AD-A054 028 ADVISORY GROUP FOR AEROSPACE RESEARCH AND DEVELOPMENT--ETC F/G 20/4
UNSTEADY AERODYNAMICS.(U)
FEB 78
UNCLASSIFIED AGARD-CP-227 NL

1 OF 7
ADA
054028

AGARD-CP-227

AGARD

ADVISORY GROUP FOR AEROSPACE RESEARCH & DEVELOPMENT

7 RUE ANCELLE 92200 NEUILLY SUR SEINE FRANCE

AGARD CONFERENCE PROCEEDINGS No. 227

Unsteady Aerodynamics

NORTH ATLANTIC TREATY ORGANIZATION

DISTRIBUTION AND AVAILABILITY
ON BACK COVER

(1) (14) AGARD-CP-227

NORTH ATLANTIC TREATY ORGANIZATION

ADVISORY GROUP FOR AEROSPACE RESEARCH AND DEVELOPMENT

(ORGANISATION DU TRAITE DE L'ATLANTIQUE NORD)

AGARD Conference Proceedings No.227

(6) UNSTEADY AERODYNAMICS.

(9) Conference proceedings.

(11) Feb 78

(12) 613p.

Papers presented at the Fluid Dynamics Panel Symposium held at the Government Conference Centre, Ottawa, Canada, 26–28 September, 1977.

400 043

JOB

THE MISSION OF AGARD

The mission of AGARD is to bring together the leading personalities of the NATO nations in the fields of science and technology relating to aerospace for the following purposes:

- Exchanging of scientific and technical information;
- Continuously stimulating advances in the aerospace sciences relevant to strengthening the common defence posture;
- Improving the co-operation among member nations in aerospace research and development;
- Providing scientific and technical advice and assistance to the North Atlantic Military Committee in the field of aerospace research and development;
- Rendering scientific and technical assistance, as requested, to other NATO bodies and to member nations in connection with research and development problems in the aerospace field;
- Providing assistance to member nations for the purpose of increasing their scientific and technical potential;
- Recommending effective ways for the member nations to use their research and development capabilities for the common benefit of the NATO community.

The highest authority within AGARD is the National Delegates Board consisting of officially appointed senior representatives from each member nation. The mission of AGARD is carried out through the Panels which are composed of experts appointed by the National Delegates, the Consultant and Exchange Program and the Aerospace Applications Studies Program. The results of AGARD work are reported to the member nations and the NATO Authorities through the AGARD series of publications of which this is one.

Participation in AGARD activities is by invitation only and is normally limited to citizens of the NATO nations.

Published February 1978

ISBN 92-835-0212-4

Printed by Technical Editing and Reproduction Ltd
Harford House, 7–9 Charlotte St, London, W1P 1HD

AGARD FLUID DYNAMICS PANEL

CHAIRMAN: Mr J.P.Hartzuiker
NLR, Anthony Fokkerweg 2
Amsterdam 1017, Netherlands

DEPUTY CHAIRMAN: Mr J.L.Jones
NASA Ames Research Ctr
Moffett Field, California 94035
USA

PROGRAM COMMITTEE MEMBERS

Professor A.D.Young (Chairman)
Department of Aeronautical Engineering
Queen Mary College
Mile End Road
London E1 4NS, UK

Professor Dr Ing. C.Buongiorno
Universita degli Studi
Scuola d'Ingegneria Aerospaziale
Via Salaria
Roma, Italy

M. l'Ing. de l'Armement A.Coursimault
Section "Etudes Générales"
Service Technique de l'Aéronautique
4 *Avenue de la Porte d'Issy*
75996 Paris Armées, France

Dr Ing. H.Försching
Head of Institute of Aeroelasticity
DFVLR
Aerodynamische Versuchsanstalt
Bunsenstrasse 10
3400 Göttingen, Germany

Dr Ing. B.Laschka
Messerschmitt Bölkow-Blohm GmbH
Unternehmensbereich Flugzeuge
Postfach 80 11 60
8000 München 80 – Germany

Dr W.J. McCroskey
Ames Directorate – US Army Air
Mobility Research and Development Lab.
Moffett Field, Ca. 94035, USA

Dr K.J.Orlik-Rückemann
National Aeronautical Establishment
National Research Council
Montreal Road
Ottawa K1A 0R6, *Canada*

Professor Dr J.A.Steketee
Department of Aeronautical Engineering
Delft Technical University
Kluyverweg 1
Delft, Netherlands

MEETING COORDINATOR

Mr P. de L.Markham
National Aeronautical Establishment
Montreal Road
National Research Council
Ottawa K1A 0R6
Canada

PANEL EXECUTIVE

Mr Michael C.Fischer

CONTENTS

SESSION I – UNSTEADY SUBSONIC AND SUPERSONIC FLOW

SESSION II – UNSTEADY TRANSONIC FLOW

---

* Not available at time of printing – see note at appropriate place in book.

SESSION III – UNSTEADY NON-SEPARATED AND SEPARATED BOUNDARY LAYERS

SESSION IV – VISCOUS – INVISCID INTERACTIONS, DYNAMIC STALL

UNSTEADY SUBSONIC AND SUPERSONIC INVISCID FLOW *

by
Holt Ashley
Department of Aeronautics & Astronautics
Stanford University
Stanford, Ca. 94305
USA

SUMMARY

Paper opens with a discussion of circumstances under which the neglect of viscosity still yields useful results in the analysis of time-dependent airflows external to shapes of aeronautical interest. The corresponding physical laws are reduced to a single differential equation, which governs the velocity potential. Determinate mathematical problem statements are summarized, capable of predicting aerodynamic loads to first-or second-order in small disturbances superimposed upon a uniform airstream. Arbitrary small motions are emphasized.

Within this framework, important methods of solution are summarized, along with some results of recent research and needs for the future. From fully linearized potential theory, information is reviewed on isolated lifting surfaces, slender bodies and interfering configurations in flight below and above the ambient speed of sound. The sonic limit of linearized theory is assessed. The findings of AGARD's comparative studies on selected wing planforms and on interfering systems are recalled.

A briefer discussion is presented on the progress and promise of second-order approximations, such as local linearization and numerical solution of the field differential equations. Finally speculations are offered about the increasing significance of numerical fluid dynamics as a practical approach to unsteady flow phenomena.

I. INTRODUCTION

In order to remain consistent with the apparent purposes of this session, I shall generally confine myself to discussing the time-dependent external flow of perfect gas produced by the motion of one or more submerged objects. Furthermore, I shall emphasize circumstances where analysis is facilitated because the direct effects of viscosity and heat conductivity can be neglected. Attention is therefore focussed on "streamlined" configurations with relatively small surface slopes and angles of attack relative to their direction of mean motion; blunted noses and leading edges are, of course, often acceptable. As has frequently been remarked, one of the miracles of Twentieth Century fluid dynamics is that we have learned when and how to account quite effectively for viscosity and even (unseparated) turbulence without necessarily including these phenomena in the equations of motion.

With certain exceptions, I also rule out the presence of strong, curved shocks and other mechanisms which might release distributed vorticity into fluid which was initially irrotational. Thus I accept the exclusion of fully hypersonic flows. Later, however, I hope to convince the audience that it is arbitrary and indefensible to eliminate any reference to "transonic" from a session concerned with Mach Numbers M_∞ both below and above unity. In passing I mention that, within the framework of linearized theory, there is a well-known equivalence between airloads caused by steady flight through a disturbed medium (e.g., atmospheric turbulence) and by analogous deformations of the same body flying in still air. A subject which deserves more study is whether such analogies can be preserved when the flow disturbances are not necessarily small.

Although my invitation solicited a review paper, I suggest that a really comprehensive summary of recent developments in our field would be presumptuous, superfluous, and practically impossible. The number of specialist conferences, survey papers, meeting sessions and round-table discussions devoted to unsteady fluid mechanics during the past few years is almost intimidating. AGARD's contribution has, by itself, been quite impressive. Among their surveys, one can cite Volumes II and VI of the Manual on Aeroelasticity (Mazet, 1968) with particular notice of the supplements by Woodcock (1971) and Rodden (1976a), as well as Rodden (1976b) and the activities of three Panels [Many authors (1975a), McCroskey (1975), Many authors (1977), and the present proceedings]. Outside of AGARD's purview and just in the U.S., there have been portions of at least two contemporary NASA Conferences [Many authors (1967a), Many authors (1975b)], the Tucson meeting (Kinney, 1975), the 13th von Kármán Lecture (Garrick, 1976), McCroskey (1976) and others. Finally, sessions at each AIAA Structures, Structural Dynamics and Materials Conference summarize selected developments in unsteady flow, not to speak of the 1977 Dynamics Specialist Conference, from which several papers receive comments in what follows. Additional sources of review information could be recalled, yet surely there are also some of which I am not aware.

---

* Preparation of this paper was supported in part by the Air Force Office of Scientific Research under Contract AFOSR 74-2712.

Let me add that a particularly welcome development is that much of this effort goes beyond the limitations to small perturbations and irrotationality, which dominated the first four decades of unsteady flow theory. We now observe serious and sophisticated attention being paid to both the measurement and analysis of time-dependent boundary layers, intermittent separation, helicopter rotors in forward flight, and nonlinear phenomena in rotating machinery.

Faced with this renaissance in research — and the evaluation of research — I have no choice but to be selective and nearly idiosyncratic in my choice of citations. If important work is omitted, its oversight could well be unintentional. I must offer the customary apology with regard to any contribution more deserving of notice than its counterparts in my reference list.

Several other papers on the present program relieve me of other responsibilities; they need not all be referenced here. Important examples are the subjects of internal flows, rotating machinery and helicopter rotor aerodynamics. Relative to propulsion systems and turbomachinery, I do wish to call attention to portions of a special issue of Journal of Aircraft (Walker, 1975), to the IUTAM Symposium (Many authors, 1976b), and to the interesting survey of aeroelasticity by Fleeter (1977).

II. FORMULATION OF THE PHYSICAL LAWS

I begin my review by recalling several ways in which the physics of unsteady flow can be embodied in differential equations and boundary conditions. This is familiar ground, but I am thus able to emphasize both the abundance of dependent variables that are available for this purpose *and the hierarchy of approximations* wherefrom the interested mathematician or computer scientist may select.

Figure 1 illustrates the typical situation with which I am concerned. External to boundary layers and wakes produced by this vehicle's translation and rotation, the fluid motion is described by a vector field of the particle velocity $\vec{Q}$, whose Cartesian components can be defined as

$$\vec{Q} = u\vec{i} + v\vec{j} + w\vec{k} \tag{1}$$

there are also coupled scalar fields of properties like static pressure p and density ρ. These quantities are, of course, governed by the principles of mass conservation, momentum conservation and thermodynamics. If one assumes a thermally and calorically perfect gas with constant specific-heat ratio γ, these principles can be expressed (e.g., Ballhaus, 1976) as a first-order matrix differential equation — a form which has proved convenient for numerical computation:

$$\frac{\partial U}{\partial t} + \frac{\partial F}{\partial x} + \frac{\partial G}{\partial y} + \frac{\partial H}{\partial z} = 0 \tag{2}$$

Here x,y,z constitute any inertial and rectangular coordinate system, and t is time.

The four column matrices or 5-vectors in (2) may be written

$$U = \begin{Bmatrix} \rho \\ \rho u \\ \rho v \\ \rho w \\ e \end{Bmatrix}, \quad F = \begin{Bmatrix} \rho u \\ \rho u^2 + p \\ \rho uv \\ \rho uw \\ u(e+p) \end{Bmatrix}, \quad G = \begin{Bmatrix} \rho v \\ \rho vu \\ \rho v^2 + p \\ \rho vw \\ v(e+p) \end{Bmatrix}, \quad H = \begin{Bmatrix} \rho w \\ \rho wu \\ \rho wv \\ \rho w^2 + p \\ w(e+p) \end{Bmatrix} \tag{3a,b,c,d}$$

The extra unknown in (2) - (3) is a "total energy per unit volume" e. For steady or unsteady motions, it is connected with the others by an algebraic "equation of state"

$$p = (\gamma - 1)\left[e - \frac{\rho}{2}(u^2 + v^2 + w^2)\right] \tag{4}$$

The full complement of boundary conditions will be discussed later. I recall here, however, that shock discontinuities can occur when locally $Q = |\vec{Q}|$ is supersonic, i.e., when the local Mach number

$$M \equiv \frac{Q}{a} = Q\left(\frac{\gamma p}{\rho}\right)^{-\frac{1}{2}} \tag{5}$$

exceeds unity. In the past shocks were usually treated as boundaries for subdivided fields of the flow, across which the Rankine-Hugoniot jump conditions were enforced. An interesting discovery* of modern computational fluid dynamics is that suitable discretizations of (2) - (4), or of certain potential equations listed below, are able to "capture" the approximate locations and strengths of shocks as an intrinsic part of the numerical solution.

Under familiar circumstances frequently encountered in aeronautical applications, the flow is nearly irrotational, the curl of $\vec{Q}$ may be assumed to vanish everywhere, and a scalar potential Φ exists such that

$$\vec{Q} = \nabla \Phi \tag{6}$$

These same circumstances imply constant entropy and a simple, universal relation between p and ρ. The mass and momentum principles can then be manipulated (cf. Sect. 1-7 of Ashley & Landahl, 1965) to yield a single differential equation

$$\nabla^2 \Phi = \frac{1}{a^2} \left\{ \frac{\partial^2 \Phi}{\partial t^2} + \frac{\partial}{\partial t} [\nabla\Phi \cdot \nabla\Phi] + \nabla \Phi \cdot \nabla \left[\frac{\nabla \Phi \cdot \nabla \Phi}{2} \right] \right\} \tag{7}$$

Also required is a formula for sound speed a. For example, if conditions remote from the body are uniform with $a = a_\infty$ and particle speed U_∞, I can write it

$$a^2 = a_\infty^2 - (\gamma - 1) \left\{ \frac{\partial \Phi}{\partial t} + \frac{Q^2 - U_\infty^2}{2} \right\} \tag{8}$$

(Body forces are neglected.) For calculating aerodynamic loads under these conditions, one needs an expression for p; the familiar dimensionless Bernoulli-Kelvin equation is

$$C_p \equiv \frac{p - p_\infty}{\frac{1}{2} \rho_\infty U_\infty^2} = \frac{2}{\gamma M_\infty^2} \left\{ \left[1 - \frac{\gamma - 1}{a_\infty^2} \left(\frac{\partial \Phi}{\partial t} + \frac{Q^2 - U_\infty^2}{2} \right) \right]^{\frac{\gamma}{\gamma - 1}} - 1 \right\} \tag{9}$$

I can state the kinematic boundary condition that goes with (7) in a situation like Fig. 1 "exactly" as (cf. Sect. F,3 of Garrick, 1957)

$$\frac{DS}{Dt} = 0 , \tag{10}$$

to be enforced at the surface $S(x,y,z,t) = 0$ of each impermeable body.

$$\frac{D}{Dt} \equiv \frac{\partial}{\partial t} + \vec{Q} \cdot \nabla = \frac{\partial}{\partial t} + \nabla \Phi \cdot \nabla \tag{11}$$

is the "substantial derivative." Equation (10) is essentially a specification of the particle velocity component v_n normal to S. For slender wings and bodies, respectively, (10) is usually rearranged so as to prescribe explicitly the Z-component w and the radial component v_r (polar coordinates centered in the axisymmetric body).

Garrick (1957) mentions four other classes of boundary conditions:

- Edge conditions, typically Kutta's requirement for smooth flow or nonsingular pressure at a sharp trailing edge.
- Wake conditions, which call for free vortices shed from trailing edges to follow the fluid motion and to obey the Helmholtz theorems. Wakes show up in small-disturbance theory as characteristic surfaces, across which Φ is discontinuous but p and v_n have zero jumps.
- Conditions at infinity, where properties uniformly approach their $(\cdots)_\infty$ values and wave trains propagate away from their sources.
- Other conditions, such as jumps at shocks and prescribed zones of influence or silence in supersonic flows.

As I proceed through the hierarchy of approximations that have been made to (7) - (9) and their auxiliary formulas, it is useful for present purposes to stick with the case of steady mean flight when U_∞ is parallel to the x-direction. Almost universally, one then replaces Φ with the disturbance potential ϕ, defined by

$$\Phi = U_\infty x + \phi (x,y,z,t) \tag{12}$$

---

*See, for instance, Sect. 2.4 of Ballhaus (1976) and references given therein, where the subject is discussed in the context of small-disturbance transonic flow. I recognize, incidentally, that propagating shocks may also appear in unsteady flows under locally subsonic conditions, but they are not important for the topics of this survey.

or the equivalent. I mention, however, that the literature contains several studies of accelerated or sinuous flight. A notable example is the extensive work of Wu and his colleagues (e.g., Wu, 1971, Chopra 1977), wherein 2-D, and more recently 3-D, incompressible theory is extended to problems connected with locomotion of fish and birds. The proper reference frame for quantifying physical laws in these cases seems to me to be one attached to the fluid at rest.

I see no profit in writing out the components of (7) or the corresponding complete equation for ϕ. Perhaps more interesting is the way it reduces when cubes of small disturbances are neglected*:

$$\nabla^2\phi - M_\infty^2\left(\frac{\partial}{\partial x}+\frac{1}{U_\infty}\frac{\partial}{\partial t}\right)^2\phi = M_\infty^2\left(\frac{\gamma-1}{U_\infty}\right)\left[\phi_x+\frac{1}{U_\infty}\phi_t\right]\nabla^2\phi$$
$$+\frac{M_\infty^2}{U_\infty}\left[\frac{\partial}{\partial x}+\frac{1}{U_\infty}\frac{\partial}{\partial t}\right]\left[\phi_x^2+\phi_y^2+\phi_z^2\right] \qquad (13)$$

(Subscript notation is used for partial derivatives when convenient.) There are in the literature a few instances where (13) has been usefully solved in 2-D unsteady flow. A notable case is Van Dyke (1954) for the supersonic oscillating airfoil. Landahl (1957) carried out an expansion in M_∞^{-2} and calculated the influence of airfoil thickness on unsteady lifting loads; he made the common assumption that thickness ratio ε is large compared to excursions in the angle of attack α.

Under the full-blown small-disturbance approximation, one usually finds (13) reduced to

$$(1-M_\infty^2)\,\phi_{xx}+\phi_{yy}+\phi_{zz}-\frac{2M_\infty^2}{U_\infty}\phi_{xt}-\frac{M_\infty^2}{U_\infty^2}\phi_{tt}=0 \qquad (14)$$

The physics here are precisely the same as in acoustic wave theory for a uniform medium.

When M_∞ is close to unity, however, it is now well known that other versions of (13) must be employed; an excellent treatment of the various forms and corresponding ranges of the governing parameters is given in Chapter 1 of Landahl (1961). Choose k to represent some dimensionless measure of flow "unsteadiness," such as reduced frequency based on semi-chord. *Then to make a long story perhaps too short, when* k *and* $|1-M_\infty|$ are of the same order of magnitude for motion of an airfoil or large-aspect-ratio wing the following form applies:

$$\left[1-M_\infty^2-\frac{M_\infty^2}{U_\infty}(\gamma+1)\,\phi_x\right]\phi_{xx}+\phi_{yy}+\phi_{zz}-\frac{2M_\infty^2}{U_\infty}\phi_{xt}-\frac{M_\infty^2}{U_\infty^2}\phi_{tt}=0 \qquad (15)$$

On the other hand, in highly unsteady flow over wings, when everywhere

$$k \gg |1-M_{LOCAL}|\,, \qquad (16)$$

one should use the fully linearized transonic version

$$\phi_{yy}+\phi_{zz}-\frac{2M_\infty^2}{U_\infty}\phi_{xt}-\frac{M_\infty^2}{U_\infty^2}\phi_{tt}=0 \qquad (17)$$

In general, the approximation to pressure equation (9) which, for wings, is consistent with (14), (15) or (17) reads

$$C_p = -2\left(\frac{1}{U_\infty}\frac{\partial}{\partial x}+\frac{1}{U_\infty^2}\frac{\partial}{\partial t}\right)\phi \qquad (18)$$

For bodies of revolution and the like, however, ϕ_x/U_∞ is found to be $O(\varepsilon^2|\ln\varepsilon|)$, whereas ϕ_y/U_∞ and ϕ_z/U_∞ remain $O(\varepsilon)$. *Then the nonlinear terms*

$$-\frac{1}{U_\infty^2}(\phi_y^2+\phi_z^2)$$

should be added to (18).

I believe more study should be devoted to the suggestion that solutions of (13) or of the small-disturbance equations be inserted back into the "exact" (9) when airloads are being calculated. Although mathematically inconsistent, some such scheme might be combined

---

* In the presence of steady or nearly steady shocks, (13) is consistent with the assumption of isentropy. For further discussion of shocks and potential flow, see Jameson (1976) among other references.

with partially nonlinear kinematic boundary conditions (e.g., see Appendix C of Rowe, Redman and Ehlers, 1975). Especially in subsonic and lower supersonic flows, I suspect that the linearity of the field differential equation may be the least restrictive part of the reduced problem statement, and the suggested steps might "nonlinearize" two other principal parts of this statement without a severe computational penalty.

Linearized versions of the boundary condition (10) will be skipped at this stage. I remark that a condition on $v_n \equiv \phi_z(x,y,t)$, which is consistent for wings with the second-order (13), can be constructed by Taylor expansion in z (cf. Landahl, 1957).

Another neglected tool of nonlinear irrotational flow theory is Prandtl's acceleration potential

$$\Psi \equiv -\int_{p_\infty}^{p} \frac{dp}{\rho} \tag{19}$$

This scalar function of position and time is inherently a disturbance quantity. Its name comes from the formula for particle acceleration,

$$\frac{D\vec{Q}}{Dt} = \nabla\Psi\ , \tag{20}$$

which one readily deduces from Euler's equations of motion when $p = p(\rho)$. Garrick (1957, pp. 663-4) discusses Ψ but gives no "exact" differential equation. My own investigation has not yielded a convenient single equation, but the following coupled relations between Φ and Ψ embody the same physics as (7):

$$\frac{D\Psi}{Dt} = [a_\infty^2 - (\gamma-1)\Psi]\,\nabla^2\Phi \tag{21a}$$

$$\nabla^2\Psi = \frac{\partial}{\partial t}(\nabla^2\Phi) + \tfrac{1}{2}\nabla^2(\nabla\Phi\cdot\nabla\Phi) \tag{21b}$$

The sound speed is connected to Ψ by the simple formula

$$a^2 = a_\infty^2 - (\gamma-1)\Psi \tag{22}$$

Also for the constant $-\gamma$ isentropic case, I derive the convenient Bernoulli equation

$$\frac{p}{p_\infty} = \left[1 - \frac{\gamma-1}{a_\infty^2}\Psi\right]^{\frac{\gamma}{\gamma-1}}\ , \tag{23a}$$

whence

$$C_p = \frac{2}{\gamma M_\infty^2}\left\{\left[1 - \frac{\gamma-1}{a_\infty^2}\Psi\right]^{\frac{\gamma}{\gamma-1}} - 1\right\} \tag{23b}$$

The kinematic boundary condition which governs Ψ at $S = 0$ specifies the normal acceleration in a not-so-attractive form:

$$\nabla S\cdot\nabla\Psi = -\left\{\frac{\partial^2 S}{\partial t^2} + 2\vec{Q}\cdot\frac{\partial\nabla S}{\partial t} + \vec{Q}\cdot\left[\vec{Q}\cdot\nabla(\nabla S)\right]\right\} \tag{24}$$

Other boundary conditions may be easier to deal with, in that they require Ψ not only to die out at infinity but to be continuous everywhere in the external flow except at shock surfaces.

Let me propose that the system (21) might offer a worthy topic of research in the field of computational fluid dynamics — perhaps as a vehicle for large-disturbance subsonic flow prediction. The second-order reductions of (21) and (24) might have some analytical interest. Finally, I recall the linearized version

$$\Psi \cong \frac{p_\infty - p}{\rho_\infty}\ , \tag{25}$$

which has already proved so useful as an alternative to ϕ in the treatment of thin lifting wings. It is an easy matter to eliminate the nonlinearities between (21a) and (21b), thus verifying the well-known result that the perturbation pressure is also governed by (14).

Within a fully linear framework, I remind that Landahl & Stark (1968) furnish the reader with informative comparisons among the numerous ways in which the foregoing tools may be adapted to deal with a single class of unsteady flows. They concentrate on thin lifting wings (or systems of planar wings) in subsonic or supersonic flight, reviewing for sinusoidal motions almost every known alternative problem statement and scheme of solution. Woodcock (1971) furnishes a similar morphology, in the context of AGARD's comparative study of planar surfaces.

III. RECENT PROGRESS ON LINEAR THEORY

I begin this discussion with the observation that the bulk of work on both subsonic and supersonic flows, where Eq. (14) with ϕ or Ψ as dependent variable is the usual starting point, involves the assumption of steady-state simple harmonic motion. Thus every entry in the tables of Woodcock (1971) is for a particular value of * $k = \omega s/U_\infty$. For flutter prediction, aerodynamic transient analysis, control system design and several other purposes it would be convenient to have solutions directly incorporating arbitrary time dependence. Inasmuch as I believe the appeal to "Fourier's theorem" is not entirely satisfactory, I plan to describe below a promising new approach due to Edwards (1977).

Irrespective of this time dependence, the linear approximation artifically gives rise to a bewildering variety of singular behaviors in the load distribution on thin lifting surfaces. Although this phenomenon received occasional systematic discussion in the literature (cf. Landahl (1968) and Ashley (1971), only the more significant subset of these singularities (e.g., the subsonic leading-edge infinity, control leading-edge logarithm, infinite slopes at sides and subsonic trailing edges) are carefully accounted for in any existing theories. Others have been avoided by such strategems as rounding off the pointed vertex at the centerline of a symmetrical swept wing (see Sect. 1.5 of Woodcock, 1971). Actually there are at least four other situations similar to this vertex. All five are identified by Roman numerals in Fig. 2, taken from the recent dissertation by Medan (1976). Therein he reviews the local mathematical treatment of each corner, providing new corrected solutions for the vicinity of IV and V. Because their influence is limited to "exponentially small" regions, I would recommend against further attempts to incorporate them into present kernel function methods — there are more profitable occupations for the mathematical aerodynamicist. Moreover, finite element methods like the doublet lattice and supersonic box schemes tend to deal cavalierly with all the singularities, yet they are often successful for practical airload predictions.

3.1 Almost Planar Wings

In my opinion, the AGARD study published by Woodcock (1971) demonstrated that subsonic and supersonic theory for lifting surfaces has matured. Even to quite high reduced frequencies for complex deformation modes of very general 3-D planforms, the best mechanizations of this theory may be used confidently in practical applications. Because they approximate the true upwash distributions with sets of smooth and continuous functions, at $M_\infty < 1$ my preference is for the so-called kernel function methods. Among the best examples are the work of Laschka (1963), Davies (1976), Rowe and collaborators (1975,1976) but several others might equally well have been cited.

It is instructive to study the many tables of generalized aerodynamic forces, for the five AGARD planforms, contained in Woodcock (1971). In those cases where several independent calculations are set side by side — and when one selects what appears to be the best-converged result from any given method — my conclusion is that the entries generally differ by no more than a few per cent. In the most favorable cases (e.g., the larger generalized forces at low k on the $M_\infty = 0$ circular Wing #1) the disagreements average less than one per cent. In order to illustrate a procedure I have found useful for evaluating some of these results, Figs. 3,4 and 5 take three of the wings in compressible flow and plot the lift force due to pitching oscillation

$$Q_{12} = Q'_{12} + i Q''_{12} \tag{26}$$

vs. reduced frequency in such a way that the high-k piston theory limit is readily included. Details of the chosen examples are given in the captions. Except for my own $k \to \infty$ computations, only tabulated numbers are shown without any attempt to pass curves through them. But my experience with plotting vs. k at fixed M_∞ suggests that such curves should be

---

*Here ω is circular frequency and s is the wing semispan, picked as a reference length. Universally one uses the complex form; e.g.,

$$\phi(x,y,z,t) = \mathrm{Re}\left\{\phi(x,y,z)\, e^{i\omega t}\right\}$$

quite smooth, even through $k = 1$ where the abscissa undergoes an inversion. Recognizing that piston theory constitutes a limit that should be approached uniformly, I see nothing in these graphs and others like them to shake my confidence. There is, of course, a familiar difficulty with linearized theory as $k \to 0$ at $M_\infty = 1$ which is apparent in Fig. 4. Moreover, one might be a little concerned about the quantitative precision of the real part of Q_{12} at $k = 4$ in the supersonic example (Fig. 5).

When studying controls (as well as complete wings), I believe it important to distinguish the question of whether linearized theoretical solutions are well-converged from the more difficult issue of comparisons with measured data. For aerodynamically-unbalanced flaps with essentially sealed gaps, the best computer programs seem to have achieved convergence. Rowe et al. (1975) not only give thorough attention to the former issue but also provide a rich collection of theory vs. experimental plots — steady and oscillatory, generalized forces and chordwise pressure distributions. The three examples chosen for reproduction as Figs. 6,7, & 8 all relate to low M_∞ (see captions for details & data sources), but high subsonic M_∞ is also covered. They and other comparisons like them seem accurate enough to suggest that future research directions should now be aimed at breaking out of the constraints imposed by the small-disturbance, inviscid approximation in parameter ranges where it is not acceptable.

Because of my preference for smooth upwash and loading functions, I shall say little about finite-element (e.g., doublet lattice) methods for subsonic flow. In fairness, it seems that the work of Albano and Rodden (1969) arrived too late for an adequate evaluation in the AGARD planar wing "competition." For interfering surfaces, their and similar procedures have proved quite successful and seem often to have an edge over the kernel function in computer time required to yield given results. On the other hand, there are still indications of convergence difficulty at the higher k's [see, for instance, some of the results on Figs. 18 and 19 of Pollock and Huttsell (1974) and Fig. 9 of Woodcock (1971)]. I am also influenced by the quotation relative to Dutch experience from Roos and Zwaan (1972), "for the cases which were calculated at the NLR with both the doublet-lattice method and the kernel method the calculation times ... were of the same order."

At supersonic speeds finite-element or box methods* seem generally less objectionable, because the associated upwash distributions, although discontinuous, avoid infinite behavior. It is, nevertheless, refreshing to see progress (e.g., Cunningham, 1974) toward efficient mechanization of the kernel function approach for $M_\infty > 1$. Among the box methods, which generate direct matrices of "aerodynamic influence coefficients," I should mention the introduction by Appa and Smith (1972 and 1973, among many references) of the arbitrary triangular area element. Not only does this bypass the familiar difficulties with representing swept leading and trailing edges, but it harmonizes better than other element shapes with computational techniques used for describing structural deformation.

Among other recent contributions to the discrete solution of oscillatory supersonic lifting surface loadings, the following certainly merit reference: Giesing and Kalman (1975); Jones and Appa (1977), who adopt the chordwise derivative of ϕ as their unknown; Young (1976) and Haviland and Yoo (1976).

Relative to the subject of planar wings, current activity is so diversified and rich that I find it necessary to close this section with an almost random list of citations:

- Work of the Princeton group (e.g., Williams et al., 1977) on wings in parallel shear flows.
- Contributions by Amiet (1975, 1976) to low- and high-frequency approximations to the loading on 2-D airfoils oscillating in subsonic flow.
- Cheng's (1975) use of matched expansions to generalize lifting-line theory for the unsteady case.
- An interesting attempt (Ušv, 1975) at extending Woodward's scheme to the oscillating wing.
- The new "piecewise continuous" kernel-function approach proposed by Nissim and Lottati (1977).
- Several recent contributions by Jordan, notably his better approximation (1976) for the subsonic kernel function and his efforts (1978) to improve the reliability of generalized forces and unsteady gust loads for 3-D wings in incompressible flow.
- The publication of more, and more accurate, wind tunnel measurements to serve as standards of reference for all theory. I find the low-speed data for wings of intermediate aspect ratio, reported by Patel at this Symposium, of particular interest. In addition to verifying the theory quite satisfactorily, a unique attempt is made to justify the principle of superposition upon which all such analysis depends.

3.2 The Specialization of Linearized Wing Theory to $M_\infty = 1$

In my view, an organic feature of the theories discussed in Sect. 3.1 is their limiting transonic behavior as $M_\infty \to 1$ from below or above. The resulting linear approximation, governed at $M_\infty = 1$ by (17), has of course been discussed and extensively applied by Landahl (1961). It embodies a similarity law (Landahl, 1961, sect. 1.8) which, at the least, furnishes the slope near $M_\infty = 1$ for plots of generalized force, etc., vs. M_∞ at fixed k.

---

*For the current best version of the durable Mach box scheme see Chipman (1976).

Perhaps greater effort should be devoted to mapping out for 3-D wings the boundaries of its practical utility as a flutter- prediction tool and the like. The limitation implied by (16) may well be too severe at moderate reduced frequencies when the aspect ratio is not very large. From the comparisons in his Figs. 1.7 and 1.8, Landahl makes clear that wings with highly-swept leading edges are much more susceptible of linearized treatment than is, for example, a rectangular planform.

A quantitative way of determining accuracy is by comparison with more rigorous theories, although this approach tends to be confined to 2-D flow where the best standards of reference exist. One good example is the work of Stahara and Spreiter (1973), from which Fig. 9 is reproduced. Their nonlinear method uses local linearization to apply a thickness correction to the unsteady airloads. For the 6%-thick biconvex profile, oscillating in pitch about a leading-edge axis, the magnitude and phase of the lifting chordwise pressure distribution are plotted for several values of $k \equiv \omega c/2U_\infty$ and compared, on the right, with wholly linear results. The authors conclude satisfactory agreement for the magnitude at $k \geq 0.5$ and for the phase at $k \geq 1.0$. Since this 2-D case offers the severest test, I feel that the simpler theory can be used with confidence at considerably lower k on many 3-D wings encountered in practice.

Dangerous failures of pure linearization will be encountered, however, whenever shocks of significant strength exist somewhere along the chord and are forced to move and change strength significantly by the motion. A dramatic instance of such failure is provided by the transonic flutter study recently reported by Farmer and Hanson (1976). Two flexible wings, with 44° leading-edge sweep, identical planforms and similar elastic & inertial properties, were tested up to neutral stability by increasing operating pressures at eleven Mach numbers ($0.6 \leq M < 1.1$) in the Transonic Dynamics Tunnel, NASA Langley Research Center. The profile sections had equal thickness ratios but differed in that one was "conventional" whereas the other was a supercritical airfoil shape, which weakens the upper surface shock and drives it aft. Up to $M_\infty = 0.85$, kernel function predictions matched both sets of flutter dynamic pressures and frequencies quite well. Figure 14 of Farmer and Hanson (copied as Fig. 10 here) shows what happened to the two boundaries in the transonic range, after the data were adjusted to account for minor differences between the model stiffnesses. The separation between these curves must be attributed entirely to aerodynamic nonlinearity, and it is especially noteworthy because flutter speed is often rather insensitive to small changes in most terms of the generalized-force matrix. The reduced frequency (based on mean aerodynamic chord) is estimated around 0.17 at the sonic flutter point — a value which is clearly too low for one to expect satisfactory precision from complete linearization.

3.3 Some Comments on Slender Bodies

For pointed, streamlined shapes both of whose characteristic dimensions normal to the flight direction are small fractions of the length, we have tended to rely heavily on generalizing the classical slender-body approximation (e.g., Ward, 1955). Various deficiencies of this convenient idealization have been pointed out, far too often for them to be summarized here. Among the corresponding theoretical improvements, expansion in powers of the thickness ratio, local linearization, and solutions of (14) with boundary conditions at the mean body surface (rather than in the limit $r \to 0$) are typical of the methods employed. Surprisingly, I do not believe the best of these to be always the ones most recently published. Moreover, the majority are restricted to axisymmetric configurations, leaving low-aspect-ratio wing-fuselage combinations, elliptic cross sections, etc. to be analyzed classically. There is one safe generalization: because disturbances tend to be "doubly small," differential equation (14) governs the near and intermediate fields throughout the M_∞ range below hypersonic — the only exception being an axisymmetric part of the flow near $M_\infty = 1$.

Subsonically the most serious attempt to deal with oscillating bodies of revolution in the United States remains that of Revell (1969). My judgment is reinforced by the fact that it is still used as a standard of comparison for simplified theories, e.g., the low-k expansion by Liu, Platzer and Ruo (1976). It is also very difficult for computational purposes, and many steps in the analysis must be repeated separately for each radius distribution $R(x)$.

Among recent refinements to slender-body theory appropriate for the transonic range, I mention the low-frequency work of Stahara and Spreiter (1976), as well as Liu, Platzer and Ruo (1977). The former brings thickness effects into the nonlinear term of (15) by means of local linearization. The latter adopts the "parabolic approximation" of replacing ϕ_x by a constant average value. When making numerical computations the authors also resort to a low-k expansion, but they succeed in treating zero-thickness wings in addition to axisymmetric shapes.

Revell (1960) published a comparable second-order investigation of supersonic bodies, again expanding in thickness ratio and carefully treating the logarithmic terms that arise. Quite a different slant on the supersonic problem, with emphasis on discontinuous body slope, was taken by Kacprzynski and Landahl (1967, plus internal M.I.T. reports referenced therein). These are refinements to the theory of steady flow over "quasi cylindrical" bodies, studied during World War II by Lighthill. Special care must be used in dealing with the pointed nose of such a body. These papers make some ingenious proposals for the nonlinear calculation of pressures and for introducing entropy changes through bow shocks, however, and their approach is worthy of more attention than received to date.

Finally, I remark that "facet methods" being developed to solve wing-body unsteady interference problems can equally well be adapted to bodies alone. The interesting paper by Woodcock (1976) does this for quite general fuselage shapes in supersonic flight and gives an application to a rather complicated configuration at $M_\infty = 1.225$.

3.4 Interference

Substantial mathematical and computational effort has been dedicated during the past decade toward extending linearized subsonic and supersonic theories so that they may be applied to the interfering combinations of bodies and lifting surfaces encountered in aeronautical practice. The AGARD study (Rodden, 1976a) deals with pairs of lifting surfaces, some of which intersect but always in the absence of fuselages, nacelles, etc. Indeed, the effects of bodies has received relatively little attention to date [cf. Roos et al. (1977), Kalman et al. (1971), and Morino (1974)], and they will therefore be omitted from consideration here. Fortunately, past experience suggests that their usual influence on problems like flutter comes mainly from their inertial or elastic properties rather than from large changes in the airloads.

My personal view is that the AGARD work should be brought up to date and expanded to include both additional contributors, more values of k and further interfering configurations. It is not "definitive" in the sense that Woodcock (1971) succeeds in being. Let me offer several reasons for this opinion. First of all, publications have recently appeared which give calculations for the AGARD and similar configurations that were not included in Report 643. Instances known to me are in Tseng and Morino (1976), Appa and Jones (1976), Cunningham (1974b), Haviland and Yoo (1976), and Stark (1974). The first three of these sources contain data that could be added directly to the existing tables, and I suspect that other similar results exist today.

I also conclude that many of the comparisons among the AGARD calculations leave something to be desired and perhaps do not justify the comments about "excellent agreement" made in Sec. 7 of Rodden (1976a). Let me try to illustrate this point with what I believe to be some fairly-chosen examples. My numbers are not picked from the airloads that are so "small" as to be excessively sensitive to difference errors, but they do have the property of being truly "interference" loads. That is to say, it does not make sense to use a generalized force induced by a wing's motion upon itself (say, in a wing-horizontal-tail calculation) when judging the accuracy of these methods.

Figure 11 reproduces Fig. 17 of Rodden (1976a), showing for $M_\infty = 0.8$ and a semispan reduced frequency of 1.5 the real and imaginary parts of wing and tail pitching moments induced by an antisymmetric elastic oscillation of the familiar "AGARD wing." Five theories are compared, from sources listed in the reference and describable as subsonic kernel-function or doublet-lattice methods. It is my opinion that the tail pitching moments here, especially the imaginary parts, do not agree to within an accuracy that would be acceptable for flutter or dynamic load predictions. Other similar cases could be cited, both subsonic and supersonic, from the figures and tables of Rodden (1976a).

In order to assess the generalized aerodynamic forces tabulated in the reference, I have found it useful to make polar plots. Figures]2 and]3 are not untypical. They relate respectively, to subsonic ($M_\infty = 0.8$) and supersonic ($M_\infty = 3.0$) tail rolling moments produced by wing bending vibration at $k = 1.5$ for the same arrangement as in Fig. 11, except that the tail is displaced upward from the wing plane by a distance 0.6 wing semispans. This case was chosen so as to permit the addition of results from Tseng and Morino (1976). The comparisons speak for themselves; some are "good," others quite unsatisfactory. Especially in the supersonic example, one is quite unable to determine in this and many other cases which theory should be regarded as the correct "standard of reference."

These remarks are not intended to denigrate the impressive work of the AGARD contributors or of others occupied with the very difficult linearized interference problem. It is certain that improvements have been made since the study was closed. It is also quite possible that $k = 1.5$ is a severe test of several theories, which may achieve much better convergence at lower reduced frequencies. There are questions as to whether systematic efforts are needed, for lifting surfaces which physically intersect, to incorporate the singular behavior along those intersection lines that was referred to in Ashley (1971) and has been addressed in a few other studies. As elaborated in Sects. V and VI below, I even have doubts as to whether bringing interference theory to the same confidence level now enjoyed by planar surface theory is a project worthy of the expert time and money it would require.

Let me finish this section by mentioning three publications on interference that surely deserve recognition. Space considerations prevent me from giving many details or from referring to several other valuable contributions, notably by European investigators. Cunningham (1971) presented an early and quite successful attempt to analyze parallel, subsonic surfaces. His emphasis was on aircraft like the F-111, and although most of his examples were for steady flow the theory seems to apply at arbitrary k.

Ichikawa and Isogai (1973a and b) published an interesting incompressible-flow formulation useful to T-tail flutter analysis. Lastly, the supersonic computer programs described by Crill and Dale (1976), which is a finite-element mechanization of the potential gradient method, appears promising.

3.5 Cascades and Wind-Tunnel Wall Effects

I am sure that several papers planned for Session V of this Symposium (e.g., Platzer, Byham & Beddoes, Fleeter) will fully address current work on unsteady motion of cascades. The recent I.U.T.A.M. Symposium (Many authors, 1976b) is another rich source of information. My purpose in mentioning the subject here is because of its relationship to the influence of parallel wind-tunnel walls on unsteady airloads. In 2-D at least, the associated boundary value problems have a great deal in common. Thus, with alternating 180° phase shifts, theories like those of Jones & Moore (1975) or Kemp & Ohashi (1976) could be adapted quite straightforwardly.

The recent measurements of Satyanarayana (1977) actually bear on both problems and furnish confidence that such foundations of isolated wing theory as the trailing-edge Kutta condition remain valid for multiple lifting surfaces in time-dependent flow.

The classical analysis of wall effect on airfoil oscillations in an incompressible stream is Timman's (1951, among other references). There is no need to detail subsequent extensions to 3-D and compressible flow. It is worth mentioning, however, that transonic steady wind-tunnel testing has quite severe limitations, based on the presence of boundaries, which have not yet been fully overcome by means of such devices as slots or perforation. There is every reason to believe that transonic oscillatory force and flutter data must also be carefully examined for similar effects — not to speak of actual "resonances."

As an instance of low-speed wall interference, let me describe some ongoing flutter research at Stanford University by Rock (1977). He is working with a 2-D "typical section," whose elastically-restrained degrees of freedom are in vertical translation and pitching; with notation similar to Theodorsen's (1935), the model properties are listed on Fig. 14. It is constructed with great attention to precision, and tests of subcritical stability and flutter are being conducted in a 0.5m. - square tunnel at speeds up to about 50 m. sec.$^{-1}$. Correlative predictions were at first based on the infinite-airstream theory of Theodorsen (1935) but proved disappointing in that the critical speed disagreed with the data by more than 10%. In view of the ratio of wind-tunnel height to chord of 2, the significance of a correction was then realized, and Timman (1951) was generalized for complex oscillation frequencies. This adjustment to the analysis resulted in the root loci, for the two aeroelastic modes, shown on Fig. 14 as solid lines in the s-plane. Comparative data are also plotted, with semidimensionless flow speed $\overline{u}$ as a parameter. The critical mode, which starts from the "bending" vibration in still air, now has its neutral stability point estimated to within 2 parts in 250 for speed and 1 part in 50 for frequency (note the zero-suppressed ordinate scale). This agreement is about as good as one ever encounters in aeroelasticity.

VI. TWO IMPORTANT NEW DEVELOPMENTS

Again let me exercise the privilege of the invited reviewer and single out two contributions to unsteady flow theory which I expect to achieve great future utility. The first is the approach to airload calculation, for rather general small motions of rather complicated configurations at $M_\infty < 1$ or > 1, that was first elaborated by Morino (1974). Among other places, sample applications for convergent, steady and divergent oscillations will be found in Tseng and Morino (1976). There is also, of course, a paper later on in this session, and it relieves me of having to give details of the SOUSSA programs.

The return by these investigators to a classical Green's function statement of the problem was inspired, not only because it reduces the order of singularities that one has to cope with in formulations of the kernel-function type, but because it quite naturally shows how influences like profile thickness and wake deformation can be incorporated while the linear field equation (14) is retained. Some programming and convergence difficulties which plagued early versions of SOUSSA seem on the way to being overcome*, and computer times have been shortened.

In fairness, I should remark that Green's function solutions applied over the actual locations of bounding surfaces have occasionally been used before; indeed, the paper by Geissler in this session appears to be such a case, with examples given for $M_\infty = 0$. Nevertheless, it is my hope that support will be provided so as to ensure broad applicability, good computational convergence and wide dissemination for what looks like a powerful design tool.

As I mentioned previously, we still have a requirement for convenient theory that handles arbitrary small motions of wings and bodies. Tseng and Morino (1976) demonstrated the potential of SOUSSA to perform this task, and practical suggestions like Richardson's (1965) have long been available. Yet I believe that a scheme for directly adopting the numerous existing computer programs now limited to simple harmonic motion, would have considerable value.** I think that Edwards (1977), building on an earlier Stanford University dissertation published as Vepa (1977), has shown us how to do this. It is their work that I have singled out for attention here.

---

*Personal communication from Professor Morino.

**It should be acknowledged that several fundamental ideas in Edwards' development were anticipated by Milne (1966).

Both authors concentrate on the s-plane, arrived at by Laplace transformation on time, and both are therefore concerned with constructing "aerodynamic transfer functions" — output-input ratios in terms of s which connect, say, a given generalized force Q_{ij} to the time variation of the generalized coordinate which produces it. Such transfer functions are not only useful for computing, by inversion, indicial time functions, but they have a direct role in the design of automatic control systems or for finding roots loci like Fig. 14. The heart of Vepa's scheme is to estimate these transfer functions in the form called Padé approximants (ratios of finite polynomials in s). The coefficients of these he calculated by fitting conventional unsteady theory at a finite number of points along the imaginary axis, where the (dimensionless) $s = ik$. In the process, he learned a great deal about the limiting behavior of various theories. His tools are appealing to control-system engineers, but they have the one disadvantage of undesirably augmenting the states of the aeroelastic systems to which they are applied.

Edwards (1977) overcame this deficiency, while preserving the full accuracy of the parent theory, by returning to the original problem statement. Using a thin wing near the x-y-coordinate plane (Fig. 1) as a model, let me recall that the kinematic boundary condition on the wing projection S may be written

$$\phi_z(x,y,0,t) = U_\infty \frac{\partial Z}{\partial x} + \frac{\partial Z}{\partial t} \tag{27}$$

Here $Z(x,y,t)$ is normal displacement of the mean surface, prescribed in cases where the motion is taken to be a superposition of normal vibration modes, etc. Other boundary conditions will not be presented in detail, because their treatment is generally obvious.

Laplace transformation of any time function is defined in the customary way:

$$\bar{\phi}(x,y,z;s) \equiv \int_0^\infty e^{-st}\,\phi(x,y,z,t)\,dt \tag{28}$$

When this operation is performed on (14) and (27), the results read

$$(1-M_\infty^2)\,\bar{\phi}_{xx} + \bar{\phi}_{yy} + \bar{\phi}_{zz} - \frac{2M_\infty^2}{U_\infty}\, s\bar{\phi}_x - \left(\frac{M_\infty s}{U_\infty}\right)^2 \bar{\phi} = 0 \tag{29}$$

$$\bar{\phi}_z(x,y,0;s) = \left[U_\infty \frac{\partial}{\partial x} + s\right]\bar{Z} - Z(x,y,t=0), \quad \text{for } (x,y) \text{ on } S \tag{30}$$

Here it is assumed that the fluid is undisturbed at $t = 0-$, but (30) contains allowance for an initially impulsive motion at $t = 0$.

By way of introduction, I recall that the solution to this problem for 2-D, incompressible flow has been well known since the late 1930's. The principal transfer function for the circulatory part of the aerodynamic loads then contains the generalized Theodorsen factor

$$C \equiv \frac{K_1(sc/2U_\infty)}{K_1(sc/2U_\infty) + K_o(sc/2U_\infty)} \tag{31}$$

K_o, K_1 are Bessel functions of imaginary argument, dependent on an appropriately nondimensionalized Laplace variable. Given this s-plane interpretation, C may be used for any complex value of its argument. When airload expressions are being inverted to the time domain, however, a cut must be respected along the negative real axis in the s-plane.

For arbitrary M_∞, let the solution of (29)-(30) be written

$$\bar{\phi} = \bar{\phi}_1(x,y,z;s) + \bar{\phi}_2(x,y,z;s) \tag{32}$$

$\bar{\phi}_2$ is chosen so as to satisfy (29) with the boundary condition

$$\left.\frac{\partial \bar{\phi}_2}{\partial z}\right|_{z=0} = -\,Z(x,y,t=0) \tag{33}$$

(Incidentially, if any flow disturbances were present at $t = 0-$, they would give rise to initial-value terms on the right of (29). The effects of these terms are then also to be included in the "particular solution" $\bar{\phi}_2$.)

Given $\overline{\Phi}_2$, we observe that $\overline{\Phi}_1$ satisfies a boundary-value problem which is formally identical to that resulting from the assumption of simple harmonic motion, except that $i\omega$ is replaced by $s \equiv \sigma + i\omega$. It appears that computer programs which predict airloads due to simple harmonic motion can be modified in a fairly straightforward way to calculate similar airloads corresponding to the $\overline{\Phi}_1$ solution. It can further be reasoned that, when they are incorporated into the Laplace-transformed structural equations of motion, the $\overline{\Phi}_1$ airloads are the only ones needed to determine asymptotic stability. That is, the flutter determinant, from which aeroelastic eigenvalues and enginvectors are to be found, can be constructed using $\overline{\Phi}_1$ alone.

This hypothesis regarding aerodynamic transfer functions has already been verified for 2-D supersonic flow, for 2-D compressible subsonic flow, and for 3-D subsonic flow where numbers for AGARD wing #2 were computed with a version of the Albano & Rodden (1969) program. There remains one piece of unfinished business: at $M_\infty < 1$, $\overline{\Phi}_1$ does not account for the finite length of the unsteady wake and therefore does not reproduce the early time history of aerodynamic indicial functions. I do not believe that this defect invalidates Edwards' conclusions regarding aeroelastic stability.

Figures 15 and 16 illustrate typical results from Edwards (1977). Figure 15 relates to 2-D incompressible flow, plotting as a function of dimensionless time $t' \equiv 2U_\infty t/c$ the coefficient of lift produced by the following history of (downward) vertical displacement of the airfoil:

$$h(t) = \frac{2U_\infty}{c[\sigma^2 + \omega^2]} \left[\omega - e^{-\sigma t}\left(\sigma \sin \omega t + \omega \cos \omega t\right)\right], \tag{34}$$

with numerical values

$$\frac{\sigma c}{2U_\infty} = \frac{\omega c}{2U_\infty} = \frac{0.2}{\sqrt{2}} \tag{35}$$

The total $c_\ell(t')$ is shown decomposed into

- the noncirculatory part $c_{\ell_{nc}}$.
- a "rational part," c_{ℓ_r}, which comes from the poles at $\sigma \pm i\omega$ when the transform $\overline{c}_\ell(s)$ is inverted.
- a "nonrational part," $c_{\ell_{nr}}$, which arises from the cut along the negative real axis.

In all cases examined, this "nonrational" term is found to fall toward zero monotonically, as an inverse integral power of time when this behavior can be determined analytically. Accordingly, stability is governed by the "rational" portion of $\overline{\Phi}_1$.

Figure 16 presents a roots-locus flutter calculation in supersonic flow. This involves a typical section model with some properties similar to those listed on Fig. 14, but an unbalanced 20%-chord trailing edge flap has been added with an uncoupled rotational frequency of 317 rad/sec. Note that both the torsion and flap degrees of freedom exhibit the familiar single-degree-of-freedom instability at low supersonic M_∞.

I hope that some of my listeners may be encouraged by the foregoing summary to examine whether computer programs available to them can be converted in this way to deal with true aeroelastic stability or with other nonsinusoidal problems in unsteady flow. One main requirement seems to be that the associated subroutines are readily adaptable to accept a complex argument in place of the real k.

V. NONLINEAR POTENTIAL UNSTEADY AERODYNAMICS

5.1 Incompressible Flow

The associated linear field differential equation makes $M_\infty \to 0$ a relatively tractable régime in which to tackle nonlinearity and a continuing source of standards against which compressible-flow approximations may be compared in the limit. Among others, Küssner and Gorup (1960) and van de Vooren and van de Vel (1964) gave analytical results for 2-D lifting airfoils. In their work the location of the wake must be assumed in advance, and the kinematic boundary condition at a time-dependent location also makes difficulties. Such troubles can be avoided, at the cost of adopting purely numerical methods, by treating the flow as an initial transient, then permitting the wake of discrete vortices to follow particle trajectories. Giesing (1968) is an early and successful example of this approach.

The transient scheme with wake generation was adapted to 3-D, thick lifting surfaces in rectilinear motion by Djojodihardjo and Widnall (1969). Summa (1976, as well as the dissertation on which it was based) shows how this can be generalized to helical paths, as in the case of a rotor or propeller. These last two papers I see as precursors to the more broadly applicable theory of Morino (1974), both in the manner of wake creation and the approximation of Green's function integrals by finite areas of constant singularity strength. All are capable of estimating the effects on loading of thickness, initial incidence, etc., but the field equation must be linear.

5.2 Local Linearization and Its Relatives

I have already mentioned techniques like local linearization, whereby the influence of thickness can be introduced into lifting problems in compressible flow. Although there is no reason why this approach should not be employed at subsonic or supersonic speeds, and partially-satisfactory attempts have been made even in 3-D (cf. Kacprzynski et al., 1968), it is near $M_\infty = 1$ where the greatest promise and need seem to lie.

Landahl (1961, Chap. 1) anticipated the potentialities of local linearization for transonic flow. Among many other contributions, I cite those of Stahara and Spreiter (1973; see also the survey by these authors in Kinney, 1975); Ruo and Theisen (1975); and Dowell (1977 among others). The last of these is particularly attractive, in that his use of Taylor series expansions for the thickness pressure distribution often enables fairly simple analytical solutions. It has recently (Dowell, 1977) been extended to steady, 3-D supersonic flow, and further developments are anticipated. As an example of what this theory can do, I show in Fig. 17 the growth of lift on an indicially plunging airfoil at $M_\infty = 1$, exactly. Three different thickness ratios are represented for the parabolic-arc airfoil. As Dowell remarks, the result for $\tau = 0$ shows the classical linearized tendency for the lift to rise indefinitely at large times. By contrast, thickness corrections cause it to approach a reasonable, finite asymptote. As τ increases, the length of the transient is found to dimish.

In the same category with local linearization, I also include the various simple and ingenious schemes that have been proposed for applying local Mach number corrections and the like to what are essentially the products of subcritical linearized theory. Section 4 of Roos (1976) described such a method, and a rather different "semi-empirical" one is developed and applied by Garner (1977).

5.3 Computational Fluid Dynamics (C.F.D) for Unsteady Motion

It is certainly not my intention to review finite-difference solution of the unsteady-flow field equations. Indeed, several papers in Session II of this Symposium go deeply into this subject. Rather, I wish to discuss the history and current status of C.F.D. in the light of what this vitally important and explosively growing computer technology has to offer for the topics of my paper: the subsonic and supersonic ranges. In the process, I shall show some results which seem especially exciting to me.

For the excellent reason that nothing else can approach its accuracy or versatility, C.F.D. is the method of choice for transonic flows — for steady motions and, at least at reduced frequencies where most aeroelastic phenomena are significant, for unsteady as well. Today the costs and limitations of high-speed digital computers restrict time-accurate unsteady C.F.D. methods to two spatial dimensions. But in the 2-D régime progress has been impressive. First, let me cite the survey by Ballhaus (1976) as a useful source of information about high Reynolds numbers generally. Then I list the papers by Magnus and Yoshihara (1976, along with several predecessors mentioned therein), Traci et al. (1975), Isogai (1977), and Beam & Ballhaus (1975) as merely representative of 2-D unsteady research. The measurements by Tijdeman and Schippers (1973, 1975) served to alert investigators to the significance and complexity of unsteady shock motions.

Finally I recommend Lomax (1976) for a definitive treatment of fundamental questions in modern C.F.D. He highlights the key issue of numerical stability and how it has been enhanced by implicit methods and other recent improvements. He notes the importance of operator splitting, which underlies the "alternate-direction" scheme for reducing central-processing time and memory requirements. He describes "marching," wherein even steady flow problems can be efficiently approached by transient calculation over time.

Not everyone in the field knows that elaborate C.F.D. programs are now routinely used for airplane design. A dramatic example is the paper by Gingrich et al. (1977), which describes the aerodynamic evolution of the Rockwell Highly Maneuverable Aircraft Technology (HIMAT) vehicle. One design point involved a rapidly turning condition at $M_\infty = 0.9$ and a lift coefficient $C_L = 1.0$; it was equivalent to requiring drag C_D (at wind tunnel Reynolds No.) to be no greater than 0.12. Configurations based on subsonic linearized theory failed this criterion, as can be seen from the curve marked with triangles on Fig. 18. A redesign was carried out, using as a principal tool the C.F.D. program developed by Bailey & Ballhaus (see Ballhaus, 1976, for references). Tunnel tests for the most refined version are identified by the inverted triangles; one sees that a drag reduction of over 20% was achieved.

The Bailey-Ballhaus method is to solve numerically the steady-flow equivalent of Eq. (15), with linearized boundary conditions at the surface of an arbitrary 3-D wing. The technique employed is able to "capture" weak shocks, with considerable accuracy and as an intrinsic part of the computation. Although intended for transonic purposes, this program has been successfully applied* to find the pressure distribution on thin wings up to $M_\infty = 1.3$. There is no reason why it would not also work subcritically.

---

*Personal communication from W.F. Ballhaus.

As illustrations of the practical utility of C.F.D. for 2-D unsteady flows, some calculations are duplicated from the program described as LTRAN2 by Ballhaus & Goorjian (1977a). It is a time-accurate, alternating-direction, implicit scheme for solving the low-frequency, 2-D version of (15). This approximation renders the time integrations much more efficient by dropping the ϕ_{tt} term. The resulting limitation on reduced frequency may be inferred from Fig. 19, where $M_\infty = 0.9$ the complex lift and midchord pitching moment per unit pitch amplitude on an oscillating thin plate are compared with linearized theory (the solid line — here used as a standard of reference). Since the abscissa is reduced frequency based on full chord, I infer that the C.F.D. results are sufficiently accurate up to an $\omega c/2U_\infty$ of about 0.15. For lower M_∞, equal or perhaps slightly better agreement is generally obtained.

Figures 20 and 21 reproduce some simple aeroelastic computations by LTRAN2, taken from Ballhaus and Goorjian (1977b). The model here is an NACA 64A006 airfoil, elastically restrained in pitch about midchord. At $M_\infty = 0.88$, a neutrally stable condition was found by forcing simple harmonic motion near resonance, then permitting the model to move freely. The middle curves correspond to a flutter point. The first and third, respectively, illustrate stable & unstable conditions obtained by suitably increasing or decreasing the structural damping. In Fig. 21, the aerodynamic nonlinearity associated with oscillating shocks at $M_\infty = 0.87$ is depicted. Here the initial forced amplitude is three times that of Fig. 20, and the nonsinusoidal behavior of midchord pitching-moment coefficient is quite evident. Incidentally, this same paper contains some remarkable checks against unsteady shock measurements due to Tijdeman and Schippers (1973).

I have said nothing about the computer times required to generate the foregoing results, and it seems fruitless to quote numbers — they are very dependent on the particular machine one uses, and they are decreasing rapidly with calendar time as programming refinements are discovered. Suffice it to point out that the programs, on which Figs. 18 through 21 are based, are sufficiently practical to be described as "engineering" by their developers and users. By contrast, programs incorporating approximations to the unsteady Navier-Stokes equations of viscous flow for high Reynolds No. still require hours of CPU time on a machine like CDC 7600 (cf. Steger, 1977) and are therefore called "research."

VI. CONCLUDING REMARKS

I begin my summary with two observations on the present state of methods for predicting unsteady subsonic and supersonic external flows. First, the collection of available tools from linearized theory is impressive, and especially for isolated thin wings one may employ them confidently within their established ranges of validity. Second, I believe that a continued & single-minded concentration by theoretical aerodynamicists on further refinement of these linearized tools would constitute misplaced effort. To increase by a few per cent the accuracy and convergence rate of complicated analyses, which too often do not properly represent the physical reality where we wish to apply them, could well be a waste of scarce resources.

I see both an analogy and a disparity with the situation in finite-element structural analysis. There also has occurred a systematic development of computer programs, which tended to utilize the full capacity of the machines for which they were written. In the words of Gallagher (1977), "This topic, which in its early phases was not even recognized as a legitimate component of solid mechanics, has crystallized as an aspect of technology that cuts across many disciplines ..." True, but what the structural analysts have going for them is that the majority of designs do closely conform to the idealizations based on small strains and moderate displacements. Moreover, most structures are so arranged that a representation in terms of bars, beams, shear webs, plates, etc. is a very accurate picture.

By contrast, what can be said of the acoustic approximation to which we have clung in unsteady aerodynamics? Especially in 3-D it has also called for programs that stretch the limits of computers. But we are extremely fortunate that it works as well as it does in the situations where we apply it. It also stretches the patience of mathematicians to work their way around and through horrendous singularities, which are there not because they are needed to describe the physics but because they are forced upon us by our approximations.

Unsteady flow theory also consists of a disorderly collection of special-purpose methods, each with its presumed, limited range of applicability and each with unknown pitfalls if it is misapplied.

Let me imagine for you an alternative approach. Let me propose that something along the lines of my vision surely deserves a future research effort on the same order as what pure momentum and habit of mind ensure will be accorded to continued work on linearized theory. My goal is a unified C.F.D. methodology, useful for steady and unsteady 3-D flows — subsonic, transonic and supersonic — applicable to general combinations of streamlined lifting surfaces and bodies, accounting for nonlinear effects whenever required but also able to reproduce linear indicial responses and transfer functions in the frequent situations where they are justified. I say "steady and unsteady," for it has already been demonstrated that steady C.F.D. flows are conveniently computed through time transients; all we require is to use time-accurate schemes (cf. Isogai, 1977) for these transients. I say "subsonic, transonic and supersonic," for we know C.F.D. can capture weak shocks even when irrotational flow is assumed. It has been pointed out to me that to take the next step from potential theory to the full Euler eqs. (3) will subsume shocks of any strength (absent severe boundary-layer separation) and will require, at most, a factor of 4 in computation time. Alas, the step to the Navier Stokes equations is a much bigger one! — although interesting 2-D unsteady results are in the literature.

For time-dependent motions whose amplitudes are not a small fraction of the thickness ratio, the biggest single roadblock in the way of my goal is the formulation of kinematic boundary conditions. C.F.D. prefers to work in curvilinear coordinates matched to the body shape, and there will be a serious penalty for changing this system at each time step. Yet I believe that, in many cases, it will be acceptable to approximate boundary conditions at the mean position of a time-dependent surface. I think a 3-D computer program, based on (15) with such conditions for an isolated thin wing, can be prepared by best C.F.D. technology today in the "engineering" category.

What about computer costs? Enough of propaganda has been written about replacing wind tunnels with the computer of the future, about thus escaping from wall effects, and the like. My observation is that C.F.D. central-processor times are even today converging downward toward those of linearized theory based on surface-distributed singularities. In personal communication, Jameson of the Courant Institute has pointed out why this should be so. Whether based on collocation or finite-differencing, methods employ grids with $0(n)$ elements in each coordinate direction. Typically, a 3-D solution would call for solving a system of n^2 algebraic equations, but the coefficient matrix will tend to be full, not sparse. By contrast, there would be n^3 elements in C.F.D. But the use of splitting and alternate-direction methods would reduce the calculation to repeated solutions of systems of n equations, and their matrices are either diagonal or block diagonal. For transient motion, both approaches would tend to operate on the same number of time steps. As n becomes large, it is not difficult to reason why C.F.D. gains an advantage.

As a final word in a survey of theory, let me emphasize the need for more careful measurements of pressures and other field variables in unsteady flow situations. Recent progress has been encouraging, and excellent instruments are now available. Only through the conscientious study of such data can the real utility of any analytical tool be established.

VII. REFERENCES

Albano, E., and Rodden, W.P. (1969), "A Doublet Lattice Method for Calculating Lift Distributions on Oscillating Surfaces in Subsonic Flow," AIAA Journal, Vol. 7, No. 2, pp. 279-285.

Amiet, R.K. (1975), "Effects of Compressibility on Unsteady Airfoil Lift Theories," in Unsteady Aerodynamics, Proceedings of a Symposium held at the University of Arizona, pp. 631-653.

Amiet, R.K. (1976), "High Frequency Thin-Airfoil Theory for Subsonic Flow," AIAA Journal, Vol. 14, No. 8, pp. 1076-1082.

Appa, K., and Smith, G.C.C. (1972), "Further Developments in Consistent Unsteady Supersonic Aerodynamics for Interfering Parallel Wings," NASA C.R. 2168.

Appa, K., and Jones, W.P. (1976), "Integrated Potential Formulation of Unsteady Supersonic Aerodynamics for Interacting Wings," J. Aircraft, Vol. 13, No. 9, pp. 695-703.

Ashley, H. (1971), "Some Considerations Relative to the Prediction of Unsteady Air Loads on Lifting Configuration," Journal of Aircraft, Vol. 8, No. 10, pp. 747-756.

Ashley, H., and Landahl, M.T. (1965), Aerodynamics of Wings and Bodies, Addison-Wesley Publishing Co., Reading, Mass.

Ballhaus, W.F. (1976), Some Recent Progress in Transonic Flow Computations, presented at the lecture series on Computational Fluid Dynamics, March 15-19, 1976, von Kármán Institute, Rhode-St-Genese, Belgium.

Ballhaus, W.F., and Goorjian, P.M. (1977a), "Computation of Unsteady Transonic Flows by the Indicial Method," Proceedings, AIAA Dynamics Specialist Conference, San Diego, March 24-25, pp. 234-244.

Ballhaus, W.F., and Goorjian, P.M. (1977b), "Efficient Solution of Unsteady Transonic Flows about Airfoils," paper presented at the AGARD Specialist Meeting referenced as Many Authors (1977).

Beals, V., and Targoff, W.P. (1953), "Control Surface Oscillatory Coefficients Measured on Low Aspect Ratio Wings," WADC T.R. NO. 53-64.

Beam, R.M., and Ballhaus, W.F. (1975), "Numerical Integration of the Small-Disturbance Potential and Euler Equations for Unsteady Transonic Flow," Aerodynamic Analyses Requiring Advanced Computers, Part II, A Conference held at Langley Research Center, Hampton, Va. March 4-6, pp. 789-810.

Cheng, H.K. (1975), "*On Lifting-Line Theory in Unsteady Aerodynamics*," in Unsteady Aerodynamics, Proceedings of a Symposium held at the University of Arizona, pp. 719-739.

Chipman, R.R. (1976), "An Improved Mach-Box Approach for the Calculation of Supersonic Oscillatory Pressure Distributions," Proceedings AIAA/ASME/SAE 17th Structures, Structural Dynamics and Materials Conference, King of Prussia, Penn., pp. 608-611.

Chopra, M.G. (1977), "Large Amplitude Lunate-Tail Theory of Fish Locomotion," Journal of Fluid Mechanics, Vol. 74, part 1, pp. 161-182.

Crill, W., and Dale, B. (1976), "General Purpose Computer Program for Interacting Supersonic Configurations," NASA C.R. NAS1-13986, Users Manual.

Cunningham, Jr., A.M. (1971), "A Collocation Method for Predicting Oscillatory Subsonic Pressure Distributions on Interfering Parallel Lifting Surfaces," Proceedings of AIAA/ASME 12th Structures, Structural Dynamics and Materials Conference, Anaheim, Ca. April 19-21.

Cunningham, Jr., A.M. (1947a), "Oscillatory Supersonic Kernel Function Method for Isolated Wings," J. Aircraft, Vol. 11, No. 10, pp. 609-615.

Cunningham, Jr., A.M. (1974b), "Oscillatory Supersonic Kernel Function Method for Interfering Surfaces," J. Aircraft, Vol. 11, No. 11, pp. 664-670.

Davies, D.E. (1976), Theoretical Determination of Subsonic Oscillatory Airforce Coefficients, Royal Aircraft Establishment, Tech. Report 76059.

Djojodihardjo, R.H., and Widnall, S.E. (1969), "A Numerical Method for the Calculation of Nonlinear Unsteady Lifting Potential Flow Problems," AIAA Journal, Vol. 7, No. 10, pp. 2001-2009.

Dowell, E.H. (1977), "A Simplified Theory of Oscillating Airfoils in Transonic Flow: Review and Extension," Proceedings, AIAA Dynamics Specialist Conference, San Diego, March 24-25, pp. 209-224.

Edwards, J.W. (1977), Unsteady Aerodynamic Modeling and Active Aeroelastic Control, SUDAAR 504, Stanford University, Dept. of Aero. and Astro., Stanford, Calif. (A summary paper by Edwards, Ashley and Breakwell will appear shortly in AIAA Journal.)

Farmer, M.G., and Hanson, P.W. (1976), "Comparison of Supercritical and Conventional Wing Flutter Characteristics," Proceedings AIAA/ASME/SAE 17th Structures, Structural Dynamics, and Materials Conference, King of Prussia, Penn., pp. 608-611.

Fleeter, S. (1977), "Aeroelasticity Research for Turbomachine Applications," Proceedings, AIAA Dynamics Specialist Conference, San Diego, March 24-25, pp. 161-173.

Gallagher, R.H. (1977), "Computerized Structural Analysis and Design - the Next Twenty Years," Journal of Computers & Structures, Vol. 7, No. 4, pp. 495-501.

Garner, H.C. (1977), A Practical Framework for the Evaluation of Oscillatory Aerodynamic Loading on Wings in Supercritical Flow, Royal Aircraft Establishment, Tech. Memo Structures 900.

Garrick, I.E. (1957), "Nonsteady Wing Characteristics," Section F, Volume VII, Princeton Series in High Speed Aerodynamics and Jet Propulsion, Princeton University Press.

Garrick, I.E. (1976), "Aeroelasticity-Frontiers and Beyond," Journal of Aircraft, Vol. 13, no. 9, pp. 641-657.

Giesing, J.P. (1968), "Nonlinear Two-Dimensional Unsteady Potential Flow with Lift," Journal of Aircraft, Vol. 5, No. 2, pp. 135-143.

Giesing, J.P., and Kalman, T.P. (1975), "Oscillatory Supersonic Lifting Surface Theory Using a Finite Element Doublet Representation," Proceedings, AIAA/ASME/SAE 16th Structures, Structural Dynamics, and Materials Conference, Denver, Co., May 27-29.

Gingrich, P.B., Child, R.D., and Panageas, G.N. (1977), Aerodynamic Configuration Development of the Highly Maneuverable Aircraft Technology Remotely Piloted Research Vehicle, Rockwell International, Los Angeles, Ca., NA-76-865, to be issued as NASA C.R. 143841.

Haviland, J.K., and Yoo, Y.S. (1976), Calculation of Subsonic and Supersonic Steady and Unsteady Aerodynamic Forces Using Velocity Potential Aerodynamic Elements, NASA C.R. 2695.

Ichikawa, T., and Isogai, K. (1973a), "Note on the Aerodynamic Theory of Oscillating T-Tails - Part 1. Theory of Wings Oscillating in Yaw and Sideslip," Transactions of the Japan Society for Aeronautical and Space Sciences, Vol. 16, No. 33, pp. 173-194.

Ichikawa, T., and Isogai, K. (1973b), "Note on the Aerodynamic Theory of Oscillating T-Tails - Part 2. Theory of Laterally Oscillating T-Tails," Transactions of the Japan Society for Aeronautical and Space Sciences, Vol. 16, No. 34, pp. 209-224.

Isogai, K. (1977), "Calculation of Unsteady Transonic Flow over Oscillating Airfoils Using the Full Potential Equation," *Proceedings, AIAA Dynamics Specialist Conference*, San Diego, March 24-25, pp. 161-173.

Jameson, A. (1976), "Numerical Computation of Transonic Flows with Shock Waves," *Symposium Transsonicum II*, Springer-Verlag, Berlin.

Jones, W.P., and Appa, Kari (1977), "Unsteady Supersonic Aerodynamic Theory by the Method of Potential Gradient," *AIAA Journal*, Vol. 14, No. 1, pp. 59-65.

Jones, W.P., and Moore, J.A. (1975), "Aerodynamic Theory for a Cascade of Oscillating Airfoils in Compressible Subsonic Flow," Texas A&M University, Aerospace Engineering Dept., TEES-3068-75-01.

Jordan, P.F. (1976), "Numerical Evaluation of the Three-Dimensional Harmonic Kernel," *Z. Flugwiss*, 24, Heft 4, pp. 205-209.

Jordan, P.F. (1978), "Reliable Lifting Surface Solutions for Unsteady Flow," AIAA 16th Aerospace Sciences Meeting, Huntsville, Alabama, to be held January 16-18.

Kacprzynski, J.J., and Landahl, M.T. (1967), "Recent Developments in the Supersonic Flow over Axisymmetric Bodies with Continuous or Discontinuous Slope," AIAA Paper No. 67-5, AIAA 5th Aerospace Sciences Meeting, New York, January 23-26.

Kacprzynski, J.J., Ashley, H., and Sankaranarayanan, R. (1968), "On the Calculation of Unsteady Nonlinear Three-Dimensional Supersonic Flow Past Wings," *Journal of Basic Engineering*, Transactions of the ASME, Vol. 90, No. 4.

Kalman, T.P., Rodden, W.P., and Giesing, J.P. (1971), "Application of the Doublet-Lattice Method to Nonplanar Configurations in Subsonic Flow," *J. Aircraft*, Vol. 8, No. 6, pp. 406-413.

Kemp, N.H., and Ohasahi, H. (1976), "Forces on Unstaggered Airfoil Cascades in Unsteady In-Phase Motion," *Journal of Fluids Engineering*, ASME Paper No. 76-FE-S.

Kinney, R.B., editor (1975), *Unsteady Aerodynamics*, Proceedings of a Symposium held at the University of Arizona, Vols. I and II.

Küssner, H.G., and Gorup, G.V. (1960), "Instationäre linearisierte Theorie der Flügelprofile endlicher Dicke in inkompressibler Strömung," *Mitteilungen des Max-Planck Inst. und der A.V.A.*, Göttingen, No. 26.

Landahl, M.T. (1957), "Unsteady Flow Around Thin Wings at High Mach Numbers," *Journal of the Aeronautical Sciences*, Vol. 24, No. 1, pp. 33-38.

Landahl, M.T. (1961), *Unsteady Transonic Flow*, Pergamon Press, New York.

Landahl, M.T. (1968), "Pressure Loading Functions for Oscillating Wings with Control Surfaces," *AIAA Journal*, Vol. 6, No. 2, pp. 345-348.

Landahl, M.T., and Stark, V.J.E. (1968), "Numerical Lifting-Surface Theory — Problems and Progress," *AIAA Journal*, Vol. 6, No. 11, pp. 2049-2060.

Laschka, B. (1963), "Zur Theorie der harmonisch schwingenden Trafläche bei Unterschallanströmung," Zeitschrift für Flugwissenschaften, Vol. 11, Heft 7.

Liu, D.D., Platzer, M.F., and Ruo, S.Y. (1976), "Stability Derivatives for Bodies of Revolution at Subsonic Speeds," *AIAA Journal*, Vol. 14, No. 2, pp. 247-250.

Liu, D.D., Platzer, M.F., and Ruo, S.Y. (1977), "Unsteady Linearized Transonic Flow Analysis for Slender Bodies," *AIAA Journal*, Vol. 15, No. 7, pp. 966-973.

Lomax, H. (1976), "Recent Progress in Numerical Techniques for Flow Simulation," *AIAA Journal*, Vol. 14, No. 4, pp. 512-518.

Magnus, R., and Yoshihara, H. (1976), "The Transonic Oscillating Flap," *AIAA 9th Fluid and Plasma Dynamics Conference*, San Diego, Ca., AIAA Paper No. 76-327.

Many authors (1975a), *Unsteady Aerodynamics - Contribution of the Structures and Materials Panel to the Fluid Dynamics Panel Round Table Discussion on Unsteady Aerodynamics, Göttengen*, AGARD Report No. 645.

Many authors (1975b), *Aerodynamic Analyses Requiring Advanced Computers*, Part II, Proceedings of a conference held at Langley Research Center, Hampton, Va. March 4-6.

Many authors (1976a), *Vortex-Lattice Utilization*, Proceedings of workshop held at Langley Research Center, Hampton, Va., May 17-18.

Many authors (1976b), Revue Francaise de Mechanique, *Symposium I.U.T.A.M.*, Paris, October 18-23.

Many authors (1977), Proceedings of Specialists Meeting on Unsteady Airloads in Separated and Transonic Flow, 44th Meeting of AGARD Structures & Materials Panel, Lisbon, Portugal.

Marchbank, W.R. (1973), Evaluation of Pressure Distributions on Thin Wings with Distorted Control Surfaces Oscillating Harmonically in Linearized, Compressible, Subsonic Flow — Part I: Details of the Mathematical Techniques Used in the Evaluation of the Pressure Distributions, and a Set of Numerical Results Including Comparisons with Experiment. British Aircraft Corp., Ltd., S&T. Memo 8-73, BR36241.

Mazet, R., Editor (1968), AGARD Manual on Aeroelasticity, Second Edition.

McCroskey, W.J. (1975), Some Current Research in Unsteady Aerodynamics — A Report from the Fluid Dynamics Panel, Presented at 46th Meeting of AGARD Propulsion and Energetics Panel, Monterey, Ca., Sept. 22-26.

McCroskey, W.J. (1976), "Current Research in Unsteady Fluid Dynamics," Freeman Scholar Lecture, presented at ASME 97th Winter Annual Meeting, New York, Dec. 8 (published by ASME).

Medan, R.T. (1976), Aerodynamic Loads Near Cranks, Apexes, and Tips of Thin, Lifting Wings in Subcritical Flow, Stanford University Dept. of Aero. & Astro., Ph.D. Dissertation.

Milne, R.D. (1966), "Asymptotic Solutions of Linear Stationary Integro-Differential Equations," British A.R.C. R. & M. No. 3548.

Morino, L. (1974), A General Theory of Unsteady Compressible Potential Aerodynamics, NASA CR-2464,

Nissim, E., and Lottati, I.(1977), "Oscillatory Subsonic Piecewise Continuous Kernel Function Method," J. Aircraft, Vol. 14, No. 6, pp. 515-516.

Oswatitsch, K., and Rues, D., editors (1976), Symposium Transsonicum II, Göttengen, International Union of Theoretical and Applied Mechanics, Sept. 8-13, Springer-Verlag.

Pollock, S.J., and Huttsell, L.J. (1974), Application of Three Unsteady Aerodynamic Load Prediction Methods, AFFDL-TR-73-147.

Revell, J.D. (1960), "Second-Order Theory for Unsteady Supersonic Flow Past Slender Pointed Bodies of Revolution," Journal of the Aerospace Sciences, Vol. 27, No. 10, pp. 730-740.

Revell, J.D. (1969), "Second-Order Theory for Steady or Unsteady Subsonic Flow Past Slender Lifting Bodies of Finite Thickness," AIAA Journal, Vol. 7, No. 6, pp. 1070-1078.

Richardson, J.R. (1965), "A More Realistic Method for Routine Flutter Calculations," AIAA Symposium on Structural Dynamics and Aeroelasticity, Boston, Mass.

Rock S. (1977), Stanford University Ph.D. Dissertation, Department of Aeronautics and Astronautics, Stanford, Ca.

Rodden, W.P. (1976a), A Comparison of Methods Used in Interfering Lifting Surface Theory, AGARD Report No. 643.

Rodden, W.P. (1976b), State-of-the-Art in Unsteady Aerodynamics, AGARD Report No. 650.

Roos, R. (1976), "Application of Panel Methods for Unsteady Subsonic Flow," NLR Report MP76010 U.

Roos, R., and Zwaan, R.J. (1972), Calculation of Instationary Pressure Distributions and Generalized Aerodynamic Forces with the Doublet-Lattice Method, National Aerospace Laboratory, The Netherlands, NLR TR 72037U.

Roos, R., Bennekers, B., and Zwaan, R.J. (1977), "Calculation of Unsteady Subsonic Flow About Harmonically Oscillating Wing/Body Configurations," J. Aircraft, Vol. 14, No. 5, pp. 447-454.

Rowe, W.S., Redman, M.C., Ehlers, F.E., and Sebastian, J.D. (1975), Prediction of Unsteady Aerodynamic Loadings Caused by Leading Edge and Trailing Edge Control Surface Motions in Subsonic Compressible Flow - Analysis and Results, NASA CR-2543.

Rowe, W.S., Sebastian, J.D., and Redman, M.C. (1976), "Recent Developments in Predicting Unsteady Airloads Caused by Control Surface Motions," J. Aircraft, Vol. 13, No. 12, pp. 955-961.

Ruo, S.Y., and Theisen, J.G. (1975), Calculation of Unsteady Transonic Aerodynamics for Oscillating Wings with Thickness, NASA CR-2259.

Satyanarayana, B. (1977), "Unsteady Wake Measurements of Airfoils and Cascades," AIAA Journal, Vol. 15, No. 5, pp. 613-618.

Stahara, S.S., and Spreiter, J.R. (1973), "Development of a Nonlinear Unsteady Transonic Flow Theory," NASA CR 2258.

Stahara, S.S., and Spreiter, J.R. (1976), "Unsteady Local Linearization Solution for Pitching Bodies of Revolution at $M_\infty = 1$: Stability Derivative Analysis," AIAA Journal, Vol. 14, No. 10, pp. 1402-1408.

Stark, V.J.E. (1974), "Application to the Viggen Aircraft Configuration of the Polar Coordinate Method for Unsteady Subsonic Flow," ICAS Paper No. 74-03, The 9th Congress of the ICAS, Haifa, Israel, August 25-30.

Steger, J.L. (1977), "Implicit Finite Difference Simulation of Flow About Arbitrary Geometries with Application to Airfoils," AIAA 10th Fluid & Plasmadynamics Conf., Albuquerque, New Mexico, June 27-29, No. 77-665.

Summa, J.M. (1976), "Potential Flow about Impulsively Started Rotors," Journal of Aircraft, Vol. 13, No. 4, pp. 317-319.

Theodorsen, T. (1935), General Theory of Aerodynamic Instability and the Mechanism of Flutter, NACA Rept. 496.

Tijdeman, H., and Schippers, P. (1973), Results of Pressure Measurements on an Airfoil with Oscillating Flap in Two-Dimensional High Subsonic and Transonic Flow (zero incidence and zero mean flap position), National Aerospace Laboratory, Amsterdam, NLR TR-73078U.

Tijdeman, H. (1975), On the Motion of Shock Waves on an Airfoil with Oscillating Flap in Two-Dimensional Transonic Flow, National Aerospace Laboratory NLR, Amsterdam, NLR TR-75038 U.

Timman, R. (1951), "The Aerodynamic Forces on an Oscillating Aerofoil Between Two Parallel Walls," National Luchtv. Lab. Publ. No. MP-61, Appl. Sci. Research, Vol. A3.

Traci, R.M., Albano, E.D., and Farr, Jr., J.L. (1975), Small Disturbance Transonic Flows about Oscillating Airfoils and Planar Wings, AFFDL-TR-75-100.

Tseng, K., and Morino, L. (1976), "Fully Unsteady Subsonic and Supersonic Potential Aerodynamics of Complex Aircraft Configurations for Flutter Applications," Proceedings AIAA/ASME/SAE 17th Structures, Structural Dynamics, and Materials Conference, King of Prussia, Penn., pp. 626-638.

Ulv Mai, H. (1975), An Unsteady Vortex Panel Method and its Application to Aeroelastic Calculations of a Fixed, Thin Wing and an Unconstrained Flying Vehicle, Helsinki University of Technology, Ph.D. Dissertation.

Van de Vooren, A.I., and van de Vel, H. (1964), "Unsteady Profile Theory and Incompressible Flow," Archiwum Mechaniki, Stosowanej, Vol. 16, No. 3, pp. 709-735.

Van Dyke, M.D. (1954), "Supersonic Flow Past Oscillating Airfoils Including Nonlinear Thickness Effects," NACA Report 1183.

Vepa, R. (1977), Finite State Modeling of Aeroelastic Systems, NASA CR 2779.

Walker, W.J., Guest Editor (1975), "Special Issue on Propulsion System Structural Integration and Structural Integrity," Journal of Aircraft, Vol. 12, No. 4, April (see especially the paper by Mikolajczak et al.).

Ward, G.N. (1955), Linearized Theory of Steady High-Speed Flow, Cambridge University Press.

Williams, M.H., Chi, R., Ventres, C.S., and Dowell, E.H. (1977), "Effects of Inviscid Parallel Shear Flows on Steady & Unsteady Aerodynamics and Flutter," AIAA Paper No. 77-158.

Woodcock, D.L. (1971), A Comparison of Methods Used in Lifting Surface Theory, AGARD Report No. 583.

Woodcock, D.L. (1976), "The Theoretical Prediction of Steady and Unsteady Aerodynamic Loading on Arbitrary Bodies in Supersonic Flow," AGARD, PRoceedings No. 204.

Wu, T.Y. (1971), "Hydromechanics of Swimming Propulsion," Part 1, Journal of Fluid Mechanics, Vol. 46, Part 2, pp. 337-355.

Young, V.Y.C. (1976), A New Finite Element Supersonic Kernel Function Method in Lifting Surface Theory, AFFDL-TR-76-3, Vols. 1 and 2.

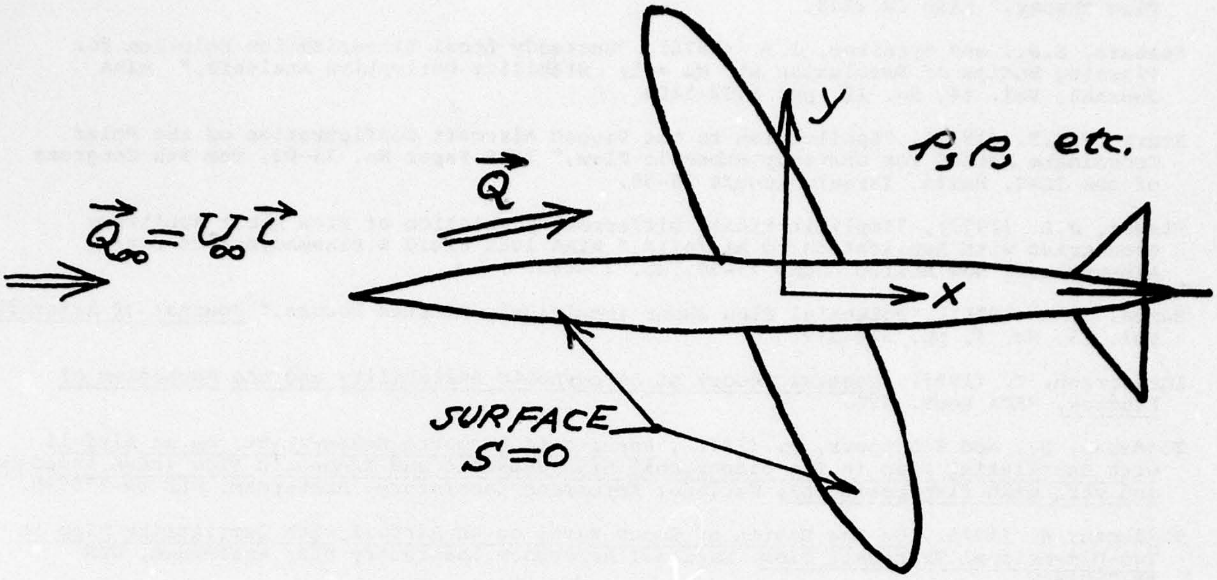

Fig. 1. Illustrating a typical aeronautical configuration, submerged in a fluid which has a parallel motion at speed U_∞ at remote distances. Coordinate system x,y,z is attached to the "mean" position, with x parallel to the free stream.

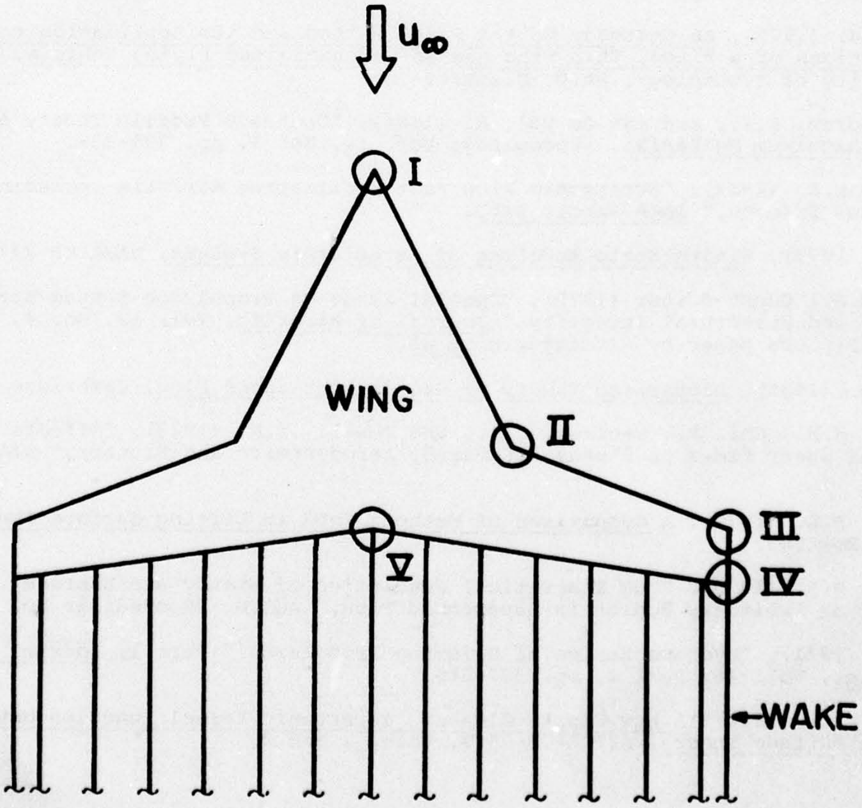

Fig. 2. Identifying the five types of corners of a wing planform projection where the loading exhibits special singular behavior. [Taken from Medan (1976).]

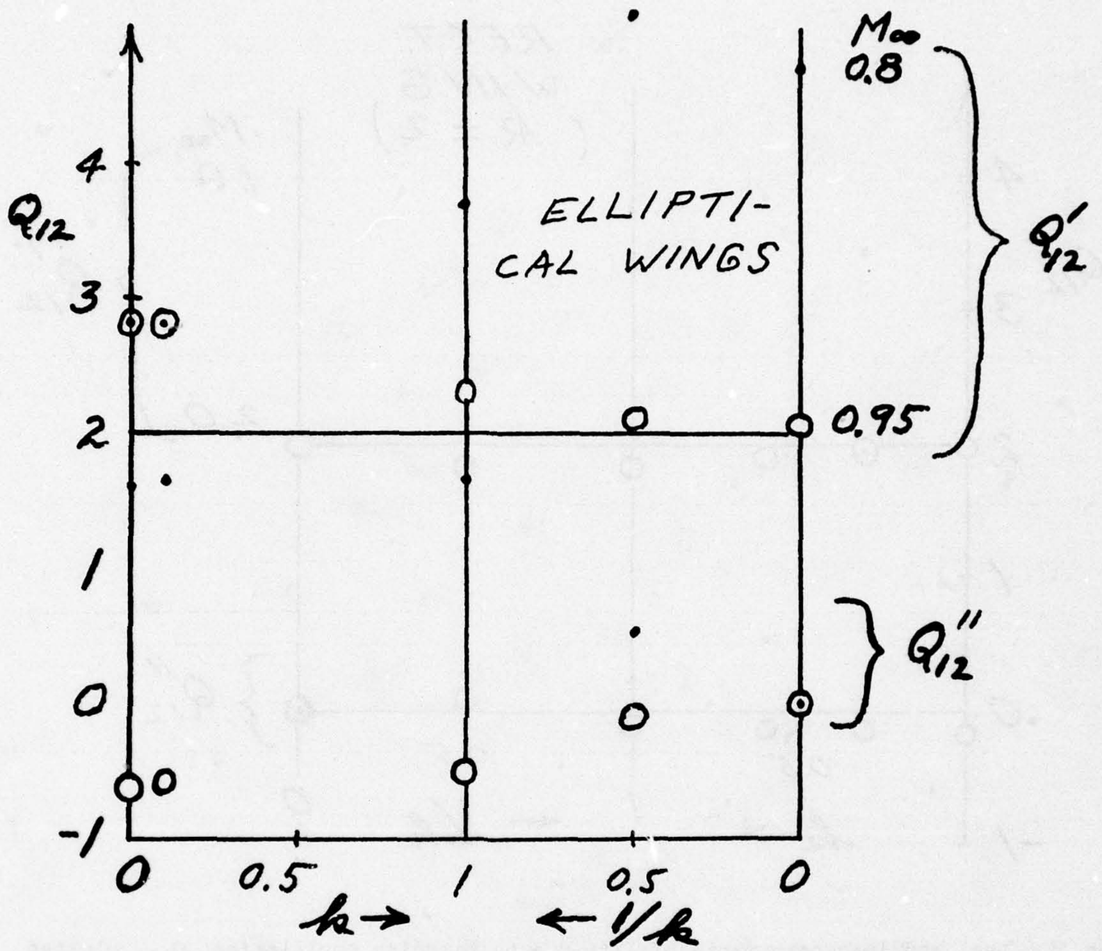

Fig. 3. Real and Imaginary parts of lift due to pitching oscillation Q_{12}, plotted <u>vs.</u> reduced frequency k, for AGARD elliptical wings at $M_\infty = 0.8$ (dots) and 0.95 (open circles). Calculations are by method of Laschka (1963) except for piston theory at (1/k) = 0.

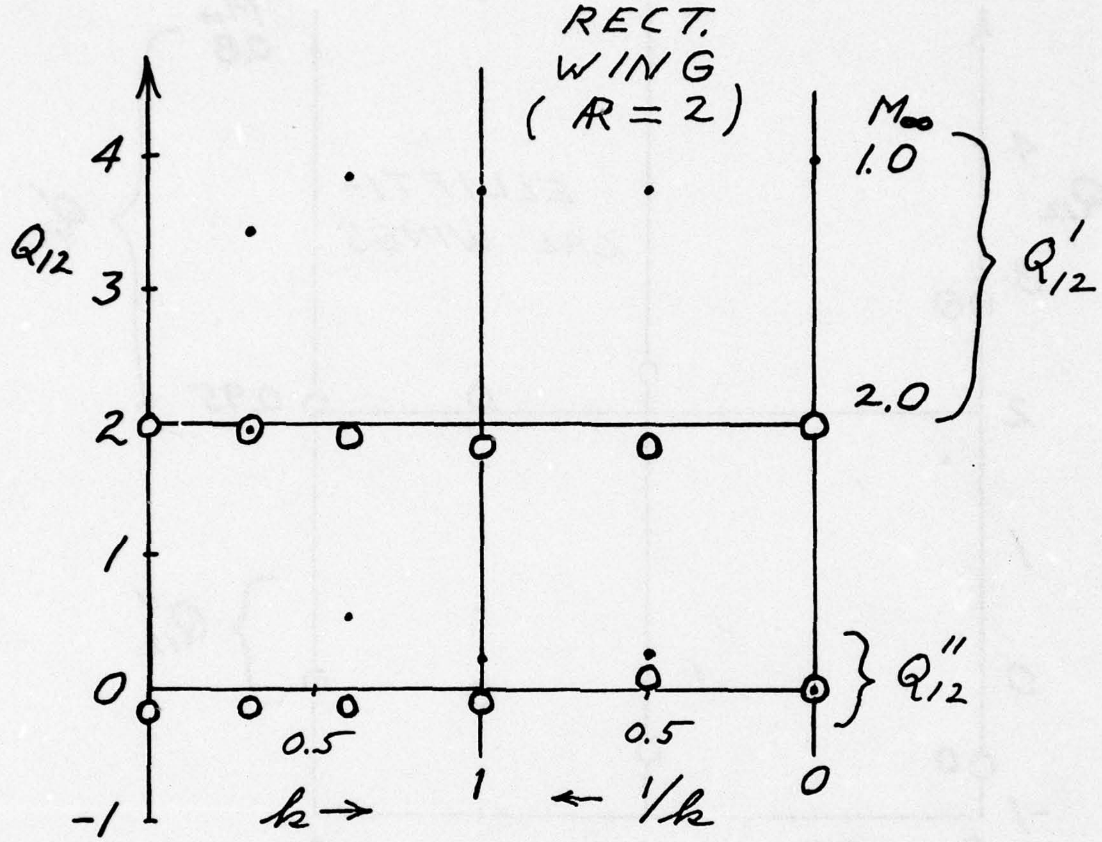

Fig. 4. Real and imaginary parts of lift due to pitching oscillation Q_{12}, plotted vs. reduced frequency k, for AGARD rectangular wing at $M_\infty = 1.0$ (dots) and 2.0 (open circles). Method of Laschka (1963) at $M_\infty = 1.0$ and Stark (see Woodcock, 1971) at $M_\infty = 2.0$ are compared with piston theory limits at $(1/k) = 0$.

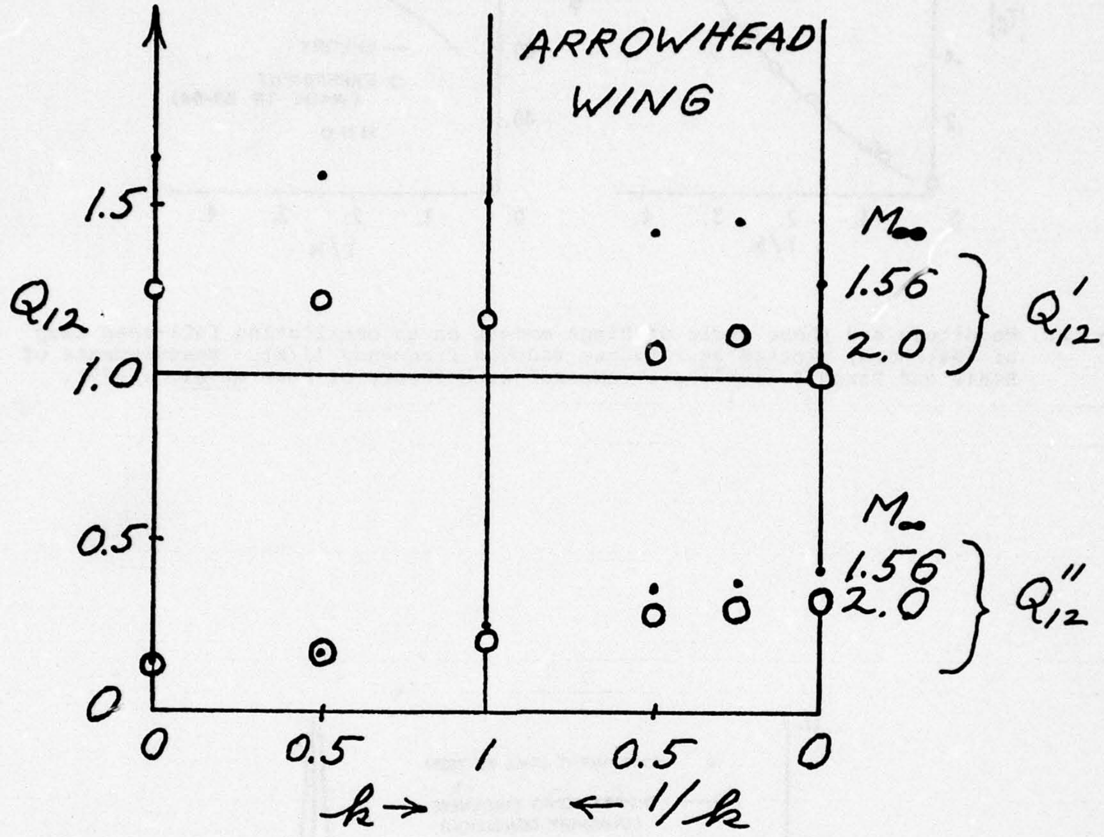

Fig. 5. Real and imaginary parts of lift due to pitching oscillation Q_{12}, plotted vs. reduced frequency k, for AGARD arrowhead wing at $M_\infty = 1.56$ (dots) and $M_\infty = 2.0$ (open circles). Calculations are by method of Stark (see Woodcock, 1971) except for piston theory at $(1/k) = 0$.

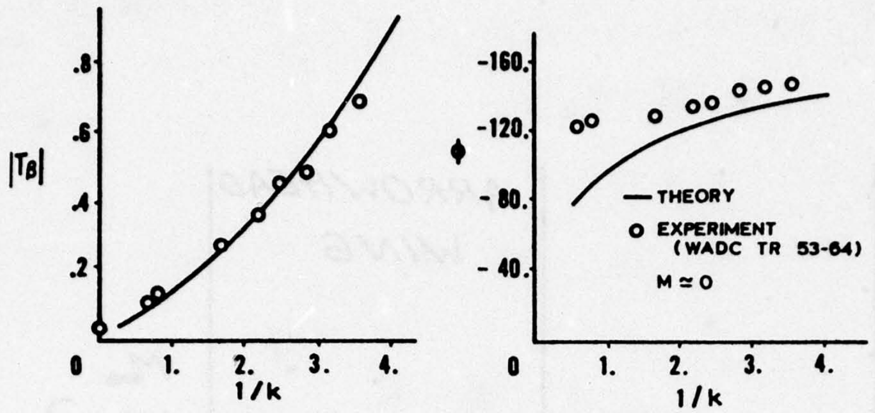

Fig. 6. Magnitude and phase angle of hinge moment on an oscillating full-span flap of 40%-chord, plotted vs. inverse reduced frequency (1/k). Measurements of Beals and Targoff (1953) are compared with theory of Rowe et al. (1975).

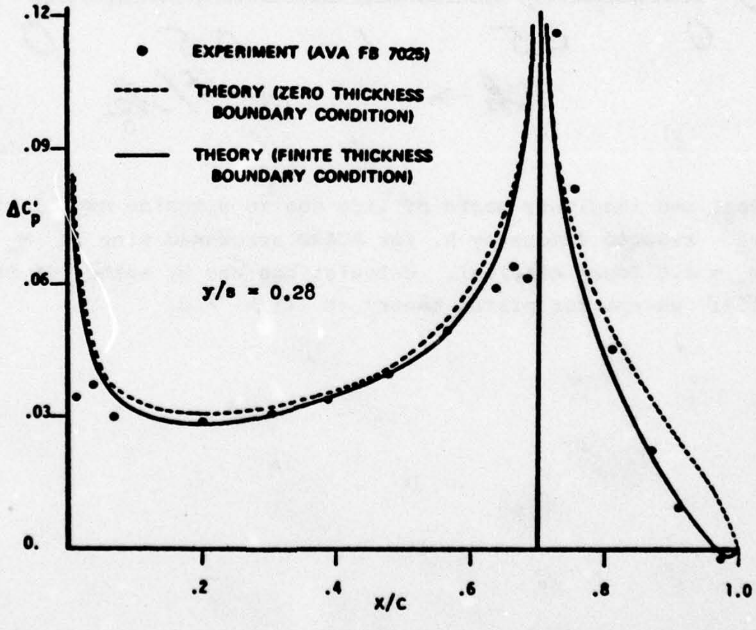

Fig. 7. In-Phase chordwise lifting pressure distribution at spanwise station (y/s) on a reduced frequency k = 0.372 and $M_\infty = 0$. Two theories of Rowe et al. (1975) are compared vs. experiment; see reference for details.

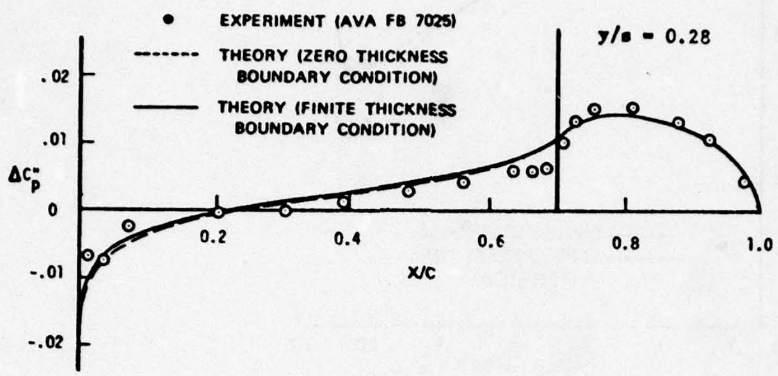

Fig. 8. 90° out-of-phase component of lifting pressure distribution for same conditions as Fig. 7.

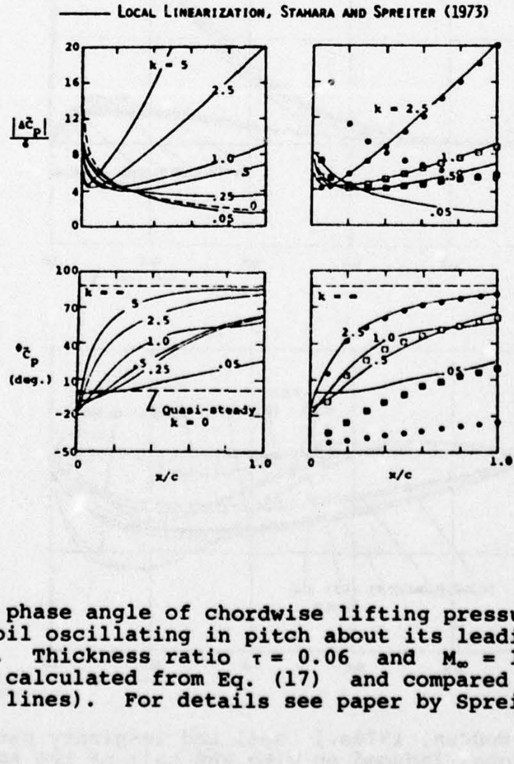

Fig. 9. Magnitude and phase angle of chordwise lifting pressure distribution on a biconvex airfoil oscillating in pitch about its leading edge at various reduced frequencies k. Thickness ratio $\tau = 0.06$ and $M_\infty = 1$; individual points on the right are calculated from Eq. (17) and compared with locally linearized theory (solid lines). For details see paper by Spreiter in Kinney (1975).

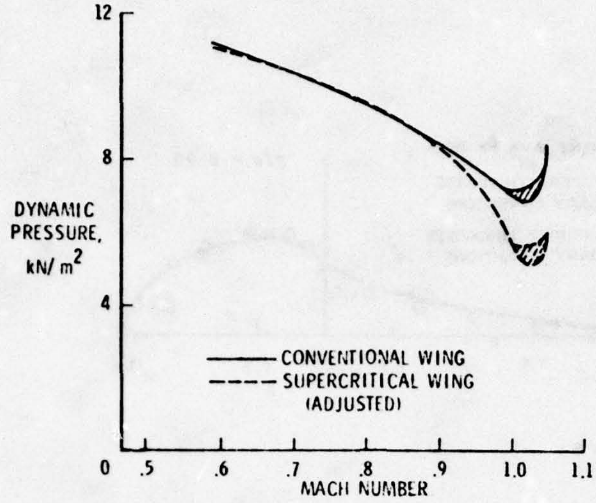

Fig. 10. Experimental flutter boundaries, plotted on a scale of dynamic pressure vs. Mach No., for two dynamically similar wings. "Conventional wing" has a modern subsonic airfoil, whereas the other has a supercritical shape of the same thickness ratio. Data are from Farmer & Hanson (1976).

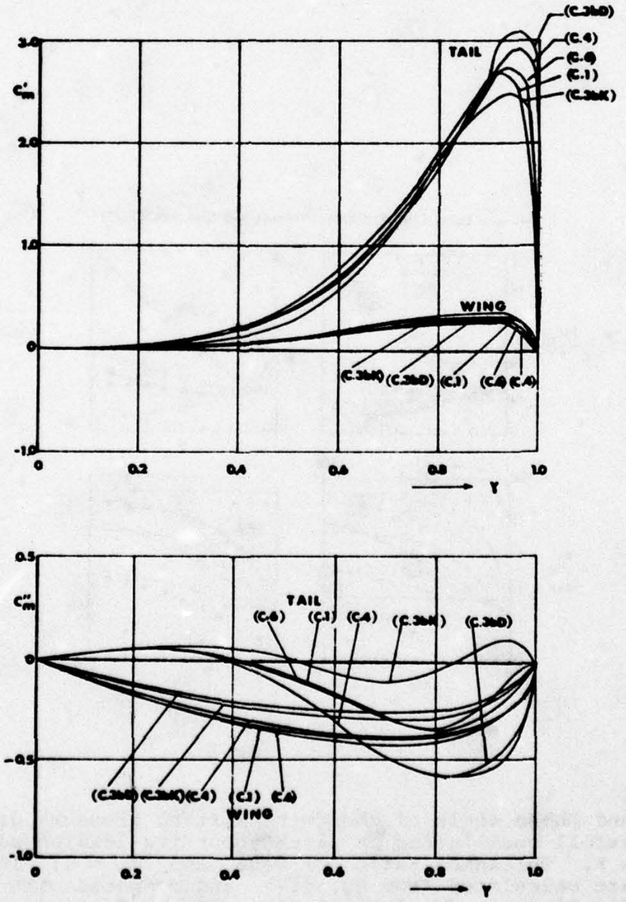

Fig. 11. [From Fig. 17 of Rodden, 1976a.] Real and imaginary parts of spanwise pitching moment distributions, induced on wing and tail of the AGARD wing-tail combination, by "antisymmetric" elastic oscillation of the wing. Five subsonic theories are compared; see reference for details.

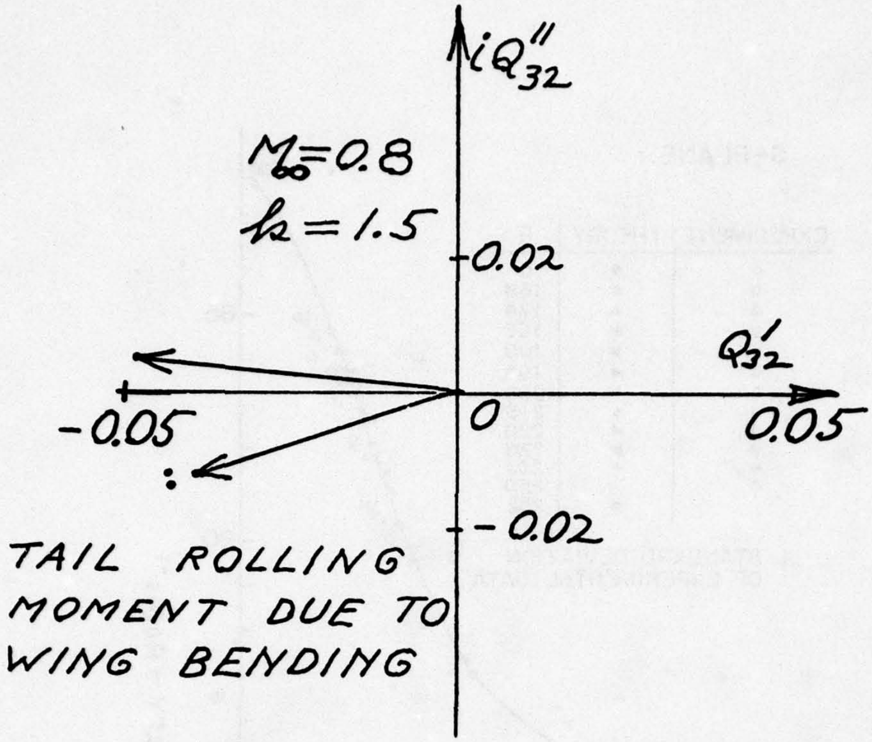

Fig. 12. Polar plot of tail rolling moment due to antisymmetrical wing bending oscillation, at $M_\infty = 0.8$ and reduced frequency $k = 1.5$, for AGARD wing-tail combination. Results of four theories are shwon from Table 4 of Rodden (1976a) and Tseng and Morino (1976). Tail is vertically displaced by 0.6 semispan.

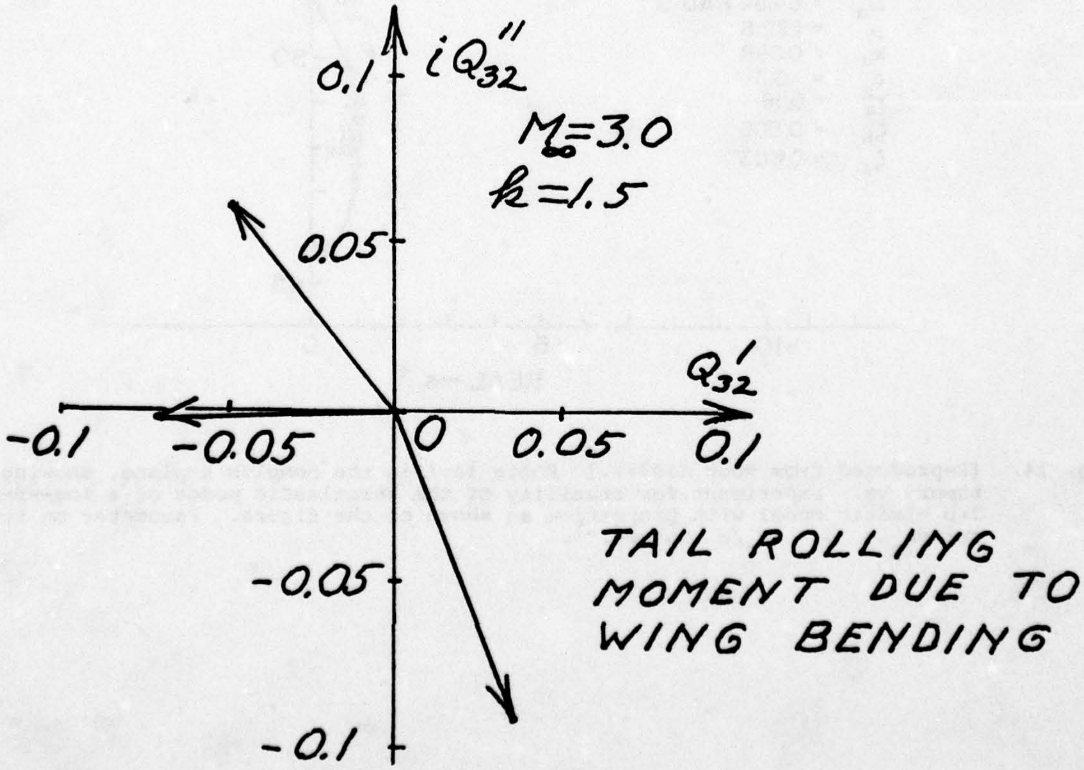

Fig. 13. Polar plot of tail rolling moment due to antisymmetrical wing bending oscillation, at $M_\infty = 3.0$ and $k = 1.5$, for AGARD wing-tail combination. Results of three theories are shown from Table 8 of Rodden (1976a) and Tseng & Morino (1976).

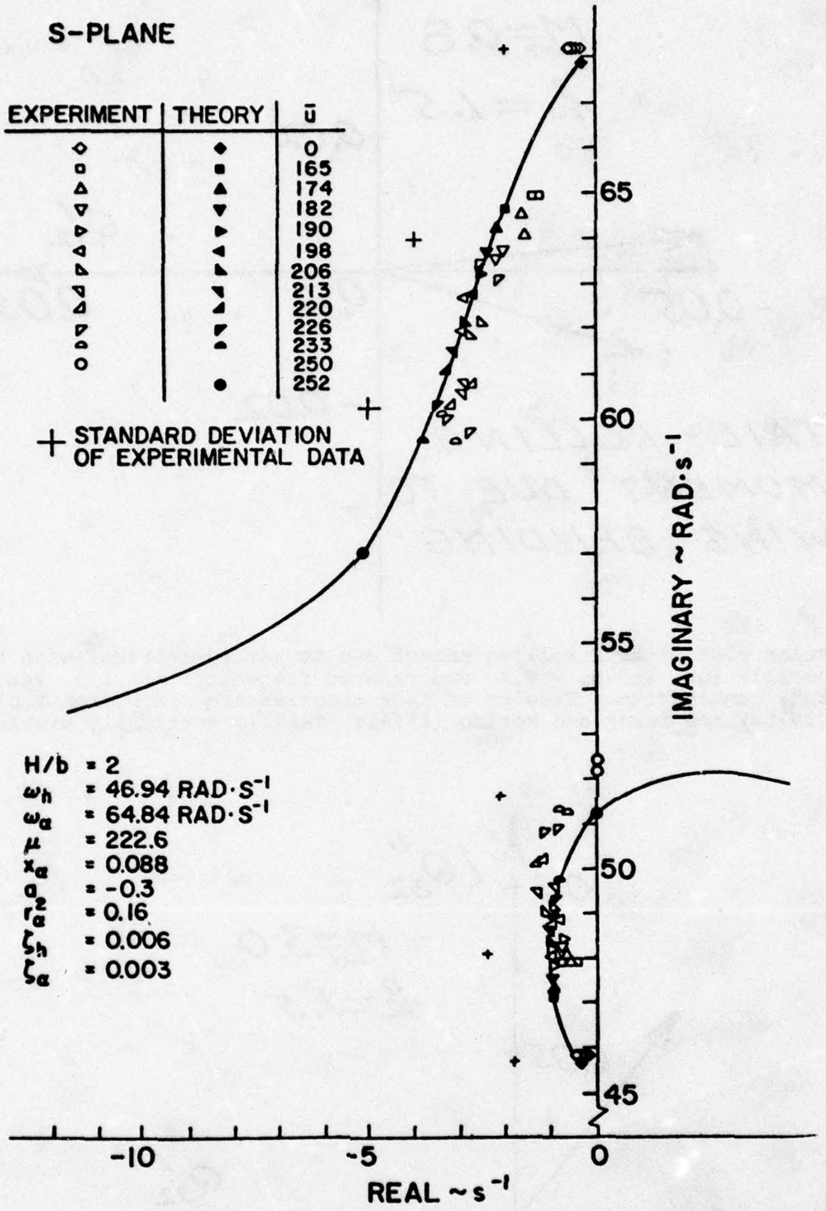

Fig. 14. [Reproduced from Rock (1977).] Roots loci in the complex s-plane, showing theory vs. experiment for stability of the aeroelastic modes of a low-speed, 2-D elastic model with properties as shown on the figure. Parameter on the curves is $\bar{u} = 2U_\infty/c$ in sec.$^{-1}$.

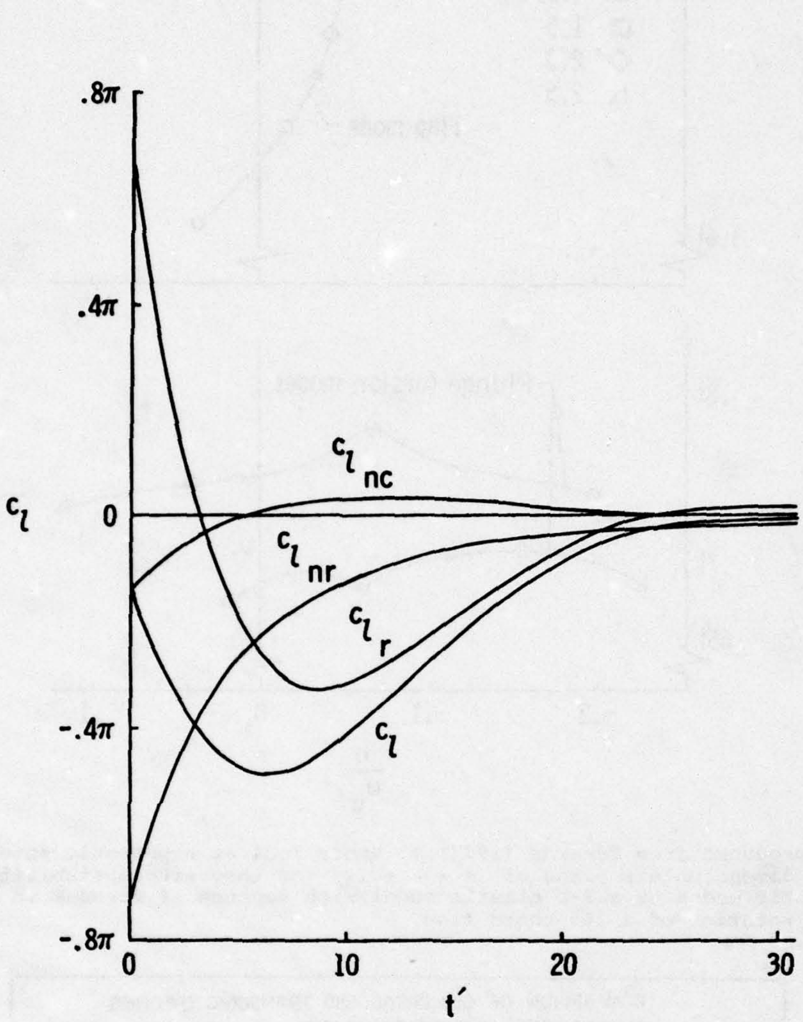

Fig. 15. [Reproduced from Edwards (1977).] Plot vs. dimensionless time $t' = 2U_\infty t/c$ of the coefficient of lift on a 2-D airfoil at $M_\infty = 0$, performing a plunging motion according to Eqs. (34)-(35). Text describes the decomposition of $c_\ell(t')$ into various parts.

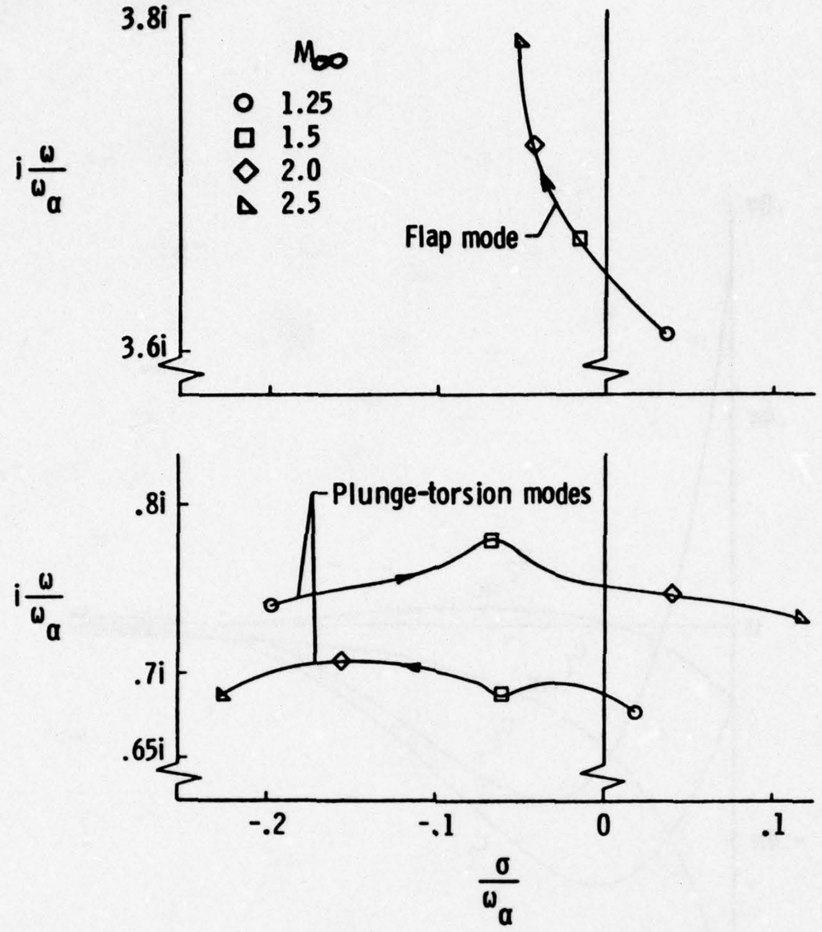

Fig. 16. [Reproduced from Edwards (1977).] Roots loci at supersonic speeds, plotted in the dimensionless plane of $s = \sigma + i\omega$, for theoreitcal stability of the aeroelastic modes of a 2-D elastic model with degrees of freedom in pitch, plunge and rotation of a 20%-chord flap.

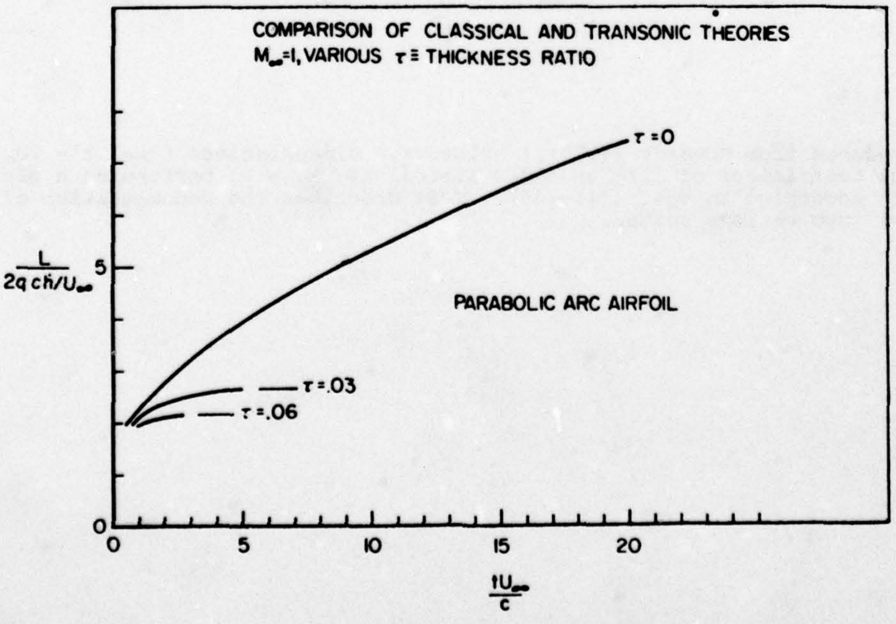

Fig. 17. [Reproduced from Fig. 7 of Dowell (1977).] Indicial growth of dimensionless lift, on 2-D airfoils at $M_\infty = 1$, following start of a constant plunging velocity h. Values for two finite thickness ratios are compared with linearized theory ($\tau = 0$).

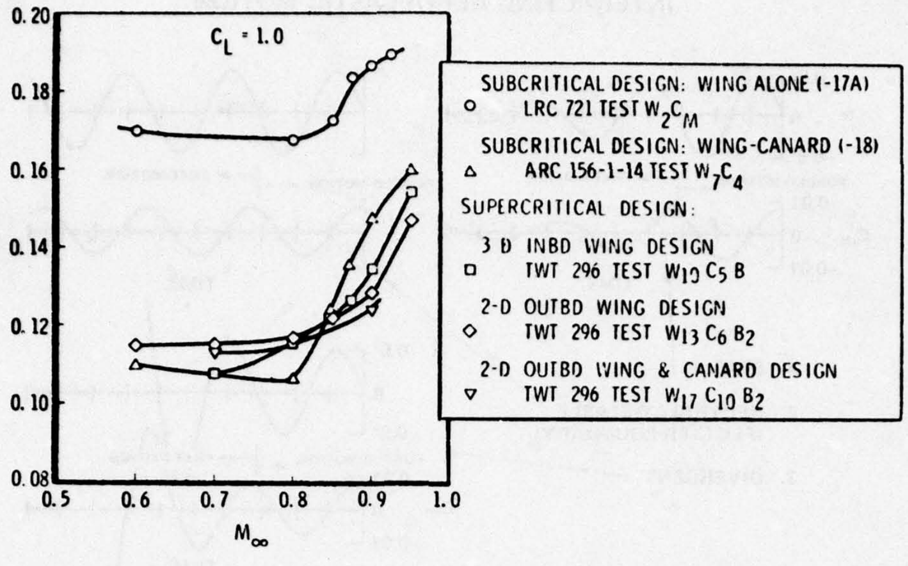

Fig. 18. Plot of drag coefficient C_D at $C_L = 1.0$ *vs.* M_∞ for various versions of the HIMAT vehicle. See text and Gingrich *et al.* (1977) for details.

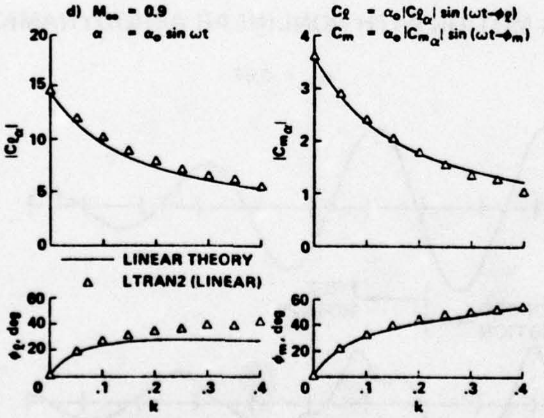

d) $M_\infty = 0.9$.

Fig. 19. [Reproduced from Ballhaus and Goorjian (1977b).] Magnitudes and Phase angles of lift and midchord pitching moment on a thin plate, per unit pitching oscillation at reduced frequency k and $M_\infty = 0.9$. Linearized theory (solid line) is compared with C.F.D. calculations (triangles).

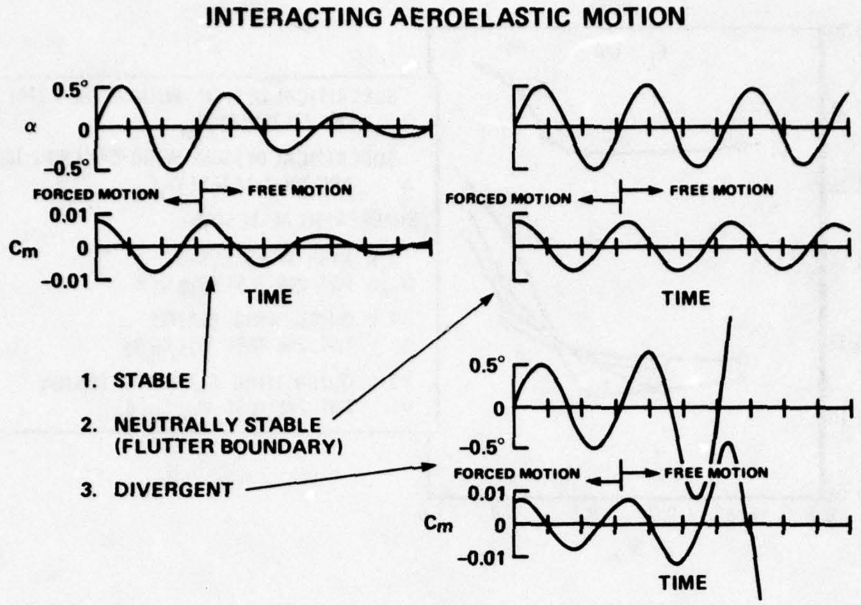

Fig. 20. [Reproduced from Ballhaus and Goorjian (1977a).] Response to initially forced oscillation in pitch at amplitude 0.5° of an elastically restrained 2-D airfoil at $M_\infty = 0.88$. Three values of rotational damping are represented; see text and reference for details.

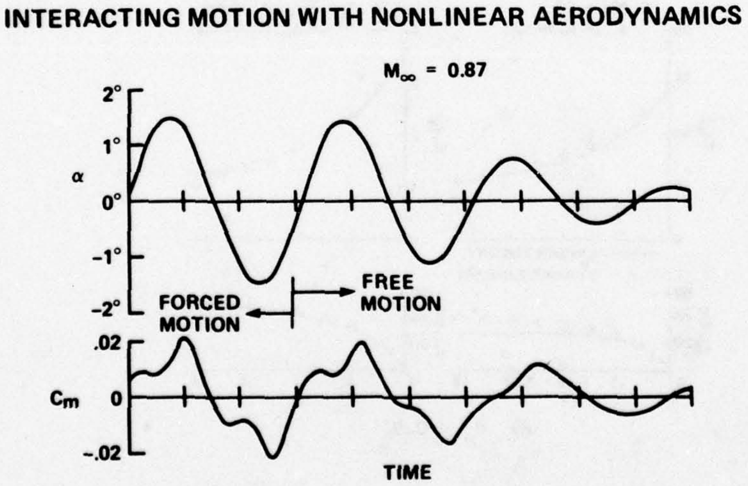

Fig. 21. [Reproduced from Ballhaus and Goorjian (1977a).] Response at $M_\infty = 0.77$ for same airfoil as Fig. 20, except that initial forcing amplitude is 1.5°.

THREE DIMENSIONAL STEADY AND UNSTEADY ASYMMETRIC FLOW PAST WINGS OF ARBITRARY PLANFORMS

by

Kandil*, O. A., Atta**, E. H. and Nayfeh***, A. H.

Department of Engineering Science and Mechanics
Virginia Polytechnic Institute and State University
Blacksburg, Virginia 24061

SUMMARY

The nonlinear-discrete vortex method has been extended to treat the problem of asymmetric flows past a wing with leading-edge separation, including steady and unsteady flows. The problem is formulated in terms of a body-fixed frame of reference and the nonlinear-discrete vortex method is modified accordingly. Although the method is general, only examples of flows past delta wings are presented due to the availability of experimental data as well as approximate theories. Comparison of our results with the experimental results of Harvey for a delta wing undergoing a steady rolling motion at zero angle of attack demonstrate the superiority of the present method over existing approximate theories in obtaining highly accurate loads. Numerical results for yawed wings at large angles of attack are also presented. In all cases, total-load coefficients, pressure distributions and shapes of the free-vortex sheets are shown.

LIST OF SYMBOLS

AR	aspect ratio
$b(x)$	local half span
C_x	rolling-moment coefficient
C_p	pressure coefficient
ΔC_p	net pressure coefficient ($C_{p_1} - C_{p_2}$)
c_r	root chord
Δc_r	winglet root chord, a characteristic length
$\bar{e}_\infty$	unit vector in the direction of the freestream velocity
$\bar{i},\bar{j},\bar{k}$	unit vectors of wing-fixed frame of reference
ℓ	length of a vortex segment
$\underline{n}$	total number of vortex segments of the model
$\bar{n}_b$	unit normal to the wing surface
$\bar{n}_w$	unit normal to the wake surface
$\bar{r}_j$	position vector of a field point
$S(\bar{r})$	wing surface
t	dimensionless time
$\bar{U}_\infty$	freestream velocity
$w(\bar{r},t)$	wake surface
x,y,z	wing-fixed frame of reference
$\alpha,\dot{\alpha}$	angle of attack and rate of pitch
$\beta,\dot{\beta}$	angle of yaw and rate of yaw
$\gamma,\dot{\gamma}$	angle of roll and rate of roll
$\bar{\omega}$	angular velocity of wing
Ω	frequency of rolling velocity
ϕ	disturbance velocity potential

Subscripts

i	source point
j	field point
k	time-step number
LE	leading edge
TE	trailing edge
ζ	tangent

I. INTRODUCTION

In recent years, development of analytical and numerical methods for predicting the aerodynamic characteristics of wings exhibiting leading-edge and/or wing-tip separation has received considerable attention. The literature contains several analytical methods

---

* Assistant Professor
** Graduate Research Assistant
*** University Distinguished Professor

which are based on simplifying assumptions. These include the assumption that the flow is conical and the assumption that the axial gradients are much smaller than the lateral gradients of the flow properties (slender-body theory). These assumptions represent inaccurate modelling of the full three-dimensional flow and violate the trailing-edge Kutta condition. Methods of this type were presented by Brown and Michael[1], Mangler and Smith[2] and Smith[3].

With the advent of high speed computers, new techniques which avoid these simplifying assumptions were developed. The nonlinear, discrete-vortex technique is among those successful techniques capable of calculating full three-dimensional flows. With this technique, the exact governing equation and the corresponding boundary conditions are satisfied and hence the solution of the inviscid problem is exact in that sense. It is not restricted by the shape of the wing planform or the range of angle of attack as long as vortex breakdown does not occur in the vicinity of the wing (stall phenomenon of wings of low-aspect ratio). However, the separation line is assumed to be known a priori along the sharp edges of the wing. Methods of this type were developed for steady symmetric flows by Belotserkovskii[4], Rehbach[5,6], Kandil[7], Kandil, Mook and Nayfeh[8-11].

Due to the accuracy and simplicity of the nonlinear discrete-vortex technique, it was extended to treat unsteady symmetric flows by Belotserkovskii and Nisht[12], Atta[13], Atta, Kandil, Mook and Nayfeh[14,15]. The source of unsteadiness in the flow may be general, e.g. a sudden translational acceleration of the wing[12], a gust wind which changes the wing angle of attack[13,14], or an oscillatory pitching motion of the wing[15]. The method is characterized by its capability of obtaining the transient as well as the steady-state aerodynamic characteristics of the wing. The technique was also extended by Kandil, Mook, and Nayfeh[16] to treat steady asymmetric flows past a large aspect-ratio rectangular wing. This case is a simulation of the problem of aerodynamic interference which arises when a small aircraft penetrates the wake of a large aircraft. Although the authors didn't account for the wing-tip separation of the trailing wing (due to its large aspect ratio), they did account for the wing-tip separation of the leading wing.

In the present paper, this technique is applied to steady and unsteady asymmetric flows past highly swept-back wings with sharp-edges. Delta wings are chosen as numerical examples due to the availability of experimental and theoretical results. Another reason for this choice is that it represents a severe numerical test of the technique owing to the presence of the vortical spiral cones which emanate from the leading edges and extend over a large portion of the wing surface. Moreover, the free-vortex surfaces are represented by a series of segmented vortex lines which approach the bound-vortex lattice representing the wing surface during the development of the numerical solution. Hence, strong singularities may arise due to the interaction of close vortex lines and therefore safeguards must be imposed to eliminate such singularities.

The problem of steady asymmetric flows was treated earlier by Pullin[17], Hanin and Mishne[18], Jones[19], and Cohen and Nimri[20]. Specifically, the steady flow past a yawed slender delta wing was considered in references 17 and 19 while the flow past a slender delta wing rolling steadily was considered in references 18 and 20. These theories are based primarily on the approximations of slender-body theory. The method of Brown and Michael was extended for the rolling wing[18,20] while the method of Mangler and Smith and the improved method of Smith were extended for the yawed wing[17,19].

Therefore, with these approximations as well as the simplified approximate modelling of the vortex sheets shed from the leading edges, one may expect substantial differences between the predicted and the experimental results. In fact, in all asymmetric results of these theories substantial errors exist in predicting the suction peak of the pressure near the leading edges. This was the case on the receding face of a rolling delta wing at zero angle of attack as reported in references 18 and 20. For the case of a yawed wing at high angle of attack, large errors were reported in predicting the suction peak of the pressure on the windward side of the wing[17,19]. In the latter case the errors were attributed to the substantial secondary separation which develops due to the adverse pressure gradients on the windward side of the wing.

From our point of view, this is only one portion of the cause because as it is well-known the problem of secondary separation is a viscous phenomenon and it cannot be treated by an inviscid model. The other portion of the cause is in fact the modelling of the separated flow and the slender-body assumption . Moreover, on the leeward side of the wing, the core of the primary vortex moves outboard as the angle of yaw is increased. Hence the suction peak on this side disappears and so does the adverse pressure gradients. Thus, secondary separation diminishes and one can expect an inviscid three-dimensional model to yield highly accurate results on the leeward side.

On the experimental side, Fink[21] and Harvey[22] considered steady flows over yawed slender-delta wings. Later, Harvey[23] considered flows over a steadily rolling delta wing. Pressure distributions, local rolling-moment coefficients, local normal-force coefficients, total-load coefficients and positions of the vortex cores were reported in these experiments. These data are used by many investigators for checking the accuracy of their theories. In the present paper, we also consider the same data to check our results for steady asymmetric flows. We also compare our results with available approximate theories. The method is also extended to the problem of unsteady asymmetric flows past a rolling wing.

II. FORMULATION OF THE PROBLEM

We consider a thin delta wing in a uniform stream and let $\overline{U}_\infty$ be the free stream velocity and oxyz be a wing-fixed frame of reference. The wing edges lie in the xy-plane, the x-axis bisects its apex angle and the xz-plane is its plane of symmetry. Euler's angles α, β and γ are used to define the angle of attack, the angle of yaw and the angle of roll of the wing, respectively, see Figure 1. To construct these angles in this order, we start from a position where $\overline{U}_\infty$ is parallel to the x-axis and successively allow for the positive rotations α, β, γ about the y, z, and x axes, respectively. The unit vector $\overline{e}_\infty$ in the direction of the freestream velocity is expressed in terms of these angles and the base unit vectors of the fixed-frame of reference by

$$\overline{e}_\infty = \cos\alpha \cos\beta \overline{i} + (\sin\alpha \sin\gamma - \cos\alpha \sin\beta \cos\gamma)\overline{j} + (\sin\alpha \cos\gamma + \cos\alpha \sin\beta \sin\gamma)\overline{k} \quad (1)$$

Next, we assume that the wing is rotating with an angular velocity $\overline{\omega}$ which can be expressed in terms of Euler's angles and their rates of change as

$$\begin{aligned} \overline{\omega} &= \omega_x \overline{i} + \omega_y \overline{j} + \omega_z \overline{k} \\ &= (\dot{\alpha} \sin\beta + \dot{\gamma})\overline{i} + (\dot{\alpha} \cos\beta \cos\gamma + \dot{\beta} \sin\gamma)\overline{j} + (-\dot{\alpha} \cos\beta \sin\gamma + \dot{\beta} \cos\gamma)\overline{k} \end{aligned} \quad (2)$$

The fluid flow is assumed to be ideal. The assumption that the wing edges are sharp fixes the separation lines along these edges. Vorticity is shed from these edges in the form of free surfaces of tangential discontinuity (free-vortex sheets). Moreover, the flow is assumed to be irrotational in the region R exterior to the wing and its free-vortex sheets. Accordingly, the flow in R is governed by Laplace's equation

$$\nabla^2 \phi = 0 \quad (3)$$

where $\phi(\overline{r},t)$ is the disturbance potential. On the boundary ∂R, ϕ satisfies the following boundary conditions. The flow must be tangent to the wing surface; that is,

$$(\overline{e}_\infty + \nabla\phi - \overline{\omega} \times \overline{r}) \cdot \overline{n}_b = 0 \qquad \text{on } S(\overline{r}) = 0 \quad (4)$$

where $\overline{n}_b = \nabla S/|\nabla S|$ is the unit normal to the wing surface S. The pressure is continuous and no flow exists across the free-vortex sheets; these dynamic and kinematic conditions yield

$$\Delta C_p = C_{p_1} - C_{p_2} = (\nabla\phi_1 - \nabla\phi_2) \cdot [2(\overline{\omega} \times \overline{r} - \overline{e}_\infty) - \nabla\phi_1 - \nabla\phi_2] - 2 \frac{\partial}{\partial t} (\phi_1 - \phi_2) = 0$$

$$\text{on } w(\overline{r},t) = 0 \quad (5)$$

$$(\overline{e}_\infty + \nabla\phi - \overline{\omega} \times \overline{r}) \cdot \overline{n}_w - \frac{1}{|\nabla w|} \frac{\partial w}{\partial t} = 0 \qquad \text{on } w(\overline{r},t) = 0 \quad (6)$$

where the subscripts 1 and 2 refer to the upper and lower surfaces of the free-vortex sheets, respectively, and $\overline{n}_w = \nabla w/|\nabla w|$ is the unit normal to the free-vortex sheets. The Kutta condition must be satisfied along the edges of separation, that is the flow leaves smoothly off the edges and the pressure is continuous across these edges. These are expressed by

$$(\overline{e}_\infty + \nabla\phi - \overline{\omega} \times \overline{r}) \cdot \overline{n}_b = 0 \qquad \text{on } S|_{TE,LE} = 0 \quad (7)$$

and

$$\Delta C_p = (\nabla\phi_1 - \nabla\phi_2) \cdot [2(\overline{\omega} \times \overline{r} - \overline{e}_\infty) - \nabla\phi_1 - \nabla\phi_2] - 2 \frac{\partial}{\partial t} (\phi_1 - \phi_2) = 0$$

$$\text{on } S|_{TE,LE} = 0 \quad (8)$$

Far from the wing and its free-vortex sheets, the disturbance velocity vanishes; that is,

$$\nabla\phi \to 0 \quad (9)$$

The complexity of the problem stems from the boundary conditions (5) and (6). These conditions are to be satisfied at the free-vortex sheets $w(\overline{r},t)$ which are unknowns of the problem. In fact, both $w(\overline{r},t)$ and $\phi(\overline{r},t)$ are dependent upon each other and hence a numerical solution is fruitful for this situation. In the next section, we discuss the method of solution of the steady problem and describe its extension to the unsteady problem.

III. METHOD OF SOLUTION

1. Nonlinear Discrete-Vortex Method for the Steady Problem

The method of solution of the steady asymmetric flow is obtained by generalizing the approach of Kandil[7] and Kandil, Mook and Nayfeh[8] for the steady symmetric flow. For the sake of completeness, we outline the basic approach and then describe the generalization to the current problem.

In the basic approach of the lifting problem, a lifting surface may be replaced by a bound-vortex sheet with unknown strength. The velocity potential of this sheet satisfies equation (3) in R and the boundary condition (9). Furthermore, this continuous vortex sheet can be accurately approximated by a lattice of bound-vortex filaments with unknown circulations (bound-vortex lattice) provided it is constructed within certain rules. This point will be undertaken later in detail in the next section.

Along the edges of separation no bound-vortex segments are placed; otherwise the Kutta condition, equation (8), will be partially violated. At these edges, the starting vortex is shed and convected with the local velocity and in a steady flow no more vortices are shed thereafter. According to the theorem of spatial conservation of circulation (Kelvin's theorem), the ends of the bound-vortex lattice lines closest to the edges are connected to vortex lines which extend downstream to infinity where the starting vortex is assumed to be. These vortex lines are called free-vortex lines and represent the free-vortex sheet $w(\bar{r})$. So far, the model satisfies equations (3) and (9) and partially satisfies the Kutta condition.

For steady symmetric flows, equations (4) - (8) immediately yield the corresponding boundary condititons upon setting $\bar{\omega} = 0$ and dropping the time dependent terms while equation (1) yields the corresponding free stream velocity upon setting $\beta = \gamma = 0$. With the discrete method, the resulting equations are satisfied at certain points on the known surface $S(\bar{r})$ and the still unknown surface $w(\bar{r})$. This is achieved by successive iterative cycles. In the first step of the cycle, we satisfy the flow tangency condition on $S(\bar{r})$ with an assumed surface $w(\bar{r})$ to find a circulation distribution Γ. In the next step, we satisfy the kinematic and dynamic boundary conditions on $w(\bar{r})$ by using the Γ distribtuion and find $w(\bar{r})$. These cycles are repeated until the Γ distribution or $w(\bar{r})$ do not change within certain prescribed tolerances. The Kutta condition is then satisfied atuomatically.

For steady asymmetric flows, equations (4) - (8) also yield the corresponding boundary conditions upon dropping the time dependent terms. Now, to obtain a steady flow it is a necessary condition, although not sufficient, that the angular velocity of the wing $\bar{\omega}$ be uniform. Moreover, the magnitude and direction of $\bar{\omega}$ as well as the orientation of the wing with respect to $\bar{e}_\infty$ (as defined by α,β,γ) must have values such that no time-dependent disturbance is generated in the flow. For a thin flat wing with $\bar{\omega} = 0$ $(\dot{\alpha} = \dot{\beta} = \dot{\gamma} = 0)$, nontrivial, steady, asymmetric flows occur in three cases. First, $\gamma = 0$ and the free stream velocity is given by

$$\bar{e}_\infty = \cos\alpha \cos\beta \ \bar{i} - \cos\alpha \sin\beta \ \bar{j} + \sin\alpha \ \bar{k} \qquad (10a)$$

This case represents the steady flow past a yawed wing at an angle of attack. It was considered in references 17, 19, and 22. Second, $\beta = 0$ and the free stream velocity is given by

$$\bar{e}_\infty = \cos\alpha \ \bar{i} + \sin\alpha \sin\gamma \ \bar{j} + \sin\alpha \cos\gamma \ \bar{k} \qquad (10b)$$

This case represents a steady flow past a wing at a banking angle and an angle of attack. Third, $\alpha = 0$ and the free stream velocity is given by

$$\bar{e}_\infty = \cos\beta \ \bar{i} - \sin\beta \cos\gamma \ \bar{j} + \sin\beta \sin\gamma \ \bar{k} \qquad (10c)$$

This case represents a steady flow past a yawed wing at a banking angle. Fourth, when all the angles α,β, and γ are different from zero and the free stream velocity is given by equation (1). All the cases considered above can be treated by the vortex lattice method as reported in references 7-10.

When the angular velocity $\bar{\omega}$ is not equal to zero, there are still two cases where the flow is steady. First, $\alpha = \beta = \dot{\alpha} = \dot{\beta} = 0$, $\bar{\omega} = \dot{\gamma}\bar{i}$ and the free stream velocity is given by

$$\bar{e}_\infty = \bar{i} \qquad (11a)$$

This case represents a steadily rolling wing about its x-axis at a zero angle of attack. It was considered in references 18, 20, and 23. Second, $\beta = \gamma = \dot{\alpha} = 0$, $\omega = \dot{\gamma}\bar{i} + \dot{\beta}\bar{k}$, $\tan\alpha = \dot{\beta}/\dot{\gamma}$ and the free stream velocity is given by

$$\bar{e}_\infty = \cos\alpha \ \bar{i} + \sin\alpha \ \bar{k} \qquad (11b)$$

This case represents a steadily rolling wing about the wind axis at an angle of attack. We can easily see that the first case is a special case of the present one. This case was considered in reference 20.

When applying the steady version of the discrete-vortex method to the last two cases, one must use a wing-fixed frame of reference; otherwise, the flow would no longer be steady.

2. Nonlinear Discrete-Vortex Method for the Unsteady-Flow Problem

The method of solution for unsteady asymmetric flows is obtained by generalizing the approach of Atta[13] and Atta, Kandil, Mook and Nayfeh[14,15] for unsteady symmetric flows. In these references, a space-fixed frame of reference was used, the wing was taken to be fixed in the flow, and the source of unsteadiness was introduced through the free stream velocity. In the present paper, a wing-fixed frame of reference is used, the wing is rotating at a nonuniform angular velocity $\bar{\omega}(t)$, and the free stream velocity is uniform.

In either case, the bound circulation around the wing continuously changes and this is accompanied by a continuous process of formation and shedding of vortexes from the edges of separation to restore the smoothness of the flow at the edges (Kutta condition). Within any infinitesimal time step, the change in the bound circulation around the wing is met by the formation of an infinitesimal vortex strip emanating from an edge of separation which has a strength of equal and opposite sense to the change of the bound circulation. This shed vortex is convected downstream with the local particle velocity. Hence a vortex sheet is continuously growing downstream as long as the unsteadiness of the flow prevails.

Now if the continuous motion of the wing is discretized into a series of impulsive changes occuring at discrete time steps, the continuously growing vortex sheet can be replaced by a growing vortex lattice in the wake. This is the salient difference between the unsteady and steady flow models. At each time step, we solve the problem using a method similar to that of the steady flow. Here, the boundary conditions, equations (4) - (8), must be satisfied at each time step. In the next section, we consider in detail the implementation of this method.

IV. IMPLEMENTATION OF THE METHOD

1. Construction of the Discrete-Vortex Model

In Figure 2, we show how the discrete-vortex model is constructed for a delta wing. Although the example discussed here is for a thin, flat, delta wing, the method is general and is not restricted by the geometrical parameters of the wing; e.g. camber, aspect or thickness ratios or wing planform.

The first step is to divide the wing into rectangular and cropped-delta winglets as shown by the dashed lines in Figure 2.a. A rectangular winglet is aerodynamically represented by a spanwise bound-vortex segment of constant circulation Γ_1. This segment is placed at the quarter-chord length of the winglet (the chord length of the rectangular winglet is the characteristic length of the problem). In addition a control point is placed at the three quarter-chord length. The choice of these positions is suggested by thin airfoil theory[24]. It can be shown that the bound-vortex sheet representing the two-dimensional flow around a flat plate at an angle of attack can be replaced by a point vortex of the same strength as that of the continuous vortex sheet under the following conditions: a) the point vortex is placed at the quarter-chord length and b) the flow tangency condition is enforced at only one point at the three-quarter-chord length.

On the other hand, a cropped-delta winglet is aerodynamically represented by a bound-vortex segment of constant circulation. This vortex segment is directed along the perpendicular from the midpoint of the winglet root chord to its leading edge. With this choice it can be seen that the vorticity of this vortex segment does not have a component along the leading edge and hence the Kutta condition is approximately satisfied along this edge.

Chordwise bound-vortex segments arise due to the differences in the strengths of the neighboring spanwise, bound-vortex segments. In this way, a bound-vortex lattice which replaces the continuous, bound-vortex sheet is constructed. The model is completed by adding free-vortex lines, representing the continuous free-vortex sheets at the ends of the bound-vortex lattice along the edges of separation - the leading and trailing edges. Each line is divided into a series of small, straight segments (near-wake region) and one semi-infinite vortex line (far-wake region). The upstream end of each segment represents a control point of the wake surface where the kinematic and dynamic boundary conditions are satisfied. The initial positions and shapes of these lines are prescribed. The resulting model is shown in Figure 2b. This model has an unknown circulation distribution and a wake that can be deformed to satisfy the boundary conditions.

The model described above is used to solve the steady-flow problem by satisfying the corresponding boundary conditions given in Section III.1. On the other hand, if the problem under consideration is for an unsteady flow which starts from a steady flow situation, then the solution of the steady-flow problem serves as an initial condition to the unsteady problem. Furthermore, if the problem under consideration is for an unsteady flow which arises from an impulsive motion of the wing, then the initial condition corresponds also to the solution of the model given above, but with the wakes removed from the model.

2. Calculation of the Velocity Field

To satisfy the boundary conditions on the wing and its wake and to calculate the surface pressure distribution, one needs an accurate method to calculate the velocity at any field point $\overline{r}_j$ at any time step t_k. If the field point is off the wing and its wake, then the velocity is given by

$$\overline{V}(\overline{r}_j,t_k) = \nabla\phi(\overline{r}_j,t_k) + \overline{e}_\infty - \overline{\omega}(t_k) \times \overline{r}_j \tag{12}$$

where

$$\nabla\phi(\overline{r}_j,t_k) = \sum_i^{n(t_k)} [\Gamma_i(t_k)/4\pi h_i(\overline{r}_j,t_k)][\cos\theta_{1i}(\overline{r}_j,t_k) - \cos\theta_{2i}(\overline{r}_j,t_k)]\overline{e}_i(\overline{r}_j,t_k) \tag{13}$$

is the induced velocity from all the vortex segments of the model. The parameters on the right-hand side of equation (13) are those of Biot-Savart's law[24]. The number of vortex segments $n(t_k)$ is a function of the time step t_k due to the growing vortex lattice in the wake in the unsteady-flow problem. To avoid extremely large velocities, artificial viscosity is introduced (as in reference 25) in the form of an exponential multiplier which causes the induced velocity to approach zero as the vortex is approached.

When the field point is on the wing surface or on the wake surface, one has to account for the induced tangential velocity due to the local strength of the vortex sheet. In Figure 2.c, we show the parameters involved in calculating the components of the induced tangential velocity in the x and y directions at a point p for a quadrilateral vortex element in the xy-plane. With linear interpolation, it is easy to show that these components are given by

$$\overline{V}_{\zeta x}(z = {}^{0^+}_{0^-}) = \pm (1/2\, \ell_1^2)[\Gamma_1(x_1 + \ell_1 - x) + \Gamma_3(x - x_1)]\overline{e}_1 \tag{14a}$$

$$\overline{V}_{\zeta y}(z = {}^{0^+}_{0^-}) = \mp (1/2\, \ell_2^2)[\Gamma_4(y_1 + \ell_2 - y) + \Gamma_2(y - y_1)]\overline{e}_2 \tag{14b}$$

where the arguments $z = 0^+$ and $z = 0^-$ correspond to the upper surface and the lower surface of the wing, respectively. Equations (14) must be added to equation (12) if one is to calculate the pressure distribution on the upper and lower surfaces by using Bernoulli's equation. Extension of equations (14) to a general, quadrilateral vortex element is straightforward.

3. Implementation of the Boundary Conditions

a. Steady-Flow Problem

The boundary conditions on the wing surface $S(\overline{r})$ and the wake surface $w(\overline{r})$ are satisfied by an iterative process. To initiate the iterative process, one needs to prescribe an initial geometry of the wake surface. It has been found from several numerical tests that the number of iterative cycles required to achieve the solution can be reduced by an appropriate choice of the initial geometry. This initial geometry depends on the problem under consideration and thus it varies from one problem to the other.

For instance, the number of iterative cycles for the steady, symmetric-flow problem is reduced by about 20% when the free-vortex lines emanating from the leading edge are prescribed to be straight lines pitched at one half the wing angle of attack. In addition, those lines emanating from the trailing edge are straight lines pitched at one third the wing angle of attack. Here, the comparison is made with respect to the number of iterative cycles required for the same problem when all the free-vortex lines are prescribed to be also straight lines but are pitched at an angle equal to the wing angle of attack.

In the case of a steadily, rolling wing at zero angle of attack, an appropriate initial guess is found to be related to an angle $\theta(\overline{r}) = \pm \frac{1}{2} \tan^{-1}|\overline{\omega}\times\overline{r}|/U_\infty$. Here, we specify the free-vortex lines emanating from the edges of the advancing side to be straight lines pitched at the angle $+\theta$ while those emanating from the edges of the receding side to be straight lines pitched at the angle $-\theta$.

Next, the flow-tangency condition and the spatial conservation of circulation are applied at the control points and node points, respectively, of the bound-vortex lattice. Thus, we obtain a set of linear algebric equations[11] which yields the circulation distribution Γ_i.

With the circulation distribution known, the kinematic and dynamic boundary conditions at the control points of the free-vortex lines are satisfied. For steady flows, these two conditions are combined into a simple condition in which we require that each vortex segment in the wake be aligned with the local velocity at its upstream end (a control point on the wake surface). This means that each vortex segment is a segment of a streamline (kinematic condition). Moreover, it means that the force on each vortex segment is zero according to Kutta-Joukowski theorem in the small (dynamic condition). This process is carried out by calculating the downstream end of each vortex segment according to

$$\bar{r}_{j+1} = \bar{r}_j + \bar{V}_j \ell_j / |\bar{V}_j| \qquad (15)$$

where $\bar{r}_j$ and $\bar{r}_{j+1}$ are the position vectors of the upstream and downstream ends, respectively, ℓ_j is the segment length and $\bar{V}_k$ is the velocity at its upstream point [equation (1) for steady flows].

The iteration scheme moves back and forth from the control points of the bound-vortex lattice to the control points of the free-vortex lines until convergence is achieved. We consider the iteration scheme converged when the variation in the circulation distribution or the displacement of the downstream ends of the free-vortex segment between two successive iteration cycles does not exceed a certain prescribed tolerance. Once convergence is achieved, we calculate the pressure distribution and the total load coefficients.

b. Unsteady-Flow Problem

Here, we consider the problem of unsteady flow which starts from a steady flow situation. We recall from Section III.2 that the continuous motion of the wing is discretized into a series of impulsive changes occuring at discrete time steps. At each time step t_k, a set of starting vortices develops along the edges of separation and are shed with the local velocities to restore the smoothness of flow at the edges (Kutta condition). In the same time, the starting vortices shed in the wake at earlier time steps are convected downstream with the local velocities without changing their strengths. This process satisfies the kinematic condition on the wake (a wake element moves along the direction of the local velocity) and it also satisfies the dynamic condition on the wake (a wake element satisfies Kelvin-Helmholtz theorem).

The position of any shed vortex $\bar{r}_j$ at any time step t_k is determined by

$$\bar{r}_j(t_k) = \bar{r}_j(t_{k-1}) + (t_k - t_{k-1})\bar{V}_j(\bar{r}_j, t_{k-1}) \qquad (16)$$

where t_{k-1} is the preceding time step and $\bar{V}_j$ is given by equation (12). The strength of any newly shed vortex is related to the change in the bound circulation. Hence, with the positions of the shed vortices known from equation (16) and with the strength of the newly shed vortices given in terms of the change of the bound circulation, the flow tangency condition at the control points of the wing yields the unknown circulation distribution. To account for the error in equation (16) because of using the velocity $\bar{V}_j(\bar{r}_j, t_{k-1})$ at the preceding time step t_{k-1} rather than the current time step t_k, an iteration procedure similar to that of the steady-flow problem is performed. In this regard, an alternative equation was given by Summa[26].

In both the steady and unsteady flows, the only difference between the symmetric and asymmetric problems is the longer computational time required for the latter problem as compared to that of the former problem. In the former problem, we need only to use half the wing to obtain the solution because of the symmetry of the flow. In the latter problem, the whole wing must be used to obtain the solution.

4. Calculation of the Pressure Coefficients

The distribution of the pressure coefficient on the upper and lower surfaces of the wing is calculated by using Bernoulli's equation in terms of a wing-fixed frame of reference[27].

$$C_p(\bar{r}_j^{\pm}, t_k) = -[\bar{v}(\bar{r}_j^{\pm}, t_k)]^2 + 2\bar{v}(\bar{r}_j^{\pm}, t_k) \cdot [\bar{\omega}(t_k) \times \bar{r}_j - \bar{e}_\infty] - 2\,\frac{\partial\phi(\bar{r}_j, t_k)}{\partial t} \qquad (17)$$

where

$$\bar{v}(\bar{r}_j^{\pm}, t_k) = \nabla\phi(\bar{r}_j, t_k) + \bar{V}_{\zeta x}(\bar{r}_j^{\pm}, t_k) + \bar{V}_{\zeta y}(\bar{r}_j^{\pm}, t_k) \qquad (18)$$

$\bar{r}_j^{\pm}$ is the position vector of the control point, the positive and negative superscripts refer to the upper surface and lower surface of the wing, respectively, and $\nabla\phi$, $\bar{V}_{\zeta x}$ and $\bar{V}_{\zeta y}$ are given by equations (13), (14a) and (14b), respectively. The pressure is calculated at the control points of the bound-vortex lattice because these are the points where the flow tangency condition is enforced.

In the steady-flow problem, the last term of the right-hand side of equation (17) is zero and all the other terms are time independent. Hence, calculating the pressure on the upper and lower surfaces is straightforward. But in the unsteady-flow problem, we need to calculate this term if the pressure coefficient is required on each of the upper and lower surfaces. To calculate the local rate of change of the disturbance velocity potential, we need to know the velocity potential at this location at two successive time steps by integrating the velocity from an undisturbed position. Because of the long computational time involved, we only calculate the net pressure force on the wing in the unsteady-flow problem. However, calculation of the pressure distribution on the upper and lower surfaces is now under consideration because it is necessary for any boundary-layer calculations.

The net pressure coefficient is given by

$$\Delta C_p(\bar{r}_j,t_k) = 4[\bar{V}_{\zeta x}(\vec{r}_j^{\,+},t_k) + \bar{V}_{\zeta y}(\vec{r}_j^{\,+},t_k)] \cdot [\bar{\omega}(t_k) \times \bar{r}_j - \bar{e}_\infty - \nabla\phi(\bar{r}_j,t_k)]$$
$$- 2[\Gamma(\bar{r}_j,t_k) - \Gamma(\bar{r}_j,t_{k-1})/(t_k - t_{k-1})] \tag{19}$$

The total-load coefficients are obtained by integrating the net pressure coefficient on the wing.

V. NUMERICAL RESULTS

A computer code which accounts for the general formulation presented here is developed. The code can be used to solve steady, unsteady, symmetric or asymmetric flow problems. Typical results obtained with this code are presented in this section. The required computation time and convergence studies are discussed in references 7-11 and 13-16.

1. Steadily Rolling Wing at Zero Angle of Attack

In Figures 3-5 we show typical solutions of the free-vortex lines of a delta wing (AR = 0.7) at different rolling velocities 0.2, 0.4 and 0.6. In each figure, a three-dimensional view and a plan view are given. The traces of the helical vortex cones are indicated on the upper view which show that the cones are antisymmetric. The size of the cone increases and it rolls-up more rapidly with increasing the rolling velocity. This is in agreement with the experimental results[23].

Figure 6 shows the spanwise pressure distribution on the upper and lower surfaces at the chordwise station $x/c_r = 0.778$, the present results are compared with the experimental results of Harvey[23] and the theoretical models of references 18 and 20. A remarkable agreement can be seen between the present results and the experimental ones. The methods of references 18 and 20 obviously overestimate the suction pressure peak and this is attributed to the simplified representation of the separated flow.

2. Yawed Wing at an Angle of Attack

In Figures 7-12 we show the effect of the yaw angle on the free-vortex lines and pressure distributions of a delta wing (AR = 0.7, $\alpha = 15°$).

The plan views in Figures 7, 9 and 11 show that the size of vortex cone emanating from the windward side of the wing increases while the size of the cone from the leeward side decreases. The former cone moves inboard while the latter cone moves outboard.

The corresponding effect on the spanwise pressure distribution at the chordwise station $x/c_r = 0.395$ and comparisons with the results of Pullin[17] and the experimental results of Harvey[22] are given in Figures 8, 10 and 12. When the angle of yaw increases, the suction pressure peak on the windward side increases while that on the leeward side decreases. The present results are in a good agreement with the experimental ones. Pullin's results overestimates the suction peak on the windward side of the wing and it shows that the error increases with increasing the angle of yaw.

3. Unsteadily Rolling Wing at Zero Angle of Attack

In Figure 13 we show the free-vortex lines at three successive time steps for a delta wing undergoing an unsteady rolling motion given by $\omega_x = 0.6 + 0.1 \sin(\pi t/6)$. The starting vortices shed from the edges of separation and later convected downstream can be seen in each view.

Figure 14 shows the spanwise pressure distribution at the chordwise state $x/c_r = 0.65$ at different time steps. The variation of the rolling-moment coefficient C_x with the frequency of the sinusoidal variation of the rolling velocity Ω is given in Figure 15. In the initial time steps, we notice that the rolling-moment coefficient decreases as the frequency increases. Finally, the variation of the rolling-moment coefficient with the rate of roll is shown in Figure 16.

VI. CONCLUDING REMARKS

We have presented a general, nonlinear, discrete-vortex method for the lifting surfaces. The method is applied to delta wings undergoing different motions. The results are compared with several results of other investigators and with the experimental results of Harvey. They show that the present method provides accurate results which could not be obtained by the existing approximate methods. Moreover, the present method is not restricted by any geometrical parameter of the lifting surface. Moreover, it is exact because it is free from any small-disturbance assumption or any corresponding linearization.

REFERENCES

1. Brown, C. E. and Michael, W. H., "On Slender Delta Wings with Leading-Edge Separation," NACA Tech. Note 3430, April 1955.
2. Mangler, K. W. and Smith, J. H. B., "A Theory of the Flow Past a Slender Delta Wing with Leading-Edge Separation," Proc. Roy. Soc. Lond. A, 251, 1959, pp. 200-217
3. Smith, J. H. B., "Improved Calculations of Leading-Edge Separation from Slender Delta Wings," Proc. Roy. Soc. Lond. A, 306, 1968, pp. 67-90.
4. Belotserkovskii, S. M., "Calculation of the Flow Around Wings of Arbitrary Planform over a Wide Range of Angle of Attack," NASA TT F-12, 391, May 1969.
5. Rehbach, C., "Calculation of Flow Around Zero-Thickness Wings with Evolute Vortex Sheets," NASA TT F-15, 183, 1973.
6. Rehbach, C., "Numerical Investigation of Vortex Sheets Issuing from Separation Line Near the Leading Edge," NASA TT F-15, 530, 1974.
7. Kandil, O. A., "Prediction of the Steady Aerodynamic Loads on Lifting Surfaces Having Sharp-Edge Separation," Ph.D. Dissertation, Dept. of Engr. Sci. and Mechanics, Virginia Polytechnic Institute and State University, Dec. 1974.
8. Kandil, O. A., Mook, D. T. and Nayfeh, A. H., "Nonlinear Prediction of the Aerodynamic Loads on Lifting Surfaces," J. of Aircraft, Vol. 13, No. 1, January 1976, pp. 27-28.
9. Kandil, O. A., Mook, D. T. and Nayfeh, A. H., "Subsonic Loads on Wings Having Sharp Leading Edges and Tips," J. of Aircraft, Vol. 13, No. 1, January 1976, pp. 62-63.
10. Kandil, O. A., Mook, D. T. and Nayfeh, A. H., "New Convergence Criteria for the Vortex-Lattice Models of the Leading-Edge Separation," NASA SP-405, No. 16, May 1976, pp. 285-300.
11. Kandil, O. A., Mook, D. T. and Nayfeh, A. H., "A Numerical Technique for Computing Subsonic Flow Past Three Dimensional Canard-Wing Configurations with Edge Separation," AIAA Paper No. 77-1, January 1977.
12. Belotserkovskii, S. M. and Nisht, M. I., "Nonstationary Nonlinear Theory of a Thin Wing of Arbitrary Planform," Fluid Dyn. 9(4), 1974, pp. 583-589.
13. Atta, E. H., "Unsteady Flow Over Arbitrary Wing-Planforms Including Tip Separation," M.S. Thesis, Dept. of Engineering Science and Mechanics, Virginia Polytechnic Institute and State University, March 1976.
14. Atta, E. H., Kandil, O. A., Mook, D. T. and Nayfeh, A. H., "Unsteady Flow Past Wings Having Sharp-Edge Separation," NASA SP-405, No. 22, May 1976, pp. 407-418.
15. Atta, E. H. Kandil, O. A., Mook, D. T. and Nayfeh, A. H., Unsteady Aerodynamic Loads on Arbitrary Wings Including Wing-Tip and Leading-Edge Separation," AIAA Paper No. 77-156, January 1977.
16. Kandil, O. A., Mook, D. T. and Nayfeh, A. H., "Application of the Nonlinear Vortex-Lattice Concept to Aircraft-Interference Problems," Advances in Engineering Science, Vol. 4, NASA CP-2001, Nov. 1976, pp. 1321-1330.
17. Pullin, D. I., "Calculations of the Steady Conical Flow Past a Yawed Slender Delta Wing with Leading Edge Separation," Imperial College of Science and Technology, Lond., I.C. Aero Report 72-17, July 1972.
18. Hanin, M. and Mishne, D., "Flow About a Rolling Slender Wing with Leading Edge Separation," Israel Journal of Technology, Vol. 11, No. 3, 1973, pp. 131-136.
19. Jones, I. P., "Flow Separation From Yawed Delta Wings," Computers and Fluids, Vol. 3, 1975, pp. 155-177.
20 Cohen, M. J. and Nimri, D., "Aerodynamics of Slender Rolling Wings at Incidence in Separated Flow," AIAA Journal, Vol. 14, No. 7, July 1976, pp. 886-893.
21. Fink, P. T., "Some Early Experiments on Vortex Separations," British R & M No. 3489, 1967.
22. Harvey, J. K., "Some Measurements on a Yawed Slender Delta Wing with Leading Edge Separation," British ARC Report 20451, 1958.
23. Harvey, J. K., "A Study of the Flow Field Associated with Steadily-Rolling Slender Delta Wing," Journal of the Royal Aeronautical Society, Vol. 68, Feb. 1964, pp. 106-110.
24. Karamcheti, K. PRINCIPLES OF IDEAL-FLUID AERODYNAMICS. John Wiley and Sons, Inc., N.Y. 1966.
25. Yager, P. M., Holland, C. H., and Strand, T., "Modified Weissinger Lifting Surface Method for Calculating Aerodynamic Parameters of Arbitrary Wing-Canard Configurations," Air Vehicle Corporation, La Jolla, Calif., Rept. 354, August 1974.
26. Summa, J. M., "Potential Flow About Three-Dimensional Lifting Configurations with Application to Wings and Rotors," AIAA Paper No. 75-126, 1975.
27. Kochin, N. E., Kibel, I. A., Roze, N.V. THEORETICAL HYDRODYNAMICS, Interscience-Wiley, New York, 1964.

ACKNOWLEDGEMENT

This work was supported by the NASA Langley Research Center under Grant NGR 47-004-090, Dr. E. C. Yates, Monitor.

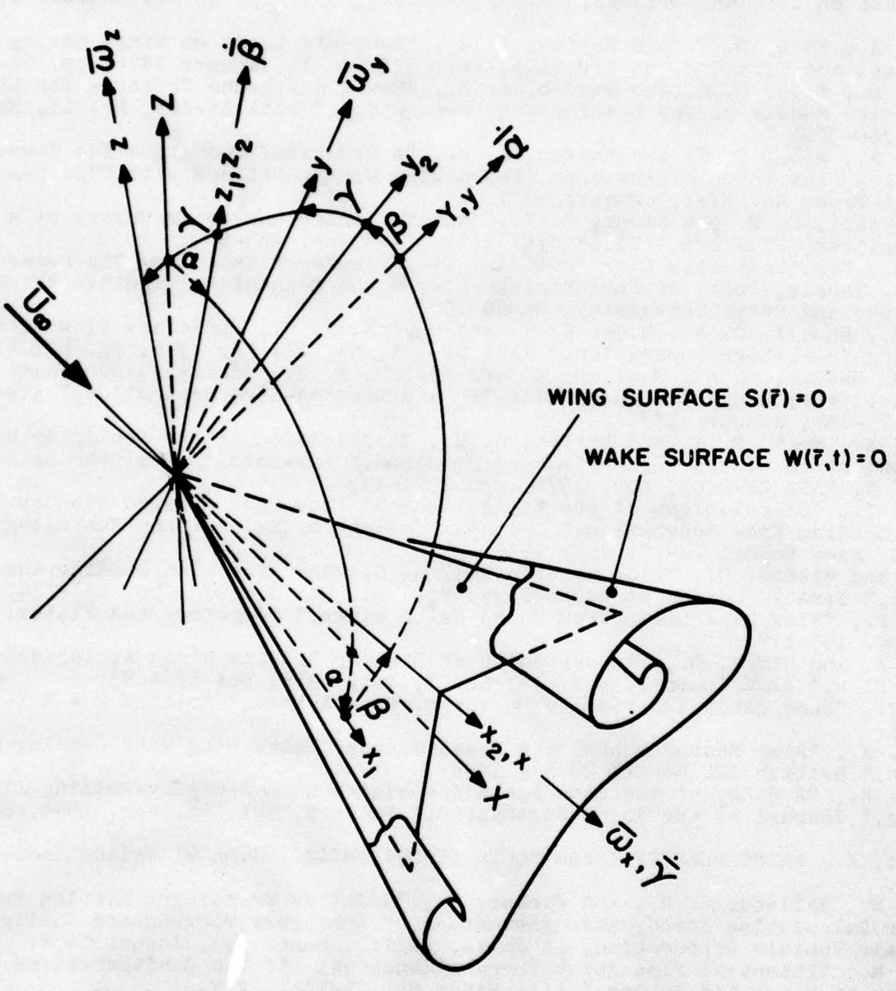

Fig. 1. Wing-fixed frame of reference (xyz) and Euler's Angles (α,β,γ).

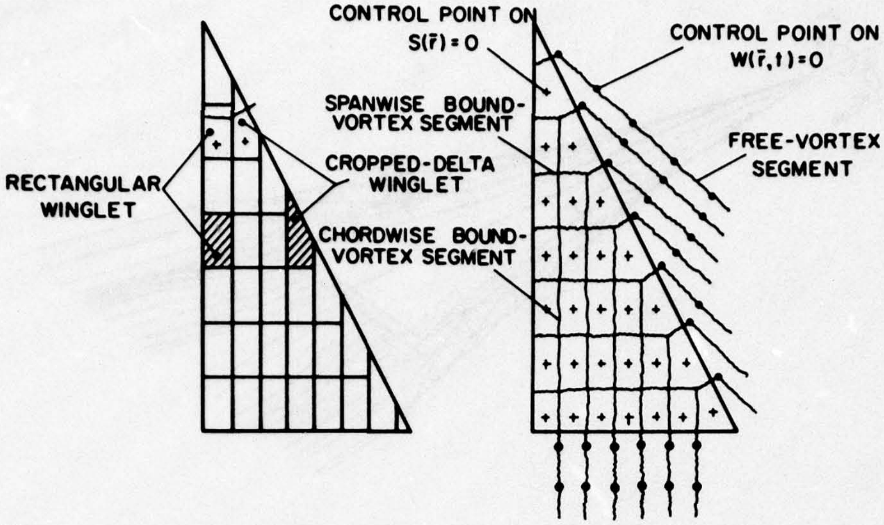

a. Discretization of wing into winglets

b. Discrete-vortex system

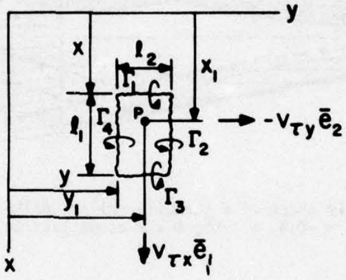

c. Induced tangential velocities

Fig. 2. Construction of the discrete-vortex system.

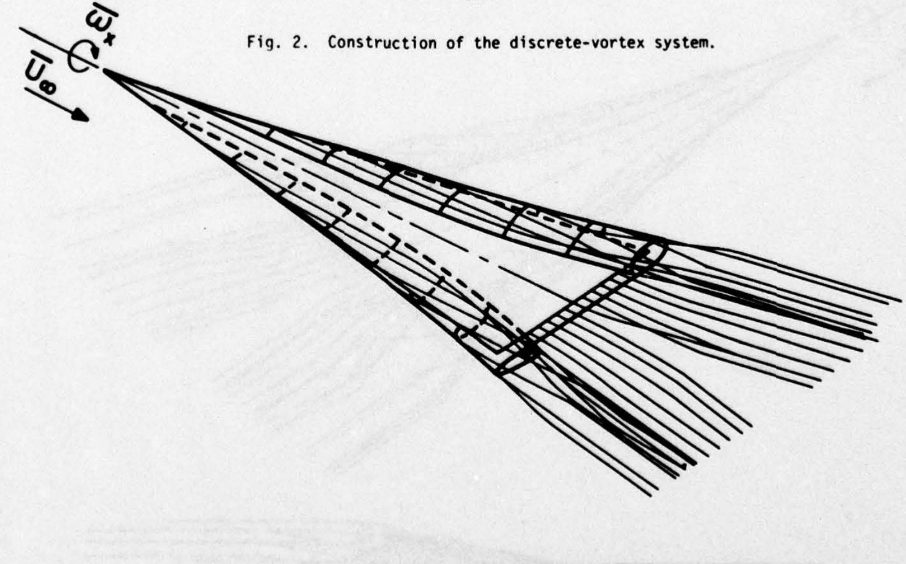

Fig. 3. Wake shape of a steadily rolling delta wing, $\omega_x = -0.2$, $\alpha = 0°$, 8 x 8 bound lattice, AR = 0.7.

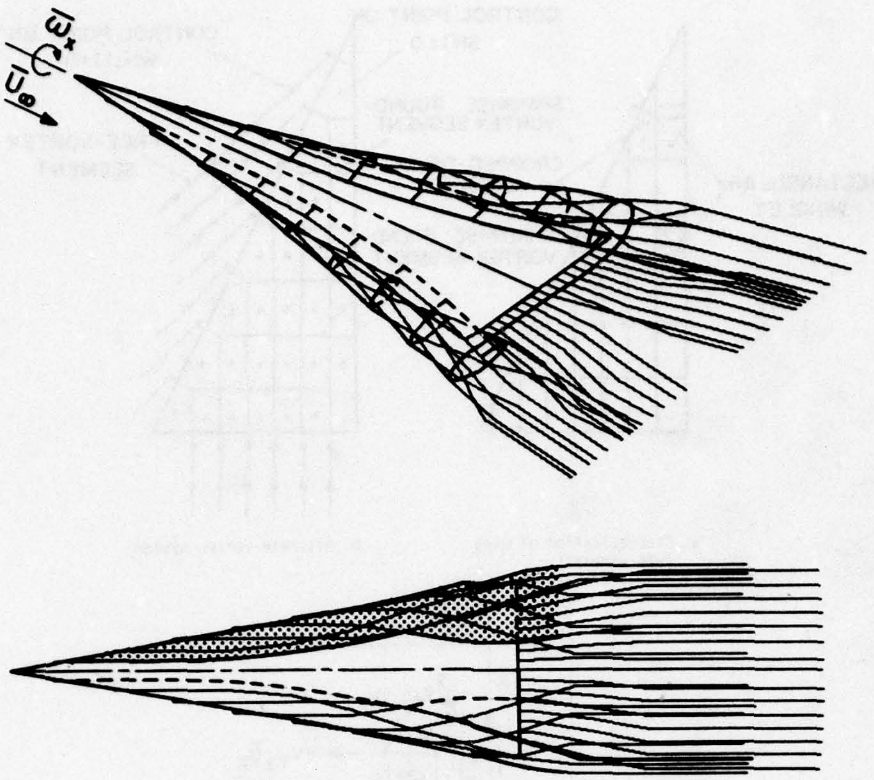

Fig. 4. Wake shape of a steadily rolling delta wing, $\omega_x = -0.4$, $\alpha = 0°$, 8 x 8 bound lattice, AR = 0.7.

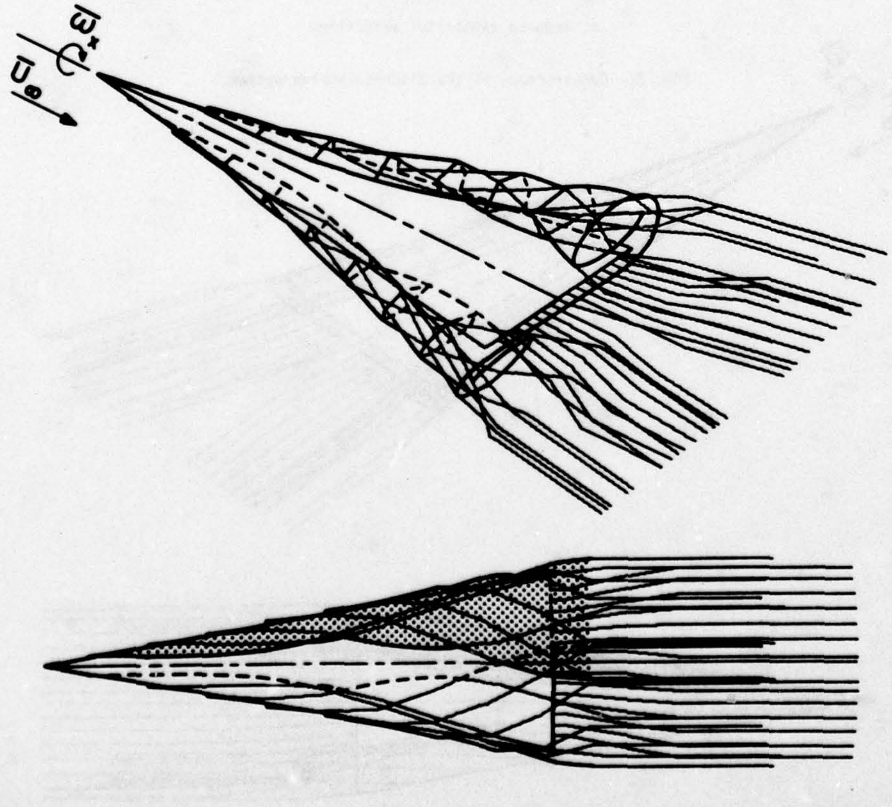

Fig. 5. Wake shape of a steadily rolling delta wing, $\omega_x = -0.6$, $\alpha = 0$, 8 x 8 bound lattice, AR = 0.7.

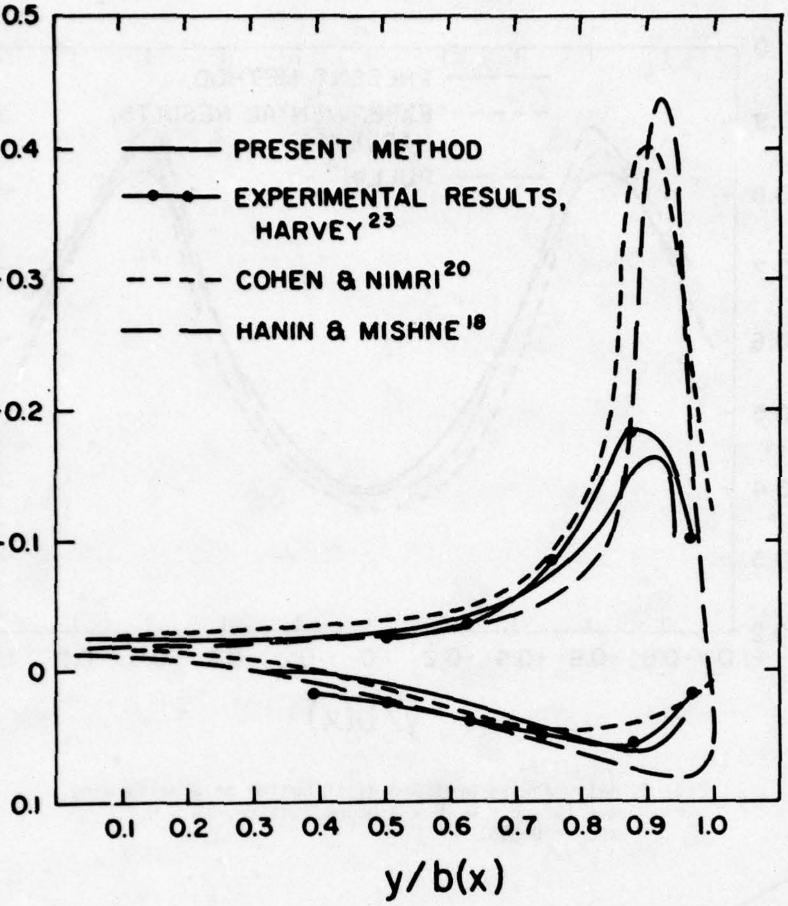

Fig. 6. Upper and lower, spanwise pressure distribution on a steadily rolling delta wing. ω_x = - 0.2, α = 0, 8 x 8 bound lattice, AR = 0.7, x/c_r = 0.778.

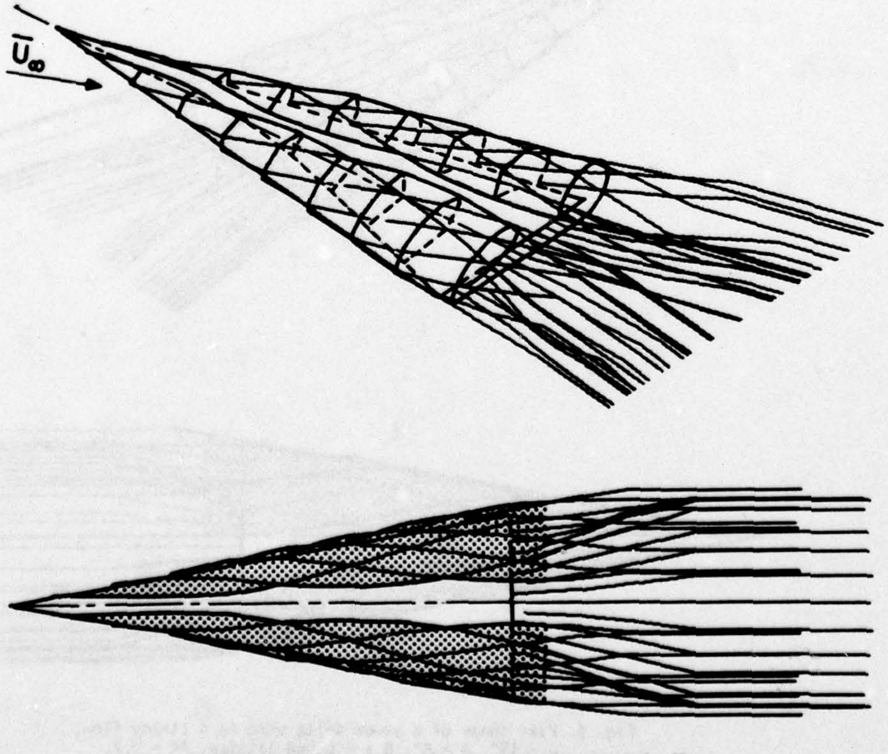

Fig. 7. Wake shape of a delta wing in a steady symmetric flow, α = 15°, β = 0.0, 8 x 8 bound lattice, AR = 0.7.

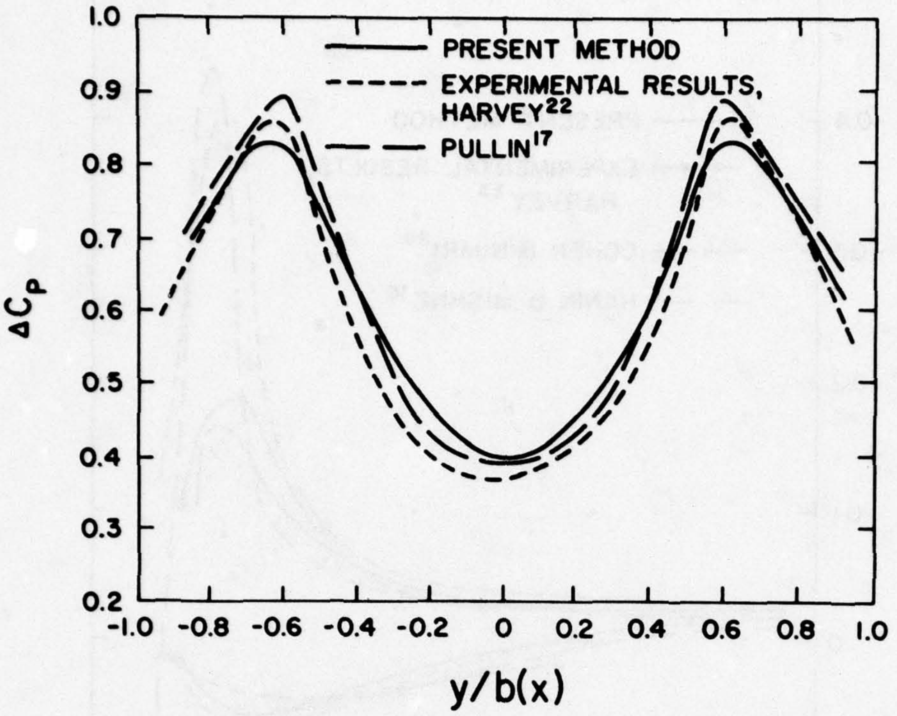

Fig. 8. Net spanwise pressure distribution on a delta wing, $\alpha = 15°$, $\beta = 0$, 8 x 8 bound lattice, AR = 0.7, $x/c_r = 0.395$.

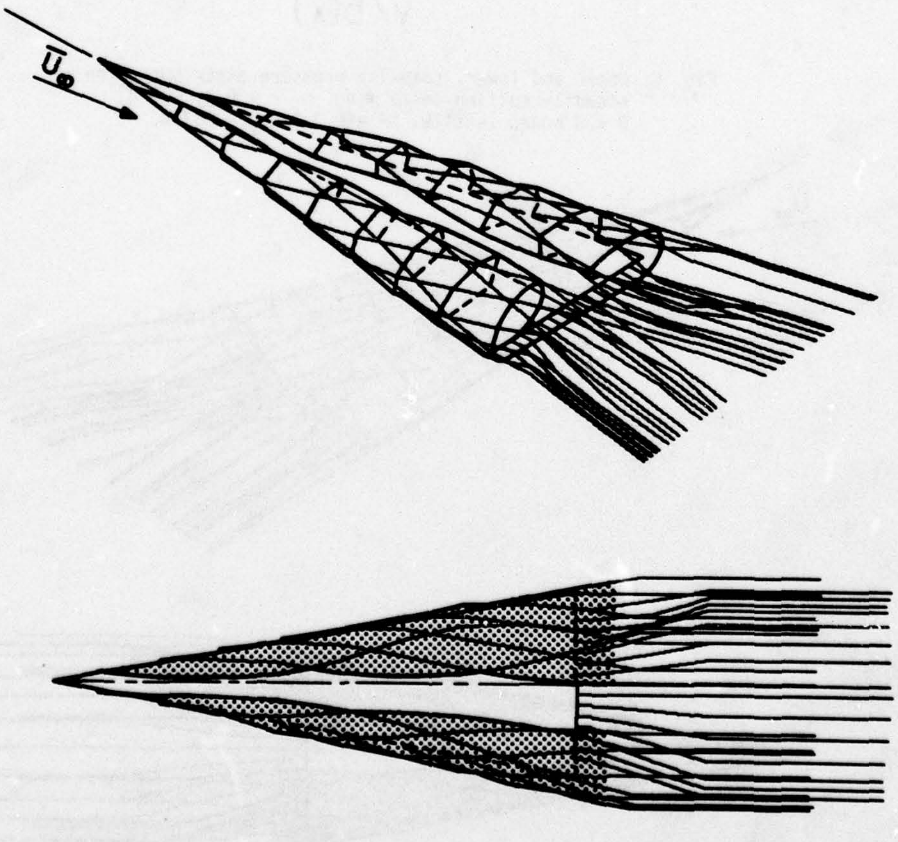

Fig. 9. Wake shape of a yawed delta wing in a steady flow, $\alpha = 15°$, $\beta = 5°$, 8 x 8 bound lattice, AR = 0.7.

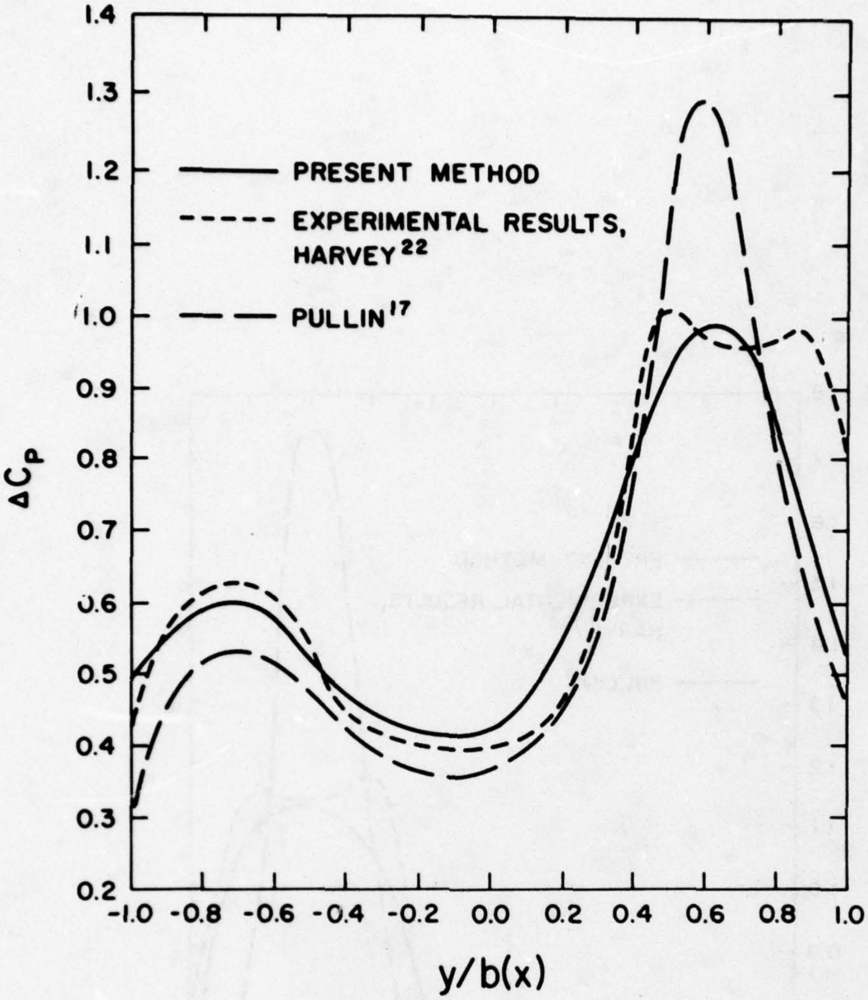

Fig. 10. Net spanwise pressure distribution on a yawed delta wing, $\alpha = 15°$, $\beta = 5°$, 8 x 8 bound lattice, AR = 0.7, $x/c_r = 0.395$.

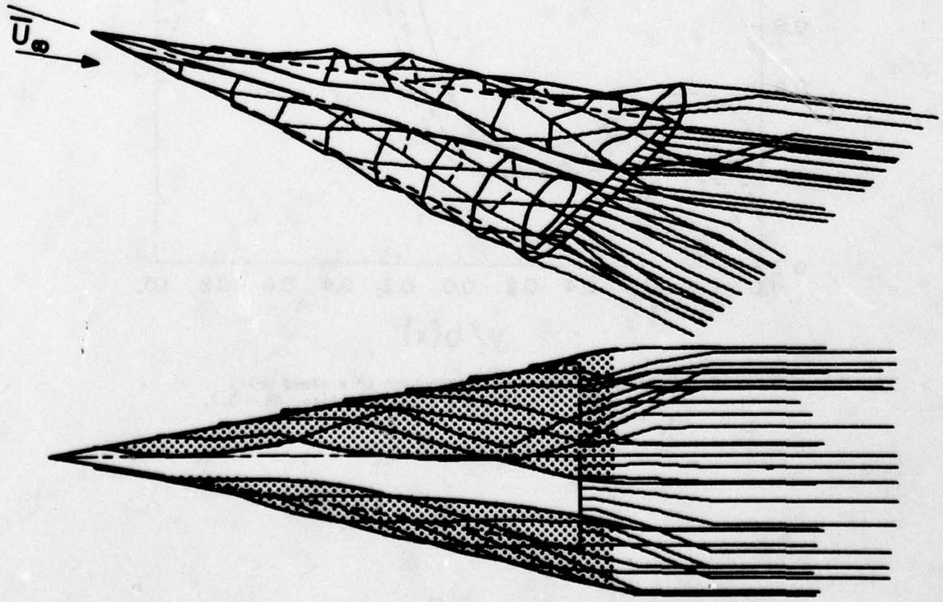

Fig. 11. Wake shape of a yawed delta wing in a steady flow, $\alpha = 15°$, $\beta = 10°$, 8 x 8 bound lattice, AR = 0.7.

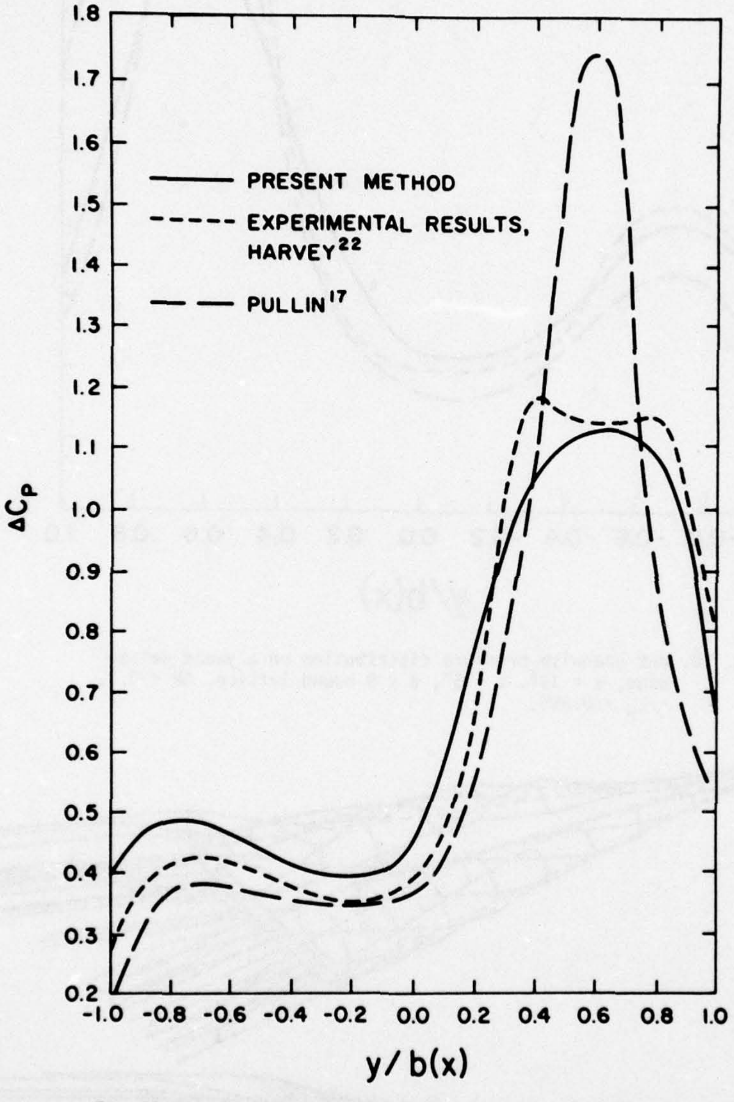

Fig. 12. Net spanwise pressure distribution on a yawed delta wing, α = 15°, β = 10°, 8 x 8 bound lattice, AR = 0.7, x/c_r = 0.395.

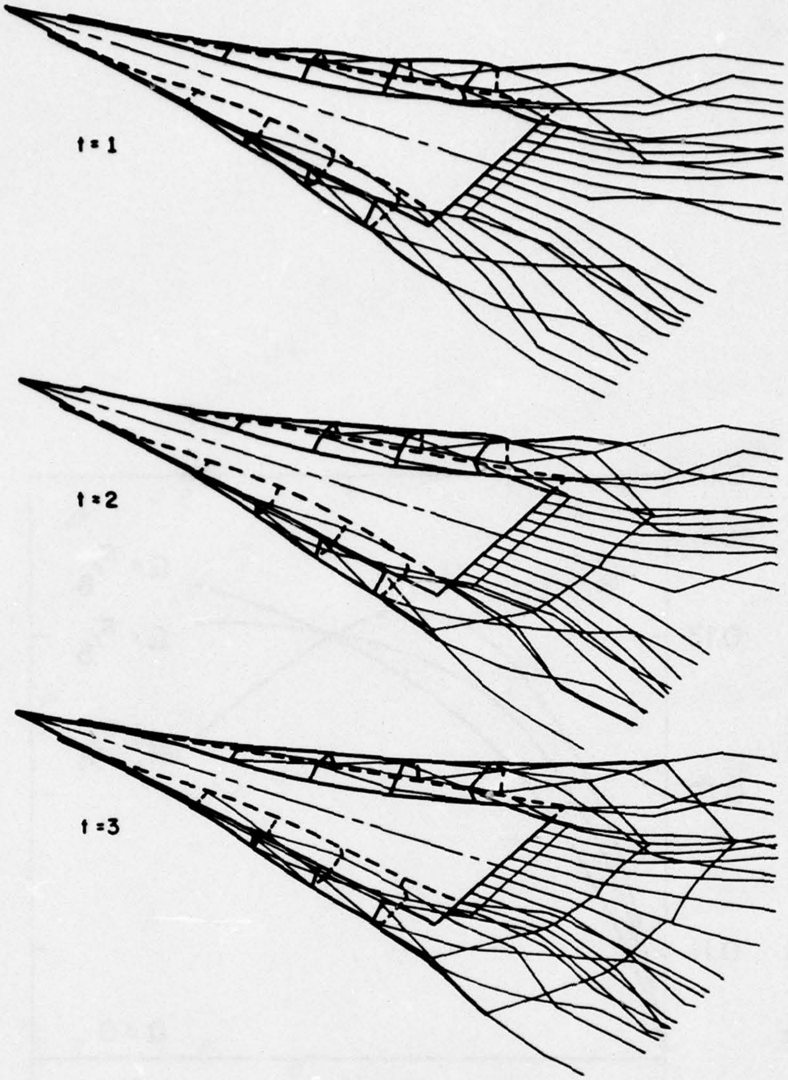

Fig. 13. Wake shape of an unsteadily rolling delta wing, $\omega_x = -0.6 - 0.1 \sin(\pi t/6)$, $\alpha = 0°$, 6 x 6 *bound* lattice, AR = 0.7.

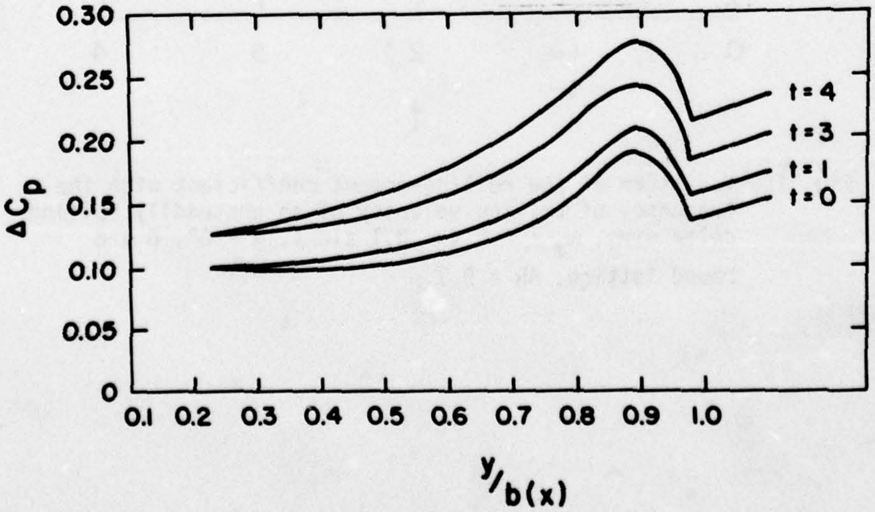

Fig. 14. Variation of the net spanwise pressure distribution with time on an unsteadily rolling delta wing, $\omega_x = -0.4 - 0.1 \sin(\pi t/4)$, $\alpha = 0°$, 6 x 6 *bound* lattice, AR = 0.7, $x/c_r = 0.65$.

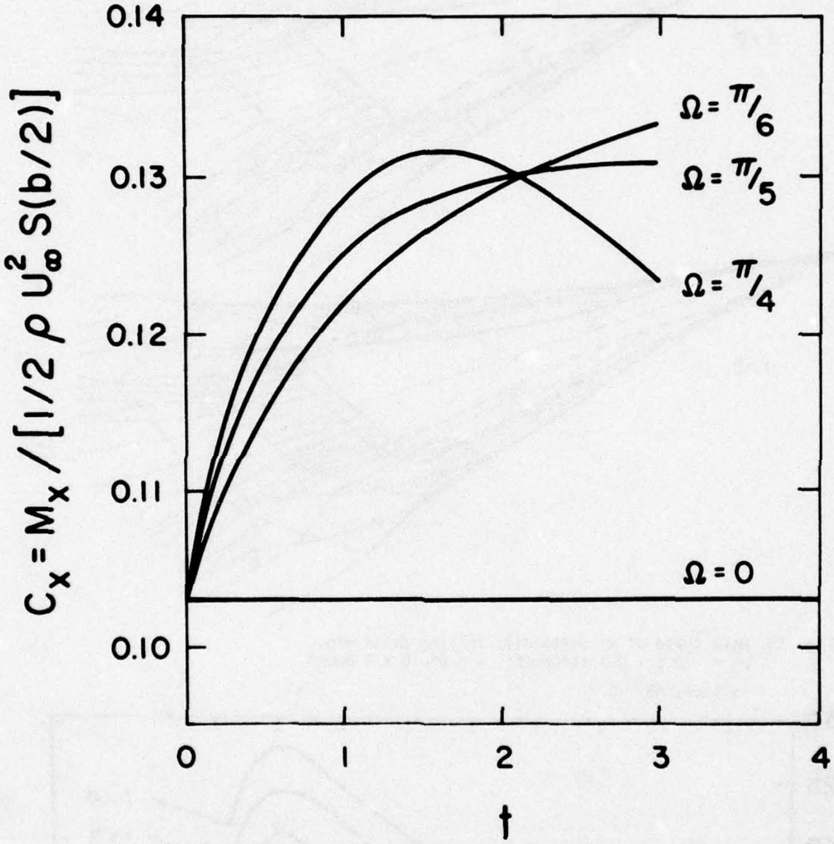

Fig. 15. Variation of the rolling-moment coefficient with the frequency of rolling velocity of an unsteadily rolling delta wing, $\omega_x = -0.4 - 0.1 \sin\Omega t$, $\alpha = 0°$, 6 x 6 bound lattice, AR = 0.7.

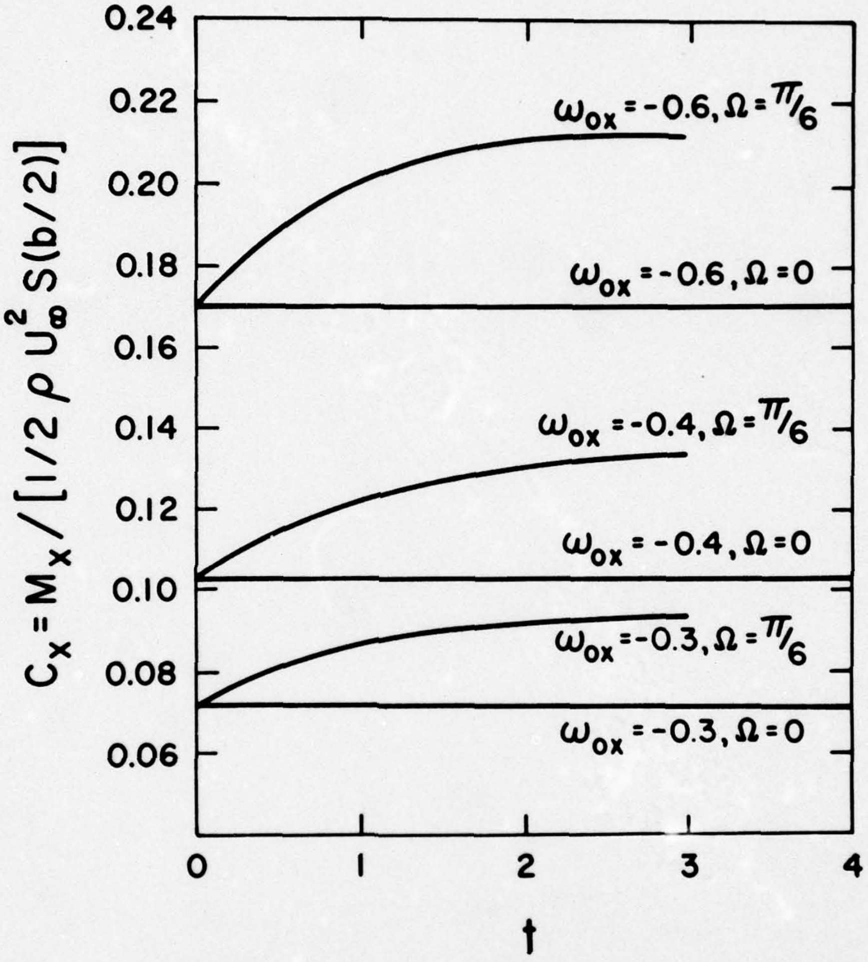

Fig. 16. Variation of the rolling-moment coefficient with the mean rate of roll of an unsteadily rolling delta wing, $\omega_x = \omega_{0x} - 0.1 \sin\Omega t$, $\alpha = 0°$, 6 x 6 bound lattice, AR = 0.7.

STEADY, OSCILLATORY AND UNSTEADY, SUBSONIC AND SUPERSONIC AERODYNAMICS (SOUSSA) FOR COMPLEX AIRCRAFT CONFIGURATIONS

by

Luigi Morino, Research Professor, Department of Aerospace and Mechanical Engineering, Boston University, Boston, Massachusetts 02215 U.S.A.
Kadin Tseng, Research Assistant, Department of Aerospace and Mechanical Engineering, Boston University, Boston, Massachusetts 02215 U.S.A.

SUMMARY

A review and recent developments of the Green's function method and the computer program SOUSSA (Steady Oscillatory and Unsteady, Subsonic and Supersonic Aerodynamics) are presented. Applying the Green's function method to the fully unsteady (transient) potential equation yields an integro-differential-delay equation. Using the finite-element method, this equation is approximated by a set of differential-delay equations in time. Using the Laplace transform yields a matrix relating the velocity potential to the normal wash. Premultiplying and postmultiplying by the matrices relating generalized forces to the potential and the normal wash to the generalized coordinates one obtains the matrix of the generalized aerodynamic forces. The frequency and mode-shape dependence of this matrix makes the program SOUSSA very useful for multiple frequency and mode-shape evaluations. Comparison with existing numerical results are presented. The results indicate that the program SOUSSA is not only general, flexible and easy to use but also accurate and fast.

SYMBOLS

a	Speed of sound
AR	Aspect ratio
b	Span
B_j	See Eq. (13)
B_{hj}	See Eq. (15)
B'_{hj}	See Eq. (17)
c	Chord
C_h	See Eq. (13)
C_{hj}	See Eq. (15)
C'_{hj}	See Eq. (17)
C_L	Lift coefficient
C_M	Moment coefficient around $x=x_M$
D_j	See Eq. (13)
D_{hj}	See Eq. (15)
D'_{hj}	See Eq. (17)
F_n	See Eq. (13)
F_{hn}	See Eq. (15)
F'_{hn}	See Eq. (17)
G_n	See Eq. (13)
G_{hn}	See Eq. (15)
G'_{hn}	See Eq. (17)
$H(P)$	See Eq. (18)
J	Number of nodes on body
k	Reduced frequency, $\omega \ell / U_\infty$
ℓ	Reference length
ℓ_w	Wake length
$L_n(P)$	Shape functions for $\Delta\Phi$

M	Mach number U_∞/a_∞
N	Normal to Σ_B
N	Number of nodes on wake
$N_n(P)$	Shape functions for Ψ and Φ
N_w	Number of wake elements in x-direction
N_x	Number of elements in chord direction
N_y	Number of elements in span direction on half-wing
p	Complex reduced frequency, $s\ell/U_\infty$
P	Point having coordinates (X,Y,Z)
P_*	Control point, (X_*, Y_*, Z_*)
R	Defined by equation (4)
R'	Defined by equation (20)
s	Complex frequency (Laplace parameter)
S_{nh}	See Eq. (11)
t	Time
T	Nondimensional time, Eq. (2)
U_∞	Velocity of undisturbed flow
x,y,z	Space coordinates
x_m	Pitch axis
x_M	Moment axis
X,Y,Z	Nondimensional space coordinates, Eq. (2)
β	$= \lvert 1-M^2 \rvert^{\frac{1}{2}}$
δ_{hj}	Kronecker delta, 1 for j=h, 0 for j≠h
$\Delta\Phi$	Discontinuity of Φ across the wake
$\Delta\Phi_n$	Nodal values of $\Delta\Phi$
Θ	Time for a disturbance to propagate from P to P_*, Eq. (5)
Θ_j	Θ for $P=P_j$
Θ_{hj}	See Eq. (15)
Θ^+_{jh}	See Eq. (17)
Θ^-_{jh}	See Eq. (17)
Π	Convection time of wake vortices, Eq. (7)
Π_n	Value of Π for $P=P_n$
Σ_B	Surface of body (X,Y,Z space)
Σ_W	Surface of wake (X,Y,Z space)
τ	Thickness ratio
φ	Velocity perturbation potential
ϕ	Velocity potential, $U_\infty x + \varphi$
Φ	Nondimensional velocity perturbation potential, $\varphi/U_\infty\ell$
Φ_j	Nodal values of Φ
$\tilde{\Phi}_j$	Laplace transform of Φ_j
Ψ	Normal wash in X,Y,Z space
Ψ_j	Nodal value of Ψ
$\tilde{\Psi}_j$	Laplace transform of Ψ_j
ω	Frequency

Subscripts:

B	Body
I	Imaginary

ℓ	Lower
R	Real part of complex number
TE	Trailing edge
u	Upper
W	Wake

Special notation:

$(\tilde{\ })$	Laplace transform of ( )
$\{\ \}$	Vector
$[\ ]$	Matrix
$[\ ]^{\Theta}$	Defined by equation (5)

INTRODUCTION

Presented here is the Green's function method for steady, oscillatory and unsteady, subsonic and supersonic, potential aerodynamics for complex aircraft configurations. Reviews of other methods in this field are given in Refs. 1 and 2 and, therefore, are not presented here. The method is based on a combination of the following techniques: Green's function method (to transform the differential equation into an integral-differential-delay equation), finite element method (to transform the equation into a set of differential-delay equations in time) and finally the Laplace transform method (to transform the differential-delay equations into algebraic equations).

GREEN'S FUNCTION METHOD

The linearized equation for the velocity perturbation potential φ is

$$a_\infty^2 \nabla^2 \varphi = \left(\frac{\partial}{\partial t} + U_\infty \frac{\partial}{\partial x}\right)^2 \varphi \tag{1}$$

where U_∞ and a_∞ are the velocity and the sound speed of the unperturbed flow.

The subsonic case, i.e., $M = U_\infty / a_\infty < 1$ is considered first. Introduce the non-dimensional variables

$$\phi = \varphi / U_\infty \ell \qquad X = x/\beta \ell \qquad Y = y/\ell \qquad Z = z/\ell \qquad T = U_\infty t/\ell \tag{2}$$

where ℓ is a reference length and $\beta = |1-M^2|^{\frac{1}{2}}$. Note that the definition of the non-dimensional time T differs from the one used in preceeding works on Green's function method: with the present definition, the limit of Eq. (1) as M goes to zero is the incompressible flow equation (Laplace equation) instead of the wave equation. By using the Green's function method, one obtains an integral-differential-delay equation (Refs. 3 and 4)

$$2\pi \phi(P_*, T) = \oiint_{\Sigma_B} \left\{ -[\psi]^{\Theta} \frac{1}{R} + [\phi]^{\Theta} \frac{\partial}{\partial N}\left(\frac{1}{R}\right) - [\dot{\phi}]^{\Theta} \frac{1}{R} \frac{\partial R}{\partial N} \right\} d\Sigma_B + \iint_{\Sigma_W} \left\{ [\Delta\phi]^{\Theta} \frac{\partial}{\partial N}\left(\frac{1}{R}\right) - [\Delta\dot{\phi}]^{\Theta} \frac{1}{R} \frac{\partial R}{\partial N} \right\} d\Sigma_W \tag{3}$$

where Σ_B is the (closed) surface of the aircraft (in the transformed X, Y, Z space), Σ_W is the (open) surface of the vortex-layer wake emanating from the trailing edge, $\vec{N}$ is the normal to Σ_B. Furthermore the control point, P_*, is located on Σ_B, whereas

$$R = |P - P_*| \tag{4}$$

is the distance between P_* and the dummy point of integration P (in the transformed space) and $[\ ]^{\Theta}$ indicates evaluation at retarded time $T-\Theta$, where

$$\Theta = \left[M^2 (X - X_*) + MR\right] / \beta \tag{5}$$

is the disturbance-propagation time. Note that the definition of Θ differs from the one used in preceeding works on Green's function method because of the different definition of T in Eq. (2). In obtaining Eq. (1) the motion is assumed to consist of infinitesimal perturbations around a steady state configuration (a more general formulation is given in Ref. 3). Therefore Σ_W is assumed to be known from the steady state analysis.

In addition note that

$$\Delta\phi(P, T) = \Delta\phi(P_{TE}, T - \Pi) \tag{6}$$

where P_{TE} is the trailing edge point of the steady-state streamline through P and Π is the steady-state convection time from P_{TE} to P (Ref. 5) which may be approximated as (the new definition of Π is also due to the new definition of T)

$$\Pi = \beta (X - X_{TE}) \tag{7}$$

Finally the normal wash $\Psi = \partial\Phi/\partial N$ is known from the boundary conditions. Therefore, Eq. (3) is an integral-differential-delay equation relating the potential, Φ, to the normal wash, Ψ. This equation and the corresponding one for supersonic flow are the basis for the Green's function method used in the program SOUSSA (Steady, Oscillatory and Unsteady, Subsonic and Supersonic Aerodynamics) presented in Refs. 6 and 7.

NUMERICAL FORMULATION

In order to obtain an efficient computational procedure, the integral-differential-delay equation is approximated by a system of differential-delay equations in time. This is obtained by using a finite-element representation, i.e., by letting

$$\Psi(P, T-\Theta) = \sum_{j=1}^{J} \Psi_j(T-\Theta_j)\, N_j(P) \tag{8}$$

$$\Phi(P, T-\Theta) = \sum_{j=1}^{J} \Phi_j(T-\Theta_j)\, N_j(P)$$

where J is the total number of nodes on the body and $\Psi_j\ (T-\Theta_j)$ and $\Phi_j\ (T-\Theta_j)$ are time-dependent values of Ψ and Φ at the node P_j at the time $T-\Theta_j$ (where Θ_j is the disturbance-propagation time from P_* to P_j); furthermore, the $N_j(P)$ are prescribed global shape functions, obtained by standard assembly of the element shape function.

Similarly, the potential discontinuity on the wake can be expressed as

$$\Delta\Phi(P, T-\Theta) = \sum_{n=1}^{N} \Delta\Phi_n(T-\Theta_n)\, L_n(P) \tag{9}$$

where N is the number of nodes on the wake, $\Delta\Phi_n(T-\Theta_n)$ is the value of $\Delta\Phi$ at the nth node $P_n^{(W)}$ on the wake at time $T-\Theta_n$ (where Θ_n is the propagation time from $P_n^{(W)}$ to P_*), and $L_n(P)$ is the global shape function relative to the nth node of the wake. Note that (Ref. 5)

$$\Delta\Phi_n(T) = \Delta\Phi_{m(n)}^{(TE)}(T-\Pi_n) \tag{10}$$

where m=m(n) identifies the trailing-edge point, $P_m^{(TE)}$, which is on the same vortex-line as the point $P_n^{(W)}$. Furthermore, Π_n is the steady-state time necessary for the vortex-point to be convected from the trailing-edge point $P_m^{(TE)}$ to the wake-point $P_n^{(W)}$. Note that $\Delta\Phi_m^{(TE)} = \Phi_{h_u} - \Phi_{h_\ell}$, where h_u and h_ℓ identify the upper and lower trailing-edge nodes on the body corresponding to the nth node on the trailing-edge. Hence it is possible to write

$$\Delta\Phi_{m(n)}^{(TE)} = \sum_{j=1}^{J} S_{nj}\, \Phi_j \tag{11}$$

where $S_{nj}=1$ $(S_{nj}=-1)$, if j identifies the upper (lower) trailing-edge point P_j on the body corresponding to the point $P_n^{(W)}$ on the wake, and $S_{nj}=0$ otherwise.

Combining Eqs. (3) through (11), one obtains a system of differential-delay equations relating Φ to Ψ_j and Φ_j:

$$\begin{aligned}\Phi(P_*, T) = {} & \sum_j B_j \Psi_j(T-\Theta_j) + \sum_j C_j \Phi_j(T-\Theta_j) + \sum_j D_j \dot{\Phi}_j(T-\Theta_j) \\ & + \sum_{n,j} F_n S_{nj} \Phi_j(T-\Theta_n-\Pi_n) + \sum_{n,j} G_n S_{nj} \dot{\Phi}_j(T-\Theta_n-\Pi_n)\end{aligned} \tag{12}$$

where (the new definitions of D_j and G_n are due to the new definition of T)

$$\begin{aligned} B_j &= \frac{-1}{2\pi} \oiint_{\Sigma_B} N_j(P)\,\frac{1}{R}\, d\Sigma_B \\ C_j &= \frac{1}{2\pi} \oiint_{\Sigma_B} N_j(P)\,\frac{\partial}{\partial N}\left(\frac{1}{R}\right) d\Sigma_B \\ D_j &= \frac{-M}{2\pi\beta} \oiint_{\Sigma_B} N_j(P)\,\frac{1}{R}\,\frac{\partial R}{\partial N}\, d\Sigma_B \\ F_n &= \frac{1}{2\pi} \iint_{\Sigma_W} L_n(P)\,\frac{\partial}{\partial N}\left(\frac{1}{R}\right) d\Sigma_W \\ G_n &= \frac{-M}{2\pi\beta} \iint_{\Sigma_W} L_n(P)\,\frac{1}{R}\,\frac{\partial R}{\partial N}\, d\Sigma_W \end{aligned} \tag{13}$$

Next, the set of differential-delay equations is replaced by a system of algebraic equations by either assuming exponential time dependence or by using the Laplace transform (indicated by a tilda, ~). Then, satisfying the equation at the nodal points, one obtains

$$\begin{aligned}\Big[\delta_{hj} - (C_{hj} + p D_{hj})\, e^{-p\Theta_{hj}} - \sum_n (F_{hn} + p G_{hn})\, e^{-p(\Theta_{hn}+\Pi_n)} S_{nj}\Big]\{\tilde{\Phi}_j\} \\ = \Big[B_{hj}\, e^{-p\Theta_{hj}}\Big]\{\tilde{\Psi}_j\}\end{aligned} \tag{14}$$

where (indicating with s the reduced frequency) $p = s\ell / U_\infty$, whereas

$$\left.\begin{aligned} \Theta_{hj} &= \Theta_j \\ B_{hj} &= B_j \\ C_{hj} &= C_j \\ D_{hj} &= D_j \\ F_{hn} &= F_n \\ G_{hn} &= G_n \end{aligned}\right\} \text{ at } P_* = P_h \tag{15}$$

The evaluation of the pressure and the aerodynamic influence coefficients for flutter analysis is given in Appendix A .

SUPERSONIC FORMULATION

For supersonic flows (i.e. $M=U_\infty / a_\infty > 1$) one obtains

$$\begin{aligned} \Big[\delta_{hj} - C'_{hj} \left(e^{-p\Theta^+_{hj}} + e^{-p\Theta^-_{hj}}\right) - p\, D'_{hj} \left(e^{-p\Theta^+_{hj}} - e^{-p\Theta^-_{hj}}\right) - \\ \sum_n F'_{hn} \left(e^{-p(\Theta^+_{hn}+\Pi_n)} + e^{-p(\Theta^-_{hn}+\Pi_n)}\right) S_{nj} - \\ \sum_n G'_{hn}\, p \left(e^{-p(\Theta^+_{hn}+\Pi_n)} - e^{-p(\Theta^-_{hn}+\Pi_n)}\right) S_{nj} \Big] \left\{\tilde{\Phi}_j\right\} = \left[B'_{hj}\left(e^{-p\Theta^+_{hj}} + e^{-p\Theta^-_{hj}}\right)\right]\left\{\tilde{\Psi}_j\right\} \end{aligned} \tag{16}$$

where (the new definitions of D'_j and G'_n are due to the new definition of T)

$$\left.\begin{aligned} B'_{hj} &= \frac{-1}{2\pi} \oiint_{\Sigma_B} N_j(P) \frac{H(P_j - P_n)}{R'}\, d\Sigma_B \\ C'_{hj} &= \frac{1}{2\pi} \oiint_{\Sigma_B} N_j(P) \frac{\partial}{\partial N^c}\left(\frac{H(P_j - P_n)}{R'}\right) d\Sigma_B \\ D'_{hj} &= \frac{-M}{2\pi\beta} \oiint_{\Sigma_B} N_j(P) \frac{H(P_j - P_h)}{R'} \frac{\partial R'}{\partial N^c}\, d\Sigma_B \\ F'_{hn} &= \frac{1}{2\pi} \iint_{\Sigma_W} L_n(P) \frac{\partial}{\partial N^c}\left(\frac{H(P_j - P_n)}{R'}\right) d\Sigma_W \\ G'_{hn} &= \frac{-M}{2\pi\beta} \iint_{\Sigma_W} L_n(P) \frac{H(P_j - P_h)}{R'} \frac{\partial R'}{\partial N^c}\, d\Sigma_W \end{aligned}\right\} \text{ at } P_* = P_h \tag{17}$$

with

$$\begin{aligned} H(P_j - P_h) &= 1 \quad \text{for} \quad X_h - X_j > \left[(Y_j - Y_h)^2 + (Z_j - Z_n)^2\right]^{1/2} \\ &= 0 \quad \text{for} \quad X_h - X_j \le \left[(Y_j - Y_h)^2 + (Z_j - Z_n)^2\right]^{1/2} \end{aligned} \tag{18}$$

In addition

$$\Theta^{\pm}_{hj} = \left[M^2 (X_h - X_j) \pm M R'\right] / \beta \tag{19}$$

and

$$R' = \left[(X_j - X_h)^2 - (Y_j - Y_h)^2 - (Z_j - Z_h)^2\right]^{1/2} \tag{20}$$

whereas

$$\frac{\partial}{\partial N^c} = - N_x \frac{\partial}{\partial X} + N_y \frac{\partial}{\partial Y} + N_z \frac{\partial}{\partial Z} \tag{21}$$

is the conormal derivative (Ref. 5). The above equations are to be interpreted within the theory of generalized functions (Ref. 3). The evaluation of the coefficients is facilitated by the use of an ad-hoc vector algebra (supersonic algebra) equivalent to a hyperbolic tensor algebra (Ref. 6).

COMMENTS

The general formulation presented above is embedded (currently with zeroth-order finite-element global shape function) in the computer program SOUSSA (Steady, Oscillatory and Unsteady, Subsonic and Supersonic Aerodynamics), which provides a unified tool for both subsonic and supersonic flows around complex aircraft configurations (Ref. 7). Application to coplanar surfaces (for instance wing wake intersecting the tail) is presented in Ref. 8. Note that no diaphragms are needed for supersonic flow. The program is general, flexible, efficient and accurate, as indicated by the results obtained thus far (see Refs. 5, 6, 7, and 8). The dependence of the coefficients upon the frequency is extremely simple as indicated by Eqs. (14) and (16). This makes the program extremely fast for multiple-frequency calculations. The dependence of the generalized aerodynamic forces is also very simple (see Appendix A). This is particularly useful for iterative structural optimal design where new mode shapes are used in each iteration.

It should be noted that, for the zeroth-order formulation, the integrals in Eqs. (13) and (17) can be evaluated analytically (Ref. 6). Recently, however, a combined analytical-numerical scheme has been used for evaluating these coefficients (Ref. 9).For while an analytical scheme is necessary for singular or near-singular integrals, numerical integration is much more efficient for integrals with relatively smooth integrands. With this combination of analytical integration for near-field integrals (near-singular integrand) and numerical Gaussian quadrature scheme for far-field integrals (smooth integrand), considerable improvement in computational efficiency is achieved while accuracy is preserved: the computer time (on an IBM 370/158 computer) for evaluating all the coefficients has been reduced by 80-90% with the same order of accuracy as obtained with the analytical scheme.

NUMERICAL RESULTS

Results for the zeroth-order formulation are in excellent agreement with existing ones (Refs. 5 to 8). Complex-frequency results for a wing-body-tail configuration, unobtainable with other methods, are given in Ref. 7. Additional results are presented in this section. The test cases selected are either well recognized (Ref. 10) or are standard AGARD configurations for which results obtained with various other methods are available (Ref. 11).

Figures 1 and 2 present the rate of convergence for the lift and moment coefficients for a rectangular wing, oscillating in pitch, with aspect ratio. AR=2, thickness ratio τ=0.01, reduced frequency k=1.0 and free stream Mach number M =0.8. It should be pointed out here that in the process of calculating the pressure coefficients and thereafter the generalized forces, a continuous distribution of the velocity potential on the surface of the aircraft (in that case, a wing) is used. In Refs. 7 and 8, these were achieved by means of an averaging scheme, which in this paper is replaced by a weighted averaging scheme (see Appendix A). Also small elements are used near the leading edge as well as the trailing edge. Considerable improvement in the convergence rate on the generalized forces is obtained with the new method.

Figures 3 and 4 present the lift and moment coefficients as a function of Mach number for a rectangular wing oscillating in pitch, with aspect ratio AR=2, thickness ratio τ=0.01, reduced frequency k=1.0. The results are compared to the ones of Ref.10.

Wing-fuselage-tail results for complex frequencies, from Ref. 7, are presented in Figs. 5 and 6. Specifications for the problem are given in Table 1. (Time-domain analysis of Eq. (12) is now underway.)

CONCLUSIONS

A general method for steady oscillatory and fully unsteady (in frequency and time domain), subsonic and supersonic aerodynamics around complex aircraft configurations has been presented. Analysis of convergence as well as comparison with existing results indicate that the method besides being intrinsically general is also accurate.

Additional features which have been recently added to the formulation include the wake roll-up (obtained through an iteration process, Ref. 11), as well as a simple approximation for the aerodynamic influence coefficients as functions of the Laplace parameter (Ref. 12). Finally the inclusion of the nonlinear effects (in the subsonic subcritical, i.e., shockfree, range) is now under investigation(Ref. 13. An assessment of the method was given by Garrick in his 13th Von Karman lecture (Ref. 14). A higher-order finite-element formulation is now under investigation.

ACKNOWLEDGMENT

This research is supported by NASA Langley Grant NGR 22-004-030, Technical Monitor, Dr. E. Carson Yates, Jr.

REFERENCES

1. Ashley, H. and Rodden, W.P., "Wing-Body Aerodynamic Interaction," Annual Review of Fluid Mechanics, Vol. 4, 1972, pp. 431-472.

2. Rodden, W.P., "State-of-the-Art in Unsteady Aerodynamics," AGARD-R-650, 1976.

3. Morino, L., "A General Theory of Unsteady Compressible Potential Aerodynamics," NASA CR-2464, 1974. (Supersedes BU-TR-72-01, 1972).

4. Morino, L., and Kuo, C.C., "Subsonic Potential Aerodynamics for Complex Configurations: A General Theory," AIAA J., Vol. 12, Feb. 1974, pp. 191-197.

5. Morino, L., and Chen, L.T., "Indicial Compressible Potential Aerodynamics Around Complex Aircraft Configuration," in NASA SP-347, 1975, pp. 1067-1110.

6. Morino, L., Chen, L.T., and Suciu, E.O., "Steady and Oscillatory Subsonic and Supersonic Aerodynamics Around Complex Configurations," AIAA J., Vol. 13, March 1975.

7. Tseng, K., and Morino, L., "Fully Unsteady Subsonic and Supersonic Potential Aerodynamics of Complex Aircraft Configurations for Flutter Applications", Proc. AIAA/ASME/SAE 17th Structures, Structural Dynamics, and Materials Conference, May 1976.

8. Tseng, K., and Morino, L., "A New Unified Approach for Analyzing Wing-body-tail Configurations with Control Surfaces," AIAA Paper No. 76-418, July 1976.

9. Tseng, K., Puglise, J.A., and Morino, L., "Recent Developments in the Green's Function Method", AIAA Paper No. 77-456, March 1977.

10. Laschka, B., "Zur Theorie der harmonisch schwingenden tragenden Flache bei Unterschallanstromung", Zeitschrift fur Flugwissenchaften, 11 (1963), Heft 7, pp. 265-292.

11. Suciu, E.O., and Morino, L., "A Nonlinear Finite-Element Analysis of Wings in Steady Incompressible Flows with Wake Roll-Up," AIAA Paper No. 76-64, January 1976.

12. Weiss, S.J., Tseng, K., and Morino, L., "State-Space Formulations for Flutter Analysis," AIAA Paper No. 77-117, Jan. 1977.

13. Tseng, K., Ph.D. Thesis, Boston University (in preparation).

14. Garrick, I.E., "Aeroelasticity-Frontiers and Beyond," Journal of Aircrafts, Vol. 13, Sept. 1976, pp. 641-657.

15. Noll, R.B., and Morino, L., "Flight Control Analysis Program (FCAP) for Arbitrary Configuration Flexible Aircraft With Active Control," Vol. I, Theoretical Analysis, Aerospace Systems, Inc., Burlington, Mass., ASI-TR-75-23, 1975.

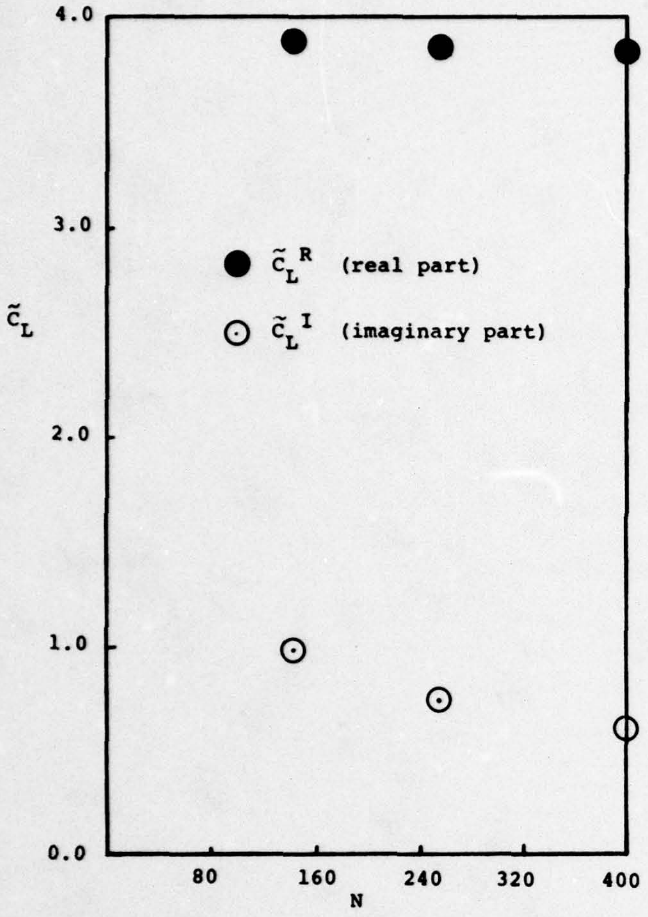

Figure 1. Convergence study of the lift coefficient, $\tilde{C}_L$ versus number of elements $N = 4N_xN_y$, for a rectangular wing oscillating in pitch, with AR=2, $\tau = 0.01$ and $N_w = 3N_x$.

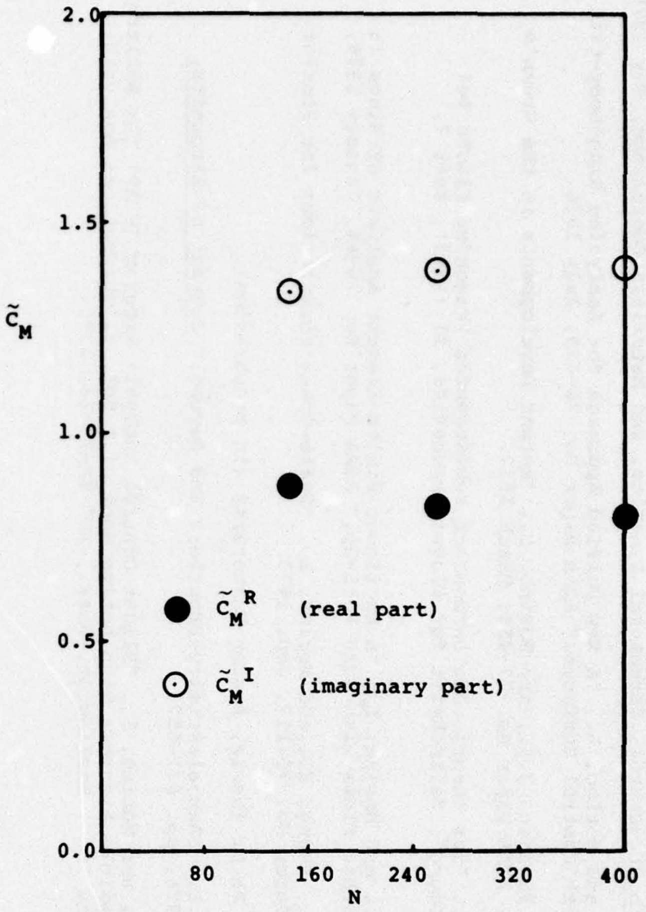

Figure 2. Convergence study of the moment coefficient, $\tilde{C}_M$, versus number of elements $N=4N_x N_y$, for a rectangular wing oscillating in pitch, with AR=2, $\tau = 0.01$ and $N_w=3N_x$.

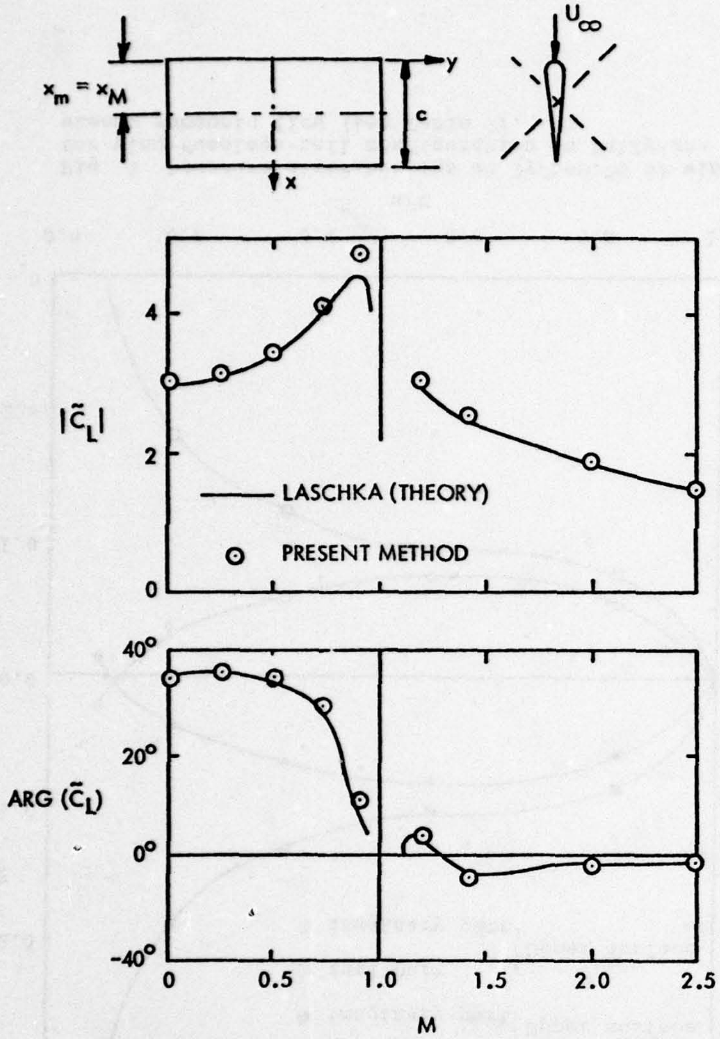

Figure 3. Lift Coefficient, $\tilde{C}_L$, Versus M, for Rectangular Wing Oscillating in Pitch, With AR=2, τ =0.01, k=1, N_x=10, N_y=6, N_w=20, ℓ_w/c=2 . Comparison With Results of Reference 10.

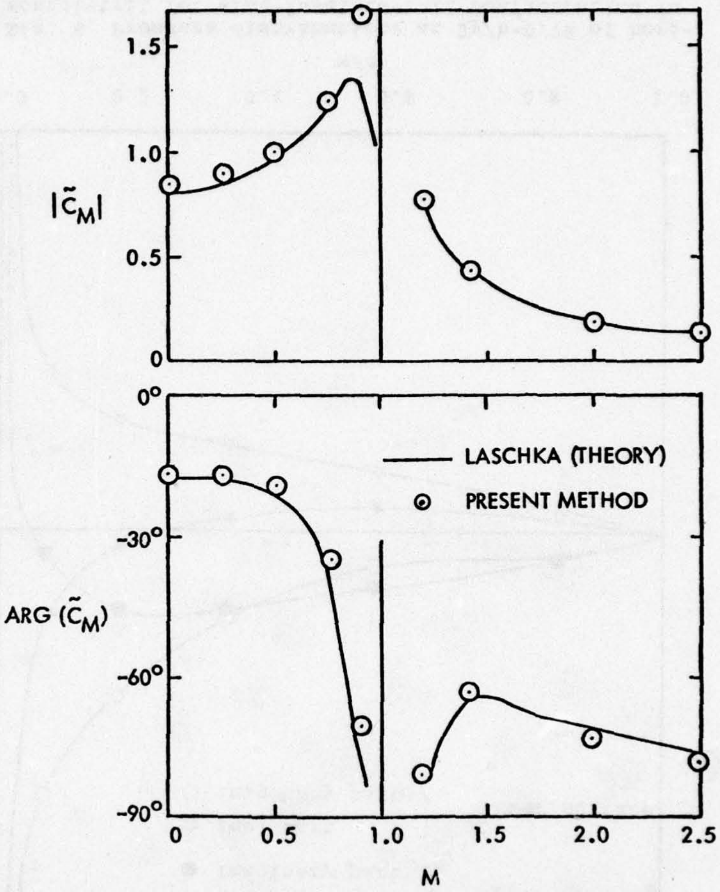

Figure 4. Moment Coefficient, $\tilde{C}_M$, Versus M, for Rectangular Wing Oscillating in Pitch, for AR=2, τ =0.01, k=1, N_x=10, N_y=6, N_w=20, ℓ_w/c=2. Comparison With Results of Reference 10.

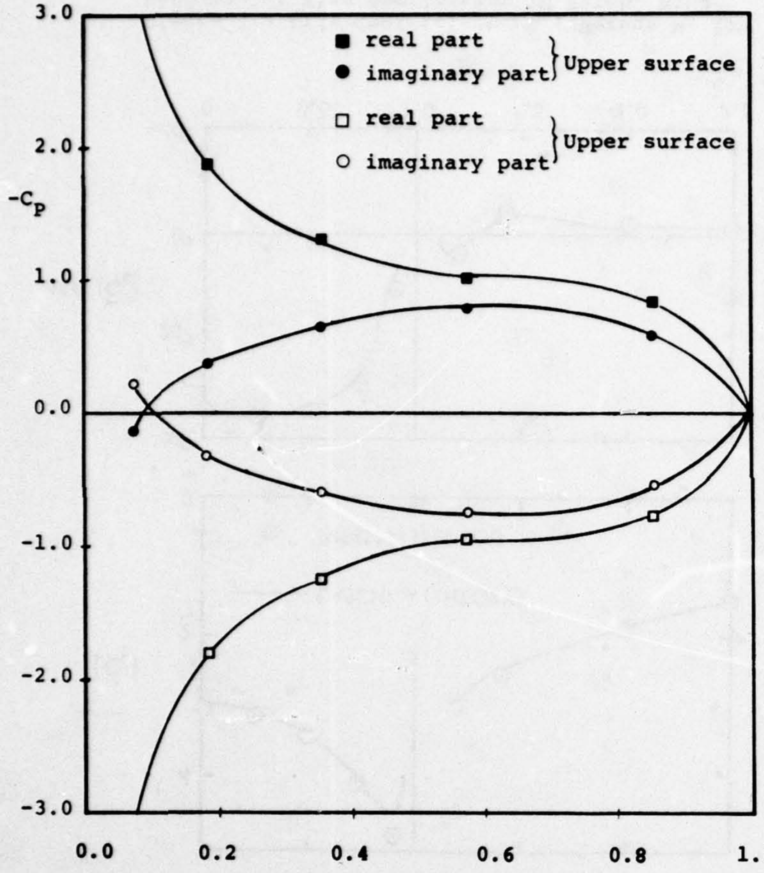

Fig. 5 Pressure distributions at 2y/b=0.78 of wing for wing-fuselage-tail configuration in fully-unsteady subsonic flow (see Table 1).

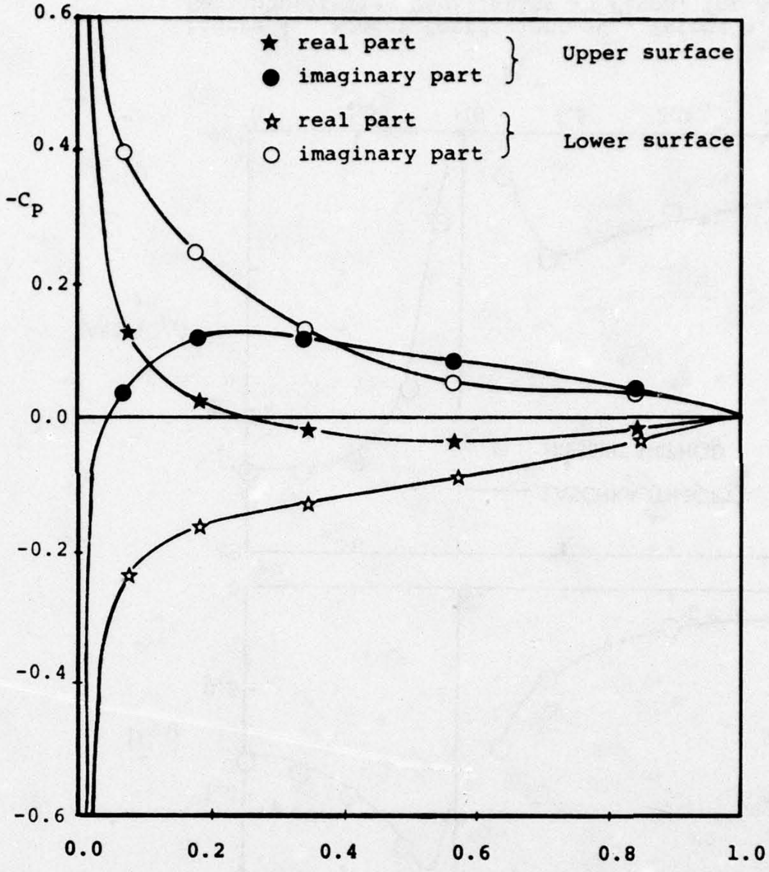

Fig. 6 Pressure distributions at 2y/b=0.78 of horizontal-tail for wing-fuselage-tail configuration in fully-unsteady subsonic flow (see Table 1).

TABLE 1

SPECIFICATION FOR PROBLEM OF FIGURES 5 AND 6

Mach Number, $M=0.5$
Reduced Frequency, $k_c = \frac{\omega \ell}{U_\infty}(\gamma + i) = 0.1 + i0.5$
Mode $\vec{M} = (x - x_{c/4})\,\ell\,\vec{\kappa}$ (on wing only)
Number of elements , $N_e = 384$
Airfoil section : circular biconvex (both wing and tail)

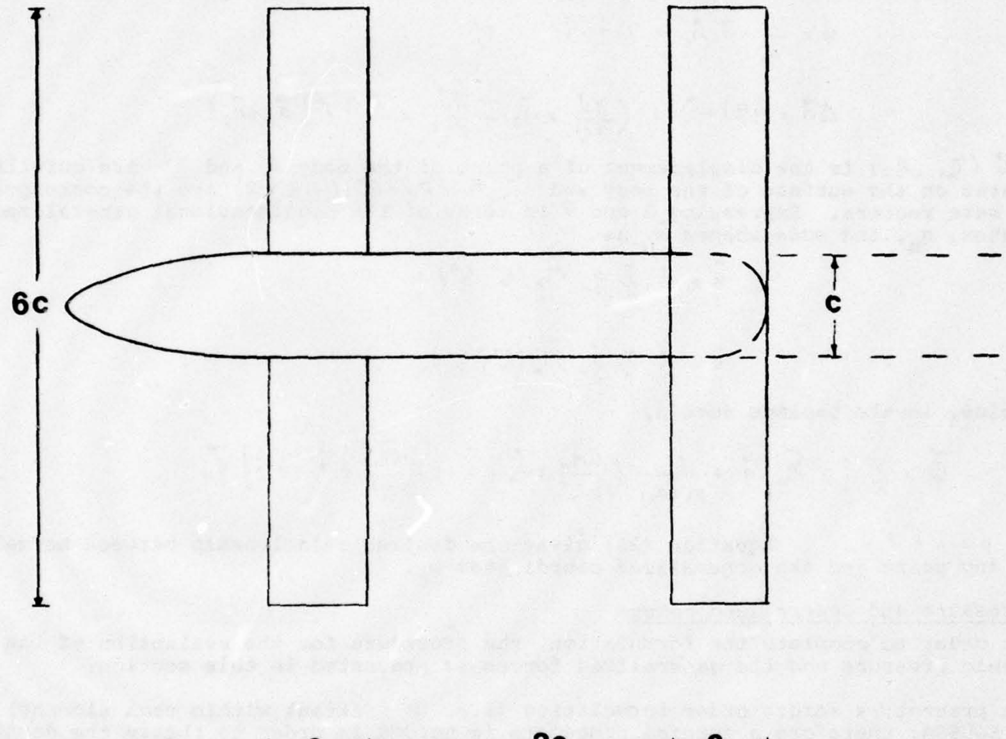

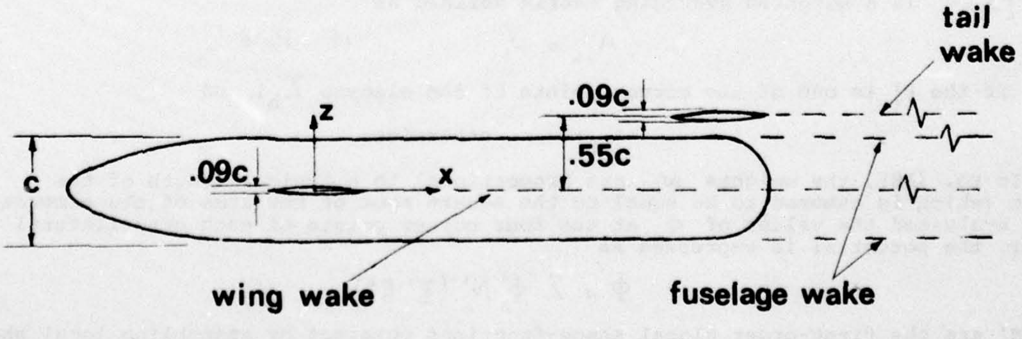

APPENDIX A

In order to evaluate the matrix relating the generalized forces to the generalized coordinates, additional relationships must be introduced. These include the relationship between normal wash and generalized coordinates and the relationship between generalized forces and potential. These relationships are briefly described in this Appendix.

A.1 Boundary Condition

The derivation of the boundary condition is given in detail in Ref. 15. Here the derivation is briefly summarized. The boundary condition is obtained by imposing that the velocity of the fluid, $U_\infty \vec{i}$, and the velocity of the body, $\vec{v}$, have the same components along the normal to the surface of the body. This yields

$$\psi = (\vec{v} - U_\infty \vec{i}) \cdot \vec{n}(t) / U_\infty \tag{A1}$$

where $\vec{n}(t)$ is the instantaneous normal to the surface of the body. The unsteady part of the boundary condition (neglecting high order terms) is given by

$$\psi = \frac{1}{U_\infty} \vec{v} \cdot \vec{n}_o + \Delta \vec{n} \cdot \vec{i} \tag{A2}$$

with

$$\Delta \vec{n} = \vec{n}(t) - \vec{n}_o = \left(\frac{\partial \vec{u}}{\partial \xi^1} \times \vec{a}_2 - \frac{\partial \vec{u}}{\partial \xi^2} \times \vec{a}_1 \right) \Big/ \left| \vec{a}_1 \times \vec{a}_2 \right| \tag{A3}$$

where $\vec{u}\,(\xi_1, \xi_2)$ is the displacement of a point of the body, ξ^1 and ξ^2 are curvilinear coordinates on the surface of the body and $\vec{a}_\alpha = \partial P / \partial \xi^\alpha$ $(\alpha = 1,2)$ are the corresponding surface base vectors. Expressing $\vec{u}$ and $\vec{v}$ in terms of the nondimensional generalized coordinates, q_n, and mode shapes $\vec{M}_n$ as

$$\vec{u} = \ell \sum_n q_n \vec{M}_n (\xi^1, \xi^2) \tag{A4}$$

and

$$\vec{v} = \ell \sum_n \dot{q}_n \vec{M}_n (\xi^1, \xi^2) \tag{A5}$$

one obtains, in the Laplace domain,

$$\tilde{\psi} = \sum_n \left[p \vec{M}_n \cdot \vec{n} + \frac{\ell}{|a_1 \times a_2|} \left(\frac{\partial \vec{M}_n}{\partial \xi^1} \times \vec{a}_2 \cdot \vec{i} - \frac{\partial \vec{M}_n}{\partial \xi^2} \times \vec{a}_1 \cdot \vec{i} \right) \right] \tilde{q}_n \tag{A6}$$

where $p = s \ell / U_\infty$. Equation (23) gives the desired relationship between normal wash at any point and the generalized coordinates q_n.

A.2 Pressure and Generalized Forces

In order to complete the formulation, the procedure for the evaluation of the aerodynamic pressure and the generalized forces is presented in this section.

At present, a zeroth order formulation (i.e. Φ constant within each element) is used in SOUSSA: therefore a special procedure is needed in order to obtain the derivative of Φ . First, consider an averaging scheme which imposes that the value of the potential Φ_k' at the node P_k' is the weighted average of the values of the potential at the centroids of the elements surrounding P_k'. In other words

$$\{\Phi_k'\} = [A_{kh}]\{\Phi_h\} \tag{A7}$$

where $[A_{kh}]$ is a weighted averaging matrix defined as

$$A_{kh} = w_h \qquad \text{if} \quad P_k' \in \Sigma_h \tag{A8}$$

(i.e., if the P_k' is one of the corner points of the element Σ_h) and

$$A_{kh} = 0 \qquad \text{otherwise} \tag{A9}$$

In Eq. (A8), the weights w_h are proportional to a typical length of the element (which is assumed to be equal to the square root of the area of the element Σ_h). Having evaluated the values of Φ at the four corner points of each quadrilateral element, the potential is expressed as

$$\Phi = \sum \Phi_h' N_h' (\xi^1, \xi^2) \tag{A10}$$

where N_h' are the first-order global shape-functions obtained by assembling local shape-functions of the type

$$N_h^{(E)} = \frac{1}{4 \Xi_k^1 \Xi_k^2} \left(\Xi_k^1 + \Xi^1 \right) \left(\Xi_k^2 + \Xi^2 \right) \tag{A11}$$

where $\Xi^1_k = \pm 1$ and $\Xi^2_k = \pm 1$ are the locations of the corners P_k of the element Σ_h (Ξ^1 and Ξ^2 are the coordinates over the element). Then

$$\frac{\partial \Phi}{\partial \xi^\alpha} = \Sigma\, \Phi'_n \frac{\partial N'_n}{\partial \xi^\alpha} \tag{A12}$$

The pressure coefficient may be evaluated from the linearized Bernoulli theorem as

$$c_p = -2 \left(p\, \Phi + \frac{\partial \Phi}{\partial x} \right) \tag{A13}$$

Expressing $\vec{\nabla}\Phi$ in terms of the tangential derivatives of Φ and neglecting the contribution of the normal component, the pressure coefficient is given by

$$c_p = -2 \left(p\, \Phi + \frac{\partial \Phi}{\partial \xi^1} \vec{a}^1 \cdot \vec{i} + \frac{\partial \Phi}{\partial \xi^2} \vec{a}^2 \cdot \vec{i} \right) \tag{A14}$$

where $\vec{a}^\alpha$ are the contravariant base vectors in the x, y, z space with $\partial \Phi / \partial \xi^\alpha$ given by Eq. (A12).

Next consider the generalized aerodynamic forces

$$e_n = -q \oiint_{\sigma_B} c_p\, \vec{n} \cdot \vec{M}_n \, d\sigma_B \tag{A15}$$

where

$$q = \frac{1}{2} \rho\, U_\infty^2 \tag{A16}$$

is the dynamic pressure.

By assuming that the pressure coefficient c_p is constant within each element (consistent with the assumption made on Φ), Eq. (A15) can be expressed as

$$\{ e_n \} = q \left[E^{(4)}_{nh} \right] \{ c_{p_h} \} \tag{A17}$$

where

$$E^{(4)}_{nh} = - \iint_{\sigma_h} \vec{n} \cdot \vec{M}_n \, d\sigma_h \tag{A18}$$

$$= - \int_{-1}^{1} \int_{-1}^{1} \vec{a}_1 \times \vec{a}_2 \cdot \vec{M}_n \, d\xi^1 \, d\xi^2 \simeq -4\, \vec{a}_1 \times \vec{a}_2 \cdot \vec{M}_n \Big|_{P = P_h}$$

where $\vec{a}_1$ and $\vec{a}_2$ are the base vectors of the element σ_h in the x, y, z space.

A.3 SOUSSA

The above formulation is implemented in the computer program SOUSSA (Steady, Oscillatory and Unsteady, Subsonic and Supersonic Aerodynamics). The computational implementation of the formulation presented above is briefly summarized here. Note first that the relationship between normal wash and generalized coordinates, Eq. (A5) may be written as*

$$\tilde{\underline{\Psi}} = \underline{E}^{(1)} \tilde{\underline{q}} \tag{A19}$$

where

$$\tilde{\underline{\Psi}} = \{ \tilde{\Psi}_n \} \tag{A20}$$

and $\underline{E}^{(1)}$ is a matrix implicitly defined by Eq. (A6). Furthermore Eq. (14) may be rewritten as

$$\tilde{\underline{\Phi}} = \tilde{\underline{E}}^{(2)} \tilde{\underline{\Psi}} \tag{A22}$$

whereas the relationship between pressure coefficient and potential may be written as

$$\tilde{\underline{c}}_p = \tilde{\underline{E}}^{(3)} \tilde{\underline{\Phi}} \tag{A23}$$

where $\tilde{\underline{E}}^{(3)}$ is obtained by combining Eqs. (A7), (A10), (A12) and (A14). Finally (see Eq. (A17)

$$\tilde{\underline{e}} = q\, \underline{E}^{(4)} \tilde{\underline{c}}_p \tag{A24}$$

or, combining Eqs. (A19, A22, A23 and A24),

$$\tilde{\underline{e}} = q\, \tilde{\underline{E}}\, \tilde{\underline{q}} \tag{A25}$$

where the matrix of the generalized aerodynamic forces, $\tilde{\underline{E}}$, is given by

$$\tilde{\underline{E}} = \tilde{\underline{E}}^{(4)} \tilde{\underline{E}}^{(3)} \tilde{\underline{E}}^{(2)} \tilde{\underline{E}}^{(1)} \tag{A26}$$

---

* In Eqs. (A19) to (A26) compact matrix notations are used. Vectors and matrices are underlined. Tildas indicate Laplace's transform or equivalent operation.

Note that $\tilde{\underline{E}}^{(1)}$ and $\tilde{\underline{E}}^{(4)}$ depend upon the modes $\vec{M}_p\ (\xi^1, \xi^2)$, whereas $\tilde{\underline{E}}^{(2)}$ and $\tilde{\underline{E}}^{(3)}$ do not. The separation of $\tilde{\underline{E}}$ into mode-dependent matrices and mode-independent matrices is particularly useful for automated optimal structural design in which the same geometry but different modes are used in each iteration. In addition $\underline{E}^{(2)}$ is the only matrix which depends in a complicated way upon the reduced complex frequency, p. However, once the coefficients of Eq. (15) are evaluated, the evaluation of $\underline{E}^{(2)}$ requires only the combination of these coefficients according to Eq. (14) and the inversion of a matrix. This is particularly useful for the evaluation of the aerodynamic influence coefficients for several frequencies, as needed for instance for flutter analysis.

FORCE MEASUREMENTS ON FINITE WINGS IN OSCILLATORY VERTICAL GUSTS

M.H. Patel
Department of Mechanical Engineering,
University College London,
Torrington Place,
London WC1E 7JE.

SUMMARY

This paper describes aerodynamic lift and pitching moment measurements on two finite wings in harmonic vertical oscillatory gusts of varying frequency parameter and gust amplitude. The variation of aerodynamic force per unit gust amplitude with frequency parameter is shown to be independent of freestream velocity, wing incidence and gust amplitude, but is strongly influenced by wing sweep. Good agreement is obtained with calculations based on a lifting surface theory. The tests on both wings are extended to the determination of aerodynamic force response to periodic vertical gusts which incorporate a combination of two harmonic frequency components. The validity of the superposition concept for unsteady attached flow over finite wings is demonstrated by comparing the components of force response at each of the two forcing frequencies to the corresponding response at the single harmonic frequency. Further measurements of lift, pitching moment and rolling moment are presented for both wings at various attitudes of skew (in yaw) to a harmonic oscillatory gust front. The effects of the resultant asymmetric lift distributions on the two wings halves are identified in the results; with particular reference to the amplitudes and phases of oscillating rolling moments that are generated.

1. INTRODUCTION

The ability to reliably predict the response of aircraft to atmospheric turbulence is important in ensuring adequate aircraft structural integrity and handling characteristics as well as in the design of active controls and gust alleviation systems. Current emphasis has been placed on these problems in relation to the high speed, low altitude flight of military aircraft.

At present, the theoretical predictions of wing loads in atmospheric turbulence are based on modelling both the continuous gusts and the aircraft response by a superposition of harmonic components. This presupposes a knowledge of the wing force response to harmonic gusts as well as the validity of superposition in then modelling the aircraft response to a realistic atmospheric gust. As a contribution to the understanding of aerodynamic wing loads due to incident gusts, without the attendant aircraft response, the characteristics of two rigid wing planforms have been measured at low speed in a known series of periodic vertical two dimensional gusts.

Three sets of tests are reported here. The first group involve measurements of lift forces and pitching moments on the wings in harmonic vertical oscillatory gusts of varying frequency parameter and gust amplitude. These results are compared with calculations using a lifting surface theory. Secondly, the tests on both wings are extended to the determination of aerodynamic force response to periodic vertical gusts which consist of combinations of two harmonic frequency components; in order to investigate the validity of the superposition concept for unsteady attached flow over finite wings. Thirdly, the effects on the wing forces of small angles of skew (in yaw) relative to an incident gust are experimentally investigated.

The two wing planforms used for most of the tests are (1) a rectangular wing of aspect ratio 6 and (2) an untapered wing of 45^o sweep and aspect ratio 4. These are designated as wings A and B respectively, for convenience.

The oscillatory gusts are generated in the low speed gust tunnel, at Queen Mary College, described by Patel & Hancock (1). Tests are reported over a frequency parameter ($\omega c/U$) range of 0.1 up to 0.8 for a constant gust amplitude ($\sim 1.8^o$) at two wing incidences for which the flow remains attached. Frequency parameter has been varied by changes in both frequency and freestream velocity. The effect of gust amplitude has also been investigated. Somewhat severe transition strips have been attached to the wings to ensure fixed transition at the leading edge for all the tests.

2. THE GUST TUNNEL FACILITY

2.1. The Wind Tunnel

The gust facility used for these tests is based on a conventional low speed wind tunnel, shown in Fig.1, with a contraction area ratio of 14.5:1 and an exit to the contraction, 0.76 m high and 0.99 m across, through which flow speeds of up to 25 m/s are available. The working section consists of a rigid semi-open structure with solid vertical sidewalls and slotted upper and lower walls. These slotted walls are necessary to produce adequate oscillatory flow characteristics in the test section.

The gust generation device, shown in Fig.2, consists of flexible extensions to the top and bottom walls at the exit to the contraction. These upper and lower extensions are fixed at their ends to an aluminium frame which can be moved up or down. Rigid sidewalls extend the contraction exit to the frame. Oscillatory motion of the frame by an electro-hydraulic servo-mechanism perturbs the shear layers above and below the semi-open test section into rolling up and forming discrete vortices in the jet mixing regions; as shown in Fig.3. The systems of rolled up vortices convect downstream with a velocity of 0.61 of the mean freestream velocity and induce an oscillatory travelling wave form of vertical gust in an irrotational flow field within the working section. The flexible nozzle is oscillated by an electro-hydraulic servo system capable of generating displacements proportional to an input voltage signal. The shape of the generated gust closely resembles this displacement - time voltage input to the movable frame. Thus, harmonic gusts at single frequencies are obtained by sinusoidal motion of the nozzle. For complex gusts at a combination of two frequencies, the required stable input signal is obtained from electronic apparatus which enables the input frequency pairs, their amplitudes and the phase differences between them to be pre-selected. Ref. 1 gives a more detailed account of the gust generation mechanism.

The oscillatory gust flow is monitored by a small aerofoil yawmeter which is situated just off one of the working section sidewalls upstream of the wing models. Signals from this yawmeter are treated as a reference for all the oscillatory measurements. A variable incidence support rig, shown in Fig.1, is used for mounting either the sting balance and wing for the force measurements or a second aerofoil yawmeter to detect the gust angle characterics at the wing position.

2.2. Working section Oscillatory Gust Conditions

For harmonic gusts at single frequencies, the oscillatory vertical velocity component on the horizontal centre plane of the working section can be written as

$$\bar{w}\,(x,t) = \bar{w}_g\, e^{i\omega(t + \frac{x}{0.61U})} \qquad (1)$$

where x is a coordinate pointing upstream, U is the mean freestream velocity, $\bar{w}$ is the nondimensionalised instantaneous vertical velocity component (= w/U), $\bar{w}_g$ is the nondimensionalised amplitude of vertical velocity oscillations (w_g/U), ω is the radian frequency and 0.61U is the downstream convection velocity of the travelling wave.

The gust amplitude, $\bar{w}_g$, is an easily calibrated function of the nozzle forcing frequency, ω, the nozzle amplitude and distance downstream aft of the nozzle. This calibration yields a usable frequency range (written in terms of frequency parameter per unit chord, in m) of $0.40 < \omega/U < 5.70$ for a gust amplitude of $\bar{w}_g = 0.0314$ or 1.80° gust incidence angle. The corresponding frequency values are from 2 to 12 Hz. For a frequency parameter of around $\omega/U = 2.2\ m^{-1}$, gust amplitudes of up to $\bar{w}_g = 0.054$ (≈ 3.10°) are also available.

The spatial distribution of gust amplitude in the working section determines the size and positioning of the test models. Figure 4 illustrates typical variations of the single frequency gust amplitude with downstream distance aft of the nozzle. For all the frequencies, a constant amplitude region is obtained downstream of a point 1.00 m from the nozzle frame. Thus, for a model positioned 1.300 m aft of the nozzle (see Fig.4), a region of constant gust amplitude is available for the wing and its wake. The wake lies in this region of constant gust amplitude up to the end of the working section sidewalls which are 1.300 m downstream of the model position.

Fig.5 shows typical variations of gust amplitude with vertical distance from the working section centreline. The 'hyperbolic cosine' type of variation of vertical velocity amplitudes is a consequence of the alternating vortices in the upper and lower shear layers (shown in Fig.3) which induce the irrotational working section gust flow. Changes in these curves due to frequency can be predicted from simple theoretical considerations, since separation distances between adjacent vortices in each shear layer are frequency dependent. The 'hyperbolic cosine' amplitude distribution is not in itself a limitation. The main restriction is the available height of irrotational flow between the upper and lower mixing regions; which as seen from Fig.5 is ± 20 cm about the centreline. This is more than adequate, however, for the thin wings used in those tests.

Measurements of the harmonic oscillatory flow in the spanwise direction across the working section reveal a closely two dimensional gust.

For the case of the more complex periodic gust at a combination of two frequencies, the incident flow is, effectively, a superposition of two gusts convecting downstream. Mathematically, this can be written as :

$$\bar{w}\,(x,t) = \bar{w}_{g1}\, e^{i\omega_1(t + \frac{x}{0.61U})} + \bar{w}_{g2}\, e^{\left[i\omega_2(t + \frac{x}{0.61U}) + \gamma\right]} \qquad (2)$$

where, in addition to the symbols defined in equation (1), $\bar{w}_{g1}$ and $\bar{w}_{g2}$ are nondimensionalised vertical velocity amplitudes at frequencies ω_1 and ω_2 respectively while γ is the phase difference between the two input frequencies and is taken with respect to the higher frequency, ω_2. The travelling wave convection velocity of this 'double frequency' gust is also 0.61U where U is the mean freestream velocity. Both $\bar{w}_{g1}$ and $\bar{w}_{g2}$ are complicated functions of the two forcing frequencies ω_1 and ω_2, the nozzle amplitudes at these frequencies, the phase difference between the two frequencies as well as distance downstream aft of the nozzle; $\bar{w}_{g1}$ and $\bar{w}_{g2}$ can, however, be calibrated for each individual case to be measured and are accurately repeatable thereafter.

The usable frequency range in this mode of tunnel operation remains unaltered from that available for the single frequency gusts. The spatial distributions of gust angle amplitudes at each of the two forcing frequencies also exhibit closely similar trends to those obtained with harmonic gusts. This applies for both the downstream (as in Fig.4) and vertical (Fig.5) variations of gust amplitude as well as to the spanwise uniformity of the gust field.

From these considerations, a suitable test model position was chosen such that the root quarter chord point of the test wing lay on the working section of centreline at 1.300 m aft of the nozzle. Here the wings and their wakes were in a region of uniform gust amplitude. Furthermore, oscillatory lift forces, pitching moments and rolling moments were measured relative to the freestream flow at the root quarter chord point.

2.3. Models and Test Equipment

As already mentioned the two wing models tested were (1) a rectangular wing of aspect ratio 6 (wing A) and (2) an untapered wing of 45° sweep and aspect ratio 4 (wing B). In addition, a few of the experiments were performed with a third wing, called C, which was untapered with 45° sweep but with an aspect ratio of 6. All three wings were made up from symmetrical 10% thick NACA 0010 aerofoil sections with wing spans of 0.60 m (60% of the working section width). The planforms had straight leading and trailing edges, no centrebodies and streamwise tips which were shaped such that the upper and lower aerofoil surfaces were joined round each tip by a half body of revolution generated by the aerofoil surface about the tip chord line. The wing chords were 0.10 m for wings A and C and 0.15 m for wing B. Roughness strips were used to provoke transition just aft of the leading edges (at 7% chord). These strips were 10 mm wide (10% chord) and were made up of silicon carbide abrasive paper with a grain height of 0.4 mm.

Fig.6 shows the reference axes system used for the tests with its origin 1.300 m aft of the nozzle at the root quarter chord point of the wing planform. For non-zero values of the skew angle, θ, these coordinates were taken to rotate with the wing. Positive incidence was taken to be nose down to ensure consistency of 'positive' lift with either wing incidence or downward gust velocity.

Aerodynamic forces on the wings were measured by a cantilever type lift, pitching moment and rolling moment sensing sting balance. The balance was designed for very low strain levels and minimum length to maximise the natural frequencies of bending and torsional vibrations. Adequate sensitivity was maintained by the use of semi-conductor strain gauges with a high gauge factor ($\sim$ 180) and a negligible level of gauge factor drift due to temperature ($\sim$ 0.022% per °C) using internal compensation.

The effects on the measurements of oscillatory deflection of the sting under oscillatory aerodynamic loads were calculated. The magnitude of resulting measurement error was shown to be extremely small due to the combination of high sting stiffness and the small aerodynamic loads that were involved. The accuracy of the measurements was, however, affected by the sting-wing system behaving as a simple two degree of freedom dynamical system in bending and torsion with natural frequencies of 60 Hz and 38 Hz respectively. A measured dynamic calibration of each sting-wing system required the amplitude of the oscillatory lifts and rolling moments to be corrected by up to about 2% and 5% respectively at the highest test frequency ($\sim$ 12 Hz). The low damping present in the system produced negligible phase errors.

The incidence gust angle and resultant wing force output signals were recorded by two different digital sampling systems.

The measurements at single frequencies were made using a system that sampled the signal to be measured at selected time instants over successive oscillation cycles. A reference signal, from an upstream gust angle measuring yawmeter, supplied the information for selecting the sampling time instants. The resulting data was a set of 'phase averages' which described the signal to be measured in relation to the reference signal. The phase average can be defined as the average value of the measured signal over several successive cycles that is obtained at a particular phase of the reference signal wave cycle.

The signals for tests at a combination of two frequencies were recorded by a fast continuous digital sampling system which had the capability of sampling the reference and a measured signal simultaneously over a number of oscillation cycles.

Data from both sampling systems were fed to a mini-computer which performed a numerical harmonic analysis of the data sets at the forcing frequencies in the reference gust angle. After calibration and correction factors had been applied, the final results were obtained as amplitude and phase angles of $\Delta C_L/\bar{w}_g$, $\Delta C_{PM}/\bar{w}_g$ and $\Delta C_{RM}/\bar{w}_g$ against frequency parameter $\omega c/U$ for each frequency in the input gust. The phase angles were relative to the undisturbed flow at the wing root quarter chord point in the absence of the wings. A measure of the experimental uncertainty in the data presented here can be estimated as approximately ±3% in amplitude values and ±2° for phase angles. Ref.1 gives further details of the sampling and data processing apparatus.

3. THE MEASUREMENTS

3.1. On Wings In Symmetric Attitudes To Harmonic Single Frequency Gusts

These tests were performed with the approaching oscillatory gust front perpendicular to the wing plane of symmetry, (i.e. with $\theta = 0°$).

Data from steady flow measurements of lift and pitching moment against incidence is condensed in Table 1 for both wings A and B together with calculated values based on inviscid lifting surface theory (Ref.2).

These show good agreement with the experiments.

As pointed out in ss.2.2, force measurements in oscillatory flow are presented relative to the freestream oscillatory gust at the root quarter chord point. A yawmeter situated at this point was used to measure the freestream gust relative to conditions at a reference upstream yawmeter in the absence of the wing. Force measurements were then made relative to the upstream yawmeter output and the two data sets combined to give amplitude and phase of $\Delta C_L/\bar{w}_g$ and $\Delta C_{PM}/\bar{w}_g$ against $\omega c/U$ relative to the undisturbed flow at the wing root quarter chord point.

A comprehensive range of tests was performed for both wings at constant gust amplitude ($\bar{w}_g = 0.0314$ or 1.8°) over a range of frequency parameters ($1.0 < \omega c/U < 5.06$) at two incidences (0° and 4°) and two freestream velocities (12.43 and 20.00 m/s). Measurements were also made on both the wings at constant frequency parameter ($\sim$ 2.2 and 2.51 per unit chord), 0° incidence and varying gust amplitude (0.0087 {0.5°} $< \bar{w}_g <$ 0.054 {3.1°}).

Results for the variation of $\Delta C_L/\bar{w}_g$ and $\Delta C_{PM}/\bar{w}_g$ with freestream gust amplitude for the wings are listed in Table 2. No significant change due to freestream gust amplitude is evident.

Fig.7 shows the effects of frequency parameter on the force results for rectangular wing A at 0° incidence. Important points to note are the close agreement between data at the two freestream velocities, the manner in which the in-phase amplitude curve in lift appears to approach zero frequency parameter and the magnitude of the lift out-of-phase component which is equivalent at high frequency parameters to a phase lag of about 23° relative to the freestream gust. The significant variation of pitching moment amplitude with frequency parameter is also of interest. Fig.8 displays the results for wing B at 0° incidence. In addition to having the features already mentioned for wing A, the effect of the 45° wing sweep is apparent in the far higher out-of-phase components in lift and pitching moment observed here. The amplitude of pitching moment is much larger than in wing A because of the rearward shift in aerodynamic centre from the wing root quarter chord point caused by wing sweep. The variations of wing forces with frequency parameter were also measured at an incidence of 4° for both wings A and B. These produced results which were identical within the bounds of experimental error to the data at 0° incidence.

3.2 On Wings in Symmetric Attitudes to Gusts at a Combination of Two Frequencies.

The type of measurements described here are illustrated by Fig.9, showing the waveforms of instantaneous gust incidence and the resultant lift response on the rectangular wing A for frequency combinations of 2 and 4 Hz and 2 and 8 Hz respectively. The lift traces display a high frequency ($\sim$ 60 Hz) ripple arising from the sting balance and wing structural vibrations in bending, in addition to the expected response at the two forcing frequencies. Measurements of spectral power density showed that the forcing and response oscillations were concentrated at the two forcing frequencies with no evidence of higher harmonics in the lift response. The additional lift output due to the sting natural vibration frequency in bending was also evident in the spectra.

As for the single frequency measurements described in ss.3.1, the double frequency tests also involved measuring both the gust angle at the test wing root quarter chord point and the wing forces relative to a reference yawmeter at a point upstream of the test wing. A numerical harmonic analysis of the data then yielded lift and pitching moment coefficients for each frequency in the form of amplitude and phase of $\Delta C_{L1}/\bar{w}_{g1}$ and $\Delta C_{PM1}/\bar{w}_{g1}$ for frequency parameter $\omega_1 c/U$ with amplitude and phase of $\Delta C_{L2}/\bar{w}_{g2}$ and $\Delta C_{PM2}/\bar{w}_{g2}$ for frequency parameter $\omega_2 c/U$.

A systematic series of tests was carried out on both wing planforms at two incidences (0° and 5°) and two freestream velocities (12.43 m/s and 20.00 m/s), by varying the two frequencies of the input gust, the amplitudes at each of these frequencies and the relative phase difference between them. These tests incorporated the following cases:

(1) Single frequency measurements, identical to those of ss.3.1, for checking the recording apparatus and for providing a data set with which the double frequency measurements could be compared.

(2) Double frequency measurements using a range of frequency pairs with the two component frequencies of each input having equal amplitude and zero phase difference relative to each other.

(3) Double frequency measurement at one frequency pair having equal amplitude components but with varying phase difference γ between the two input frequencies.

(4) Double frequency measurements at one frequency combination having zero phase difference between the two frequencies but with a constant amplitude for one and a varying amplitude for the other frequency.

Fig.10 shows the results for wing A at 0° incidence for input gusts described in case (2) above. These data are plotted over the single frequency results, shown by full lines, for comparison purposes. Each double frequency response measurement is split up into the component amplitude of force at each frequency before being plotted at the two frequency parameter abscissae values by identical symbols. For example, in Fig.10, the dual frequency response at 20.00 m/s for an 'input' gust frequency combination of 5 and 10 Hz is represented at corresponding frequency parameter abscissae points of 0.157 and 0.314 by the + (plus) symbol. Agreement between the single frequency and each component of the double frequency is good with little scatter. Data at the two freestream velocities are differentiated throughout by using open symbols (e.g. +, x) for 20.00 m/s and closed symbols (e.g. O , △) for 12.43 m/s.

Fig.11 displays corresponding results to those described above for the lift response of wing A at an incidence of 5°. The data points have been plotted over the 0° incidence results and show that the validity of superposition is unaffected by the wing angle of incidence in attached flow.

Fig.12 illustrates variation of the lift response for wing A at 0° incidence (U = 12.43 m/s) due to changes in the phase difference between the two input frequencies (3 and 6 Hz) which are kept at equal amplitudes. The corresponding single frequency data are plotted to show that the response remains unchanged in the presence of the two frequencies in the incident flow. Similar trends were obtained for the lift and pitching moment variations with amplitudes of the two frequencies making up the input gust. These data are not plotted here.

The complete set of tests discussed so far were repeated for swept wing B. Figs.13 and 14 show typical data from some of the tests. Fig.13 illustrates the results at 0^o incidence for double frequency combinations of equal amplitude and zero phase difference between the input frequencies, again plotted with the single frequency response for comparison. Fig.14 displays the effect of wing incidence on the double frequency response. These results for wing B also exhibit generally good agreement between the single frequency response data and the components of the double frequency response.

3.3 On Wings in Attitudes of Skew (in Yaw) to Harmonic Single Frequency Gusts

These tests were carried out with planforms A and C mounted at attitudes of skew (in yaw) relative to an incident two-dimensional gust field. The force balance used for previous tests was modified to incorporate a wing mount which could be skewed by up to 20^o.

Initial experiments, with the wings positioned symmetrically in the gust field, yielded data which conformed with previous such results. Tests with the wings in skewed attitudes were carried out for both planforms at angles of skew (θ) of 10^o and 20^o with wing incidence angles of 0^o and 3^o at two freestream velocities (12.43 and 20.00 m/s) and over a range of frequency parameters. The gust amplitude was, how ever, kept constant at $\bar{w}_g = 1.8^o$ for these tests.

Steady flow experiments at skew angles of $\theta = 10^o$ and 20^o for both wings yielded trends in measured rolling moments which were due to the differential sweep of the two wing halves in the flow. This effect was virtually non-existent for rectangular wing A but was quite marked for wing C with a 45^o sweep angle. These results are condensed in Table 3 in terms of the lift and moment curve slopes. The lift curve slope for wing A at $\theta = 0^o$ measured here is slightly lower than the value reported in ss 3.1 for the equivalent experiment. This is believed to be due to the aerodynamic effects of the bulkier sting mounting at the wing root which is required for rotating the wing in skew.

In the oscillatory flow tests for wing A, the lift and pitching moment distributions with frequency parameter at a skew angle of $\theta = 10^o$ were virtually identical to the symmetric response ($\theta = 0^o$). Fig.15, however, shows such data for lift at $\theta = 20^o$, and these results do differ markedly from the symmetric values. Significant effects of skew angle are evident in the rolling moment measurements displayed in Fig.16. The amplitude of rolling moment increases almost linearly with frequency parameter but for both $\theta = 10^o$ and 20^o, the phase angle variation remains constant at about 110^o lag. These characteristics are consistent with the manner in which the rolling moment develops on the rectangular planform in oscillatory flow. The phase lag of 110^o arises because, for a rectangular wing at an angle of skew, the rolling moment due to the gust incidence distribution with distance downstream lags the freestream oscillation by 90^o and the resultant lift further lags the incidence angle by approximately 20^o.

For wing C, Fig.17 shows the lift and pitching moment variations against frequency parameter at skew angles of $\theta = 0^o$ and 20^o. As for wing A, these results display a small effect of skew angle on lift and pitching moment although the results for $\theta = 0^o$ and 10^o do agree closely with each other. The rolling moment distributions for $\theta = 0^o$, 10^o and 20^o are shown in Fig.18. A non-zero, in-phase rolling moment at $\theta = 0^o$ indicates some small asymmetry in the two wing halves. However, for $\theta = 10^o$ and 20^o, the rolling moment changes mirror the differential lifts from the two wing halves due to their unequal sweep angle to the flow. In contrast to the results for wing A, these data exhibit a constant rolling moment amplitude and increasing phase lag with frequency parameter for each value of skew angle θ. This latter effect can be accounted for by the large downstream extent of the highly swept wing C being influenced by the streamwise incidence variations of the travelling wave gust field which become more pronounced with increasing frequency parameter. The larger rolling moment amplitudes observed for wing C are a consequence of the highly asymmetric lift distributions that must exist on the two wing halves.

4. DISCUSSION AND CONCLUSIONS

All the experiments in this investigation were performed with attached flow on the wing surfaces at all times and at low Reynolds numbers (up to 2×10^5 based on root chord) with transition strips on both surfaces just aft of the leading edges to simulate the boundary layer at higher Reynolds number. No wind tunnel corrections have been applied to the acquired data. The steady flow lift force, pitching and rolling moment curve slopes are used for the zero frequency cases in the oscillatory flow results.

In the following disucssion a few general points are considered first.

All the tests indicate that the measured lift forces and moments are proportional to the freestream gust amplitude. Table 2 lists typical data and shows $\Delta C_L/\bar{w}_g$, $\Delta C_{PM}/\bar{w}_g$ to be constant with $\bar{w}_g$ over the available range of gust amplitudes ($0 < \bar{w}_g < 3.1^o$).

The lift and pitching moment amplitude ($\Delta C_L/\bar{w}_g$ and $\Delta C_{PM}/\bar{w}_g$) variations with frequency parameter ($\omega c/U$) for all the wings show that results for the two freestream velocities are closely consistent with each other in that they collapse on to the same curve when plotted in terms of the frequency parameter, $\omega c/U$. Furthermore these results remain independent of wing incidence. The variation of phase lag with frequency parameter appears to depend primarily on sweep angle, so that the higher the sweep, the greater is the phase lag increase with frequency. This effect is to be expected since the phase of the incident gust distribution alters with distance downstream. Fig.19 shows these phase changes with sweep for wings A and C, both of aspect ratio 6 but with sweep angles of 0^o and 45^o respectively.

An important part of the present study is the comparison of acquired experimental data with existing theories. In oscillatory flow, the travelling wave nature of the incident gust has to be accounted for within a theoretical solution of the problem. For the experiments reported here, the gust convection velocity is 0.61 of the freestream velocity. An oscillatory gust which is convecting downstream with the freestream velocity can be expressed mathematically as:

$$\bar{w}\,(x,\,t) = \bar{w}_g\, e^{i\omega(t\,+\,x/U)} \qquad (3)$$

with the notation of Fig. 6 and equation (1). Taking $\nu = \omega c/U$ and $\bar{x} = x/c$ gives

$$\bar{w}\,(x,\,t) = \bar{w}_g\, e^{i\nu\bar{x}}\, e^{i\omega t} \qquad (4)$$

where c is the mean chord of a stationary wing in the flow field. The problem can be solved for the aerodynamic force amplitude per unit gust amplitude ($\bar{w}_g$) in terms of the frequency parameter ν.

However, the oscillatory single frequency gust in the test facility can be written as

$$\bar{w}\,(x,\,t) = \bar{w}_g\, e^{i\omega\,(t\,+\,x/0.61U)}$$

and transformed to a gust of the form

$$\bar{w}\,(x,t) = \bar{w}_g\, e^{i\nu\bar{x}/0.61}\, e^{i\omega t} \qquad (5)$$

incident on a stationary wing. This problem is identical to the preceding one except for an effective change of the oscillatory gust wavelength. Therefore, comparisons between theories based on gusts moving with the freestream velocity and the present experiments can be made by interpreting the change in wavelength as specifying an 'effective' frequency parameter ν', for the experiments to be

$$\nu' = \frac{\nu}{0.61} = \frac{\omega c}{0.61U} \qquad (6)$$

Several theoretical models are currently available for the calculation of harmonic oscillatory inviscid flow around finite wings. One of these is lifting surface theory: see Multhopp (3), Garner(4),Garner and Fox (5). Computations using this method (Garner and Davies (2)) have been performed for wings A and B. The calculated results are plotted in Figs. 7 and 8 for comparison with experiment. The calculations incorporate the effective frequency parameter required to account for the travelling wave velocity of the incident gust.

Force measurements on wings A and B in periodic gusts consisting of combinations of two frequencies are summarised in Figs. 10 to 14. The measured forces are split up into their respective components at the two forcing frequencies and then compared with a previously recorded response at single frequencies in order to provide a measure of the applicability of superposition. The results demonstrate that the superposition principle applies generally for any double frequency gust by tests which have systematically varied the frequency pairs making up the input, the phase difference between the two frequencies and the amplitude levels of each frequency.

Further measurements of lift, pitching moment and rolling moment are presented in Figs. 15 to 18 for wings A and C at angles of skew of $\theta = 10^\circ$ and 20° to the incident gust front. These results show that the total oscillatory lifts and pitching moment amplitudes are not unduly affected by the skewed wing attitude but the asymmetric lift distributions on the two wing halves do generate significant rolling moments which are quantified in Figs. 16 and 18 for wings A and C respectively.

The experiments described in this paper are a small part of the overall programme of research into unsteady aerodynamics using two gust tunnels at Queen Mary College. It is felt that these results should prove useful in reaching a better understanding of the unsteady flow around finite wings as well as in providing test cases for comparison with currently available calculation methods.

5. REFERENCES

1. Patel, M.H. and Hancock, G.J. A gust tunnel facility. A.R.C. R. & M. 3802, 1977.

2. Garner, H.C. and Davies, D.E. Private communication.

3. Multhopp, H. Methods for calculating the lift distribution of wings (subsonic lifting surface theory). A.R.C. R. & M. 2884, 1950.

4. Garner, H.C. Multhopp's lifting surface theory for wings in slow pitching oscillations. A.R.C. R. & M. 2885, 1952.

5. Garner, H.C. and Fox, D.A. Algol 60 program for Multhopp's low frequency subsonic lifting surface theory. A.R.C. R. & M. 3517, 1966.

6. NOTATION

$\underline{x}$,y,z	Cartesian frame of reference axes shown in Fig.6
x	Nondimensionalised x coordinate (= x/c)
x_{ac}	Aerodynamic centre position aft of wing apex
t	Time dimension
A	Wing aspect ratio
C_L	Lift coefficient ($=L/\frac{1}{2}\rho U^2 S$)
C_{PM}	Pitching moment coefficient ($= M_P/\frac{1}{2}\rho U^2 Sc$)
C_{RM}	Rolling moment coefficient ($= M_R/\frac{1}{2}\rho U^2 Sc$)
c	Wing chord
L	Lift force
M_P, M_R	Pitching moment and rolling moment about y and x axes respectively
S	Wing area in plan
U	Mean freestream velocity
$\underline{w}$	Instantaneous vertical velocity (downwash) component of gust
w	Instantaneous angle of incident gust (= w/U)
$\underline{w}_g$	Amplitude of vertical velocity (downwash) component in oscillatory flow
w_g	Amplitude of incident gust angle in oscillatory flow ($= w_g/U$)
α	Angle of incidence of test wing; positive nose down about y axis (Fig.6)
γ	Phase difference between the two frequencies of the double frequency gust in terms of the higher frequency ω_2
θ	Wing angle of skew (rotation about z axis)
ΔC_L	Amplitude of lift coefficient ($= \Delta L/\frac{1}{2}\rho U^2 S$)
ΔC_{PM}	Amplitude of pitching moment coefficient ($= \Delta M_P/\frac{1}{2}\rho U^2 Sc$)
ΔC_{RM}	Amplitude of rolling moment coefficient ($= \Delta M_R/\frac{1}{2}\rho U^2 Sc$)
ΔL	Amplitude of lift force
ΔM_P	Amplitude of pitching moment about y axis
ΔM_R	Amplitude of rolling moment about x axis
Λ	Sweep angle of wing quarter chord line
ν	Frequency parameter (= ωc/U)
ν'	'Effective' frequency parameter (= ωc/0.61U)
ρ	Air density
φ	Phase lead between wing force or moment and freestream oscillation
ω	Radian frequency

Subscripts

1	Quantities referring to the lower of a combination of two frequencies
2	Quantities referring to the higher of a combination of two frequencies

7. TABLES

Wing	Lift Curve Slope $\partial C_L/\partial\alpha$		Pitching Moment Curve Slope $\partial C_{PM}/\partial\alpha$		Aerodynamic Centre Position x_{ac}/c	
	Expt.	Theory	Expt.	Theory	Expt.	Theory
A	4.03	4.21	0.0	0.0	0.25	0.25
B	2.84	3.02	2.48	2.78	1.12	1.17

Steady Flow Results : Symmetric Wing Attitude ($\theta = 0^\circ$)

Table 1.

Wing	Frequency Parameter $\omega c/U$	Freestream Gust Amplitude $\bar{w}_g$/degs	ΔC_L / $\bar{w}_g$		ΔC_{PM} / $\bar{w}_g$	
			i.p.	o.p.	i.p.	o.p.
A	0.202	0.97	3.08	-1.12	-0.31	-0.18
		1.97	3.14	-1.15	-0.36	-0.17
		2.80	3.19	-1.15	-0.44	-0.17
	0.251	0.97	2.88	-1.07	-0.53	0.11
		1.94	3.03	-1.24	-0.55	0.092
		2.74	3.06	-1.19	-0.57	0.049
B	0.303	0.97	1.52	-1.74	-1.00	1.66
		1.97	1.66	-1.82	-1.15	1.83
		2.80	1.66	-1.96	-1.14	2.05
	0.377	0.93	1.44	-1.73	-0.97	1.84
		1.99	1.47	-1.80	-0.96	1.91
		3.05	1.44	-1.75	-1.03	1.80

Oscillatory Flow Results At Symmetric Wing Attitudes ($\theta = 0^o$) :
Effect of Freestream Gust Amplitude

Table 2.

Wing	Skew Angle θ /degs.	$\partial C_L / \partial \alpha$	$\partial C_{PM} / \partial \alpha$	$\partial C_{RM} / \partial \alpha$
A	0	3.90	0.0	0.0
	10	3.87	0.0	-0.23
	20	3.80	0.0	-0.29
C	0	2.91	3.93	-0.22
	10	2.87	4.20	-1.05
	20	2.71	3.88	-1.68

Steady Flow Results : Skewed Wing Attitudes

Table 3.

This work has been carried out with the support of Procurement Executive, Ministry of Defence, U.K.

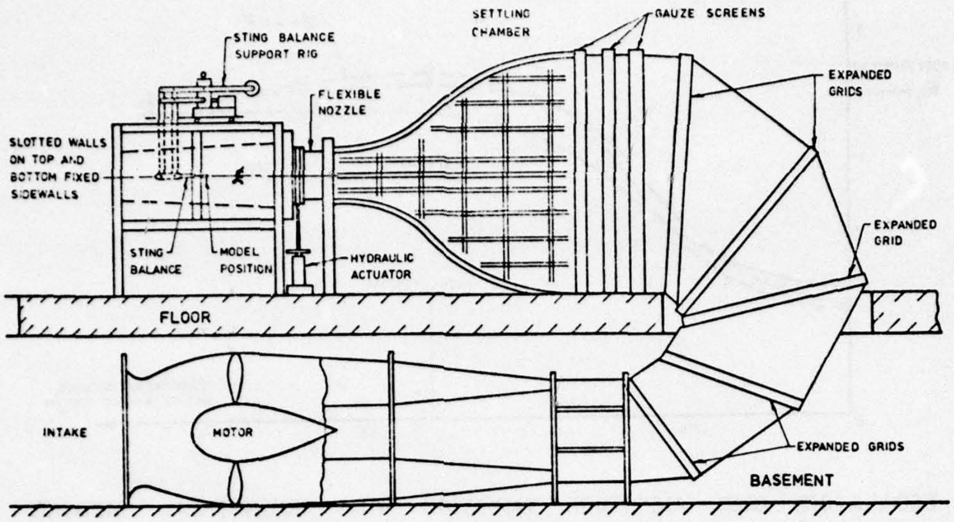

THE GUST TUNNEL

Fig. 1

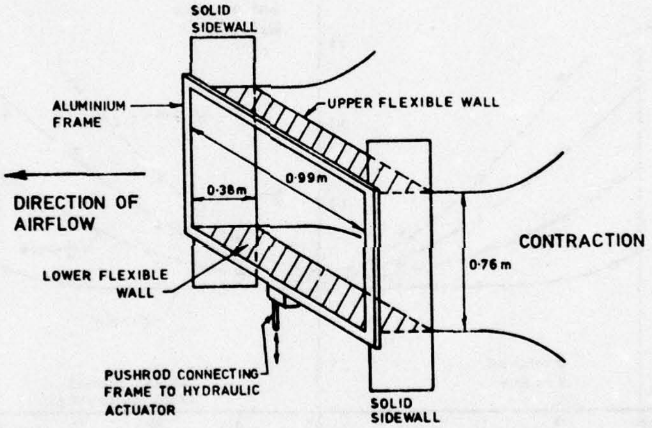

FLEXIBLE NOZZLE DETAILS

Fig. 2

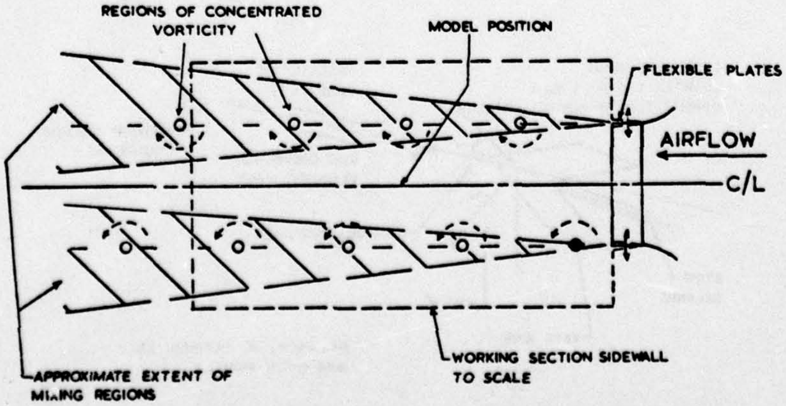

THE WORKING SECTION FLOW FIELD

Fig. 3

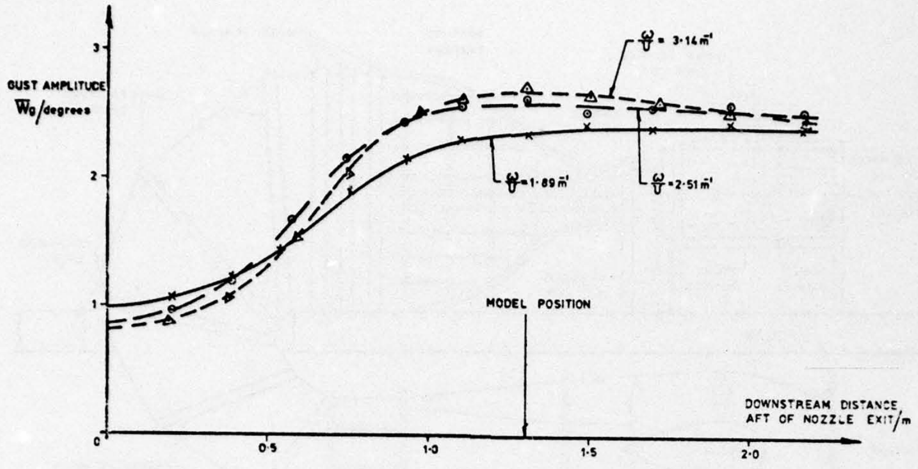

OSCILLATORY GUST AMPLITUDE VARIATION WITH DOWNSTREAM DISTANCE

Fig. 4

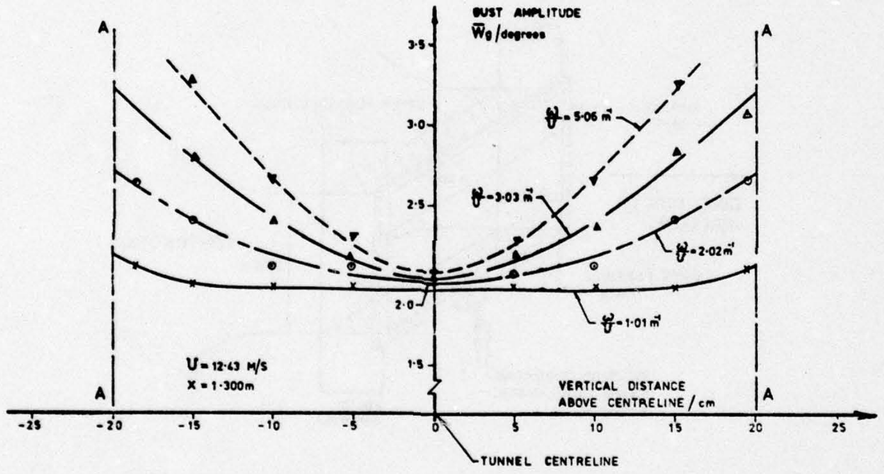

LINES AA DENOTE APPROXIMATE
MIXING REGION BOUNDARIES

OSCILLATORY GUST AMPLITUDE VARIATION WITH VERTICAL DISTANCE

Fig. 5

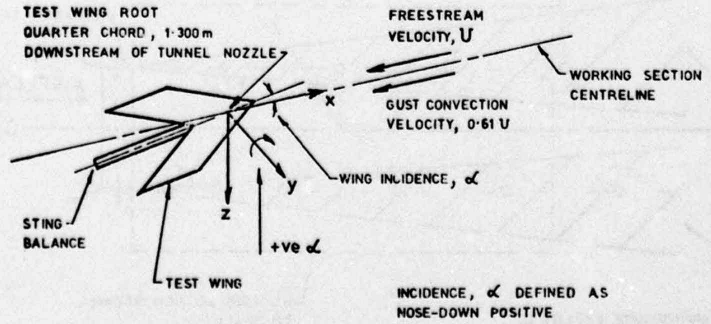

INCIDENCE, α DEFINED AS
NOSE-DOWN POSITIVE

THE WING REFERENCE AXES SYSTEM

Fig. 6

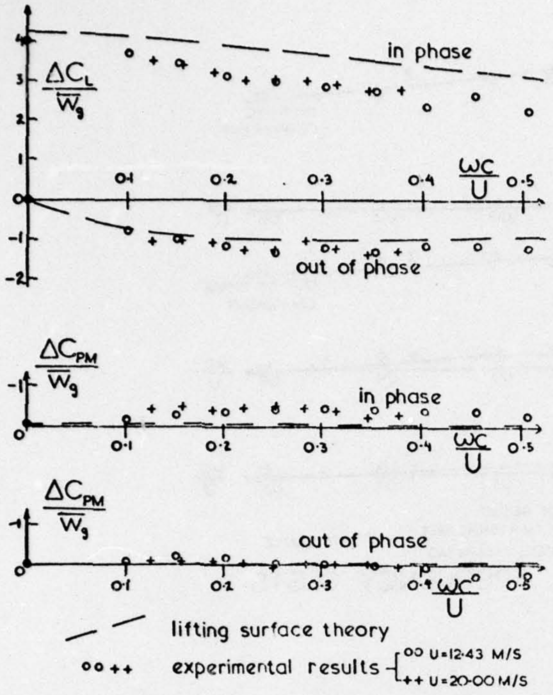

Forces On Rectangular Wing (A = 6)
In Oscillatary Gusts
Fig. 7

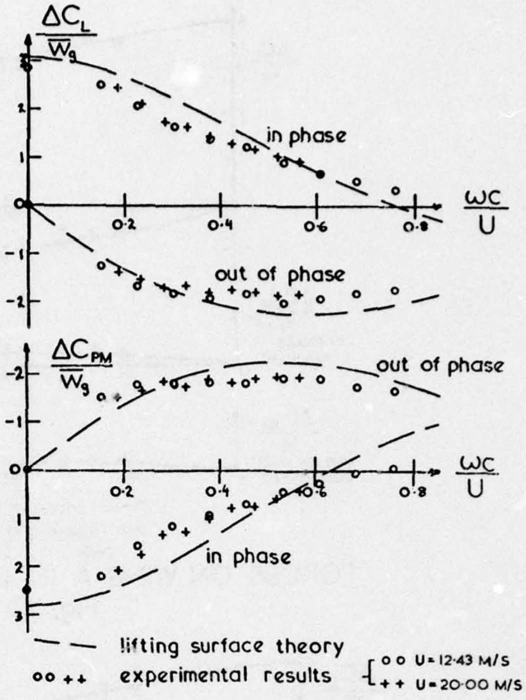

Forces On Swept Wing (Λ=45°, A = 4)
In Oscillatory Gusts
Fig. 8

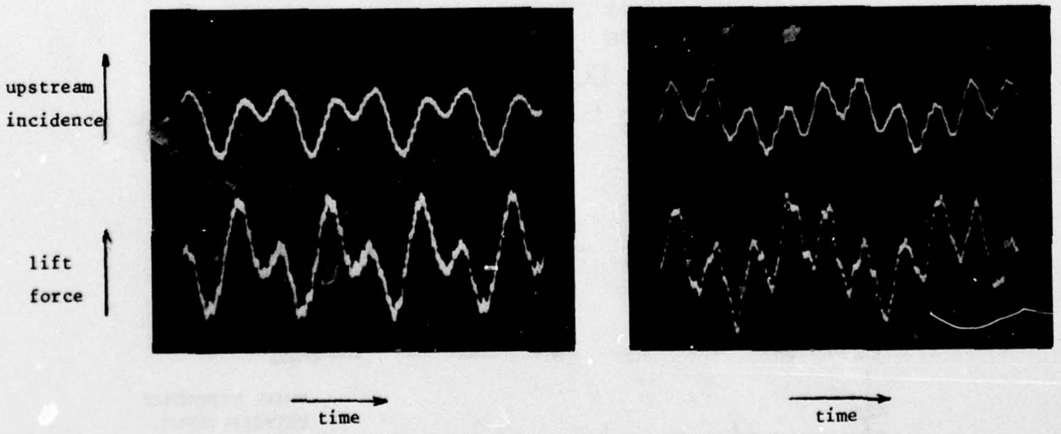

2 & 4 HZ

2 & 8 HZ

U = 12.43 m/s

Test model :- Rectangular planform, aspect ratio 6

TYPICAL WAVEFORMS OF GUST ANGLE AND LIFT FORCE

FIG. 9

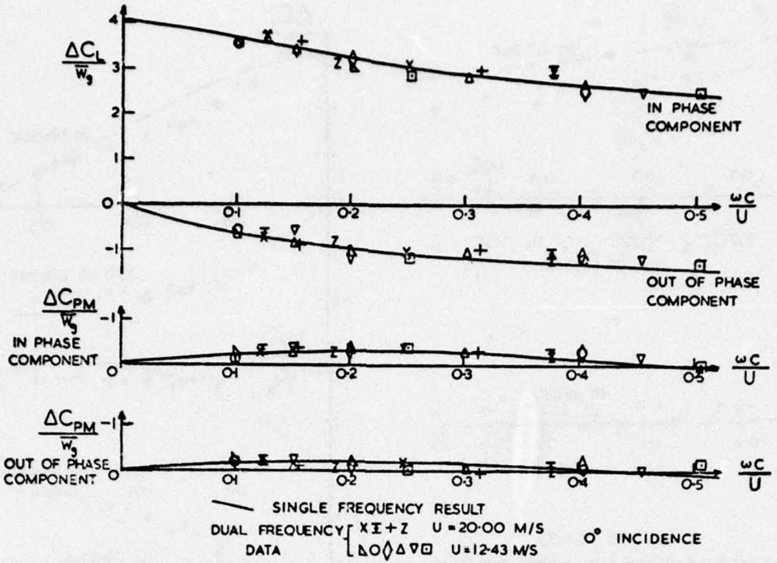

FORCES ON WING A IN DUAL FREQUENCY GUSTS
Fig. 10

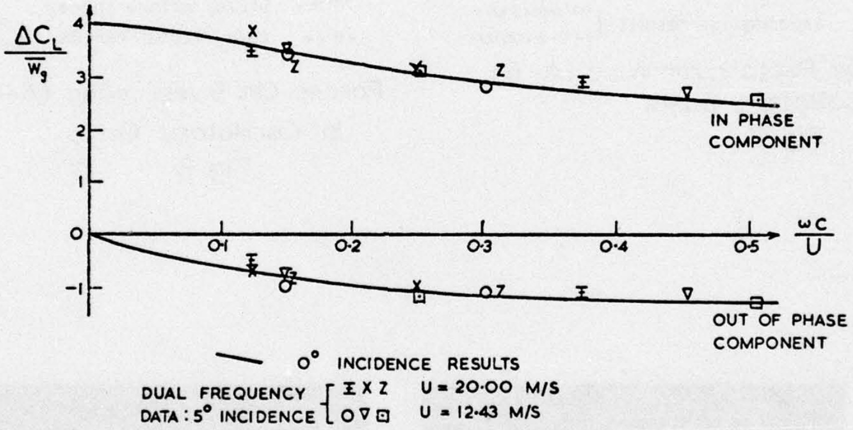

LIFT ON WING A IN DUAL FREQUENCY GUSTS
Fig. 11

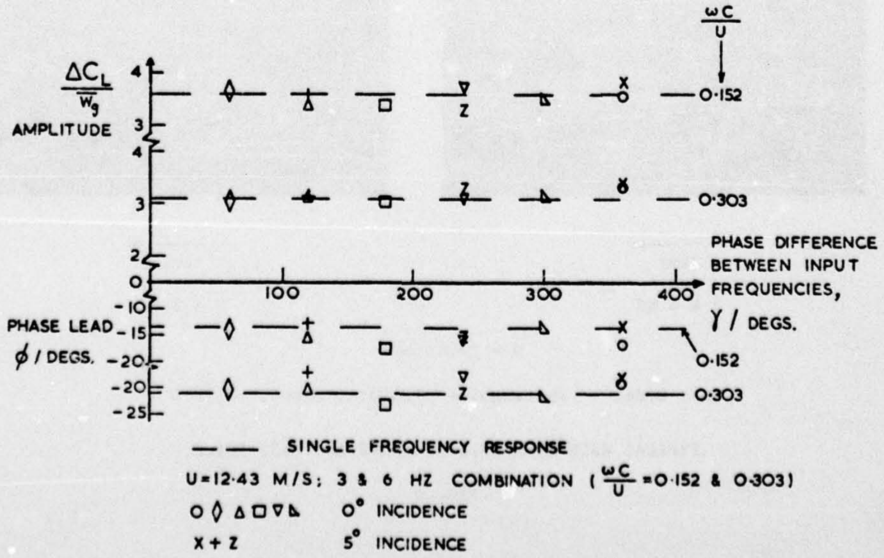

LIFT ON WING A IN DUAL FREQUENCY GUSTS
Fig. 12

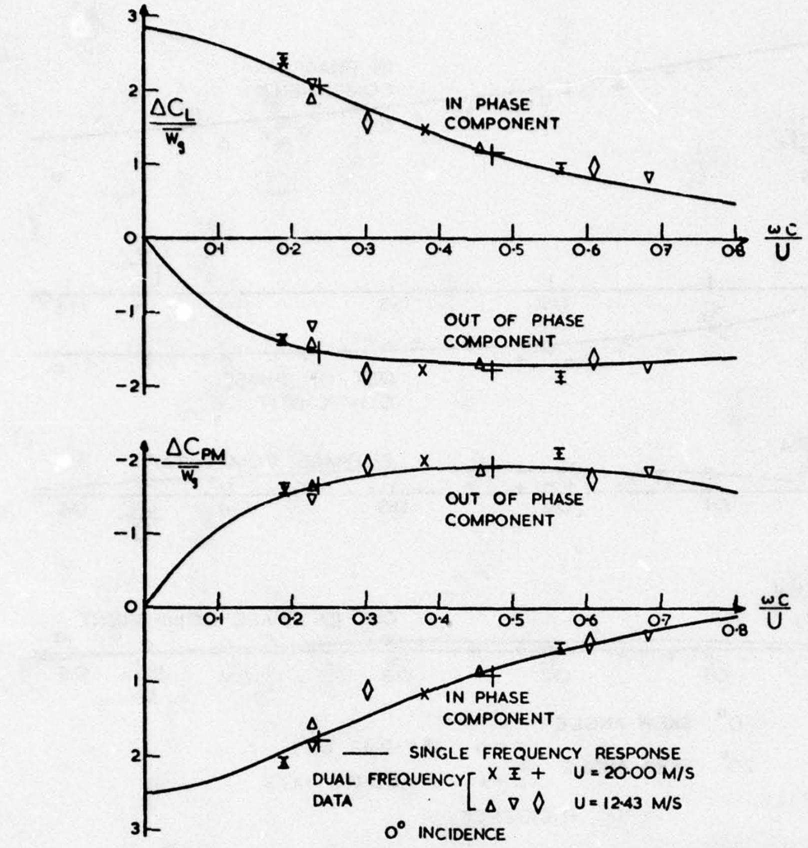

FORCES ON WING B IN DUAL FREQUENCY GUSTS

Fig. 13

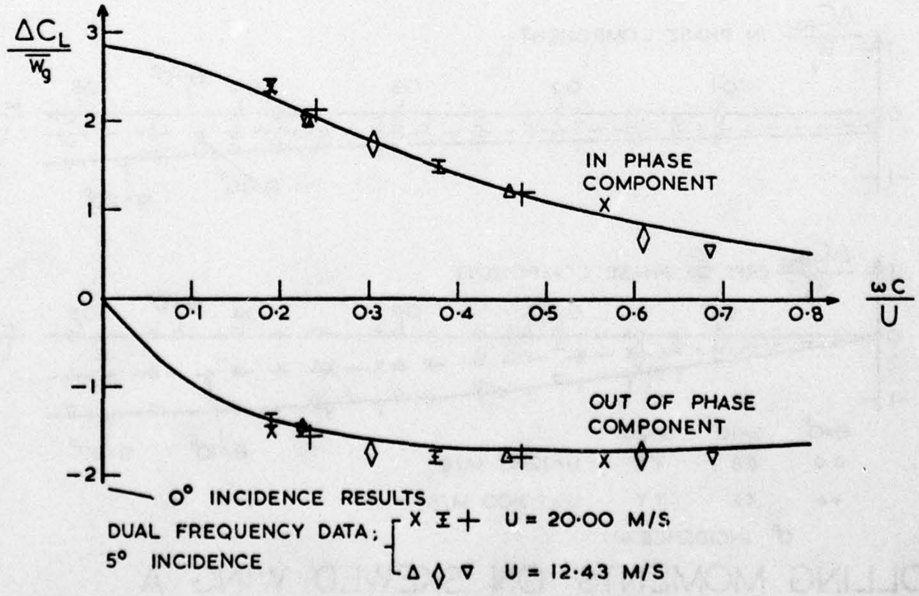

LIFT ON WING B IN DUAL FREQUENCY GUSTS

Fig. 14

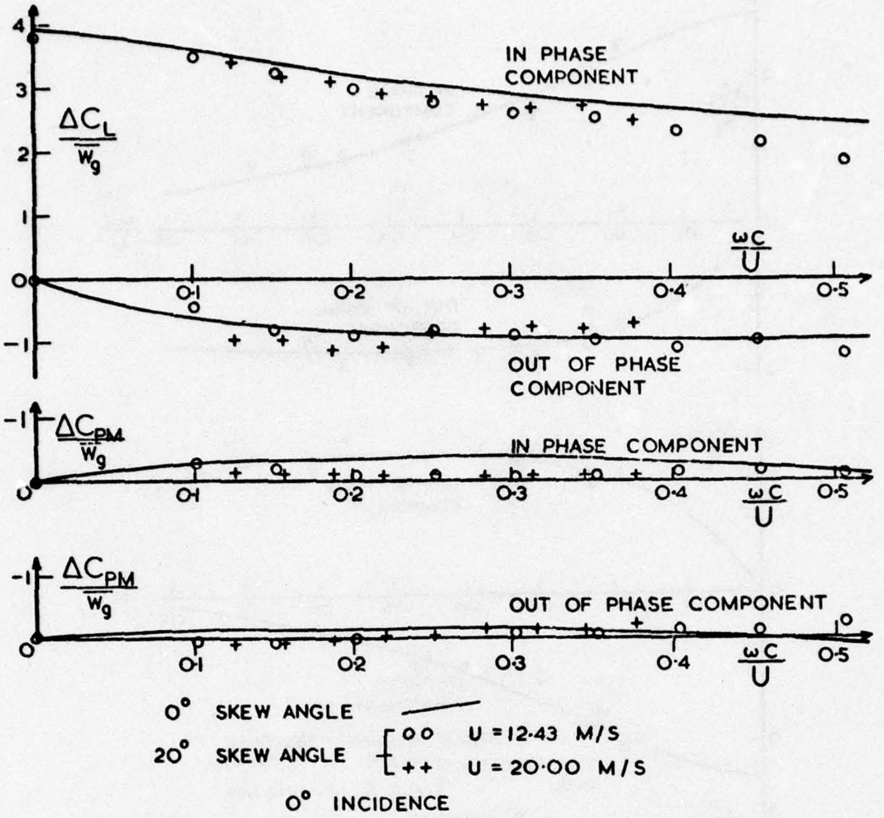

FORCES ON WING A WITH Θ = 20°

Fig. 15

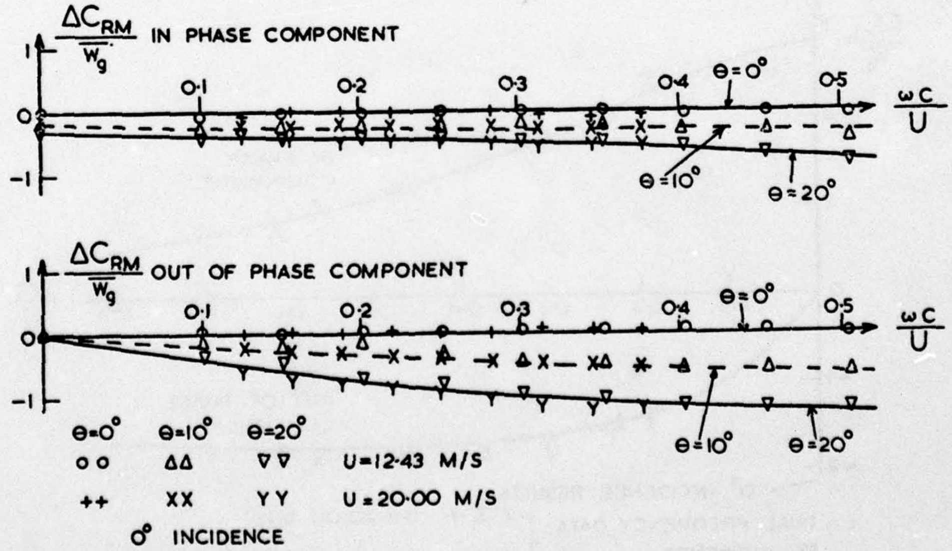

ROLLING MOMENTS ON SKEWED WING A

Fig. 16

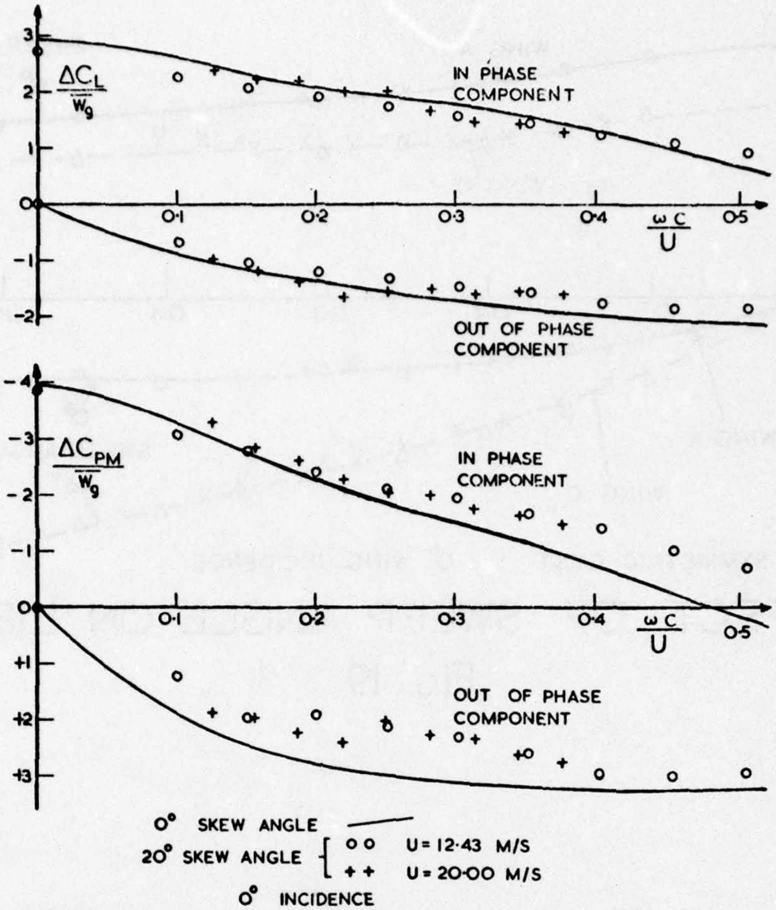

FORCES ON WING C WITH Θ = 20°
Fig. 17

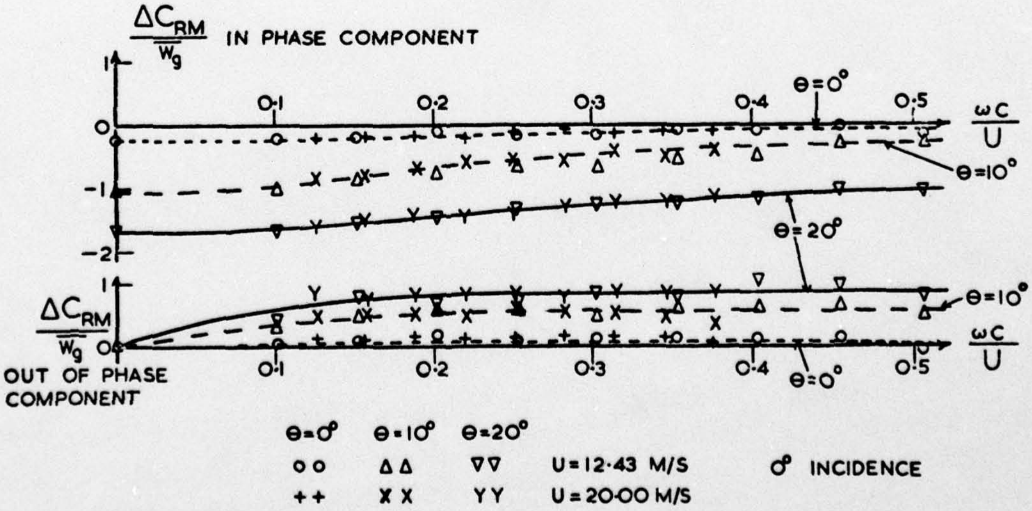

ROLLING MOMENTS ON SKEWED WING C
Fig. 18

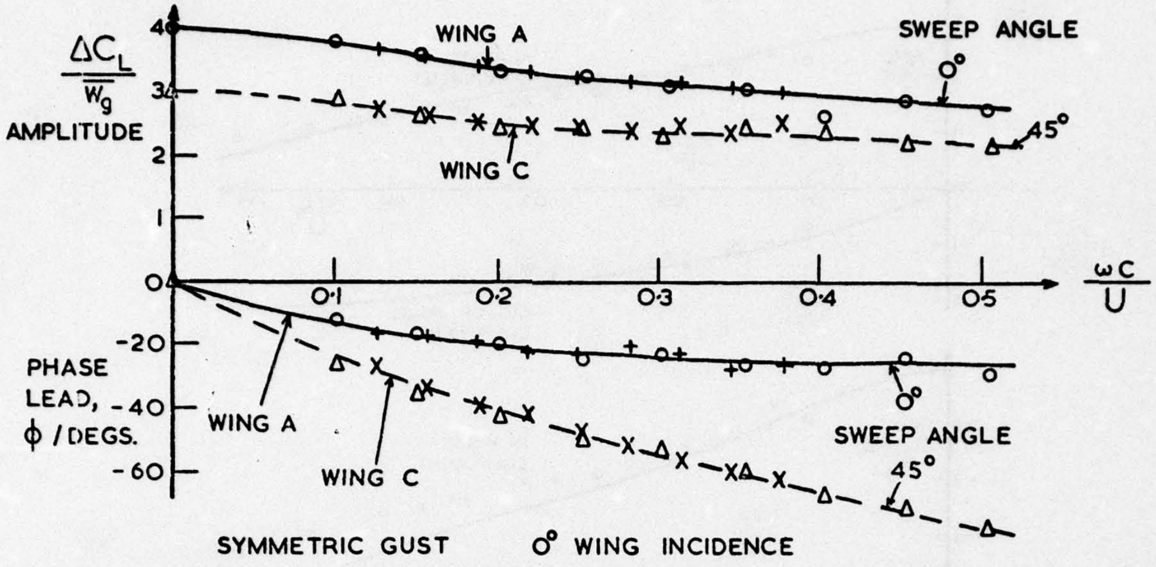

EFFECT OF SWEEP ANGLE ON LIFT

Fig. 19

CALCULATION OF UNSTEADY AIRLOADS ON OSCILLATING THREE-DIMENSIONAL WINGS AND BODIES

by

Wolfgang Geißler
Deutsche Forschungs- und Versuchsanstalt für Luft- und Raumfahrt E. V.
- Aerodynamische Versuchsanstalt Göttingen -
Institut für Aeroelastik
3400 Göttingen, Bunsenstraße 10, Germany

SUMMARY

The exact prediction of unsteady airloads on arbitrary oscillating configurations is of fundamental importance for a detailed flutter analysis. For these aeroelastic investigations, a numerical method has been developed to calculate the steady and unsteady pressure distributions on harmonically oscillating three-dimensional wings and bodies in subsonic flow.

The method is based on a complex velocity potential represented by appropriate singularity distributions on the real oscillating surfaces. Therefore, the exact geometric boundary condition on the arbitrary body surface can be taken into account.

The following three different cases

- **oscillating three-dimensional thin wings**
- **oscillating bodies at incidence**
- **oscillating three-dimensional wings with finite thickness and incidence**

have been investigated intensively.

Numerical results for a variety of problems have been checked against other analytical methods as well as against experimental data. The agreement was found to be very satisfactory.

LIST OF SYMBOLS

x, y, z	cartesian coordinates
x, r, φ	cylindrical coordinates
ξ, η, ζ	panel coordinates (ζ perpendicular to the panel surface)
l_0, l	reference length
ϕ, Φ	velocity potential
U_∞	main flow velocity
a_∞	velocity of sound
Ma_∞	Mach number, $Ma_\infty = U_\infty / a_\infty$
p	static pressure
ρ	density
q_∞	dynamic pressure of undisturbed flow, $q_\infty = \frac{1}{2} \rho U_\infty^2$
c_p	pressure coefficient, $c_p = \frac{p - p_\infty}{q_\infty}$
$\bar{c}_p$	complex unsteady pressure coefficient, $\bar{c}_p = \bar{c}'_p + i\,\bar{c}''_p$
α	angle of incidence

α', ζ'	amplitude of oscillation
t	time
ω	frequency
ω^*	reduced frequency, $\omega^* = \frac{\omega \cdot l_0}{U_\infty}$
F	area

1. INTRODUCTION

For the calculation of unsteady pressure distributions on oscillating wing surfaces, a variety of semi analytical and numerical methods have been developed in recent years. The best known are the kernel function methods [1], [2], which use analytically defined pressure distribution functions, and the doublet lattice method [3]. The latter is a fully numerical concept which represents the wing surface by a large number of small surface panels. Both kernel function and doublet lattice method use the acceleration potential with a corresponding acceleration doublet distribution on the wing surface to match the boundary condition. The advantage of this concept is that the wake of the wing has not to be taken into consideration - there is no pressure jump through the wake surface.

In [4] a method is described which is based on the velocity potential and uses velocity doublet distributions on the wing surface. First two dimensional results using this concept are discussed.

For the present numerical methods, the same velocity potential concept has been used. Two advantages characterize this method

1. The aerodynamic influence functions are rather simple compared to the equivalent expressions for the acceleration potential
2. The method is not restricted to linearized lifting surface theory, but can be extended to arbitrary surfaces in a straightforward manner.

A disadvantage is that the wake has to be taken into account, thus leading to rather complicated semi-infinite wake integrals. A method has been developed to evaluate these wake integrals by numerical methods.

In the following, the theoretical background and the numerical handling of the following three different problems:

a) 3d-mean surface unsteady theory

b) oscillating body at incidence

c) 3d-oscillating wing with finite thickness and incidence

on the basis of the velocity potential, will be discussed, and numerical results will be presented which have been obtained by the corresponding three computer programs developed for each case. The numerical results are compared with corresponding experimental data.

2. TRANSFORMATION OF THE UNSTEADY SUBSONIC POTENTIAL EQUATION

The linearized time-dependent potential equation, serving as a starting point for all unsteady potential theories, reads for subsonic flow

$$(1) \qquad \left(1 - Ma_\infty^2\right)\frac{\partial^2\phi}{\partial x^2} + \frac{\partial^2\phi}{\partial y^2} + \frac{\partial^2\phi}{\partial z^2} - \frac{2\,Ma_\infty}{a_\infty^2}\frac{\partial^2\phi}{\partial x\,\partial t} - \frac{1}{a_\infty^2}\frac{\partial^2\phi}{\partial t^2} = 0$$

with Ma_∞ as the Mach number of the undisturbed flow, and ϕ as the time dependent velocity potential.

In the case of harmonic time-dependency, the well known transformation

$$(2) \qquad \phi(x,y,z,t) = U_\infty\, l_0\, \Phi(X,Y,Z)\, e^{i(\lambda X + \omega^* T)}$$

can be used to reduce Eq. (1) to the Helmholtz wave equation

$$(3) \qquad \frac{\partial^2\bar{\Phi}}{\partial X^2} + \frac{\partial^2\bar{\Phi}}{\partial Y^2} + \frac{\partial^2\bar{\Phi}}{\partial Z^2} + \varkappa^2\,\bar{\Phi} = 0$$

with

$$\varkappa = \frac{Ma_\infty \omega^*}{\beta^2} \quad ; \quad \beta^2 = 1 - Ma_\infty^2$$

and

$$\lambda = \varkappa \cdot Ma_\infty \quad .$$

The cartesian coordinates and the time are made dimensionless in the usual way by

$$X = x/l_0 \; ; \quad Y = y\cdot\beta/l_0 \; ; \quad Z = z\cdot\beta/l_0 \; ; \quad T = t\cdot U_\infty/l_0 \quad .$$

In Eqs. (2) and (3), the reduced frequency

$$\omega^* = \frac{\omega \cdot l_0}{U_\infty} \tag{4}$$

occurs as the most important unsteady parameter.

The Helmholtz wave equation quite obviously reduces to the simple Laplace equation for the transformed velocity potential Φ in two limiting cases:

a) Incompressible flow ($Ma_\infty = 0$)

Here the time dependency is only expressed by the fact that the transformed potential is a complex quantity with both real and imaginary parts. The mode and the frequency of oscillation do only enter the problem by the boundary condition. For this special incompressible case, a numerical procedure for the calculation of unsteady airloads on oscillating bodies and wings with arbitrary surface geometries has been developed.

b) Compressible steady flow ($\omega^* = 0$)

This is the steady case with a Prandtl-Glauert type of transformation for the body coordinates. For the more arbitrary case of unsteady compressible flow, the Helmholtz wave equation can be transformed into an integral equation by use of Greens theorem

$$\frac{\partial\bar{\Phi}}{\partial Z} = \lim_{Z \to 0} \iint_{F+W} \Delta\bar{\Phi} \, \frac{\partial^2}{\partial Z^2}\left(\frac{e^{-i\varkappa r}}{r}\right) dX\,dY \tag{5}$$

where r is the distance between the source point and the control point on the wing surface. $\partial\bar{\Phi}/\partial Z$ expresses the normal velocity on the wing induced by a doublet distribution of harmonically oscillating strength.

The integral in Eq. (5) has to be taken over the wing and wake surfaces, respectively. Due to the governing linearized potential equation, *the wing surface is now assumed to be infinitely thin.* The wake is located in the plane of the wing. $\Delta\bar{\Phi}$ expresses the velocity potential difference between the upper and lower surfaces of the wing.

The prescribed downwash velocity on the wing due to the oscillating movement is given by

$$W = -\left(\frac{\partial\Phi}{\partial Z}\right)_{Z=0} = \frac{1}{\beta}\left(\bar{f}\, i\omega^* + U_\infty \frac{\partial\bar{f}}{\partial x}\right) e^{-i(\lambda X + \omega^* T)} \tag{6}$$

with f as the displacement of a surface point due to the oscillation

$$f = \bar{f}(X, Y)\, e^{i\omega^* T} \quad .$$

In addition to the boundary condition on the wing surface, the Kutta condition at the trailing edge of the wing has to be applied. This leads to a potential distribution in the wake

$$\Delta\bar{\Phi}(X, Y)_{Wake} = \Delta\bar{\Phi}(X_t, Y)\, e^{-i\nu(X - X_t)} \tag{7}$$

with $\nu = \omega^*/\beta^2$ and X_t as the location of the wing trailing edge. It follows from Eq. (7) that in the unsteady case, the potential in the wake is no longer a constant.

Once the integral equation (5) is solved for the unknown potential differences $\Delta\bar{\Phi}$, the unsteady pressure coefficient $\Delta\bar{c}_p$ as the pressure difference between the wing lower and upper surface can be determined by means of Bernoulli's theorem:

$$\Delta\bar{c}_p = \frac{\Delta\bar{p}}{\frac{\rho}{2} U_\infty^2 \alpha'} = 2\left[i\nu\,\Delta\bar{\Phi} + \partial(\Delta\bar{\Phi})/\partial X\right] e^{i\lambda X} \quad . \tag{8}$$

with

$$\Delta\bar{c}_p = \Delta\bar{c}'_p + i\,\Delta\bar{c}''_p \quad .$$

3. NUMERICAL SOLUTION OF THE INTEGRAL EQUATION AND RESULTS

For the solution of Eq. (5) a panel type discretisation procedure is applied, dividing the oscillating surface into a large number of small plane surface elements. Fig. 1 shows a typical panel arrangement for a swept wing with control surfaces at the trailing edge. The panels are concentrated at the wing and control surface leading edges, respectively, accounting for the large gradients of $\Delta\Phi$ in these regions. Assuming constant doublet strengths for each panel Eq. (5) can be written in discretized form

$$\overline{W} = \frac{1}{4\pi} \sum_{n=1}^{I \cdot J} \Delta\overline{\Phi}_n \iint_{\Delta F_n} \frac{\partial^2}{\partial Z^2} \left(\frac{e^{-i\kappa r}}{r} \right)_{Z \to 0} dX\, dY \; + \tag{9}$$

$$+ \frac{1}{4\pi} \sum_{q=1}^{J} \Delta\overline{\Phi}_{tq} \iint_{\Delta W_q} e^{-i\nu (X - X_{tq})} \frac{\partial^2}{\partial Z^2} \left(\frac{e^{-i\kappa r}}{r} \right)_{Z \to 0} dX\, dY$$

where $\partial\overline{\Phi}/\partial Z$ is replaced by the amplitude of the prescribed downwash $\overline{W}$ (Eq. (6)). The second term in Eq. (9) represents the influence of the wake, taking into account the Kutta condition (Eq. (7)) at the wings trailing edge.

The remaining surface integrals in Eq. (9) over each panel surface - the aerodynamic influence function - must be evaluated by numerical means. In [5] it is shown in detail that the surface integrals can be reduced to line integrals along the panel edges. All integrals can be expressed by both incompressible and compressible terms. The wake integral is complicated by the exponential function occuring in the integrand. In [5] it is mentioned that the integration in the spanwise direction can be done analytical. The remaining integral of the type

$$J = \int_0^{\infty} e^{ist} f(t)\, dt \tag{10}$$

can be reduced to an integral with a finite boundary by the transformation

$$\tau = \pi / |s| \quad .$$

Using the periodic behavior of the exponential function $e^{is(t+n\tau)}$, $n = 1, 2, \ldots$ one obtains

$$J = \int_0^{\tau} e^{ist} \{ f(t) - f(t+\tau) + f(t+2\tau) - + \ldots \, dt \} \tag{11}$$

where only a finite number of terms in the infinite series is taken into account. The final calculation of J is done by use of Simpsons rule.

Once the aerodynamic influence functions of both wing surface and wake panels have been calculated, Eq. (9) can be solved in the usual way as a linear system of equations with the potential differences $\Delta\overline{\Phi}$ as the solution vector. In Eq. (8), the streamwise derivative of $\Delta\overline{\Phi}$ is necessary to calculate the pressure coefficients $\Delta\overline{c}_p$. This differentiation is done numerically by a spline interpolation process. For the determination of local lift and moment coefficients this differentiation is avoided and only a simple numerical integration remains.

3.1 THREE-DIMENSIONAL THIN WINGS

The velocity-potential panel method will first be applied to the limiting case of a thin 3d-wing with arbitrary planform, including one or more control surfaces at the trailing edge. Fig. 1 shows a wing with two control surfaces (inner and outer flap) which has been investigated experimentally in incompressible flow [6]. Fig. 2 gives results in two spanwise sections for the case of the inner and outer flaps oscillating in anti-phase. The wing remaines in a stationary position. The agreement between numerical and experimental results is quite good. Some small differences can only be observed at the control surface leading edge. This is due to a small gap there in the experimental case.

Fig. 3 shows quasi-steady and unsteady pressure distributions for the case of a rectangular wing with an oscillating control surface at high subsonic flow. Two-dimensional experimental data [7] are plotted for comparison. To represent the limiting two dimensional case a rectangular wing of aspect ratio $\Lambda = 8$ is used for the numerical calculation. The results in Fig. 3 are obtained in a spanwise section close to the plane of symmetry. The results show that the mean surface theory predicts the experimental data very well, even up to high subsonic flow velocities. At Mach numbers $Ma_{\infty} > 0.8$ the influence of the shock leads to increasing differences. It is remarkable that the lift and moment coefficients are well predicted by the lifting surface theory to even higher Mach numbers [5]. More results for different wing planforms and oscillation modes are given in [5].

3.2 OSCILLATING BODIES AT INCIDENCE

It is the advantage of the velocity potential panel method that it can be applied in a straightforward manner also to bodies of more complicated geometry. It has already been pointed out that in the limiting case of incompressible flow, the Helmholtz wave equation reduces to Laplace's equation with a simple type of Green's function.

The main influence of a body with reasonable thickness is the displacement effect, which can be well represented by a surface source-sink distribution. If the same discretisation procedure is applied for the body surface, splitting it up into small plane panels, the aerodynamic influence function (induced normal velocity) of a source panel is expressed by

$$\frac{\partial \Phi_q}{\partial \zeta} = \frac{1}{4\pi} \sigma_{qn} \iint\limits_{\Delta F_n} \frac{\partial}{\partial \zeta}\left(\frac{1}{r}\right) dF \tag{12}$$

with σ_q as the yet unknown source strength. The normal velocity components induced in a control point by the influence of all source panels must be equal but opposite in sign to the prescribed normal velocity on the real body surface due to the oscillatory movement of the body and due to the influence of the mainflow. This kinematic boundary condition leads to the integral equation, and further on to the linear system of equations, for the evaluation of the unknown σ_q-vector.

Fig. 4 shows a body of revolution at incidence undertaking oscillations about a pitching axis through the midpoint. In contrast to the linearized boundary condition of the mean surface theory, where steady and unsteady parts are completely separated, now the prescribed normal velocity contains both steady and unsteady parts as follows:

a) Velocity due to the oscillatory movement

If r' is the perpendicular distance of the surface point from the axis of rotation (Fig. 4), the displacement of this point is

$$f = r' \alpha' e^{i\omega^* T} \tag{13}$$

and the velocity

$$\vec{V} = \frac{\partial f}{\partial t} = i\omega^* \frac{U_\infty}{l_0} r' \alpha' e^{i\omega^* T} \tag{14}$$

with a component normal to the body surface

$$V_\zeta = - i\omega^* \alpha' e^{i\omega^* T} [r \cdot \sin\alpha^* + (X - X_a) \cos\alpha^*] \cos\varphi \quad . \tag{15}$$

In Eq. (15) α^* is the angle between the surface tangent and the axis of rotation (Fig. 4).

2. Velocity due to mainflow

The complete angle of attack can be expressed by both a steady and a harmonic oscillating part (Fig. 4):

$$\alpha_t = \alpha + \alpha' e^{i\omega^* T} \tag{16}$$

leading to a time dependent normal velocity component of the mainflow velocity

$$U_\zeta = - \sin\alpha^* \cos(\alpha + \alpha' e^{i\omega^* T}) - \cos\alpha^* \sin(\alpha + \alpha' e^{i\omega^* T}) \cos\varphi \tag{17}$$

which can be expressed by steady, first, and higher harmonic parts

$$U_\zeta = U_{\zeta s} + \bar{U}_{\zeta i1} \alpha' e^{i\omega^* T} + \bar{U}_{\zeta i2} \alpha'^2 e^{2 i\omega^* T} + \ldots \tag{18}$$

In the following, the series in Eq. (18) will be truncated after the second harmonic part. Due to the linear behavior of the governing Laplace equation the flow potential can also be expressed by steady and unsteady parts:

$$\Phi = \Phi_s + \bar{\Phi}_{i1} \alpha' e^{i\omega^* T} + \bar{\Phi}_{i2} \alpha'^2 e^{2i\omega^* T} + \ldots \tag{19}$$

Differentiation of Eq. (19) with respect to the surface normal direction ζ and introduction of the boundary condition Eqs. (15) and (18) yields:

$$\frac{\partial\Phi_s}{\partial\zeta} + \frac{\partial\bar{\Phi}_{i1}}{\partial\zeta}\alpha' e^{i\omega^*T} + \frac{\partial\bar{\Phi}_{i2}}{\partial\zeta}\alpha'^2 e^{2i\omega^*T} + \ldots = - \left\{U_{\zeta s} + (\bar{U}_{\zeta i1} + \bar{V}_\zeta)\alpha' e^{i\omega^*T} + \bar{U}_{\zeta i2}\alpha'^2 e^{2i\omega^*T} + \ldots\right\} \quad . \tag{20}$$

The aerodynamic influence functions on the left hand side of Eq. (20) are given by Eq. (12) and are identical for the steady and unsteady cases respectively. The integral equation (20) can be solved separately for the steady and the unsteady cases forming linear systems of equations with three or more right hand sides and resulting in three or more σ_{qn}-vectors.

It can be shown that the unsteady Bernoulli equation represented in body fixed coordinates can also be expressed separately by steady and unsteady parts:

$$c_p = \frac{p - p_\infty}{q_\infty} = \frac{(\vec{U}_\infty + \vec{V})^2}{U_\infty^2} - \frac{2}{U_\infty^2}\frac{\partial\Phi}{\partial t} - \frac{\mathfrak{w}\cdot\mathfrak{w}}{U_\infty^2} = c_{ps} + \bar{c}_{p1}\alpha' e^{i\omega^*T} + \bar{c}_{p2}\alpha'^2 e^{2i\omega^*T} \tag{21}$$

where $\mathfrak{w}$ *defines the resulting* flow velocity vector relative to the moving surface, and $\vec{V}$ is given by Eq. (14).

Fig. 5 shows some typical results for a spheroid at incidence with steady, first and second harmonic pressure distributions along meridians. In the unsteady cases, the axis ratio of the spheroid serves as a parameter. It should be mentioned that the second harmonics are proportional to α'^2, so in the case of small amplitudes, these pressure terms may be neglected.

Fig. 6 gives first harmonic pressure distributions along three meridians for a spheroid with cylindrical afterbody at pitching oscillations about the midchord axis. The numerical results are compared with corresponding unsteady pressure measurements [8]. Except in the afterbody region, where separation seems to occur, the experimental data are well predicted by the theoretical pressure curves.

3.3 THREE-DIMENSIONAL WINGS WITH FINITE THICKNESS AND STATIC ANGLE OF ATTACK

For the extension of the mean surface theory described in a previous section to 3d-wings with finite thickness, two different types of singularity distributions are now taken into account:

1. Source-sink distribution on the real body surface (Eq. (12)) corresponding to the body-case
2. Doublet distribution also on the real body surface.

This concept has already been used for steady cases by HESS [9].

The aerodynamic influence function for a dipol distribution (induced normal velocity) becomes

$$\frac{\partial\Phi_d}{\partial\zeta} = \frac{1}{4\pi}\sigma_d \iint\limits_{\Delta F} \frac{\partial^2}{\partial\zeta\,\partial\zeta'}\left(\frac{1}{r}\right) dF + \frac{1}{4\pi}\iint\limits_{\Delta W} \Delta\Phi_{dW} \frac{\partial^2}{\partial\zeta\,\partial\zeta'}\left(\frac{1}{r}\right) dF \quad . \tag{22}$$

The first term in Eq. (22) gives the influence of a wing surface panel. The second term expresses the influence of a wake strip. The panel arrangement for an arbitrary 3d-wing at incidence is shown in Fig. 7.

In contrast to the source strengths, which vary from panel to panel, the doublet strength of a wing section *n* (Fig. 7) is a prescribed *linearly varying function*, which is represented by a step function of yet unknown reference strength. The doublet distribution in the spanwise direction is also represented by a step function. The unknown doublet strengths of each spanwise section are calculated by applying the Kutta condition at the wings trailing edge.

It is shown in detail in [10] that the Kutta condition can also be handled separately for the steady and the unsteady part of the problem:

Now two different conditions have to be fulfilled:

1. No static pressure jump
2. No unsteady pressure jump

at the trailing edge. Both conditions are applied at the two panel midpoints on the wing upper and lower surfaces adjacent to the trailing edge.

The overall calculation process for a finite thick wing in unsteady motion is now similar to the steady case described in [9]:

The influences of the doublet sheets of each wing section are added to the right-hand side of the integral equation (Eq. (20)), assuming unit doublet strength. This must be done separately for the steady and the unsteady case, due to the fact that the unsteady wake integral, similar to Eq. (10), is quite different compared to the steady wake integral with constant $\Delta\Phi_W$. This leads to an integral equation with $2N+2$ right hand sides, if N is the number of wing sections (Fig. 7).

This formulation of the integral equation has the advantage that the aerodynamic influence functions on the left hand side of Eq. (20) - the induced normal velocities of source panels - are unchanged for both steady and unsteady calculations. After the linear systems of equations have been solved for the $2N+2$ source strength vectors, the Kutta condition for the steady and the unsteady part of the problem can be applied. This leads in the steady case to a quadratic, and in the unsteady case to a linear system of equations, resulting in $2N+2$ steady and unsteady doublet strengths, respectively. With all source and doublet strengths known, the steady and unsteady pressure coefficients can be determined using Eq. (21). It should be emphasized at this point that the steady and unsteady velocity components forming the resulting velocity vector $\mathfrak{w}$ in Eq. (21) are joined together. The unsteady pressures can only be calculated after the steady velocity vectors are known.

Results of this method are given in Figs. 8 and 9 for a rectangular wing of aspect ratio $\Lambda = 4$ with a NACA 0012 profile. The wing oscillates in pitching mode about the midchord axis (perpendicular to the x-z-plane, Fig. 7). Fig. 8 shows real and imaginary parts in two spanwise sections for symmetric flow ($\alpha = 0^o$), and Fig. 9 gives the corresponding results for the wing at $\alpha = 3^o$ incidence. The reduced frequency is in both cases $\omega^* = 0.418$. In the symmetric case (Fig. 8), the results of the mean surface theory are included. Experimental data in these plots are described in [11]. The results show good agreement between the present method and the experimental data, except for the incidence case (Fig. 9) in the tip region of the wing, where the tip vortex influences the unsteady pressure distribution mainly on the upper surface. The steady pressure distribution shows a similar behavior in this region. The experimental results have been obtained with a cut-off tip. The results for a rounded wing tip gave smaller deviations from the calculated results.

4. CONCLUSIONS

Numerical methods have been developed to calculate unsteady airloads on oscillating three-dimensional configurations using the velocity-potential panel concept. The surfaces of the bodies are broken up into large numbers of surface panels, each with a source or doublet distribution of constant strength. The integral equation representing the surface boundary condition is reduced to a linear system of equations for the unknown singularity strengths. Once the source or doublet strengths are known, the pressures can be calculated by means of Bernoulli's equation.

The velocity potential concept has been applied to the linearized mean surface theory calculating unsteady pressures on 3d-wing surfaces in subsonic flow. One or more control surfaces at the trailing edge have been taken into account.

The method has been extended to oscillating bodies in incompressible flow using a source-sink distribution on the real surface. Static, first and second harmonics of the pressure distributions have been calculated for this case.

For a wing with finite thickness, both a source and doublet distribution have been used. The first one is needed to represent the kinematic boundary condition on the wing surface, and the second one to fulfill the Kutta condition, and therefore to represent the circulation around the wing. Results have been given for a rectangular wing undergoing pitching oscillations with and without mean incidence.

The comparison of the numerical results with experimental data show good agreement in most cases.

5. REFERENCES

[1] LASCHKA, B.	Zur Theorie der harmonisch schwingenden tragenden Fläche bei Unterschallströmung. Z. Flugwiss., Bd. 11 (1963) S. 265-292.
[2] ROWE, W. S. WINTHER, B. A. REDMAN, M. C.	Unsteady Subsonic Aerodynamic Loadings Caused by Control Surface Motions. J. Aircraft, Vol. 11, No. 1, January 1974.
[3] ALBANO, E. RODDEN, W. P.	A Doublet Lattice-Method for Calculating Lift Distributions on Oscillating Surfaces in Subsonic Flow. AIAA Journal, Vol. 7 (1969) pp. 279-285.

[4] JONES, W. P.
MOORE, J. A.
Simplified Aerodynamic Theory of Oscillating Thin Surfaces in Subsonic Flow.
AIAA-Journal, Vol. 11, No. 9 (1973) pp. 1305-1309.

[5] GEISSLER, W.
Ein numerisches Verfahren zur Berechnung der instationären aerodynamischen Druckverteilung der harmonisch schwingenden Tragfläche mit Ruder in Unterschallströmung.
Teil II: Theorie und Ergebnisse für kompressible Strömung.
DLR-FB 77-15 (1977).

[6] FÖRSCHING, H.
TRIEBSTEIN, H.
WAGENER, J.
Pressure Measurements on a Harmonically Oscillating Swept Wing with Two Control Surfaces in Incompressible Flow.
DLR-FB 70-47 (1970).

[7] TIJDEMANN, H.
SCHIPPERS, P.
Results of Pressure Measurements on an Airfoil with Oscillating Flap in Two-Dimensional High Subsonic and Transonic Flow.
(Zero Incidence and Zero Mean Flap Position).
NLR-TR 73078 U (1973).

[8] TRIEBSTEIN, H.
Instationäre Druckverteilungsmessungen an Flügel-Außenlastkombinationen in inkompressibler Strömung.
DLR-FB 77-12 (1977).

[9] HESS, J. L.
The Problem of Three-Dimensional Lifting Potential Flow and its Solution by Means of Surface Singularity Distribution.
Computer Methods in Applied Mechanics and Engineering 4 (1974) pp. 283-319.

[10] GEISSLER, W.
Berechnung der Druckverteilung an oszillierenden dreidimensionalen Tragflächen mit endlicher Dicke in inkompressibler Strömung.
DFVLR-AVA-Bericht 253 - 76 J 05 (1976).

[11] TRIEBSTEIN, H.
Instationäre Druckverteilungsmessungen an angestellten Rotorblattspitzen in inkompressibler Strömung.
DLR-FB 76-42 (1976).

AD-A054 028   ADVISORY GROUP FOR AEROSPACE RESEARCH AND DEVELOPMENT--ETC   F/G 20/4
UNSTEADY AERODYNAMICS.(U)
FEB 78

UNCLASSIFIED   AGARD-CP-227   NL

2 OF 7
ADA
054028

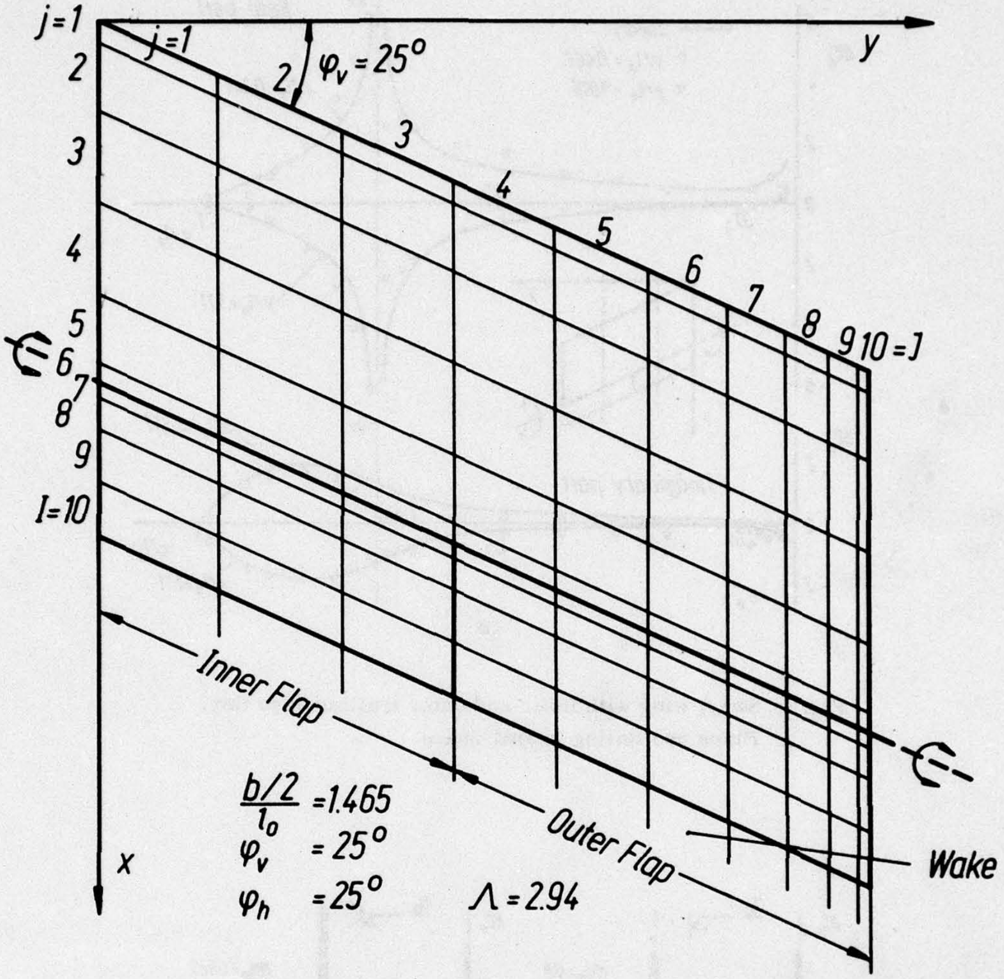

Fig. 1: Panel arrangement for a swept wing with inner and outer trailing edge flap

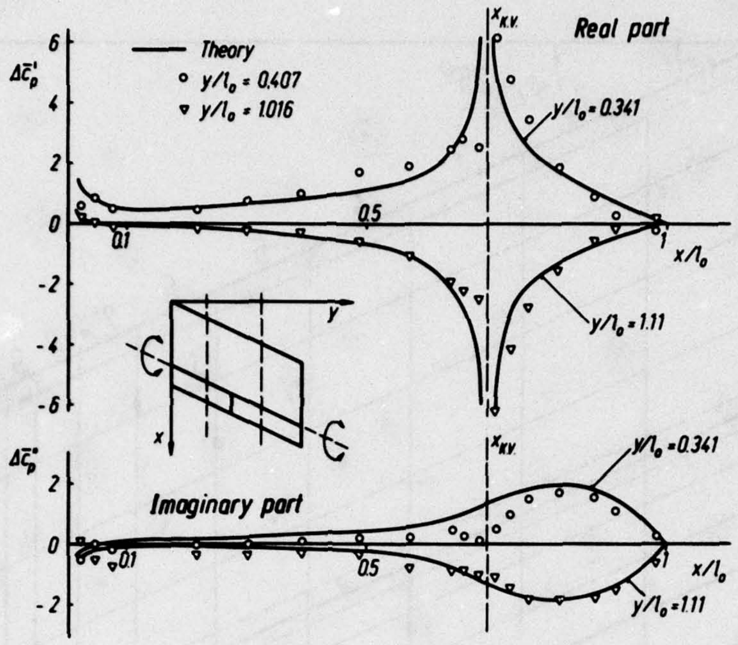

Fig. 2: Swept wing with inner and outer trailing edge flap. Flaps oscillating in anti-phase

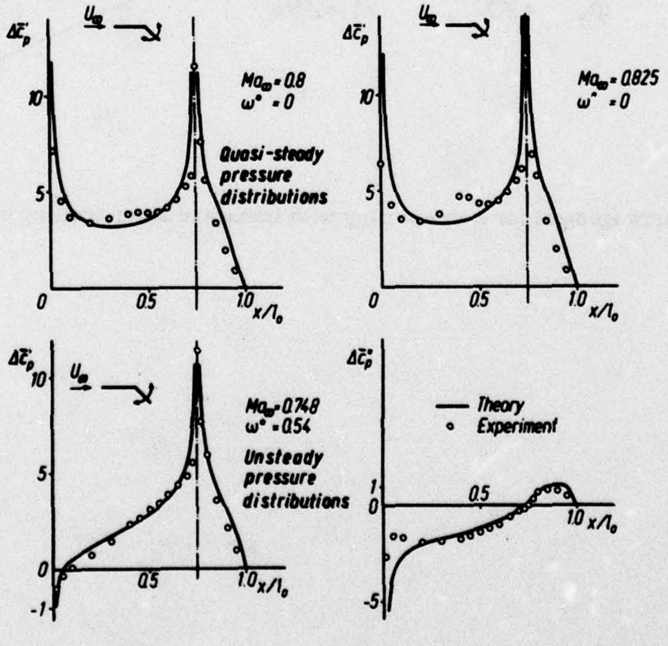

Fig. 3: Rectangular wing with oscillating flap in high subsonic flow.
Comparison with 2-d measurements [7]

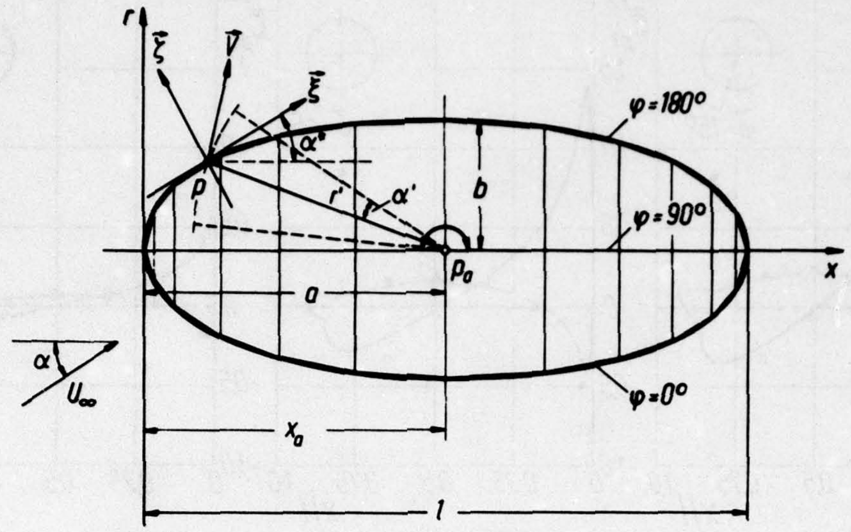

Fig. 4: Oscillating body at incidence

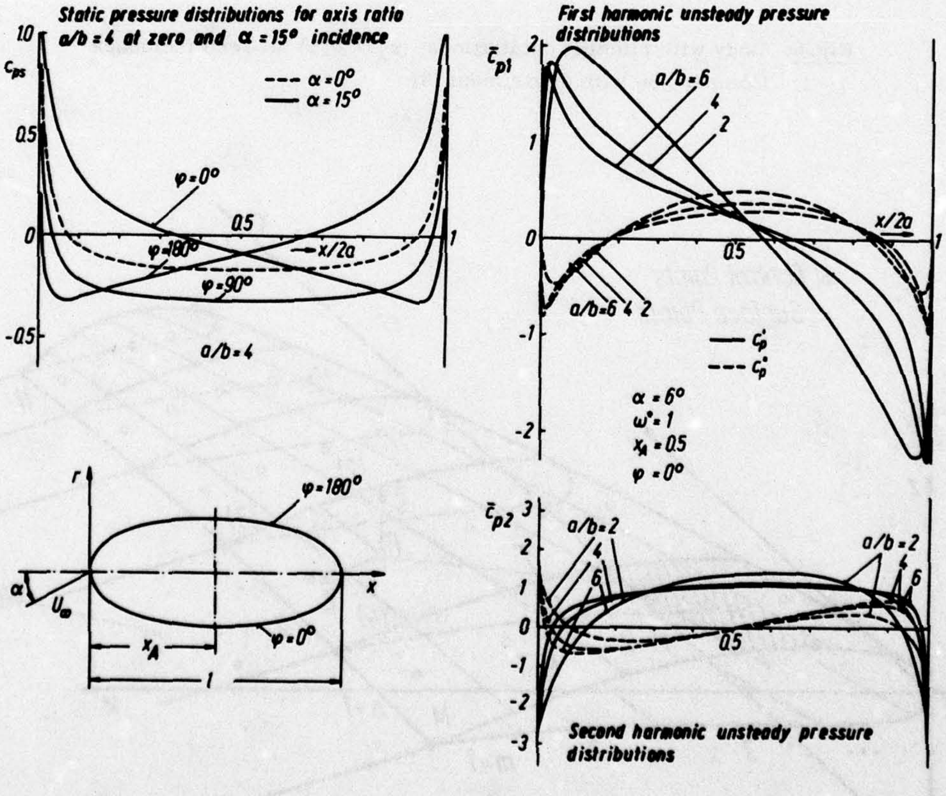

Fig. 5: Spheroid at incidence with pitching oscillations (x_A = 0, 5)

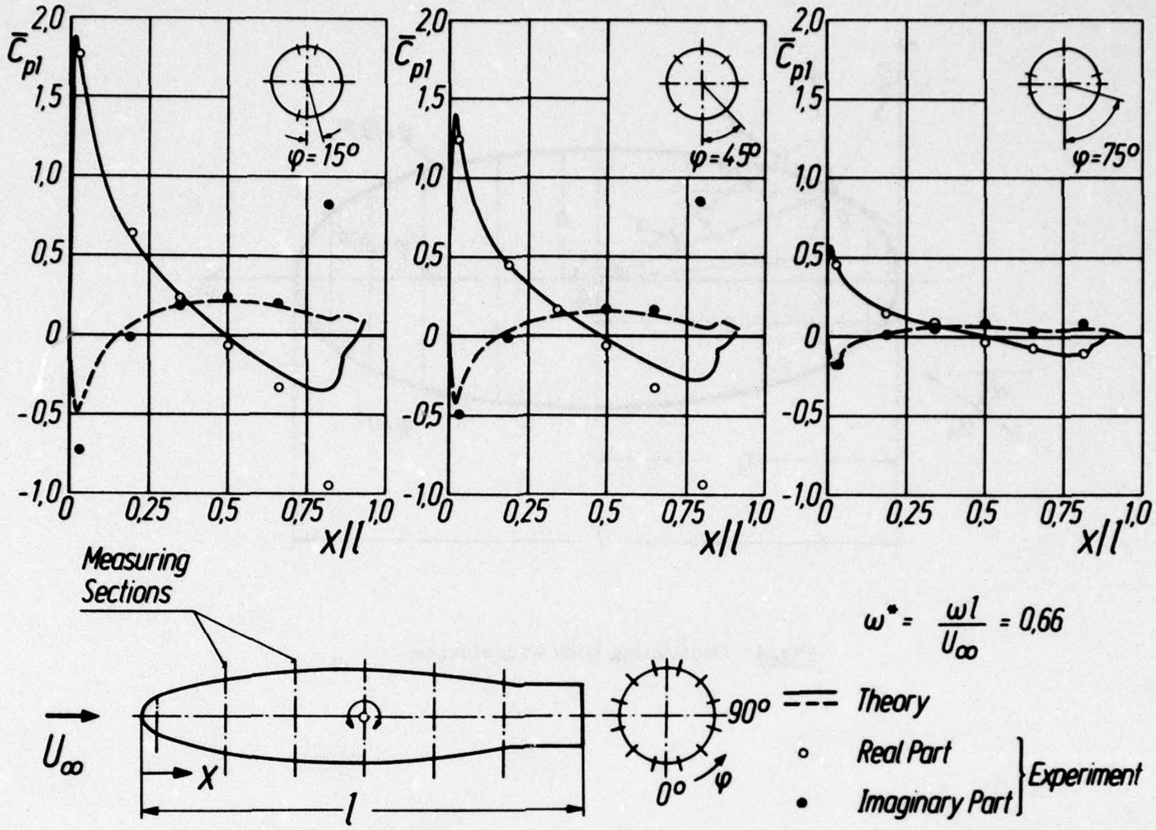

Fig. 6: Body with pitching oscillations ($x_A = 0,5$) at zero incidence
Comparison with experiment [8]

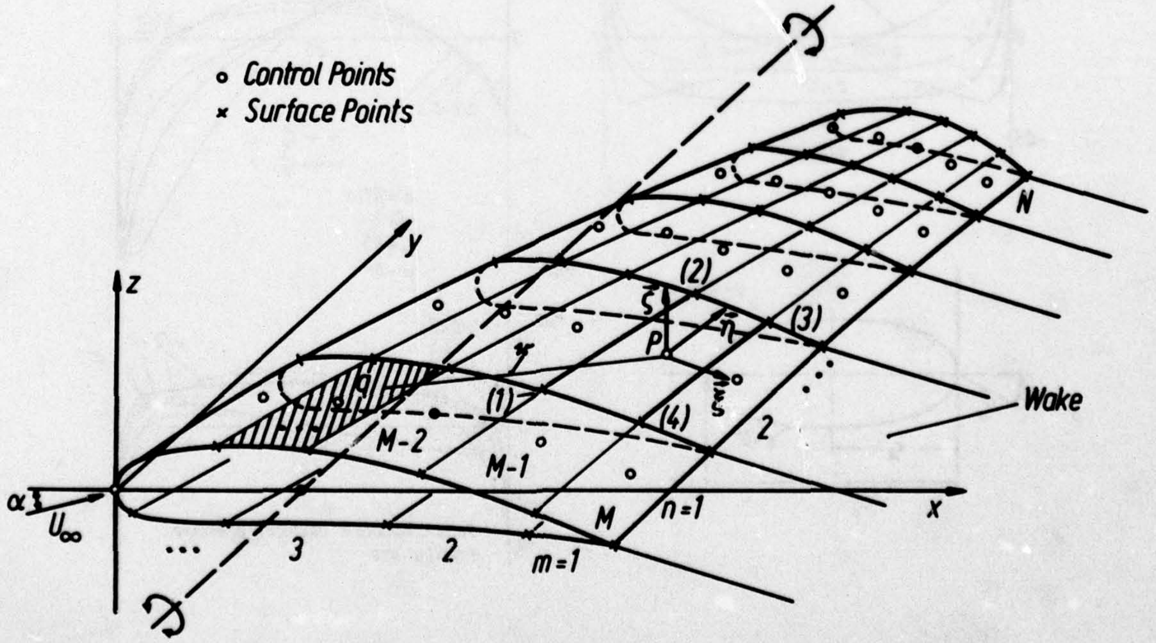

Fig. 7: Panel arrangement for a thick wing at incidence

100

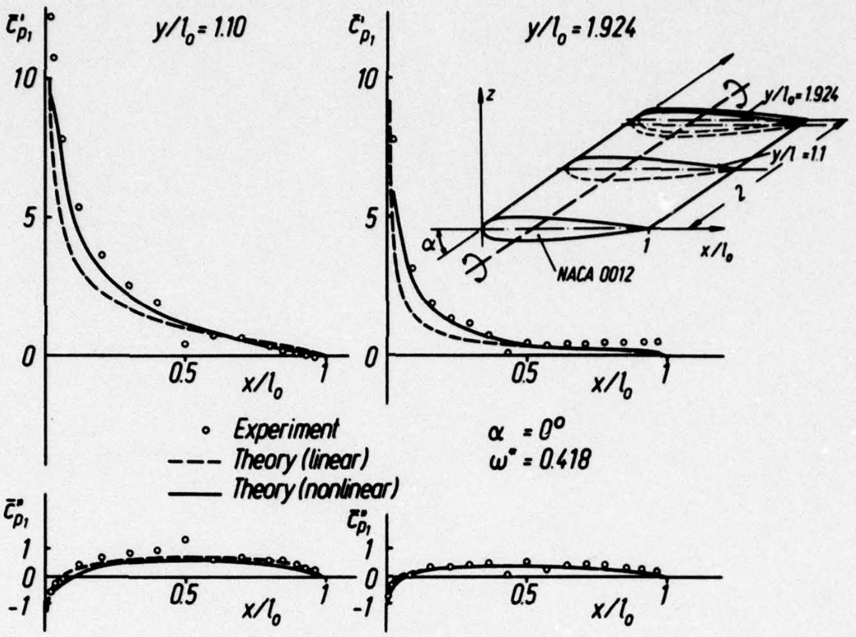

Fig. 8: Rectangular wing with pitching oscillations at zero incidence. Comparison with mean surface theory [5] and experiments [11]

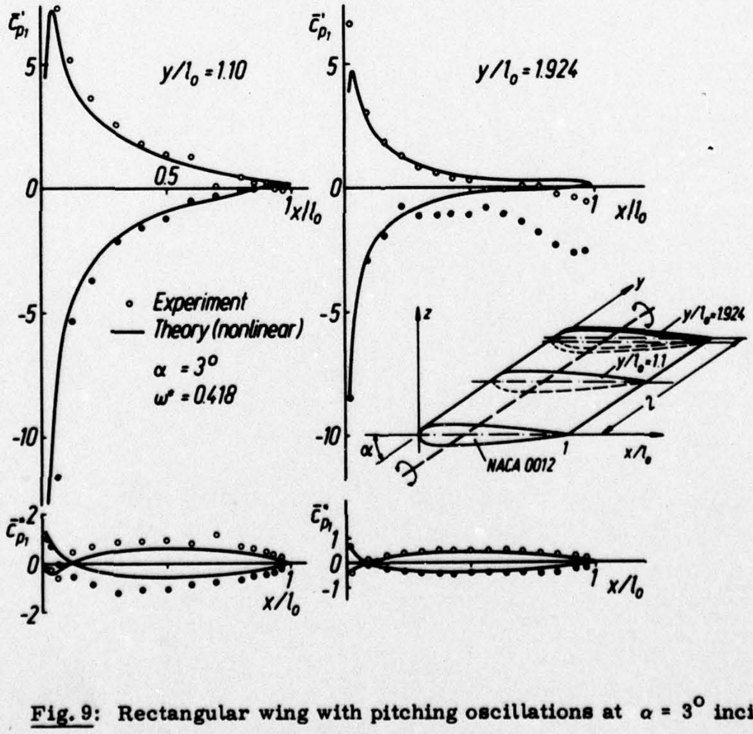

Fig. 9: Rectangular wing with pitching oscillations at $\alpha = 3^o$ incidence. Comparison with experiments [11]

SOME BASIC AND NEW ASPECTS ON THE DISTURBANCE FIELDS OF UNSTEADY SINGULARITIES IN UNIFORM MOTION

Arabindo Das +)
Institut für Aerodynamik der DFVLR, Braunschweig, Germany

SUMMARY

The treatment of disturbance propagation from unsteady singularities in motion is a classical problem, whose formal methods of solution are extensively dealt with in standard literature.

The objective of this paper is to analyze in detail the influence factors arising from the motion of the singularities and to derive generally valid expressions for these effects. In order to achieve the generalization, uniform translatory motion of the singularity and of the field point relative to the medium is allowed, both having arbitrary velocities and path orientations in space.

In the linearized theory the aerodynamic and aeroacoustic problems can be dealt with by means of a unified treatment. The derived expressions for the influence factors can be given general forms which are uniformly valid for subsonic and supersonic velocities of the singularities.

The unsteady singularities which are commonly encountered in the field of aerodynamics and aeroacoustic can be represented as sources, dipoles and quadrupoles - the last two appearing in various orientations. The expressions for the near-field and far-field disturbances of the various moving singularities are presented.

The resulting changes in the disturbance fields of moving singularities compared to those of space-fixed singularities in an unbounded medium at rest may be denoted as Mach number effect. The usual global notation of this effect as compressibility effect is neither true nor applicable, when linearized theory of disturbance fields is considered.

Finally the problem of disturbance propagation from singularities in motion is treated in a moving reference frame by applying the Lorentz transformation in a nondimensional form, which preserves the physical quantities defined in the medium-fixed system, such as singularity strength, phase relations, etc. The significance of the Lorentz transformation is elucidated by presenting the field of a moving source in the space-time continuum. The solution of the disturbance potential of the moving source can be obtained very easily for different Mach numbers from a universal diagram.

CONTENT

+) Prof. Dr.-Ing.
Head of the Theoretical Aerodynamics Dept.

NOTATIONS

Geometrical quantities

h	radial distance of a field point normal to the path of a singularity
l	reference length
$P; P_o; P_\nu$	location of field point, singularity and corresponding emission point
r	radial distance in a spherical polar coordinate system
r_o	radial distance between P and P_o
r_ν	radial distance between P and P_ν
r^*	equivalent distance between P and P_ν accounting for the influence factor due to the motion of the singularity
F_o	control surface
$\bar{F}_o = F_o/l^2$	dimensionless control surface
V_o	control volume
$\bar{V}_o = V_o/l^3$	dimensionless control volume
x, y, z	cartesian coordinates
ξ, η, ζ	dimensionless cartesian coordinates
$\hat{\varepsilon}_o$	space-matching parameter for P, P_o and P_ν used in the delta function
$\vartheta_o, \vartheta_\nu$	angle of inclination of r_o and r_ν with the direction of motion of the singularity
Ψ	angle of inclination between the P-P_o-P_ν-plane and the vertical plane

Aerodynamic and aeroacoustic quantities

a	sound speed
a_∞	sound speed in a stationary medium
c_p	static pressure coefficient
$\bar{D}$	doublet strength
E	energy density in the disturbance field
$G; \bar{G}; \hat{G}$	disturbance functions in the potential equation
i	static enthalpy
I	energy intensity in the disturbance field
Q	volume flow of a source
$k = \frac{2\pi}{\lambda} = \frac{\omega}{a_\infty}$	wave number
K	external disturbance force per unit mass of volume element
K_x, K_y, K_z	components of external disturbance in the corresponding directions
L	rate of energy flow through a closed control surface
$\bar{M}$	quadrupole strength
$Ma_S = V_S/a_\infty$	Mach number of the moving singularity
$\hat{Ma}_E$	Mach number component of a moving field point projected on the P-P_o-P_ν-plane
p	static pressure in the disturbance field
p_∞	static pressure in the stationary medium
$\Delta p = p - p_\infty$	pressure perturbation
q_∞	nominal dynamic pressure
R	gas constant
$\bar{s} = \frac{\Delta\rho}{\rho_\infty} = \frac{\Delta p}{\kappa p_\infty}$	dimensionless density- and pressure-perturbation
$\bar{S}$	source strength
t	time
t_o	time instant for signals reaching a field point
$t_\nu = t_o - \frac{r_\nu}{a_\infty}$	retarded time instant of emission of the signal
T_{ij}	source tensor to describe a quadrupole singularity per unit mass of volume element
u, v, w	perturbation velocities
v_r	particle velocity in the disturbance field
V_S	translatory motion of the singularity
V_E	translatory motion of the field point
V_∞	translatory motion of the medium
V	resultant velocity of a volume element of the medium in the disturbance field
$\beta = \sqrt{[1 - Ma_S^2]}$	Mach-number parameter
δ	delta function to match P, P_o and P_ν
ε	aberration angle between r_o and r_ν
$\kappa = c_p/c_v$	ratio of specific heats
$\hat{\kappa}_o$	time-matching parameter for P, P_o, P_ν
$\lambda = 2\pi/k$	wave length
μ	Mach angle
ρ	local density of the medium in the disturbance field
$\Delta\rho = \rho - \rho_\infty$	density perturbation
$\sigma_D; \sigma_V; \sigma_R$	influence parameters
σ_F	frequency parameter at a moving field point due to signals from a moving source
$\tau = ta_\infty/l$	dimensionless time
φ	perturbation potential
$\bar{\varphi} = \varphi/a_\infty l$	dimensionless perturbation potential
ω	circular frequency of a harmonic disturbance function
$\bar{\omega} = \frac{\omega}{a_\infty}$	reduced frequency
$\bar{\Omega}; \tilde{\Omega}$	disturbance function

Subscripts

o	momentary position or time of the singularity
ν	emission point ($\nu = 1$ for $Ma_S < 1$; $\nu = 1; 2$ for $Ma_S > 1$)

1. INTRODUCTION

The propagation of disturbances from space fixed sound sources in an unbounded compressible medium at rest has been the subject of investigation since the times, when thermodynamic laws were quite unknown [1] to [3]. Still, the theoretical derivation of the sound speed which corresponds to the adiabatic process of disturbance propagation was given correctly in [3], as could be verified later. The physical process of disturbance propagation from space fixed singularities in an unbounded medium at rest leads to the classical wave equation. The first solution of the wave equation in two dimensional form in connection with mechanical oscillations was derived in [4], while the problem of disturbance propagation in compressible medium as sperical waves was first solved in [5].

Some elegant methods of solution of the wave equation in connection with electromagnetic waves was presented in [6]. For harmonic disturbances the solution of the inhomogeneous wave equation as given in [7] is very useful. Extensive treatment on disturbance propagation from space-fixed singularities in a compressible medium at rest is given in standard texts on acoustics [8] and hydrodynamics [9].

The problem of disturbance fields from moving unsteady singularities was treated at first for electromagnetic waves and subsequently for sound as presented in the contribution [10] to [12]. Some basic treatment of the classical wave equations in moving reference system has been given in [13] to [15]. A general introduction into the theory of the wave equation can be found in [16].

With the advancement of aerodynamics to motions of bodies in compressible medium, disturbance fields originating from moving singularities had to be considered. The first basic attempts were restricted to the very special case of time independent steady singularities in motion, with the disturbance field accompanying them in the moving reference frame. Basic contributions on the treatment of stationary disturbance fields for subsonic and supersonic velocities of the singularities were first made in the references [17] to [29]. They were then followed by a very large number of contributions known in the literature as cited in [29].

While treatment of the problem of unsteady singularities in motion had been taken up thereafter indicating some basic contributions and further developments in [30] to [36], intensive advancements on the theory of sound fields originating from moving sources proceeded also during the same period as can be seen from references [37] to [47].

The treatment of sound fields in aeroacoustics often has to overcome a major difficulty due to the fact, that the singularity strengths can not always be precisely defined, specially when it arises due to fluctuations in mass flow or forces in some regions of the medium itself. Some basic theoretical and experimental work on this topic has been contributed in [48] to [55] leading to a better understanding of the subject.

The significance of unsteady aerodynamics is well known in the field of aircraft design, some basic works [57] to [58] being cited as typical illustrations.

The present paper deals with the analysis of the effect of motion of the unsteady singularities on the disturbance propagation - regarding their strengths, phase relations and frequencies. These effects will be expressed as influence factors and put into general forms which are valid for subsonic and supersonic motion of the singularities. A very general expression for the Doppler parameter accounts for uniform translatory motion of the singularity and the field point, having arbitrary velocities and path orientations in space. By applying a modified Lorentz transformation, the disturbance fields of moving sources will be illustrated in a space-time continuum.

2. BASIC EQUATIONS AND KINEMATICS OF THE DISTURBANCE FIELDS ORIGINATING FROM UNSTEADY SINGULARITIES IN MOTION

The fundamental equation of the disturbance field of a moving singularity in an unbounded compressible medium is obtained from the laws of conservation of mass, momentum and energy. If friction and heat conduction is neglected, then the field of small disturbances can be assumed as isentropic, thus enabling the introduction of a perturbation potential for the treatment of the problem. The potential field can be described in various ways depending on the reference system for the coordinates used, i.e. moving or fixed with respect to the medium in space.

2.1 The linearized equation of the perturbation field

The exact nonlinear equation of the perturbation potential due to a singularity in uniform motion in an unbounded medium can be expressed in a moving reference system, accompanying the singularity, in the following way:

$$\nabla^2 \varphi - \frac{1}{a^2}\frac{D^2 \varphi}{Dt^2} = \Omega(t)\,\delta(x-V_S t,\, y,\, z) \qquad (2\text{-}1)$$

with ∇^2 as the Laplace operator; $\frac{D}{Dt}$ as the substantial derivative in space and $\Omega(t)$ as the disturbance function, the δ-function notation denoting the spatial location of Ω in the medium at time t.

The speed of sound a is given by the isentropic relation

$$a^2 = a_\infty^2 \left[1 + \frac{\Delta\rho}{\rho_\infty}\right]^{\kappa-1} \qquad (2\text{-}2)$$

where $\Delta\rho = \rho - \rho_\infty$ denotes the density perturbation. For small values of $\Delta\rho$ Eq. (2-2) can be approximated as

$$a^2 \approx a_\infty^2 \left[1 + (\kappa-1) \frac{\Delta\rho}{\rho_\infty} \right] \approx a_\infty^2 \qquad (2\text{-}3)$$

Using now two distinct steps, i.e. letting the negative x-axis coincide with the direction of motion of the singularity relative to the medium and introducing the assumption of small perturbation, enabling higher order terms to be neglected, Eq. (2-1) simplifies to

$$\nabla^2 \varphi - \frac{1}{a_\infty^2} \left[\frac{\partial}{\partial t} + V_S \frac{\partial}{\partial x} \right]^2 \varphi = \Omega(t)\ \delta(x-V_S t,\ y,\ z) \qquad (2\text{-}4)$$

The Laplace operator ∇^2 can be expressed in the corresponding form depending on the coordinate system used. Eq. (2-4) written out fully takes the following, commonly form used

$$(1 - Ma_S^2)\varphi_{xx} + \varphi_{yy} + \varphi_{zz} - \frac{2}{a_\infty} Ma_S\, \varphi_{xt} - \frac{1}{a_\infty^2} \varphi_{tt} = \Omega(t)\ \delta(x-V_S t,\ y,\ z) \qquad (2\text{-}5)$$

It is often advantageous to express Eq. (2-4) or Eq. (2-5) in a space fixed coordinate system with the medium at rest. For this purpose the Galilean transformation is to be used, namely

$$\hat{x} = x - V_S t; \quad \hat{y} = y; \quad \hat{z} = z; \quad \hat{t} = t \qquad (2\text{-}6)$$

This transformation being introduced in Eq. (2-5), the potential equation of the disturbance field simplifies to the classical wave equation

$$\nabla^2 \varphi - \frac{1}{a_\infty^2} \varphi_{tt} = \Omega(t)\ \delta(\hat{x},\hat{y},\hat{z}) \qquad (2\text{-}7)$$

Due to the linearization of the problem, where linear dependence between the potential φ and the pressure or density perturbation $\bar{s}$ exists, the wave equation is equally applicable to the perturbation quantities, giving

$$\nabla^2 \bar{s} - \frac{1}{a_\infty^2} \bar{s}_{tt} = \frac{\Omega^*}{a_\infty^2}(t)\ \delta(\hat{x},\hat{y},\hat{z}) \qquad (2\text{-}8)$$

The disturbance function $\Omega(t)$ and $\Omega^*(t)$ can be given the general expression:

$$\Omega(t) = G(t) + \{\nabla \cdot \bar{G}\}(t) + \{\nabla \cdot \nabla \cdot \hat{G}_{ij}\}(t) \qquad (2\text{-}9a)$$

$$\Omega^*(t) = g(t) - \{\nabla \cdot K_i\}(t) + \{\nabla \cdot \nabla \cdot T_{ij}\}(t) \qquad (2\text{-}9b)$$

denoting the three terms G, $\bar{G}$ and $\hat{G}_{ij}$ in their respective order as equivalent source, dipole or quadrupole singularities. The correspondence between Ω and Ω^* follows at once from the relation between $\bar{s}$ and φ in the space fixed reference system with the medium at rest, as is derived in the subsequent section.

2.2 Equations for the density and pressure perturbations in the disturbance field

The perturbation quantities in the disturbance field of an unsteady singularity in motion have essentially nonstationary character, when the field point is fixed or has arbitrary motion in the medium. If the field point is made to accompany the moving reference system, then the disturbances there undergo only a time variation corresponding to the unsteady singularity - and, in case of a time independent steady disturbance, reduce to a stationary perturbation field.

If the disturbance field in the medium is considered to be at rest, then the perturbations caused by the moving singularity reveal two distinct contributions, i.e. a time dependent and a convective change of the disturbances.

The pressure or density perturbation in the disturbance field can be derived from the general Bernoulli equation:

$$\frac{\partial\varphi}{\partial t} + \frac{V^2}{2} + \frac{a^2}{\kappa-1} = \frac{V_S^2}{2} + \frac{a_\infty^2}{\kappa-1} = f(t) \qquad (2\text{-}10)$$

The isentropic relations between pressure or density perturbations and the local sound of speed yields the following expression:

$$\frac{\Delta p}{p_\infty} = \frac{p}{p_\infty} - 1 = \left(\frac{a}{a_\infty}\right)^{\frac{2\kappa}{\kappa-1}} - 1 \qquad (2\text{-}11)$$

Putting this relation into Eq. (2-10) and using a moving reference system the pressure or density perturbation in the field takes the following form:

$$\bar{s} = \frac{\Delta\rho}{\rho_\infty} = \frac{\Delta p}{\kappa p_\infty} = -\frac{1}{a_\infty^2} \left[\frac{\partial\varphi}{\partial t} + V_S \frac{\partial\varphi}{\partial x} + \frac{(\nabla\varphi)^2}{2} \right] \qquad (2\text{-}12)$$

If a medium fixed reference system is considered then the perturbation equation simplifies to the following expression

$$\bar{s} = \frac{\Delta\rho}{\rho_\infty} = \frac{\Delta p}{\kappa p_\infty} = -\frac{1}{a_\infty^2}\left[\frac{\partial\varphi}{\partial t}(\hat{x},\hat{y},\hat{z},\hat{t}) + \frac{(\nabla\varphi)^2}{2}\right] \tag{2-13}$$

The square term in the bracket of Eq. (2-12) and Eq. (2-13) is usually small and can often be neglected. If the field point is also in motion without creating any disturbance in the medium, then evidently it has no influence on the potential field of the moving singularity. The motion of the field point causes however a change in the time sequence of the signals passing through it and thus imposes a change in the frequency compared to that at emission of the disturbance.

2.3 The kinematic and space-time relations for the disturbance propagation from moving singularities

With V_S as the velocity of the singularity in the negative x-direction and V_E the velocity of a field point along an arbitrary straight path in space, both velocities being defined relative to the medium, it is very simple to determine the kinematic relation at a given time instant t_o, when a disturbance meets the field point. The disturbance propagation and the corresponding kinematic relations for subsonic and supersonic velocity of the singularity is depicted in Fig. 1.

At time t_o with $P_o(x_o,t_o)$ as the momentary position of the singularity and $P(x,t_o)$ as the momentary position of the field point with disturbance signals meeting it, one can find the emission point $P_\nu(x_\nu,t_\nu)$ at a retarded time t_ν easily, since the velocity of propagation a_∞ of the spherical waves is also known.

The kinematic relations can be established based on the velocity V_S of the singularity or on V_E, the velosity of the field point. It is preferable to choose V_S because V_E vanishes when determining perturbation magnitudes in the medium itself. Using Fig. 2 the following relation can be set up:

$$a_\infty^2 (t_o - t_\nu)^2 = V_S^2 (t_o - t_\nu)^2 + r_o^2 + 2r_o V_S (t_o - t_\nu) \cos\vartheta_o \tag{2-14}$$

or

$$\beta^2 a_\infty (t_o - t_\nu)^2 - 2r_o \cos\vartheta_o\, a_\infty Ma_S (t_o - t_\nu) - r_o^2 = 0 \tag{2-15}$$

with $\nu = 1$ for $Ma_S < 1$ and $\nu = 1; 2$ for $Ma_S > 1$.

The general solution of this quadratic equation yields the space-time relations of the disturbance propagation linking P_o, P and P_ν:

$$a_\infty (t_o - t_\nu) = \frac{r_o}{1 - Ma_S^2}\left[Ma_S \cos\vartheta_o + (-1)^{\nu+1}\sqrt{1 - Ma_S^2 \sin^2\vartheta_o}\right] \tag{2-16}$$

or, with $V_S(t_o - t_\nu) = x_o - x_\nu$, the alternative form

$$(x_\nu - x_o) = \frac{Ma_S\, r_o}{1 - Ma_S^2}\left[Ma_S \cos\vartheta_o + (-1)^{\nu+1}\sqrt{1 - Ma_S^2 \sin^2\vartheta_o}\right] \tag{2-17}$$

is obtained. Further relations connecting r_o, ϑ_o to r_ν, ϑ_ν are (see Fig. 2)

$$r_\nu (\cos\vartheta_\nu - Ma_S) = r_o \cos\vartheta_o \tag{2-18}$$

$$r_\nu \sin\vartheta_\nu = r_o \sin\vartheta_o \tag{2-19}$$

$$r_\nu (1 - Ma_S \cos\vartheta_\nu) = (-1)^{\nu+1}\left[r_o (1 - Ma_S^2 \sin^2\vartheta_o)^{1/2}\right] \tag{2-20}$$

$$r_\nu (1 - Ma_S^2) = r_o\left[Ma_S \cos\vartheta_o + (-1)^{\nu+1}\cdot(1 - Ma_S^2 \sin^2\vartheta_o)^{1/2}\right] \tag{2-21}$$

$$\sin\varepsilon = Ma_S \sin\vartheta_o \tag{2-22}$$

with $\nu = 1$ for $Ma_S < 1$ and $\nu = 1; 2$ for $Ma_S > 1$.

For $Ma_S > 1$ the following relation connects the two emission times and locations corresponding to the two signals, which meet the field point $P(x,t_o)$ at a time instant t_o:

$$t_{\nu 1} - t_{\nu 2} = \frac{2r_o\sqrt{1 - Ma_S^2 \sin^2\vartheta_o}}{a_\infty (Ma_S^2 - 1)} \tag{2-23}$$

$$x_{\nu 1} - x_{\nu 2} = \frac{2\, Ma_S\, r_o \sqrt{1 - Ma_S^2 \sin^2 \vartheta_o}}{(Ma_S^2 - 1)} \tag{2-24}$$

For a space fixed point $P(\hat{x})$ the following basic invariant expression proves to be an important property in the nature of disturbance propagation

$$(x - x_\nu)^2 + y^2 + z^2 - a_\infty^2 (t - t_\nu)^2 = 0 \, . \tag{2-25}$$

This expression also forms the fundamental equation in electromagnetic wave propagation for the representation of the solution of disturbance fields in a space-time continuum.

3. DERIVATION OF THE INFLUENCE FACTORS IN THE DISTURBANCE FIELDS OF SINGULARITIES IN MOTION

The kinematics of the disturbance propagation from moving sources leads to space-time relations, which connect the momentary position $P_o(x_o,t_o)$ of the singularity with the location $P_\nu(x_\nu,t_\nu)$ from where the signal, which reaches the field point $P(x,t_o)$ at a time t_o, has been emitted. The kinematic relations are basically defined through three main parameters, i.e. the Mach number Ma_S of the singularity, the instantaneous relative orientation between the field point and the singularity, denoted by r_o and ϑ_o.

If the geometric position of an elementary singularity $P_o(x_o,t_o)$ undergoes a small change in its location, due to shifting by an infinitesimal interval, then the emission point of its signal which just reaches the field point $P(x)$ at time t_o also undergoes a shifting but by a different amount, as imposed by the kinematic relations.

The perturbation intensity at a field point will therefore be defined by the effective emission volume of the singularity and further by the effective shift of the elementary sources at the emission point when higher order singularities are concerned. Besides, the change in the time sequence of the signals while passing through the field point will bring an additional effect, the so called Doppler effect. These physical phenomena will be elucidated in the following treatment and their analytical derivation will lead to the influence factors arising from the motion of the singularity. In connection with this topic the interpretations given in [43] may be mentioned.

3.1 The effective emission volume of a source in motion

If an elementary three dimensional source in uniform motion is considered to have an infintesimal length dx_o, then the corresponding emission element dx_ν from which the signals reach a specified field point simultaneously at the time t_o can be obtained from the Eq. (2-17) by taking its partial derivative with respect to x_o, yielding

$$\begin{aligned} \frac{dx_\nu}{dx_o} = 1 + \frac{Ma_S}{1 - Ma_S^2} \Bigg[& \frac{\partial r_o}{\partial x_o} \Big\{ Ma_S \cos \vartheta_o + (-1)^{\nu+1} \sqrt{1 - Ma_S^2 \sin^2 \vartheta_o} \; - \\ & - \frac{r_o\, \partial \vartheta_o}{\partial x_o} \Big\{ Ma_S \sin \vartheta_o + (-1)^{\nu+1} \cdot \frac{Ma_S^2 \sin 2\vartheta_o}{2\sqrt{1 - Ma_S^2 \sin^2 \vartheta_o}} \Big\} \Bigg] \Bigg] \end{aligned} \tag{3-1}$$

For a medium fixed field point the partial derivatives of r_o und ϑ_o can be replaced by

$$\frac{\partial r_o}{\partial x_o} = \cos \vartheta_o \; ; \quad \frac{\partial \vartheta_o}{\partial x_o} = - \frac{\sin \vartheta_o}{r_o} \tag{3-2}$$

Introducing these relations into Eq. (3-1) one obtains the volume parameter σ_V of emission:

$$\sigma_V = \frac{dx_\nu}{dx_o} = \frac{1}{(1 - Ma_S^2)} \left[1 + (-1)^{\nu+1} \cdot \frac{Ma_S \cos \vartheta_o}{\sqrt{1 - Ma_S^2 \sin^2 \vartheta_o}} \right] \tag{3-3}$$

with $\nu = 1$ for $Ma_S < 1$; $\nu = 1$; 2 for $Ma_S > 1$.

Using the kinematic relations given by Eq. (2-18) and Eq. (2-20) the influence factor σ_V reduces to:

$$\sigma_V = \frac{dx_\nu}{dx_o} = (-1)^{\nu+1} \frac{1}{(1 - Ma_S \cos \vartheta_\nu)} \tag{3-4}$$

or

$$\sigma_V = \frac{r_\nu}{r^*} \tag{3-5}$$

where

$$r^{*} = (-1)^{\nu+1}\, r_{\nu}(1 - Ma_S \cos \vartheta_{\nu}) \tag{3-6a}$$

or

$$r^{*} = \sqrt{(x - x_o)^2 + (1 - Ma_S^2)\,(y^2 + z^2)}\ . \tag{3-6b}$$

The physical process involved is depicted in Fig. 3, where the signals lying on the wave front 1-1 and originating from dx_{ν} reach the field point P simultaneously at the time t_o, thus changing the signal strength by a factor σ_V.

3.2 The effective shift of sources at the emission point for higher order singularities in motion

When using higher order singularities like dipoles and quadrupoles the corresponding sources and sinks are displaced about the momentary central position $P_o(x_o,t_o)$ of the moving singularity. The kinematic relation in Eq. (2-17) imposes an effective shifting of their positions at the location of the emission point $P_{\nu}(x_{\nu},t_{\nu})$, such that the signals meet the field point simultaneously at the time instant t_o.

For a dipole, the moving singularity may have two basic orientations depending on the displacement of the source and sink along or normal to the x-axis. For a quadrupole, the arrangement of the sources and sinks may be achieved in three different orientations, i.e. placing the two source - sink pairs both aligned along or normal to x and in a squire arrangement.

The fundamental effect of such shifting of singularities at $P_o(x_o,t_o)$ on the relative displacements at the emission point can well be studied by giving the source elements at P_o elementary displacements dx_o along the x-axis or dh_o normal to it. The following kinematic relations, already illustrated in Fig. 2, can be used:

$$\begin{aligned} Ma_S\, r_{\nu} &= x_{\nu} - x_o \\ r_{\nu} \cos \vartheta_{\nu} &= x_{\nu} - x \\ r_{\nu} \sin \vartheta_{\nu} &= h - h_o \\ h_{\nu} - h_o &= 0 \end{aligned} \tag{3-7}$$

The effect of local shifting of a singularity at P_o on the changes at the emission point can be derived from Eq. (3-7) and is illustrated in Figs. 4a and 4b.

For source shifted along x:

$$\frac{dr_{\nu}}{dr_o} = \frac{\cos \vartheta_{\nu}}{1 - Ma_S \cos \vartheta_{\nu}}\ ; \quad r_{\nu} \frac{d\vartheta_{\nu}}{dx_o} = -\frac{\sin \vartheta_{\nu}}{1 - Ma_S \cos \vartheta_{\nu}} \tag{3-8}$$

$$\frac{dx_{\nu}}{dx_o} = \frac{1}{1 - Ma_S \cos \vartheta_{\nu}}$$

For source shifted normal to x:

$$\frac{dr_{\nu}}{dh_o} = -\frac{\sin \vartheta_{\nu}}{1 - Ma_S \cos \vartheta_{\nu}}\ ; \quad r_{\nu} \frac{d\vartheta_{\nu}}{dh_o} = \frac{\cos \vartheta_{\nu} - Ma_S}{1 - Ma_S \cos \vartheta_{\nu}} \tag{3-9}$$

$$\frac{dx_{\nu}}{dh_o} = -\frac{Ma_S \sin \vartheta_{\nu}}{1 - Ma_S \cos \vartheta_{\nu}}\ ; \quad \frac{dh_{\nu}}{dh_o} = 1$$

As illustrated in Fig. 4 it is evident that the relative displacements of the corresponding sources at the location of emission differ from the original shifting by a factor, depending on the Mach number of the moving singularity and the orientation ϑ_{ν} between the field point and the emission point. The same relation can be obtained for supersonic Mach number of the singularity. This influence factor due to a change in the effective shift will be denoted as σ_R, with

$$\sigma_R = (-1)^{\nu+1} \cdot \frac{1}{1 - Ma_S \cos \vartheta_{\nu}} \tag{3-10}$$

with $\nu = 1$ for $Ma_S < 1$ and $\nu = 1;\ 2$ for $Ma_S > 1$.

3.3 The Doppler effect in the disturbance field of moving singularities

The Doppler effect at a field point depends on the time sequence with which the perturbation signals pass through the field point as compared to the time sequence with which they are emitted. In general, the time sequence of the signals at the field point will be determined by the motions of the singularity and of the field point relative to the medium and by the orientation of the paths of their motions in space defined by ϑ_o and ϑ_{oE} as measured from the radial line joining the momentary positions of both at time t_o.

For determining the density or pressure perturbation in the medium in which case the time sequence of the change of perturbation potential at a medium-fixed elementary volume is involved, the corresponding field point will be taken as stationary relative to the medium. However, for the signal frequency at a moving field point, its motion is to be accounted for in the Doppler effect.

The relation between the time sequence of signals passing through a field point and of those emitted at the corresponding emission point can be derived from Eq. (2-16) and is, in general, valid both for a moving and for a fixed field point. The time derivation yields the following expression:

$$\frac{dt_\nu}{dt_o} = 1 - \frac{\partial r_o/\partial t_o}{1 - Ma_S^2}\left[Ma_S \cos\vartheta_o + (-1)^{\nu+1}\sqrt{1 - Ma_S^2 \sin^2\vartheta_o}\right] + \qquad (3\text{-}11)$$

$$+ \; r_o \frac{\partial\vartheta_o/\partial t_o}{1 - Ma_S^2}\left[Ma_S \sin\vartheta_o + (-1)^{\nu+1} \frac{Ma_S^2 \sin 2\vartheta_o}{2\sqrt{1 - Ma_S^2 \sin^2\vartheta_o}}\right]$$

with $\nu = 1$ for $Ma_S < 1$ and $\nu = 1;\ 2$ for $Ma_S > 1$.

The time derivations of r_o and ϑ_o can be given the general expressions:

$$\frac{\partial r_o}{\partial t_o} = -\left(Ma_S \cos\vartheta_o + \bar{M}a_E \cos\bar{\vartheta}_o\right) \qquad (3\text{-}12)$$

$$r_o \frac{\partial\vartheta_o}{\partial t_o} = \left(Ma_S \sin\vartheta_o + \bar{M}a_E \sin\bar{\vartheta}_o\right)$$

where $\bar{M}a_E$ represents the component of Ma_E, i.e. the field point Mach number relative to the medium in the P_o-P-P_ν-plane, and $\bar{\vartheta}_o$ denotes the angle between $\bar{M}a_E$ and r_o in the same plane.

For $\bar{M}a_E = 0$, Eq. (3-11) reduces to

$$\sigma_D = \left.\frac{dt_\nu}{dt_o}\right|_{\bar{M}a_E=0} = \frac{1}{1 - Ma_S^2}\left[1 + (-1)^{\nu+1} \cdot \frac{Ma_S \cos\vartheta_o}{\sqrt{1 - Ma_S^2 \sin^2\vartheta_o}}\right] \qquad (3\text{-}13)$$

Using the relations given in Eq. (2-20) and Eq. (2-21) the Doppler factor σ_D simplifies to

$$\sigma_D = (-1)^{\nu+1} \frac{1}{(1 - Ma_S \cos\vartheta_\nu)} \qquad (3\text{-}14)$$

For a field point moving with $\bar{M}a_E \neq 0$, the expression for the Doppler-frequency effect takes the form

$$\sigma_F = \frac{dt_\nu}{dt_o} = \frac{1}{1 - Ma_S^2} + \frac{Ma_S\, \bar{M}a_E \cos(\vartheta_o + \bar{\vartheta}_o)}{1 - Ma_S^2} + (-1)^{\nu+1} \frac{(Ma_S \cos\vartheta_o + \bar{M}a_E \cos\bar{\vartheta}_o)}{(1 - Ma_S^2)\sqrt{1 - Ma_S^2 \sin^2\vartheta_o}} - \qquad (3\text{-}15)$$

$$- \; (-1)^{\nu+1} \frac{Ma_S^2\, \bar{M}a_E \sin\vartheta_o \sin(\vartheta_o + \bar{\vartheta}_o)}{(1 - Ma_S^2)\sqrt{1 - Ma_S^2 \sin^2\vartheta_o}}$$

In view of the kinematic relations connecting r_o, ϑ_o to r_ν and ϑ_ν as given in Eq. (2-18) to Eq. (2-21) an alternative form for σ_F in terms of r_ν and ϑ_ν can be obtained:

$$\sigma_F = \frac{dt_\nu}{dt_o} = \frac{1}{1 - Ma_S^2} - \frac{Ma_S\,\bar{M}a_E}{1 - Ma_S^2} + \frac{Ma_S\,(\cos\vartheta_\nu - Ma_S) - \bar{M}a_E\left\{\cos\vartheta_\nu - Ma_S\cos(\vartheta_\nu + \bar{\vartheta}_\nu)\right\}}{(1 - Ma_S^2)\,(1 - Ma_S\cos\bar{\vartheta}_\nu)} -$$

$$- \frac{Ma_S^2\,\bar{M}a_E\,\sin\vartheta_\nu\,\sin(\vartheta_\nu + \bar{\vartheta}_\nu)}{(1 - Ma_S^2)\,(1 - Ma_S\cos\vartheta_\nu)} \tag{3-16}$$

with $\nu = 1$ for $Ma_S < 1$ and $\nu = 1;\ 2$ for $Ma_S > 1$.

It can be easily verified that for $\bar{M}a_E = 0$ the two Doppler factors σ_D and σ_F are equal. Eq. (3-15) and Eq. (3-16) are valid for uniform translatory motions of the singularity and of the field point relative to the medium both having arbitrary path orientations in space. All known special cases regarding the motion of the field point, which are often dealt with in standard texts, can be obtained from this general expression. Some typical cases illustrating the physical phenomenon which causes a change of the time sequence of the signals at a field point are shown in Fig. 5a and Fig. 5b.

An important feature of the kinematics of the disturbance field of moving singularities is illustrated in Fig. 6. It shows, that on a ray from the instantaneous position of the singularity all disturbance waves meeting the ray at the time instant t_o are emitted under the same angle ϑ_ν and that the influence factors σ given by the ratio r_ν/r^* have the same values on each single ray.

4. THE GENERAL SOLUTIONS OF THE LINEARIZED EQUATIONS FOR THE DISTURBANCE FIELDS OF UNSTEADY SINGULARITIES

In order to obtain generally valid solutions of the problem, it is preferable to express all the quantities in dimensionless form. Based on a characteristic length l and on the sound velocity a_∞ considered as constant, the following nondimensional quantities can be defined

$$\xi = \frac{x}{l}\,; \quad \eta = \frac{y}{l}\,; \quad \zeta = \frac{z}{l}\,; \quad \tau = \frac{t a_\infty}{l}$$

$$\bar{\varphi} = \varphi/a_\infty l\,; \quad \bar{\Omega} = \Omega \cdot \frac{l}{a}\,; \quad \bar{\Omega}^* = \Omega\,\frac{l^2}{a_\infty^2} \tag{4-1}$$

$$\tau_o - \tau_\nu = (t_o - t_\nu)\,\frac{a_\infty}{l} = \frac{r_\nu}{l} = \bar{r}_\nu$$

Thus, the operator for the substantial derivative becomes

$$\frac{D}{D\tau} = \left[\frac{\partial}{\partial\tau} + Ma_S\,\frac{\partial}{\partial\xi}\right] \tag{4-2}$$

and the linearized equation of the perturbation potential is expressed as

$$\nabla^2\bar{\varphi} - \frac{D^2\bar{\varphi}}{D\tau^2} = \bar{\Omega}(\tau)\;\delta(\xi - Ma_S\tau,\ \eta,\ \zeta) \tag{4-3}$$

or

$$\nabla^2\bar{\varphi} - \bar{\varphi}_{\tau\tau} - 2\,Ma_S\,\bar{\varphi}_{\xi\tau} - Ma_S^2\,\bar{\varphi}_{\xi\xi} = \bar{\Omega}(\tau)\;\delta(\xi - Ma_S\tau,\ \eta,\ \zeta) \tag{4-4}$$

with $\bar{\Omega}(\tau)$ as the disturbance function.

4.1 The solution of the classical wave equation including the kinematic relations of disturbance fields as auxiliary condition

The linearized potential equation of the disturbance field of moving singularities in the moving reference system can be converted to the classical wave equation in a fixed reference system by applying a Galilean transformation as already described in section 2.

If at a time instant $\tau = 0$ both the systems coincide, then the following relations are valid:

$$\hat{\xi} = \bar{\xi} - Ma_S\bar{\tau}\,; \quad \hat{\eta} = \bar{\eta}\,; \quad \hat{\zeta} = \bar{\zeta}\,; \quad \hat{\tau} = \bar{\tau}\,. \tag{4-5}$$

With these conventions Eq. (4-3) and Eq. (4-4) simplify to

$$\nabla^2\bar{\varphi} - \bar{\varphi}_{\hat{\tau}\hat{\tau}} = \bar{\Omega}(\hat{\tau})\;\delta(\hat{\xi},\hat{\eta},\hat{\zeta}) \tag{4-6}$$

In the linear theory the wave equation is equally valid when $\bar{\varphi}$ is replaced by the perturbation quantity $\bar{s}$ denoting the density or pressure variations in the disturbance field as given in Eq. (2-13). This leads to

$$\nabla^2 \bar{s} - \bar{s}_{\hat{\tau}\hat{\tau}} = \bar{\Omega}^{*}(\hat{\tau})\, \delta(\hat{\xi},\hat{\eta},\hat{\zeta}) \tag{4-7}$$

with

$$\bar{s} = -\frac{\partial \bar{\varphi}}{\partial \hat{\tau}} \quad \text{and} \quad \bar{\Omega}^{*} = \frac{\partial \bar{\Omega}}{\partial \hat{\tau}} \tag{4-8}$$

The solution of the inhomogeneous wave equation with an harmonic disturbance function is given in [7] to [9]. For arbitrary disturbance function $\bar{\Omega}(\tau)$ the given method of solution can be generalized by making use of Fourier integrals.

The solution of Eq. (4-6) can be obtained by applying Green's theorem and as given in [7] has the general form:

$$\bar{\varphi}(P) = \frac{1}{4\pi} \iiint\limits_{\bar{V}_o} \frac{\bar{\Omega}(\hat{\tau}_\nu)}{\hat{r}_\nu}\, d\bar{V}_o \tag{4-9}$$

With $P(\hat{\xi},\hat{\tau}_o)$ as the field point and $P_\nu(\hat{\xi}_\nu,\hat{\tau}_\nu)$ as the emission point. The disturbance function $\bar{\Omega}(\tau_\nu)$ exists only in an elementary volume $\bar{V}_o$ in the medium, representing the singularity.

The basic solution of the homogeneous wave equation with $\bar{\Omega}(\tau_\nu) = 0$ in Eq. (4-6) is presented in [6] and has the form:

$$\bar{\varphi}(P) = \frac{1}{4\pi} \iint\limits_{\bar{F}_o} \left[-\frac{1}{\hat{r}_\nu} \frac{\partial \varphi}{\partial \bar{n}} + \bar{\varphi} \frac{\partial}{\partial \bar{n}} \left(\frac{1}{\hat{r}_\nu} \right) - \frac{1}{a_\infty \hat{r}_\nu} \frac{\partial \hat{r}_\nu}{\partial \bar{n}} \frac{\partial \bar{\varphi}}{\partial \hat{\tau}_\nu} \right] d\bar{F}_o \tag{4-10}$$

Eq. (4-9) represents a trivial solution of the problem, although it gives a correct picture of the wave propagation with continuous shift of the emission points with time. This contrast in the solution compared to that of a space fixed singularity is brought about by the Galilean transformation, as illustrated in Fig. 7. However Eq. (4-9) fails to give the correct strength of the perturbation signals at the field point. This is due to the fact that in the formal solution given in Eq. (4-9) the kinematic relations of the perturbation fields leading to the influence factors is not considered.

For determining the perturbation potential it is necessary to introduce the kinematic relations into Eq. (4-9) with the help of a Delta-function localizing the correct emission point and accounting for the influence factors σ_V and σ_R, thus yielding the corresponding changes in the perturbation signal strength due to the motion of the singularity.

For this purpose the shifting property of the Delta-function can be used by introducing an auxiliary variable $\hat{\varepsilon}_o$, whereby the following condition is imposed:

$$\hat{\varepsilon}_o = \left[\hat{\xi}'_\nu - Ma_S\, \hat{r}_\nu - \hat{\xi}_o \right]_{\hat{\xi}'_\nu \to \hat{\xi}_\nu} = 0 \text{ for } \hat{\xi}'_\nu = \hat{\xi}_\nu \tag{4-11}$$

yielding

$$d\hat{\varepsilon}_o = \left[\hat{\xi}'_\nu - Ma_S\, \hat{r}_\nu - \hat{\xi}_o \right]_{\hat{\varepsilon}_o \to 0} \equiv \hat{\xi}'_o - \hat{\xi}_o = d\hat{\xi}_o\,. \tag{4-12}$$

Application of the Delta-function leads to the following solution for the perturbation potential

$$\bar{\varphi}(P) = \frac{1}{4\pi} \sum_\nu \iiint\limits_{\bar{V}_o} d\hat{\xi}_o\, d\hat{\eta}_o\, d\hat{\zeta}_o \int_{-\infty}^{\infty} \left[\frac{\Omega}{\bar{r}_\nu} (\hat{\xi}_\nu - \hat{\varepsilon}_o)\, \delta(\hat{\varepsilon}_o) \frac{d\hat{\xi}_\nu}{d\hat{\xi}_o} \right]_{\hat{\varepsilon}_o \to 0} d\hat{\varepsilon}_o \tag{4-13}$$

or

$$\bar{\varphi}(P) = \frac{1}{4\pi} \sum_\nu \iiint\limits_{\bar{V}_o} \frac{\bar{\Omega}(\hat{\xi}_\nu)}{\hat{r}_\nu} \cdot \frac{1}{(1 - Ma_S \cos \vartheta_\nu)}\, d\hat{\xi}_o\, d\hat{\eta}_o\, d\hat{\zeta}_o \tag{4-14}$$

With $\bar{\Omega}$ as source density, $\Delta\bar{V}_o$ as an elementary volume containing the disturbance source and $\hat{\xi}_\nu$ yielding τ_ν from Eq. (4-11) with $\hat{\varepsilon}_o = 0^\circ$, one obtains for the source strength the following relation:

$$\bar{\Omega}(\hat{\tau}_\nu)\,\Delta\bar{V}_o = -\frac{q(\hat{\tau}_\nu)\,\Delta\bar{V}_o}{a_\infty l^2} = \frac{4\pi a_\infty l^2 \bar{S}(\hat{\tau}_\nu)}{a_\infty l^2} = 4\pi\bar{S}(\hat{\tau}_\nu) \tag{4-15}$$

Thus, the solution for the perturbation potential of a source in uniform motion becomes:

$$\bar{\varphi}(P) = \sum_\nu \frac{\bar{S}(\hat{\tau}_\nu)}{\hat{r}_\nu^{*}} = \sum_\nu \frac{\bar{S}(\tau_\nu)}{\bar{r}_\nu^{*}} \tag{4-16}$$

with $\hat{r}_\nu^{*} = (-1)^{\nu+1}\cdot\hat{r}_\nu(1 - Ma_S\cos\vartheta_\nu)$; $\nu = 1$ for $Ma_S < 1$ and $\nu = 1;\ 2$ for $Ma_S > 1$.

The pressure or density perturbation in the disturbance field of moving singularities is expressed in the space fixed reference system of stationary medium as

$$\bar{s} = \frac{\Delta\rho}{\rho_\infty} = \frac{\Delta p}{\kappa p_\infty} = \frac{\partial\bar{\varphi}}{\partial\hat{\tau}_o}(\hat{\xi}, \hat{\eta}, \hat{\zeta}, \hat{\tau}_o) \tag{4-17}$$

According to Eq. (4-16) the perturbation potential $\bar{\varphi}(P)$ is dependent on the retarded time τ_ν at the emission point whereas the density or pressure perturbation at the field point is determined by the time sequence τ_o for the change in potential. Both time sequences however are, connected by the kinematic relations, which can again be accounted for by introducing a Delta function with a new variable such that,

$$\hat{\kappa}_o = \left|\tau_o - \tau'_\nu - \bar{r}_\nu\right|_{\tau'_\nu \to \tau_\nu} = 0 \text{ for } \tau'_\nu = \tau_\nu \tag{4-18}$$

yielding

$$d\hat{\kappa}_o = \left|\tau_o - \tau'_\nu - \bar{r}_\nu\right|_{\hat{\kappa}_o \to 0} \equiv \tau_o - \tau'_o = d\tau_o$$

$$\left.\frac{d\tau_\nu}{d\tau_o}\right|_{\hat{\kappa}_o \to 0} = \frac{1}{1 - Ma_S\cos\vartheta_\nu} \tag{4-19}$$

Hence, the density or pressure perturbation may be expressed in the following form, where the Delta function fulfills the kinematic relations imposed by Eq. (4-18) and Eq. (4-19).

$$\bar{s} = \frac{\Delta\rho}{\rho_\infty} = \frac{\Delta p}{\kappa p_\infty} = \frac{\partial}{\partial\tau_o}\int_{-\infty}^{\infty}\left[\bar{\varphi}(\tau_o - \hat{\kappa}_o)\ \delta(\hat{\kappa}_o)\right]_{\hat{\kappa}_o \to 0} d\hat{\kappa}_o \tag{4-20}$$

The formal partial derivation of Eq. (4-20) with respect to τ_o, considering that the time derivative of $\delta(\hat{\kappa}_o)$ has the significance of a convective change with τ_o given by

$$\frac{\partial\delta(\hat{\kappa}_o)}{\partial\tau_o} = Ma_S\frac{\partial\delta(\hat{\kappa}_o)}{\partial\xi_o}, \tag{4-21}$$

the perturbation quantity $\bar{s}$ takes the form

$$\bar{s} = \frac{\partial\bar{\varphi}}{\partial\tau_o} + Ma_S\frac{\partial\bar{\varphi}}{\partial\xi_o} \tag{4-22}$$

Introducing the expression for the perturbation potential from Eq. (4-16) one gets

$$\bar{s} = \sum_\nu\left[\frac{1}{\bar{r}_\nu^{*}}\,\frac{\partial\bar{S}(\tau_\nu)}{\partial\tau_\nu}\cdot\left|\frac{\partial\tau_\nu}{\partial\tau_o}\right|_{\kappa\to 0} + Ma_S\,\bar{S}(\tau)\,\frac{\partial}{\partial\xi_o}\left(\frac{1}{\bar{r}_\nu^{*}}\right)\right] \tag{4-23}$$

Thus, the density or pressure perturbation due to a moving unsteady source is

$$\bar{s} = \sum_{\nu} \left[\frac{\bar{S}'(\tau_\nu)}{r_\nu \, (1 - Ma_S \cos \vartheta_\nu)^2} + \frac{\bar{S}(\tau_\nu) \, Ma_S \, (\cos \vartheta_\nu - Ma_S)}{r_\nu^2 \, (1 - Ma_S \cos \vartheta_\nu)^3} \right] \qquad (4\text{-}24)$$

The first term is the dominant one in the far-field while the second term is significant in the near-field.

4.2 Application of the Lorentz-transformation to solve the wave equation in a moving reference system

In order to treat the disturbance propagation from a singularity placed in a moving reference system, it is very useful to apply the Lorentz-transformation because it possesses four remarkable properties:

> The equation of the perturbation potential retains the form of the classical wave equation.
>
> The kinematics of the disturbance field of a moving source is continually fulfilled.
>
> The existance of a basic invariant of the form $(\xi-\xi_\nu)^2 + \eta^2 + \zeta^2 - (\tau-\tau_\nu)^2 = 0$ in the disturbance field allows the results to be depicted in a space-time continuum.
>
> The time sequences of the signals passing through a field point in another reference system can be easily derived.

In order to differentiate the quantities in various reference systems the following symbols are introduced

$\tilde{x}, \tilde{y}, \tilde{z}, \tilde{t}$ - coordinates in Lorentz-space

$\bar{x}, \bar{y}, \bar{z}, \bar{t}$ - coordinates in a moving system in physical space

$\hat{x}, \hat{y}, \hat{z}, \hat{t}$ - coordinates in a fixed reference system in physical space

With all three systems coinciding at the time $\tilde{t} = \bar{t} = \hat{t} = 0$ the following relations between the three coordinate system can be established

$$\tilde{x} = \frac{\hat{x} + V_S \hat{t}}{\sqrt{1 - Ma_S^2}} = \frac{\bar{x}}{\sqrt{1 - Ma_S^2}} \; ; \quad \tilde{y} = \bar{y} = \hat{y} \; ; \quad \tilde{z} = \bar{z} = \hat{z}$$

$$\tilde{t} = \frac{a_\infty^2 \hat{t} + V_S \hat{x}}{a_\infty^2 \sqrt{1 - Ma_S^2}} = \frac{a_\infty^2 \bar{t} + V_S (\bar{x} - V_S \bar{t})}{a_\infty^2 \sqrt{1 - Ma_S^2}} \qquad (4\text{-}25)$$

Introducing now dimensionless quantities based on the characteristic lengths $\tilde{l}$ and $\bar{l}$ in the two moving reference systems, where $\tilde{l} = \bar{l}/\sqrt{1 - Ma_S^2}$, one has

$$\tilde{\xi} = \frac{\tilde{x}}{\tilde{l}} \; ; \quad \bar{\xi} = \frac{\bar{x}}{\bar{l}} \; ; \quad \tilde{h} = \frac{h}{\tilde{l}} \; ; \quad \bar{h} = \frac{h}{\bar{l}}$$

$$\tilde{\tau} = \frac{a_\infty \tilde{t}}{\tilde{l}} \; ; \quad \bar{\tau} = \frac{a_\infty \bar{t}}{\bar{l}} \; . \qquad (4\text{-}26)$$

The Lorentz-transformation in Eq. (4-25), rewritten in dimensionless form, reduces to (see Fig. 8)

$$\tilde{\xi} = \bar{\xi} = \hat{\xi} + Ma_S \hat{\tau}$$

$$\tilde{\eta} = \bar{\eta} \sqrt{1 - Ma_S^2} = \hat{\eta} \sqrt{1 - Ma_S^2}$$

$$\tilde{\zeta} = \bar{\zeta} \sqrt{1 - Ma_S^2} = \hat{\zeta} \sqrt{1 - Ma_S^2} \qquad (4\text{-}27)$$

$$\tilde{\tau} = (1 - Ma_S^2) \, \bar{\tau} + Ma_S \, \bar{\xi} = \hat{\tau} + Ma_S \, \hat{\xi} \; .$$

The kinematic relations can then be expressed as

$$\tilde{\tau}_\nu = \tilde{\tau}_o - \tilde{r}_\nu = (1 - Ma_S^2)\,\bar{\tau}_o + Ma_S\,\bar{\xi} - \bar{r}_\nu^{*} = (1 - Ma_S^2)\bar{\tau}_\nu$$

$$\tilde{r}_\nu \cos\tilde{\vartheta}_\nu = r_\nu(\cos\vartheta_\nu - Ma_S) \tag{4-28}$$

$$\tilde{r}_\nu = \bar{r}_\nu^{*} = \bar{r}_\nu \left| 1 - Ma_S \cos\vartheta_\nu \right|$$

The physical quantities involved in the disturbance function possess the following relations

$$Q = 4\pi a_\infty \tilde{l}^2\tilde{S} = 4\pi a_\infty \bar{l}^2\bar{S}$$

$$\tilde{\omega}\, d\tilde{\tau}_\nu = \bar{\omega}\, d\bar{\tau}_\nu$$

$$\tilde{\omega} = \frac{\bar{\omega}}{1 - Ma_S^2} \;; \quad d\tilde{\tau}_\nu = d\bar{\tau}_\nu(1 - Ma_S^2) \tag{4-29}$$

$$\tilde{\Omega} = \bar{\Omega} \;; \quad d\tilde{V}_o = d\bar{V}_o(1 - Ma_S^2) \;; \quad \tilde{S} = \bar{S}(1 - Ma_S^2)$$

$$\tilde{\varphi} = \bar{\varphi}\,(1 - Ma_S^2)$$

Applying the corresponding Lorentz-transformation to the basic equation of the disturbance field in moving reference system as given in Eq. (4-4) or to the classical wave equation in space fixed reference system as given in Eq. (4-6) one gets the following exact relation

$$\tilde{\varphi}_{\tilde{\xi}\tilde{\xi}} + \tilde{\varphi}_{\tilde{\eta}\tilde{\eta}} + \tilde{\varphi}_{\tilde{\zeta}\tilde{\zeta}} - \tilde{\varphi}_{\tilde{\tau}\tilde{\tau}} = \tilde{\Omega}(\tilde{\tau}_\nu/\beta^2)\ \delta(\tilde{\xi},\frac{\tilde{\eta}}{\beta},\frac{\tilde{\zeta}}{\beta}) \tag{4-30}$$

The solution of this classical wave equation is well known and it yields for the perturbation potential

$$\tilde{\varphi}(P) = \sum_\nu \frac{\tilde{S}(\tilde{\tau}_\nu)}{\tilde{r}_\nu} \tag{4-31}$$

with $\nu = 1$ for $Ma_S < 1$ and $\nu = 1;\ 2$ for $Ma_S > 1$.

In this solution the kinematic relations of the disturbance propagation from moving source is already included, since $\tilde{r}_\nu = \bar{r}^*$ denoting the effective radial distance between emission point and field point. The solution in the physical space follows at once:

$$\bar{\varphi}(P) = \frac{\tilde{\varphi}(P)}{1 - Ma_S^2} = \sum_\nu (-1)^{\nu+1} \frac{\bar{S}(\bar{\tau}_\nu)}{\bar{r}_\nu(1 - Ma_S \cos\vartheta_\nu)} \tag{4-32}$$

For stationary disturbance fields with source strength $\bar{S}$ = const. and the field point accompanying the moving coordinate system, Eq. (4-32) reduced to the wellknown solution of the perturbation potential

$$\bar{\varphi}(P) = \frac{\bar{S}}{\bar{r}^*} \qquad \text{for } Ma_S < 1\,,$$

$$\bar{\varphi}(P) = \frac{2\bar{S}}{\bar{r}^*} \qquad \text{for } Ma_S > 1\,, \tag{4-33}$$

where $\bar{r}^* = \left[(\xi - \xi_o)^2 + (1 - Ma_S^2)\,(\eta^2 + \zeta^2)\right]^{1/2} = \bar{r}_\nu \left| 1 - Ma_S \cos\vartheta_\nu \right|$.

The density or pressure perturbation can be easily deduced now to be

$$\bar{s} = \frac{\Delta\rho}{\rho_\infty} = \frac{\Delta p}{\kappa p_\infty} = \frac{Ma_S}{\beta^2}\frac{\partial\tilde{\varphi}}{\partial\tilde{\xi}} + \frac{\partial\tilde{\varphi}}{\partial\tilde{\tau}_o} = Ma_S\frac{\partial\bar{\varphi}}{\partial\bar{\xi}} + \frac{\partial\bar{\varphi}}{\partial\bar{\tau}_o} \tag{4-34}$$

After carrying out the partial differentiation and using the kinematic relations one gets for the harmonic disturbance function:

$$\bar{s} = \sum_{\nu} \frac{\tilde{S}_o\, e^{-i\tilde{\omega}_S \tilde{\tau}_\nu}}{(1 - Ma_S^2)} \left[\frac{Ma_S\, \tilde{\xi}}{\tilde{r}_\nu^3} + \frac{i\tilde{\omega}_S\,(1 - Ma_S \cos\tilde{\vartheta}_\nu)}{\tilde{r}_\nu} \right] \tag{4-35}$$

with $\cos\tilde{\vartheta}_\nu = \frac{\tilde{\xi}}{\tilde{r}_\nu}$ as depicted in <u>Fig. 9</u>. Eq. (4-35) can be rewritten in terms of coordinates in physical space, yielding

$$\bar{s} = \sum_{\nu} (-1)^{\nu+1}\; \bar{S}_o\, e^{-i\bar{\omega}_S \bar{\tau}_\nu} \left[\frac{Ma_S\,(\cos\vartheta_\nu - Ma_S)}{\bar{r}_\nu^2 (1 - Ma_S \cos\vartheta_\nu)^3} + \frac{i\bar{\omega}_S}{\bar{r}_\nu (1 - Ma_S \cos\vartheta_\nu)^2} \right], \tag{4-36}$$

with $\nu = 1$ for $Ma_S < 1$ and $\nu = 1;\ 2$ for $Ma_S > 1$.

In order to determine the frequency at the field point, fixed or moving, the following general relation may be used:

$$\bar{\omega}_E\, d\bar{\tau}_o = \bar{\omega}_S\, d\bar{\tau}_\nu = \tilde{\omega}_S\, d\tilde{\tau}_\nu \tag{4-37}$$

giving

$$\bar{\omega}_E = \tilde{\omega}_S \frac{d\tilde{\tau}_\nu}{d\bar{\tau}_o} = \frac{\bar{\omega}_S}{(1 - Ma_S^2)} \frac{\partial}{\partial\bar{\tau}_o} \left[(1 - Ma_S^2)\tau_o + \left(Ma_S\, \bar{r}_o \cos\vartheta_o - \bar{r}_o \sqrt{1 - Ma_S^2 \sin^2\vartheta_o} \right) \right]. \tag{4-38}$$

The factor of $\bar{\omega}_S$ in Eq. (4-38) is identical to the expression obtained from the kinematic relations in Eq. (3-11) and hence to Eq. (3-15). Thus, Eq. (4-38) reduces to the simple expression

$$\bar{\omega}_E = \bar{\omega}_S\, \sigma_F \tag{4-39}$$

with σ_F representing the Doppler effect given in Eq. (3-15) or Eq. (3-16).

Thus, the application of Lorentz-transformation presents all the results given in chapter 4.1 with only very few steps needed.

The disturbance fields of a source with subsonic velocities are depicted in the space-time continuum in <u>Fig. 10a</u> and <u>Fig. 10b</u> giving directly the $\tilde{r}_\nu$ or $\bar{r}^*$ values of spherical waves meeting the field point. In <u>Fig. 10b</u> for <u>$Ma_S > 1$</u> it illustrates the meeting of two waves at a field point with their corresponding influence factors contained in $\bar{r}_\nu^*$.

4.3 <u>The variation of perturbations at a space fixed field point with time due to a disturbing source in uniform motion</u>

Based on the fact that for a uniform motion of the disturbing source the velocity V_S is constant, and that in the linearized theory the velocity of sound a_∞ in the disturbance field is assumed constant, it is possible to express all the kinematic relations in terms of time. For this purpose the vertical distance h of the field point from the x-axis may be replaced by an hypothetical time factor τ_h, which is a constant. Setting $\tau = 0$ at the time instant when the moving source is at $\xi_o = \xi$, the various distances between P_o, P and P_ν in the field may be expressed as:

$$\xi - \xi_o = Ma_S \tau_S \;;\quad \bar{h} = Ma_S \tau_h \;;\quad \bar{r}_\nu = \tau_S - \tau_\nu \tag{4-40}$$

with τ_S as the time instant for the location of the singularity, when the emitted signal at a retarded time τ_ν just reaches the field point. The kinematic relations for the disturbance field may then be written as:

$$(\tau_S - \tau_\nu)^2 = Ma_S^2 \tau_\nu^2 + Ma_S^2 \tau_h^{\,2} \tag{4-41}$$

yielding for the value of τ_ν the expression

$$\beta^2 \tau_\nu = \left[\tau_S + (-1)^{\nu+1} \cdot Ma_S \sqrt{\tau_S^2 + \beta^2 \tau_h^2} \right] \tag{4-42}$$

with $\beta^2 = (1 - Ma_S^2)$.

The location of the emission point is given by

$$\bar{r}_\nu = \tau_S - \tau_\nu$$

$$\cos\vartheta_\nu = -\frac{Ma_S \tau_\nu}{\tau_S - \tau_\nu} \tag{4-43}$$

For the perturbation values at the field point the required value of $\bar{r}_\nu^*$ is given by:

$$\bar{r}_\nu^* = Ma_S \tau_h \sqrt{(1 - Ma_S^2) + \left(\frac{\tau_S}{\tau_h}\right)^2} \tag{4-44}$$

with $\nu = 1$ for $Ma_S < 1$ and $\nu = 1;\ 2$ for $Ma_S > 1$.

While at subsonic motion of the source the perturbations are felt at the field point at all time instants with $-\infty \leq \tau_S \leq +\infty$, at supersonic velocity of the source the perturbations exists only for $\tau_S \geq (Ma_S^2 - 1)\tau_h$. The variation of the perturbation and of the influence factors with time at a space fixed field point is exhibited in Fig. 11 and Fig. 12. The variation of $\bar{\varphi}$, $\bar{s}_F$ and σ_D at the field point as a function of time reveals the characteristic features of disturbance fields from singularities moving with subsonic and supersonic velocities.

5. THE NEAR-FIELD AND FAR-FIELD SOLUTIONS FOR THE DISTURBANCE FIELDS OF SINGULARITIES IN MOTION

The disturbance fields of singularities in uniform motion in an unbounded medium can be described by the classical wave equation, either by using a fixed reference system or by applying a Lorentz-transformation in a moving reference system. The methods of solution of the classical wave equation for singularities in motion are treated and discussed in detail in section 4. The nature of the disturbing source is defined by the disturbance function $\Omega(\tau_\nu)$, the first term representing a source, the second a dipole, and the third a quadrupole type singularity.

5.1 Disturbance field of an unsteady harmonic source in uniform motion

The perturbation potential of a moving unsteady source as derived in section 4 has the solution:

$$\bar{\varphi}(P) = \sum_\nu (-1)^{\nu+1} \cdot \frac{\bar{S}_o\, e^{-i\bar{\omega}_S \tau_\nu}}{\bar{r}_\nu (1 - Ma_S \cos \vartheta_\nu)} \tag{5-1}$$

The density or pressure perturbation at a field point is given by

$$\bar{s} = \frac{\Delta\rho}{\rho_\infty} = \frac{\Delta p}{\kappa p_\infty} = \sum_\nu (-1)^{\nu+1}\ \bar{\bar{S}}_o\, e^{-i\bar{\omega}_S \tau_\nu} \left| \frac{Ma_S (\cos \vartheta_\nu - Ma_S)}{\bar{r}_\nu^2 (1 - Ma_S \cos \vartheta_\nu)^3} + \frac{i\bar{\omega}_S}{\bar{r}_\nu (1 - Ma_S \cos \vartheta_\nu)^2} \right| \tag{5-2}$$

with $\nu = 1$ for $Ma_S < 1$ and $\nu = 1;\ 2$ for $Ma_S > 1$.

While the first term is predominant in the near-field, the second term mainly defines the far-field disturbances. The near-field and far-field pressure perturbations are shown in Fig. 13.

5.2 Disturbance field of an unsteady harmonic dipole in uniform motion

The disturbing source originating from an oscillating force is denoted by the second term of $\bar{\Omega}(\tau_\nu)$ where the axis of oscillation may have an arbitrary orientation with respect to the direction of motion. Two basic types of orientations for the oscillation may be defined, i.e. an oscillation axis lying along x or this axis being placed normal to x.

The solution for the perturbation potential of harmonically oscillating forces having uniform motion is given by the general expression:

$$\bar{\varphi}_D(P) = \sum_\nu \frac{(-1)^{\nu+1}}{4\pi} \iiint \frac{(\nabla \cdot \bar{G}_o) e^{-i\bar{\omega}_S \tau_\nu}\, d\xi_o\, d\eta_o\, d\zeta_o}{\bar{r}_\nu (1 - Ma_S \cos \vartheta_\nu)} \tag{5-3}$$

with $\bar{G}(\tau_\nu) = \int_0^{\tau_\nu} \bar{K}_i(\tau_\nu)\, d\tau_\nu$, where $\bar{K}_i = K_i \frac{1}{a_\infty^2}$ denotes the dimensionless oscillating force per mass of the medium contained in the volume element of the singularity.

For an harmonically oscillating force the following relations are valid:

$$\bar{G}(\tau_\nu) = -\frac{i}{\bar{\omega}_S} \bar{K}_{oi}\, e^{-i\bar{\omega}_S \tau_\nu} \tag{5-4}$$

The perturbation potential of oscillating forces in motion with the two basic orientations of the force axis may be expressed as

$$\bar{\varphi}_{D1}(P) = \sum_{\nu} \frac{i\bar{K}^{*}_{o1}}{4\pi\bar{\omega}_S} \cdot \frac{\partial}{\partial\xi_o}\left\{\frac{(-1)^{\nu+1}\, e^{-i\bar{\omega}_S\tau_\nu}}{\bar{r}_\nu(1 - Ma_S \cos\vartheta_\nu)}\right\} \tag{5-5}$$

and

$$\bar{\varphi}_{D2}(P) = \sum_{\nu} \frac{i\bar{K}^{*}_{o2}}{4\pi\bar{\omega}_S} \cdot \frac{\partial}{\partial\eta_o}\left\{\frac{(-1)^{\nu+1}\, e^{-i\bar{\omega}_S\tau_\nu}}{\bar{r}_\nu(1 - Ma_S \cos\vartheta_\nu)}\right\} \tag{5-6}$$

respectively, where

$$\bar{K}^{*}_{o} = \iiint_{V_o} \bar{K}_{oi}\, d\xi_o\, d\eta_o\, d\zeta_o$$

with $\nu = 1$ for $Ma_S < 1$ and $\nu_S = 1$; 2 for $Ma_S > 1$.

The bracketed terms in Eq. (5-5) and Eq. (5-6) denote the basic solution of a moving source, and hence the perturbation field of an oscillating force is equivalent to that of a dipole, whose solution can be directly obtained from the partial derivative of the source solution, with the equivalent dipole strength given by

$$\bar{D}_o = \frac{i\bar{K}^{*}_{o}}{4\pi\bar{\omega}_S} \tag{5-8}$$

The density and pressure perturbation can be obtained from the Eq. (4-17) yielding the near-field and far-field terms, a graphical display of which is shown in Fig. 14.

5.3 Disturbance fields of unsteady harmonic quadrupoles in uniform motion

Quadrupole-type singularities arise when a pair of oscillating forces is used or is activated through shearing motions in the medium. The treatment of quadrupole sources in aeroacoustics was first presented in [43]. The disturbance function is denoted by the third term of $\Omega(\tau_\nu)$ in Eq. (2-9). The solution of the perturbation potential in the disturbance field of quadrupoles may be obtained from the same general expression which is applicable to sources and dipoles. For harmonic fluctutation of the quadrupole singularities one has

$$\bar{\varphi}_{M}(P) = \sum_{\nu} \frac{(-1)^{\nu+1}}{4\pi} \iiint \frac{(\nabla\cdot\nabla\cdot\hat{G}_{oij})\, e^{-i\bar{\omega}_S\tau_\nu}\, d\xi_o\, d\eta_o\, d\zeta_o}{\bar{r}_\nu(1 - Ma_S \cos\vartheta_\nu)} \tag{5-9}$$

where $\bar{T}_{ij} = \frac{\partial}{\partial\tau_\nu}\hat{G}_{ij}$ can be denoted as a shearing stress tensor yielding the relation

$$\hat{G}_{ij} = -\frac{i}{\bar{\omega}_S}\bar{T}_{ij} = -\frac{i}{\omega_S} T_{ij} \cdot \frac{1}{a_\infty l} \tag{5-10}$$

Thus, $\bar{T}_{ij}$ defines a dimensionless stress tensor based on the mass of the medium contained in the volume element of the singularity - its integral over the elementary volume being denoted by $\bar{T}^{*}_{o}$.

The solution of the perturbation potential for the three basic orientations of the quadrupole axes may be expressed as follows:

$$\bar{\varphi}_{M1}(P) = \sum_{\nu} \frac{i\,\bar{T}^{*}_{o1}}{4\pi\bar{\omega}_S} \cdot \frac{\partial^2}{\partial\xi_o^2}\left[\frac{(-1)^{\nu+1}\, e^{-i\bar{\omega}_S\tau_\nu}}{\bar{r}_\nu(1 - Ma_S \cos\vartheta_\nu)}\right] \tag{5-11}$$

$$\bar{\varphi}_{M2}(P) = \sum_{\nu} \frac{i\,\bar{T}^{*}_{o2}}{4\pi\bar{\omega}_S} \cdot \frac{\partial^2}{\partial\xi_o\partial\zeta_o}\left[\frac{(-1)^{\nu+1}\, e^{-i\bar{\omega}_S\tau_\nu}}{\bar{r}_\nu(1 - Ma_S \cos\vartheta_\nu)}\right] \tag{5-12}$$

$$\bar{\varphi}_{M3}(P) = \sum_{\nu} \frac{i\,\bar{T}^{*}_{o3}}{4\pi\bar{\omega}_S} \cdot \frac{\partial^2}{\partial\zeta_o^2}\left[\frac{(-1)^{\nu+1}\, e^{-i\bar{\omega}_S\tau_\nu}}{\bar{r}_\nu(1 - Ma_S \cos\vartheta_\nu)}\right] \tag{5-13}$$

The bracketed terms denote again the source solution from which the quadrupol solution may be directly obtained by a double differentiation. The equivalent quadrupole strength becomes

$$\bar{M}_o = \frac{i\,\bar{T}_o^{*}}{4\pi\bar{\omega}_S} \qquad (5\text{-}14)$$

The density and pressure perturbations for the near-field and the far-field can be obtained again from Eq. (4-17). The pressure perturbation for the type-2 quadrupole are illustrated in Fig. 15.

6. ENERGY DENSITY AND ENERGY FLOW IN THE DISTURBANCE FIELD OF MOVING SINGULARITIES

From the pressure perturbations and particle velocities in the disturbance field one can easily determine the kinetic and potential energy content in an elementary volume of the disturbance field as well as calculate the intensity of the radiated energy propagated with the disturbance waves. In case of unsteady disturbance fields the perturbation energy content in an elementary volume of the medium is defined by the mean-square values of the disturbance quantities, while the perturbation intensity denotes the mean rate of flow of energy per unit area due to the disturbance propagation. To gain a basic insight into this topic, standard texts [8], [9], and some detailed analyses in [39] and [43] are referred to.

In this section a short derivation of the energy propagated in the disturbance field will be given, using control surfaces which are better adapted to the case of moving singularities. Considering the near-field and far-field terms of the disturbance field originating from disturbing sources in motion, one can write

$$\Delta p = \Delta p_N + \Delta p_F \quad \text{and} \quad v_S^2 = v_{SN}^2 + v_{SF}^2 + 2v_{SN}v_{SF}\cos\alpha_{NF} \qquad (6\text{-}1)$$

where v_S denotes the disturbance velocities with α_{NF} being the angle between v_{SN} and v_{SF}.

For the time average of harmonic functions use will be made of the following properties

$$\overline{\cos\omega t \cdot \sin\omega t} = 0 \quad \text{and} \quad \overline{\cos^2\omega t} = \overline{\sin^2\omega t} = \frac{1}{2}\,. \qquad (6\text{-}2)$$

Hence, the following relations hold

$$\overline{(\Delta p)^2} = \overline{(\Delta p_N)^2} + \overline{(\Delta p_F)^2} \qquad \text{and} \qquad \overline{v_S^2} = \overline{v_{SN}^2} + \overline{v_{SF}^2} \qquad (6\text{-}3)$$

The energy fluxes $\hat{I}_F$ and I_F at a field point in the fixed and moving reference systems, respectively, are interrelated by the time sequence of signals passing through it, as shown in Fig. 5, whence

$$\hat{I}_F\, dt_o = I_F\, dt_\nu\,. \qquad (6\text{-}4a)$$

This yields

$$\hat{I}_F = I_F\,\sigma_D \quad \text{and} \quad \hat{E}_F = E_F\,\sigma_D \qquad (6\text{-}4b)$$

with

$$\sigma_D = (1 - Ma_S\cos\vartheta_\nu)^{-1}\,.$$

6.1 Energy density and energy flow due to the far-field radiative terms

The energy density due to the far-field terms consisting of the radiative part of the disturbance quantities can be expressed in the moving reference frame, when the time average is based on $\Delta\tau_\nu$ and thus

$$E_F = \frac{1}{2}\rho_\infty a_\infty^2 \left| \frac{\overline{v_{SF}^2}}{a_\infty^2} + \frac{\overline{(\Delta p_F)^2}}{(\kappa p_\infty)^2} \right| \qquad (6\text{-}5)$$

In the far-field the following relation holds for the radiative component of the disturbances, v_{SF} being identical with the particle velocity v_{rF} directed radially to the propagating spherical waves

$$\rho_\infty a_\infty v_{SF} = \rho_\infty a_\infty v_{rF} = \Delta p_F\,. \qquad (6\text{-}6)$$

Hence, Eq. (6-5) simplifies to

$$E_F = \rho_\infty a_\infty^2 \left[\frac{\overline{v_{rF}^2}}{a_\infty^2} \right] = \rho_\infty a_\infty^2 \frac{\overline{(\Delta p_F)^2}}{(\kappa p_\infty)^2}\,. \qquad (6\text{-}7)$$

The energy intensity defined as the rate of energy flow through a unit surface normal to v_{rF} amounts to

$$I_F = \overline{\Delta p_F \cdot v_{rF}} = \rho_\infty a_\infty^3 \frac{\overline{(\Delta p_F)^2}}{(\kappa p_\infty)^2} \,, \tag{6-8a}$$

giving also the relation $I_F = a_\infty E_F$. (6-8b)

Further the convecting part of the energy flow through a unit surface normal to V_S will be given by

$$I_{KF} = a_\infty Ma_S \, E_F \,. \tag{6-9}$$

Thus, the rate of energy flow through a moving control surface, in general, is given by the expression:

$$L_F = \int\limits_{F_o} (\vec{I}_F - \vec{I}_{KF}) \cdot n dF_o - \int\limits_{V_o} \frac{\partial E_F}{\partial t} dV_o \tag{6-10}$$

The mean energy density in the control volume accompanying the moving reference system being constant, the volume integral vanishes and Eq. (6-10) assumes a simple form containing the known values from Eq. (6-8) and Eq. (6-9).

In order to calculate the time rate of total energy flow in the radiative field it is natural to consider in the moving reference system a spherical control surface of radius r_ν, which coincides, at a time $t = t_o$, with an emitted disturbance wave, as shown in Fig. 16. Being in the moving reference system, the control surface will always be met by corresponding disturbance waves, coincident with it, but undergoing a time variation of their strengths. The time average of the rate of total energy flow through the spherical control surface will then give the mean radiative power output of the disturbing source.

The rate of energy flow through the moving spherical surface will then amount to

$$L_F = \int\limits_{F_o} E_F(\vec{a}_\infty - \vec{V}_S) \cdot n dF_o = 2\pi r_\nu^2 \int\limits_o^\pi a_\infty E_F (1 - Ma_S \cos\vartheta_\nu) \sin\vartheta_\nu \, d\vartheta_\nu \tag{6-11}$$

With the value of Δp_F from Eq. (5-2) put into the expressions relating E_F and I_F as given in Eq. (6-7) and Eq. (6-8) leads to the following value for the mean radiative power output of the disturbing source

$$L_F = 2\pi l^2 \rho_\infty a_\infty^3 \frac{\bar{\omega}_S^2 \, \bar{S}^2}{(1 - Ma_S^2)^2} \tag{6-12}$$

with l as a characteristic reference length, being constant for the system chosen and $\bar{S}$ denoting the strength of the disturbing source. Thus, the expression in Eq. (6-12) is independent of the control-surface radius and is equally valid for all r_ν-values. This also proves the pure radiative nature of the far-field disturbances, which propagate outward without undergoing any losses. One obtains the same result for L_F if an infinitely long cylindrical control-surface of radius h about the x-axis is chosen and the control surface is made to move with the singularity.

The expression for the mean power output of the far-field disturbances, Eq. (6-12), is equally valid for subsonic and supersonic velocities of the source, where in the latter case the integration of Eq. (6-11) possesses the generalized principal value.

6.2 Energy density and energy flow due to the near-field perturbation terms

The energy density and the energy flow due to the near-field terms can be determined in a similar way as for the far field, by using a moving spherical control-surface of radius r_o about the singularity itself, as is shown in Fig. 16.

One obtains

$$E_N = \frac{1}{2} \rho_\infty a_\infty^2 \left| \frac{\overline{v_{SN}^2}}{a_\infty^2} + \frac{\overline{(\Delta p_N)^2}}{(\kappa p_\infty)^2} \right| \tag{6-13}$$

and

$$I_N = \overline{\Delta p_N \, v_{rN}} = \rho_\infty a_\infty^3 \, Ma_S \left[\frac{\overline{u_N \, v_{rN}}}{a_\infty^2} \right]$$

with u_N being the x-component of the near-field term of disturbance velocity and v_{rN} the radial component through the spherical control surface.

The convective part of the energy flow is given by

$$I_{KN} = a_\infty \, Ma_S \, E_N \tag{6-15}$$

Thus, the mean power output due to the near field perturbation terms is given by

$$L_N = 2\pi r_o^2 \int_o^\pi (I_N - I_{KN} \cos \vartheta_o) \sin \vartheta_o \, d\vartheta_o \tag{6-16}$$

$$L_N = 0 \quad \text{for } Ma_S < 1 \, . \tag{6-17}$$

With the disturbance quantities being known, it is easy to evaluate the integral in Eq. (6-16) for a subsonic velocity of the disturbing source. This gives $L_N = 0$ as stated in Eq. (6-17), due to the assymetric nature of the integrand with respect to ϑ_o, thus stating that there is no mean power output due to the near-field perturbation terms of a singularity in subsonic motion. This fact is well established, verifying again that bodies in steady subsonic motion in a frictionless medium experience no drag.

For supersonic motion of the singularity, however, the evaluation of the value of L_N is somewhat involved, due to the fact that the disturbance quantities on a Mach line, according to the linearized theory, becomes indeterminate. In this case the use of an infinitely long cylindrical control surface about the x-axis is appropriate. The rate of energy flow L_N through the cylindrical surface due to a moving singularity at supersonic speed, however, assumes a finite value, giving rise to the well known wave drag.

7. CONCLUSIONS

Based on the linearized theory of disturbance propagation the perturbation field of moving instationary singularities is determined. The unified treatment applies, both, to aerodynamics and to aeroacoustics. The perturbation fields of stationary aerodynamics are contained in it as special cases.

In this investigation the main emphasis is laid on the kinematics of the disturbance fields. The analysis of their physical character leads to the derivation of the main influence factors arising from the motion of the singularities. The derivations, which follow from the kinematics of the disturbance propagation using linear theory, confirm that the effect of the motion of a singularity, the so called Mach number effect, is purely a kinematic effect, not a compressibility effect. A true compressibility effect can arise only if nonlinear theory is applied.

The generalized formula given for the Doppler effect admits uniform linear motion of the singularity as well as of the field point considered, both having arbitrary orientations in space. All expressions derived for the influence factors are uniformly valid for subsonic and supersonic motion of the singularities.

The solution for the perturbation field of moving singularities is derived in two different ways: first, by using the classical wave equation and by inserting the kinematic relations of the disturbance propagation as auxiliary conditions, and alternatively by applying the Lorentz-transformation in a nondimensional form. Both methods are applicable to subsonic and to supersonic motion of the singularities.

The source solution is presented in a space-time continuum revealing the interesting features of the Lorentz-transformation. Unsteady moving singularities in the form of sources, dipoles and quadrupoles are studied extensively, yielding the near-field and the far-field perturbation potentials and, accordingly, the density and pressure perturbations.

REFERENCES

[1] NEWTON, I. Philosophiae naturalis prinzipia mathematica (1687, 1713, 1726).
Mathematical Principles of Natural Philosophy, translated by A. Molte (1729), revised by A. Cajory, Univ. of California Press (1946).
Mathematische Prinzipien der Naturlehre. Edited by J.Ph. Wolfers (1872).

[2] BIOT, J.B. Sur la théorie du son. Jour. Phys. 55 (1802) pp. 173-182.

[3] LAPLACE, P.S. Sur la vitesse du son dans l'air et dans l'eau. Ann. de Chim. et de Phys. III (1816), p. 238 ff.

[4] D'ALEMBERT, J.L. Recherches sur la courbe que forme une corde tendue mise en vibration. Kgl. Akad. Wiss. Berlin 3 (1747), p. 214 ff.

[5] POISSON, S.D. Mémoire sur la théorie du son. Jour. de l'Ecole Polytechn. VII (1807), pp.334-338.

[6] KIRCHHOFF, G. Zur Theorie der Lichtstrahlen. Berl. Ber. (1882) p. 641 ff.
Vorlesungen über Mechanik, Leipzig (1897).

[7] v. HELMHOLTZ, H. Theorie der Luftschwingungen in Röhren mit offenen Enden. Crelle, Vol. LVII (1860), p. 1 ff.

[8] LORD RAYLEIGH The Theory of Sound. 2 Vols. (1878), 2nd Ed. Dover Publication New York (1945).

[9] LAMB, H. Hydrodynamics, 6th Edition. Cambridge Univ. Press, London (1932). Reprinted 1945, Dover Publication, New York.

[10] DOPPLER, C. Über den Einfluß der Bewegung auf die Erscheinungen der Äther-Luft- und Wasserwellen. Abh. d. Böhmischen Ges. d. Wiss., V. Folge, Vol. 161 (1847).

[11] MACH, E.; SALCHER, P. Photographische Fixierung der durch Projektile in der Luft eingeleiteten Vorgänge. Wiener Ber., Vol. 95 (1887), p. 764 ff.

[12] VOIGT, W. Über das Doppler'sche Prinzip. Nachrichten von der kgl. Ges. d. Wiss., 2 (1887), pp. 41-51.

[13] LORENTZ, H.A. Abhandlungen über theoretische Physik. Vol. 1, Teubner Verlag (1907).

[14] SOMMERFELD, A. Vorlesungen über theoretische Physik. Vol. 4, Akademische Verlagsgesellschaft, Leipzig (1964).

[15] KÜSSNER, H.G. Lösungen der klassischen Wellengleichung für bewegte Quellen. ZAMM 24, No. 5 and 6 (1944), pp. 243-250.

[16] SCHMIDT, H. Einführung in die Theorie der Wellengleichung. Barth Verlag, Leipzig (1931).

[17] JANZEN, O. Beitrag zu einer Theorie der stationären Strömung kompressibler Flüssigkeiten. Phys. Zeitschr. 14 (1913), pp. 639-643.

[18] LORD RAYLEIGH On the flow of compressible fluid past an obstacle. Phil. Mag. 32 (1916), pp. 1-6.

[19] GLAUERT, H. The effect of compressibility on the lift of an airfoil. Proc. Roy. Soc. A 118 (1925), pp. 113-119.

[20] PRANDTL, L. Über Strömungen, deren Geschwindigkeit mit der Schallgeschwindigkeit vergleichbar sind. Jour. Aero. Research Inst., Univ. of Tokyo 63 (1930), pp. 14 ff.

[21] PRANDTL, L. Allgemeine Betrachtungen über die Strömung zusammendrückbarer Flüssigkeiten. Proc. 5, Volta Kongress, Rome (1935), pp. 169-197.

[22] v. KÁRMÁN, Th. The Problem of Resistance in Compressible Flow. Proc. 5, Volta Congress, Rome (1935), pp. 232-277.

[23] ACKERET, J. Luftkräfte auf Flügel, die mit größerer als Schallgeschwindigkeit bewegt werden. Zeitschr. f. Flugtech. u. Motorluftschiffahrt 16 (1925), pp. 72-74.

[24] v. KÁRMÁN, Th.; MOORE, N.B. Resistance of Slender Bodies Moving with Supersonic Velocities, with Special Reference to Projectiles. Trans. ASME 54 (1932), pp. 303-310.

[25] FERRARI, C. Campi di corrente ipersonora altorna a solidi di rivoluzione. Aerotechnica 17 (1937), pp. 507-518, Brown Univ. Transl. A 9-T-29.

[26] TSIEN, H.S. Supersonic Flow Over an Inclined Body of Revolution. Journ. Aero. Sci. 5 (1938), pp. 480-483.

[27] PRANDTL, L. Theorie des Flugzeugtragflügels im zusammendrückbaren Medium. Luftfahrtforschung, Vol. 13 (1936), pp. 313-319.

[28] SCHLICHTING, H. Tragflügeltheorie bei Überschallgeschwindigkeit. Luftfahrtforschung, Vol. 13 (1936), pp. 320-335.

[29] HEASLET, M.A.; LOMAX, H. Supersonic and Transonic Small Perturbation Theory. General Theory of High Speed Aerodynamics, Section D, High Speed Aerodynamics and Jet Propulsion, Vol. VI (Ed. W.R. Sears), Princeton Univ. Press (1954).

[30] KÜSSNER, H.G. Allgemeine Tragflächentheorie. Luftfahrtforschung 17 (1940), pp. 370-378. NACA Tech. Mem. 979 (1941).

[31] GARRICK, I.E. Moving Sources in Nonsteady Aerodynamics and in Kirchhoffs Formula. Proc. First U.S. Natl. Congr. Appl. Mech., Chicago (1951). Trans. Am. Soc. Mech. Engrs. 74 (1952), pp. 732-739.

[32] GARRICK, I.E. Nonsteady Wing Characteristics. Aerodynamic Components of Aircraft at High Speeds, Section F, (Editors A.F. Donovan and H.R. Lawrence), High Speed Aerodynamics and Jet Propulsion, Vol. VII, Princeton University Press (1957).

[33] ROBINSON, A.; LAURMAN, J.A. Wing Theory. Cambridge Univ. Press (1956).

[34] TEMPLE, G. Modern Developments in Fluid Dynamics (Unsteady Motion). Clarendon Press, Oxford (1953).

[35] SEARS, W.R. Small Perturbation Theory. General Theory of High Speed Aerodynamics, Section C. High Speed Aerodynamics and Jet Propulsion, Vol. VI (Ed. W.R. Sears), Princeton Univ. Press (1954).

[36] MILES, J.W. The Potential Theory of Unsteady Supersonic Flow. Cambridge Univ. Press (1959).

[37] PRANDTL, L. Über Schallausbreitung bei rasch bewegten Körpern. Schriften d. Deutschen Akademie d. Luftfahrtforsch. H 7 (1938), pp. 1-14.

[38] HÖNL, H. Über das Schallfeld einer gleichförmig-translatorisch bewegten punktförmigen Schallquelle. Annalen d. Phys. Leipzig, Vol. 43 (1943), pp. 437-464.

[39] ROTT, N. Das Feld einer rasch bewegten Schallquelle. Mitteilung Nr. 9, Mitteil. d. Inst. f. Aerodynamik, Eidg. Tech. Hochschule, Zürich (1945).

[40] BILLING, H. Geradlinig bewegte Schallquellen. ZAMM Vol. 29 (1949), pp. 267-274. Das Feld geradlinig gleichförmig bewegter Schallquellen, AVA Bericht Nr. 45/J/15 (1945).

[41] WALTERS, A.G. On the Propagation of Disturbances from Moving Sources. Cambridge Phil. Soc. (1951), pp. 109-126.

[42] OESTREICHER, H.L. The Effect of Motion on the Accoustic Radiation of a Sound Source. Centr. Air. Docum. Off. (Washington). Tech. Data Digest 16 No. 9 (1951), pp. 16-19.

[43] LIGHTHILL, M.J. On Sound Generated Aerodynamically. I. General Theory. Proc. Roy. Soc. A 211 (1952), pp. 564-587.

[44] ZATZKIS, H. The Sound Field of a Moving Source. Jour. Acoust. Soc. America, Vol. 25 (1953), pp. 897-898.

[45] GARRICK, I.E.
WATKINS, C.E. Theoretical Study of the Effect of Forward Speed on the Free-Space Sound-Pressure Field around Propellers. NACA TR 1198 (1954).

[46] OESTREICHER, H.L. Field of a Spatially Extended Moving Sound Source. Jour. Acoust. Soc. America, Vol. 29 (1957), pp. 1223-1232.

[47] LOWSON, M.V. The Sound Field of Singularities in Motion. Proc. Roy. Soc. A 286 (1965), pp. 559-572.

[48] PARKAR, E.N. Acoustical Radiation from the Velocity Field in a Compressible Fluid. Phys. Review, Vol. 90 (1953), pp. 240-242.

[49] LIGHTHILL, M.J. On Sound Generated Aerodynamically, II. Turbulence as a Source of Sound. Proc. Roy. Soc., A 222 (1954), pp. 1-32.

[50] CURLE, N. The Influence of Solid Boundaries upon Aerodynamic Sound. Proc. Roy. Soc., A 231 (1955), pp. 505-514.

[51] MEECHAM, W.C.
FORD, G.W. Acoustic Radiation from Isotropic Turbulence. Jour. Acoust. Soc. America, Vol. 30 (1958), pp. 318-322.

[52] RIBNER, H.S. The Generation of Sound by Turbulent Jets. Advances in Appl. Mech., Vol. 8, Academic Press (1964), pp. 103-182.

[53] LILEY, G.M. On the Noise from Air Jets. Aero. Research Council ARC 20, 376-N40-FM 2724 (1958).

[54] FFOWCS WILLIAMS, J.E. The Noise from Turbulence Convected at High Speed. Phil. Trans. Roy. Soc. (London), A 255 (1963), pp. 468-503.

[55] MICHALKE, A.
FUCHS, H.V. Introduction to Aerodynamic Noise Theory. Progress in Aero-Space Sci. (Ed. D. Küchemann), Pergamon Press, Oxford,Vol. 14 (1973), pp. 227-297.

[56] KÜSSNER, H.G. A General Method for Solving Problems of the Unsteady Lifting Surface Theory in the Subsonic Range. Jour. Aero. Sci. 21 (1954), pp. 17-27.

[57] LASCHKA, B. Zur Theorie der harmonisch schwingenden, tragenden Fläche bei Unterschallströmung. Zeitschr. f. Flugwiss., Vol. 11 (1963), pp. 265-292.

[58] JONES, W.P. Supersonic Theory of Oscillating Wings of any Plan Form. Brit. ARC Report & Mem. 2655 (1953).

[59] COURANT, R.
HILBERT, D. Methoden der mathematischen Physik. Vols. 1 and 2, Springer Verlag Berlin (1968).

[60] BATEMAN, H. Partial Differential Equations of Mathematical Physics. Dover Publication (1944).

---

*Acknowledgement is due to Prof. H.S. Ribner, Institute of Aerospace Studies, University of Toronto, for his valuable comments to the preprint and especially for his suggestion to introduce the δ-function notation in Sec. 2 and to define in Sec. 6 the energy density in the respective reference frames.

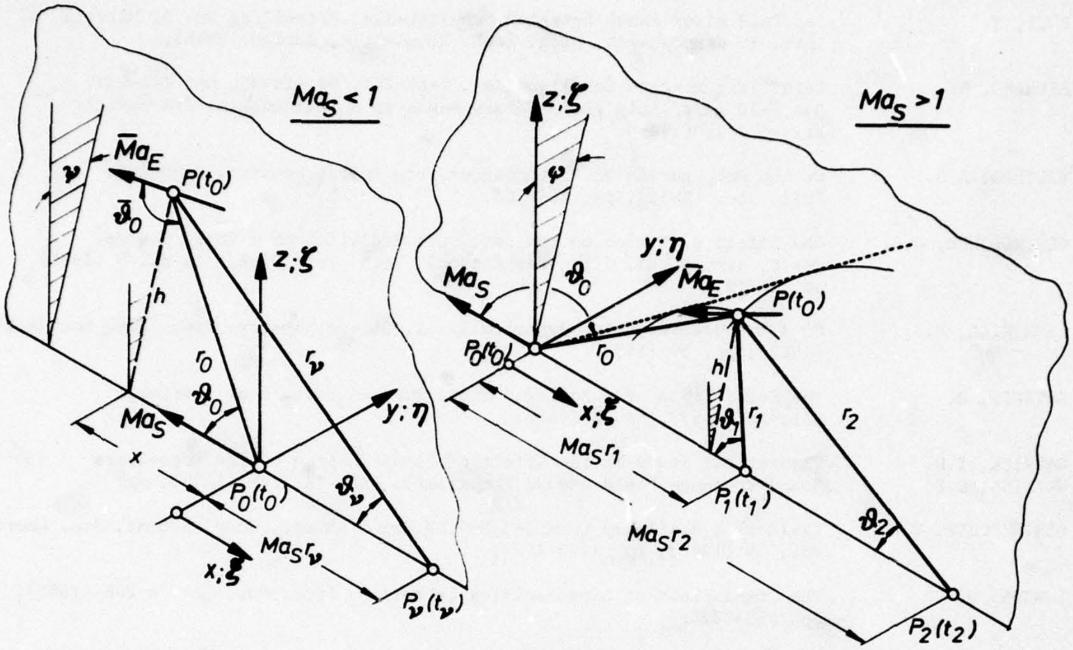

Fig. 1: Disturbance propagation from singularities in uniform motion, showing at a time instant t_0 the relative positions of the singularity and of a given field point, which is just met by a signal emitted at a retarded time t_ν.

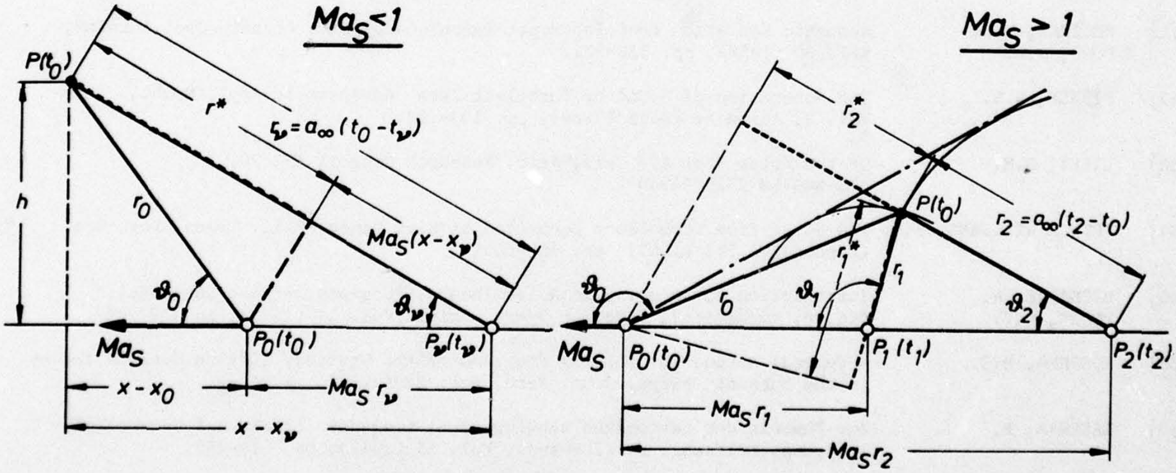

Fig. 2: The kinematic relations in the disturbance fields of singularities in uniform motion at subsonic and supersonic velocities.

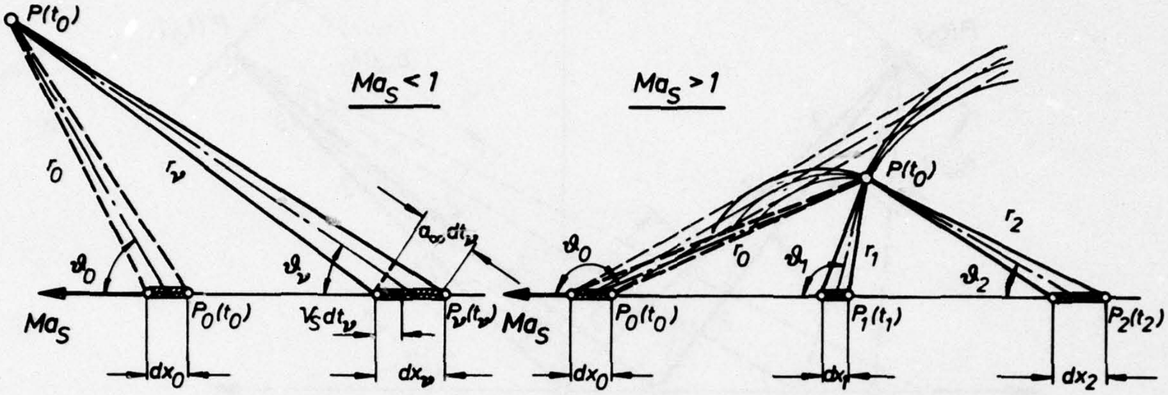

Fig. 3: The influence factor σ_V due to the change in effective emission volume of a singularity in uniform motion.

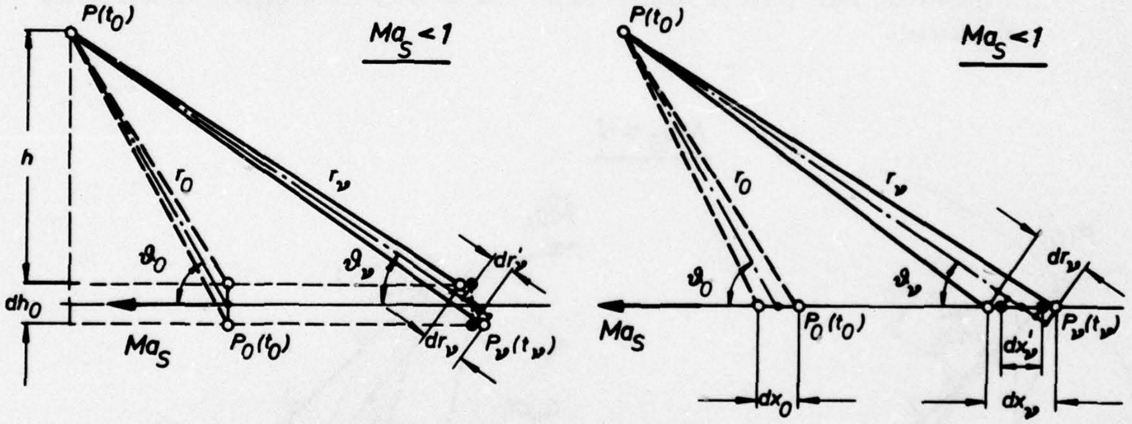

Fig. 4: The influence factor σ_R due to the effective shift of the emitting position of the sources composing higher order singularities in uniform motion.

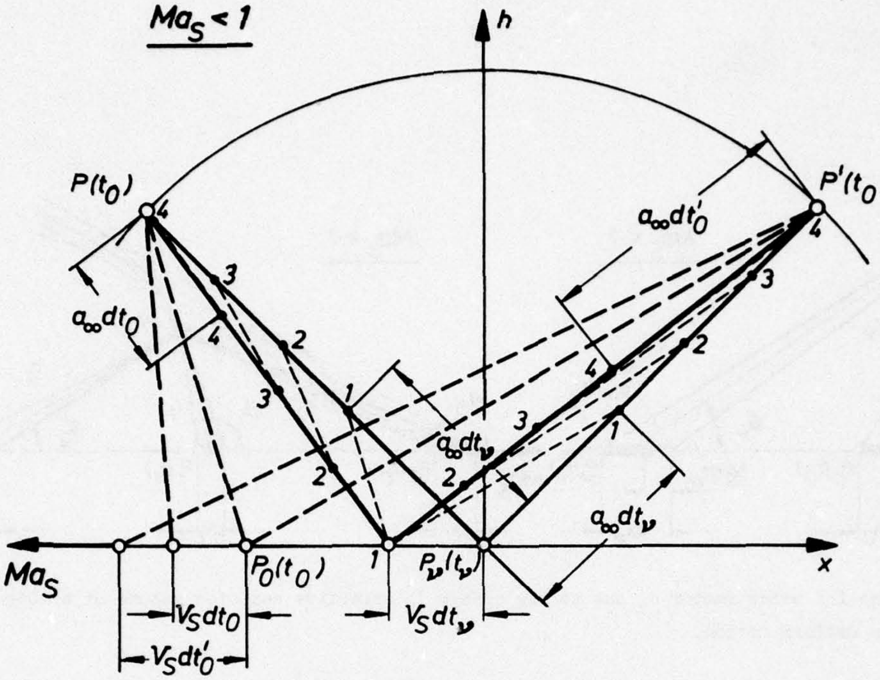

Fig. 5a: The Doppler parameter σ_D arising from the changed time sequence of signals passing through a space-fixed field point in relation to the time sequence during emission from a moving singularity.

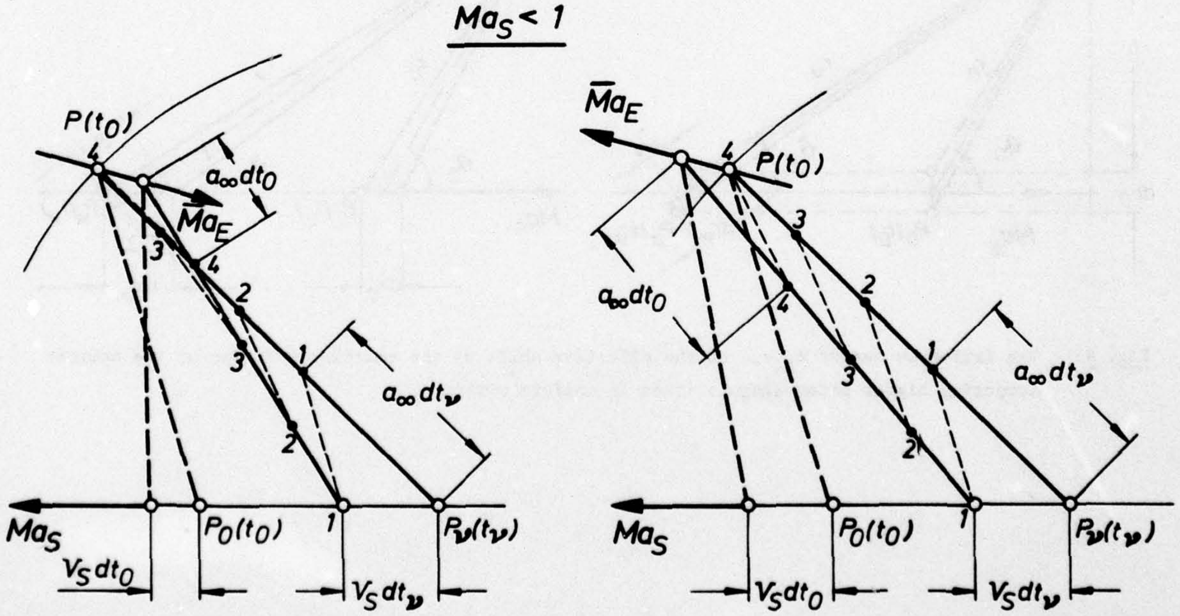

Fig. 5b: The Doppler-frequency parameter σ_F arising from the changed time sequence of signals passing through a moving field point in relation to the time sequence during emission from a moving singularity.

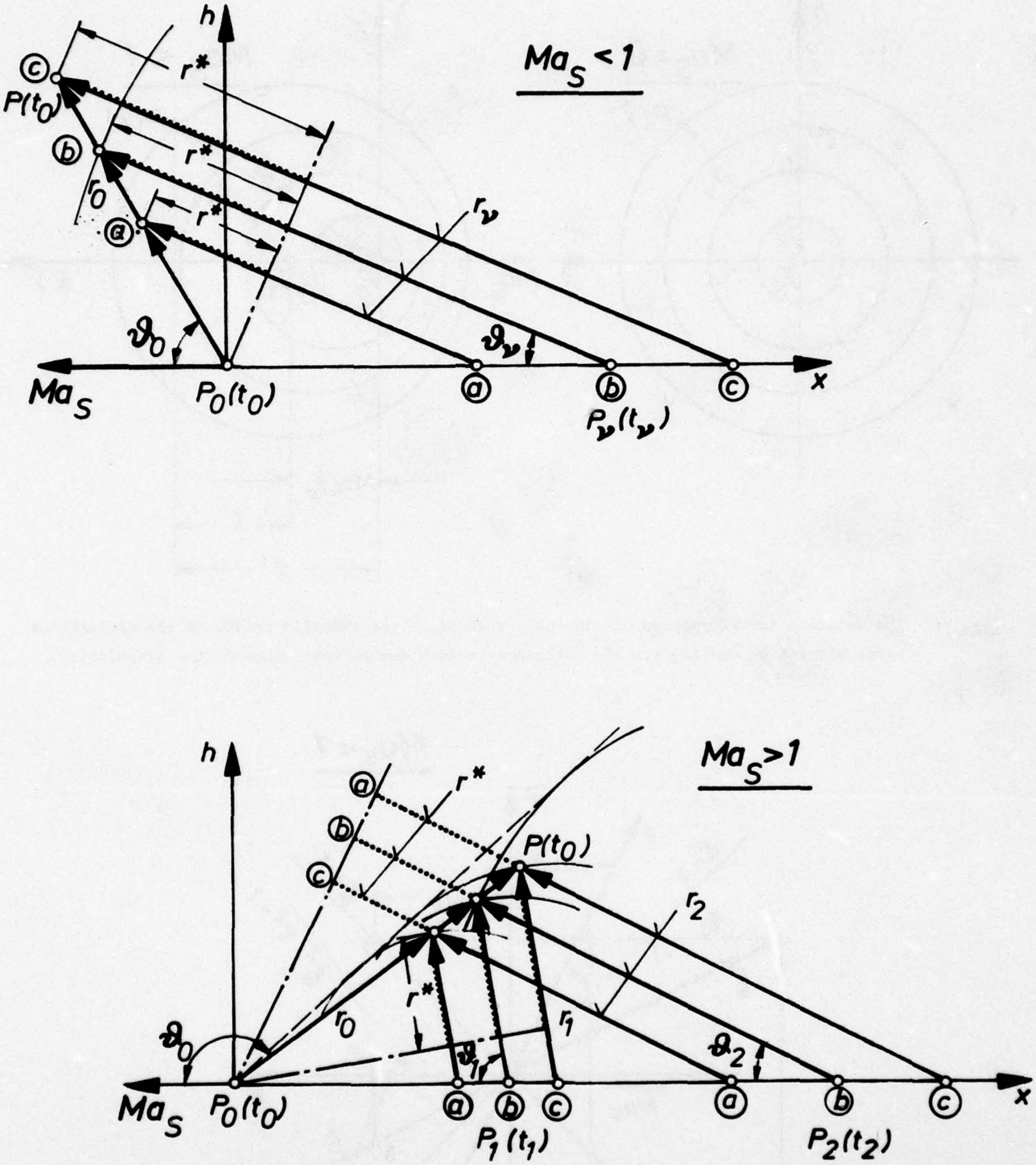

Fig. 6: Kinematic relations giving constant influence factor $\sigma = r_\nu/r^*$ for field points lying on a ray from the singularity in the moving reference system.

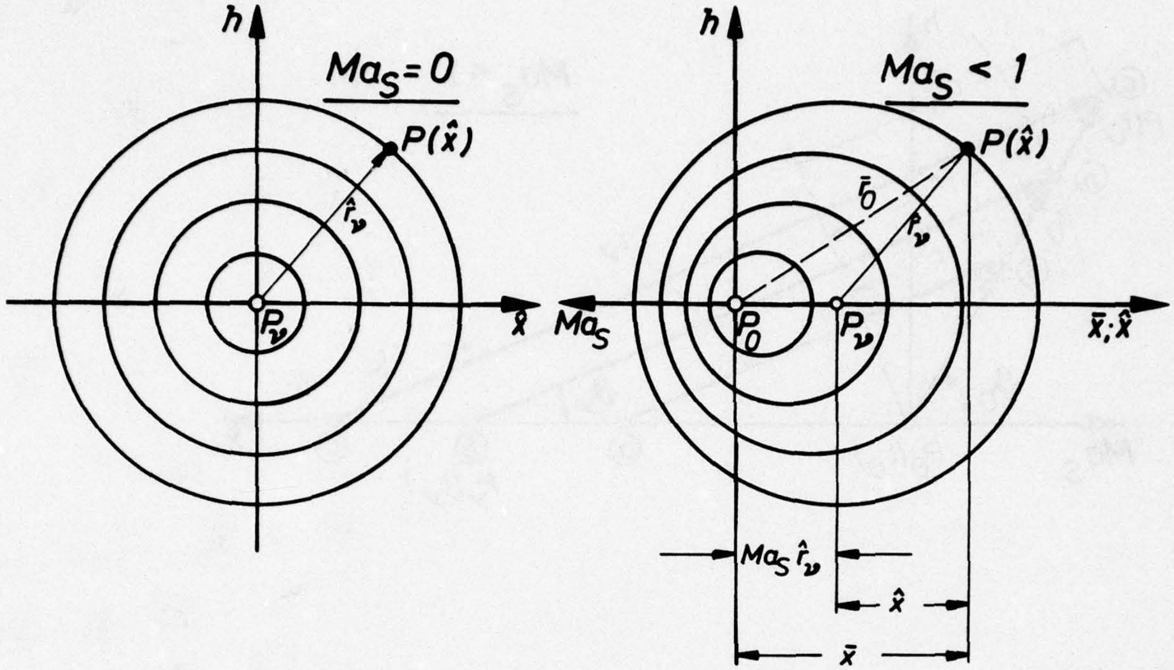

Fig. 7: The Galilean transformation causing only a shift of the emission points of the disturbance waves without accounting for the influence factors due to the motion of the singularity.

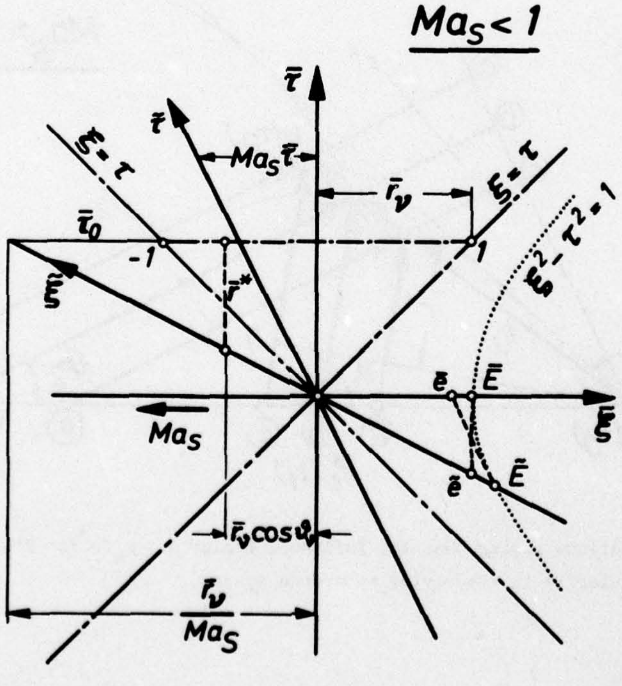

Fig. 8: The use of Lorentz-transformation to determine the perturbation fields of disturbance sources having uniform translatory motion.

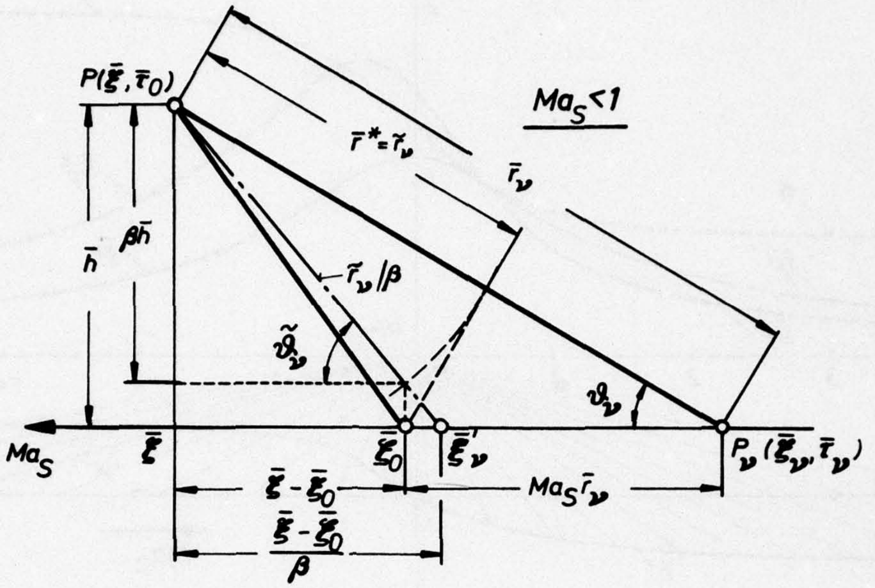

Fig. 9: Some kinematic relations defined by the Lorentz-transformation presented in the physical plane.

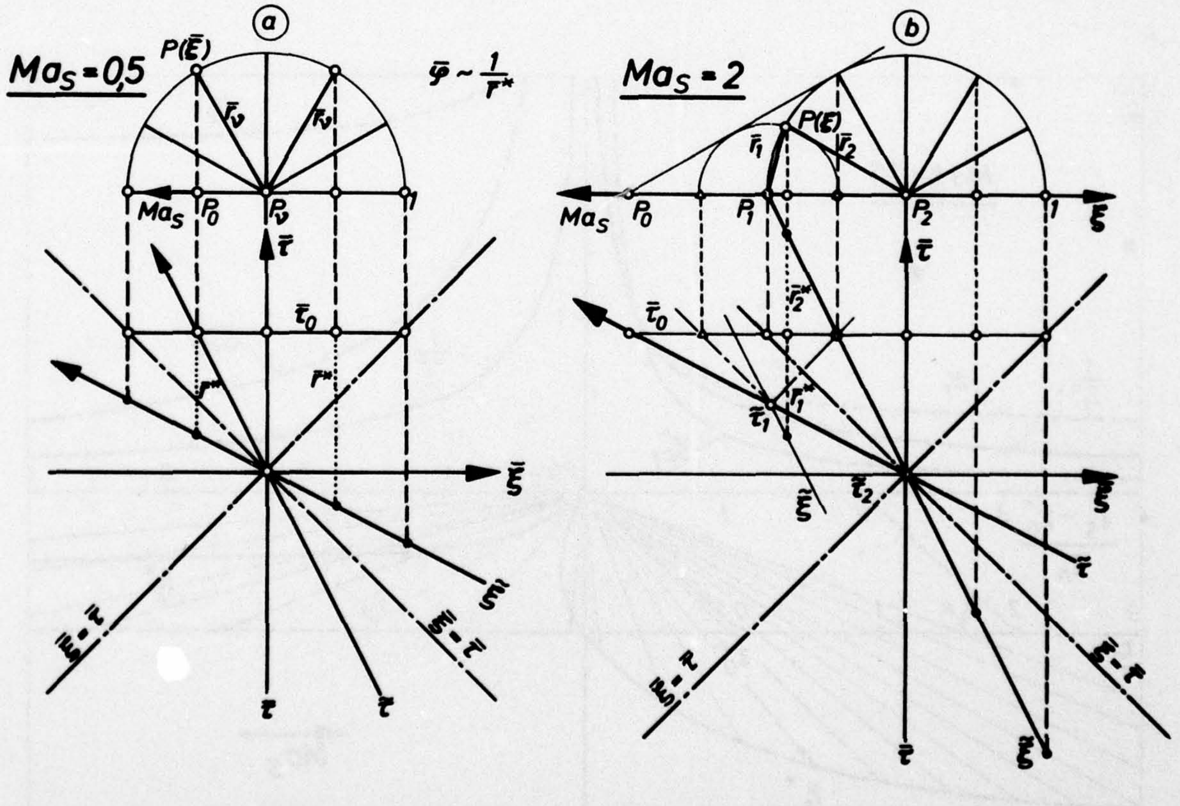

Fig. 10: The source solution presented in the space-time continuum for subsonic and supersonic motion of the singularity.

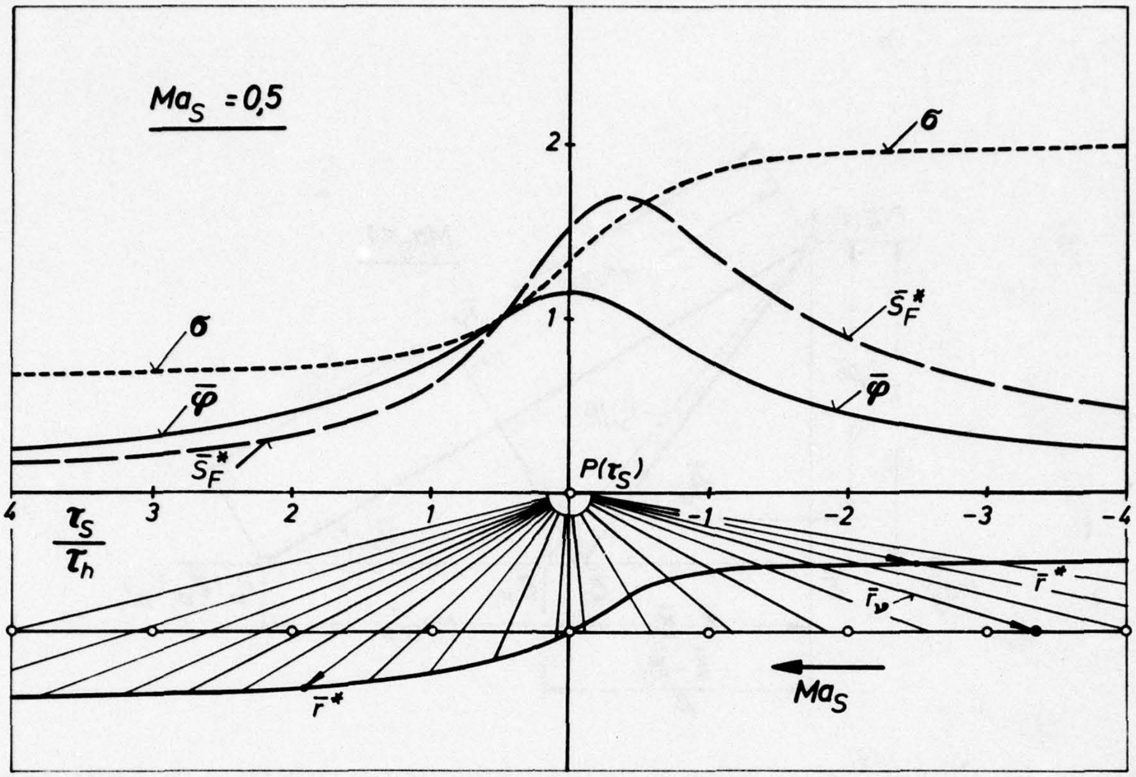

Fig. 11: Time history of perturbation quantities at a space-fixed field point due to a singularity in uniform translatory motion at subsonic velocity.

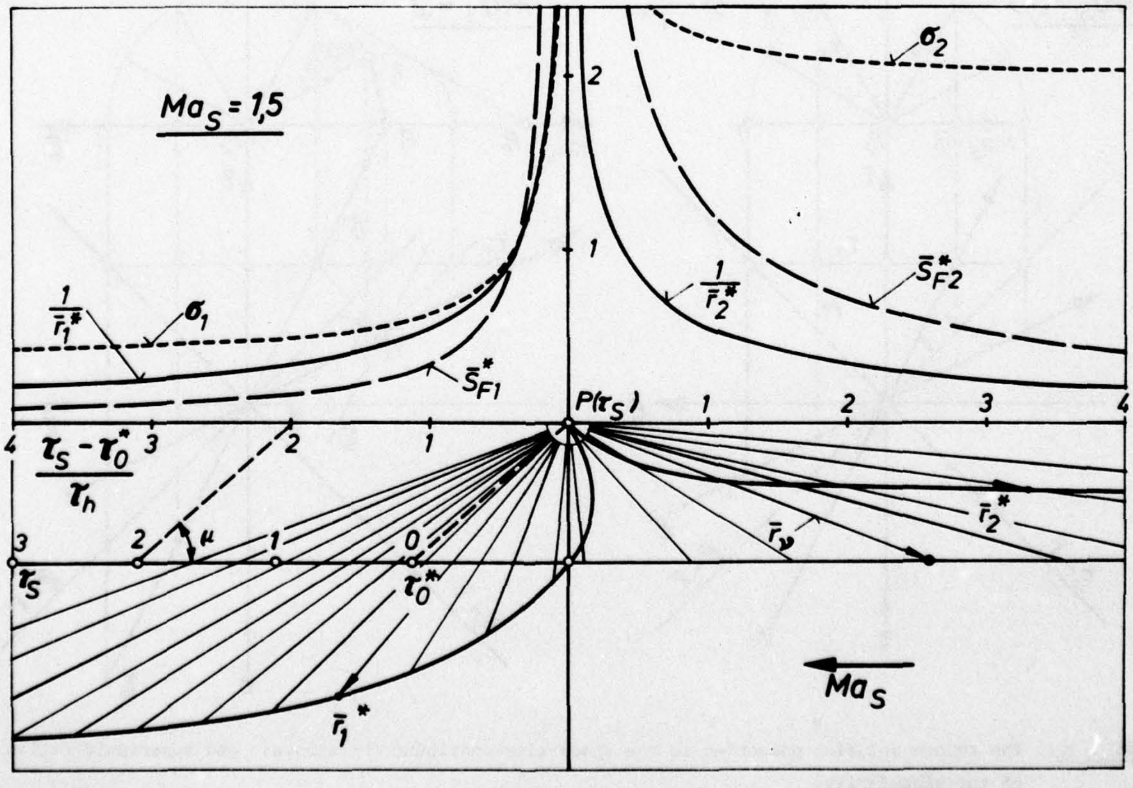

Fig. 12: Time history of perturbation quantities at a space-fixed field point due to a singularity in uniform translatory motion at supersonic velocity.

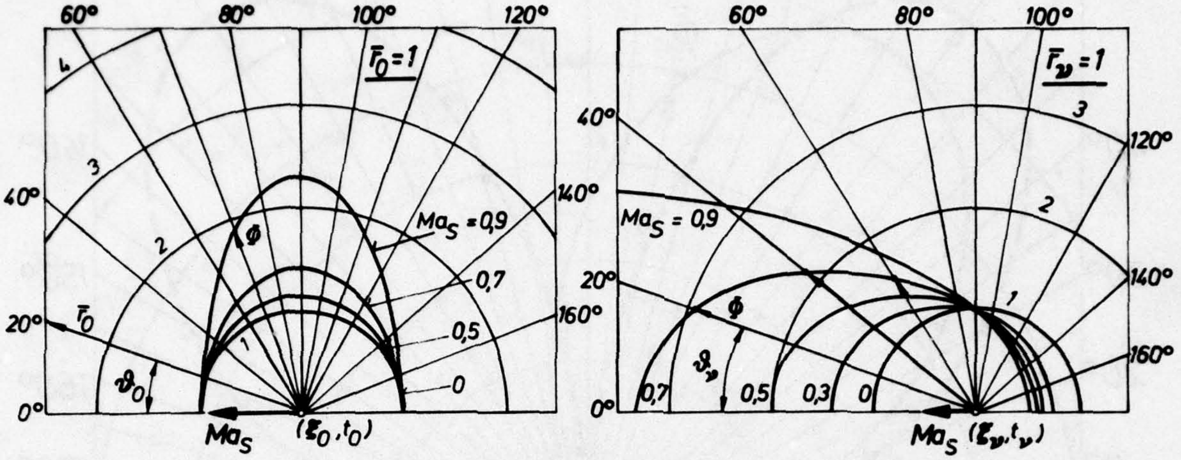

Fig. 13: Perturbation potential on a unit sphere about P_o and P_ν of a source in uniform motion at various Mach numbers ($\bar{\Phi}_N = \bar{\Phi}_F = \frac{\bar{\varphi}}{\bar{S}_o}$).

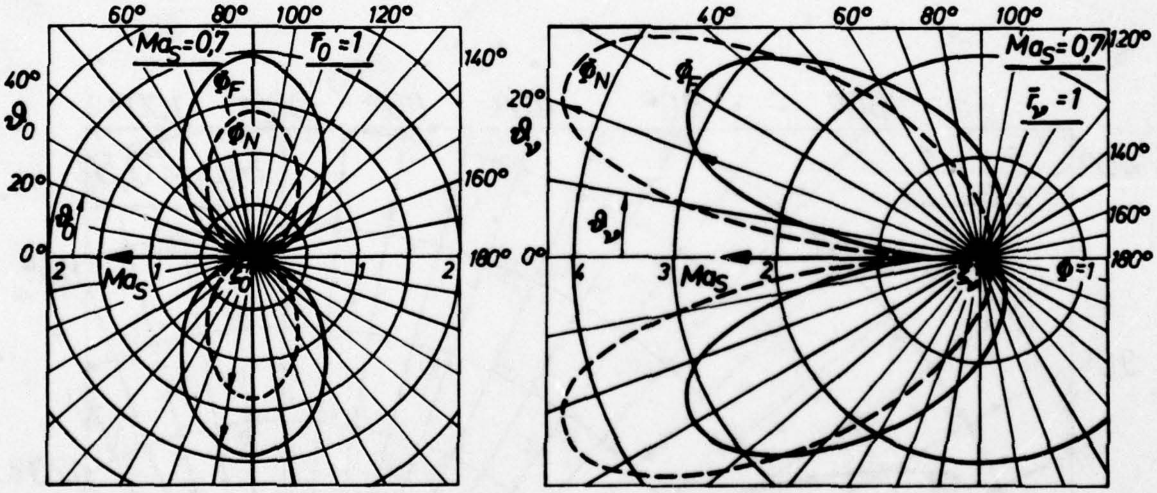

Fig. 14: Near-field and far-field perturbation potentials on a unit sphere about P_o and P_ν of a dipole in uniform motion ($\bar{\Phi}_N = \bar{\varphi}_N / \bar{D}_o \cos\Psi$; $\bar{\Phi}_F = \bar{\varphi}_F / \bar{D}_o \bar{\omega} \cos\Psi$).

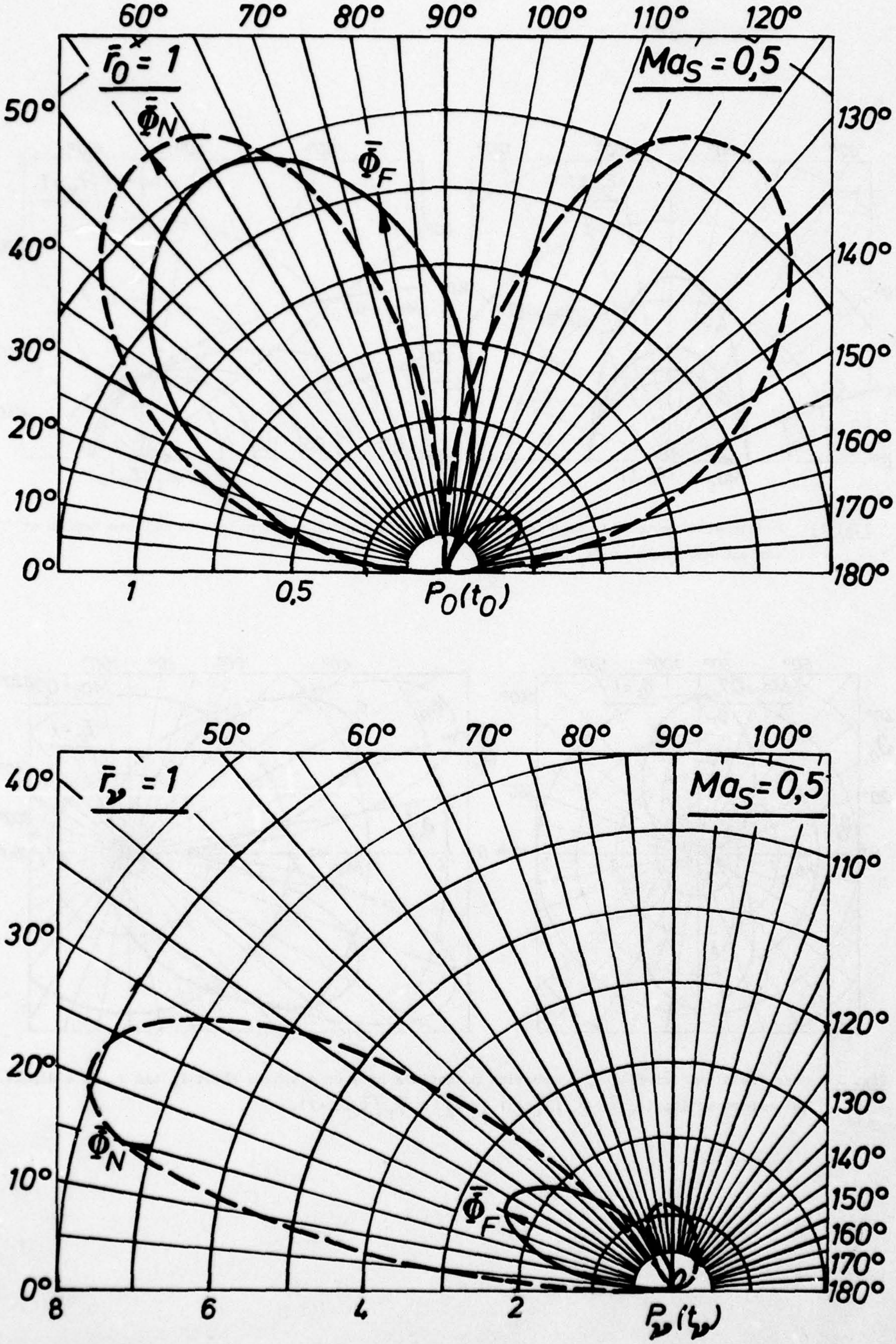

Fig. 15: Near-field and far-field perturbation potentials on a unit sphere about P_o and P_ν of a quadrupole in uniform motion ($\bar{\Phi}_N = \bar{\varphi}_N / \bar{M}_o \cos\Psi$; $\bar{\Phi}_F = \bar{\varphi}_F / \bar{M}_o \bar{\omega}^2 \cos\Psi$).

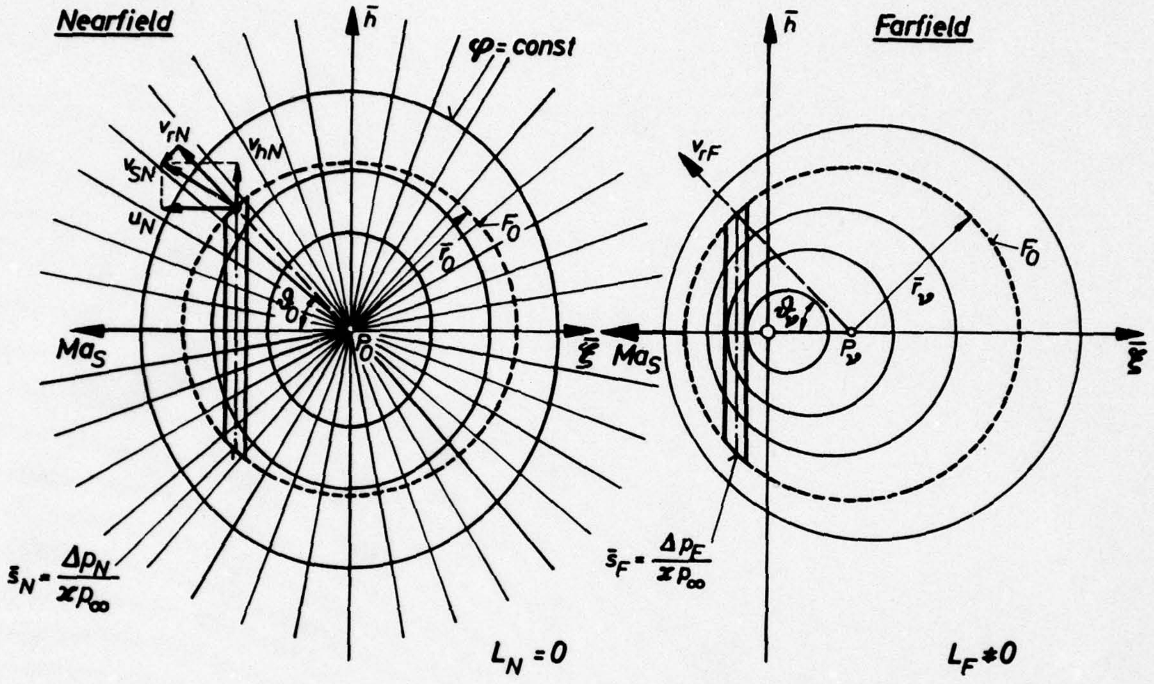

Fig. 16: Control surface used to determine the energy fluxes due to the near-field and far-field perturbation terms of unsteady sources in uniform motion.

INTERFERING AIRFOILS IN TWO-DIMENSIONAL UNSTEADY INCOMPRESSIBLE FLOW

by
Helmut Bosch
Führungsakademie der Bundeswehr
Manteuffelstrasse 20
2000 Hamburg 55
Germany

SUMMARY

This investigation deals with the interference of two or more lifting surfaces in two-dimensional unsteady incompressible flow. The integral relations relating the unsteady flow components around a harmonically oscillating airfoil to the pressure distribution are presented. These relations are then applied to treat two problems: first, calculation of the flow field around a single airfoil for a given pressure distribution and, second, calculation of the aerodynamic forces acting on the lifting surfaces. Special consideration is given to the longitudinal force component, i.e. drag or propulsion, acting on the lifting surfaces, and to the propulsion efficiency. Besides the well-known fact that aerodynamic forces induced by interference may reach considerable values, the results show that for both the plunging motion and the pitching motion, a lifting surface at rest located behind an oscillating airfoil considerably improves the propulsion efficiency. For the plunging motion the propulsion efficiency is very close to 100 %, almost independent of the reduced frequency and the backward position of the aft surface.

LIST OF SYMBOLS

a_n	coefficients of the pressure distribution
$\vec{a}_n = (a_n)$	vector of the coefficients a_n
$C_D(t)$	drag coefficient
$\bar{C}_D$	time average of C_D over one oscillation cycle
$\bar{C}_{DT}$	$\bar{C}_D$ of a tandem wing configuration
$\bar{C}_{DS}$	$\bar{C}_D$ of a single airfoil
$\bar{C}_{Dtotal}$	drag coefficient of a lifting surface combination (time average over one oscillation cycle)
Ci	cosine integral
C_L	lift coefficient
C_M	pitch moment coefficient
C_{P_x}	coefficient of the longitudinal force component P_x
C_S	coefficient of the "suction" force
Δc_p	pressure difference between upper and lower wing surface referred to dynamic pressure
D	drag (or propulsion)
$\bar{D}$	time average of D over one oscillation cycle
$D(x_o,z;k)$	influence function of the velocity potential, Eq.(2)
$Ei(-k\cdot\lvert z\rvert)$, $\overline{Ei}(k\cdot\lvert z\rvert)$	exponential integrals
E, E_1	influence functions of the longitudinal wash, Eq.(12) and (15)
$\bar{f}(x;t) = f(x)\cdot\exp(i\omega t)$	harmonic motion of the airfoil
$f_n(\varphi)$	pressure distribution
$k = \frac{\omega\cdot l}{V}$	reduced frequency
K, K_1, K_2	influence functions of the upwash, Eq.(4),(6),(8)
l	semi-chord; reference length
P	force per unit span resulting from the pressure distribution
P_x	component of P in flow direction
S	"suction" force per unit span
Si	sine integral
t	time
$T = \frac{2\pi}{\omega}$	period of oscillation
u	longitudinal wash referred to V
V	flight speed; reference speed
v	flow deflection on a lifting surface referred to V
$\vec{v} = (v(x_p))$	vector of the flow deflection

w	upwash referred to V
$\vec{w} = (u,w)$	vectorial velocity referred to V
$W_{ij} = (W_{nij}(x_p))$	matrices of the linear equations system
$\bar{W}$	work per unit time required to maintain the oscillations (time average over one oscillation cycle)
$x,x',y,y',z,x_o=x-x'$	coordinates referred to l
x_p	coordinate of the collocation points referred to l
$\bar{x}, \bar{z}$	rear and upward position of lifting surface 2 of the tandem wing configuration
α	angle of attack
η_S	propulsion efficiency of an airfoil
η_{T1}, η_{T2}	propulsion efficiency of the tandem wing configuration (index T1: lifting surface 1 oscillates, index T2: lifting surface 2 oscillates)
ρ	density
$\varphi = \frac{\varphi^*}{l \cdot V}$	dimensionless velocity potential
ω	circular frequency
$\nabla = (\partial/\partial x, \partial/\partial z)$	operator

1. INTRODUCTION

In the past years, great efforts have been made to investigate the phenomena of mutual aerodynamic interference of oscillating planar and nonplanar airfoils. The theories on three-dimensional flow have been developed very extensively. They allow now the prediction of general aerodynamic forces for nearly arbitrary lifting surface configurations, refs. 1,2,3.

The two-dimensional interference problem has not been investigated during this process; the investigation of this problem was overleaped. In order to reduce the gap in knowledge, the problem of interfering airfoils in two-dimensional unsteady incompressible flow has been studied.

Up to now, only little emphasis has been given to the determination of the longitudinal force components acting on interfering oscillating airfoils. Besides the general desire of having methods available to calculate the thrust, knowledge of these force components might be of special importance for aircraft with variable sweep where longitudinal degrees of freedom may occur. Therefore, in addition to the usual general aerodynamic forces acting on interfering airfoils, as desired for stability and flutter prediction, the mechanism of propulsion occurence has been investigated.

The interference problem has been treated by means of the lifting surface theory following the method given for the three-dimensional flow in ref. 1.

Parts of the results have been published in ref. 4.

2. INTEGRAL RELATIONS FOR PRESSURE AND FLOW FIELD

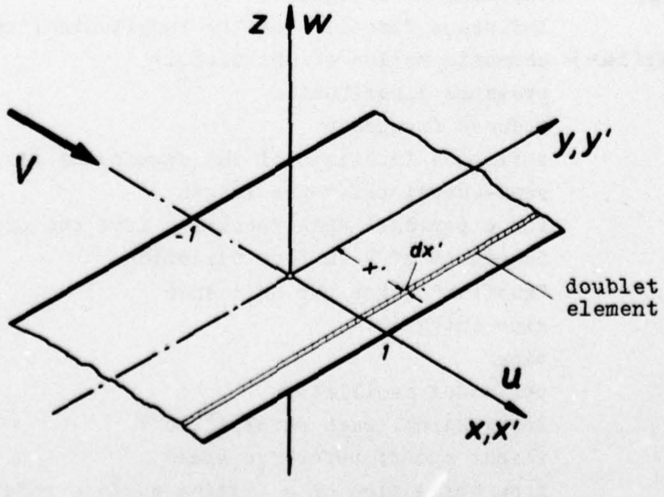

Fig. 1. Coordinates

The thin, infinitely long airfoil is located in the plane z = 0, and each point of it is undergoing harmonic translations of small amplitude at reduced frequency k.

On the basis of the acceleration potential and by means of doublets, the following integral relation which relates the vectorial disturbance velocity at any field point to the pressure distribution on the lifting surface can be deduced:

$$\vec{w} = \nabla\varphi(x,z;k) = \nabla\int_{-1}^{1}\Delta c_p(x')\cdot D(x_o,z;k)\cdot dx' \tag{1}$$

where

$$D(x_o,z;k) = \frac{1}{4\pi}\cdot e^{-ikx_o}\int_{-\infty}^{x_o} e^{ik\eta}\cdot\frac{z}{\eta^2 + z^2}\cdot d\eta \tag{2}$$

From Eq.(1) the relations given below for the velocity components, i.e. upwash and longitudinal wash, may be derived.

2.1 Upwash

For the case k·z ≠ 0 we obtain the following expression for the upwash

$$w(x,z;k) = \int_{-1}^{1}\Delta c_p(x')\cdot K(x_o,z;k)\cdot dx' \tag{3}$$

where

$$K(x_o,z;k) = \frac{1}{4\pi}\left\{-\frac{x_o}{x_o^2 + z^2} + e^{-ikx_o}\left[-\frac{\pi}{2}k\cdot e^{-k|z|} + i\frac{k}{2}\left(e^{-k|z|}\overline{Ei}(k|z|) + e^{k|z|}Ei(-k|z|)\right) + \right.\right.$$
$$\left.\left. + ik\int_{0}^{x_o/|z|} e^{ik|z|\tau}\frac{\tau}{1+\tau^2}d\tau\right]\right\} \tag{4}$$

The integral in Eq.(4) can be exactly evaluated after series expansion of the exponential function.

Treating of the special case z → 0 leads to the well-known relation, ref. 5

$$w(x,z=0;k) = \int_{-1}^{1}\Delta c_p(x')\cdot K_1(x_o,z = 0;k)dx' \tag{5}$$

where

$$K_1(x_o,z = 0;k) = \frac{1}{4\pi}\left[-\frac{1}{x_o} + ike^{-ikx_o}\left(Ci(kx_o) + i\left(Si(kx_o) + \frac{\pi}{2}\right)\right)\right] \tag{6}$$

The kernel function $K_1(x_o,z = 0;k)$ becomes singular for $x_o = 0$. The singularities are of the order $1/x_o$ and $\ln(kx_o)$, where the logarithmic singularity is contained in the cosine integral.

For larger distances from the lifting surface ($x \rightarrow \pm\infty$) the relation for the upwash simplifies considerably.

$$w(x\rightarrow\pm\infty,z;k) = \int_{-1}^{1}\Delta c_p(x')\cdot K_2(x\rightarrow\pm\infty,z;k)\,dx' \tag{7}$$

where

$$K_2(x \to \pm\infty, z; k) = -\frac{1}{8}\left(1 + \frac{x}{|x|}\right) k e^{-k|z|} \cdot e^{-ikx_o} \tag{8}$$

Eq.(7) shows that the upwash behind the airfoil in flow direction approaches a sinusoidal function, whereas it disappears far ahead of the wing.

For the steady case k = 0 we obtain the well-known equations

$$w(x,z;k=0) = -\frac{1}{4\pi}\int_{-1}^{1} \Delta c_p(x')\frac{x_o}{x_o^2 + z^2}dx' \tag{9}$$

and

$$w(x,z=0;k=0) = -\frac{1}{4\pi}\int_{-1}^{1} \Delta c_p(x')\frac{1}{x_o}dx' \tag{10}$$

2.2 Longitudinal Wash

For the case $k \cdot z \neq 0$ the expression for the longitudinal wash becomes

$$u(x,z;k) = \int_{-1}^{1} \Delta c_p(x') \cdot E(x_o,z;k)dx' \tag{11}$$

where

$$E(x_o,z;k) = \frac{z}{|z|}\cdot\frac{1}{4\pi}\left\{\frac{|z|}{x_o^2 + z^2} - ike^{-ikx_o}\left[\frac{\pi}{2}e^{-k|z|} - \frac{i}{2}\left(e^{-k|z|}\,\overline{Ei}(k|z|) - e^{k|z|}Ei(-k|z|)\right) + \int_{0}^{x_o/|z|} e^{ik|z|\tau}\frac{1}{1 + \tau^2}d\tau\right]\right\} \tag{12}$$

The factor $z/|z|$ denotes that for field points above the plane z = 0 the direction of the longitudinal wash u is in the positive direction and for field points below the plane z = 0 in the negative direction of the x-axis. The integral in Eq.(12) can be soved exactly after series expansion of the exponential function.

The special case $z \to 0$ has to be treated carefully, as only doublet elements upstream of the field point P(x,0) contribute to the longitudinal wash. The integral relation becomes

$$u(x,z=0;k) = \frac{z}{|z|}\cdot\frac{1}{4}\left(\Delta c_p(x) - ik\int_{-1}^{x}\Delta c_p(x')e^{-ikx_o}\,dx'\right) \tag{13}$$

Eq.(13) reveals that in the plane z = 0 the longitudinal wash disappears ahead of the wing, whereas it exists in the wake. The latter statement is contrary to the steady case. The term $\Delta c_p(x)$ is valid only for field points on the lifting surface.

For large distances from the lifting surface $(x \to \pm\infty)$ the integral relation may be reduced to the simple form

$$u(x \to \pm\infty, z; k) = \int_{-1}^{1}\Delta c_p(x')\cdot E_1(x \to \pm\infty, x'; k)dx' \tag{14}$$

where

$$E_1(x \to \pm\infty, x', z; k) = -i\frac{1}{8}\cdot\frac{z}{|z|}\left(1 + \frac{x}{|x|}\right)ke^{-k|z|}\cdot e^{-ikx_o} \tag{15}$$

Behind the lifting surface the longitudinal wash approaches a sinusoidal function, whereas it disappears ahead of the wing. A comparison with the corresponding relation for the upwash (Eq.(8)) shows that the phase-shift between the velocity components is $\pi/2$. With respect to the vertical distance z, upwash and longitudinal wash decrease exponentially. The decrease is proportional to the reduced frequency.

For the steady case k = 0 the well-known equations follow:

$$u(x,z;k=0) = \frac{z}{|z|}\cdot\frac{1}{4\pi}\int_{-1}^{1}\Delta c_p(x')\frac{|z|}{x_o^2 + z^2}dx' \tag{16}$$

and

$$u(x,z=0;k=0) = \frac{z}{|z|}\cdot\frac{1}{4}\Delta c_p(x) \tag{17}$$

2.3 Summary

With Eq.(3) through (17) the integral relations relating the flow field around an oscillating airfoil to the pressure distribution on the airfoil are available in a numerically treatable form. This allows solving of the following problems:

(a) Calculation of upwash and longitudinal wash at any point of the flow field for a given pressure distribution.

(b) Calculation of the pressure distribution on an oscillating airfoil or on a static airfoil in an oscillating flow field, where the upwash on the airfoil is given by the well-known relation for the tangential flow condition

$$v(x;k) = \frac{\partial f(x)}{\partial x} + ikf(x) = w(x,0;k) \tag{18}$$

For a single airfoil the exact solution of this problem is well-known. In the case of interfering airfoils however, the pressure distribution on each of the airfoils can be determined by approximate methods only, at least at the present time.

3. PRESSURE DISTRIBUTION

For representation of the pressure the following series is suitable:

$$\Delta c_p(\varphi') = \frac{2}{\pi}\sum_{(n)} a_n f_n(\varphi') \tag{19}$$

where $f_n(\varphi') = \dfrac{\cos(n\varphi') + \cos(n+1)\varphi'}{\sin\varphi}$, $x' = -\cos\varphi$, $n = 0(1)N, 0<\varphi<\pi$

This series has the advantage that the lift is given by a_o and the pitch moment by a_o and a_1, see Eq.(24) and (25).

4. CALCULATION OF THE UNSTEADY FLOW FIELD AROUND AN AIRFOIL

Calculation of the unsteady flow field around an airfoil makes it necessary to determine the values of the coefficients a_n of the pressure distribution. For a given motion of the airfoil this can be achieved by comparison of the above pressure series with the well-known series of the exact solution of the two-dimensional problem as given, for instance, in ref. 5.

The interation over x' may conveniently be performed by aid of the GAUSS-JACOBI quadrature formulae, ref. 2. As there is no need to calculate the upwash on the lifting surface, no difficulties arise from the singularities contained in Eq.(6).

Results

Numerical calculations were carried out for the plunging motion $\bar{f}(x;t) = \exp(i\omega t)$ and the pitching motion $\bar{f}(x;t) = - x\cdot\exp(i\omega t)$ of the airfoil. Some of the results are presented in figs. 2 through 6.

For the plane z = 0 figs. 2 through 5 show the upwash and longitudinal wash distribu-

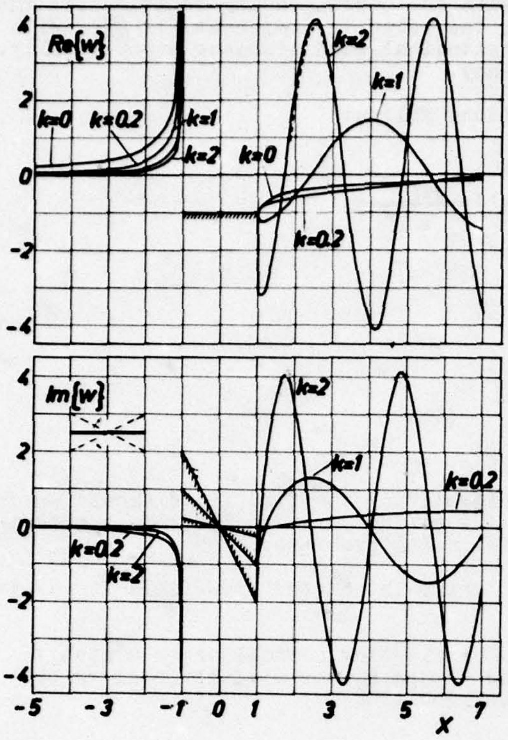

Fig. 2
Upwash.Pitching motion. z = 0.
--- Asymptotic approximation.

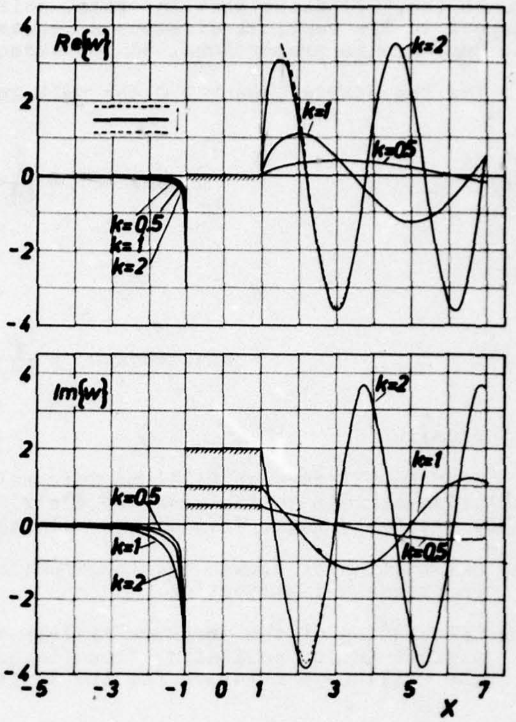

Fig. 3
Upwash. Plunging motion. z = 0.
--- Asymptotic approximation.

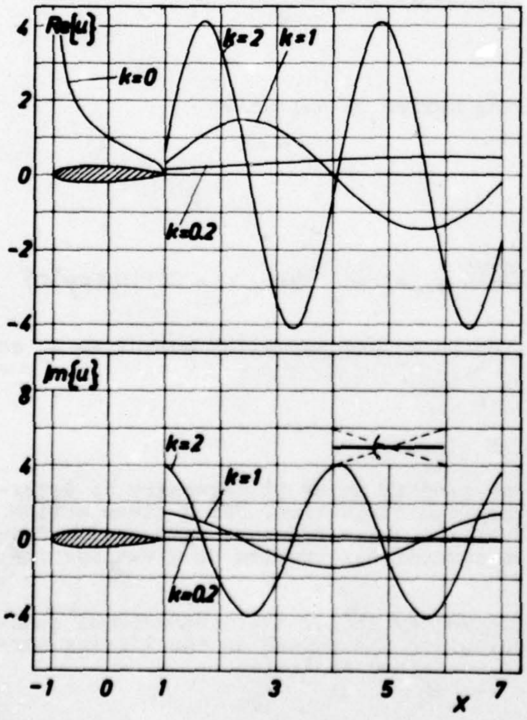

Fig. 4
Longitudinal wash. Pitching motion.
z = 0

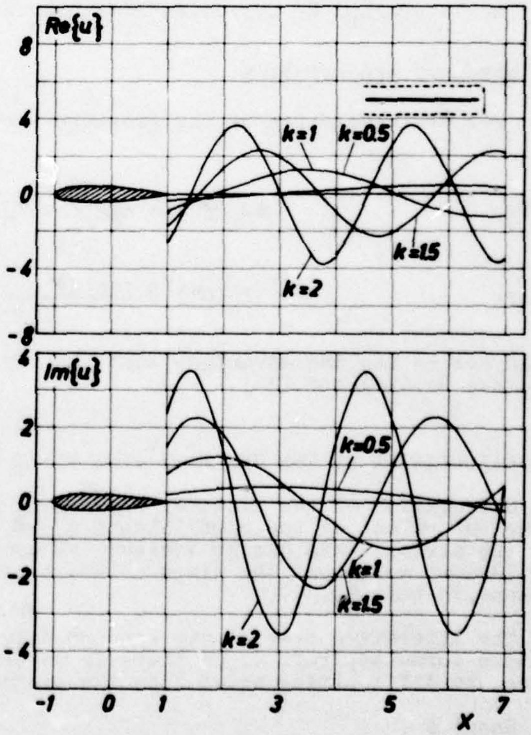

Fig. 5
Longitudinal wash. Plunging motion.
z = 0

tion in front of and behind the airfoil at several reduced frequencies. In front of the wing the longitudinal wash is zero and the upwash vanishes very rapidly. Behind the wing both upwash and longitudinal wash vary considerably in flow direction. The distributions are almost sinusoidal, and the amplitudes are proportional to the reduced frequency. The maximum values of the real and imaginary parts of the upwash exceed the values given by the tangential flow condition. This result implies that considerable unsteady aerodynamic forces will be induced when another lifting surface is located in this flow field. The magnitude of the induced aerodynamic forces depends essentially on the backward position of the lifting surface.

The results obtained by applying the approximate formulae are, for $x > 5$ and large reduced frequencies, in good agreement with those obtained using the exact formulae.

Fig. 6 shows the exponential decreasing of the upwash with respect to the vertical distance z at several reduced frequencies for the pitching motion.

In fig. 7 a result of this calculation is compared with an exact solution given by E. LAPIN, R. COOKSHANKS and H. F. HUNTER, ref. 6, for the upwash at five semi-chord distance behind a wing in plunging motion. Both results are in good agreement.

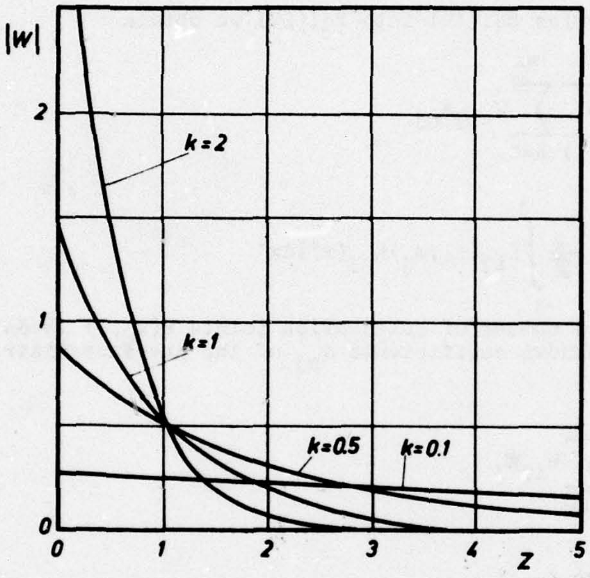

Fig. 6
Exponential decreasing of the upwash with respect to the vertical distance z. Pitching motion. $x = 5$.

$$|w| = \sqrt{(\mathrm{Re}(w))^2 + (\mathrm{Im}(w))^2}$$

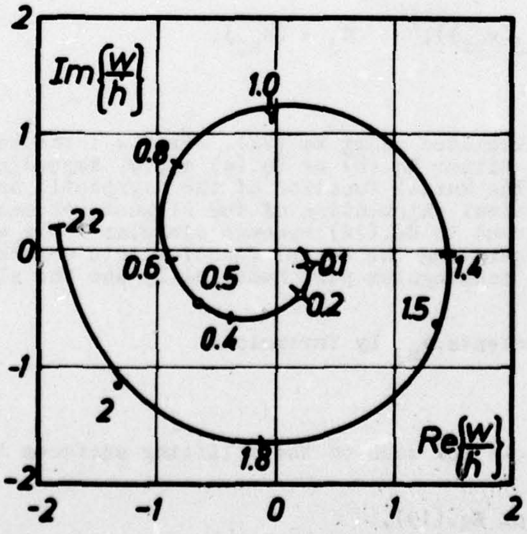

Fig. 7
Polar diagram for upwash at a distance of five semi-chords behind wing mid-chord.
Parameter: Reduced frequency
w - upwash
ḣ - plunging velocity
+ values given in ref. 6
∘ values of this calculation

5. CALCULATION OF THE AERODYNAMIC FORCES ACTING ON INTERFERING AIRFOILS

5.1 Solution of the Interference Problem

Calculation of the aerodynamic forces acting on m interfering airfoils requires of including the upwash induced by one lifting surface on another lifting surface into the boundary condition. On each of the lifting surfaces, the boundary condition is defined by its self-induced upwash as well as by the upwash induced by the other lifting surfaces on the lifting surface under consideration, ref. 1. This may be expressed as follows:

$$v_i = \frac{\partial f_i}{\partial x_i} + ik_i f_i = \sum_{(j)} w_{ij} = \sum_{(j)} \int_{-1}^{1} \Delta c_{pj}(x') K_{ij}(x_o, z_j) dx' \tag{20}$$

Index i $(i=1(1)m)$ denotes the lifting surface for which the upwash has to be evaluated; index j $(j=1(1)m)$ denotes the lifting surface inducing the upwash.

Eq.(20) represents a system of m coupled integral equations for the m unknown pressure distributions Δc_{pj}. It may be solved by application of the collocation method described in detail in ref. 1.

After introducing the pressure series Eq.(19) into Eq.(20) we obtain

$$v_i = \sum_{(j)} \sum_{n=0}^{N_j} W_{nij} a_{nj} \tag{21}$$

where

$$W_{nij} = \frac{2}{\pi} \int_{-1}^{1} K_{ij}(x_o, z_j) f_{nj}(x') dx' \tag{22}$$

Fulfilling the boundary condition in a number of collocation points $P(x_p, 0)$ leads to a system of linear equations for the unknown coefficients a_{nj} of the pressure distributions. In matrix form we can write:

$$\bar{v}_i = \sum_{(j)} W_{ij} \bar{a}_j \tag{23}$$

where

$$\bar{v}_i = \left(\frac{\partial f_i(x_{pi})}{\partial x_i} + ik_i f_i(x_{pi}) \right),$$

$$W_{ij} = (W_{nij}(x_{pi})), \qquad \bar{a}_j = (a_{nj}),$$

and $p = 0(1)N$, $n = 0(1)N$.

The elements of matrix W_{ij} may be calculated using Eq.(22). For $j = i$ the kernel function Eq.(6) has to be used; for $j \neq i$ either Eq.(6) or Eq.(4) apply, depending on the vertical position of lifting surface j. The kernel function of the asymptotic approximation (Eq.(8)) may also be used. The numerical calculation of the elements of matrices W_{ii} involves some difficulties, as the integrand in Eq.(22) becomes singular for $x_p = x'$. These difficulties may be overcome by seperating the kernel function into a nonsingular part and a singular part and solving the nonsingular part numerically and the singular part in closed form, ref.2.

Eq.(23) may be solved for the coefficients a_{nj} by inversion.

5.2 Aerodynamic Forces

Knowledge of the coefficients $\bar{a}_j$ allows for each of the m lifting surfaces the calculation of

(a) the pressure coefficient Δc_p by aid of Eq.(19),

(b) the lift coefficient C_L and the pitch moment coefficient C_M with respect to the axis $x = x_a$ (positive nose up)

(24) $$C_L = a_o$$

(25) $$C_M = \frac{a_o}{2}\left(\frac{1}{2} + x_a\right) + \frac{1}{4}\cdot a_1$$

(c) the generalized aerodynamic forces.

6. SPECIAL CONSIDERATION OF THE LONGITUDINAL FORCE COMPONENT

6.1 Drag or Propulsion Coefficient

The forces acting on a thin, infinitely long plane plate are shown in fig. 8. P denotes the force per unit span length resulting from the pressure distribution, P_x the component of P in flow direction, and S represents the well-known "suction" force. For small angles of attack α we obtain for the resulting longitudinal force component D

(26) $$D = P_x - S$$

or in coefficient form

(27) $$C_D = C_{P_x} - C_S$$

A relation for the "suction" force has been given by I. E. GARRICK, ref. 5. With the pressure distribution used in this paper and after changing from complex to real quantities, we get for the coefficient C_S

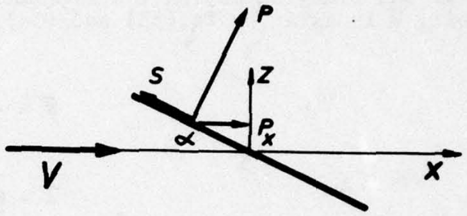

Fig. 8

(28) $$C_S(t) = \frac{1}{2\pi}\left(\sum_{n=0}^{N} A_n\right)^2$$

where

$$A_n = \mathrm{Re}(a_n)\cos\omega t - \mathrm{Im}(a_n)\sin\omega t$$

Integration of the real part of the pressure distribution over the surface yields for the coefficint $C_{P_x}(t)$

(29) $$C_{P_x}(t) = -\frac{1}{\pi}\sum_{n=0}^{N} A_n \int_0^{\pi} (\cos(n\varphi) + \cos(n+1)\varphi)\frac{\partial \mathrm{Re}(\bar{f}(x;t))}{\partial x}\,d\varphi$$

where $x = x(\varphi) = -\cos\varphi$. $\partial\mathrm{Re}(\bar{f}(x;t))/\partial x$ denotes the real part of the local slope of the lifting surface.

In order to get the information whether the longitudinal force acting on the airfoil is either drag (positive sign) or propulsion (negative sign), we determine the time average over one oscillation cycle:

(30) $$\bar{C}_D = \frac{1}{T}\int_0^T C_D(t)\,dt = -\frac{1}{T\pi}\int_0^T \sum_{n=0}^{N} A_n \int_0^{\pi} (\cos(n\varphi) + \cos(n+1)\varphi)\frac{\partial \mathrm{Re}(\bar{f}(x;t))}{\partial x}\,d\varphi\cdot dt - $$
$$- \frac{1}{4\pi}\left[\left(\sum_{n=0}^{N} \mathrm{Re}(a_n)\right)^2 + \left(\sum_{n=0}^{N} \mathrm{Im}(a_n)\right)^2\right]$$

The total longitudinal force acting on a combination of m lifting surfaces is the sum of the longitudinal forces acting on each of the lifting surfaces. In coefficient form we get

(31) $$\bar{C}_{D_{total}} = \sum_{i=1}^{m} \bar{C}_{D_i}$$

with $\overline{C}_{D_i}$ given by Eq.(30).

6.2 Efficiency Factor

Special information concerning the situation in longitudinal direction can be gained by introducing the efficiency factor η_S, which is defined as follows:

$$\eta_S = \frac{\overline{D} \cdot V}{\overline{W}} \tag{32}$$

$\overline{D} = \rho l V^2 \overline{C}_D$ represents the average propulsion or drag force per unit span, and $\overline{W}$ the average work per unit time required to maintain the oscillations of a lifting surface against the acting aerodynamic forces and moments, ref. 5.

For a lifting surface combination $\overline{D}$ represents the resultant propulsion or drag force, and $\overline{W}$ the total work per unit time required to maintain the oscillations of all the lifting surfaces.

For the plunging motion $\overline{f} = \exp(i\omega t)$ and the pitching motion $\overline{f} = -x \cdot \exp(i\omega t)$ of an airfoil, $\overline{W}$ is given by Eq.(33) and (34), respectively.

$$\overline{W} = \frac{\rho}{2} V^3 l k \operatorname{Im}(C_L) \tag{33}$$

$$\overline{W} = \rho V^3 l k \operatorname{Im}(C_M) \tag{34}$$

7. RESULTS FOR A TANDEM WING CONFIGURATION

Numerical calculations were carried out for a tandem configuration as shown in fig. 9.

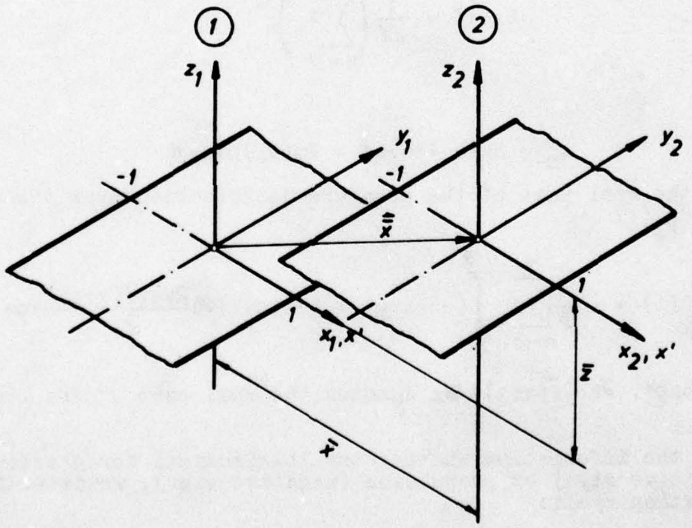

Fig. 9. Tandem wing configuration.

Index 1 refers to lifting surface 1, index 2 to lifting surface 2. Both lifting surfaces have the same semi-chord l.

As in sect. 4, the following harmonic motions of the airfoils were selected:

Plunging motion	$f_1 = \exp(i\omega t)$	$f_2 = \exp(i\omega t)$
Pitching motion	$f_1 = -x_1 \cdot \exp(i\omega t)$	$f_2 = -x_2 \cdot \exp(i\omega t)$
Reduced frequency	$k_1 = \frac{\omega l}{V} = k$	$k_2 = \frac{\omega l}{V} = k$

For the calculation the first three coefficients of the pressure distributions have been retained.

According to ref. 1, it is sufficient for a basic description of the aerodynamic forces to consider the two special cases:

(a) Lifting surface 1 oscillates in mode f_1, surface 2 being steady, i.e. $v_1 \neq 0$, $v_2 = 0$.

(b) Lifting surface 2 oscillates in mode f_2, surface 1 being steady, i.e. $v_1 = 0$, $v_2 \neq 0$.

The coefficients of the aerodynamic forces corresponding to the two special cases are denoted by indices as shown in fig. 10.

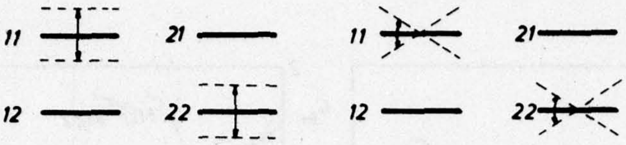

Fig. 10. Indices of the aerodynamic coefficients.

In figs. 11 through 25 a selection of the results contained in the original paper, ref. 7, is presented. Where the real and imaginary parts of the aerodynamic coefficients are plotted the following notations are used: $C_L' = \mathrm{Re}(C_L)$, $C_L'' = \mathrm{Im}(C_L)$, $C_M' = \mathrm{Re}(C_M)$, $C_M'' = \mathrm{Im}(C_M)$.

7.1 Lift and Pitch Moment Coefficients

Figs. 11 and 12 show the lift and pitch moment coefficients as function of the reduced frequency for the pitching motion. In figs. 13 and 14 the coefficients are presented as functions of the rear position of lifting surface 2. The coefficients marked by index 21 reach considerable values and show considerable variations. The effect of oscillating lifting surface 2 on lifting surface 1 is small.

7.2 Longitudinal Force Component

The drag (propulsion) coefficients for the pitching motion, as function of the aft position of lifting surface 2, are presented in figs. 15 through 17 and as function of the reduced frequency in fig. 18. The force acting on the lifting surface at rest is always a propulsion force (index 12 or 21), whereas the force acting on the oscillating lifting surface (index 11 or 22) is, depending on the reduced frequency, either drag or propulsion.

With a lifting surface at rest located behind an airfoil oscillating in pitching motion, the transition of the lifting surface combination from drag to propulsion is, compared with a single airfoil, shifted to lower reduced frequencies. The influence of a lifting surface at rest located in front of the oscillating surface is negligible.

The result for the steady case, fig. 15, is interesting, as the absolute value of the propulsion force acting on the horizontal lifting surface (index 12 or 21) is equal to the absolute value of the drag force acting on the lifting surface at incidence. This reflects the fact that in a steady flow the drag of a wing is zero.

For the plunging motion figs. 19 and 20 indicate the propulsion coefficients as function of the aft position of lifting surface 2, and fig. 21 as function of the reduced frequency. All forces are propulsion forces. A lifting surface at rest located behind a lifting surface in plunging motion effects a considerable increase in the total propulsion force acting on the lifting surface combination. The effect of a lifting surface at rest located in front of the oscillating airfoil is negligible.

7.3 Propulsion Efficiency

Figs. 22 and 23 show the propulsion efficiency of the tandem configuration and the single airfoil as function of the reduced frequency. A positive propulsion efficiency denotes propulsion, a negative one drag.

The airfoil at rest located behind the oscillating airfoil improves the propulsion efficiency considerably. In the case of the plunging motion, fig.22, the propulsion efficiency is close to 100 % and nearly independent of the reduced frequency. If the airfoil is performing pitching motions, also a considerable increase in propulsion efficiency is noticeable and, in addition, the transition from drag to propulsion is, compared with the single airfoil, shifted to lower reduced frequencies.

For small values of reduced frequency in pitching motion, the propulsion efficiency becomes smaller than -1. This indicates a loss of damping. The necessary energy is extracted from the airstream.

Figs. 24 and 25 indicate that for both the plunging motion and the pitching motion, the propulsion efficiency is almost independent of the aft position of lifting surface 2, which is at rest.

An airfoil at rest located in front of the oscillating airfoil is of negligible influence on the propulsion efficiency of the lifting surface combination.

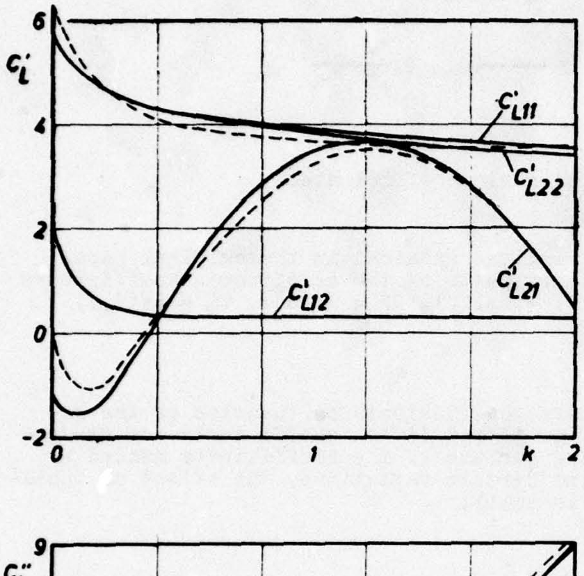

Fig. 11
Lift coefficient as function of the reduced frequency k. Pitching motion. Distance from wing mid-chord to wing mid-chord four semi-chords. $\bar{x} = 0$.
--- Asymptotic approximation.

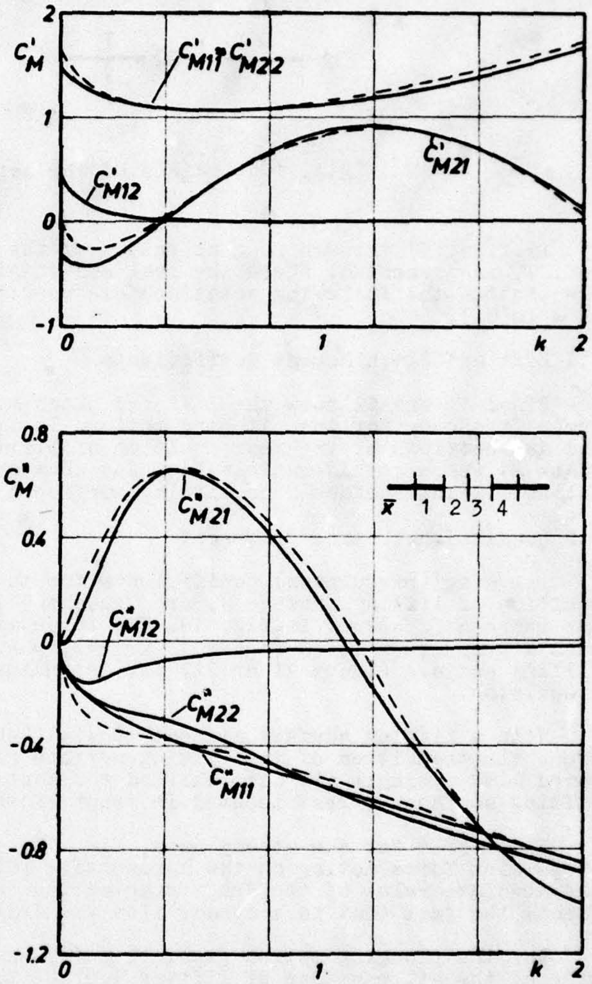

Fig. 12
Pitch moment coefficient as function of the reduced frequency k. Pitching motion about axis $x_a = 0$. Distance from wing mid-chord to wing mid-chord four semi-chords. $\bar{x} = 0$.
--- Asymptotic approximation.

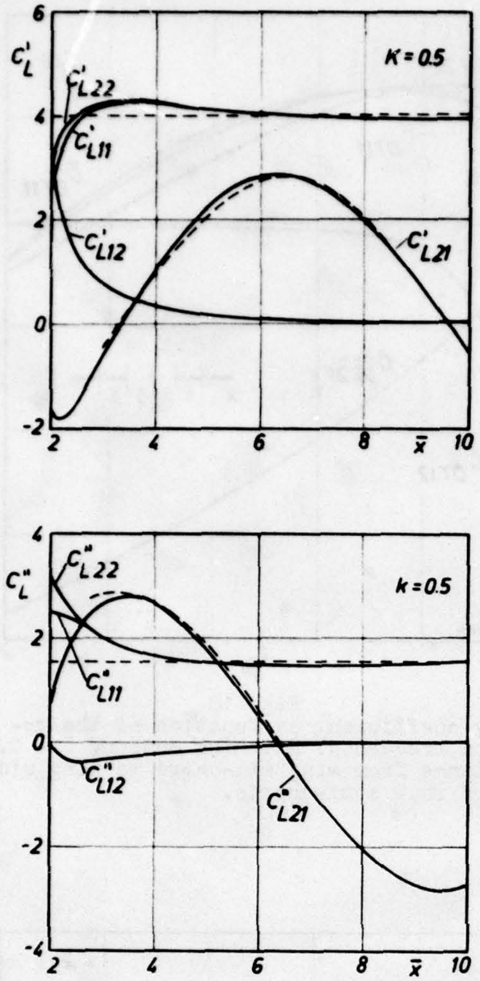

Fig. 13
Lift coefficient as function of the aft position of lifting surface 2. Pitching motion. $\bar{\bar{z}}$ = 0. k = 0.5.
--- Asymptotic approximation.

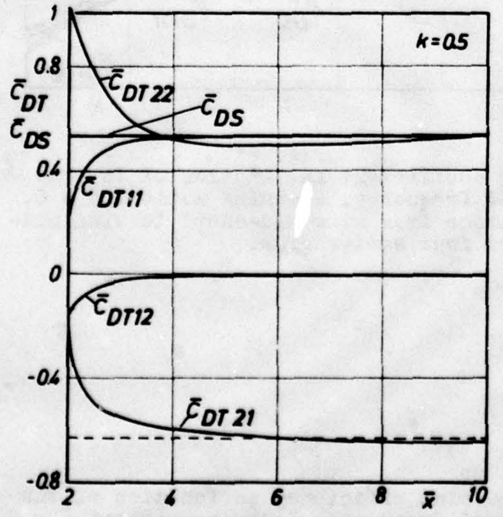

Fig. 16
Drag coefficient as function of the aft position of lifting surface 2. Pitching motion. $\bar{\bar{z}}$ = 0. k = 0.5.

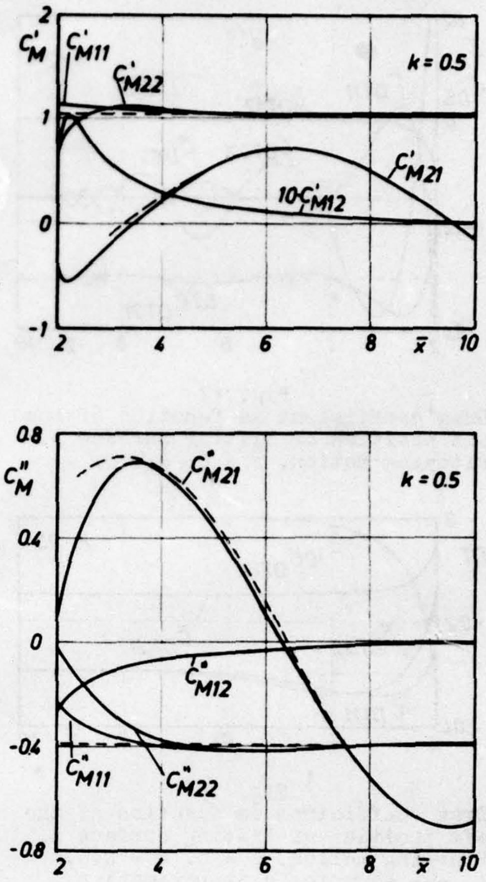

Fig. 14
Pitch moment coefficient as function of the aft position of lifting surface 2. Pitching motion about axis x_a=0. $\bar{\bar{z}}$=0. --- Asymptotic approximation

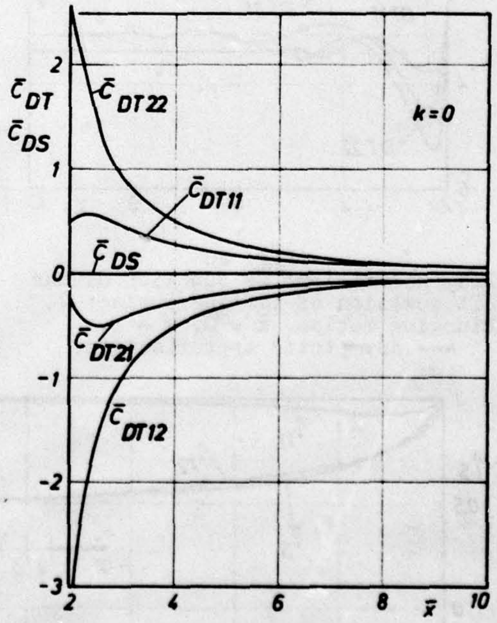

Fig. 15
Drag coefficient as function of the aft position of lifting surface 2. Pitching motion. $\bar{\bar{z}}$ = 0. k = 0.

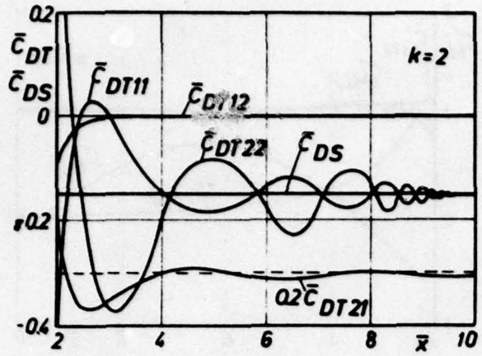

Fig. 17
Drag coefficient as function of the aft position of lifting surface 2. Pitching motion. $\bar{z} = 0$. $k = 2$.

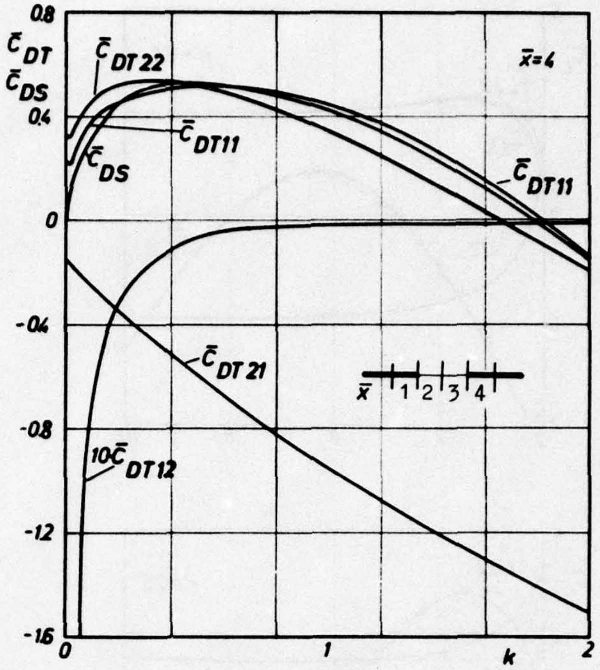

Fig. 18
Drag coefficient as function of the reduced frequency. Pitching motion. $\bar{z} = 0$. Distance from wing mid-chord to wing mid-chord four semi-chords.

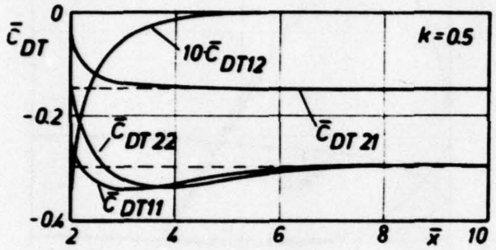

Fig. 19
Drag coefficient as function of the aft position of lifting surface 2. Plunging motion. $\bar{z} = 0$. $k = 0.5$.
--- Asymptotic approximation.

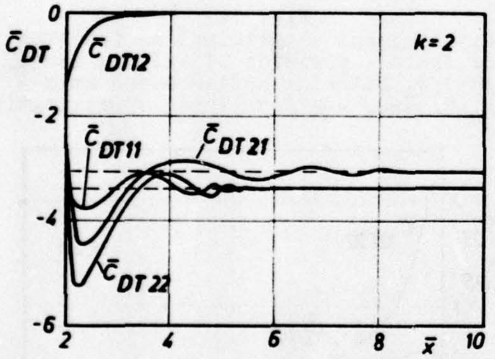

Fig. 20
Drag coefficient as function of the aft position of lifting surface 2. Plunging motion. $\bar{z} = 0$. $k = 2$.
--- Asymptotic approximation.

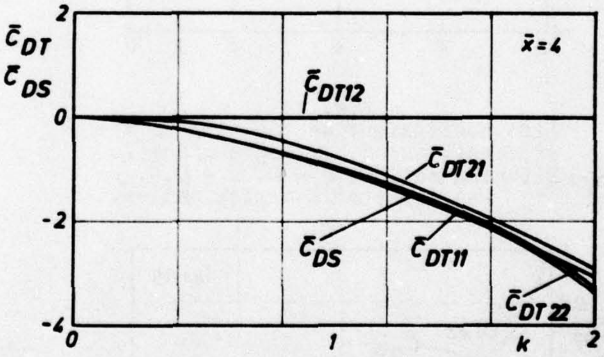

Fig. 21
Drag coefficient as function of the reduced frequency. Plunging motion. $\bar{z} = 0$. Distance from wing mid-chord to wing mid-chord four semi-chords.

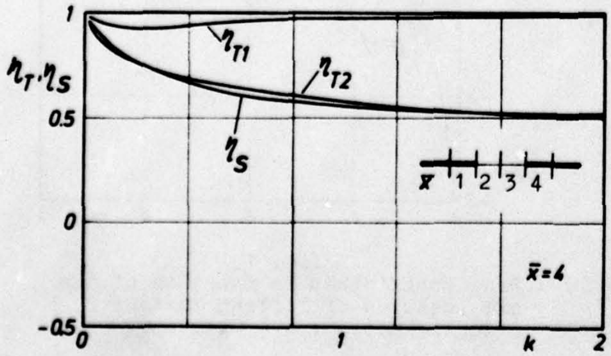

Fig. 22
Propulsion efficiency as function of the reduced frequency. Plunging motion. $\bar{z} = 0$. Distance from wing mid-chord to wing mid-chord four semi-chords. Index T1: Lifting surface 1 oscillates. Index T2: Lifting surface 2 oscillates. Index S: Single wing.

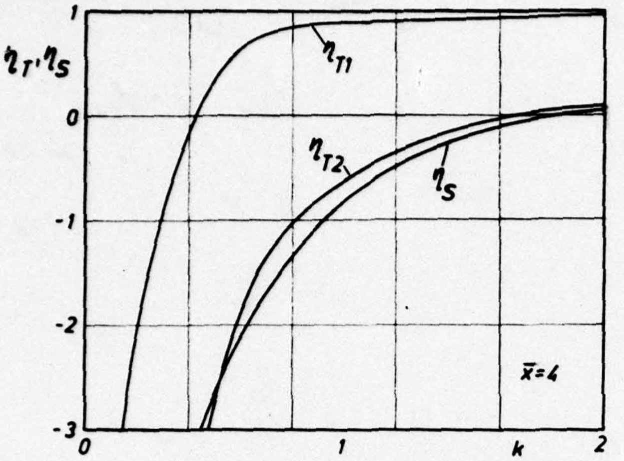

Fig. 23
Propulsion efficiency as function of the reduced frequency. Pitching motion. $\bar{z}$ = 0. Distance from wing mid-chord to wing mid-chord four semi-chords.

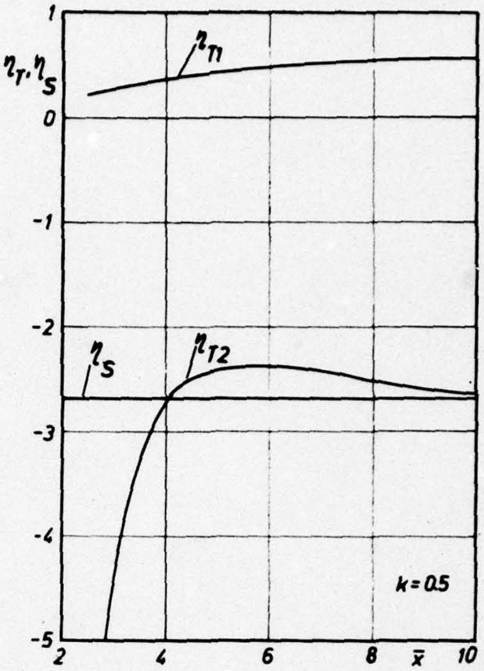

Fig. 25
Propulsion efficiency as function of the aft position of lifting surface 2. Pitching motion. $\bar{z}$ = 0. k = 0.5.

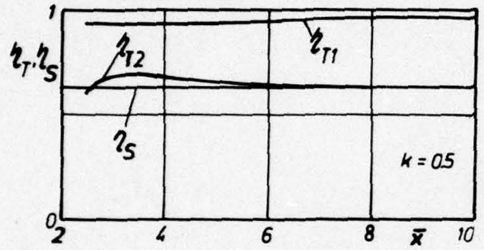

Fig. 24
Propulsion efficiency as function of the aft position of lifting surface 2. Plunging motion. $\bar{z}$ = 0. k = 0.5.

8. REFERENCES

1 B. Laschka, H. Schmid — Unsteady Aerodynamic Forces on Coplanar Lifting Surfaces in Subsonic Flow (Wing - Horizontal Tail Interference). Jahrbuch 1967 der WGLR, pp. 211 - 222.

2 B. Laschka — Interfering Lifting Surfaces in Subsonic Flow. Zeitschrift für Flugwissenschaften, Bd. 18, Heft 9/10, 1970.

3 J.P. Giesing, T.P. Kálmán, W.P. Rodden — Subsonic Unsteady Aerodynamics for General Configurations, Part I, Direct Application of Nonplanar Doublet-Lattice Method. US Air Force Flight Dynamics Labratory, AFFDL - TR - 71 - 5, 1971

4 B. Laschka — Unsteady Aerodynamic Prediction Methods Applied in Aeroelasticity. AGARD Report No. 645 on Unsteady Aerodynamics, 1975

5 I.E. Garrick — Nonsteady Wing Characteristics, published in "Aerodynamic Components of Aircraft at High Speeds (Edited by A. F. Donovan, H. R. Lawrence), Princeton University Press, Princeton, N. J., 1957

6 E. Lapin, R. Crookshanks, H.F. Hunter — Downwash Behind a Two-Dimensional Wing Oscillating in Plunging Motion, J. Ae. Sc. Vol. 19, July, 1952, pp. 447 - 450.

7 H. Bosch — Instationäre Luftkräfte eines Tragflügelpaares in Tandemanordnung in ebener inkompressibler Strömung, Diplom-Ingenieur Thesis, Technical University Munich, 1972

ÉTUDE D'UN PROFIL SUPERCRITIQUE AVEC GOUVERNE OSCILLANTE EN ÉCOULEMENT SUBSONIQUE ET TRANSSONIQUE

par Richard GRENON et Jean THERS

Office National d'Etudes et de Recherches Aérospatiales (ONERA)
92320 Châtillon - France

On présente les résultats des mesures de pression instationnaire effectuées sur un profil supercritique équipé d'une gouverne de bord de fuite de 25 % de profondeur animée d'un mouvement d'oscillation harmonique en écoulement bidimensionnel subsonique et transsonique.

L'étude a mis en évidence les différences importantes entre le régime subcritique sans choc et le régime supercritique avec chocs. Dans ces deux cas, on a étudié l'influence des paramètres «instationnaires», tels que la fréquence et l'amplitude des oscillations, et l'influence des paramètres «stationnaires», tels que le braquage moyen du volet et l'incidence de l'aile.

Il ressort de cette étude l'importance des phénomènes visqueux et des phénomènes liés aux mouvements des chocs, et la nécessité de développer des méthodes de calculs pouvant prendre en compte ces phénomènes.

STUDY OF A SUPERCRITICAL PROFILE WITH OSCILLATING CONTROL SURFACE IN SUB- AND TRANSONIC FLOWS

The paper presents results of unsteady pressure measurements performed on a supercritical profile equipped with a 25 %-chord trailing edge control surface in harmonic motion, in two-dimensional sub- and transonic flows.

Important differences appeared between the subcritical regime without shock, and the supercritical regime with shock. In both cases, we studied the influence of the "unsteady" parameters, such as oscillation frequency and amplitude, and that of "steady" ones, such as mean flap setting and wing angle of attack.

This study brought to light the importance of viscous and shock-related phenomena, and the necessity to develop calculation methods taking these phenomena into account.

NOTATIONS

a	vitesse du son
ρ	masse volumique
V	vitesse de l'écoulement
M	nombre de Mach
c	corde
α	incidence du profil
δ	braquage du volet, positif vers le bas
δ_m	braquage moyen du volet
δ_i	amplitude des oscillations du volet
t	temps
ω	fréquence circulaire
$f = \frac{\omega}{2\pi}$	fréquence des oscillations (Hz)
$k = \frac{\omega c}{2 V_\infty} = \frac{\pi f c}{V_\infty}$	fréquence réduite
P	pression instantanée
P_m	pression moyenne
ΔP	fluctuation de pression
$K_P = \frac{P - P_\infty}{1/2 \rho_\infty V_\infty^2}$	coefficient de pression instantanée (ou stationnaire)
$C_P = \frac{\Delta P}{1/2 \rho_\infty V_\infty^2 \cdot \delta_i}$	coefficient de pression instationnaire
K_P^*	valeur de K_P lorsque $M_\ell = 1$
C_z	coefficient de portance stationnaire
C_{z_δ}	coefficient de portance instationnaire
C_{m_δ}	coefficient de moment de tangage instationnaire
C_{mc_δ}	coefficient de moment de charnière instationnaire
φ	angle de phase
P_i	pression génératrice
R_e	nombre de Reynolds

INDICES

m	valeurs moyennes (δ, P)
ℓ	valeurs locales (a, V, M)
∞	valeurs à l'infini amont (a, V, M)
1	indice affecté au 1er harmonique du module et de la phase de C_p

1 - INTRODUCTION

Devant l'intérêt manifesté pour les techniques de contrôle actif généralisé (CAG ou CCV) qui requièrent l'utilisation de gouvernes rapides, l'ONERA a entrepris une étude expérimentale approfondie des effets instationnaires d'une gouverne oscillante dans le domaine subsonique et surtout transsonique, où le calcul des forces aérodynamiques instationnaires est incertain.

Cette étude a été faite en écoulement bidimensionnel sur un profil supercritique du type utilisé actuellement dans les projets d'avions de transport.

Une première partie, consacrée à la description du montage original de la maquette et aux essais en soufflerie, sera suivie de l'analyse des résultats obtenus.

2 - MONTAGE DE LA MAQUETTE ET MESURES -

2.1 - Montage maquette

Le profil retenu est un profil supercritique de 16 % d'épaisseur relative développé par la Société Aérospatiale. La maquette est une aile droite en acier de 560 mm d'envergure et de 180 mm de corde. La gouverne, de profondeur relative 25 %, est en duralumin. Le programme d'essai comporte une étude en écoulement stationnaire et une étude en écoulement instationnaire. Il faut donc disposer d'une excitation permettant des braquages statiques et dynamiques importants de la gouverne à des fréquences élevées. Pour remplir de telles conditions, un vérin hydraulique asservi a été réalisé.

Le montage en veine se présente alors de la manière suivante (fig. 1). L'aile est encastrée à ses deux extrémités par un talon sur les deux tourelles-parois soufflerie. L'axe de la gouverne est lié à l'aile par 4 paliers en bronze et à chaque extrémité il est accouplé à l'axe des vérins droit et gauche. Chaque vérin est commandé par une servo-valve pilotée par un générateur.

La maquette est équipée de 78 prises de pression statique et de 32 capteurs de pression instationnaire type Kulite à court temps de réponse (16 en intrados et 16 en extrados). Douze accéléromètres, placés pour moitié dans l'aile et dans le volet, permettent de contrôler le mouvement de la gouverne par rapport à l'aile. Quatre ponts de jauges indiquent les efforts auxquels sont soumis l'aile et la gouverne. Un capteur angulaire fixé en bout de chaque axe vérin permet d'accéder à la fois au braquage moyen et à l'amplitude du braquage dynamique de la gouverne. Les deux capteurs angulaires permettent d'asservir les vérins entre eux par l'intermédiaire des servo-valves.

Ce système d'excitation forcée répond bien aux conditions exigées : couple disponible important, braquage moyen et amplitude dynamique réalisables simultanément, variation de fréquence continue. Toutes les variations de paramètres se faisant sans aucun démontage, il n'y a pas de perte de temps lors des essais en soufflerie.

Ce montage permet des oscillations du volet de ± 1° à 100 Hz, cette amplitude pouvant atteindre ± 5° à 20 Hz. La limitation d'amplitude est donnée d'une part par le débit du groupe hydraulique ou de la servo-valve et d'autre part par les efforts d'inertie que peut supporter le volet.

2.2 - Mesures en soufflerie -

Le programme d'essai comprenait une partie stationnaire et une partie instationnaire pour des nombres de Mach compris entre 0,3 et 0,8

L'influence d'une variation des paramètres suivants a été étudiée : l'incidence α du profil, le braquage moyen δ_m de la gouverne, le nombre de Reynolds et de plus en instationnaire, l'amplitude δ_i et la fréquence des oscillations.

La variation du nombre de Reynolds est obtenue en faisant varier la pression génératrice, d'où le choix de la soufflerie S3 Modane ($1{,}2 < P_i < 4$bars).

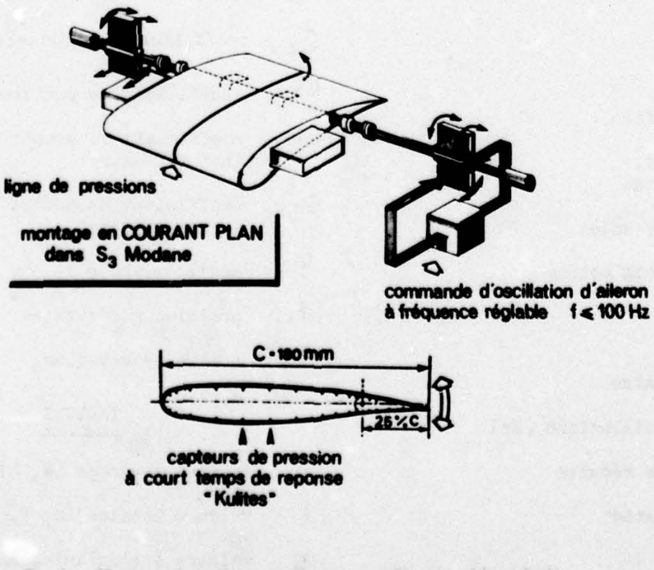

Fig. 1 – Montage d'un aileron oscillant sur profil supercritique épais.

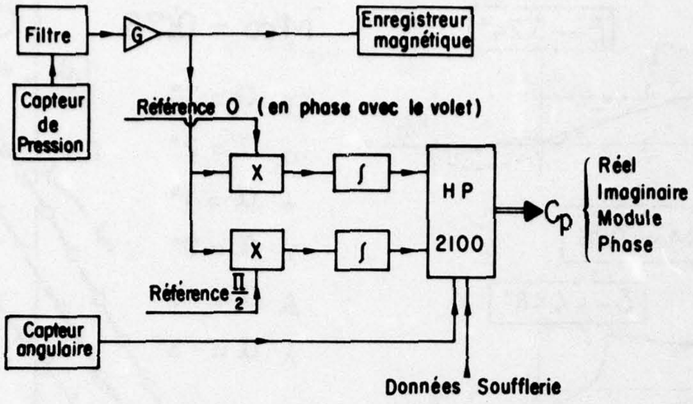

Fig. 2 – Chaîne de mesures instationnaires.

Tous les essais ont été effectués en transition naturelle. Un banc de strioscopie permet de visualiser les ondes de choc de l'écoulement au voisinage de la partie extrados du profil. En instationnaire, un signal synchronisé avec le mouvement de la gouverne déclenche 25 prises de vue successives avec un déphasage de 15°, plus un nombre entier de périodes entre chaque photo. La série des 25 photos permet de reconstituer l'écoulement au cours d'une période complète du mouvement du volet et de suivre le déplacement du choc.

2.3 - Chaînes d'acquisition -

Pour les essais statiques, exécutés séparemment, l'acquisition est celle utilisée habituellement à S3Modane. Pour les essais dynamiques, le traitement du signal recueilli par les capteurs Kulite est celui représenté par la figure 2.

3 - ANALYSE DES RESULTATS -

3.1 - Essais stationnaires

A incidence nulle et braquage nul du volet, la zone supersonique localisée au bord d'attaque extrados à $M = 0,7$ s'étend vers le bord de fuite à mesure que le nombre de Mach croît, et une seconde zone supersonique apparaît à l'intrados(fig.3). Les zones supersoniques à $M = 0,76$ sont profondément modifiées par un braquage de 5 degrés en plus ou en moins du volet (fig. 4). On constate cependant que le volet reste chargé positivement dans les deux cas (la charge s'annule pour un braquage voisin de $\delta_m = -10°$).

Le coefficient C_z évolue linéairement en fonction du braquage pour des braquages négatifs ; de $M = 0,3$ à $M = 0,7$ la pente $\frac{dC_z}{d\delta}$ reste sensiblement constante, elle augmente ensuite jusqu'à $M = 0,76$ pour diminuer au delà ($M = 0,8$).

L'efficacité de la gouverne diminue lorsque le braquage dépasse 2° en positif en raison de l'épaississement de la couche limite et du décollement qui se produit à l'extrados du volet.

Si l'on met le profil en incidence, on observe (figure 5) une variation assez faible de la pente des courbes $C_z(\delta)$ dans leur partie linéaire. L'étendue de la plage linéaire est maximale pour l'incidence de 1° et diminue rapidement pour les incidences de part et d'autre de 1°.

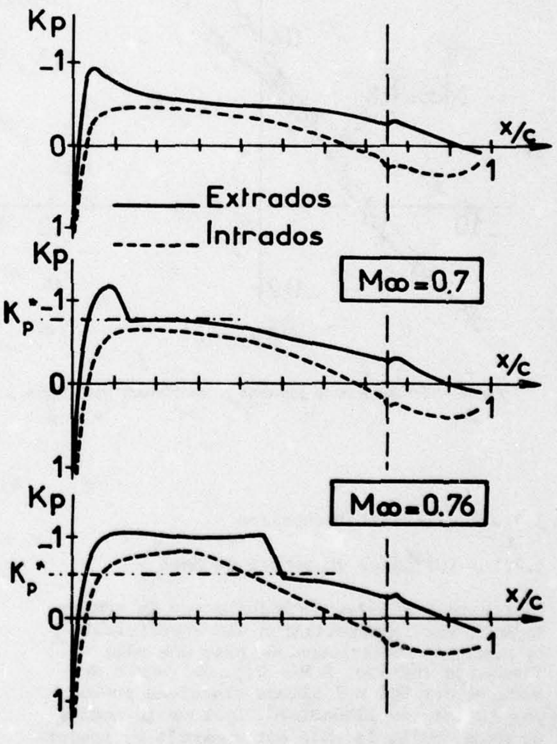

Fig. 3 – Profil SNIAS 16SC1 - $\alpha = 0°$; $\delta \simeq 0°$ - Répartitions de pression en écoulement stationnaire.

L'effet Reynolds a été étudié pour l'incidence de 0° et pour les braquages compris entre 0 et - 5° ; dans ce cas, il est assez modéré, la pente $dC_z/d\delta$ n'augmentant que de 7% pour une variation du nombre de Reynolds de 3 à 7 10^6 mais il est probable que l'effet aurait été plus important pour des essais dans la zone non linéaire des courbes

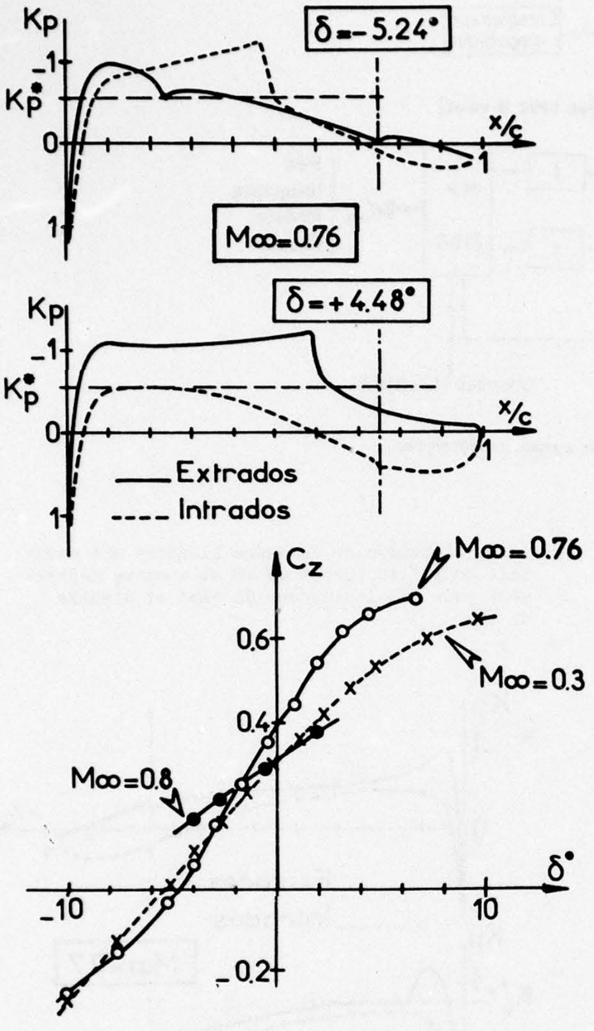

Fig. 4 – Efficacité de la gouverne en écoulement stationnaire. α = 0.

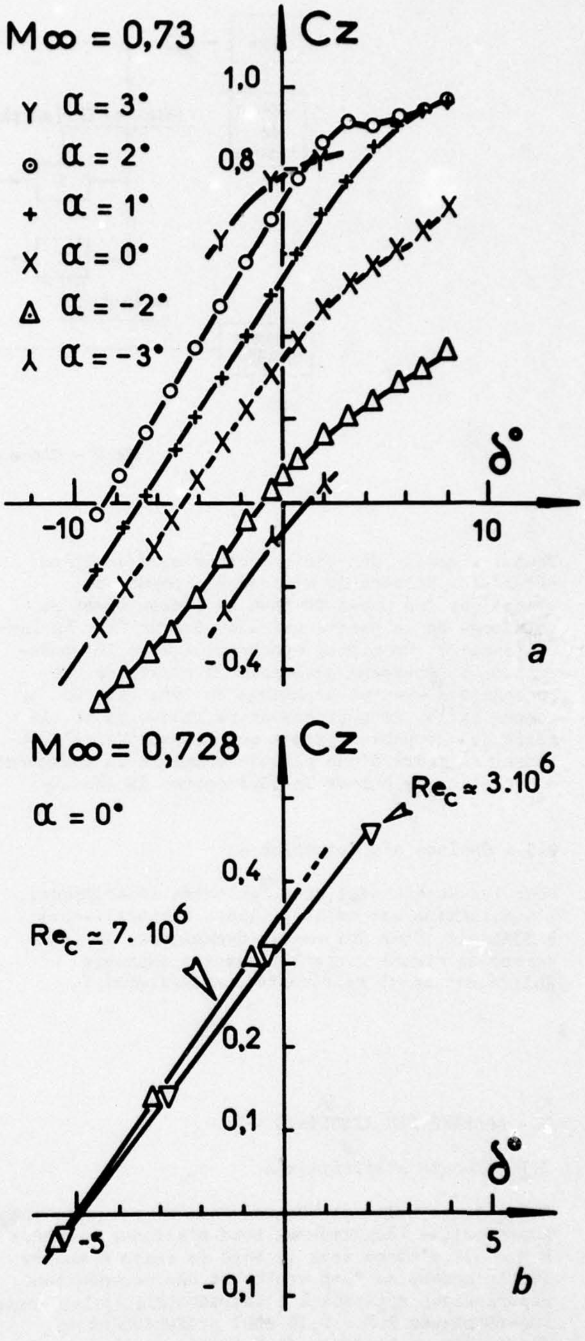

Fig. 5 – Efficacité de la gouverne. a) Influence de l'incidence - b) Influence du nombre de Reynolds.

3.2 - Essais instationnaires -

3.2.1 - Influence du nombre de Mach -

La figure 6 représente l'influence du nombre de Mach sur la répartition des coefficients de pression instationnaire pour une même fréquence réduite. A M = 0,3, la courbe des modules des **Cp1** a l'allure classique prévue par la théorie linéarisée. Lorsque le nombre de Mach croît, le choc qui apparaît se traduit par un pic sur la courbe des C_{p1} qui va en grandissant et en reculant. Le déphasage s'accroît avec le nombre de Mach, mais il reste constant dans la zone supersonique et présente un brusque saut au niveau du choc. On voit que l'allure des répartitions de pression instationnaire est très différente selon que l'on est en régime subcritique ou supercritique.

3.2.2. - Influence de l'amplitude des oscillations

L'influence de l'amplitude des oscillations est représentée sur la figure 7. Les 3 courbes relatives aux trois amplitudes δ_i = ± 1° , ± 3° et ± 5° sont pratiquement confondues en module et phase sauf dans la zone balayée par le choc. Les non linéarités n'apparaissent qu'au niveau du mouvement du choc et de l'apparition des décollements. Le volet décolle pour un braquage de 3° en stationnaire à M = 0,73 et on constate bien que les plus gros écarts sont entre les courbes correspondant à ± 1° et ± 3°.

Un essai à M = 0,3, pour des amplitudes de 1° et de 5° n'a montré aucun écart significatif entre les deux répartitions de C_{p1}. Dans ce cas le phénomène est parfaitement linéaire.

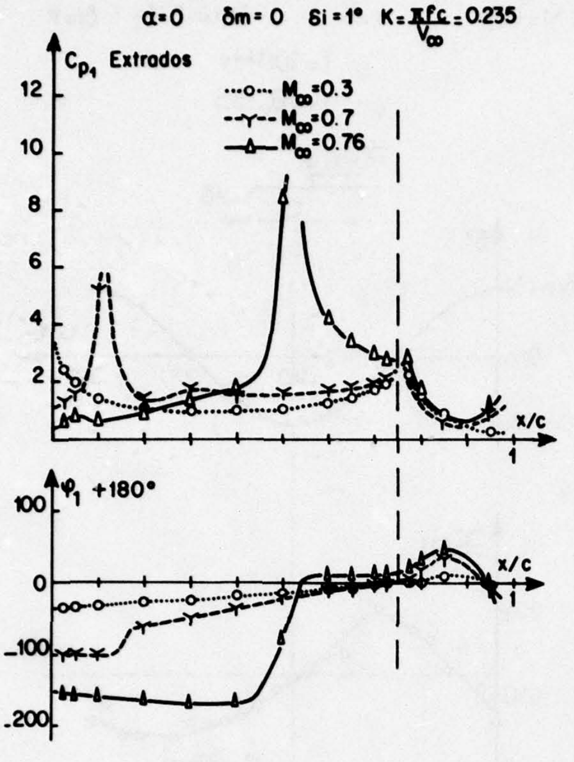

Fig. 6 – Influence du nombre de Mach sur les pressions instationnaires.

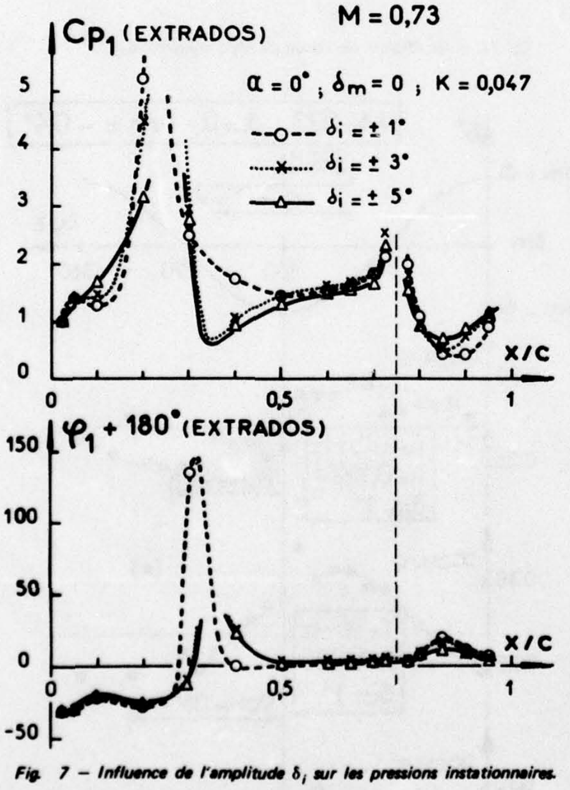

Fig. 7 – Influence de l'amplitude δ_i sur les pressions instationnaires.

3.2.3 - Influence de la fréquence réduite -

Les figures 8 et 9 donnent l'évolution des C_{p1} extrados pour 3 fréquences réduites à M = 0,3 et M = 0,76. En régime subcritique M = 0,3, le module des pressions diminue et le retard de phase en amont de la charnière augmente lorsque la fréquence croît. En régime supercritique M = 0,76 où la zone supersonique s'étend de 10 à 50 % de la corde, l'évolution est différente en amont et en aval du choc. On a porté sur cette figure le cas quasi-stationnaire, c'est-à-dire K = 0, cas limite de la fréquence nulle. Ces valeurs quasi-stationnaires sont obtenues à partir des valeurs des K_p correspondant à 2 braquages voisins de la position moyenne du volet

$$C_{pes} = \left[K_p(\delta_m+\Delta\delta) - K_p(\delta_m-\Delta\delta)\right] / 2\Delta\delta$$

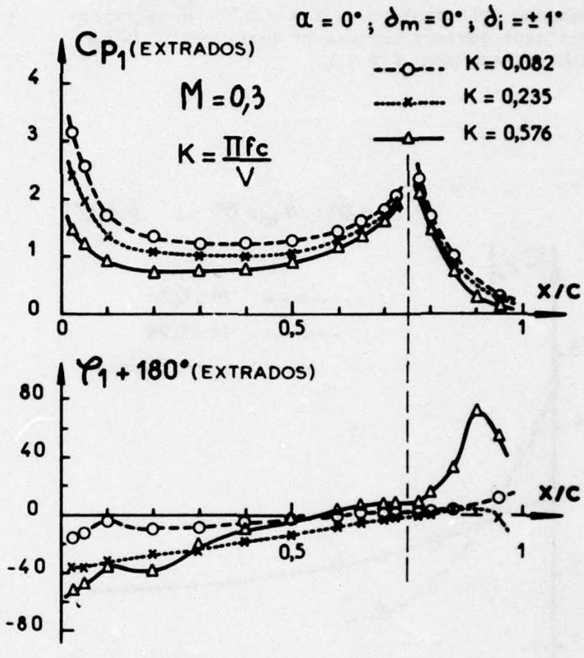

Fig. 8 – Influence de la fréquence réduite sur les pressions instationnaires.

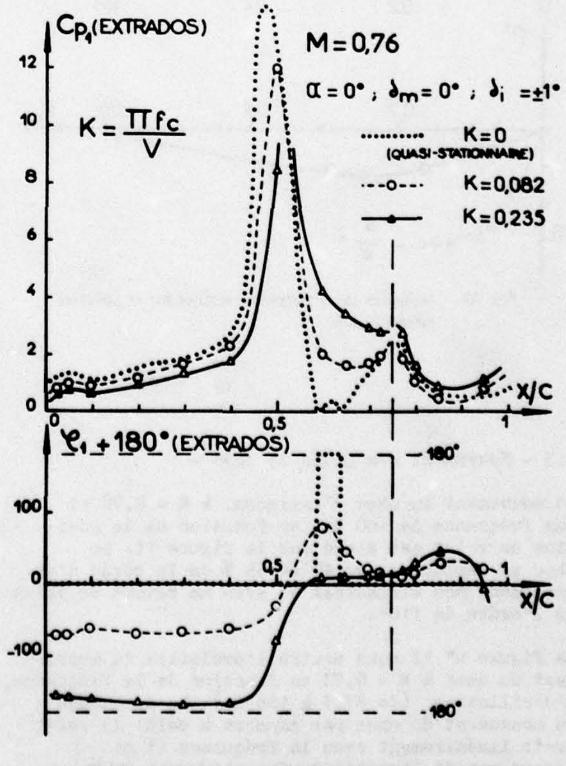

Fig. 9 – Influence de la fréquence réduite sur les pressions instationnaires.

Il faut remarquer que l'évolution du module de C_p en aval du choc est de signe opposé de celle en amont du choc lorsque la fréquence réduite croît.

L'influence de la fréquence réduite sur le coefficient global de portance instationnaire $C_{z\delta}$ est représentée sur la figure 10 pour M = 0,3 et M = 0,76. A M = 0,3 la portance instationnaire $|C_{z\delta}|$ décroît lentement avec une pente plus faible aux fréquences élevées tandis qu'elle diminue très rapidement à M = 0,76. $|C_{z\delta}|$ supercritique devient rapidement inférieur à $|C_{z\delta}|$ subcritique pour K > 0,1.

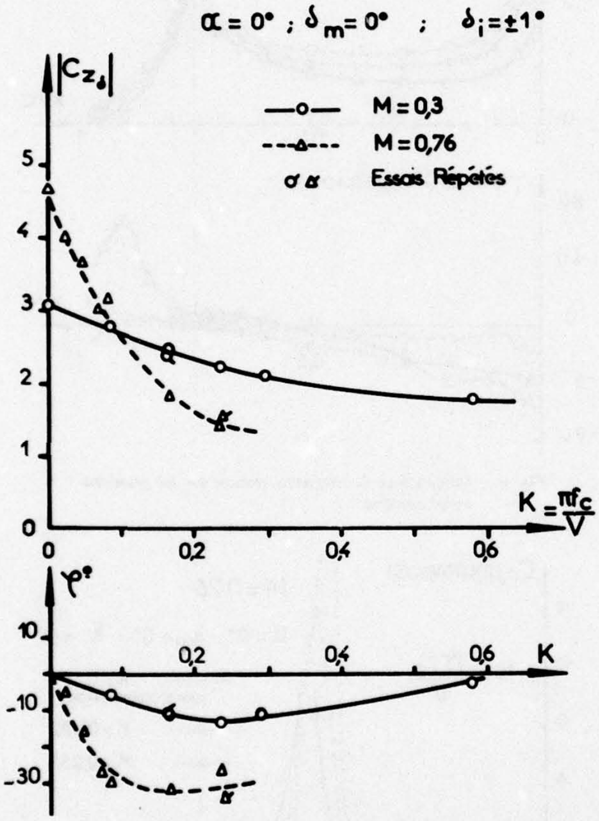

Fig. 10 – Influence de la fréquence réduite sur la portance instationnaire.

3.3 - Mouvement des ondes de choc -

Le mouvement du choc d'extrados, à M = 0,76 et une fréquence de 100 Hz, en fonction de la position du volet est donné par la figure 11. Le choc se déplace entre 47 et 55 % de la corde d'un mouvement non sinusoïdal et avec un retard de phase de l'ordre de 110°.

La figure n° 12 nous montre l'évolution du mouvement du choc à M = 0,73 en fonction de la fréquence d'oscillation (de 67,5 à 106 Hz). Le déphasage du mouvement du choc par rapport à celui du volet croît linéairement avec la fréquence et ne dépend pas de l'amplitude dynamique, de façon analogue à ce qui a été observé réf.[1] et réf.[2].

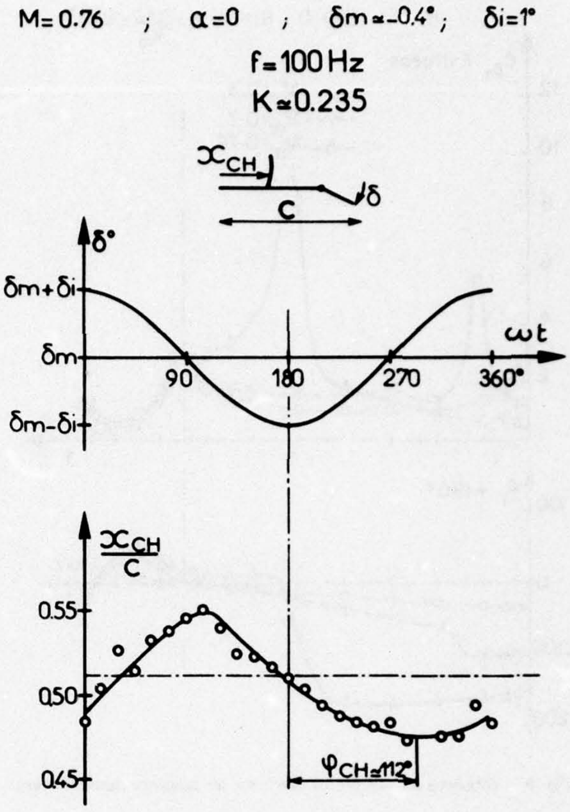

Fig. 11 – Oscillations de l'onde de choc d'extrados.

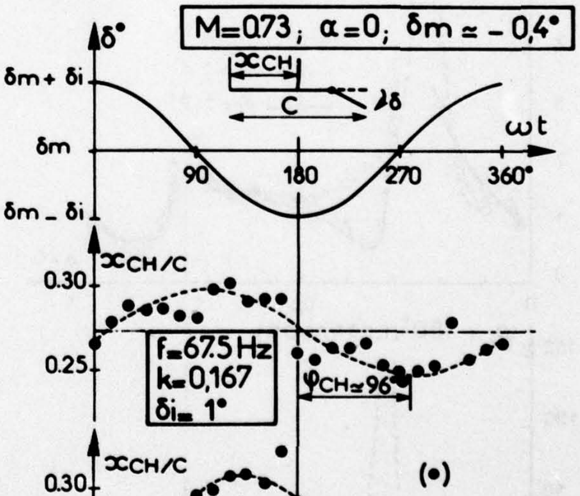

Fig. 12 – Oscillations de l'onde de choc d'extrados.

3.4 - Interactions stationnaire-instationnaire

Les théories linéarisées couramment utilisées en instationnaire comme celle de Théodorsen [réf. 3], ne prévoient pas les effets de cambrure et d'incidence [écoulement moyen]. Elles ne mettent en évidence que l'effet du nombre de Mach et des paramètres instationnaires qui déterminent le mouvement.

En fait, la réponse instationnaire dépend de l'écoulement moyen, même en régime subcritique et pour des oscillations très faibles (1° d'amplitude). Cela est mis en évidence sur les figures 13 et 14 qui présentent les répartitions de pression instationnaire d'extrados à une fréquence réduite et une amplitude d'oscillation données pour trois braquages moyens, respectivement en régime subcritique à M = 0,6 et en régime supercritique à M = 0,73 : lorsque le braquage moyen augmente, accroissant ainsi la charge moyenne de l'aile, les modules des pressions instationnaires diminuent, et les phases évoluent légèrement dans le sens d'une avance. On remarque de plus une forte augmentation des pressions instationnaires au bord de fuite lorsque le volet oscille de plus en plus près du décollement (δm = 2,5° dans le cas présent). En régime supercritique, on observe en plus une translation du pic de la courbe des modules et du saut de la courbe des phases correspondant au déplacement de la position moyenne du choc.

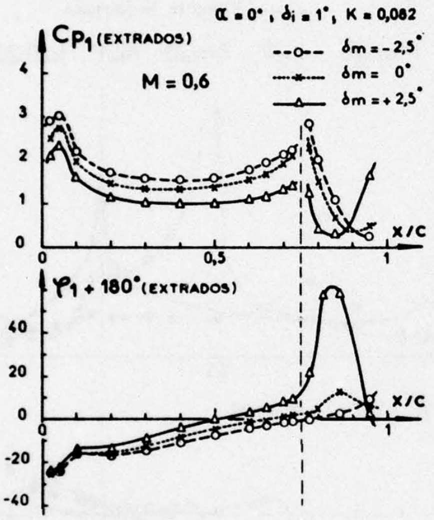

Fig. 13 – Influence du braquage moyen δ_m sur les pressions instationnaires.

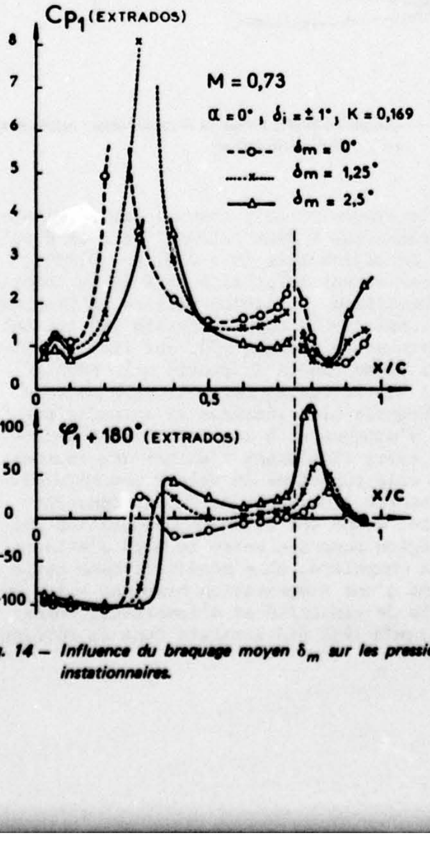

Fig. 14 – Influence du braquage moyen δ_m sur les pressions instationnaires.

La figure 15 présente la portance instationnaire à une fréquence réduite et une amplitude d'oscillation données, en fonction du braquage moyen du volet. On a superposé le cas subcritique à M = 0,3 et le cas supercritique à M = 0,73 pour la même fréquence réduite. Dans les deux cas, la portance instationnaire semble maximale vers δm = - 5°, ce qui correspond à une portance moyenne nulle. Lorsque le braquage moyen et la charge moyenne de l'aile croissent, la portance instationnaire diminue d'abord avec une pente plus forte en régime supercritique qu'en subcritique, puis semble atteindre un palier lorsqu'un décollement apparaît sur le volet (pour un braquage de 2 à 3° à M = 0,73 et de 5 à 7° à M = 0,3).

La phase évolue assez peu, aussi bien en régime subcritique qu'en régime supercritique, tant qu'on est éloigné du décollement. Elle augmente dans le sens d'une avance de phase lorsqu'on approche du décollement, puis diminue une fois que le volet est bien décollé.

On voit que la réponse instationnaire dépend de façon sensible de l'écoulement moyen et que les interactions entre les divers phénomènes sont particulièrement complexes en régime supercritique.

Néanmoins, en régime subcritique, tant que l'on est éloigné des décollements, on voit sur la figure 15 qu'il existe une zone autour du Cz moyen nul, c'est-à-dire pour δm compris entre - 10° et 0° environ, où la portance instationnaire dépend assez peu de l'écoulement moyen. Cela justifie donc l'emploi de théories linéarisées lorsque l'aile est modérément chargée.

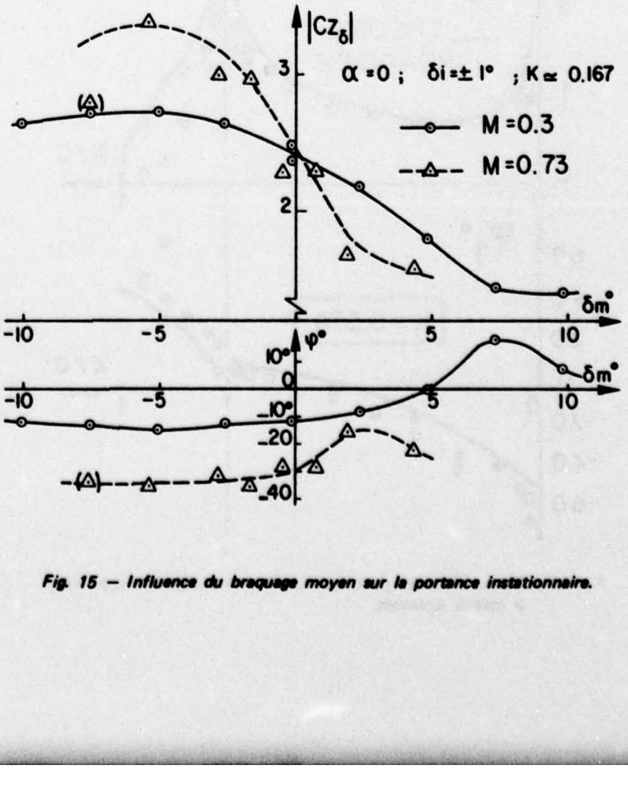

Fig. 15 – Influence du braquage moyen sur la portance instationnaire.

3.5 - Comparaison avec les méthodes de prévision.

Des calculs effectués avec la théorie linéarisée de la plaque plane suivant la méthode de Théodorsen [3] montrent (figure 16) que pour le cas subcritique à M = 0,3, la correspondance théorie-expérience est satisfaisante, bien que la théorie ne fasse pas de différence entre extrados et intrados. Les plus gros écarts en module se trouvent sur le volet à l'extrados; pour la phase l'écart est supérieur à 10° aux fréquences élevées. Cette différence doit être attribuée aux effets de cambrure, d'épaisseur et surtout de viscosité.

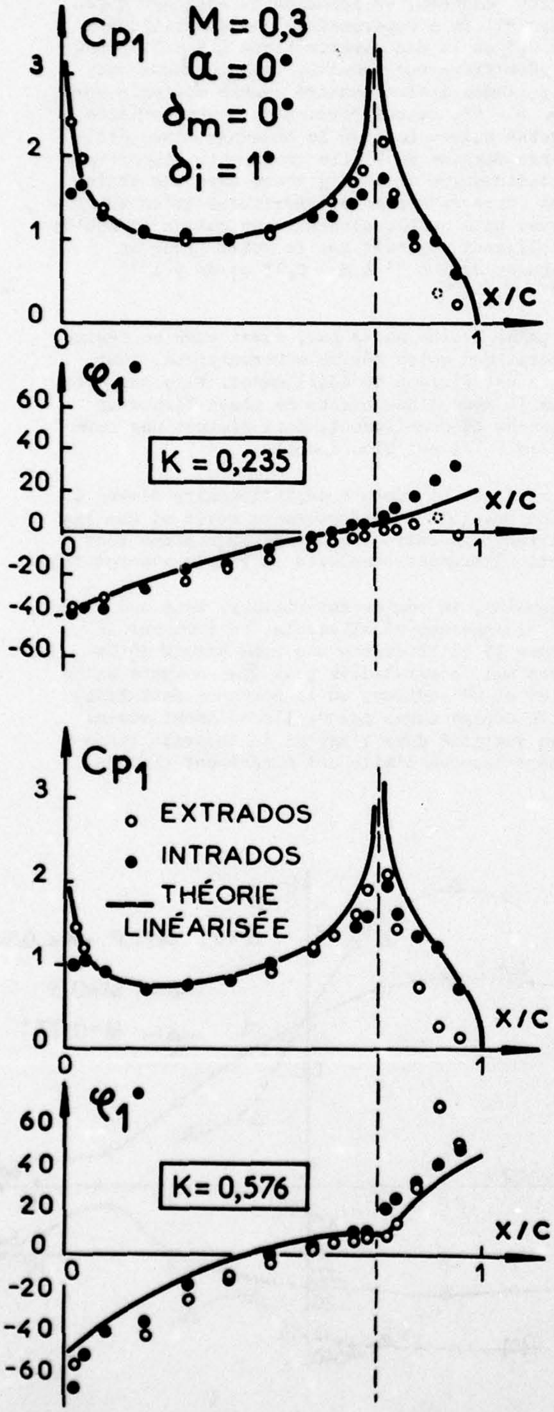

Fig. 16 – Comparaison des pressions instationnaires expérimentales avec la théorie linéarisée.

La même comparaison faite en régime supercritique à M = 0,76 (fig. 17) montre que la théorie linéarisée devient tout à fait inadéquate pour représenter l'évolution des C_p aussi bien en module qu'en phase. Car pour un tel profil les écoulements d'extrados et d'intrados sont très différents.
Si l'on étend cette comparaison à M = 0,76 aux coefficients globaux de portance, de moment de tangage et de moment de charnière instationnaires (fig. 18), on s'aperçoit alors que les écarts théorie-expérience sont très importants, ils atteignent 100 % et plus pour $|C_{mc\delta}|$ l'évolution générale n'est même plus respectée pour les coefficients de moment. A M = 0,3 (fig. 19), la correspondance est meilleure, l'évolution est respectée mais les écarts atteignent 50 % pour $|C_{mc\delta}|$.

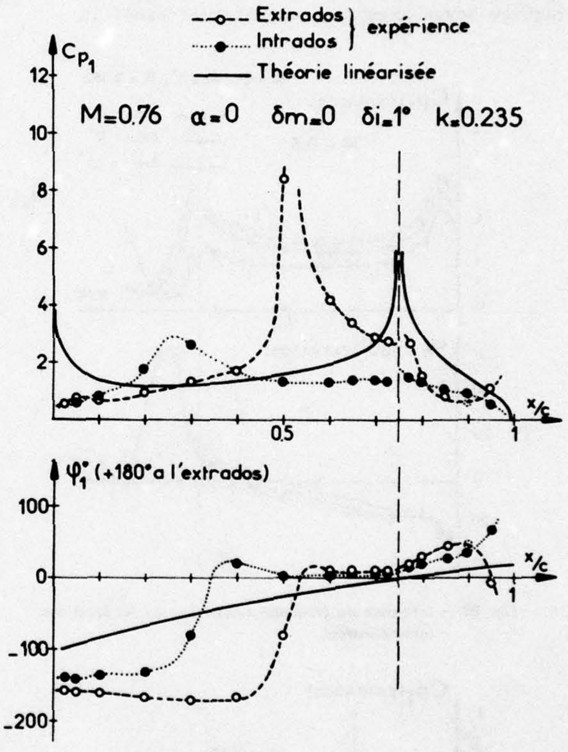

Fig. 17 – Comparaison des pressions instationnaires expérimentales avec la théorie linéarisée.

Sur la figure 20 on a comparé les résultats expérimentaux à deux calculs faits en écoulement incompressible (M = 0,3, K = 0,235), le premier est celui déjà cité de la théorie de Théodorsen, le second utilise un programme développé par la Société Bertin [4] suivant la méthode de Giesing [5], qui tient compte de la forme exacte du profil mais néglige aussi la viscosité. Cette seconde méthode différencie bien intrados et extrados au bord d'attaque et à la charnière et reproduit assez fidèlement l'allure des courbes, mais elle surestime la valeur des modules. La théorie linéarisée de Théodorsen, par contre, donne une bonne représentation dans la région comprise entre le bord d'attaque et la charnière, elle bénéficie dans cette région d'une compensation heureuse entre les effets de viscosité et d'épaisseur, comme cela avait déjà été constaté dans la référence [6].

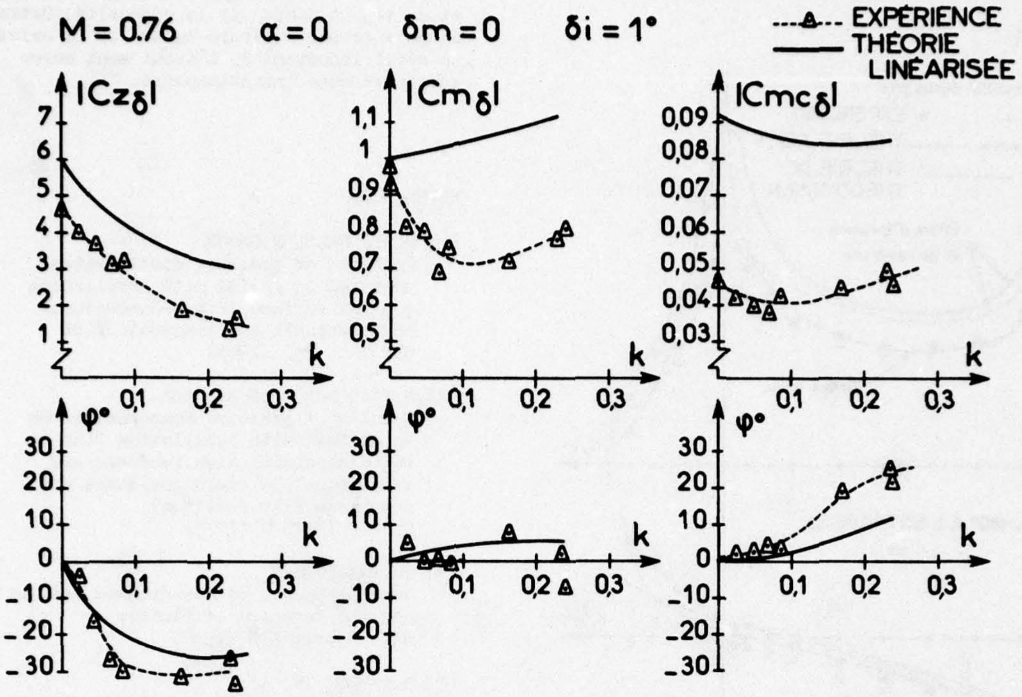

Fig. 18 – Coefficients de portance, de moment de tangage et de moment de charnière instationnaires : comparaison des résultats expérimentaux avec la théorie linéarisée.

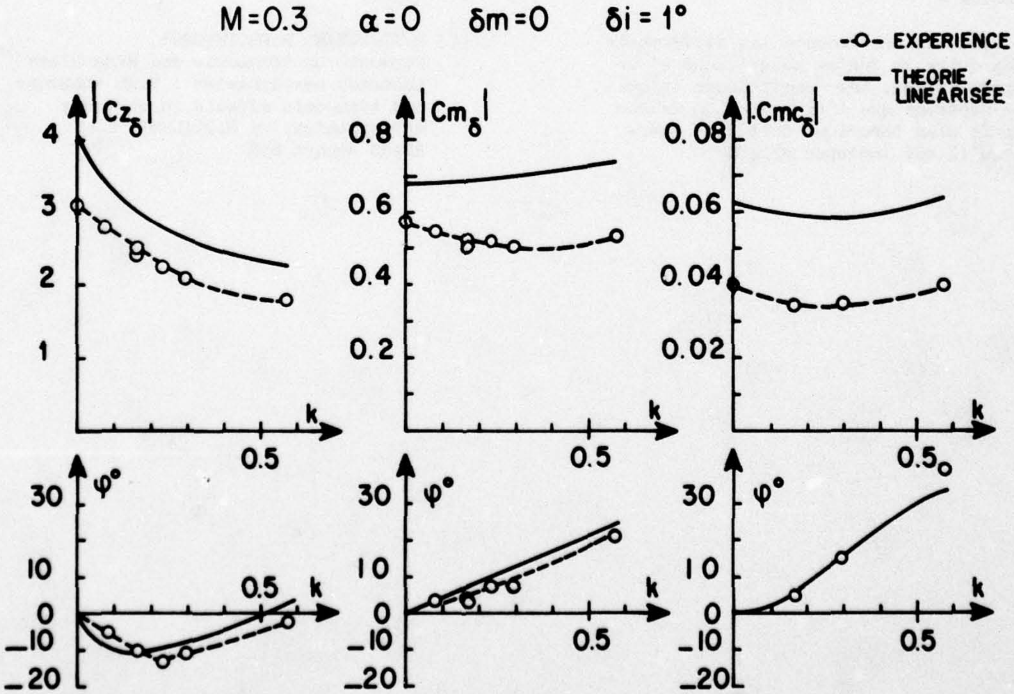

Fig. 19 – Coefficients de portance, de moment de tangage et de moment de charnière instationnaires : comparaison des résultats expérimentaux avec la théorie linéarisée.

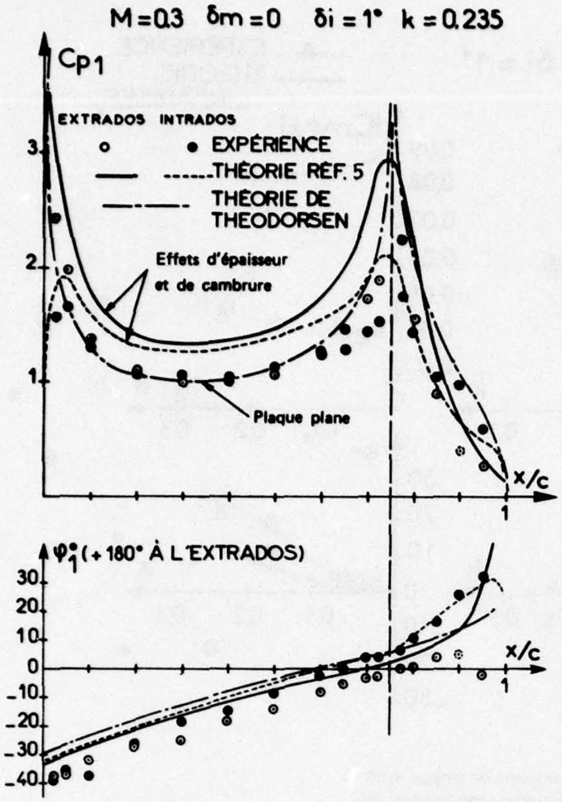

Fig. 20 – Comparaisons calcul – expérience : introduction des effets d'épaisseur et de cambrure dans les calculs.

4 - CONCLUSION -

Ces essais ont mis en évidence les différences importantes entre le régime subcritique et le régime supercritique. Les comparaisons calcul-expérience montrent que l'exploitation de ces essais sur le plan théorique doit être poursuivie et qu'il est indispensable de développer des méthodes de calcul permettant de traiter les cas supercritiques avec choc et en tenant compte de la viscosité. Cette étude aura par ailleurs montré qu'il existe un effet important de l'écoulement moyen sur la réponse instationnaire.

REFERENCES

[1] H.TIJDEMAN, H.BERGH
Analysis of pressure distributions measured on a wing with oscillating control surface in two-dimensional high subsonic and transonic flow
NLR TR F 253 (1963)

[2] H.TIJDEMAN, P.SCHIPPERS
Results of pressure Measurements on an airfoil with oscillating flap in two-dimensional high subsonic and transonic flow (zero incidence and zero mean flap position)
NLR TR 73078 U (1973)

[3] TH.THEODORSEN
General theory of Aerodynamic instability and the Mecanism of flutter
NACA Report 496 (1935)

[4] N.BAUDU, TH. LE
Etude du comportement aérodynamique d'un profil avec gouverne oscillante
Rapport de Synthèse finale - BERTIN note 75 CC 06 (1975)

[5] J.P.GIESING
Non linear two dimensional unsteady potential flow with lift
Journal of Aircraft, vol.5 n° 2 (1968)

[6] H.TIJDEMAN, R.DESTUYNDER
Comments on transonic and Wing store unsteady aerodynamics : High subsonic and transonic effects in unsteady aerodynamics, by H.TIJDEMAN
AGARD Report 636

INVESTIGATION OF THE UNSTEADY AIRLOADS ON WING-STORE CONFIGURATIONS IN SUBSONIC FLOW *

by

J.W.G. van Nunen, R. Roos and J.J. Meijer
National Aerospace Laboratory NLR
Anthony Fokkerweg 2
1059 CM Amsterdam
The Netherlands

SUMMARY

A description and results are given of an extensive research program set up to determine the unsteady aerodynamic loading on oscillating wing-store configurations. It is shown that the tools developed in the course of the program allow for a more accurate prediction of the unsteady airforces introduced by wing mounted stores.

LIST OF SYMBOLS

$[A]$	submatrix of aerodynamic influence coefficients
a	velocity of sound
C_p	unsteady pressure coefficient; $C_p = p_1 s/q_\infty d$
C_y	local side load coefficient ; C_y = side load/$q_\infty \ell$
C_z	local normal load coefficient ; C_z = normal load/$q_\infty \ell$
c	local chord
$\bar{c}$	mean chord
c_r	root chord
d	displacement of reference point ($x/c = 0.871$, $y/s = 0.143$)
f	frequency ; $f = \omega/2\pi$
k	reduced frequency ; $k = \omega s/U_\infty$
ℓ	reference length ; wing : $\ell = c$, body : ℓ = max.diam.
M	Mach number
p_1	unsteady pressure
p_o	stagnation pressure
$\vec{q}$	velocity vector
q_∞	dynamic pressure
S	surface of wing or body
s	semi span
t	time
U_∞	free stream velocity
x,y,z	right-hand cartesian coordinate system
ΔC_p	unsteady pressure jump between the lower and upper wing surface
δ	angular coordinate on the body
σ	source strength
ϕ	velocity potential
φ	perturbation velocity potential
ω	oscillation frequency

Superscripts

B	referring to the body
D	referring to the lifting surface
'	referring to the component in phase with the motion
''	referring to the component in quadrature with the motion

Subscripts

o	referring to the steady flow field
1	referring to the unsteady flow field
∞	referring to the freestream conditions

---

* This investigation was carried out under contract for the Scientific Research Division, Directorate of Materiel, RNLAF.

1 INTRODUCTION

In the last decade the development of military aircraft has shown a clear tendency towards larger stores, being carried in close proximity to the wing and the fuselage. To investigate the implications of this on the aeroelastic characteristics of an aircraft (flutter, gust response and manoeuvring loads), the NLR has carried out an extensive research program. This program was focussed on an accurate determination of the unsteady aerodynamic loading on complex wing-store configurations. It consisted of three distinct parts:

1. the development of a calculation method to compute the unsteady loading on such oscillating configurations.
2. unsteady pressure measurements on an oscillating wing-tiptank-store windtunnel model.
3. the verification of the calculation method in a series of flutter tests, both with the (adapted) windtunnel model and with the real aircraft.

In this paper the different facets of this research program are touched upon. First a short outline of the calculation method is given, followed by a description of the experimental investigation on the unsteady pressure distributions. Results of these tests are shown in a comparison with theoretically obtained unsteady pressure and load distributions. Finally, both flutter experiments are described and their results are compared with flutter data obtained by using theoretically determined aerodynamic loads.

2 THE "NLRI" CALCULATION METHOD

2.1 General observations.

Until recently the unsteady loading on oscillating airplane configurations was approximated by "thin wing theory", such as lifting surface or lifting lattice techniques. The effects introduced by the fuselage and / or the stores were neglected or taken into account by using slender body theory. Kalman, Roddan and Giesing (Ref. 1) were the first to attempt a more thorough computation of wing/body interference effects. Lately, their original ring-wing concept as applied in the doublet lattice method has evolved into a more complete method (ref. 2), which can be expected to produce satisfactory results as far as unsteady aerodynamic coefficients are concerned. Recently, Morino et al (ref. 3 and 4) have developed a computer program, which can treat complex configurations in steady and unsteady, subsonic and supersonic flow. As far as unsteady flow is concerned, an evaluation of both methods still awaits a comparison with experimental data for a complex wing/body configuration.

The method developed at NLR (NLRI-method) is set up to meet two requirements. It should provide:

1. the unsteady aerodynamic forces on wing/body configurations for aeroelastic analysis
2. detailed pressure distributions to support unsteady windtunnel measurements and to obtain more information about the distribution of the loading over the configuration.

This means that the method has to compute both local and overall aerodynamic coefficients and generalized aerodynamic coefficients as well as detailed pressure distributions on both the body and the wing. These requirements have been met by combining the already existing doublet lattice method with an unsteady source panel method.

The next chapter gives a short outline of the NLRI-method. For a more detailed description of the method and its formulations, the reader should consult references 5 and 6.

2.2 Outline of the method.

The flowfield about a configuration is described with a velocity potential $\phi = U_\infty x + \varphi$. The perturbation potential φ satisfies the linearized equation:

$$(1-M_\infty^2)\varphi_{xx} + \varphi_{yy} + \varphi_{zz} - \frac{1}{a_\infty^2}\varphi_{tt} - \frac{2M_\infty}{a_\infty}\varphi_{xt} = 0 \qquad (1)$$

The flow is assumed to remain tangential to the surface of the configuration as is expressed by the boundary condition

$$\frac{DS}{Dt} = \frac{\partial S}{\partial t} + q.\nabla S = 0 \quad (S = 0) \qquad (2)$$

in which $S(x,y,z,t) = 0$ describes this surface. The configuration is taken to perform harmonic oscillations about a steady mid-position. Therefore the perturbation potential φ is split into a steady part φ_o and an unsteady part $\varphi_1 e^{i\omega t}$. This results in a decoupling of the steady and the unsteady flowfields, for which the governing equations can be reduced to the Laplace equation and the Helmholtz equation respectively. The solution for both flow fields can be found in terms of an integral over a source distribution on the surface of the configuration and a dipole distribution on the camber surface and the wake. The strength of these distributions is found by applying boundary condition (2) in which now S represents the surface of the harmonically oscillating surface.

The result is a set of integral equations for both the steady and the unsteady flowfield, of which for practical applications a solution can be found only with a panel method approach.

The approach used here is a combination of a lifting lattice method for the lifting surfaces and a constant source panel method for the bodies. In particular for the unsteady flowfield the choice fell on the well-known doublet lattice method and an unsteady source panel method of the type described by Hess (ref.7). The doublet lattice method is chosen because of its established success and flexibility in applications on interfering lifting surfaces. The constant source panel method is preferred in view of the experience available at the NLR with this method for steady flowfields.

With the discretization in panels the integral equations are reduced to sets of algebraic equations which in matrix form read:

$$\left[\begin{array}{c|c} A^{BB} & A^{BD} \\ \hline A^{DB} & A^{DD} \end{array}\right] * \left[\begin{array}{c} \sigma \\ \hline \Delta C_p \end{array}\right] = \left[\begin{array}{c} F^B \\ \hline F^D \end{array}\right] \qquad (3)$$

with σ being the yet unknown source strengths on the body panels (B) and ΔC_p the group of lifting line strengths (equivalent to the pressure jump across the surface) for the 1/4-chord lines of each lifting surface panel (D). F^B and F^D stand for the prescribed normal velocity (boundary condition) in all collocation points of respectively the body and lifting surface panels. The matrix of aerodynamic influence coefficients is partitioned into four submatrices. The coefficients in the submatrices $[A^{BB}]$ and $[A^{DB}]$, which represent the normal velocity induced by a body panel with a unit source strength, are computed with the formulations of the constant source panel method for respectively steady and oscillatory flow. The coefficients in the submatrices $[A^{BD}]$ and $[A^{DD}]$ represent the normal velocity induced by a lifting surface panel with a lifting line of unit strength. These are computed following the lines of the vortex and doublet lattice methods.

For the solution of the matrix equation a method is used based on the expected properties of the sub-matrices. First the subset of equations containing $[A^{BB}]$ is solved with an iterative Gauss-Seidel process. Then, the residue is determined and used to solve the set containing $[A^{DD}]$ with a direct Crout process. The residue is determined again and the process is started from the beginning. This iteration process is repeated several times until the increment, which during each run is added to the solution of σ and ΔC_p has become smaller than a certain value. A relaxation factor takes care of large oscillations during the first few iteration steps.

From the computed source strength σ the velocity and pressure distribution on the bodies can be determined while the pressure jump ΔC_p across the lifting surfaces is known already. Integration leads to both local and overall aerodynamic coefficients.

A schematic diagram, indicating the important steps in the calculation method is given in figure 1. As was mentioned before dividing the perturbation potential in a steady and an oscillatory part results in a decoupling of the steady and unsteady flowfields. As indicated in figure 1, the coupling is restored if in the unsteady boundary condition and the expression for the unsteady pressure at the body surface the effects of the local changes in the steady flowfield due to the presence of the bodies are taken into account. The realization of this coupling requires the computation of second order derivatives of the steady perturbation potential, which on certain parts of the configuration turn out to violate the small perturbation assumption (the first derivative remains small). Clearly a constant source panel method is not suited to compute higher order derivatives. Therefore in the computations which yielded the results mentioned in this paper, the coupling was ignored, which means that first order boundary conditions and pressure formula were used.

3 UNSTEADY WINDTUNNEL MEASUREMENTS

3.1 The experiment.

To obtain an insight into the aerodynamic consequences of the addition of stores on a wing oscillating in subsonic flow and further to have a first check on results computed with the NLRI-method, a windtunnel experiment was performed. The model concerned was a swept tapered wing equipped with a tiptank and a detachable under-wing store (see figure 2). A sketch of the model, showing the planform and its overall dimensions is given in figure 3.

The model could be driven into sinusoidal pitching oscillations with adjustable frequencies and two locations of the pitch axis (15% and 50% of the rootchord). To determine the vibration mode of the model during the tests, the wing and stores were equipped with miniature accelerometers. Using the NLR unsteady pressure measuring system, which employs pressure tubes connected to scanning valves, a detailed mapping of the unsteady pressure distribution was obtained on the wing as well as on the tiptank and the store. The number of pressure orifices totalled 160 on the wing, 78 on the tiptank and 86 on the under-wing store. Dynamic calibration of the measuring system was provided by some miniature pressure transducers built in the wing.

The measurements were carried out for several combinations of Machnumber, frequency and pitch axis location. Further,all tests were run for two model configurations: wing with tiptank and wing with tiptank and under-wing store.

A more detailed description of the experiment was given by Renirie (Ref. 8), who also presented some preliminary data. In this paper a few additional results, taken from reference 6, are shown. Here the data are used as a check on the results obtained with the aforementioned NLRI-method.

3.2 Comparison of experimental and theoretical results.

The results presented next concern both configurations, with and without store, pitching about the 15% chord axis with a frequency of 11 Hz at a Machnumber 0.45.

For the wing with tiptank figure 4 contains the chordwise distribution of the unsteady pressure jump ΔC_p across the wing in a section close to the tiptank. The experimental data are seen to be in satisfactory agreement with the theory. Since the model tiptank was not detachable its influence could not be determined separately, but the computed results for the wing with and without tiptank show this influence clearly. Apparently addition of the tiptank results in an increase of the pressure jump near the wing tip.

The measured and calculated pressure distribution in axial direction on the tiptank (fig. 5) shows a rather good agreement except at the rear where in reality separation is present. Both theory and experiment show the influence of the wing in terms of the relatively large pressures near the attachement position. Integration of the pressure distribution in angular direction leads to the unsteady normal force distribution presented in figure 6.

Figure 7 shows the spanwise unsteady normal load distribution for the two different configurations. The theoretical curves show that the tiptank acts as an endplate, preventing the loading to go to zero at the tip. Addition of the pylon and store under the wing is seen to introduce a jump in the spanwise load distributions. This jump indicates that circulation is carried off by the pylon towards the store. As a result of this, the pylon and store will experience an outward pointing side load. Although the magnitude of the jump and the trend of the theoretical and experimental curves are about the same, the overall level of the measurements is somewhat lower, at least for the in phase loading. This feature is common for "flat plate" theories, which exhibit an infinite pressure peak at the leading edge.

An example of an unsteady pressure distribution along the under-wing store is given in figure 8. The agreement between experiment and theory is rather satisfactory except near the rear of the store,where separation is present. The calculations made for the isolated store and the wing with the store only show that the presence of the wing and pylon introduces a marked interference, which is largest near the attachment of the pylon with a maximum near the wing leading edge. Adding the tiptank has only a marginal effect.

In figure 9 and 10 the normal and side load distributions along the store are presented for the same three configurations. On the isolated store the normal load distribution is antisymmetrical, reflecting the fact that the front and rear end are identical. In figure 10 the isolated store is missing since for a rotational symmetric body the side load is zero. Interference effects introduced by wing and pylon are clearly visible in both figures. The side load on the store is in agreement with the observations made on the jump in the normal load distribution on the wing.

When comparing the load distributions on the wing, the tiptank and the store it is essential to notice that they are nondimensionalized in a different way. The scaling factors are given in the figures. For the case considered here(15% pitch axis)it is found that the loading on the tiptank and store is of the order of 7% to 10% of the wing loading. However, as will become evident in the last part of this paper, this does not necessarily mean that these loadings can be neglected in aeroelastic calculations.

4 FLUTTER TESTS

4.1 General.

Considering the reasons for developing the NLRI-method, a further check on the quality of the results of this method was obtained by applying them in a flutter investigation. To acquire data for comparison, flutter experiments were carried out on complex configurations to which it was sensible to apply the NLRI-method. These experiments consisted of flutter test in the windtunnel on the model previously used for the unsteady pressure measurements, as well as a series of flight tests with the aircraft on which the model was based (except for a difference in under-wing store). In the following these tests are discussed shortly and the data are compared with results of flutter calculations with aerodynamic input from the NLRI-method.

4.2 Model experiments.

To convert the model, used for the pressure measurements, into a simple flutter model its suspension mechanism was modified (see fig. 11). The root of the model was suspended in a set of elastic springs resulting in a two degree of freedom system: pitch and roll. The stiffness of the springs was designed such, that a flutter condition could be reached within the test limits of the variable density windtunnel HST of the NLR. A further requirement set to the stiffness of the springs was that the resonance frequencies of the model remained within the range of frequencies covered in the earlier unsteady pressure measurements. Moreover, at these frequencies the model itself could be regarded as almost stiff thus leading to rather simple vibration modes.

In order to get as complete a check on the NLRI-procedure as possible the model was tested in three different configurations: the plain wing, the wing with tiptank and finally the wing with tiptank and under-wing store. All three configurations were tested at about the same resonance frequencies and vibration modes. This was achieved by replacing the tiptank and the pylon-store combination, when not present, by additional masses outside the airstream, thus keeping the inertia characteristics the same. In this manner all differences in the flutter behaviour of the three configurations should in principle be attributed to the variations in the unsteady aerodynamics as caused by the presence of the bodies and not to the combined variation of unsteady aerodynamics and inertial characteristics.

Finally the flutter experiments were carried out at a constant Mach number but varying stagnation pressure. The Mach number was fixed at $M_\infty = 0.7$ in order to avoid transonic effects, which are not included in the unsteady aerodynamic theory.

The results of the flutter experiments performed on the three configurations are gathered in figure 12. This flutter diagram gives the behaviour of the hysteresis damping and frequency of the various modes as a function of the stagnation pressure at a constant Mach number. It should be mentioned that the results shown are obtained by averaging the data of several repeated tests. Further, all windtunnel tests were carried out for conditions below the actual flutter points. The latter were determined by applying the method of Zimmerman and Weissenburger (ref. 9).

From figure 12 it can be observed that the flutter behaviour of the three configurations is very different indeed. While the two frequencies and the damping for the bending mode remain relatively unaffected by the change in configuration, the damping for the torsion mode and the predicted flutter point vary considerably. The more complex this configuration becomes, the lower the damping in torsion and the lower the stagnation pressure required for flutter will be. Evidently this effect is caused by the unsteady aerodynamic loads generated by the external bodies, for the differences in inertial characteristics between the various configurations are made negligibly small.

A comparison between the theoretical and experimental flutter characteristics is presented in fig. 13 through 15. In the first plot (fig. 13) the flutter diagram is shown for the bare wing. As can be expected the agreement between computed and measured flutter behaviour is rather good. Both resonance frequencies and the development of the corresponding dampings are predicted very well. Only at higher stagnation pressures a small difference between theoretical and experimental results can be observed. Then the two vibration modes appear to couple less in theory than in the experiment and as a consequence the theoretical flutter point occurs at a higher stagnation pressure than when predicted on the basis of the subcritical experimental data points. Thus the unsteady aerodynamic forces appear to be a little more effective than predicted by theory. In this respect it should be noted that when the results are transformed to actual flight speed, these differences amount to not more than about 3 per cent. This means that for the purpose of flutter speed prediction an excellent agreement is obtained.

The theoretical and experimental flutter results for the configuration of the wing with tiptank are compared in figure 14. Although the trend is predicted correctly, the agreement is not as good as in the case above. The theory predicts flutter to occur at a lower stagnation pressure than indicated by the experimental data. Apparently, the unsteady aerodynamic forces are slightly overestimated by the theory.

To find out to what extent the unsteady aerodynamic forces generated by the tiptank itself contribute to the flutter behaviour of the present configuration, additional calculations were performed in which the unsteady aerodynamic loads on the tiptank were omitted. The unsteady interference loads from the tiptank onto the wing were not excluded. Although the flutter characteristics develop in the same manner as before (fig. 14), the difference in the damping curves of the two vibration modes is remarkable. The stagnation pressure at which flutter is predicted has shifted considerably: from about $p_o = 1.53$ bar for the case the unsteady loads on the tiptank are taken into account to about $p_o = 1.76$ bar for the case these loads are omitted from the calculations. Apparently the unsteady aerodynamic loads on the tiptank decrease the dynamic pressure at which flutter is encountered by about 12%.

The flutter results for the wing with tiptank and pylon-store combination, are presented in fig. 15. When comparing the experimental data with the results predicted by theory, again a rather good agreement is found, be it that the experiments lead to a lower flutter stagnation pressure than predicted by theory. For this configuration the unsteady aerodynamic loads are slightly underestimated by the theory.

For this configuration also it was analysed to what extent the flutter characteristics are governed by the unsteady aerodynamic loads on the externally mounted bodies. To that end two sets of additional calculations were performed: firstly, flutter calculations in which the unsteady aerodynamic loads on both the tiptank and the store were omitted and secondly calculations with only the unsteady loads on the tiptank omitted.
In both cases the interference loads from tiptank and store onto the wing were taken into account. The results of these calculations are incorporated in fig. 15. As can be expected from comparison with the previous configuration, the omittance of the unsteady loads on the external bodies leads to more stable configurations. When the aerodynamic forces on the tiptank are omitted, the stagnation pressure at which flutter is predicted goes up from about $p_o = 1.3$ bar to about 1.5 bar. Neglecting the aerodynamic loading on the under-wing store also, causes the pressure to rise to about $p_o = 1.65$ bar, which compared to the complete configuration means an increase of 25 per cent. Comparing these figures it may be observed that some 40% of the difference between the configuration with and without external bodies can be attributed to the unsteady aerodynamic loads on the store under the wing. Evidently the remaining 60% of the difference is due to the unsteady loads on the tiptank. The cause for this is very much related to the location of the two bodies as compared to the two vibration modes of the model.

4.3 Flight tests.

The flight flutter tests were performed on a fighter airplane of which the wings were equipped with a tiptank and two external stores mounted at two separate wing stations: an outboard and an inboard station. The test data were gathered at a constant altitude and varying Mach number.

The two basic vibration modes that are important here are: first wing bending and first wing torsion. In both cases the tiptank exhibits a considerable amount of pitch roughly about its midpoint.

An illustrative result of these flight flutter tests is presented in fig. 16. It concerns the flutter characteristics for a flight Mach number of $M_\infty = 0.8$. The theoretical results in figure 16 have become available from flutter calculations in which various assumptions were made with respect to the unsteady aerodynamic forces taken into account. First of all calculations were made in which the unsteady loads on the external bodies were neglected. A comparison of these theoretical results with the experimental data reveals, that especially for the damping values the theoretical prediction is rather poor. However, adding the unsteady aerodynamic forces on the tiptank brings the theoretical values of the damping for both the bending and the torsion mode much more in agreement with the experimental values. A further expansion of the unsteady aerodynamic forces with those on the inboard and outboard store on the other hand hardly modifies the result obtained already. It may be concluded that in this case unsteady forces generated by the underwing stores hardly contribute to the flutter behaviour of the airplane. Apparently this is due to the fact that the vibration modes under concern both have a considerable and effective displacement in the region of the tiptank, whereas at the location of the inboard and outboard store the amplitude of vibration is rather small .

5 CONCLUSION

In the present paper a description is given of an extensive investigation of the unsteady airloads on wing-store configurations oscillating in subsonic flow and of their effect on the flutter characteristics. This has resulted in a theoretical method to predict these unsteady airloads, which is verified by two different types of experiments: unsteady pressure measurements and flutter tests in both the windtunnel and free flight. It is found that reliable predictions can be obtained and that the unsteady aerodynamic loads on the external bodies, although being small in comparison with the unsteady loads on the wing, may influence the flutter characteristics greatly.

6 REFERENCES

1. Kalman, T.P., Rodden, W.P. and Giesing, J.P. — Application of the doublet lattice method to nonplanar configurations in subsonic flow. J. Aircraft, Vol.8, No. 6, 1971, pp 406-413.

2. Giesing, J.P., Kalman, T.P. and Rodden, W.P. — Subsonic steady and oscillatory aerodynamics for mutiple interfering wings and bodies. J. Aircraft, Vol.9, No. 10, 1972, pp 693-702.

3. Morino, L. — A general theory of unsteady compressible potential aerodynamics. NASA CR-2464, Dec. 1974.

4. Tseng, K. and Morino, L. — Fully unsteady subsonic and supersonic potential aerodynamics of complex aircraft configurations for flutter applications. Proc. AIAA/ASME/SAE 17th Struc. Dyn. and Materials Conf., King of Prussia, Pa, May 1976, pp 626-638.

5. Bennekers, B., Roos, R. and Zwaan, R.J. — Calculation of aerodynamic loads on oscillating wing/store combinations in subsonic flow. AGARD Specialists Meeting on Wing-with-Stores Flutter, CP-162, Paper No. 4, Munich, 1974.

6. Roos, R., Bennekers, B. and Zwaan, R.J. — Calculation of unsteady subsonic flow about harmonically oscillating wing/body configurations. J. Aircraft, Vol. 14, No. 5, 1977, pp 447-454.

7. Hess, J.L. — Calculation of acoustic fields about arbitrary three-dimensional bodies by a method of surface source distributions based on certain wave number expansions. Douglas Aircraft Comp., Long Beach, Calif., DAC 66901, March 1968.

8. Renirie, L. — Analysis of measured aerodynamic loads on an oscillating wing-store combination in subsonic flow. AGARD Specialists Meeting on Wing-with-Stores Flutter, CP-162, Paper No. 5, Munich, 1974.

9. Zimmerman, N.H. and Weissenburger, J.T. — Prediction of flutter onset speed based on flight testing at subcritical speeds. J. Aircraft, Vol. 1, No. 4, 1964, pp 190-202.

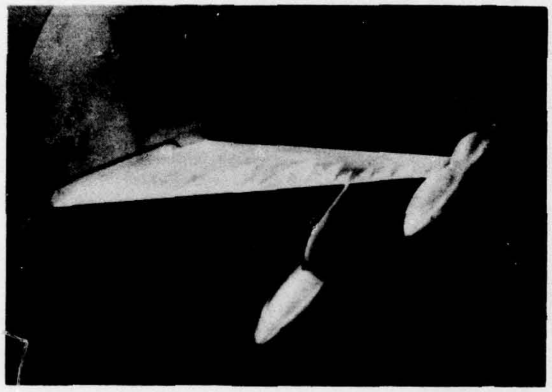

Fig. 2 Model of the wing with tip tank and store mounted in the testsection of the wind tunnel

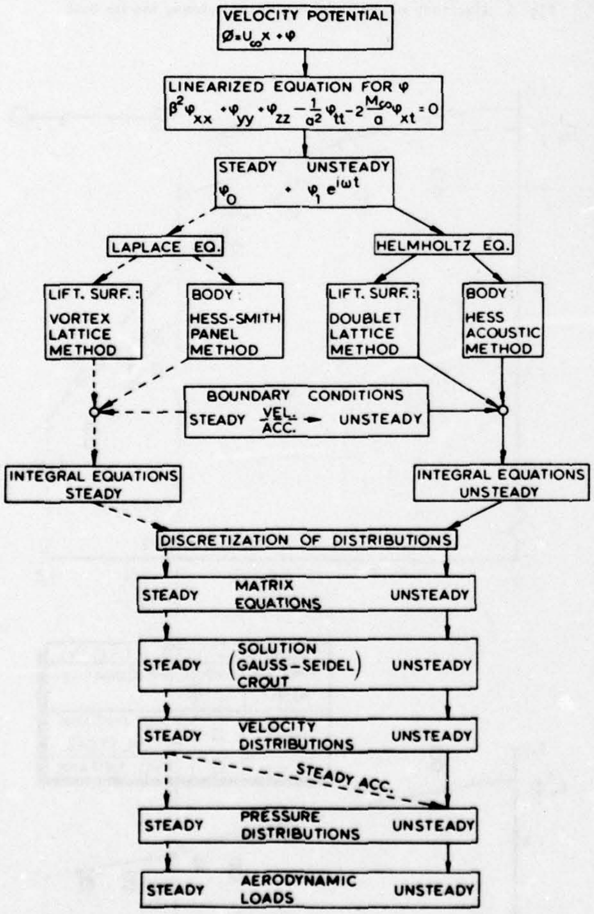

Fig. 1 Schematic outline of the NLR1 –method

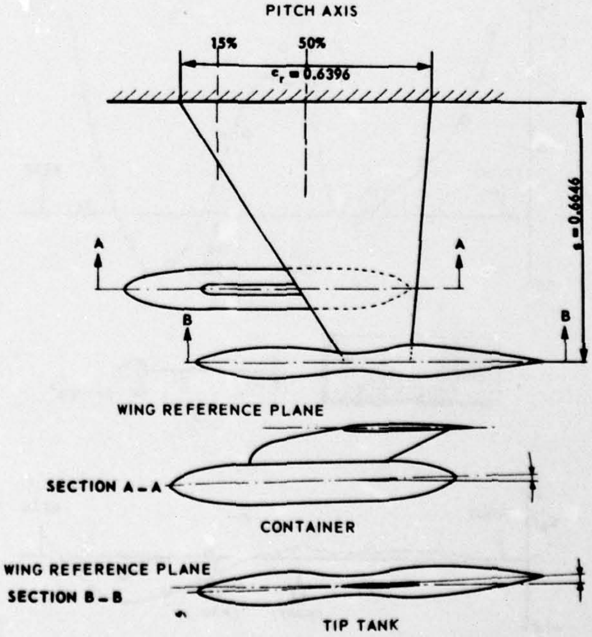

Fig. 3 Sketch of the wing/tip tank/store configuration

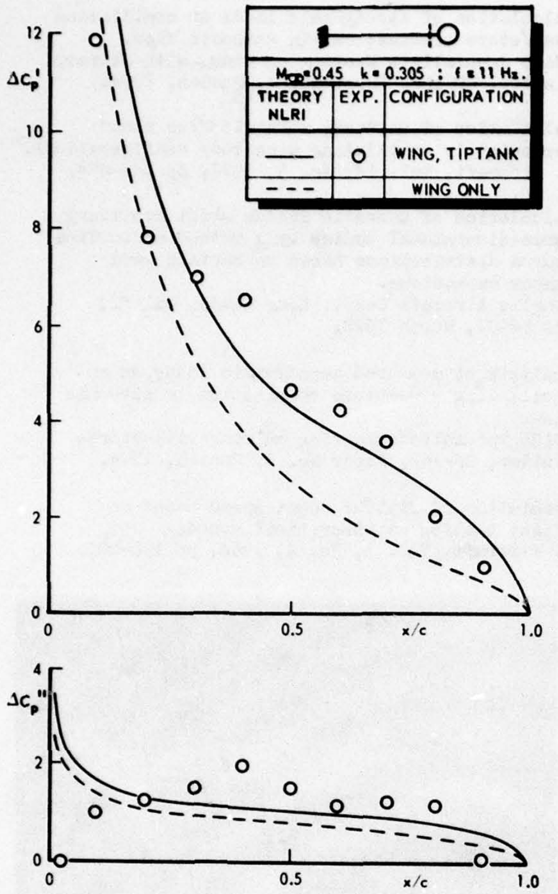

Fig. 4 Chordwise distribution of the unsteady pressure jump across the wing near the tip tank

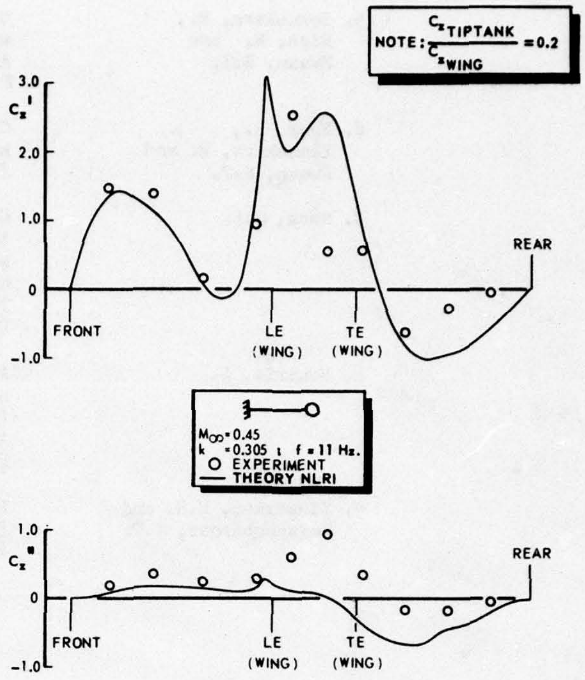

Fig. 6 Unsteady normal load distribution along the tip tank

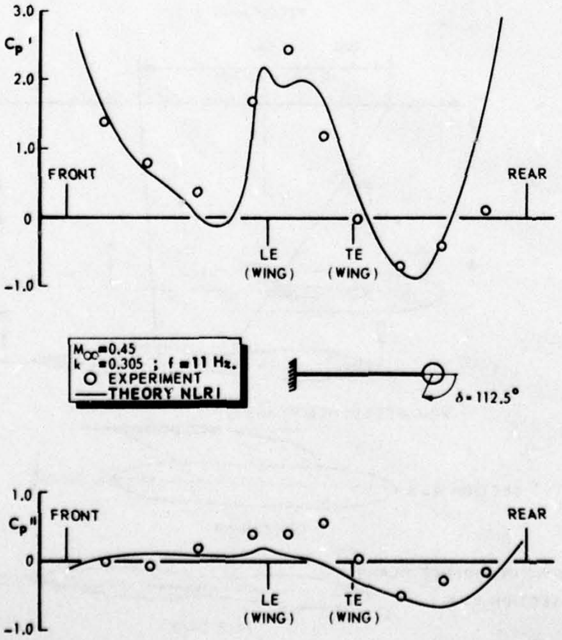

Fig. 5 Unsteady pressure distribution along the tip tank

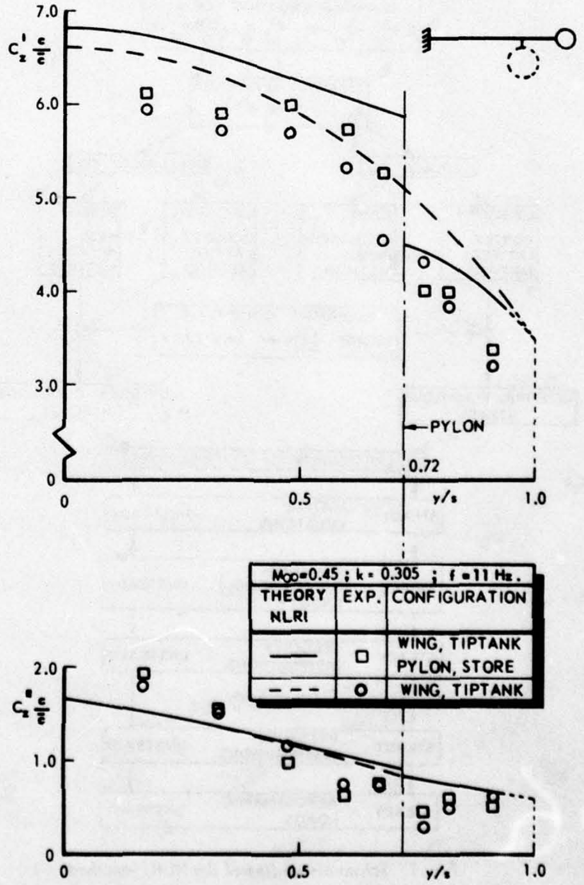

Fig. 7 Normal load distribution on the wing for the different configurations

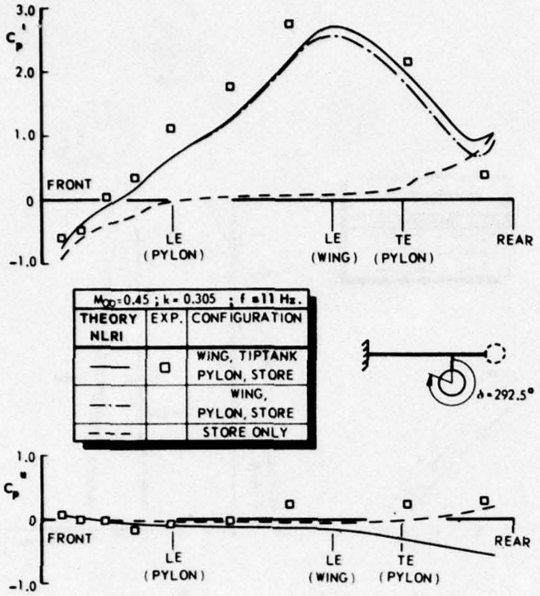

Fig. 8 Unsteady pressure distribution along the store

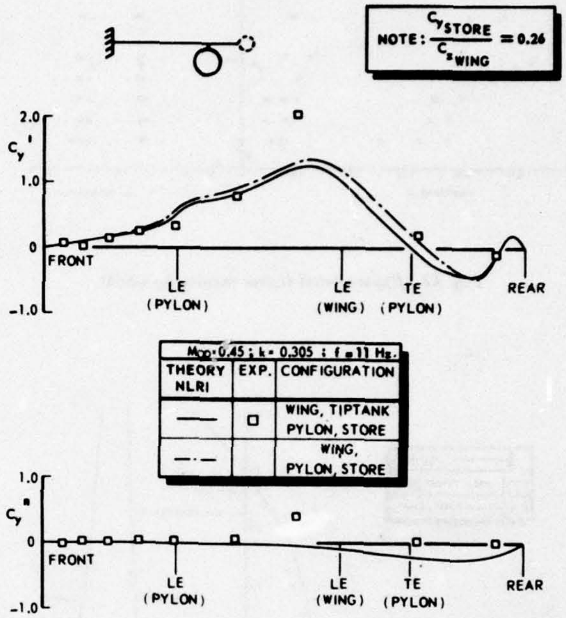

Fig. 10 Unsteady side load distribution along the store

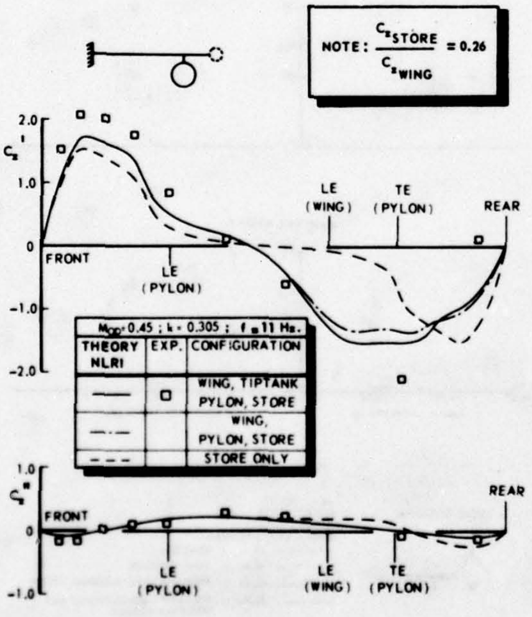

Fig. 9 Unsteady normal load distribution along the store

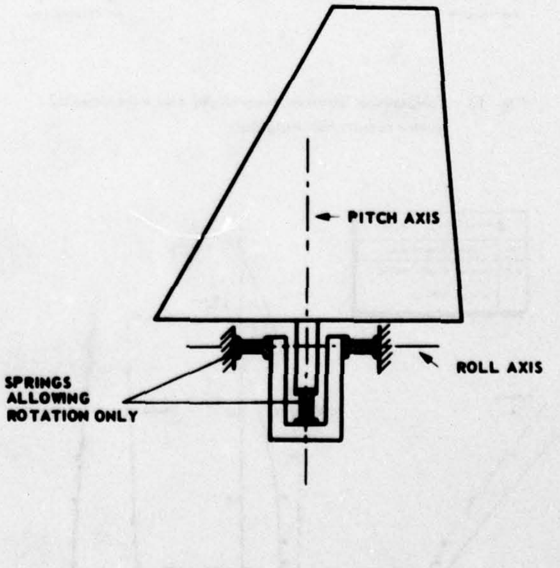

Fig. 11 Sketch of fluttermodel

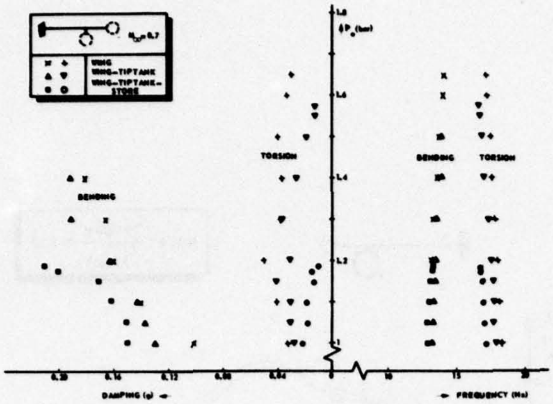

Fig. 12 Experimental flutter results for model

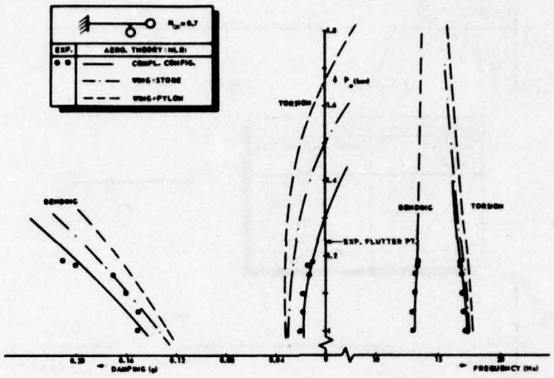

Fig. 15 Comparison between theoretical and experimental flutter results for wing with tip tank and underwing store

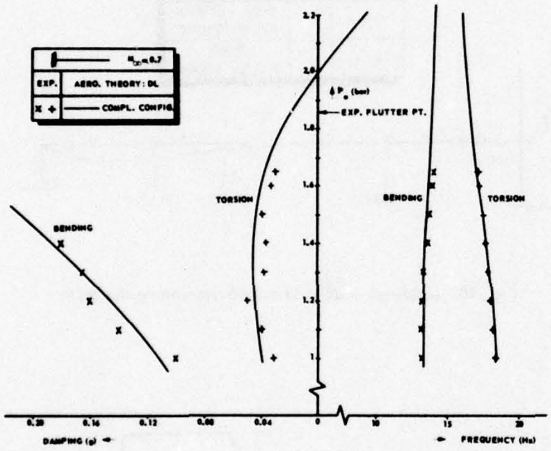

Fig. 13 Comparison between theoretical and experimental flutter results for wing only

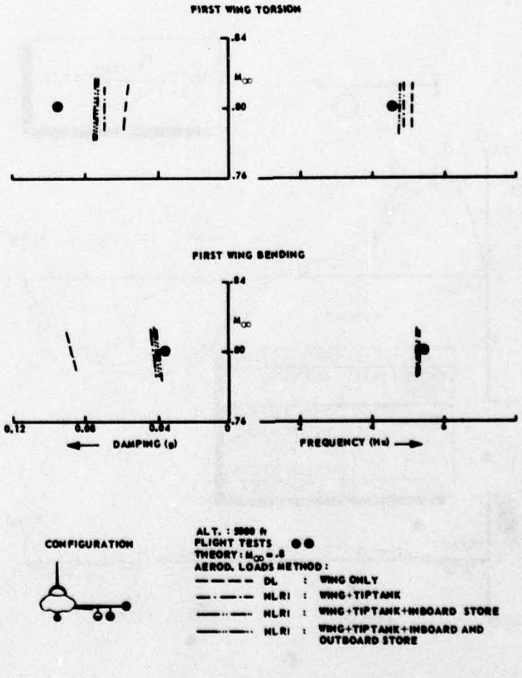

Fig. 16 Comparison of theoretical and experimental flutter results for aircraft equipped with stores

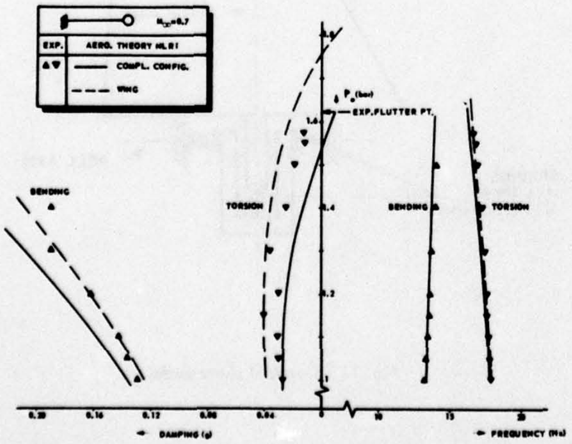

Fig. 14 Comparison between theoretical and experimental flutter results for wing with tip tank

PAPER No. 10 – A review paper for Session II on Unsteady Transonic Flow by Dr H.Tijdeman, was not provided by the author for publication in the Conference Proceedings.

The material presented in Dr Tijdeman's Symposium paper is part of that contained in his recent dissertation entitled "Investigations of the Transonic Flow Around Oscillating Airfoils", NLR Report TR 77090. Interested readers are referred to Dr Tijdeman's dissertation.

COMMENT

by

T.Hsieh
Sverdrup
ARO, Inc. AEDC Division
Arnold Air Force Station
Tennessee 37389
USA

First, I would like to congratulate Dr Tijdeman for his excellent review paper. In some of your slides, you showed good agreement in the unsteady surface pressure data obtained by using pressure tubes and in-situ transducers in both subsonic and transonic flow regimes. I think this is an important contribution because the tube system can reduce the initial cost of the test and is more convenient to set up. Would you please comment about: (1) what difficulties that one would expect in using the tube system? (2) What is the procedure to obtain the transfer function? Is it time consuming? (3) What is the dimensions of the tubes you used in your test? What is the maximum length one can use for good results?

UNSTEADY TRANSONIC FLOW COMPUTATIONS

by
A. R. Seebass, N. J. Yu, and K-Y. Fung
Department of Aerospace and Mechanical Engineering
University of Arizona
Tucson, Arizona 85721

SUMMARY

We investigate the effects of unsteady modes of motion on two-dimensional transonic flows; we do so in the context of the inviscid small perturbation approximation. The study is a numerical one and draws upon the alternating-direction implicit procedure developed for such calculations by Ballhaus and his co-workers at the NASA Ames Research Center. Our numerical algorithm treats shock waves as moving discontinuities. Results of nonlinear and time-linearized calculations of the transonic flow past an NACA 64A006 airfoil experiencing harmonic motions in several of its modes are presented and discussed.

1. INTRODUCTION

In unsteady transonic flows, relatively small periodic changes in the boundary conditions can lead to substantial changes in the loads and moments with marked phase lags. These are of major concern in the aerodynamic design of aircraft that operate in the transonic regime. A short, but timely, review of various aspects of unsteady transonic flow may be found in Reference 1. Of particular concern are aeroelastic behavior, and flutter and buffet boundaries. Here the unsteady perturbations may sometimes be small enough that linearization about a nonlinear steady flow, as suggested by Landahl (2) long ago, is possible.

In such flows the behavior of the boundary layer, especially as it is affected by the pressure rise caused by any shock waves in the flow, is clearly of major importance. Additionally, in the neighborhood of the leading edge the flow perturbations are large; consequently, highly accurate inviscid results require the use of the full potential equation. It seems likely that eventually the computational algorithms used in routine studies of unsteady transonic flows will use the Reynolds averaged Navier-Stokes equations now used in research studies. However, such algorithms (3) currently require substantial computer time and are too inefficient for exploratory studies such as this one. The ability of these algorithms to model complex unsteady transonic flow phenomena, such as buffet, has recently been demonstrated (4).

An important consideration in constructing an algorithm for unsteady transonic flows is the treatment of moving shock waves. The experimental observations of Tijdeman (5-7) indicate that even for simple airfoil motions shock wave motions can be complicated, and that they can strongly affect aerodynamic force and moment variations. Time-linearized methods, i.e., methods that assume the unsteady perturbations are small compared to the basic steady disturbance have not usually considered shock motions (8, 9), although they can be modified to do so for small shock excursions (10). Time-integration methods (11-18) treat shock waves by "capturing" them, a procedure that can present a number of difficulties.

Unsteady experiments (5-7), analysis (10) and numerical studies (10) all indicate that the amplitude of the shock wave motions increases inversely with reduced frequency. Thus some of the most important effects occur with low-frequency motions. This is not surprising; nonlinear behavior is suppressed at higher frequencies, with the small perturbation equation becoming linear for frequencies higher than the two-thirds power of the airfoil's thickness-to-chord ratio. Explicit finite-difference schemes are not efficient when applied to low-frequency cases because the stability restriction on the time step is substantially more severe than that required for accuracy. As a result, efficient semi-implicit methods (13) and even more efficient fully implicit methods (11, 12, 17, 18) have been developed. Caradonna and Isom (17) use an iterative implicit procedure, i.e., the nonlinear implicit finite-difference equations must be solved iteratively at a given time level. In an earlier, unpublished, study we also used such a procedure. Ballhaus and Steger (11) and Beam and Warming (18) constructed more efficient algorithms that solve the nonlinear equations directly by the solution of simple matrix equations generated by an alternating-direction implicit (ADI) procedure. This method has proven to be so efficient that it is now used as an alternative to successive line over-relaxation (SLOR) for steady flow calculations (Reference 19 and Yu and Seebass, unpublished).

As mentioned above, these implicit schemes "capture" shock waves, i.e., shock waves evolve automatically as part of the numerical solution. Shock capturing produces shock profiles that are distorted in a manner that depends on the truncation errors in the finite-difference scheme. The use of mixed-difference schemes (11, 18) can improve the situation for cases in which the flow changes from supersonic to subsonic across the shock. However, when this condition is not satisfied the differencing cannot be switched across the shock and shock resolution is poor. In any case, shock capturing requires spatial grid spacings, in regions where shock waves are anticipated, that are sufficiently small to resolve the shock waves. The grid spacing required to do this is usually much smaller than that required to resolve flow variable gradients in most of the rest of the flow field. Shock fitting removes the large gradients from the finite difference solution and permits equivalent flow field resolution with fewer grid points, both in space and time (20, 21). If shock waves are not treated as discontinuities, but are to be captured correctly, the difference equations must be solved in conservation form. This imposes an additional constraint on the construction of finite-difference schemes that can be difficult to satisfy.

A need for shock fitting also arises in computing time-linearized solutions for very small unsteady perturbations. Time-linearized solutions for indicial motions can be used to determine force and moment coefficient variations at various reduced frequencies, obviating the need for a numerical solution at each reduced frequency (see, e.g., Reference 22).

Traci, et al., (8, 23, 24) have developed relaxation methods for solving the resulting time-linearized equations of motion for harmonic disturbances. Less complete, but comparable, studies have been made by Weatherill et al. (25); these derive from an earlier study by Ehlers (26). In both of these studies shock motions, which contribute substantially to the time-varying loads and moments, are neglected. Difficulties also arise in the convergence of the iterative numerical scheme. Unsteady small amplitude motions have shock wave excursions that are the order of the amplitude of the motion divided by the reduced frequency of the motion. Consequently, these shock motions dominate other low frequency contributions to the lift and moment coefficients. Such time-linearized shock motions can be computed in a rational way, but the accuracy of the results depends critically on an accurate resolution of the steady flow field in the vicinity of the shock wave (10); this is best accomplished by shock fitting.

This paper briefly reviews the numerical procedures we have developed for computing nonlinear and time-linearized small perturbation unsteady transonic flows. We use an ADI scheme and treat shock waves as discontinuities in the flow. Calculations of the transonic flow past an NACA 64A006 airfoil experiencing harmonic or indicial pitching and flap oscillations are discussed.

2. FORMULATION

We write the unsteady small disturbance equation for low frequency transonic flows in the commonly used form

$$-2KM_\infty^2\phi_{xt} + \{1 - M_\infty^2 - (\gamma + 1)M_\infty^2\phi_x\}\phi_{xx} + \phi_{yy} = 0. \tag{1}$$

The spatial coordinates, the time, and the velocity potential in (1) have been non-dimensionalized by the chord, the reciprocal of the angular frequency, and the free stream velocity times the chord, respectively. Other, perhaps more useful and suitable, forms are given in References 21 and 27. This equation results from a systematic expansion of the velocity potential in the thickness ratio τ and applies for reduced frequencies $K = 0(\tau^{2/3})$ where $K = \omega c/U$, i.e., the angular frequency multiplied by the time it takes the flow to traverse the airfoil chord. Lin, Reisner and Tsien (28) showed that, with restriction to small perturbations throughout the flow, this is the only nonlinear equation that arises. For moderate frequencies the equation

$$-K^2\phi_{tt} - 2K\phi_{xt} + \{1 - M_\infty^2 - (\gamma + 1)M_\infty^2[\phi_x + \frac{\gamma - 1}{\gamma + 1} K\phi_t]\}\phi_{xx} + \phi_{yy} = 0$$

is frequently used, with or without the ϕ_t term, and may provide results that apply at higher frequencies than those obtained from (1).

The boundary condition on the body takes the simple form

$$\phi_y(x,0,t) = \tau[Y_x^\circ + \frac{\delta}{\tau}(Y_x^u + KY_t^u)], \quad -\frac{1}{2} \le x \le \frac{1}{2}, \tag{2}$$

where $Y(x,t)$, the instantaneous body shape, has been decomposed into a steady part, Y°, and an unsteady part, Y^u. Here δ is the amplitude of the unsteady oscillation. Because $K = 0(\tau^{2/3})$, the last term in (2) is dropped unless $Y_x^u \equiv 0$ or is small. For this reason, the time-linearized perturbation velocity potential for plunging motions ($Y_x^u = 0$) is just K times that for the analogous pitching motion, where $Y^u(x,t) = (x - x_o)\sin t$.

Numerical studies conducted by Magnus (15) show that erroneous boundary data on a finite domain can lead to significant errors. The low frequency approximation implies that any changes in the circulation are communicated instantly downstream to infinity. Consequently, the simplest boundary conditions are $\phi_x = 0$ on the downstream boundary and $\phi = 0$ on the other boundaries. Ballhaus and Goorjian (12) used these boundary conditions in their study and obtained satisfactory results. The validity of such far-field boundary conditions can only be justified by numerical experiments; i.e., near the boundary the disturbance quantities ϕ_x, and ϕ_y, must be much smaller than the values at the airfoil surfaces. For the lifting case, ϕ depends on the instantaneous circulation, Γ. This dependence can be derived theoretically by assuming that in the far field all the perturbations are small compared to the basic steady state (see, e.g., Reference 27). Here we use a stretched coordinate system that maps the doubly infinite domain into $|\xi| \le 1$, $|\eta| \le 1$, and set $\phi_x = 0$ on the downstream boundary $\xi = 1$ and $\phi = 0$ elsewhere on the boundary of this domain. As a numerical test for this procedure we have computed the steady state circulation about an NACA 64A006 airfoil for various flap deflection angles, using the ADI method with appropriate far-field values of ϕ, corrected for the usual steady state circulation contribution. These results have been compared with the results obtained by the ADI calculations with the boundary conditions employed here for an unsteady flap deflection to the correct angle. These results are identical within the accuracy with which we have computed the solutions.

Any shock wave that exists in the flow field must satisfy the jump relation derived from the conservative form of the governing equation (1), namely

$$-2KM_\infty^2[\![\phi_x]\!]^2(\frac{dx}{dt})_s - \{1 - M_\infty^2 - (\gamma + 1)M_\infty^2\bar{\phi}_x\}[\![\phi_x]\!]^2 + [\![\phi_y]\!]^2 = 0 \tag{3}$$

together with the condition derived from the assumption of irrotationality,

$$(\frac{dy}{dx})_s = -[\![\phi_x]\!]/[\![\phi_y]\!]. \tag{4}$$

Here $\tilde{\phi}_x$ refers to the mean value of ϕ_x evaluated on each side of the discontinuity, and $\llbracket \phi_x \rrbracket$ indicates the jump in ϕ_x across the discontinuity; the subscript "s" denotes the quantity evaluated at the shock surface.

The pressure coefficient, defined so that it vanishes at sonic conditions, takes the form

$$C_p = -2 \left\{ \frac{M_\infty^2 - 1}{(\gamma + 1)M_\infty^2} + \phi_x \right\} . \tag{5}$$

In the small disturbance approximation, the Kutta condition is imposed by requiring that C_p be continuous at $y = 0$ for $x > 1/2$.

2.1 Time-Linearized Equations

We now assume that the unsteady disturbances, characterized by δ, are small enough that we may write

$$\phi(x,y,t) = \phi^\circ(x,y) + \delta\psi(x,y,t) + o(\delta) \tag{6}$$

and neglect higher-order terms in δ. The restriction imposed on δ for this to be true will depend on the other parameters of the problem, viz., $\kappa \equiv (1 - M_\infty^2)/[(\gamma + 1)M_\infty^2\tau]^{2/3}$ and K. This gives

$$\{1 - M_\infty^2 - (\gamma + 1)M_\infty^2\phi_x^\circ\}\phi_{xx}^\circ + \phi_{yy}^\circ = 0, \quad \phi_y^\circ(x,0) = \tau Y^{\circ\prime}(x), \quad -\frac{1}{2} \leq x \leq \frac{1}{2} ; \tag{7}$$

$$-2KM_\infty^2\psi_{xt} + \{[1 - M_\infty^2 - (\gamma + 1)M_\infty^2\phi_x^\circ]\psi_x\}_x + \psi_{yy} = 0, \quad \psi_y(x,0,t) = Y_x^u + KY_t^u, \quad -\frac{1}{2} \leq x \leq \frac{1}{2} . \tag{8}$$

The solution to (7) must satisfy the steady version of the shock relations (4) and (5). The shock relations for (8) are discussed in Section 2.2.

We avoid writing

$$\psi(x,y,t) = \mathrm{Re}\{\bar{\psi}(x,y)e^{i\omega t}\} \tag{9}$$

as this restricts the study to harmonic motions. Because indicial motions can be superimposed to obtain the results for any frequency, they seem more important. Equation (9) results in an equation for a complex-valued ψ which may be solved by line relaxation. Our experience with unsteady ADI techniques has been that they are at least as effective as line relaxation for problems of this type, and hence there is *no advantage to the decomposition (9).*

The numerical algorithm developed in Reference 21 and described briefly in Section 3 can be used to solve the basic equation (1) subject to the boundary conditions (2), the shock conditions, (3) and (4), the far-field boundary conditions and the Kutta condition. Steady state solutions, $\phi^\circ(x,y)$, may be obtained rapidly by subjecting a basic steady state, such as undisturbed flow, to rapidly changing boundary data until a new steady configuration is prescribed. This, then, determines the steady state result for (7) needed to solve (8).

2.2 Shock Fitting

The basic algorithm for shock fitting in mixed flows was developed in a previous study of steady transonic flows (20). A different approach to shock fitting has also been used by Hafez and Cheng (29) in their study of steady transonic flow problems. Their procedure essentially replaced the shock-point operator of Murman (30) by an analogous difference statement derived from the shock jump conditions. Subsequently, the velocity potential on each side of the shock wave is extrapolated to locate the shock wave.

To understand the shock-fitting procedure for unsteady transonic flow calculations it is necessary to recall how shock waves form in an unsteady field. Shock waves are generated when the local flow becomes supersonic and compressive. While the initial shock formation may not be predicted exactly by the numerical solution when shock fitting is used in the early stages of shock wave formation, it eliminates spurious oscillations in the numerical solution and does provide the correct development of the shock wave in later stages of the calculations (31). The criteria that we set for the initial shock formation is that the local flow become sonic (relative to the airfoil) and compressive. In the body-fixed coordinate system, a shock wave can exist both in the usual supersonic-supersonic and supersonic-subsonic transitions, but also in a purely subsonic flow field, sometimes referred to as a "subsonic-subsonic" shock. In any case, the flow ahead of the shock relative to a coordinate system fixed on the shock must be always supersonic. Consequently, the correct judgment for the existence of a shock wave in the unsteady field is to evaluate the local flow velocity ahead of a prospective shock with respect to the coordinate system fixed on it; i.e., if the local flow is supersonic a shock may exist, if the local flow becomes sonic the shock strength diminishes, and if it is subsonic a shock cannot exist.

Any shock wave that exists in the flow field must satisfy the jump relations (3) and (4). In two-dimensional small perturbation transonic flows the shock waves that usually occur are nearly normal to the flow direction. While it is not necessary to do so, in the numerical calculations reported here we have assumed that if the basic steady flow has a shock wave, then this shock may be approximated by a shock wave normal to the free stream flow. To be consistent with this approximation we must also assume that the motion of any shock wave that arises from unsteady changes in the flow, as well as the motion of existing shock waves, is also calculated by this normal shock approximation. For this simplified model, (3) and (4) reduce to

$$\llbracket\phi\rrbracket = 0 \quad \text{on} \quad \dot{x}_s \equiv \left(\frac{dx}{dt}\right)_s = \frac{\gamma+1}{2K}\left\{\frac{M_\infty^2 - 1}{(\gamma+1)M_\infty^2} + \tilde{\phi}_x\right\}, \tag{10}$$

which gives the speed of the normal shock in the flow field. For steady flows $\tilde{\phi}_x$ is a function of x alone; this, of course, still permits $\llbracket\phi_x\rrbracket$ to vary with y. For unsteady flows, while $\dot{x}_s$ is a function of t alone, the strength of the shock will still vary with y.

For time-linearized flows the steady state result for ϕ°_x with normal shock fitting will give a steady state shock position x°_s, $0 \le |y| \le y^*_\pm$. We now determine the shock wave's motion by writing the perturbed shock position as $x_s = x^\circ_s + \delta\chi(t)$ and using the time-linearized version of (10); we note that an expression of the form $x^\circ_s + \delta\chi(t)/K$ would probably be more appropriate. From (10), we conclude that the shock motion is governed by

$$\frac{d\chi}{dt} = \frac{\gamma+1}{2K}\tilde{\psi}_x(x,0,t) \quad \text{with} \quad \llbracket\phi\rrbracket = \llbracket\phi^\circ\rrbracket + \delta\llbracket\psi\rrbracket = 0 \tag{11}$$

on the shock. Linearizing the expression in (11) for the velocity potential about the steady shock position we find

$$\begin{aligned}\phi(x_s,y,t) &= \phi(x^\circ_s,y,t) + \phi_x(x^\circ_s,y,t)\delta d\chi \\ &= \phi^\circ(x^\circ_s,y) + \phi^\circ_x(x^\circ_s,y)\delta d\chi + \delta\psi(x^\circ_s,y,t) + 0(\delta^2).\end{aligned}$$

Because we have treated the shock as a normal one, y appears here simply as a parameter. Now $\llbracket\phi(x_s,y,t)\rrbracket$ and $\llbracket\phi^\circ(x^\circ_s,y)\rrbracket$ are both zero; consequently we have

$$\llbracket\psi(x^\circ_s,y,t)\rrbracket = -\frac{(\gamma+1)}{2K}\llbracket\phi^\circ_x(x^\circ_s,y)\rrbracket\int_0^t \tilde{\psi}_x(x^\circ_s,0,\hat{t})d\hat{t} \tag{12}$$

which must be integrated in time in conjunction with the solution to (8).

3. NUMERICAL PROCEDURES

In a preliminary study of the unsteady transonic flows a normal shock-fitting procedure was implemented in an implicit-iterative scheme. Satisfactory results were obtained, but the procedure was time-consuming because of the iterative process required at each time step. The recent studies of Ballhaus and Steger (11) and Ballhaus and Goorjian (22) show that an ADI scheme is more efficient that the implicit-iterative scheme in treating the low frequency transonic flows. The shock-fitting algorithm was modified and implemented with an ADI scheme. In this section the ADI procedure and the method used for unsteady shock fitting are briefly reviewed.

3.1 Coordinate Stretching

To minimize the far-field boundary effects on the numerical results a relatively large computational region is usually required. For some of the cases studied in this paper the shock excursions are large and the unsteady disturbances carried several chord lengths away from the airfoil; thus, the use of a relatively large computational domain seems desirable. A simple and straightforward way of computing the solution in a large computational domain is to use nonuniform mesh distributions with most of the mesh points concentrated in the region of interest. An alternative is to introduce analytical coordinate stretchings. In the present study, we use the following coordinate stretchings:

$$\xi = \pm\{1 - \exp(\mp a_1 x)\} \quad \text{for} \quad x \gtrless 0 \quad \text{and} \quad \eta = \pm\{1 - \exp(\mp a_2 y)\} \quad \text{for} \quad y \gtrless 0,$$

where a_1 and a_2 are constants that control the mesh distributions. The infinite physical domain is transformed into the finite computational domain bounded by $|\xi| \le 1$, and $|\eta| \le 1$. The transformation provides a concentrated mesh distribution near the airfoil which is suitable for the present study. While this scaling is not consistent with the known algebraic decay of the perturbations, calculations made with an algebraic scaling, viz., $\xi = x/(|x| + a_1)$ etc., gave essentially identical results. The exponential variation used here seems more desirable near the airfoil.

The governing equation (1), written in the stretched coordinate system, is

$$\left\{\frac{-2KM_\infty^2}{a_2^2(1-|\eta|)}\phi_\xi\right\}_t - \left\{\frac{(\gamma+1)M_\infty^2}{2a_2^2(1-|\eta|)}\left[\frac{M_\infty^2-1}{(\gamma+1)M_\infty^2} + a_1(1-|\xi|)\phi_\xi\right]^2\right\}_\xi + \left\{\frac{1-|\eta|}{a_1(1-|\xi|)}\phi_\eta\right\}_\eta = 0. \tag{13}$$

Because (13) is in divergence-free form, a conservative difference approximation can be constructed if the shock wave is to be "captured" rather than "fitted."

The normal shock jump relation follows directly from (13); this relation and the boundary condition on the airfoil surface are now

$$\left(\frac{d\xi}{dt}\right)_s = \frac{a_1(1-|\xi|)(\gamma+1)}{2K}\left\{\frac{M_\infty^2-1}{(\gamma+1)M_\infty^2} + a_1(1-|\xi|)\tilde{\phi}_\xi\right\} \tag{14}$$

and

$$\phi_\eta(0,\xi) = \frac{a_1}{a_2}(1-|\xi|)\frac{\partial Y(\xi,t)}{\partial\xi} + \frac{K}{a_2}\frac{\partial Y(\xi,t)}{\partial t}, \quad -1+\exp(a_1/2) \le \xi \le 1-\exp(-a_1/2).$$

Equations analogous to (13) and (14) for the time-linearized results are given in Reference 10.

3.2 Alternating-Direction Implicit (ADI) Method

The low frequency equation in the stretched coordinate system is solved by the alternating-direction implicit scheme developed by Ballhaus and Steger (11). To simplify this discussion, equation (13) is rewritten in the form

$$\Psi_{\xi t} + F_\xi + G_\eta = 0, \tag{15}$$

where the function Ψ, F and G may be determined by comparing equations (13) and (15). The solution is advanced from time level "n" to level "n+1" by the following two-step procedure:

$$\frac{1}{\Delta t}(\Psi_\xi^+ - \Psi_\xi^n) + D_\xi F^+ + \delta_\eta G^n = 0; \quad \frac{1}{\Delta t}(\Psi_\xi^{n+1} - \Psi_\xi^+) + \frac{1}{2}\delta_\eta(G^{n+1} - G^n) = 0. \tag{16}$$

Here "+" refers to an intermediate value of Ψ, D_ξ is the type-dependent difference operator for ξ-derivatives and δ_η the central-difference approximation for η-derivative. The backward difference approximation for Ψ_ξ^n can be either a first-order or a second-order difference approximation, with the latter giving improved results. The nonlinear term F is evaluated, using a linearization somewhat different from the two-time level averaging procedure of Ballhaus and Steger. The difference approximations described above provide first- or second-order accuracy for $\Psi_{\xi t}$, second-order accuracy for F_ξ and G_η in subsonic regions, and first-order accuracy for F_ξ in supersonic regions. A local analysis shows that the procedure is unconditionally stable.

In the first step a quadradiagonal system is generated and can be easily solved by direct elimination. For lifting calculations two grid lines are used to represent the lower and upper surfaces of the airfoil. The circulation, Γ, is calculated by $\Gamma = \phi_{ITE}^U - \phi_{ITE}^L$ through each sweep. Here "ITE" denotes the upper and lower values at the first grid point behind the trailing edge. This circulation is incorporated into the construction of the η-derivatives behind the airfoil for $\eta = 0$.

In the second step a tridiagonal system is generated by the body. Ahead of the leading edge and behind the trailing edge the double grid notation for $\eta = 0$ destroys the tridiagonal system. However, ahead of the leading edge, $\phi^U = \phi^L$, and behind the trailing edge, $\phi^U = \phi^L + \Gamma$; thus the difference equations can be reordered to give a tridiagonal system. On the airfoil surface, the matrix equations above and below the airfoil are decoupled; they can either be solved separately or simultaneously by packing the matrix equations together.

Again, analogous but somewhat simpler equations and procedures are used for the time-linearized calculations. In these calculations the type dependent operator, D_ξ, changes at the steady state sonic line and shock wave. The coefficient, $f(\xi,\eta)$, that appears in (8) in the form $\{f(\xi,\eta)\psi_\xi\}_\xi$ depends on the steady state results $\phi^\circ(\xi,\eta)$ and must be stored. On the other hand, the matrices used do not depend on the solution ψ and, consequently, need only be inverted once. In its present form our algorithm does not take advantage of this feature.

3.3 Shock Fitting

We start the unsteady nonlinear flow calculations by using an ADI scheme. When the local flow becomes sonic and compressive, we introduce the shock-fitting algorithm described in detail in Reference 21. Sonic, compressive points are treated as shock points where differentiation in t and ξ across discontinuities is avoided. Initially, the shock has zero strength and is stationary. The flow properties ahead of and behind the shock can be easily extrapolated from neighboring points. The shock wave can either increase or decrease in strength during the unsteady process. This results in three possibilities for shock motion that have to be considered separately in the fitting procedure: The shock moves upstream and crosses grid points; the shock remains stationary or moves within a grid spacing; the shock moves downstream and crosses grid points. At each new time level the shock position is determined by applying (10). The formulations of the difference approximations for each case are quite similar.

For time-linearized calculations the solution is advanced in time using the time-linearized analogues of (16) coupled with (12) in the form

$$\|\psi\|^+ = -C(\eta)\Delta t\tilde{\psi}_\xi^n + \|\psi\|^n; \quad \|\psi\|^{n+1} = -C(\eta)\Delta t\tilde{\psi}_\xi^{n+1} + \|\psi\|^+.$$

Here

$$C(\eta) = \frac{\gamma+1}{4K}a_1^2(1-|\xi_s^\circ|)^2\|\phi_\xi^\circ(\xi_s^\circ,\eta)\|,$$ and ξ_s° denotes the steady state position of the shock wave.

This procedure corrects the ψ values for shock motions as the solution progresses. The shock motion is easily determined simultaneously by using (11) and (12) in the form

$$\chi^{n+1}(0,t) = -[\psi(x_s^\circ,0,t)]^{n+1}/[\phi_x(x_s^\circ,0)].$$

Further details are given in Reference 10.

4. RESULTS AND DISCUSSION

Both the nonlinear and time-linearized algorithms have been used to compute the flow past an NACA 64A006 airfoil subjected to indicial, i.e., step, changes and harmonic motions in pitch and flap oscillation. The latter calculations have included a range of Mach numbers, amplitudes for the nonlinear algorithm, and reduced frequencies for the harmonic changes. The nonlinear algorithm has also been used to compute the flow past a pulsating parabolic arc airfoil. In this latter flow, at $M_\infty = 0.85$, as the airfoil thickens a shock wave forms and moves downstream until shortly after mid-cycle. As the airfoil thins, the shock wave moves upstream with increasing speed, eventually leaving the airfoil. A comparison of the results, with and without shock fitting (21), indicates that shock fitting predicts the formation of the shock wave more accurately. It also properly defines the shock wave when it becomes "subsonic-subsonic" in the fixed grid system. The shock wave decays slowly as it propagates into the free stream after passing the location of the leading edge when the airfoil's thickness has just become zero.

4.1 NACA 64A006 Airfoil, Nonlinear Calculations

Steady state solutions were computed as discussed in Section 2.1 for an NACA 64A006 airfoil for various values of the freestream Mach number by using the ADI scheme with shock fitting outlined in Section 3. The free stream Mach number was varied between 0.8 and 0.9. The mesh system had 101 by 82 grid points in the x- and y-directions respectively. About 250 to 450 time steps were required for the solution to converge $|\Delta\phi|_{max} \leq 10^{-4}$. These steady state solutions are used as initial data for the nonlinear and time-linearized unsteady flow calculations.

Results were computed for the airfoil with quarter-chord flap for various values of the reduced frequency, the free stream Mach number, and the oscillation amplitude, in order to simulate the shock motions observed by Tijdeman (5, 6). These motions were classified by him as: type A - small shock oscillation; type B - the shock becomes very weak or disappears during part of a cycle; type C - the shock leaves the airfoil. Results for type A motions are not given, as they are easy to treat computationally. For all cases studied it took three to six cycles for the flow field to become periodic. Stability seems to require that the time step be small enough that Δt(in degrees)/$K < 10$.

Figure 1 illustrates the pressure coefficients on the airfoil surface at various times for $M_\infty = 0.854$, $K = 0.358$ and $\delta = 1°$. For these conditions Ballhaus and Goorjian (12) were able to simulate type B motion where the shock disappears during some part of the cycle. Here the shock does not disappear during the cycle; rather, it becomes quite weak during a small portion of the cycle. This difference is probably due in part to the assumption of a normal shock, which results in a stronger shock than would normally occur, and to the use of shock fitting, which is able to resolve very weak shock waves.

Figure 2 depicts the pressure coefficient on the airfoil surfaces for $M_\infty = 0.822$, $K = 0.496$ and $\delta = 2°$, simulating type C shock motion. Because we have used less spatial resolution and have not scaled the equation and boundary conditions with various powers of the Mach number, a slightly larger deflection angle seems to be needed in order to generate the type C shock motion; that is, we need a 2° deflection angle rather than the 1.5° of Reference 12 to obtain analogous behavior. In this case the flow field is subcritical during most of the cycle, where the shock wave is barely "captured" in the non-shock-fitting procedure. During the unsteady process the shock moves toward the leading edge. However, the strong singular behavior in pressure at the leading edge prevents the shock from propagating off the airfoil. The perturbation velocity becomes large and is negative; thus, the flow used to calculate the relative velocity ahead of the shock can no longer support a shock wave. Normal shock-fitting calculations determine the shock speed from the pressure jump across the shock at the airfoil surface. This eliminates the possibility that a portion of the shock may propagate off the leading edge in the computations. But this does not imply it cannot occur; rather this is a limitation of the normal shock fitting.

Magnus and Yoshihara (15) have solved the Euler equations using an explicit procedure for the conditions of Figure 1. Their results are compared with our calculation in Figure 3 for two angular times chosen to represent the least and the largest discrepancies. These discrepancies are thought to be mainly due to the inaccuracy of the small perturbation solution near the leading edge. Small errors there change the size and shape of the sonic line and influence the shock's position. For the conditions considered, the shock is nearly normal and the normal shock approximation should be a good one. Rather good agreement is obtained.

Additional nonlinear calculations have been carried out for $M_\infty = 0.880$ and $K = 0.48$. Both pitching and flap motions have been calculated for indicial and harmonic changes. For these conditions very small unsteady changes lead to very small shock motions and the shock wave remains between grid points. Because of the extrapolation procedure used in the shock-fitting, the ξ mesh distribution used here can introduce errors, albeit small ones, in the shock's position when a grid line is crossed. We wished to eliminate these errors in order to use the nonlinear calculations to judge the accuracy of time-linearized calculations. These results indicate that for pitching about mid-chord, nonlinear, amplitude dependent, behavior occurs for $\delta/\tau \geq 0.1$ for $K = 0.48$. Because the amplitude of the shock motions increases with decreasing K, nonlinear effects occur at smaller values of δ/τ at lower reduced frequencies.

Indicial motions require about eight hundred time steps of varying size to resolve the response. For harmonic motions, initiated from rest, three to ten cycles are required for the solution to become harmonic, with large values of K and M_∞ requiring more cycles. The pitching mode requires more cycles than the flap mode. The amplitude of the positive and negative phases of the motion could be varied from

cycle to cycle to reduce the number of cycles required. Each cycle requires 60 to 180 time steps to compute, with more steps required for smaller values of K. Each time step takes about 5 seconds of CPU time on a CDC 6400, or about 0.25 seconds of CPU time on a CDC 7600.

4.2 NACA 64A006 Airfoil, Time-Linearized Calculations

Time-linearized results have been computed for an NACA 64A006 airfoil experiencing harmonic and indicial pitching and flap motions. As noted earlier, in the low frequency approximation made here pitching and plunging motions lead to the same result except that the time-linearized perturbations are proportional to the maximum pitch angle for the former, and K times the maximum amplitude for the latter. Harmonic motions initiated from a steady state become nearly periodic in three to ten cycles, with the changes induced by flap oscillations becoming periodic more rapidly than those resulting from pitching oscillations. More cycles were required for larger reduced frequencies and, to a lesser degree, higher Mach numbers.

In order to confirm the validity of the time-linearized calculations, both the time-linearized and nonlinear algorithms were used to compute the response to a step change in angle of attack and the harmonic response to pitching motions. Figure 4 compares the nonlinear and time-linearized results for the normalized circulation and shock position for harmonic pitching motions at $M_\infty = 0.88$ and $K = 0.48$. Results are given for the fifth cycle; note that the nonlinear results are not yet periodic. Figure 5 compares the nonlinear and time-linearized pressure deviation from steady state at six angular times for the same conditions. Good agreement between the results is obtained for δ/τ less than 0.1.

Time-linearized pressure distributions at six angular positions for an oscillating quarter-chord flap with $K = 0.06$ and $M_\infty = 0.875$ are shown in Figure 6. The flap deflection is downward during the first half of the cycle. The results for the second half of the period, for the symmetrical problem shown here, are just the results shown with the lower and upper surface pressures interchanged. Thus the results for 0° are not given as they are just those for 180° with the lower and upper surface pressures reversed. Because the flap hinge occurs very close to the steady state shock location, the pressure singularity due to the change in flow direction at the hinge is missed. The circulation and shock excursion obey the following relations:

$$\Gamma(t)/\delta = 9.26 \sin (t - 59°),$$

$$\chi(t) = 12 \sin (t - 51°).$$

Note the substantial phase lag in the circulation and the shock's position.

Time-linearized pressure distributions at six angular positions for an oscillating airfoil with $K = 0.12$ and $M_\infty = 0.875$ are depicted in Figure 7. If these results are multiplied by K, then they represent the pressure perturbations for a plunging airfoil. As in the previous case of an oscillating flap, changes in forces and moments of $O(\delta/K)$ occur due to shock wave motion. In this case

$$\Gamma(t)/\delta = 5.48 \sin (t - 70°),$$

$$\chi(t) = 5.62 \sin (t - 87°).$$

Analogous computations have been carried out for $K = 0.12$, 0.24, 0.36, and 0.48. Figure 8 depicts the shock wave's excursion and maximum circulation as a function of K^{-1}. The nearly linear variation of the shock excursion substantiates an observation made in a one-dimensional model where the shock wave excursion is directly proportional to $1/K$ (see Reference 10).

In these calculations the circulation gives an immediate evaluation of the lift coefficient as a function of time; the moment coefficient must be evaluated by integrating the moment of the pressure coefficient. This is done by integrating the moment of pressure perturbations with the shock wave in its steady-state position and then correcting these results for the moment due to the shock wave motion, assuming that the shock's strength is defined by the steady-state pressure field. This makes an error in the shock strength of $O(\delta)$, but the effect on the moment is $O(\delta^2/K)$; because we have neglected other higher-order terms it is consistent to neglect this change in the strength of the shock wave.

Figure 9 depicts the absolute value and phase angle of the normalized lift and moment coefficients, as a function of the inverse reduced frequency K^{-1}, for harmonic flap and pitching motions at $M_\infty = 0.875$.

The time-linearized algorithm used here is a derivative of that used for the nonlinear calculations. Consequently, computational times are not greatly reduced from those required for the nonlinear calculations. The linearity of these computations may make it possible to greatly reduce the computational effort required. A local stability analysis shows that the computations should be unconditionally stable, but numerical experience has shown some difficulties for Δt(in degrees)$/K \geq 50$. Each time step requires about two seconds of CPU time on a CDC 6400, or about 0.1 seconds on a CDC 7600. The number of time steps required for a given computation is somewhat less than those required for the nonlinear computations at small values of K, and comparable at larger values of K.

5. CONCLUSION

Efficient and accurate methods for computing low frequency, unsteady behavior in transonic flows have been developed. They utilize the ADI procedure developed at NASA Ames for the small perturbation equation, but treat shock waves as discontinuities. The time-linearized calculations allow shock wave motions, which are shown to be $O(\delta/K)$ and often dominate changes in the force and moment coefficients. Comparison

of the time-linearized results with fully nonlinear calculations delineates their range of applicability. The unsteady behavior due to harmonic pitching and flap oscillations of an NACA 64A006 airfoil is discussed.

ACKNOWLEDGMENT

This research was sponsored by the AFOSR through Grant 76-2954B, the NASA through Grant 2112, and the ONR through Contract N0014-76-C-0182.

REFERENCES

1. Ballhaus, W. F.: Some Recent Progress in Transonic Flow Computations. VKI Lecture Series on Computational Fluid Dynamics, von Karman Institute for Fluid Dynamics, Rhode-St-Genese, Belgium, 1976.
2. Landahl, M. T.: Unsteady Transonic Flow. Pergamon Press, New York, 1961, 111-113.
3. MacCormack, R. W.: An Efficient Numerical Method for Solving the Time-Dependent Navier-Stokes Equations at High Reynolds Number. NASA TM X-73129, 1976.
4. Levy, L. L., Jr.: An Experimental and Computational Investigation of the Steady and Unsteady Transonic Flow Field About an Airfoil in a Solid-Wall Test Channel. AIAA Paper No. 77-678, 1977.
5. Tijdeman, H.: On the Motion of Shock Waves on an Airfoil with Oscillation Flap in Two-Dimensional Transonic Flow. NLR TR 75038U, 1975.
6. Tijdeman, H.: On the Motion of Shock Waves on an Airfoil with Oscillating Flap. Ed. K. Oswatitsch and D. Rues, IUTAM Symposium Transsonicum II, Göttingen, 1975, 49-56.
7. Tijdeman, H., Schippers, P., and Persoon, A. J.: Unsteady Air Loads on an Oscillating Supercritical Airfoil. NLR MP 77008 U, 1977.
8. Traci, R. M., Albano, E., and Farr, J. L.: Perturbation Method for Transonic Flows about Oscillating Airfoils. AIAA J., Vol. 14, No. 9, 1976, 1258-1265.
9. Weatherill, W. H., Ehlers, R. E., and Sebastian, J. D.: Computation of the Transonic Perturbation Flow Fields Around Two- and Three-Dimensional Oscillating Wings. NASA CR-2599, 1975.
10. Fung, K-Y., Yu, N. J., and Seebass, A. R.: Small Unsteady Perturbations in Transonic Flows. Informal report, submitted for publication 1977.
11. Ballhaus, W. F. and Steger, J. L.: Implicit Approximate-Factorization Schemes for the Low-Frequency Transonic Equation. NASA TM X-73082, 1975.
12. Ballhaus, W. F. and Goorjian, P. M.: Implicit Finite Difference Computations of Unsteady Transonic Flows about Airfoils, Including the Treatment of Irregular Shock Wave Motions. AIAA Paper 77-205, 1977.
13. Ballhaus, W. F. and Lomax, H.: The Numerical Simulation of Low Frequency Unsteady Transonic Flow Fields. Lecture Notes in Physics, Springer-Verlag, Vol. 35, 1975, 57-63.
14. Magnus, R. and Yoshihara, H.: Unsteady Transonic Flows Over an Airfoil. AIAA J., Vol. 13, No. 12, 1975, 1622-1628.
15. Magnus, R. and Yoshihara, H.: The Transonic Oscillating Flap. AIAA Paper No. 76-327, 1976.
16. Magnus, R. J.: Computational Research on Inviscid, Unsteady, Transonic Flow over Airfoils. ONR Report CASD/LVP 77-010, 1977.
17. Caradonna, F. X. and Isom, M. P.: Numerical Calculation of Unsteady Transonic Potential Flow Over Helicopter Rotor Blades. AIAA J., Vol. 14, No. 4, 1976, 482-488.
18. Beam, R. M. and Warming, R. F.: An Implicit Finite-Difference Algorithm for Hyperbolic Systems in Conservation-Law Form. Journal of Computational Physics, Vol. 22, No. 1, 1976, 87-110.
19. Ballhaus, W. F., Jameson, A., and Albert, J.: Implicit Approximate Factorization Schemes for the Efficient Solution of Steady Transonic Flow Problems. AIAA 3rd Computational Fluid Dynamics Conference, June, 1977, 27-34.
20. Yu, N. J. and Seebass, A. R.: Inviscid Transonic Flow Computations with Shock Fitting. Ed. K. Oswatitsch and D. Rues, IUTAM Symposium Transsonicum II, Göttingen, 1975, 449-456.
21. Yu, N. J., Seebass, A. R., and Ballhaus, W. F.: An Implicit Shock-Fitting Scheme for Unsteady Transonic Flow Computations. AIAA 3rd Computational Fluid Dynamics Conference, June, 1977, 13-26.
22. Ballhaus, W. F. and Goorjian, P. M.: Computation of Unsteady Transonic Flows by the Indicial Method. AIAA Paper No. 77-477, 1977.
23. Traci, R. M., Albano, E. D., and Farr, J. L., Jr.: Perturbation Method for Transonic Flow about Oscillating Airfoils. AIAA Paper No. 75-877, 1975.

24. Traci, R. M., Albano, E. D., Farr, J. L., Jr., and Cheng, H. K.: Small Disturbance Transonic Flows about Oscillating-Airfoils. Air Force Flight Dynamics Laboratory, Wright-Patterson Air Force Base, Ohio, AFFDL-TR-75-100, 1974.

25. Weatherill, W. A., Ehlers, F. E., and Sebastian, J. D.: Computation of the Transonic Perturbation Flow Field Around Two- and Three-Dimensional Oscillating Wings. NASA CR-2599, 1975.

26. Ehlers, F. E.: A Finite Difference Method for the Solution of the Transonic Flow About Harmonically Oscillating Wings. NASA CR-2257, 1974.

27. Krupp, J. A. and Cole, J. D.: Studies in Transonic Flow IV, Unsteady Transonic Flow. UCLA Engineering Report 76104, 1976.

28. Lin, C. C., Reissner, E., and Tsien, H. S.: *On Two-Dimensional Non-Steady Motion of a Slender Body in a Compressible Fluid.* J. Math. and Physics, 27, 1948, 220-231.

29. Hafez, M. M. and Cheng, H. K.: Shock-Fitting Applied to Relaxation Solutions of Transonic Small-Disturbance Equations. AIAA J. Vol. 15, No. 6, 1977, 786-793.

30. Murman, E. M.: Analysis of Embedded Shock Waves Calculated by Relaxation Methods. AIAA J., Vol. 12, No. 5, 1973, 626-633.

31. Moretti, G.: Thoughts and Afterthoughts about Shock Computations. PIBAL Report No. 72-37, 1972.

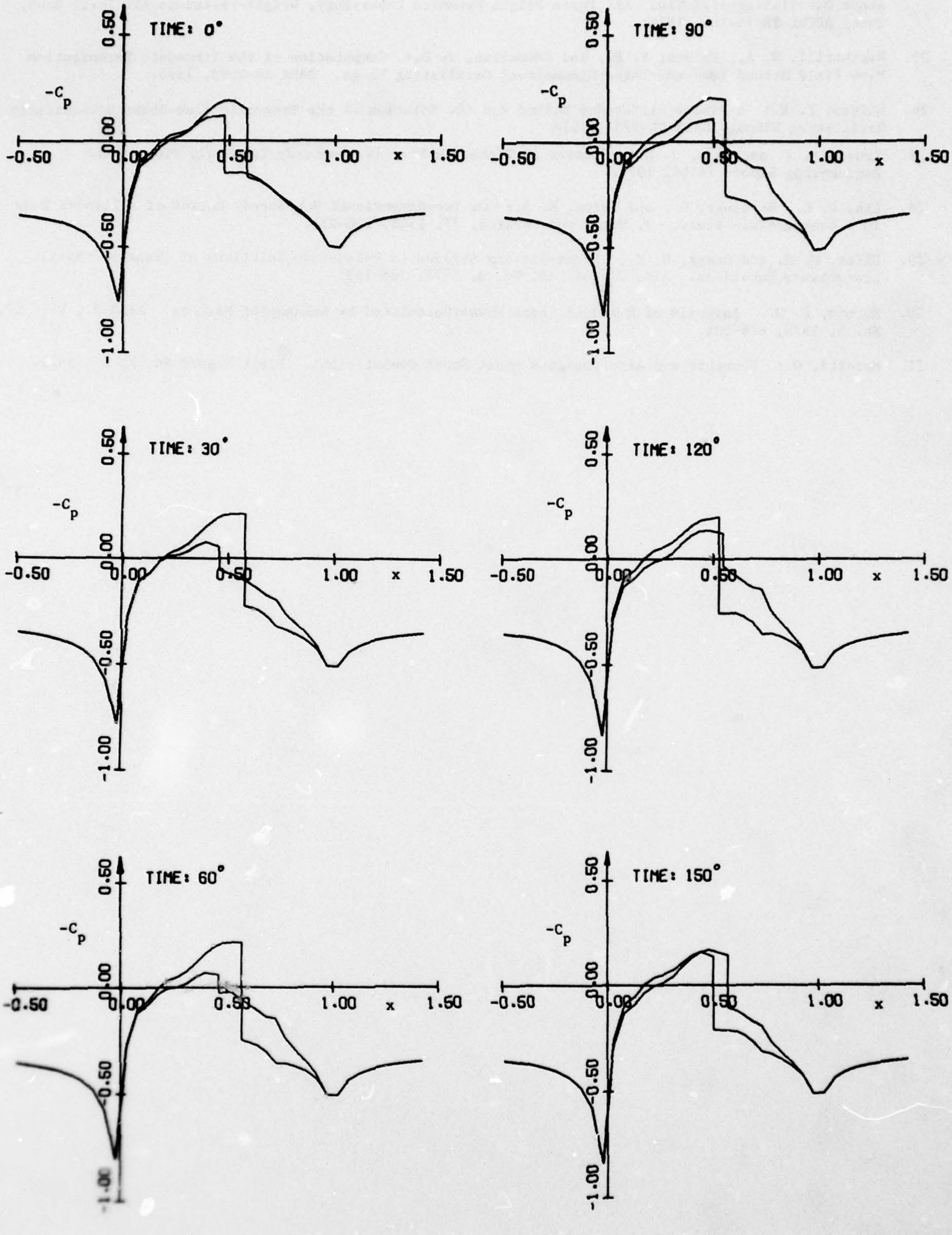

FIGURE 1. C_p ON AN NACA 64A006 AIRFOIL AT $M_\infty = 0.854$, $K = 0.358$ WITH $\delta = 1° \sin t$ (NONLINEAR CALCULATIONS).

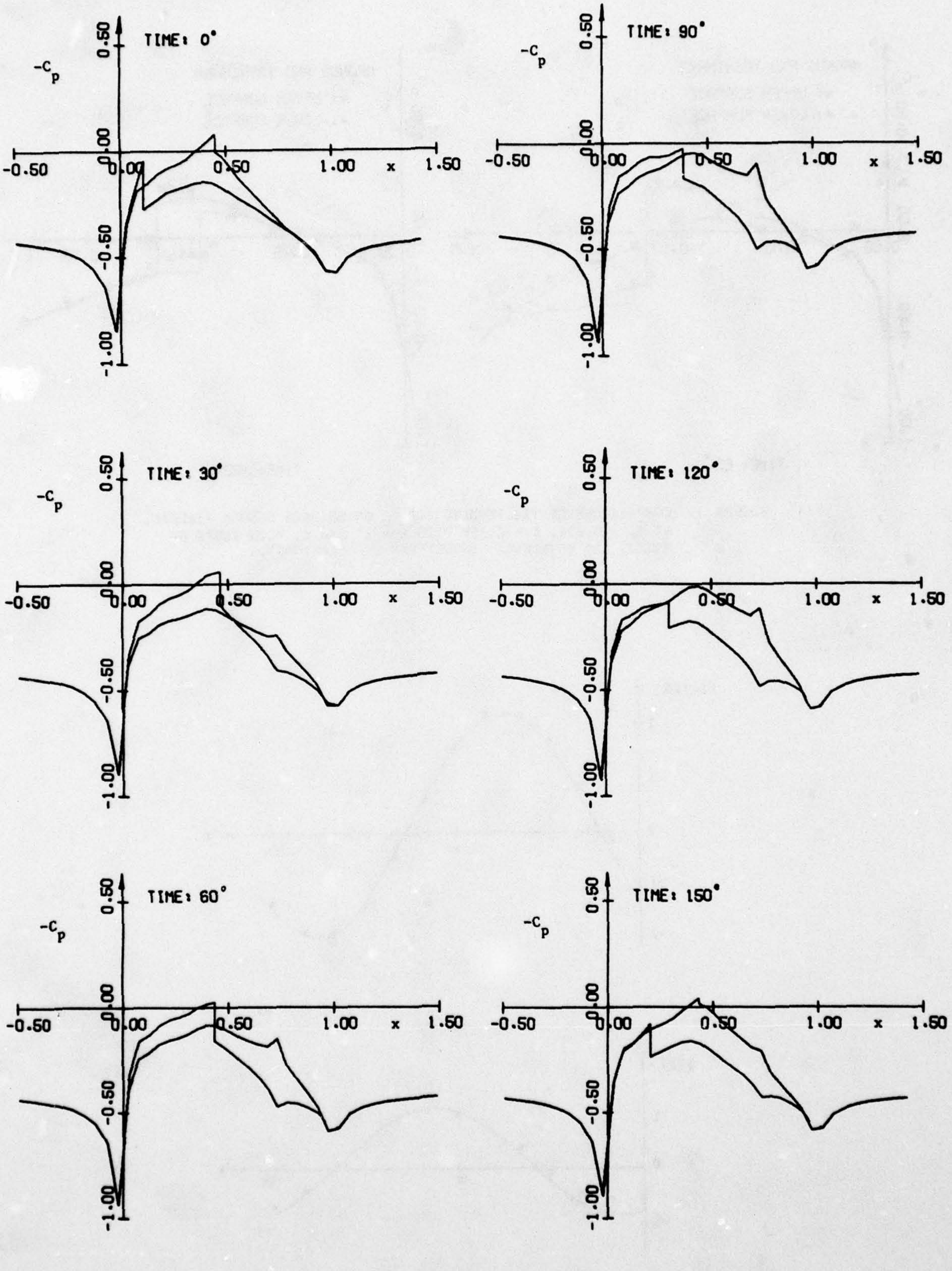

FIGURE 2. C_p ALONG AN NACA 64A006 AIRFOIL AT $M_\infty = 0.822$,
$K = 0.496$ WITH $\delta = 2° \sin t$ (NONLINEAR CALCULATIONS).

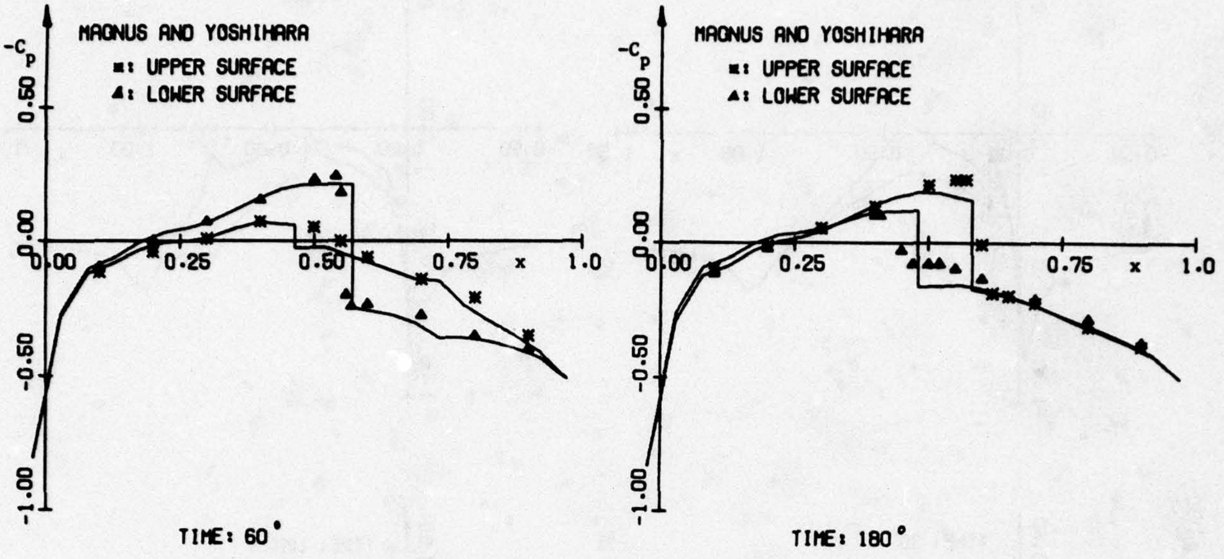

FIGURE 3. COMPARISONS OF THE RESULTS FOR C_p ON AN NACA 64A006 AIRFOIL, AT $M_\infty = 0.854$, $K = 0.358$ WITH $\delta = 1° \sin t$, WITH THOSE OF MAGNUS AND YOSHIHARA (NONLINEAR CALCULATIONS).

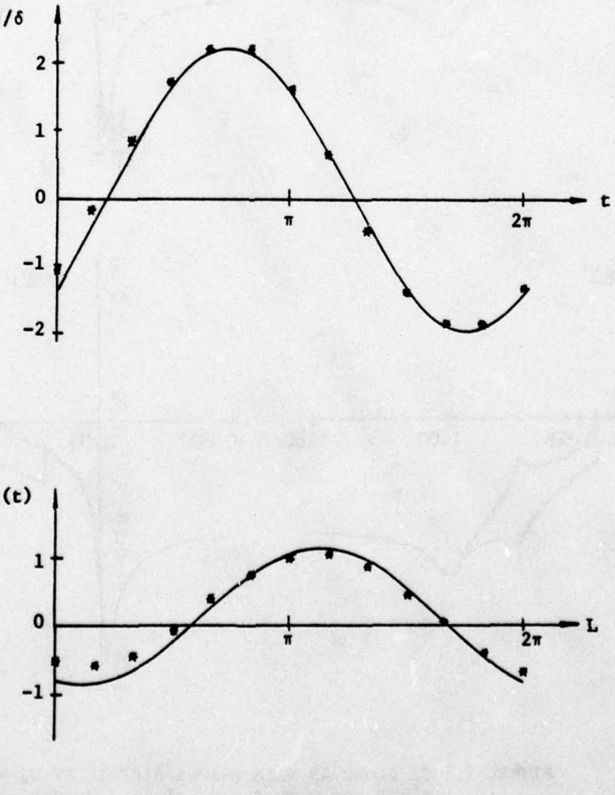

FIGURE 4. NONLINEAR (***) AND TIME-LINEARIZED(——) CIRCULATION AND SHOCK POSITION FOR THE PITCHING MOTION OF AN NACA 64A006 AIRFOIL. RESULTS SHOWN ARE FOR THE FIFTH CYCLE. THE NONLINEAR RESULTS ARE FOR $\delta = 0.1°$ AND ARE NOT YET PERIODIC. $M_\infty = 0.880$, $K = 0.48$.

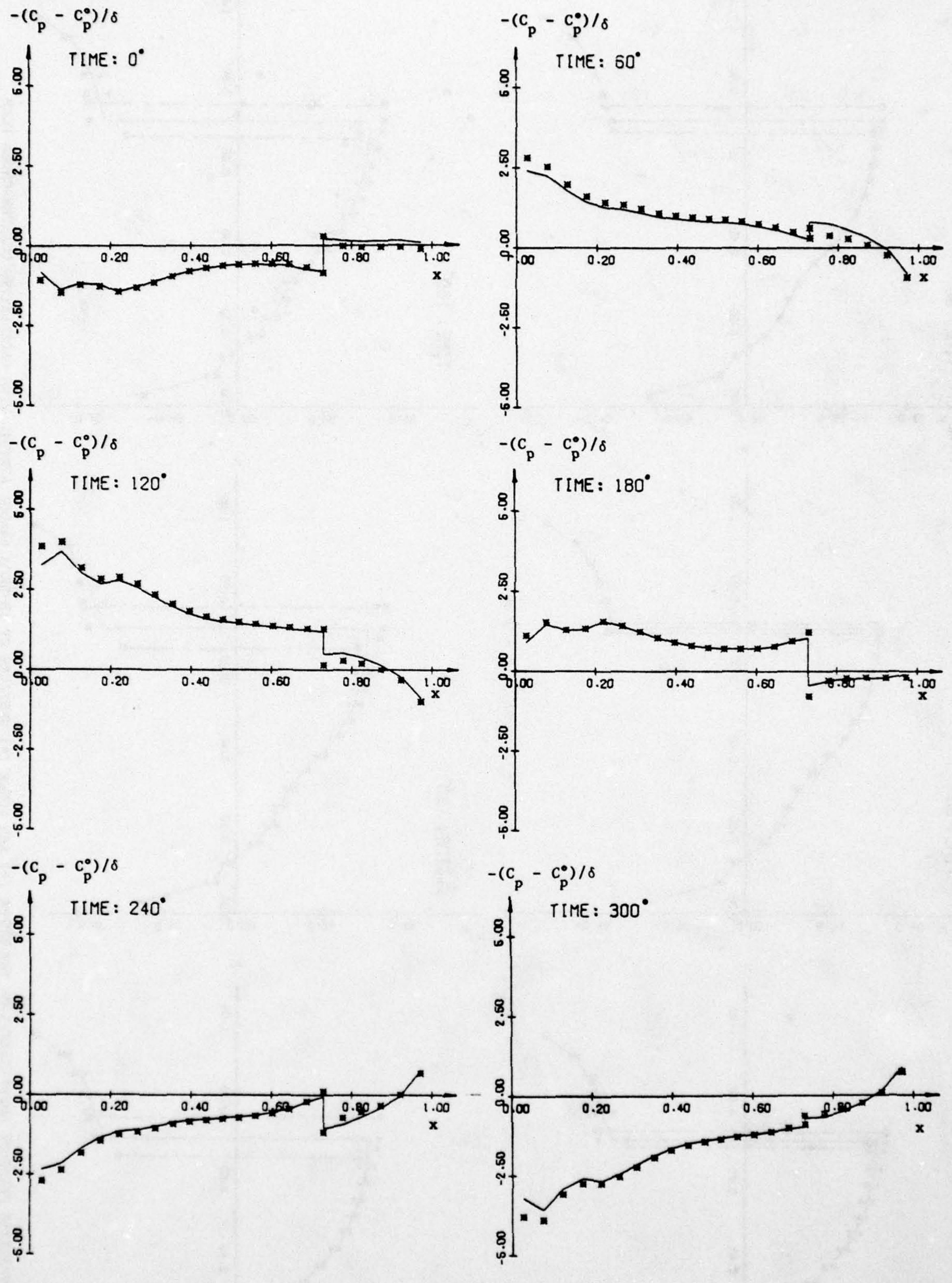

FIGURE 5. NORMALIZED NONLINEAR (****) AND TIME-LINEARIZED (——) PRESSURE PERTURBATIONS ON THE UPPER SURFACE OF AN NACA 64A006 AT SIX TIMES. PITCHING MOTION WITH $M_\infty = 0.880$, $K = 0.48$. FOR THE NONLINEAR CALCULATIONS $\delta = 0.1°$.

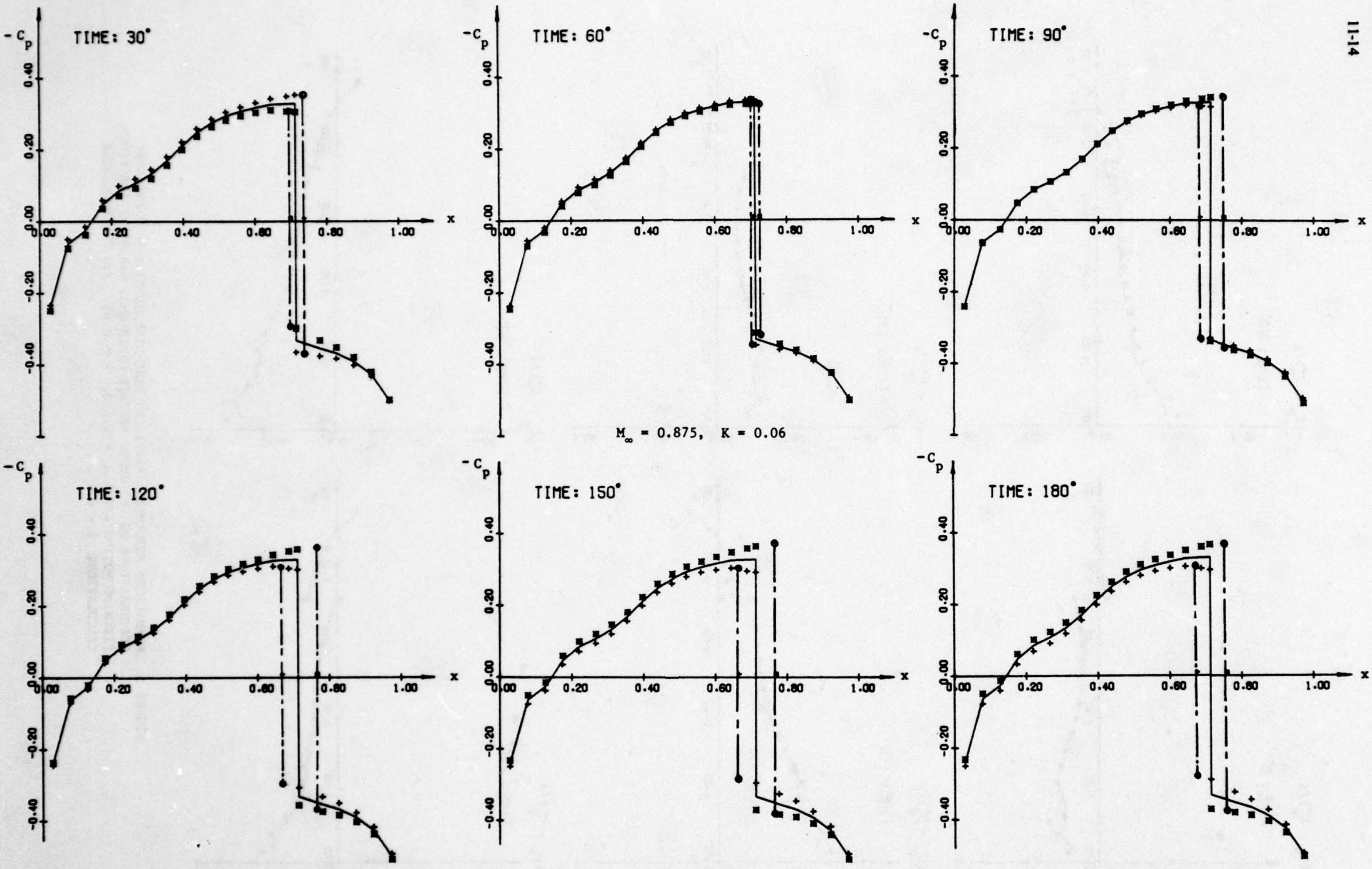

FIGURE 6. TIME-LINEARIZED PRESSURE COEFFICIENTS ON THE UPPER (+) AND LOWER (*) SURFACES OF AN NACA 64A006 AIRFOIL WITH OSCILLATING QUARTER-CHORD FLAP

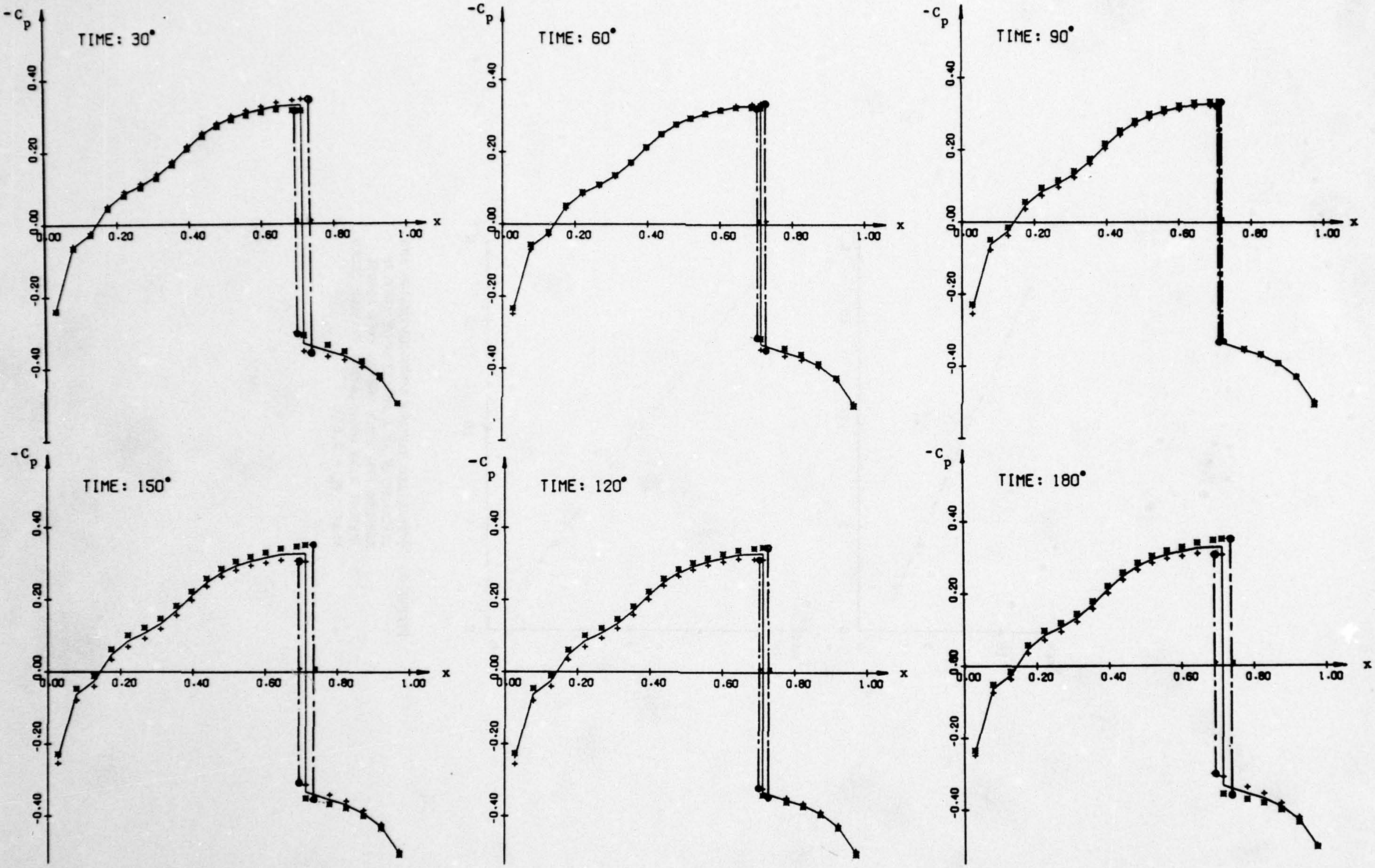

FIGURE 7. TIME-LINEARIZED PRESSURE COEFFICIENTS ON THE UPPER (+) AND LOWER SURFACES OF AN NACA 64A006 AIRFOIL OSCILLATING IN PITCH ($\delta = 1/4°$). $M_\infty = 0.875$, $K = 0.12$.

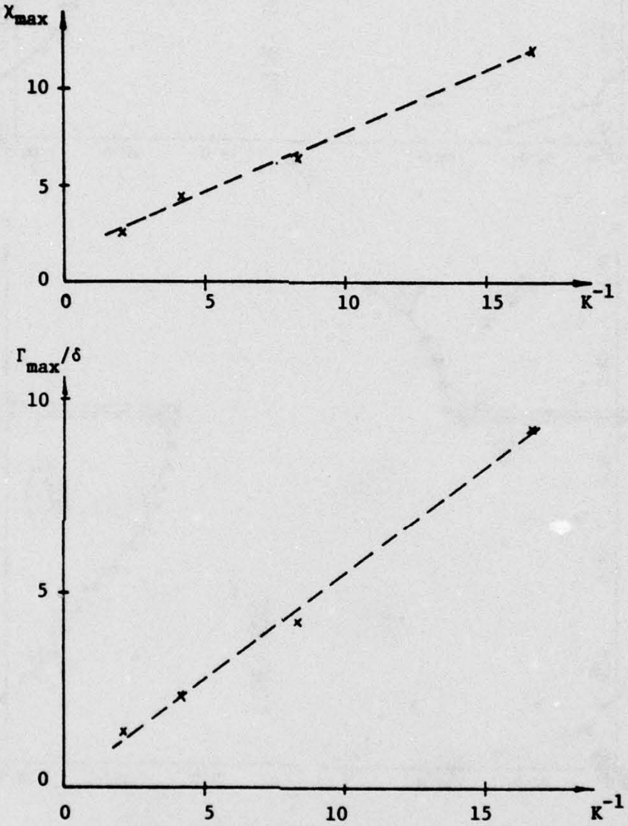

FIGURE 8. NORMALIZED MAXIMUM SHOCK EXCURSION AND CIRCULATION AS A FUNCTION OF INVERSE REDUCED FREQUENCY FOR AN NACA 64A006 AIRFOIL WITH OSCILLATING QUARTER-CHORD FLAP. $M_\infty = 0.875$.

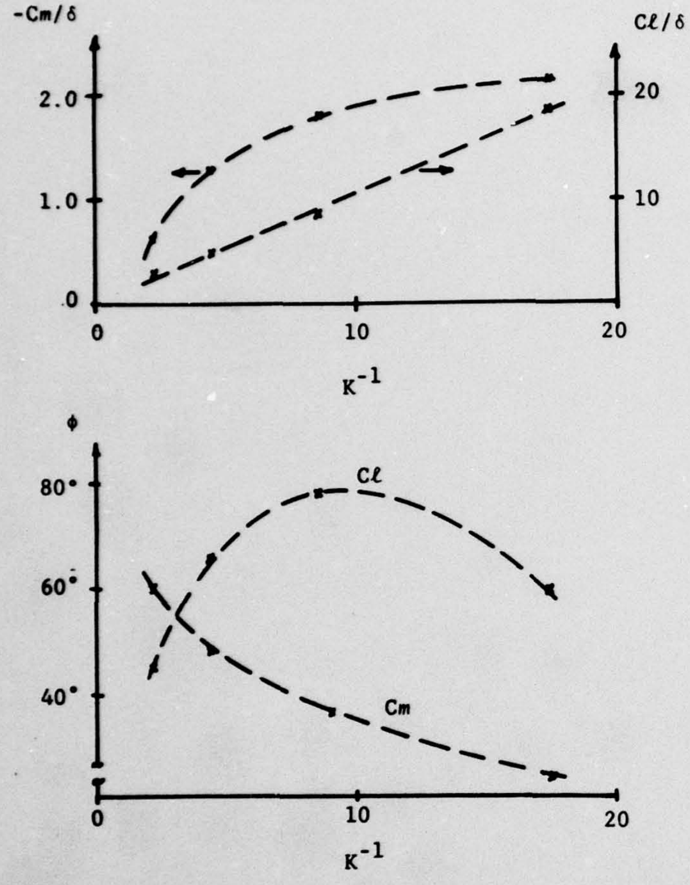

NORMALIZED LIFT AND MID-CHORD MOMENT COEFFICIENT AMPLITUDES AND PHASE LAGS FOR AN NACA 64A006 AIRFOIL WITH HARMONIC FLAP OSCILLATIONS AT M_∞ = 0.875.

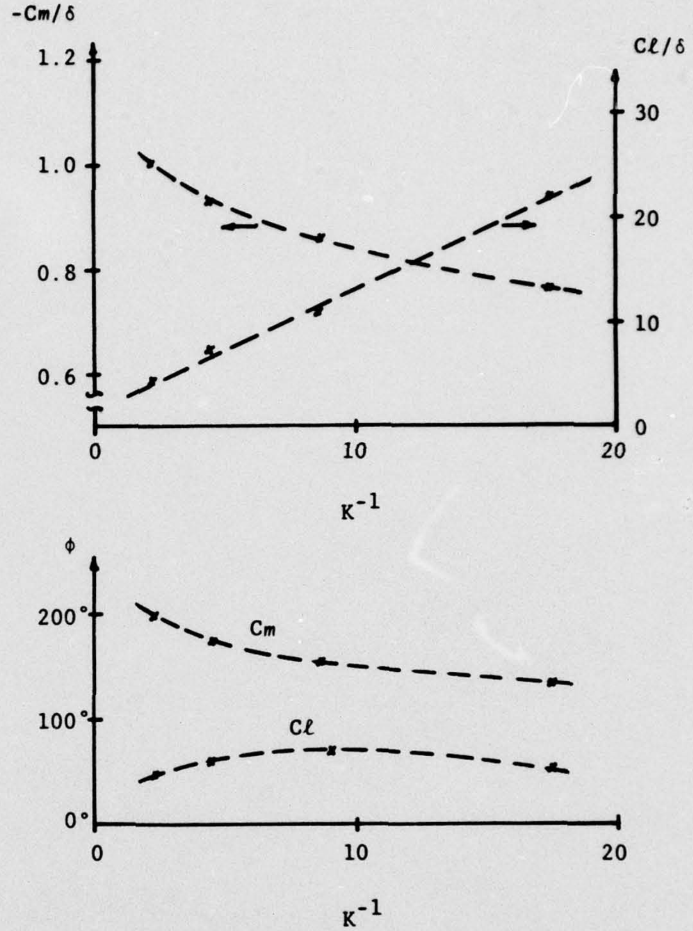

NORMALIZED LIFT AND MID-CHORD MOMENT COEFFICIENT AMPLITUDES AND PHASE LAGS FOR HARMONIC PITCHING MOTIONS OF AN NACA 64A006 AIRFOIL AT M_∞ = 0.875.

FIGURE 9.

TOWARDS A MIXED KERNEL FUNCTION APPROACH FOR UNSTEADY TRANSONIC FLOW ANALYSIS

D.D. Liu
and
B.A. Winther

NORTHROP CORPORATION
Aircraft Division
3901 West Broadway
Hawthorne, California 90250

SUMMARY

A new formulation in adopting multikernel functions, according to the mixed-flow structure, for three-dimensional analyses of the oscillatory transonic flow problems is proposed. It is aiming at a unified approach that would bridge the previous subsonic and supersonic lifting-surface methods through the regime of linearized transonic flow. The present analysis attempts to include the effect of the transonic shock wave; a mildly oscillatory shock-jump condition is derived and its compatible boundary condition considered. The only provision of the present approach is that the nonlinear mean-flow distribution must be supplied by other experimental or theoretical means.

The question of the Transonic Acceleration-Potential Equation suitable for the present kernel-function formulation is first examined. Based on the concept of local linearization, unsteady wave patterns are derived to illustrate the present model. The same concept is then applied for obtaining various kernel functions. Contour integration and frequency-perturbation techniques are suggested for evaluation of these functions. The proposed scheme for paneling of the wing is outlined and preliminary computed results are presented only for the linearized subsonic and supersonic cases. Finally, assessments of the present approach and other transonic kernel function methods are given.

Nomenclature

(x,y,z) = nondimensional carterian coordinates, normalized by the true chord length L
U = freestream velocity
t = $\bar{t}L/U$ nondimensional time
$\bar{t}$ = true time
k = $\omega L/U$, reduced frequency
ω = true angular frequency of pitch
α = angle of pitch of main wing
β = angle of pitch of flaps
Ω = time-dependent small-disturbance velocity potential normalized by $(UL)^{-1}$
$|L_\beta|$, $\phi_{L\beta}$ = magnitude and phase angle of the wing lift due to an oscillatory flap (see Reference 42 for definition

1. INTRODUCTION

The conventional engineering tool for handling the unsteady aerodynamic problems of an aeroelastic system has been the lifting surface method, also known as the kernel function method [1]. The advantage of using such a method is clear in that both the edge and the wake conditions can be absorbed into the integral formulation once and for all and the flexibility in incorporating various modes or flap motions into the flutter calculation scheme has been evidenced by numerous works in the past [2]. However, this method is largely restricted to the purely subsonic and supersonic flow cases where the perturbed velocity potential equation is a purely linearized one.

Generally, the lifting and unsteady problems in the inviscid transonic regime is a nonlinear one (e.g., [3],[4]), which usually complicates the flow field by the movements of moving shock waves on the wing planform [5]. In this case, it seems that one must resort to the current computational methods for accurate flow field details (e.g., [6,7]). But for aeroelastic considerations such as transonic flutter prediction, it may be sufficient to assume that the wing performs small amplitude oscillation as this assumption is compatible with one on which the equation of motion is based. Thus, an unsteady linearized transonic equation can be derived as a result of the small amplitude perturbation [8]. Consequently, the main position of the shock wave is essentially fixed. Let the time-dependent small-disturbance velocity potential be $\Omega(x,y,z,t)$ and it can be split into two parts, i.e.,

$$\Omega = \phi(x,y,z) + \varphi(x,y,z)e^{ikt}$$

where ϕ represents the steady mean flow potential, φ the oscillatory flow potential and k is the reduced frequency of the oscillatory motion. Apart from a few exceptional wing planform configurations, and certain flow conditions†, the approximate governing equation for oscillatory flow can be written as

$$\Box\varphi = \nu_\infty(\phi_x\varphi_x)_x \qquad (1a)$$

---

†More terms should be added to Equation (1) in the case of a sweepback, large aspect ratio wing (e.g., C-141 wing) and also when the flow field is in the proximity of a transonic shock wave.

where

$$\Box = (1 - M_\infty^2)\frac{\partial^2}{\partial x^2} + \frac{\partial^2}{\partial y^2} + \frac{\partial^2}{\partial z^2} - 2ikM_\infty^2\frac{\partial}{\partial x} + k^2M_\infty^2 \qquad (1b)$$

$$(\;)_x = \frac{\partial}{\partial x}$$

$$\nu_\infty = (\gamma + 1)M_\infty^2$$

and γ is the specific heat ratio of the gas. The mean flow potential ϕ now assumes its value at the mean flow surface $z = 0$.

Equation (1) is a plausible equation insofar as the steady flow is stable [9] and the sweep back angle is slight for wings with large aspect ratios [10]. In recent years, considerable attempts were made to solve this equation. The approaches can be broadly divided into three categories [9], [11]; 1) semi-analytical methods for sonic or near sonic flows (e.g. [8], [12] through [16]); 2) computation methods by finite difference or finite element schemes (e.g., [17] through [22]): and 3) kernel-function type of approach (e.g., [23] through [25]). While in Method 1, almost all cases are inapplicable for the supercritical flow, Method 2 continues to be in the developing stage and yet rather costly to operate particularly for the three-dimensional calculation. On the other hand, there is indeed an increasing demand for an improved flutter prediction scheme suitable for industrial practice in the transonic regime. Therefore, we conceive that if an improved kernel function method can be formulated in such a way that the mixed flow nature and the shock condition can be properly patched into the formulated scheme, then it would still be the most attractive for industrial application. It is so at least in the forseeable future. Similar assessment was given in Landahl's and Tijdeman's recent review articles [9], [26]. Subsequently, we found that it is possible to formulate a more general kernel function scheme on a more fundamental basis than those of previous attempts [23,24].

Hence, the purpose of this paper is to present two main issues of the mixed kernel function formulation. First, we present our current progress towards the development of a proposed mixed kernel function method for three-dimensional unsteady transonic flow analysis [27]. It is aiming at a unified three-dimensional approach that would bridge the previous subsonic and supersonic methods through the transonic regime. The present analysis also includes the oscillatory imbedded shock wave; a mildly unsteady three-dimensional shock jump condition is derived and its compatible boundary condition considered. The only provision of the present approach is that the mean flow solution ϕ_x must be assumed known, a priori, either from experiment or from other nonlinear theories. Secondly, we present our recent development of a constant pressure panel (CPP) scheme, which bears the unified feature for both unsteady purely subsonic and purely supersonic flows [42]. Emphasis will be placed on subjects that are of primary importance for our future development of the mixed kernel function method, 1) the transonic receding wave effects due to various approximate models, 2) the evaluation of kernel functions according to the parabolic approximation, and 3) the calculation of unsteady loads in purely subsonic and supersonic flow by CPP method.

2. TRANSONIC ACCELERATION POTENTIAL EQUATION

2.1 The Acceleration Potential

For purely subsonic and supersonic flow, the kernel function formulation is conveniently realized by the utilization of the linearized pressure, known as the acceleration potential, as a single dependent variable in the formulation. Consequently, the acceleration potential satisfies the same equation as the disturbance velocity potential equation in the pure linearized theory. For the linearized transonic flow, this is however not the case, because the equation (Eq. (1)) contains variant coefficients due to the mean flow influence. Two related questions then arise. First, the question of a valid transonic acceleration potential has not been resolved in the past [49]. An approximate linearized transonic pressure expression based on a one-dimensional mean flow has been given recently by H.C. Garner [25] and further discussed by Dowell [28]. The latter author has shown that at least for a slowly accelerated flow the pressure correction due to the nonuniform mean flow is not severely different from the purely linearized pressure. Hence, before a rigorous three-dimensional transonic acceleration potential can be established and for simplicity of the present analysis, it is assumed that the acceleration potential used for the subsequent development is defined in the usual sense, i.e.,

$$\psi \equiv \Lambda\cdot\varphi \qquad (2a)$$

where

$$\Lambda\cdot = \frac{\partial}{\partial x} + ik \qquad (2b)$$

However, we have to keep in mind that such an assumption may be applicable to the most part of the airfoil but caution must be taken in the neighborhood of the shock wave where the nonlinearity predominates. We shall come back to this point in a later stage. Secondly, there exists the question of a valid transonic acceleration potential equation, which will be discussed in the following paragraphs.

2.2 Transonic Acceleration Potential Equation

Applying operator $\Lambda\cdot$(Eq. 2b)) to Eq. (1a) and making use of Eq. (2a) results

$$\Box\psi = \nu_\infty[(\phi_x\psi_x)_x + (\Phi_x\varphi_x)_x] \qquad (3a)$$

where $\Phi \equiv \Lambda\cdot\phi$

Clearly, Eq. (3a) contains two known variant coefficients ϕ_x and Φ_x and it also consists of two dependent variables, ψ and φ. Nevertheless, the latter two are related by Eq. (2a). Following the line of Küssner [29], Richardson [30], Watkins, et al. [31], Landahl [36], the integral relation between ψ and φ reads

$$\varphi = e^{-ikx}\, I[\psi] \tag{4a}$$

where

$$I[\cdot] = \int_{-\infty}^{x} [\cdot]\, e^{ik\lambda} d\lambda \tag{4b}$$

for subsonic flow

$$= \int_{Br}^{x} [\cdot]\, e^{ik\lambda} d\lambda \tag{4c}$$

for supersonic flow

where $B = \sqrt{(M_\infty^2 - 1)}$ and $r = \sqrt{y^2 + z^2}$

Therefore, without loss of generality, we can now recast Eq. (3a) into an integro-differential equation for ψ alone, i.e.,

$$\Box\psi - \nu_\infty[(\phi_x\psi_x)_x + \Phi_x(\psi_x - ik\psi) + \Phi_{xx}\psi] = -ik\nu_\infty\varphi(\phi_{xxx} + k^2\phi_x) \tag{5}$$

where φ on the right-hand side (RHS) can be expressed in terms of ψ in an integral form (Eq. (4a)). Although it is difficult to solve Eq. (5) as is, it is possible to seek approximate solutions of it at least in the lower frequency range (i.e., $0 \leq k < 1$). If we assume that the mean flow is accelerated at a fairly slow rate such that $\phi_{xxx} \sim O(k^2)$, and all the third order terms in k are negligible, the integral term on the RHS of Eq. (5) can be dropped. The approximate form of Eq. (5) then becomes

$$[(1 - M_\infty^2) - \nu_\infty\phi_x]\psi_{xx} + \psi_{yy} + \psi_{zz} - [2\nu_\infty\phi_{xx} + ik(2M_\infty^2 + \nu_\infty\phi_x)]\psi_x$$

$$+ [k^2(M_\infty^2 - \nu_\infty\phi_x) - \nu_\infty\phi_{xxx}]\psi = O(k^3) \tag{6}$$

In passing, we note that for higher order approximations of Eq. (5), a frequency perturbation scheme can be formally formulated. That is, variables Φ, ψ, and φ in Eq. (5) can be expressed in terms of an ascending asymptotic series of (ik), i.e.,

$$\Pi = \sum_{n=0}^{N} (ik)^n \cdot \Pi^{(n)} \tag{7a}$$

where Π symbolically represents any one of Φ, ψ, and φ. Consequently, substituting Eq. (7a) into Eq. (5) yields a general recurrance equation for $(ik)^n$, i.e.,

$$\Box\psi^{(n)} - \nu_\infty \cdot \left[(\phi_x\psi_x^{(n)})_x + (\phi_{xx}\psi^{(n)})_x\right] = \nu_\infty \cdot \left\{\left[\phi_x\psi_x^{(n-1)} - \phi_{xxx}\varphi^{(n-1)}\right] - \phi_x\left[\psi^{(n-2)} - \varphi^{(n-3)}\right]\right\} \tag{7b}$$

where n = 0, 1, 2...

In this way, the integral term ignored in Eq. (5) can be recovered iteratively by the above successive approximation.

In the subsequent development, we will however restrict our attention to Eq. (6), keeping in mind that the solution of it is only accurate up to $O(k^3)$.

2.3 Comparative Study of Different Approaches

Eq. (6) can be written in a compact form as

$$\beta_o^2\psi_{xx} + \psi_{yy} + \psi_{zz} + A\psi_x + B\psi = 0 \tag{8a}$$

where

$$\beta_o^2 = (1 - M_\infty^2 - \lambda)$$

$$A = -2\Gamma - ik(2M_\infty^2 + \lambda)$$

$$B = k^2(M_\infty^2 - \lambda) - \sigma \tag{8b}$$

parameters λ, Γ, and σ are steady-mean-flow coefficients defined as

$$\lambda = \nu_\infty\phi_x \quad , \quad \Gamma = \nu_\infty\phi_{xx} \quad , \text{and} \quad \sigma = \nu_\infty\phi_{xxx} \tag{8c}$$

Earlier methods [23], [24] suggested to replace the freestream Mach Number M_∞ by a local Mach number M_L in the doublet lattice program, which have provided some improved results. If one ignores the $O(\phi_x^2)$, these earlier approximations then differ from Eq. (8a) by a complex coefficient $(2\Gamma - ik\lambda)$ in A and a real coefficient $(-2k^2\lambda - \sigma)$ in B. Clearly, it implies that these methods have partially neglected the wave damping mechanism due to the steady mean flow. On the other hand, if one employs Eq. (1) as a basic equation for ψ, then the differences from Eq. (8a) are a complex coefficient $(\Gamma + ik\lambda)$ in A and a real coefficient $(-k^2\lambda - \sigma)$ in B. Again, a part of the wave damping mechanism was absent.

3. UNSTEADY WAVE PATTERNS

3.1 Parabolic Approximation

To further elucidate the wave damping (or amplification) mechanism due to the steady mean flow influence, we must retrieve the general time dependent form of Eq. (1), i.e.,

$$\beta_\infty^2\hat{\varphi}_{xx} + \hat{\varphi}_{yy} + \hat{\varphi}_{zz} - 2M_\infty^2\hat{\varphi}_{xt} - M_\infty^2\hat{\varphi}_{tt} = \Gamma\hat{\varphi}_x + \lambda\hat{\varphi}_{xx} \tag{9}$$

where

$$\hat{\varphi} = \varphi(x,y,z;k)e^{ikt}$$

Moreover, in order to *simplify the analysis effectively, we now make use of the parabolic approximation*, i.e., setting Γ and λ as constants. This approximation has been extensively employed first by Teipel and Hosakawa (p.459 and p. 184, [34]) and later by Liu, et al., [32] for slender bodies analysis and Kimble, et al., [12] for slender wing analysis. More recently, Stahara and Spreiter [14], [32] have extended the method based on Spreiter's local linearization concept; Dowell [16] has also devloped a simplified method that accounts for a higher-order approximation in a systematic manner. In the latter two methods, it is however, necessary to consider the parabolic-approximation solutions as fundamental solutions. From a mathematical viewpoint, the parabolic approximation only provides simplified equations in a different transonic flow regime but from which exact solutions can be found insofar as the parameters Γ and λ can be justified as constants at this stage. Putting $\lambda = 0$, one returns to the original parabolic approximation assumption by Oswatitsch and Maeder that the flow model must be restricted to cases where only slow variation of the steady mean flow velocity components are admissible. On the other hand, retaining both constants, one would imply either Dowell's first-order equation in which Γ and λ are coefficients for a series representation of a steady flow distribution, or a basic step toward the application of the local linearization concept.

3.2 One-Dimensional Acoustic Disturbances

Let us first consider the one-dimensional cases of Eq. (9) based on the parabolic approximation. In the subsonic uniform stream, a unit oscillating source solution placed at $x = \xi$ simply takes the forms

$$\hat{\varphi}^+ = \exp\left\{ikt + (\alpha - \sqrt{\chi})\, X\right\} \tag{10a}$$

for $x > \xi$

$$\hat{\varphi}^- = \exp\left\{ikt + (\alpha + \sqrt{\chi})\, X\right\} \tag{10b}$$

for $x < \xi$

where $(\ )^+$ indicates the advancing wave and $(\ )^-$ indicates the receding wave; the parameters α and $\sqrt{\chi}$ are

$$\alpha = \frac{\Gamma + 2ikM_\infty^2}{2\beta_o^2} \tag{10c}$$

$$\chi = \frac{\Gamma^2/4 - k^2M_\infty^2 + ikM_\infty^2\Gamma}{\beta_o^4} \tag{10d}$$

If one is allowed in use the simplified representation for pressure in the transonic regime, the solutions (10a) and (10b) can be considered as acoustic disturbances with transonic mean flow, satisfying the approximate Eq. (9). It can be shown that these pressure waves indeed contain variable amplitudes [27]. Consequently, both waves can be attenuated, or amplified, depending on the mean flow parameters such as Γ, β_o^2, M_∞ and the pulsating frequency k. For example, the advancing wave grows in amplitude if $\Gamma > 2kM_\infty$ whereas constant amplitude results for both waves when Γ is put to zero.

The one-dimensional wave patterns are sketched in Figure 1. It is clear that leaving out the $\Gamma\varphi_x$ term in Eq. (9) amounts to removing the damping mechanism (case 1). Replacing the freestream Mach number by the local Mach number amounts to changing the local slope of the characteristics, hence the phase angle (case 2).

3.3 Three-Dimensional Unit Source

Next, consider a unit oscillatory source located at $x = \xi$, which is placed in a three-dimensional subsonic/transonic mean flow. Using the parabolic approximation, the source solution can be obtained immediately, i.e.,

$$\hat{\varphi} = -\frac{1}{4\pi R}\cdot\exp\left\{ik(t + \tilde{\alpha}\, X - \widetilde{\sqrt{\chi}}\, R)\right\} \tag{11}$$

where $\tilde{\alpha} = \alpha/(ik)$

$\widetilde{\sqrt{\chi}} = \sqrt{\chi}/(ik)$

$R = [X^2 + \beta_o^2\,(y^2+z^2)]^{1/2}$

For a large value of X such that $X^2 \gg \beta_o^2\,(y^2+z^2)$, the following asymptotic wave solutions can be derived from Eq. (11), i.e.,

$$\hat{\varphi}_x^{\pm} = \frac{1}{4\pi X}\left[\frac{1}{|X|} \mp ik(\tilde{\alpha} \mp \widetilde{\sqrt{\chi}})\right]\cdot\exp\left\{ik[t + (\tilde{\alpha} \mp \widetilde{\sqrt{\chi}})X]\right\} \tag{12}$$

where $(\ )^+$ represents the advancing wave (i.e., $X > 0$) and $(\ )^-$ represents the receding wave (i.e., $X < 0$). When Γ and λ approach zero, $\tilde{\alpha} - \sqrt{\chi}$ becomes $-M_\infty(1 + M_\infty)^{-1}$ whereas $\tilde{\alpha} + \sqrt{\chi}$ becomes $M_\infty(1 - M_\infty)^{-1}$, as expected. Hence Equations (12) generalize the purely subsonic solution given previously by Landahl (p. 12 [8]). Having obtained the wave solutions (12), we can conduct a series of testing cases for comparison of various models based on different degrees of approximations. As the advancing waves possess speed of order $O(M_L/(1 + M_L))$, they usually smoothly decay while being carried downstream by the mean flow; hence, they are of little concern. By contrast, special attention should be emphasized on the receding waves, as they propagate upstream with speed of $O((M_L - 1)/M_L)$. In many instances it is the receding wave portion that alters drastically the unsteady pressure distributions. For further discussion of the characteristics of these waves, we refer to Landahl's book [8].

From Figures 2a through 2d, the mean flow model is based on a linear accelerated flow in the local Mach number (p. 428 [9]), i.e.,

$$\text{Case A:} \quad M_L = 0.95 + 0.05X$$

$$\text{Case B:} \quad M_L = 0.9 + 0.1X$$

Figure 2a confirms the findings of the one-dimensional wave study. It is seen that letting $\Gamma = 0$ (but with $\lambda = \lambda(x)$) indeed lessens the damping effect, whereas whether letting $\lambda = 0$ or not but with $\Gamma = \Gamma(x)$ makes essentially little difference to the wave velocities. Landahl's solution by asymptotic expansion seems to give shorter waves and less damping than the present approach. Figure 2b shows that in Case B, a more rapid acceleration damps out the oscillatory wave quickly and it brings the present result closer to that given by Landahl. However, there still exists a difference in the phase angle. Figure 2c presents some trivial cases with frequency variations, however, it is interesting to see that the Case A acceleration with $k = 0.5$ amounts to nearly the same effect for the Case B acceleration at higher frequency $k = 1$ (see Fig. 2b). Figure 2d presents that all approximations (Cases 1, 2, and 3) make little change in the wave velocity for a more rapidly accelerated mean flow (Case B). Hence, the lesson learned from these wave pattern studies is that the Γ term is definitely a more significant one for the approximate transonic equation under consideration, whereas the additional inclusion of the λ-term shows comparatively less influence. Furthermore, there is also little difference between cases where Γ is being a constant or presumed to be a local variable in these wave patterns. This probably explains the reason for the close agreement between recent studies by the parabolic approximation [32] and by the local linearization procedure [33] for axisymmetric unsteady transonic flow analyses.

4. TRANSONIC KERNEL FUNCTIONS

In this section, we shall formulate three types of kernel functions according to Eq. (8), in which all the mean flow quantities are set to be constants for the time being. In this way, the basic solutions that are required in the kernel functions can then be obtained in closed forms. The classical kernel function approach can now be generalized to a multikernel formulation, i.e.,

$$K_m(X,Y,0) = \left\{ \lim_{z \to 0} \frac{\partial^2}{\partial z^2} \int_{-\infty}^{X} e^{ikx_0} \psi_m(x_0, Y, z)\, dx_0 \right\} e^{-ikX} \tag{13}$$

where X and Y are the relative distance between the sending point $(\xi, \eta, 0)$ and the receiving point $(x, y, 0)$ The subscript $m = 0,1,2$, corresponds to the case of sonic, supersonic and subsonic flow, respectively. The elementary solutions ψ_m should satisfy Eq. (8) in each case.

4.1 General Basic Solutions

Based on Eq. (8), three elementary solutions, which have been previously derived by Hosokawa and Miyoshi [34], adopted later by Liu, Platzer and Ruo [32], and by Stahara and Spreiter [33], can be written as

- Sonic Flow ($M \simeq 1.0$)*

$$\psi_0 = \begin{cases} \dfrac{e^{-\left[A_0 X + \frac{Ar^2}{4X}\right]}}{X} & \\ 0 & , \quad X \le 0 \end{cases} \tag{14a}$$

- Transonic/Supersonic Flow ($M \ge 1.0$)*

$$\psi_1 = \begin{cases} \dfrac{\cosh(\sqrt{A_2}\, R)\, e^{-A_1 X}}{R} & \\ 0 & , \quad X \le |\beta| r \end{cases} \tag{14b}$$

- **Transonic/Subsonic Flow ($M \leq 1.0$)***

$$\psi_2 = \frac{e^{-A_1 X + A_2 R}}{R} \quad \text{for all } X \tag{14c}$$

where

$$A_0 = B/A \;;\quad A_1 = -A/2\beta_0^2 \;;\quad A_2 = -(A^2 - 4\beta_0^2 B)^{1/2}/2\beta_0^2$$

$$R = (X^2 + \beta^2 r^2)^{1/2} \;;\quad r = (Y^2 + z^2)^{1/2}$$

$$X = x - \xi \text{ and } Y = y - \eta$$

It should be clarified that the Mach numbers in the brackets ( )* could be defined either as the free-stream Mach number or the local Mach number. When one applies the parabolic approximation, M becomes M_∞ and as only one type of these basic solutions will be used throughout the kernel function procedure, it is a much simplified procedure. Otherwise, for later application of the local linearization procedure, M becomes M_L, all of these basic solutions will be used for a mixed kernel function procedure (see Section 6). In the latter case, the basic solutions ψ_m above should be named as locally-sonic flow, locally-supersonic flow, and locally-subsonic flow for Eqs. (14a), (14b), and (14c), respectively. It is apparent that when $\Gamma = \lambda = \sigma = 0$ the above basic solutions, hence the kernel functions Eq. (13), reduce to their purely sonic, supersonic, and subsonic counterparts in the classical theories (e.g., [31] and [35]).

4.2 Kernel Function Evaluation

To evaluate the kernel functions defined in Eq. (13) is a laborious task. In the past, the purely subsonic kernel function has been carried out analytically to some extent or numerically by numerous investigators. In what follows, we will only outline the evaluation procedure of the transonic/subsonic kernel function.

Substituting Eq. (14c) into Eq. (13) and after rearrangement, we obtained the generalized subsonic kernel function as

$$K_2(X,Y,0) = \left\{ \frac{1}{r_0}\frac{\partial}{\partial r_0} \int_{-\infty}^{X} \frac{e^{\frac{ik}{\beta^2_*}(x_0 - NR)}}{R}\, dx_0 \right\} \cdot e^{-ikX} \tag{15a}$$

where

$$\beta_*^2 = \beta_0^2/\mu_0$$

$$N = \frac{iA_2\beta_0^2}{k\mu_0}$$

$$\mu_0 = \beta_0^2[1 + iA_1/k] \quad \text{and} \quad \frac{1}{r_0}\frac{\partial}{\partial r_0} \equiv \lim_{z\to 0}\frac{1}{r}\frac{\partial}{\partial r} \tag{15b}$$

The above parameters reduce to the corresponding purely subsonic expression as Γ, λ, and σ are put to zero, i.e., $\beta_*^2 = \beta_0^2$, $\mu_0 = 1$, hence $N = M_\infty$. Following Rodemich-Landahl's procedure [36], K_2 can be integrated by parts consecutively to yield,

$$K_2(X,Y,0) = -|Y|^{-2} \cdot \left\{ \left(\frac{N\beta_0^2|Y|}{c\,\beta_*^2 R_0} - u_1 \right) \cdot \frac{e^{-ik_1u_1}}{\sqrt{1 + u_1^2}} + ik_1\,\Pi_0 \right\} \tag{16a}$$

where

$$\Pi_0 = \int_{u_1}^{\infty} \frac{ue^{-ik_1u}}{\sqrt{1 + u^2}}\, du \quad , \tag{16b}$$

$$k_1 = k|Y| \;,\quad R_0 = (X^2 + \beta_0^2Y^2)^{1/2},\quad c = \beta_0(1 - N^2)/\beta_*^2 \;,\ \text{and}\quad u_1 = \frac{NR_0 - X}{c\beta_*^2|Y|}$$

Basically, Eqs. (16) appear to be in the same form as Rodemich-Landahl's subsonic expression. However, the lower limit u_1 of Π_0 here is a complex variable. This greatly complicates the matter, for the convenient exponential substitution by Laschka (e.g., see [37]) would cease to apply.

Nonetheless, a numerical evaluation scheme can be formulated. The integral Π_0 can be recast and split into two terms, i.e., $\Pi_0 = \Pi_a + \Pi_b$

$$\Pi_0 = \Pi_a + \Pi_b \tag{17a}$$

AD-A054 028 ADVISORY GROUP FOR AEROSPACE RESEARCH AND DEVELOPMENT--ETC F/G 20/4
UNSTEADY AERODYNAMICS.(U)
FEB 78

UNCLASSIFIED AGARD-CP-227 NL

3 OF 7
ADA
054028

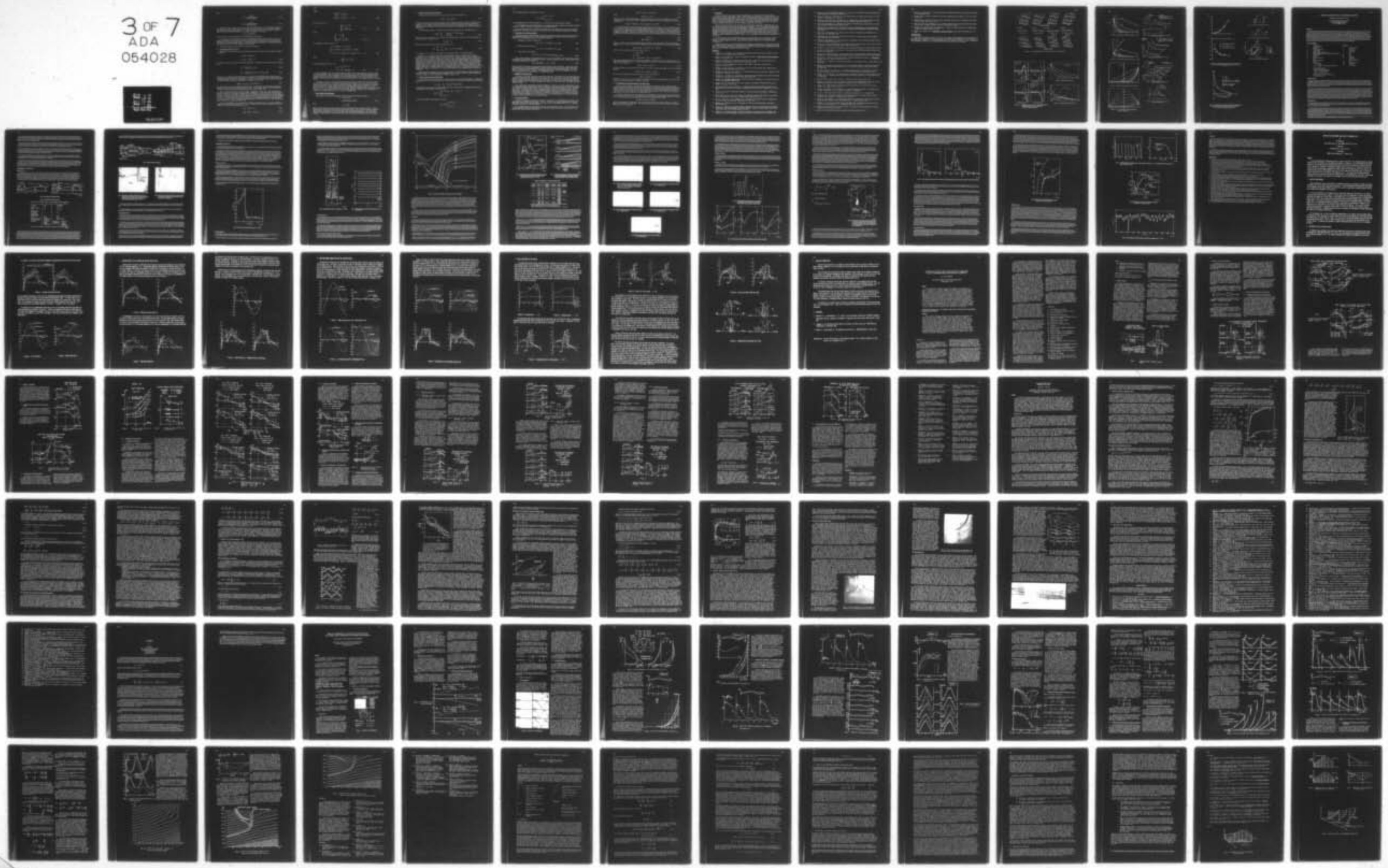

where

$$\Pi_a = \int_0^{\infty} \frac{e^{-ik_1\tau}}{\sqrt{1 + (\tau + u_1)^2}}\, d\tau \tag{17b}$$

$$\Pi_b = \int_0^{\infty} \frac{\tau e^{-ik_1\tau}}{\sqrt{1 + (\tau + u_1)^2}}\, d\tau \tag{17c}$$

Now some care must be taken in order to evaluate these integrals by the contour integral technique. Both integrals Π_a and Π_b contain two poles, but their positions can appear in any quadrant depending on the given flow conditions such as M_∞, Γ, λ, σ, and k. For example, for the case of $R_e[u_1] > 0$ with a defined contour in the fourth quadrant, Π_a is eventually equated to an integral

$$\Pi_a = i \int_0^{\infty} f(\rho) e^{-k\rho} d\rho$$

which can then be evaluated numerically by the Gauss-Laguerre Quadrature.

An alternative way of evaluation is the hybrid approximation method proposed in [27]. We split the kernel in two parts: the near-field kernel and the far-field kernel. Then the near-field part can be integrated in terms of an infinite series in (ik_1), whereas the far-field part can be integrated in the same manner as the purely subsonic kernel, by Laschka's exponential substitution, provided that ignoring the Γ-term effect in the far-field integral can be justified.

We refer to Reference 27 for details in both evaluation methods.

4.3 Low-Frequency Kernel Functions

Expanding the kernel functions and the acceleration potential for small reduced frequency according to Eqs. (7),

$$K_m = K_m^{(0)} + ikK_m^{(1)} + \cdots$$

$$\psi_m = \psi_m^{(0)} + ik\psi_m^{(1)} + \cdots \tag{18a}$$

and making use of Eq. (13) yields the following expressions for in-phase and out-of-phase kernel functions, i.e.,

$$K_m^{(0)} = \frac{1}{r_0} \frac{\partial}{\partial r_0} \int_{-\infty}^{X} \psi_m^{(0)} dx_0 \tag{18b}$$

$$K_m^{(1)} = \frac{1}{r_0} \frac{\partial}{\partial r_0} \left\{ \int_{-\infty}^{X} \psi_m^{(1)} dx_0 + \int_{-\infty}^{0} \bar{x} \psi_m^{(0)} d\bar{x} \right\} \tag{18c}$$

where $\bar{x} = x_0 - X$. Since our main interest here is to derive the low frequency kernel functions, the acceleration potential ψ_m involved only needs to satisfy the low frequency form of Eq. (8a), which amounts to dropping the terms of $O(k^2)$ in the equation. As a heuristic step, further simplification of Eq. (8a) is made by resuming the parabolic approximation in letting $\lambda = \sigma = 0$, i.e.,

$$\beta_\infty^2 \psi_{xx} + \psi_{yy} + \psi_{zz} - 2(\Gamma + ikM_\infty^2)\psi_x = 0 \tag{19}$$

The in-phase and out-of-phase acceleration potential $\psi_m^{(0)}$ can be derived from expanding the given basic solutions, of Eqs. (14), in the small parameter of $(ik)^n$. Alternatively, they can also be obtained by directly solving the frequency perturbation scheme set up earlier in Eqs. (7b).

Next, the evaluation of $K_m^{(0)}$ and $K_m^{(1)}$ requires integrations of Eqs. (18). To perform these integrations is, however, not altogether straightforward. Nonetheless, we have sucessfully obtained closed-form exact results for these kernel functions in all flow regimes, insofar as Eq. (19) is a valid approximation. It should be added that for later improvement the integration schemes used here remain essentially the same for evaluation of the more general kernel functions in which terms involving λ and σ are included. At any rate, all these integration procedures appear to be quite lengthy and some are rather laborious. For this reason, we shall only present the final expressions of these kernel functions. The detailed derivation of them will be reported elsewhere [38].

With some rearrangements, the transonic kernel functions obtained $K_m^{(i)}$ $(i = 0, 1)$ can be expressed in terms of the classical kernel functions $\kappa_m^{(i)}$ $(i = 0, 1)$, based on purely linearized equations [31,35], in combination with various tabulated functions, i.e.,

$$\bar{K}_m^{(0)} = \bar{\kappa}_m^{(0)} \cdot f_m \tag{20a}$$

$$\bar{K}_m^{(1)} = \bar{\kappa}_m^{(1)} \cdot g_m + h_m \tag{20b}$$

where

$$\begin{cases} \bar{K}_m^{(i)} \equiv Y^2 K_m^{(i)}/R \\ \bar{\kappa}_m^{(i)} \equiv Y^2 \kappa_m^{(i)}/R \qquad i = 0,\ 1 \end{cases} \tag{20c}$$

For sonic flow (m = 0)

$$\begin{cases} f_o = g_o = e^{-\Gamma\eta} \\ h_o = 2\Gamma\eta E_i(-\Gamma\eta) \qquad ,\eta > o \end{cases} \tag{21a}$$

where

$$\begin{cases} \eta = \dfrac{Y^2}{2X} \\ E_i[-\Gamma\eta] = \displaystyle\int_{-\infty}^{-\Gamma\eta} \frac{e^u}{u}\,du \qquad \text{for } \Gamma\eta > o \end{cases}$$

For transonic/supersonic flow (m = 1)

$$\begin{cases} f_1 = e^{\rho\zeta}[\cosh\rho - \zeta^{-1}\sinh\rho] \\ g_1 = e^{\rho\zeta}[\cosh\rho - \beta_\infty^2\zeta\sinh\rho/(1 - M_\infty^2\zeta^2)] \\ h_1 = \rho(1-\zeta^2)\,\{E_i[\rho(\zeta-1)] - E_i[\rho(\zeta+1)]\} \qquad ,\zeta \geq 1 \end{cases} \tag{21b}$$

where

$$\rho = \frac{\Gamma R}{\beta_\infty^2} \quad \text{and} \quad \zeta = \frac{X}{R}$$

For transonic/subsonic flow (m = 2)

$$\begin{cases} f_2 = g_2 = e^{\rho(\zeta-1)} \\ h_2 = \rho(1-\zeta^2)E_i[\rho(\zeta-1)] \qquad ,|\zeta| \leq 1 \end{cases} \tag{21c}$$

Some investigations on various limiting cases are needed. When Γ approaches zero, f_m and g_m become unity and h_m vanishes, thus, all transonic kernel functions reduce to their classical counterparts [31], [35] as they should be. When M_∞ approaches one, both transonic/supersonic and transonic/subsonic kernel functions, Eqs.(21b) and (21c), converge to the sonic kernel functions, Eq. (21a), as expected. Furthermore, all the transonic kernel functions are no more singular than Y^{-2} that appears in all the classical cases.

In Figures 3a and 3b, it is seen that the sonic kernel functions $\mp Y^2 K_o^{(i)}$ reach the classical limits at $\eta = 0$, for all Γ values. This implies that the only receiving point that is free from the transonic thickness effect (due to Γ) is located at downstream infinity. Figures 4a and 4b are plots of supersonic kernel function $Y^2K_1^{(i)}$, Figures 5a and 5b are plots of subsonic kernel functions $\mp Y^2K_2^{(i)}$. It can be observed that for all ρ values, again both types of kernel functions reach the classical limits at $\zeta = 1$. Finally, we note that in both in-phase cases, the plots are implicitly dependent on the Mach number, whereas it is not so for the out-of-phase cases. For sonic kernel functions, the in-phase plot is implicitly dependent on X, whereas again it is not so for the out-of-phase plot.

5. MIXED KERNEL FUNCTION APPROACH

The formulation of the kernel functions is aiming at solving the integral equation

$$\begin{aligned} \varphi_z &= w(x,y,0;\ M_\infty,k) \\ &= a_0 \iint p(\xi,\eta) K_m(X,Y,0)\,d\xi\,d\eta \end{aligned} \tag{22}$$

where

$$a_0 = -\frac{1}{8\pi}\ .$$

This equation represents the normal velocity-pressure relation evaluated on the wing planform. With the downwash given, the pressure function $p(\xi,\eta)$ is the solution sought. The technique of pressure evaluation can be broadly classified as the classical method (or the pressure-mode method e.g., [31], [35], [39]) and the discrete-element method (e.g., [40], [41], [42]). For the present approach, the latter method appears to be more suitable. The reason for this and the evaluation procedure are described as follows.

5.1 Constant-Pressure-Panel (CPP) Method

Ordinarily the pressure function $p(\xi,\eta)$ is sought in the following form, i.e.,

$$p(\xi,\eta) = \sum_{j=1}^{N} b_j f_j(\xi,\eta) \tag{23a}$$

In the pressure mode method, further knowledge of f_j is required, this hence restricts the applicability in general. As one type of the discrete element methods, the CPP method was originally developed by Woodward [41] for a unified application to the lifting subsonic and supersonic flow. Rodden [43] later suggested the generalization to the unsteady flow, which led to the subsequent development by Winther [42] at Northrop.

The method simply replaces a "sending" point on the panel element by the "sending" panel, i.e.,

$$f_j(\xi,\eta) = \begin{cases} 1 & ,(\xi_{j-1},\eta_{j-1}) < (\xi,\eta) < (\xi_j,\eta_j) \\ 0 & ,\text{otherwise} \end{cases} \tag{23b}$$

where subscript 'j' is referred to the location of the sending panel. Now Eq. (22) can be expressed in the form of a matrix equation, i.e.,

$$W_i = \sum_j D_{ij} \cdot b_j \tag{24a}$$

where for the linearized version of D_{ij}, K_m becomes κ_m, i.e.,

$$D_{ij} = \int_{\xi_{j-1}}^{\xi_j} \int_{\eta_{j-1}}^{\eta_j} \kappa_m(x_i - \xi, y_i - \eta, 0; M_\infty, k)\, d\xi\, d\eta \tag{24b}$$

the subscript 'i' is referred to the location of the receiving point (or collocation point).

Reference [42] certainly provided some very encouraging results. It demonstrated the method by applying it to a rectangular wing of aspect ratio Æ = 2.0. In Figures 6 and 7, the lift slope coefficients for the case in Figure 6 differ by less than 3 percent between collocation points situated at the panel center and at the panel trailing edge. Besides, a rather coarse paneling scheme (6 x 8 points on semiwing) was used, and yet the results compare favorably with other known solutions. Figure 8 presents the result for a rectangular wing with a deflected control surface. Figure 9 shows that the CPP method indeed gives accurate lift slope coefficients in both linearized flow ranges for rectangular wings with different aspect ratios. For unsteady subsonic calculations, Figure 10a presents the unsteady lift and its phase angle for a rectangular wing due to an oscillatory flap at $M_\infty = 0$; Figure 10b shows the unsteady pressure distribution at midspan location of a rectangular wing, of Æ = 3.0, oscillating in the first bending mode. Again, in both cases, it is seen that the comparison with experiments and with theory are excellent.

Hence, from these preliminary results, one may conclude that the CPP method is indeed applicable for unified treatments of unsteady subsonic and supersonic flows. A natural extension of such a method is, of course, to apply it for the treatments of unsteady transonic flow.

5.2 The Mixed Kernel Function (MKF) Method

Two typical transonic flow patterns are considered here for the proposed MKF schemes: 1) supercritical flow (Figure 11a), 2) sonic flow (Figure 11b). The D_{ij} matrix now contains the transonic kernel functions K_m as

$$K_m = K_m[x_i - \xi, y_i - \eta, 0; M_\infty, \Gamma(\xi), \lambda(\xi), \sigma(\xi), k]$$

For simplicity consider Case 1 in the two-dimensional case. The D_{ij} matrix is represented by three different matrices in the mixed flow regions, i.e.,

$$D_{ij} = E_{ij}, \begin{cases} 0 < \xi_j < x_* \quad \text{and} \quad x_s < \xi_j < 1 \\ 0 < x_i < 1 \end{cases} \tag{25a}$$

in the locally-subsonic flow region (m = 2); and

$$D_{ij} = H_{ij}, \begin{cases} x_* < \xi_j < x_s \\ \xi_j < x_i < 1 \end{cases} \tag{25b}$$

in the locally-supersonic flow region ($m = 1$); and

$$D_{ij} = P_{ij}, \begin{cases} x_*^- < \xi_j < x_*^+ \\ \xi_j < x_i < 1 \end{cases} \tag{25c}$$

in the neighborhood of the sonic line where $m = 0$. Note that x_* is the sonic point location.

In the neighborhood of the shock location $x = x_s$, extreme care must be exercised in forming the matrix equation, Eq. (24a). This will be elaborated in the following section.

For sonic freestream (Case 2) without the imbedded shock wave, the situation becomes much simplier. Although we may still have to use all the kernel functions, we are effectively dealing with two regions.

5.3 Comparison of the Previous Methods

Having outlined our proposed procedure, we can now compare the kernel-matrix with two existing kernel function methods currently in use for the transonic flow calculation [23,24]. These kernel function matrices in the two-dimensional case can be expressed simply as

1. Cunningham's matrix (two types) [23]

$$D_{ij} = D(x_i - \xi_j;\ M_i, \omega L/U_i) \ ;\ M_i = M(x_i) \tag{26a}$$

2. NLR's matrix (one type) [24]

$$D_{ij} = D(x_i - \xi_j;\ M_j, \omega L/U_\infty) \ ;\ M_j = M(\xi_j) \tag{26b}$$

3. Present matrix (three types)

$$D_{ij} = D(x_i - \xi_j;\ M_\infty,\ [\Gamma(\xi_j),\ \lambda(\xi_j), \sigma(\xi_j)],\ \omega L/U_\infty) \tag{26c}$$

In Eq. (26a), apparently the normalization of ω by U_i is quite arbitrary. For the selection of local Mach number, M_i in Eq. (26a) is incorrectly assigned. Rather, M_j should be chosen. However, based on the pressure-mode method, D_{ij} is defined as

$$D_{ij} = \iint f_j(\xi, \eta) K(x_i - \xi,\ y_i - \eta)\ d\xi d\eta \tag{26d}$$

where the index j only refers to the jth pressure mode instead of the jth elements. In this case, since the selection of a single M_j corresponding to a particular mode function f_j would not make sense, some thought is required in reformulating the mixed-kernel version of the pressure-mode method. On the other hand, in Eqs. (26b) and 26c), j refers to the sending panel element, so that the assignment of a local (or a mean) Mach number to each element is a straightforward task.

6. TREATMENT OF THE SHOCK WAVE

In the past, oscillatory shock wave condition has been derived and "patched" to the various linearized transonic solutions by Coupry and Piazzoli [44], Landahl [8], and Eckhaus [45]. The former two works were based on the potential model, whereas the latter was based on the linear perturbation of Euler's equation. They all, however, assume the steady shock position is known, a priori, and let it be represented by a one-dimensional normal shock. An unsteady one-dimensional shock wave is then evaluated at the steady mean position of the shock.

On the other hand, recent numerical studies by Ehlers [17], Traci, et al. [18], and Weatherill, et al. [19], have ignored the prescribed shock condition altogether. Some effort has been put forth by Cunningham in patching his transonic kernel function with the oscillatory shock condition that he derived. We found that, however, his shock condition does not approach Landahl's expression corresponding to the low frequency limit. Furthermore, all the upstream perturbations were ignored in his shock condition. Earlier investigators such as Eckhaus did so because they had adopted a flat plate model to simplify the flow condition upstream of the shock for the convenience of control surface analysis. But for a general program of kernel function development as such, the terms due to the upstream perturbation must be fully retained in order to include the influence of the nonuniform flow.

6.1 Shock-Jump Condition

To simplify the physical situation, we proposed a condition for a three-dimensional oscillatory shock wave based on a cylindrical mean shock wave. That is, we assume that the mean steady shock wave is one-dimensional (normal shock) at each spanwise $y = c$ plane, but it is two-dimensional on the $z = 0$ planform, with given shock shape $x = S(y)$ (see Figure 12).

The perturbed oscillatory shock shape is assumed three-dimensional, however. We further impose that the amplitude and frequency of shock oscillation is the same as that performed by the wing motion. The general shock shape can then be described as

$$F(x,y,t) = F_0(x,y) - \delta(y,z)e^{ikt} = 0 \tag{27a}$$

where

$$F_0(x,y) = x - S(y) \tag{27b}$$

and $\delta(y,z)$ is the perturbed shock shape. All flow properties then need to be transferred to the mean shock position $F_0 = 0$ by means of Taylor's expansion; for example, the mean flow potential now should be expressed as

$$\phi(x,y,z) = \phi_0(S(y),y,z) + F_0(x,y)\phi_{0_x}(S(y),y,z) + O(\delta^2) \tag{27c}$$

To be consistent with our low-frequency approximation, we only attempt to derive the mildly unsteady shock condition. Thus, recasting the mildly unsteady equation for potential Ω (set, $\Omega_{tt} = 0$) in a conservative form and making use of the divergence theorem yields a set of difference equations for mean flow potential ϕ_0 and another set for the oscillatory flow potential φ_0. The former set is the well-known two-dimensional shock polar. Meanwhile, we require that the total perturbed potential Ω be continuous across the shock wave on the premise that only the weak shock solution is admissible; hence two conditions result, i.e.,

$$\langle \phi_0 \rangle = 0 \tag{28a}$$

$$\langle \varphi_0 \rangle + \delta\langle \phi_{0x} \rangle = 0 \tag{28b}$$

where $<\cdot> = (\cdot)^{\oplus} - (\cdot)^{\ominus}$ is the shock jump difference operator. Now, making use of these two conditions together with the mean-flow shock polar, we obtain the oscillatory shock condition after some rearrangement, i.e.,

$$\langle c_0\varphi_{0x} \rangle + (ikc_1 - d_0 + 2S'd_1)\langle \varphi_0 \rangle = 2S'\langle \varphi_{0y} \rangle \tag{29a}$$

where all the coefficients are due to the mean flow, i.e.,

$$c_0 = \beta_\infty^2 - \nu_\infty\phi_{0x}$$

$$c_1 = -2M_\infty^2$$

$$d_0 = \langle c_0\ \phi_{0xx} \rangle / \langle \phi_{0x} \rangle \quad \text{and} \quad d_1 = \langle \phi_{0yx} \rangle / \langle \phi_{0x} \rangle$$

Next, several degenerate cases of Eq. (29a) are considered. When $S'(y)$ is set to a constant slope m, the mean shock shape then maintains a constant skewed angle θ to the mean flow direction; and when m is set to zero, Eq. (29a) reduces to

$$\langle c_0\varphi_{0x} \rangle + (ikc_1 - d_0)\langle \varphi_0 \rangle = 0 \tag{29b}$$

On the other hand, when the perturbed shock shape is related to the mean shock shape by $\delta_y = S'(y)$, Eq. (29a) becomes

$$\langle c_0\varphi_{0x} \rangle + (ikc_1 - d_0)\langle \varphi_0 \rangle = 2S'\langle \phi_{0y} \rangle \tag{29c}$$

For a strictly one-dimensional mean shock wave, Eq. (29c) then reduces to

$$\langle c_0\varphi_{0x} \rangle + ikc_1\langle \varphi_0 \rangle = 0 \tag{29d}$$

Evidently, Eq. (29d) is no more than Landahl's one-dimensional unsteady shock condition [8, Eq. (10.13)], which is the unsteady counterpart of Prandtl's relation.

6.2 The Compatible Boundary Conditions at the Shock Point

At the foot of the shock, a very delicate region appears for both the steady and unsteady cases. Oswatitsch and Zierep [46] have resolved the local solution which shows that for a convex body there exists a rapid expansion region followed by a smoothed compression in the downstream neighborhood of the shock. In order to achieve a consistent condition, which would both satisfy the shock-jump condition and the tangency condition, the shock slope at $x = x_s$ must be normal to the surface. This leads to the well-known singularity in the local solution due to a steady shock wave.

A similar situation exists in the unsteady case. Avoiding the detailed investigation on the unsteady Oswatitsch-Zierep problem for the time being, we are really interested in achieving a compatible condition at $x = x_s$, which would satisfy the jump condition and the tangency condition, namely

$$w(x,y,0;k) = h_x(x,y) + ikh(x,y)$$

where $h(x,y)$ represents the mode shape. Once the compatible condition is properly derived at the shock point, we then proceed to incorporate it into the matrix equations (24) and (25). Such effort for the two-dimensional case is in progress.

7. DISCUSSIONS

We have outlined the basic steps toward a new development of the mixed kernel function method as a transonic lifting surface theory. Several issues, which are considered as the building blocks of the present theory, have been examined in detail. In fact, the present work takes a close look into the feasibility of a mixed kernel function method, whereas much of the necessary investigations has been ignored in an earlier study by Cunningham [23]. Still, we feel that further analytical investigations are required before a meaningful numerical work can be put forth. For example, the question of an exact equation for transonic acceleration potential in the full frequency range is not yet resolved.

The present kernel functions have been based on the parabolic approximation. Admittedly, this is a crude model by itself which may contain unsatisfactory flow details. It is nevertheless a global method in that the global numbers such as stability derivatives or flutter speeds at low frequencies (with fairly low order mode shapes) can be accounted for expediently. Besides, we have shown that it can be readily extended to other methods relating the concept of local linearization or Dowell's model. As seen from the receding wave studies in Figures 2, however, the phase angle of all these models may not turn out to be desirable. This was pointed out by Landahl recently [9]. The remedy for the present model is perhaps to take up an earlier suggestion of Landahl's ([34], p. 427) to superpose a phase correction potential on the formulation.

On the other hand, the formulated MKF method does not require necessarily to couple with a fixed pressure evaluation scheme such as CPP. Other discrete element methods, the classical pressure-mode methods, or a hybrid method [47] with proper modification may work equally well in combination with the MKF method.

Finally, we believe that the present method, once developed, should provide a useful tool as a scheme for unsteady transonic calculations for unbounded flow, or even for internal flows in turbomachinery, e.g., [48]. For industrial application, it should be more cost-effective than the current computational methods particularly in analyzing a complicated aeroelastic system.

REFERENCES

1. Landahl, M.T., and Stark, V.J.E., "Numerical Lifting-Surface Theory: Problems and Progress," AIAA J. Volume 6, No. 11, November 1968, pp. 2049-2059.

2. Ashley, H., and Rodden, W.P., "Wing-Body Aerodynamic Interaction," Annual Review of Fluid Mechanics, Volume 4, 1972, pp. 431-472.

3. Cheng, H.K., and Hafez, M.M., "Transonic Equivalence Rule: A Nonlinear Problem Involving Lift," Journal of Fluid Mechanics, Volume 72, Part 1, 1975, pp. 161-187.

4. Cole, J.D., "Modern Developments in Transonic Flow," SIAM J. Appl. Math., Volume 29, No. 4, December 1975, pp. 763-787.

5. Tijdeman, H., "On the Motion of Shock Waves on an Airfoil with Oscillating Flap," Symposium Transonicom II (IUTAM) Gottingen, 1975, pp. 49-56.

6. Ballhaus, W., Magnus, R., and Yoshihara, H., "Unsteady Transonic Flow Calculations," CASD-NSC-75-005, September 1975, Also AIAA Paper 75-98.

7. Yoshihara, H., and Magnus, R., "The Transonic Oscillation Flap," AGARD Specialist Meeting on Unsteady Aerodynamics in Separated and Transonic Flow, Lisbon, April 1977.

8. Landahl, M.T., Unsteady Transonic Flow, International Series of Monographs in Aeronautics and Astronautics, Pergamon Press, London, 1961.

9. Landahl, M.T., "Some Developments in Unsteady Transonic Flow Research," Symposium Transsonicum II (IUTAM), Gottingen, 1975, pp. 1-32.

10. Ballhaus, W.F., Bailey, F.R., and Frick, J., "Improved Computational Treatment of Transonic Flow about Swept Wings," NASA CP-2001 Advances in Engineering Science, Volume 4, November 1976, pp. 1311-1320.

11. Bland, S.R., "Comments on NASA Langley Research in Transonic Unsteady Aerodynamics," AGARD Report No. 611, 1973.

12. Kimble, K.R., Liu, D.D., Ruo, S.Y., and Wu, J.M., "Unsteady Transonic Flow Analysis for Low Aspect Ratio, Pointed Wings," AIAA Journal, Volume 12, April 1974, pp. 516-522.

13. Ruo, S.Y., Yates, E.C. Jr., and Theisen, J.G., "Calculation of Unsteady Transonic Aerodynamics for Oscillating Wings with Thickness," AIAA Paper No. 73-326, 1973.

14. Stahara, S.S., and Spreiter, J.R., "Development of a Nonlinear Unsteady Transonic Flow Theory," NASA CR-2258, 1973.

15. Isogai, K., "A Method for Predicting Unsteady Aerodynamic Forces on Oscillating Wing with Thickness in Transonic Flow Near Mach Number 1," National Aerospace Laboratory Technical Report NAL-TR-468T, Tokyo, Japan, June 1974, Also AIAA Paper No. 74-360.

16. Dowell, E.H., "A Simplified Theory of Oscillating Airfoils in Transonic Flow," Proceedings of the Symposium on Unsteady Aerodynamics, University of Arizona, Tucson, Volume II, pp. 655-679, 1975.

17. Ehlers, F.E., "A Finite Difference Method for the Solution of the Transonic Flow around Harmonically Oscillating Wings," NASA CR-2257, January 1974.

18. Traci, R.M., Farr, J.L., and Albano, E., "Perturbation Method for Transonic Flows about Oscillating Airfoil," AIAA Paper 75-877, June 1975.

19. Weatherill, W.H., Ehlers, F.E., and Sebastian, J.D., "Computation of the Transonic Perturbation Flow Fields around Two- and Three-Dimensional Oscillating Wings," NASA CR-2599, April 1975.

20. Beam, R.M., and Warming, R.F., "Numerical Calculations of Two-Dimensional, Unsteady Transonic Flows with Circulation," NASA TN D-7605, February 1974.

21. Ballhaus, W.F., and Goorjian, P.M., "Implicit Finite-Difference Computations of Unsteady Transonic Flows about Airfoils, Including the Treatment of Irregular Shock-Wave Motions," AIAA Paper 77-205, January 1977.

22. Chan, S.T.K., and Brashears, M.R., "Finite Element Analysis of Transonic Flow," AFFDL-TR-74-11, March, 1974, Also AIAA Paper 75-875.

23. Cunningham, A.M., "An Oscillatory Kernel Function Method for Lifting Surfaces in Mixed Transonic Flow," AIAA Paper No. 74-359, 1974.

24. Tijdeman, H., And Zwaan, R.J., "On the Prediction of Aerodynamic Loads on Oscillating Wings in Transonic Flow," NLR MP 73025, April 1973.

25. Garner, H.C., "A Practical Approach to the Prediction of Oscillatory Pressure Distributions on Wings in Supercritical Flow," RAE Technical Report 74181, February 1975.

26. Tijdeman, H., "High Subsonic and Transonic Effects in Unsteady Aerodynamics," NLR TR 75079U, May 1975.

27. Liu, D.D., "A Mixed Kernel Function Method for Unsteady Transonic Flow Calculations," Northrop Tech-Brief PC 20-59, March 1976.

28. Dowell, E.H., "A Simplified Theory of Oscillating Airfoils in Transonic Flow: Review and Extension," AIAA/ASME 18th Structural Dynamics Conference, San Diego, California, March 21-23, 1977, pp. 209-224.

29. Küssner, H.G., "General Lifting Surface Theory," in AIAA Selected Reprints Volume V, Aerodynamics Flutter, Editor I.E. Garrick, March 1967, pp. 36-39.

30. Richardson, J.R. "A Method for Calculating the Lifting Forces on Wings," ARC Tech. Report R&M No. 3157, April 1955.

31. Watkins, C.E., Runyan, H.L., and Woolston, D.S., "On the Kernel Function of the Integral Equations Relating the Lift and Downwash Distribution of Oscillating Finite Wings in Subsonic Flow," NACA RPT 1234, 1955

32. Liu, D.D., Platzer, M.F., and Ruo, S.Y., "Unsteady Linearized Transonic Flow Analysis for Slender Bodies," AIAA Jornal, Volume 15, No. 7, July 1977, pp. 966-973, Also see AIAA Paper 70-1970.

33. Stahara, S.S., and Spreiter, J.R., "Unsteady Local Linearization Solution for Pitching Bodies of Revolution at $M_\infty = 1$: Stability Derivative Analysis," AIAA Journal, Volume 14, No. 10, October 1976, pp. 1402-1408.

34. Symposium Transsonicum, Volume I, Edited by Oswatitsch, Springer-Verlag, Berlin, 1962.

35. Watkins, C.E., and Berman, J.H., "On the Kernel Function of the Integral Equation Relating Lift and Downwash Distributions of Oscillating Wings in Supersonic Flow," NACA RPT 1257, 1957.

36. Landahl, M.T., "Kernel Function for Nonplanar Oscillating Surfaces in a Subsonic Flow," AIAA J. Volume 5, No. 5, May 1967, pp. 1045-46.

37. Giesing, J.P., Kalman, T.P., and Rodden, W.P., "Subsonic Unsteady Aerodynamics for General Configurations," AFFDL-TR-71-5, Part 1, Volume 1, November 1971, Appendix A.

38. Liu, D.D., "Some Kernel Function Results for Linearized Transonic Flow," to be published.

39. Cunningham, A.M., "Oscillatory Supersonic Kernel Function Method for Isolated Wings," Journal of Aircraft, Volume II, Number 10, October 1974, pp. 609-615.

40. Albano, E., and Rodden, W.P., "A Double-Lattice Method for Calculating Lift Distributions on Oscillating Surfaces in Subsonic Flows," AIAA Journal, No. 11, November 1969, p. 2192.

41. Woodward, F.A., "Analysis and Design of Wing-Body Combination at Subsonic and Supersonic Speeds," Journal of Aircraft, Volume 5, No. 5, November-December 1968, pp. 528-534.

42. Winther, B., "A Consistent Finite Element Approach to Linearized Unsteady Aerodynamics," Northrop Technical Brief NB 75-218, July 1975.

43. Rodden, W.P., Private Communication (Consultant to Northrop Corporation) 1975.

44. Coupry, G., and Piazzoli, G., "Etude du Flottement en Regime Transsonique," La Recherche Aeronautique No. 63, March-April 1958.

45. Eckhaus, Wiktor, "A Theory of Transonic Aileron Buzz Neglecting Viscous Effects," J.A.S., June 1962, pp. 712-718.

46. Oswatitsch, K., & Zierep, J., "Das Problem des Senkrechten Stosses an Einer Gekrummten Wand," ZAMM, Volume 40, Suppl. 1960, ppl T143-144.

47. Shen, C.C., Lopez, M.L., and Wasson, N.F., "A Jet-Wing Lifting-Surface Theory Using Elementary Vortex Distributions," Journal of Aircraft, Volume 12, May 1975, pp. 448-456.

48. Platzer, M.F., "Unsteady Flows in Turbomachines - A Review of Current Developments," AGARD Unsteady Aerodynamic Symposium, Ottawa, Sept. 1977.

49. Ashley, H.R., Landahl, M.T., Aerodynamics of Wings and Bodies, Addison-Wesley Publishing Co., Inc. 1965.

ACKNOWLEDGEMENT

The authors are grateful to Ms. P.A. Hill for her assistance in the computations of the present work. They would like to thank Dr. W.P. Rodden, Professor H.K. Cheng of the University of Southern California and Professor M.F. Platzer of the Naval Postgraduate School for valuable discussions. Also the suggestions forthe manuscript offered by Dr. R. Schamberg of Northrop Corporation were very helpful.

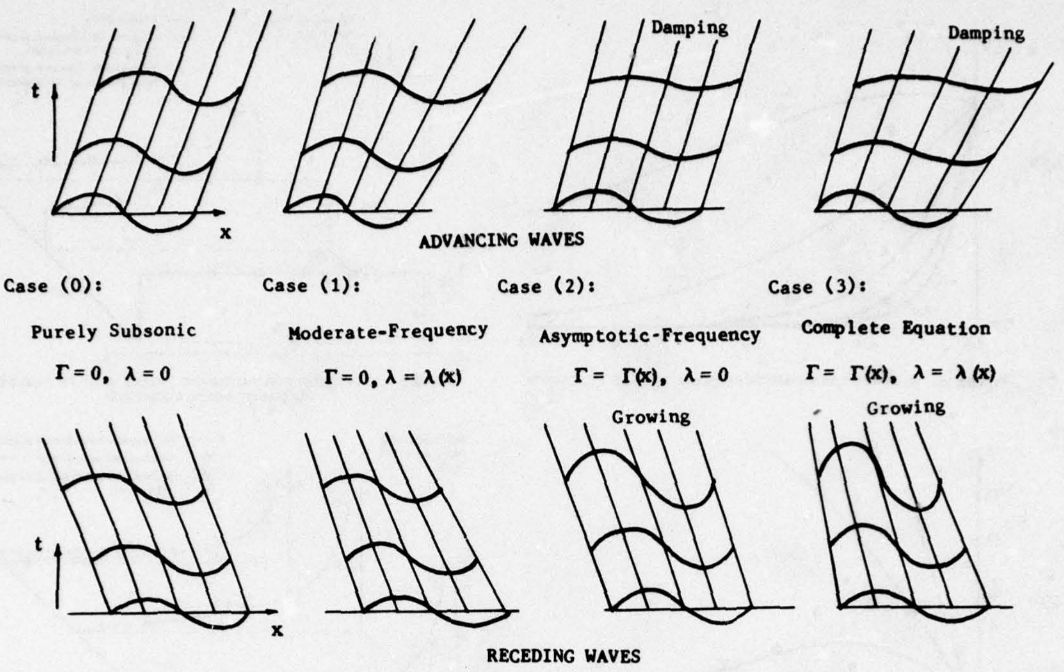

Figure 1 Wave Propagations According to Various Approximations

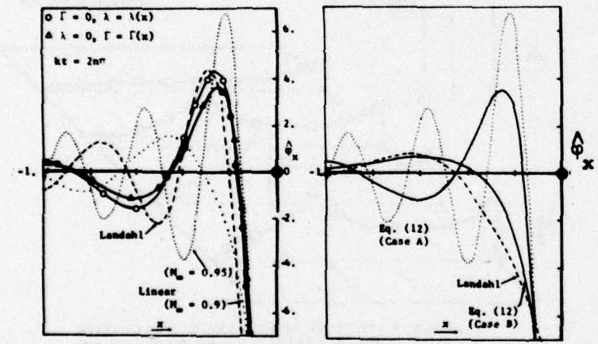

(a) Case A acceleration

(b) Comparison of Case A and Case B accelerations

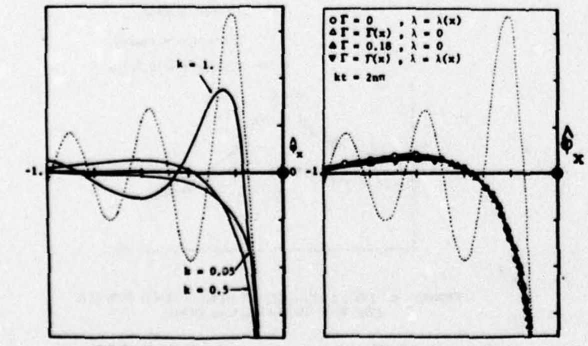

(c) Frequency effects

(d) Case B acceleration

Figure 2. Receding Waves due to a Three-Dimensional Dimensional Unit Source According to Various Approximations

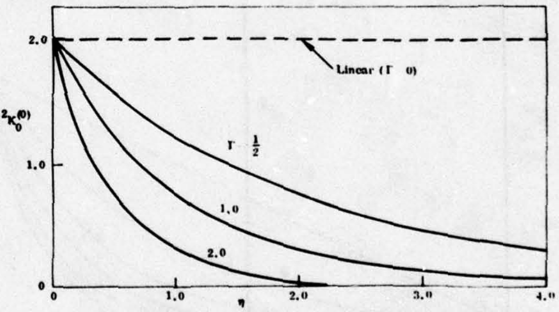

FIGURE 3a. IN-PHASE SONIC KERNEL FUNCTIONS

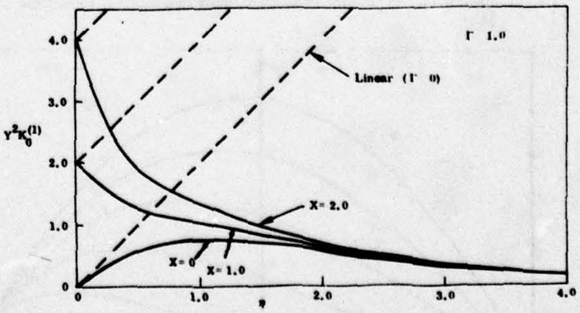

FIGURE 3b. OUT-OF-PHASE SONIC FLOW KERNEL FUNCTION

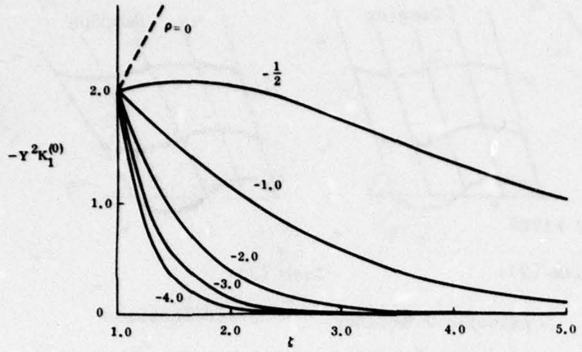

FIGURE 4a. IN-PHASE TRANSONIC/SUPERSONIC KERNEL FUNCTIONS

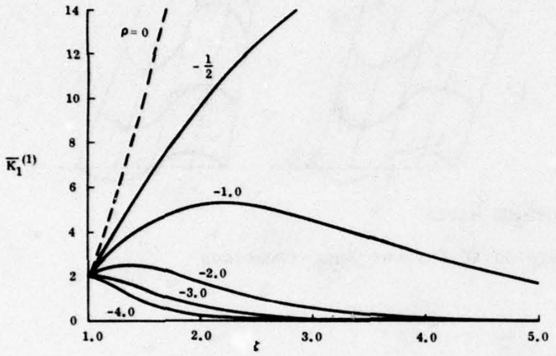

FIGURE 4b. OUT-OF-PHASE TRANSONIC/SUPERSONIC KERNEL FUNCTIONS

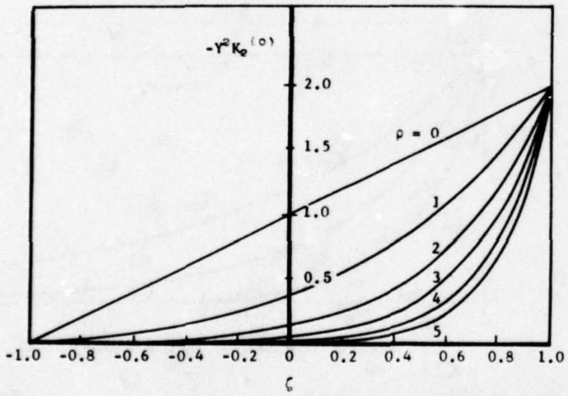

Figure 5a. In-Phase Transonic/Subsonic Kernel Functions

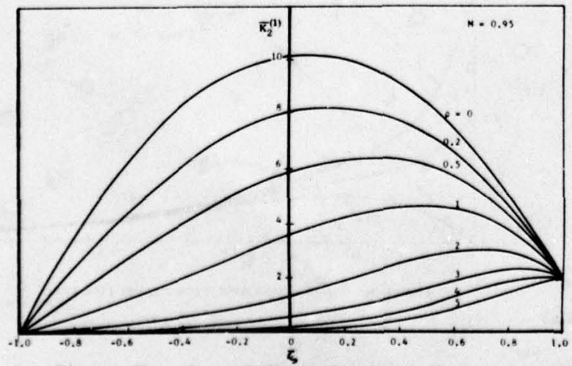

Figure 5b. Out-of-Phase Transonic/Subsonic Kernel Functions

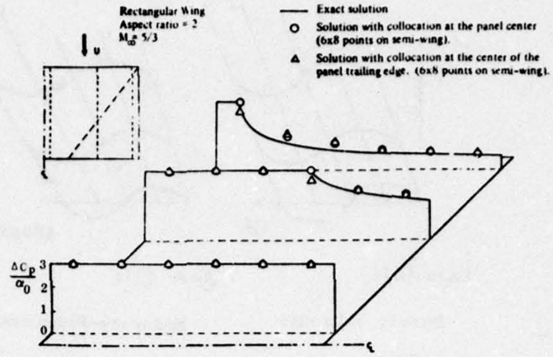

FIGURE 6. SOLUTION FOR SUPERSONIC FLOW WITH TWO DIFFERENT CONTROL POINT LOCATIONS

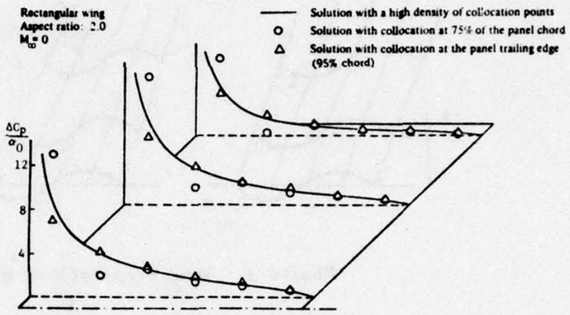

FIGURE 7. SOLUTION FOR SUBSONIC FLOW WITH TWO DIFFERENT CONTROL POINT LOCATIONS

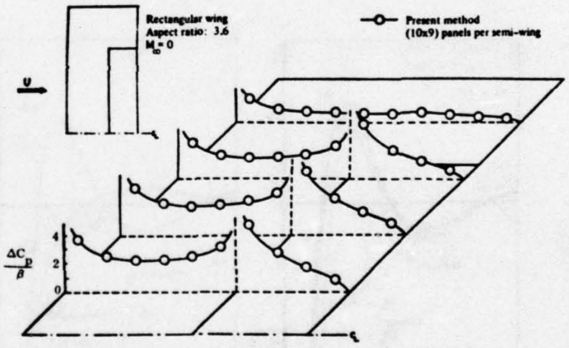

FIGURE 8. PRESSURE DISTRIBUTION DUE TO CONTROL SURFACE DEFLECTION AT $M_\infty = 0$

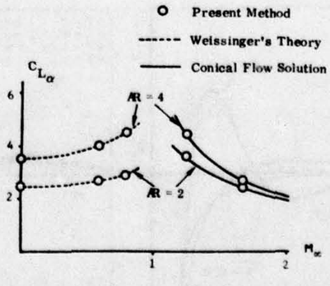

FIGURE 9. LIFT CURVE SLOPE VERSUS MACH NUMBER FOR TWO RECTANGULAR WINGS

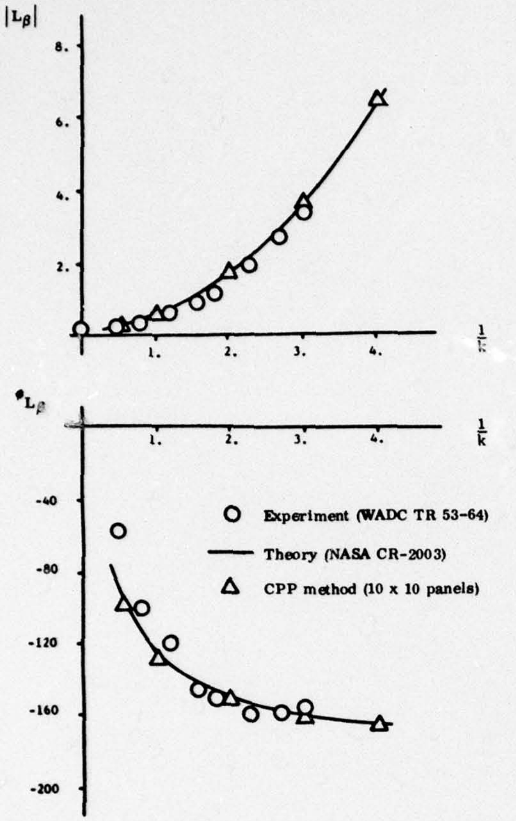

FIGURE 10a. MAGNITUDE AND PHASE ANGLE OF THE LIFT FOR A RECTANGULAR WING WITH OSCILLATING CONTROL SURFACES ($M_\infty = 0$, Æ = 2.0)

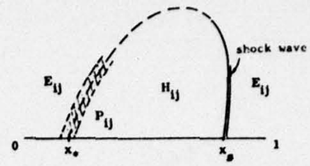

Figure 11a. Mixed Kernel Functions Related to Mixed Flow (1

Figure 11b. Mixed Kernel Functions Related to Mixed Flow (2)

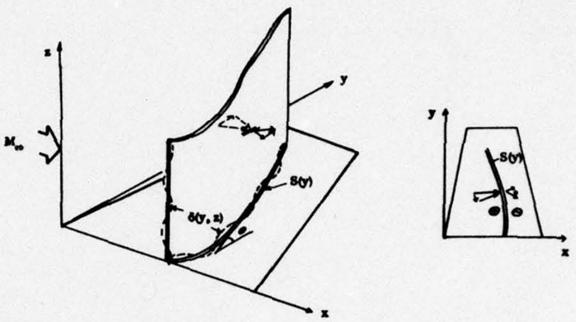

Figure 12. Oscillatory Shock Wave Showing Notation

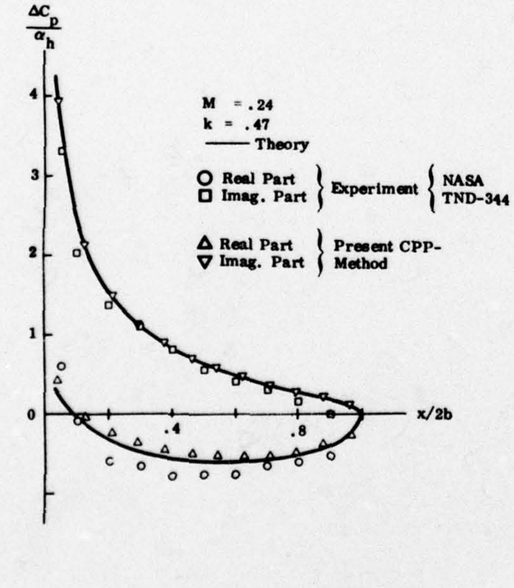

FIGURE 10b. MEASURED AND PREDICTED PRESSURE DISTRIBUTIONS AT 50% SPAN OF AN ASPECT RATIO 3.0, RECTANGULAR WING OSCILLATING IN THE FIRST BENDING MODE

UNSTEADY TRANSONIC FLOW IN A TWO-DIMENSIONAL DIFFUSER*

M. Sajben, J.C. Kroutil, and C.P. Chen

McDonnell Douglas Research Laboratories
McDonnell Douglas Corporation
St. Louis, Missouri 63166

SUMMARY

Two-dimensional diffuser flows including a normal shock near the throat were investigated using a model with a 2.36 exit-to-throat area ratio. Reynolds numbers based on the 48 mm throat height ranged to 10^6; the largest time-mean shock Mach number was 1.45. Extensive sidewall and corner boundary layer control produced reasonable two-dimensionality of the time mean flow. The flow was separated at all transonic conditions. Observation and subsequent quantitative analysis of high-speed schlieren films show that the investigated system exhibits low-frequency fluctuations, highly correlated over the entire diffuser length. Shock oscillations occur mostly in the 70-160 Hz range; the maximum shock displacement amplitudes are comparable to the throat height. Time mean shock Mach number strongly influences shock and separation bubble configurations. Upstream propagating trains of weak normal shocks, prominant in the post-shock core flow zone, appear to be important in determining fluctuation properties.

LIST OF SYMBOLS

a	acoustic speed
A	cross-sectional area
f	frequency
G	power spectral density
h	channel height
ℓ	diffuser length from shock to exit
l	diffuser length from throat to end of divergent section
M	Mach number
p	pressure
R	perfect gas constant
t	time
T	absolute temperature
u	velocity
w	mass flow rate
$\tilde{w}$	$= 0.685 \dfrac{w\sqrt{RT_{to}}}{A_* p_{to}}$ = *dimensionless mass flow rate*
δ	boundary layer thickness
λ	length scale of shock displacement
ν	$= p_{to}/p_{s2}$ = overall pressure ratio
ν_t	$= p_{t2}/p_{to}$ = total pressure ratio
τ	*time scale for boundary layer readjustment*
—	(overbar) time average

Subscripts

0	plenum condition
1	inlet station
2	exit station
*	throat station
s	static
t	total
SH	shock
S	*separation*
R	reattachment
e	boundary layer edge
w	wall
rms	root-mean-square
max	maximum
c	sonic (critical)

INTRODUCTION

In supersonic flight, the subsonic diffuser portion of aircraft inlet systems may display self-excited, large-scale, low-frequency flow fluctuations which adversely influence compressor operation. These fluctuations, commonly referred to in propulsion technology as *dynamic inlet distortion, constitute a major limitation on off-design, maneuvering performance of fighter aircraft.* The fluid mechanical processes causing these fluctuations are poorly understood, and development of new inlet designs having acceptable levels of dynamic distortion must therefore proceed empirically.

In order to characterize the fluid mechanical processes responsible for the unsteady behavior of such systems, a detailed experimental exploration of two-dimensional, transonic diffuser flows was undertaken. The flow chosen for investigation accelerates to supersonic speeds across a minimum-area throat, passes through a shock shortly thereafter, and decelerates subsonically in a diverging section. The post-shock adverse pressure gradient causes the flow to separate from the top wall at all transonic flow conditions. The experiment is believed to contain most essential elements of flows commonly present in inlets operating supercritically; intense low-frequency oscillations believed equivalent to those primarily responsible for distortion problems in full-scale inlets are displayed. Furthermore, the fluctuations appear to have many characteristics *common with transonic fluctuations* observed over airfoil and control surfaces (related to buffet and/or buzz); the possibility of synergism between airfoil-related research and this area is evident.

BACKGROUND

The engineering problem motivating this study (dynamic inlet distortion) has been extensively investigated and documented.[1,2] The principal physical mechanisms involved, however, are not well understood; experiments aimed at clarifying them are scarce, and few directly applicable theoretical studies exist.

The largest class of relevant analyses deals with inviscid, compressible, unsteady flows in variable-area channels and treats the problem in a one-dimensional approximation. The first important contribution in this category came from Kantrowitz[3] who showed that smooth, transonic deceleration (in a throat) is unstable to compression pulses coming from the rear of the divergent channel and that the shock position is stable only in divergent channels. Hurrell[4] showed that the displacement of the shock lags a downstream perturbation, and that the time lag depends inversely on the rate of cross-sectional area change at the shock location. A weak dependence on shock Mach number was also found.

**This research was conducted under the McDonnell Douglas Independent Research and Development Program*

Jacob^5 computed the response of a normal shock in a diffuser to various types of upstream and downstream perturbations using a linearized theory. He found the largest response when the perturbation frequency was $\sim a_2/\ell$, where ℓ is the diffuser length from shock to exit and a_2 is the sonic speed at the duct exit. His predictions show that a 1% change in exit static pressure may cause shock displacements up to 4% of the diffuser length.

The latest and most relevant analyses by Adamson, Sichel, Richey and Messiter$^{6-8}$ dealt with the problem of unsteady, inviscid, two-dimensional channel flows including shock waves; similarity solutions and perturbation methods were used to solve several variants of the problem. These studies represent the state-of-the-art in theoretical description of the underlying phenomena.

The present authors are not aware of any attempt to construct a theory which formally includes viscous effects. The only known major experimental effort directed at the unsteady aspects of transonic channel flows was conducted by Meier^9 who used high-speed interferometry to diagnose the flow in a Laval nozzle with hyperbolic contours. He found a nearly periodic, pulsating flow, governed by complex interactions between the shock and a separated flow zone.

Fortunately, many publications deal with selected features of the entire complex flow pattern of the present study. Studies of steady, normal-shock/boundary-layer interactions form one such class. The oscillations displayed by such interactions are discussed by Trilling^{10}, Fiszdon^{11}, Fiszdon and Mollo-Christensen^{12} and Plotkin.^{13}

Much peripherally relevant information is available from studies of unsteady transonic flowfields over airfoils. The wall pressure distribution on the suction side of airfoils is often similar to that on diffuser walls, and many of the dynamic features are also similar. In particular, upstream propagation of pressure perturbations of significant amplitude has been established in both situations.^{14,15} Little is known about how such flows behave in real diffusers. It follows that the present experiment is necessarily exploratory; its primary goal is to describe the flows found under the available range of externally controllable parameters.

EXPERIMENTAL APPARATUS

Diffuser Model

Investigations began with a diffuser of area ratio 2.5 (model A) whose contours are shown on the left of Fig. 1. The model was equipped with five vertical suction slots on each sidewall to enhance two-dimensionality of the flow. Early tests showed that the flow in this model exhibited the expected unsteady behavior, but that it also contained an unrealistically large, separated flow zone. The model was redesigned with a smaller area ratio and less severe contour curvatures. The new configuration, model B-1 (right, Fig. 1), also contained vertical boundary layer control (BLC) sidewall slots and several new features, such as a variable-contour top wall and relocation of the throat within the field-of-view of the schlieren system. A comparison of features is given in Table 1.

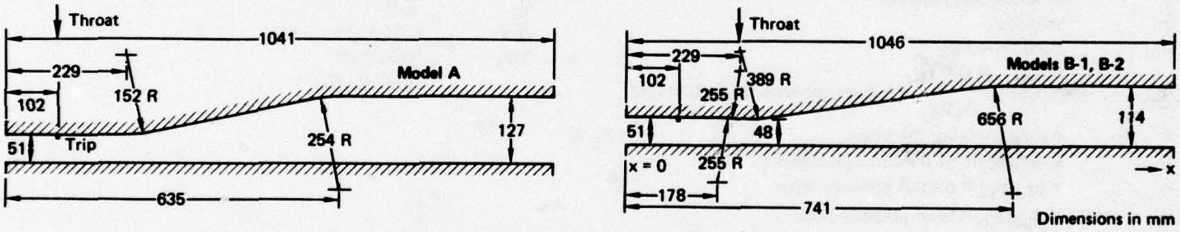

GP77-0678-1

Fig. 1 Wall contours of diffuser models

Table 1. Comparison of diffuser models

	A	B-1	B-2
Top contour	Fixed	Variable shape	
Area ratio	2.5	1.84 to 2.37	
Maximum divergence angle	11°	5.4° to 8.8°	
Divergent-length/ throat-height	8	10.6	
Radius of throat contour curvature to throat height	3	8 to 13	
Throat	Hidden	In view	
Approach BL thickness control on top wall by	Single element roughness trip	Single element trip	
Sidewall BLC	Vertical slots; multiple, staggered sidewall panels	Vertical slots; multiple, flush sidewall panels	Streamwise slots in top corners; single-piece sidewall panel

GP77-0678-24

Detailed checkouts using shadowgraph and oil-flow methods showed that the separation bubble size was reduced, but the sidewall slots were still inadequate to ensure acceptable two-dimensionality. Furthermore, minute misalignments of individual glass panels caused multiple focal points in the optical system, which did not harm shadowgraphy but made it impossible to use a knife-edge to produce schlieren images. Both problems were eliminated by using single-panel glass sidewalls and suction slots along both top corners. The model with this BLC configuration, designated B-2, displayed good optical properties for both shadowgraph and schlieren purposes, and the flow had a satisfactory degree of two-dimensionality and a separated zone of modest size, comparable to what might occur in a realistic inlet. Most of the results given below were obtained with this configuration. The layout and principal dimensions are shown in Fig. 2, a photograph of the model is given as Fig. 3, and the experimental facility is shown in Fig. 4.

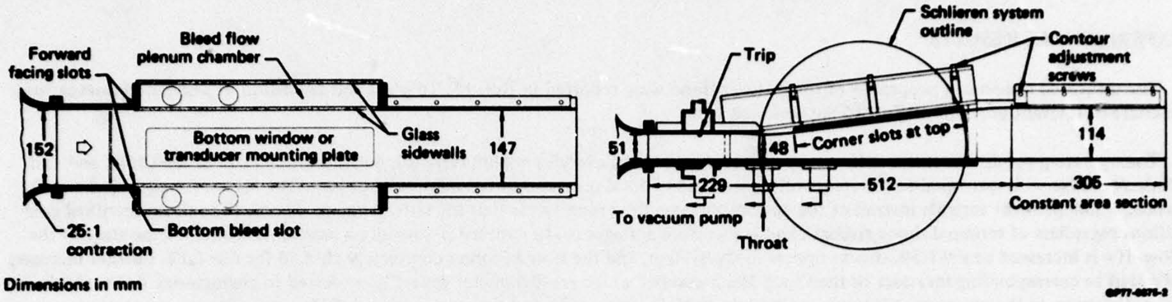

Fig. 2 Details of diffuser model B-2

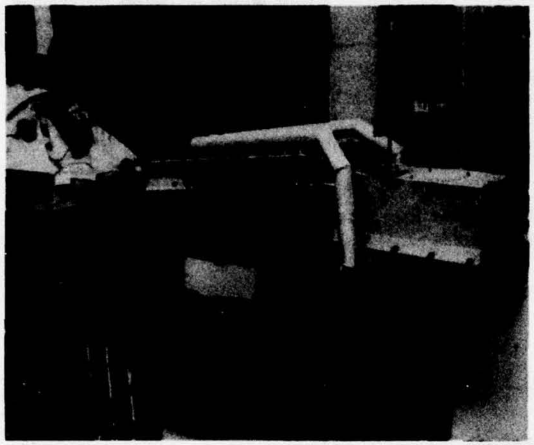

Fig. 3 Photograph of diffuser model B-2. Mirror in foreground is part of schlieren system. Overhead manifold services top corner suction slots. Vertical actuator with a dummy probe is shown at $\tilde{x} = 11.4$.

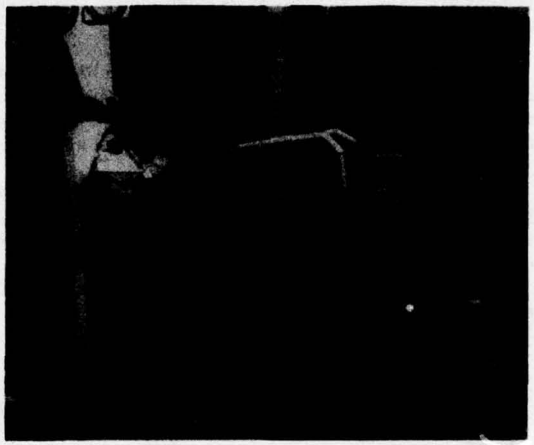

Fig. 4 Photograph of experimental facility. Light source and far-side mirror visible behind probe actuator. High-speed camera in foreground.

The model was attached to a plenum chamber with a 25:1 contraction and was supplied with filtered, dry air at precisely measured rates. A separate flow meter was used to measure the total of all bleed flows, amounting to approximately 5% of the maximum flow rate.

Flow rates ranged up to 2.2 kg/s, corresponding to a maximum Reynolds number of 10^6, based on the 48 mm throat height and the average throat velocity. Test conditions were set by controlling plenum chamber pressure.

INSTRUMENTATION

Wall pressure distributions were determined using 75 0.4-mm diam wall taps, connected to two 48-channel scanivalves, each housing a ± 34 kPa transducer (Druck model PECR-22). The same scanivalves were used to sense pressures from a total pressure rake consisting of 11 probes, mounted at midspan of the exit station. The inside and outside diameters of the probes were 0.4 and 0.8 mm, respectively. Temperatures were sensed by iron/constantan thermocouples with ice-bath reference junctions.

An optical system was constructed using two 51-cm diam concave mirrors with 320-cm focal length, operable either in shadowgraph or schlieren modes. Shadowgraphs were adequate to clearly show the shock motion; the more sensitive schlieren technique was required to display the turbulent structures in the boundary layers. The system was used with a steady mercury light source to obtain high-speed movies at 5500 frames/s with a Hycam camera. Sharp images could be obtained with a 20 ns duration spark source, used in conjunction with a commercial 35 mm reflex camera.

Oil-flow traces were used to detect the direction of time-mean skin friction. The surface patterns were converted into a permanent record by adsorbing them onto a paper strip, applied with a roller. These "blots" were used to judge the two-dimensionality of the flow and to determine separation/reattachment locations.

Shock-position records were obtained from high-speed schlieren films using a semi-automatic digitizer arrangement. The streamwise position of the intersection between the upstream edge of the shock and a horizontal line 2.54 cm above the straight (bottom) wall was recorded for film segments containing 2000-3000 frames. Since the dominant frequencies were below 200 Hz, the 5 kHz sampling rate was adequate to contain all significant information about the shock motion. Shock thickness, temporal shock-shape variations and camera-related image jitter amounted to ±2 mm and were the principal factors affecting data precision.

The position vs time information was subsequently processed digitally to determine statistical properties of the oscillations.

EXPERIMENTAL RESULTS

The measured time-mean properties of the diffuser flows were reported in Ref. 15. To place the discussion of associated fluctuations in context, relevant portions of Ref. 15 are reviewed here.

The operating conditions in the diffuser are characterized by an overall pressure ratio (ν), defined as the ratio of inlet total and exit static pressures. ν is *not* equal to the frequently used ratio of total pressures at the inlet/exit stations. The reason for choosing ν as the principal independent variable instead of the customary mass flow ratio ($\tilde{w}$) is that the latter remains constant for all supercritical conditions regardless of terminal shock strength and is therefore ambiguous. In contrast, ν provides a unique definition of the state of the flow. If ν is increased to $\nu = 1.10$, shocks appear in the system, and the flow becomes completely choked for $\nu > 1.12$. Further increases of ν lead to corresponding increases of the shock Mach number which is a parameter generally preferred to characterize flows of this type. However, in the presence of intense oscillations, both the definition and the measurement of M_{SH} pose serious problems; therefore, it is advantageous to retain the temporally constant and precisely measurable ν as the principal test variable.

Inlet/Exit Conditions

The streamwise location at $\tilde{x} = -1.66$ was arbitrarily designated as the model inlet station. Mean velocity traverses made with total pressure probes at three spanwise locations showed that the core flow velocity at this station was uniform within 1%, across the channel and in the spanwise direction.

The bottom boundary layer (developing after a BLC suction slot spanning the duct upstream of the inlet station) was thin, and no attempt was made to determine its details. The top wall boundary layer, developing after a 0.51-mm high trip at $\tilde{x} = -2.52$, had a velocity profile characteristic of a turbulent boundary layer with zero pressure gradient. The boundary layer at the inlet station had a momentum thickness of $\theta = 0.28$ mm, changing only slightly over the supercritical range of flow conditions.

A Kulite transducer mounted at $\tilde{x} = -3.69$ showed that top-wall pressure fluctuations were less than 0.1% of the core flow dynamic pressure under all supercritical flow conditions (Fig. 5). It is thus unlikely that the large fluctuations observed during the test are a direct result of disturbances originated upstream, although upstream fluctuations could act as trigger events for various instabilities.

The flow exhausted to the test cell at atmospheric pressure, which imposed a constant static pressure boundary condition at the exit station ($\tilde{x} = 17.0$).

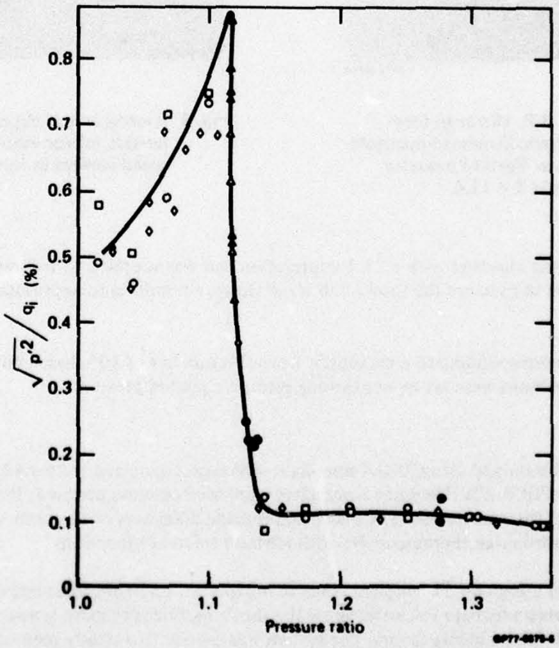

Fig. 5 Top wall static pressure fluctuations at $\tilde{x} = -3.69$

Two-Dimensionality

Since the value of results from this experiment depends on the extent of two-dimensionality achieved, this aspect of the flow was checked carefully using tufts, oil-flow techniques, schlieren photography and velocity profile measurements.

The oil-flow method is the most sensitive and was used as the ultimate criterion to select the best arrangement of suction slots.

Figure 6 shows the oil-flow pattern for the largest pressure ratio (shock strength) tested. The symmetric, dipole-like recirculating pattern is evident within the separation bubble, which is similar to those found in the experiments of Alber et al.[16] No tested combination of sidewall and/or corner slots eliminated this pattern; indeed, two-dimensional, separated flow in a rectangular duct may be impossible even with sidewall boundary layer removal.

Spanwise variation of wall static pressures was negligible for all pressure ratios at the inlet station, at $\tilde{x} = 5.1$ (Fig. 7), and at the exit station where static pressure uniformity was imposed by the atmosphere. Spanwise non-uniformity of velocity profiles at $\tilde{x} = 5.1$ increased with increasing pressure ratio.

The two-dimensionality of the shock front was evaluated from schlieren photographs and oil-flow patterns. The time-mean shape deviated from a mean plane by at most ± 1 cm (Fig. 6) while instantaneous bulges were smaller; only at the highest pressure ratio did the bulges reach ~ 1 cm. In comparison to the 15 cm channel width, these irregularities are tolerable, and the conclusions reported here are not likely to be significantly affected by them.

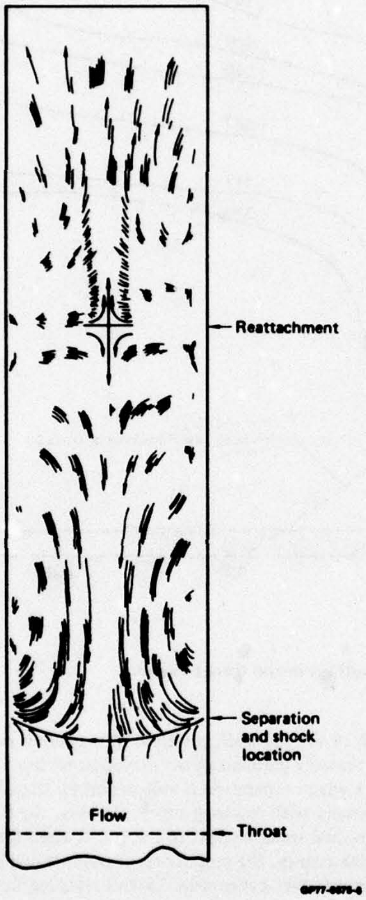

Fig. 6 Typical oil-flow pattern on top wall at ν = 1.340

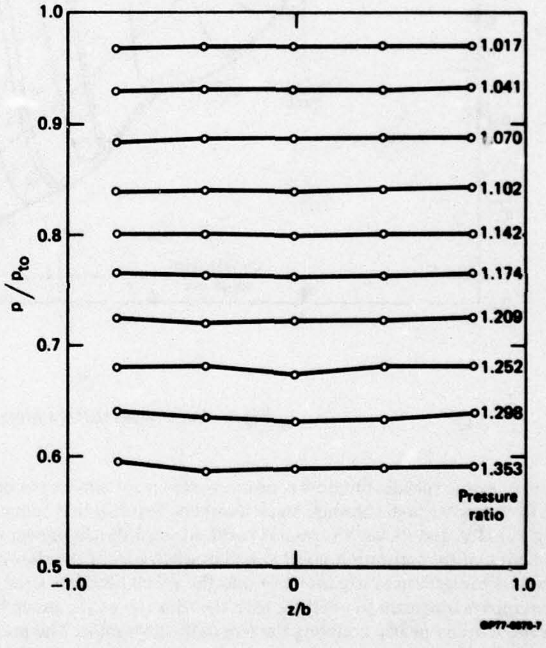

Fig. 7 Spanwise wall static pressure distributions at $\tilde{x} = 5.1$ (b = 7.37 cm)

Overall Performance

Time-mean measurements of conventional performance parameters were made for the entire pressure ratio range. The parameters included normalized mass flow ($\tilde{w}$), exit-to-inlet total pressure ratios based on mass-flow-weighted averages (ν_t), and various distortion indices computed from the measured exit station total pressure (and velocity) profiles. Detailed results, discussed in Ref. 15, show that the total pressure ratio (representing losses) is equal to 0.95 near the point of choking ($\nu \cong 1.1$), which is comparable to values encountered in inlet design practice.

Wall static pressure distributions were determined on both the top and bottom walls. The more interesting top-wall distributions are given in Fig. 8 for a channel segment near the throat, including all the supersonic flow; the inviscid, one-dimensional result for supersonic flow is also shown. Wall contour curvature and boundary layer displacement effects cause the measured pressures to be significantly below the theoretical line. The post-shock static pressures are less than expected from the Rankine-Hugoniot relations. This discrepancy is typical for normal-shock/boundary-layer interactions and will be discussed in more detail later.

Shock Locations and Separation Bubble Properties

Separation and reattachment points (more precisely, lines) were determined from oil-flow traces, and time-mean shock positions were extracted from the high-speed films. The results are shown in Fig. 9.

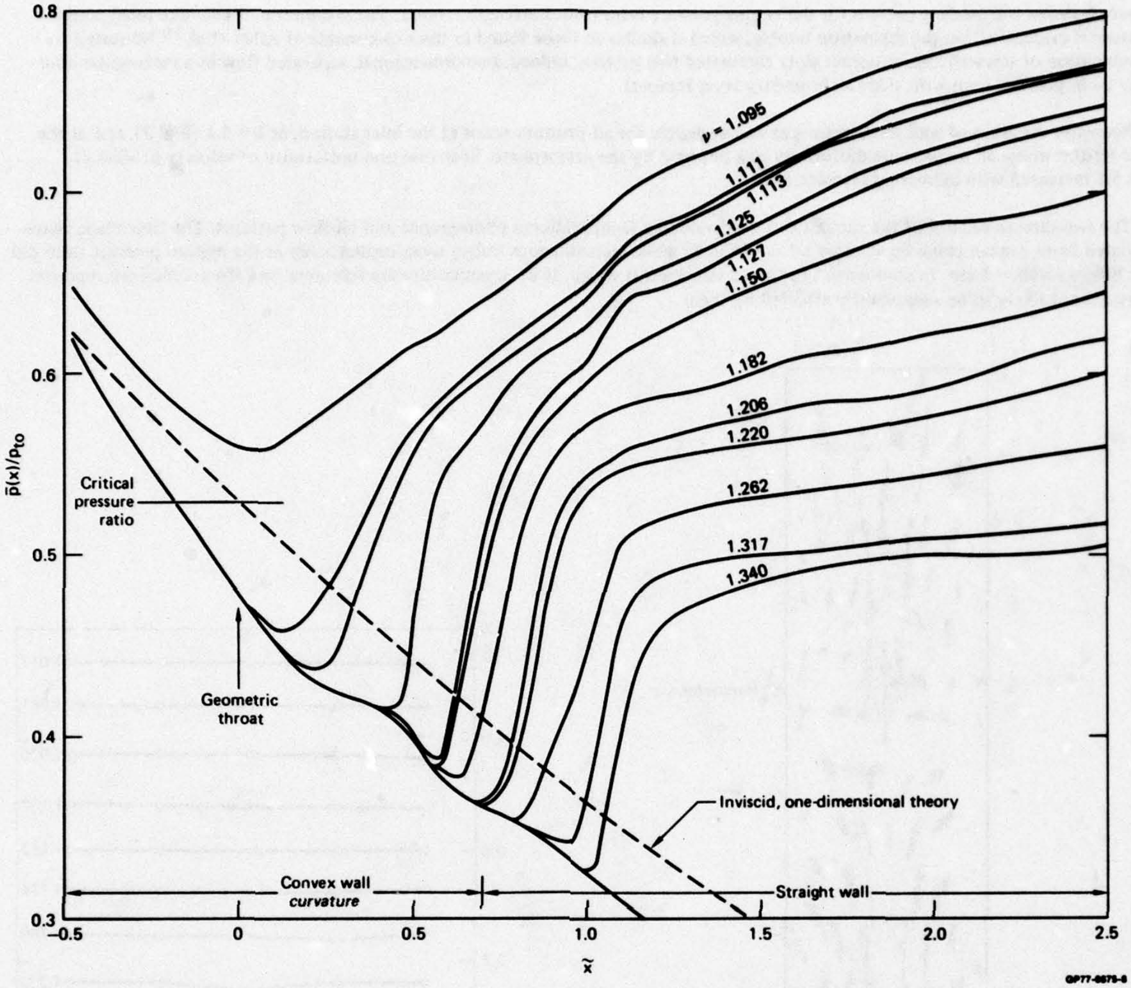

Fig. 8 Time-mean surface pressure distributions in the throat region

At subsonic speeds, the flow is near separation for almost the entire length of the top-wall, and flow reversal does not occur until the flow reaches high subsonic Mach numbers. Separation is induced by the pressure gradient in the divergent section. The bubble is long initially, and its length remains constant until shocks appear near $\nu = 1.1$ where separation is still caused by the adverse pressure gradient and the separation point is well downstream of the shock. Coincidentally with reaching supercriticality, the bubble begins to shrink as the pressure ratio increases and the shock becomes stronger. This gradual trend persists to $\nu = 1.150$ when the separation point moves upstream to coincide with the location of the shock foot. Simultaneously, the reattachment point is displaced downstream, thereby nearly doubling the length of the bubble. The pressure-gradient-induced separation is thus replaced by shock-induced separation.

Additional increases of ν move the shock and the separation point further downstream. The x_{SH} and x_S loci given in Fig. 9 are not identical because the shock position was defined as the x coordinate of the intersection point between the upstream edge of the shock image and a horizontal reference line 2.54 cm above the bottom (straight) wall. This point always lies further downstream than the foot of the upstream leg of a lambda shock, as illustrated in the Fig. 9 insert.

Flow Modes

All measurements discussed thus far refer to the time-mean properties of the flow. The characteristics of the fluctuations were identified from the high-speed shadowgraph and schlieren films. These observations led to a classification of flow conditions on the basis of dynamic behavior. Eight modes were identified and are described below.

Subsonic Modes – Mode 1 is subsonic flow without separation. The top wall boundary layer is near incipient separation; oil dots placed on the divergent part of the top wall retained their original shapes without alteration. Mode 2 is fully subsonic, but intermittent separation occurs. This pattern was termed transitory stall by Fox and Kline.[18] Mode 3 contains a separation bubble at all times (fully separated flow), but the flow remains subsonic at all points. The three subsonic modes observed were not studied in detail; interest was concentrated on modes including shocks.

Supercritical Modes – Five supercritical flow modes were observed. Simplified drawings depicting the flow patterns in each mode are given in Fig. 10. Table 2 contains a summary of their principal features, including shock Mach number ranges for each mode.

Mode 4 occurs in the lowest range of pressure ratios in which shocks appear ($1.110 < \nu < 1.115$). In general, several weak shocks (shocklets) are visible most of the time, each constantly changing in intensity and position. They may merge, split apart, or even

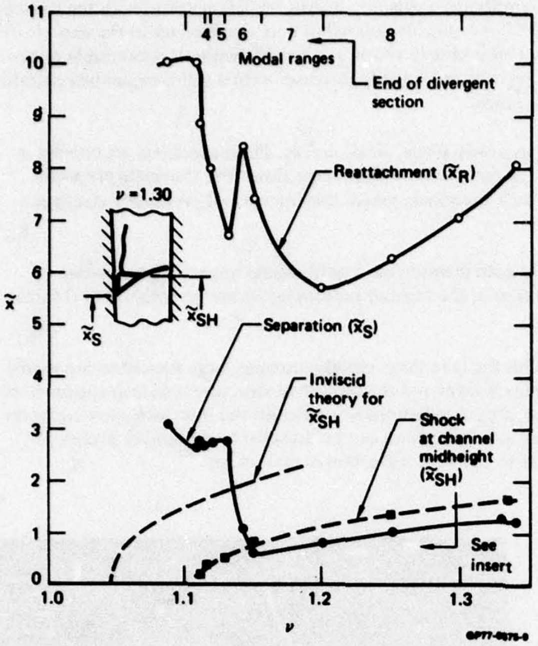

Fig. 9 Shock, separation and reattachment locations; inviscid shock position also shown for comparison. Insert illustrates why $\tilde{x}_S \neq \tilde{x}_{SH}$ for $\nu > 1.15$

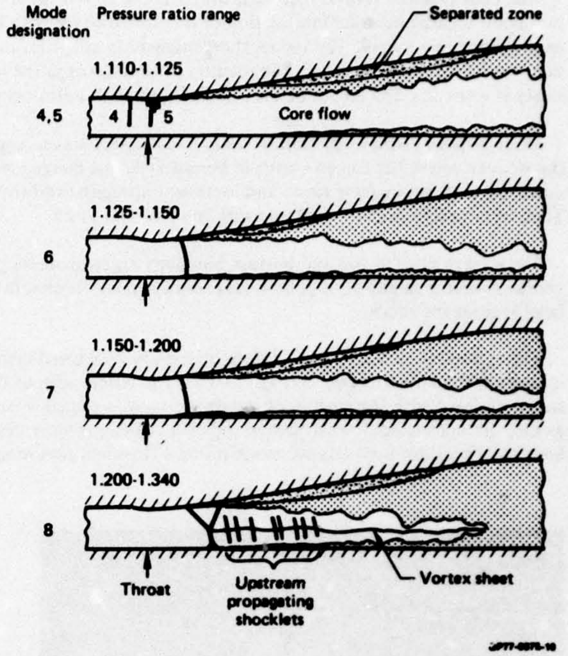

Fig. 10 Typical instantaneous flow patterns for supercritical modes. Shock labeled 4 in top pattern signifies occasional presence of shock upstream of throat

Table 2. Characteristics of supercritical flow modes

Mode designation	Pressure ratio	M_{SH}*	Presence of a supersonic *region is*	Presence of shock(s) is	Shock geometry	Separation induced by
4	1.110- 1.115	1.11- 1.17	Intermittent	Intermittent	Multiple, normal	Adverse pressure gradient
5	1.115- 1.125	1.17- 1.25	Persistent	Intermittent	Multiple, normal	
6	1.125- 1.150	1.25- 1.28	Persistent	Persistent	Single, normal	
7	1.150- 1.200	1.28- 130	Persistent	Persistent	Single, normal (or small lambda?)	Shock
8	1.200- 1.340	1.30- 1.38	Persistent	Persistent	Single, lambda	

*M_{SH} was computed from the ratio of plenum total pressure to the minimum wall pressure at shock, thus representing the minimum value.

GP77-0675-36

disappear. Occasionally, a striking event occurs: shocks propagate upstream, across the throat and eventually disappear in the convergent section, leaving subsonic flow throughout the model. Subsequently, the flow reaccelerates to supersonic speeds, generating new shocks. This type of shock passage across the throat generally occurs when the weak shocklets merge to form a single, relatively strong shock. This behavior was also observed by Meier[9] in a two-dimensional, symmetric Laval nozzle with hyperbolic contours, operated *near the point of choking.* Mode 4 behavior can be summarized as intermittently transonic and intermittently shock-free flow, since for some fraction of time the flow is subsonic everywhere in the field, and the shocks are present only part of the time.

Mode 5 ($1.115 < \nu < 1.125$) is also an intermittently shock-free, multiple-shocklet pattern, but in this case shocks never cross the throat. Presumably, a sonic line and a small supersonic zone of varying size exist at all times. The supersonic Mach numbers are close to one, and no visible shocks occur for some fraction of time. For these reasons Mode 5 is characterized as persistently transonic, intermittently shock-free flow.

Mode 6 ($1.125 < \nu < 1.15$) displays a single, approximately normal shock at all times. Multiple, weak shock patterns are absent. The shock shape is somewhat curved, and the shock angles close to the wall are large enough to describe the shock as oblique, with a pressure rise considerably below that for a normal shock. The shock does not cause immediate separation.

Mode 7 appears at $\nu = 1.15$, where the separation point abruptly moves upstream and assumes the same position as the shock foot while the length of the separation bubble is nearly doubled. Spark photographs suggest that the foot of the shock may be split to form a miniature lambda pattern, in which the bifurcation point is at most twice as far from the wall than the visible edge of the approach boundary layer. However, the scale of the pattern is below the tolerance placed on the two-dimensionality of this experiment and this finding should be considered tentative. This pattern persists for a wide pressure ratio range, up to about $\nu = 1.2$. Oscillation amplitudes increase slightly, and the bubble length decreases with ν in this range.

When the pressure ratio is increased over 1.2, the top of the shock intermittently splits into a large lambda pattern, with the separation point located near the intersection of the upstream leg with the wall. This mode, designated as 8, is observed up to the experimental limit of $\nu = 1.34$. The vortex sheet originating at the bifurcation point is clearly visible and persists without appreciable diffusion throughout the core flow. The fraction of time spent in the lambda formation gradually increases until a full-time lambda pattern exists at $\nu \cong 1.25$. The length of the bubble grows with ν throughout this range.

Mode 8 flows display upstream-propagating pressure waves, appearing as nearly plane, weak shocks. These shocklets are created in the vicinity where the top and bottom boundary layers merge, i.e., near the end of the uniform core flow. The shocklets propagate upstream with diminishing speed and increasing strength until they approach the shock, where they merge and eventually disappear. They were never observed to merge with the terminal shock.

The growth rates of top and bottom boundary layers increase gradually with pressure ratio until shocks appear. The presence of shocks is accompanied by rapidly thickening boundary layers. In modes 6 to 8, the top and bottom layers merge within 4 to 6 throat heights from the shock.

The top-wall boundary layer exhibits a coarsely structured interface with the core flow; rapidly growing, large structures are visible in spark schlieren photographs (Figs. 11-15). The visible edge of the boundary layer and the individual structures (eddies) appear to be well correlated with the motion of the shock; shock excursions are followed by undulations or ripples on the interface, growing larger as they are convected downstream in the duct. When reaching the diffuser exit, the eddies can be detected by stationary probes as large total pressure fluctuations, constituting a flowfield that is equivalent to dynamic distortion in real inlets.

GP77-0875-11

Fig. 11 Spark schlieren photograph of model B-2 flowfield at $\nu = 1.111$ (mode 4). Reference grid dimension is 2.54 mm x 1.27 mm. Throat is at first (partially covered) vertical line at left

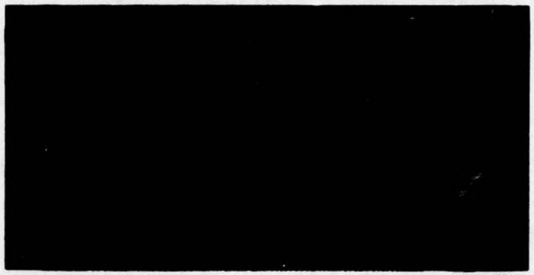

GP77-0875-12

Fig. 12 Spark schlieren photograph of model B-2 flowfield at $\nu = 1.128$ (mode 6)

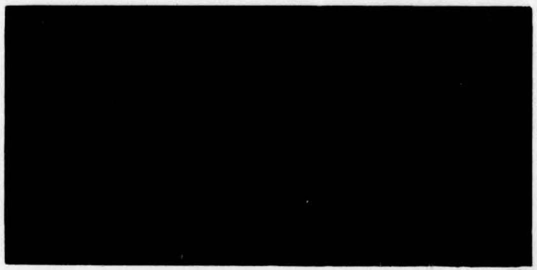

GP77-0875-13

Fig. 13 Spark schlieren photograph of model B-2 flowfield at $\nu = 1.140$ (mode 6)

GP77-0875-14

Fig. 14 Spark schlieren photograph of model B-2 flowfield at $\nu = 1.250$ (mode 8)

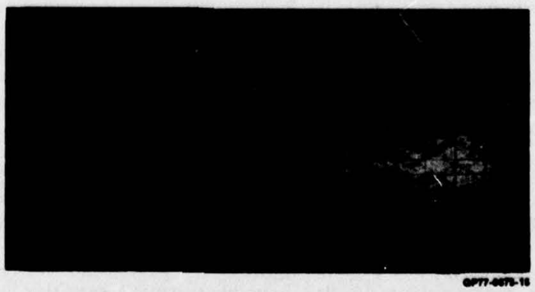

GP77-0875-15

Fig. 15 Spark schlieren photograph of model B-2 flowfield at $\nu = 1.340$ (mode 8)

The scheme proposed here is similar to and partially builds upon classification systems evolved by other investigators for different but similar types of flows. The studies of Fox and Kline[18] led to the determination of distinct regimes in incompressible diffuser flows: our work is a limited extension of theirs into the transonic speed range. Pearcey and associates[19] identified several types of steady, transonic flowfields around airfoils that could be characterized by relative positions of the shock, separation and reattachment points. The time-mean properties of the various modes described here closely parallel their classification scheme.

The unsteady aspects of our modal classification have counterparts in the work of Tijdeman[20] who investigated flows around a *thin airfoil* with a 25% flap which oscillated harmonically with small amplitudes, with freestream Mach numbers ranging from 0.85 to 0.9. He identified three types of shock oscillations (A,B,C) which correspond to our modes 6, 5 and 4. The correspondence is not complete: Tijdeman's definitions, based on shock kinematics, are suited to harmonic oscillations but are not readily applicable to random ones. For this reason, we used gas dynamic criteria to distinguish between modes 4, 5 and 6. These criteria are less descriptive of the specific shock position histories but have broader applicability and include Tijdeman's three types as special cases.

Oscillation Properties

The shock position records were smoothed and interpolated in one digital process to create a secondary file with equal time steps of 0.5 ms. These histories cover time periods of 0.3-0.6 s and are adequately long to provide basic statistical information. The most important questions concern how the oscillation amplitudes, frequencies, and shock speeds depend on the principal test variable, the overall pressure ratio.

Oscillation Amplitudes

The simplest way to characterize the fluctuation amplitudes is through the probability density distribution functions (PDF's) for position, shown in Fig. 16. The distributions are normalized such that the areas under the curves are identical.

The data of Fig. 16 define the time-mean shock positions for each ν, which have already been included in Fig. 9. The root-mean values of the displacement amplitudes (λ_{rms}) are also implicit and are shown in Fig. 17 as a function of ν. Figure 17 also shows λ_{max}, defined as the difference between the maximum and minimum instantaneous shock locations.

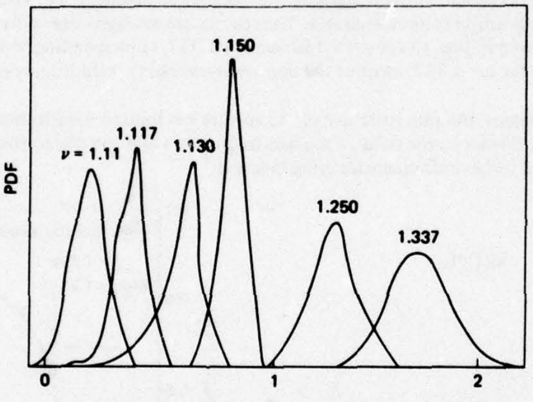

Fig. 16 Probability density distribution for shock position at six different values of pressure ratio. Vertical scale arbitrary but common to all distributions

Fig. 17 Characteristic length, frequency and velocity scales of shock oscillations

Figure 17 shows that the maximum displacement amplitudes are comparable to the throat height. The amplitudes show an increasing trend up to $\nu = 1.13$, abruptly dropping to less than half the previous maximum at $\nu = 1.15$, and increase slowly with increasing ν over the remaining range of pressure ratios. The first group of points displaying an upward trend corresponds to modes 4, 5 and 6, all of which contain a pressure-gradient-induced separation. The second group of points forming another upward trend, on the other hand, corresponds to modes 7 and 8 which are associated with shock-induced separation. The amplitude trends thus seem to be related to the direct cause of separation. The amplitude trends thus seem to be related to the direct cause of separation. The character of surface pressure distributions also changes with the onset of shock-induced separation (See Fig. 8, $\nu = 1.15$, 1.182), and the exit velocity profiles also undergo a marked change at the same time.[15]

The PDF's (Fig. 16) obtained at low pressure ratios ($\nu < 1.130$) display a sharp peak and are skewed in the upstream direction. Contributions to the upstream tail are accumulated during rare, but large, upstream excursions of the shock that are evident on the films. In the case of mode 4, these excursions penetrate into the subsonic zone upstream of the throat. The distribution functions obtained with shock-induced separation ($\nu > 1.150$) are more symmetric and resemble Gaussian distributions.

The time-mean wall static pressure distributions necessarily reflect the fact that the shock position covers a broad range: the pressure rise caused by the shock becomes gradual and extends over a distance comparable to the range of shock oscillation. Figure 18 shows selected (bottom) wall pressure distributions, together with the independently measured shock position PDF's, strongly suggesting that oscillations are the primary factor determining the streamwise extent of the "footprint" of the shock in this flow. Figure 18 also shows the pressure distributions expected from the Rankine-Hugoniot relations when the shock is located at the experimentally determined time-mean shock position. Pre-shock total pressure was assumed equal to the plenum pressure, and pre-shock static pressure was obtained by extrapolating the supersonic wall pressures to the mean shock position.

The experimental curve is too gradual to permit a clear definition of the pressure rise across the shock, but almost any definition leads to the conclusion that the measured pressure rise is less than the theoretical expectation. This is typical of (nominally) normal shock-boundary layer interactions: in our case it can be largely explained by the obliqueness of the shock near the wall.[17]

Oscillation Frequencies

The second basic property of the fluctuations is their characteristic frequency or time scale. These were obtained by calculating the Fourier power spectra for each shock-position history available. The spectra are averaged over only 16 realizations, but magnitudes and trends are clear. Sample spectra are given in Fig. 19 for $\nu = 1.150$ and $\nu = 1.337$, corresponding to the smallest and largest frequencies found. The frequencies are low: even for $\nu = 1.337$, most of the contributions come from frequencies below 300 Hz.

Because of the small number of samples, the fine structure of the spectra has limited significance. In order to clarify the pressure-ratio dependence (and to increase confidence in the data), a median frequency $\bar{f}$ was calculated from each spectrum. $\bar{f}$ is defined such that half the fluctuation energy would reside in frequencies lying below it:

$$\int_0^{\bar{f}} G(f)df = \frac{1}{2}\int_0^{f_{max}} G(f)df,$$

where f_{max} satisfied the criteria:

$$G(f_{max}) = 0.02\,G_{max}$$

and

$$[G(f)]_{f > f_{max}} \leq 0.02\,G_{max}.$$

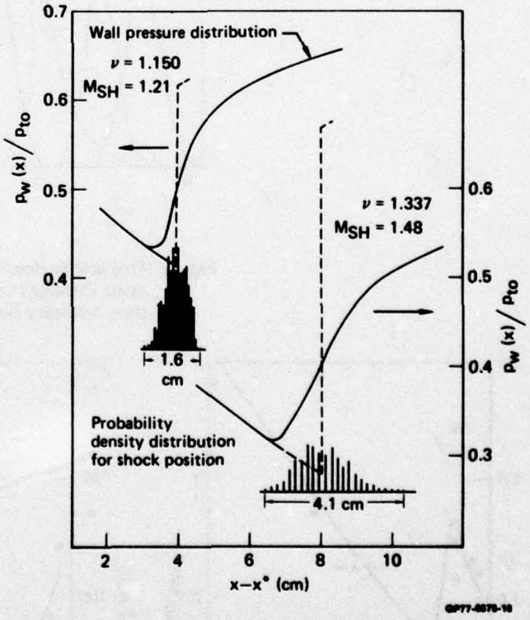

Fig. 18 **Comparison of time-mean (bottom) wall pressure and shock position probability distributions for two selected pressure ratios. Inviscid distributions for stationary shock at mean shock positions are shown (dashed lines)**

The median frequencies obtained by this procedure are plotted in Fig. 17 as functions of ν. The frequencies decrease until $\nu = 1.150$ where a minimum of 63 Hz is reached. After this point the frequencies increase to a maximum of ≈ 160 Hz at $\nu = 1.337$.

The high frequencies at the low-pressure-ratio end of the scale can be attributed to the combination of multiple shock patterns observed in this range and to the manner in which the measurements were made. One shock position was recorded for each frame. At low pressure ratios, however, there were several weak shocks visible at any given time. When one shock was stronger that the rest, its position was recorded; otherwise the shock located most-upstream was considered representative.

Multiple shock patterns repeatedly displayed a shock-shock interaction in which the strength of the leading (upstream-most) shock decreased while the adjacent second shock gradually became stronger and eventually became dominant. This seems to occur when the pressure perturbations, arriving at the vicinity of the throat from downstream, reach strengths comparable to the weak shock already residing there. Through the continuous changes in the strength of each, the new shock may evolve into the "resident" shock while the original one decays completely. In the recording procedure followed, this caused a sudden shift of the recorded position from the first shock to the second, which in turn translated to high-frequency contributions to the Fourier spectrum. The apparent high frequencies are thus largely caused by the changing "identity" of the recorded shock.

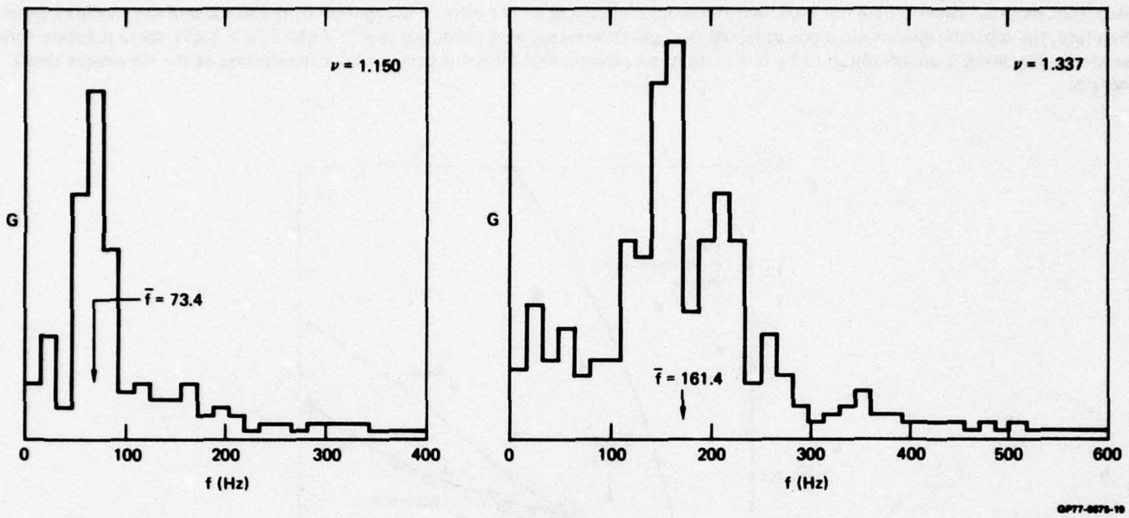

Fig. 19 Power spectra for shock position at pressure ratios corresponding to the two extreme values of the median frequency

The shock was a single, distinctly defined entity for pressure ratios $\gtrsim 1.13$, and the trend of rising frequencies for $\nu \gtrsim 1.15$ is not influenced by the fine structure of the shock. It is more likely that the times required for the propagation of disturbances from some source region to the shock control the frequency.

The dominant source of pressure disturbances is probably the separation bubble. Additional disturbances may be originated from the zone where the top and bottom wall boundary layers merge, i.e., from the end regions of the core flow. Analysis of time-dependent wall pressure data, presently in progress, should clarify this question.

One important consequence of these findings is that the time scales are long enough to permit the shock/boundary-layer interaction to be treated as if it were quasi-steady. The shortest period (at $\nu = 1.334$) found is 7×10^{-3} s. The characteristic time scale needed by the boundary layer to readjust to a changed shock position or strength is expected to be of the order of δ/u_e. Taking the conservative estimates of $\delta = 0.5$ cm, $u_e = 150$ m/s and $\tau = \delta/u_e = 3.3 \times 10^{-5}$s, which is two orders of magnitude shorter than the shock oscillation periods. Thus the known properties of normal shock/boundary-layer interactions can be expected to apply at any instant to a good approximation. It follows that known properties of a stationary shock/boundary-layer interaction can be expected to be similar to those of a moving interaction, provided the pressure ratio across the shock is the same for both cases.

Shock Speed Scales

An estimate of shock speeds can be obtained as a product of length and frequency scales (Fig. 17). The low-pressure-ratio values may be difficult to interpret as explained previously, but data for $\nu > 1.125$ are relevant to the motion of a single shock. Figure 17 shows that the velocity scales rapidly grow with increasing ν, because of the increase of both amplitudes and frequencies. The greatest rms value is 1.1 m/s at $\nu = 1.337$, while the greatest speed based on λ_{max} is 6.4 m/s. The maximum instantaneous speed can be estimated by analogy to harmonic oscillations where $u_{max} = 2\pi f A$, where A is the displacement amplitude. Taking $A = 0.5\ \lambda_{max}$, $u_{max} \cong 20$ m/s for $\nu = 1.337$.

Shock velocities of this magnitude can significantly change the instantaneous shock strength, which is determined by the relative speed between the fluid and the shock. In the case of an upstream moving shock, the fluid and shock speed in the laboratory frame are added, making the shock stronger than a downstream moving one located at the same streamwise position. Assuming, for example, a peak shock speed of 20 m/s and a flow speed of 350 m/s, the relative speeds and thereby shock Mach numbers can vary within a factor of 1.12, depending on which direction the shock moves. The instantaneous pressure rise thus depends on both the direction and speed of the shock, and so do details of the shock/boundary-layer interaction.

Shock Mach Numbers

The study of shock/boundary-layer interactions in steady flows established the shock Mach number (M_{SH}) as the most important variable determining the properties of the interaction. Equivalent information would be desirable for the unsteady case also. Unfortunately, the direct measurement of this quantity as a function of time is an almost impossible experimental task and was not attempted. The question whether meaningful time-mean Mach numbers can be deduced from the available data therefore assumes considerable importance and will be discussed briefly.

The Mach number of most interest is the freestream value at the outer edge of the boundary layer, just upstream of the shock. (In the case of a lambda pattern, the upstream leg of the shock defines the location of interest.) One possibility is to compute a Mach number from the minimum (pre-shock) pressure found in the time-mean wall pressure distributions (Fig. 8), using the plenum pressure as the local freestream total pressure. Since the minimum in the p(x) distribution corresponds to the upstream end of the shock motion range and since the shock speed is necessarily zero at the extremal position, this procedure should give a good representation of the minimum shock Mach numbers reached during the oscillations. Mach numbers calculated by this method are given in Fig. 20 and Table 2.

A time-mean Mach number is the Mach number determined by the time-mean position of the foot of the shock (i.e., its intercept with the wall) and the wall pressure when the flow is supersonic at this location. The schlieren films can be used to evaluate the shock position, and the pressures can be obtained using the supersonic segments of the pressure distributions. At the time of this writing, the shock foot motion histories were not available: the records discussed earlier refer to the motion of the shock midway in the channel. Therefore, the separation point locations obtained from oil-flow traces were used. For modes 7 and 8 ($\nu > 1.15$), these coincide with the shock. The Mach numbers obtained by this method are given in Fig. 20 as the best available description of the time-mean shock strength.

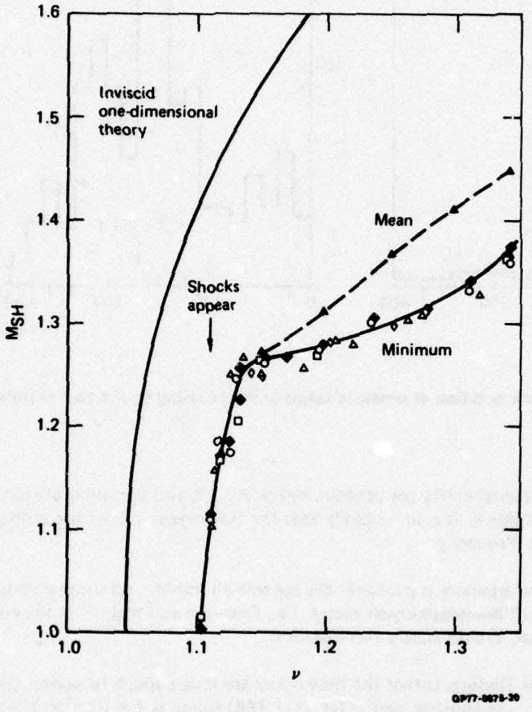

Fig. 20 Minimum and mean shock Mach numbers as functions of overall pressure ratio

Repetitive Events

The initial phase of this work included a partial investigation of diffuser model A, which had a greater area ratio (2.5) and shorter divergent length ($l/h_* = 8$). The flow in this model was not sufficiently similar to the ultimate applications of this effort (inlets), and its study was discontinued. However, high-speed films of the shock motion and surface pressure distributions were obtained. The films showed a nearly cyclic behavior of the shock motion, which was not seen in model B-2. Figure 21 shows a representative segment of a typical $x_{SH}(t)$ record. The cycle began with the appearance of several weak shocks which merged after 1.2 ms of random motion. The resultant shock then moved upstream (out of the field-of-view) at a rapidly increasing speed. This process was repeated at an average frequency of ∿ 190 Hz. The individual periods varied from 2 to 12 ms, but a clearly identifiable cycle was always present. The phenomenon was remarkably similar to that observed by Meier[9] in a Laval nozzle with hyperbolic contours. The frequency is notably higher than the values found in model B-2, and the shock excursions are greater (4-5 cm within view of the schlieren system, probably much longer).

The wall pressure distributions for the two models are shown in Fig. 22 for comparable mean shock strengths (which occurred at different pressure ratios). The accelerating, upstream motion of the shock in model A occurred in a long, constant-area region throughout which the uniform core flow Mach number was nearly constant and slightly over unity. In contrast, shocks in model B-2 must propagate into a large, negative-pressure gradient that apparently limits the excursion within a relatively short distance.

Having observed a definitely cyclic event in model A, the question arises whether there is a sequence of underlying basic events buried in the more randomly appearing shock motion records of model B-2. Direct observation of selected segments (Fig. 23) strongly suggests that this may be the case. However, reliable detection of a regularity of this type is difficult, and results to date are not conclusive.

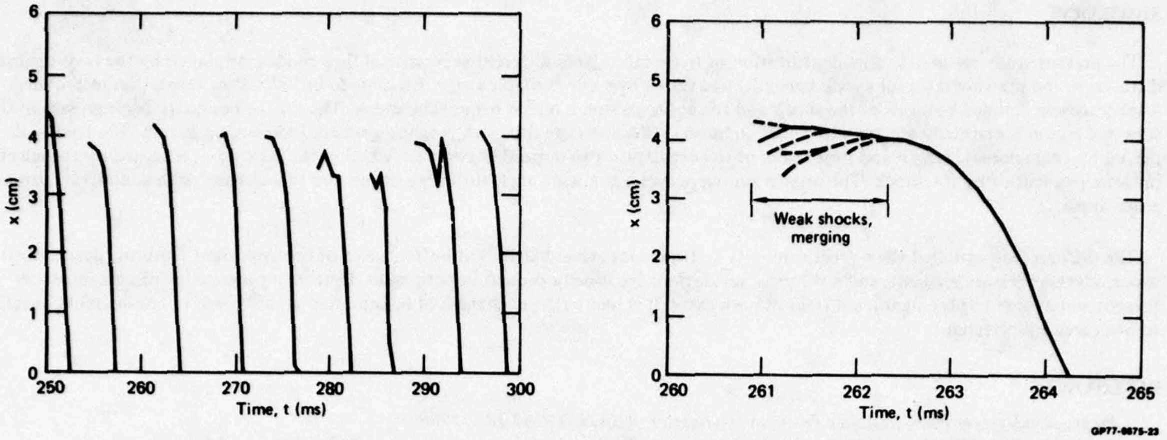

Fig. 21 Typical segment of a shock position vs time record for model A at $\nu = 1.21$. Right part shows a single cycle at greatly enlarged time scale

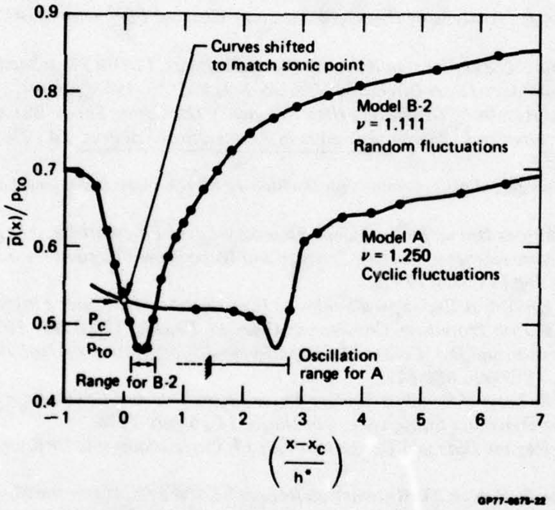

Fig. 22 Comparison of time-mean top wall static pressure distributions for model A and B-2

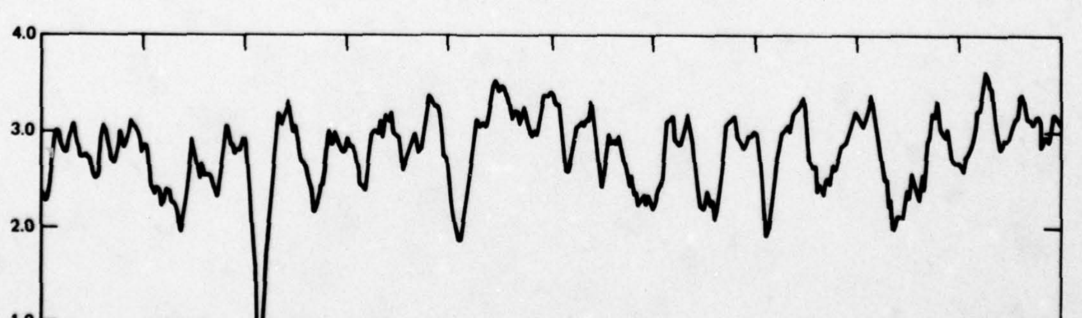

Fig. 23 Typical segment of shock position vs time record for model B-2 at $\nu = 1.130$

SUMMARY

The present study resulted in the identification of five qualitatively different supercritical flow modes, displayed by the investigated diffusers as the pressure ratio (or shock strength) was varied over the available range. Each mode includes flow separation. All modes display closely coupled motions of the shock and the entire subsonic region behind the shock. The rate of boundary layer growth in the subsonic region is markedly greater with shock-induced separation than it is with pressure-gradient-induced separation. The trends displayed by characteristic length and time scales of the oscillation also depend strongly on whether the separation is caused by the adverse pressure gradient or by the shock. The oscillations were cyclic in a wide angle diffuser and random in a diffuser with a moderate divergence angle.

The diffuser flows studied show great similarity to flowfields around airfoils in buffet: most of the important features (shock, post-shock adverse pressure gradient, and a subsonic separation) are usually present in both cases. Upstream propagating disturbances are present and appear to play significant roles in both cases. It is likely that exchanges of information would result in considerable benefits to both areas of research.

REFERENCES

1. *Propulsion System Flow Stability Program (Dynamic), AFAPL-TR-68-142, 1968.*
2. *Supersonic Inlet Design and Airframe-Inlet Integration Program (Project Tailor Mate) AFFDL-TR-71-124, 1973.*
3. *A. Kantrowitz, The Formation and Stability of Normal Shock Waves in Channel Flows, NACA TN 1225, 1956.*
4. *H.G. Hurrell, Analysis of Shock Motion in Ducts During Disturbances in Downstream Pressure, NACA TN 4090, 1957.*
5. *D. Jacob, On Some Aspects of Shock Wave Oscillations in Supersonic Diffusers, Ph.D. Thesis, University of Tennessee Space Institute, 1968; summary of work given in AFFDL-TR-69-103.*
6. *T.C. Adamson, Jr., Unsteady Transonic Flows in Two-Dimensional Channels, J. Fluid Mech., Vol. 52, 1972, pp. 437-449.*
7. *A.F. Messiter and T.C. Adamson, Jr., On the Flow Near a Shock Wave Downstream of a Nozzle Throat, J. Fluid Mech., Vol. 69, 1975, pp. 97-108.*
8. *G.K. Richey and T.C. Adamson, Jr., Analysis of Unsteady Transonic Channel Flow with Shock Waves, AIAA J., Vol. 14, 1976, pp. 1054-1061.*
9. *G.E.A. Meier, Shock Induced Flow Oscillations, in AGARD Proceedings No. 168 on Flow Separation, 1974.*
10. *L. Trilling, Oscillating Shock Boundary-Layer Interation, J. Aero. Sci. Vol. 25, 1958, pp 301.*
11. *W. Fiszdon, Some Experimental Results of Generating High Frequency Oscillating Shock Waves and Oscillating Shock-Wave Boundary Layer Interaction at Supersonic Speeds, Advances in Aeronautical Sciences. Ed., Th. von Karman (Pergamon Press, New York, 1962) Vol. 3, pp. 433.*
12. *W. Fiszdon and E. Mollo-Christensen, An Experiment on Oscillatory Shock-Wave Boundary-Layer Interaction, J. of Aero/Space Sci. Vol. 27, pp. 71 (1960).*
13. *K.J. Plotkin, Shock Wave Oscillations Driven by Turbulent Boundary-Layer Fluctuations, AIAA J., Vol. 13, 1975, pp. 1036-1040.*
14. *F.W. Roos and D.W. Riddle, Measurements of Surface-Pressure and Wake-Flow Fluctuations in the Flow Field of a Whitcomb Supercritical Airfoil, NASA TN D-8443, Aug 1977.*
15. *M. Sajben, C.P. Chen, and J.C. Kroutil, A High-Speed Schlieren Investigation of Diffuser Flows with Dynamic Distortion, AIAA Paper 77-875, AIAA/SAE 13th Propulsion Conference, Orlando, Florida, 11-13 July 1977.*
16. *I.E. Alber, J.W. Bacon, B.S. Masson, and D.J. Collins, An Experimental Investigation of Turbulent Transonic Viscous-Inviscid Interactions, AIAA J., Vol. 11, 1973, pp. 620-627.*
17. *G.R. Inger, Analysis of Transonic Normal-Shock/Boundary Layer Interaction and Comparison with Experiment, AIAA Paper 76-331, AIAA Fluid and Plasma Dynamics Conference, San Diego, 14-16 July 1976.*
18. *R.W. Fox and S.J. Kline, Flow Regime Data and Design Methods for Curved Subsonic Diffusers, J. of Basic Engr., Vol. 84, Ser. D., 1962, pp. 303-312.*
19. *H.H. Pearcey, J. Osborne, and A.B. Haines, The Interaction Between Local Effects and the Shock and Rear Separation - A Source of Significant Scale Effects in Wind-Tunnel Tests on Airfoils and Wings, AGARD CP-35, 1968.*
20. *H. Tijdeman, High Subsonic and Transonic Effects in Unsteady Aerodynamics, NLR Rept. TR 75070U (1975).*

UNSTEADY FORCE AND MOMENT ALLEVIATION IN TRANSONIC FLOW

BY

W. BALLHAUS

AMES DIRECTORATE, U.S. ARMY AMRDL, MOFFETT FIELD, CA.

P. GOORJIAN

INFORMATICS INC., PALO ALTO, CA.

H. YOSHIHARA

BMAD, BOEING AEROSPACE CO., SEATTLE, WA.

SUMMARY

IN FLUTTER SUPPRESSION, CONTROLLED STABILITY, OR GUST ALLEVIATION IN THE TRANSONIC REGIME, AN UNDERSTANDING OF HOW THE UNSTEADY LIFT AND MOMENT ARE GENERATED IS ESSENTIAL. FINITE DIFFERENCE CALCULATIONS BASED ON THE 2D UNSTEADY SMALL-DISTURBANCE EQUATION ARE FIRST USED TO DEMONSTRATE THE ESSENTIAL FLOW ADJUSTING MECHANISMS. BASED ON THIS BACKGROUND, CONTROL DEVICES SITUATED IN THE "SENSITIVE" PARTS OF THE AIRFOIL ARE NEXT INVESTIGATED TO MODERATE THE CHANGES IN THE LIFT AND MOMENT ARISING IN THE CASE OF THE PITCHING OSCILLATION OF A NACA 64A-006 AIRFOIL AT $M = 0.85$. HERE THE PITCHING AMPLITUDE IS 1^{o} ABOUT AN ANGLE OF ATTACK OF 0^{o} WITH THE REDUCED PITCH FREQUENCY OF 0.2. THE CONTROL DEVICES INVESTIGATED ARE LEADING AND TRAILING EDGE FLAPS AND VARIABLE BUMPS LOCATED IN THE NEIGHBORHOOD OF THE SHOCK. RESULTS SHOW SUCCESSFUL ALLEVIATION OF THE PITCHING LIFT AND MOMENT BY USE OF LEADING AND TRAILING EDGE FLAPS.

1. OBJECTIVE AND APPROACH

VEHICLE STRUCTURAL WEIGHT CAN BE REDUCED IF AERODYNAMIC MEANS CAN BE DEVELOPED TO COUNTER THE FORCES AND MOMENTS THAT DRIVE FLUTTER AND DYNAMIC INSTABILITY. THESE CONSIDERATIONS HAVE MAGNIFIED SIGNIFICANCE IN THE TRANSONIC REGIME WHERE EXTREME FLOW SENSITIVITIES LEAD TO LARGE FORCE AND MOMENT CHANGES, PARTICULARLY THROUGH THE DISPLACEMENT OF SHOCK WAVES.

IT WILL BE THE PURPOSE OF THE PRESENT STUDY TO INVESTIGATE NUMERICALLY THE EFFECTIVITY OF CONTROLS TO NULLIFY SUCH FORCE AND MOMENT CHANGES. IN PARTICULAR WE SEEK THE PROGRAMMING OF LEADING AND TRAILING EDGE DEVICES TO NEGATE AN A PRIORI GIVEN LIFT AND MOMENT DUE TO THE PITCHING OSCILLATION OF A NACA 64A-006 AIRFOIL AT $M = 0.85$. FOR THE CALCULATIONS THE BALLHAUS-GOORJIAN UNSTEADY TRANSONIC SMALL DISTURBANCE METHOD (REF. 1) IS USED WHICH EMPLOYS AN ALTERNATING DIRECTION IMPLICIT DIFFERENCE SCHEME. THE LOW FREQUENCY LIMIT OF THE PERTURBATION POTENTIAL EQUATION IS USED WHERE THE UNSTEADINESS IS EMBODIED IN THE ADDITION OF AN X,T DERIVATIVE TO THE CLASSICAL STEADY PERTURBATION EQUATION. IN THIS LIMIT THE QUASI-PLANAR AIRFOIL CONDITION IS ESSENTIALLY QUASI-STEADY WITH THE LOCAL PLUNGING OF THE SURFACE HAVING A NEGLIGIBLE CONTRIBUTION. A CONSERVATIVE SHOCK CAPTURE IS EMPLOYED; AND THE ESSENTIAL VISCOUS INTERACTIONS ARE OMITTED IN THE PRESENT INVESTIGATION.

AS A PRELIMINARY STEP, IN PART TO IMPROVE OUR UNDERSTANDING OF THE UNSTEADY FORCE AND MOMENT GENERATION PROCESS, WE SHALL CALCULATE THE ISOLATED EFFECTS OF AN OSCILLATING LEADING OR TRAILING EDGE FLAP WITH THE AIRFOIL KEPT AT A FIXED ANGLE OF ATTACK. THE LATTER FLOW IS OF COURSE REASONABLY FAMILIAR HAVING BEEN INVESTIGATED EARLIER (REFS. 2 AND 3). BASED ON THESE RESULTS, THESE DEVICES ARE THEN DEPLOYED ON THE PITCHING AIRFOIL. THE RESULTS ARE PRESENTED IN TERMS OF PRESSURE DISTRIBUTIONS AND THE LIFT AND MOMENT HISTORIES.

2. THE RESULTS FOR THE PITCHING AIRFOIL

THE UNSTEADY LIFT AND MOMENT VARIATIONS TO BE NEGATED ARE THOSE FOR THE PITCHING OSCILLATION ABOUT THE MIDCHORD OF A NACA 64A-006 AIRFOIL AT $M = 0.85$. THE PITCH AMPLITUDE IS 1^{o} ABOUT 0^{o} ANGLE OF ATTACK, AND THE REDUCED FREQUENCY IS 0.2. (ALL REDUCED FREQUENCIES USED HEREIN ARE REFERENCED TO THE AIRFOIL CHORD.)

IN FIGURE 1 THE RESULTING UPPER SURFACE PRESSURE DISTRIBUTIONS DURING THE PITCH CYCLE ARE SHOWN.

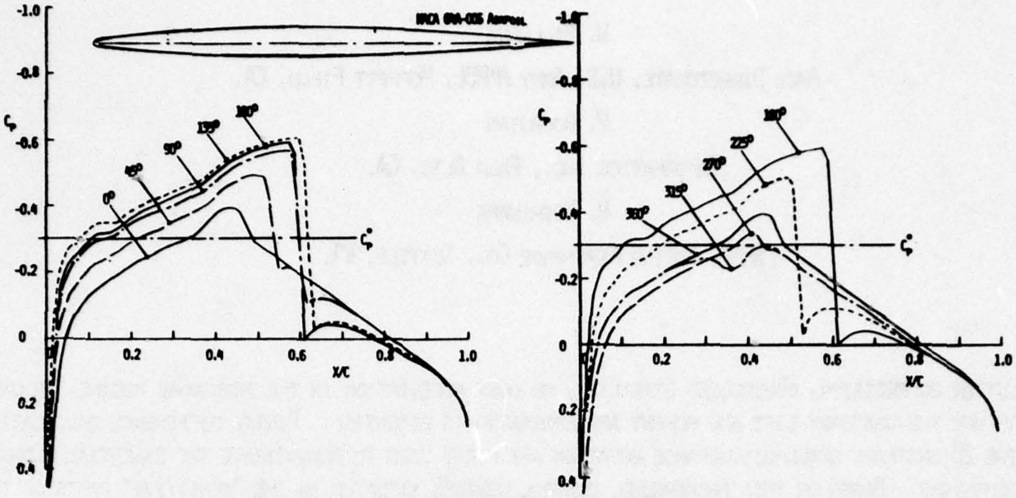

FIGURE 1. MIDCHORD PITCHING OSCILLATION

FOR THE PRESENT 0^0 MEAN ANGLE OF ATTACK CASE THE CORRESPONDING LOWER SURFACE PRESSURE DISTRIBUTIONS ARE OBTAINED BY SHIFTING THE PHASE OF THE UPPER SURFACE DISTRIBUTIONS BY 180^0. IT IS SEEN HERE THAT AT A PHASE ANGLE OF 315^0 A WEAK SHOCK PERSISTS EVEN THOUGH THE UPSTREAM FLOW IS SUBCRITICAL. SUCH A POSSIBILITY IS NOT UNCOMMON IN UNSTEADY FLOW WHERE THE REQUIRED UPSTREAM SUPERCRITICALITY RELATIVE TO THE SHOCK IS MAINTAINED BY THE UPSTREAM MOVEMENT OF THE SHOCK. (TIJDEMAN'S TYPE C SHOCK MOTION)

IN FIGURES 2 AND 3 THE CORRESPONDING VARIATIONS OF THE LIFT AND MOMENT COEFFICIENTS ARE SHOWN, THE LATTER TAKEN ABOUT THE MIDCHORD OF THE AIRFOIL. (CURVES FOR SUBSEQUENT CASES ARE ALSO SHOWN HERE, AND THEY SHOULD BE DISREGARDED FOR THE MOMENT.) RELATIVE TO THE AIRFOIL MOTION, THERE IS A LAG OF 38^0 IN THE LIFT CURVE, WHILE THERE IS A LAG OF 56^0 FOR THE MOMENT. NOTE ALSO THE DISTORTION FROM A HARMONIC IN THE MOMENT CURVE.

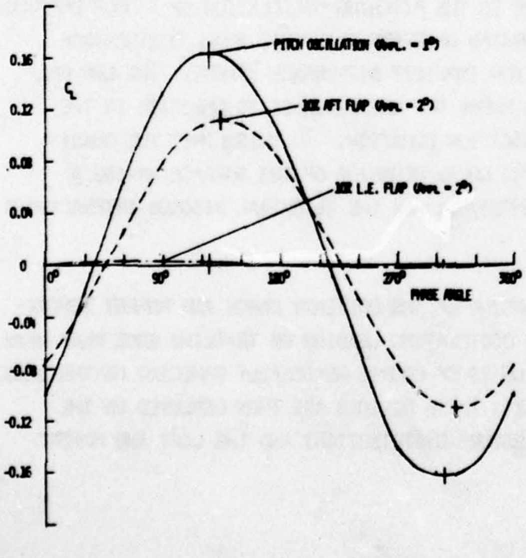

FIGURE 2. LIFT VARIATIONS

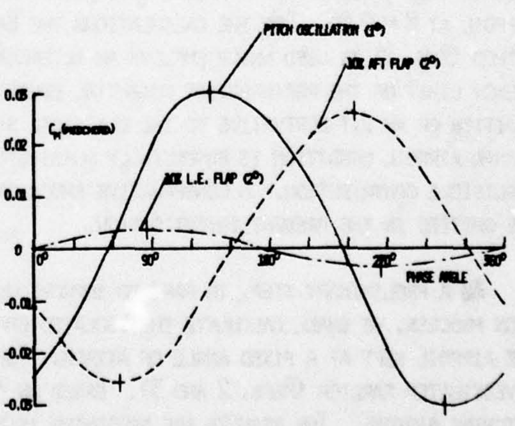

FIGURE 3. MOMENT VARIATIONS

3. ISOLATED EFFECTS OF THE LEADING AND TRAILING EDGE DEVICES

Consider first the case of a 10% chord trailing edge flap oscillating sinusoidally with an amplitude of 2° at a reduced frequency of 0.2. The resulting pressure distributions are shown in Figure 4, while the lift and moment coefficients are compared in Figures 2 and 3 with those of the pitching airfoil. In the latter figures it is seen that the phase lag for the lift is approximately the same as for the pitching airfoil, but there is a considerably greater lag in the moment. The cause for this greater lag can be seen in the pressure distributions of Figure 4 and is due in large part to the delay in the generation of the forward loading by the slow upstream propagation of the aft flap effect.

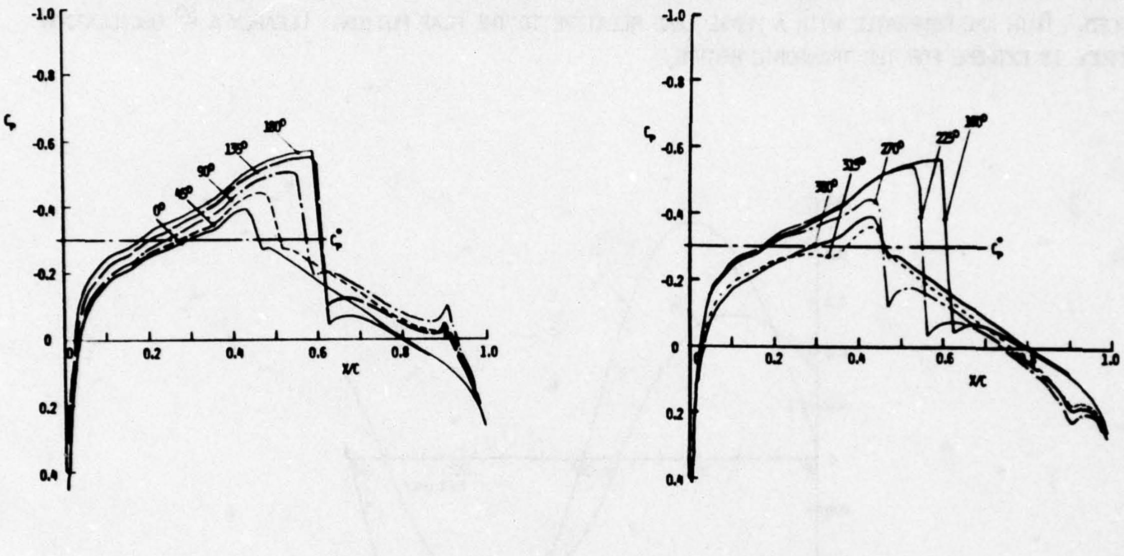

Figure 4. 10% Chord Trailing Edge Flap

The consequence of the above is that the phase of the aft flap can be timed with respect to the airfoil pitch to cancel either the lift or the moment, but not both. This then leads naturally to the consideration of an oscillating leading edge device such as a flap to provide a more timely forward loading. In Figure 5 we show the pressure distributions for the case of a 10% chord leading edge flap oscillating with an amplitude of 2° at the reduced frequency of 0.2, while the corresponding lift and moment variations

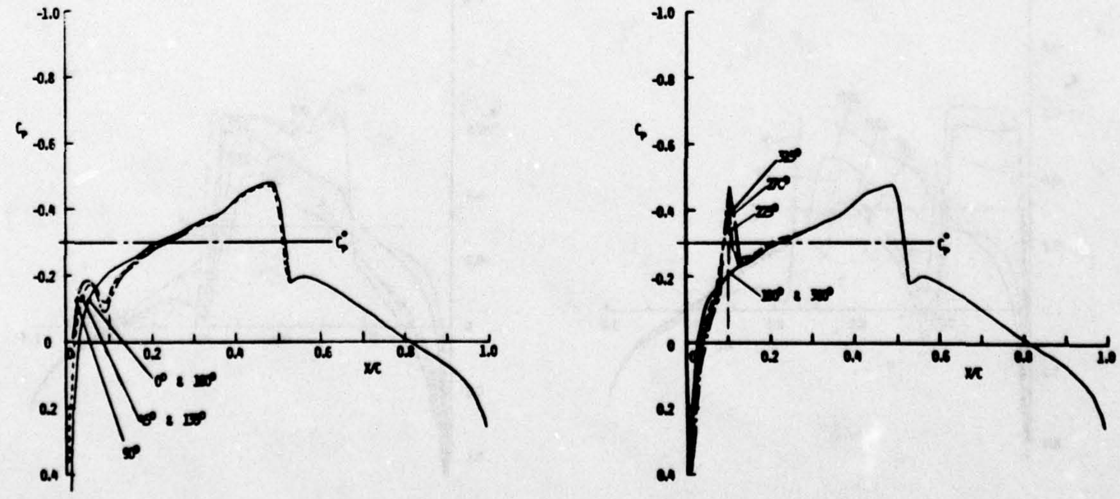

Figure 5. 10% Leading Edge Flap

ARE COMPARED TO THE PREVIOUS CASES IN FIGURES 2 AND 3. WE SEE HERE THAT THE LEADING EDGE FLAP IS INEFFECTIVE IN GENERATING EITHER LIFT OR THE DESIRED MOMENTS. THE CAUSE IS IMMEDIATELY EVIDENT IN THE PRESSURE DISTRIBUTIONS. IN CONTRAST TO THE AFT FLAP WHICH EFFECTS GLOBAL PRESSURE DISTRIBUTION CHANGES VIA THE KUTTA CONDITION, THE EFFECTS OF THE LEADING EDGE FLAP ARE CONFINED PRIMARILY TO THE FLAP ITSELF. MOREOVER LOADING CHANGES ON THE FORWARD PART OF THE FLAP ARE SEEN TO BE NEGATED BY AN OPPOSITE LOADING GENERATED AT THE KINKS IN THE AIRFOIL AT THE FLAP HINGE LINE.

GREATER EFFECTS OF THE LEADING EDGE FLAP CAN BE OBTAINED BY INCREASING ITS CHORD AND THE OSCILLATION AMPLITUDE. IN FIGURE 6 WE SHOW THE RESULTS FOR THE CASE OF A 25% CHORD AND AN AMPLITUDE OF 4°. IT IS SEEN HERE THAT THE DESIRABLE LEVEL OF THE PITCHING MOMENT IS GENERATED WITH LITTLE ADDITIONAL LIFT BEING PRODUCED. BOTH ARE GENERATED WITH A PHASE LEAD RELATIVE TO THE FLAP MOTION. CLEARLY A 4° OSCILLATION AMPLITUDE IS EXTREME FOR THE TRANSONIC REGIME.

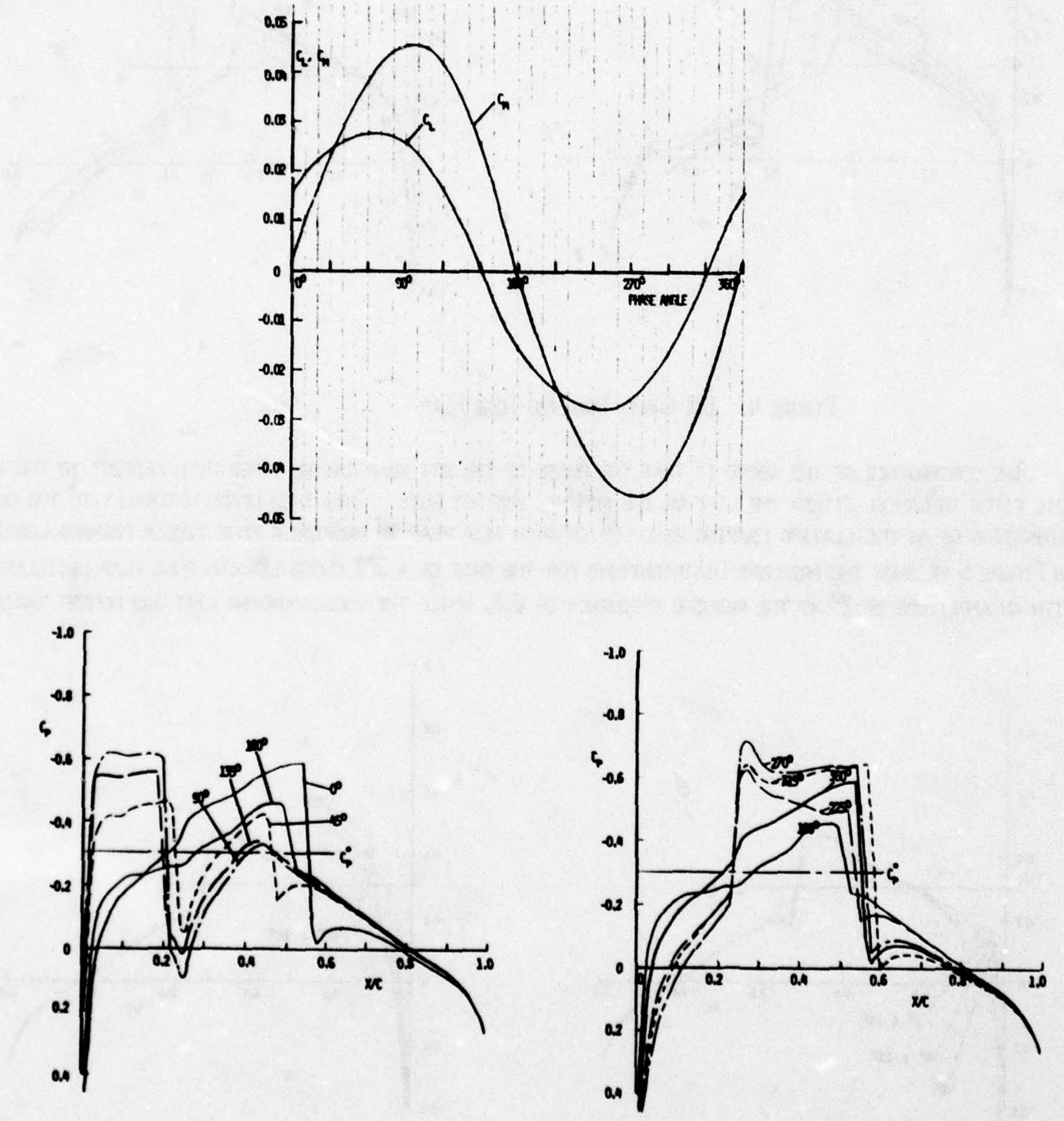

FIGURE 6. LEADING EDGE FLAP - INCREASED CHORD AND AMPLITUDE

4. FORCE AND MOMENT CANCELLATION ON THE PITCHING AIRFOIL

WE SEEK NEXT TO CANCEL THE LIFT AND MOMENT FOR THE PITCHING AIRFOIL EMPLOYING OSCILLATING LEADING AND TRAILING EDGE FLAPS. IN FIGURE 7 WE SHOW FIRST THE USE OF A 15% CHORD AFT FLAP TO CANCEL ONLY THE MOMENT OF THE PITCHING AIRFOIL. HERE THE MOTION OF THE FLAP LAGS THE PITCHING MOTION OF THE AIRFOIL BY 80°, AND THE FLAP AMPLITUDE IS 2°. IN THE ABOVE PHASE RELATION, 180° PHASE DIFFERENCE IS REQUIRED TO CHANGE THE SIGN OF THE FLAP CONTRIBUTION, SO THAT THE BALANCE IS CLOSELY APPROXIMATED BY THE PHASE DIFFERENCE BETWEEN THE PITCHING ALONE AND THE FLAP ALONE. WE SEE HERE THAT A LARGE REDUCTION IN THE MOMENT VARIATION IS OBTAINED WITH SOME INCREASE IN THE LIFT OSCILLATION AMPLITUDE. NOTE HERE THAT THE RESIDUAL MOMENT IS DOMINANTLY OF A HIGHER HARMONIC. IN FIGURE 8 WE SHOW COMPARABLE RESULTS WHERE ONLY THE LIFT OSCILLATION HAS BEEN REDUCED. HERE THE FLAP PHASE LAG IS 171°, AND THE OSCILLATION AMPLITUDE IS INCREASED TO 2¼°.

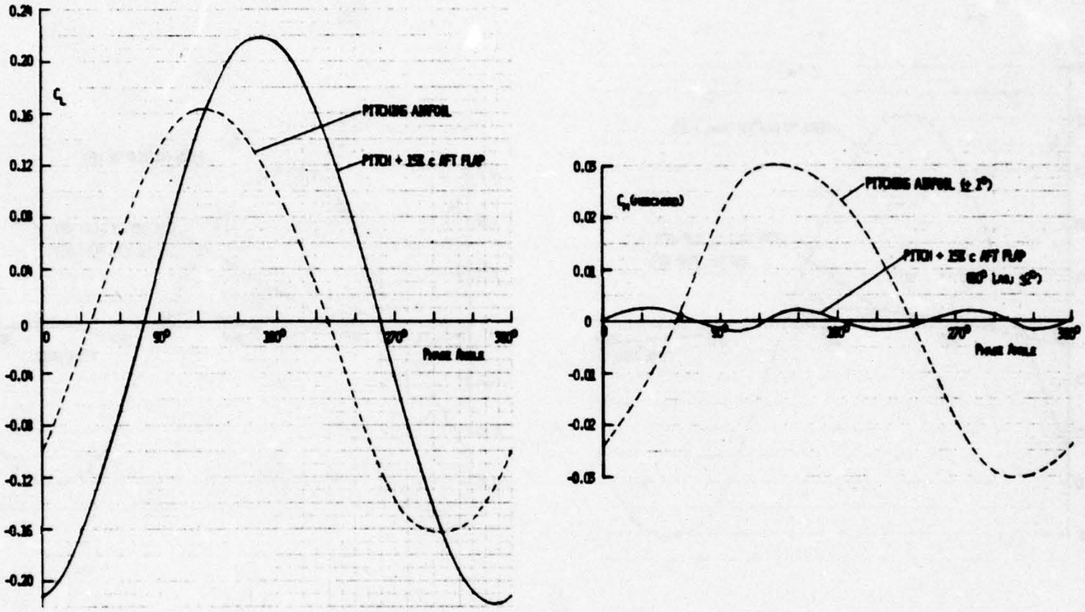

FIGURE 7. MOMENT CANCELLATION WITH A 15% CHORD AFT FLAP

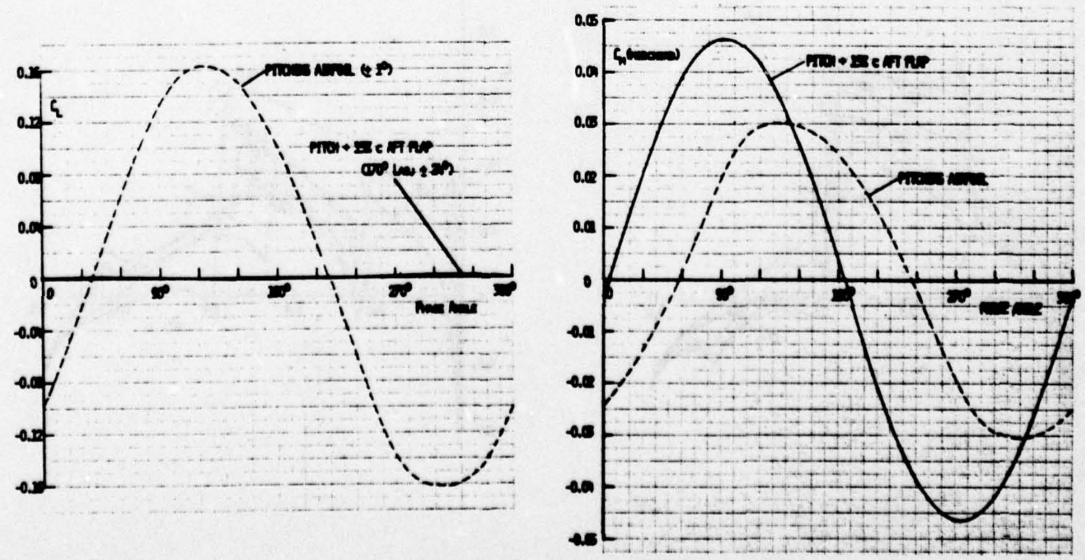

FIGURE 8. LIFT CANCELLATION WITH A 15% CHORD AFT FLAP

FINALLY IN FIGURE 9 WE SHOW THE USE OF BOTH LEADING AND TRAILING EDGE FLAPS TO REDUCE BOTH THE LIFT AND MOMENT OF THE PITCHING AIRFOIL. HERE THE 25% CHORD LEADING EDGE FLAP IS DEPLOYED WITH A PHASE LAG OF 190.5° WITH AN AMPLITUDE OF 4°, WHILE THE 15% CHORD TRAILING EDGE FLAP HAS A PHASE SHIFT OF 180° AND AN AMPLITUDE OF 2°. ALL OSCILLATIONS ARE AT A REDUCED FREQUENCY OF 0.2. THE RESULTS SHOW SIGNIFICANT REDUCTIONS OF BOTH THE LIFT AND MOMENT VARIATIONS WHERE THE RESIDUAL MOMENT AGAIN CONTAINS PRIMARILY A HIGHER HARMONIC IN CONTRAST TO THE LIFT RESIDUAL WHICH STILL IS DOMINATED BY THE BASE HARMONIC. THE LATTER SUGGESTS THAT FURTHER TUNING OF THE FLAP MOTIONS IS REQUIRED. IN THE ABOVE RESULT THE LEADING EDGE FLAP WAS ESSENTIALLY USED TO CANCEL THE MOMENT WHEREAS THE TRAILING EDGE FLAP WAS USED TO CANCEL THE LIFT. INTERESTINGLY THE REQUIRED PHASES FOR THE FLAPS CAN BE ESTIMATED FROM THE ISOLATED EFFECTS OF THE FORE AND AFT FLAPS.

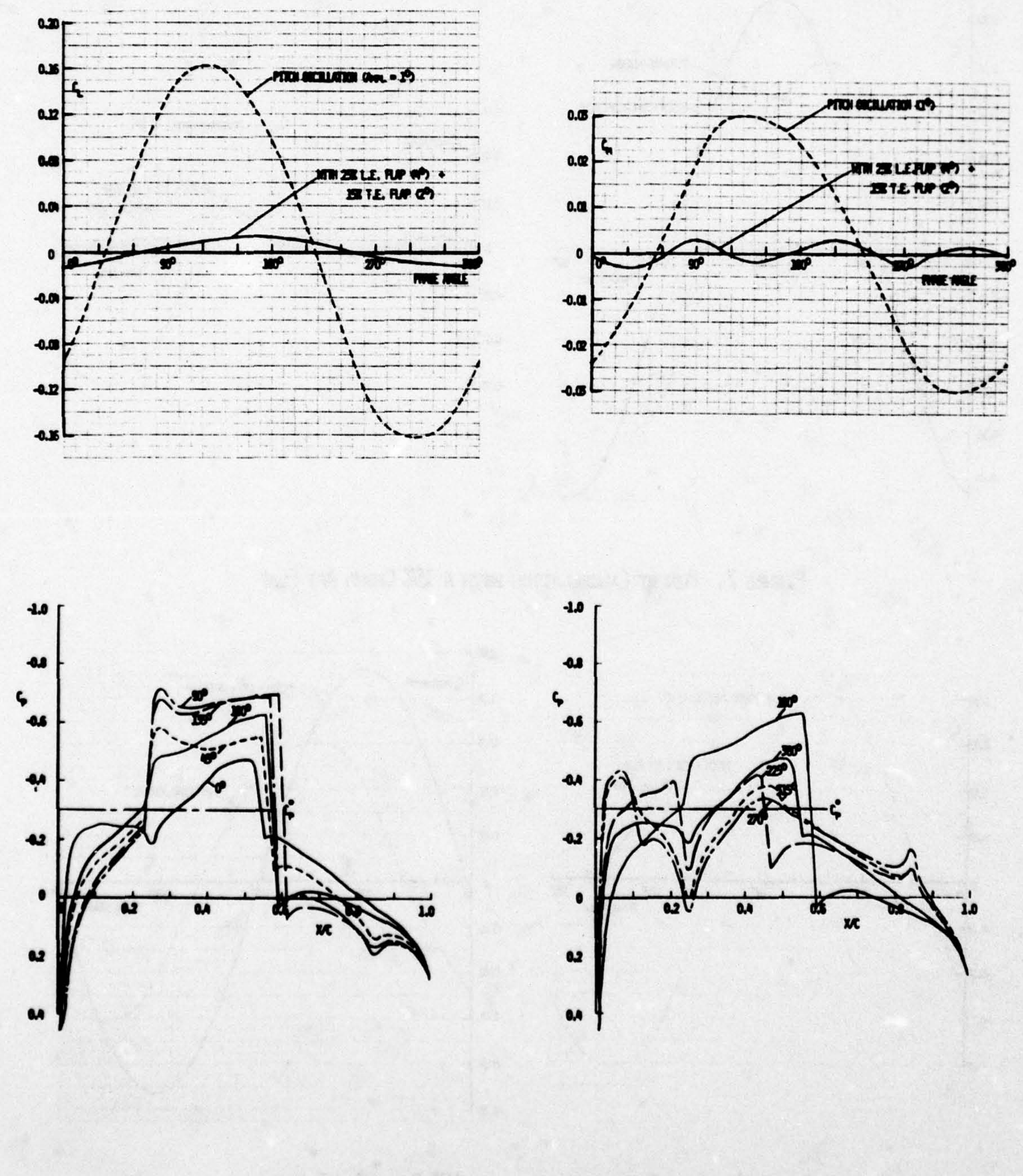

FIGURE 9. SIMULTANEOUS LIFT AND MOMENT CANCELLATION

5. OSCILLATING BUMPS ON THE AIRFOIL

TO INFLUENCE THE SHOCK POSITION, THEREBY SEEKING TO MODERATE THE LIFT AND MOMENT VARIATIONS, SMALL BUMPS WERE OSCILLATED IN THE NEIGHBORHOOD OF THE SHOCK. THE BUMPS WERE SINE-SHAPED WITH A CHORD OF 10% AND A MAXIMUM HEIGHT OF 2% OF THE BUMP CHORD AND OSCILLATED AT A REDUCED FREQUENCY OF 0.2. THE ANGLE OF ATTACK OF THE AIRFOIL WAS CONSTANT AT EITHER 1° OR 0°. THE RESULTING PRESSURE DISTRIBUTIONS FOR THE BUMP LOCATED JUST UPSTREAM OF THE SHOCK FOR THE 1° ANGLE OF ATTACK CASE IS SHOWN IN FIGURE 10. IT IS SEEN HERE THAT THE BUMP HAD NEGLIGIBLE EFFECT ON THE SHOCK POSITION, IN FACT CHANGING THE PRESSURE DISTRIBUTION ESSENTIALLY ONLY ON THE BUMP ITSELF. THE RESULTS FOR A BUMP LOCATED JUST DOWNSTREAM OF THE SHOCK ARE SHOWN IN FIGURE 11, WHERE A COMPARABLE INEFFECTIVITY IS SEEN. IT MIGHT HAVE BEEN CONJECTURED THAT THE PRESSURE PERTURBATIONS FROM THE BUMP WOULD PROPAGATE UPSTREAM, IMPINGING ON THE BACK SIDE OF THE SHOCK, TO THEN CAUSE A SHOCK DISPLACEMENT.

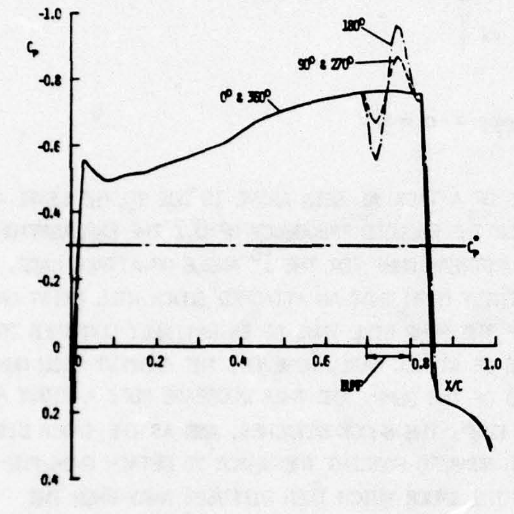

FIGURE 10. UPSTREAM BUMP - $\alpha = 1^0$

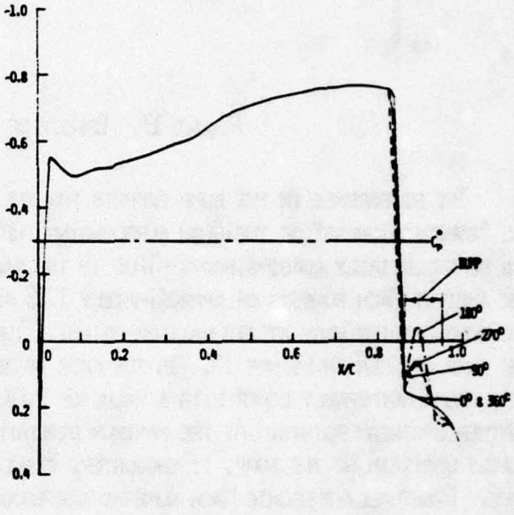

FIGURE 11. DOWNSTREAM BUMP - $\alpha = 1^0$

THE OSCILLATING BUMPS WERE NEXT DEPLOYED WITH THE AIRFOIL SET AT 0° ANGLE OF ATTACK. THE RESULTING PRESSURE DISTRIBUTIONS ARE SHOWN IN FIGURES 12 AND 13 FOR THE FORE AND AFT BUMPS. IN CONTRAST TO THE 1° ANGLE OF ATTACK CASE, THERE IS A SIGNIFICANT EFFECT OF THE BUMPS.

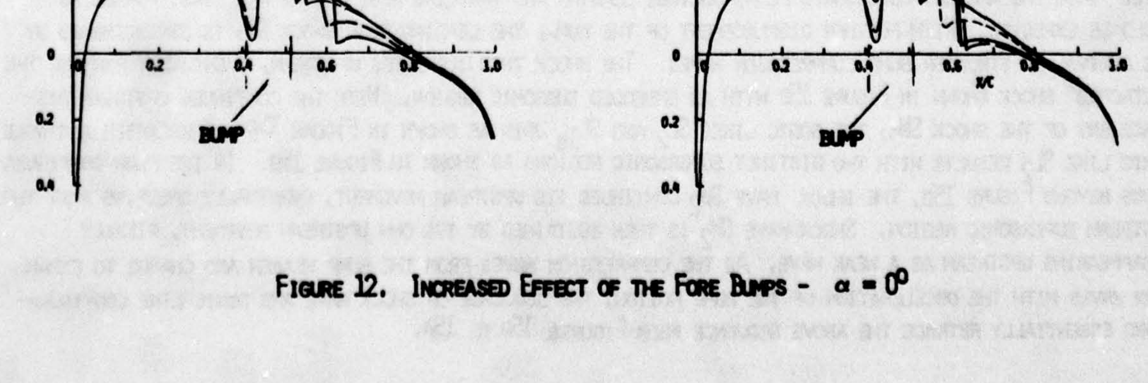

FIGURE 12. INCREASED EFFECT OF THE FORE BUMPS - $\alpha = 0^0$

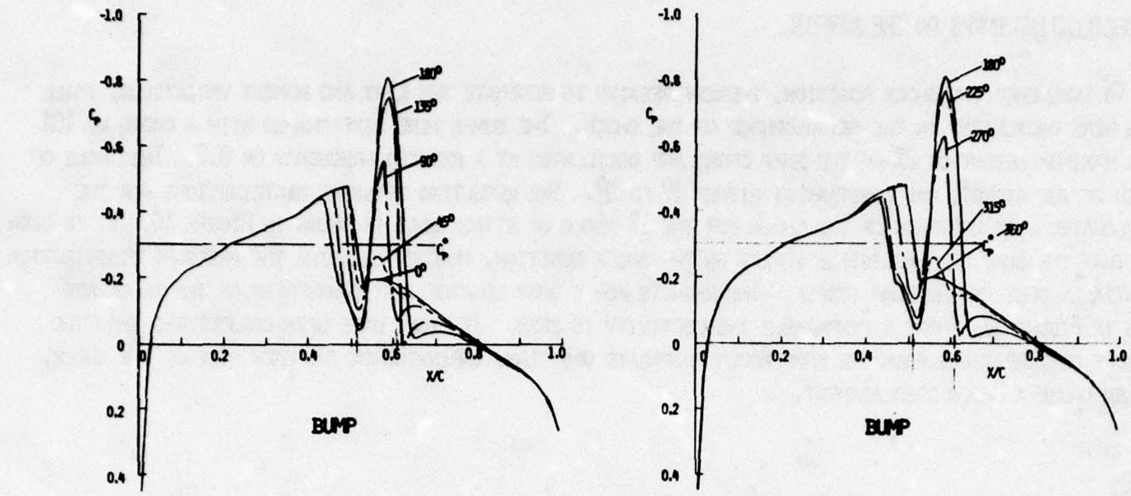

Figure 13. Effect of the Aft Bumps - $\alpha = 0^0$

The difference in the bump effects for the two angles of attack as seen above is due to the level of the "supersonicness" of the flow surrounding the bumps. For the reduced frequency of 0.2 the explanation can be essentially quasi-steady. Thus in the case of the upstream bump for the 1^0 angle of attack case, the ambient Mach numbers of approximately 1.25 are sufficiently high that an attached shock will exist on the bump leading edge at its maximum height. The effect of the bump will thus be essentially confined to the bump as seen in Figure 10. In the case of the 0^0 angle of attack case, however, the ambient Mach numbers are considerably lower with a value of 1.07 just ahead of the bump, and they decrease more rapidly at further upstream points. At the maximum deployment of the bump, the shock detaches, and as the shock displaces upstream of the bump, it encounters still lower Mach numbers forcing the shock to detach even further. Eventually subsonic Mach numbers are encountered by the shock which then diffuses away when the shock velocity is insufficient.

In the case of the aft bumps, the primary cause of the differences between the 0^0 and 1^0 case is the strength of the primary terminating shocks which manifests its effects in two ways. In the first, the 1^0 shock leads to post-shock Mach numbers approaching the bump that are considerably lower than in the case of the 0^0 case. This then leads to a bump flow that is significantly less supercritical in the latter case. In the second way, the unsteady waves, though bucking a higher headwind, have a greater relative influence in moving the shock for the 0^0 case with the weaker shock, thus accounting for the more pronounced upstream displacement of the shock in this case.

Finally a 4% bump was oscillated directly beneath the shock with the angle of attack of 0^0. The resulting pressure distributions are shown in Figure 14, while the corresponding shock wave and sonic line configurations are sketched in Figure 15. The latter were deduced from the surface pressure distributions since calculated flow field data were not recorded.

In Figure 15a the shock wave and sonic line are shown for zero bump displacement. As the bump moves into the ambient supersonic flow, oblique leading and trailing edge shocks are first formed as would be expected. With further displacement of the bump, the leading edge shock SW_2 is strengthened by the arrival of stronger bump compression waves. The shock then displaces upstream, eventually forming the "detached" shock shown in Figure 15b with an embedded subsonic region. With the continued upstream displacement of the shock SW_2, the sonic lines SL_2 and SL_{1B} join as shown in Figure 15c. Thereafter a single sonic line SL_2 results with two distinct supersonic regions as shown in Figure 15d. In the flow configurations beyond Figure 15d, the shock wave SW_2 continues its upstream movement, eventually sweeping away the upstream supersonic region. Shock wave SW_2 is then sustained by its own upstream movement, finally disappearing upstream as a weak wave. As the compression waves from the bump weaken and change to expansion waves with the deceleration of the bump motion, the sequence of shock wave and sonic line configurations essentially retrace the above sequence from Figures 15d to 15a.

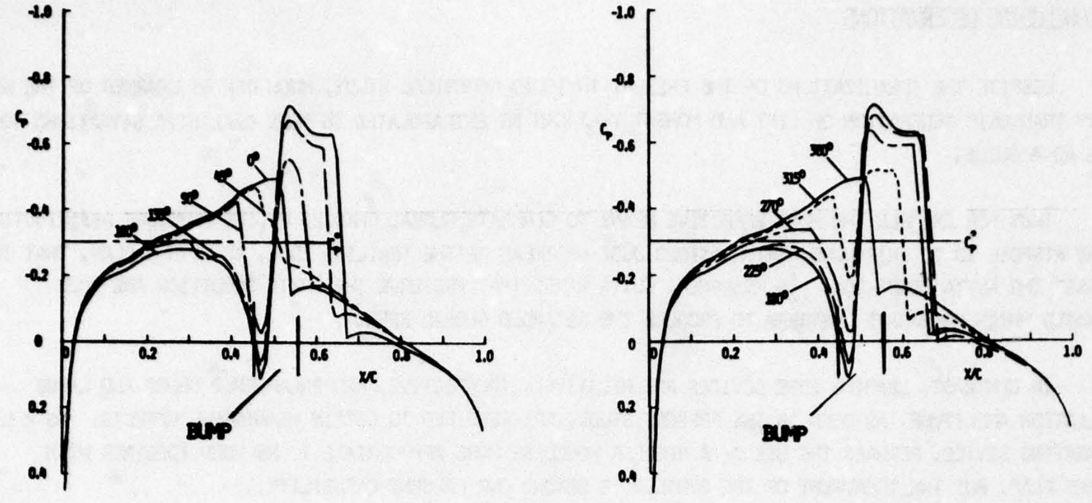

FIGURE 14. OSCILLATING BUMP UNDER SHOCK WAVE

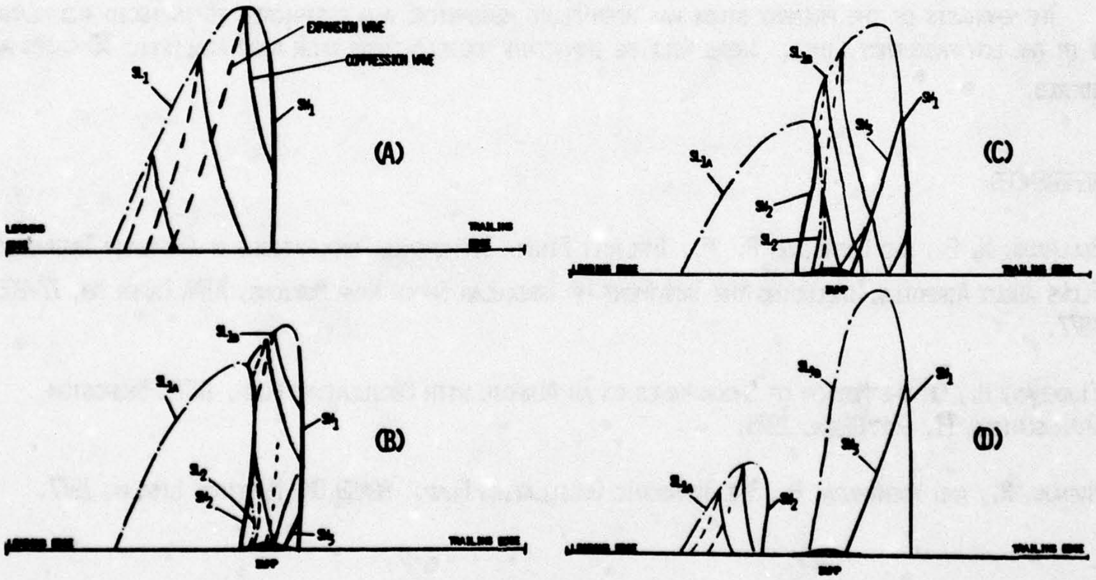

FIGURE 15. CORRESPONDING CONJECTURED FLOW FIELDS

6. CONCLUDING OBSERVATIONS

Despite the idealizations of the present inviscid numerical study, much can be learned of the unsteady transonic generation of lift and moment that can be extrapolated to more realistic situations to serve as a guide.

Thus for example the most effective means to generate global changes of the pressure distribution on the airfoil is to introduce perturbations just upstream of the trailing edge, as with a flap, that tend to upset the Kutta condition. In response, Kutta waves that preserve the Kutta condition are then generated which propagate upstream to produce the retarded global effect.

In contrast, leading edge devices are relatively ineffective, and enlargened chord and large oscillation amplitude, as used in the present study, are required to obtain meaningful effects. As a lift attenuating device, perhaps the use of a spoiler would be more appropriate to be used together with the aft flap, but the treatment of the spoiler is beyond our present capability.

The present results show that the proper phasing of either the leading or trailing edge flap to cancel a given variation of lift or moment can be obtained from the isolated effects of the given device. Moreover, the effects of a given device depend strongly on the environment in which the device must operate, as shown by the oscillating bumps in the vicinity of the shock. The effectivity of the aft flap will suffer accordingly if extended supersonic regions are present upstream of the flap.

The emphasis of the present study has been fluid mechanical and restricted to inviscid and planar flows in the low frequency limit. There will be important modifications when more realistic 3D cases are considered.

7. REFERENCES

1. Ballhaus, W. F., and Goorjian, P. M., Implicit Finite Difference Computations of Unsteady Transonic Flows about Airfoils, including the Treatment of Irregular Shock Wave Motions, AIAA Paper No. 77-205, 1977.

2. Tijdeman, H., On the Motion of Shock Waves on an Airfoil with Oscillating Flap, IUTAM Symposium Transsonicum II, Göttingen, 1975.

3. Magnus, R., and Yoshihara, H., The Transonic Oscillating Flap, AGARD SMP Meeting, Lisbon, 1977.

Appended Note: We have omitted details of the numerical process. For the reader interested in these details, he is referred to Ref. 1.

INFLUENCE DU NIVEAU DE BRUIT DES SOUFFLERIES TRANSSONIQUES SUR LES CARACTÉRISTIQUES AÉRODYNAMIQUES DES MAQUETTES

par Xavier VAUCHERET

Office National d'Etudes et de Recherches Aérospatiales (ONERA)
92320 Châtillon - France

Résumé

En vue d'étudier l'influence du bruit des souffleries transsoniques, les parois perforées de la soufflerie ONERA S2 de Modane ont été recouvertes d'une gaze : le niveau de bruit a alors été réduit à celui des spécifications LEHRT. L'étude a porté sur des maquettes étalons. Hormis un décalage des moments de tangage, le bruit n'affecte pas les caractéristiques stationnaires globales. Les positions des chocs ne sont nettement modifiées par le bruit que lorsque des décollements de pied de choc existent. En l'absence de décollements, les perturbations acoustiques sont d'autant plus perçues que la portance est plus faible ; les valeurs efficaces des pressions instationnaires peuvent être décuplées. Avec décollement et suppression du bruit des parois, les capteurs de pression décèlent les vibrations de la voilure sur ses modes propres. Sans suppression du bruit, cette réponse est totalement masquée, ce qui peut fausser les conclusions concernant les couplages aérodynamique-structure. En présence de décollements intenses, l'effet du bruit devient nul. En transition déclenchée, l'influence des perturbations est atténuée sans décollements, mais exacerbée en leur présence.

INFLUENCE OF THE NOISE LEVEL IN A TRANSONIC WIND TUNNEL TEST SECTION ON THE AERODYNAMIC CHARACTERISTICS OF *MODELS*

Summary

With a view to study the influence of noise in transonic wind tunnels, the perforated walls of the ONERA S2 Modane wind tunnel have been covered with a gauze : the noise level is then reduced to that specified in the LEHRT project. The study was carried out with standard models. Except a shift of the pitching moment, the noise does not affect the overall steady characteristics. The shock locations are strongly modified by the noise, but only when the separation occurs at the shock foot. Without separation, the edge tones were heard clearly by the pressure transducers, all the more as the lift decreases ; RMS values can be increased tenfold. With separation and suppression of wall noise, the transducers reveal wing vibrations on their natural modes. Without noise suppression this response is completely drawned, which may alter the conclusions concerning aerodynamics-structure coupling. With strong separation, the noise effect disappears. For fixed transition, the edge tones effect is damped without separation, but amplified with separation.

INTRODUCTION

L'utilisation de parois perméables pour diminuer le blocage et atténuer la réflexion des ondes de choc issues des maquettes [1,2] a été retenue pour la conception des souffleries transsoniques actuellement en service.

En léger supersonique, la réduction souhaitable de la perméabilité des parois conduisait à adjoindre aux parois perforées, des plaques perforées coulissantes situées du côté de l'enveloppe étanche. Une telle solution fut ainsi adoptée dans les souffleries 6ft de S2 Modane, 4ft de l'AEDC ou 14 inches de NASA-MSFC.

A l'occasion de difficultés rencontrées en 1966 [3] au cours d'essais de flottement dans la soufflerie S2 de Modane, l'analyse spectrale des fluctuations de pression de l'écoulement fit apparaître des fréquences privilégiées liées aux parois perforées. Un simple déplacement des plaques coulissantes permit alors de déplacer les fréquences dues aux perforations vers des valeurs plus élevées non dommageables pour les maquettes.

Des formules empiriques [4,5] puis théoriques [6] permirent de préciser les fréquences des perturbations acoustiques émises par les cavités constituées par les perforations des parois (edge tones). Les conditions d'existence de ces perturbations dans des domaines Mach, Reynolds bien définis [7] , la prédominance de certains harmoniques d'edge tones, la détermination de plusieurs nombres de Mach de résonnance liés aux dimensions de la veine d'essais [8] permirent de mieux comprendre le mécanisme de production du bruit en soufflerie.

Une qualification de l'écoulement des souffleries transsoniques de grandes dimensions fut entreprise à l'aide d'un même étalon constitué par un cône de 10 degrés d'ouverture. Les nombres de Reynolds de transition et les niveaux de bruit obtenus dans les souffleries de AEDC, ARA, NASA Ames et Langley, NLR, ONERA Modane et RAE Bedford furent confrontés en 1974 [9,10]. Une corrélation transition-bruit fut établie [11,12].

Tandis qu'ainsi l'environnement aérodynamique instationnaire des souffleries transsoniques était de mieux en mieux connu, avec le développement d'avions à haute performance, les phénomènes aérodynamiques instationnaires prenaient un aspect de plus en plus important dans la conception des projets [13]. Ce n'est en fait qu'à partir de 1972 que des essais [14,15] illustrent l'influence significative du bruit des veines d'essais sur la transition de la couche limite à portance élevée et sur les caractéristiques d'entrée en tremblement des maquettes d'avions. Pour assurer une prévision raisonnable des limites de tremblement, un niveau maximal des perturbations de l'écoulement fût proposé. Cette préoccupation se répand alors et conduit à émettre d'abord des recommandations sur le niveau de bruit des souffleries transsoniques futures [16], puis à formuler des spécifications précises sur ce niveau pour les souffleries participant au projet LEHRT [17]. L'appellation de "souffleries propres" fait son apparition par opposition aux veines d'essais transsoniques en service.

Il importait donc, pour les souffleries transsoniques existantes, de développer des moyens aptes à réduire leur niveau de bruit jusqu'à une valeur fixée par les nouvelles spécifications. Cette valeur est celle du seul bruit engendré par la couche limite turbulente sur parois solides [18], considérée comme irréductible. Partant du principe qu'en soufflerie continue, la majeure partie du bruit en veine provient des parois, plusieurs recherches furent menées parallèlement pour éliminer les perturbations acoustiques des parois perforées.

Un type particulier de solution concerne des parois d'un nouveau concept (rod wall) [19]. Une autre solution consiste à détruire le tourbillon générateur de perturbation, en insérant dans chaque perforation une cloison mince placée parallèlement au vent [20]. Outre une laborieuse mise en place due au nombre de perforations, cette solution a l'inconvénient d'être irréversible.

La solution la plus simple consiste à déplacer les fréquences des edge tones vers des valeurs supérieures à celles intéressant les phénomènes instationnaires des maquettes. Il suffit pour cela d'utiliser des parois avec des perforations d'un diamètre inférieur à 4 mm [12] soit, à la limite, des parois en métal fritté [21]. Dans ce dernier cas, la mauvaise résistance mécanique des parois rend technologiquement cette solution d'un emploi difficile. Une autre solution a été recherchée dans le but de conserver les parois d'origine : elle consiste à appliquer sur ces parois, du côté de la veine, une gaze à maille fine. Simultanément une gaze en polyester [12] et une gaze métallique [22], de caractéristiques très voisines, ont été proposées. Des essais avec un tissu à forte perméabilité [21] sont venus confirmer les résultats obtenus avec les gazes.

Il apparaît donc, à partir de 1975, qu'un moyen simple et très économique permet, dans des souffleries à parois perforées conventionnelles, d'environnement acoustique élevé, non seulement de ramener le bruit au niveau de celui d'une paroi solide, mais encore par pose et dépose de la gaze, de disposer d'une veine à deux niveaux de bruit différents. Les critiques émises du point de vue acoustique à l'encontre des parois perforées ne sont donc plus fondées, et, en outre, il est possible d'étudier toutes choses égales par ailleurs, l'effet du niveau de bruit sur les phénomènes aérodynamiques. Dans la soufflerie S2 de Modane, il est ainsi permis de réaliser deux niveaux de bruit fort différents et dans le cas du niveau le plus élevé, le déplacement des plaques coulissantes autorise un déplacement des zones de fréquences à forte énergie.

Les seuls résultats publiés sur l'influence du bruit dans une même soufflerie concernent les répartitions de pressions stationnaires et les emplacements de la transition. Sur un cône cylindre, les pressions ne sont pas modifiées dans une large gamme de Mach de 0,6 à 1,3 [20]. Seul un léger recul du choc est observé à Mach 0,95 [20]. sur une voilure et un empennage. Une élévation du niveau de bruit par un moyen situé en aval de la veine d'essais ne modifie pas le décollement d'un profil mais provoque un léger recul de la transition [23].

Devant le faible nombre de renseignements dont il était possible de disposer, surtout en instationnaire, des expériences ont été menées dans la soufflerie S2 de Modane. Les résultats présentés ici concernent l'influence du niveau de bruit tant sur les caractéristiques stationnaires globales et locales que sur le comportement instationnaire de maquettes tridimensionnelles dans le domaine transsonique.

1 - NOTATIONS

b	Demi envergure de voilure
$\overline{C}$	*Corde aérodynamique* moyenne de voilure
$C_{1,2}$	Corde de section 1,2
C_A	Coefficient de force axiale
C_m	Coefficient de moment de tangage (pris par rapport à 25 % de $\overline{C}$)
C_N	Coefficient de force normale
C_{N_α}	Gradient de portance
C_p	Coefficient de pression locale
f	Fréquence
f_c	Fréquence liée au régime du compresseur
M	Nombre de Mach
$F(n)$	Fonction spectrale (voir paragraphe 3)
n	Fréquence réduite (voir paragraphe 3)
P	Pression locale stationnaire
P_i	Pression génératrice
q	Pression dynamique
$\mathcal{R}_C$	Nombre de Reynolds, calculé sur une longueur C
x/c	Position relative en profondeur d'une pression d'une section de longueur
y/b	Position relative en envergure d'une section équipée de prises de pressions
$x/\overline{c}$	Position du point neutre de la maquette = 25 % - dCm/dCn
α	Incidence du fuselage
α_W	Incidence de la voilure ($\alpha_W = \alpha + 4^\circ$)
σ_B	Signal du pont de jauge de flexion à l'emplanture voilure

Indices

$K_{1,2}$	caractérise une pression mesurée par le capteur Kulite situé dans la section 1,2
M	caractérise une pression mesurée par le microphone situé à la paroi de la veine d'essais
$\sim$	caractérise une valeur efficace d'un signal

Indications particulières

B,T	modes de flexion, torsion de voilure
1,1',2,3	numéro d'harmonique d'edge tones

2 - MOYENS D'ESSAIS

La veine transsonique de la soufflerie continue à pression variable S2 de Modane est une veine de section carrée de 6 ft de côté. Les parois verticales sont pleines, tandis que les parois horizontales sont perforées à trous de 18 mm de diamètre inclinés à 60 degrés complétés de plaques coulissantes, de même perforation, situées du côté de l'enveloppe étanche de très grande dimension (diamètre 13 mm) entourant la veine (figure 1). Le dispositif de réduction du bruit consiste en une gaze en fils de polyester de 30/100 mm tressés en mailles de 0,8 mm. Cette gaze est appliquée, côté veine, sur toute la partie perforée des parois horizontales de 5,4 m de longueur.

Les maquettes tridimensionnelles utilisées sont les maquettes étalons ONERA (figure 1) ayant servi à une large confrontation [24] de 14 souffleries transsoniques industrielles américaines et européennes et à des études de corrections des effets de parois [25] . Ces maquettes sont représentatives d'un avion de transport d'allongement 7,3 de la classe Mach 0,85 (le Mach de divergence de traînée est 0,87). Le même profil PEAKY, symétrique de 10,5 % d'épaisseur relative, équipe toutes les surfaces portantes de génération conique. La voilure est calée à 4 degrés sur le fuselage. L'absence de vrillage et de cambrure sur ces ailes en flèche de grand allongement confère aux maquettes des caractéristiques de décrochage prématuré en bout d'aile avec une intéressante susceptibilité des seuils de pitch up et des phénomènes de décollement et interaction choc-couche limite aux nombres de Mach et de Reynolds. Comme on dispose de maquettes homothétiques et d'une soufflerie à pression génératrice variable, il devient plus facile dans certaines conditions de séparer les effets du nombre de Reynolds, des parois et du niveau de bruit. La conception monobloc des maquettes permet une meilleure reproductibilité des essais et une identification sûre des résultats.

Les deux maquettes étalons ONERA utilisées sont :

- la maquette M1 d'envergure 0,29 m présentant une obstruction en veine de 0,05 % dont les résultats peuvent être assimilés à ceux qui seraient obtenus en atmosphère illimitée.
- la maquette M5 d'envergure 0,98 m présentant une obstruction de 0,59 % et un rapport entre envergure et largeur de veine de 0,56 comparable aux valeurs utilisées en essais industriels. Bien entendu, la taille de cette maquette présente l'avantage de permettre un équipement plus complet que celui de la petite maquette.

L'équipement des deux maquettes comprend une balance dynamométrique à 6 composantes et un capteur de pression instationnaire situé à 65 % de profondeur de la corde à mi-envergure. La maquette M5 comprend en outre un second capteur de pression instationnaire à 83 % de profondeur de la corde à 81 % d'envergure, un pont de jauges mesurant la flexion à l'emplanture de voilure et deux sections S_1 et S_2 équipées chacune de 40 prises de pressions stationnaires situées à 50 et 81 % de l'envergure.

L'environnement acoustique de la veine d'essais est mesuré à l'aide d'un microphone monté affleurant à la paroi verticale pleine, à mi-hauteur ; il est placé respectivement à 1,42 m et 0,57 m en amont du nez des maquette M1 et M5.

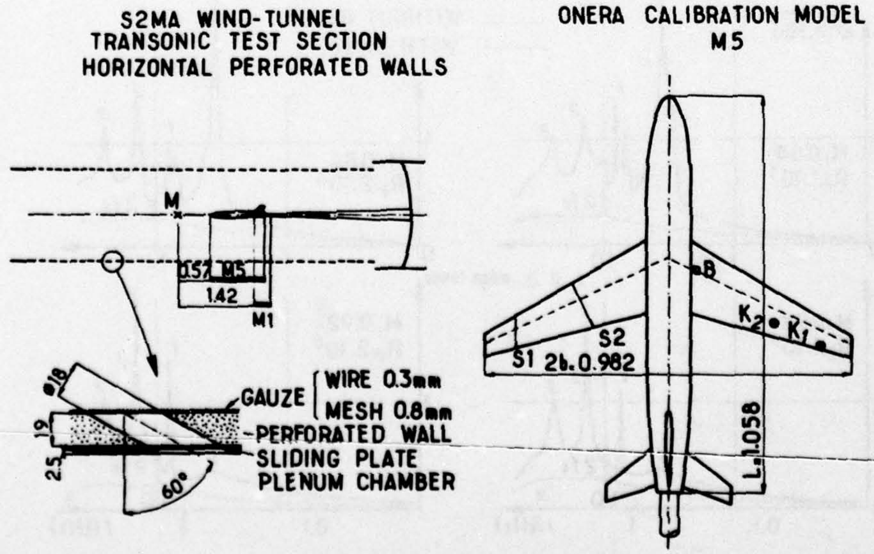
S2MA WIND-TUNNEL TRANSONIC TEST SECTION HORIZONTAL PERFORATED WALLS

ONERA CALIBRATION MODEL M5

Figure 1 Soufflerie S2MA - Maquettes étalons ONERA

3 - ESSAIS ET MESURES EFFECTUEES

L'ensemble des essais est systématiquement effectué en présence et en l'absence de gaze sur les parois horizontales perforées. Les plaques coulissantes des parois sont maintenues en position ouvertes.

Les essais sont effectués à différents nombres de Reynolds en transition naturelle (pression génératrice variable de 0,5 à 1,8 bar). Quelques essais en transition déclenchée (perles de verre de 0,12 mm collées à 7 % de profondeur de corde extrados et intrados) sont réalisés sur la maquette M5 ; des visualisations classiques de la transition de la couche limite sont faites à Mach 0,92, et incidence $\alpha = 3{,}3°$ (CN $\sim$ 0,6), au nombre de Reynolds de 2 millions sur la maquette M5 sans rugosité.

Les mesures de pressions instationnaires sont présentées en utilisant les coordonnées sans dimension : fréquence réduite $n = fl/U$ (l = côté de la veine carrée) et fonction spectrale $F(n)$ telle que

$$\frac{\overline{p^2}}{q^2} = \int_{n=0}^{n=\infty} F(n)\, dn = \int_{\log n=-\infty}^{\log n=\infty} n\,F(n)\, d \log n$$

Ainsi que préconisé pour le LEHRT [26], les spectres de puissance sont présentés en termes $\sqrt{nF(n)}$ en fonction de logn.

4 - NIVEAUX DE BRUIT EN VEINE

Les spectres de fluctuations de pressions mesurées avec le microphone, situé en amont de la maquette M5, à Mach 0,84 et 0,92, $\mathcal{R}_{\bar{c}}$ de 1 et 2 millions, en présence et en l'absence de gaze, sont comparés figure 2.

Dans l'état d'origine des parois (sans gaze) les spectres comportent des zones à forte énergie très marquées correspondant aux trois harmoniques d'edge tones, numérotés 1, 2 et 3. A Mach 0,84 le premier harmonique est prépondérant alors qu'à Mach 0,92 il est très atténué et le second harmonique prédomine. Sur ces 2 modes d'edge tones, les densités spectrales normalisées $\sqrt{nF(n)}$ dépassent 0,02. Autour de $n = 8$, une quatrième *zone d'énergie numérotée* 1' moins importante apparaît : son origine n'a pas été identifiée, car elle ne semble pas être assimilable à un harmonique des fréquences de perturbation acoustique de trous [12]. Enfin, une raie de très faible énergie, située à $n = 10$, *correspond* à la *fréquence* double du régime compresseur.

La présence de la gaze rabote toutes les zones de forte ou moyenne énergie et diminue les densités spectrales dans toute la gamme de fréquence. Seule la raie, liée au compresseur, à n = 10 subsiste. La répartition de densité spectrale est voisine de celle obtenue sur paroi solide et répond donc aux spécifications imposées pour le LEHRT.

5 - RESULTATS AERODYNAMIQUES STATIONNAIRES

5-1 - Gradients de portance - points neutres

Les gradiens de portance et position de points neutres ne sont pas modifiés par le niveau de bruit ainsi que le montrent les courbes tracées en fonction de C_N à Mach fixe ou en fonction du Mach à C_N fixe (figure 3). Les très légers écarts constatés sont attribuables à la méthode numérique de détermination des valeurs C_{N_α} et $x/\bar{c}$ (de l'ordre de 1 % de C_{N_α} ou 1 % de corde en position de point neutre). Ces faibles écarts ne sont pas de l'ordre de grandeur, ni de l'effet du nombre de Reynolds (courbes 1 et 2 de la figure 4 sur maquette M5), ni de l'effet des interactions dues aux parois, ainsi que le montre la comparaison des courbes 2 et 3 de la figure 4 obtenues à l'aide de valeurs non corrigées des effets de parois.

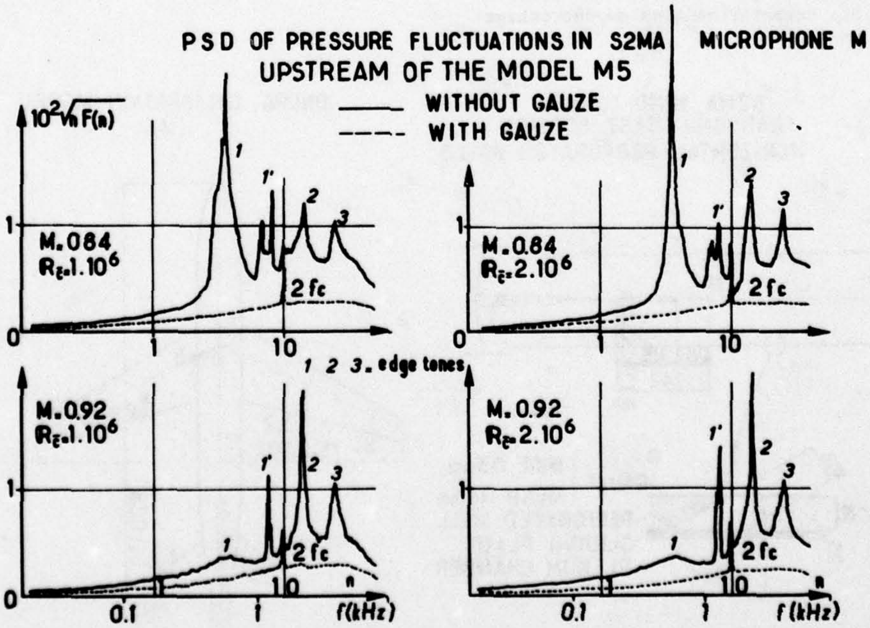

Figure 2 Spectres de fluctuations de pressions de S2MA : microphone M à la paroi de la soufflerie.

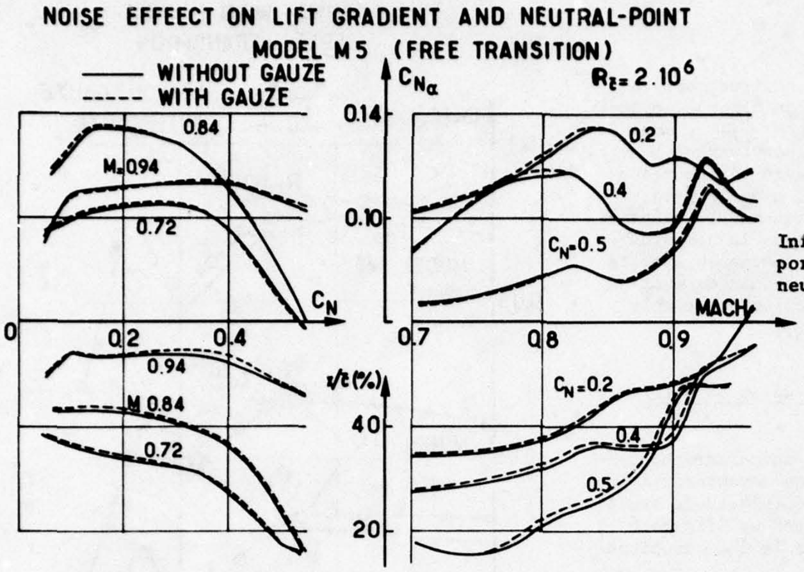

Figure 3

Influence du bruit sur gradients de portance et positions de points neutres - M5 - $R_\ell = 2.10^6$

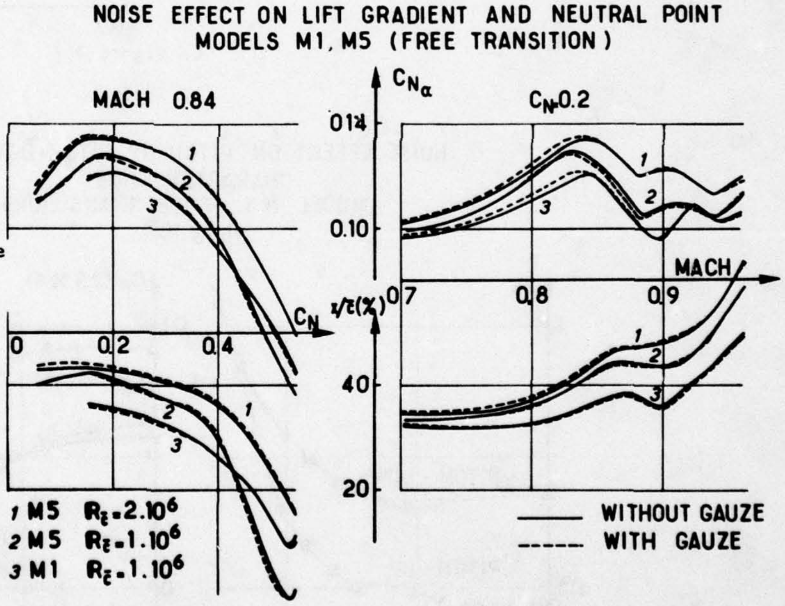

Figure 4

Influence du bruit sur gradients de portance et positions de points neutres - M1, M5 -

Comme la perméabilité aérodynamique moyenne des parois perforées est déterminée expérimentalement à partir des gradients de portance [25], l'examen des figures 3 et 4 montre bien que la présence de la gaze, sans effet sur C_{N_α}, n'altère pas la porosité des parois. Cette constatation est sans doute attribuable à la très grande porosité des parois de la soufflerie S2MA, assimilable à une veine libre [25] : une légère modification de la perméabilité géométrique des parois ne change alors pas la porosité aérodynamique moyenne très élevée.

5-2 - Moments de tangage

Si les positions de points neutres sont indépendantes du niveau de bruit, on observe cependant un décalage systématique des C_m , au-dessous de Mach 0,84 et 0,90 respectivement pour les deux maquettes M5 et M1 (figure 5). La réduction du niveau de bruit, obtenue avec la gaze, provoque un couple cabreur pratiquemment indépendant du nombre de Reynolds. Lors de la comparaison de diverses souffleries transsoniques avec la même maquette M5 [24] , de tels décalages avaient été constatés, même après correction des effets de parois.

5-3 - Caractéristiques de Pitch up et de Pitch down

Les constatations énoncées au paragraphe précédent restent vérifiées pour les caractéristiques de pitch-up : l'influence du niveau de bruit est nulle sur la portance de pitch-up (figure 6) ; elle se manifeste légèrement sur le C_m de pitch-up au-dessous de Mach 0,8.

Au delà du pitch up, le développement des décollements accroît l'effet du niveau de bruit, qui se fait sentir sur le moment de tangage de pitch-down au-dessous de Mach 0,84 (figure 6). Une légère modification de la portance de pitch-down existe à Mach 0,7.

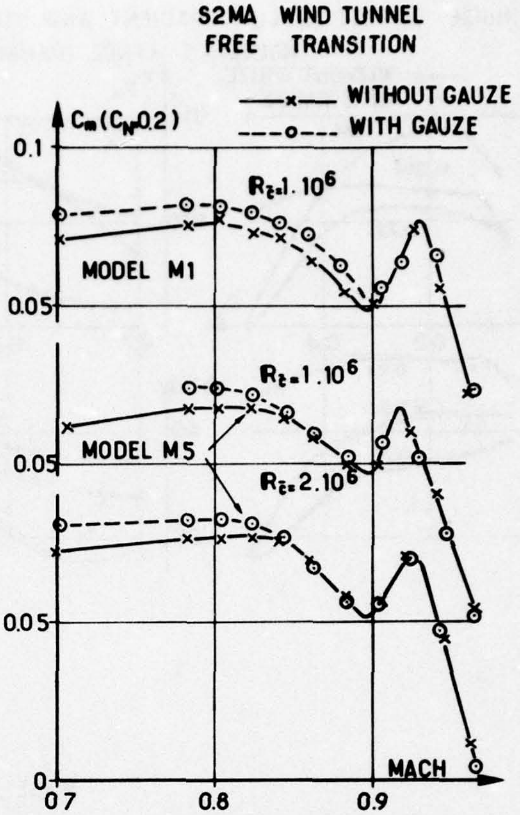

Figure 5 Moment de tangage à CN = 0,2 en fonction de M

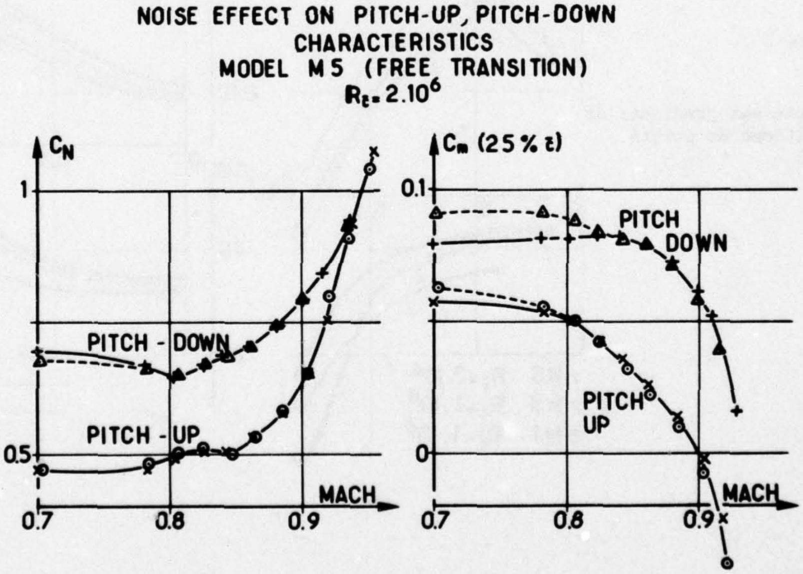

Figure 6 Influence du bruit sur les caractéristiques de pitch up et de pitch down

5-4 - Coefficients de traînée nette

En l'absence de décollements, le coefficient de traînée axiale nette ne dépend pas du niveau de bruit (figure 7). Au fur et à mesure que les décollements prennent de l'importance, la réduction du niveau de bruit accroît la traînée. Le maximum des écarts dus au niveau de bruit atteint 4 % de CA à Mach 0,7 et CN 0,6. Ces écarts ne dépendent pas du nombre de Reynolds (figure 8) ; ils sont nettement inférieurs aux variations de traînée dues à une variation du nombre de Reynolds, surtout au-dessous de 1 million, et aux effets des parois ainsi que le montre la comparaison des CA, non corrigés des effets de parois, obtenus sur les deux maquettes M1 et M5 d'obstructions très différentes.

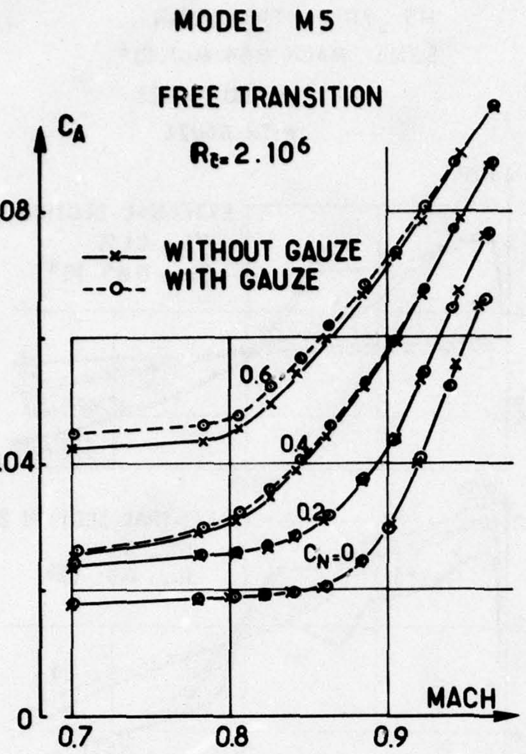

Figure 7 Traîné- en fonction de M - M5 - $\mathcal{R}_{\bar{c}} = 2.10^6$

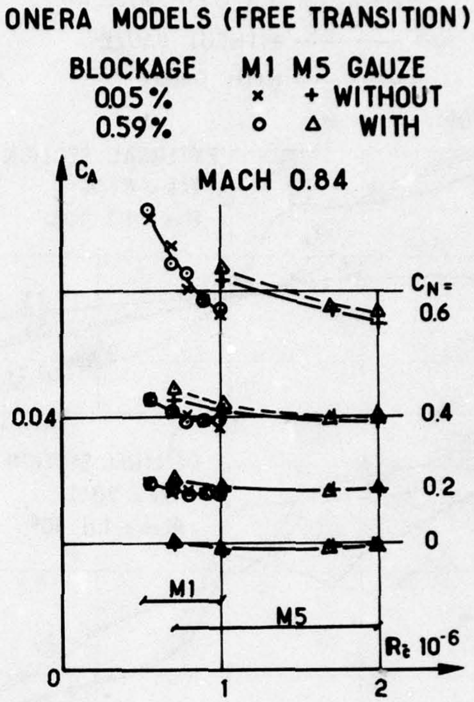

Figure 8 Traînée en fonction de $\mathcal{R}_{\bar{c}}$ - M1 - M5 - Mach 0,84

5-5 - Répartitions de pressions

5-5-1 - Transition naturelle

A Mach 0,84, en l'absence de décollements au bord de fuite(α_W = 3,3° pour section 1. α_W = 3,3° et 5,3° pour section2) les répartitions de pressions mesurées en transition naturelle ne dépendent pas du niveau de bruit (figures 9 a et b).

En présence de décollements au bord de fuite, la réduction du bruit en veine a pour effet d'étendre légèrement le décollement et d'avancer le choc (au maximum de 4 % de la corde locale).

A Mach 0,92 (figures 10 a et b), dans la section 2 au centre de la voilure, le choc, situé en arrière du profil, recule lorsque le bruit diminue en l'absence de décollements de bord de fuite (α_W = 3,3 et 5,3) : le recul du choc est plus accusé en présence d'un décollement de pied de choc (α_W = 5,3) et atteint 2 % de la corde. Lorsque le décollement de bord de fuite existe (α_W = 7,3) le bruit modifie très peu les répartitions de pression.

Au même nombre de Mach, dans la section 1 de bout d'aile, le bruit provoque des modifications profondes du choc, sans que la pression de bord de fuite soit altérée, qu'il y ait ou non un décollement à cet endroit. Ces modifications importantes de la position du choc et des répartitions de pression entre les essais effectués avec et sans gaze ne peuvent être expliquées par les écarts d'incidence (0,02 degré) ou de Mach (0,005) entre les essais et doivent donc être attribuées au bruit. Au plus grand nombre de Reynolds (figure 10a), à l'incidence de 3,3 degrés avec un faible décollement de bord de fuite, le choc est reculé, lorsque le bruit diminue, d'environ 12% de la corde ainsi que le décollement de pied de choc qui prend de l'extension. A l'incidence de 5,3 degrés, en présence d'un décollement de bord de fuite, la réduction de bruit entraîne un recul du choc de 18% de la corde. A 7,3 degrés d'incidence, en présence d'un décollement encore plus prononcé du bord de fuite, l'effect du bruit est plus modéré : la réduction du bruit résorbe le décollement de pied de choc, ne modifie pratiquement pas l'emplacement du choc, ce qui conduit à une réduction des pressions à partir du maitre couple du profil.

Les lignes de transition visualisées à l'incidence voilure de 7,3 degrés, à Mach 0,92 et $\mathcal{R}_{\bar{c}} = 2.10^6$ sont strictement identiques pour les 2 niveaux de bruit. Dans la section 2, la ligne visualisée est à 66 % de profondeur et correspond au pied de choc (figure 10 a) précédé d'un très léger décollement. Dans la section 1, la ligne visualisée se situe à 45 % de profondeur, donc sensiblement en fin de choc placé pratiquement au même endroit pour les 2 niveaux de bruit.

Dans le cas de cette incidence de 7,3 degrés et de la section 2, il semble donc que la ligne visualisée corresponde à la zone de recollement turbulent assez distante du décollement de bord de fuite. Malheureusement, aucune visualisation n'a été effectuée aux incidences plus faibles, ce qui ne permet pas d'expliquer l'important effet du bruit sur les chocs.

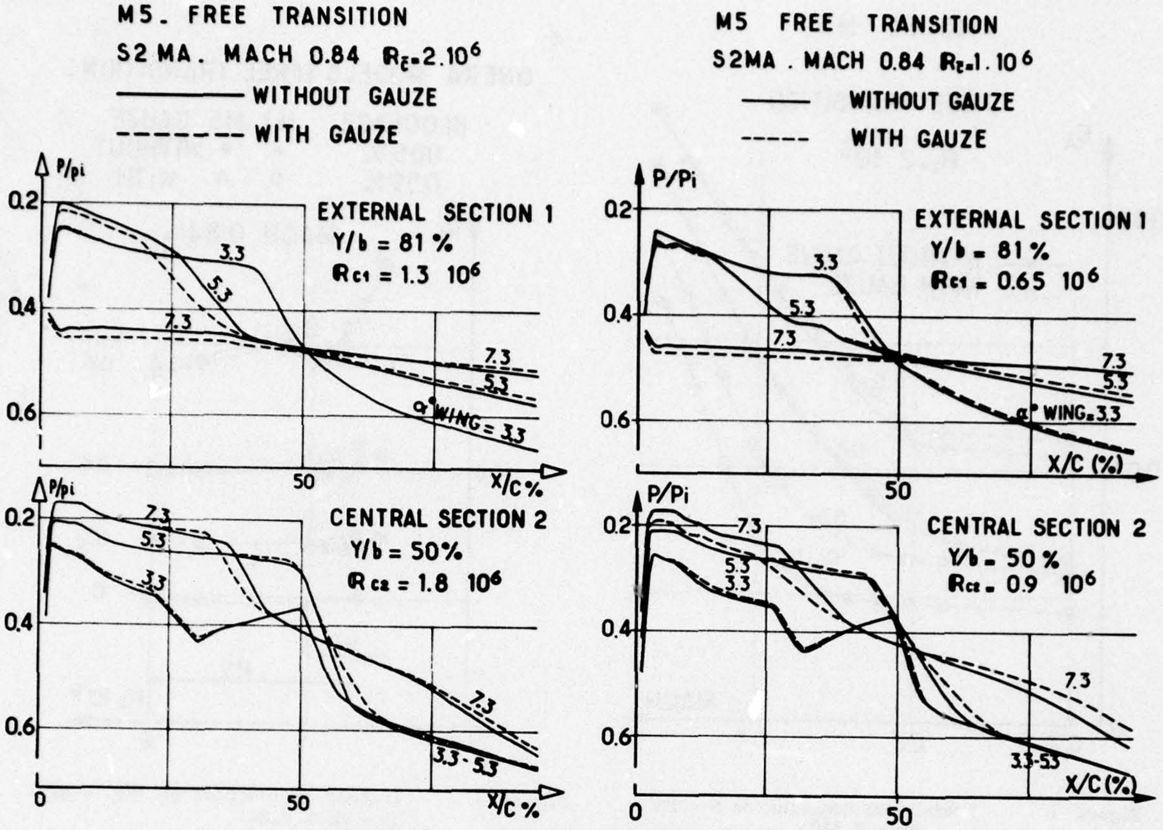

Figure 9 Répartitions de pressions - M5 - transition naturelle - Mach 0,84
figure 9a $R_{\bar{c}} = 2.10^6$
figure 9b $R_{\bar{c}} = 1.10^6$

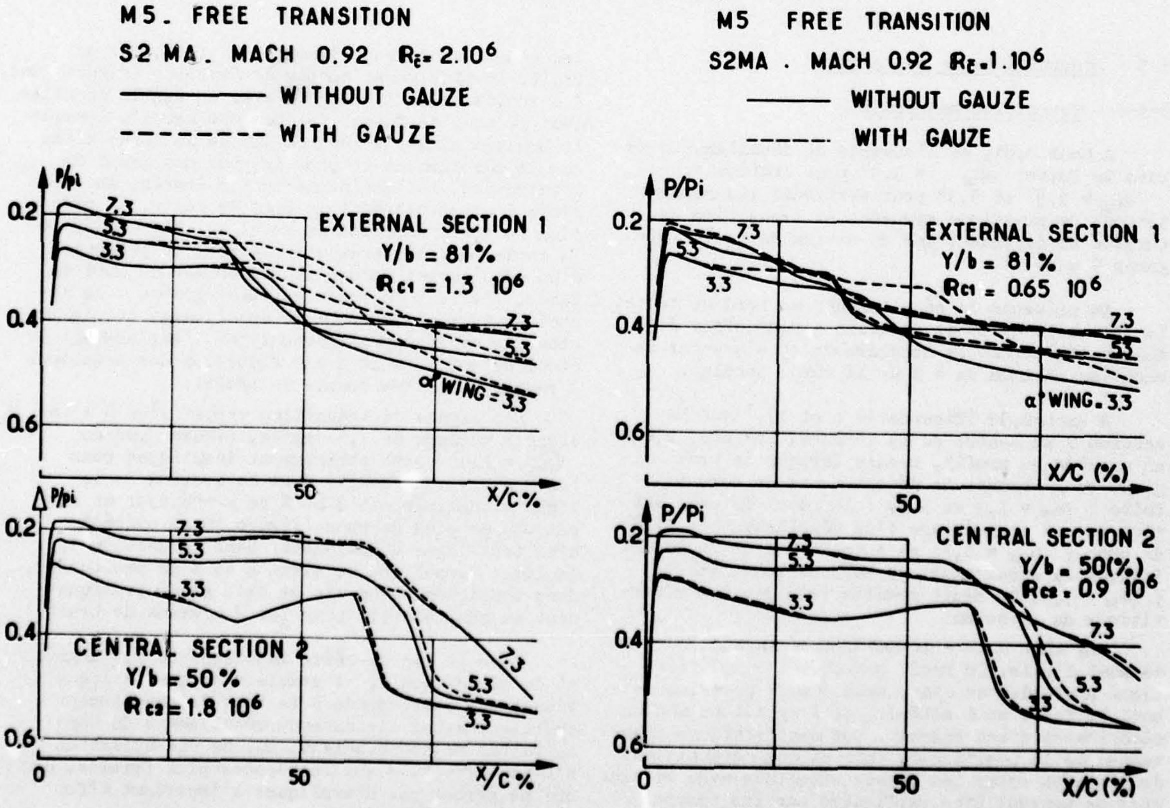

Figure 10 Répartitions de pressions - M5 - transition naturelle - Mach 0,92

a

b

figure 10a $R_{\bar{c}} = 2.10^6$
figure 10b $R_{\bar{c}} = 1.10^6$

5-5-2 - Transition déclenchée

Dans le cas d'une transition déclenchée par des rugosités surabondantes ayant provoqué une importante avancée des chocs, pouvant atteindre 24 % de la corde [24], l'effet du niveau de bruit reste modéré quels que soient la section de mesure, le Mach, l'incidence ou le nombre de Reynolds. Avec cette transition déclenchée à 7 % de profondeur, les décollements de pied de choc ont disparu, mais les décollements de bord de fuite sont plus marqués qu'en transition naturelle. La réduction du bruit recule le choc au maximum de 1 % de corde (figure 11).

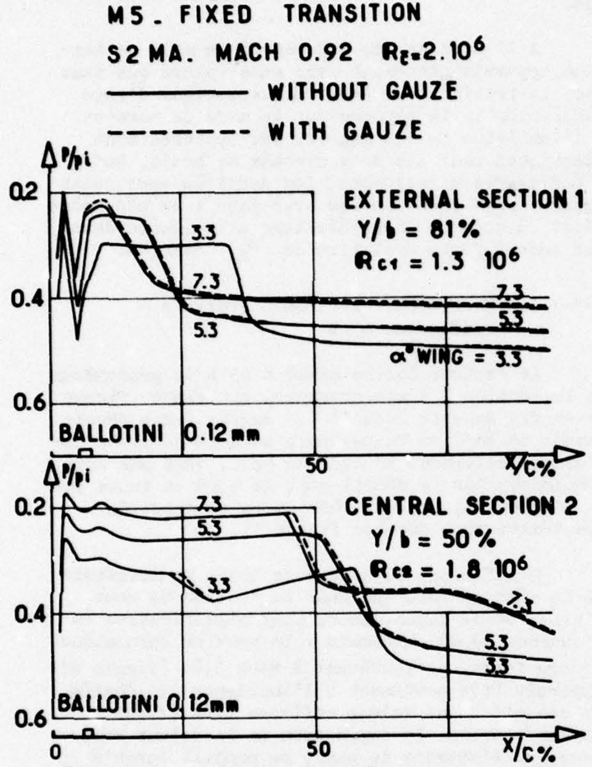

Figure 11 Répartitions de pressions - M5 - transition déclenchée - $R_\xi = 2.10^6$

5-6 - Pressions au bord de fuite - Portance d'une section

L'entrée en buffeting peut être déterminée par la méthode classique [27] de l'incidence de divergence des pressions de bord de fuite ou l'analyse des pertes de portance dans une section de voilure. Aucune influence du bruit n'a pu être mise en évidence sur ces grandeurs, même lorsqu'une modification sensible de la position des chocs existe.

6 - RESULTATS AERODYNAMIQUES INSTATIONNAIRES

Parmi les méthodes d'investigation des phénomènes instationnaires transsoniques, et en particulier du buffeting, récemment passées en revue [28], les mesures des signaux de jauges d'emplanture d'aile et de capteurs de pressions instationnaires sont couramment utilisées, en vol et en soufflerie. Les résultats présentés ici ne prétendent pas à une étude du buffeting ou des couplages entre fluctuation de pression et réponses des structures qui nécessiteraient un équipement important des maquettes [29]. Le but des expériences effectuées est simplement d'examiner si le niveau de bruit des veines d'essais transsoniques affecte les mesures de contraintes ou de pressions instationnaires.

6-1 - Signaux instationnaires de balance

Dans les spectres des signaux de balance apparaissent des raies aux fréquences des modes de suspension de la maquette et de flexion voilure. Dans le cas des ponts de traînée, moment de tangage et roulis, les raies sont limitées au deuxième mode de flexion de voilure, situé à 140 Hertz (n = 1). L'intensité des raies n'est pas modifiée par le changement de niveau de bruit qui ne se manifeste pas de façon importante pour cette gamme de n (figure 2). Dans le cas du pont de portance, des raies supplémentaires existent vers 340 et 750 Hertz : toutes les raies sont situées en dehors des zones à forte énergie dues aux edge tones.

Compte tenu de la très forte rigité des maquettes, leur réponse aux excitations contenues dans l'écoulement, vue au travers des ponts de la balance, est une réponse filtrée sur des modes à très faible amortissement sans énergie. Une telle fonction de transfert, dont les raies de fréquences sont en dehors des zones d'excitation modifiées par les perturbations acoustiques des perforations, conduit à une réponse indépendante du niveau de bruit : ceci est vérifié tant sur les répartitions de densités spectrales que sur les valeurs efficaces des ponts de balance.

6-2 - Signaux de jauges de flexion à l'emplanture de voilure

Les valeurs efficaces (figure 12) sont identiques pour les 2 cas de bruit étudiés, sauf à faible portance, quels que soient les nombres de Mach et de Reynolds. Cette modification ayant lieu avant la divergence des courbes $\tilde{\sigma}_B/q = F(C_N)$ conduit à une réduction de la portance de divergence, utilisée pour caractériser l'entrée en buffeting, lorsque le bruit diminue.

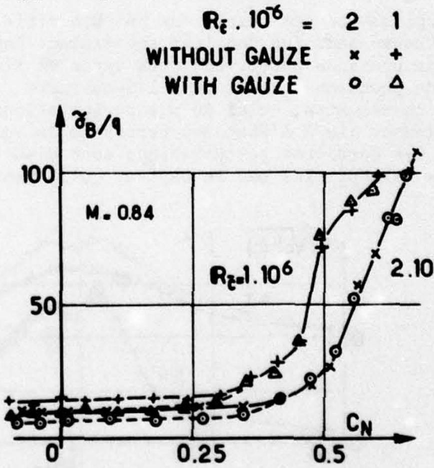

Figure 12 Valeurs efficaces de la flexion à l'emplanture de voilure
M5 - transition naturelle

6-3 - Signaux de pressions instationnaires

Les exemples de modification des pressions instationnaires par un changement du niveau de bruit sont issus des mesures effectuées à l'aide de 2 capteurs Kulite qui, selon leur emplacement, réagissent différemment, du fait de leur position relative par rapport aux chocs et aux décollements dans la section de mesure de la voilure. Il sera donc permis de dégager, dans quelles conditions, l'effet du bruit extérieur à la maquette modifie les réponses des pressions instationnaires. Les effets du bruit sont successivement examinés à 2 emplacements fort différents pour 2 nombres de Mach, 2 nombres de Reynolds, en fonction de l'incidence de la voilure étudiée en transition naturelle, puis déclenchée.

6-3-1 - Transition naturelle

6-3-1-1 - Mach 0,84 - section 1 de bout d'aile - Profondeur 83 %

Dans ce cas, le capteur de pression situé à 83 % de profondeur de la section 1 de bout d'aile, est en aval du choc (figure 9) dans une zone dont le décollement partant du bord de fuite s'intensifie avec la mise en incidence. Les répartitions de densités spectrales et les valeurs efficaces sont fournies en fonction de l'incidence ou de CN sur la figure 13.

En l'absence de bruit (avec gaze), la valeur efficace est d'un niveau faible et constant jusqu'à CN de 0,2 puis croit jusqu'à un maximum, dépendant fortement du nombre de Reynolds et situé à une portance CN variant de 0,65 à 0,4 selon $\mathcal{R}_{\bar{c}}$. Au-delà, les valeurs efficaces diminuent par suite d'une organisation des décollements.

A fort niveau de bruit (sans gaze), les valeurs efficaces sont 10 fois supérieures, à portance nulle, à celles mesurées avec faible bruit ; lorsque CN croit, elles diminuent jusqu'au début de décollement puis croissent de la même manière qu'à faible bruit pour passer par un maximum à même CN qu'avec gaze. En règle générale, les valeurs efficaces obtenues suivent les mêmes évolutions pour les 2 niveaux de bruit mais sont d'autant plus élevées que le bruit augmente : l'effet du bruit est d'autant moins important que les décollements sont intenses.

L'explication des écarts des valeurs efficaces se trouve dans les densités spectrales. Les capteurs de pression perçoivent deux types de fluctuations de pression : celui dû à l'écoulement propre de la maquette, celui dû aux perturbations de l'écoulement lié à l'état des parois de la veine d'essais. Ces dernières perturbations sont d'autant moins perceptibles par le capteur qu'il est situé dans une zone de fluctuation intense du champ propre à la voilure c'est-à-dire, lorsqu'il est situé dans une zone de décollements intenses.

L'identification des pointes de densités spectrales est réalisée à partir des harmoniques d'edge tones (figure 2) et des fréquences des modes de structure de voilure.

A l'incidence de 3,3 degrés, il est clair que le capteur perçoit tous les edge tones (numérotés 1 - 1' - 2 et 3 de la figure 2) qui disparaissent en présence de la gaze, ce qui explique les différences considérables des valeurs efficaces.

A l'incidence de 5,3 degrés le mode de torsion apparaît nettement avec gaze, alors que sans gaze la proximité du deuxième harmonique d'edge tones amortit la réponse sur le mode de torsion. A l'incidence de 7,3 degrés, les spectres sont identiques pour les deux niveaux de bruit. Enfin à 8,3 degrés d'incidence, les densités spectrales apparaissent plus élevées avec gaze : ce phénomène n'est dû qu'à un léger décalage d'incidence dans une zone à forte évolution de P_{K_1} avec CN.

6-3-1-2 - Mach 0,84 - section 2 centrale - Profondeur 65 %

Le capteur Kulite situé à 65 % de profondeur de la section 2 à mi-envergure, est placé (figure 9) en fin de choc jusqu'à 5,3 degrés (sans décollement de bord de fuite) puis au delà de cette incidence, nettement en aval du choc, dans une zone contaminée par le décollement de bord de fuite dès 5,3 degrés. Les valeurs efficaces et densités spectrales sont données figure 14.

L'influence du niveau de bruit se manifeste de la même manière que dans la section de bout d'aile, et de façon encore plus significative en l'absence de décollements : le premier harmonique d'edge tones, prépondérant à Mach 0,84 (figure 2) apparaît très nettement à l'incidence 3,3 degrés et conduit à une valeur efficace très élevée à portance nulle. La diminution de la valeur efficace, en l'absence de gaze, se produit jusqu'à CN = 0,35.

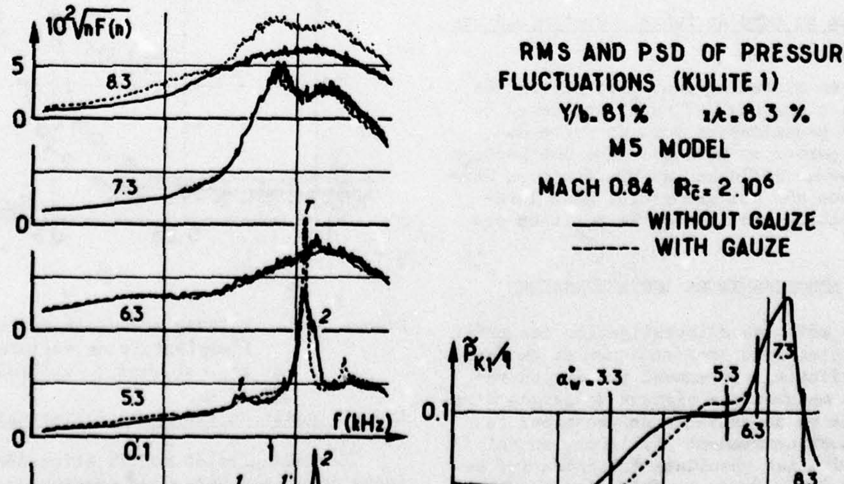

Figure 13 **Valeurs efficaces et spectres de pression -capteur kulite 1 - M = 0,84**

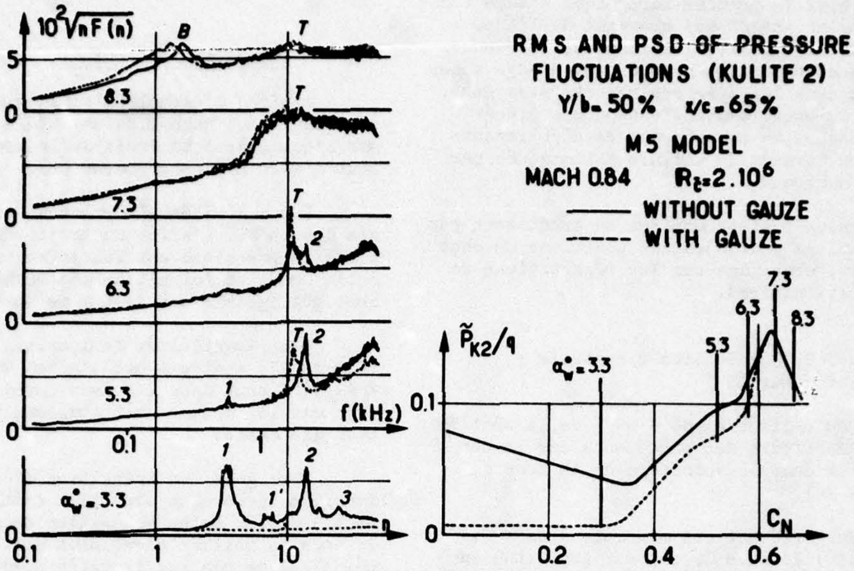

Figure 14 Valeurs efficaces et spectres de pression - capteur kulite 2 - M = 0,84

Comme la valeur efficace reste faible et constante, en l'absence de perturbations acoustiques, la diminution observée sans gaze ne peut provenir du champ des fluctuations de l'écoulement propre à la voilure. Il semble que lorsque l'incidence croît, le choc qui recule et s'intensifie, protège en quelque sorte le capteur des perturbations acoustiques de la veine d'essais qu'il perçoit de moins en moins.

Le mode de torsion bien visible avec gaze, n'émerge pas des spectres en présence de l'edge tones 2 qui le masque. A l'incidence de 8,3 degrés, après le maximum des valeurs efficaces, les spectres sont très voisins pour les deux niveaux de bruit : ils décèlent une organisation de l'écoulement dans les zones décollées favorisant le mode de flexion voilure.

Il est donc manifeste que la présence de perturbations acoustiques, perçues nettement par la voilure en l'absence de décollement, peut masquer des réponses sur les modes de structure de voilure.

6-3-1-3 - Mach 0,92 - Section 1 de bout d'aile Profondeur 83 %

A Mach 0,92 le capteur placé à 83 % de profondeur de la section 1 est situé toujours en aval du choc (figure 10) dans une zone influencée par le décollement de bord de fuite. Il a été vu au paragraphe 5-5-1 que dans ce cas l'influence du niveau de bruit était très importante sur le choc, qu'une réduction de bruit reculait jusqu'à 18 % de longueur de corde. Le capteur sera donc d'autant moins en aval du choc que le bruit sera faible. Toutefois il a été indiqué que la pression stationnaire du bord de fuite était indépendante du bruit.

Les valeurs efficaces (figure 15) sont toujours élevées car le capteur est placé dans la zone décollée naissant au bord de fuite. L'évolution de ces valeurs efficaces en fonction de C_N est faible ; les valeurs sont légèrement réduites par l'emploi de la gaze.

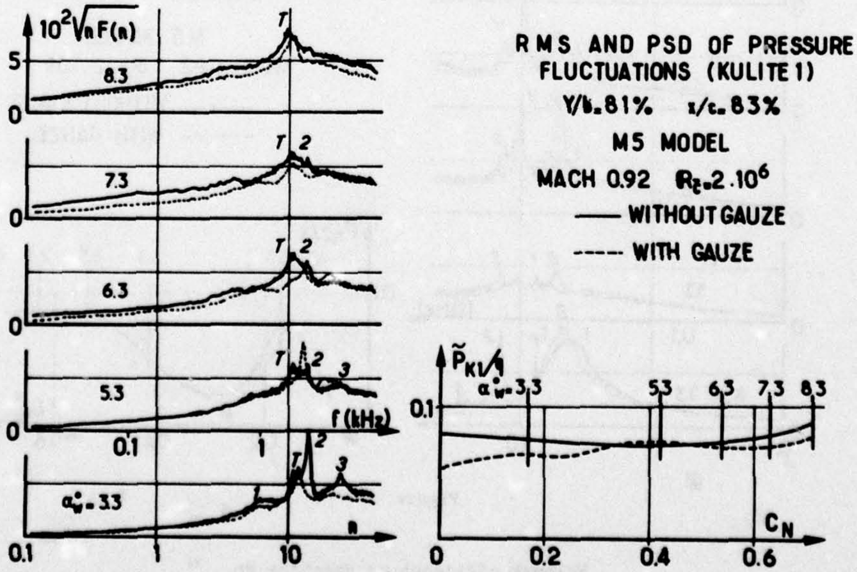

Figure 15 Valeurs efficaces et spectres de pression - capteur kulite 1 - M = 0,92

A Mach 0,92 le premier harmonique d'edge tones est pratiquement absent des spectres de l'écoulement (figure 2). Seules les zones de fréquences des deuxième et troisième harmoniques d'edge tones apparaissent dans les spectres mesurés sans gaze. L'influence du bruit se manifeste comme précédemment, à Mach 0,84 en présence de décollements : la réponse en torsion de voilure est masquée par l'edge tone numéro 2.

Les signaux instationnaires ne traduisent pas les modifications profondes des positions de choc dues au bruit, observées sur les répartitions de pressions stationnaires.

6-3-1-4 - Mach 0,92 - Section 2 centrale - Profondeur 65 %

Le cas du capteur situé à 65 % de la section 2 à Mach 0,92 diffère des précédents car le capteur est situé dans le voisinage de la zone de choc (figure 16).

La valeur efficace est maximale à CN = 0,15 (α_W = 3,3°) lorsque le capteur est situé en fin de choc. Lorsque CN croît, la valeur efficace passe par un minimum à CN = 0,3, correspondant à un début de décollement. Au delà, la valeur efficace croît jusqu'à une valeur modérée : le capteur situé alors au pied du choc ressent l'influence du léger décollement de pied de choc. Bien que les valeurs efficaces soient très voisines pour les 2 niveaux de bruit, les spectres diffèrent notablement. Il y a compensation des densités spectrales obtenues, sans gaze, sur les modes d'edge tones, par les densités spectrales obtenues, avec gaze, sur les modes de structure voilure. Ainsi, avec les parois d'origine, le deuxième harmonique d'edge tones, prépondérant à Mach 0,92 dans l'écoulement, est toujours perçu par le capteur. Avec gaze, les modes de torsion et flexion voilure apparaissent nettement à partir de l'incidence de 6,3 degrés alors que les edge tones 1 et 2 les masquent sans gaze. Dans ce dernier cas, le mode de torsion n'arrive à émerger qu'au delà de l'incidence de 7,3 degrés.

6-3-2 - Transition déclenchée

A titre d'exemple l'influence de rugosités est examinée à Mach 0,84 et $\mathcal{R}_{\bar{c}}$ = 2 millions sur l'écoulement au droit de la section 1 de bout d'aile à la profondeur 83%.

Les rugosités ont provoqué une nette avancée des chocs. L'effet du bruit sur les répartitions de pressions est faible en transition naturelle comme en transition déclenchée et pratiquement négligeable sur le C_p de bord de fuite.

Les répartitions de densités spectrales (figure 17) montrent que l'effet du bruit est très différent dans les deux cas de transition bien que le capteur soit toujours nettement en aval des chocs.

Avec gaze, en transition déclenchée, les densités spectrales sont plus faibles à α_W = 3,3 et 5,3 degrés qu'en transition naturelle. Le mode de torsion voilure n'est plus visible avec rugosité. A 7,3 degrés les densités spectrales sont voisines pour les 2 types de transtion, lorsque la section est profondément décollée.

La présence d'edge tones dans les spectres, très nettement visible en transition naturelle en l'absence de décollement, est, au contraire, peu perçue en transition déclenchée. En présence de décollements l'inverse se produit : edge tones non visibles en transition naturelle, exacerbés en transition déclenchée. Pour une section entièrement décollée (α_W = 7,3 degrés) la présence des rugosités avec un fort niveau de bruit produit des densités spectrales très élevées. L'influence du bruit qui était nulle en transition naturelle multiplie par 2,6 les valeurs efficaces en transition déclenchée.

Ces considérations s'appliquent également aux mesures, non reportées ici, effectuées dans la section 2.

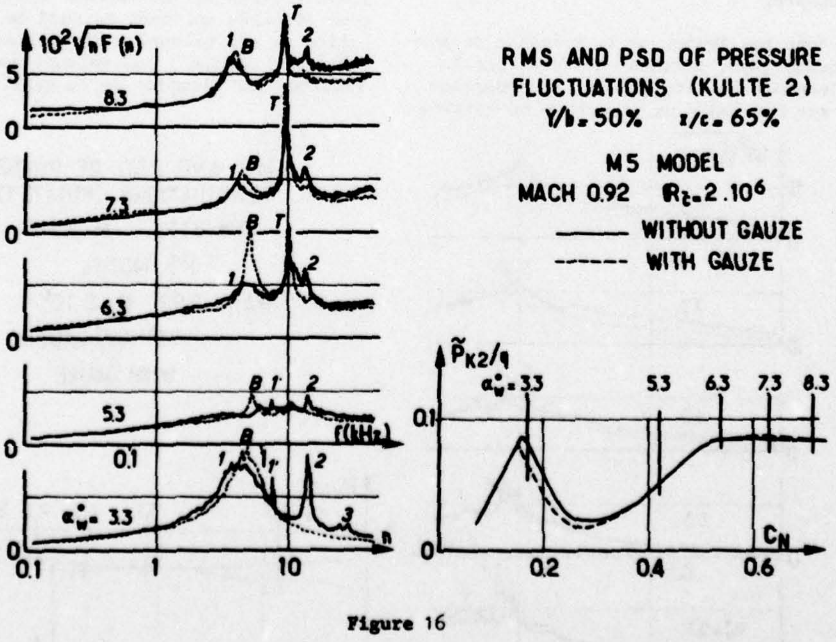

Figure 16

Valeurs efficaces et spectres de pression - capteur Kulite 2 - M = 0,92

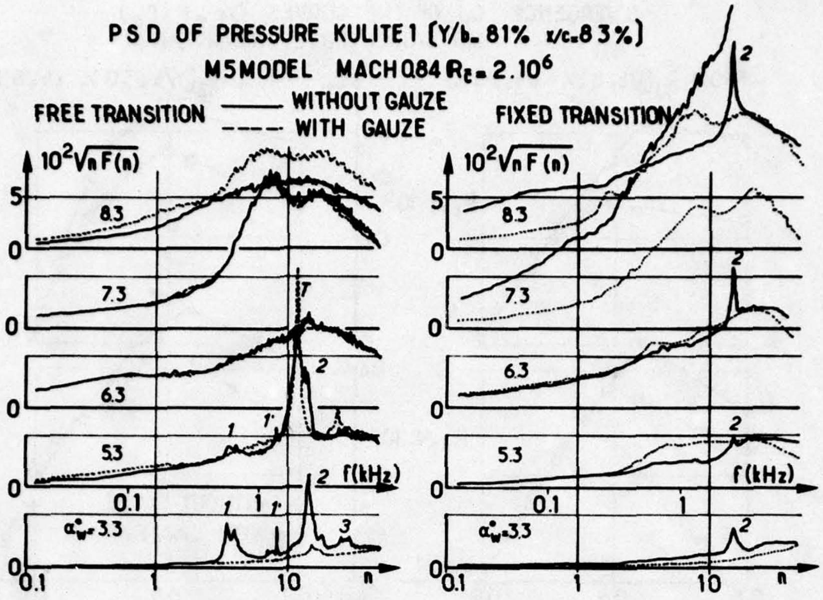

Figure 17 Influence de rugosités sur spectres de pression - M = 0,84

Il apparaît donc que la modification, par suite d'une transition avancée, de l'état de la couche limite à la naissance du choc et que l'épaississement de couche limite par les rugosités contribuent à :

-atténuer l'effet des perturbations acoustiques, en absence de décollements,

-exarcerber leur effet en présence de décollements,

-éliminer la présence des modes de structure dans les réponses des capteurs de pressions.

6-3-3 - Influence de la maquette

Les deux maquettes M1 et M5 étant équipées d'un même capteur situé en un point homologue, la comparaison des valeurs efficaces des pressions mesurées à la paroi de la veine d'essais et par le capteur de voilure permet d'apprécier au même nombre de Reynolds $\mathcal{R}_{\bar{c}} = 1.10^6$ l'influence des dimensions de la maquette sur les phénomènes instationnaires. D'une part la fonction de transfert de la maquette est différente, par déplacement des fréquences vers les valeurs plus élevées lorsque la maquette est plus petite, d'autre part les perturbations acoustiques sont reçues par une voilure de surface 11 fois plus petite pour la maquette M1 que pour la maquette M5.

La figure 18 Montre que :

-sans edge tones, avec gaze, les valeurs efficaces de pressions sont accrues pour la petite maquette M1 à portance nulle. Les variations de $\tilde{P}_K$ avec CN sont plus réduites.

-avec edge tones, sans gaze, les valeurs efficaces de pressions, toujours à portance nulle, sont au contraire moins élevées pour la petite maquette. A Mach 0,84 $\tilde{P}_K$ reste constante avant divergence pour M1 alors que pour M5 $\tilde{P}_K$ décroît fortement : le minimum de $\tilde{P}_K$ pour M5 est égal à la valeur constante de $\tilde{P}_K$ pour M1 (0,05). La différence de perception des edge tones par les deux maquettes provient sans doute du rapport des surfaces de voilure.

A CN = 0,5 les valeurs efficaces sont plus faibles pour M1 que pour M5 ; l'effet du bruit est encore nettement ressenti par la petite maquette alors qu'il n'existait pas pour la grande maquette. Cette différence de comportement des deux maquettes provient sans doute de la position relative des fréquences des modes de structure et des edge tones.

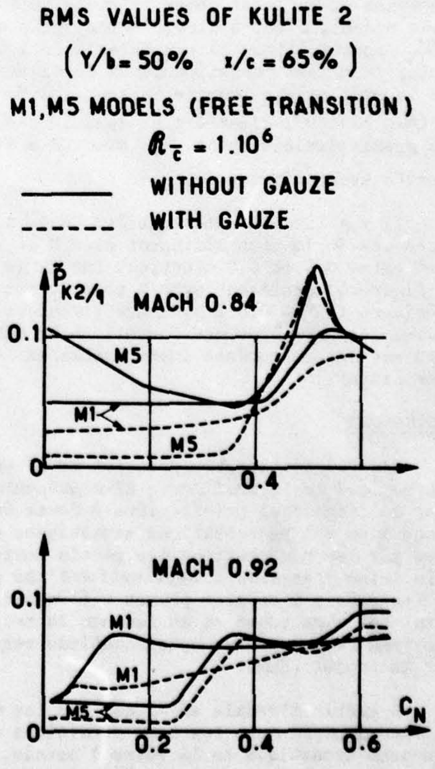

Figure 18 - Influence de la maquette Transition naturelle $\mathcal{R}_{\bar{c}} = 1.10^6$

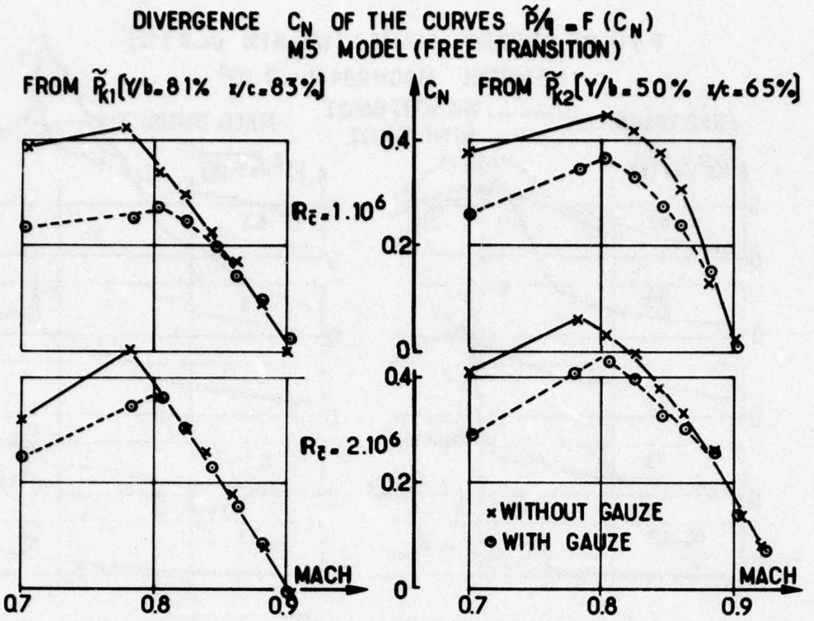

Figure 19 CN de divergence des courbes $\tilde{P}_K$ (CN)
M5 - transition naturelle

6-4 - <u>CN de divergence des courbes $\tilde{P}_K$ (CN)</u>

Les coefficients de portance pour lesquels la divergence des courbes $\tilde{P}_K$ (CN) apparaît sont portés figure 19. En l'absence d'edge tones, il s'agit du CN à partir duquel $\tilde{P}_K$ croît ; avec edge tones il peut s'agir du minimum de la courbe (CN). Dans ce cas, le CN de divergence dépend du niveau de bruit et croît avec celui-ci. Les différences apparaissent dans la zone d'activité des edge tones et évoluent comme l'intensité du bruit qu'ils créent, c'est-à-dire d'autant plus que M et $\mathcal{R}_{\bar{c}}$ sont faibles. Il est caractéristique que la plus important variation du CN de divergence avec le bruit existe pour le capteur 1 à Mach 0,78 et $\mathcal{R}_{\bar{c}} = 1.10^6$, c'est-à-dire dans le cas où la plus grande diminution de $\tilde{P}_K$ avec CN a été observée avant divergence.

Il y a lieu de noter que les CN de divergences des $\tilde{P}$ locales diminuent avec M et se situent entre 0,4 et 0,0 alors que les CN de pitch up (figure 6) croissent avec M et sont nettement supérieurs (CN de 0,5 à 1,1) aux portances auxquelles les premières manifestations de décollements sur les phénomènes instationnaires locaux apparaissent.

<u>CONCLUSIONS</u>

Les fluctuations de pression de la veine transsonique de la soufflerie S2MA présentent des zones de fréquences privilégiées à forte énergie sonore dues aux perturbations acoustiques engendrées par les perforations des parois horizontales de la veine d'essais. L'application d'une gaze sur les parois d'origine permet d'éliminer totalement les edge tones et de ramener le bruit à un niveau répondant aux spécifications requises pour le projet LEHRT.

A partir d'essais effectués sur les maquettes étalons ONERA dans les deux conditions d'environnement acoustique de la veine d'essais, avec et sans gaze, les conclusions suivantes peuvent être dégagées :

Si les essais ne visent qu'à la connaissance de caractéristiques globales stationnaires, d'autocabrage ou de limites de tremblement à partir des techniques de pressions de bord de fuite ou de mesures à l'emplanture des ailes, l'influence du bruit n'a pas à être considérée, sauf pour la valeur absolue du moment de tangage ; le bruit semble bien à l'origine de la disparité des C_{m_0} dans les comparaisons de souffleries.

Si les essais comportent des mesures de pressions stationnaires et surtout instationnaires il apparaît indispensable d'obvier à l'effet des perturbations acoustiques qui risquent de compromettre la qualité des données aérodynamiques instationnaires. L'élimination des edge tones, à l'aide d'un moyen simple, tel que la gaze utilisée ici, permet de mettre en évidence des couplages entre modes de structure et phénomènes aérodynamiques instationnaires, qui ne sont pas décelables sans élimination du bruit des parois.

La différence de perception des perturbations acoustiques par les pressions instationnaires selon que l'essai est effectué en transition naturelle ou en transition déclenchée fait ressortir l'importance de l'état de la couche limite avant choc. Il serait donc nécessaire de compléter les résultats présentés par des essais à des nombres de Reynolds plus élevés, tels qu'en transition naturelle la transition de couche limite soit située nettement en amont des chocs. Pour les mêmes raisons, il serait souhaitable d'examiner si l'influence du bruit est spécifique du type de profil étudié et si les susceptibilités au nombre de Reynolds et au niveau de bruit sont liées.

<u>REFERENCES</u>

1 - GOETHERT B.H -"Transonic wind tunnel testing"- Pergamon Press (1961).

2 - LUKASIEWICZ J. -"Effect of boundary layer and geometry characteristics of perforated walls for transonic wind tunnels"- Aerospace eng. vol 20 n°4 (1961).

3 - CHRISTOPHE J. - LONIEWSKI J. -"Reduction of pressure fluctuations in a transonic test section"- ONERA TP n° 567 (1968).

4 - Mc CANLESS Jr G.F -"Additional corrections of 4% SATURN V protuberance test data"- NASA 30517 - Technical Report HSM RI-71 (1971).

5 - CREDLE O.P -"Perforated wall noise in the AEDC PWT 16 ft and 4 ft transonic tunnels"- AEDC TR 71-216 (1971).

6 - BILANIN A.J - COVERT E.E -"Estimation of possible excitations frequencies for shallows rectangular cavities"- AIAA "Journal vol II n°3 (1973).

7 - COX R.N - FREESTONE M.M -"Design of ventilated walls with special emphasis on the aspect of noise generation"AGARD Report 602 (1973).

8 - VARNER M.O -"Noise generation in transonic wind tunnels" - AEDC TR-74 126 (1975).

9 - DOUGHERTY Jr N.S - STEINLE Jr F.W - "Transition Reynolds number comparisons in several major transonic tunnels"- AIAA Paper 74627 (1974).

10 - VAUCHERET X -"Evolution of acoustic frequency peaks generated by perforated walls of a transonic test section with variable porosity factor"- ONERA TP n° 1324 (1974).

11 - BENEK J.A - HIGH M.D -"A method for the prediction of the effect of free stream disturbances on boundary layer transition"- AEDC TR 73 158 (1973).

12 - VAUCHERET X -"Fluctuations acoustiques engendrées par les parois perméables d'une soufflerie transsonique"- AGARD Conference Proceedings n°174 - Londres (1975).

13 - CARRIERE P-"Current problems of applied transonic aerodynamics"- EUROMECH 40 colloquium(1973).

14 - GREEN J.E. -"On the influence of free stream turbulence on a turbulent boundary layer as it relates to wind tunnel testing at subsonic speeds"- RAE TR 72201 (1972).

15 - MABEY D.G -"Beyond the buffet boundary"- the Aeronautical Journal vol 27 n° 748 (1973).

16 - "The need for large wind tunnels in Europe"- AGARD Report n°60 (1972).

17 - "On the flow quality necessary for the large European High-Reynolds number transonic wind tunnel LEHRT"- AGARD Report n° 644 (1976).

18 - LOWSON M.V -"Prediction of boundary layer pressure fluctuations"- AFFDL - TR 67 167 (1966).

19 - GILLIAM F.T -"An experimental investigation of the acoustic and wave attenuation characteristics of a rod wall wind tunnel in transonic flow"- AIAA Paper n° 76-215 (1976).

20 - DOUGHERTY Jr N.S - ANDERSON C.F - PARKER Q.L -"An experimental investigation of techniques to suppress edge tones from perforated wind tunnel walls"- AEDC TR 75-88 (1975).

21 - VERGNOLLE J.F -"Bruit de parois transsoniques"- NT 1/5015 DN CERT (1976).

22 - SCHUTZENHOFER L.A - HOWARD P.W - "Suppression of background noise in a transonic wind tunnel test section"- AIAA Journal vol 13 n° 11 (1975).

23 - ROSS R. - ROHNE P.B -"The character of flow unsteadiness and its influence on steady state transonic wind tunnel measurements"- AGARD Conf. Proc. 174 (1975).

24 - VAUCHERET X - BAZIN M - ARMAND C -"Comparaison d'essais transsoniques bi et tridimensionnels effectués dans diverses grandes souffleries"- AGARD Conf. Proc. CP 187 (1975).

25 - VAUCHERET X - VAYSSAIRE J.C -"Corrections de parois en écoulement tridimensionnel transsonique dans des veines à parois ventilées"- AGARD Conf. Proc. CP 174 (1975).

26 - MABEY D.G -"The influence of flow unsteadiness on wind tunnel measurements at transonic speeds"- Laws Paper n° 38 (1972).

27 - PEARCEY H.H - HOLDER D.W -"Simple methods for the prediction of wing buffeting resulting from bubble type separation"- NPL Aero report 1024 ARC 23884 (1962).

28 - LAMAR W.E -"Effects of buffeting and other transonic phenomena"- AGARD Conf. Proc. 187 (1975).

29 - COE C.F - RIDDLE D.W - HWANG C. - "Separated flow unsteady pressures and forces on elastically responding structures"- AGARD SMP Meeting, Lisbonne, 17-22 avril 1977 (à paraître).

UNSTEADY BOUNDARY LAYERS,
SEPARATED & ATTACHED

Demetri P. Telionis

Department of Engineering Science & Mechanics
Virginia Polytechnic Institute and State University
Blacksburg, Virginia 24061 USA

SUMMARY

The area of unsteady boundary layers is investigated very actively today as a part of the effort to fully understand and calculate unsteady flows and their applications. As a result a number of review articles has already appeared quite recently. The present review is therefore a supplement to earlier contributions and in particular one prepared two years ago by the author of this paper. Emphasis will be given here to areas in which considerable progress has been achieved recently. However it appears that in most of the interesting areas today, as for example in experimental investigation of unsteady turbulent boundary layers, modeling of unsteady separation and separated flows, all the investigators are presently continuing their efforts. There is no particular program that has been completed. This review article, therefore, will be a kind of a unified progress report which will hopefully capture the spirit of the work in progress in different countries of the western world and will identify potential difficulties and future needs.

1. INTRODUCTION

Potential flow theory has been an invaluable tool for the designer in a variety of engineering applications of aerodynamics. It is well known, however, that this has been possible only via appropriate heuristic assumptions, as for example the Kutta-Joukowski condition, which replaces the catalytic role played by viscosity. Alternatively potential theory may be supplemented with a boundary-layer calculation. Today it is widely accepted that viscous effects, although very often confined in small areas, control and regulate basic features of the flow field, as for example, circulation. As a result, aerodynamic characteristics of significant engineering importance, like lift and drag, depend on the development of a viscous layer and its downstream fate which may or may not experience transition to turbulence and separation to a wake.

In unsteady aerodynamics viscosity has again reserved for us some unexpected surprises. It is the agent responsible for phenomena that cannot be predicted or explained with potential theory and quasi-steady viscous models. Some typical examples: dynamic stall of lifting surfaces, stall flutter of helicopter rotor blades, rotating stall in engine compressor blades, etc. Most of such phenomena can be attributed to the nonlinear character of the viscous layers that generate space and time phase differences, non-linear secondary streaming, separation delay, viscous damping, etc.

As of today, efforts have been mostly confined to first order theories and very few attempts have been made to assess the importance of the interaction between the unsteady viscous and inviscid fields. The problem becomes even more difficult if the elastic properties of the aerodynamic surfaces and their coupling with the aerodynamics is brought into play. In this paper we will be exclusively concerned with the response of the viscous part of the flow to fluctuations imposed externally. We will therefore exclude unsteady effects that may be generated hydrodynamically, as for example windloads on bluff bodies that for a certain range of Strouhal numbers, experience side forces alternating in sign. We will not deal with the very important area of coupling between the aerodynamic and elastic forces. Moreover, in the spirit of this symposium and the interests of AGARD, we will confine our attention to external flows with the exception of special cases where work has been very successful and the results appear to have global significance.

The present author was invited only a few years ago to prepare a similar review article[1]. The opportunity to return and prepare a new paper on the topic is mostly welcomed. Clearly the responsibility to cover inclusively all the basic areas is now greater, since overlooking twice an important contribution would be inexcusable. However the present article should have its own character and goals and such earlier contributions will be included only if their context integrates smoothly with the material of the following section. The tremendous amount of publications and of course the inevitable delay in the publication of an article, make it almost necessary in our times to resort again to private communication. This has been pursued very actively. Omission of some most recent contributions is however inevitable.

At first it was thought that it would be more appropriate to group the material according to the different methods of attack. Certainly it would appeal more to the investigators, if separate sections were devoted to numerical methods, analytical methods, experimental methods, etc. The geometrical features of the problem could also be a good criterion for grouping the material. However it was decided instead to adopt, with some minor adjustments, the section headings used in the earlier review of the present author[1]. This will preserve the continuity and will make the present article a supplement of the earlier one.

Some very interesting earlier papers were brought to the attention of this author after the publication of Ref. 1. Excellent review articles have in fact appeared earlier containing a lot more information on the topic[2-8]. In the present article it will not be attempted to give a complete account of contributions in the area. It will be pursued to present a picture of today's state of the art by listing and commenting upon the most recent successful efforts and identifying the needs for further research.

In the past two years, little has been done in the area of transient viscous flows and a section on this topic will not be included here. In the second section of this paper we will examine oscillating flows but we will concentrate more on oscillations with a non-vanishing mean. More emphasis will now be given to compressible flows and unsteady heat transfer. In the third section we will discuss the problem of modeling fluctuating turbulent flows which has been attacked vigorously in the last few years. Finally in the last section we will consider the problem of unsteady separation and unsteady separated flows. The topics of the last two sections have finally stimulated the interest of experimentalists and we can report today on some initial data that have already become available.

2. LAMINAR FLUCTUATING BOUNDARY LAYERS

It is believed that the problem of finding the response of a two-dimensional laminar boundary layer to fluctuations of the outer stream is today solved and adequately understood. A variety of analytical methods has been used to attack this problem: a) Asymptotic expansions in powers of a small amplitude (Lighthill[9]); b) Averaging methods similar to the classical treatment of turbulent boundary layers (Lin[10]); c) Expansions in powers of a frequency parameter (Moore[11]); d) Numerical methods solving exactly the problem in a three-dimensional coordinate space[1,7]. A great number of publications that follow the above guidelines has appeared already in this area (see recent reviews in Refs. 1, 5-7).

Some of the advantages and disadvantages of these methods are enumerated below. In the first category, following Lighthill,[9] the assumption of a small amplitude automatically restricts the method to flows with external disturbances smaller than 10% of the mean flow. To improve the accuracy one would have to proceed to terms of order ε^2 where ε is the amplitude ratio. Surprisingly enough, none of the investigators listed in Ref. 1 has attempted this type of an expansion. Instead the problem was further simplified by expanding in powers of a frequency parameter or its inverse. Such methods are thus limited to extreme values of frequency. The technique of expanding in powers of ε is however quite versatile and its capabilities and possible extensions will be commented upon later in this section.

The second and third method, following Lin[10] and Moore[11] respectively, has not been pursued further adequately. They are both limited to large or small values of the frequency parameter only. The fourth method, that is numerical calculations in the three-dimensional coordinate space (x, y and t) is perhaps the most unambiguous and accurate method but suffers from the need of large computer sotrage and time. The literature in this area has been adequately surveyed very recently[1,6-8] and it was decided here not to reference earlier publications again.

It is the opinion of the present author that most of the engineering problems of today can be treated effectively with an expansion method of the type described under the first category. Compared to the exact numerical solutions that require storage of information in a two-dimensional space, this method requires information stored in two or three columns only. Moreover it provides physical insight that will guide the investigator to avoid basic conceptual erros as it will be described in the present and the next sections.

Very few investigators attempted experiments in this area but the work of Hill & Stenning[12] is quite extensive and perhaps adequate. The problem is straightforward and its physics is well understood. In fact all of the basic trends like velocity overshoots, phase advances or delays, etc., are quite accurately predicted by almost all of the analytical methods. Therefore today the problem of two-dimensional incompressible oscillations imposed on laminar boundary layers does not pose any conceptual, physical or methodological difficulties and is considered a test case for investigators who intend to attack more complex situations. In this subsection most recent contributions will be referenced, some minor physical pecularities disclosed recently will be described and some comments on the validity of the available mathematical models will be made.

Oscillations of Incompressible Flows

Patel[13] recently considered the problem of laminar fluctuations generated by a system of vortices that are being convected downstream with a speed $Q = 0.77U_0$ where U_0 is the velocity of the outer mean flow. This corresponds to an outer flow velocity distribution of the form

$$U_e(x,t) = U_0 + U_1(x)e^{i\omega(t-x/Q)} \tag{2.1}$$

with U_0 = const, U_1 a linear function of x, and Q the velocity of the traveling wave. Patel's experimental investigation provides velocity and phase shift profiles for reduced frequencies of 0.314 up to 1.57. He finds that the mean flow is unaffected by the outer flow fluctuations which should be expected since his $\varepsilon=U_1/U_0$ is less than 10%. It appears however that other experimentalists (Hill & Stenning[12], Karlsson[14]) the latter for turbulent flows, reported the same finding for a stationary wave and for amplitudes of oscillations up to 30% of the main flow. According to the asymptotic theory[1], the correction to the mean flow will appear in the terms of order ε^2. For $\varepsilon = 0.3$ we should therefore expect a contribution approximately equal to 10% of the mean flow. Such deviations from the quasi-steady solution should be experimentally detectable. The only available numerical calculations[15] indicate that the actual values of the streaming terms, i.e. the non-fluctuating coefficients of the term that multiplies ε^2 in the series expansion are indeed rather small. If this is true, then the problem would be simplified considerably, except perhaps in the neighborhood of separation.

In the same paper Patel describes an extension of Lighthill's method which appears to give results comparing favorably with the experimental data for extreme values of the frequency parameter. Patel's experimental velocity profiles indicate overshoots of the order of magnitude of 50% or even 60% and undershoots, or in his terminology, "dips" of the profiles of the order of 10% or 20%. He also demonstrates some peculiar features of the flow in the neighborhood of $\omega x/U_0 \sim 1$. This behavior is illustrated in Fig. 1 where wall phase lag of velocity fluctuations for traveling wave and pure time dependent oscillations as functions of the frequency parameter are shown.

In Ref. 1 the present author included an alert with regard to the validity of the mathematical models commonly used. The differential equations that govern the steady streaming terms were explicitly displayed but no solutions were available at this time. Numerical solutions of the streaming equations have appeared most recently[15-17]. Some basic equations are repeated here from Ref. 15 in order to clarify some aspects of the problem.

For an outer flow velocity distribution given by

$$U_e = U_0 + \frac{\varepsilon}{2} U_1 e^{i\omega t} + \frac{\varepsilon^2}{2} U_2 e^{2i\omega t} + \ldots + CC \tag{2.2}$$

where U_i's are real functions, ω is the frequency of the oscillation, ε is a small dimensionless parameter and CC stands for the complex conjugate of the preceding quantity, the properties of the shear layer are assumed in the form

$$f = f_0 + \frac{\varepsilon}{2}(f_1 e^{i\omega t} + \bar{f}_1 e^{-i\omega t}) + \frac{\varepsilon^2}{2}(f_2 e^{2i\omega t} + \bar{f}_2 e^{-2i\omega t}) + \varepsilon^2 f_s + \ldots \tag{2.3}$$

In the above equation f may represnet the velocity components u, v, the pressure p, or the temperature T, and an overbar denotes the complex conjugate.

Substitution of such expressions in the Navier-Stokes equations and collection of like powers of ε generates sets of differential equations that can be solved successively. For the zeroth order quantities, u_0, v_0, p_0, it can be easily shown that the problem reduces to the classical steady state boundary-layer equations provided that the Reynolds number $R_0 = U_0 L/\nu$ is very large. Here L is a typical length of the problem and ν is the kinematic viscosity.

Collection of terms of order ε then yields

$$\frac{\partial u_1}{\partial x} + \frac{\partial v_1}{\partial y} = 0 \tag{2,4}$$

$$i\omega u_1 + u_0 \frac{\partial u_1}{\partial x} + u_1 \frac{\partial u_0}{\partial x} + v_0 \frac{\partial u_1}{\partial y} + v_1 \frac{\partial u_0}{\partial y} = -\frac{1}{\rho}\frac{\partial p_1}{\partial x} + \nu\left[\frac{\partial^2 u_1}{\partial x^2} + \frac{\partial^2 u_1}{\partial y^2}\right] \tag{2.5}$$

$$i\omega v_1 + u_0 \frac{\partial v_1}{\partial x} + v_1 \frac{\partial u_0}{\partial x} + v_0 \frac{\partial v_1}{\partial y} + v_1 \frac{\partial v_0}{\partial y} = -\frac{1}{\rho}\frac{\partial p_1}{\partial y} + \nu\left[\frac{\partial^2 v_1}{\partial x^2} + \frac{\partial^2 v_1}{\partial y^2}\right] \tag{2.6}$$

In these forms the above equations represent a linear elliptic disturbance to the boundary layer equations. The thickness of the oscillatory layer, commonly known as a Stokes layer, is of the order of $\sqrt{\nu/\omega}$ and for most practical applications, it is very small. The ratio of the Stokes layer thickness to the thickness of the mean boundary layer is therefore $\delta_1/\delta_0 = (U_0/\omega L)^{1/2}$ and if this number is small, then the boundary-layer assumption can be recalled in order to arrive at the familiar boundary layer form of Eqs. (2.4-6). For a specific situation this condition provides a lower bound for ω. The boundary layer approximation is applicable provided that the external disturbance amplitude, $U_1(x)$, is a smooth function of x. However if $U_1(x)$ has large derivatives or if it is periodic, with a wavelength comparable to the thickness of the boundary layer[5], then we should expect that $\partial u_1/\partial x$ and $\partial^2 u_1/\partial x^2$ and hence $\partial p_1/\partial y$ are not negligible compared to the other terms of the equation and the problem must be treated as an elliptic one.

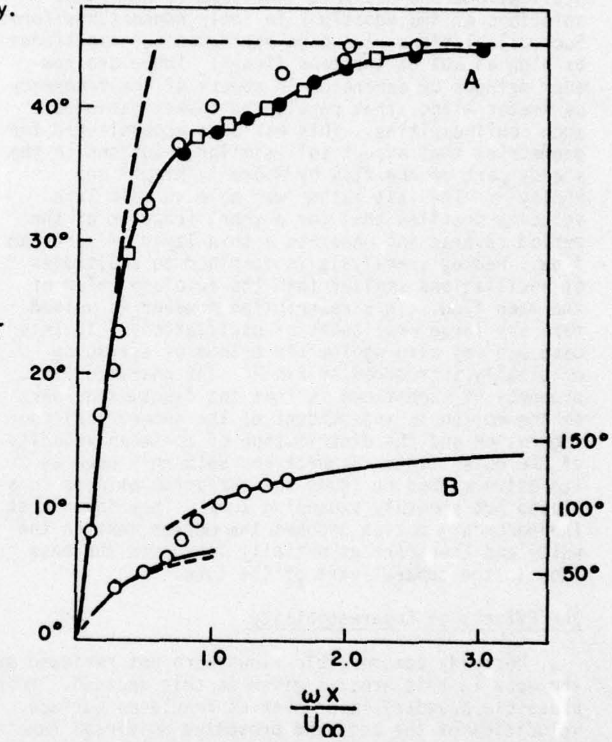

Fig. 1. The skin friction phase angle as a function of the frequency parameter. A. Oscillating outer flow, $U_0 + U_1 \cos(\omega t)$; - - -, Lighthill[9]; ——, Telionis and Romaniuk[17]; ○, McCroskey and Philippe; □, Cebeci[16]; •, Ackerberg and Philips[34]; B. Traveling Wave, $U_0 + U_1 \cos(\omega t - kx)$; Patel[13]: ○, experiment; ——, - - -, high and low frequency approximations.

In the case considered by Patel[13], the traveling wave has a wave number equal to ω/Q and a wavelength equal to $2\pi Q/\omega$. It therefore appears that the validity of the boundary layer form of the equations that govern the fluctuating part of the flow imposes an upper bound on ω as well. For example for $Q/U_0 = 0.7$ which is a consequence of Patel's experimental set up and for $L \sim 0.05$m and $U_0 = 10$m/sec even $\omega L/U_0 \sim 10$ gives a wavelength equal to 0.02m which could be of the same order of magnitude with the mean boundary layer thickness.

Collecting the non-fluctuating terms of order ε^2, that is the steady-streaming terms we arrive again at a set of elliptic linear differential equations of a form quite similar to Eqs. (2.4-6). Stuart[5] has indicated that for no mean flow, $u_0 = v_0 = 0$, the streaming terms do not attain the free stream value at the edge of the Stokes layer. Following Stuart's line of thought[17] we can arrive at the conclusion that the ratio of the streaming layer thickness to the fluctuating layer thickness is $\delta_s/\delta_1 = \omega L/U_0$ and therefore the streaming Reynolds number should be defined as $R_s = (\nu\omega/U_0^2)^{1/2}$. To derive the boundary layer form of the streaming equations we need to assume that R_s is large. However at this level of approximation we may find that terms neglected at the zeroth order level may be comparable to the streaming terms if the product $\varepsilon^2 R_0$, with R_0 the mean flow Reynolds number, is of order one. The complete form of the streaming boundary-layer equations then is

$$\frac{\partial u_s}{\partial x} + \frac{\partial v_s}{\partial y} = 0 \tag{2.7}$$

$$u_0 \frac{\partial u_s}{\partial x} + v_0 \frac{\partial u_s}{\partial y} + u_s \frac{\partial u_0}{\partial x} + v_s \frac{\partial u_0}{\partial y} = - 2R[\bar{u}_1 \frac{\partial u_1}{\partial x} + \bar{v}_1 \frac{\partial u_1}{\partial y}] + U_1 \frac{dU_1}{dx} + \frac{\partial^2 u_s}{\partial y^2} + \frac{1}{\varepsilon^2 R_0} \frac{\partial^2 u_0}{\partial x^2}$$
$$+ \frac{1}{R_s} \frac{\partial^2 u_s}{\partial x^2} \qquad (2.8)$$

In this equation all the symbols represent dimensionless quantities and R denotes the real part of the expresion that follows. Fig. 2 shows streaming velocity profiles for oscillatory Howarth flow[15]. It appears that next to the wall and for adverse pressure gradients the secondary flow is opposing the mean flow and eventually closes a loop to form an elongated vortex.

To account for nonlinear phenomena and the response of the boundary layer to large amplitude oscillations one may have to resort to numerical solutions of the equations in their nonpertubed form. Such calculations have been performed for amplitudes as high as 60% of the mean flow[18]. There are however methods of expansion in powers of the frequency parameter alone, that permit the investigation of such nonlinearities. This has been accomplished for geometries that accept self-similar solutions to the steady part of the flow by Moore[11], King[19] and Pedley[20]. The last author was able to calculate velocity profiles that for a short fraction of the period reverse and generate a thin layer of upstream flow. Pedley's analysis is confined to amplitudes of oscillations smaller than the absolute value of the mean flow. This restriction however is waived for very large amplitudes of oscillations. In this case one may also employ the method of averaging originally introduced by Lin[10]. The characteristic property of such flows is that the fluctuating part of the motion is independent of the geometrical configuration and the distribution of the mean velocity of the outer flow. Schneck and Walburn[21] used an iterative method to study the streaming effects in a closed but smoothly expanding tube. They found that the secondary motion opposes the motion next to the walls and therefore essentially increases the mass flow in the central part of the tube.

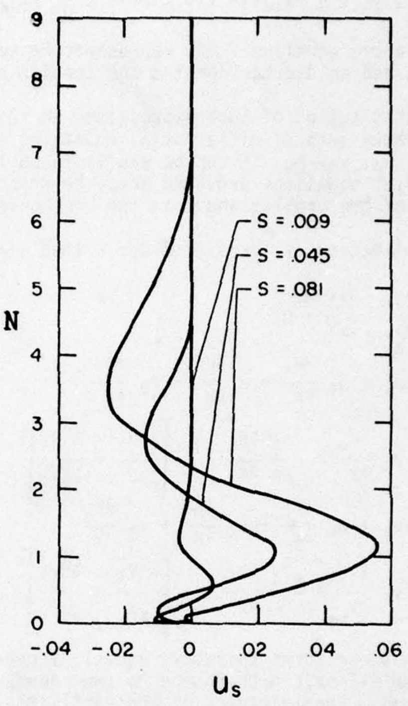

Fig. 2. Steady Streaming profiles for oscillatory flow[15] with the outer flow velocity given by $U_e = 1 - s$. Here $s = \frac{x}{L}$, $N = y\left(\frac{U_\infty L}{\nu}\right)^{1/2}$

The Effects of Compressibility

Unsteady compressible flows were not reviewed extensively earlier[1] and a more complete account of the work in this area is given in this section. Moore[11] was first to consider the unsteady laminar compressible boundary layer over an insulated surface. He studied the case of continuous time-dependent velocities of the body and presented universal functions from which the deviations of the velocity and temperature profiles from the quasi-steady state can be determined. Ostrach[22] and later Moore and Ostrach[23] extended the theory to include the effects of heat transfer but confined their attention to flat plate flows only. The momentum equation can then be uncoupled from the energy equation and the fact that the outer velocity has no space gradient further simplifies the problem. Illingworth[24] also considered a flat plate and studied the effect of high wall temperatures on skin friction and heat transfer due to sound waves carried by the main stream. This was actually the first paper that treated the case of fluctuating compressible outer flows in the form of an acoustic wave which accounts for fluctuations in the velocity and temperature but corresponds to a vanishing mean pressure gradient.

It should be emphasized here that for compressible flows the two problems of fixed bodies in oscillating flows or oscillating bodies in steady uniform flows cannot be treated mathematically through the same model. In other words it is not possible to derive one flow field from the other by a simple transformation of the frame of reference. This is due to the fact that the inertia term introduced when transforming the coordinate system to match one case with the other, involves the term $\rho_e \partial U_e/\partial t$ in the one case and $\rho \partial U_e/\partial t$ in the other case where ρ, U_e and t are the density, the edge velocity and time respectively. The two effects are equivalent only if $\rho = \rho_\infty$. Gribben[25,26] considered the flow in the neighborhood of a stagnation point, which accounts for pressure gradient effects, albeit in a narrow sense. Gribben was mainly interested in the effects of a very hot surface and therefore assumed constant outer flow density and temperature. Vimala and Nath[27] presented most recently a quite general numerical method for solving the problem of compressible stagnation flow.

Flows with nonvanishing mean pressure gradients, for example flows about wedges, were considered first by Sarma[28]. Sarma employed double expansions in powers of the distance along the wall and time. However, he studied only impulsive changes of the outer flow. This introduces a considerable simplification since fluctuations in velocity and pressure are missing from the outer flow which is thus rendered isenthalpic. To clarify this point let us consider the governing equations for two-dimensional or axisymmetric laminar compressible boundary-layer flow

$$\frac{\partial \rho}{\partial t} + \frac{1}{r^j} \frac{\partial}{\partial x} (\rho r^j u) + \frac{\partial}{\partial y} (\rho v) = 0 \qquad (2.9)$$

$$\rho\left(\frac{\partial u}{\partial t} + u\,\frac{\partial u}{\partial x} + v\,\frac{\partial u}{\partial y}\right) = -\,\frac{\partial p}{\partial x} + \frac{\partial}{\partial y}\left(\mu\,\frac{\partial u}{\partial y}\right) \tag{2.10}$$

$$\rho C_p\left(\frac{\partial T}{\partial t} + u\,\frac{\partial T}{\partial x} + v\,\frac{\partial T}{\partial y}\right) - \left(\frac{\partial p}{\partial t} + u\,\frac{\partial p}{\partial x}\right) = \frac{C_p}{Pr}\,\frac{\partial}{\partial y}\left(\mu\,\frac{\partial T}{\partial y}\right) + \left(\mu\,\frac{\partial u}{\partial y}\right)^2 \tag{2.11}$$

In the above equations u, v and x, y are the velocity components and the distances parallel and perpendicular to the wall, ρ, p and T are the density, pressure and temperature, and C_p, μ and Pr are the specific heat for constant pressure, the viscosity and the Prandtl number respectively. The quantity $r = r(x)$ defines the body of revolution for axi-symmetric flow and j takes the values 0 and 1 for two-dimensional and axisymmetric flow respectively. The above system can be closed if we specify the equation of state: assumming for example the gas to be perfect

$$p = \rho RT \tag{2.12}$$

The boundary conditions require for a fixed wall with no suction

$$u = v = 0 \qquad \text{at } y = 0 \tag{2.13}$$

$$T = T_w \qquad \text{at } y = 0 \tag{2.14}$$

while at the edge of the boundary layer the flow joins smoothly, within the boundary-layer approximation, with the outer flow

$$u \to U_e,\ T \to T_e \qquad \text{as } y \to \infty \tag{2.15}$$

where the subscript e denotes properties of the outer flow.

The outer flow distributions cannot be prescribed arbitrarily as in the case of incompressible flow. The outer flow pressure, velocity, density and temperature distributions must be compatible and should satisfy the following equations

$$-\,\frac{\partial p}{\partial x} = \rho_e\left(\frac{\partial U_e}{\partial t} + U_e\,\frac{\partial U_e}{\partial x}\right) \tag{2.16}$$

$$\frac{\partial p}{\partial t} = \rho_e C_p\left(\frac{\partial}{\partial t} + U_e\,\frac{\partial}{\partial x}\right)\left(T_e + U_e/2C_p\right) \tag{2.17}$$

and the equation of state, Eq. (2.12). For incompressible flow any distribution of the outer flow velocity corresponds to the evaluation at $y = 0$, that is the inner limit, of some potential flow. For compressible flow, one may choose arbitrarily the distribution of one of the quantities p, ρ_e, U_e, T_e. The other three quantities should be calculated from the system of Eqs. (2.12, 16 and 17). The reader should notice now in Eq. (2.17) that for unsteady compressible flow the total enthalpy is not constant but fluctuates with the time derivative of the pressure.

In Sarma's work[28] the outer flow velocity and temperature distributions are given an impulsive change and for $t > 0$ both functions are constants. As a result the right hand side of equation (2.17) is zero, the outer flow enthalpy is constant and the pressure does not vary with time. King[19] also considered wedge flows, but only for the case of hypersonic flow. In this particular case the outer flow velocity may be assumed constant and only pressure fluctuations have to be taken into account. King's work is nevertheless quite interesting as it presents a perturbation method independent of the small amplitude assumption. Telionis & Gupta[29] have studied the fluctuating compressible flow over a wedge or a cone but for the very special case of a wall temperature equal to the adiabatic wall temperature. This is perhaps the first attempt to study a flow with nonzero pressure gradients and purely unsteady outer flow conditions. For this flow enthalpy ceases to be constant and varies proportionally to the time derivative of the pressure. However in this work[29] the enthalpy variations are of one order of magnitude higher than the level of the terms retained. Moreover the simplifying assumptions are quite restrictive since the solution is valid for a conducting wall with a temperature equal to the adiabatic temperature.

In a later publication[30], the same authors consider a more general class of problems by assuming arbitrary wall temperatures and velocity distributions that correspond to wedges and cones. The physical picture appears to be very interesting. A wedge that fluctuates in orientation forces the attached shock wave to continuously change its slope with the same period. This message however travels with the speed of sound along the shock and as a result the shock wave is not straight but wavy. The flow behind the shock is not isentropic but homoentropic. Closer to the skin of the wedge the velocity varies with time and the enthalpy again fluctuates. This time however the fluctuation occurs along a streamline as well since the pressure varies with temperature as Eq. (2.17) indicates.

The Effects of Heat Transfer and Three-Dimensionality

Heat transfer effects were considered quite early and in fact some of the earlier contributions have slipped the attention of the present author[1]. Sparrow and Gregg[31] studied the compressible flow over a flat plate and proposed series expansions similar to those of Moore[11]. In Refs. 11 and 23 the deviations from the quasi-steady flow due to slow variations of the outer flow velocity were investigated while in Ref. 22 a steady flow was assumed and the effect of slow variations of wall temperatures was investigated. More recently Watkins[32] looked into the classical problem of impulsive motion over a flat plate and extended the theory to include impulsive temperature changes. Similar experimental and theoretical studies, again for the flat plate and including the effects of conduction and radiation were reported by Karvinen[33]. However this study is confined to transient flows. Heat transfer rates were also calculated in the special case considered in Ref. 27 as a deviation from the adiabatic flow and then again in Ref. 28 for a more general situation when the temperature of the wall is prescribed.

The present author and one of his associates[17] reconsidered laminar incompressible flows and via asymptotic expansions of the form presented in this section, investigated the effects of hot and cold wall temperatures and for the first time dissipation, on heat transfer rates. It is interesting to note here that a typical nonlinear streaming phenomenon appears again. The differential equation for the temperature is of course linear but the nonlinear terms of the velocity field feed energy into the temperature field and thus generate a steady component of temperature in excess of the average quasi-steady temperature profile. More specifically, assuming that the temperature is expanded according to Eq. (2.3) the streaming component of energy satisfies the equation

$$u_0 \frac{\partial T_s}{\partial x} + v_0 \frac{\partial T_s}{\partial y} + u_s \frac{\partial T_0}{\partial x} + v_s \frac{\partial T_0}{\partial y} = \frac{1}{Pr} \quad \frac{\partial^2 T_s}{\partial y^2} + \frac{1}{\varepsilon^2 R_0} \frac{\partial^2 T_0}{\partial x^2} \quad + 2E_c \quad \frac{\partial u_0}{\partial y} \frac{\partial u_s}{\partial y} + \frac{1}{\varepsilon^2 R_0} \frac{\partial u_0}{\partial y}^{2} \qquad (2.18)$$

where Pr and Ec are the Prandtl and Eckert numbers respectively. The streaming terms, u_s and v_s, influence the convective and dissipative part of the process. From the physical point of view the phenomenon is perhaps of considerable importance. It appears that imposed velocity fluctuations may result in increased rates of heat transfer as compared to quasi-steady values. Unfortunately the analysis in Ref. 17 is confined to small amplitude of oscillations and as a result the domain of large deviations from the mean cannot be investigated. However, the phenomenon may have interesting engineering applications since larger amplitudes of oscillation may result in substantial changes of the mean heat transfer.

The numerical analysis of the problem[17]shows that temperature profiles do not have monotonic derivatives, much like the curves shown in Fig. 1. Such "wiggly" variations may have been inherited from the velocity field and appear even for large values of the frequency parameter. In fact the asymptotic values are approached in a damped oscillatory fashion, as observed earlier for the velocity field by Ackerberg and Phillips[34]. This behavior was attributed to the neglect of initial conditions upstream at x=0, which are transmitted downstream by exponentially small oscillatory eigenfunctions. Ackerberg and Phillips have verified this by numerical experiments and by fitting numerical results to some eigenfunctions determined by Lam and Rott[35]. However there is some controversy with regard to the correctness of the eigenfunctions determined by Lam and Rott because the eigenfunctions of higher order appear to grow faster than the eigenfunctions of lower order. Brown and Stewartson[36,37] have proposed a different set of eigenfunctions based on the physical argument that the outer Blasius flow controls the motion, rather than the inner Stokes flow and that signals from the leading edge propagate downstream with finite velocity. For more details the reader may look into the papers referenced as well as the review article of Riley[6]. The present paper is confined here to give hospitality to Ackerberg's rebuttal. Ackerberg[37] maintains that the argument of Brown and Stewartson makes no physical sense because the flow under consideration is <u>absolutely</u> periodic in time and has been so for an infinite amount of time. There are no transient signals emanating from the leading edge, just absolutely periodic ones. Therefore, every point in the flow downstream of the leading edge has been "aware" of the periodic conditions at the leading edge for an infinite amount of time. If the conditions at the leading edge are <u>not</u> periodic in time, then Stewartson's argument is probably correct.

It is certainly true that Lam and Rott's eigenfunctions are not very useful, but that is not sufficient reason to doubt their validity. There are several possible ways by which Lam and Rott's and Brown and Stewartson's eigenfunctions can both be correct:

1. Asymptotic expansions are not always unique.
2. Stewartson's eigenfunctions may be a different (and more useful) representation of Lam and Rott's eigenfunctions, i.e., one can expand an eigenfunction in terms of another set of eigenfunctions.
3. A double limit is involved in the derivation of these eigenfunctions. Lam and Rott have obtained eigenfunctions for $t \to \infty$ first and then $x \to \infty$, while in Refs. 36, 37 eigenfunctions correspond to $x \to \infty$ first, followed by $t \to \infty$. Brown and Stewartson's physical argument would then apply since transient signals would still be propagating downstream with the main stream velocity when $x \to \infty$ before one allows $t \to \infty$. More simply stated, the limits $x \to \infty$ and $t \to \infty$ are not commutative.

Although the problem of laminar two-dimensional oscillations has received extensive attention in the last 25 years and may be considered solved, very little has been done to extend these theories to three-dimensional flows. A typical example where such flows are encountered is the helicopter blade and the urgent need to have an engineering solution to the problem have prompted various investigators[39-43] to propose approximate solutions. It appears that a small frequency assumption is acceptable for this problem and in all the above references only the first approximation is derived which essentially corresponds to large distances from the center of rotation. McCroskey and Laggy[41] indicate that in this case the spanwise flow is independent of the crosswise flow and proceed to investigate the effects on separation. A transformation to treat the same problem and in particular separation was proposed by Young and Williams[43]. More recently[44] an effort has been made to capture the oscillating components of the spanwise flow and the cross-flow. This could be considered as the first order unsteady correction to earlier studies. However the work in Ref. 44 is confined to the flow over a yawed but infinite cylinder of arbitrary cross-section. Some of the results are quite interesting. With oscillations of the outer flow only in the spanwise direction, it appears that the coupling of the differential equations allows the disturbances to be transferred to the cross flow. As a result cross flow fluctuating profiles are generated. No attempt has been made to attack the problem for more general situations.

It is the opinion of the present author that numerical solutions in the space of 4 independent variables (x, y, z, t) should be excluded, at least for the time being. An application of perturbation methods will be necessary and we feel that the most appropriate would be an extension of the one proposed for two-dimensional flow by Lighthill[9]. The oscillatory part of the flow then, following the notation of this section, would be governed by the equations

$$\frac{\partial u_1}{\partial x} + \frac{\partial v_1}{\partial y} + \frac{\partial w_1}{\partial t} = 0 \tag{2.19}$$

$$i\omega u + u_0 \frac{\partial u_1}{\partial x} + u_1 \frac{\partial u_0}{\partial x} + v_0 \frac{\partial u_1}{\partial y} + v_1 \frac{\partial u_0}{\partial y} + w_0 \frac{\partial u_0}{\partial z} + w_1 \frac{\partial u_0}{\partial z} = - \frac{1}{\rho} \frac{\partial p_1}{\partial x} + \nu \frac{\partial^2 u_1}{\partial y^2} \tag{2.20}$$

$$i\kappa\omega_1 + u_0 \frac{\partial w_1}{\partial x} + u_1 \frac{\partial w_0}{\partial x} + v_0 \frac{\partial w_1}{\partial y} + v_1 \frac{\partial w_0}{\partial y} + w_0 \frac{\partial w_1}{\partial z} + w_1 \frac{\partial w_0}{\partial z} = - \frac{1}{\rho} \frac{\partial p_1}{\partial z} + \nu \frac{\partial^2 w_1}{\partial z^2} \tag{2.21}$$

Integration of the system of steady state equations that govern the quantites u_0, v_0 and w_0 and Eqs. (2.19-21) can proceed numerically in the three-dimensional space x, y, z for a general body configuration and for a specific value of the frequency ω. In this way no restriction will be imposed on the geometry of the aerodynamic surface or the value of the frequency of the oscillation. The only requirement is that the amplitude of the oscillation is a small.

Finally we should emphasize here that one area of laminar fluctuations remains almost untouched. It is the problem of strong interaction with the outer inviscid flow. The author is aware that an effort in this direction is under way[45]. Moreover a modest attempt to initiate the work in this area has already appeared in print. Afzal and Rizvi[46] studied the higher order boundary layer effects for a transient flow in the neighborhood of a stagnation point. The boundary layer equations may be confining for the investigation of such problems. Indeed many authors have employed more general models including of course the use of the full Navier Stokes equations. A review of such efforts can be found in Ref. 47.

3. TURBULENT FLUCTUATING BOUNDARY LAYERS

Interest in this area has been suddenly revived in the early seventies. As a result the experimentalists were caught unprepared, while many theoreticians have rushed to propose a variety of solutions, extending the well established steady flow models to unsteady flows (see earlier review of the present author[1]). Some of the investigators compared their theoretical predictions to the only available at the time experimental data, those of Karlsson[14]. The agreement in most cases is not very satisfactory. The profile of the mean flow* is usually predicted with reasonable accuracy. However theoretical in-phase and out-of-phase velocity profiles and phase advances appear to deviate very much from the experimental data. Even more disheartening is the fact that unacceptable disagreement exists between the results of various theoretical methods. The necessity for more experimental information has emerged more and more urgent. In the last year or two some experimental studies have started appearing. Therefore it is appropriate to start this section with a description of the most recent experimental results.

Recent Experimental Information

If a fluctuation of a specified frequency is imposed on a turbulent boundary layer, it is necessary to device a method of identifying separately the organized response to the external oscillation and the random fluctuation of the turbulent field. A method to identify experimentally these quantities, albeit for different physical situations, is described by Acharya and Reynolds[48], Houdeville et. al.[49], Schachenman et. al.[50] and Soutif et. al.[51]. A triple decomposition is necessary. A field quantity f is decomposed as follows

$$f = \bar{f} + \tilde{f} + f' \tag{3.1}$$

In this expression $\bar{f}$ is the time average of the quantity and according to our terminology, the mean. The quantity $\tilde{f}$ is derived by an ensemble averaging process which, however, is based on a conditional sampling technique. Acharya and Reynolds[48] call it "periodic sampling" or "phase averaging". It is the ensemble average of instantaneous values selected at a specific phase of the outer flow oscillation. Let

$$\langle f(t) \rangle = \lim \frac{1}{N} \sum_{n=0}^{N} f(t + nT) \tag{3.2}$$

where T is the period of the imposed oscillation. The quantity $\tilde{f}$ which represents the organized fluctuations, is defined according to the formula

$$\tilde{f} = \langle f \rangle - \bar{f} \tag{3.3}$$

while the random fluctuations are

$$f' = f - \langle \bar{f} \rangle \tag{3.4}$$

Similar decompositions have been used by Townsend[52] and Phillips[53]. The above definitions are depicted schematically in Fig. 3. Acharya and Reynolds provide a detailed discussion on this decomposition as well as the differential equations that govern the field of the mean and the fluctuating quantities. A boundary layer form of their equations in the classical notation should be:

for the mean flow:

$$\frac{\partial \bar{u}}{\partial x} + \frac{\partial \bar{u}}{\partial y} = 0 \tag{3.5}$$

---

*It is proposed to avoid confusion here by the following convention for the terminology. Let the term "average" be used whenever a statistical ensemble average is involved. Let the term "mean" be reserved only for the overall mean of the deterministically oscillating and randomly fluctuating motion.

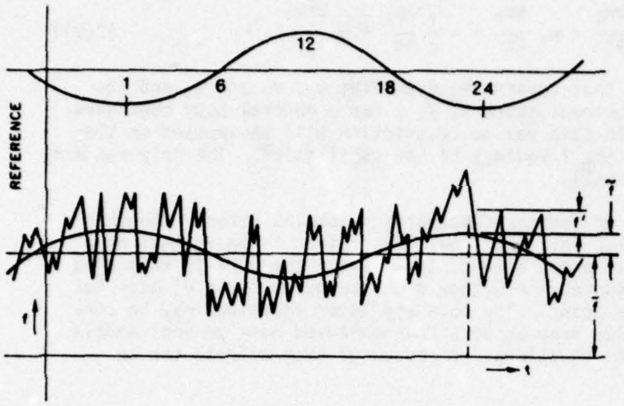

Fig. 3. Schematic representation of the triple decomposition (from Ref. 48).

$$\bar u \frac{\partial \bar u}{\partial x} + \bar v \frac{\partial \bar u}{\partial y} = - \frac{1}{\rho} \frac{\partial \bar p}{\partial x} + \nu \frac{\partial^2 u}{\partial y^2} - \frac{\partial}{\partial y} (\overline{u' v'})$$

$$- \frac{\partial}{\partial y} (\overline{\tilde u \tilde v}) \qquad (3.6)$$

and for the oscillating flow:

$$\frac{\partial \tilde u}{\partial x} + \frac{\partial \tilde v}{\partial y} = 0 \qquad (3.7)$$

$$\frac{\partial \tilde u}{\partial t} + \tilde u \frac{\partial \bar u}{\partial x} + \bar u \frac{\partial \tilde u}{\partial x} + \tilde v \frac{\partial \bar u}{\partial y} + \bar v \frac{\partial \tilde u}{\partial y} = - \frac{1}{\rho} \frac{\partial \tilde p}{\partial x}$$

$$+ \nu \frac{\partial^2 u}{\partial y^2} + \frac{\partial}{\partial y} (\overline{\tilde u \tilde v} - \tilde u \tilde v)$$

$$- \frac{\partial}{\partial y} (\langle u' v' \rangle - \overline{u' v'}) \qquad (3.8)$$

Reynolds stress terms appear in these equations both from the random as well as the organized fluctuations and we have assumed here that within the boundary layer approximation, normal Reynolds stresses are negligible.

Acharya and Reynolds provide extensive experimental data that includes mean profiles, averaged profiles, normal and shear Reynolds stresses, correlations etc. However they investigate internal fully developed turbulent flows which are beyond the scope of the present review. Their results could provide an excellent test case for approximate theoretical models of unsteady turbulent boundary layers.

Some very interesting features of oscillating turbulent boundary layers were disclosed by the experimental efforts of a group of investigators from Toulouse[49,54,55]. All of these experiments are characterized by not so small amplitudes of oscillation, of the order 30% to 40% of the mean outer flow. As a result some clear nonlinear effects become obvious. Perhaps their most exciting discovery, in the opinion of the present author, is that the turbulence level at a fixed point in space fluctuates with the same frequency as the outer flow. That is, the random disturbances tend to follow the periodic variation of the outer flow fluctuations. Figure 4 is taken from Ref. 49 and corresponds to a reduced frequency of oscillation $\omega\delta_1/U_0 = 3.7 \times 10^{-3}$ where δ_1 and U_0 are the displacement thickness and outer flow velocity respectively. It shows the reduced turbulence level variation, $(\overline{u'^2}/(\overline{u'^2})_m)^{1/2}$, and the reduced averaged flow U/U_m. In the notation of Ref. 49 the subscript m denotes a time average. In our notation the quantity U/U_m should be $\langle u \rangle / \bar u$. We observe that the turbulence level follows with some delay the fluctuations of the ensemble averaged motion but as one proceeds away from the wall and approaches the edge of the boundary layer, larger phase shifts and a periodic intermittency phenomenon appears. More surprising, near the edge of the boundary layer, at a certain instant and while the averaged velocity and boundary layer thicknesses are at a maximum and minimum respectively, the turbulence level increases violently. In other words when the boundary layer goes through its smallest thickness, the turbulence suddenly bursts out into the free flow. Inspecting the ensemble averaged profiles which are given only for four points of the period - not shown here - we also observe a clear asymmetry of the periodic variation, that is a deviation from the sinusoidal behavior.

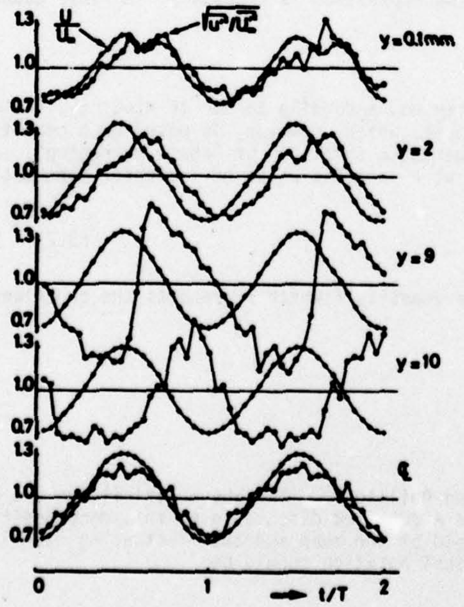

Fig. 4. The time history of the level of turbulence, $(u'^2)^{1/2}$, at different distances from the wall (from Ref. 49).

In a later publication[55] and

for a higher frequency parameter $\omega\delta_1/U_0 = 12.7 \times 10^{-3}$, the same authors give instantaneous profiles for the quantities $(\overline{u'^2})^{1/2}$ and $-(\overline{u'v'})$. In Fig. 5 we have carried over the experimental data from Ref. 55 as well as from Patel[56] who undertook a similar investigation. However, Patel used a time constant larger than the period of oscillation and essentially obtained the average of the instantaneous turbulence level profiles give by Cousteix et. al.[55]. It should be made very clear here, that the data of Fig. 5 correspond to different frequencies and amplitude parameters. Therefore comparison of different experimental results can be accomplished only at the qualitative level. The profiles shown in Fig. 5 seem to indicate that the turbulent energy is convected in an oscillatory manner and in a direction perpendicular to the wall with the frequency of the outer flow. However it appears that the flux of $(u'^2)^{1/2}$ shown in this Figure, may be conserved across the boundary layer.

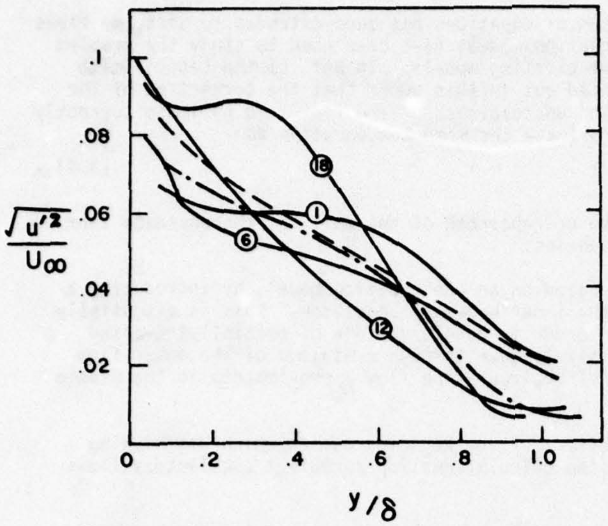

Fig. 5. The level of turbulence profiles: ____, four characteristic instances of a period $\omega t = 0, \pi/2, \pi$ and $3\pi/2$ (curves 1, 6, 12 and 18 respectively as shown in Fig. 3), Ref. 55; - - -, averaged through a period and steady flow, Ref. 56; -·-·-, steady flow, Ref. 57.

Fluctuating turbulent boundary layers with an adverse pressure gradient were investigated experimentally by Schachenmann and Rockwell[50] in a conical diffuser. In this study the frequency parameter was varied between 0.63 and 7.33 but the amplitude of the oscillations was only $\epsilon \equiv \tilde{U}/\bar{U} = 0.069$. However the pressure gradient effect appears to have a strong influence on the fluctuating part of the motion. First, the overshoot of the fluctuating component $\tilde{u}$ increases with downstream distance. Overshoot values reach magnitudes 60% higher than the value of the outer stream. The same effects were encountered in a numerical study for laminar oscillations by Telionis and Tsahalis[58]. Second, the profile of the fluctuating velocity component for large frequencies of oscillations indicates two peaks, and away from the wall it undershoots the value of the outer flow. Such a behavior was also encountered by Telionis and Romaniuk[17] and was found to carry over to temperature profiles as well. Third, for distances further downstream, the phase angle shows some negative values and eventually it becomes negative across the entire thickness of the boundary layer. The velocity fluctuations follow the fluctuations of the outer flow. Unfortunately the statistical information is not extensive. The root mean square of the total velocity is given and it is shown to increase with downstream distance. However if this quantity contains the RMS of the organized fluctuations, then the turbulence level is buried in this quantity and very little can be deduced about the statistics of the unsteady turbulent boundary layer.

Charnay and Mathieu[59] have also investigated fluctuating turbulent flows but measured only the effects of mean flow fluctuations on the free turbulence in a wind tunnel. The response of a turbulent boundary layer on an air-foil to fluctuations of the outer stream was investigated by Satyanarayana[60]. A wind tunnel with flexible walls was used to provide a stream that fluctuates in magnitude or in direction. In Ref. 60 averaged velocity profiles are given but little information on the statistical properties of turbulence is supplied.

Some very interesting problems that probably belong to the same family, although not strictly dealing with external turbulent boundary layers were investigated most recently. Soutif, Favre-Marinet and Binder[51] investigated the response of a turbulent jet to oscillations generated by two flaps that fluctuate symmetrically or antisymmetrically. The authors presented instantaneous profiles and the downstream evolution of periodic and turbulent intensities. Most important of all, they indicated that the externally imposed fluctuation may transfer energy to the turbulent motion. Indeed 20 jet thicknesses downstream of the disturbance, the periodic fluctuations die out but the turbulent intensity grows to a value 35% larger than the corresponding undisturbed jet intensity. Thomas and Shukla[61] have looked into the wall region of fully developed fluctuating turbulent pipe flow. They report on the interaction between the bursting effect and the imposed fluctuations and compare their experimental results with the theoretical model based on the concept of surface renewal. The work of Binder and Didelle[62], Mainardi and Pandai[63]and Mainardi et. al.[64] may be also found useful to the investigators of unsteady turbulent boundary layers.

Recapitulating, we may say that a clear picture has started to emerge from the available experimental data. There are of course many parameters involved and a lot more work is necessary to provide a complete description of the phenomenon. The frequency parameter is not easy to vary in all the experimental lay-outs. However a relatively wide range has been explored by different investigators. The amplitude parameter is fixed or very difficult to adjust for some of the experimental set-ups. Very little information is available for flows with pressure gradients which have been proved to have a strong influence on the fluctuating part of the motion. One of the most surprising conclusions that has emerged from many experimental studies[14,49,64] is that the mean profile is very little affected even for large amplitudes of oscillation.

Comparing the results of different experiments will be very difficult and it has been attempted in this paper but with no enthusiasm. This is due to the fact that the parameter $\omega x/U_0$ is no longer a similarity variable as is the case in laminar flows. In the laminar flow equations the independent variables x and t appear always in the combination $\partial/\partial t + u\partial/\partial x$. However, in the turbulent flow equations, x is introduced also in the Reynolds stress. The parameters $\omega\delta/U_0$ or $\omega\theta/U_0$ have been suggested for comparison but these too cannot be used for a global presentation of the experimental data. It appears that the only method of comparing experimental data could be through analytical extrapolations based on a successful theoretical method.

Modeling of the Unsteady Turbulent Boundary Layer

Most of the existing models for closing the system of equations has been extended to unsteady flows as reviewed in Ref. 1. At that time zero- and one-equation models have been used to study the problem. Since then, efforts have been continued to improve the existing models. In Ref. 65 the Cebeci-Smith eddy viscosity model is further improved. It is pointed out in this paper that the correction of the damping effect due to unsteadiness is influenced by the unsteadiness of the flow. To estimate correctly the shear τ_S at the edge of the sublayer one may approximate the momentum equation as

$$\rho \frac{\partial u}{\partial t} = - \frac{\partial p}{\partial x} + \frac{\partial \tau}{\partial y} \tag{3.9}$$

The convective terms could be ignored in the immediate neighborhood of the wall but the unsteady term, $\partial u/\partial t$, may be significant, especially for large frequencies.

Patel and Nash[67-70] extended their earlier work based on an one-equation model, by introducing a refinement in the neighborhood of the wall, to meet the inner boundary condition. This is essentially the law of the wall with appropriate modifications in order to handle regions of partially reversed flow. Patel and Nash investigate a flow that progressively goes through a minimum of the outer flow velocity. This generates a small but growing region of recirculating flow approximately in the middle of the domain of integration.

Cebeci[16] included in his well known models the effect of low Reynolds number which was missing from the development of Refs. 66 and 71 and repeated the calculations for turbulent oscillatory flows over a flat plate.

It has been argued that the agreement between the numerical results of some of the above methods and the experimental data is imperfect but probably adequate for engineering purposes. It has been also claimed that the existing discrepancies can be probably attributed, at least in part, to experimental scatter. The present author disagrees with such excuses. Instead he feels that in all the above models something fundamental is missing and many of the investigators clearly admit it. The argument of course and the controversy is carried over from steady turbulent flows, but here it is felt that our models do not even seem to predict the physical tendencies correctly. The reader will be convinced if he would simply throw a glance on Fig. 6. In this Figure we have collected experimental and analytical information on the variation of the skin friction phase angle as a function of the frequency parameter $\omega x/U_0$. Unfortunately the definition of these quantities is not very clear in some of the references. A 2π is implied sometimes and the distance x is not always specified or clearly defined. As a result our interpretation of data may not be very accurate. Moreover the interpretation of Karlsson's experimental results is very difficult and the points shown in the Figure may contain a possible error of up to 20%.

All the existing analytical models were carried over from steady flow. The only adjustments made were confined to incorporation of the term $\partial u/\partial t$ wherever it was appropriate. The two-equation models[75] may be a little more promising. In fact they have been used, again with no major adjustments to account for unsteadiness, in Refs. 49, 54 and 55. Successful modeling of the turbulent boundary layer is a clear challenge to the theoreticians. They will have to invent new models that would take into account the interaction between the organized fluctuations of the outer flow and the random fluctuations of turbulence. The process may even involve energy transfer from the deterministic to the random fluctuations, a phenomenon already observed experimentally[51]

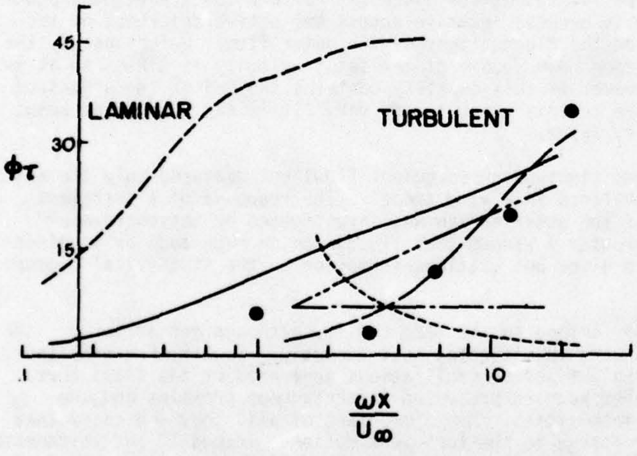

Fig. 6. The skin friction phase angle for turbulent oscillations as a function of the frequency parameter $\omega x/U_0$. Theoretical Results; -----, Kuhn & Nielsen[72]; - • • • -, Nash et al[72], Re = 10^7; ———, Telionis & Tsahalis[71], - .. - .. , Cebeci[16], —— McCrosky and Philippe[74]. Experiment: •, Karlsson[14].

The fallacy in using the steady flow models for unsteady turbulent flows becomes obvious if one simply observes the equations that govern the mean and the organized fluctuations of the motion, Eqs. (3.5 through 3.8). The Reynolds stresses appearing in the equations for the fields $\bar{u}$, $\bar{v}$ and $\tilde{u}$, $\tilde{v}$ are fundamentally different. Using a steady flow model and integrating numerically in the space x, y, t amounts to an arbitrary distribution of the steady Reynolds stress in the Reynolds stresses of Eqs. (3.6) and (3.8).

An alternative and more straightforward approach that clearly indicates the necessity of modeling separately the Reynolds stresses for the two fields was recently put forward[76] and will be repeated here briefly.

Consider an outer flow velocity distribution of the form

$$U_e(x,\ t) = U_0(x) + \frac{\varepsilon}{2}\, U_1(x)[e^{i\omega t} + CC] \tag{3.10}$$

where ε is a small dimensionless parameter and CC stands for the complex conjugate of the preceding quantity. We assume the response of the viscous layer in the form

$$\begin{aligned} u(x,\ y,\ t) &= u_0(x,\ y) + \frac{\varepsilon}{2}\,[u_1(x,\ y)e^{i\omega t} + CC) + O(\varepsilon^2) \\ v(x,\ y,\ t) &= u_0(x,\ y) + \frac{\varepsilon}{2}\,[u_1(x,\ y)e^{i\omega t} + CC] + O(\varepsilon^2) \end{aligned} \tag{3.11}$$

where u and v are the velocity components parallel and perpendicular to the wall respectively. The quantities u_0 and u_1 are, in general, random complex quantities. We therefore assume here that the boundary layer will respond to the outer flow with a deterministic fluctuation of the same frequency and an amplitude that contains the random turbulent fluctuations. We further assume that the organized fluctuations are small compared to the mean flow. However the random part of u_0 and u_1 does not have to be small compared to the mean of u_0 and u_1.

The steps that follow will be only described here briefly. We first substitute the above expressions in the full Navier-Stokes Equations, eliminate a few terms on the basis of the boundary layer approximation and collect powers of the small parameter ε. The process of making the boundary layer assumption and collecting the powers of ε may be interchanged under certain conditions and comments on the proper procedure are included in Ref. 17. At this stage we have two sets of differential equations: the first is nonlinear and governs the mean flow $(u_0,\ v_0)$. The second is linear and governs the amplitude of the fluctuations $(u_1,\ v_1)$. Both sets of equations are stochastic and describe exactly the turbulent boundary layer phenomena, within an error of order ε^2.

We now further decompose the velocity components as follows

$$\left.\begin{aligned} u_i &= \bar{u}_i + u_i' \quad &(3.12) \\ v_i &= \bar{v}_i + v_i' \quad &(3.13) \end{aligned}\right\} i = 0,\ 1,\ \ldots$$

where bars and primes denote the ensemble average and the random fluctuation respectively, i = 0, 1, ... and by definition $\bar{u}_i' = \bar{v}_i' = 0$. It is easy to show that both the averaged and the fluctuating components defined in Eqs. (3.12-13) satisfy the continuity equation in the form

$$\frac{\partial \bar{u}_i}{\partial x} + \frac{\partial \bar{v}_i}{\partial y} = 0 \quad , \quad i = 0,\ 1,\ \ldots \tag{3.14}$$

Substitution of the expressions (3.12) and (3.13) into the momentum equations of order 1 and ε, ensemble-averaging and using Eq. (3.14), yields

$$\bar{u}_0 \frac{\partial \bar{u}_0}{\partial x} + \bar{v}_0 \frac{\partial \bar{u}_0}{\partial y} = U_0 \frac{dU_0}{dx} + \nu \frac{\partial^2 u_0}{\partial y^2} - \frac{\partial}{\partial y}\,(\overline{u_0'v_0'}) - \frac{\partial}{\partial x}\,(\overline{u_0'^2} + \overline{v_0'^2}) \tag{3.15}$$

$$\begin{aligned} i\omega\bar{u}_1 + \bar{u}_0 \frac{\partial \bar{u}_1}{\partial x} + \bar{u}_1 \frac{\partial \bar{u}_0}{\partial x} + \bar{v}_0 \frac{\partial \bar{u}_1}{\partial y} + v_1 \frac{\partial \bar{u}_0}{\partial y} &= i\omega U_1 + U_0 \frac{dU_1}{dx} + U_1 \frac{dU_0}{dx} + \nu \frac{\partial^2 \bar{u}_1}{\partial y^2} - \frac{\partial}{\partial y}\,(\overline{u_0'v_1'} + \overline{u_1'v_0'}) \\ &\quad - 2\,\frac{\partial}{\partial x}\,(\overline{u_0'u_1'} + \overline{v_0'v_1'}) \end{aligned} \tag{3.16}$$

Equation (3.15) is identical to the steady-state turbulent boundary layer equation. If the x-derivative of the random fluctuations is assumed negligible and the Reynolds stress modeled according to one of the phenomenological theories widely accepted[75], then the theory shows that within an error of order ε, the mean and ensemble averaged flow is identical to the quasi-steady flow. In Eq. (3.16) it becomes now clear that the nonlinear contributions to the organized fluctuations $(\bar{u}_1,\ \bar{v}_1)$ would require special attention. There is no justification at all to assume that the Reynolds stress $\partial/\partial y\ (\overline{u_0'v_1'+u_1'v_0'})$ is modeled in exactly the same way as the Reynolds stress $\partial/\partial y\ (\overline{u_0'v_0'})$. In all the earlier calculations this is essentially what was done. The steady state model of the Reynolds stress was assumed and a straightforward integration in the three-dimensional space (x, y, t) was performed.

In a preliminary investigation[76] it was decided to perform calculations for the simplest kind of modeling possible. To this end, a classical eddy viscosity model for the mean flow Reynolds stress was used and the nonlinear random contributions in Eq. (3.16) were completely ignored. This assumption is essentially equivalent to a laminar oscillatory correction on a steady turbulent boundary-layer. It is felt that this is physically justified. It is well known that the boundary layer, laminar or turbulent, responds locally in an almost inviscid manner. The hypothesis here is that the local organized pressure disturbance is instantly carried through the turbulent boundary layer without interaction with the random fluctuations. Or equivalently that the turbulent eddies undergo an oscillatory deformation that does not affect their entity and the process of their mutual interaction. The effect of viscosity is confined to a thin Stokes-type layer and shrinks further with larger frequencies. In other words the inviscid response, that is a velocity fluctuation with a uniform profile, grows larger and approaches the wall as the frequency of the outer fluctuation increases. It should be mentioned here that a similar suggestion is included in Ref. 48 but it was proved that this idea did not produce satisfactory results in the case of internal flows.

A classical test of a theoretical method is the calculation of the harmonics of the organized part of the velocity, in the terminology of Karlsson: the in-phase and out-of-phase velocity components. No published theoretical results have predicted up to now overshoots of the in-phase component larger than 1% or 2%. Yet Karlsson's data and all the most recent experimental information indicate that the overshoot may reach 10% or even 20% of the mean flow. In Fig. 7 we plot for a specific situation, experimental data as well as theoretical predictions. Some improvement is obvious but the out-of phase comparison is still poor.

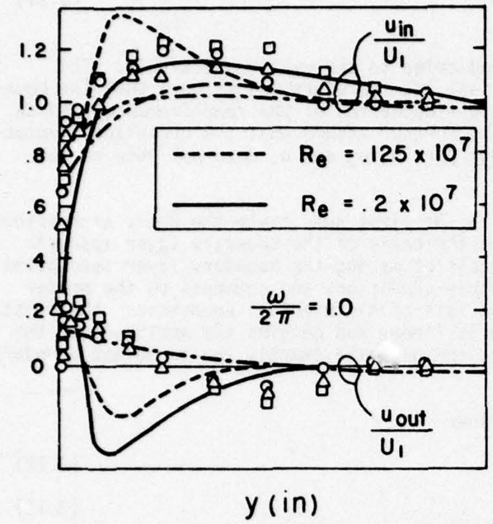

Fig. 7. The in-phase and out-of-phase velocity components for a fluctuating turbulent boundary layer. Theoretical results: - • - • -, Telionis[66] and Cebeci[16]; - - -, ——, Telionis & Romaniuk[76]. Experimental data: ∘, Δ, □, Karlsson[14] (different amplitudes); - .. - .. -, Cousteix, et al[55].

Let us try to gain some physical insight into the problem. Let us assume here a zero equation model and accept the mixing length expression for the Reynolds stress in unsteady flow:

$$- \overline{u'v'} = \rho \ell^2 \left| \overline{\frac{\partial u}{\partial y}} \right| \overline{\frac{\partial u}{\partial y}} \tag{3.17}$$

The mixing length could be expressed in terms of any of the exotic functions that improve the comparison with the experimental data. If this expression is substituted in the unsteady turbulent boundary layer equations, an expansion like the one given by Eqs. (3.11) is assumed and terms of order 1 and ϵ are collected, we arrive at the conclusion that the Reynolds stresses appearing in Eqs. (3.15) and (3.16) are

$$- \overline{u_0'v_0'} = \rho \ell^2 \left(\frac{\overline{\partial u_0}}{\partial y}\right)^2 \tag{3.18}$$

$$- \overline{u_0'v_1'} - \overline{u_1'v_0'} = \rho \ell^2 \frac{\overline{\partial u_0}}{\partial y} \frac{\overline{\partial u_1}}{\partial y} \tag{3.19}$$

This process corresponds to an asymptotic solution of the equations solved numerically in Refs. 16, 65 and 70. However the distribution of the Reynolds stress in the mean and the organized motion is absolutely arbitrary. The author and his colleagues have run some numerical examples and arrived at exactly the same results: almost no overshoot in the in-phase component of the velocity. It remains a great enigma to the present author how the calculations in Ref. 56 that follow the model given by (3.18) and (3.19) have resulted in large overshoots.

There is some physical meaning in the decomposition of the Reynolds stress implied by Eq. (3.18) and (3.19). The expression in Eq. (3.19) represents an eddy viscosity $\rho\ell^2\ \partial u_0/\partial y$ which is the same as the eddy viscosity of the mean flow. This is simply a factor to the shear $\partial \bar{u}_1/\partial y$ of the velocity field $\bar{u}_1$, $\bar{v}_1$. Acharya and Reynolds[48] list this assumption as one of the possible closures of the Eqs. (3.5-3.8). It is believed that this assumption as well as the over-simplified assumption[76] of a vanishing $\overline{u_0'v_1'} + \overline{u_1'v_0'}$ are not adequate. A more sophisticated model is urgently needed.

4. UNSTEADY SEPARATION AND SEPARATED FLOWS

The study of viscous phenomena and in particular boundary layers has interested investigators for a variety of reasons. It is certainly needed to know the distribution of skin friction and heat transfer across the interface of fluids and solids. For internal fluid mechanics this information and the properties of viscous regions per se, as for example velocity profiles, flow rates and perhaps the effect of viscosity on mixing and chemical reactions, is a final goal in itself. However in external fluid dynamics it is necessary to consider the interaction between the viscous layer and the outer inviscid flow. Viscous flow theories are employed in order to determine the location of separation which controls basic characteristics of lifting surfaces and perhaps the properties of small separated regions or even wakes. Boundary-layer technology has been successful in predicting with reasonable accuracy the location of separation in steady fields (see review articles by Brown and Stewartson[73] and Williams[78]). In the last decade it has been actively pursued to demonstrate that the classical theories can be used to determine the properties of unsteady flow fields. A breakthrough in this effort has been the identification of the fact that the classical criterion of separation for steady flow, that is the vanishing of skin friction is no longer valid for unsteady flows. This idea was presented at first in a form of a conjecture[79-81]. Some numerical evidence appeared later (see review article by Sears & Telionis[82]). This consists essentially of numerical integrations of laminar and turbulent boundary layers that were carried through the point of zero skin friction and into a region of partially reversed flow without any evidence of the separation singularity. Almost at the same time Despard and Miller[83] published their experimental results and argued that separation in oscillatory flow is displaced with respect to its steady state location but remains unaffected by the oscillations of the outer stream. The point of zero skin friction oscillates back and forth thus generating a thin layer of reversed flow that shoots upstream from the location of separation and then disappears again.

There have been some misunderstandings over the precise definitions suggested in Refs. 83 and 84 and a clarification, although repetitious, is perhaps necessary here. Let it be clear from the very beginning that by 'separation' we mean the location on the solid boundary where the flow stops creeping over the skin of the body and breaks away from the wall, thus generating a turbulent wake. This phenomenon, encountered mostly in external flows with relatively large Reynolds numbers, controls the overall pressure distribution and quantities like lift and drag. This was essentially the definition adopted in Ref. 84 where the authors have further argued that abrupt changes of boundary layer properties in the first order boundary layer equations, may signal the approach to the point of separation. Such properties have been studied extensively and are referred to as the Goldstein singularity. Despard and Miller[83] define separation as the furthest downstream station at which the shear fluctuates between zero and some negative value.

The work in this area has been reviewed in Refs. 1, 8, 78 and 82, all of which appeared very recently. In this section we will give a brief account of most recent contributions to the area and we will discuss the problems of unsteady separated flows.

The Glorified Moving Wall Case

Moore, Rott and Sears[84] have argued in the late fifties that there is an intrinsic qualitative similarity between steady separation over fixed walls and unsteady separation over moving walls. In fact to investigate the problem of unsteady separation, experiments were at first conducted at the Cornell Aeronautical Laboratory with steady flow over rotating cylinders[78,84]. A few years ago Telionis and Werle[85] have carried out numerical calculations of boundary layer flow over a parabola at an angle of attack. Allowing the skin of the parabola to move downstream they were able to demonstrate that the point of zero skin friction is not singular and that a Goldstein type singularity appears further downstream, at a point where the M.R.S. criterion is met, that is $\partial u/\partial y = 0$ at $u = 0$. Williams and Johnson[86,87] introduced a transformation that maps the steady flow over a moving wall to unsteady flow over a fixed wall. They were thus able to capture at least one special case of unsteady flow, where sepatation and the separation singularity occur at a station where the M.R.S. criterion is met, if the flow is viewed by an observer moving with the speed of separation. The same problem was attacked numerically quite earlier by Moore[81], through the self-similar equations of Falkner and Skan. This idea was further pursued by Telionis[88]. In Ref. 88 it was demonstrated that a singularity accompanies the profiles that satisfy the M.R.S. criterion for downstream moving walls. However this is not the case for upstream moving walls. It soon became clear that the problem of separation over upstream moving walls posed much greater difficulties than anticipated as Williams also notes[78].

At this point it is felt that a clarification is necessary. The Goldstein singularity or better, a characteristic singular behavior similar to the one studied by Goldstein[77], appears in a numerical calculation in the form of a sharp growth of quantities like the v-component of velocity, derivatives $\partial/\partial x$, etc. In all the cases studied the sharp growth is proportional to the inverse square root of a variable. This variable, in non-similar flow, is the upstream distance from separation. For self-similar solutions the quantities mentioned above blow up with the inverse square root of the pressure gradient parameter β. Fansler and Danberg[89] demonstrated that a similar phenomenon occurs in an integral analysis of the unsteady boundary layer equations. In this case the square root singularity appears if one plots the quantity H versus K, where H is the ratio of the displacement thickness to the momentum thickness and K is the energy thickness divided by the momentum thickness.

Tsahalis[90] attempted to investigate, for the first time numerically, the phenomenon of separation over upstream moving walls. Considering a non-similar flow, one encounters a small region of steady reversed flow. Integration in this case cannot proceed further with a steady state scheme of calculations. To overcome this difficulty Tsahalis employed an unsteady method of solution, started with a fixed wall and introduced gradually the upstream motion of the skin. Thus he was able to arrive at a converged steady state solution, which contains a region of partially reversed flow and a station where a Goldstein singularity appears. At this station the M.R.S. criterion is "nearly" met. Tsahalis explains that the boundary layer equations cannot accept an M.R.S. condition for upstream moving walls and that his analysis indicates that the M.R.S. criterion should probably be met at this station if the full Navier Stokes equations are employed. Fansler and Danberg[89] employ an integral method that makes use of self-similar profiles to investigate non-similar separation flows. They find that for upstream moving walls the MRS profile corresponds to a station near the point and not exactly at the point on the H-K curve where a singularity appears. However for upstream moving walls the point on the H-K curve that corresponds to an MRS profile is quite far from the singularity. Fansler and Danberg adopt essentially the definition of Ref. 80 and assume that separation occurs at the point where the H-K curve shows singular behavior. They proceed to compare their results to experimental data with acceptable success, at least for the case of downstream moving walls.

The present author has prepared a report[91] on this topic collecting information on analytical, numerical and experimental works. In the same report an asymptotic expansion is proposed to prove that even for the smallest speed of the skin of the body, the points of stagnation are removed from the body. The streamlines then form a saddle point configuration, identical to the one originally proposed by Moore, Rott and Sears.

Two experimental investigations in this area have been conducted in the last few years. Huq[92] has measured unsteady

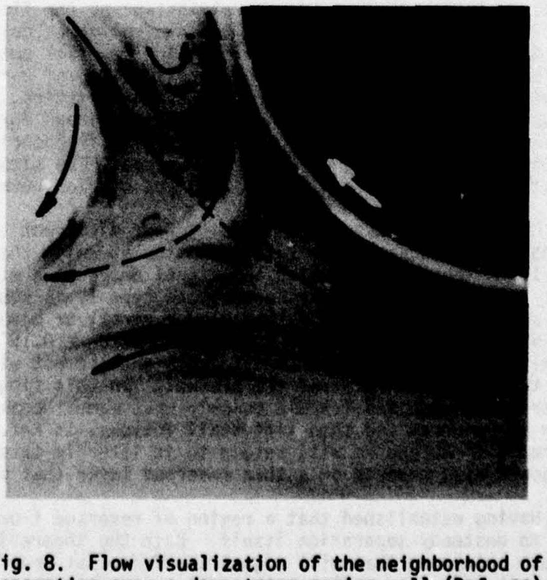

Fig. 8. Flow visualization of the neighborhood of separation over a downstream moving wall (Ref. 93).

boundary layer properties in a towing tank. Using titanium dioxide particles for surface observations, he also looked into the flow around a rotating cylinder. However, due to the small thickness of the viscous region, it appeared difficult to visualize details within the boundary layer. Huq instead directed his attention to the problem of an impulsively started flat plate.

In another effort undertaken at VPI & SU a mixture of glycerin and water was used to achieve thicker boundary layers with not so small velocities. With Reynolds numbers of the order of 100 or 200, laminar wakes permitted the capture of all four of the critical streamlines that form a saddle point at separation. Flow visualization was achieved again by surface pellets. Some preliminary results were reported in Ref. 91. A more detailed description of this work can be found in Ref. 93. The immediate neighborhood of separation over the upstream and the downstream moving walls is given here in Figs. 8 and 9. In these photographs the camera film was exposed for 1/4 of a second and therefore it tracked each particle on a portion of its path. The cylinder has a diameter of 13 cm and it rotates with a surface speed equal to 30% of the mean flow velocity. The area shown in the picture represents approximately 4 cm^2 in the immediate neighborhood of the stagnation points.

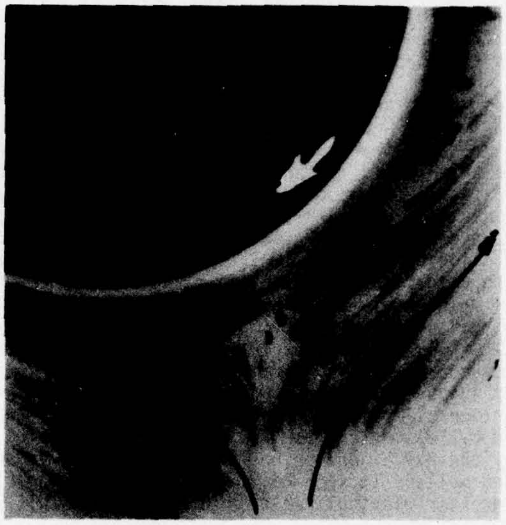

Fig. 9. Flow visualization of the neighborhood of separation over an upstream moving wall (Ref. 93).

Unsteady Separation

A lot of effort has been directed in the last decade towards solving this difficult problem. However many questions remain unanswered. We may be able to state with certainty that the point of zero skin friction is not related to separation in unsteady flows. A large number of numerical calculations (see review articles in Refs. 1, 78, 82) have proved that in unsteady flow one may proceed through the point of zero skin-friction without any evidence of singular behavior. In this way a thin layer of reversed flow may be captured, upstream of the location of separation. At first such arguments did not appear convincing. After all, there is no definite proof that the boundary layer equations contain information about the extent of their own validity. Experimental verification that thin layers of reversed flow can be embedded at the bottom of an attached boundary layer was supplied first by Despard and Miller[83] for oscillatory flows. A similar investigation was reported by Ruiter et al[94].

In their investigation of unsteady stall Carr, McAlister and McCroskey[95] employ a multiplicity of sensing and measuring devices: smoke-flow visualization, surface tufts, hot wire probes and surface-pressure transducers. They observe universally flow reversal on the skin of the airfoil prior to any discernible disturbances of the outer flow or any detectable normal-force or pitching moment deviation. In fact they report that in several instances, the flow at the surface reverses over a major portion of the airfoil before variations in integral force data can be detected. For an airfoil with typical trailing-edge stall characteristics, flow reversal smoothly creeps upstream and eventually reaches the leading-edge of the airfoil before any sign of unsteady separation and stall can be detected. For airfoils with leading-edge stall characteristics, flow reversal seems to be initiated for higher frequencies at the leading-edge of the airfoil and for lower frequencies almost simultaneously over the entire surface of the airfoil. For high frequencies flow reversal originates upstream and travels downstream as the angle of attack increases. The situation is quite complicated for other types of airfoils that appear to have a mixed type of flow reversal characteristics (NACA 0012).

Carr and his associates identify four different types of flow reversing signals as detected by the hot wire probes. Type I is the point at which the hot wire signal indicates an abrupt breakdown. Type II is the point at which the signal drops to a minimum. Type III is defined on the basis of the first fluctuation that reaches zero and type IV is some distinct change in the character of the signal that seems symptomatic of either flow reversal or boundary layer separation. Figure 10 is taken from Ref. 95 and shows for $\alpha = 15 + 10 \sin\omega t$, $\omega x/U_0 = 0.15$ and $Re = 2.5 \times 10^6$, the angle of attack, the normal and pitching moment coefficients and the hot wire signal for different spanwise locations. All four types of flow reversal are present. In this figure the onset of flow reversal appears first near the trailing edge and travels quickly upstream. Moment stall occurs when practically all the boundary layer is reversed and then lift stall follows. In Ref. 95 we find more information about separation and separated flows and we will return to it later in this section. In a paper presented at this conference Kenison[93] also reports on a thin reversed layer that precedes separation in unsteady flows.

Having established that a region of reversed flow may precede the location of separation we now return to unsteady separation itself. Both the theoretical analysis and the experiment require an unambiguous criterion that will signal the fact that separation is occuring. As almost always is the case with unsteady viscous flows, theoretical analysis preceded the experiment. Telionis and Tsahalis[71,97,98] and the group of Nash, Carr, Singleton, Patel and Shruggs[67-70], integrating through the point of zero skin friction, reach a station where all the familiar properties of a separation singularity appear. They in fact study the upstream excursions of the point of zero skin friction which is followed by the point of separation. However no experimental information is available for comparison. As a result there has been some justified criticism. Riley[6] correctly notes that there is some disagreement between the numerical results of Refs. 98 and 100, 101. It is felt however that the work of Proudman and Johnson[98] and Robins and Howarth[99] is not at all in variance with the ideas presented in Ref. 82. Stewartson (private communication) expressed in the past some concern over the numerical results of Ref. 98 whereby a singularity suddenly appears away from the rear stagnation point, in a cylinder started impulsively from rest. In a recent publication Bodonyi and Stewartson[104] examine the unsteady flow on a rotating disk in a counter-rotating fluid and discover that this is indeed possible. They propose mutually consistent numerical and analytical solutions of an unsteady boundary layer flow which is initially well behaved but breaks down after a finite interval of time. Finally in a most recent analytical effort, Schneck[105] employs the Despard and Miller definition to study separation in pulsatile internal flow. He finds that the point of separation moves progressively downstream and towards its stead-state location, as the frequency of oscillation increases.

Carr, McAlister and McCroskey[95] describe in their experimental study the formation of large scale vortices that grow and create large scale disturbances of the potential flow. It appears from their flow visualization that such vortices receive their energy from a shear layer that separates from the skin of the airfoil and rolls over to generate a growing but well organized separated region. Similar experimental studies with unsteady flows over airfoils that indicate the formation of similar vortices have been performed by Ericsson and Reding[106], Maresca, Rebont and Valensi[107], Lang[108] and others.

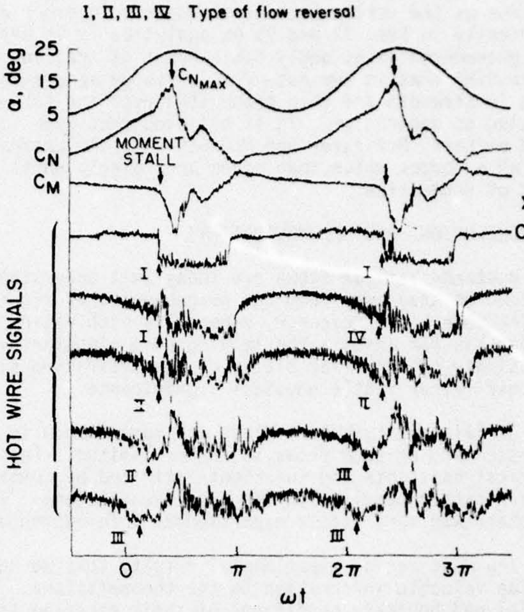

Fig. 10. The angle of attack, coefficients of lift and moment, and the hot wire signals as a function of time for a NACA 0012, $\omega x/U_0 = 0.15$, $Re = 2.5 \times 10^6$ and $\alpha = 15^0 + 10^0 \sin \omega t$ (Ref. 95).

The author, with the support of the Army Research Office, has undertaken an experimental study of unsteady separation and some preliminary findings are reported here. Experiments are being performed in a water tunnel with a long test section to achieve relatively thick boundary layers with not so small velocities. Most favorable conditions for such studies are also achieved by using glycerin-water mixtures. A thin sheet of light illuminates a plane parallel to the mean flow direction. Through the same optical path, a flash of light can also be directed. The flow is visualized via amberlite and pliolite particles which have densities very close to the density of the water. The camera exposes the film for a short period of time, t_0 and the particles appear in the film as short segments of length, say s_i. The average speed of a particle i can be thus approximated by the ratio s_i/t_0, provided that the lengths s_i are sufficiently small. The foot of all these segments is marked by a brighter spot which is accomplished by a strong flash at the beginning of the time interval t_0. In this way the directionality of the flow can be investigated. Dyes are also used in the wake rather than in the mean flow, in contrast with the use of smoke by Carr et al. A more detailed description of the experimental lay-out will be included in a later publication.

The transient flow in the vicinity of separation is thus investigated. Steady separation at two distinct locations, S_I and S_{II}, over a circular arc was accomplished by giving a flap located downstream two extreme positions. Starting with the steady flow that separates at S_I, the flap inclination is then changed impulsively and the transient flow is investigated. In Fig. 11 we show the flow as visualized by the method described above at an instant t = 0.5 sec. after the initiation of the impulsive change. It should be noted that for Reynolds numbers of the order of 1000, the wake of the steady flow is fully

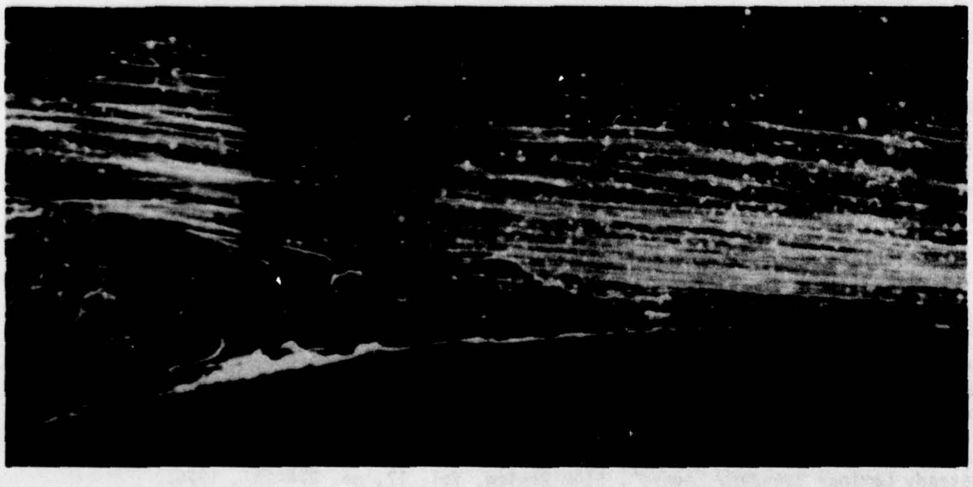

Fig. 11. Flow visualization of the neighborhood of separation for an impulsive change of the pressure distribution.

turbulent and this has been captured in flow visualization photographs. It is therefore quite interesting to note that with the impulsive change of the pressure gradient, a strong vortex is formed in the wake. At the first instant of the flow, the vortex appears to force all the slow moving particles to order themselves, while the location of separation remains unaffected. The boundary of the wake thus thickens as the vortex becomes stronger. In other words there is a time delay similar to the one observed numerically in Ref. 97 and 99 or analytically in Ref. 109. We should also emphasize here the fact that this phenomenon is strongly reminiscent of trailing edge separation as described in Ref. 95. It is very interesting that in our case too, unsteady separation takes the form of a well organized vortex that grows in strength and then propagates over the surface of our rigid body to arrive eventually at the new position of separation. It is believed that even for very large Reynolds numbers, as in the cases examined by Carr, McAlister and McCroskey[95], the unsteadiness reactivates the dead fluid and gives it the form of a vortex which then moves accordingly until its upstream boundary reaches the new location of the point of separation.

5. CONCLUSIONS AND RECOMMENDATIONS

Unsteady laminar flows are today well understood and theory and experiment are in good agreement provided we stay away from the neighborhood of separation. A few weak points in the theory may still require some basic research, especially with regard to the singularities that appear. Such singularities however, as for example the leading edge singularity and its offspring that travels downstream over an impulsively started flat plate, or the separation singularity, etc., are creations of our approximations and bear rather little physical significance.

Oscillating turbulent flows are more common in engineering applications but for the time being, our understanding of such flows is rather limited. The analytical models proposed up to now are based on empirical constants and functions estimated by comparison to steady flows, hence their "postdictions" compare rather poorly with the experimental data. This may be due to the fact that until only a year ago there was very little experimental information available.

The most recent experimental results that we have described in the present paper should definitely provide valuable information to the theoreticians. However the experimentalists should provide accurate initial and boundary conditions of their experiments that are necessary in order to perform calculations. It has been common practice in the past to initialize the theoretical calculations at a certain station far downstream of the leading edge or the stagnation point. Starting with most of the characteristic features of the flow already built-in, it is not surprising that the results, a few stations further downstream, compare favorably with the experimental data. A reliable theoretical model should have the capability to predict the flow, even if integrated from the earlier steps of the shear layer formation. To avoid confusion with unsteady transition and oscillatory disturbances that may be convected downstream, experimentalists may have to trip their boundary layers and make sure that transition is controlled.

Theoretical investigations may soon run into nonlinear phenomena that permit the transfer of energy between the organized and random fluctuations. All of the experimental information on external oscillating turbulent boundary layers pertains to imposed frequencies outside the spectrum of turbulence. However it has been recently pointed out that in the case of a fluctuating jet the externally imposed oscillations transfer energy into the turbulent motion.

Unsteady separation and the determination of the size and shape of the wake or a growing recirculating bubble remains open for investigation. Quite a few recent studies of unsteady flow over airfoils have indicated various unsteady flow patterns and identified the formation of large eddies that grow and propagate over the airfoil. However the physical justification of such phenomena and their analytical prediction appears to be very difficult. Some investigators believe that such phenomena could be reproduced via first order boundary layer theories. No attempt has been made up to now to compare theoretical predictions with experimental data. One of the reasons for failure to attempt such comparison is the fact that all of the available experimental information concerns complex flow fields that involve unsteady transition and unsteady turbulent boundary layers. The work in this direction would require the definition of a simple unsteady flow which could be easily reproduced in the laboratory. Finally, it is the opinion of the present author that transient separation phenomena should be much closer to real-life engineering problems like unsteady stall. Indeed, in most cases, separation performs a rapid excursion and is followed by an overall breakdown of the flow. Oscillatory flow fields with steady separation or separation that oscillates with a small and well controlled manner appear to have little or no engineering importance.

ACKNOWLEDGEMENTS

This work was partially supported by the U. S. Army Research Office under Grant No. DAHC04-75-0067. Miss Maria Romaniuk, one of the author's associates and Mrs. Marlene Taylor have offered great help in preparing this manuscript; the first with criticism and meaningful discussions and the second with editing and typing of the manuscript. Their contribution is gratefully acknowledged.

REFERENCES

1. Telionis, D. P., "Calculations of Time-Dependent Boundary Layers", in Unsteady Aerodynamics, ed. R. B. Kinney, Vol. 1, pp. 155-190, 1975.
2. Stewartson, K., "The Theory of Unsteady Laminar Boundary Layers" in Advances in Applied Mechanics, Vol. 6, pp. 1-37, Academic Press, New York, 1960.
3. Stuart, J. T., "Unsteady Boundary Layers" in Laminar Boundary Layers, L. Rosenhead (ed.), Oxford, pp. 349-406, 1964.
4. Rott, M., "Theory of Time Dependent Laminar Flows", in Theory of Laminar Flows, F. K. Moore (ed.), Princeton University Press, Princeton, N. J., 1964.
5. Stuart, J. T., "Unsteady Boundary Layers" in Recent Research of Unsteady Boundary Layers, E. A. Eichelbrenner (ed.), Vol. 1, pp. 1-46, 1971.
6. Riley, N., "Unsteady Laminar Boundary Layers", SIAM Review, Vol. 17, pp. 274-297, 1975.

7. Wirz, H. J., "Computation of Unsteady Boundary Layers", Lecture Notes in Physics, No. 41, Progress in Numerical Fluid Dynamics, Wirz, H. J., ed., Springer-Verlag, Berlin, pp. 442-476, 1975.
8. McCroskey, W. J., "Some Current Research in Unsteady Fluid Dynamics - The 1976 FREEMAN SCHOLAR LECTURE", Journal of Fluids Eng., Vol. 99, pp. 8-38, 1977.
9. Lighthill, M. J., "The Response of Laminar Skin Friction and Heat Transfer to Fluctuations in the Stream Velocity", Proc. Roy. Soc., Vol. 224A, pp. 1-23, 1954.
10. Lin, C. C., "Motion in the Boundary Layer with a Rapidly Oscillating External Flow", Proc. 9th Int. Congr. Appl. Mech., Brussels, Vol. 4, pp. 155-169, 1956.
11. Moore, F. K., "Unsteady Laminar Boundary-Layer Flow", NACA TN 2471, 1951.
12. Hill, P. G., and Stenning, A. H., "Laminar Boundary Layers in Oscillatory Flow", Journal of Basic Engr., Vol. 82, pp. 593-608, 1960.
13. Patel, M. H., "On Laminar Boundary Layers in Oscillatory Flow", Proc. Royal Soc. Lond., Vol. A347, pp. 99-123, 1975.
14. Karlsson, S. K. F., "An Unsteady Turbulent Boundary Layer", J. Fluid Mech., Vol. 5, pp. 622-636, 1959.
15. Telionis, D. P. and Romaniuk, M. S., "Non-Linear Streaming in Boundary Layer Flow", Proceedings of the 12th Annual Meeting of the Society of Engineering Science, pp. 1169-1180, 1975.
16. Cebeci, T., "Calculation of Unsteady Two-Dimensional Laminar and Turbulent Boundary Layers with Fluctuations in External Velocity", to appear in the Proc. Royal Soc., London.
17. Telionis, D. P. and Romaniuk, M. S., "On the Response of Skin Friction and Heat Transfer to Fluctuating Boundary Layers", AIAA Paper No. 77-235, 1977.
18. Tsahalis, D. Th., and Telionis, D. P., "Oscillating Boundary Layers with Large Amplitude", in Unsteady Flows in Jet Engines, F. O. Carta (ed.), pp. 407-416, 1974.
19. King, W. S., "Low Frequency, Large Amplitude Fluctuations of the Laminar Boundary Layer", AIAA Journal, Vol. 4, pp. 994-1001, 1966.
20. Pedley, T. J., "Two-Dimensional Boundary Layers in a Free Stream Which Oscillates Without Reversing", J. Fluid Mech., Vol. 55, pp. 359-383, 1972.
21. Schneck, D. J. and Walburn, F. J., "Pulsatile Blood Flow in a Channel of Small Exponential Divergence - II Steady Streaming Due to the Interaction of Viscous Effects with Convected Inertia", J. of Fluids Eng., Vol. 98, pp. 707-714, 1976.
22. Ostrach, S., "Compressible Laminar Boundary Layer and Heat Transfer for Unsteady Motions of a Flat Plate", NACA TN 3569, 1955.
23. Moore, F. K. and Ostrach, S., "Displacement Thickness of the Unsteady Boundary Layer", Journal of the Aeronautical Sciences, Vol. 124, pp. 77-85, 1957.
24. Illingworth, C. R., "The Effects of a Sound Wave on the Compressible Boundary Layer on a Flat Plate", Journal of Fluid Mechanics, Vol. 3, pp. 471-493, 1958.
25. Gribben, R. J., "The Laminar Boundary Layer on a Hot Cylinder Fixed in a Fluctuating Stream", Journal of Applied Mechanics, Vol. 28, pp. 339-346, 1961.
26. Gribben, R. J., "The Fluctuating Flow of a Gas Near a Stagnation Point on a Hot Wall", Journal of Applied Mechanics, Vol. 38, pp. 820-828, 1971.
27. Vimala, C. S. and Nath, G., "Unsteady Laminar Boundary Layers in a Compressible Stagnation Flow", Journal of Fluid Mechanics, Vol. 70, pp. 561-572, 1975.
28. Sarma, G. N., "A General Theory of Unsteady Compressible Boundary Layers with and without Suction or Injection", Proceedings of the Cambridge Philosophical Society, Vol. 61, pp. 975-807, 1965.
29. Telionis, D. P. and Gupta, T. R., "Unsteady Heat Convection in Three Dimensional Compressible Flow", XXVIth Congress of the International Astronautical Federation, Portugal, 1975, Paper No. 75-047, also to appear in Acta Astronautica.
30. Telionis, D. P. and Gupta, T. R., "Compressible Oscillating Boundary Layers", AIAA Journal, Vol. 15, pp. 974-983, 1977.
31. Sparrow, E. M. and Gregg, J. L., "Nonsteady Surface Temperature Effects on Forced Convection Heat Transfer", Journal of the Aero. Science.
32. Watkins, C. B., "Heat Transfer in the Laminar Boundary Layer Over an Impulsively Started Flat Plate", Journal of Heat Transfer, pp. 482-484, 1975.
33. Karvinen, R., "Steady State and Unsteady Heat Transfer Between a Fluid and a Flat Plate with Coupled Convection, Conduction and Radiation", Acta Poly. Scandinavica, Mech. Eng. Ser. No. 73, 1976.
34. Ackerberg, R. C., and Phillips, J. H., "The Unsteady Laminar Boundary Layer on a Semi-Infinite Plate Due to Small Fluctuations in the Magnitude of the Free-Stream Velocity", J. Fluid Mech., Vol. 51, pp. 137-157, 1972.
35. Lam, S. H. and Rott, N., "Theory of Linearized Time-Dependent Boundary Layers", Cornell Univ. GSAE Rep. AFOSR TN-60-1100, 1960.
36. Brown, S. N. and Stewartson, K., "On the Propagation of Disturbances in a Laminar Boundary Layer, II", Proc. Cambridge Philos. Soc., Vol. 73, pp. 505-514, 1973.
37. Brown, S. N. and Stewartson, K., "On the Propagation of Disturbances in a Laminar Boundary Layer. I", Ibid., Vol. 73, pp. 493-504, 1973.
38. Ackerberg, R. C., private communication.
39. Fogarty, L. E., "The Laminar Boundary Layer on a Rotating Blade", J. Aerospace Sciences, Vol. 18, p. 247, 1951.
40. Rott, N. and Smith, W. E., "Some Examples of Laminar Boundary Layer Flow on Rotating Blades", J. Aerospace Sciences, Vol. 23, p. 991, 1956.
41. McCroskey, W. J. and Yaggy, P. F., "Laminar Boundary Layers on Helicopter Rotors in Forward Flight", AIAA J., Vol. 6, p. 1919, 1968.
42. Young, W. H., and Williams, J. C., "The Boundary Layer on Rotating Blades in Forward Flight", AIAA Paper No. 70-49, 1970.
43. Young, W. H. and Williams, J. C., "Boundary-Layer Separation on Rotating Blades in Forward Flight", AIAA Journal, Vol. 10, pp. 1613-1619, 1972.
44. Gupta, T. R. and Telionis, D. P., "Cross Flow Effects in Oscillating Boundary Layers", Proceedings of Heat Transfer and Fluid Mechanics Institute, pp. 420-435, 1976.
45. Young, W. H., private communication.
46. Afzal, N. and Rizvi, S. M. A., "Second-Order Unsteady Stagnation-Point Boundary-Layer Solutions", AIAA Journal, Vol. 15, pp. 1051-1053, 1977.

47. McCroskey, W. J., "Some Current Research in Unsteady Aerodynamics - A report from the Fluid Dynamics Panel: AGARD Propulsion and Energetics Panel, California, 1976.
48. Acharya, M. and Reynolds, W. C., "Measurements and Predictions of a Fully Developed Turbulent Channel Flow with Imposed Controlled Oscillations", Stanford University, Thermosciences Division, Technical Report, TF-8, 1975.
49. Houdeville, R., Desopper, A. and Cousteix, J., "Experimental Analysis of Average and Turbulent Boundary Layer, ONERA TP, No. 30, 1976, also Rech. Aerosp. No. 1976-4.
50. Schachanemann, A. A. and Rockwell, D. A., "Oscillating Turbulent Flow in a Conical Diffuser", J. of Fluids Eng., Vol. 98, pp. 695-702, 1976.
51. Soutif, M., Favre-Marinet, M., Binder, G., "Diffusion and Periodic Structure of Flapping Jets", to appear.
52. Townsend, A., The Structure of Turbulent Shear Flow, Cambridge Univ. Press, 1956.
53. Phillips, D. M., The Dynamics of the Upper Ocean, Cambridge University Press, 1967.
54. Cousteix, J., Desopper, A. and Houdeville, R., "Recherches Sur les Couches Limites Turbulentes Instationnaires, ONERA TP No. 147, 1976.
55. Cousteix, J., Desopper, A. and Houdeville, R., "Structure and Development of a Turbulent Boundary Layer in an Oscillatory External Flow", ONERA TP 14, 1977; also presented at the Symposium on Turbulent shear Flows, Penn. State University, Pennsylvania, April 1977.
56. Patel, M. H., "On Turbulent Boundary Layers in Oscillatory Flow", Proc. Royal Soc., Vol. A353, pp. 121-144, 1977.
57. Klebanoff, P. S., "Characteristics of Turbulence in a Boundary Layer with Zero Pressure Gradient", NACA TN 3178, 1954.
58. Telionis, D. P. and Tsahalis, D. Th., "Oscillating Laminar Boundary Layers and Unsteady Separation", AIAA J., Vol. 12, pp. 1469-1476, 1974.
59. Charnay, G. and Mathieu, J., "Periodic Flow in a Wind Tunnel Produced by Rotating Shutters", Journal of Fluids Engineering, Trans. ASME, Series I, Vol. 98, No. 2, pp. 278-283, June 1976.
60. Satyanarayana, B., "Some Aspects of Unsteady Flow Past Airfoils and Cascades", AGARD Conference Proc. No. 177, Unsteady Phenomena in Turbomachinery, Paper No. 25, Sept. 1975.
61. Thomas, L. C. and Shukla, R. K., "Theoretical and Experimental Study of Wall Region Periodicity for Turbulent Pulsatile Flow", J. Fluids Eng., Vol. 98, pp. 27-32, 1976.
62. Binder, G. and Didelle, H., "Improvement of Ejector Thrust Augmentation by Pulsating of Flapping Jets", 2nd Symposium on Jets Pumps and Ejectors and Gas Lift Techniques, Paper No. E2, 1975.
63. Mainardi, H. and Panday, P. K., "A Study of Turbulent Pulsating Flow in a Circular Pipe", to appear.
64. Mainardi, H., Barriol. R. and Panday, P. K., "Characteristics of an Orifice Plate in Pulsating Flow", Int. J. of Mass Transfer, to appear.
65. Miller, J. A., "Heat Transfer in the Oscillating Turbulent Boundary Layer", ASME Paper No. 69-67-34, 1969.
66. Telionis, D. P., "On the Dynamics of Eddy Viscosity Models for Turbulent Boundary Layers", Archives of Mechanics, Vol. 28, pp. 997-1010, 1976.
67. Nash, J. F. and Patel, V. C., "Calculations of Unsteady Turbulent Boundary Layers with Flow Reversal", NASA CR-2546, 1975.
68. Patel, V. C., and Nash, J. F., "Unsteady Turbulent Boundary Layers with Flow Reversal", in Unsteady Aerodynamics, ed. R. B. Kinney, Vol. 1, 1975.
69. Patel, V. C. and Nash, J., "Some Solutions of the Unsteady Turbulent Boundary Layer Equations", in Recent Research on Unsteady Boundary Layers, ed. A. F. Eichelbrenner, 1972.
70. Nash, J. F., "Further Studies of Unsteady Boundary Layers with Flow Reversal", NASA CR-2767, 1976.
71. Telionis, D. P. and Tsahalis, D. Th., "Unsteady Turbulent Boundary Layers and Separation", AIAA Journal, Vol. 14, pp. 468-474, 1975.
72. Kuhn, G. D. and Nielsen, J. N., "Studies of an Integral Method for Calculating Time Dependent Turbulent Boundary Layers", Nielsen Engineering and Research, Inc., Rept. NEAR TR 57, 1973.
73. Nash, J. F., Carr, L. W. and Singleton, R., "Unsteady Turbulent Boundary Layers in Two-Dimensional Incompressible Flow", AIAA J., No. 13, pp. 167-172, 1975.
74. McCroskey, W. J. and Philippe, J. J., "Unsteady Viscous Flow on Oscillating Airfoils", AIAA J., No. 13, pp. 71-79, 1975.
75. Reynolds, W. C., "Computation of Turbulent Flows", in Annual Review of Fluid Mechanics, Vol. 8, pp. 183-208, 1976.
76. Telionis, D. P. and Romaniuk, M. S., "Deterministic and Random Disturbances on a Boundary Layer", to appear.
77. Brown, S. N. and Stewartson, K., "Laminar Separation" in Annual Rev. of Fluid Mech., W. R. Sears (ed.), Vol. 1, pp. 45-72, 1969.
78. Williams, J. C., "Incompressible Boundary-Layer Separation", in Annual Review of Fluid Mechanics, Vol. 9, 1977.
79. Sears, W. R., "Some Recent Developments in Airfoil Theory", J. Aero. Sci., Vol. 23, pp. 490-499, 1956.
80. Rott, N., "Unsteady Viscous Flow in the Vicinity of a Stagnation Point", Quart. J. Appl. Math., Vol. 13, pp. 444-451, 1956.
81. Moore, F. K., "On the Separation of the Unsteady Laminar Boundary Layer", in Boundary Layer Research, Proc. Symp. of Int. Union of Theoret. and Appl. Mech., H. Gortler (ed.), pp. 296-311, 1957.
82. Sears, W. R. and Telionis, D. P., "Boundary Layer Separation in Unsteady Flow", Presented at the Int. Symp. in honor of the 70th Birthday of Prof. Sydney Goldstein, Haifa, Israel, 1973; also SIAM Journal of Appl. Math., Vol. 28, pp. 215-135, 1975.
83. Despard, R. A. and Miller, J. A., "Separation in Oscillating Boundary-Layer Flows", Journal Fluid Mech., Vol. 47, pp. 21-31, 1971.
84. Sears, W. R. and Telionis, D. P., "Unsteady Boundary-Layer Separation" in Recent Research of Unsteady Boundary Layers, E. A. Eichelbrenner (ed.), Vol. 1, pp. 404-447, 1971.
85. Telionis, D. P. and Werle, M. J., "Boundary Layer Separation from Downstream Moving Boundaries", Journal Appl. Mech., Vol. 40, No. 2, pp. 369-374, 1973.
86. Williams, J. C., III and Johnson, W. D., "Semi-similar Solutions to Unsteady Boundary-Layer Flows Including Separation", AIAA Journal, Vol. 12, pp. 1388-1393, 1974.
87. Williams, J. C., III and Johnson, W. D., "Note on Unsteady Boundary-Layer Separation", AIAA Journal, Vol. 12, pp. 1427-1429, 1974.

88. Telionis, D. P., "A Comment on Some Falkner-Skan Solutions", Journal of Fluids Eng., Vol. 97, pp. 117-118, 1975.
89. Fansler, K. S. and Danberg, J. E., "Boundary-Layer Spearation on Moving Walls Using an Integral Theory", AIAA Journal, Vol. 15, pp. 274-276, 1977.
90. Tsahalis, D. Th., "Laminar Boundary Layer Separation from an Upstream Moving Wall", AIAA Journal, Vol. 15, pp. 561-566, 1977.
91. Telionis, D. P., "Critical Points and Streamlines in Viscous Flows", Virginia Polytechnic Institute and State University Engineering Report, VPI-E-76-28, 1976.
92. Huq, R., "An Experiment for Quantitative Visualization of Boundary-Layer Flow", Masters Thesis, Cornell University, 1975.
93. Telionis, D. P. and Koromilas, C., "Separation and Wake Phenomena over Moving Boundaries", presented at the XIII Biennial Fluid Dynamics Symposium, Poland, September 1977.
94. Ruiter, G. H., Nagib, H. M. and Fejer, A. A., "Unsteady Boundary-Layer Separation over Oscillating Airfoils", Fluid Dynamics of Unsteady, Three-Dimensional and Separated Flows, F. J. Marshall, ed., Atlanta, Georgia; pp. 423-426, 1971.
95. Carr, L. W., McAlister, K. W. and McCroskey, W. J., "Analysis of the Development of Dynamic Stall Based on Oscillating Airfoil Experiments", NASA TN D-8382, 1977.
96. Kenison, R. C., "An Experimental Study of the Effect of Oscillatory Flow on the Separation Region in a Turbulent Boundary Layer", contribution to the present symposium.
97. Telionis, D. P. and Tsahalis, D. Th., "The Response of Unsteady Boundary-Layer Separation to Impulsive Changes of Outer Flow", AIAA Journal, Vol. 12, pp. 614-619, 1974.
98. Telionis, D. P. and Tsahalis, D. Th., "Unsteady Laminar Separation over Impulsively Moved Cylinders", Acta Astronautica, Vol. 1, pp. 1487-1505, 1974.
99. Nash, J. F., Carr, L. W. and Singleton, R., "Unsteady Turbulent Boundary Layers in Two-Dimensional Incompressible Flow", AIAA Journal, Vol. 13, pp. 167-172, 1975.
100. Belcher, R. J., Burggraf, O. R., Cooke, J. C., Robins, A. J. and Stewartson, K., "Recent Research on Unsteady Boundary Layers", Laval University Press, Quebec, Canada, pp. 1444-1466, 1972.
101. Collins, W. M. and Dennis, S. C. R., "Flow Past an Impulsively Started Circular Cylinder", Journal Fluid Mech., Vol. 60, pp. 105-128, 1973.
102. Proudman, I. and Johnson, K., "Boundary-Layer Growth Near a Rear Stagnation Point", Journal Fluid Mech., Vol. 12, pp. 161-168, 1962.
103. Robins, A. J. and Howarth, J. A., "Boundary-Layer Development at a Two-Dimensional Rear Stagnation Point", Journal Fluid Mech., Vol. 56, pp. 161-171, 1972.
104. Bodonyi, R. J. and Stewartson, K., "The Unsteady Laminar Boundary Layer on a Rotating Disk in a Counter-Rotating Fluid", Journal Fluid Mech., Vol. 79, pp. 669-688, 1977.
105. Schneck, D. J., "Pulsatile Blood Flow in a Channel of Small Exponential Divergence - III. Unsteady Flow Separation", Journal of Fluids, Eng., Vol. 99, pp. 333-338, 1977.
106. Ericson, L. E. and Reding, J. P., "Dynamic Stall Analysis in Light of Recent Numerical and Experimental Results", AIAA Paper No. 75-26, 1975.
107. Maresca, C., Rebont, J. and Valensi, J., "Caracteristiques Aerodynamiques d'un Profil d Aile en Mouvement Instationnaire", 14th International Congress of Theoretical and Applied Mechanics, The Netherlands, 1976.
108. Lang, J. D., "The Dynamics of a Growing Separation Region on an Airfoil", Air Force Systems Command, Report No. SRL-TR-75-0005, 1975.
109. Buckmaster, J., "The Unsteady Evolution of the Singularity at Separation", Journal Eng. Math., Vol. 7, pp. 223-230, 1973.

COMMENT

by

M.H.Patel
Dept. of Mechanical Engineering
University College London
Torrington Place
London WC1E 7JE

It is not clear from the review paper that the response of the oscillating turbulent boundary layer to purely time-dependent free stream oscillations is inherently different from the response to oscillations incorporating a travelling-wave type convection velocity. This point can be best illustrated by considering the free stream equations for two simple oscillatory conditions. The purely time-dependent free stream velocity can be written as

$$V = V_0 + V_1 e^{i\omega t} \tag{1}$$

while, for the travelling wave type, we have

$$V = V_0 + V_1 e^{i\omega(t-x/Q)} \tag{2}$$

using a constant mean free stream velocity, V_0. Equation (2) incorporates an oscillatory component of free stream velocity which varies with downstream distance, x, while Equation (1) is only a special form of (2), with $Q \to \infty$. If Equation (2) is substituted into the free stream terms of the boundary layer equations, we have for the first order perturbation terms

$$\frac{\partial V}{\partial t} + V\frac{\partial V}{\partial x} = i\omega V_1 e^{i\omega(t-x/Q)} - i\omega \frac{V_0}{Q} V_1 e^{i\omega(t-x/Q)} \tag{3}$$

There are several deductions arising from this equation. For the purely time-dependent free stream oscillation, with $Q \to \infty$, the second term on the right-hand side of Equation (3) vanishes. Then, the free stream forcing term in the boundary layer equations (or the oscillating pressure gradient) leads the free stream by 90° and results in the velocity phase leads within the boundary layer which have been observed for this case by so many researchers. For the travelling-wave type of free stream oscillation, however, if $Q < V_0$, then the second term on the right-hand side of Equation (3) is dominant and the oscillating pressure gradient lags the free stream by 90°. This gives rise to a velocity phase lag within the boundary layer as is reported in References 13 and 56 of the review paper for both laminar and turbulent boundary layers. This point needs to be made especially clear for the results reproduced in Figure 1 of the review paper.

Furthermore, for the travelling-wave type of free stream, with $Q < V_0$, the oscillating pressure gradient tends to have larger amplitudes then for the case with $Q \to \infty$. This leads to higher overshoots in velocity amplitude since, for $Q < V_0$, the accelerative influence of the oscillating pressure gradient on the slower-moving fluid within the boundary layer is proportionately greater. These higher overshoots are a feature of both laminar and turbulent flows as reported for the experiments in Reference 13 and 56.

The major conclusion to be drawn here is that the response of an unsteady laminar or turbulent boundary layer can be drastically affected if a time dependent component of the free stream velocity varies significantly with distance downstream.

There appears to be an error in Figure 5 of the review paper. Here, two significantly different curves are presented from Reference 56 for the longitudinal turbulence intensity distributions within the boundary layer. However, in the work reported in Reference 56, no consistent difference was found, within the constraints of experimental error, between the steady flow and time averaged turbulence intensities for the oscillating turbulent boundary layer. It is not clear how the curves of Figure 5 were obtained from Reference 56.

It is stated in the review paper that, for the laminar boundary layer calculations reported in Reference 13, the validity of the boundary layer equations could impose an upper bound on frequency, ω, when the travelling wave length is of the same order as the boundary layer thickness. This is certainly true but in the numerical example given, for $L \sim 0.25$ m, $V_0 = 10$ m/s and $Q/V_0 = 0.77$, $\omega L/V_0 \sim 5$ gives, in fact, a wavelength of 0.24 m which is hardly of the same order as the boundary layer thickness. For the data reported in Reference 13, the ratio of travelling wave length to mean boundary layer thickness has a minimum value of 200 for the experiments and a minimum value of 40 for the theory at the highest frequency parameter presented, $\omega L/V_0 = 8$.

Finally, I have a comment regarding the calculations reported around Equations 3.17 to 3.19 of the review paper. It is suggested that the lack of a predicted overshoot was not a consequence of the turbulence model but due to the fact that the laminar sublayer and the buffer regions between it and the fully turbulent flow were not modelled sufficiently well. It is instructive that the only calculation which gave Telionis and his coworkers anything close to a realistic overshoot was the quasi-laminar model reported in the review paper for Reference 72. This kind of calculation would have come closest to modelling the region very near the wall in a realistic manner.

RÉSULTATS EXPÉRIMENTAUX ET MÉTHODES DE CALCUL RELATIFS AUX COUCHES LIMITES TURBULENTES EN ÉCOULEMENT INSTATIONNAIRE

par Jean COUSTEIX, Robert HOUDEVILLE, André DESOPPER

Office National d'Etudes et de Recherches Aérospatiales (ONERA)
Centre d'Etudes et de Recherches de Toulouse (CERT)
31055 Toulouse, France

RESUME

On présente l'étude expérimentale d'une couche limite turbulente se développant en présence d'un écoulement extérieur pulsé.

Pour analyser séparément la composante périodique de la vitesse et sa fluctuation turbulente, une analyse statistique des données provenant d'anémomètres à fil chaud est mise en jeu.

Parallèlement, une méthode de résolution des équations locales a été mise au point en utilisant soit un schéma de longueur de mélange, soit un système d'équations de transport. Une technique pratique faisant appel à la résolution des équations globales est également présentée.

Le problème du décollement ou de la formation de singularités dans le calcul de couche limite à vitesse extérieure imposée est abordé en utilisant la méthode intégrale.

EXPERIMENTAL RESULTS AND CALCULATING METHODS CONCERNING TRANSITIONAL AND TURBULENT BOUNDARY LAYERS IN UNSTEADY FLOW

A turbulent boundary layer developing in an oscillating external flow is experimentally studied.

We analyse the periodic component and the turbulent fluctuation of the velocity separately with the aid of a statistical treatment of data from hot wire anemometers.

We also present a numerical method for solving the local equations by using a mixing length scheme or a transport equation model. An integral method of prediction is also used.

The question of separation or of occurence of singularities in the boundary layer calculation with an imposed external velocity are approached by using the integral method.

1 - INTRODUCTION

Dans une étude systématique que nous avons entreprise sur les effets de pulsation de l'écoulement sur le développement d'une couche limite turbulente, deux buts essentiels ont été poursuivis :

- Obtenir à partir de l'expérience des renseignements détaillés relatifs aux effets de l'instationnarité sur les caractéristiques de la couche limite. Il s'agit là en fait d'une étude fondamentale destinée à préciser la structure de la turbulence en écoulement pulsé et réalisée à l'aide d'une méthode d'analyse statistique permettant d'étudier séparément les composantes moyenne et aléatoire de la vitesse.
- Utiliser les conclusions de cette étude expérimentale à la fois comme support pour établir les hypothèses à mettre en oeuvre dans l'établissement de méthodes de calcul et comme moyen de contrôle de la validité des résultats auxquels elles conduisent. Plusieurs méthodes ont été mises en oeuvre.

L'une, de type intégral, est déduite très simplement d'une méthode établie antérieurement en stationnaire.
Deux autres font intervenir la résolution des équations locales où l'on utilise soit un schéma de longueur de mélange, soit un modèle d'équations de transport pour l'énergie cinétique de turbulence et pour son taux de dissipation.

D'autres problèmes importants sont ceux du décollement, de l'apparition de singularités dans le calcul de la couche limite et des conditions de leur formation. Une méthode d'analyse de ces problèmes est proposée quand on utilise la méthode intégrale.

2 - CONDITIONS DE L'ETUDE EXPERIMENTALE EFFECTUEE.

2.1 - Le montage expérimental

Un écoulement instationnaire périodique est créé à l'aide d'un papillon tournant dans le diffuseur d'une soufflerie subsonique (Fig. 1).

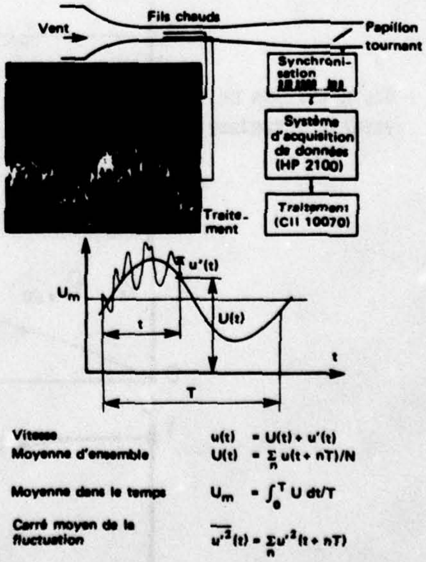

Vitesse $u(t) = U(t) + u'(t)$
Moyenne d'ensemble $U(t) = \sum_n u(t+nT)/N$
Moyenne dans le temps $U_m = \int_0^T U\,dt/T$
Carré moyen de la fluctuation $\overline{u'^2}(t) = \sum_n u'^2(t+nT)$

FIG. 1 : DISPOSITIF EXPERIMENTAL.

Le développement de la couche limite est étudié le long du plancher de la veine dont la section rectangulaire a pour dimensions 100 mm X 110 mm. Les mesures de vitesse sont effectuées au moyen d'anémomètres à fil chaud à température constante. Une sonde, immobile dans l'écoulement extérieur, est utilisée comme référence. Elle est placée à l'aplomb d'une seconde sonde qu'on peut déplacer perpendiculairement à la paroi pour explorer la couche limite. Quatre stations ont été sondées ; si $X_1 = 0$ est l'abscisse de la première, les autres sont $X_2 = 70$ mm, $X_3 = 140$ mm, $X_4 = 210$ mm.

Les tensions de sortie des anémomètres sont d'abord enregistrées sous forme numérique sur une bande magnétique ; elles sont ensuite traitées sur ordinateur.

2.2 - Exploitation des données.

Le traitement consiste d'abord à transformer la tension en grandeur physique en utilisant la loi d'étalonnage ; il consiste ensuite à effectuer une analyse statistique des données qui permettra d'étudier séparément la composante moyenne de la vitesse et sa fluctuation. Une moyenne est entendue ici au sens moyenne d'ensemble déterminée à partir d'un grand nombre de réalisations du même phénomène. Contrairement au cas d'un écoulement stationnaire il est clair que moyenne d'ensemble et moyenne dans le temps ne sont pas équivalentes.

Puisque l'écoulement est périodique, chaque période constitue une réalisation particulière du même phénomène. Si la fréquence de pulsation est faible devant les temps caractéristiques de la turbulence, on peut considérer de plus que deux mesures espacées d'une période sont pratiquement indépendantes l'une de l'autre. Ainsi, pour calculer par exemple la moyenne U de la vitesse instantannée u, nous faisons la somme des valeurs prises par u à des instants correspondant, dans les périodes successives, à un angle de phase identique dans la période de l'écoulement extérieur.

Le repérage de l'angle de phase est assuré par un système de synchronisation par cellule photoélectrique, directement lié à la rotation du papillon. Ce système délivre un train d'impulsions découpant la période en 24 intervalles et il pilote la chaîne d'acquisition de données en agissant comme horloge externe : on enregistre ainsi les mesures à des instants bien déterminés dans la période.

La fluctuation u', dont la moyenne d'ensemble est nulle, est calculée par différence entre U et u. Elle est analysée séparément à l'aide par exemple de son écart type $(\overline{u'^2})^{1/2}$ calculé aussi à partir d'une moyenne d'ensemble ; elle est analysée aussi à l'aide de moments d'ordre supérieur ou encore par sa densité de probabilité.

A l'aide de sondes à fils croisés, nous avons aussi mesuré la composante transversale $\overline{v'^2}$ et la tension turbulente $-\rho\overline{u'v'}$

2.3 - Conditions d'écoulement extérieur.

Deux configurations ont été étudiées, différant essentiellement l'une de l'autre par les distributions de la vitesse extérieure, représentées sur la figure 2 à l'aide de l'analyse harmonique. Dans les deux cas la fréquence a été choisie de telle façon que la distorsion harmonique soit très faible.

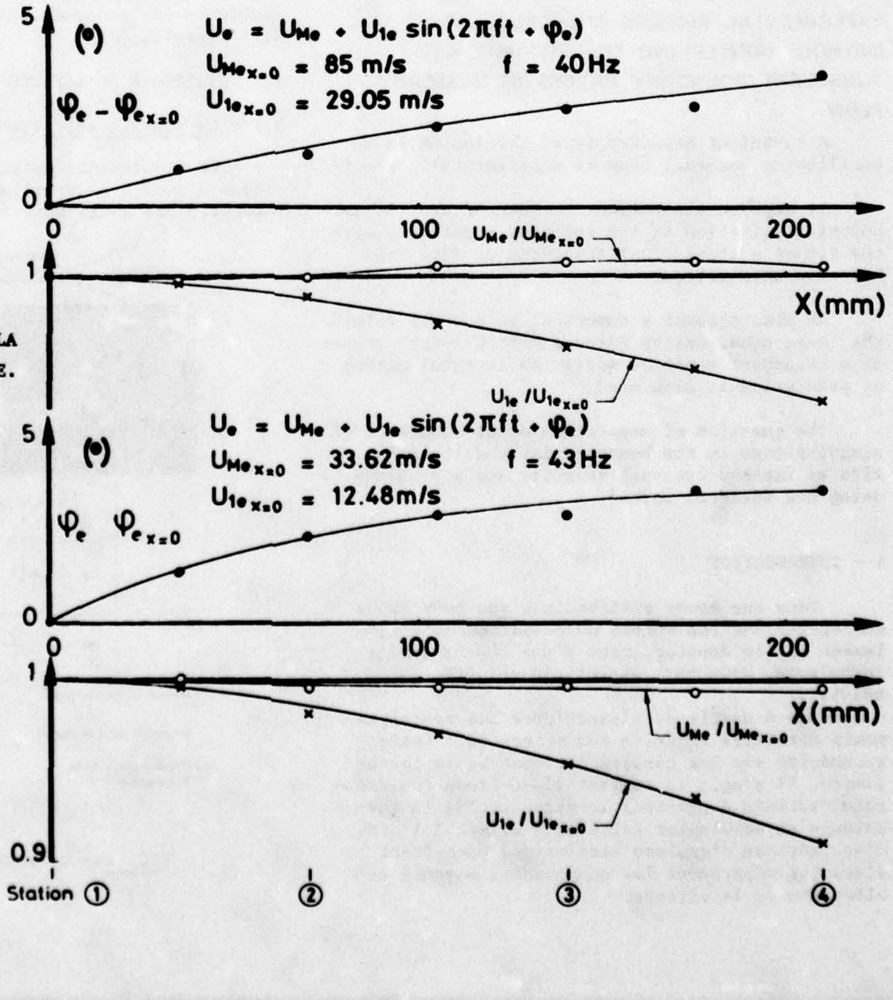

FIG. 2 : DISTRIBUTIONS DE LA VITESSE EXTERIEURE.

A un instant donné, la vitesse extérieure n'est pas constante : il se forme en effet un système d'ondes qui se réfléchissent et interfèrent. Entre le premier et le dernier point de mesure, on note un déphasage de l'ordre de 4° correspondant à une vitesse de convection de l'onde de l'ordre de 770 m/s, c'est à dire très supérieure à la vitesse moyenne de l'écoulement.

L'analyse harmonique montre aussi que la composante continue de la vitesse extérieure varie peu alors que l'amplitude décroît d'environ 10 %.

Pour les deux configurations étudiées l'amplitude relative de variation de la vitesse extérieure est du même ordre de grandeur : elle est voisine de 35 %.Les deux configurations diffèrent par les valeurs du nombre de Reynolds et du nombre de Strouhal :

Configuration 1 : $X_\omega = \frac{\omega X}{U_{Me}} = 2,5 \qquad R_{ex} = \frac{U_{Me} X}{\nu} = 4\,10^6$

Configuration 2 : $X_\omega = 5 \qquad R_{ex} = 10^6$

La distance X intervenant ici est une distance fictive nécessaire au développement d'une couche limite stationnaire sans gradient de pression, dont l'épaisseur serait l'épaisseur moyenne de la couche limite instationnaire à la première station de sondage.

Dans les deux cas le taux de turbulence $(\overline{u'^2})^{1/2} / U$ de l'écoulement extérieur est de l'ordre de 7%.

3 - ANALYSE DES RESULTATS.

3.1 - Oscillogrammes.

Une première analyse qualitative du comportement de la couche limite est l'observation de l'enregistrement du signal de sortie de l'anémomètre. Dans les deux configurations les observations sont identiques et nous donnons ici seulement les oscillogrammes correspondant à la deuxième configuration (Fig. 3).

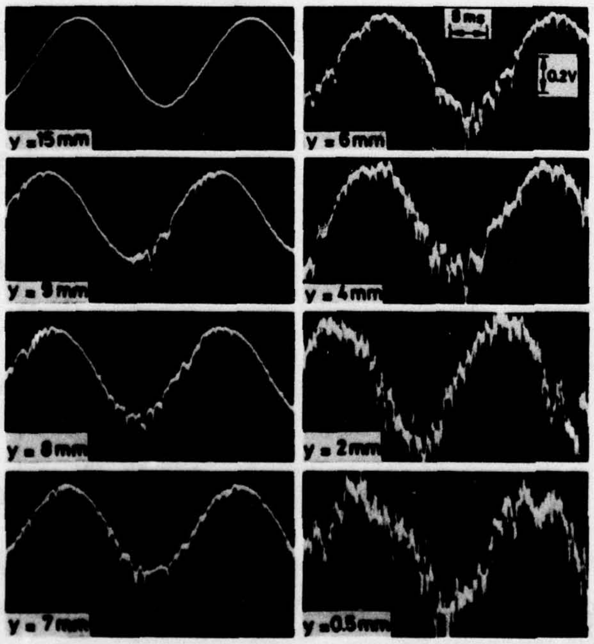

FIG. 3 : SIGNAL DE L'ANEMOMETRE.

Près de la paroi, le signal est formé de fluctuations importantes superposées à une tendance moyenne périodique. Un peu plus loin de la paroi, ces fluctuations sont nettement dissymétriques et apparaissent comme des pics dirigés vers les valeurs négatives. De plus, il est clair que ces fluctuations se localisent dans une partie bien délimitée de la période. Cette dernière observation s'explique par une variation périodique forcée de la frontière libre de la couche limite : périodiquement la sonde se trouve plongée dans la couche limite où l'intensité de turbulence est plus importante que dans l'écoulement extérieur. Ce mouvement contrôlé de la frontière de couche limite se superpose en fait à un mouvement aléatoire qui fait l'objet de nombreuses études en écoulement stationnaire.

L'étude expérimentale que nous allons décrire est consacrée en grande partie maintenant à l'analyse des phénomènes suggérés par l'observation de ces photographies.

3.2 - Vitesses moyennes.

La vitesse moyenne U a été déterminée comme moyenne d'ensemble sur 600 périodes. Elle dépend de trois variables indépendantes x, y, t. Aussi pour avoir une image précise de son évolution nous avons utilisé deux types de représentation.

Evolution de U en fonction du temps. Analyse harmonique.

La réponse de la couche limite à la perturbation extérieure peut être étudiée simplement à l'aide de l'analyse harmonique de la vitesse moyenne. Sur la figure 4 nous présentons les résultats de cette analyse en nous limitant à ceux concernant la fréquence fondamentale.

On note d'abord que les profils de la composante continue U_M / U_{Me} sont voisins pour les deux configurations étudiées. L'allure et les caractéristiques de ce profil sont d'ailleurs très sensiblement celles que l'on aurait pour une couche limite stationnaire de plaque plane. Ceci confirme le fait noté aussi par d'autres auteurs [4 - 6] que les termes non linéaires n'ont qu'une faible influence sur la composante continue de la vitesse.

L'analyse harmonique montre aussi que dans la région externe de la couche limite, l'amplitude de la composante en phase est supérieure à la valeur imposée à l'écoulement extérieur. Ceci peut s'expliquer en considérant le tracé de l'évolution de U en fonction du temps à différentes altitudes dans la couche limite (Fig. 4) et en remarquant, comme nous le verrons plus loin, que la variation forcée d'épaisseur de couche limite est grossièrement en opposition de phase avec la vitesse extérieure. Comparons en effet les courbes tracées pour y = 15 mm et y = 4 mm : à l'instant t/T = 0.5 l'épaisseur de couche limite est voisine de son minimum alors qu'à l'instant t/T = 1 elle est voisine de son maximum ; ainsi pour y = 4 mm U est plus voisin de U_e à l'instant t/T = 0.5 qu'à l'instant t/T = 1 et l'amplitude de U en y = 4 mm est supérieure à celle de U_e.

On remarque aussi que le profil de la composante en phase et le maximum du déphasage sont décalés vers les valeurs plus faibles de y pour la deuxième configuration. Ceci est imputable certainement à la variation du nombre de Strouhal. Il est connu en effet que le rapport de l'épaisseur de la couche instationnaire, c'est à dire de la région où les effets instationnaires sont significatifs, à l'épaisseur moyenne de la couche limite, décroît quand le nombre de Strouhal augmente ; quand le nombre de Strouhal devient très grand les effets instationnaires sont confinés à une couche très mince près de la paroi.

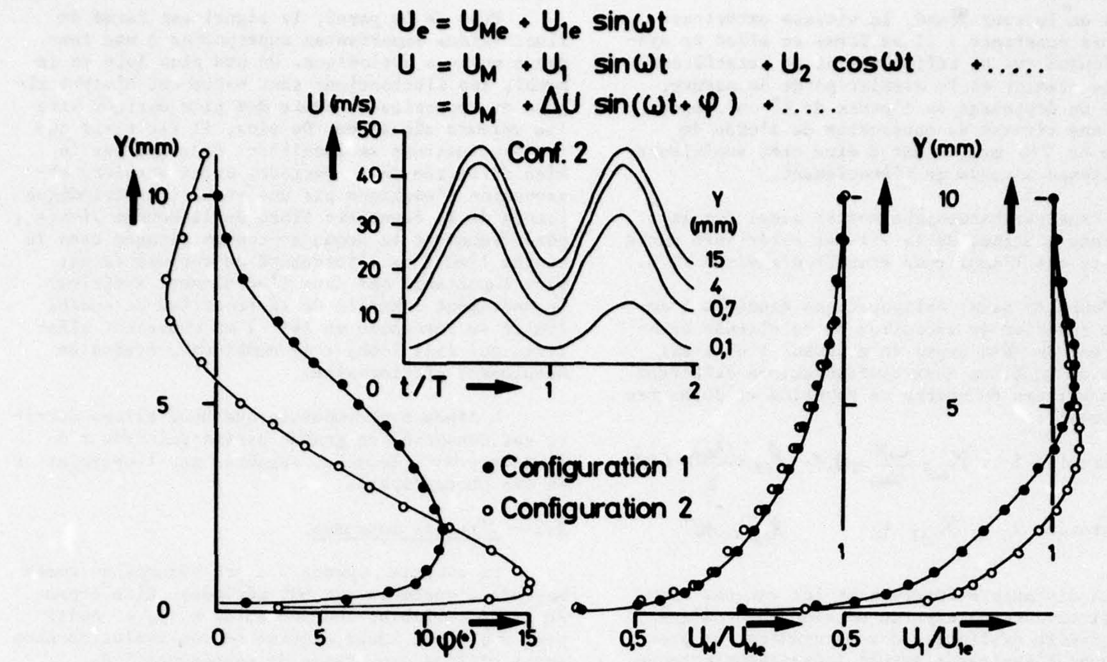

FIG. 4 : ANALYSE HARMONIQUE DE LA VITESSE MOYENNE (station 4).

Dans les deux configurations on observe des valeurs positives de l'angle de phase à l'intérieur de la couche limite. Ceci s'explique par le fait que dans la couche limite, la vitesse étant plus faible que dans l'écoulement extérieur, l'inertie y est plus faible. La réponse au gradient de pression est donc plus rapide dans la région interne de la couche limite. Le gradient de pression $\sim \frac{\partial U_e}{\partial t}$ étant en avance de phase de 90° par rapport à la vitesse extérieure, il n'est pas paradoxal de trouver des déphasages positifs dans la couche limite.

Dans la région externe de la couche limite des valeurs négatives du déphasage ont été mesurées dans la deuxième configuration, mais ceci n'a pas été observé dans la première étude. Il se peut que dans ce cas l'angle de phase était trop petit pour être mesuré avec une précision suffisante. Ce même phénomène est d'ailleurs décelable aussi dans les expériences de KARLSSON [4]. Ajoutons encore qu'en écoulement laminaire le calcul et l'expérience indiquent que le maximum du retard de phase présente une valeur maximale quand on varie systématiquement le nombre de Strouhal.

Les résultats qui viennent d'être présentés et qui décrivent la réponse de la vitesse dans la couche limite sont susceptibles d'être très différents selon la nature de la pulsation. PATEL [6] a étudié l'influence de la vitesse de convection de l'onde et a montré en particulier que le profil du déphasage peut être totalement modifié à cause de la présence dans le terme de gradient de pression du terme $U_e \frac{\partial U_e}{\partial x}$ qui joue un rôle important.

Profils de vitesses.

Une seconde représentation consiste à tracer à différents instants les profils de vitesses en une station donnée. Chaque profil est obtenu pour une valeur fixée de l'angle de phase dans la période de l'écoulement extérieur, et il est rendu sans dimension en divisant la vitesse par sa valeur extérieure. Ces profils sont donnés figures 5a et 5b pour les deux configurations à la station 4.

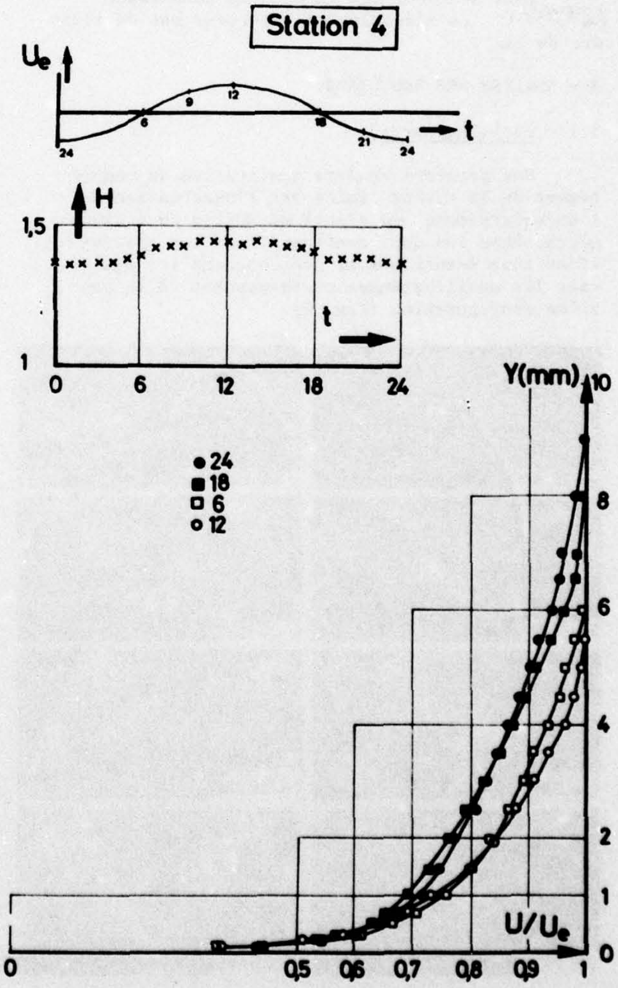

FIG.5 a : PROFILS DE VITESSE MOYENNE (configuration 1).

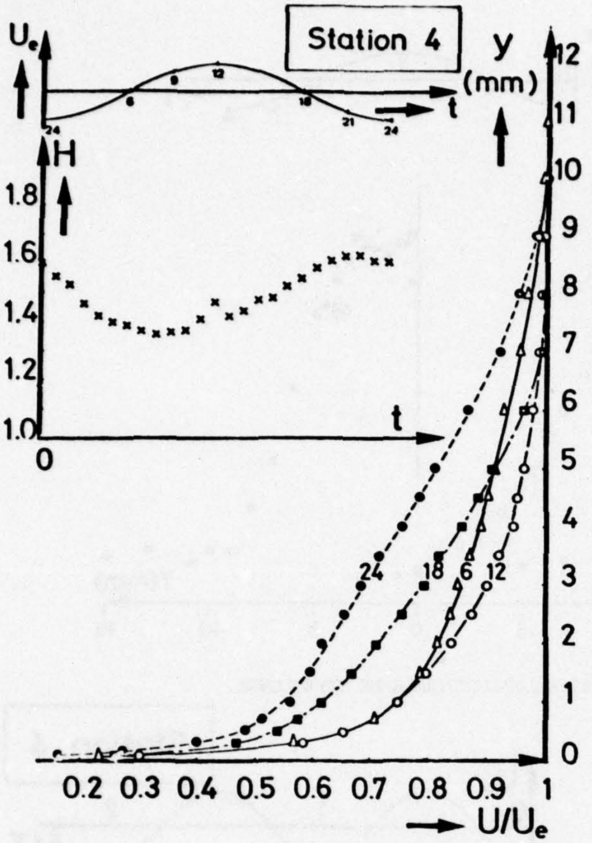

FIG. 5

b : PROFILS DE VITESSE MOYENNE (configuration 2).

Une partie de l'évolution des profils est due à la variation forcée de l'épaisseur de couche limite ; cependant on observe une variation de forme de ces profils liée à l'alternance de gradients de pression instantanés positifs et négatifs. On remarque d'ailleurs que cette déformation est plus accentuée dans la deuxième configuration. En effet un paramètre essentiel qui définit la forme du profil de vitesses est relié à la quantité $\frac{\delta}{u_e^2}\frac{\partial p}{\partial x} = -\frac{\delta}{u_e^2}\frac{\partial u_e}{\partial t}$ dont les variations sont beaucoup plus importantes dans le deuxième cas. Corrélativement on observe l'évolution du facteur de forme H qui traduit bien la variation de forme des profils. On note encore que H varie autour d'une valeur moyenne plus élevée dans la deuxième configuration : ceci s'explique certainement par la différence de nombres de Reynolds.

3.3 - Intensité de turbulence - Frottement turbulent.

Les fluctuations turbulentes u' de la vitesse longitudinale sont calculées par différence entre la vitesse instantanée u et la moyenne d'ensemble U. L'écart-type $(\overline{u'^2})^{1/2}$ définit la composante longitudinale de l'énergie cinétique de turbulence.

L'effet du gradient de pression variable dans la période peut encore être mis en relief en traçant les profils $(\overline{u'^2})^{1/2}/U_e$ (Fig. 6a et 6b), *pour lesquels apparaît une variation de forme tout* à fait caractéristique. On note aussi que cette déformation est moins accentuée pour la première configuration. Les mêmes observations peuvent être répétées si l'on considère l'évolution des profils de la tension turbulente (Fig. 13).

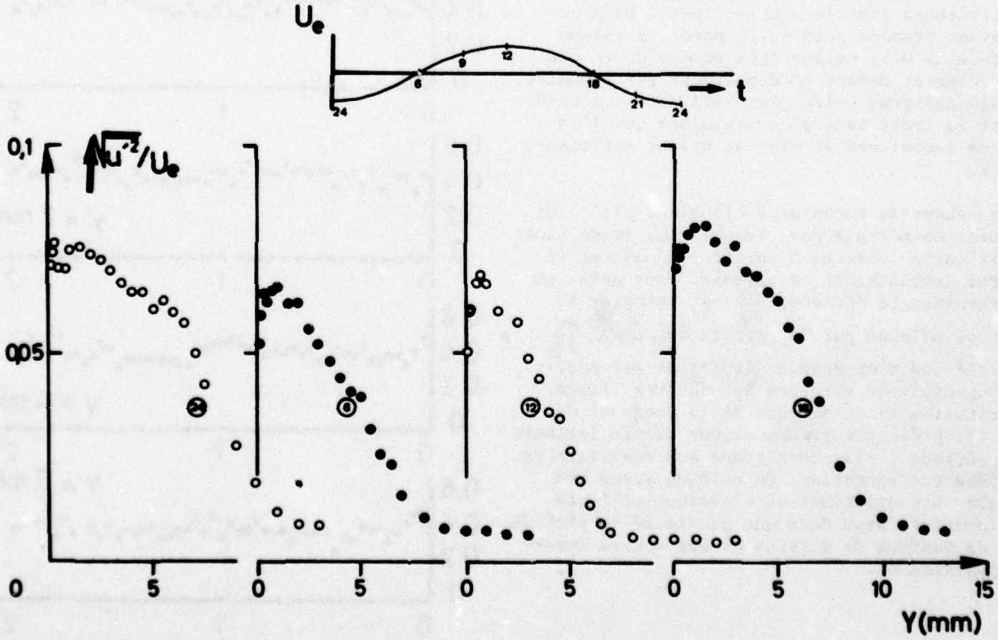

FIG. 6a : PROFILS DE L'INTENSITE LONGITUDINALE DE TURBULENCE

(configuration 1).

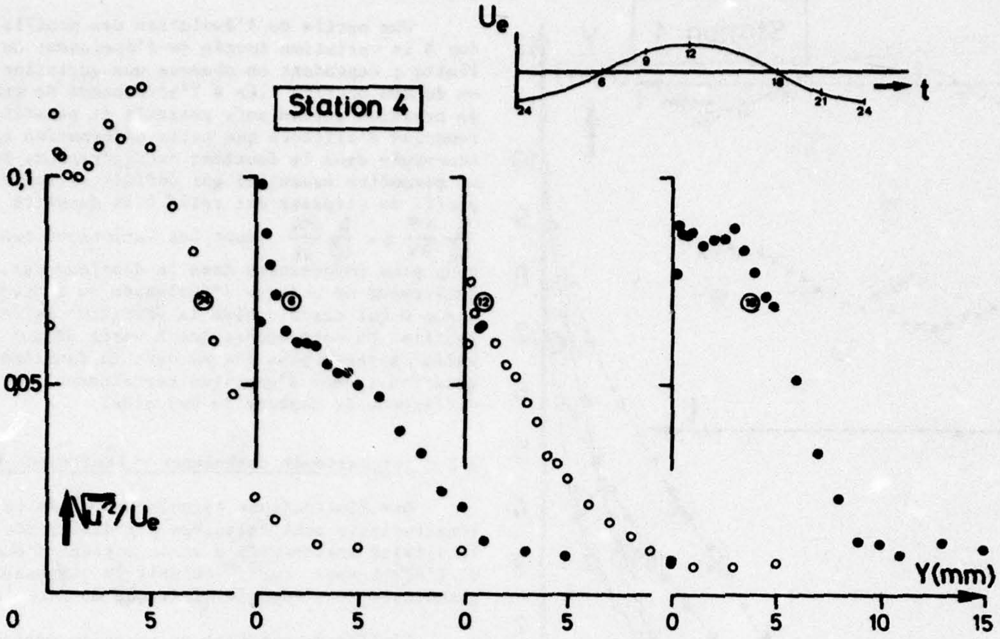

FIG. 6b : PROFILS DE L'INTENSITE LONGITUDINALE DE TURBULENCE (configuration 2).

Les mesures de la tension turbulente permettent de plus d'analyser des quantités qui jouent un rôle important dans de nombreuses méthodes de calcul. Par exemple on a calculé le coefficient de corrélation $-\overline{u'v'}/(\overline{u'^2}.\overline{v'^2})^{1/2}$ qui est représenté figure 7 comme une fonction du temps pour différentes altitudes dans la couche limite. Dans une région assez étendue près de la paroi sa valeur est voisine de 0.5, valeur très proche de ce qui est généralement mesuré en écoulement stationnaire. Ce coefficient tend évidemment vers zéro à l'extérieur car le frottement s'annule alors que l'intensité de turbulence atteint sa valeur extérieure non nulle.

Un schéma de turbulence classique est celui de longueur de mélange pour lequel nous avons tenté une vérification directe à partir des mesures de frottement turbulent et de vitesse. Pour cela, on doit déterminer la dérivée $\frac{\partial U}{\partial y}$ et calculer la longueur de mélange par le rapport $\ell = (-\overline{u'v'})^{1/2} / \frac{\partial U}{\partial y}$; pour éviter une trop grande dispersion des résultats les profils de vitesses ont dû être lissés. La distribution ainsi obtenue de la longueur de mélange est présentée figure 8 pour quatre instants dans la période ; elle correspond aux résultats de la deuxième configuration. On note un assez bon accord avec une distribution classique utilisée en stationnaire, sauf dans une partie de la période voisine du maximum de vitesse où des écarts importants apparaissent.

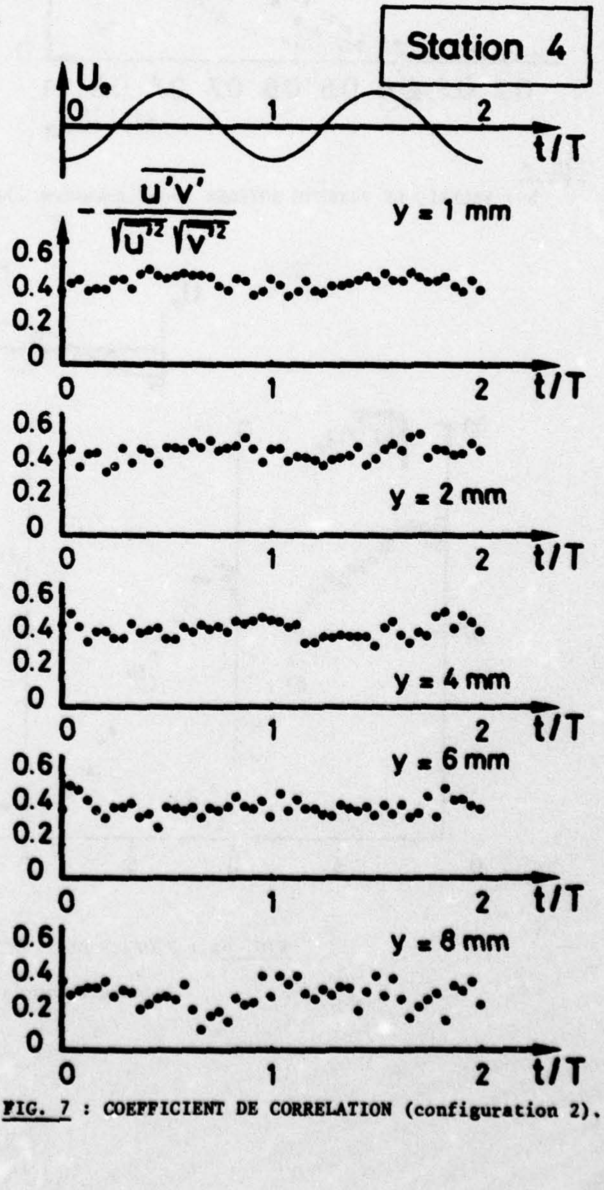

FIG. 7 : COEFFICIENT DE CORRELATION (configuration 2).

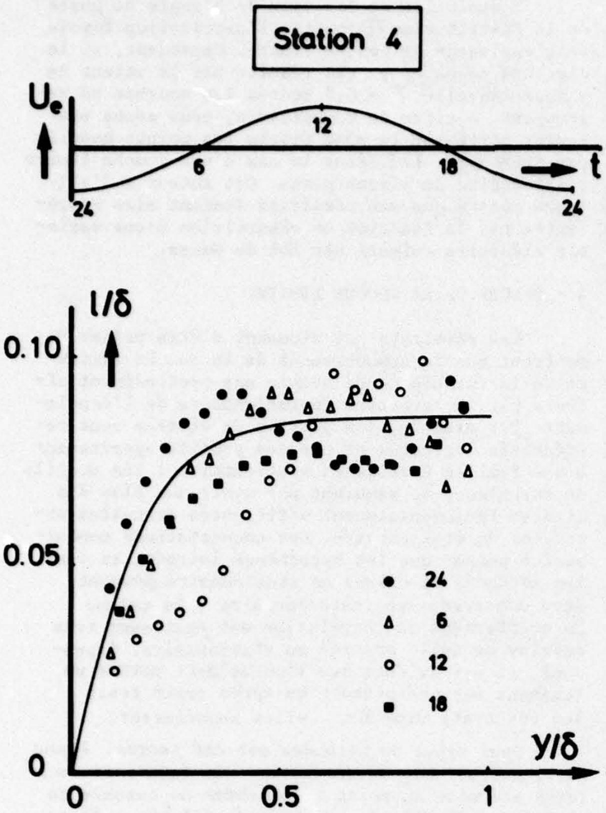

FIG. 8 : DISTRIBUTION DE LONGUEUR DE MELANGE (configuration 2).

3.4 - Etude statistique de la fluctuation u'.

Densité de probabilité.

Des informations complémentaires intéressantes sont tirées de l'analyse de la distribution statistique des fluctuations turbulentes de la vitesse longitudinale. La densité de probabilité de u' a été déterminée et quelques résultats sont présentés sur la figure 9 pour deux instants (7 et 19) à différentes altitudes dans la couche limite ; ces résultats correspondent à la deuxième configuration.

Les courbes, portées en fonction de la variable centrée et normalisée $u'/(\overline{u'^2})^{1/2}$ sont comparées à la densité de probabilité d'une variable aléatoire qui suit la loi de Gauss. On peut constater que près de la paroi et dans l'écoulement extérieur, la fluctuation turbulente suit à peu près une loi de Gauss ; entre ces deux régions, la densité de probabilité de u' est fortement déformée. Qualitativement, pour un angle de phase donné, le comportement de cette fonction est très voisin de celui observé en écoulement stationnaire [7] . Si on se réfère à ce cas, la déformation de la densité de probabilité est la conséquence du phénomène d'intermittence qui résulte lui-même du mouvement aléatoire de la frontière libre de la couche limite. Quand la sonde est à l'extérieur des bouffées turbulentes, on mesure une vitesse à peu près constante et peu fluctuante, alors qu'à l'intérieur des bouffées, elle est beaucoup plus agitée. La valeur mesurée à l'extérieur est ainsi beaucoup plus probable que les autres et conduit à un pic de la densité de probabilité. D'autre part la vitesse à l'intérieur des tourbillons étant, près de la frontière, plus faible qu'à l'extérieur, ce pic se produit pour des valeurs positives de u'.

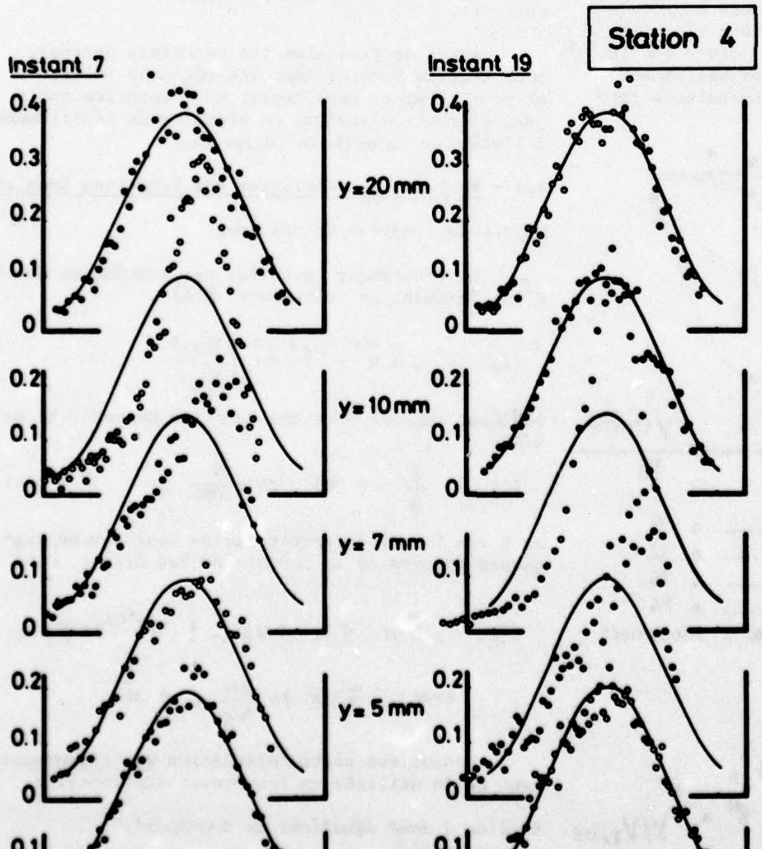

FIG. 9 : DENSITE DE PROBABILITE DE u' (configuration 2).

La position instantanée de la frontière libre de la couche limite est une grandeur aléatoire dont la fonction de répartition est le facteur d'intermittence γ ; la courbe $\gamma(y)$ représente donc la probabilité pour que la frontière extérieure de la couche limite soit supérieure à y.
En écoulement stationnaire, mais dans ce cas seulement, $\gamma(y)$ représente aussi le rapport du temps pendant lequel on observe un écoulement turbulent, au temps total d'observation à l'altitude y.

Dans l'écoulement extérieur, la densité de de probabilité de u' est quasiment gaussienne comme c'est le cas de la turbulence derrière une grille en écoulement stationnaire.

On note enfin que l'évolution suivant y de la courbe de la densité de probabilité dépend fortement de l'angle de phase ; ceci s'explique en grande partie par les oscillations forcées de l'épaisseur de couche limite.

Facteur d'aplatissement.

Sous certaines hypothèses, (valeurs moyennes de la vitesse dans les régimes turbulents et non turbulents confondues, fluctuations de vitesse nulles en régime non turbulent), ce coefficient est lié au facteur d'aplatissement F par la formule :

$$\gamma = 3 / F \qquad \text{avec} \qquad F = (\overline{u'^4}) / (\overline{u'^2})^2$$

Nous avons utilisé ce procédé simple pour apporter quelques informations sur le mouvement de la frontière (Fig. 10). Près de la paroi, la distribution de u' est pratiquement gaussienne ; en conséquence le facteur γ est voisin de 1 : on est en présence d'un régime toujours turbulent. La diminution de γ à partir de valeurs faibles de y est une indication de la grande amplitude du mouvement aléatoire de la frontière libre. A l'extérieur, γ redevient égal à 1 parce que la fluctuation u' suit à nouveau approximativement une loi de Gauss comme le fait la turbulence derrière une grille.

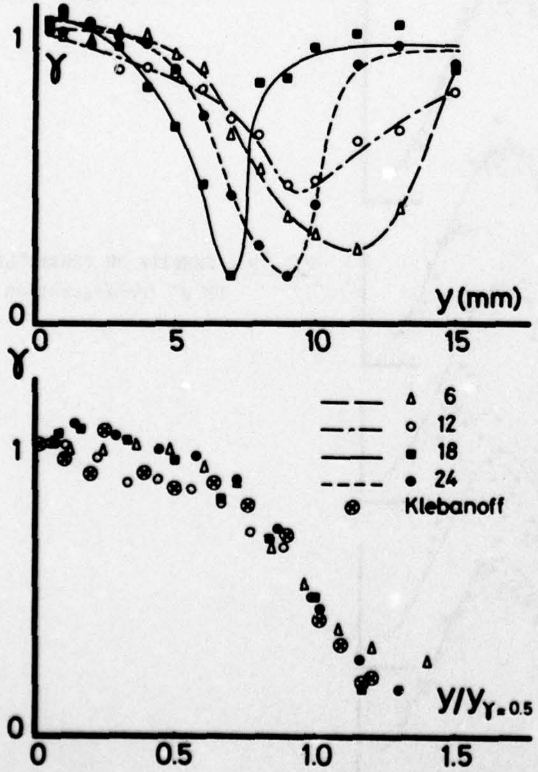

FIG. 10 : FACTEUR D'APLATISSEMENT (configuration 2).

L'évolution en fonction de l'angle de phase de la distribution $\gamma(y)$ montre l'oscillation forcée de l'épaisseur de couche limite. Cependant, si la distance normale y est réduite par la valeur de y pour laquelle $\gamma = 0.5$ toutes les courbes se regroupent. A titre de comparaison, nous avons également porté sur le même graphe les points mesurés par KLEBANOFF [7] dans le cas d'une couche limite stationnaire de plaque plane. Cet auteur a d'ailleurs montré que ses résultats étaient bien représentés par la fonction de répartition d'une variable aléatoire suivant une loi de Gauss.

4 - CALCUL DE LA COUCHE LIMITE.

Les résultats qui viennent d'être présentés montrent que le comportement de la couche limite et de la turbulence ne semble pas profondément affecté par le caractère instationnaire de l'écoulement. Par exemple, les profils de vitesse sont représentés correctement par des profils appartenant à une famille établie en stationnaire ; les profils de turbulence ne semblent pas avoir non plus des allures fondamentalement différentes de celles observées en stationnaire. Ces constatations conduisent à penser que les hypothèses introduites dans les méthodes de calcul en stationnaire peuvent être conservées en instationnaire ; la valeur du coefficient de corrélation est également très voisine de celle mesurée en stationnaire. Cependant, il est évident que l'on ne peut porter un jugement sur une méthode qu'après avoir testé les résultats auxquels elles aboutissent.

Deux types de méthodes ont été testés. D'une part, une méthode de résolution des équations locales a été mise au point ; le schéma de turbulence est soit un modèle de longueur de mélange soit un modèle d'équations de transport. D'autre part, une méthode de résolution des équations globales a été analysée.

Avant de présenter les résultats obtenus, nous décrirons brièvement les méthodes utilisées et pour terminer nous tenterons d'apporter quelques éléments d'analyse du problème du décollement à l'aide de la méthode intégrale.

4.1 - <u>Méthodes de résolution des équations locales.</u>

Modèle de longueur de mélange.

Le frottement turbulent est exprimé au moyen d'une formulation classique [15] :

$$(1) \qquad -\overline{u'v'} = F^2 \ell^2 \left(\frac{\partial U}{\partial y}\right)^2$$

où ℓ/δ est supposé être une fonction universelle de y/δ :

$$(2) \qquad \frac{\ell}{\delta} = 0.085 \quad \text{th} \frac{\chi}{0.085} \frac{y}{\delta} \qquad \chi = 0.41$$

et F une fonction correctrice de sous couche visqueuse déduite de la formule de Van Driest [15] :

$$(3) \qquad F = 1 - \exp(-\ell (\tau\rho)^{1/2} / 26 \chi \mu)$$

$$\text{avec} \qquad \tau = \mu \frac{\partial U}{\partial y} - \rho \overline{u'v'}$$

Notons que cette formulation est rigoureusement celle utilisée en écoulement stationnaire.

Modèles à deux équations de transport.

Ces dernières années, différents modèles plus élaborés que celui de longueur de mélange ont été développés en faisant appel à des équations de transport pour décrire le développement de différentes quantités turbulentes.

Dans les études précédentes, [8] nous avons utilisé avec succès, un modèle à deux équations de transport qui a été développé à l'Imperial College [9].

Il consiste en un système décrivant l'évolution de l'énergie cinétique de turbulence k et celle de son taux de dissipation ε . Aux nombres de Reynolds élevés des écoulements turbulents établis, les équations s'écrivent :

$$(4)\quad \frac{Dk}{Dt} = -\overline{u'v'}\frac{\partial U}{\partial y} - \varepsilon + \frac{\partial}{\partial y}\left(\frac{C_\mu}{\sigma_k}\frac{k^2}{\varepsilon}\frac{\partial k}{\partial y}\right)$$

$$(5)\quad \frac{D\varepsilon}{Dt} = -C_{\varepsilon_1}\frac{\varepsilon}{k}\overline{u'v'}\frac{\partial U}{\partial y} - C_{\varepsilon_2}\frac{\varepsilon^2}{k} + \frac{\partial}{\partial y}\left(\frac{C_\mu}{\sigma_\varepsilon}\frac{k^2}{\varepsilon}\frac{\partial \varepsilon}{\partial y}\right)$$

Et le frottement turbulent a pour expression :

$$(6)\quad -\overline{u'v'} = C_\mu \frac{k^2}{\varepsilon}\frac{\partial U}{\partial y}$$

Dans ces équations, les constantes ont pour valeurs :

$C_\mu = 0{,}09 \quad C_{\varepsilon_1} = 1{,}45 \quad C_{\varepsilon_2} = 2 \quad \sigma_k = 1{,}1 \quad \sigma_\varepsilon = 1{,}1$

Par rapport à un écoulement stationnaire, seuls sont ajoutés les termes de dérivée partielle par rapport au temps intervenant dans les termes de convection. Il est important de souligner que la modélisation mise en oeuvre pour le stationnaire est intégralement conservée.

Ce modèle comme nous l'avons déjà précisé est établi pour les nombres de Reynolds de turbulence élevés. Par conséquent, il est en défaut près de la paroi où un traitement spécial est nécessaire. Deux solutions ont été retenues. La première consiste à remplacer, près de la paroi, le système (4), (5), (6) par le modèle de longueur de mélange (1), (2), (3). On abandonne ce traitement à une distance y quand la fonction F est assez voisine de 1 (F = 0.99), c'est à dire quand le nombre de Reynolds de turbulence est assez élevé. On assure un raccordement en y_r en imposant la continuité des valeurs de $U, \frac{\partial U}{\partial y}, \tau$ et on admet que :

$$k = (\tau/\rho) / C_\mu^{1/2}$$

$$\varepsilon = \frac{C_\mu}{\tau/\rho}\, k^2 \frac{\partial U}{\partial y}$$

La seconde solution retenue est d'introduire des modifications adéquates dans le système des équations de transport comme cela a été fait par JONES-LAUDER [10] pour aboutir à une version "faible nombre de Reynols" du modèle.

Quel que soit le schéma de turbulence adopté les équations locales de couche limite ont été résolues numériquement pas à pas au moyen d'une méthode de différences finies décrite plus largement dans la référence [11].

4.2 - <u>Méthode de résolution des équations globales</u>.

Dans de nombreuses applications pratiques, il n'est pas nécessaire de faire appel à des méthodes aussi complexes que celles qui viennent d'être décrites. Si l'on ne s'intéresse qu'à l'évolution de quantités globales, comme l'épaisseur δ_1 ou le coefficient de frottement pariétal, une méthode intégrale peut se révéler efficace.

Le principe d'une telle méthode repose sur la résolution simultanée des équations globales de continuité et de quantité de mouvement. En négligeant la variation de la masse volumique, elles s'écrivent :

$$(7)\quad \frac{\partial \delta}{\partial x} - \frac{v_e}{u_e} = \frac{1}{u_e}\frac{\partial}{\partial x} u_e(\delta - \delta_1)$$

$$(8)\quad \frac{C_f}{2} = \frac{\partial \theta}{\partial x} + \theta\frac{H+2}{u_e}\frac{\partial u_e}{\partial x} + \frac{1}{u_e^2}\frac{\partial}{\partial t}(u_e\delta_1)$$

Cinq inconnues apparaissent dans ce système :

$\frac{\partial \delta}{\partial x} - \frac{v_e}{u_e}, \; C_f, \; \delta_1, \; \theta, \; \delta \quad (H = \delta_1/\theta)$

La résolution de ces équations nécessite donc des relations supplémentaires entre les inconnues. En stationnaire elles peuvent être obtenues par l'établissement de solutions de similitude [15] qui ont été étendues au cas d'un écoulement instationnaire [12]. Ces relations sont des lois reliant les grandeurs caractéristiques de la couche limite, exprimées par les formules suivantes :

$$(9)\quad \frac{\delta_1}{\delta} = \gamma F_1(G) \qquad \gamma = (C_f/2)^{1/2}$$

$$(10)\quad \frac{\delta_1}{\theta} = \frac{1}{1 - G\gamma}$$

$$(11)\quad \frac{\partial \delta}{\partial x} - \frac{v_e}{u_e} = \gamma P(G) - \frac{1}{u_e}\frac{\partial \delta}{\partial t}$$

$$(12)\quad \frac{1}{\gamma} = \frac{1}{\chi}\ln\frac{u_e\delta_1}{\nu} + D^*(G) \qquad \chi = 0{,}41$$

où F_1, P et D sont des fonctions de G, paramètre de Clauser $\left(G = \int_0^1 \left(\frac{u_e - u}{\gamma u_e}\right)^2 d\frac{y}{\delta} \Big/ \int_0^1 \frac{u_e - u}{\gamma u_e}\, d\frac{y}{\delta} \right)$

déterminées par l'analyse des solutions de similitude et représentées par les formules suivantes :

$F_1 = 0{,}613\, G - (3{,}6 + 76{,}86\, (1/G - 0{,}154)^2) / G$

$P = 0{,}074\, G - 1{,}0957 / G$

$D^* = 2\, G - 4{,}25\, G^{1/2} + 2{,}12$

Le système des équations globales (7), (8) complété par les relations (9), (10), (11), (12) a été résolu numériquement pas à pas à l'aide d'une technique de différences finies.

4.3 - <u>Application aux expériences présentées</u>.

Les différentes méthodes qui viennent d'être présentées ont été appliquées au cas des expériences décrites plus haut. Pour les deux configurations, des résultats comparables ont été obtenus et nous nous limiterons à présenter ceux relatifs à la deuxième configuration.

Quelle que soit la méthode utilisée, la distribution de la vitesse extérieure est une donnée du calcul de couche limite. Pour cela, nous avons utilisé l'analyse harmonique de sa distribution présentée figure 2. Quand le schéma de turbulence est un modèle d'équations de transport, on doit de plus imposer le niveau de turbulence extérieure ke et de son taux de dissipation ε_e . En fait il est facile de voir que l'on peut calculer ke (x,t) et ε_e (x,t) à l'aide des équations (4) et (5) écrites à l'extérieur à condition d'imposer les distributions ke (o,t), ε_e (o,t), ke (x,o), ε_e (x,o). On a pris $k_e/U_e^2(o,t) = k_e/U_e^2(x,o) = 5\ 10^{-5}$, ce qui correspond sensiblement aux valeurs mesurées. Les conditions sur $\mathcal{E}_e$ (o,t) et $\mathcal{E}_e$ (x,o) sont plus arbitraires mais leur influence sur le résultat du calcul est en fait des plus réduites.

On a également besoin de fixer les profils U(y), k(y) et $\mathcal{E}$ (y) dans les plans x = o et t = o ; les profils de vitesses sont donnés par l'expérience et les profils de k et $\mathcal{E}$ ont été déduits de ceux de U au moyen d'une formule de longueur de mélange.

L'application de la méthode intégrale est plus simple : elle nécessite seulement la connaissance de δ_1 et θ en x = o et en t = o. Ces données sont facilement déterminées à partir des profils de vitesses mesurés.

Notons enfin que pour chaque méthode, les conditions en t = o sont peu importantes car au bout d'un temps suffisamment long, une solution périodique indépendante de ces conditions est obtenue.

Sur la figure 11, les évolutions calculées de $\delta_1 = \int_0^\delta (1 - u/u_e)\,dy$ et $\theta = \int_0^\delta u/u_e(1 - u/u_e)\,dy$ sont comparées aux valeurs mesurées. Les différentes méthodes conduisent à des résultats cohérents, voisins de ceux de l'expérience et ceci aux différentes abscisses , rappelons qu'à la première station les données de l'expérience sont retenues comme données initiales du calcul.

Par souci de simplification, on peut être tenté de calculer le développement de la couche limite par une méthode quasi-stationnaire. Il s'agit de résoudre les équations stationnaires pour différents instants dans la période en imposant comme distribution de la vitesse extérieure celle qui existe effectivement à l'instant donné. Un tel calcul a été effectué à l'aide de la méthode intégrale. La seule différence avec le calcul instationnaire est le terme $\frac{1}{u_e^2}\frac{\partial}{\partial t}(u_e\delta_1)$ de l'équation globale de quantité de mouvement (8). La comparaison des résultats de cette méthode aux données expérimentales (Fig. 11) montre que des écarts importants apparaissent dans une grande partie de la période.

La résolution des équations locales permet de connaître l'évolution des profils de vitesses, de frottement turbulent ou d'énergie cinétique de turbulence. La comparaison des profils de vitesses (Fig. 12) indique que toutes les méthodes utilisées reproduisent bien leur déformation au cours de la période. Les résultats donnant l'évolution des profils de frottement (Fig. 13) sont plus dispersés ; cependant la forme de ces profils et le niveau des valeurs sont correctement calculés.

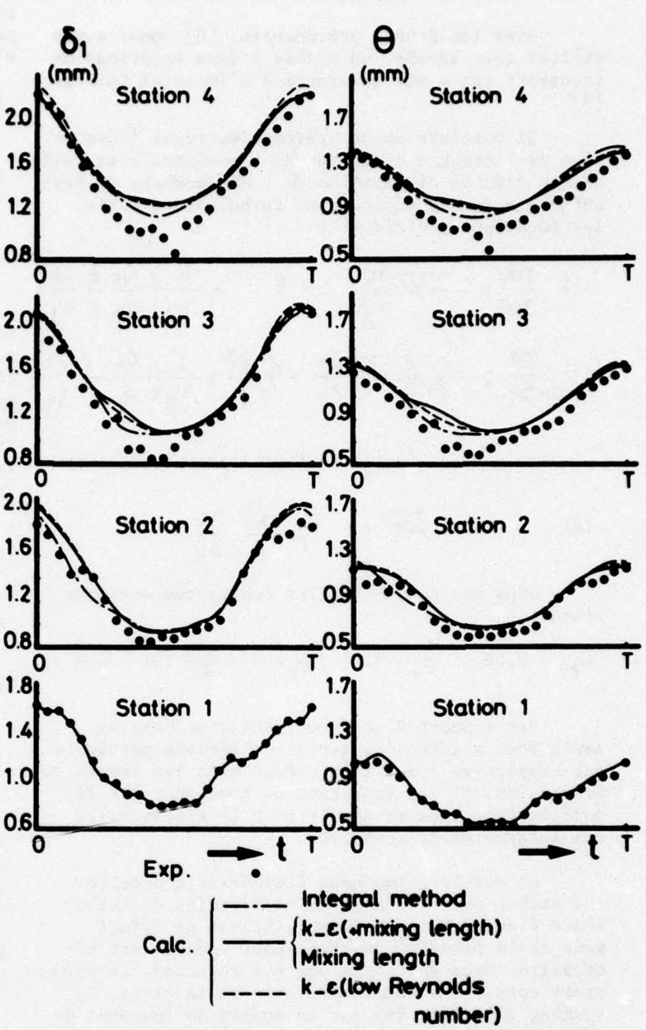

FIG. 11 : COMPARAISON CALCULS - EXPERIENCES - EPAISSEURS INTEGRALES (configuration 2).

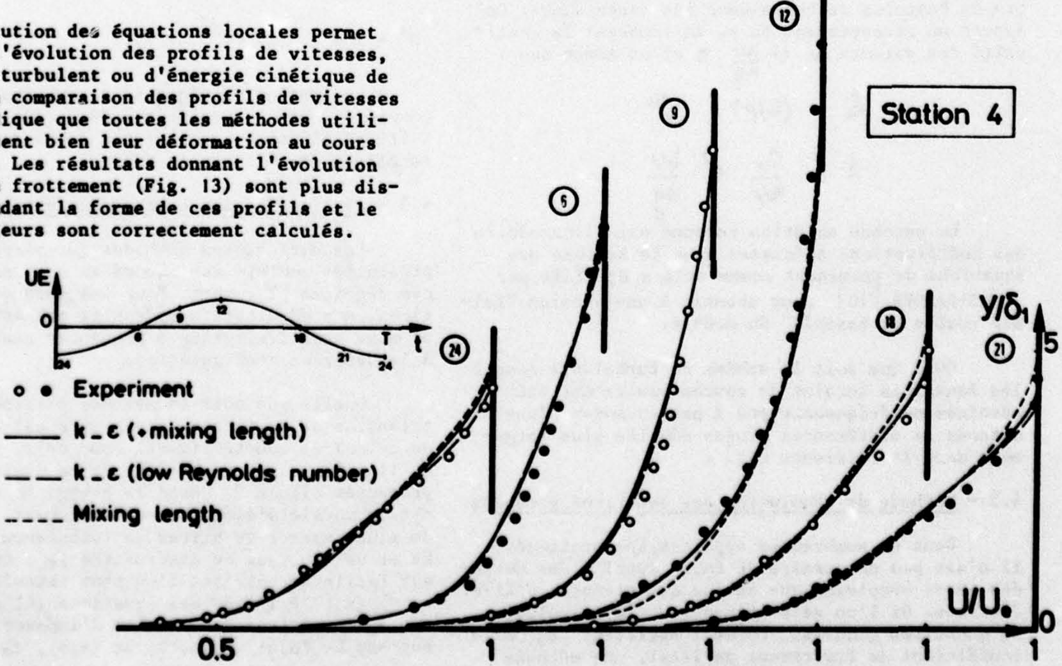

FIG. 12 : CALCUL DE LA COUCHE LIMITE. PROFILS U/U_e (configuration 2).

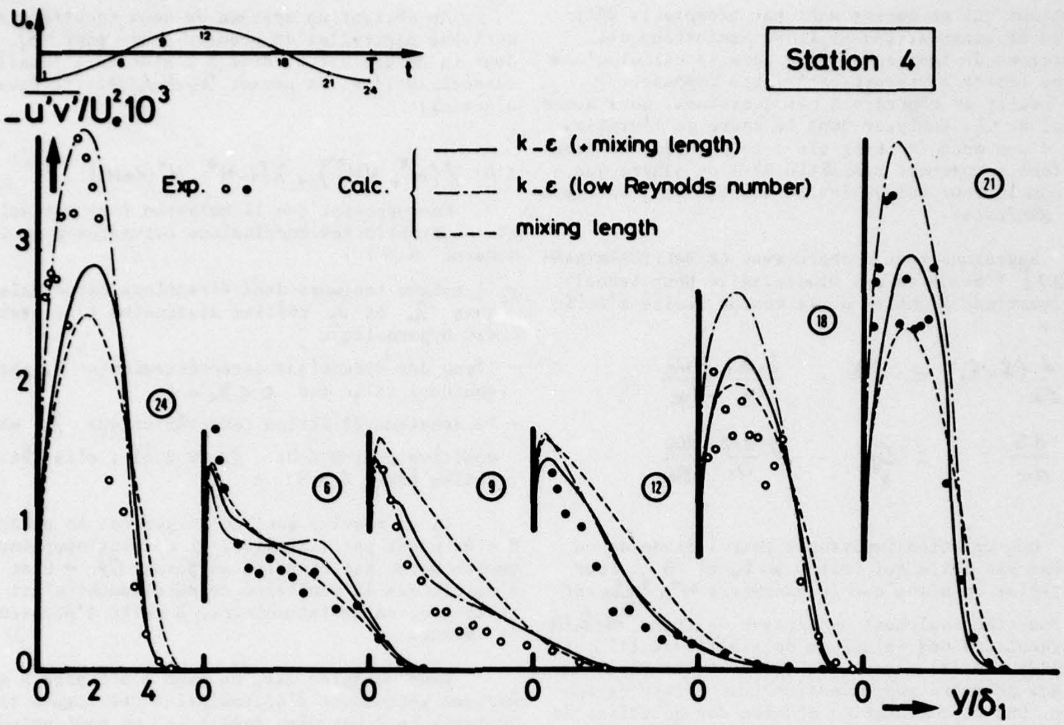

FIG. 13 : CALCUL DE LA COUCHE LIMITE. PROFILS $-\overline{u'v'}/U_e^2$ (configuration 2).

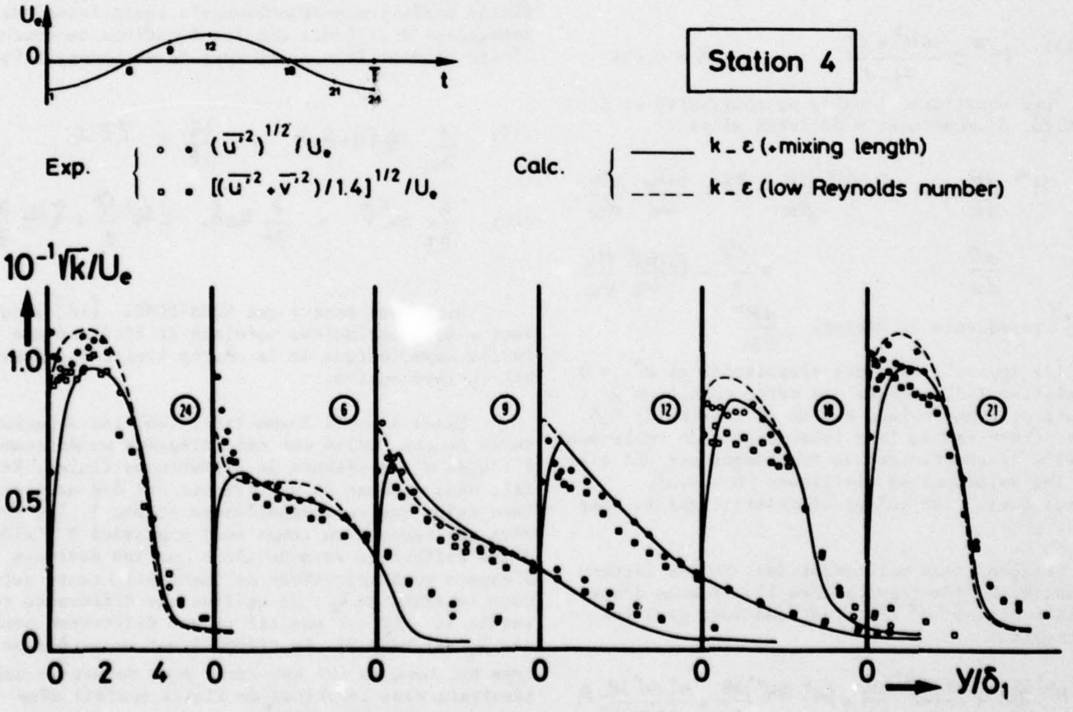

FIG. 14 : CALCUL DE LA COUCHE LIMITE. PROFILS $\sqrt{k}/U_e$ (configuration 2).

Quand on utilise le schéma de longueur de mélange, l'énergie cinétique de turbulence n'est pas explicitement calculée ; nous n'avons donc comparé que les résultats obtenus par le modèle d'équations de transport (Fig. 14). Dans l'expérience , seules les composantes $\overline{u'^2}$ et $\overline{v'^2}$ ont été mesurées. Deux hypothèses ont été utilisées pour calculer l'énergie totale : dans le premier cas on admet $\overline{u'^2} = k$; dans le second $\overline{w'^2} = 0,3\,k$ et l'énergie est calculée par $k = (\overline{u'^2} + \overline{v'^2}) / 1,4$. Les résultats obtenus sont voisins et le modèle d'équations de transport reproduit bien leur évolution.

4.4 - Problème du décollement - Analyse de cas théoriques.

La prévision du point de décollement à l'aide des équations de couche limite a suscité de nombreuses études, mais il apparaît que ce problème n'est pas encore totalement éclairci surtout en écoulement instationnaire [1-2-3-16-17-22-]. Les

questions qui se posent sont par exemple la définition de singularités et la détermination des conditions de leur apparition dans le calcul d'une couche limite à vitesse extérieure imposée.
Pour tenter de répondre à ces questions, nous avons choisi de les analyser dans le cadre de l'utilisation d'une méthode intégrale ; le problème se trouve alors grandement simplifié et l'on espère que les conclusions auxquelles on aboutit sont suffisamment générales.

Reprenons tout d'abord avec LE BALLEUR-MIRANDE [17] l'étude du cas stationnaire pour lequel les équations globales de la couche limite s'écrivent :

$$\frac{d}{dx}(\delta-\delta_1) = P\gamma - \frac{\delta-\delta_1}{u_e}\frac{du_e}{dx}$$

$$\frac{d\theta}{dx} = \frac{C_f}{2} - \theta\,\frac{H+2}{u_e}\frac{du_e}{dx}$$

Une relation importante pour l'étude de ce système est celle qui relie $\delta-\delta_1$ et θ . Pour simplifier on admet que le paramètre $H^* = \frac{\delta-\delta_1}{\theta}$ est une fonction seulement du facteur de forme $H = \delta_1/\theta$: les résultats des solutions de similitude [15] et l'expérience [17] montrent qu'une telle dépendance est une première approximation tout à fait raisonnable. Une représentation déduite des solutions de similitude, valable particulièrement au voisinage du point $C_f = 0$, est :

$$H^* = \frac{\alpha H^2 + H}{H-1} \quad \text{avec} \quad \alpha = 0{,}631 \tag{13}$$

Les équations globales de continuité et de quantité de mouvement s'écrivent alors :

$$H^*\frac{d\theta}{dx} + \theta\,H^{*\prime}\frac{dH}{dx} = P\gamma - \frac{\delta-\delta_1}{u_e}\frac{du_e}{dx} \tag{14}$$

$$\frac{d\theta}{dx} = \frac{C_f}{2} - \theta\,\frac{H+2}{u_e}\frac{du_e}{dx} \tag{15}$$

où $H^{*\prime}$ représente la dérivée $\frac{dH^*}{dH}$

Il apparaît donc une singularité si $H^{*\prime} = 0$. La relation (13) indique que cette condition se produit pour une valeur H = Hc de l'ordre de 2,6. Cette valeur est en fait très voisine de celle pour laquelle le coefficient de frottement est nul d'après les solutions de similitude (H = 2,35).
On peut aussi voir qu'une singularité existe pour H = 1.

Plaçons nous maintenant dans le cas instantionnaire. En admettant encore l'existence d'une relation unique $H^*(H)$, les équations globales s'écrivent :

$$H^{*\prime}\frac{\partial\delta_1}{\partial x} + \frac{1+H^{*\prime}}{u_e}\frac{\partial\delta_1}{\partial t} + (H^* - HH^{*\prime})\frac{\partial\theta}{\partial x} + \frac{H^* - HH^{*\prime}}{u_e}\frac{\partial\theta}{\partial t} = A \tag{16}$$

$$\frac{1}{u_e}\frac{\partial\delta_1}{\partial t} + \frac{\partial\theta}{\partial x} = B \tag{17}$$

$$A = P\gamma - \frac{\delta-\delta_1}{u_e}\frac{du_e}{dx}$$

$$B = \frac{C_f}{2} - \theta\,\frac{H+2}{u_e}\frac{\partial u_e}{\partial x} - \frac{\delta_1}{u_e^2}\frac{\partial u_e}{\partial t}$$

On obtient un système de deux équations aux *dérivées partielles du premier ordre pour* δ_1 et θ dont la nature est étudiée à l'aide de l'équation caractéristique. En posant $\lambda = dx/u_e dt$ cette équation s'écrit :

$$\lambda^2(H^* - HH^{*\prime}) + \lambda(1 - H^* + H^{*\prime}(1+H)) - H^{*\prime} = 0 \tag{18}$$

En supposant que la relation (13) est valable on établit les conclusions suivantes pour le domaine $H > 1$:

- il existe toujours deux directions caractéristiques λ_1 et λ_2 réelles distinctes : le système est hyperbolique
- l'une des directions caractéristiques λ_1 est toujours telle que $0 < \lambda_1 < 1$
- la deuxième direction caractéristique λ_2 est positive pour $H < Hc$ (Hc ≃ 2.6) ; elle est négative pour $H > Hc$.

Il en résulte donc qu'en général le point H = Hc n'est pas singulier. Or on peut supposer que ce point est très lié au point $C_f = 0$ et il s'ensuit que la condition de décollement n'est pas rattachée, en instationnaire, à celle d'écoulement de retour.

Dans certains cas, on peut s'attendre à obtenir des phénomènes d'accumulation des lignes caractéristiques d'une même famille et on peut prévoir aussi la formation de chocs analogues à ceux qu'on peut rencontrer dans l'étude des écoulements de fluide parfait monodimensionnels instationnaires. Remarquons d'ailleurs que les équations de couche limite peuvent être mises sous forme conservative :

$$\frac{\partial}{\partial x}u_e(\delta-\delta_1) + \frac{\partial\delta}{\partial t} = P\gamma u_e \tag{19}$$

$$\frac{\partial}{\partial x}u_e^2\theta + \frac{\partial}{\partial t}u_e\delta_1 = u_e^2\frac{C_f}{2} - \delta_1 u_e\frac{\partial u_e}{\partial x} \tag{20}$$

Signalons encore que SHEN-NENNI [18] aboutissent à des conclusions voisines en étudiant une solution asymptotique de la couche limite incompressible instationnaire.

Mises sous la forme (19), (20) les équations de la couche limite ont été intégrées numériquement à l'aide d'une méthode de différences finies. En fait deux schémas de différences ont été utilisés. Dans celui que nous appellerons schéma 1, les dérivées par rapport au temps sont exprimées à l'aide d'une différence avancée alors que les dérivées d'*espace sont approchées de façon différente suivant le signe de* λ_2 : on utilise une différence retardée si λ_2 est positif et une différence centrée si λ_2 est négatif. Le schéma 2 est un schéma de type Mac Cormack qui est connu pour donner de bons résultats dans le calcul de fluide parfait même avec onde de choc [21].

Le premier exemple d'application de cette méthode est un cas théorique proposé par SINGLETON et al [19] qui ont eux-mêmes calculé ce cas à l'aide d'une méthode de résolution des équations locales, dans laquelle le schéma de turbulence est un modèle à une équation de transport pour la tension turbulente. Pour cet exemple les conditions de vitesse extérieure sont résumées figure 15. Des conditions initiales simples sont imposées en x = 0 : $\frac{\delta}{\delta_0} = \left(\frac{u_e}{u_0}\right)^{-0.2}$ $\delta_0 = 0{,}0044$ m H = 1,4. Au temps t = 0, des conditions de couche limite de plaque plane sont utilisées.

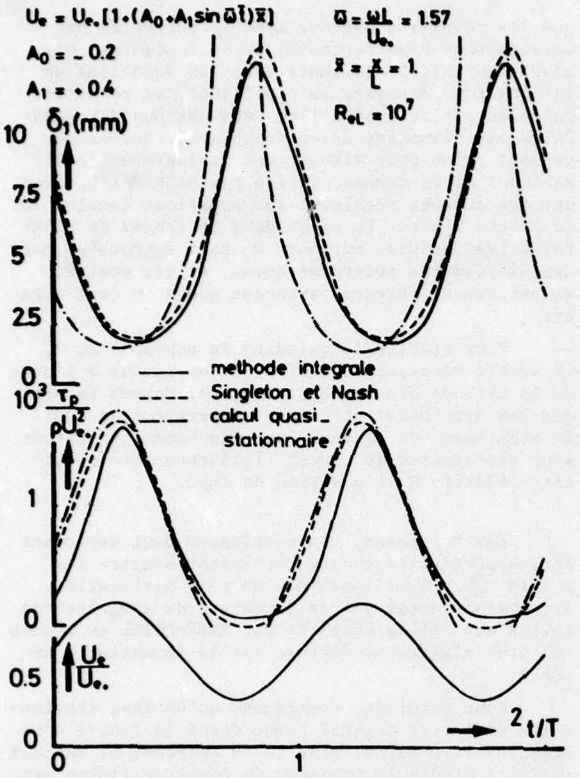

FIG. 15 : ANALYSE D'UN CAS THEORIQUE [Référence 19] . GRANDEURS GLOBALES

A l'échelle de la figure 15 où sont reportés les résultats, les schémas 1 et 2 donnent des résultats identiques ; en fait ce calcul ne présente pas de difficulté et les deux directions caractéristiques sont partout positives sauf dans une région très réduite. Figure 15, on a porté les résultats obtenus par SINGLETON et al. [19] et ceux provenant d'un calcul quasi-stationnaire par la méthode intégrale. Les deux calculs instationnaires conduisent à des résultats vosins alors que la méthode quasi-stationnaire indique en certains points de la période le décollement de la couche limite pour des valeurs de $\bar{x}$ inférieures à 1 (c'est pour cette raison que les résultats ne figurent pas dans cette zone). Ces résultats sont complétés par le tracé des caractéristiques (Fig. 16). Rappelant qu'une tangente verticale à une ligne caractéristique correspond à H = Hc on constate que même au voisinage de tels points aucun phénomène particulier n'apparaît.

Dans une deuxième exemple proposé par NASH-PATEL [20] la distribution de vitesse extérieure est schématisée figure 17. En $x = 0$ on a imposé $\delta = 0.00444$ m $H = 1,4$; en $t = 0$ des conditions de couche limite de plaque plane sont utilisées.

Signalons dès à présent que dans cette configuration, une zone avec écoulement de retour existe et l'on a dû pour la calculer faire un certain nombre d'hypothèses parfois grossières : nous avons supposé que la relation (13) $H^*(H)$ est valable, que $C_f = 0$ et que $P\gamma = 0,042$ (coefficient d'entrainement constant égal à sa valeur au point $C_f = 0$). Il est bien évident que dans les régions sans écoulement de retour, nous avons conservé le système de relations (9), (10), (11), (12).

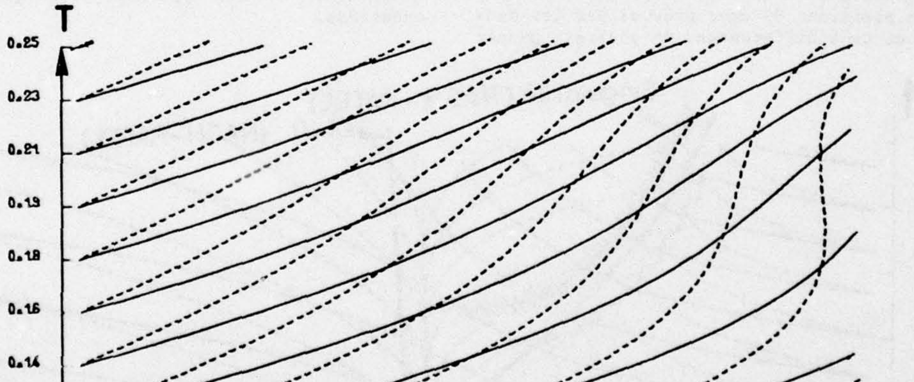

FIG. 16 : ANALYSE D'UN CAS THEORIQUE [Référence 19] . TRACE DES LIGNES CARACTERISTIQUES.

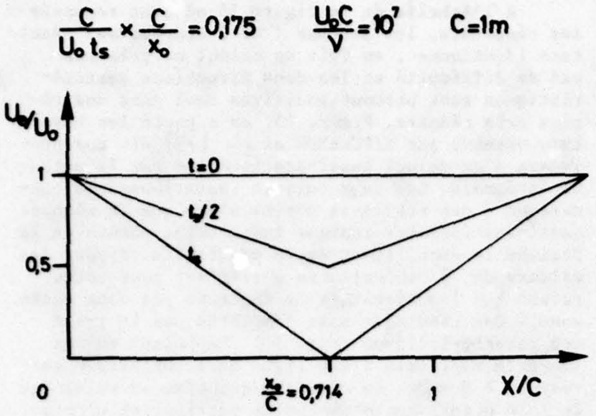

FIG. 17 : ANALYSE D'UN CAS THEORIQUE [Référence 20]
DISTRIBUTION DE LA VITESSE EXTERIEURE.

Figure 18, on donne le tracé des caractéristiques obtenues par le schéma 1 et figure 19 le tracé relatif au schéma 2. On a également reporté sur la figure 18 quelques résultats calculés par NASH-PATEL qui donnent [20] le lieu des points $C_f = 0$ et le lieu d'une singularité que ces auteurs définissent comme étant caractérisée par d'importants gradients longitudinaux et une déflection très forte des lignes de courant, les équations de couche limite cessant alors d'être valables.

Jusqu'au temps t = 0.035 les schémas 1 et 2 donnent des résultats très voisins. Pour les valeurs supérieures de t , les deux schémas indiquent une focalisation des lignes caractéristiques qui donne naissance à un choc. Cependant, on observe que les positions du choc prévues par les deux schémas sont très différentes. On pourrait penser que les résultats obtenus avec le schéma de Mac Cormack sont plus corrects car ce schéma est bien adapté au calcul des chocs avec les équations de la dynamique des gaz. La similitude des résultats calculés par le schéma 1 et ceux obtenus par NASH-PATEL est néanmoins assez troublante. Notons cependant qu'on peut établir une analogie entre le schéma 1 et le schéma utilisé par NASH-PATEL, bien que ces auteurs résolvent les équations locales de la couche limite. En effet dans le schéma de NASH-PATEL les dérivées suivant x sont approchées par des différences retardées quand u est positif et par des différences avancées quand u est négatif.

Pour établir la validité du schéma 1 ou 2, il semble nécessaire d'effectuer un calcul à l'aide de la méthode des caractéristiques. Notons encore que les hypothèses utilisées en particulier pour le traitement de la zone avec écoulement de retour sont discutables et peuvent influencer les résultats relatifs à la position du choc.

Dès à présent, une conclusion peut cependant être apportée. En écoulement instationnaire les points $C_f = 0$ ne jouent pas un rôle particulier. Il apparaît aussi que la formation de singularités telles que celles décelées par NASH-PATEL se trouve ici très clairement définie par la formation d'un choc.

Pour terminer, remarquons qu'un état stationnaire peut être regardé comme étant la limite d'un état instationnaire. Dans cette optique, LE BALLEUR [22] a étudié le problème du couplage fluide parfait-couche limite avec décollement en utilisant une méthode d'analyse analogue à celle que nous venons de présenter, et il a pu ainsi compléter le point de vue des approches classiques de ces questions.

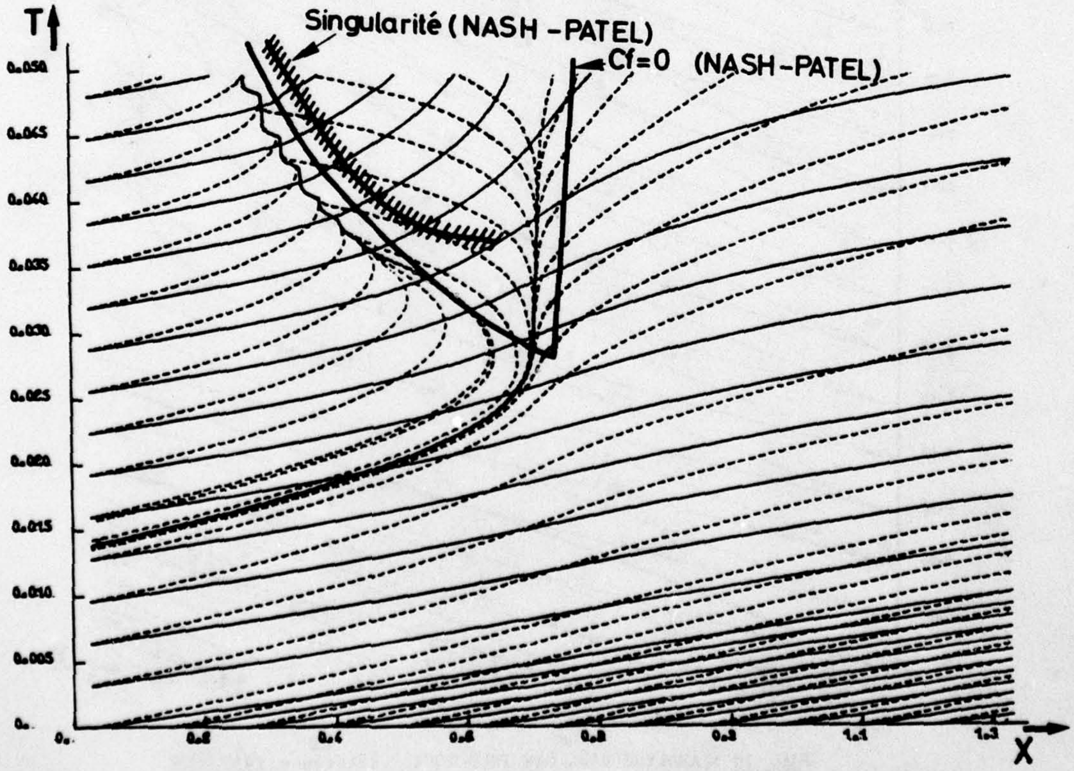

FIG. 18 : ANALYSE D'UN CAS THEORIQUE [Référence 20].
TRACE DES LIGNES CARACTERISTIQUES (schéma 1).

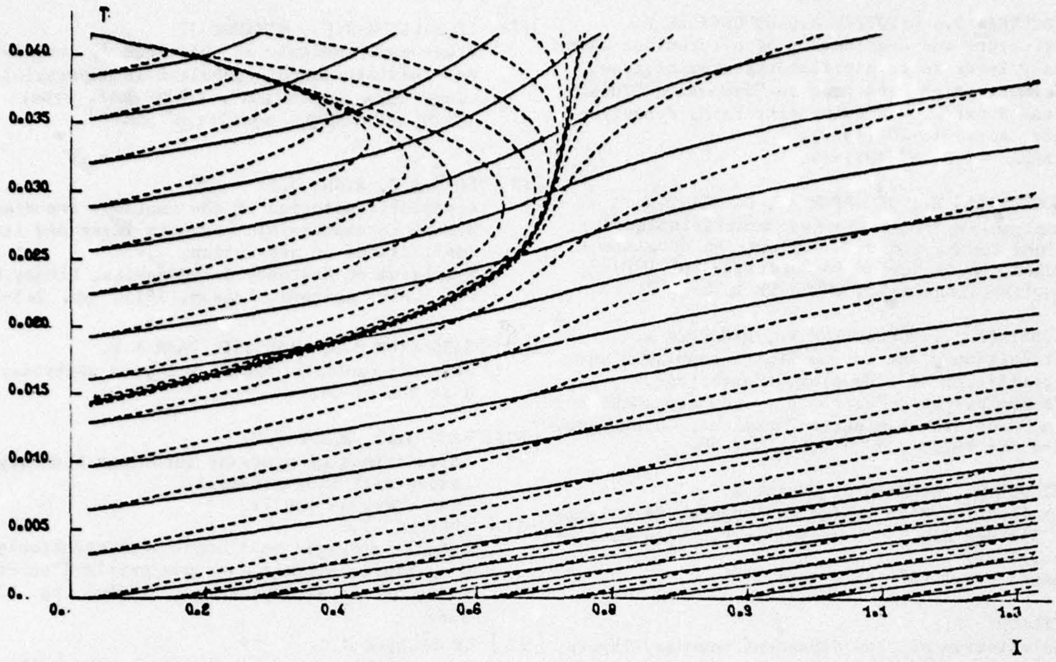

FIG. 19 : ANALYSE D'UN CAS THEORIQUE [Référence 20] .
TRACE DES LIGNES CARACTERISTIQUES (schéma de Mac Cormack).

CONCLUSIONS

L'étude expérimentale d'une couche limite turbulente se développant en présence d'un écoulement extérieur oscillant a montré que le comportement général de la couche limite et que la structure de la turbulence ne sont pas fondamentalement affectés par l'instationnarité de l'écoulement. Cependant, il doit être noté que dans nos expériences, la fréquence imposée est faible devant celles qui caractérisent la turbulence. Des valeurs plus grandes du nombre de Strouhal ou la présence d'un gradient de vitesse moyenne peuvent éventuellement jouer un rôle important.

L'application d'un modèle de longueur de mélange et d'un modèle d'équations de transport a montré que ces schémas de turbulence gardent leur validité en écoulement instationnaire, tout au moins dans des conditions similaires à celles de nos expériences. Pour les applications pratiques, il apparaît aussi qu'une méthode simple telle que la méthode intégrale présentée peut se révéler très efficace. Cependant, il est clair que des expériences systématiques avec des conditions plus sévères sont nécessaires pour permettre de tester plus largement les méthodes de calcul.

A l'aide d'une méthode intégrale on a présenté une méthode d'analyse rigoureuse des singularités pouvant intervenir dans le calcul de la couche limite. La comparaison des résultats obtenus avec ceux d'autres méthodes indique des recoupements très intéressants.

REFERENCES

[1] EICHELBRENNER E.A.
Recherches récentes sur les couches limites instationnaires. Proc. of the IUTAM Symp. Québec 1971.

[2] Mc CROSKEY W.J.
Some current research in Unsteady Fluid Dynamics. The 1976 freeman scholar lecture. Journal of Fluids Engineering, Vol. 99, March 1977.

[3] ABBOTT D.E., WU J.C.
Fluid dynamics of unsteady three dimensional and separated flows. Proceedings of a SQUID Workshop. 10-11 June 1971.

[4] KARLSSON S.K.F.
An unsteady turbulent boundary layer. Journ. of Fluid Mech., Vol. 5, 1969, P. 622-636.

[5] CHARNAY G., MELINAND J.P.
Etude de la structure des couches limites turbulentes qui se développent en présence d'un écoulement extérieur pulsé.
Contrat DRME 72-774 (1975).

[6] PATEL M.H.
On turbulent boundary layers in oscillatory flows. - Proc. R. Soc. Lond. A.353 121-144 (1977).

[7] KLEBANOFF P.S.
Characteristics of turbulence in a boundary layer with zero pressure gradient.
NACA Rep. 1247 (1955).

[8] COUSTEIX J.
Progrès dans les méthodes de calcul des couches limites turbulentes bi et tridimensionnelles.
ONERA, N.T. N° 1976-15.

[9] LAUNDER B.E.
Prediction methods for turbulent flows.
VKI Lecture Series 76 (1976).

[10] JONES W.P., LAUNDER B.E.
The prediction of laminarization with a two equation model of turbulence.
Int. Jour. of Heat and Mass Transfer, Vol. 15, n° 2 (1972).

[11] COUSTEIX J., DESOPPER A., HOUDEVILLE R.
Recherches sur les couches limites instationnaires - La Recherche Aérospatiale n° 1977-3 (p.167 - 177).

[12] COUSTEIX J., DESOPPER A., HOUDEVILLE R.
Structure and development of a turbulent boundary layer in an oscillatory external flow.
Communication présentée au "Symposium "Turbulent Shear Flows" University Park, Pensylvanie, April 18-20 (1977).
ONERA - T.P. N° 1977-14.

[13] HOUDEVILLE R., DESOPPER A., COUSTEIX J.
Analyse expérimentale des caractéristiques d'une couche limite turbulente en écoulement pulsé. La Recherche Aérospatiale n° 1976-4.
English Translation ONERA TP 1976-30 E.

[14] COUSTEIX J., HOUDEVILLE R., DESOPPER A.
Transition d'une couche limite soumise à une oscillation de l'écoulement extérieur.
Communication présentée à la réunion AGARD sur la Transition Laminaire-Turbulent, Copenhague, 2-4 Mai 1977.- ONERA T.P. 1977-55.

[15] MICHEL R., QUEMARD C, DURANT R.
Application d'un schéma de longueur de mélange à l'étude des couches limites turbulentes d'équilibre.
ONERA - N.T. n° 154 (1969).

[16] TELIONIS D.P.
Calculation of time dependent boundary layers.
Unsteady Aerodynamics, Vol. 1, ed. R.B. Kinney (1975), P. 155-190.

[17] LE BALLEUR J.C., MIRANDE J.
Etude expérimentale et théorique du recollement bidimensionnel turbulent incompressible, dans "Flow Separation", AGARD Conf. Proc. n° CP 168 (1975), mémoire n° 12.

[18] SHEN S.F, NENNI J.P.
Asymptotic solution of the unsteady two-dimensional incompressible boundary layer and its implications on separation.
Symposium on Unsteady Aerodynamics, Kinney R.B. ed., Univ. Arizona, Tucson, 1975, pp. 245-259.

[19] SINGLETON R.E, NASH J.F, CARR L.W.
Unsteady turbulent boundary layers analysis.
NASA TMX-62-242.

[20] NASH J.F., PATEL V.C.
Calculations of unsteady turbulent boundary layers with flow reversal.
NASA -CR-2546 (1974).

[21] VEUILLOT J.P.
Calcul numérique de l'écoulement transsonique d'un fluide parfait dans une grille d'aubes.
La Recherche Aerospatiale N° 1975-6, pp. 327-338.

[22] LE BALLEUR J.C.
Couplage visqueux-non visqueux. Calcul d'écoulements transsoniques ou supersoniques avec décollements.
La Recherche Aérospatiale (à paraître).

UNSTEADY BOUNDARY LAYERS WITH REVERSAL AND SEPARATION

by

John F. Nash and Roy M. Scruggs
Sybucon Inc., Atlanta, Georgia 30339
USA

SUMMARY

A review is made of a theoretical study of the mechanics of unsteady boundary-layer reversal and separation. The study has involved computational experimentation based, largely, on first-order boundary-layer theory, which is valid at the point of flow reversal and over some domain, beyond it, whose extent varies with the degree of unsteadiness implicit in the flow.

The paper describes the development of an appropriate computation scheme, for both laminar and turbulent flows, exploiting the validity of the first-order theory, and then proceeds with a survey of some of the numerical experiments which have been conducted to date. The topics addressed include the effect of time-dependence on flow reversal, the nature of unsteady reversal and separation, and the relevance of the results to engineering problems - notably the dynamic-stall problem. In conclusion, some brief comments are made about the direction which this research is expected to take over the next few years.

NOTATION

$A_1, \cdots, A_6$	Matrix coefficients
a_2	Empirical diffusion function
c	Chord of the plate
D	Total derivative
F	Vector dependent variable
f	Arbitrary function of time
L	Dissipation length
P, Q, R	Matrices in the numerical formulation
p	Static pressure
q	Resultant fluctuating velocity
t	Time
U, V, W	Ensemble average velocity components
u, v, w	Fluctuating velocity components about U, V, W
x, y, z	Cartesian coordinates
δ	Boundary-layer thickness
ν	Kinematic viscosity
ρ	Density

Subscripts

o	Reference value
e	Value at the outer edge of the boundary layer
f	Value at the time of freezing of the external flow
1, 2	Stations on the plate

I. INTRODUCTION

Unsteady boundary-layer separation is a limiting factor in the performance of many aerodynamic systems: helicopter rotors, turbine blades, lifting-surfaces of high-maneuverability vehicles, and so forth [1]. The successful design of such systems is far from straightforward because of the complexity of the associated fluid mechanics, and because experimental data are scarce and costly to obtain. In the absence of comprehensive measurements, knowledge of unsteady separating flows is being acquired largely through the intelligent use of numerical experimentation. Again because of the lack of comprehensive measurements, the numerical experiments are being performed using models whose validity can only be inferred by extrapolation of results from other flow regimes: primarily steady flows. The need for this extrapolation places increased emphasis on the need for fundamental correctness in the models themselves, and appropriate sophistication of the calculations is called for, subject to the obvious economic constraints.

Extensive calculations have been carried out, over the last several years, to investigate the properties of time-dependent boundary layers [2-7]. Much of this work has been addressed to the problems of flow reversal and separation. An important feature of unsteady flows is the distinction between reversal, which is a surface-flow event, and separation, which (in the sense of detachment of the external stream from the body) is an event - or perhaps a sequence of events - occuring further away from the surface. In unsteady flows the boundary layer can, at least temporarily, remain thin despite the presence of reversed flow close to the surface. In this thin-boundary-layer regime the conventional first-order boundary-layer approximations remain valid, permitting the study of reversed flows using nothing more than the simple first-order theory. The development of calculation methods which exploit this fortunate

---

This work was supported under contracts from the U.S. Army Air Mobility Research and Development Laboratory (Ames Directorate) and NASA Langley Research Center, and currently, is supported by the Army Research Office under Contract DAAG29-76-C-0045.

situation is discussed in Section II.

With regard to the ability to calculate unsteady flows, it is recognized that, for the laminar case at least, the Navier-Stokes equations offer the ultimate tool applicable to almost any unsteady flow of engineering interest. On the other hand, the solution of these equations may be prohibitively expensive, particularly if it is attempted over a whole flow field, or may not yet be possible for other reasons. As a practical matter, therefore, less generally applicable tools often have to be deployed. The use of first-order boundary-layer theory can be justified by just such an argument. For the turbulent case, there is no generally valid tool and all useful calculations have to be done by means of methodologies having certain limitations. Boundary-layer theory, together with a reliable turbulence model, may well be superior to higher-order methods for which the associated turbulence modeling is at a more primitive stage of development.

Later sections of this paper present an overview of some of the numerical experiments which have been conducted as part of this ongoing research program. An attempt has been made to extract results which can be expected to have a measure of generality beyond the particular circumstances of the original calculations. Section III deals with the effect of time-dependence on the onset of reversed flow. Section IV discusses the fundamental properties of unsteady reversal and separation. Section V deals with the relevance of these results to problems in engineering. Section VI describes extensions to the various methodologies which are currently being implemented, and further research which will be carried out when the more general tools become available. Finally, Section VII lists some conclusions which have been drawn from the research conducted to date.

II. CALCULATION OF UNSTEADY FLOWS WITH REVERSAL

Since the first-order boundary-layer approximations evidently remain valid, over some range of conditions beyond the onset of flow reversal, the generation of reversed-flow solutions depends only on the development of a suitable numerical scheme and the provision of relevant boundary conditions. Details are given here of the method currently being used for incompressible laminar and turbulent flows; a method for compressible flows is also available.

For incompressible time-dependent, boundary-layer flow over an infinite yawed cylinder whose generators are parallel to the z-axis, the ensemble-average equations of motion can be written

$$\frac{DU}{Dt} + \frac{1}{\rho}\frac{\partial p}{\partial x} - \nu\frac{\partial^2 U}{\partial y^2} + \frac{\partial}{\partial y}(\overline{uv}) = 0 \tag{1}$$

$$\frac{DW}{Dt} - \nu\frac{\partial^2 W}{\partial y^2} + \frac{\partial}{\partial y}(\overline{vw}) = 0, \tag{2}$$

where the convective derivative is defined by

$$\frac{D}{Dt} = \frac{\partial}{\partial t} + U\frac{\partial}{\partial x} + V\frac{\partial}{\partial y}, \tag{3}$$

and the continuity equation is

$$\frac{\partial U}{\partial x} + \frac{\partial V}{\partial y} = 0. \tag{4}$$

As a consequence of the first-order approximations the pressure is taken to be constant through the boundary layer. The terms $\overline{uv}$, $\overline{vw}$ represent the ensemble-average Reynolds stress terms. In our work closure has been obtained via the empirically modified turbulent kinetic-energy equation

$$\frac{D}{Dt}(\overline{q^2}) + \overline{uv}\frac{\partial U}{\partial y} + \overline{vw}\frac{\partial W}{\partial y} + \frac{\partial}{\partial y}(a_2\overline{q^2}) + \frac{(\overline{q^2})^{3/2}}{L} = 0 \tag{5}$$

where $\overline{q^2}$ is the ensemble-average square of the velocity fluctuations:

$$\overline{q^2} = \overline{u^2} + \overline{v^2} + \overline{w^2}, \tag{6}$$

and a_2 and L (the diffusion function and dissipation length) are the usual empirical functions of distance through the boundary layer [8]. In our earlier work [9], following Bradshaw et al [10], the shear stress components were taken to be proportional to $\overline{q^2}$; more recently we have used the isotropic-eddy-viscosity formulation*

$$\overline{uv} = -k(\overline{q^2})^{1/2} L \frac{\partial U}{\partial y} \tag{7}$$

$$\overline{vw} = -k(\overline{q^2})^{1/2} L \frac{\partial W}{\partial y}$$

---

*It will be noted that this eddy viscosity is not prescribed but varies from point to point as the square-root of the turbulent intensity. More general calculations have been done in which $\overline{uv}$ and $\overline{vw}$ have been modeled as nonlinear functions of the dimensionless rate of mean strain.

in which k is an empirical constant (equal to about 0.023). The two formulations give closely similar results in most cases. For laminar flow, of course, $\overline{uv} = \overline{vw} = 0$.

The principle governing equations (Equations (1), (2), (5)) can conveniently be written in matrix-vector form as

$$A_1F + A_2\frac{\partial F}{\partial t} + A_3\frac{\partial F}{\partial x} + A_4\frac{\partial F}{\partial y} + A_5\frac{\partial^2 F}{\partial y^2} + A_6 = 0 \qquad (9)$$

where F(x,y,t) is the vector of local dependent variables:

$$F^T = [U, W, \overline{q^2}] \qquad (10)$$

and the A's are matrix coefficients. This equation is parabolic, and can be integrated, over some domain, by means of a forward-marching procedure advancing in the positive t-direction (Figure 1). In our work the thickness of the domain is allowed to vary, in both space and time, proportion to the local boundary-layer thickness. Appropriate finite differencing converts Equation (9) into a relationship between values of F(x,y) at the forward time level and values at previous time levels. Our earlier work (which was restricted to turbulent flows) involved an explicit method of solution, with wall-law matching. Now, an alternating-direction implicit method is being used, which can handle both laminar and turbulent flows and in which wall-law matching is no longer needed: the numerical integration extends all the way to the body surface.

At each time level, the x-y plane is scanned, first in the horizontal direction, and then in the vertical direction (Figure 2). A tridiagonal matrix formulation is applied recursively producing partial solutions which extend over the whole domain as the scan is completed. To illustrate, when the scanning procedure advances in the x-direction, the formulation is

$$PQ = R \qquad (11)$$

where P is a tridiagonal matrix (each of whose elements is a square submatrix), Q is the vector of unknowns containing values of F for each node point in the y-direction and R is a column matrix of the same dimension as Q. When the scanning procedure advances in the y-direction a similar formulation emerges, except that Q then contains values of F at each node point in the z-direction. Equation (11) is nonlinear because P and R are functions of F, but it can be solved via a quasi-linearization technique with or without iteration to update these matrices. Iteration at each time step permits larger time steps to be taken for the same accuracy level, and so there is a trade-off between the number of iterations and the number of time steps. The optimization of this trade-off is still under investigation; currently an iterative scheme is being used, but for some applications, a non-iterative one may be optimal.

An important element of a successful method for calculating flows with reversal is the provision for switching from a backward difference to a forward difference for $\partial F/\partial x$ as the local U-component of velocity changes sign. Switching is advisable, for first- or second-order accurate difference approximations, to avoid convective instability (information is always convected "downstream" relative to the local direction of the flow). In our own work switching from a backward to a forward difference is also employed to the approximation of $\partial F/\partial y$, according to the sign of V; this procedure effectively removes any cell-Reynolds-number limitation on the magnitude of V and/or the fineness of the mesh. Second-order difference approximations are used throughout.

The existence of the reversed-flow region will necessitate the provision of downstream boundary conditions if the region extends to the edge of the domain of integration. Unfortunately some research workers still attempt to perform calculations without specifying the downstream conditions; even if solutions can be obtained in this way they are non-unique. The provision of the downstream conditions would present appreciable difficulties in a practical case. In order to avoid such difficulties, all of the computations we have carried out have related to situations involving closed reversed-flow regions, i.e. in which forward flow is re-established across the whole of the boundary layer by the time the flow reaches the downstream end of the domain (see Figure 1). In these situations, only initial (i.e. at some initial time) and upstream boundary conditions have to be furnished, together with the usual conditions at the wall and in the external stream.

Most of our calculations have involved prescribed external U-component velocity distributions of the form:

$$U_e = U_0, \text{ for } t \leq 0 \text{ and all } x \qquad (12)$$

$$\frac{U_e}{U_o} = 1 - \frac{x}{x_1}\{1 - f(t)\}, \text{ for } t \geq 0 \text{ and } 0 \leq x \leq x_1 \qquad (13)$$

$$\frac{U_e}{U_o} = 1 - \frac{x_2 - x}{x_1}\{1 - f(t)\}, \text{ for } t \geq 0 \text{ and } x_1 \leq x \leq c \qquad (14)$$

where U_0 is some reference velocity, x_1 and x_2 are prescribed values of x: $x_1 = 5c/7$ (= 0.714c), $x_2 = 2x_1$, and f(t) is some function of time. Suitable choice of the function, f, permits the imposition of a variety of external velocity distributions. The calculations discussed, herein, are all two-dimensional, and are based on the form

$$f = 1 - (1 - f_f)\, t/t_f, \text{ for } 0 \leq t \leq t_f \qquad (15)$$

and

$$f = f_f, \text{ for } t > t_f \tag{16}$$

These flows, which are illustrated in Figure 3, are termed "frozen flows" [11] because the external velocity distributions become independent of time for $t > t_f$.* Oscillatory flows can be produced by taking f to be harmonic functions of time [11].

III. EFFECT OF TIME-DEPENDENCE ON REVERSAL AND SEPARATION ONSET

It has been mentioned that time-dependence has an impact on the significance of flow reversal. Time-dependence also has a pronounced effect on the point of onset of reversal, relative to the development of the external velocity field [5].

Sometimes a time-dependent flow will exhibit reversal whereas no such reversal would occur in a "corresponding" steady flow. An example is oscillatory flow over a two-dimensional flat plate. If the amplitude, or the frequency is high enough, reversal can be provoked during part of each cycle [5, 11]. (The steady-flow equivalent would be a sequence of constant-velocity flows each having an external velocity equal to the instantaneous external velocity at a different point in the cycle of the oscillatory flow. None of them would experience reversed flow.) In this example the time-dependence could be said to be responsible for the reversal. It makes its effect felt via the pressure gradient associated with the term $\partial U_e/\partial t$ in the momentum equation; the pressure gradient is adverse during the part of the cycle when $\partial U_e/\partial t$ is negative.

More generally, for any two-dimensional flow, $\partial U_e/\partial t$ makes a contribution to the pressure gradient:

$$-\frac{1}{\rho}\frac{\partial p}{\partial x} = U_e\frac{\partial U_e}{\partial x} + \frac{\partial U_e}{\partial t} \tag{17}$$

If $\partial U_e/\partial t$ is negative any adverse pressure gradient due to the spatial variation of U_e is augmented; if $\partial U_e/\partial t$ were positive then the adverse pressure gradient would be alleviated. In cases where the effects of time-dependence are to alleviate the adverse pressure gradient one would therefore expect reversal onset to be delayed by the effects of time-dependence. In other words, one would expect the net spatial decrease of U_e from some upstream reference point to the point of incipient flow reversal, to be larger in a time-dependent flow than in an equivalent steady flow. Such is, in fact, the case, and the effect is substantial [5]. It has been shown that this effect partly explains the ability of a pitching airfoil to reach higher values of $C_{L_{max}}$, before stall than could be sustained by the same airfoil at a fixed angle of incidence [12] (See Section V, below).

What was unexpected was the observation, from computational experiments [5], that unsteadiness could sometimes delay the onset of reversal even though the local pressure gradients were strongly augmented by the $\partial U_e/\partial t$ term. This observation indicated that the impact of time-dependence on reversal could not be explained entirely via the effects on the pressure gradient; some other mechanism must evidently be present too. In Reference [5] it was suggested that this additional mechanism took the form of an "inertia" effect limiting the rate at which the necessary reorganization of velocities, within the boundary layer, can take place. In terms of an external flow field which imposes a progressively severe adverse pressure gradient on the boundary layer, the finite time required for the reorganization may allow the retardation to reach a stage substantially in excess of what could be accommodated by an attached steady flow.

Cases in which the effects of time-dependence are to delay reversal onset appear to be more common than those (such as the oscillatory flat-plate flow) in which the effects are to provoke reversal. In the cases where reversal onset is delayed, separation onset is delayed even more by unsteadiness. Except possibly in situations where the extent of reversed flow is decreasing with time, separation (to the extent that it can be identified) seems to occur downstream of reversal. Or, at a given station on a body surface, reversal occurs first followed, some time later, by separation. The rapid growth of the boundary layer, necessary to provoke detachment of the outer streamlines, evidently implies a further reorganization of the velocities within the layer, and requires an additional time increment, over and above that required for reversal.

IV. THE PROPERTIES OF UNSTEADY REVERSAL AND SEPARATION

A familiar concept in boundary-layer theory is the notion that the boundary layer separates when the wall shear stress falls to zero. Numerous text books have reproduced a schematic diagram, published originally by Prandtl, showing how a dividing streamline leaves the body surface, initiating a region of reversed flow within the boundary layer, and immediately provoking detachment of the external stream from the body contour. So familiar is this conceptual picture that it is widely believed that it portrays the general pattern of separation. Actually, Prandtl's representation is accurate only for two-dimensional, steady, incompressible, laminar flow. In almost all other cases there are deviations from this representation and, in some, the actual picture is substantially different.

In time-dependent flow the wall shear stress can often pass through zero, ushering in a region of reversed flow, without there being any significant disruption of the external stream or breakdown of the boundary-layer equations [13]. Figure 4 depicts the process schematically, and Figures 5, 6 show some

---

*The flows, mentioned in Section IV, in which the external gradients are alleviated, involve some variations beyond $t = t_f$; also the spatial distributions of U_e depart, to some extent, from Equations (13), (14).

calculated velocity profiles, for laminar and for turbulent flow, respectively, which illustrate this smooth passage through the point of reversal.

From a conceptual standpoint, the occurrence of reversal, unaccompanied by disruption of the outer flow, is highly significant. It means that the direction of the flow near the body surface is essentially uncorrelated with the inclination of the outer streamlines, and that a change in this direction is not necessarily indicative of rapid boundary-layer thickening. This result has important consequences in engineering because the loads on a body are highly dependent on the rate of boundary-layer growth and the associated displacement effect; the direction of the surface flow, by contrast, is of little concern. Section V below, includes a further discussion of the engineering implications of unsteady reversal and separation.

Although the first onset of unsteady reversal is uncoupled from rapid boundary-layer thickening and does not signal the immediate breakdown of the first-order boundary-layer equations, those events may occur some time later. It is often found that rapid thickening occurs, and steep gradients develop within the boundary layer, subsequent to the onset of reversal (Figure 7). The calculations frequently break down, shortly thereafter, indicating the presence of a singularity in the equations. The existence of the singularity has been discussed by Sears and Telionis [2] who argued that it is simply the counterpart of the Goldstein singularity in steady laminar flow, but that it happens to occur at some location other than the reversal point. Certainly the behavior of boundary-layer solutions near the point of breakdown in unsteady flow bears similarities to their behavior near the Goldstein singularity [14].

Two questions remain, however. The first is whether the development of a singularity in the first-order theory inevitably occurs subsequent to the formation of a region of reversed flow. This question will be addressed below. The second is whether the singularity has any physical significance or any physical counterpart. In response to this second question, a plausible argument would be that, even though a singularity, per se, could not occur in a real fluid, the associated rapid boundary-layer thickening would be observable. Moreover, the rapid thickening and subsequent breakdown of the boundary layer would correspond to "separation", in the sense of detachment of the outer flow from the body contour. According to this interpretation a well-defined and predictable sequence of physical events runs parallel to the events encountered in the boundary layer calculations.

Probably there are physically realizeable flows in which this whole sequence of events takes place: reversal, further development of a thin boundary layer (with embedded reversed flow near the surface) and, finally, rapid thickening and separation. On the other hand, there is now considerable doubt as to whether the rapid thickening and breakdown of the first-order boundary layer -- interpreted as physical separation or not -- is an inevitable feature of flows with reversal. Calculations for the same types of flow, performed using the full Navier-Stokes equations failed to exhibit a singularity or any abrupt thickening of the viscous layer which might correspond to it [11]. The Navier-Stokes solutions were almost disappointingly uneventful. It was even found possible to relax the solutions to a steady-state condition, containing embedded reversed flow, without any gross thickening of the viscous layer becoming apparent.

The sharply contrasting behavior of the first-order solution, on the one hand, and that of the Navier-Stokes solution, on the other, supports a viewpoint somewhat at variance from the one linking developments in the boundary-layer calculations to physical separation. This second viewpoint would hold that the rapid thickening of the first-order boundary layer, and its subsequent breakdown, may be nothing more than anomalies resulting from the unrealistic nature of the boundary-layer approximations. Studies of the rapid thickening, far from shedding light on the separation process, would be of no physical relevance. This viewpoint may be exaggerated; as suggested before, probably there are classes of flow in which the rapid thickening does occur. The particular Navier-Stokes solution may have belonged to a different class which could not be distinguished from the others by the first-order theory. However the possibility that the rapid thickening may simply be a consequence of the boundary-layer approximations is a serious one and needs to be explored further.

The boundary-layer approximations include the neglect of diffusive transport parallel to the body surface and the neglect of the pressure gradient normal to it. It can readily be shown that longitudinal or lateral diffusion plays a minimal role in the mechanics of the flow, at the Reynolds numbers of the calculations (10^4 for laminar flow and 10^7 for turbulent flow), and is not powerful enough to suppress the rapid thickening. The focus of interest accordingly shifts to the normal pressure gradient. The normal gradient is associated with momentum transport through the boundary layer, but it can also be regarded as a means for redistributing the longitudinal gradients; the existence of a finite $\partial p/\partial y$ allows $\partial p/\partial x$ to vary with y. The average, and effective, value of $\partial p/\partial x$ in the inner part of the boundary layer may differ significantly from its value in the adjacent external stream. The Navier-Stokes solution reflects this redistribution, whereas the first-order boundary-layer solution does not.

In order to study the possible effects of redistribution of the longitudinal pressure gradients, some first-order calculations have been performed in which $\partial p/\partial x$ could automatically be alleviated over regions in which rapid thickening of the boundary layer would otherwise occur. A simple (but somewhat ad hoc) scheme was devised for locally reducing $\partial p/\partial x$ if $\partial\delta/\partial x$ (where δ is the physical thickness) exceeded some threshold value. The intent was to simulate, very roughly, the effects of allowing the boundary layer to interact with an outer flow field. Calculations were done for both laminar and turbulent flow, and the results are shown in Figures 8 through 13. For laminar flow, Figures 8, 9 show plots of displacement thickness and wall shear stress for increasing time levels. The solid curves show the solution obtained with the alleviated pressure gradients, and it will be seen that calculations extend to a nondimensional time of 5 without any sign of breakdown. In contrast, the solution obtained with the prescribed pressure gradients, shown by the dashed lines, suffers rapid boundary-layer thickening and breakdown at about 3 time units. The external velocity distributions corresponding to these solutions is shown in Figure 10. It will be seen that most of the alleviation of the external gradients is confined to the region where the singularity would otherwise be expected to develop. Figures 11 - 13 show similar results for turbulent flow. Again, as a result of alleviation, it was found possible to continue the calculation substantially further than could be done without alleviation of the external gradients. Indeed, it would appear that the solutions could be relaxed to steady-state conditions, to produce steady flow solutions containing embedded reversal.

The conclusion, from these calculations, seems to be that the rapid thickening, and subsequent breakdown, of conventional first-order solutions result largely from the prescription of the longitudinal pressure gradients. These trauma are not inevitable and can be avoided if the gradients are relaxed over critical regions of the flow, in favor of some other criterion of development. This conclusion, for time-dependent flow, parallels one reached some years ago, that the Goldstein singularity in steady flow could similarly be avoided by alleviation of the pressure gradients [15, 16]. In a real flow the alleviation of the gradient arises from the interaction between the boundary layer and the outer flow field. Presumably, in some cases this alleviation is sufficient to delay rapid thickening for an extended period; in others the alleviation is less effective and early separation takes place.

V. RELEVANCE TO ENGINEERING PROBLEMS

As noted in Section I, unsteady reversal and separation impact on a number of important engineering problems. In some cases the unsteadiness is "unintentional" and embarrassing, as for example, in the various problems of aeroelasticity, including aileron buzz. In others, time-dependence is an intentional feature of the flow and, far from being an embarrassment, improves the range of operating conditions over and above what might be possible in steady flow. An area in this latter category, which has been extensively explored, is that of dynamic stall.

Reduced to its simplest terms, the flow in question is that over an airfoil in pitching motion. During the "upstroke" (increasing incidence) the airfoil reaches a higher angle of attack and a higher lift coefficient, before stall occurs, than would be possible if the same airfoil were held at constant incidence. An important question arises concerning the mechanism by which the boundary layer manages to remain attached during the phases of the motion when the instantaneous angle of incidence exceeds the value for static stall (i.e., during the C_L overshoot). This question was addressed in References [12, 17], and it was shown that a sizeable delay in the onset, and forward movement, of flow reversal could be explained by

(a) the effect of unsteadiness in the potential flow, in the form of an alleviation of the local spatial rates of retardation

(b) the effect of unsteadiness in the boundary layer, in the form of a delay in reversal for given spatial rates of retardation.

These two effects seemed to be of roughly equal magnitude and, together, were large enough to explain the C_L overshoot. But it was also shown that they were only just large enough, and that the increase of $C_{L_{max}}$, predicted simply on the basis of delay in reversal onset, roughly correlated with the increase observed experimentally. The correlation led to the suggestion, in Reference [12], that flow reversal in the boundary layer (when it finally does occur) somehow contributes to the collapse of the flow about the airfoil. This suggestion met with considerable hostility from the more vocal proponents of competing dynamic-stall models, particularly from the proponents of models which focus on the bursting of a leading-edge bubble. Experiments conducted since that time, however, have indicated that the suggestion had considerable merit. It has been demonstrated [18] that in many cases, including the familiar NACA 0012 airfoil, stall is associated with breakdown of the boundary layer, initiated by forward movement of the reversal point. It should be noted that the reversal point can move upstream on the airfoil without immediately causing strong boundary layer thickening. Indeed, with appropriate alleviation of the external gradients the boundary layer can, as shown earlier in this paper, remain thin for a relatively long time. The point at which strong thickening or "separation" finally occurs will lie further aft, moving forward in pursuit, as it were, of the reversal point.

There are two mechanisms by which reversal and/or separation can contribute to stall (Figure 14). The first involves the forward movement of the region of gross thickening of the boundary layer, and its associated detrimental effect on the circulation about the airfoil. This mechanism, which is reminiscent of rear (or trailing-edge) stall but is not necessarily limited to events over the aft portion of the airfoil, can operate whether or not a leading-edge bubble is present. The second is applicable in those cases where a bubble is known to form, and has to do with the interaction between the bubble and the reversed flow which spreads forward from further aft on the airfoil. The tongue of reversed flow penetrates the oncoming boundary layer and, eventually, can feed mass into the leading-edge bubble, allowing it to increase in size and subsequently to burst. Thus, even if bubble bursting features significantly in certain types of dynamic stall, the bursting process may well be triggered by forward movement of the reversal point.

Unsteady effects within the boundary layer evidently play a larger role in the dynamic stall story than was believed only a few years ago. Not only do they explain the delay in stall, but it is now recognized that they may hold the key to the stall mechanism itself.

VI. EXTENSIONS AND FUTURE WORK

The basic computational scheme has been formulated for both two-dimensional and infinite-yawed-cylinder flows, and for incompressible and compressible flows. To date, the numerical experimentation has been confined to incompressible flows and, with a few exceptions, to two-dimensional conditions. Considerable scope therefore exists, already, to perform calculations for a wider range of flows. Uncertainties regarding the validity of the turbulence modeling may be of increasing concern over this wider range, but they are not absent even for the simplest cases of two-dimensional, incompressible flow.

Some work remains to be done to refine the computational scheme and to improve upon typical run-times. The major thrust of the work now in hand, however, is to upgrade the method by the inclusion of higher-order terms in the governing equations. Within the existing numerical structure it is possible to upgrade the method to the status of the full Navier-Stokes equations. The marching procedure can, of course, be retained because the Navier-Stokes equations are parabolic with respect to time.* Upgrade of the turbulence model to two-equation status is also in hand to provide the capability necessary for handling this wider range of flow conditions. The intention at this stage, is to confine the research to flows which are boundary-layer like, i.e., to flows, close to solid boundaries, whose longitudinal extent of interest is large compared to their thickness. Important classes of flows have these characteristics -- flows which are intermediate, in terms of complexity, between those simple enough to conform to the first-order boundary-layer theory and those so complex that their computation requires access to specially-developed computing facilities. The present authors feel a strong commitment to the development of calculation tools which are within the means of private industry to use for engineering purposes.

Regardless of the status of the equations used to treat the viscous/turbulent flow near the solid boundary, there is a strong need to couple the solutions to potential flow solutions for an outer flow field. In this way the redistribution of longitudinal pressure gradients, arising from the displacement effects, can be properly accounted for. As noted earlier (Section IV above) this redistribution has a major influence on the ability of a calculation to proceed beyond the initial stages of reversal without encountering singular breakdown.

VII. CONCLUSIONS

This research is aimed both at the development of computational tools for unsteady flows with reversal and separation, and at the use of these tools to study the associated fluid mechanics. The simple tool of first-order boundary-layer theory has proved to have a surprising degree of versatility, and an impressive range of validity. The observation, made several years ago, that reversal onset did not signal the breakdown of the boundary-layer approximations, meant that the first-order theory could be used to study the early development of embedded reversed-flow regions. The observation, made herein, that the breakdown of those approximations does not inevitably occur -- even for extended times beyond reversal onset -- means that the theory can be used to study the mechanics of mature reversed flows, possibly to the point of their asymptotic approach to steady-state conditions.

The observation that the boundary-layer equations do not inevitably break down subsequent to reversal helps to clarify a number of important issues:

1. The singularity identified by Sears and Telionis is not a necessary feature of the first-order theory, but develops when the theory is interpreted in a particular manner: in terms of prescribed longitudinal pressure gradients.

2. The singularity can evidently be avoided if alleviation of the pressure gradients is permitted, in certain critical regions, as would occur if the boundary layer were allowed to interact with an outer potential flow.

3. The rapid thickening of the boundary layer, observed in certain calculations, may correspond to physical separation, or detachment of the outer streamlines, but may simply reflect the breakdown of the first-order theory due to inappropriate longitudinal pressure gradients.

4. When it does occur, physical separation usually takes place at a later time than flow reversal. The effects of time-dependence are typically to delay reversal onset (compared to conditions in an equivalent steady flow) and to delay separation onset even more. The time interval between reversal onset, at some station on a body, and separation onset may be indefinitely long depending on the temporal and spatial development of the pressure field.

5. Unsteady effects within the boundary layer appear to be capable of explaining two classes of dynamic stall: one in which rapid thickening of the layer, and separation, bring about a collapse of the circulation, and the other in which the layer remains thin but a tongue of reversed flow penetrates a leading-edge bubble causing it to grow and burst.

Coupling of a first-order boundary layer with a potential-flow model of the external flow field would appear to provide a tool for studying a wide variety of unsteady flows with embedded reversal. For many such flows use of the full Navier-Stokes equations, or their turbulent analog, would offer few advantages and poorer economy. Comparison between the solutions obtained by the two alternate approaches would serve to establish the range of validity of the former. For flows which are of the boundary-layer type, but in which the first-order approximations are inadequate, higher-order terms should be retained in the equations. The solution of the resulting set of equations, having a status lying between that of the first-order theory and the Navier-Stokes equations, should, again, be matched to an outer potential-flow model.

---

* In time-dependent flow no approximation needs to be made in order to produce this parabolic status.

REFERENCES

1. W. J. McCroskey, "Some Current Research in Unsteady Fluid Dynamics", J. Fluid Eng. 90, p.8, March 1977.
2. W. R. Sears and D. P. Telionis, "Unsteady Boundary-Layer Separation", Recent Research On Unsteady Boundary Layers, E. A. Eichelbrenner (Ed.) 1, p.404, 1971.
3. V. C. Patel and J. F. Nash, "Some Solutions of the Unsteady Turbulent Boundary Layer Equations", Recent Research On Unsteady Boundary Layers, E. A. Eichelbrenner (Ed.) 1, p. 1106, 1971.
4. D. P. Telionis, D. Th. Tsahalis, and M. J. Werle, "Numerical Investigation of Unsteady Boundary-layer Separation", Phys. Fluids, 16, p.968, 1973.
5. J. F. Nash, L. W. Carr, and R. E. Singleton, "Unsteady Turbulent Boundary Layers in Two-Dimensional Incompressible Flow", AIAA J. 13, p. 167, Feb. 1975.
6. D. P. Telionis, "Calculations of Time-Dependent Boundary Layers", Unsteady Aerodynamics, R. B. Kinney (Ed.), 1, p.155, 1975.
7. K. C. Reddy and W. L. Sickles, "Computation of Unsteady Boundary Layers", Unsteady Aerodynamics, R. B. Kinney (Ed.) 1, p.221, 1975.
8. J. F. Nash and V. C. Patel, "Three-Dimensional Turbulent Boundary Layers", SBC Technical Books, 1972.
9. R. E. Singleton and J. F. Nash, "A Method for Calculating Unsteady Turbulent Boundary Layers in Two-and Three-Dimensional Flows", AIAA J., 12, p.590, 1974.
10. P. Bradshaw, D. H. Ferris, and N. P. Atwell, "Calculation of Boundary-Layer Development Using the Turbulent Energy Equation", J. Fluid Mech., 28, p.593, 1967.
11. J. F. Nash, "Further Studies of Unsteady Boundary Layers with Flow Reversal", NASA CR-2767, 1976.
12. R. M. Scruggs, J. F. Nash, and R. E. Singleton, "Analysis of Flow-Reversal Delay for a Pitching Airfoil", AIAA Paper No. 74-183, 1974.
13. V. C. Patel and J. F. Nash, "Unsteady Turbulent Boundary Layers with Flow Reversal", Unsteady Aerodynamics, R. B. Kinney (Ed.), 1, p.191, 1975.
14. J. C. Williams, and W. D. Johnson, "New Solutions to the Unsteady Laminar Boundary Layer Equations Including the Approach to Unsteady Separation", Unsteady Aerodynamics, R. B. Kinney (Ed.), 1, p.261, 1975.
15. D. Catherall, and K. W. Mangler, "The Integration of the Two-Dimensional Laminar Boundary-Layer Equations Past the Point of Vanishing Skin Friction", J. Fluid Mech., 26, p.163, 1966.
16. J. N. Nielson, L. L. Lynes, F. K. Goodwin, and M. Holt, "Calculation of Laminar Separation With Free Interaction by the Method of Integral Relations", AIAA Paper No. 65-50, 1965.
17. R. M. Scruggs, J. F. Nash, and R. E. Singleton, "Analysis of Dynamic Stall Using Unsteady Boundary-Layer Theory", NASA CR-2462, 1974.
18. L. W. Carr, K. W. McAlister, and W. J. McCroskey, "Analysis of the Development of Dynamic Stall Based on Oscillating Airfoil Experiments", NASA TN D-8382, 1977.

FIGURES

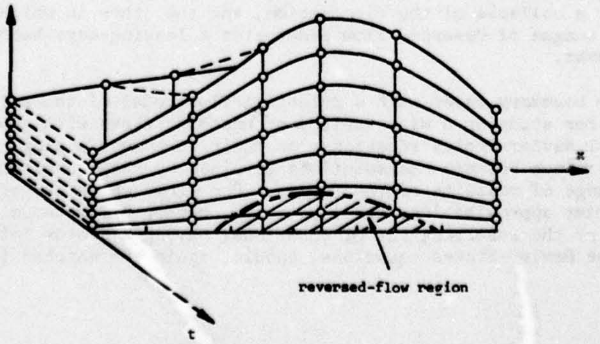

Figure 1 INTEGRATION DOMAIN FOR TIME-DEPENDENT BOUNDARY LAYERS

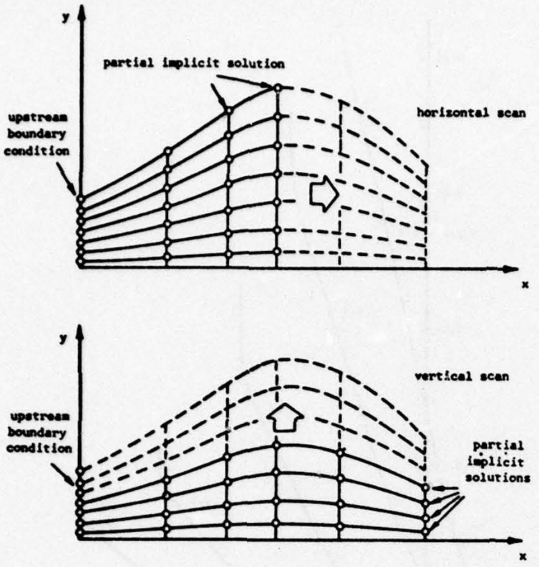

Figure 2 SCANNING OF THE x - y PLANE USING THE ALTERNATING-DIRECTION TECHNIQUE

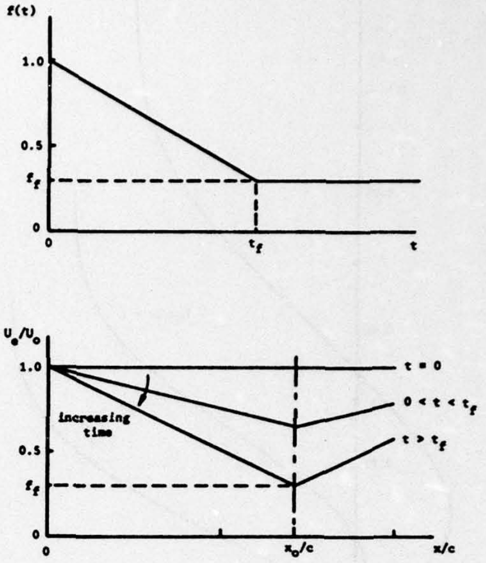

Figure 3 EXTERNAL VELOCITY DISTRIBUTIONS FOR "FROZEN FLOWS"

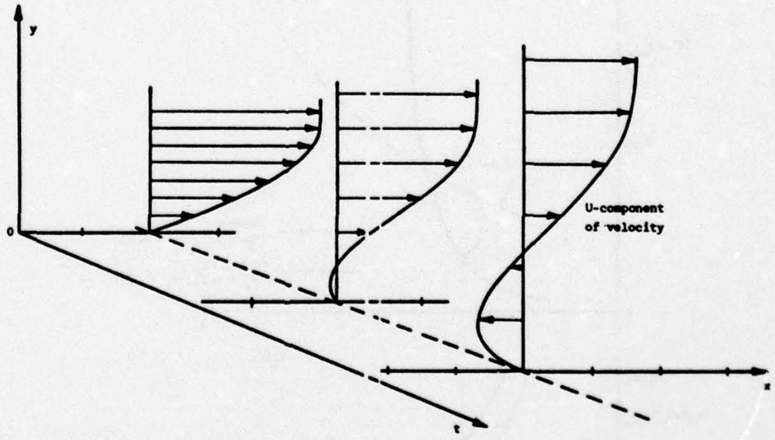

Figure 4 REVERSAL ONSET IN A TIME-DEPENDENT BOUNDARY LAYER

AD-A054 028 ADVISORY GROUP FOR AEROSPACE RESEARCH AND DEVELOPMENT--ETC F/G 20/4
UNSTEADY AERODYNAMICS.(U)
FEB 78

UNCLASSIFIED AGARD-CP-227 NL

4 OF 7
ADA
054028

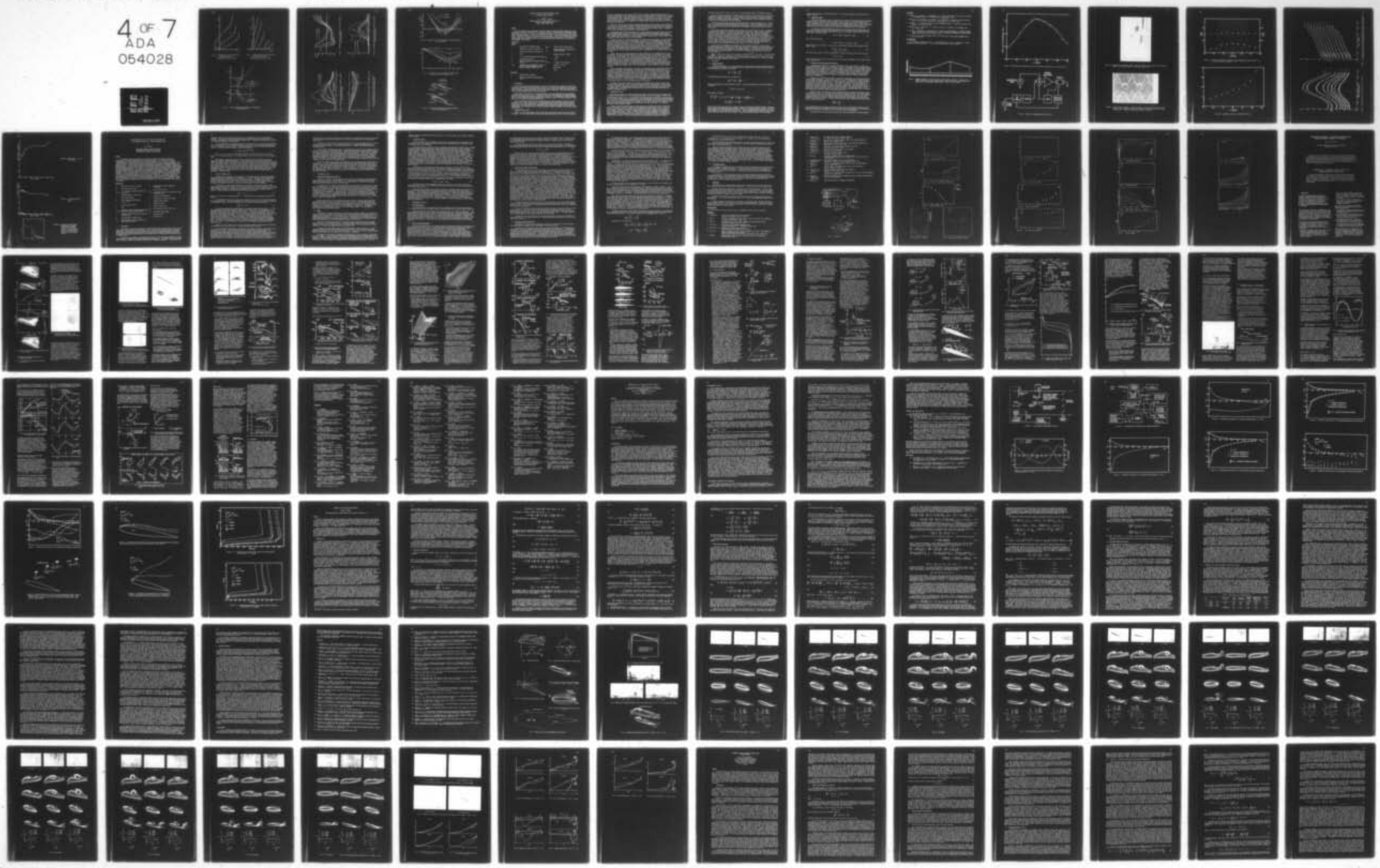

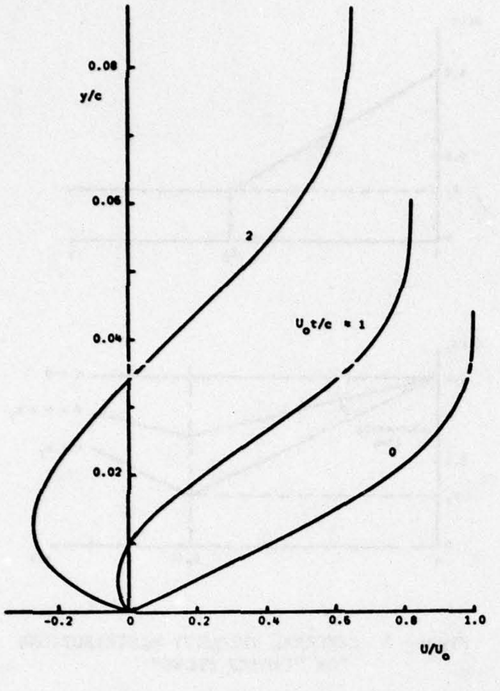

Figure 5 LAMINAR BOUNDARY LAYER PENETRATING A REVERSED-FLOW REGION (Laminar Frozen Flow: $R_e = 10^4$, $f_f = 0.5$, $t_f = 2.0$, $x/c = 0.5$)

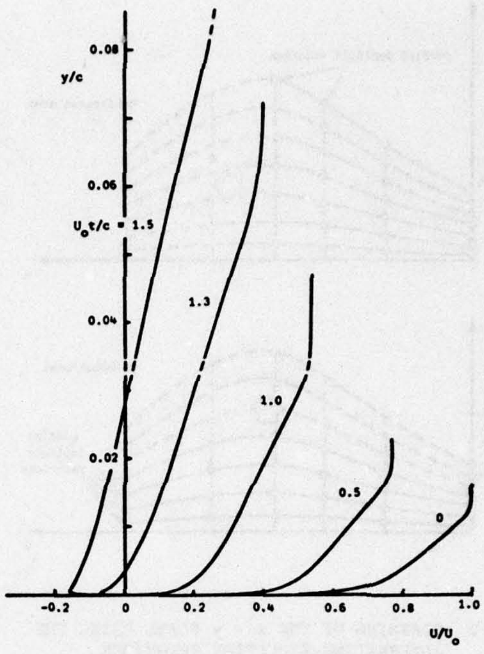

Figure 6 TURBULENT BOUNDARY LAYER PENETRATING A REVERSED-FLOW REGION (Turbulent Frozen Flow: $R_e = 10^7$, $f_f = 0.25$, $t_f = 1.5$, $x/c = 0.66$)

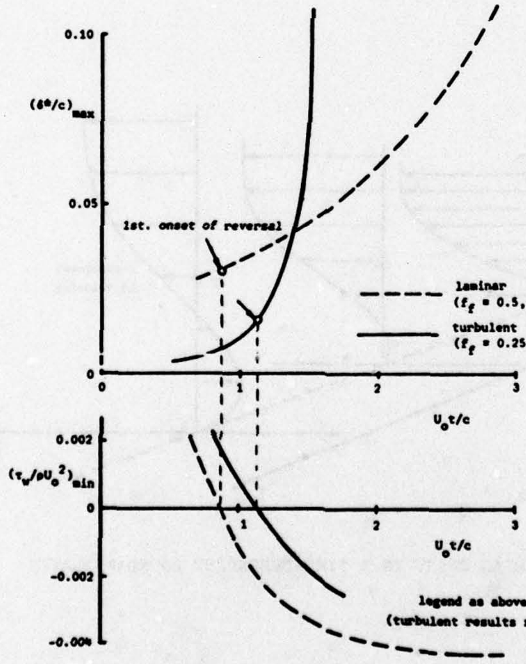

Figure 7 *RAPID THICKENING OF THE BOUNDARY LAYER SUBSEQUENT TO REVERSAL ONSET*

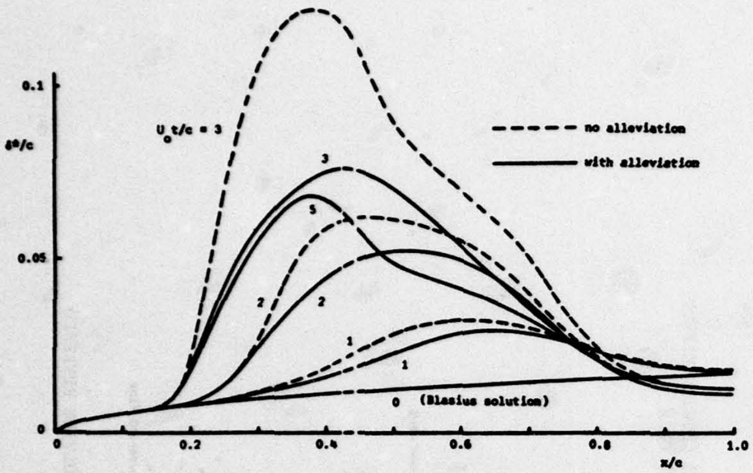

Figure 8 LAMINAR FLOW WITH ALLEVIATION OF PRESSURE GRADIENTS: *DISPLACEMENT THICKNESS*

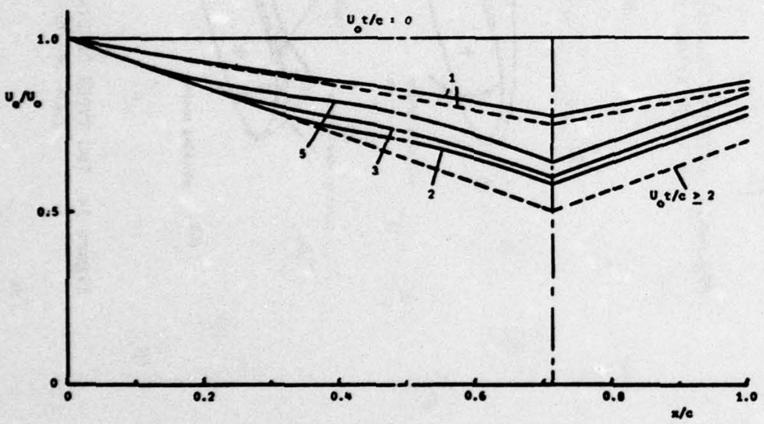

Figure 10 EXTERNAL VELOCITY DISTRIBUTIONS SHOWING EFFECTS OF ALLEVIATION: FROZEN LAMINAR FLOW

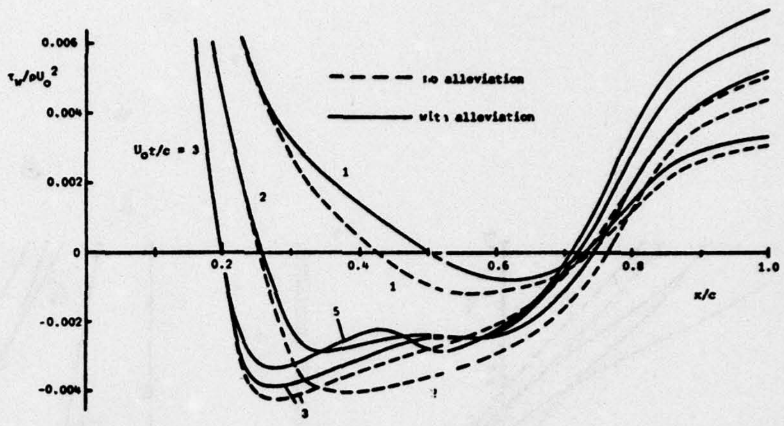

Figure 9 LAMINAR FLOW WITH ALLEVIATION OF PRESSURE GRADIENTS: WALL SHEAR STRESS

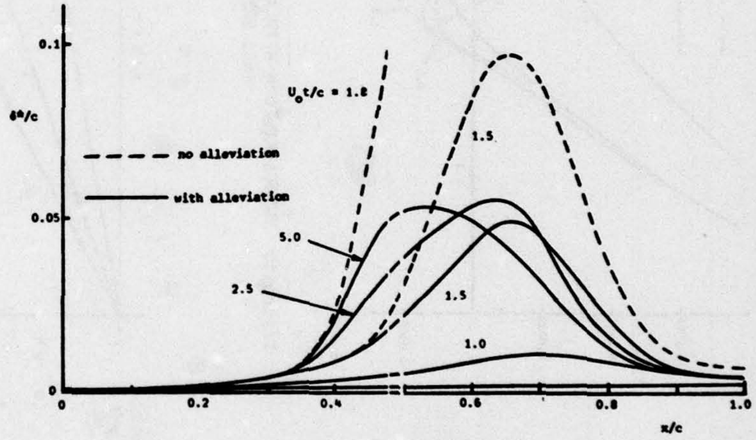

Figure 11 TURBULENT FLOW WITH ALLEVIATION OF PRESSURE GRADIENTS: DISPLACEMENT THICKNESS

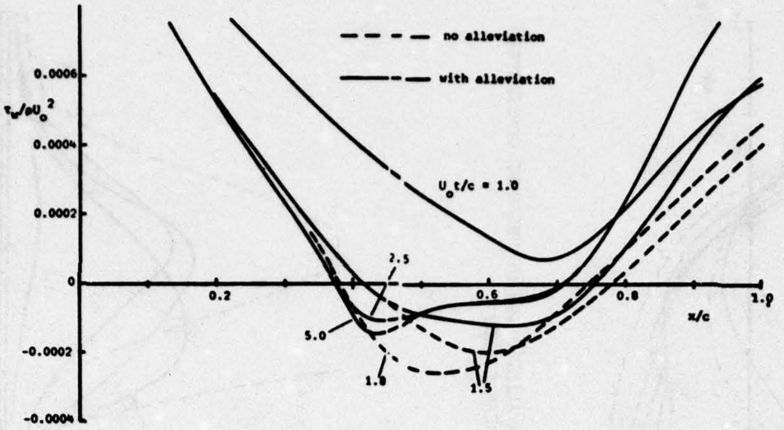

Figure 12 TURBULENT FLOW WITH ALLEVIATION OF PRESSURE GRADIENTS: WALL SHEAR STRESS

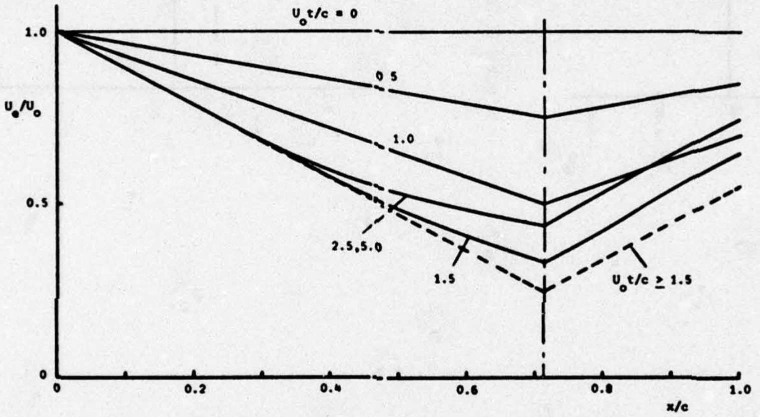

Figure 13 EXTERNAL VELOCITY DISTRIBUTIONS SHOWING EFFECT OF ALLEVIATION: FROZEN TURBULENT FLOW

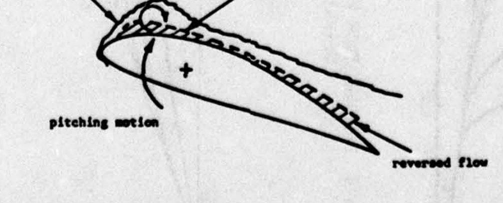

Figure 14 TWO TYPES OF DYNAMIC STALL INVOLVING REVERSED FLOW IN THE BOUNDARY LAYER

FEATURES OF UNSTEADY TURBULENT BOUNDARY LAYERS AS REVEALED FROM EXPERIMENTS

by
R. L. Simpson, Professor
Department of Civil and Mechanical Engineering
Southern Methodist University
Dallas, Texas 75275 USA

SUMMARY

The first results from an experimental research program on unsteady turbulent boundary layers near separation are presented. The test flow is a periodic, nominally two-dimensional, incompressible turbulent boundary layer on a flat surface. A programmable flow damper is used to produce the almost single harmonic velocity variation. It was found that the periodic flow in the viscous sublayer of the boundary layer is strongly influenced by the oscillating pressure gradient. *Within the semi-logarithmic velocity* profile region there is no phase variation. Since the characteristic frequencies of the turbulence decrease markedly near separation, there is much more interaction between the periodic oscillation and the turbulence in this region.

NOMENCLATURE

Symbols

C	characteristic streamwise length
f	frequency of periodic oscillation, Hz
n	characteristic bursting frequency, Hz
t	time
U	$= \overline{U} + \hat{U}$, ensemble-averaged velocity, fps
$\overline{U}$	time-averaged velocity
$\hat{U}$	periodic component of ensemble-averaged velocity
U_1, U_2	amplitude of the fundamental and second harmonic frequency components of the periodic ensemble-averaged velocity
$U_w(t)$	velocity scale for wall region
$\widehat{\overline{u^2}}$	ensemble-averaged streamwise mean square fluctuation
y	distance from wall, inches
y_w	$= yU_w/\nu$
y_∞	$= y/\delta$
$\delta(x,t)$	$= y$ where $U = 0.99\,U_\infty(x,t)$
ν	kinematic viscosity
ϕ	phase angle
ω	$= 2\pi f$

Subscripts

e	denotes entrance condition
∞	freestream condition outside boundary layer

1. INTRODUCTION

The results from experiments described in this paper are concerned with a periodic, nominally two-dimensional, incompressible turbulent boundary layer on a flat surface which separates due to an adverse pressure gradient. Several experimental investigations have been made of unsteady turbulent boundary layers, but few have measured the flow behavior as separation is approached. The results from ciné films of the unsteady separation behavior are also presented.

These results are the first in this research program to provide needed quantitative experimental information about this type of flow. A directionally sensitive laser anemometer to determine quantitatively the flow structure downstream of separation will be used. This information is clearly important since it is well recognized that this separated flow strongly influences the freestream potential flow, which in turn influences the upstream flow behavior.

Some of the important results that have been deduced from these experiments to date are (1) that the periodic flow in the viscous sublayer is strongly affected by the oscillating pressure gradient, (2) that there is no phase variation in a semi-logarithmic velocity profile region, and (3) that the characteristic large-scale eddies of the turbulence strongly influence the phase variation within the boundary layer. Near separation there is strong interaction between the boundary layer and the inviscid freestream flow.

2. EQUIPMENT AND TEST FLOW

Figure 1 is a side view schematic of the 25 feet long, three foot wide test section of the blown wind tunnel. The test boundary layer on the steel-reinforced wind tunnel floor is an airfoil type for

velocities corresponding to the average oscillating flow velocities at each streamwise location. An elaborate active boundary layer control system is used to eliminate preferential separation of the curved top wall boundary layer. Highly two-dimensional wall jets of high velocity air (110 fps) are introduced at the beginning of each of the eight feet long sections. At the latter two streamwise locations the oncoming boundary layer is partially removed by a highly two-dimensional suction system. All experimental data were obtained with the temperature and average entrance velocity being maintained essentially constant at 77°F and 54 fps.

Velocity profiles at several spanwise locations indicated that the mean velocity is two-dimensional within about 1%. Just upstream of the blunt leading edge of the test wall, 33 smoke ports are located spanwise across the wind tunnel contraction. A baffle plate deflects the smoke in the free-stream direction and tends to produce a uniform spanwise distribution of the dioctyl phthalate smoke. A spanwise sheet of laser light indicated two-dimensional time-averaged flow.

A programmable rotating-blade flow damper [1] is located downstream of the free-stream flow blower. The fixed setting damper is used to adjust the mean velocity while the programmable rotating-blade damper produces the flow unsteadiness. This is about 30 feet upstream of the wind tunnel contraction exit. Between these two locations are located a blower silencer, ductwork with a sound absorbing liner, honeycomb and seven screens, as well as the contraction.

As shown in figures 3, six-inch-chord symmetrical aluminum extrusions mounted on 1/2 inch diameter steel shafts are used for the five rotating blades. Only one or all of the blades may be used at any relative orientation to one another. Six-inch-pitch-diameter spur gears connect these shafts while other gears provide the drivetrain from a 0.3 hp DC motor. A specially built programmable motor power controller makes possible periodic variations of the angular velocity of the damper blades. This makes possible adjustment of the periodic velocity waveform at the test section entrance. An optical switch and a chopper blade mounted on the first damper blade shaft are used with the controller to maintain the period of each rotation constant within about 0.25% of a preselected crystal oscillator period. The blade angular velocity variation within each period is programmable with 16 adjustable motor voltage variations.

Figure 4 shows an oscilloscope photograph of several quantities for the 0.596Hz periodic flow described here. The three top blades rotate and are parallel when open while the fourth is fixed open and the fifth is fixed closed. The velocity varies from 36 to 72 fps. The straight line is a common voltage ground or zero velocity line. The top fuzzy triangular-shaped wave-form is the output voltage and associated noise from a voltage generator tachometer connected to the motor. Note that this smoothed shape closely corresponds to the smoothed low-pass filtered voltage variations in the 16 different voltage steps and shown in the bottom portion of the photograph. The linearized hot-wire anemometer signal at the test section entrance and the pure sine wave indicate that the velocity variation is approximately sinusoidal. The velocity time derivative is also observed to be not extremely far from a consine wave although there is more than 90 degrees of phase difference with the velocity variation.

Hot-wire anemometers and linearizers constructed from integrated circuits and Thermo-Systems Model 1218 probes with 0.00015 inches diameter wires were used in the measurements reported here. The averages of signals over an integral number of period cycles of the crystal oscillator were obtained using a voltage-controlled oscillator (VCO) and a digital counter. The signal was input to the VCO and the digital counter displayed the ratio of the crystal oscillator frequency to the average VCO frequency. Simultaneously the signals from the hot-wires located in the boundary layer and in the freestream and the reference signal from the crystal oscillator passed through line driver amplifiers to 16 bit A/D converters. These digitized signals were sampled by a Fortran programmable EAI Model 640 Digital Computer at 96 different phases of the fundamental period to educt the periodic variation of the boundary velocity $\hat{U}$ and the streamwise velocity fluctuation $\hat{\overline{u^2}}$.

The smoke-filled turbulent flow was illuminated by a streamwise vertical sheet of laser light along the tunnel centerline. Ciné films with a Paillard-Bolex H16M camera capable of framing rates of 16 to 64 frames/sec. were made to visualize the separating flow. Styrofoam balls about 1/16 inches in diameter were used to approximately mark the variation of the mean separation location during the oscillation period. These balls were rolled about on the test floor by the opposing upstream and downstream aerodynamics forces.

3. EXPERIMENTAL RESULTS

Based upon the average test section entrance velocity $\overline{U}e_\infty$ of 54 fps and the 16 feet length of the converging-diverging section for C, the length Reynolds number for this flow is $\frac{\overline{U}e_\infty C}{\nu} = 5.1\text{x}10^6$ and the reduced frequency $\omega C/2\overline{U}e_\infty = 0.55$. The free-stream oscillation amplitude is about 1/3 of the mean velocity. These values are near the values encountered in some turbomachinery and helicopter blade applications. Fourier analysis of the ensemble-averaged free-stream velocity indicates that only 0.2% of the oscillation energy lies in the harmonics greater than the fundamental. While this flow may be considered near quasi-steady, the moderate oscillation amplitude introduces some non-linear effect that is of interest, particularly in the separation region.

As shown in figure 2, the mean velocity of the freestream in the oscillating flow is almost the same up to 90 inches as that for a steady flow with the same entrance velocity. The ratio of the oscillation amplitude to the mean velocity of the fundamental only slightly deviates from a constant value as shown in figure 5a. The second harmonic contribution reaches a maximum at the minimum flow area and decreases downstream. There is increasing phase lead of the fundamental as the separation region is approached as shown in figure 5b. There is little streamwise variation of the phase of the second harmonic. The test boundary layer near separation is several inches thick, so freestream and boundary layer interaction is believed to produce the deviation between the unsteady and steady freestream results shown in figure 2 as well as the increasing phase lead of the freestream velocity.

The ciné films for steady flow at an entrance velocity of 54 fps indicate that there is considerable unsteadiness introduced by separation. Previous research in this tunnel [2] indicates that turbulent boundary layer separation is unsteady by nature, moving up and down stream over a streamwise distance of the order of several boundary layer thicknesses. Some unsteadiness is also introduced into the free-stream flow by the turbulent-non-turbulent interface.

The movies for the unsteady flow show the periodic movement of the mean separation line. Unsteadiness is also introduced into the freestream by the boundary layer. There is approximately 30° - 50° phase lag between the free-stream and the movement of the separation line as indicated by the styrofoam balls. This lag is due to the time required for the large eddies in the outer shear layer to supply the backflow.

Figure 6 shows the periodic ensemble-averaged results for the 87.56 inches location. The momentum thickness Reynolds number at this location varies between 4300 and 6700. There is significant phase lead in the viscous sublayer as shown in the bottom trace. Figure 7 shows the periodic ensemble-averaged velocity profiles for several cycle phases with a distinct semi-logarithmic region near the wall and a distinct wake region near the freestream. Figure 8 shows the phase for the fundamental harmonic as a function of distnace from the wall. The greatest phase lead occurs in the viscous sublayer. As proven below, the phase in the semi-logarithmic velocity profile region must be constant and is observed to be so. Note that the boundary layer thickness δ is a periodic function of the cycle phase. The outer region of the U/U_∞ vs. y/δ profile does not vary significantly with phase when the local U_∞ and δ values for the same phase are used. Near the wall in the semi-logarithmic region there is a small deviation from the average velocity profile, shown as a solid line in figure 7.

Figure 9 shows the amplitude of the fundamental U_1 and the second harmonic U_2 of the periodic ensemble-averaged results normalized by the local mean velocity $\overline{U}$ as a function of distance from the wall. The ratios $U_1/\overline{U}$ and U_2/U are the greatest in the viscous sublayer. As discussed below this occurs because the oscillating pressure gradient has the greatest influence on the relatively low velocity flow in the sublayer. The flow downstream of this location but upstream of separation exhibits the same qualitative behavior.

There is little phase variation of the turbulence fluctuation $\left(\widehat{\overline{u^2}}\right)^{\frac{1}{2}}$ near the wall. The outer region of the $\left(\widehat{\overline{u^2}}\right)^{\frac{1}{2}}/\ U_\infty$ profile is correlated for different phases when the local U_∞ and δ values for the same phase are used. Based upon the previous work on steady free-stream separation [3], the hot-wire signals indicated intermittent backflow at 106.3 inches.

4. DISCUSSION

4.1 Sublayer behavior

From these experiments it is now clear that the periodic variation of viscous sublayer velocities can be markedly out of phase with the freestream velocity. Neglecting the turbulence and the convective terms, the equation of motion can be written

$$\frac{\partial U}{\partial t} = \frac{-1}{\rho}\frac{dP}{dx} + \nu\frac{\partial^2 U}{\partial y^2} \qquad (1)$$

The freestream pressure gradient can be expressed as

$$\frac{\partial U_\infty}{\partial t} + U_\infty\frac{\partial U_\infty}{\partial x} + \frac{1}{\rho}\frac{dP}{dx} = 0$$

from the one-dimensional inviscid equation of motion. If the free-stream velocity varies approximately according to

$$U_\infty = \overline{U}_\infty(x) + U_{1\infty}\cos(\omega t) \qquad (2)$$

then equation (1) becomes

$$\frac{\partial U}{\partial t} - \nu\frac{\partial^2 U}{\partial y^2} = -U_{1_\infty}\,\omega\sin(\omega t) + \overline{U}_\infty\frac{d\overline{U}_\infty}{dx} + \left(\overline{U}_\infty\frac{dU_{1\infty}}{dx} + U_{1\infty}\frac{d\overline{U}_\infty}{dx}\right)\cos(\omega t)$$

$$+ \frac{U_{1_\infty}}{2}\frac{dU_{1_\infty}}{dx}\left[1 + \cos(2\omega t)\right] \qquad (3)$$

The first term on the right side of this equation is due to the unsteady free-stream velocity. The other terms are the steady pressure gradient, the major component to the unsteady pressure gradient, and the non-linear component to the unsteady pressure gradient. In the low frequency moderate amplitude oscillations examined here, the first and the last terms are small. Thus the unfavorable oscillating pressure gradient and the freestream velocity are almost in phase. The pressure gradient strongly acts on the viscous sublayer flow to produce a significant phase lead. The non-linear component also has some effect as shown in figure 9.

4.2 Logarithmic region

Based upon dimensional grounds, it is possible to prove that the phase variation of the ensemble averaged velocity is zero within a semi-logarithmic region. That is, if a semi-logarithmic velocity profile is observed, the phase shift with respect to the freestream does not vary in that region. It is well established that in a steady free-stream turbulent boundary layer one set of velocity and length scales exists for the velocity profile near the wall, as expressed by the "law-of-the-wall", while another set exists for the velocity near the freestream, as expressed by the "law-of-the-wake".

In the region of overlap between these regions, the velocity profile varies with ln/y/. Two such sets of velocity and length scales apparently exist for a periodic unsteady turbulent boundary layer at each streamwise location, $U_w(t)$ and $\nu/U_w(t)$ for the wall region, and $U_\infty(t)$ and $\delta(t)$ for the outer region. Thus near the wall

$$U(y,t) = \overline{U}(y_w) + U_1(y_w) f(\omega t + \phi(y_w)) \tag{4}$$

while in the outer region

$$U(y,t) = \overline{U}(y_\infty) + U_1(y_\infty) f(\omega t + \phi(y_\infty)) \tag{5}$$

where the function f is periodic. In the region of overlap both relations should produce the same result. Thus,

$$\frac{U_w}{\nu} \frac{\partial U}{\partial y_w} = \frac{\partial U}{\partial y} = \frac{1}{\delta} \frac{\partial U}{\partial y_\infty} \tag{6}$$

Since this overlap region is formally independent of viscosity, then $\partial U/\partial y_w$ must vary as $1/y_w$ and

$$U(y,t) \sim \ell n/y/ \tag{7}$$

Only if $\phi(y_\infty)$ equals $\phi(y_w)$ and is constant can each of the terms in equations (4) and (5) have a logarithmic variation in y.

4.3 Periodic oscillation-turbulence interaction

A characteristic frequency of the large-scaled eddies of the outer region of a steady free-stream turbulent boundary layer is the "bursting" frequency. These coherent structures supply momentum and energy to the wall region from the outer region flow and are responsible for the engulfment of free-stream fluid in the entrainment process. They can agglomerate into larger structures and new structures can be formed by flow instabilities. The behavior of these structures is the subject of much current turbulent shear layer research [4]. In most of the experiments that have been reported for unsteady freestream flows, the oscillation frequency was much below the bursting frequency. No appreciable effect on the turbulence structure was noted, i.e., turbulence models for steady freestream flows appeared to be adequate [5].

However, it is important to note that as separation is approached, the characteristic bursting frequency greatly decreases. Figure 10 shows the variation of the characteristic bursting frequency for the steady freestream separating flow of Simpson, et al [2]. The beginning of intermittent separation (backflow on an intermittent basis) occurred at about 121 inches and the zero average surface shearing stress occurred at about 132 inches. The ratio of the periodic oscillation frequency to the characteristic bursting frequency increases as separation is approached. The oscillating pressure gradient and the turbulent structure become more strongly coupled. Thus, even though there may not be appreciable interaction upstream, there will be more interaction in the separation region. In the present flow, there is moderate phase lead of the boundary layer ensemble-averaged velocities upstream, while downstream the backflow lagged the freestream by about 40°.

Whether a lead or lag occurs near the wall depends partially on whether the pressure gradient oscillation leads, lags, or is in phase with the free-stream velocity variation. For example, there was a low amplitude traveling wave oscillation in the flat plate experiments of Patel [6]. The favorable pressure gradient part of the cycle lagged the freestream velocity by about 90°. There was little interaction between the oscillation and the turbulence; the oscillation frequency was well below the boundary layer bursting frequency. In that case the logarithmic region lagged the freestream velocity. This lag can be expressed by

$$\frac{\phi_{lag}}{2\pi} \approx 10 \frac{f\delta}{\overline{U}_\infty}$$

It is interesting that Simpson et al. [2] found that $n\delta/U_\infty \approx 1/10$ for the bursting frequency in their separating boundary layer. Noting the similarity of these latter two expressions, it is reasonable to expect that the phase shift near the wall is also related to the bursting frequency.

The questions that have been raised by these results are being addressed in further research.

REFERENCES

1. Simpson, R. L., Sallas, J. J., and Nasburg, R. E., "Tailoring the Waveform of a Periodic Flow with a Programmable Damper," to be submitted to J. Fluids Engrg., 1977.
2. Simpson, R. L., Strickland, J. H., and Barr, P. W., "Features of a Separating Turbulent Boundary Layer in the Vicinity of Separation," J. Fluid Mech., 79, pp. 553-594, 1977.
3. Simpson, R. L., "Interpreting Laser and Hot-film Anemometer Signals in a Separating Boundary Layer," AIAA J., 14, pp. 124-126, 1976.
4. Davies, P. O. A. L. and Yule, A. M., "Coherent Structures in Turbulence," J. Fluid Mech., 69, pp. 513-537, 1975.
5. Cousteix, J., Desopper, A., and Houdeville, R., "Structure and Development of a Turbulent Boundary Layer in an Oscillatory External Flow," paper 8B, Proceedings of Symposium on Turbulent Shear Flows, April 18-20, 1977, Pa. State Univ., 1977.
6. Patel, M. H., "On Turbulent Boundary Layers in Oscillatory Flow," Proc. R. Soc. London A. 353, pp. 121-144, 1977.

ACKNOWLEDGMENTS

This research was supported by the U. S. Army Research Office. Dr. Y.-T. Chew and E. B. Bowles obtained and reduced these data; J. J. Sallas solved the many minor computer problems.

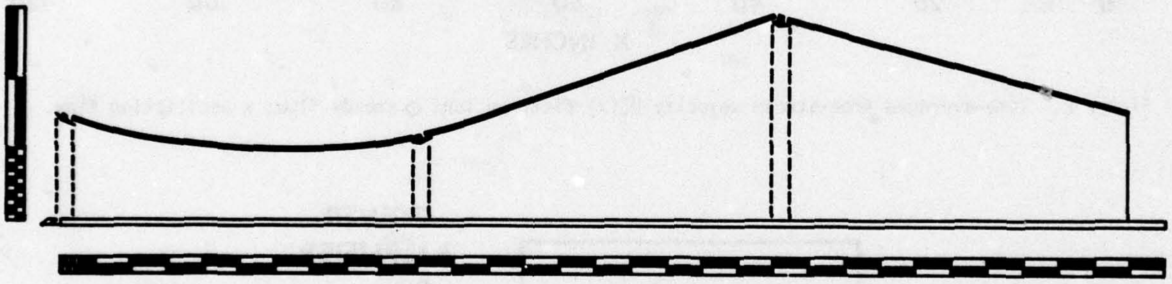

Figure 1. Sideview schematic of the test section. Major divisions on scales: 10 inches. Note baffle plate upstream of blunt leading edge on bottom test wall and side and upper wall suction and wall jet boundary layer controls. Flow from left to right.

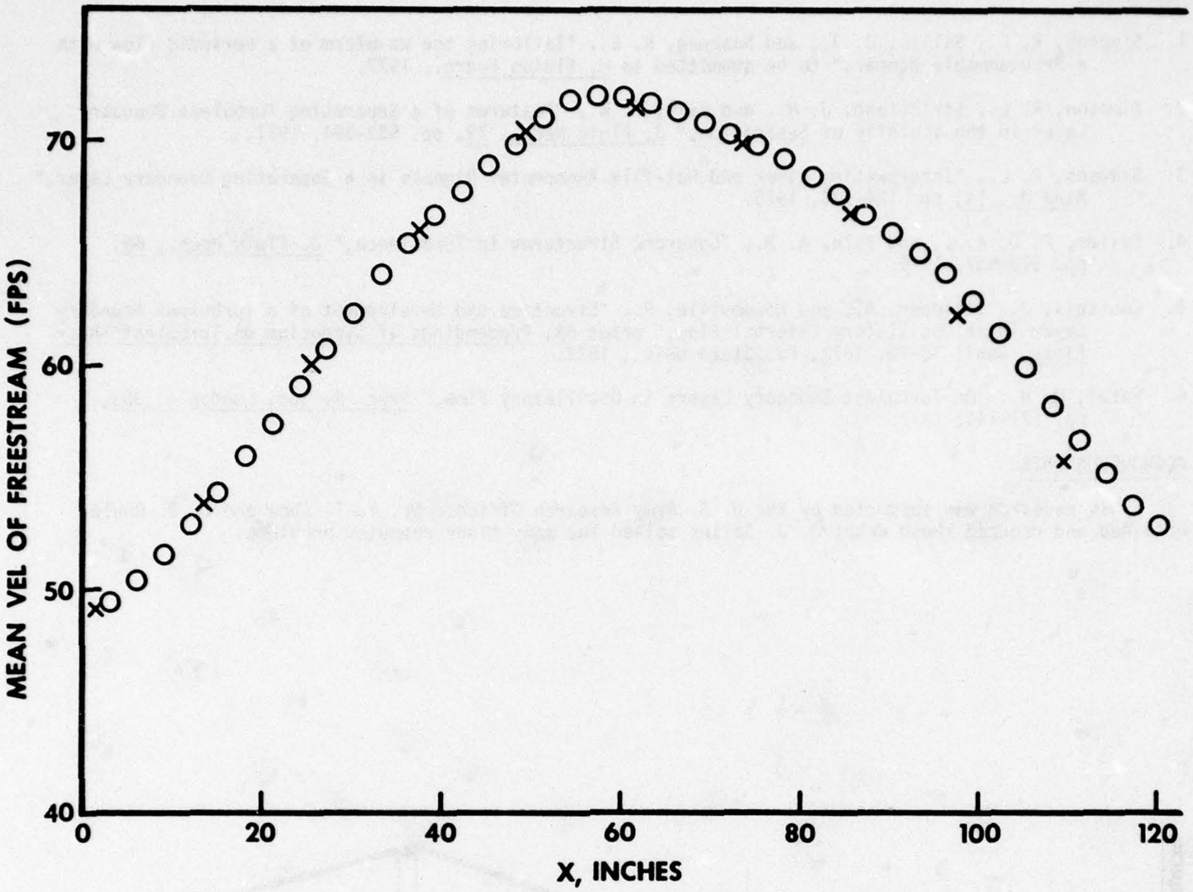

Figure 2. Time-averaged free-stream velocity $U_1(x)$ distribution: ○ steady flow; x oscillating flow.

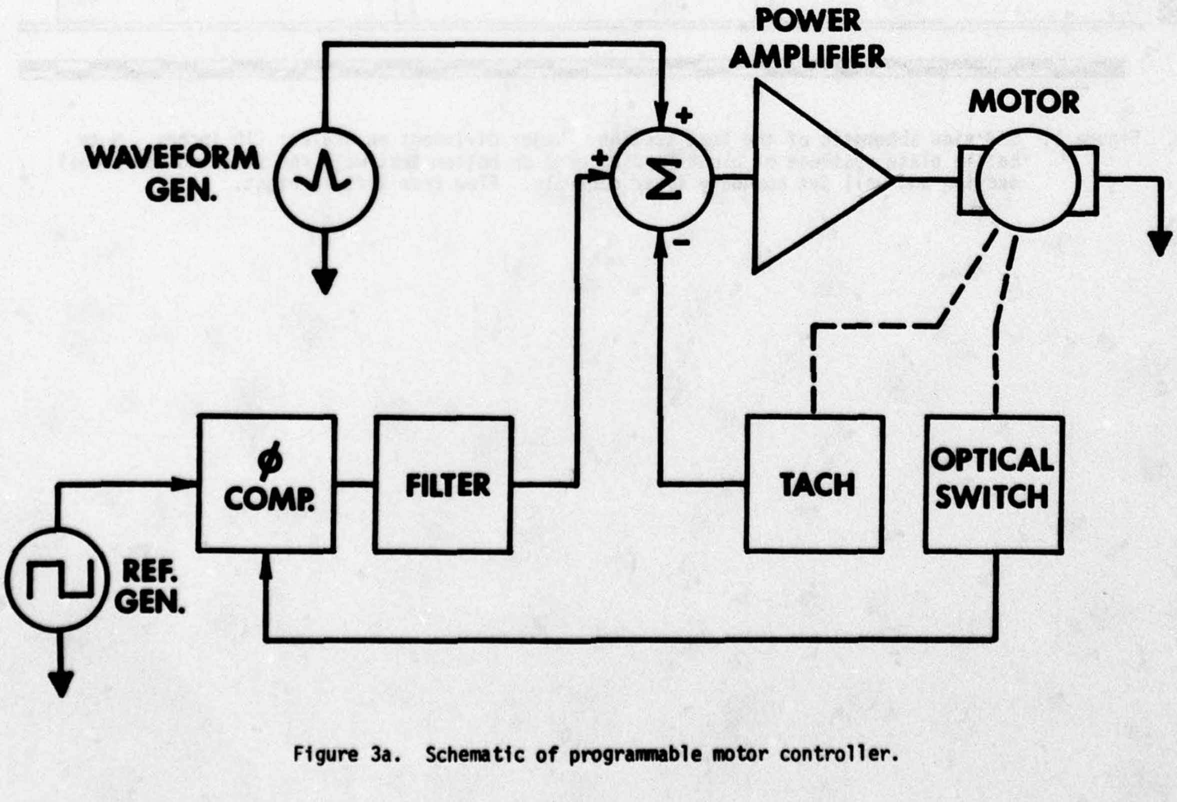

Figure 3a. Schematic of programmable motor controller.

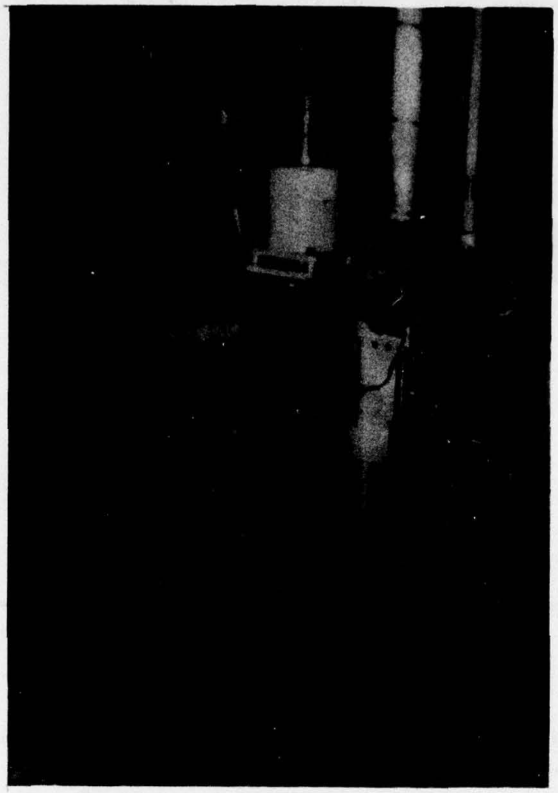

Figure 3b. Photograph of programmable damper. Note fixed damper at right, gear train for rotating blades in the center, and motor and tachometer at center top.

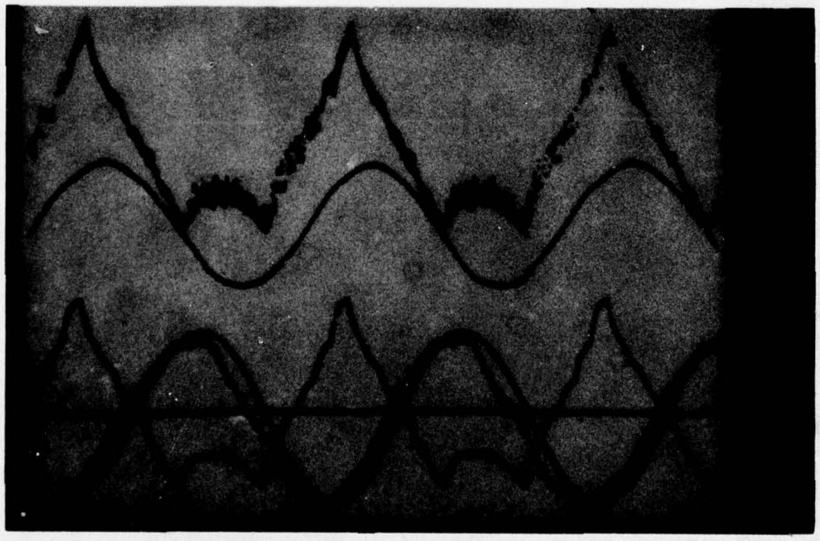

Figure 4. Time variation of signals. From top to bottom: angular velocity variation, tunnel velocity, input voltage variation, time derivative of tunnel velocity, pure cosine, common ground. 2 volts/div. vertical; 0.5 sec/div. horizontal.

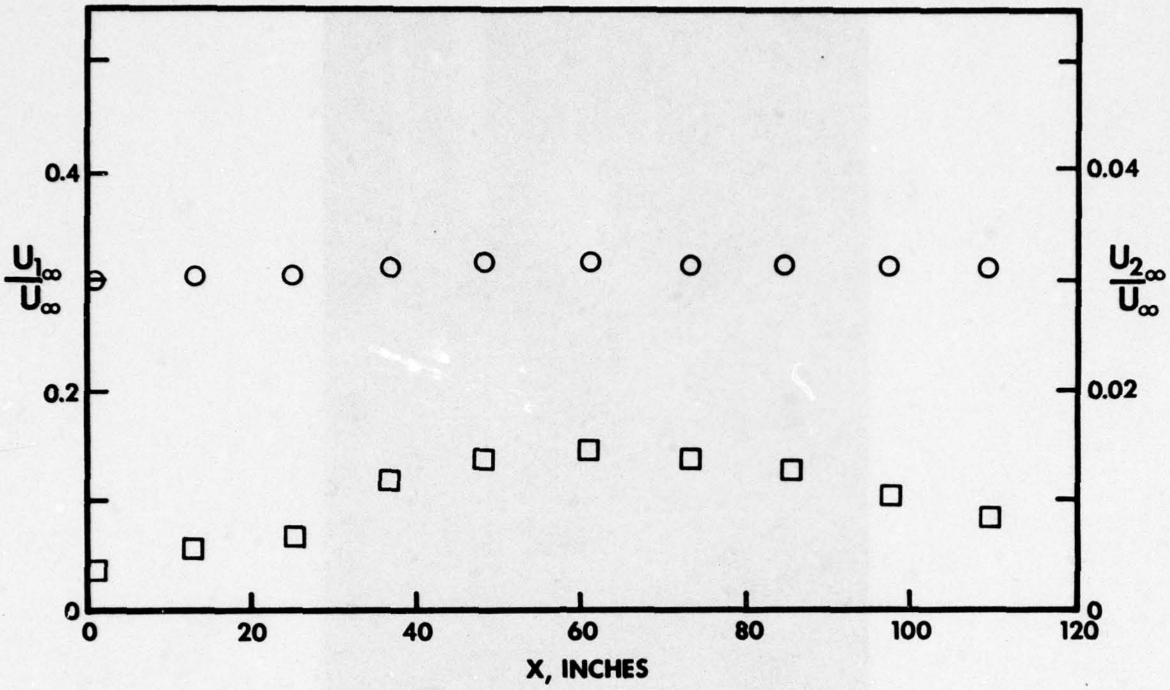

Figure 5a. Normalized oscillation amplitudes for the fundamental and second harmonics, $U_{1_\infty}(x)/\overline{U}_\infty(x)$ and $U_{2_\infty}(x)/\overline{U}_\infty(x)$. □

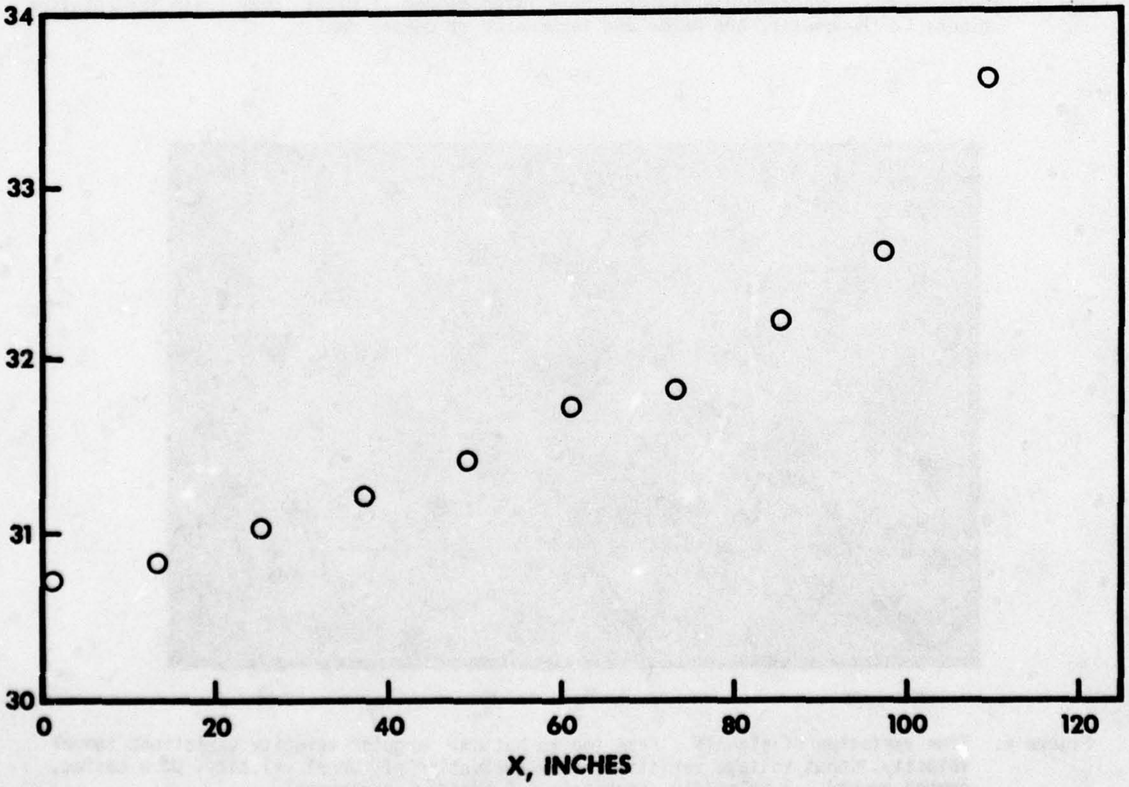

Figure 5b. Streamwise variation of the phase angle of U_{1_∞}.

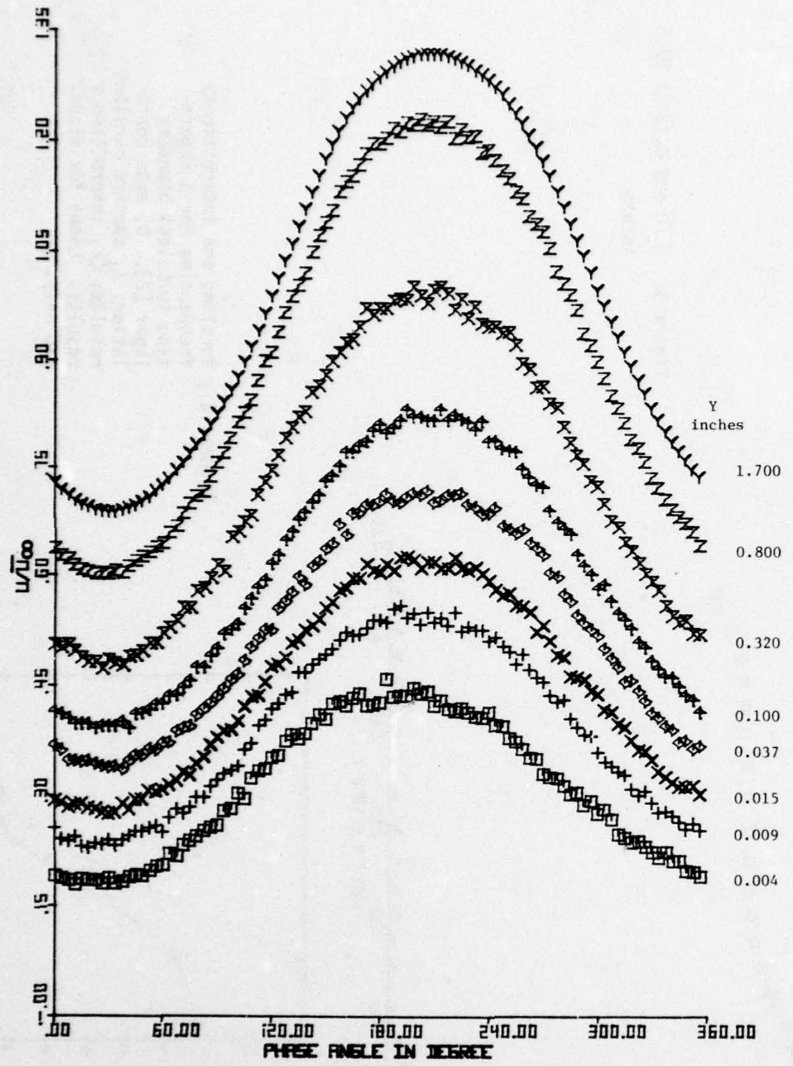

Figure 6. Phase variation of mean velocity at 87.5 inches.

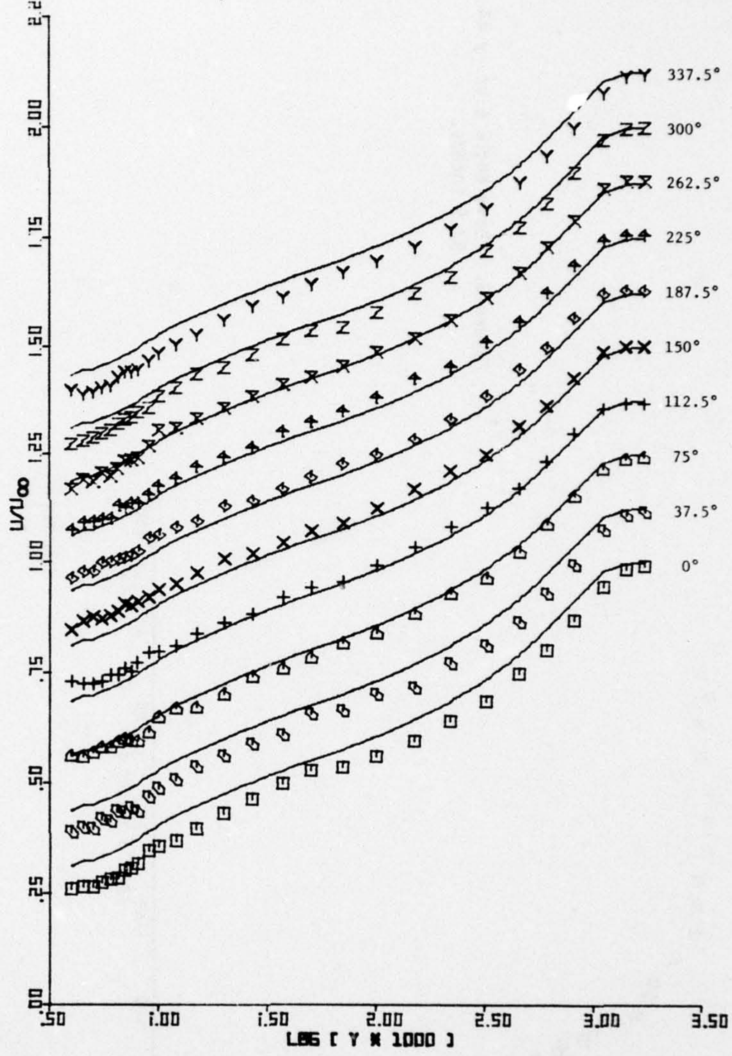

Figure 7. Velocity profiles at several cycle phases, 87.5 inches. Note ordinate scale offset of 0.125. Time-average velocity denoted by solid line.

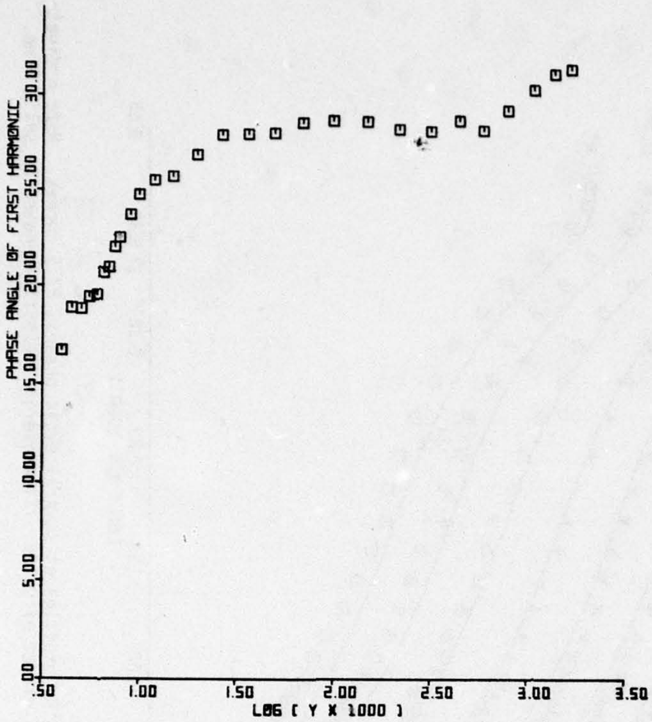

Figure 8. Phase angle ϕ vs. y at 87.5 inches.

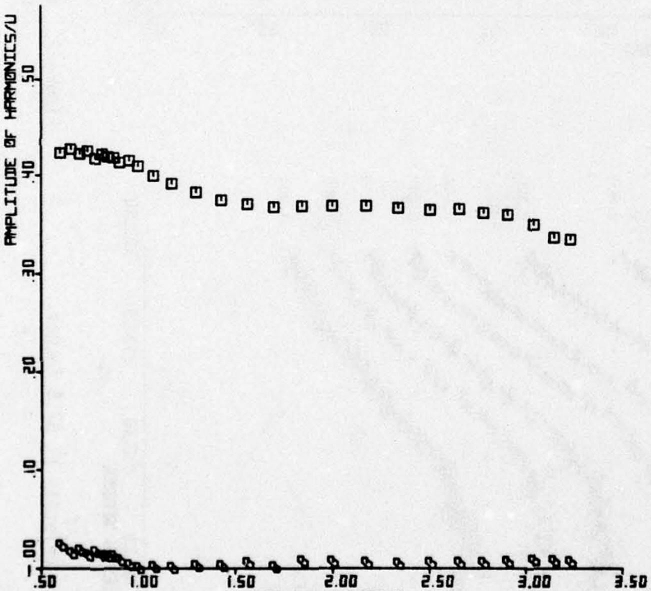

Figure 9. $U_1/\overline{U}$ and $U_2/\overline{U}$ at 87.5 inches.

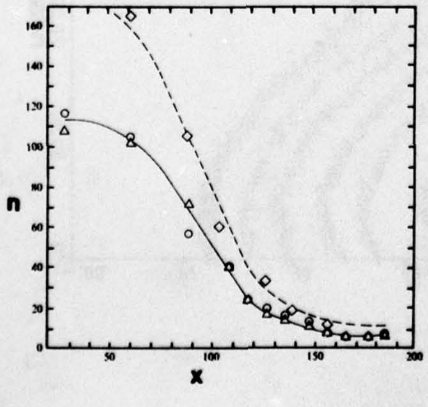

Figure 10. Bursting and intermittency frequencies for a separating turbulent boundary layer [2]. O, auto correlation; Δ, spectra bursting results; ◇, intermittency results. Lines for visual aid only.

AN EXPERIMENTAL STUDY OF THE EFFECT OF OSCILLATORY FLOW ON THE SEPARATION REGION IN A TURBULENT BOUNDARY LAYER

by

R. C. Kenison

Queen Mary College, University of London
Department of Aeronautical Engineering
Mile End Road, London, E1 4NS, England

SUMMARY

A separated turbulent boundary layer on a plate was subjected to harmonic oscillations superimposed on the mean adverse freestream velocity distribution. The resulting effects were investigated over a range of frequencies up to 6 Hz and amplitudes up to 13 per cent of the mean freestream velocity. Measurements were made of boundary velocity profiles, turbulence components, static pressures and skin friction at various points along the plate surface before and immediately after the separation point. For the range of frequencies and amplitudes examined the oscillating freestream had a negligible effect on the mean distributions of skin friction, static pressures, turbulence intensities and the mean separation position. The variation of velocity amplitudes in the boundary layer, which exceeded the freestream amplitude at certain positions, was dependent on frequency and distance from leading edge. The phase of these oscillations consistently lagged behind the freestream oscillations. Instantaneous measurements of skin friction showed that it oscillated at the same frequency as the fundamental forcing frequency. As the separation point for steady flow was approached from upstream, the oscillating skin friction at some point became negative for part of the oscillatory cycle. This negative portion of the cycle increased as the mean separation point was approached. However the oscillating reversed flow region ahead of separation position for steady flow produced very little variation in momentum thickness and shape parameter, i.e. there was no associated convection of vorticity into the main stream. There was similarly a region showing oscillation in flow direction and skin friction downstream of the position of separation.

NOMENCLATURE

C_f	mean local skin friction $\tau_w/\frac{1}{2}\rho U_1^2$
C_p	mean pressure coefficient
$C_{p_{r.m.s}}$	root mean square of pressure coefficient $P_{r.m.s}/\frac{1}{2}\rho U_1^2$
d	outside diameter of Preston tube
H	mean shape parameter
P_a	static pressure amplitude ratio $P_{1_{r.m.s.}}/\frac{1}{2}\rho U_0^2$
Q	travelling wave velocity
t	time
$U_{1_{r.m.s}}$	root mean square of the freestream velocity amplitude at edge of boundary layer
U_1	mean local freestream velocity at edge of boundary layer
U_a	peak amplitude in boundary layer
U_{1_a}	peak amplitude of freestream velocity at edge of boundary layer.
u'	mean turbulent velocity component in x-direction
u_τ	skin friction velocity
$\lvert U_{1_i} \rvert$	instantaneous velocity in freestream at edge of boundary layer
x	distance from leading edge
y	perpendicular distance from surface
δ	boundary layer thickness
θ	momentum thickness
τ_w	mean wall shear stress
τ_{w_a}	peak amplitude of wall shear stress
ϕ_ℓ	phase angle (lag) degrees
ω	pulsatance ($2\pi f$)
ρ	density of air

1. INTRODUCTION

The effects of an oscillating freestream on turbulent and laminar boundary layers are of practical importance in various fields of fluid dynamics. A few illustrations of basic applications include the stator blades in turbo-machinery which are subjected to oscillatory flow generated by the passing rotor blades, wings under flutter conditions, aerofoil lift hysteresis and flow over helicopter rotor blades. The importance of understanding the effects of oscillatory flows can eventually improve the design of new aerodynamic systems.

Experimental and theoretical investigations of separation of two dimensional turbulent and laminar boundary layers in steady flow has been well documented for many years. The numerical methods available are still unable to predict exact boundary layer profiles at and beyond separation. The location of the separation point can be determined almost precisely, thus a knowledge of the limiting parameters is essential. There have been very few theoretical and no experimental studies into the effects of an oscillating freestream on a separating turbulent boundary layer. Therefore the required data to predict oscillatory flow separation is not available.

This paper describes an experimental examination of the response of a separated turbulent boundary layer under the effect of an oscillating freestream. Comprised of a mean freestream superimposed upon this is a disturbance, which is convected in the downstream direction at less than the mean freestream velocity. Hence the freestream velocity is given by the equation

$$U_{1_i} = U_1(x) + U_{1_a}(x)e^{i\omega(t - \frac{x}{Q})} \qquad (1)$$

where $|U_{1_i}|$, U_1, U_{1_a} are the instantaneous, mean and oscillatory amplitude of the freestream velocity, ω is the radian frequency, Q the travelling wave velocity and x the distance from the leading edge.

Measurements included pressure distributions, velocity profiles, Preston tube readings and longitudinal turbulence velocity measurements. Examination was made of the region close to and immediately beyond the steady flow separation point, to determine the effect of the oscillatory freestream on the onset of flow reversal at the wall. This condition is defined as the wall shear stress reaching zero at any instant in time. It has been emphasised that for laminar flow and theoretically for turbulent flow, separation does not necessarily mean the boundary layer becomes detached from the body. In these experiments oscillating zero wall shear stress was observed without separation ahead of the known steady flow separation point. It was hoped the data acquired during these experiments may help in the development of more exact theoretical models, and give an indicationg of the limiting parameters for separation in oscillating flows.

2. REVIEW OF PREVIOUS WORK

Several recent investigations into the effects of oscillatory flow on separation have produced important advances in the knowledge of this phenomenon. It has only been during the last decade that unsteady or oscillatory flows have been studied to any great extent. Recently there have been some reviews written which cover this broad topic by Stewartson[1] (1960), Rott[2] (1964), Stuart[3] (1971), Telionis[4] (1975) and Williams[5] (1977). From these reviews it was clear that the majority of the work has been biased towards the theoretical aspects and the development of numerical methods.

The criteria for steady flow two dimensional separation was first stated by Prandtl in 1904. Prandtl described separation as "the point from which the flow ceases to follow the contours of that body". Separation marks the end of the boundary layer and the beginning of the wake or separation bubble. In an ideal situation the approach to separation is accompanied by the vanishing of the shear stress at the surface. Prandtl's definition of two dimensional separation was given by:

$$\frac{\partial U}{\partial y} = 0 \quad \text{at} \quad y = 0 \qquad (2)$$

where U was the velocity in the boundary layer, y is the perpendicular distance measured away from the surface.

The Prandtl definition for separation has been shown not to be valid for all cases of steady flow, by Moore Rott and Sears. These three independently studied steady flows over moving walls and proposed that simultaneous vanishing of shear and velocity was an indicator for separation, defined by

$$\frac{\partial U}{\partial y} = 0 \quad \text{at} \quad U = 0 \qquad (3)$$

The two flows considered were steady flow with an upstream and downstream moving wall. In both cases the boundary layer flow is divided by the wake at a stagnation point. This hypothesis was experimentally verified by Vidal[6] (1959) and Ludwig[7] (1964). Tsahalis D.T. and Telionis D.P.[8] (1973) developed a numerical method which confirmed these results, for the downstream moving wall only. The separation of the boundary layer appears at the point defined by equation 3, rather than at the point for zero skin friction defined by equation 2. The criteria of Moore, Rott and Sears has been proven for steady flows over moving walls. Williams and Johnson[9] (1974) showed that for the special case of unsteady flow over stationary walls it may be mathematically transformed into steady flow over moving walls. The method of semi-solutions was used. The results of this study showed that the separation point is characterised by simultaneous vanishing of both shear and velocity at a point in the boundary layer flow. This is a singular behaviour in the solution of the boundary layer equations near the separation point.

Danberg & Fansler[10] (1975) have verified the relationship between unsteady flow over a fixed wall and steady flow over a moving wall, but for the downstream moving wall case only.

The first experiments undertaken in unsteady flow, to determine the effects on separation, were by Despart & Miller[11] (1969). These experiments indicated that the laminar separation appears to be stationary but displaced upstream from the location that corresponds to steady separation. The correlation between experimental data indicated that the frequency, Reynolds number and dynamic history of the boundary layer are the dominant parameters, and the oscillatory amplitude has a negligible effect on the separation points displacement. An interesting observation made was that reversed flow and consequently zero wall shear profiles were observed to occur periodically at points on the surface in the adverse pressure region, upstream of the region of wake formation. Despard and Miller proposed the following definition of laminar separation in oscillating flow as "commencing with the initial occurrence of zero velocity or reversed flow at some point in the velocity profile which occurs throughout the entire cycle".

Tsahalis and Telionis[12] (1974) using numerical calculation, found some agreement with the results of Despard and Miller, but not for all situations considered. The experimental data available on oscillating flow with separation is not sufficiently conclusive to permit a thorough comparison with theoretical studies.

To the author's knowledge there has been no experimental work carried out to investigate turbulent boundary layer separation in oscillatory flows. There has been some work on turbulent boundary layers for cases of zero mean axial pressure gradient by Karlsson[13] (1959) and M.H. Patel[14] (1976). Analogies were found between laminar and turbulent boundary layer oscillatory flows. Patel's experimental study was carried out under very similar working conditions as those used in these experiments. Recently Schachenmann and Rockwell[15] (1976) experimented with an oscillating freestream on a turbulent boundary layer with an adverse pressure gradient along a diffuser without separation. Results indicated the effects of oscillations on the mean velocity profiles in the adverse pressure gradients were insignificant irrespective of the frequency of disturbance tested.

Theoretical studies into unsteady turbulent boundary layers at separation have recently achieved some results. V.C. Patel & Nash[16] (1975) later extended by J.F. Nash[17] (1976) solved the unsteady turbulent boundary layer equation numerically using the rate equation for the Reynolds stress to obtain closure. It was shown that for unsteady flow the point of zero skin friction is not singular and hence the calculations could proceed into a partially reversed flow region. This method of calculation is only valid for certain types of unsteady flow. Similar investigations into the unsteady separation where the theoretical calculation enters the partially reversed flow have also been studied by Telionis and Tsahalis[18] (1976).

3. EXPERIMENTAL DETAILS

3.1 Tunnel and Oscillatory flow facility

Figure No. 1 illustrates the wind tunnel used in the study of the separated turbulent boundary layer under oscillatory flow. The wind tunnel is of low speed open circuit type, with side walls, capable of producing steady and unsteady flow within a velocity range of 0 to 25 metres per second. A velocity of 22.0 metre/second was used in all experiments.

The working section in which the model was mounted had an exit throat cross-section of 1.0 metre wide by 1.4 metres high. The tunnel had a contraction ratio of diffuser area to throat area of 5.8 to 1.0. The oscillatory flow was generated by two horizontal flaps which were positioned at the top and bottom of the tunnels exit nozzle. These two flexible flaps were rigidly fixed at one end, nearest the contraction, and free at the other. The free end was driven vertically up and down in harmonic oscillation by a shaft attached to a cammed rotor arm. The flaps oscillated harmonically in phase, with a frequency range of 0 to 6 Hz. Mechanical limitations prevented higher frequencies being attained. This gave a non-dimensional frequency parameter ($\omega x/U_0$) in the range of 0 to 3.0 over the model being tested. The flaps produced a maximum root mean square amplitude ratio of oscillation ($U_{1_{r.m.s.}}/U_1$) of 10% at the edge of the boundary layer.

The oscillatory flow in the freestream over the test section was induced by the moving flaps interfering with the shear layers at the edge of the tunnels exit jet. The interference causes the shear layers to roll up into discrete vortices in the mixing region, which are convected downstream by the jet. The rolled up vortices affect the velocity components in the jet flow. Equation (1) gives the definition of the obtained flow, which is a travelling type of unsteadiness. The harmonic oscillation of the flaps generate a sinusoidal flow in the working section. The wave travels at 0.65 of the undisturbed freestream velocity.

3.2 Model

The model used in these experiments was a flat plate of 2.0 metres in length with a round nose section and a width of 1.0 metre. At the rear of the plate positioned 1.85 metres from the leading edge a slotted spoiler inclined at 50° to the horizontal axis. The spoiler had vertical height of 25 centimetres from the surface. Slots cut into the spoiler produced stability in the wake and prevented undue unsteady fluctuations of the steady separation point. The spoiler induced the adverse pressure gradient and separation of the turbulent boundary layer over the flat plate.

The model was positioned horizontally on the centre line of the tunnel with the leading edge extending 0.3 metres into the throat section. The model protruded upstream of the flaps to prevent "bubble" formation over the leading edge caused by incidence changes in the freestream due to the flap oscillations. The model was symmetrical about the horizontal axis.

A diagram of the experimental layout in the working section is shown in figure 2. A strip of rough paper was placed close to the leading edge to trip the boundary layer giving a well developed turbulent boundary layer over the region under investigation. The plate had at short intervals pressure tappings on and either side of the centre line in the region of separation,

The support traversing gear, was magnetically attached to the plate, and held the Preston tube or the hot-wire probes. It was designed to be able to make measurements within the boundary layer at any position. Experiments showed the support column had no interference effects on the probe upstream. For measurements close to separation the traversing equipment was mounted behind the inclined spoiler and the probe held on a telescopic support arm, protruded into the flow through the centre slot. This was ideally suited to have minimal flow obstruction effects in a sensitive region, where premature separation could be induced.

4. MEASUREMENT METHODS

In the experiments hot-wire anemometers were used for instantaneous velocity measurements within the boundary layer. Pressure from the Preston tube and static pressure tappings in the model surface were measured by pressure transducers.

As the flow varied as a function of time, instantaneous measurements were needed to gain a complete knowledge of changes in the boundary layer flow during one period of oscillation of the freestream. A digital electronic triggering device was designed and constructed at Queen Mary College, to produce a trigger signal for the reading instruments. The digital unit required an input reference signal of the forcing frequency. This was obtained from a hot-wire placed in the freestream at the edge of the boundary layer which responded to the harmonic oscillations of the flow. The D.C. component of the signal was eliminated and the triggering unit processed the signal to give trigger impulses at specified time instances derived from the input frequency. The output from the unit was fed into a voltmeter; the trigger signal instructing the voltmeter to read the input signal applied to it. The input signal i.e. the measured signal, was either obtained from a second hot-wire or the pressure transducer. The digital data was automatically fed into and stored in a Hewlett Packard 9821A calculator. Knowing the time when the sample was recorded relative to a reference signal analysis of the signals was determined by simple fourier analysis. Calculations of the mean and amplitude of the signal and the phase difference between the reference and measured signals were determined from an average of 320 individual sample readings.

Calculation of the longitudinal turbulence intensity component of velocity $\sqrt{\overline{u'^2}}$ inside the boundary layer presented a special problem. The hot-wire signal output was composed of the fluctuations due to the forced oscillations and the freestream turbulence. Amplitude measurements of the unfiltered signal gave the total amplitude of the signal (a_{total}). An electronic filter with a frequency setting of 5% and attenuation insertion loss of 3DB at the cutoff frequency and 36DB/octave after cutoff was used to eliminate from the signal all turbulent fluctuations above the forcing frequency and measure the resultant amplitude of the oscillating components only (a_{oscil}). This was possible because a negligible amount of turbulent spectra occurs in the 0 to 6 Hz range. From these two measurements the amplitude of the signal due to turbulent fluctuations was determined from the equation

$$a^2_{turb.} = a^2_{total} - a^2_{osc.} \qquad (4)$$

Calibration of the constant temperature hot-wire was carried out in the tunnel and followed conventional static methods. In oscillating flows the signal response of the various measuring devices from the flow input is critical.

Static calibration was made of the pressure transducers to determine whether the response time of the input pressures from the flow was fast enough for the range of frequencies considered in these experiments. The main parameters in determining the response was the volume of air between the point of measurement and the transducer diaphragm and the inlet hole diameter. Pressure differences measured by the transducer had to be arranged to have identical tube connections on either side, thus ensuring that inputs to the transducer had the identical response times. This was particularly important for measurements made with the Preston tube. An outside diameter of 1.0 mm was used, with an approximate internal to external radius of 0.6. The inside hole diameter of pressure transducer and static pressure tapping were identical.

5. MEASUREMENT AND RESULTS

5.1 Flow Visualisation

The two dimensionality of the flow was initially investigated by flow visualisation techniques. This indicated that there was an acceptable degree of flow uniformity over the central region of the plate.

Flow visualisation was used to determine the approximate position of steady flow separation. The method adopted was to paint a special mixture on the surface of the plate. Whilst the tunnel was running ammonia vapour was introduced into the wake. The mixture and ammonia would chemically react when they came into contact causing a change in the colour of the mixture from yellow to purple. As ammonia was sucked forward by the recirculating wake, a line could be seen where the separation point occurred. When these tests were repeated for oscillatory flow, it was found that the fairly straight line produced with steady flow became streaked. These streaks of purple reached further upstream than the line of steady separation.

5.2 Static Pressure Measurements

Preliminary measurements made of the spanwise pressure distribution confirmed the two dimensionality over the centre region of the plate. The longitudinal pressure distribution was obtained from static pressure tappings over the plate surface, between 0.55 and 1.83 metres from the leading edge. The majority of the readings were obtained close to the spoiler. The mean pressure coefficient C_p distribution along the plate surface for steady and oscillating flow, for each frequency tested, were obtained and plotted in figure 3. The variation between steady and oscillating flow was too small to include all the points for each measuring position. The vertical line indicates the maximum variation from 2 to 6 Hz. The variation due to the oscillating freestream is consistent along the distribution except for the region close to the spoiler, where the variation is slightly reduced. The distribution of the mean pressure coefficient in figure 3 shows a slight initial favourable pressure gradient, due to the leading edge section of the model lying within the throat of the tunnel. From x = 0.8 metres from the leading edge the pressure continually increased until about 1.7 metres, after which the pressure remains almost constant.

To determine the magnitude of the oscillations in static pressures induced by the freestream oscillations, measurements of the root mean square of static pressure (P_a) were made. From these results the non-dimensional root mean square of static pressure amplitude was obtained, where this is defined by

$$P_a = P_{1_{\text{r.m.s.}}} / \tfrac{1}{2}\rho U_0^2 \tag{5}$$

Figure 4 shows the distribution of the root mean square of static pressure amplitude ratio for steady and oscillating flow. The steady flow results show a marginal rise along the surface. The oscillating results have much larger values, as would be expected. The amplitude increases with frequency up to 5 Hz until at 6 Hz there is a slight reduction. This was due to a tunnel characteristic, dependent upon the vertical height of the exit throat, where the peak oscillation occurs about 5 Hz, rather than the response of the fluctuations in the freestream oscillations to an adverse pressure gradient. In the oscillating situation the distribution along the plate indicates slightly different patterns. At 2 and 3 Hz P_a reduces initially and then increases. The higher frequencies show a general increased P_a along the plate up to the spoiler. A similar type of distribution of amplitude is shown later for skin friction and freestream velocity at the edge of the boundary layer.

5.3 Skin friction results (Preston tube)

As stated previously the skin friction measurements over the model were obtained from a Preston tube. V.C. Patels[19] (1965) calibration was used to determine the wall shearing stress from the difference in pressures between pitot tube and wall static pressure. The Preston tube diameter d was chosen so that $u_\tau d/\nu$ was less than 50, where u_τ is the friction velocity $(\tau_w/\rho)^{\frac{1}{2}}$. The centre of tube was within or close to the lower boundary of the "log law" region, provided the boundary exhibited this type of profile. Measurements of the mean skin friction were made from x = 1.19 metres up and beyond the steady flow separation point for each oscillating frequency and steady flow. A graph of these mean skin friction coefficient was plotted (figure 5), to compare the mean steady results, and the calculation method of Bradshaw et al[20] (1967). Satisfactory agreement was achieved. The mean oscillating skin friction results show very little difference with varying oscillation frequency and follow the same type of distribution as those of the steady flow. Steady flow results indicate that flow separation occurs at 1.72 metres from the leading edge. A set of results for the instantaneous skin friction were also obtained. A specimen example of the type of distribution is shown in figure 6 for the 5 Hz frequency, the eight instantaneous readings during one cycle are plotted for each measuring position up to and beyond the steady separation point. The variations in the wall shear stress were found to oscillate at the fundamental forcing frequency. The phase difference along the surface between measuring positions has been removed. As the separation point for steady flow was approached from upstream the mean of the oscillating wall shear stress reduced. At some point, depending on the amplitude of oscillation of the freestream at the edge of the boundary layer, the wall shear stress became negative for part of the cycle. For the 5 Hz frequency results, this initially occurred at 1.62 metres from the leading edge. This negative portion of the cycle increases as the separation point is approached. At the mean steady flow separation point the oscillating flow exhibits positive and negative wall shear stress on the surface during one cycle. The oscillations in positive and negative wall shear stress are also observed in the oscillating flow behind the steady flow separation point.

In figure 5 the mean of the oscillating skin friction is plotted, but close to steady separation readings are absent because the sampling system was recording negative pressures referring to a negative wall shear stress. The readings of the Preston tube were invalid in this region, hence it was impossible to obtain mean averaged results.

For the five frequencies tested the amplitude of the oscillations in wall shear stress (τ_{w_a}) were plotted (figure 7). The 2 Hz flap oscillation, the amplitude has a continual decline up to and beyond the mean separation point. The 3, 4, 5 and 6 Hz have a gradual decline until about 1.43 metres from the leading edge, then an increase to the onset of zero wall shear stress. The arrows denote the onset of negative zero wall shear stress during part of an oscillation.

The amplitude of the oscillations in skin friction are directly related to the oscillations in freestream velocity. The largest oscillations in freestream velocity were expected to have the maximum effect on skin friction.

5.4 Boundary Layer Velocity Profile

Measurements of the mean velocity, amplitude of the velocity fluctuations and the phase angle difference between the boundary layer and freestream oscillations were made.

The mean velocity distribution showed little variation with frequency and minimal changes were observed when results were compared with the measurements obtained from steady flow. A representative distribution of the velocity profiles measured at various points along the plate is plotted in figure 8. the graph shows the development of a typical turbulent boundary layer velocity profile in an adverse pressure gradient approaching separation. It was concluded that the mean results are unaffected by freestream oscillation, this agrees with the experimental work of M.H. Patel[14] (1976), Schachenmann and Rockwell[15] (1976) and Karlsson[13] (1959) all of whom used a range of freestream amplitudes of oscillation corresponding to those used here but with higher frequencies of oscillation.

The mean momentum thickness (θ) and shape parameter (H) were determined from each mean velocity profile for steady and oscillatory flow. The momentum thickness variation with distance from the leading edge is plotted in figure 9, this shows a little scatter between the results, due mainly to the slight errors in velocity measurements. The graph shows the development of the momentum thickness, with a rapid rise close to separation. A similar graph showing the distribution of the shape parameter is plotted in figure 10. These results compare favourably with the Preston tube measurements which also indicated the freestream oscillation had a negligible effect on the turbulent boundary layer before the steady flow separation point under the frequencies and amplitudes tested. No thickening of the boundary layer was observed in the region of oscillating zero wall shear stress ahead of the steady flow separation.

The root mean square of the velocity amplitude at the edge of the boundary layer non-dimensionalised by the local mean freestream velocity ($U_{1_{r.m.s.}}/U_1$) is plotted in figure 11 for each frequency against distance from the leading edge. The results show an increase in amplitude with frequency up to 5 Hz and a decline in the 6 Hz reading. A continual rise along the plate of the amplitude was observed. The 4 to 6 Hz frequency readings are of a higher amplitude and may explain the differences which occur in some of the distributions in phase lag and velocity amplitude ratios in the boundary layer compared with those at 2 and 3 Hz.

The amplitude of velocity measurements were made inside the boundary layer. The amplitude ratio (U_a/U_{1_a}) plotted against non-dimensional perpendicular distance from the surface (y/δ) is shown in figure 12. The general distribution shown for the specimen frequency of 5 Hz indicates the peak amplitude to always occur approximately half way through the boundary layer ($y/\delta = 0.5$). For 5 Hz distributions close to separation the peak falls below the freestream amplitude ratio of 1.0. The distribution measured in the earlier part of the adverse pressure gradient experiences a sharp increase in amplitude ratio close to the wall. The amplitude ratio profiles measured further into the adverse pressure gradient have a sharp increase close to the wall, but the rise finishes at a lower amplitude ratio before following the more gradual profile. Close to separation profiles no longer experience any sharp rise at the wall. This type of distribution appears to be directly related to the mean velocity profile distribution. Sharp increase in velocity close to the wall, large $\partial U/\partial y$, which occur in the early part of the adverse pressure gradient, cause large changes in amplitude ratio. At separation the velocity profile has an almost linear distribution of velocity with distance from the surface. Thus no sharp increase in amplitude ratio would be anticipated (figure 12). Similar type of patterns occur in the longitudinal turbulence intensity distributions, which no longer exhibit such a sharp rise in turbulence close to the wall near separation.

The reason for the dip in the amplitude ratio profiles in the outer region of the boundary layer observed in the measurements close to separation is not known.

A graph of the peak amplitude ratio obtained for all frequencies is shown in figure 13. The 2 and 3 Hz peaks show a continual rise in amplitude ratio up to spoiler, whereas for the higher frequencies there is a fairly constant peak value up to about 1.35 metres and then the peak amplitude values decline. All the individual amplitude profiles at each frequency follow the similar distributions to the specimen example shown in figure 12. The change in the peak amplitude distribution between 2 to 3 Hz and 4 to 6 Hz was thought to be due to the difference in freestream amplitudes of oscillation as mentioned earlier.

Phase angle distributions between the outer edge of the boundary layer and any point inside the boundary layer are shown in figure 14 for every measuring position at the 5 Hz frequency. The sharpest rise in phase lag is experienced in the "outer region" of the boundary layer velocity profile. In the inner region the gradient is gradual until the wall, then close to the sublayer a sharp rise occurs in the phase lag, followed by a reduction. This rise increased as measurements were taken further downstream from the leading edge where the adverse pressure gradient is larger. Accuracy of the measurements of phase was not affected by heat loss effects on the hot-wire close to the wall. Determining variation of the phase through the viscous sub layer was not possible due to the layer being too thin for an extensive investigation. A graph of the peak phase lag immediately adjacent to the wall was plotted for each frequency tested in figure 15. Every frequency follows a very similar distribution of maximum phase lag. The lag increases with increase in distance from the leading edge.

The phase lag through the boundary layer is mainly due to the pressure gradient in the freestream which is obtained from two sources; the travelling wave type of flow experienced in the freestream and the adverse pressure gradient. The Bernouilli equation for time dependent flow is given by

$$-\frac{1}{\rho}\frac{\partial P}{\partial x} = \frac{\partial U_{1_i}}{\partial t} + U_{1_i}\frac{\partial U_{1_i}}{\partial x} \qquad (6)$$

Substituting U_1 from equation (1)

$$-\frac{1}{\rho}\frac{\partial P}{\partial x} = U_1\frac{\partial U_1}{\partial x} + \left\{U_1\frac{\partial U_{1_a}}{\partial x} + U_{1_a}\frac{\partial U_1}{\partial x}\right\} e^{i\omega(t - x/Q)}$$

$$+ i\omega e^{i\omega(t - x/Q)}\left\{U_{1_a} - U_1\frac{U_{1_a}}{Q}\right\} \qquad (7)$$

McCroskey[21] (1977) has indicated that in an adverse pressure gradient the effect of $U_{1_i} \partial U_{1_i}/x$ in equation 6, if it is dominant over the other parameters, will induce a lag of the boundary layer response behind the quasi-steady behaviour.

The phase lags measured during these experiments are larger than those obtained by M.H. Patel(1976) who carried out experiments under similar conditions on a turbulent boundary without pressure gradients and a higher travelling wave velocity.

During the profile measurements special attention was made to the velocity amplitude of the double frequency response of the hot-wire signal in the region where the skin friction was known to oscillate between positive and negative values. The hot-wire would respond to positive and negative flow but the output signal would only behave as though the flow was positive. Hence the output signal of oscillating forward and reverse flow would be at twice the frequency of the fundamental forcing frequency. These readings were made close to the surface to give the approximate thickness of the oscillating reversed region. These results indicated the region to be thin compared with the boundary layer thickness. The conclusions drawn from these results are that there is a thin oscillating layer close to the surface. There is reversed flow in this region for part of the oscillatory freestream flow cycle, without the boundary layer breaking away from the surface. The approximate size and shape of the region of oscillating positive and negative flow close to the wall for 5 Hz frequency was measured and is shown in a schematic diagram in figure 16.

5.5 Turbulence Intensity

The longitudinal turbulence intensity was measured for both steady and oscillating flows along the surface of the model. Readings were taken into the outer region of the viscous sub-layer where the turbulence levels began to drop significantly. The maximum turbulence intensity near separation was approximately 13%. Variation with frequency in the early part of the adverse pressure gradient up to $x = 1.59$ was negligible.

In this part of the flow there appears to be no interaction between the turbulent eddies and freestream oscillations. Near separation the turbulence intensity variation begins to grow very slightly, it appears that there may be some interaction with the wake, which affects the turbulence levels upstream of this region. Figures 17 and 18 show the distribution of longitudinal turbulence $\sqrt{\overline{u'^2}}/U_1$ for oscillating flow at 5 Hz and steady flow respectively.

6. CONCLUSION

The separation of a turbulent boundary layer has been subjected to periodic oscillations of the mean freestream over a range of frequencies and amplitudes. The conclusions of the main results are:

The mean separation in steady flow is affected by the oscillating freestream. Periodic forward and reversed flow occurs ahead of the point of steady separation, this only occurs in a very thin layer. It has been noted that it does not have a dramatic effect on the boundary layer. This was confirmed by the fact that the mean velocity profiles, skin friction, momentum thickness, shape parameter, coefficient of pressure and turbulence intensities were not affected.

The amplitude of velocity fluctuations within the boundary layer can exceed the boundary layer edge conditions. At the lower freestream amplitudes there is a very large maximum amplitude ratio close to separation.

The phase difference of the velocity oscillations in the boundary layer continually lags behind the freestream oscillation. The phase lag increases with downstream movement. The phase lags in the adverse pressure gradient are much larger than experimental results of M.H. Patel (1976) with a turbulent boundary layer without a pressure gradient.

Acknowledgement

This work has been carried out with the support of Procurement Executive, Ministry of Defence.

REFERENCES

1. Stewartson K. The theory of unsteady laminar boundary layers. Advances in App. Mech. Vol. 6, 1-37, 1960.

2. Rott N. Theory of Time dependent laminar flows. In Theory of Laminar Flows, edited by F.K. Moore, Princeton Univ. Press, 1964.

3. Stuart J. Unsteady Boundary Layers. Recent Research on Unsteady Boundary Layers. Proceedings of Symp. IUTAM. Vol. 1, 1971.

4. Telionis D.P. Calculation of time dependent Boundary Layers. Unsteady Aerodynamics, Vol. 1, Edited R.B. Kinney, 1975.

5. Williams J.C. III. Incompressible Boundary Layer Separation. Annual Review of Fluid Mechanics, Vol. 9, 1977.

6. Vidal R.J. Research on Rota-ing Stall in axial flow compressor, Part III - Experiments on Laminar Separation from a moving wall. Wright Air Development Center TR-59-75 Wright-Patterson AFB, Dayton, Ohio.

7. Ludwig G. An Experimental investigation of Laminar Separation from a moving wall. AIAA Paper 64-6, 1964.

8. Tsahalis D.T. & Telionis D.P. The effect of blowing on a laminar separation J. of Appl. Mech. Vol. 40, 1133-34, 1973.

9. Williams J.C. III & Johnson Semi solution to Unsteady Boundary Layer Flow including Separation. AIAA Vol. 12, p.1388-93, 1974.

10. Danberg J.E. & Fansler K.S. Separation like similarity solutions on two dimensional moving walls. AIAA Journal, Vol. 13, 110-12, 1975.

11. Despard R.A. & Miller J.A. Separation in oscillating laminar Boundary Layer Flow. J.F.M. Vol. 47, pp.21-31, 1971.

12. Tsahalis D.T. & Telionis D.P. Unsteady laminar boundary layers and separation. AIAA, Vol. 12, No. 11, 1974.

13. Karlsson S.K.F. An Unsteady Turbulent Boundary Layer. JFM, Vol. 5, part IV, 1959.

14. Patel M.H. On Turbulent Boundary Layers in Oscillatory Flow, Proceedings of the Royal Society, London Series A. No. 1672, Vol. 353, p.121-144, 1976.

15. Schachenmann A.A. & Rockwell D.O. Oscillating Turbulent Flow in a Conical Diffuser, Transactions of ASME J. of Fluids, p.695-701, Dec. 1976.

16. Patel V.C. & Nash J.F. Calculation of Unsteady Turbulent Boundary Layers with Flow Reversal, N.A.S.A. CR 2546, May 1975.

17. Nash J.F. Further Studies of Unsteady Boundary Layers with Flow Reversal, N.A.S.A. CR 2767, Dec. 1976.

18. Telionis D.P. & Tsahalis D.T. Unsteady Turbulent boundary layer and separation, AIAA Vol. 14, No. 4, April 1976.

19. Patel V.C. Calibration of a Preston tube and Limitations on its use in pressure gradients JFM, Vol. 23, pp.185, 1965.

20. Bradshaw P., Ferris D.H. & Atwell N.P. Calculation of Boundary Layer Development using the Turbulent Energy equation. JFM, Vol. 28, p.593, 1967.

21. McCroskey W.J. Some Current Research in Unsteady Fluid Dynamics,

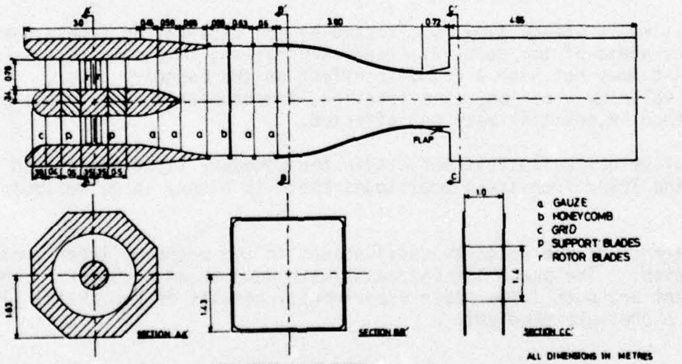

LOW SPEED WIND TUNNEL

FIGURE No:1

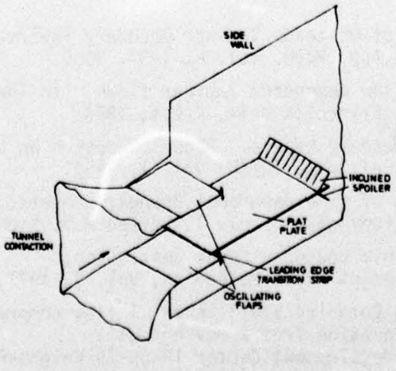

FIGURE No 2 EXPERIMENTAL LAY-OUT

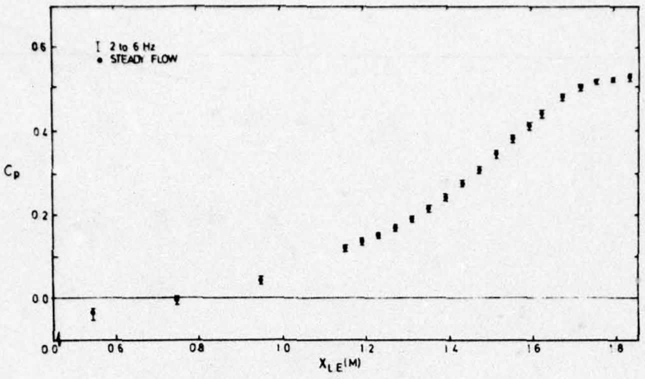

FIGURE No 3 DISTRIBUTION OF COEFFICIENT OF PRESSURE

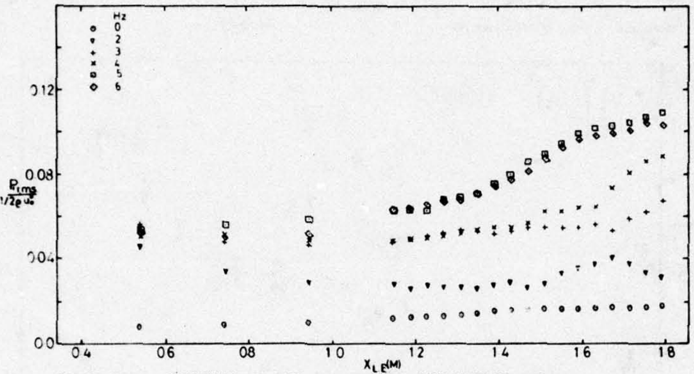

FIGURE No.4 DISTRIBUTION OF ROOT MEAN SQUARE OF STATIC PRESSURE AMPLITUDE.

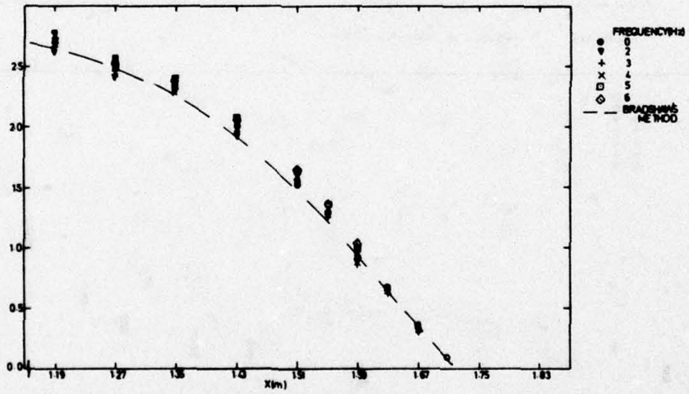

FIGURE No:5 DISTRIBUTION OF COEFFICIENT OF FRICTION

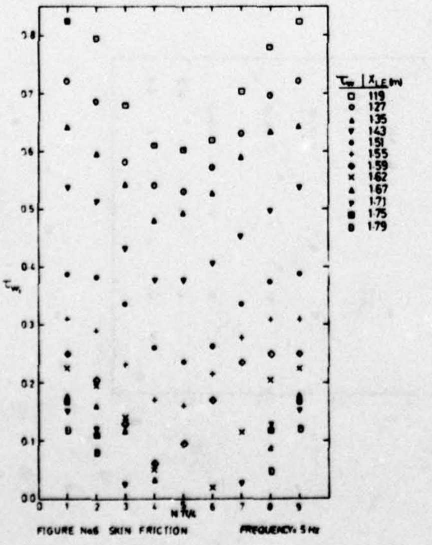

FIGURE No6 SKIN FRICTION FREQUENCY = 5 Hz

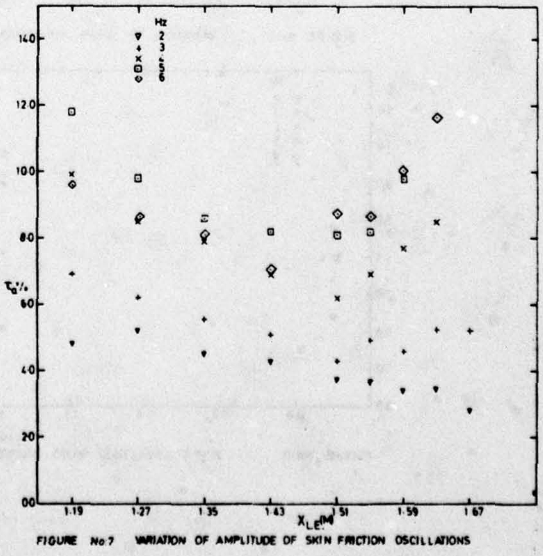

FIGURE No 7 VARIATION OF AMPLITUDE OF SKIN FRICTION OSCILLATIONS

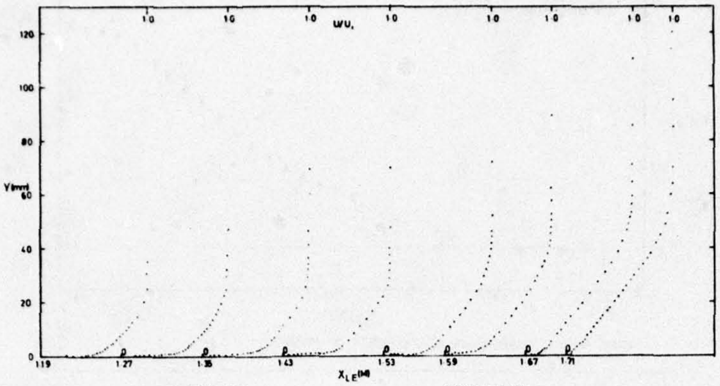

FIGURE No.8 MEAN VELOCITY PROFILES FREQUENCY = 5 Hz

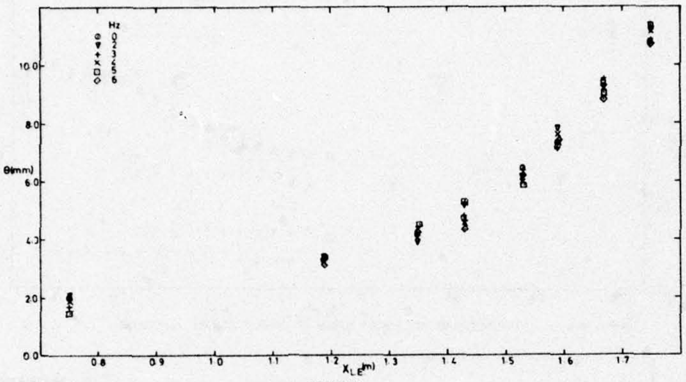

FIGURE No.9 VARIATION OF MOMENTUM THICKNESS

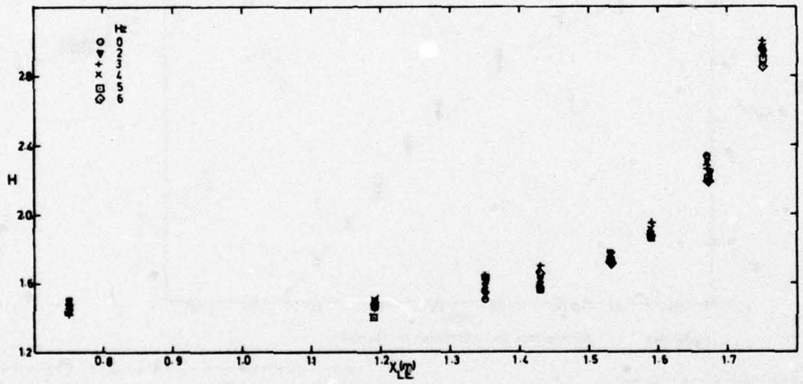

FIGURE No.10 VARIATION OF SHAPE PARAMETER.

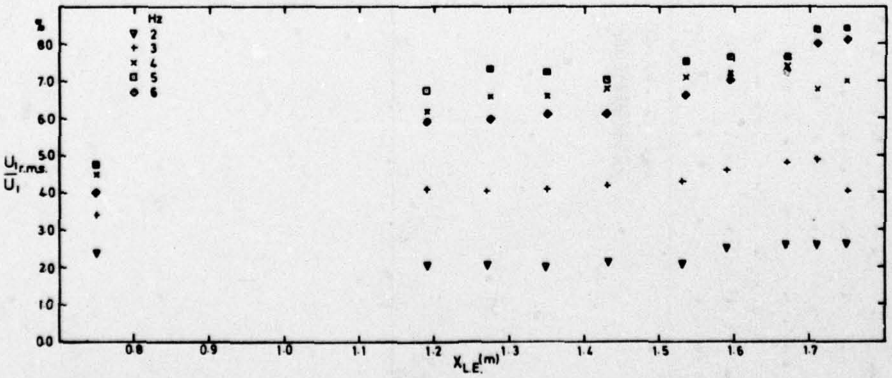

FIGURE No.11 R.M.S AMPLITUDE RATIO DISTRIBUTION.

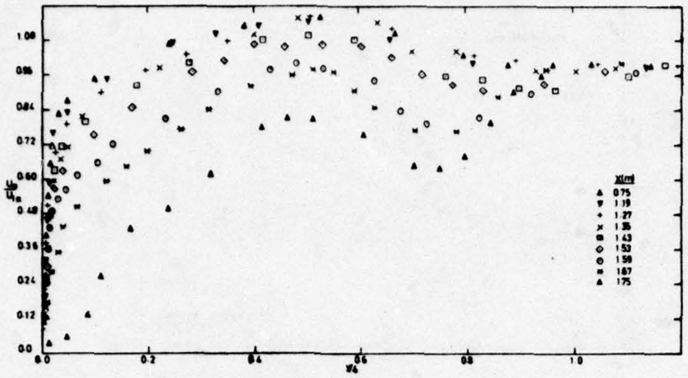

FIGURE No:12 VARIATION OF AMPLITUDE RATIO IN BOUNDARY LAYER

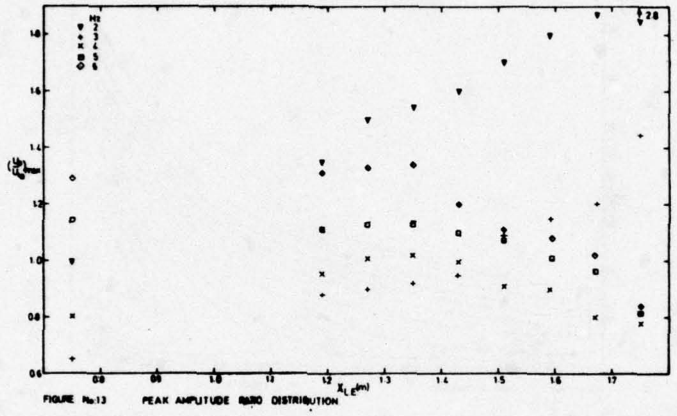

FIGURE No:13 PEAK AMPLITUDE RATIO DISTRIBUTION

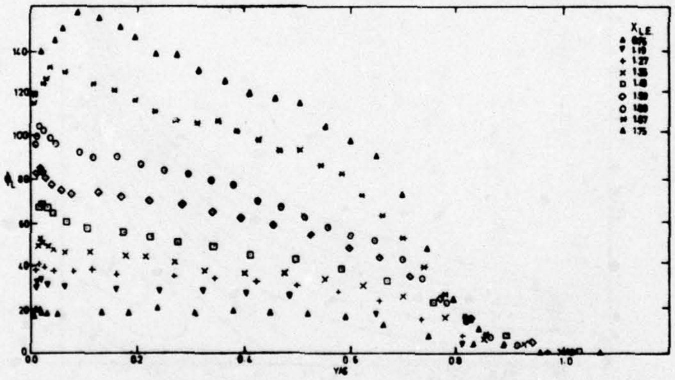

FIGURE No:14 VARIATION OF PHASE LAG IN BOUNDARY LAYER FREQUENCY = 5Hz

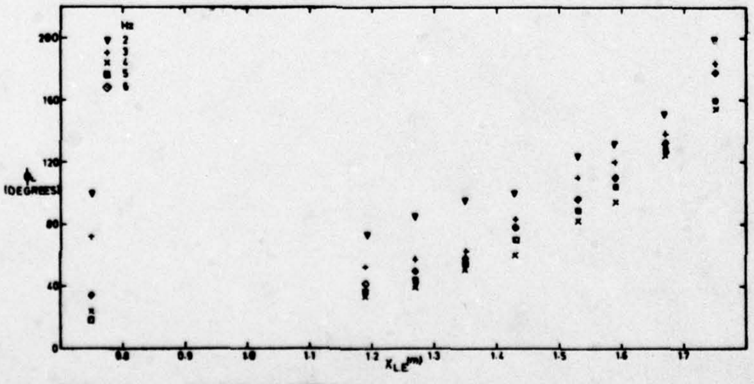

FIGURE No:15 PEAK PHASE LAG DISTRIBUTION

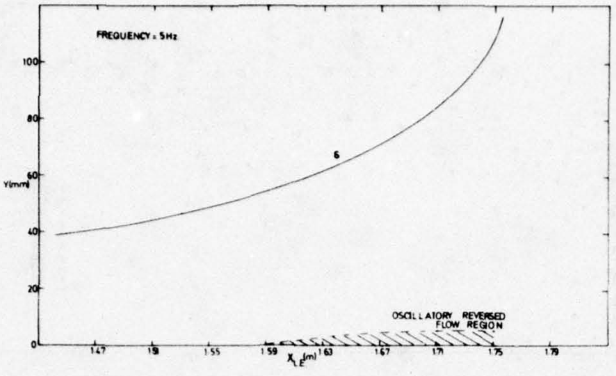

FIGURE No.16 BOUNDARY LAYER GROWTH & REGION OF OSCILLATORY REVERSING FLOW.

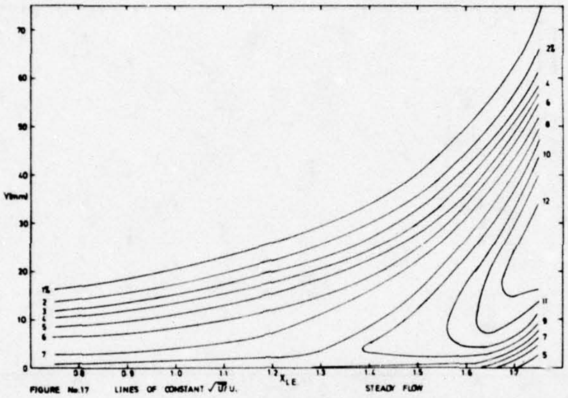

FIGURE No.17 LINES OF CONSTANT $\sqrt{\overline{U'}}/U_1$ STEADY FLOW

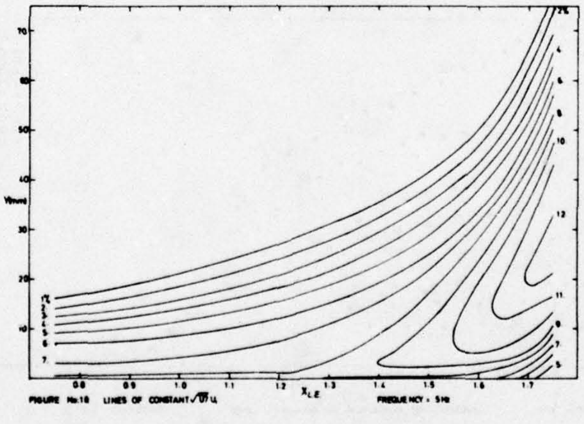

FIGURE No.18 LINES OF CONSTANT $\sqrt{\overline{U'}}/U_1$ FREQUENCY = 5Hz

LE DÉCROCHAGE DYNAMIQUE : UN EXEMPLE D'INTERACTION FORTE ENTRE ÉCOULEMENTS VISQUEUX ET NON-VISQUEUX

par Jean-Jacques PHILIPPE

Office National d'Etudes et de Recherches Aérospatiales (ONERA)
92320 CHATILLON - France

Ce mémoire fait le point sur les phénomènes liés aux profils en configuration de décrochage dynamique et plus spécialement sur ceux liés aux profils oscillants en tangage. Les résultats expérimentaux les plus caractéristiques sur les décollements à caractère tourbillonnaire et leurs répercussions au niveau des pressions locales et forces globales sont analysés. Quelques aspects des méthodes de prévision des écoulements en présence (ou non) de décollement de la couche limite sont examinés, ainsi que les principales méthodes simplifiées disponibles à ce jour pour le calcul des forces globales dans de telles configurations.

DYNAMIC STALL : AN EXAMPLE OF STRONG INTERACTION BETWEEN VISCOUS AND INVISCID FLOWS

This paper surveys the phenomena concerning profiles in dynamic stall configuration, and more specially those related to pitch oscillations. The most characteristic experimental results on flow separations with a vortex character, and their repercussions on local pressures and total forces are analyzed. Some aspects of the methods for predicting flows with the presence (or not) of boundary layer separation are examined, as well as the main simplified methods available to date for the calculation of total forces in such configurations.

1 - INTRODUCTION

Le terme "décrochage dynamique" regroupe un ensemble de phénomènes aérodynamiques qui se produisent lorsqu'un profil, un élément de pale, une aile ou un appareil se trouve soumis à des conditions aérodynamiques variables dans le temps, se traduisant par des chutes de portance ou des accroissements brutaux de moment de tangage caractéristiques des configurations de décrochage.

Par exemple, dans certaines configurations de vol d'un hélicoptère, les pales du rotor peuvent être soumises périodiquement à des conditions de décrochage et de recollement dynamique. En effet, les incidences sur la pale reculante du rotor peuvent être bien supérieures aux angles de décrochage stationnaire des profils tandis que les incidences sont faibles en pale avançante.

Pour illustrer les principaux phénomènes liés à une variation d'incidence d'un profil autour de son incidence de décrochage, la figure 1 tirée de la référence 1 montre que, par rapport aux caractéristiques aérodynamiques stationnaires, le profil peut :

- atteindre des portances bien supérieures à celles obtenues en écoulement stationnaire, tout en étant le siège de décollements importants à caractère tourbillonnaire organisé, visualisés ici par l'émission de fumées en différents points du profil,
- présenter, pendant la phase critique où le profil est soumis à des décollements, des moments de tangage de très fortes intensités (décrochage en moment précédant le décrochage en portance),
- être soumis à des forces aérodynamiques telles que le travail de ces forces devenu positif, tende à rendre instable le mouvement d'incidence.

Dans ce qui suit, on analysera les divers aspects de ce phénomène et on fera le point des connaissances sur :

- les écoulements visqueux instationnaires avec décollement et recollement sur un profil en mouvement cyclique,
- les conséquences de tels écoulements sur les pressions locales et les efforts aérodynamiques globaux instationnaires,
- les méthodes de calculs des écoulements autour des profils, pouvant s'appliquer à des configurations de décrochage dynamique,
- les méthodes pratiques que peuvent employer les industriels pour évaluer les performances aérodynamiques dans de telles conditions.

Pour la rédaction de ce document, l'auteur a été beaucoup aidé par W.J. McCROSKEY et son équipe de l'USAAMRDL d'Ames grâce aux travaux effectués en commun concernant le décrochage dynamique et aux publications de synthèse sur ce sujet (réf. 1 et 2). Qu'ils en soient ici remerciés.

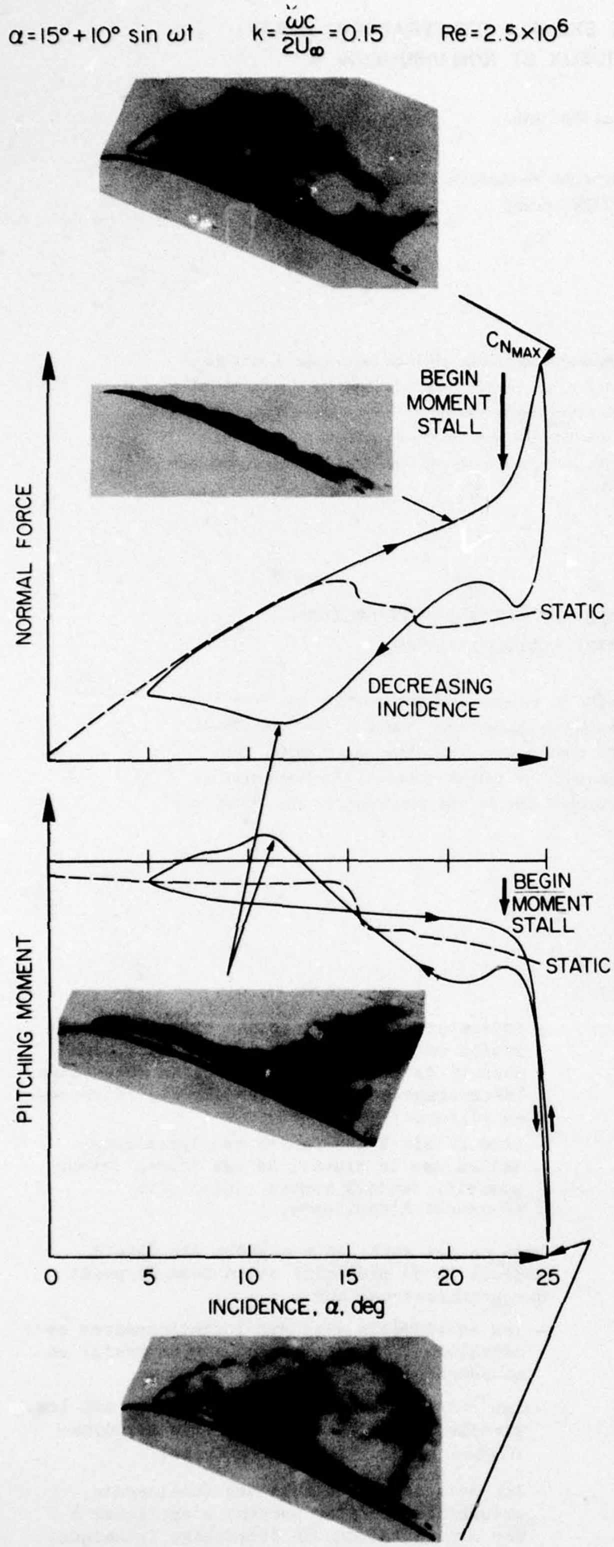

Fig. 1 – Exemple d'évolution des forces et moments de tangage en stationnaire et en instationnaire.

2 – ANALYSE DES CARACTERES PRINCIPAUX DU DECROCHAGE DYNAMIQUE

2.1 – Le caractère tourbillonnaire des écoulements décollés.

Les visualisations des écoulements autour des profils permettent d'analyser le type et la structure des écoulements dont dépendent les caractéristiques aérodynamiques des profils. L'ONERA possède un tunnel hydrodynamique, qui s'est avéré un moyen d'investigation très utile pour les études d'aérodynamique instationnaire (réf. 3).

La figure 2 concerne le profil NACA 0012 en oscillations harmoniques de tangage de part et d'autre de l'incidence de décrochage stationnaire. Lorsque l'incidence croît on peut dépasser largement cette incidence sans voir apparaître de décollement notable sur le profil (photo 2a). Il arrive cependant un moment du cycle où des décollements importants se produisent ; ceux-ci présentent un caractère tourbillonnaire marqué. Comme on peut le voir sur la figure 2b un tourbillon formé au voisinage du bord d'attaque se déplace vers le bord de fuite du profil.

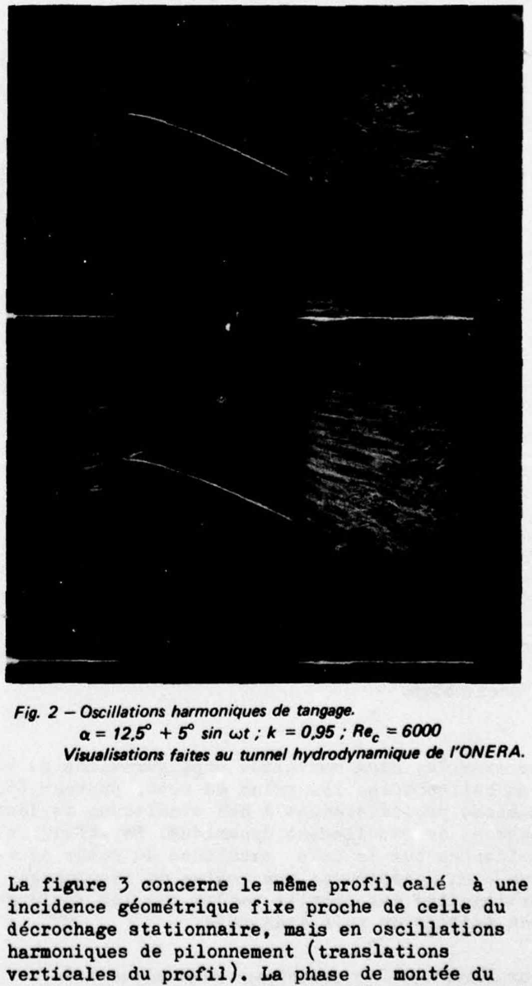

Fig. 2 – Oscillations harmoniques de tangage.
$\alpha = 12{,}5° + 5° \sin \omega t$; $k = 0{,}95$; $Re_c = 6000$
Visualisations faites au tunnel hydrodynamique de l'ONERA.

La figure 3 concerne le même profil calé à une incidence géométrique fixe proche de celle du décrochage stationnaire, mais en oscillations harmoniques de pilonnement (translations verticales du profil). La phase de montée du profil retarde l'apparition du décrochage sur le profil, comme dans la phase d'incidence croissante du profil oscillant en tangage (photo 3a). Lorsque les décollements apparaissent sur le profil, ils présentent également un caractère tourbillonnaire. On observe alors, à partir d'un point proche du bord d'attaque, la formation puis le déplacement vers l'aval d'un tourbillon (photo 3b).

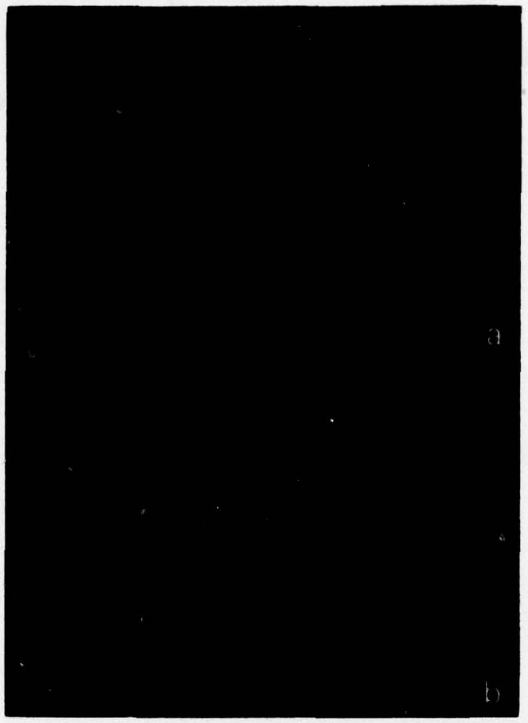

Fig. 3 – Oscillations harmoniques de pilonnement.
$\alpha = 12{,}5^\circ$; $\Delta z = 0{,}25\, c \sin \omega t$; $k = 0{,}95$; $Re_c = 6000$
Visualisations effectuées au tunnel hydrodynamique de l'ONERA.

La figure 4 concerne toujours le même profil calé à une incidence géométrique fixe, mais il est animé d'un mouvement harmonique de tamis (translations horizontales du profil). Les visualisations révèlent que la zone décollée sur l'extrados du profil qui avance est le siège d'une formation continue de tourbillons entraînés par le courant (photo 4a), tandis que dans le cas du profil reculant (photo 4b) le caractère tourbillonnaire est plus diffus.

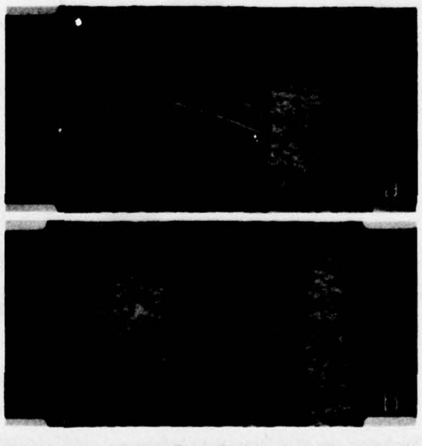

Fig. 4 – Oscillations harmoniques de tamis.
$\alpha = 12{,}5^\circ$; $\Delta x = 1{,}5\, c \sin \omega t$; $k = 0{,}1075$; $Re_c \simeq 6000$
Visualisations effectuées au tunnel hydrodynamique de l'ONERA.

Ces visualisations dans l'eau concernent des nombres de Reynolds(rapportés à la corde) faibles de l'ordre de 6000. L'USAAMRDL d'Ames dispose d'un tunnel hydrodynamique qui permet des études jusqu'à des nombres de Reynolds de l'ordre de $0{,}5 \times 10^6$ (réf. 4). Les visualisations sont assurées par bulles d'hydrogène produites par électrolyse suivant une technique développée par K.W. McAlister de l'US Army AMRDL d'Ames. Les photos de la figure 5 tirées d'un document à paraître (réf. 5) montrent la bonne qualité des visualisations ainsi obtenues sur profil NACA 0012 modifié en oscillations de tangage.

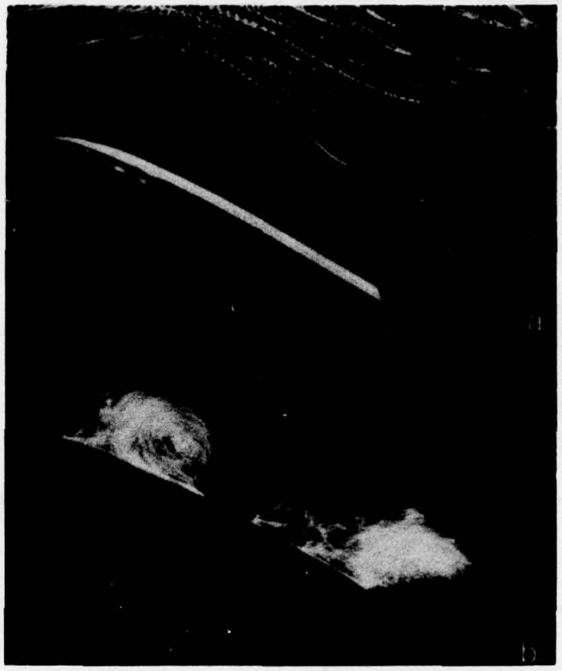

Fig. 5 – Visualisations par bulles d'hydrogène (USAAMRDL Ames)
NACA 0012 modifié oscillant en tangage.
$\alpha = 15^\circ + 10^\circ \sin \omega t$; photos prises à $\alpha = \alpha_{MAX}$.

Les visualisations effectuées dans l'air par l'émission de fumées à partir de différents points d'un profil (fig. 1) sont aussi très intéressantes en écoulement subsonique. Lors d'une étude très détaillée du décrochage dynamique, l'USAAMRDL d'Ames a construit un profil NACA 0012 de 1,20 m de corde pour sa soufflerie 7 x 10 ft (réf. 6 et 7). Les essais ont couvert des nombres de Reynolds de 1 à $3{,}5 \times 10^6$ pour le NACA 0012 et des profils derivés obtenus en changeant la forme du bord d'attaque.

Un film qui sera présenté au cours de ce symposium montre :

- un décrochage dynamique de bord d'attaque de type "éclatement du bulbe laminaire de bord d'attaque", lorsque le rayon du bord d'attaque du profil NACA 0012 est réduit à une valeur de 0,4 % au lieu de 1,58 classique,
- un décrochage dynamique de bord de fuite de type "remontée progressive des décollements de bord de fuite vers le bord d'attaque" lorsque le NACA 0012 est équipé d'une extension cambrée définie par l'ONERA,
- un décrochage dynamique complexe pour le NACA 0012 de référence, puisqu'il s'agit d'un décrochage turbulent brutal de bord d'attaque mais précédé par une remontée non négligeable de décollements de bord de fuite.

On reviendra en détail sur ces différents types de décrochage dynamique lors du paragraphe suivant mais il est à noter que dans chacun des cas, on a la présence, dans la phase critique de décollement généralisé, de tourbillons plus ou moins organisés et complexes comme le montre les photos de la figure 6.

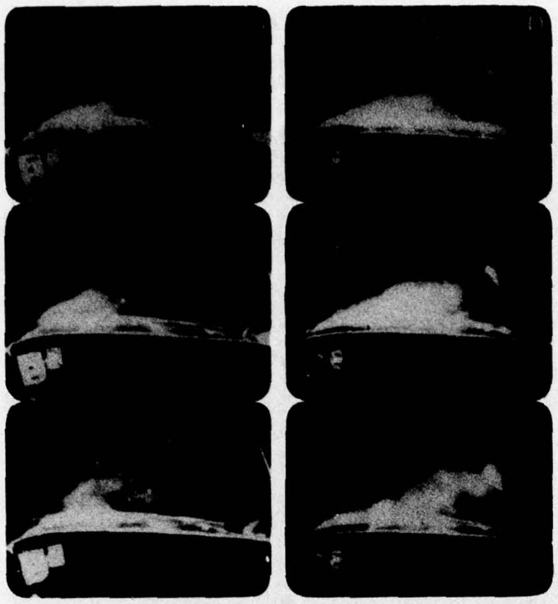

Fig. 6 – *Evolution des décollements à caractère tourbillonnaire sur profil oscillant.*
a) NACA 0012 à rayon de bord d'attaque réduit ;
b) NACA 0012 à extension cambrée ;
$Re_c = 2,5 \times 10^6$; $\alpha = 15° + 10° \sin \omega t$; $k = 0,15$;
essais USAAMRDL Ames.

2.2.- Les décollements instationnaires de la couche limite turbulente.

Les films chauds sont de bons détecteurs de flux de chaleur. Le flux convecté dépend étroitement de l'état laminaire, turbulent ou décollé de la couche limite au droit du film chaud (réf. 8).

C'est ainsi, figure 7, que lors d'essais à la soufflerie S10 du CEA de Toulouse on a mis en évidence une remontée progressive des décollements turbulents naissant au bord de fuite sur le profil NACA 0012 à extension cambrée oscillant en tangage de part et d'autre de son incidence de décrochage stationnaire (réf. 9). Cette phase précède celle du décollement généralisé à caractère tourbillonnaire décrite dans le paragraphe précédent.

Le même type d'informations peut être obtenu par des fils chauds placés très près de l'extrados du profil. Cette technique a été utilisée par l'USAAMRDL d'Ames (réf. 10) lors de la campagne d'essai sur le profil NACA 0012 et sur ses dérivés, citée précédemment. La figure 8, tirée de la référence 2, montre l'évolution des décollements sur les différents profils essayés en fonction du temps ou de l'incidence géométrique des profils. Pour obtenir cette figure on a assimilé ici, ce qui n'est pas très rigoureux, le point où naît le décollement avec le point où apparaît pour la première fois un écoulement inverse.

Il est cependant clair, que, dans des conditions d'oscillations en tangage identiques :

- le NACA 0012 à rayon de bord d'attaque réduit voit les décollements naître et se propager principalement du bord d'attaque vers le bord de fuite,
- le NACA 0012 à extension cambrée voit les décollements naître et se propager du bord de fuite vers le bord d'attaque,

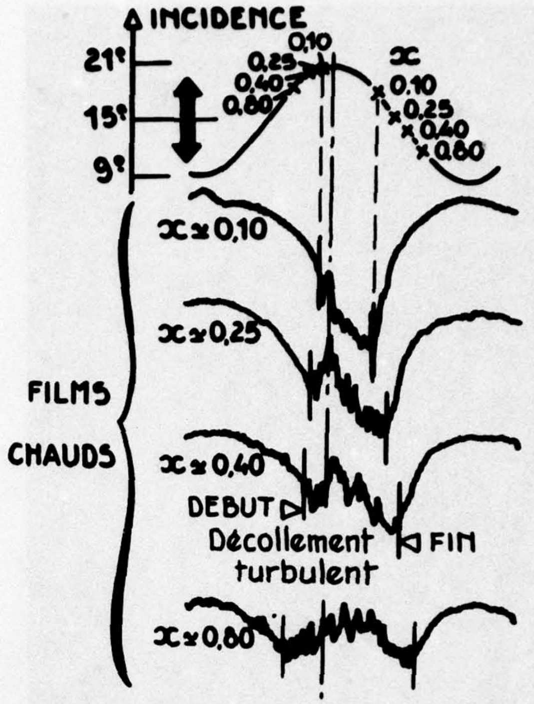

Fig. 7 – *Evolution des décollements turbulents sur profil NACA 0012 à extension cambrée.*
$M = 0,2$; $k = 0,114$; $Re_c = 1,9 \times 10^6$.

- le NACA 0012 voit d'abord un décollement de bord de fuite remonter vers le bord d'attaque, puis un décollement brutal se déclencher du bord d'attaque avant que ceux du bord de fuite n'aient atteint le bord d'attaque, que la transition soit ou non déclenchée.

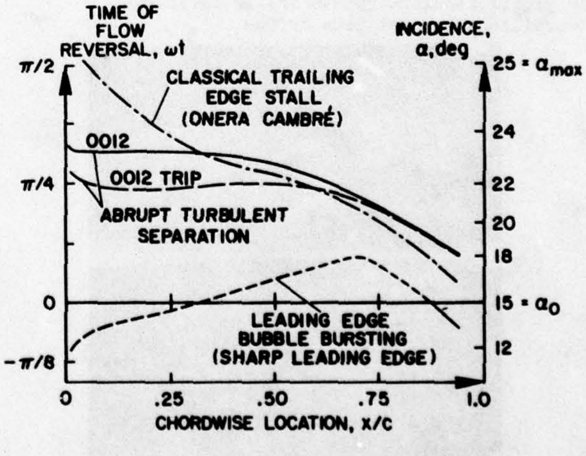

Fig. 8 – *Evolution des décollements turbulents sur profil oscillant.*
$\alpha = 15° + 10° \sin \omega t$; $k = 0,15$; $Re = 2,5 \times 10^6$.

Ces décollements de la couche limite turbulente dépendent, comme en écoulement stationnaire, de nombreux paramètres :

- ceux qui conditionnent la valeur du gradient de pression locale :
  - . le profil lui-même comme l'a illustré la figure 8 précédente,
  - . l'incidence moyenne et l'amplitude des oscillations en tangage,

- la fréquence réduite de l'oscillation, puisque les dérivées temporelles de l'incidence du profil lui sont directement proportionnelles.

La figure 9 adaptée de la figure 26 de la référence 10 illustre d'ailleurs l'influence de ce paramètre. Plus la fréquence réduite de l'oscillation est élevée, plus l'apparition des décollements est tardive. Cela retarde d'autant le décollement généralisé sur le profil.

- Ceux qui sont liés à la viscosité :

  - le nombre de Reynolds,
  - la position de la transition de la couche limite, que celle-ci s'effectue naturellement ou artificiellement.

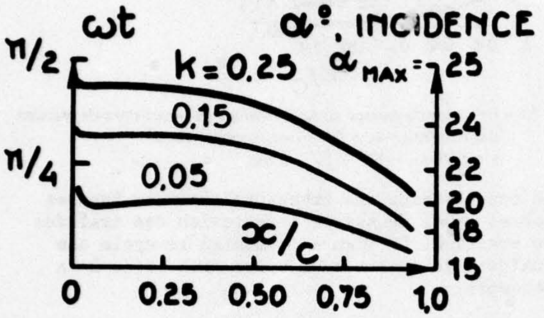

Fig. 9 – Influence de la fréquence réduite sur l'évolution des décollements NACA 0012. $\alpha = 15° + 10° \sin \omega t$.

La figure 10 adaptée de la figure 32 de la référence 10 illustre l'influence du nombre de Reynolds. Plus celui-ci est élevé, plus les décollements apparaissent et se développent tardivement.

L'influence des conditions aval sur le décollement sera discutée au paragraphe 4.3.

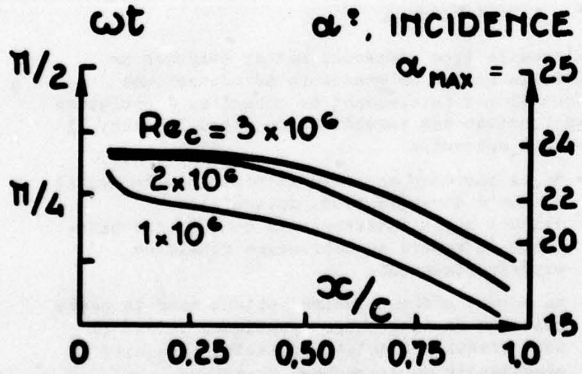

Fig. 10 – Influence du nombre de Reynolds sur l'évolution des décollements NACA 0012. $\alpha = 15° + 10° \sin \omega t$; $k = 0,15$.

x abscisse du point de décollement.

3 - EFFORTS GLOBAUX ET PRESSIONS LOCALES SUR LES PROFILS EN DECROCHAGE DYNAMIQUE.

3.1 - Exemple type d'un profil en oscillations harmoniques de tangage.

La figure 11 tirée de la référence 2 reprend les cycles de portance et de moment de tangage du profil NACA 0012 oscillant en tangage déjà présentés figure 1, mais en associant à différents moments du cycle d'incidence les principaux évènements du décrochage dynamique décrits en détail au paragraphe précédent.

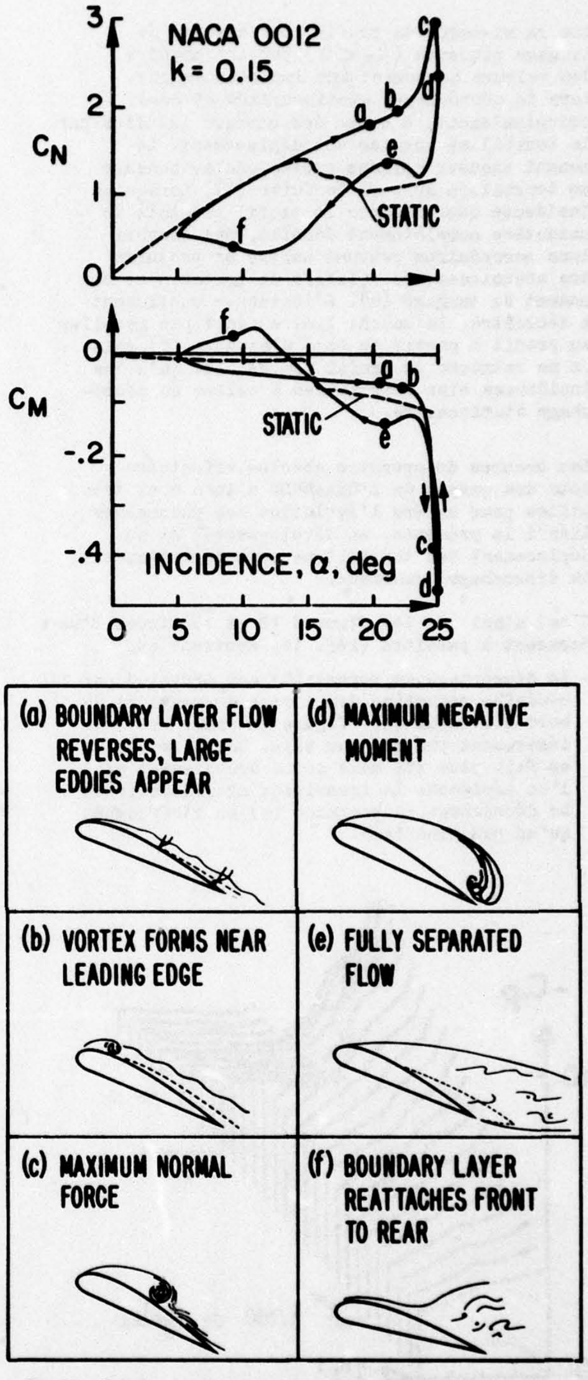

Fig. 11 – Principaux évènements liés au profil NACA 0012 en configuration de décrochage dynamique. $Re = 2,5 \times 10^6$.

On remarquera surtout que la portance du profil continue à croître avec l'incidence, bien au dela de la valeur maximale obtenue en écoulement stationnaire et ceci, malgré la présence d'écoulements inverses au sein d'une couche limite de plus en plus turbulente et épaisse sur une grande partie de la corde du profil (a). Un tourbillon se crée près du bord d'attaque (b) et la portance continue à croître encore plus rapidement avec l'incidence. Le départ du tourbillon vers le bord de fuite provoque le décrochage en moment du profil, mais le décrochage en portance (c) n'arrive qu'un peu plus tard, lorsque le tourbillon a dépassé, dans ce cas particulier, un peu plus que la mi-corde du profil. Les moments de tangage piqueurs ($C_m < 0$) peuvent prendre des valeurs nettement plus importantes que lors de décrochages stationnaires et ceci, principalement, à cause des charges induites par le tourbillon lors de son déplacement. Le moment piqueur maximum correspond au passage du tourbillon au bord de fuite (d). Lorsqu'en incidence décroissante le profil présente un caractère complètement décollé, des tourbillons secondaires peuvent naître et produire des accroissements relatifs de portance et de moment de tangage (e). L'incidence continuant à décroître, la couche limite finit par recoller au profil à partir du bord d'attaque (f) mais on ne retrouve un profil non décollé qu'à des incidences bien inférieures à celles du décrochage stationnaire.

Les mesures de pression absolue effectuées lors des essais de l'USAAMRDL d'Ames sont très utiles pour suivre l'évolution des phénomènes liés à la présence, au développement et au déplacement des tourbillons caractéristiques du décrochage dynamique.

C'est ainsi que les figures 12 et 13 tirées d'un document à paraître (réf. 11) montrent que :

- le décrochage en moment (b) est provoqué par la soudaine réduction des fortes dépressions de bord d'attaque (a) -figure 12- mais est légèrement précédé par elle. Cette réduction se fait plus tôt mais moins brusquement si l'on déclenche la transition artificiellement. Le décrochage en portance (c) ne s'effectue qu'un peu plus tard.

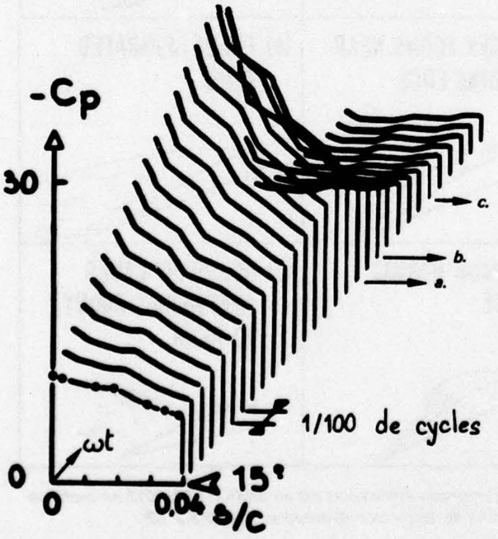

Fig. 12 – Evolution des pressions dans la région du bord d'attaque. Cas du profil NACA 0012 en transition libre.
$\alpha = 15° + 10° \sin \omega t$; $k = 0,15$.

- le tourbillon se déplace le long de l'extrados du profil en développant sur son passage des dépressions locales (fig. 13), dont le maximum permet de localiser le tourbillon ; on trouve que la vitesse de déplacement de ce tourbillon est généralement inférieure à la moitié de la vitesse de l'écoulement à l'infini amont. Une étude détaillée de ce phénomène est faite également dans la référence 12 par F.O. CARTA, à partir d'essais effectués par Sikorsky en 1972 sur profil NACA 0012.

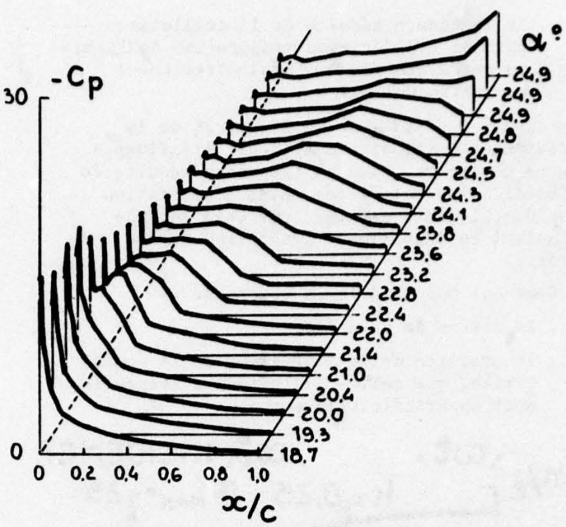

Fig. 13 – Influence du passage du tourbillon sur les répartitions de pression. Cas du profil NACA 0012 avec transition fixée.
$k = 0,15$; $\alpha = 15° + 10° \sin \omega t$.

La connaissance des pressions absolues locales permet aussi de suivre l'évolution des traînées de pression. La figure 14 montre le cycle des traînées de pression dans les axes liées à la maquette.

La technique des mesures des pressions absolues a également été adoptée par d'autres chercheurs comme A.G. PARKER (réf. 13) et plus anciennement par R.I. WINDSOR (réf. 14) ; ces travaux sont très utiles car ils fournissent aussi une base de comparaison pour la mise au point des méthodes de calcul des écoulements instationnaires en présence ou non de décrochage dynamique.

3.2 - Grandeurs aérodynamiques caractéristiques des profils en oscillations harmoniques de tangage.

L'exemple type précédent met en évidence un certain nombre de grandeurs aérodynamiques dont il est intéressant de connaître l'évolution en fonction des paramètres de l'oscillation. Il s'agit surtout :

- de la portance maximale atteinte par le profil en cours d'oscillation, puisqu'elle traduit quantitativement la conséquence bénéfique du retard au décrochage constatée expérimentalement,
- du moment piqueur maximal obtenu dans la phase critique du décrochage dynamique, puisqu'il peut traduire quantitativement l'intensité pénalisante du décrochage dynamique.

Un autre point important des configurations de décrochage dynamique concerne les échanges d'énergie entre le profil et le courant d'air, qui conditionnent donc la stabilité aérodynamique.

L'aire intérieure des cycles de moment de tangage en fonction de l'angle d'incidence est proportionnelle au travail des forces aérodynamiques ($\oint C_m \, d\alpha$). Si le cycle est parcouru dans le sens inverse des aiguilles d'une montre, le travail des forces aérodynamiques est négatif, l'amortissement aérodynamique est positif et le mouvement est stable. Par contre, si le cycle est parcouru dans le sens des aiguilles d'une montre, le travail des forces aérodynamiques est positif, l'amortissement aérodynamique est négatif et cela peut entraîner une instabilité en torsion de la pale.

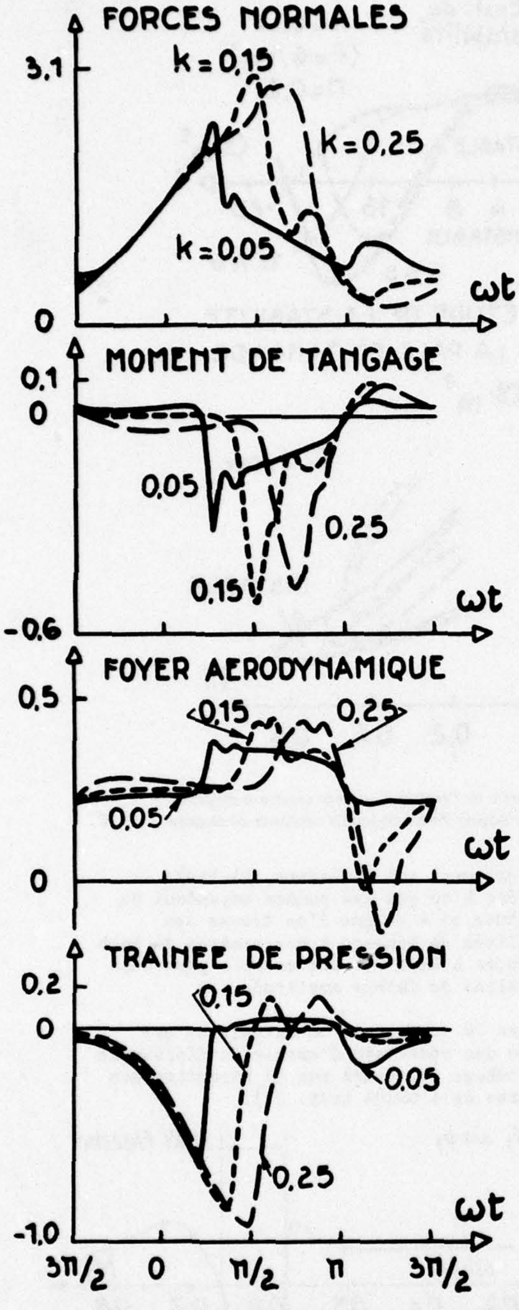

Fig. 14 – Influence de la fréquence réduite. Cas du profil NACA 0012 en transition libre.
$\alpha = 15^\circ + 10^\circ \sin \omega t$.

Les essais très complets effectués en 1968 et 1969 par Boeing-Vertol sur 4 profils (réf. 16 et 17) équipés de capteurs de pressions différentiels en mouvement de tangage et de pilonnement et en faisant varier la fréquence réduite, l'amplitude et l'incidence moyenne des oscillations et le nombre de Mach permettent d'établir l'influence de ces paramètres sur les performances aérodynamiques instationnaires des profils.

Il n'est pas question ici de fournir l'ensemble des résultats caractéristiques obtenus mais d'attirer l'attention sur les principaux effets et notamment celui :

- de l'incidence moyenne de l'oscillation et de l'amplitude associée car les effets sont très différents suivant que la plage d'incidences balayées se situe avant, de part et d'autre ou après l'incidence de décrochage stationnaire du profil. La figure 15 montre un exemple de cycles obtenus. On remarquera que, c'est dans une oscillation de part et d'autre de l'incidence de décrochage stationnaire que les effets sont les plus marqués et conduisent à des portances maximales importantes et à la possibilité d'instabilité en tangage. Lorsque le profil oscille continuement en écoulement décollé, aux fortes incidences moyennes, le mouvement redevient stable mais en général cela s'accompagne de fortes valeurs de moments de tangage piqueurs.

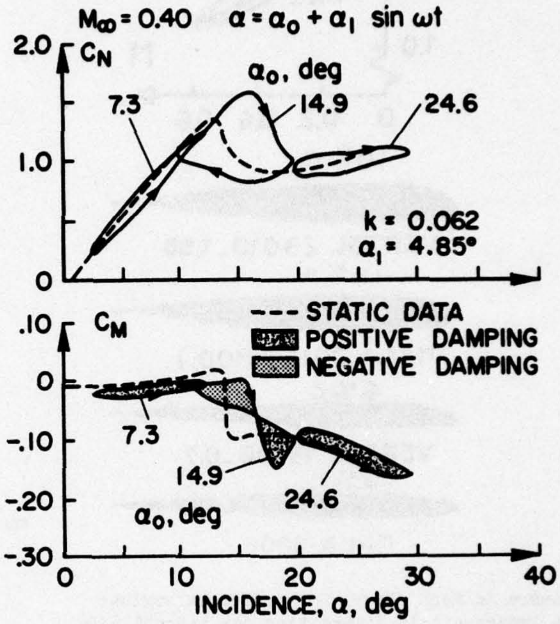

Fig. 15 – Cycles des forces et moments obtenus sur profil Vertol 23010 en oscillations harmoniques de tangage ($Re_c = 4,8 \times 10^6$).

- du nombre de Mach car dès que ce paramètre augmente un peu et qu'on se trouve à des incidences élevées, les problèmes liés à la compressibilité apparaissent. La figure 16 tirée de la référence 2 montre les cycles obtenus à différents nombres de Mach pour des incidences moyennes légèrement supérieures aux incidences de décrochage stationnaires correspondantes. Si l'allure générale des cycles reste la même, on notera que la portance maximale diminue avec le nombre de Mach et qu'en général les moments piqueurs maximaux sont moins importants à

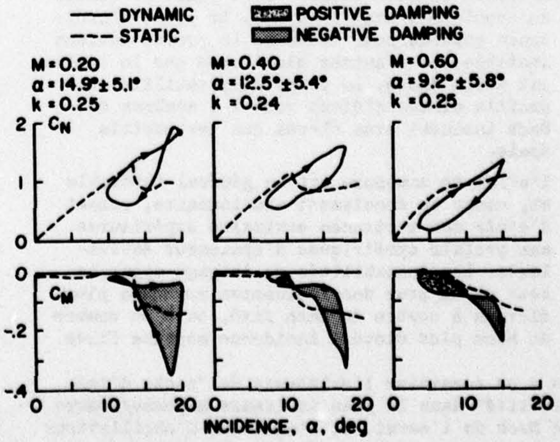

Fig. 16 – Effet du nombre de Mach sur les caractéristiques instationnaires du profil NACA 0012.

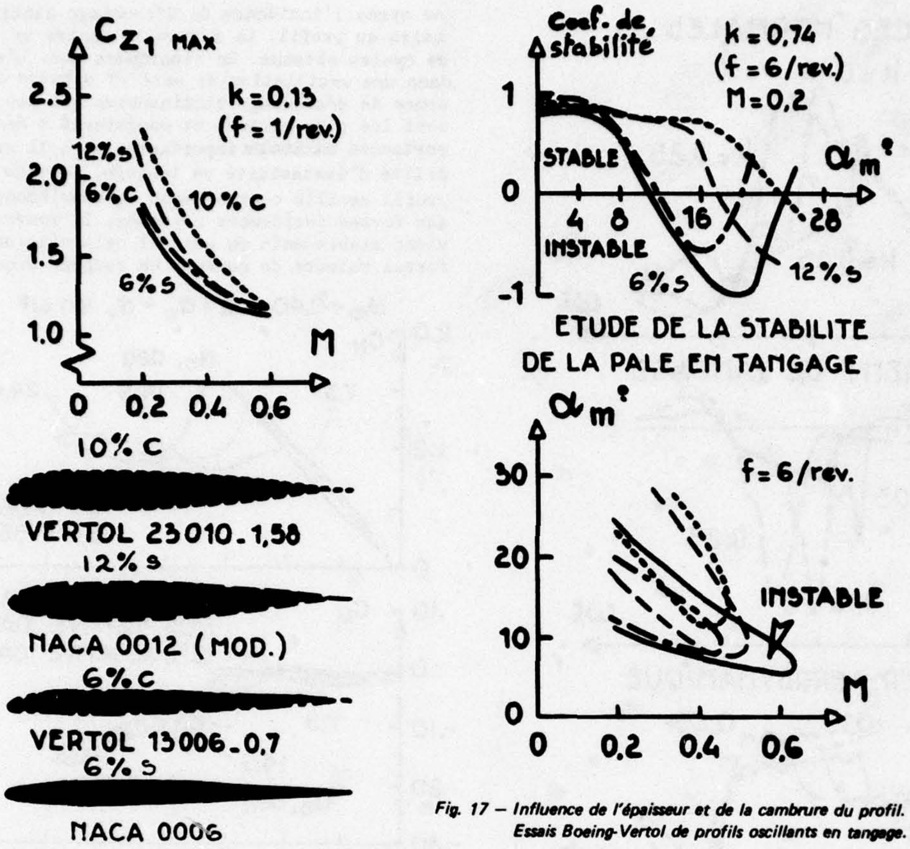

Fig. 17 — Influence de l'épaisseur et de la cambrure du profil.
Essais Boeing-Vertol de profils oscillants en tangage. $\bar{\alpha} = \pm 5°$.

nombre de Mach élevé. On remarquera surtout la tendance à *la disparition des instabilités* en tangage à Mach élevé. Ceci peut être dû à un développement tourbillonnaire moins fort lorsqu'une onde de choc est présente près du bord d'attaque du profil.

Ces essais ont été analysés par de nombreux auteurs (réf. 2, 18, 19 et 20 par exemple).

L'influence de la forme des profils essayés est non négligeable, comme l'illustre la figure 17, rassemblant les figures 7, 8 et 9 de la référence 19.

On notera que :

- dans la gamme des épaisseurs relatives essayées, plus l'épaisseur d'un profil est faible, plus ses performances de portance maximale instationnaire sont limitées (comme en écoulement stationnaire). De plus, l'incidence moyenne pour laquelle le profil devient instable est d'autant plus basse que le profil est moins épais. La poche d'instabilité des profils minces s'étend vers les nombres de Mach incident plus élevés que les profils épais.
- l'effet de cambrure est en général favorable et, comme en écoulement stationnaire, permet d'avoir des portances maximales supérieures aux profils symétriques d'épaisseur équivalente. Les instabilités en tangage apparaissent alors pour des incidences moyennes plus élevées à nombre de Mach fixé, ou à un nombre de Mach plus élevé à incidence moyenne fixée.

On a pu constater l'existence de "poche d'instabilité" dans le plan incidence moyenne/nombre de Mach de l'essai. Il s'agit ici d'oscillations d'amplitudes moyennes (± 5°). Les phénomènes liés tant à la compressibilité qu'au décrochage étant fortement non linéaires, il faut *s'attendre à ce que ces poches dépendent* de l'amplitude et à ce que l'on trouve des instabilités de tangage à des nombres de Mach supérieures à Mach 0,6 par exemple pour des oscillations de faible amplitude.

La figure 18 en fournit un exemple et est extraite des résultats d'essais de flottement de décrochage effectués par la Direction des Structures de l'ONERA (réf. 21).

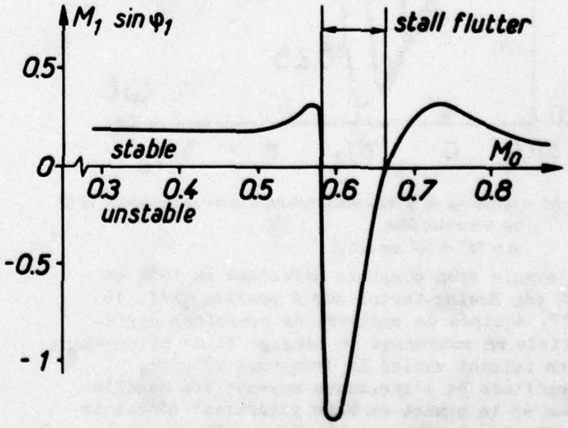

Fig. 18 — Exemple de résultat obtenu dans une étude de flottement de décrochage - Axe d'oscillation situé à 0,375 c. NACA 63A015 en oscillations de tangage - $\alpha_0 = 10°$.

En dehors des essais déjà cités, on peut obtenir des renseignements sur les caractéristiques instationnaires d'autres profils grâce aux essais effectués par le RAE sur le NPL 9615 par exemple (réf. 22) ou par le CEAT de Toulouse en France sur le profil SA 13109 par exemple (réf. 23). De nouveaux bancs d'essais destinés plus spécialement aux essais à des nombres de Mach élevés sont en cours de montage ou viennent de commencer à fonctionner. Il s'agit par exemple de bancs prévus à Ames et Langley Field par la NASA, ou à l'ARA de Bedford sous l'égide du RAE.

3.3 - Autres mouvements.

Si l'analyse des phénomènes de décrochage dynamique a été faite sur des mouvements d'incidence de la maquette, c'est que l'on dispose de très nombreux renseignements sur ce type de mouvement.

On distingue aussi :

- les mouvements de pilonnement du profil obtenus en le soumettant à des variations cycliques de translation perpendiculaire à la vitesse de l'écoulement à l'infini amont U_∞. Quelques résultats caractéristiques des essais effectués par Boeing-Vertol (réf. 16 et 17) sont fournis dans les références 18 et 19. On notera cependant que ce mouvement revient, en première approximation, à une variation d'incidence du profil de module $h\omega/U_\infty$, h étant l'amplitude du mouvement de pilonnement et ω sa pulsation. Les différences proviennent de ce que sur le profil la loi de répartitions des vitesses induites par le mouvement est linéaire *dans le mouvement* d'oscillation de tangage tandis qu'elle est constante dans le mouvement de pilonnement. La figure 19 montre un exemple de cycles obtenus, et confirme la possibilité d'avoir des portances instationnaires là encore supérieures à celles du décrochage stationnaire mais au prix de moments piqueurs importants et d'instabilités du mouvement. La figure 20 montre l'évolution des principales grandeurs caractéristiques des configurations de décrochage dynamique en fonction de l'incidence de calage du profil et du nombre de Mach de l'écoulement à l'infini amont,
- le mouvement de tamis du profil. Le mouvement est alors une translation cyclique du profil parallèlement à la vitesse de l'écoulement à l'infini amont U_∞. On obtient en fait une modulation cyclique de la vitesse d'attaque du profil, reproduisant par exemple, les conditions de vitesse d'attaque sinusoïdale pour une section de pale d'hélicoptère en vol de translation. C'est l'IMF de Marseille qui travaille sur ce sujet en France (réf. 24, 25). Là encore il y a possibilité d'obtenir lors de ces mouvements des portances supérieures à celles que l'on obtient en stationnaire, suivant les valeurs de l'incidence de calage du profil (supérieures ou égale à l'incidence de décrochage stationnaire) de la fréquence réduite du mouvement $k = \pi f c/U_\infty$ et de son amplitude réduite $\lambda = A\omega/U_\infty$ (A étant l'amplitude réelle du mouvement de tamis). La figure 21 adaptée de la figure 1 de la référence 26 illustre ce point mais la communication faite par les ingénieurs de l'IMF de Marseille durant ce meeting (réf. 27) permettra d'entrer beaucoup plus dans les détails des écoulements liés à ce mouvement et des performances aérodynamiques ainsi obtenues. Cette variation de vitesse d'attaque peut également s'effectuer en faisant varier la vitesse de l'écoulement dans la soufflerie, le profil restant fixe. Ce type de montage a été adopté aux Etats Unis à l'Université de Monterey en Californie, à celle du Texas et à celle de l'Illinois. Les essais effectués sur un profil NACA 0012 dans cette dernière installation seront présentés lors de ce meeting par L.S. SAXENA, AA. FEJER et M.V. MORKEVIN (communication n° 22).

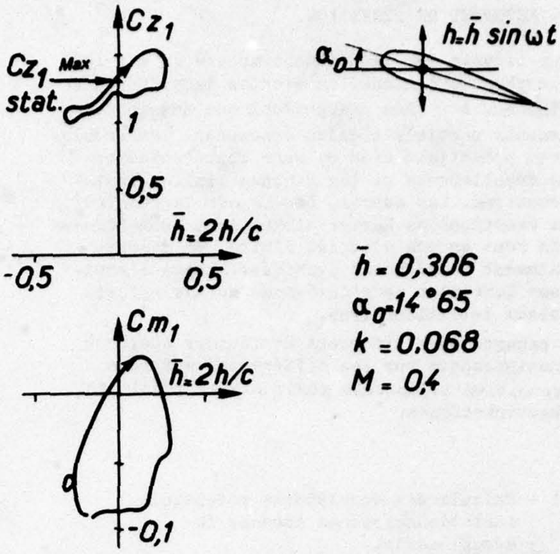

Fig. 19 – Exemple de cycles instationnaires obtenus en oscillations de pompage du profil Vertol 23010-1,58.

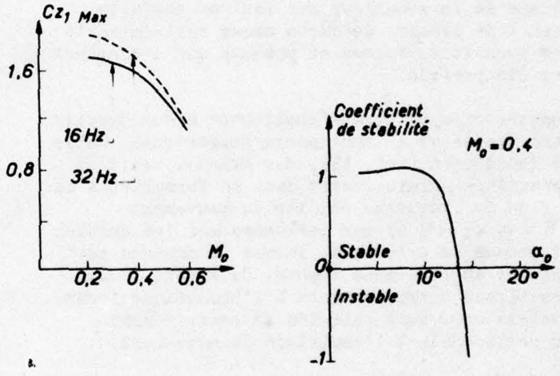

Fig. 20 – Portances maximales et coefficients de stabilité du profil Vertol 23010 en oscillations de pompage.

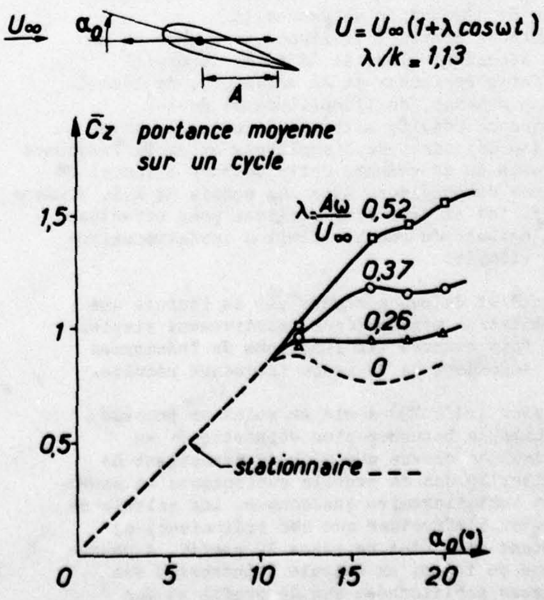

Fig. 21 – Oscillations harmoniques de tamis sur un profil NACA 0012 - $1 < Re_c < 2 \times 10^6$.

4 - METHODES DE PREVISION.

Pour prévoir le phénomène complexe qu'est le décrochage dynamique, on dispose de différentes méthodes. Les unes n'apportent que des renseignements partiels ; elles concernent les écoulements potentiels avec ou sans représentation des décollements et les couches limites instationnaires. Les autres, basées sur la résolution des équations de Navier-Stokes sont prometteuses mais sont encore d'emploi limité. On dispose également de méthodes pratiques à base d'empirisme lorsqu'on ne s'intéresse qu'aux efforts globaux instationnaires.

Ce paragraphe s'efforcera de fournir quelques renseignements sur les différentes méthodes disponibles illustrées par quelques résultats caractéristiques.

4.1 - Calculs des écoulements potentiels instationnaires en absence de décollements.

Lorsque les profils ne sont pas soumis à des décollements ou à des effets visqueux importants, la résolution des équations instationnaires de la mécanique des fluides parfaits permet de décrire de façon assez satisfaisante les pressions, forces et moments qui s'exercent sur les profils.

Les théories de base s'appliquent à des profils sans épaisseur en mouvements harmoniques. Celle de Théodorsen (réf. 15), par exemple, fait apparaître naturellement dans sa formulation la notion de fréquence réduite du mouvement ($k = \omega c/2U_\infty$) et son influence sur les modules et phases des pressions, forces et moments par rapport au mouvement imposé. Cependant, seuls les termes correspondants à l'harmonique fondamentale en ω sont calculés et ceux-ci sont proportionnels à l'amplitude du mouvement.

Une extension simple de cette méthode aux cas des profils épais a été proposée par W.J. McCROSKEY (réf. 28) qui fournit les répartitions de vitesse à l'extrados et à l'intrados des profils oscillants. Associée à la résolution de l'équation de Bernoulli la méthode montre l'existence de termes en ω qui dépendent alors de la forme du profil (effet d'épaisseur et de cambrure), de l'incidence moyenne, de l'amplitude et de la fréquence réduite mais aussi celle de termes en 2ω dépendant de l'amplitude et de la fréquence réduite du mouvement. Cette méthode a fourni de bonnes comparaisons avec les essais de R.I. Windsor (réf. 14) et peut être utilisée pour effectuer des calculs de couches limites instationnaires par exemple.

L'intérêt de ces méthodes est de fournir une formulation mathématique relativement simple, une fois connues les fonctions de Théodorsen qui dépendent de la seule fréquence réduite.

Giesing (réf. 29) a mis au point un procédé de calculs beaucoup plus sophistiqués en mettant en oeuvre une méthode permettant de traiter le cas de profils quelconques en mouvement instationnaire quelconque. Les calculs ne peuvent s'effectuer que sur ordinateur, en partant d'un état de repos du profil. A chaque étape en temps, on calcule l'intensité des sources positionnées sur le profil et des tourbillons liés disposés à l'intérieur du profil et la position des tourbillons libres lachés du bord de fuite pour former le sillage instationnaire, dont on calcule aussi le développement dans l'espace. Compte tenu de la condition de Kutta-Joukowski, ce calcul permet de prévoir l'évolution des pressions, forces et moments agissant sur le profil. Si quelques procédés de calculs des écoulements instationnaires, en absence de tout décollement sur le profil, ont été rappelés ici, c'est parce que :

- pour toute configuration de décrochage dynamique, il existe des instants où il n'y a pas de décollements sur le profil
- l'analyse des résultats fournis par ces méthodes peuvent partiellement expliquer le retard au décrochage.

La théorie de Théodorsen montre par exemple que, lorsque les incidences d'un profil oscillant en tangage croissent, les gradients de pression le long de la corde sont inférieurs à ceux que l'on obtient en stationnaire. Cette constatation faite par F.O. CARTA (réf. 30) peut-elle suffire à expliquer le retard au décrochage ? La figure 22 tirée de la référence 1 montre le résultat obtenu en supposant que le décrochage instationnaire (α_{DS}) ne se produit que lorsque le gradient de pression instationnaire près du bord d'attaque (à $x/c = 0.1$) du profil atteint la valeur théorique correspondant au décollement en stationnaire. Le calcul prévoit bien, comme dans l'expérience, que l'incidence de décrochage instationnaire augmente avec la fréquence réduite du mouvement mais le calcul est loin de pouvoir prédire la valeur absolue de l'accroissement d'incidence de décrochage dans les configurations de décrochage dynamique.

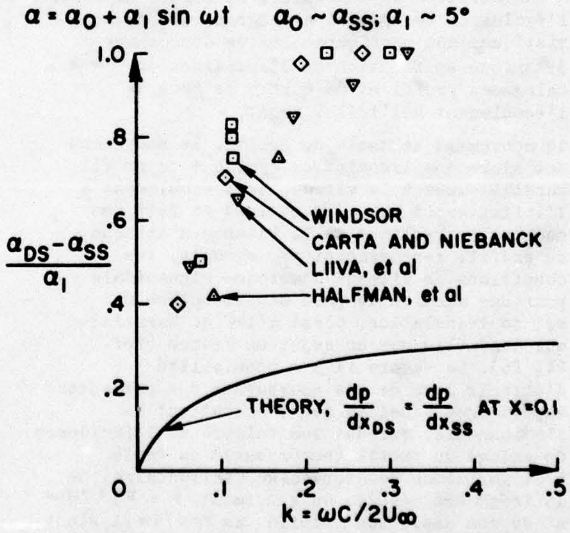

Fig. 22 – Augmentation de l'incidence du décrochage instationnaire α_{DS} par rapport à l'incidence de décrochage stationnaire α_{SS}.

4.2 - Calculs de configurations de décrochage dynamique à l'aide des écoulements potentiels.

On a vu qu'expérimentalement l'une des phases importantes du décrochage dynamique était celle de la formation et du déplacement d'un tourbillon sur l'extrados des profils.

- Le Pr. HAM (réf. 31) a simulé cette phase en émettant au voisinage du bord d'attaque une série de tourbillons et en les laissant s'échapper vers le bord de fuite à la vitesse de l'écoulement local. Ce calcul a été effectué pour le cas d'un profil infiniment mince.

La figure 23 tirée de la référence 31 montre les trajectoires suivies par les tourbillons dans le cas d'une plaque plane soumise brutalement à un échelon d'incidence de 30°. On voit très bien une masse tourbillonnaire se former et se déplacer vers le bord de fuite.

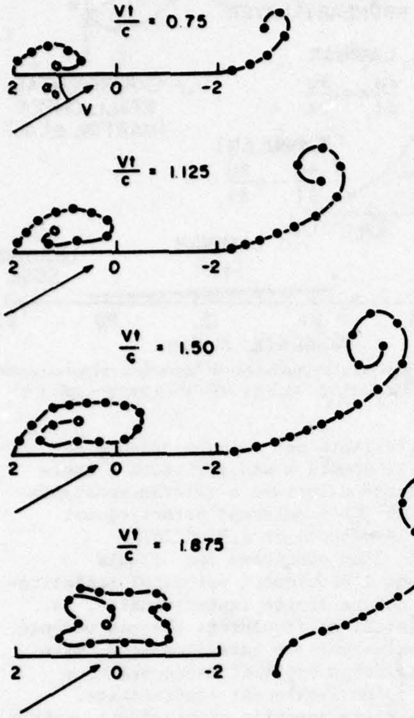

Fig. 23 – Trajectoires calculées des tourbillons émis lors d'une mise en incidence brutale à 30°.

La figure 24 tirée également de la référence 31 montre un accord satisfaisant avec l'expérience en ce qui concerne le niveau des pressions locales sur un profil oscillant en tangage entre 10° et 30° à une fréquence réduite de 0,35 (essais effectués au MIT).

Il est cependant à noter qu'il faut s'imposer l'instant du début d'émission des tourbillons de bord d'attaque. De plus les calculs ne peuvent pas prendre en compte des décollements de bord de fuite.

- La Société BERTIN en France (réf. 32 et 33) a utilisé cette schématisation en l'appliquant au cas d'un profil. Mais c'est le décollement de la couche limite qui se produit vers le bord d'attaque qui engendre une nappe tourbillonnaire. Celle-ci se développe à partir de ce point et est alimentée en rotationnel par la couche limite. Suivant Sarpkaya (réf. 34) le débit de rotationnel est donné par la formule :

$$\Delta\gamma / \Delta t = -1/2 \, (u^2 - u_r^2)$$

où u est la vitesse de l'écoulement au droit du point de décollement laminaire et U_r est la vitesse maximale de l'écoulement de recirculation induit par l'enroulement tourbillonnaire.

A chaque étape en temps, on émet donc des tourbillons discrets dont on calcule la trajectoire. On détermine les vitesses induites à la paroi du profil par l'ensemble des singularités correspondant à la méthode de J.P. Giesing (réf. 29) et par les tourbillons libres émis au bord d'attaque.

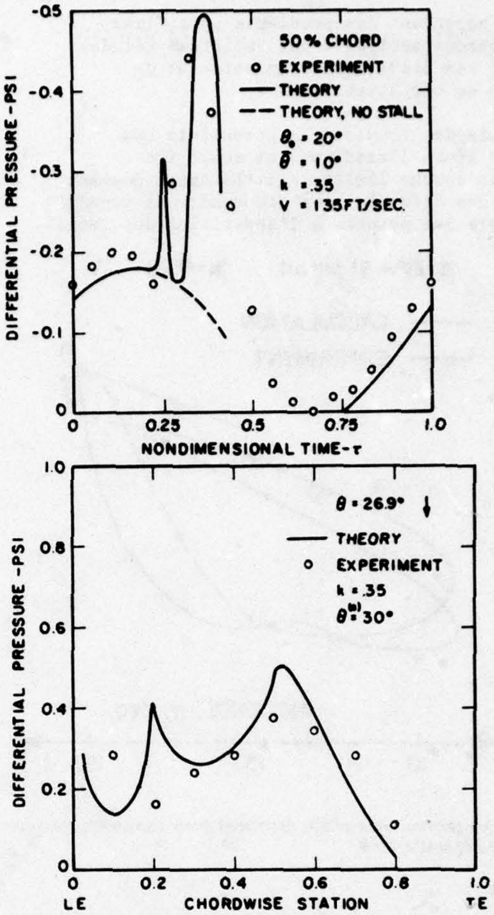

Fig. 24 – Evolution calculée et expérimentale des pressions sur un profil en configuration de décrochage dynamique.

La figure 25 tirée de la référence 33 montre les comparaisons des lignes tourbillonnaires calculées et les visualisations par fumées effectuées par l'USAAMRDL d'Ames (Réf. 6). Les comparaisons au niveau des cycles de portances obtenues sont aussi assez encourageantes comme le montre la figure 26 tirée de la référence 2.

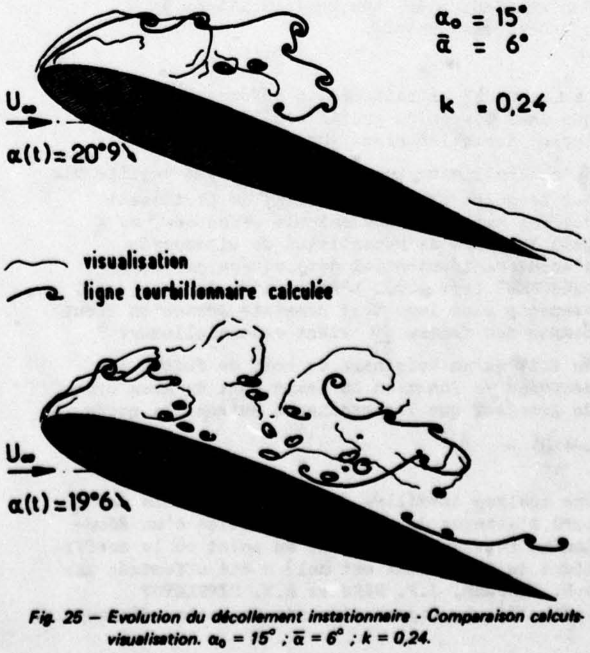

Fig. 25 – Evolution du décollement instationnaire - Comparaison calcul-visualisation. $\alpha_0 = 15°$; $\bar{\alpha} = 6°$; k = 0,24.

Il reste cependant des problèmes pour fixer soit rigoureusement soit par empirisme (études en cours) les conditions d'émission et de diffusion de ces tourbillons.

Les calculs des écoulements potentiels ont cependant leurs limitations et seuls les calculs de couche limite instationnaire peuvent apporter des éléments pour comprendre et prévoir si possible les retards à l'apparition des décollements.

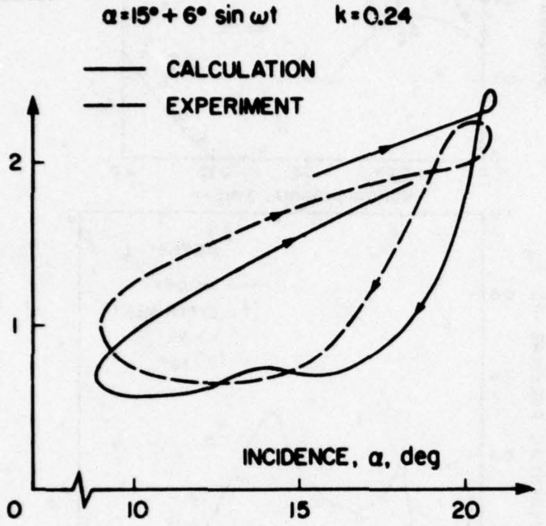

Fig. 26 – Comparaison entre calculs BERTIN et essais USAAMRDL (Ames). Profil NACA 0012.

4.3 - Calculs des couches limites instationnaires

Une des sessions de ce meeting d'aréodynamique instationnaire est consacrée aux problèmes de couche limite instationnaire décollée ou non ; elle est précédée d'une présentation générale par D.P. Telionis ; il n'est donc pas utile ici de développer ce sujet.

On ne rappelle ici que quelques problèmes fondamentaux liés aux configurations de décrochage dynamique.

La figure 27 extraite de la référence 1 montre que dans le cas du profil oscillant, l'effet de termes instationnaires $\frac{\partial u}{\partial t}$ des équations de couche limite turbulente n'est pas négligeable sur le point où le coefficient de frottement devient nul. Dans les calculs effectués, on a pris les lois de répartition de vitesse de l'écoulement potentiel déterminées par W.J. McCROSKEY (réf. 28). L'effet d'hysteresis beaucoup plus important constaté lorsqu'on tient compte des termes $\frac{\partial u}{\partial t}$ vient essentiellement du fait qu'au voisinage du bord de fuite, ces dérivées en fonction du temps sont du même ordre de grandeur que les gradients suivant la corde $u\frac{\partial u}{\partial x}$.

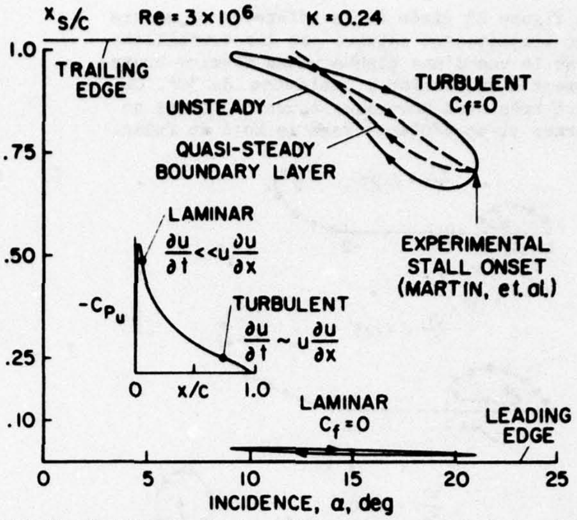

Fig. 27 – Evolution du point de coefficient de frottement nul sur un profil oscillant NACA 0012 - Re = 3 x 10⁶ ; k = 0,24 ; α = 15° + 6° sin ωt.

Une analyse détaillée de la remontée vers le bord d'attaque du point d'apparition d'un écoulement inverse (équivalent au point où le coefficient de frottement est nul) a été effectuée par R.M. SCRUGGS, J.F. NASH et R.E. SINGLETON (réf. 35). La figure 28 tirée de cette référence montre les résultats des calculs obtenus pour un profil soumis à une variation d'incidence croissante effectuée à vitesse constante entre 0° et 25°. L'écoulement potentiel est calculé par la méthode de J.P. GIESING (réf. 29). Si l'on considère les calculs effectués avec l'écoulement potentiel instationnaire et la couche limite instationnaire, le point où apparaît un écoulement inverse remonte plus tardivement vers le bord d'attaque, mais lorsque l'incidence croît, de façon beaucoup plus rapide qu'en écoulement stationnaire.
Le retard à cette remontée proviendrait, selon les auteurs, en partie de l'écoulement potentiel instationnaire, en partie des couches limites instationnaires, comme le montrent les différentes courbes de la figure 28.

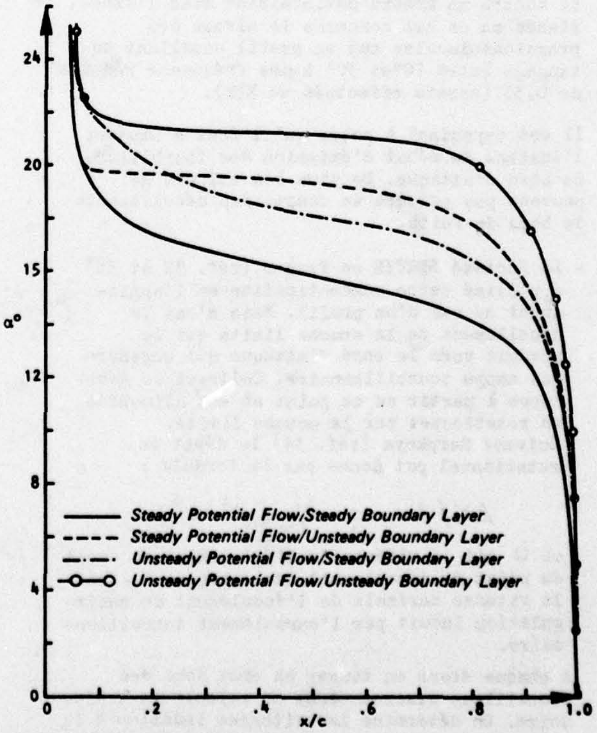

Fig. 28 – Mouvement du point d'apparition de l'écoulement inverse. (Incidence croissante et cα̇/u∞ = 0,04).

Il est aussi significatif de voir (fig. 29, tirée de la référence 35) que, si l'on considère l'incidence d'apparition à mi-corde du point d'écoulement inverse, celle-ci augmente avec la vitesse de variation angulaire du profil de façon très comparable à celle de l'incidence de décrochage instationnaire en portance. Cette augmentation est d'abord très rapide pour les faibles valeurs de $c\dot{\alpha}/2U_\infty$ puis il apparaît une sorte de saturation des effets instationnaires aux valeurs élevées de $c\dot{\alpha}/2U_\infty$. Ce phénomène caractéristique proviendrait lui aussi en partie de l'écoulement potentiel instationnaire et en partie des couches limites instationnaires.

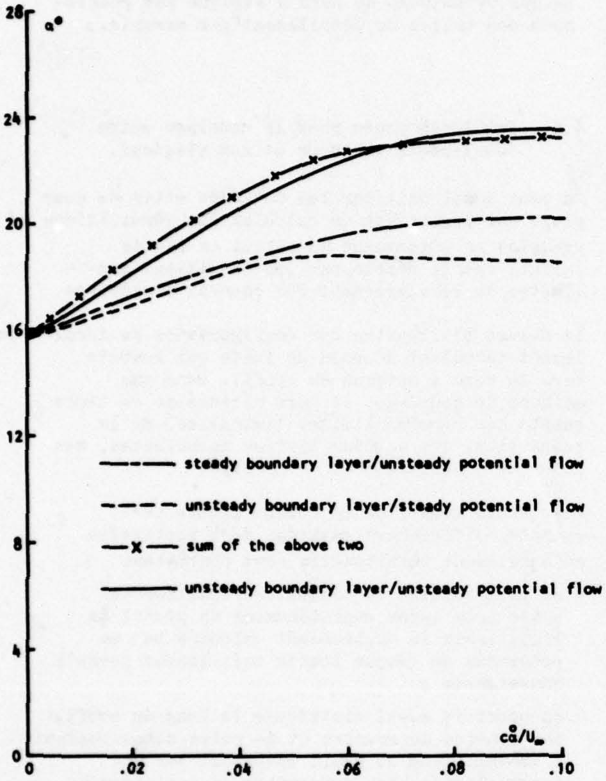

Fig. 29 – Incidence pour laquelle l'écoulement inverse atteint la mi-corde du profil, en fonction de la vitesse angulaire du profil.

Il faut cependant dire que ces calculs ne peuvent être vraiment significatifs que si le point d'apparition d'écoulement inverse n'est pas suivi à l'aval d'un décollement de la couche limite trop important, qui modifierait alors les répartitions de vitesse sur l'ensemble du profil (ce qui semble le cas lors des essais effectués à Ames sur le profil NACA 0012 muni ou non de son extension cambrée).

Un point important lié à la nature instationnaire des couches limites est la distinction à faire entre le point d'apparition d'un écoulement inverse et le point de décollement. De très nombreux travaux ont été effectués sur ce sujet et le lecteur pourra se reporter, par exemple , à certaines communications :

- celles faites au Symposium IUTAM sur les couches limites instationnaires organisé par l'Université Laval à Québec en Mai 1971 (réf. 36) ;
- celles faites au Symposium organisé par l'Université d'Arizona à Tucson en Mars 1975 (réf. 37) sur l'Aérodynamique instationnaire.

Il n'apparaît pas en fait de singularités au point d'écoulement inverse, comme en écoulement stationnaire. Le critère de décollement n'intervient par exemple qu'à l'apparition de la divergence de l'épaisseur du déplacement.
Cela se situe en aval du point d'apparition d'écoulement inverse, comme le montre le schéma de la figure 30 proposé par W.R. Sears et D.P. Telionis (réf. 38). On peut donc continuer à décrire la couche limite en aval du point d'écoulement inverse ($C_f = 0$). V.C. PATEL et J.F. NASH (réf. 39) ont pu calculer l'évolution dans le temps d'une bulle de décollement turbulent créée par une décélération suivie d'une accélération de l'écoulement extérieure, variable dans le temps. La figure 31 tirée de la référence 2 illustre les résultats obtenus qui montrent la naissance de la bulle de décollement avec écoulement inverse, son extension vers le bord d'attaque et l'apparition finale d'un décollement due au brusque accroissement de l'épaisseur de la couche limite. Ces phénomènes de bulles de décollement turbulent instationnaire sont également étudiés de façon intensive par L.W. CARR de l'USAAMRDL d'Ames.

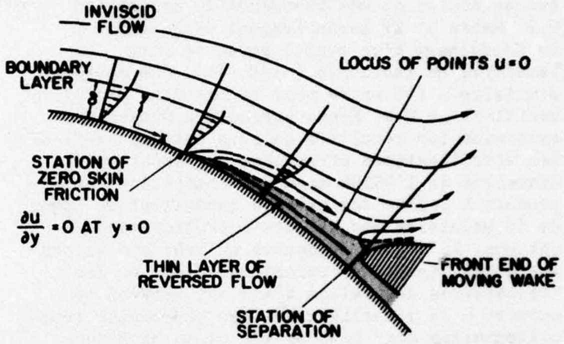

Fig. 30 – Modèle de Sears et Telionis pour un décollement d'une couche limite remontant vers le bord d'attaque.

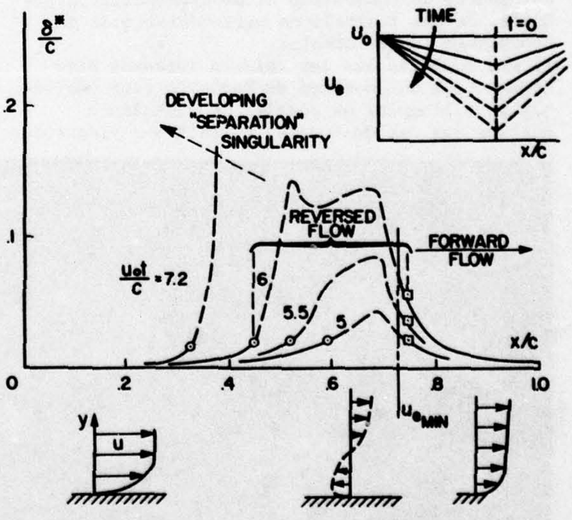

Fig. 31 – Calcul de la variation de l'épaisseur de déplacement d'une couche limite turbulente instationnaire avec écoulements inverses.

De nombreuses méthodes de calcul des couches limites turbulentes instationnaires existent, mais il est à noter que les modèles de turbulence choisis sont pour l'instant toujours basés sur des critères valables en écoulement stationnaire. Il semble donc fondamental dans ce domaine de vérifier que ces modèles sont adaptés à l'aérodynamique instationnaire. Les expériences basées sur la recherche de caractéristiques des couches limites instationnaires sont donc très utiles et à titre d'exemple on citera celle menée au CERT-ONERA de Toulouse pour des plaques planes soumises à des écoulements pulsés. Ces travaux feront l'objet d'une présentation lors de la session III de ce meeting (réf. 40)

En conclusion, les calculs d'écoulements potentiels et de couches limites fournissent des renseignements partiels intéressants et permettent de comprendre certaines phases du décrochage instationnaire. Mais ils demeurent incomplets.

4.4 - Calcul des équations de Navier-Stokes

Dans un problème aussi complexe d'interaction entre les écoulements potentiels et visqueux la résolution des équations de Navier-Stokes devrait permettre d'aborder le problème du décrochage dynamique dans son ensemble.

En résolvant l'équation de propagation du tourbillon et celle de Poisson pour la fonction de courant par un schéma implicite aux différences finies et une procédure de relaxation U.B. Mehta et Z. Lavan avaient déjà étudié le décrochage d'un profil après sa mise impulsive en incidence (réf. 41). Une approche similaire a été prise pour le cas d'un profil oscillant et U.B. Mehta présentera durant ce symposium les résultats qu'il a obtenus (réf. 42). Des visualisations effectuées au tunnel hydrodynamique de l'ONERA dans des conditions correspondant à celles des calculs permettent de juger de la précision des résultats préliminaires obtenus. La figure 32 montre un très bon accord entre les lignes de courant calculées et les trajectoires des bulles d'air qui servent de support à la visualisation. Les phénomènes tourbillonnaires sont bien prévus et on peut donc espérer que les calculs pourront décrire de façon satisfaisante le processus physique de naissance, de convection et de dissipation éventuelle de ces tourbillons caractéristiques du décrochage instationnaire.

Il est souhaité que les calculs puissent être effectués à des nombres de Reynolds plus réalistes avec l'emploi de modèles de turbulence adaptés aux cas de fortes interactions visqueuses.

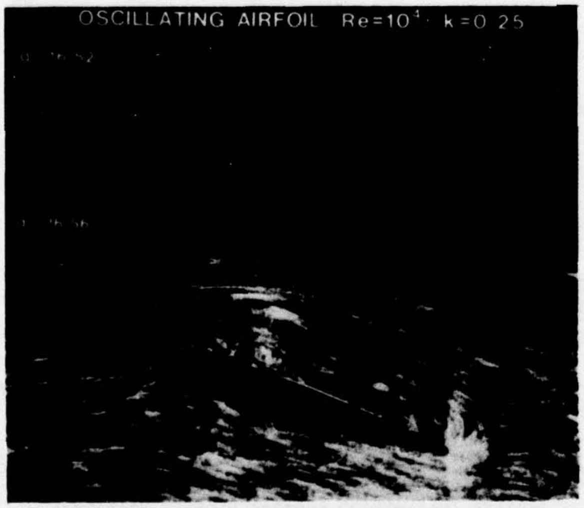

Fig. 32 – Profil NACA 0012 oscillant en tangage.
$\alpha = 10^\circ + 10^\circ \sin \omega t$; $k = 0,25$; $Re_c = 10000$

D'autres communications, durant ce meeting, traitent aussi de la résolution des équations de Navier-Stokes. Celle de J.C. Wu et N.L. Sankar concerne aussi une aile oscillante (réf. 43) et celle de R.B. Kinney traite du cas d'une aile fixe soumise à des écoulements instationnaires (réf. 44). Les méthodes employées pour la résolution des équations de Navier-Stokes pouvant être différentes, il sera intéressant de savoir si certaines peuvent étendre leurs applications à des nombres de Reynolds plus élevés sans nécessiter pour cela des temps de calcul prohibitifs.

Une autre application des équations de Navier-Stokes a été faite par S.J. Shamroth et J.P. Kreskowsky (réf. 45) en ne les utilisant qu'au voisinage du bord d'attaque. Les calculs fournissent une description assez fine des décollements laminaires de bord d'attaque et pourraient donc être utilisés pour des décrochages dynamiques du bord d'attaque par éclatement des bulles de décollement par exemple.

4.5 - Problèmes posés pour le couplage entre écoulements visqueux et non visqueux.

On peut aussi utiliser les méthodes dites de couplage qui permettent de calculer les répartitions de pression en effectuant un calcul en fluide parfait tenant compte, par les conditions aux limites, du développement des couches visqueuses.

La figure 33 illustre une configuration de décollement turbulent de bord de fuite qui remonte vers le bord d'attaque du profil. Dans une méthode de couplage, il sera nécessaire de tenir compte des couches limites laminaires, de la transition, des couches limites turbulentes, des zones de décollement et du sillage.

Pour tenir compte de la couche limite par exemple, différentes méthodes déjà appliquées en écoulement stationnaire sont possibles:

- on peut refaire le calcul des écoulements potentiels après engraissement du profil de l'épaisseur de déplacement calculée par un programme de couche limite puis itérer jusqu'à convergence ;
- on pourrait aussi distribuer le long du profil une densité de sources et de puits correspondant à la variation du débit intéressé par la couche limite, les intensités de ces singularités ($q = d/ds(\rho_e u_e \delta^*)$) étant calculées à partir des résultats de calculs des écoulements potentiels et visqueux de l'itération précédente.

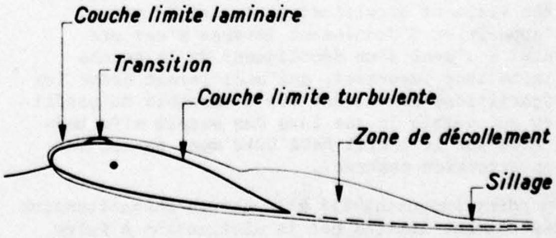

Fig. 33 – Exemple de zones visqueuses sur un profil en configuration de décrochage dynamique.

La transition s'effectue dans de nombreux cas par l'intermédiaire d'une bulle de décollement laminaire. Les conditions instationnaires auxquelles est soumis le profil peuvent retarder son éclatement. Les travaux menés par J.D. LANG (réf. 46) sont, par exemple, intéressants à cet égard. Le rôle de cette bulle de décollement laminaire peut surement devenir important dans le cas de profils qui en stationnaire décrochent par éclatement de cette bulle. On doit citer également les études faites sur ce sujet au M.I.T. par N.D. HAM et son équipe (réf. 72, 73, 76).

Le problème de la zone de décollement et du sillage demeure beaucoup plus complexe et mériterait des études approfondies.

On peut citer les études de P. Crimi (réf. 47 et 48) qui, dans ses travaux de prévision des forces et moments des profils en configurations de décrochage dynamique, fait par exemple l'hypothèse d'une pression constante dans la bulle de décollement.

Le point de décollement sur le prôfil est supposé connu, mais est remis en cause à chacune des itérations successives entre calculs des écoulements potentiels et visqueux jusqu'à convergence de ce point.

En se fixant une loi de déplacement du point de décollement sur un profil oscillant, F. SISTO et P.V.K. PERUMAL (réf. 49) ont calculé l'évolution des forces et moments. Ils ont utilisé pour les calculs d'écoulements potentiels une méthode de potentiel d'accélération. Les calculs effectués pour une plaque plane en oscillations de tangage et de pompage montrent que l'on peut ainsi obtenir des cycles des forces et moments pouvant entraîner le flottement. En fait, le choix de singularités adaptées pour représenter les zones de décollement et le sillage visqueux provenant de la confluence des couches limites extrados et intrados semble encore demander des analyses approfondies.

Cependant, l'aspect théorique de ce problème a été examiné récemment par W.R. SEARS (réf. 50) qui pose notamment le délicat problème de la condition de Kutta-Joukowski en instationnaire.

Il serait peut être intéressant de développer des méthodes analogues à celles développées pour la prévision de la portance maximale des profils en écoulement stationnaire, comme viennent de le faire B. MASKEW et F.A. DVORAK (réf. 51).

Le problème de couplage entre écoulements visqueux et non visqueux va certainement demander encore beaucoup d'efforts mais le but à atteindre est des plus attractifs puisqu'il devrait permettre un calcul beaucoup plus précis des configurations de décrochage dynamique et des qualités aérodynamiques des profils dans ce cas.

4.6. - Méthodes empiriques pour la prévision des forces globales.

Les paragraphes précédents montrent les différents problèmes fondamentaux qui sont à résoudre pour décrire de façon précise les différentes phases du décrochage dynamique. Depuis des années, en vue de leur utilisation pour les applications, de nombreux chercheurs se sont attachés à trouver des méthodes plus simples de représentation des forces instationnaires pour les profils rencontrant des régimes de décrochage dynamique au cours de mouvements instationnaires.

Le problème consiste surtout à trouver une formulation très générale à partir d'essais effectués dans des configurations simples (profil oscillant par exemple) en faisant varier de nombreux paramètres : profil, nombre de Mach, incidence et amplitude, etc ..

Méthode UARL (α, A, B).

Cette méthode a été mise au point par F.O. CARTA et repose sur le fait que la portance et le moment de tangage instantanés doivent être fonctions comme en écoulement instationnaire non décollé de l'incidence α , de la vitesse angulaire $\dot{\alpha}$ et de l'accélération angulaire $\ddot{\alpha}$

En fait, CARTA utilise, pour plus de généralités, les paramètres réduits suivants :

$\sigma = \alpha / \alpha_{DS}$ $A = \dot{\alpha} c / 2U_\infty$ $B = \ddot{\alpha} c^2 / 4U_\infty^2$

α_{DS} : incidence de décrochage stationnaire

On dispose de tables (réf. 52 et 53) fournissant pour toute incidence des valeurs moyennes de C_z ou C_m correspondantes à des valeurs associées A et B.

Cette méthode a permis de résoudre de nombreux problèmes liés aux configurations de décrochage dynamique ou d'apparition d'instabilité aérodynamique (flottement) sur rotor d'hélicoptère ou de compresseur (réf. 54 à 56).

Plus récemment, R.L. BIELAWA de l'United Technologies Research Center à Hartford (réf. 57) a développé une méthode permettant de s'affranchir des tabulations des valeurs A et B. Des fonctions non linéaires, dont seuls les coefficients seront tabulés, synthétisent les courbes Cz (ou Cm) = $f(\alpha, A, B)$.

Ces méthodes peuvent s'appliquer par exemple à la détermination des incidences prises par une maquette globalement flexible en torsion lorsqu'elle se trouve en oscillations forcées de tangage. La figure 34 tirée de la référence 57 montre la très bonne comparaison des résultats de calcul avec l'expérience.

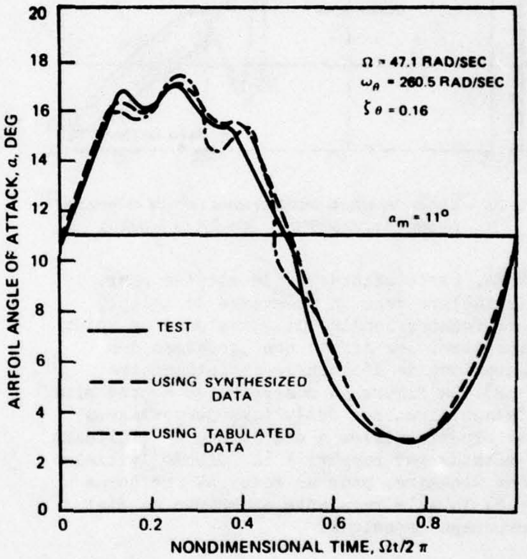

Fig. 34 – Comparaison des incidences prises par une maquette flexible mise en oscillations forcées en tangage (ω_θ/Ω = 5,53).

Méthode Boeing-Vertol.

Cette méthode a été developpée à la suite des campagnes d'essais sur profils oscillants en tangage et en pompage effectués par Boeing-Vertol (réf. 16 et 17). Elle repose sur le fait constaté expérimentalement que les effets instationnaires sont en général d'autant plus importants que la variation d'incidence imposée au profil se fait plus rapidement. D.W. Gross et F.D. Harris (réf. 58) ont montré que le retard au décrochage est proportionnel à $\sqrt{c\dot{\alpha}/2U_\infty}$. F.D. Harris et F.J. Tarzanin (réf. 59 et 60) ont alors mis au point un calcul des forces aérodynamiques en associant à la théorie de base de Théodorsen une incidence pseudo-dynamique ou de référence instationnaire qui traduit la possibilité d'avoir, en incidence croissante, un retard au décrochage.

R.E. Gormont (réf. 61) a décrit de façon très complète la méthode Boeing-Vertol qui a l'avantage, bien que basée sur un certain empirisme, d'une formulation mathématique qui ne nécessite que la connaissance des seuls polaires stationnaires des profils

La figure 35 tirée de la référence 60 montre que les calculs permettent de prévoir avec une certaine précision les cycles des forces et moments de tangage pour des profils en absence ou en présence de décrochage total ou partiel.

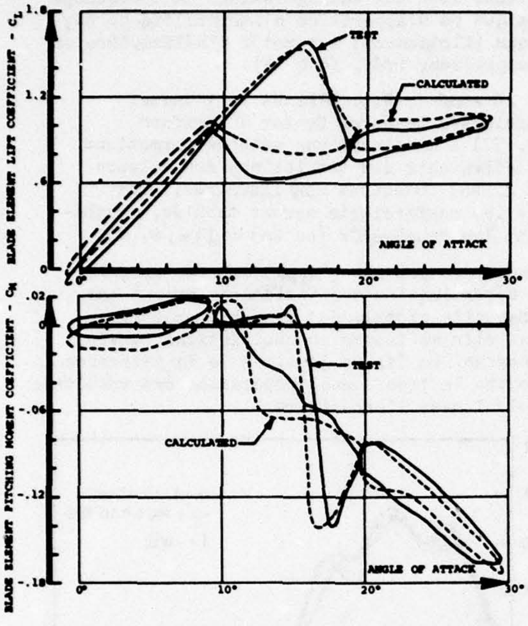

Fig. 35 – Cycles des efforts instationnaires calculés et mesures. (Profil Vertol 23010 - M = 0,4 ; k = 0,062).

A l'ONERA, cette méthode a été adaptée pour pouvoir inclure dans un programme de calculs des performances locales et globales d'un rotor d'hélicoptère, les effets non linéaires des configurations de décrochage instationnaire (réf. 62). La figure 36 montre qu'un accord plus satisfaisant avec les évolutions de portances locales expérimentales a été obtenu en utilisant cette méthode par rapport à la méthode initiale purement linéaire, pour un rotor où une bonne partie de la pale reculante se trouve en état de décrochage dynamique.

Méthode du temps de retard au décrochage dynamique (Time delay method).

Cette méthode est basée sur l'idée simple qu'il pourrait exister deux valeurs de temps réduit τ_1 et τ_2 qui fixent le retard au décrochage en moment et au décrochage en portance. Si t_0 est le temps origine, au moment où le profil possède une incidence instantanée égale à celle où il décroche en stationnaire, les temps t_1 et t_2 pour lesquels, dans des conditions instationnaires, le profil décroche en moment et en portance, correspondent à des temps réduits

$$\tau_1 = (t_1 - t_0) \times \frac{U_\infty}{c} \qquad \tau_2 = (t_2 - t_0) \times \frac{U_\infty}{c}$$

où τ_1 et τ_2 sont des constantes "universelles".

Pour Sikorsky (réf. 63) τ_1 et τ_2 valent 2 et 6 ; pour Westland (réf. 64), τ_1 et τ_2 valent 2,44 et 5,41 après un examen détaillé des essais Boeing-Vertol (réf. 16 et 17) pour lesquels ces valeurs moyennes seraient valables dans plus de 120 configurations. De ce résultat, quelque peu surprenant, est venue une méthode simple de calculs des forces aérodynamiques instationnaires dans le cas de décrochage dynamique. Les 4 phases principales du calcul sont illustrées par la figure 37.

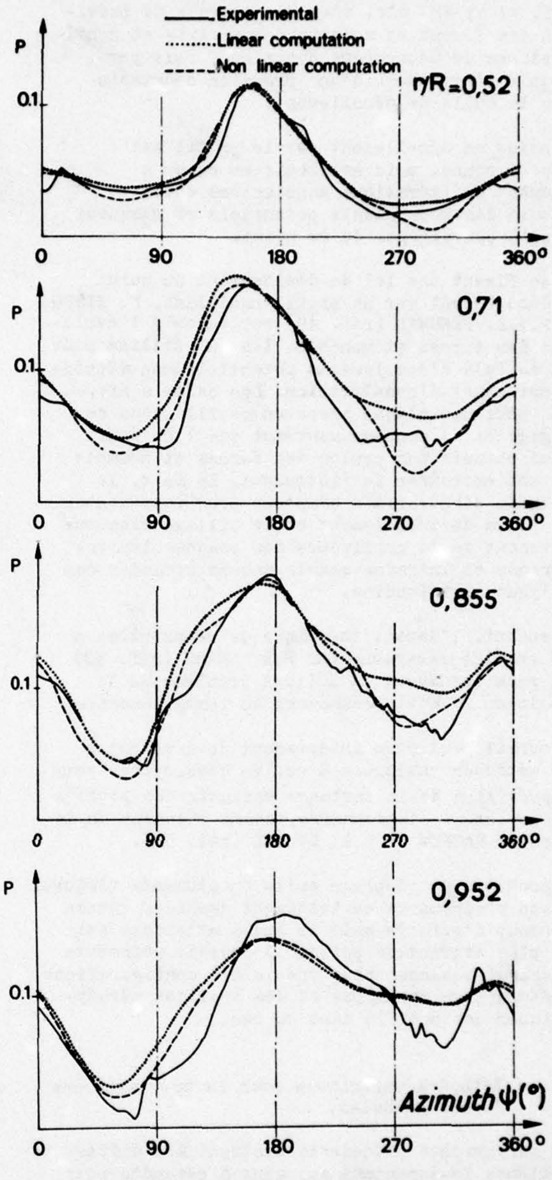

Fig. 36 – Evolution des charges locales sur un rotor tripale fortement chargé.

1) Tant que le profil n'atteint pas l'incidence correspondante au décrochage instationnaire en moment, le calcul s'effectue en écoulement potentiel sans décollement.

2) Pour des temps intermédiaires entre le décrochage en moment et le décrochage en portance, on continue de calculer les portances pour des écoulements non décollés mais le moment est calculé en s'imposant une loi linéaire en fonction du temps du recul du foyer aérodynamique jusqu'à une position équivalente à celle obtenue en écoulement stationnaire totalement décollé.

3) Lorsque le décrochage instationnaire en portance intervient, on impose une loi de diminution exponentielle de cette portance en fonction du temps vers des valeurs correspondantes à une polaire quasi-stationnaire d'écoulement décollé sur un profil

4) Enfin lorsque l'incidence redevient égale ou inférieure à l'incidence de décrochage stationnaire, on retourne vers les polaires stationnaires par un processus de recollement qui s'exprime aussi mathématiquement.

Avec cette méthode, on arrive aussi à assez bien reproduire les cycles expérimentaux de portance et de moment de tangage sur profils en configuration de décrochage dynamique comme le montre la figure 38 extraite des travaux de T.S. Beddoes (réf. 64). Cependant comme dans le cas des méthodes précédentes, l'accord n'est pas toujours très bon.

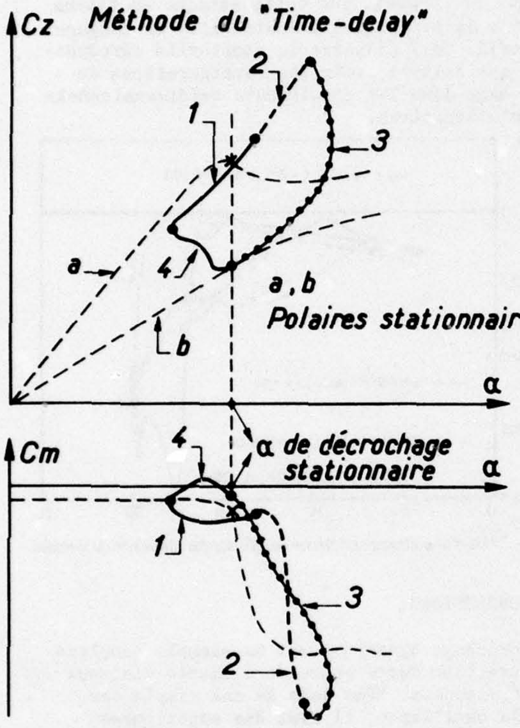

Fig. 37 – Principales phases du calcul effectué dans la méthode du « Time-delay ».

Méthode Lockheed.

L.E. Ericsson et J.P. Reding basent leurs analyses des résultats et leurs méthodes de prévision sur une décomposition mi-théorique, mi-empirique du retard au décrochage.

Les formules mathématiques associées sont développées dans la référence 65. Leur application au cas des essais effectués à Ames par l'USAAMRDL donnent parfois de bons résultats comme le montre la figure 39 tirée de la référence 66. La phase d'apparition du décrochage en moment est bien prévue. La phase du décrochage en portance et celle d'apparition du moment piqueur maximal sont liées à une vitesse de propagation du tourbillon égale à 0,55 U_∞ et à son passage soit à 70 % de la corde soit au bord de fuite du profil.

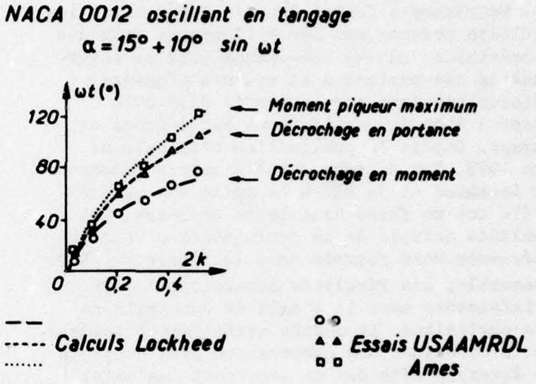

Fig. 39 – Prévisions d'évènements liés au décrochage dynamique des profils oscillants. NACA 0012 oscillant en tangage - α = 15° + 10° sin ωt.

Les méthodes développées par L.E. Ericsson et J.P. Reding ont fait l'objet de nombreux documents (réf. 67 à 70) portant notamment sur le décrochage instationnaire, le flottement ou les effets dynamiques liés au décollement derrière les ondes de choc. Lors de ce meeting, ces auteurs présentent une communication (réf. 71) qui pose le problème d'échelle de similitude des résultats acquis en soufflerie qu'il faut transposer à l'échelle grandeur des appareils dans le cadre des essais dynamiques où le nombre de Reynolds joue un rôle très important.

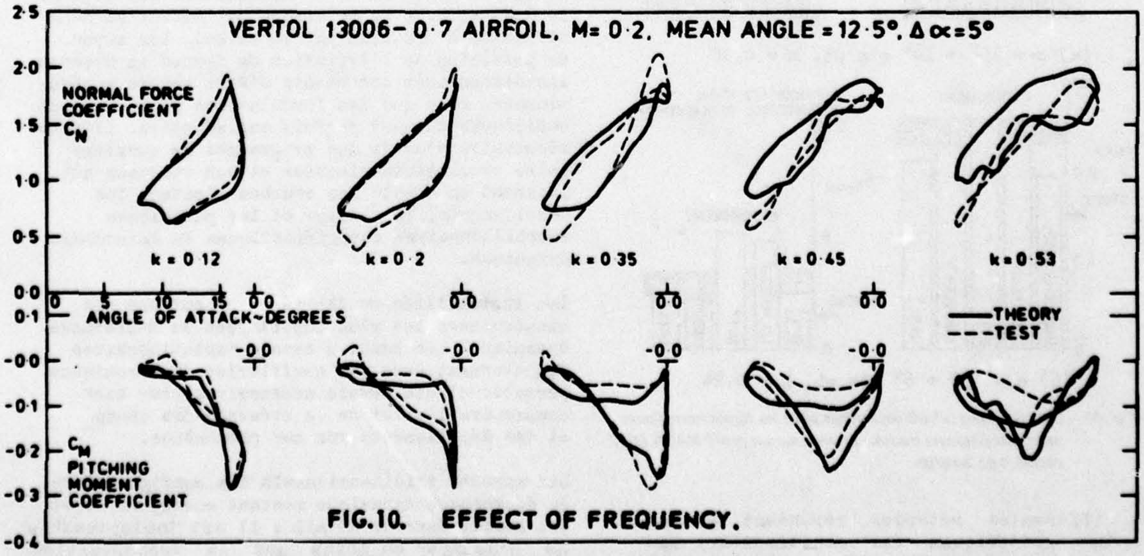

Fig. 38 – Effet de la fréquence réduite des oscillations harmoniques de tangage sur le profil Vertol 13006 (M = 0,2 ; α_0 = 12,5° ; α_1 = 5°).

Méthode MIT

Elle est basée sur les connaissances acquises au MIT par le Pr. HAM et son équipe, sur le plan expérimental et théorique (réf. 72 et 73). W. Johnsson (réf. 74 et 75) a montré que la portance maximale et le moment de tangage maximal sont liés linéairement au paramètre de vitesse angulaire $c\dot{\alpha}/2U_{\infty}$ mais qu'il y a des valeurs limites à leurs accroissements. L'angle de décrochage instationnaire est estimé par des formules semi-empiriques établies par W. Johnsson et N.D. Ham, réf. 76. A titre d'exemple, la référence 75 fournit les résultats obtenus par cette méthode et celles développées chez Boeing-Vertol et l'UARL dans la détermination des charges locales sur un rotor d'hélicoptère.

W.J. McCroskey a fourni dans la référence 1 les résultats obtenus par les différentes méthodes de prévision citées ci-dessus pour la détermination des portances et moments piqueurs maximaux atteints sur le profil NACA 0012 essayé à Ames en oscillations harmoniques de tangage. Depuis la publication originale de mars 1975, les calculs ont été repris notamment par Lockheed et le MIT à la suite des progrès qu'ils ont pu faire dans leurs méthodes. Les résultats actuels de la confrontation calculs-expérience sont fournis dans la figure 40. Dans l'ensemble, les résultats apparaissent fort satisfaisants mais il s'agit de comparaisons très partielles. Il serait certainement intéressant d'effectuer une comparaison plus complète des diverses méthodes en regardant également les phases auxquelles se produisent les principaux évènements sur les cycles de portance et surtout sur le cycle des moments.

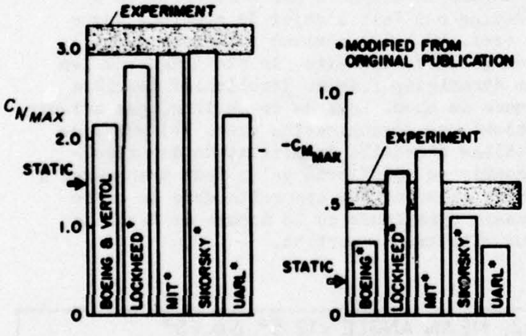

(a) $\alpha = 15° + 14° \sin \omega t$, k = 0.10

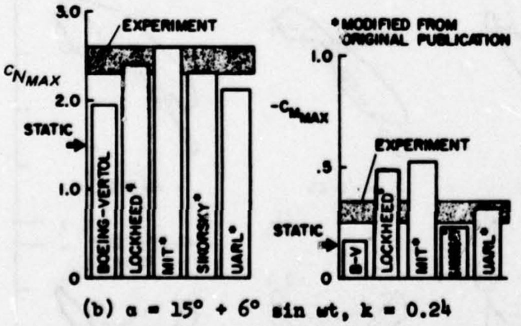

(b) $\alpha = 15° + 6° \sin \omega t$, k = 0.24

Fig. 40 – Comparaisons calculs-expérience pour les forces normales et moments piqueurs maxima atteints sur un profil NACA 0012 oscillant en tangage.

Ces différentes méthodes répondent à des besoins spécifiques des constructeurs et des chercheurs. Les applications concernent essentiellement les rotors d'hélicoptère dont certaines des configurations de vol imposent la présence de décrochage sur la pale reculante. Charges dynamiques, contraintes et déformations induites par le décrochage de la pale sont nettement mieux prévues actuellement par l'utilisation des méthodes précédentes, qu'il y a quelques années. Il n'en reste pas moins des écarts locaux ou instantanés importants qui justifient la poursuite de la recherche de nouvelles méthodes de prévision de plus en plus sophistiquées, ou d'essais instationnaires avec effet tridimensionnel. La figure 41 tirée de la référence 77 montre les résultats d'essais acquis récemment par l'UTRC à Hartford sur profils oscillants attaqués en flèche et les différences significatives obtenues entre une flèche de 30° et une flèche nulle, au niveau des cycles des moments aérodynamiques. Il apparaît que cette attaque en flèche augmente la tendance à l'instabilité en tangage du profil. Cela illustre la complexité aérodynamique que doivent avoir les configurations de décrochage dans les écoulements tridimensionnels et instationnaires.

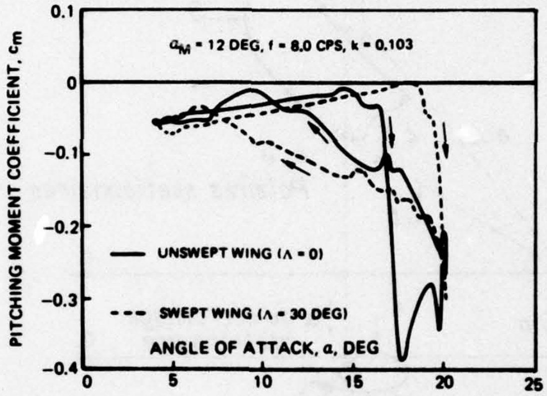

Fig. 41 – Effet d'une attaque en flèche de 30° sur les moments de tangage.

5 - CONCLUSIONS.

Le décrochage dynamique est un exemple complexe d'interaction forte entre écoulements visqueux et non visqueux. Même dans le cas simple des profils oscillants, il faut des expériences regroupant des moyens de mesures et de visualisations très complets pour pouvoir interpréter au mieux les phénomènes complexes liés à de telles configurations. Le processus physique de la formation et de l'alimentation des tourbillons d'extrados reste encore mal défini et donc difficile à traduire par le calcul. Les moyens de prévision de l'évolution de forces et moments instationnaires ont besoin d'être encore perfectionnés. Bien que des formulations plus ou moins empiriques donnent parfois satisfaction, il sera nécessaire d'avoir des programmes de couplage entre écoulements visqueux et non visqueux qui prennent en compte les couches limites, les décollements, le sillage et les phénomènes tourbillonnaires caractéristiques du décrochage dynamique.

Les instabilités ou flottements sont une des conséquences les plus importantes du décrochage dynamique. Les bancs d'essais instationnaires fonctionnant dans des souffleries transsoniques permettront des essais nécessaires pour bien comprendre l'effet de la présence des chocs et des décollements sur ces phénomènes.

Les aspects tridimensionnels des configurations de décrochage dynamique restent encore un sujet peu abordé dans le détail ; il est indispensable de s'assurer au moins que la transposition des résultats acquis en écoulement bidimensionnel est suffisamment précise pour la résolution des problèmes pratiques qui se posent aux constructeurs.

Dans cette communication, seuls certains aspects du décrochage dynamique ont pu être abordés pour des raisons de clarté de la présentation mais il est certain que d'autres intéressants travaux mériteraient d'être cités.

De plus, les communications qui seront faites lors de ce congrès sur l'aérodynamique instationnaire apporteront de nouveaux résultats et de nouveaux éléments de *réflexion* qui *feront* sans aucun doute avancer la compréhension et la prévision des phénomènes liés aux configurations de décrochage dynamique.

REFERENCES

[1] W.J. McCROSKEY
Recent Developments in Dynamic Stall
Symposium on Unsteady Aerodynamics
Tucson, March 1975 (published in "Unsteady Aerodynamics" Vol. 1 - Kinney R.B. University of Arizona, July 1975).

[2] W.J. McCROSKEY
Some Current Research in Unsteady Fluid Dynamics
The 1976 Freeman Scholar Lecture.
Journal of Fluids Engineering, Vol. 99, March 1977.

[3] H. WERLE - M. GALLON
Ecoulement plan autour d'un modèle animé d'un mouvement périodique
Note Technique ONERA n° 239 (1974)

[4] J. OLSEN - H.T. LIU
The construction and operation of a water tunnel in application to flow visualization studies of an oscillating airfoil.
Flow Res. Rep. n° 13 - NASA CR 114696 (May 1973)

[5] K.W. McALISTER - L.W. CARR
Water tunnel research
NASA Report to be published in Summer 77.

[6] J.M. MARTIN, R.W. EMPEY, W.J. McCROSKEY F.X. CARADONNA
An Experimental Analysis of Dynamic Stall on an Oscillating Airfoil
J. of AHS - Vol. 19 - N° 1 - January 1974

[7] W.J. McCROSKEY - L.W. CARR, K.W McALISTER
Dynamic Stall Experiments on Oscillating Airfoils
AIAA Journal, Vol. 14, N° 1, January 1976

[8] W.J. McCROSKEY - E.J. DURBIN
Flow Angle and Shear Stress Measurements, Using Heated Films and Wires.
ASME Transactions : Journal of Basic Engineering - Vol. 94 n° 1 - March 1972

[9] W.J. McCROSKEY - J.J. PHILIPPE
Unsteady Viscous Flow on Oscillating Airfoils
AIAA Journal, Vol. 13 n° 1, January 1975 (also AIAA Paper 74-182)

[10] L.W. CARR - K.W. Mc ALISTER - W.J. McCROSKEY
Analysis of the Development of Dynamic Stall Based on Oscillating Airfoil Experiments.
NASA TND - 8382 - January 1977

[11] K.W. McALISTER, L.W. CARR, W.J. McCROSKEY
Dynamic Stall Experiments on the NACA 0012 Airfoil
NASA TN, to be published in 1977

[12] F.O. CARTA
Chordwise Propagation of Dynamic Stall Cells on an Oscillating Airfoil
AIAA Paper n° 75-25, January 1975

[13] A.G. PARKER
Force and Pressure Measurements on an Airfoil Oscillating Through Stall
Final Report Part II - NASA CR 145877 - August 1975

[14] R.I. WINDSOR
Measurements of Aerodynamic Forces on an Oscillating Airfoil
US Army AVLABS TR 69-98 March 1970

[15] Th. THEODORSEN
General Theory of Aerodynamic Instability and the Mecanisms of Flutter.
NASA TR 496 - 1940

[16] J. LIIVA - F.J. DAVENPORT - L. GRAY I.C. WALTON
Two-Dimensional Tests of Airfoils Oscillating Near Stall
US Army AVLABS TR 68-13, 1968

[17] L. GRAY - J. LIIVA - F.J. DAVENPORT
Wind-Tunnel Tests of Thin Airfoils Oscillating Near Stall
US Army AVLABS TR 68-89, 1969

[18] J. LIIVA
Unsteady aerodynamic and stall effects on helicopter rotor blade airfoil sections
6th Aerospace Sciences meeting - AIAA
New-York - January 1968

[19] J. LIIVA - F.J. DAVENPORT
Dynamic Stall of Airfoil Sections for High-Speed Rotors
24th Annual National Forum - AHS - Washington - May 1968

[20] J.J. PHILIPPE
Le Décrochage Instationnaire d'un Profil
Aéronautique et Astronautique n° 27, 1971-3.

[21] E. SZECHENYI
Experimental studies of dynamic forces on fixed and vibrating two dimensional airfoils
3rd European Rotorcraft and Powered Lift Aircraft Forum
Aix en Provence - Septembre 1977. A paraitre dans la Rech. Aérosp.

[22] A.W. MOORE - N.C. LAMBOURNE - L. WOODGATE
Comparison between dynamic stability boundaries for NPL 9615 and NACA 0012 aerofoils pitching about the quarter-chord.
ARC - CP 1279 - 1974

[23] J. RENAUD - F. NIBELLE
Effects of the Airfoil Choice on Rotor Aerodynamic Behaviour in Forward Flight
Second European Rotorcraft and Powered Lift Aircraft Forum. Bückeburg - Allemagne Fédérale - Septembre 1976

[24] J. VALENSI, J. REBONT, J. RENAUD, G. VINGUT
Effets aérodynamiques sur un profil d'aile animé d'un mouvement harmonique parallèle à l'écoulement
AGARD CP n° 111 "Aerodynamics of Rotary wings" 1973.

[25] C. MARESCA, J. REBONT, J. VALENSI
Separation and reattachment of the boundary layer on a symmetrical aerofoil oscillating at fixed incidence in a steady flow.
Symposium on "Unsteady Aerodynamics" - University of Tucson - Arizona - March 1975

[26] C. MARESCA - J. REBONT - J. VALENSI
Caractéristiques aérodynamiques d'un profil d'aile en mouvement instationnaire.
14th International Congress of Theoritical and Applied Mechanics - Delft - Septembre 1976

[27] J. REBONT, C. MARESCA, D. FAVIER, J. VALENSI
Dynamic reattachment on an aerofoil performing oscillations parallel to the undisturbed stream
FDP AGARD meeting on "Unsteady Aerodynamics"
Ottawa - September 77

[28] W.J. McCROSKEY
Inviscid flow field of an oscillating airfoil
AIAA Journal - Vol. 11 n° 8 (August 1973)

[29] J.P. GIESING
Non linear two-dimensional unsteady potential flow with lift
Journal of Aircraft - Vol. 5 n° 2 - March-April 1968

[30] F.O. CARTA
Effect of unsteady pressure gradient reduction on dynamic stall delay
Journal of Aircraft - Vol. 8 - N° 10 - October 1971

[31] N.D. HAM
Aerodynamic loading on a two-dimensional airfoil during dynamic stall
AIAA Journal Vol: 6 - N° 10 - October 1968

[32] J.J. PHILIPPE -M. SAGNER
Calculs et mesures des forces aérodynamiques sur un profil oscillant
AGARD CP n° 111 "Aerodynamics of Rotary wings" 1973.

[33] N. BAUDU - M. SAGNER - J. SOUQUET
Modélisation du décrochage dynamique d'un profil oscillant
AAAF - 10ème Colloque d'Aérodynamique Appliquée, Lille, Novembre 1973

[34] T. SARPKAYA
An analytical study of separated flow about circular cylinders
Trans. ASME, J. Basic Engineering 90-511 1968

[35] R.M. SCRUGGS - J.F. NASH - R.E. SINGLETON
Analysis of dynamic stall using unsteady boundary layer theory
NASA CR 2462 - October 1974

[36] IUTAM Symposium 1971 "Recent research on unsteady boundary layers"
Editeur : E.A. Eichelbrenner - Les Presses de l'Université de Laval - Québec - 1972

[37] R.B. KINNEY - W.R. SEARS
Unsteady Aeordynamics - Vol. 1 et 2
Editeur : Université d'Arizona - Tucson - 1975

[38] W.R. SEARS - D.P. TELIONIS
Boundary layer separation in unsteady flow
SIAM Journal on Applied Mathematics
Vol. 28 n° 1, January 1975

[39] V.C. PATEL - J.F. NASH
Unsteady turbulent boundary layers with flow reversal
Symposium on unsteady Aerodynamics - Tucson 1975 (réf.37) ; also NASA CR 2546,May 1975

[40] J. COUSTEIX - R. HOUDEVILLE - A. DESOPPER
Experimental results and calculating methods concerning transitional and turbulent boundary layers in unsteady flows
FDP AGARD meeting on Unsteady Aerodynamics - Ottawa - September 1977

[41] U.B. MEHTA - Z. LAVAN
Starting Vortex, Separation Bubbles and Stall : A Numerical Study of Laminar Unsteady Flow around an Airfoil -
Journal of Fluid Mechanics , Vol. 67, Part 2, January 1975

[42] U.B. MEHTA
Dynamic Stall of an Oscillating Airfoil
FDP AGARD meeting on Unsteady Aerodynamics
Ottawa - September 1977

[43] J.C. WU - N.L. SANKAR - S. SAMPATH
A Numerical Study of Unsteady Viscous Flows Around Airfoils
FDP AGARD meeting on Unsteady Aerodynamics
Ottawa - September 1977

[44] R.B. KINNEY
Two-Dimensional Viscous Flow Past on Airfoil in an Unsteady Airstream
FDP AGARD meeting on Unsteady Aerodynamics
Ottawa - September 1977

[45] J.S. SHAMROTH - J.P. KRESKOVSKY
A Weak Interaction Study of the Viscous Flow about Oscillating Airfoils
NASA CR 132 425, May 1974

[46] J.D. LANG
On predicting leading egde bubble bursting on an airfoil in unsteady incompressible flow
Cranfield Memo 109 - April 1976

[47] P. CRIMI
Dynamic Stall
AGARD - AG - 172 - November 1973

[48] P. CRIMI
Investigation of non linear inviscid and viscous flow effects in the analysis of dynamic stall
NASA CR - 2335 - February 1974

[49] P.V.K. PERUMAL - F. SISTO
Lift and Moment Prediction for an Oscillatory Airfoil with a Moving Separation Point.
Trans. ASME, Series A, Vol. 96, N° 4, October 1974 - on Journal of Engineering for Power - Paper n° 74-GT-28

[50] W.R. SEARS
Unsteady Motion of Airfoils with Boundary Layer Separation.
AIAA Journal - Vol. 14, N° 2 - February 76

[51] B. MASKEW, F.A. DVORAK
Investigation of Separation Models for the Prediction of Cl Max.
33rd Annual National Forum of the AHS - Washington - May 1977

[52] P.J. ARCIDIACONNO, F.D. CARTA, L.D. CASELLINI, H.L. ELMAN
Investigation of helicopter control loads induced by stall flutter.
USA AVLABLS TR 70-2 - March 1970

[53] F.O. CARTA, G.L. COMMERFORD, R.G. CARLSON, R.H. BLACKWELL
Investigation of airfoil dynamic stall and its influence a helicopter control loads.
USA AMRDL TR 72-51, September 1972

[54] F.O. CARTA
Unsteady normal force on an airfoil in a periodically stalled inlet flow
J. of Aircraft - Vol. 4 n° 5, 1967

[55] F.O. CARTA, L.M. CASELLINI, P.J. ARCIDIACONNO H.L. ELMAN
Analytical study of helicopter rotor blade flutter
26th Annual National Forum AHS - June 1970

[56] F.O. CARTA, G.L. COMMERFORD, R.G. CARLSON
Determination of Airfoil and Rotor Blade Dynamic Stall Response
J. of the AHS - Vol 18 - N° 2 - April 73

[57] R.L. BIELAWA
Synthesized Unsteady Airfoil Data with Applications to Stall Flutter Calculations
31st Annual National Forum of the AHS, May 1975

[58] D. GROSS, F.D. HARRIS
Prediction of inflight stalled airloads from oscillating airfoil data
25th Annual National Forum - AHS - May 1969

[59] F.D. HARRIS - F.J. TARZANIN - R. FISHER
Rotor high speed performance - Theory versus Test.
J.of the AHS - Vol. 15 - N° 3 - July 1970

[60] F.D. TARZANIN
Prediction of control loads due to blade stall
J. of the AHS - Vol. 17 - N° 2 - April 1972

[61] R.E. GORMONT
A Mathematical Model of Unsteady Aerodynamics and Radial Flow for Application to Helicopter Rotors
USAAMRDL TR 72-67 - May 1973

[62] J.J. COSTES
Rotor Response Prediction with non linear Aerodynamics Loads on the Retreating Blade
Second European Rotorcraft and Powered Lift Aircraft Forum - Bückeburg - 20-22 September 1976, also : Recherche Aérospatiale N° 1975-3

[63] R.G. CARLSON - R.H. BLACKWELL - G.L. COMMERFORD - P.H. MIRICK
Dynamic stall modeling and correlation with experimental data on airfoils and rotors
AHS/NASA Ames - Spécialists' Meeting on Rotorcraft Dynamics - February 1974

[64] T.S. BEDDOES
A synthesis of unsteady aerodynamics effects including stall hysteresis
1st European Rotorcraft and Powered Lift Aircraft Forum - University of Southampton England, September 1975

[65] L.E. ERICSSON - J.P. REDING
Dynamic stall analysis in light of recent ~~numerical and experimental results.~~
J. of Aircraft - Vol. 13 n° 4 - April 1976
(AIAA Paper 75-26 - January 1975).

[66] L.E. ERICSSON - J.P. REDING
Quasi-steady and transient dynamic stall characteristics
AGARD FDP Symposium on "Prediction of Aerodynamics Loading" - Ames - Sept. 1976

[67] L.E. ERICSSON - J.P. REDING
Unsteady airfoil stall, review and extension
J. of Aircraft - Vol. 8 N° 8 - August 1971

[68] L.E. ERICSSON - J.P. REDING
Dynamic stall of helicopter blades
J. of the AHS - Vol. 17 N° 1 - January 72

[69] L.E. ERICSSON - J.P. REDING
Stall flutter analysis
J. of Aircraft. vol. 10 N° 1 January 1973.

[70] L.E. ERICSSON
Dynamics effects of shock-induced flow separation
J. of Aircraft - February 1975

[71] L.E. ERICSSON - J.P. REDING
Scaling problems in dynamic tests of aircraft like configurations
AGARD FDP Symposium on "Unsteady Aerodynamics" Ottawa - September 1977

[72] N.D. HAM
Aerodynamic loading on a two-dimensional airfoil during dynamic stall
AIAA Journal - Vol. 6 n° 10 - October 1968

[73] N.D. HAM - M.S. GARELICK
Dynamic stall considerations in helicopter rotors
J. of the AHS - Vol. 13 N° 2 - April 1968

[74] W.JOHNSON
The effect of dynamic stall on the response and airloading of helicopter rotor blades
J. of AHS - Vol. 14 n° 2, april 1969

[75] W. JOHNSON
Comparison fof three methods for calculating of helicopter rotor blade loading and stresses due to stall
NASA TN D-7833 - November 1974

[76] W. JOHNSON - N.D. HAM
On the mechanism of dynamic stall
J. of AHS, Vol. 17 - n° 4 - October 1974

[77] A.J. LANDGREBE, R.C. MOFFIT, D.R. CLARK
Aerodynamic Technology for Advanced Rotorcraft
Journal of the American Helicopter Society
Part 1 - Vol. 22 n° 2 - April 1977
Part 2 - Vol. 22 n° 3 - July 1977

FEATURES OF UNSTEADY FLOWS OVER AIRFOILS

by
L.S. Saxena, A.A. Fejer and M.V. Morkovin
Department of Mechanics, Mechanical & Aerospace
Engineering
Illinois Institute of Technology
Chicago
Illinois 60616 - U.S.A.

SUMMARY

This is a study of sinusoidally oscillating flows over stationary NACA 0012 airfoils at angles of attack close to the angle of stall in steady flow (α_{crit}) by means of hot wire surveys of the velocity field, surface pressure measurements and diagnostics with surface film gages and tufts. At the moderate amplitudes of these tests (18% of the mean velocity) stall occurred at $\alpha=\alpha_{crit}$, and the flow was quasi-steady below and above the angle when the frequency was low. At higher frequencies this quasi-steady behavior persisted below α_{crit} but the unsteadiness did alter some of the details of the flow. However, above α_{crit} the flow lost its quasi-steady character completely, with the instantaneous normal force exhibiting large periodic fluctuations and its average exceeding the steady flow values by 60%. Comparison with flows incorporating boundary layer trips revealed Reynolds number independence. Our studies suggest that below α_{crit} oscillating flows can be treated analytically with confidence. But the drastic changes above α_{crit} seem to imply that in wind tunnel studies of the dynamic stall of helicopter rotors one should add fluctuations of the freestream to the usual oscillations of the airfoil.

LIST OF SYMBOLS

α	Angle of attack
k	Reduced frequency = $\pi fc/U_\infty$
c	Chord length
$U_\infty(t)$	Freestream velocity = $\bar{U}_\infty + u_\infty(t)$
$C_p(x,t)$	Pressure coefficient = $p(x,t)/\frac{1}{2}\rho U_\infty^2(t)$
N_a	Amplitude ratio = $\Delta U_\infty/\bar{U}_\infty$

INTRODUCTION

The present study was motivated by the desire to contribute to the understanding of the class of problems involving unsteady flows over lifting surfaces, and in particular the dynamic stall of helicopter rotors. Earlier investigations (1) suggest that the complex three-dimensional flow over the rotors, during the forward flight of the helicopter, can be modeled by a two-dimensional sinusoidally oscillating airstream over an airfoil oscillating in pitch. While many experimentalists have studied the case of a steady flow over an oscillating airfoil (summarised in a recent report by McCoskey (2)), not much attention has been paid to the effects of the oscillating airstream. The primary objective of the present study was, therefore, to investigate experimentally the basic features of unsteady flow fields generated by sinusoidally oscillating airstreams over a stationary airfoil at fixed angles of attack close to the angle of static stall.

In particular, angles just below and just above the angle of static stall were explored, with the reduced frequency expressing the relative magnitude of the velocity of rotation to the velocity of flight serving as the primary flow parameter. Two such frequencies were used. The lower one of these reduced frequencies was of the same order as that at the tip of a rotor blade of a typical helicopter in high speed forward flight, while at the higher frequency, the unsteady effects were expected to be more pronounced. Sensitivity of the flow field to airfoil roughness was studied by means of a boundary layer trip to simulate the higher Reynolds numbers of the rotors.

The investigations were carried out by means of hot wire surveys of the velocity field around the airfoil (NACA 0012 profile) and pressure measurements on the surface of the airfoil. This information was supplemented by data provided by heated surface film gages and flow visualization achieved with the aid of silk tufts. Reduced frequencies of 0.18 and 0.9 were used at the oscillation amplitude ratio of 0.18 and a Reynolds number of 250,000. Periodic sampling and averaging techniques were used to obtain "instantaneous" boundary layer and wake mean velocity profiles and pressure coefficient distributions at different instants of the cycle of oscillations of the freestream.

EXPERIMENTAL SET-UP

The investigations, reported here, were conducted in the Illinois Institute of Technology closed-circuit oscillating flow wind tunnel described by Miller and Fejer (3), where the oscillations in freestream velocity are generated by a set of four rotating blades, mounted on equally spaced horizontal shafts, located at the downstream end of the test section. Signals provided by a magnetic pick-up installed near one of the rotating blades serve as phase reference and also indicate frequency of oscillation. The test section with the airfoil and the associated experimental set up is shown in Figure 1. The freestream velocity and static pressure oscillations in the test section for a typical set of parameters are presented in Figure 2.

A hollow aluminum airfoil with NACA 0012 profile of 12 inch chord and supported at the quarter chord point was used. The airfoil is equipped with a surface pressure acquisition system located near the quarter chord point. It consists of a solenoid actuated remotely controlled 24 port Scanivalve S-9 pressure switch and a Setra-237 capacitance type pressure transducer. There are eighteen pressure taps along the center-line on the upper surface of the airfoil including one at the leading edge, spaced progressively closer near the leading edge where the pressure gradients are larger. The airfoil is also equipped with seven surface hot film gages bounded to the upper surface and three holes for smoke injection.

A tungsten hot wire, operated in the constant temperature mode, was used for velocity measurements around the airfoil and in the wake. The mean velocity of the freestream was monitored by a Statham PM5TC pressure transducer, through a static pressure tap and a total head probe inside the tunnel (see Figure 1), while a Pitran PTM2 pressure transducer, mounted at the tunnel wall, measured the AC part of the unsteady freestream static pressure.

The signals proportional to the velocity and pressure obtained from the hot-wire and the pressure transducer systems were further processed using the scheme shown in Figure 3. In most cases these signals were composed of periodic and random components. Periodic sampling and averaging techniques (eduction) were used to extract the periodic components. For a flow variable f(t), this averaging procedure is defined as

$$f_e(t) = \lim_{p\to\infty} \frac{1}{p} \sum_{n=1}^{p} f(t+nT)$$

were p and n are integers and T is the time period of the freestream oscillations.

The instantaneous velocity and pressure signals were observed on a DC coupled oscilloscope and sometimes recorded photographically by means of a polaroid camera. The educted signals were compared with the instantaneous signal traces shown by the scope, and then recorded by a XY plotter.

The eduction was performed with the help of a Princeton Applied Research "Waveform Eductor" model TDH-9 which was used in DC mode. The timing pulses to trigger the eductor were provided by the magnetic pick-up referred to earlier. The number of cycles used for each eduction was of the order of 100, the actual number depending on the time required by the educted signal to reach a limiting value.

The educted velocity and pressure data were recorded as functions of time at discrete spacewise locations. These were used to compute ensemble averaged "instantaneous" boundary layer and wake velocity profiles and chordwise surface pressure distributions at various phases of the freestream oscillation cycle. Lift coefficients at various instants of the oscillation cycle were determined by evaluating the areas enclosed by the instantaneous pressure coefficient distributions.

Part of the flow field investigations around the airfoil were carried out with the boundary layer tripped at the leading edge. The criteria used for designing and constructing the trip were: (a) the transition to turbulence should occur upstream of the point of laminar separation at all instants of the freestream oscillation cycle, and thereby preclude the formation of a laminar separation bubble throughout the cycle, (b) the characteristics, specifically the thickness, of the two turbulent boundary layers over the airfoil in the tripped and untripped cases, should be as close to each other as possible. A two-dimensional trip, which is normally used in steady boundary layers, introduces a locally separated region just downstream of itself. Since very little is known about the response of locally separated regions to oscillations in the external flow, this trip is undesirable in the case of unsteady boundary layers. Most effective tripping in oscillating boundary layers is achieved by three-dimensional trips. The trip devised for our experiments consisted of beads of glue about 1½ mm in height and 2½ mm in diameter, bonded about 5 mm apart to a strip of masking tape. The trip was taped to the leading edge of the airfoil with the row of beads positioned on the leading edge.

EXPERIMENTAL RESULTS AND DISCUSSION

The steady flow field over the airfoil was first investigated as a base-flow reference. One of the basic features of the steady flow was the existence of a Reynolds number dependent angle of attack, α_{crit}, at which the flow separated abruptly at the leading edge. At angles larger than $6\frac{1}{2}°$ but less than α_{crit}, there was a laminar separation bubble near the leading edge, having a length of about 2% of the chord. The bubble structure was determined by hot-wire and pressure measurements and was found to be consistent with published information. Typical pressure distributions over the airfoil, at angles below the critical angle (revealing the presence of the separation bubble) and in the stalled region above the critical angle, are shown in Figures 4 and 5.

Oscillating flow fields were studied at angles above and below α_{crit}. Eductable flow fields at angles closest to α_{crit}, were chosen for investigation.

The value of α_{crit} is not affected noticeably by the presence of freestream oscillation. The leading edge separation occurs at an angle very near α_{crit} (steady), but is sporadic - i.e., there are several cycles of attached flow followed by several cycles of fully separated flow. This intermittency which occurs within a small band of angles in the vicinity of α_{crit}, is random and not related in phase to the oscillation. This was anticipated based on our understanding of the mechanisms of transition.

At angles less than the critical angle, it was found that the basic structure of the flow field over the airfoil in an oscillating freestream was the same as that in a steady freestream. Laminar separation bubbles with a reattached turbulent boundary layer were observed at both the low and high frequencies. The bubbles were found to be periodically modulated and their behaviour was experimentally documented. Typical pressure distributions over the airfoil are shown in Figures 6 and 7.

At the low frequency, $f = 2.22$ Hz ($k = 0.18$), the behavior was quasi-steady, with the separation point remaining almost fixed. But the transition and consequently the reattachment points oscillated in response to the periodically changing Reynolds number of the flow. Thus there were periodic changes in the bubble size in phase with the freestream oscillations. In contrast to the bubbles in steady flow, the flow in the downstream portion of the unsteady bubble was turbulent. The turbulent fluid appears to have been injected into the bubble at the point of reattachment during the decelerating phase of the freestream oscillations.

At the higher frequency, $f = 9.66$ Hz, ($k = 0.9$), the Reynolds number dependent behavior of the flow was substantially modified, with the increase in wall generated vorticity due to the higher unsteady pressure gradients being a probable major cause. As a result both the separation and the reattachment points were found to be oscillating in response to the unsteady freestream, and the periodic changes in the bubble size were much larger than at the low frequency. Part of the turbulent fluid that appeared to have been injected into the bubble at the point of reattachment during freestream deceleration, was relaminarized during the accelerating part of the cycle.

Although the process of separation-reattachment in the leading edge region was very different in the oscillating flow from that in steady flow, this did not result in any major changes in the overall features of the flow, i.e., the unsteady normal force coefficients were not very different from the steady force coefficients. The departures in the unsteady values were the largest in the case of the higher reduced frequency when the boundary layer was not tripped. This is indicative of the extra sensitivity of the bubble to the unsteady freestream pressure gradients.

Since the magnitude of the unsteady pressure gradients produced by the oscillating freestream is proportional to the product of the reduced frequency and the amplitude ratio it would appear desirable to repeat the experiments with $\alpha<\alpha_{crit}$, using larger amplitude ratios, that can be readily obtained by using rotating shutters of larger width.

The investigations at angles larger than the critical angles, revealed that at the lower frequency $f = 2.22$ Hz ($k = 0.18$), the surface pressure distributions (see Figures 5 and 8) did not differ significantly from the corresponding steady pressure distributions. The departures of the instantaneous normal force coefficients from the steady flow values were of the same order as in the cases of $\alpha<\alpha_{crit}$. The basic flow structure was not very different from the steady separated flow.

At $k = 0.9$, $\alpha>\alpha_{crit}$, the increased unsteady pressure gradients completely altered the structure of the separated flow over the airfoil. This is clear from the pressure distributions shown in Figures 5 and 9. Here the average normal force coefficient was 60% larger than the corresponding steady flow value, and the instantaneous force coefficients showed large periodic variations, ranging from 1.26 to 1.83 times the steady flow value. Surveys made with a single hot-wire indicated that in this flow, vortical disturbances shed from the leading edge region were being convected downstream with an average velocity of $0.7\bar{U}_\infty$ (see Figure 10). Mean velocity profiles indicated a large "flapping" motion of the separated region which was synchronous with the oscillating freestream (see Figures 12). This should be compared with the boundary layer thickness along the chord at an angle smaller than the critical angle (see Figure 11). The structure of the separated flow with large k, needs to be investigated further using two moveable flow sensors.

Some of the phenomena described above are revealed by the samples of educted boundary layer profiles shown in Figures 13 and 14. These profiles were obtained during the high frequency oscillations at a number of phase points of the cycle, with the airfoil set at the sub-critical angle. Figure 13 shows the cyclic changes in the boundary layer near the leading edge at a location which is occupied by the laminar separation bubble during a part of the cycle. Figure 14 shows profiles that were taken farther downstream.

As far as the effects of the leading edge trip are concerned no significant difference was observed between the flows with and without the leading edge trip, except for the presence of the separation bubble in the latter case. The turbulent boundary layers generated by the trip and the separation bubble showed a similar development over the airfoil chord, revealing increasingly large frequency-dependent phase shifts in the velocity relative to the freestream towards the trailing edge. The tripped boundary layer was thinner than the untripped boundary layer near the leading edge but thicker near the trailing edge. Also the tripped boundary layer separated somewhat upstream of the corresponding untripped boundary layer. Since the trip provided uniform transition throughout the oscillating cycle, it may be particularly useful in making comparisions with theoretical computations of unsteady turbulent boundary layers.

SUMMARY AND CONCLUSIONS

At the moderate amplitude ratios (N_a = 0.18-0.19) of our experiments, the following major findings were made:

(a) The angle of stall, α_{crit}, is about the same in steady and oscillating flows.

(b) At a low frequency (f=2.22 Hz, k = 0.18) of freestream oscillation, the flow over the airfoil is quasi-steady at angles both above and below α_{crit}.

(c) At a high frequency (f = 9.66 Hz, k = 0.9) at angles below α_{crit} the global features of the flow (e.g., the force coefficients) are again quasi-steady. However, the details of the flow, specifically the leading edge separation bubble, show more pronounced unsteady effects than in (b).

(d) At a high frequency, and angles above α_{crit}, the flow field around the airfoil is completely different from that in steady flow. There are large periodic fluctuations in the instantaneous normal force coefficients and the average value of the coefficient is 60% larger than in steady flow.

(e) At angles below α_{crit}, tripping of the boundary layer at the leading edge of the airfoil eliminates the separation bubble throughout the oscillation cycle. However, the overall flow field does not differ significantly from the flow in the untripped case. This is suggestive of Reynolds number independence of the oscillating flows.

Below the angle of static stall the minor changes in the boundary layer structure and local separation should make it possible in that region to attack the problem analytically with confidence. A possible approach would be to determine first the inviscid unsteady pressure distributions, and to modify these by means of turbulent boundary layer calculations starting from the point of closure of the bubble with steady flow pressure distributions serving as a guide.

Above the angle of static stall the changes are sufficiently drastic suggesting that proper wind tunnel simulation of the dynamic stall of helicopter rotors may require combining the oscillations of the airfoil with those of the freestream.

REFERENCES

(1) McCroskey, W.J., and Fisher, R.K., Jr., "Detailed Aerodynamic Measurements on a Model Rotor in the Blade Stall Regime," J. American Helicopter Society, Vol. 17, No. 1, 1972.

(2) McCroskey, W.J., "Recent Developments in Dynamic Stall", Symposium on University Aerodynamics, Tucson, March 1975.

(3) Miller, J.A., and Fejer, A.A., "Transition Phenomena in Oscillating Boundary Layer Flows", J. Fluid Mechanics, Vol. 18, 1964.

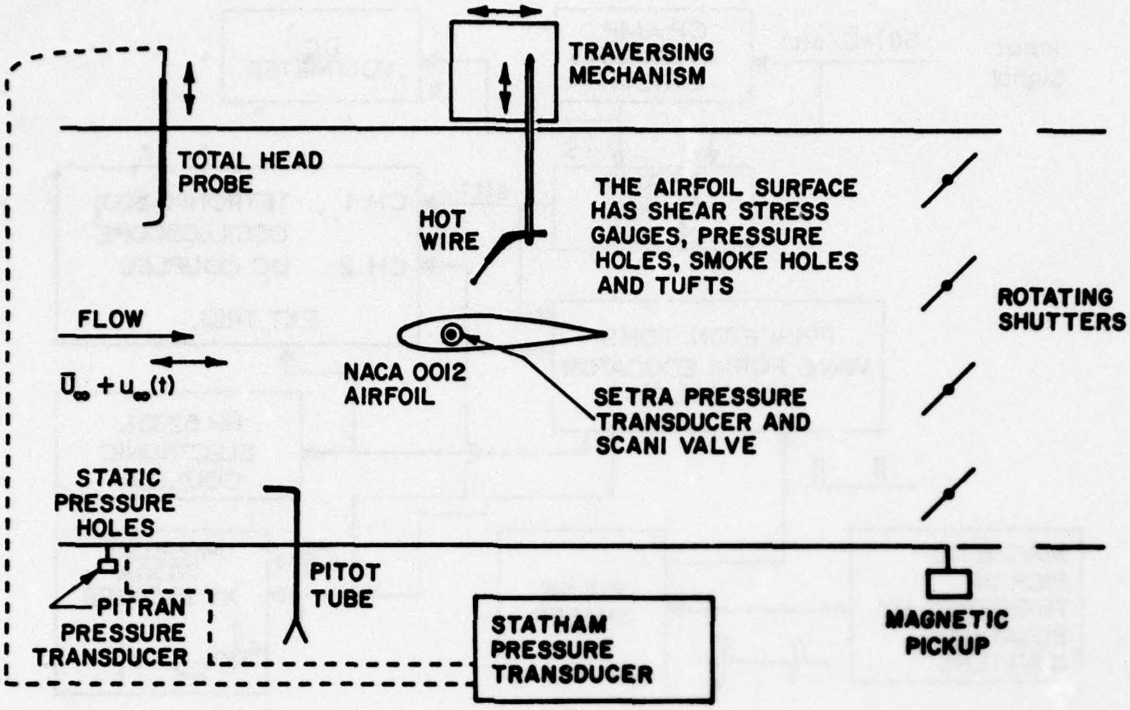

Figure 1. Test Section Experimental Set-up

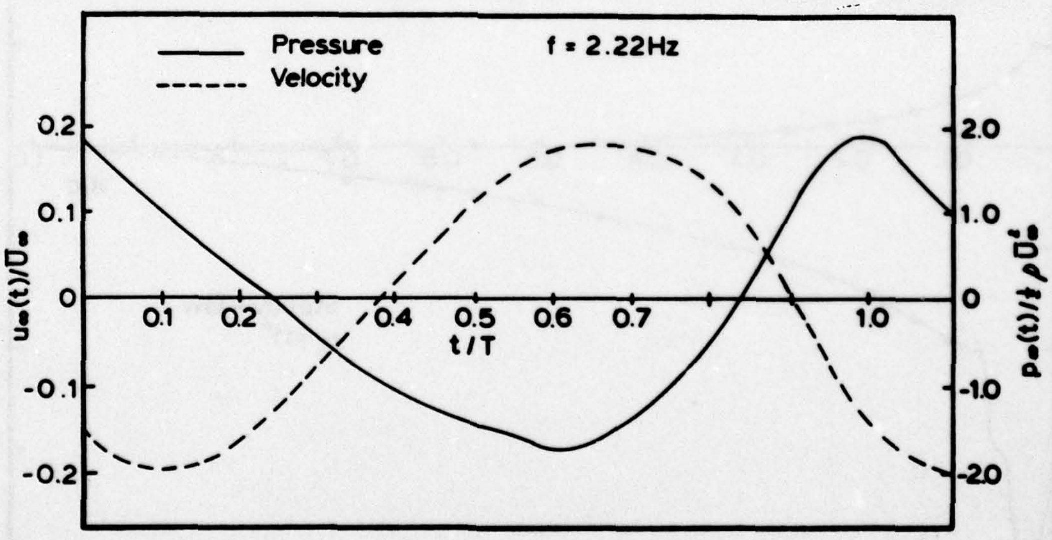

Figure 2. Freestream Velocity and Static Pressure Oscillations in Test Section, f = 2.22 Hz

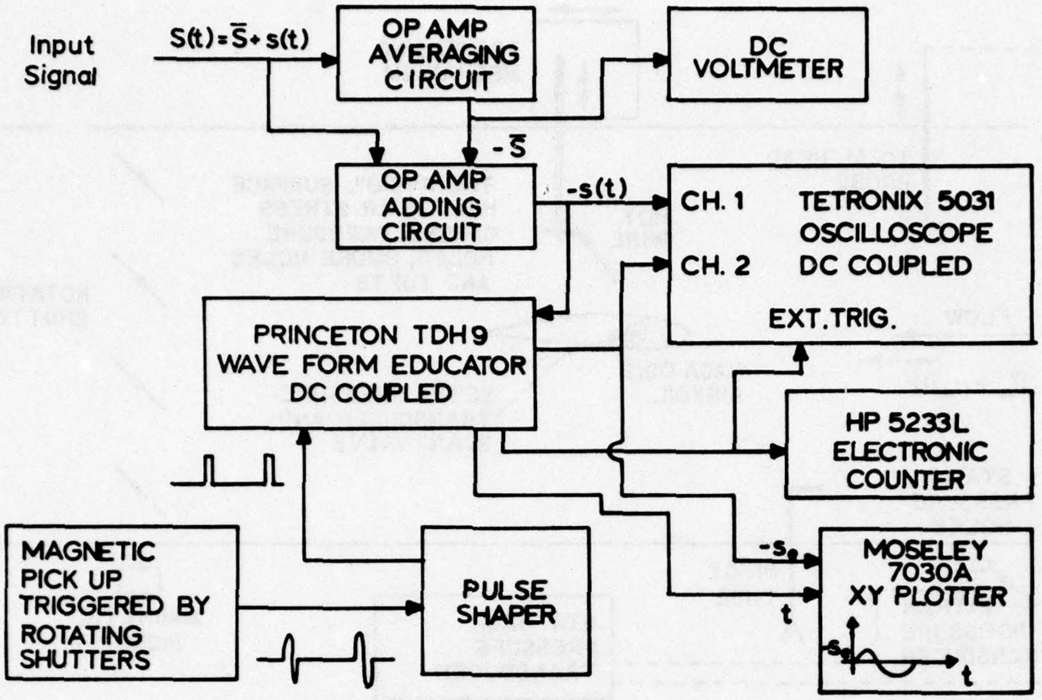

Figure 3. Instrumentation Schematic for Signal Processing

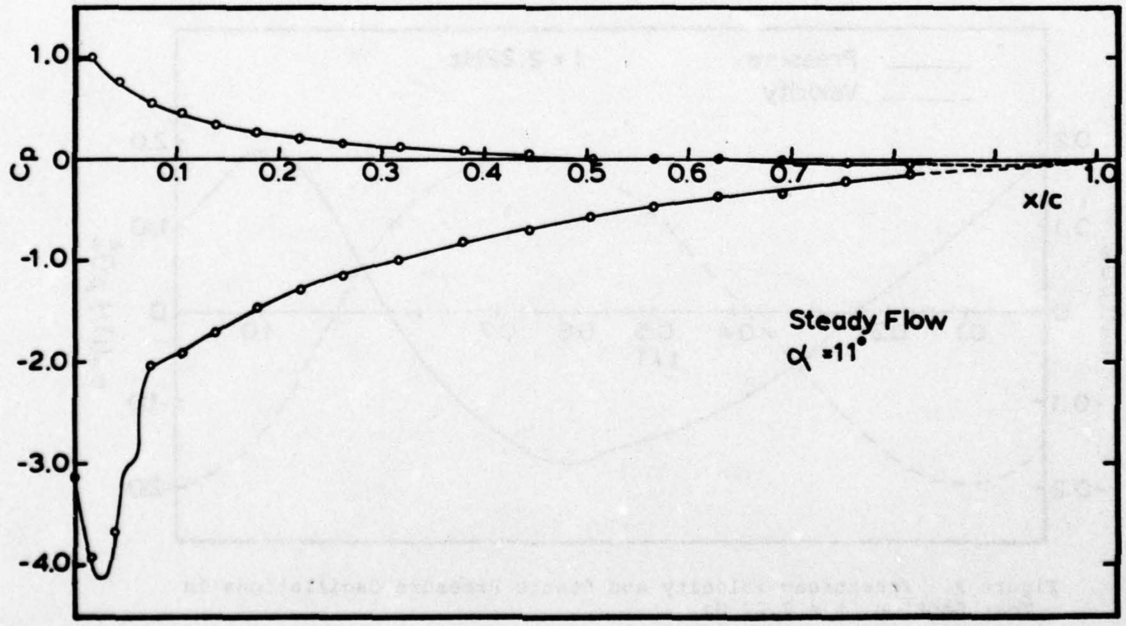

Figure 4. Chordwise Distribution of Pressure Coefficients, $\alpha = 11°$

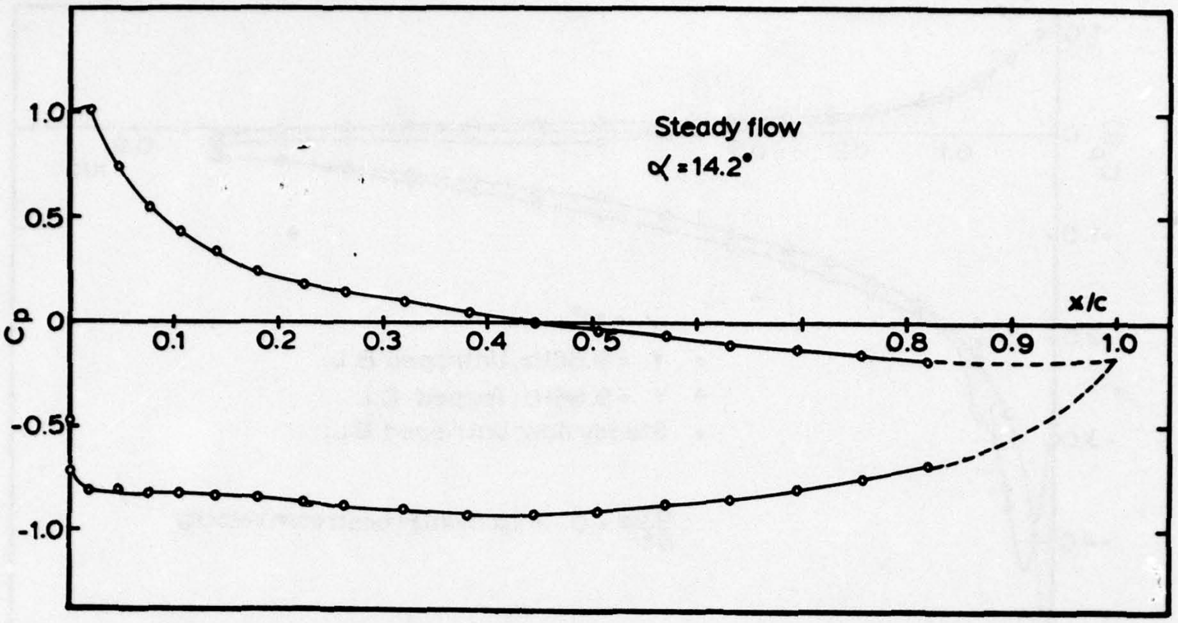

Figure 5. Chordwise Distribution of Pressure Coefficients, α = 14.2°

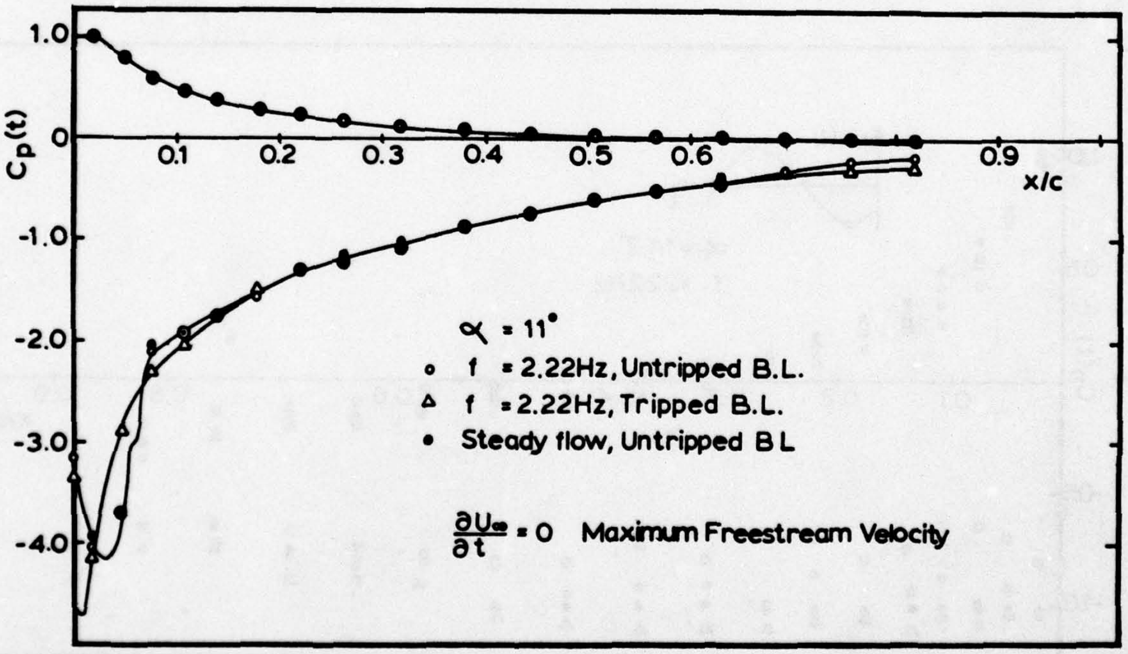

Figure 6. Chordwise Distribution of Instantaneous Pressure Coefficients

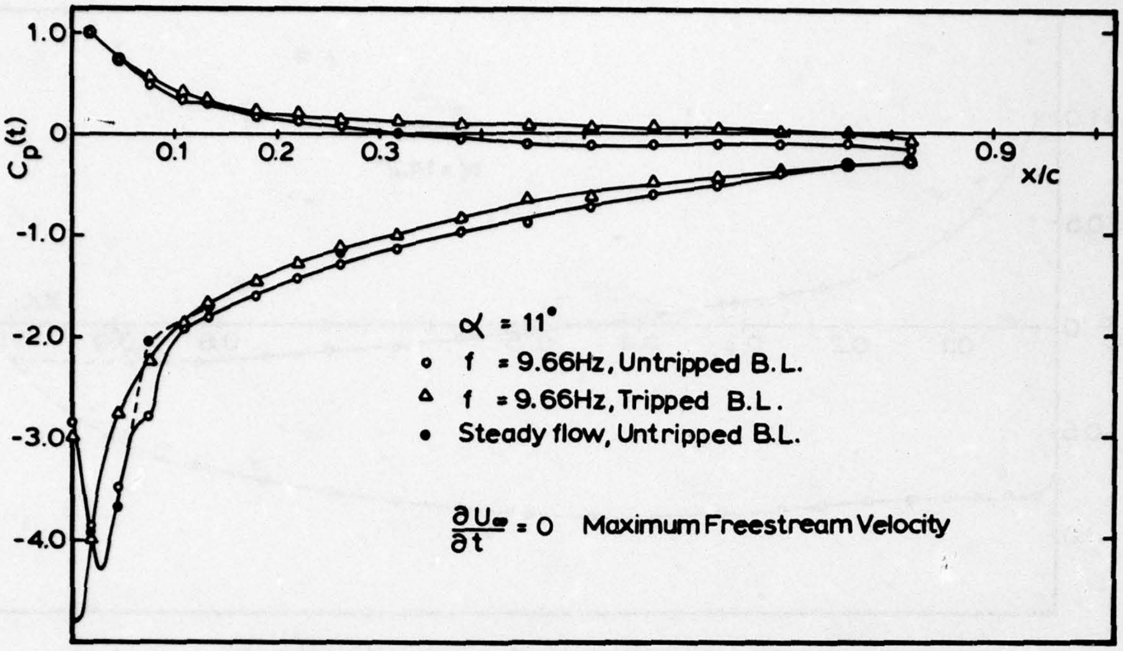

Figure 7. Chordwise Distribution of Instantaneous Pressure Coefficients

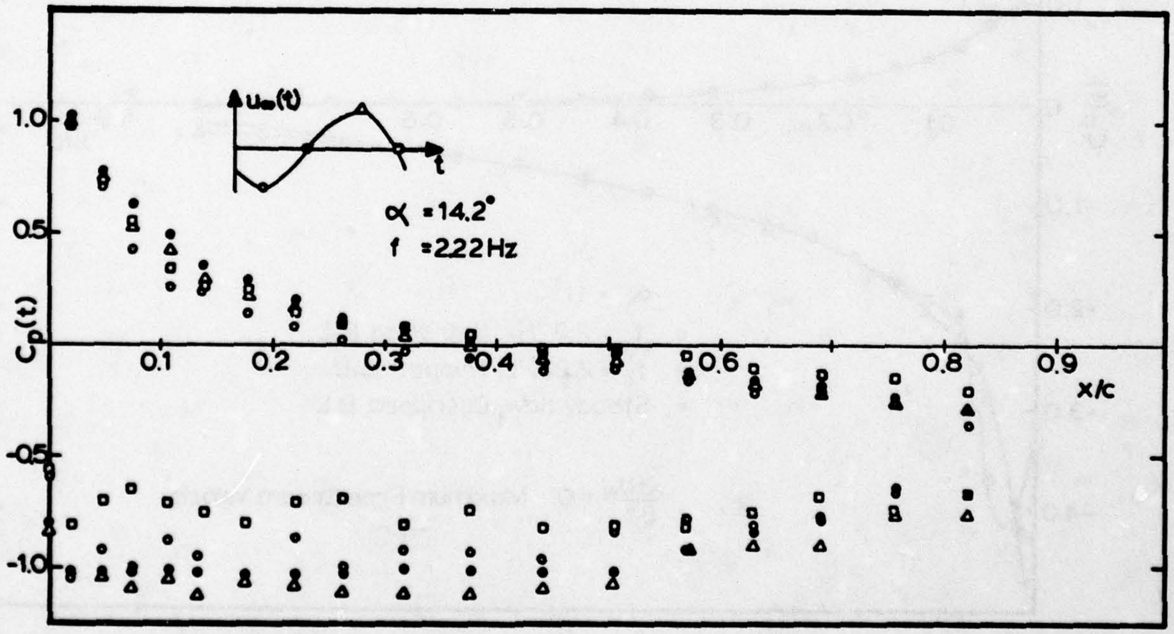

Figure 8. Chordwise Distribution of Instantaneous Pressure Coefficients

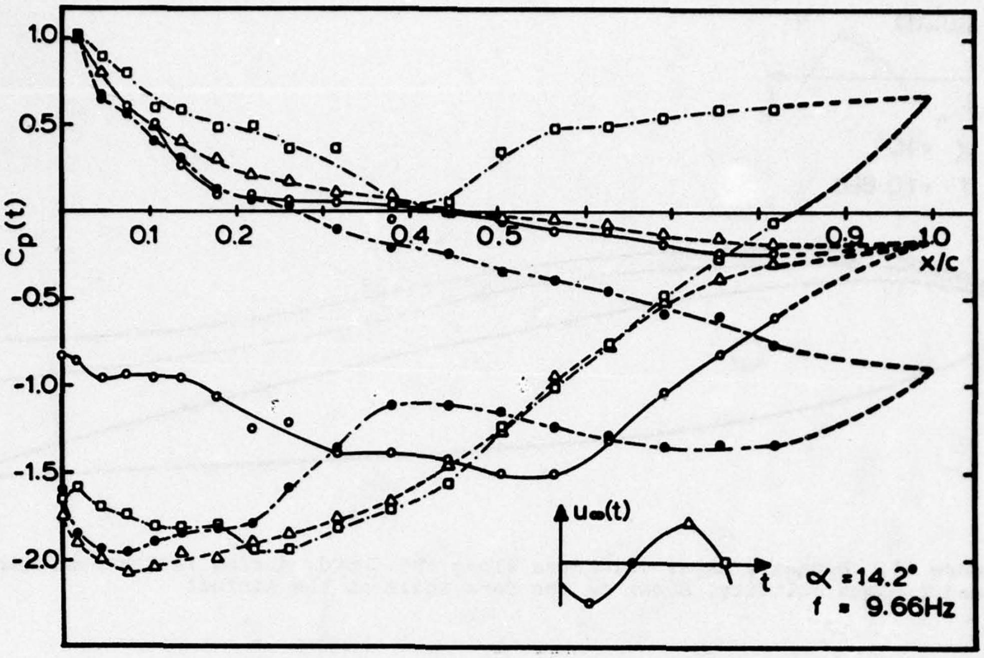

Figure 9. Chordwise Distribution of Instantaneous Pressure Coefficients

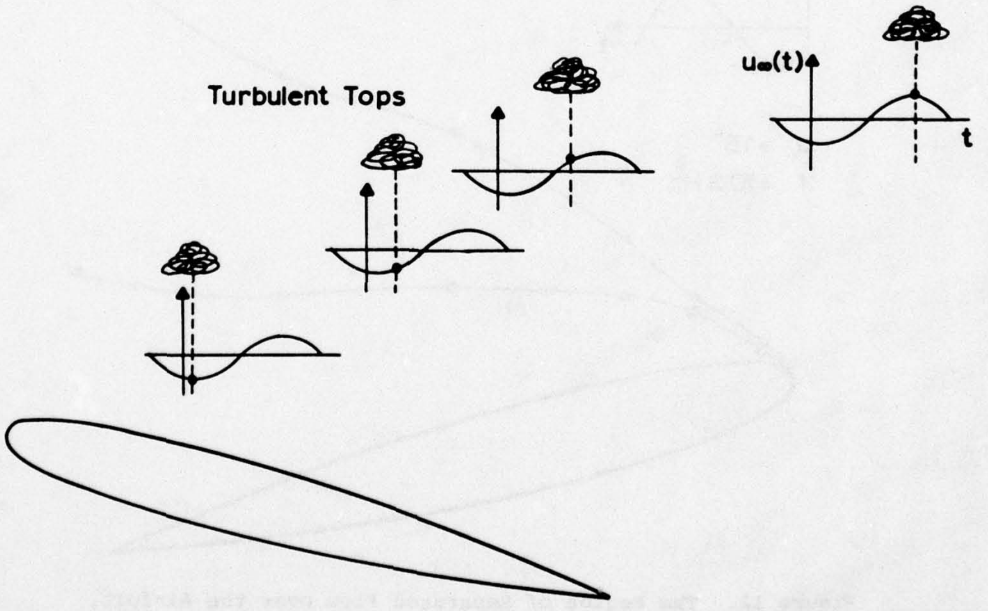

Figure 10. Downstream Convection of Vortical Disturbances Shed from the Leading Edge, α = 14.2°, f = 9.66 Hz (Chord Length 12 inches). The Height of the Turbulent Tops avove the Airfoil is Shown on the Same Scale as the Airfoil

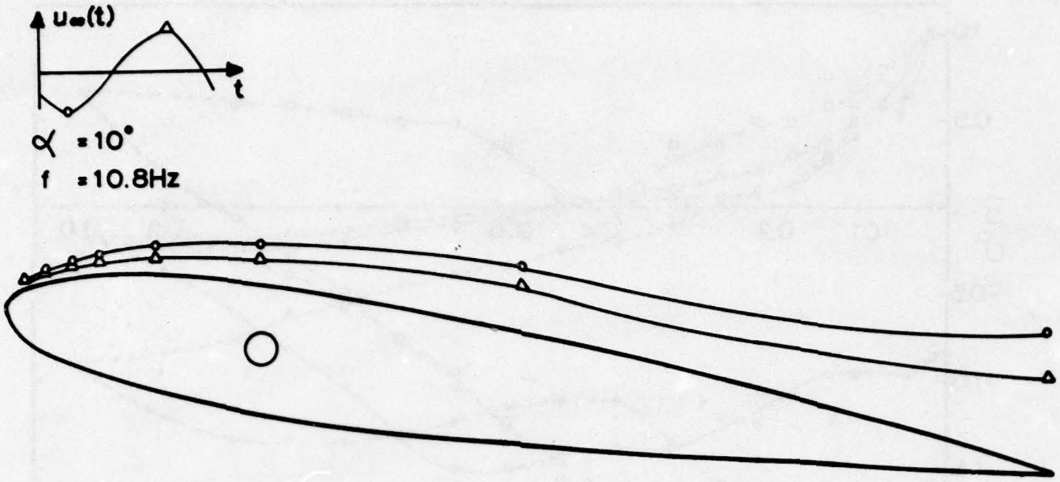

Figure 11. Boundary Layer Thickness along the Chord, during Instants of Maximum and Minimum Velocity, Shown on the Same Scale as the Airfoil

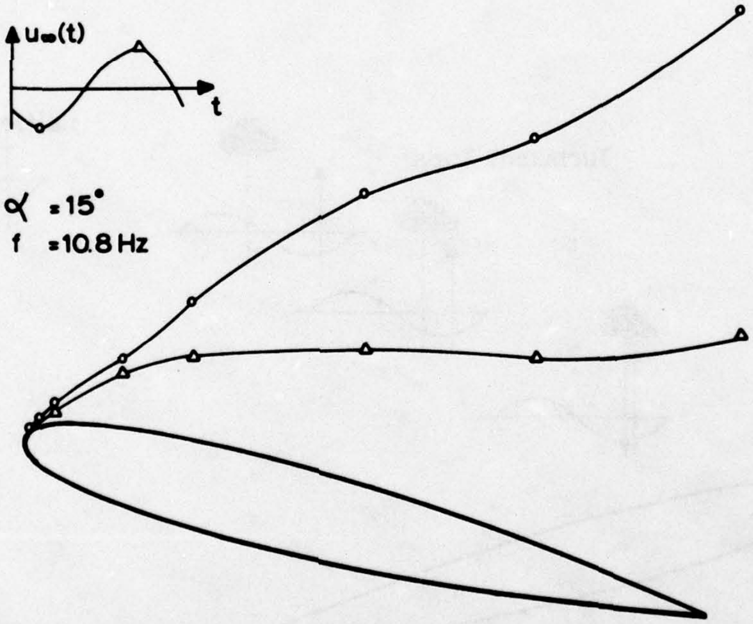

Figure 12. The Region of Separated Flow over the Airfoil, Shown on the Same Scale as the Airfoil, at Instants of Maximum Freestream Velocity (Chord Length = 8 inches)

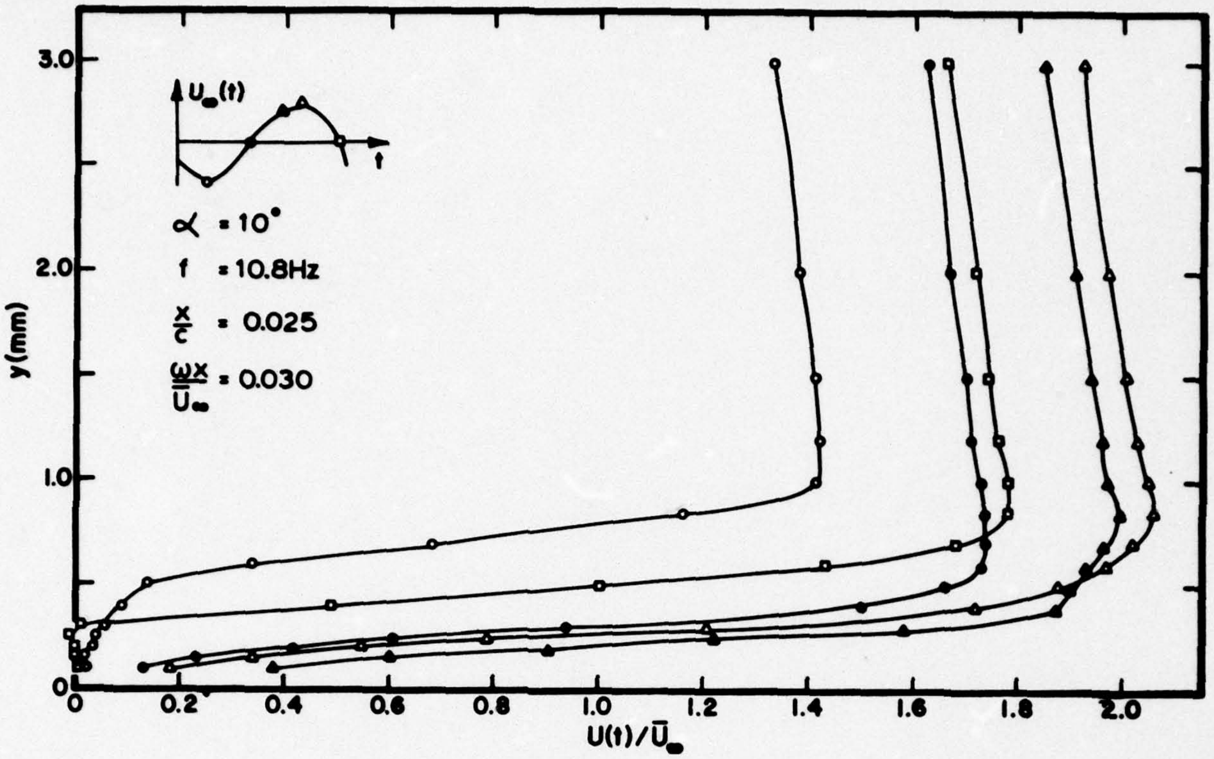

Figure 13. Instantaneous Boundary Layer Mean Velocity Profiles (Chord Length = 8 inches)

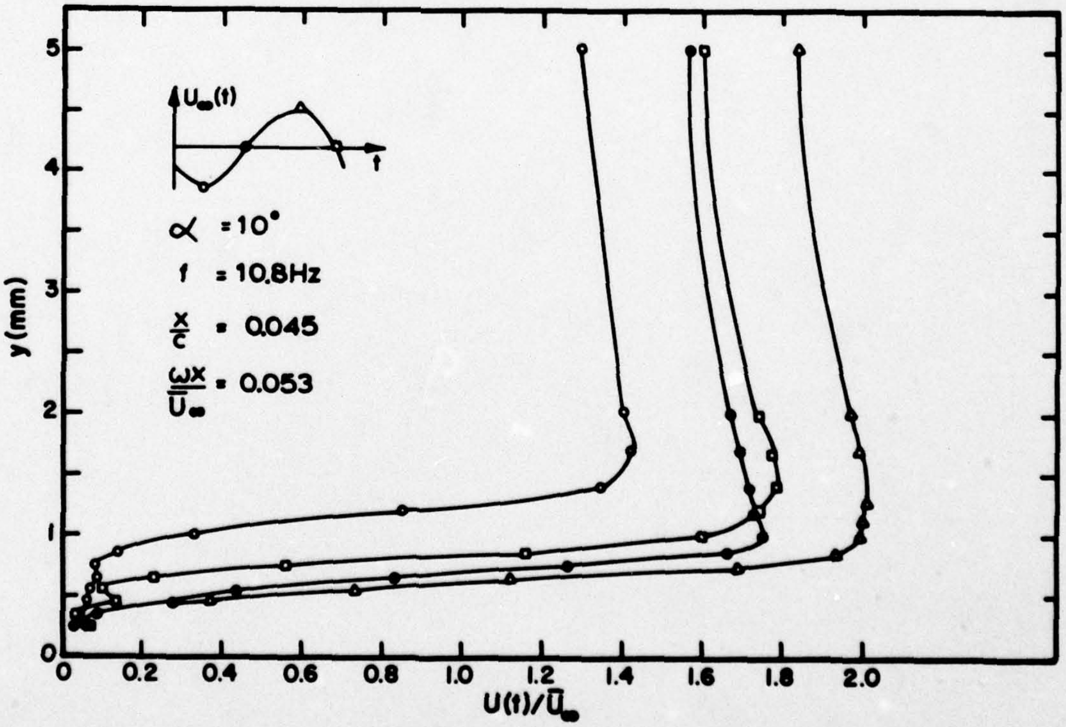

Figure 14. Instantaneous Boundary Layer Mean Velocity Profiles (Chord Length = 8 inches)

DYNAMIC STALL OF AN OSCILLATING AIRFOIL

Unmeel B. Mehta*

Ames Research Center, NASA, Moffett Field, California 94035, U.S.A.

SUMMARY

Unsteady, separated boundary layers and wakes are studied by investigating flow past an oscillating airfoil which, in part, models the retreating-blade stall on the helicopters. The Navier-Stokes equations in terms of the vorticity and stream function for laminar flow are solved to determine the flow field around a modified NACA 0012 airfoil. The computations are done for two cases: (1) $R = 5{,}000$ and $k = 0.5$, and (2) $R = 10{,}000$ and $k = 0.25$, where the Reynolds number R is based on airfoil chord, and the reduced frequency of oscillation k is based on half chord.

After a fully developed flow is determined at zero incidence, the airfoil is oscillated in pitch through an angle-of-attack range from 0° to 20°. The computed streamlines, during this pitch-up motion, are in qualitative agreement with the trajectories of air bubbles observed in ONERA water tunnel experiments conducted with a NACA 0012 airfoil under the same conditions. However, during the pitch-down motion of the airfoil, the computed flow patterns cannot be compared with the experiments because the trajectories of air bubbles intersect. An analysis of these patterns is done to gain insight into the fundamental mechanisms of dynamic stall on oscillating airfoils.

1. INTRODUCTION

Engineers are increasingly confronted with problems which require a thorough understanding, prediction, and control of unsteady fluid dynamic effects (Ref. 1). The most complex of these effects are the ones which involve flow separation. Buffet of the wing, tail, or control surfaces of an aircraft during a rapid pull-up maneuver, stall flutter of marine propellers, rotating stall of compressors, and retreating-blade stall of helicopter blades are a few examples. The common features of these problems, unsteady separated boundary layers and wakes, are studied in this paper by investigating flow past a pitching airfoil (Fig. 1), which partially models the retreating-blade stall on helicopter blades. The primary objective is to gain some physical insight into dynamic stall on pitching airfoils. The secondary objective is to develop a numerical technique which satisfactorily solves moderate Reynolds number, external flow problems. The motivations behind these objectives are discussed below, starting with a brief description of the dynamic stall problem. (Further details concerning this problem may be found in a review paper that M. Phillipe is presenting at this symposium.)

When a helicopter is in forward flight, the local approaching airflow relative to the individual blade varies periodically with large amplitude fluctuations in magnitude, chordwise incidence, and yaw angle. This produces unsteady three-dimensional transonic effects on the advancing blade and stall on the retreating blade. The spanwise component of velocity $U \cos \Omega t$ (Fig. 2), and the centrifugal effects due to blade rotation appear to play a minor role during the initial stages of the stall development, which occur for $180° < \phi < 270°$, where $\phi = \Omega t$ (Refs. 2 and 3). Therefore, the retreating-blade stall problem can be treated as the dynamic stall on a two-dimensional airfoil oscillating sinusoidally in pitch in an airstream of varying velocity.

Generally, experimenters study either the case of an oscillating airfoil in a steady flow or that of oscillating airflow past a stationary airfoil. In oscillating airfoil studies, frequently the flow includes, before dynamic stall, laminar separation on the upper surface near the leading edge, transition to turbulence in the separated shear layer, and reattachment of this shear layer forming a separation bubble. Subsequently, the turbulent boundary layer separates near the trailing edge. Recently, McCroskey et al. (Ref. 4) reported that this attached turbulent boundary appears to break down, causing the airfoil to stall in three different ways: (1) the classical trailing-edge stall resulting from the gradual upstream extension of the separated region; (2) the abrupt turbulent separation on the forward portion of the airfoil, following an initial progression of flow separation from the trailing-edge; and (3) the leading-edge bubble bursting mechanism. Previously, Ham (Ref. 5) and Ham and Garelick (Ref. 6) had provided a conceptual description of how dynamic stall proceeds. A vortexlike disturbance grows near the leading edge, breaks out of the boundary layer, and passes over the upper surface of the airfoil. This description applies to case (3) above and possibly to cases (1) and (2).

The passage of the vortexlike disturbance over the upper surface of the airfoil distorts the chordwise pressure distribution which produces transient forces and moments that are significantly different from those observed during static stall. Prediction of these unsteady loads and the unsteady separated boundary layer is impossible with traditional potential-flow theory, boundary-layer theory, and thin-layer approximations. In addition, the empirical modeling procedures in current use are unsatisfactory for predicting loads in engineering applications. These procedures await a better theoretical understanding of dynamic stall (Ref. 7). The inherent limitations of the above approaches and the engineering procedures can, in principle, be overcome by the use of the Navier-Stokes equations. In addition, the main advantage of the solution of these equations is that all of the details of the flow field are available, which is never true in experiments.

The solutions of the Navier-Stokes equations still require modeling of transition and unsteady turbulence. Although substantial advances have been made over the past decade in the prediction of simple turbulent flows, regions involving moderate or large, separated, turbulent flows cannot, at present, be quantitatively predicted satisfactorily. In the case of small separated regions, it is not always possible to predict both the skin friction or the surface pressure distribution simultaneously. In addition,

---

*Contractor. Affiliated with Stanford University, Stanford, California.

much work needs to be done in predicting transition and unsteady-in-the-mean turbulent flows, particularly when the characteristic time scales for transition and turbulence are different.

As discussed above, the main features of dynamic stall are unsteadiness, flow separation, transition, and turbulence. We consider here only the first two. The theoretical approach described by Mehta and Lavan (Ref. 8) for stationary airfoils is extended to treat oscillating airfoils. The governing equations in terms of the vorticity and stream function for laminar, unsteady, incompressible flow of a Newtonian fluid are solved numerically around an oscillating modified NACA 0012 airfoil. In Ref. 8, these equations were solved using a successive over-relaxation procedure with an implicit finite differencing of the vorticity equation. In the present study, the vorticity equation is solved with an implicit factored algorithm; and the stream-function equation is solved using a direct-solution procedure.

A few comments concerning computation of viscous, external flow problems are in order. Currently, there is a Reynolds number restriction on laminar flow simulations. To different investigators, the actual value of this Reynolds number limit is different. This restriction primarily arises because all scales of fluid motions are not resolved during the computation of the flow field. Usually, high frequencies or short-wave lengths in the Fourier sense are not properly represented. These unresolved scales have a tendency to grow and contaminate or distort some of the scales that are resolved, thus making the computations meaningless at times. This situation becomes worse as the kinematic viscosity is decreased. On the other hand, in turbulent flows, the effective eddy viscosity is generally two or three (or more) orders of magnitude larger than the kinematic viscosity. This greatly helps the turbulent, "Navier-Stokes" computations. For the present study, in order to compute laminar flows satisfactorily at moderate Reynolds number, $R \sim O(10^4)$, by resolving higher frequencies than those resolved by second-order schemes, a higher order numerical technique was developed.

The rest of the paper is outlined as follows: Section 2 presents governing equations in rotating or body coordinate system with initial and boundary conditions. The numerical procedure is presented in Section 3 to solve these equations. In Section 4, we give the actual problem definition, parameters that are considered, some preliminary remarks and results. Section 5 discusses results for $R = 5{,}000$ and $k = 0.5$ and $R = 10{,}000$ and $k = 0.25$, where the reduced frequency k expresses the ratio of angular velocity of oscillation to the velocity of flight. The final section presents concluding remarks.

2. THEORETICAL FORMULATION

The field exterior to a Joukowski airfoil or a cylinder is mapped into a unit circle using the transformation

$$ze^{i\alpha} = \frac{1}{\kappa} + \gamma + \frac{\kappa c^2}{1 + \gamma\kappa} - \sigma \tag{1}$$

where $z = x + iy$, $\kappa = re^{i\theta}$, $\gamma = \xi + i\eta$, α is the angle of attack, and σ is a real constant. The value of σ fixes the origin of the coordinate system along the chord about which the airfoil may be oscillated. The shape of the trailing edge of the airfoil is controlled by

$$c = [\xi + (1 - \eta^2)^{1/2}](1 - \delta) \tag{2}$$

where $0 < \delta << 1$.

In place of Eq. (1), the conformal transformation procedure of Theodorsen and Garrick (Ref. 9) could be used to transform any two-dimensional body into a circle, as recently demonstrated by Ives (Ref. 10). The theoretical formulation and numerical procedures given below are still applicable as long as the Jacobian of transformation is nonzero everywhere. On the other hand, the procedure of Thompson et al. (Ref. 11) introduces cross derivative terms whenever there is a Laplacian operator in the governing equations of the physical plane z. Consequently, these authors have used time-consuming, successive, over-relaxation procedure to solve the governing equations in the transformed plane. Steger (Ref. 12) has invoked thin-layer assumptions and neglected these cross derivative terms. In the present moderate Reynolds number study, these terms are significant near the trailing and leading edges, the front stagnation point, and in the vicinity of separation and reattachment points for flow fields that contain large separated regions and when the airfoil is at large incidence.

The Navier-Stokes equations for an incompressible fluid in an inertial or fixed coordinate system is

$$\left(\frac{D\vec{q}_I}{Dt}\right)_I = -\vec{\nabla}p + \frac{L}{R}\nabla^2\vec{q}_I \tag{3}$$

where subscript I refers to inertial coordinate system. The Reynolds number is $R = u\ell/\nu$ where ℓ and ν are, respectively, the chord length and kinematic viscosity. Variables $\vec{q}$, p, and L are dimensionless velocity, pressure, and chord length, respectively. The free-stream velocity U and the radius of the circle a to which the airfoil is transformed are the characteristic scales. (The radius of the circle is taken as a characteristic length for the convenience of computing in the interior of a unit circle.) The characteristic time T is chosen such that $UT/a = 1$.

If the coordinate system representing z in Eq. (1), as shown in Fig. 3 is fixed with respect to the airfoil which is rotating with angular velocity $\vec{\Omega}$, relative to the inertial system, the velocity $\vec{q}$ relative to the rotating coordinate system of a point located by the vector $\vec{r}$ is given by

$$\vec{q}_I = \vec{q} + \vec{\Omega}\times\vec{r} \tag{4}$$

The angular velocity is defined positive in counter-clockwise direction. Equation (3) in the rotating system is

$$\frac{\partial \vec{q}}{\partial t} + \frac{1}{2}\vec{\nabla}(\vec{q}\cdot\vec{q}) - \vec{q}x(\vec{\nabla}x\vec{q}) + \frac{d\vec{\Omega}}{dt}x\vec{r} + 2\vec{\Omega}x\vec{q} + \vec{\Omega}x(\vec{\Omega}x\vec{r}) = -\vec{\nabla}p + \frac{L}{R}\nabla^2\vec{q} \tag{5}$$

This equation in κ-plane in terms of the vorticity ω is

$$H^2r^2\,\frac{R}{L}\,\frac{\partial\omega}{\partial t} = r^2\,\frac{\partial^2\omega}{\partial r^2} + r\,\frac{\partial\omega}{\partial r} + \frac{\partial^2\omega}{\partial\theta^2} - r\,\frac{R}{L}\,J\left(\frac{\omega,\Psi}{r,\theta}\right) - 2\,\frac{d\Omega}{dt}\,H^2r^2\,\frac{R}{L} \tag{6}$$

with the stream function Ψ defined by

$$r^2\,\frac{\partial^2\Psi}{\partial r^2} + r\,\frac{\partial\Psi}{\partial r} + \frac{\partial^2\Psi}{\partial\theta^2} = -H^2r^2\omega \tag{7}$$

where

$$H^2 = \left(\frac{\partial x}{\partial r}\,\frac{\partial y}{\partial\theta} - \frac{\partial x}{\partial\theta}\,\frac{\partial y}{\partial r}\right)\Big/ r$$

Equations (6) and (7), respectively, describe the kinetic and kinematic aspects of the flow field. Furthermore, they are valid both on the boundary and in the interior of the computational domain as is Eq. (5).

The problem of grid resolution in the radial coordinate is addressed by transforming the variable r as

$$\rho = (k_1 + k_2)^{-1}[\tanh^{-1}(rk_3 - k_4) + k_2] \tag{8}$$

with

$$k_3 = (\tanh k_1 + \tanh k_2)[1 - r_o/(r_o - 1)]$$

and

$$k_4 = \tanh k_2 - r_o(\tanh k_1 + \tanh k_2)/(r_o - 1)$$

The constants r_o, k_1, and k_2 (all positive) determine the value of ρ. As r varies from r_o to 1, ρ varies from 0 to 1. The stretching function (8) is introduced to obtain a better distribution of grid points in the physical plane. Constant increments in ρ give more condensed grid spacing next to the surface, and less expanded spacing away from it than that given by constant increments in r. Equations (6) and (7) are rewritten for computational convenience using Eq. (8) as

$$H^2r^2\,\frac{R}{L}\,\frac{\partial\omega_I}{\partial t} = \left(r\,\frac{d\rho}{dr}\right)^2\frac{\partial^2\omega_I}{\partial\rho^2} + \left(r\,\frac{d\rho}{dr} + r\,\frac{d^2\rho}{dr^2}\right)\frac{\partial\omega_I}{\partial\rho} + \frac{\partial^2\omega_I}{\partial\theta^2} - r\,\frac{d\rho}{dr}\,\frac{R}{L}\,J\left(\frac{\omega_I,\Psi}{\rho,\theta}\right) \tag{9}$$

and

$$\left(r\,\frac{d\rho}{dr}\right)^2\frac{\partial^2\psi}{\partial\rho^2} + \left(r\,\frac{d\rho}{dr} + r^2\,\frac{d^2\rho}{dr^2}\right)\frac{\partial\psi}{\partial\rho} + \frac{\partial^2\psi}{\partial\theta^2} = -H^2r^2\omega_I \tag{10}$$

where

$$\omega_I = \omega + 2\Omega \tag{11}$$

and

$$\Psi = \psi + y + \frac{\Omega}{2}(x^2 + y^2) \tag{12}$$

Both Eqs. (9) and (10) are subjected to periodicity in θ direction. On the surface ($\rho = 1$), the constraint of no slip is applied in the form

$$\Psi = 0 \quad \text{or} \quad \psi = -y - \frac{\Omega}{2}(x^2 + y^2) \tag{13}$$

and

$$\frac{\partial\Psi}{\partial\rho} = 0 \quad \text{or} \quad \frac{\partial\psi}{\partial\rho} = -\frac{dr}{d\rho}\left[\frac{\partial y}{\partial r} + \frac{\Omega}{2}\,\frac{\partial(x^2 + y^2)}{\partial r}\right] \tag{14}$$

The kinematic condition of vanishing velocity component normal to the surface is given by the condition (13), and the dynamic condition of zero tangential velocity component is specified by Eq. (14). These together give the surface vorticity from kinematic Eq. (7) as

$$\omega = -\frac{1}{H^2}\left(\frac{d\rho}{dr}\right)^2\frac{\partial^2\Psi}{\partial\rho^2} \tag{15}$$

Drs. Kinney and Wu, who are separately presenting at this symposium their method of calculating external flow fields, determine the surface vorticity differently. Their approach and the present one (Eq. 15), both give the value of vorticity on the surface that would enforce the no-slip condition. Wu (Ref. 13) primarily objects to the manner in which expressions like Eq. (15) are implemented in a numerical procedure. He does not object to the kinematic relations (7) and (15). The question of how Eq. (15) is implemented in the present study is taken up in the next section.

The flow at the far boundary is governed with first-order differential relations obtained from the Navier-Stokes equations by dropping the tangential derivative of the pressure and viscous terms, i.e., the inertia terms are dominant:

$$H^2 r \frac{\partial \omega_I}{\partial t} = -\frac{d\rho}{dr} J\left(\frac{\omega_I, \Psi}{\rho, \theta}\right) \tag{16}$$

and

$$\frac{\partial \psi}{\partial \rho} = -\frac{dr}{d\rho}\left[u_2 H + \frac{\partial y}{\partial r} + \frac{\Omega}{2}\frac{\partial(x^2+y^2)}{\partial r}\right] \tag{17}$$

in which u_2 is obtained from the θ-component of the Navier-Stokes equation:

$$\frac{\partial u_2}{\partial t} = -\left[\frac{1}{2rH}\frac{\partial(u_1{}^2 + u_2{}^2)}{\partial \theta} + u_1\omega_I + \frac{d\Omega}{dt}\frac{1}{2H}\frac{\partial(x^2+y^2)}{\partial r} - \frac{\Omega^2}{2rH}\frac{\partial(x^2+y^2)}{\partial \theta}\right] \tag{18}$$

The velocity components in terms of the disturbance stream function ψ are defined as

$$u_1 = \frac{1}{rH}\left[\frac{\partial \psi}{\partial \theta} + \frac{\partial y}{\partial \theta} + \frac{\Omega}{2}\frac{\partial(x^2+y^2)}{\partial \theta}\right] \tag{19}$$

and

$$u_2 = -\frac{1}{H}\left[\frac{d\rho}{dr}\frac{\partial \psi}{\partial \rho} + \frac{\partial y}{\partial r} + \frac{\Omega}{2}\frac{\partial(x^2+y^2)}{\partial r}\right] \tag{20}$$

The main difficulty in specifying the downstream boundary conditions across a wake is that the boundary values are part of the solution and hence not known a priori. The above boundary conditions are based on physical insight into the nature of the flow at the boundary, and therefore, they are more appropriate than to specify either potential flow or uniform velocity since "eddies" or vortices can pass through the downstream boundary at the local velocity. In addition, since the velocity at the boundary is not specified, it can change with time as the vorticity field changes in the flow field. In Eq. (18), the absence of the tangential pressure derivative, will not significantly affect the motion of a vortex through the downstream boundary (where also the grid resolution usually is not satisfactory). In addition, the overall flow field near the surface would not be affected because the downstream boundary is several chord lengths away from the trailing edge. These boundary conditions have been used satisfactorily by Mehta and Lavan (Ref. 8) for a stalled stationary airfoil. Lugt and Haussling (Ref. 14) and Lugt and Ohring (Ref. 15) have used successfully a similar set at the downstream half of the boundary. The primary difference is that they have used the free-stream velocity as a convection velocity instead of the local velocity. On the other hand, in the integro-differential formulation (Ref. 16), the domain of computation must be increased as time advances, because vorticity cannot be allowed to escape the downstream boundary.

Equation (18) is solved all along the outer boundary when solutions of flow past a stationary airfoil are determined. However, the oscillating airfoil results are obtained with Eq. (18) applied only along the downstream half of the boundary, and the free-stream velocity prescribed along the upstream half of the boundary. This change for oscillating airfoil was necessary when a fourth-order scheme was used for Eq. (18) because $2\Delta\theta$ oscillations (where $\Delta\theta$ is a grid increment) near the upstream stagnation streamline were difficult to control even with added numerical dissipation. The prescription of free-stream velocity results into following boundary conditions from $\theta = \pi/2$ to $3(\pi/2)$:

$$\omega_I = 0 \tag{21}$$

and

$$\frac{\partial \psi}{\partial \rho} = \frac{dr}{d\rho}\left[-(\sin\alpha - x\Omega)\frac{\partial x}{\partial r} + (\cos\alpha + y\Omega)\frac{\partial y}{\partial r} - \frac{\partial y}{\partial r} - \frac{\Omega}{2}\frac{\partial(x^2+y^2)}{\partial r}\right] \tag{22}$$

The initial condition for computing flow field past a stationary airfoil is irrotational flow (without circulation), i.e., $\omega = 0$. It is determined by solving Eq. (10) with

$$\frac{\partial \psi}{\partial \rho} = \frac{dr}{d\rho}\left(\frac{1}{r^2}\sin\theta + \sin\theta - \frac{\partial y}{\partial r}\right) \tag{23}$$

at the outer boundary and on the surface. The computed results for the oscillating airfoil are determined after a fully developed flow is obtained at zero incidence.

The surface pressure distribution is obtained by integrating the tangential component of the Navier-Stokes Eq. (5):

$$p = \int_0^\theta \left[\frac{L}{R}\frac{d\rho}{dr}\frac{\partial \omega_I}{\partial \rho} - \frac{d\Omega}{dt}\frac{1}{2}\frac{\partial(x^2+y^2)}{\partial r} + \frac{\Omega^2}{2}\frac{\partial(x^2+y^2)}{\partial \theta}\right] d\bar{\theta} + p_o \tag{24}$$

The constant p_o is determined such that p from Eq. (24) at a grid point on the surface just upstream of the front stagnation point is the same as that obtained from integration of the radial component of Eq. (5):

$$\frac{\partial u_1}{\partial t} + \frac{1}{2}\frac{1}{H}\frac{d\rho}{dr}\frac{\partial}{\partial \rho}(\vec{q}\cdot\vec{q}) - u_2\omega_I - \frac{d\Omega}{dt}\frac{1}{2rH}\frac{\partial(x^2+y^2)}{\partial \theta} - \Omega^2\frac{1}{2H}\frac{\partial(x^2+y^2)}{\partial r} = -\frac{1}{H}\frac{d\rho}{dr}\frac{\partial p}{\partial r} - \frac{1}{rH}\frac{L}{R}\frac{\partial \omega_I}{\partial \theta} \tag{25}$$

The constant of integration in this case is the defect in the kinetic energy, $1.0 - (u_1{}^2 + u_1{}^2)_I$, at the upstream boundary.

The pressure coefficient C_p is equal to $2p$. On the surface, the tangential stress is given by $\sigma_{12} = (L/R)\omega_I$. Both p and σ_{12} are made dimensionless with ρU^2. The conventional expressions for the coefficients of lift, drag, and moment around the origin of the z plane, which is also the point of oscillation, are:

$$C_L = \frac{\text{lift}}{(1/2)\rho U^2 \ell}\ , \qquad C_D = \frac{\text{drag}}{(1/2)\rho U^2 \ell}\ , \qquad C_M = \frac{\text{moment}}{(1/2)\rho U^2 \ell^2}\ ,$$

with

$$C_{LP} = -\frac{2}{L}\int_0^{2\pi} p\,\frac{\partial x_I}{\partial\theta}\,d\theta\ , \qquad C_{LF} = -\frac{2}{R}\int_0^{2\pi} \omega_I\,\frac{\partial y_I}{\partial\theta}\,d\theta\ ,$$

$$C_{DP} = \frac{2}{L}\int_0^{2\pi} p\,\frac{\partial y_I}{\partial\theta}\,d\theta\ , \qquad C_{DF} = -\frac{2}{R}\int_0^{2\pi} \omega_I\,\frac{\partial x_I}{\partial\theta}\,d\theta\ ,$$

$$C_{MP} = \frac{2}{L^2}\int_0^{2\pi} p\left(x_I\,\frac{\partial x_I}{\partial\theta} + y_I\,\frac{\partial y_I}{\partial\theta}\right)d\theta$$

$$C_{MF} = \frac{2}{RL}\int_0^{2\pi} \omega_I\left(-y_I\,\frac{\partial x_I}{\partial\theta} + x_I\,\frac{\partial y_I}{\partial\theta}\right)d\theta$$

where the subscripts P and F, respectively, represent the contributions due to pressure and viscous forces, and where the moment is considered positive in the clockwise direction.

Equations developed in this section are valid for both stationary airfoil ($\Omega = 0$) and the oscillating airfoil. Hence, the same computer program may be used for determining flow past either one of these airfoils.

3. COMPUTATIONAL PROCEDURES

The vorticity Eq. (9) may be solved in a number of ways. One needs to use, however, an implicit method for the viscous terms, since the time step restriction of an explicit method becomes severe for moderate Reynolds number flows. A numerical scheme may be devised such that the convective and viscous terms are respectively treated explicitly and implicitly. However, for the sake of simplicity and uniformity in computer programming, we consider implicit schemes for both convective and viscous terms. As stated in Section 2, the point or line successive over-relaxation (SOR) procedure for the implicit finite-difference representation of this equation is extremely time consuming for long time computations of moderate Reynolds number flows on machines comparable to the CDC 7600. The other possible candidates are the strongly implicit procedure (SIP) proposed by Stone (Ref. 17) or one of the fractional-step methods (Ref. 18) such as the alternating-direction implicit methods (Ref. 19) which result from approximate factorization. Instead of using these methods, an exact factorization procedure is developed as discussed below.

The SIP method requires Dirichlet boundary conditions, and we have periodicity in θ direction. Lin et al. (Ref. 20) studied the Karman vortex street from a circular cylinder with this method by fixing the front stagnation point and assigning the value of vorticity along the θ line radiating from this stagnation point. However, during the phenomena of vortex shedding from the upper and lower surface of the cylinder, the location of the stagnation point does move. Wu and Sampath (Ref. 21) have used the SIP method to determine flow past an airfoil. They have divided the solution domain into four blocks along constant θ lines, applied the SIP method in each block, and used the line SOR method for obtaining vorticity values along the dividing constant θ lines. This procedure is questionable for long time computations with time increments larger than for an explicit scheme because the implicit coupling between the blocks is destroyed. Sampath (Ref. 48) does overcome this limitation by iterating (without upgrading stream function).

The domain bounded by $0 \le \theta \le 2\pi$ and $\rho_0 \le \rho \le 1$ is divided into a rectangular network. The increments θ, ρ, and t are specified by $\Delta\theta$, $\Delta\rho$, and Δt with i, j, and n as the corresponding indices. A time-implicit form of the vorticity Eq. (9) is

$$\left(1 - \frac{2\Delta t}{AT_1}\,\partial_\theta{}^n\right)\left(1 - \frac{2\Delta t}{AT_1}\,\partial_\rho{}^n\right)\omega_I{}^n = -\frac{1}{T_1}\left(T_2\omega_I^{n-1} + T_3\omega_I^{n-2}\right) + \frac{4\Delta t^2}{T_1{}^2}\,\frac{\partial_\rho{}^n}{A}\,\frac{\partial_\omega{}^n}{A}\,\omega_1{}^n + O\left(\Delta t^{m+1}\right) \qquad (26)$$

where

$$A \equiv H^2 r^2\,\frac{R}{L}$$

$$\partial_\rho{}^n \equiv \left(\frac{d\rho}{dr}\,r\right)^2 \frac{\partial^2}{\partial\rho^2} + \left(\frac{d\rho}{dr}\,r + \frac{d^2\rho}{dr^2}\,r^2\right)\frac{\partial}{\partial\rho} - r\,\frac{d\rho}{dr}\,\frac{R}{L}\,\frac{\partial(\partial\Psi^n/\partial\theta)}{\partial\rho} \qquad (27)$$

and

$$\partial_\theta{}^n \equiv \frac{\partial^2}{\partial\theta^2} + r\,\frac{d\rho}{dr}\,\frac{R}{L}\,\frac{\partial(\partial\Psi^n/\partial\rho)}{\partial\theta} \qquad (28)$$

The three-point backward time differencing is given by $T_1 = 3$, $T_2 = -4$, $T_3 = 1$, and $m = 2$; whereas, the two-point backward difference is formulated with $T_1 = 2$, $T_2 = -2$, $T_3 = 0$, and $m = 1$. The latter formulation is used following the impulsive start and whenever the time step is cut in half, for the next two time steps. The operators ∂_ρ and ∂_θ do not commute, and the convective term, in these operators, is in conservative form. In a numerical procedure to solve Eq. (26), one may treat the cross derivative term, the nonlinear terms and the surface vorticity in several ways. A few of these are discussed below and the procedures used in this study are stated.

Neglecting the cross derivative term from the right-hand side of Eq. (26) gives a first-order time, approximate factorization procedure. Further, the term $(\partial_\theta/A)(\partial_\rho/A)\omega_I$ is large around the leading and trailing edge of the airfoil at incidence. The product

$$\frac{4\Delta t^2}{T_1^2}\,\frac{\partial_\theta^{\,n}}{A}\,\frac{\partial_\rho^{\,n}}{A}\,\omega_I^{\,n}\ ,$$

therefore, may be larger than Δt^2. On the other hand, schemes of evaluating this product at either $n - 1$ or $n - 1$ and $n - 2$ time levels may not be satisfactory in unsteady computations, again near the leading and trailing edge of the airfoil at incidence.

The nonlinear terms in Eq. (26) may be linearized in order to avoid an iterative procedure for determining Ψ^n. In operators (27) and (28), if superscript n is replaced by $n - 1$, as Wu and Sampath (Ref. 21) have done, then the numerical procedure is first order in time. Another approach is to expand the stream function in a Taylor series of time and obtain an estimate for Ψ^n:

$$\Psi^n = 2\Psi^{n-1} - \Psi^{n-2} + O(\Delta t^2)$$

This gives formally a second-order time differencing scheme. Linearization procedures such as these are generally used with an iterative scheme for determining the surface vorticity at n time level (see, for example, Briley, Ref. 22 and Briley and McDonald, Ref. 23). That is, either the stream function or velocity field is computed at each iteration in order to compute the surface vorticity and yet, the convection of vorticity near the surface is done with extrapolated or old $(n - 1)$ values of velocity. This procedure is particularly recommended when only steady state is required.

In the present unsteady computations, the vorticity equation is not linearized, although the number of iterations required for convergence of wall vorticity may be more than when it is linearized. Further, the cross derivative term in Eq. (26) is retained at n time level. It can be observed from these discussions that an attempt is made to reduce the different sources of numerical error when possible.

Equation (26) is actually solved in the following two steps:

$$\left(1 - \frac{2\Delta t}{AT_1}\,\partial_\theta^{\,n}\right)\bar{\omega} = -\frac{1}{T_1}\left(T_2\omega_I^{n-1} + T_3\omega_I^{n-2}\right) + \frac{4\Delta t^2}{T_1^2}\,\frac{\partial_\theta^{\,n}}{A}\,\frac{\partial_\rho^{\,n}}{A}\,\omega_I^{\,n} \tag{29}$$

and

$$\left(1 - \frac{2\Delta t}{AT_1}\,\partial_\rho^{\,n}\right)\omega_I^{\,n} = \bar{\omega} \tag{30}$$

The derivatives with respect to θ variable in operator ∂_θ are replaced by fourth-order-accurate rational fractions or Padé forms (refs. 24 and 25):

$$\frac{\partial f}{\partial\theta} = \frac{D_0 f}{\left(1 + \frac{\Delta\theta^2}{6}D_+D_-\right)} + \frac{\Delta\theta^4}{180}\,\frac{\partial^5 f}{\partial\theta^5} \tag{31}$$

and

$$\frac{\partial^2 f}{\partial\theta^2} = \frac{D_+D_- f}{\left(1 + \frac{\Delta\theta^2}{12}D_+D_-\right)} + \frac{\Delta\theta^4}{240}\,\frac{\partial^6 f}{\partial\theta^6} \tag{32}$$

where

$$D_0 f = (f_{i+1} - f_{i-1})/2\Delta\theta$$

and

$$D_+D_- f = (f_{i+1} - 2f_i + f_{i-1})/\Delta\theta^2$$

These fourth-order accurate expressions partially address the usual problem of grid resolution in θ direction. (The next section further deals with this problem.)

Using the above expressions, Eq. (29) is replaced by a set of two equations:

$$\begin{aligned}\left[\left(AT_1 + \frac{6\Delta t}{\Delta\theta}\,r\,\frac{d\rho}{dr}\,\frac{R}{L}\,\frac{\partial\Psi}{\partial\rho}\right)\bar{\omega}\right]_{i-1,j} &+ (4AT_1\bar{\omega})_{i,j} + \left[\left(AT_1 - \frac{6\Delta t}{\Delta\theta}\,r\,\frac{d\rho}{dr}\,\frac{R}{L}\,\frac{\partial\Psi}{\partial\rho}\right)\bar{\omega}\right]_{i+1,j} - 2\Delta t\bar{\omega}^{\theta\theta}_{i-1,j} - 8\Delta t\bar{\omega}^{\theta\theta}_{i,j} - 2\Delta t\bar{\omega}^{\theta\theta}_{i+1,j}\\ &= (AT_1\bar{R})_{i-1,j} + (4AT_1\bar{R})_{i,j} + (AT_1\bar{R})_{i+1,j}\end{aligned} \tag{33}$$

and

$$-\frac{12}{\Delta\theta^2}\,\bar{\omega}_{i-1,j} + \frac{24}{\Delta\theta^2}\,\bar{\omega}_{i,j} - \frac{12}{\Delta\theta^2}\,\bar{\omega}_{i+1,j} + \bar{\omega}^{\theta\theta}_{i-1,j} + 10\bar{\omega}^{\theta\theta}_{i,j} + \bar{\omega}^{\theta\theta}_{i+1,j} = 0 \tag{34}$$

where, with s as the iteration counter,

$$\bar{R} = -\frac{1}{T_1}\left(T_2\omega_I^{n-1} + T_3\omega_I^{n-1}\right) + \frac{4\Delta t^2}{T_1^2}\,\frac{\partial_\theta^{\,n,s}}{A}\,\frac{\partial_\rho^{\,n,s}}{A}\,\omega_I^{\,n,s} \tag{35}$$

and the superscript θ denotes differentiation with respect to θ coordinate. Equations (33) and (34) give a periodic block tridiagonal system with 2×2 blocks that is solved to obtain $\bar{\omega}$ for $j = 2$ to $JL - 1$. Except when $m = 1$, at the start of the iterative procedure, $\omega_I^{\,n}$ and Ψ^n that appear in the cross derivative term of Eq. (35) are respectively estimated by $2\omega_I^{n-1} - \omega_I^{n-2}$ and by using $2\psi^{n-1} - \psi^{n-2}$ for the estimate of Ψ^n. The value of ψ^n at the wall is given by Eq. (13).

Next, Eq. (30) is solved with a second-order, central difference formulae for the derivatives with respect to ρ. This choice of a second-order accuracy is partly motivated by the fact that the stretching function (8) gives the flexibility of appropriately distributing the grid points in ρ direction. In addition, the use of rational fractions to achieve a fourth-order accuracy requires a solution of a block tridiagonal system with 3×3 blocks. The finite difference form of Eq. (30) is

$$2\Delta t\left[-\left(r\frac{d\rho}{dr}\right)_j^2 + \frac{\Delta\rho}{2}\left(\frac{d\rho}{dr}r + \frac{d^2\rho}{dr^2}r^2\right)_j - \frac{\Delta\rho}{2}\left(r\frac{d\rho}{dr}\right)_j \frac{R}{L}\left(\frac{\partial\Psi}{\partial\rho}\right)_{i,j-1}\right]\omega^n_{Ii,j-1} + \left[AT_1\Delta\rho^2 + 4\Delta t\left(r\frac{d\rho}{dr}\right)^2\right]_{i,j}\omega^n_{Ii,j}$$

$$+ 2\Delta t\left[-\left(r\frac{d\rho}{dr}\right)_j^2 - \frac{\Delta\rho}{2}\left(\frac{d\rho}{dr}r + \frac{d^2\rho}{dr^2}r^2\right)_j + \frac{\Delta\rho}{2}\left(r\frac{d\rho}{dr}\right)_j \frac{R}{L}\left(\frac{\partial\Psi}{\partial\theta}\right)_{i,j+1}\right]\omega^n_{Ii,j+1} = \Delta\rho^2(AT_1\bar{\omega})_{i,j} \qquad (36)$$

The above scalar tridiagonal system is solved for $i = 2$ to $IL - 1$ to determine ${\omega_I}^n$. The derivatives of Ψ in Eqs. (33) and (36) are determined by calculating derivatives of ψ with fourth-order-accurate rational fraction of the form given by Eq. (31). Equations (33), (34), and (36) together give the finite-difference form, with a truncation error of $O[(\Delta\rho)^2 + (\Delta\theta)^4 + (\Delta t)^m]$, of the vorticity equation.

The disturbance stream function ψ is computed from Eq. (10) using a fourth-order scheme both in ρ and θ directions below. The Fourier transform of ψ and $-H^2r^2\omega_I$ in Eq. (10) gives

$$\left(r\frac{d\rho}{dr}\right)^2\hat{\psi}^{\rho\rho} + \left(\frac{d\rho}{dr}r + \frac{d^2\rho}{dr^2}r^2\right)\hat{\psi}^{\rho} - \tilde{k}^2\hat{\psi} = \hat{\omega} \qquad (37)$$

where $\hat{\psi}$ and $\hat{\omega}$ are respectively the Fourier transforms, superscript ρ indicates differentiation with respect to ρ

$$\tilde{k}^2 = \frac{12}{\Delta\theta^2}\left[\frac{1 - \cos(k'\Delta\theta)}{5 + \cos(k'\Delta\theta)}\right] \qquad (38)$$

with k' being the wave number. The above equation is determined by substituting $e^{ik'\theta}$ and $-\tilde{k}^2e^{ik'\theta}$, respectively, for f and $d^2f/d\theta^2$ in Eq. (32) and neglecting the truncation error (Ref. 49). The following two equations are solved in place of Eq. (37) for $i = 2$ to $IL - 1$:

$$\left\{\frac{12}{\Delta\rho^2} - \frac{{\tilde{k}_i}^2}{[r(d\rho/dr)]^2_{j-1}}\right\}\hat{\psi}_{i,j-1} - \left\{\frac{24}{\Delta\rho^2} + \frac{10{\tilde{k}_i}^2}{[r(d\rho/dr)]^2_j}\right\}\hat{\psi}_{i,j} + \left\{\frac{12}{\Delta\rho^2} - \frac{{\tilde{k}_i}^2}{[r(d\rho/dr)]^2_{j+1}}\right\}\hat{\psi}_{i,j+1}$$

$$+\left\{\frac{r(d\rho/dr) + (d^2\rho/dr^2)r^2}{[r(d\rho/dr)]^2}\right\}_{j-1}\hat{\psi}^{\rho}_{i,j-1} + 10\left\{\frac{r(d\rho/dr) + (d^2\rho/dr^2)r^2}{[r(d\rho/dr)]^2}\right\}_j\hat{\psi}^{\rho}_{i,j} + \left\{\frac{r(d\rho/dr) + (d^2\rho/dr^2)r^2}{[r(d\rho/dr)]^2}\right\}_{j+1}\hat{\psi}^{\rho}_{i,j+1}$$

$$= \frac{\hat{\omega}_{i,j-1}}{[r(d\rho/dr)]^2_{j-1}} + 10\frac{\hat{\omega}_{i,j}}{[r(d\rho/dr)]^2_j} + \frac{\hat{\omega}_{i,j+1}}{[r(d\rho/dr)]^2_{j+1}} \qquad (39)$$

and

$$\frac{6}{2\Delta\rho}\hat{\psi}_{i,j-1} - \frac{6}{2\Delta\rho}\hat{\psi}_{i,j+1} + \hat{\psi}^{\rho}_{i,j-1} + 4\hat{\psi}^{\rho}_{i,j} + \hat{\psi}^{\rho}_{i,j+1} = 0 \qquad (40)$$

At the airfoil surface, $j = JL$, the no-slip condition is exactly enforced by specifying both $\hat{\psi}$ and $\hat{\psi}^{\rho}$ from Eqs. (13) and (14). At the outer boundary, $\hat{\psi}^{\rho}$ is obtained from either Eq. (17) or (22). An additional relation between $\hat{\psi}$ and $\hat{\psi}^{\rho}$ that is required at this boundary is given by

$$2{\hat{\psi}_1}^{\rho} + 4{\hat{\psi}_2}^{\rho} - \frac{1}{\Delta\rho}(-5\hat{\psi}_1 + 4\hat{\psi}_2 + \hat{\psi}_3) = 0 \qquad (41)$$

which is third-order accurate. According to Kreiss and Oliger (Ref. 26) and Bramble and Hubbard (Ref. 27), this decrease in order of accuracy by one at the boundary may not reduce the accuracy in interior of the computational domain. The block tridiagonal system with 2×2 blocks resulting from Eqs. (39) and (40) and the boundary conditions are solved from $j = 2$ to $JL - 1$ for each value of i. The inverse Fourier transform of $\hat{\psi}$ gives ψ.

There are two major advantages of solving the stream-function equation as described above. First, *the stream function is determined with both the tangential and normal velocity exactly zero at the surface.* This alleviates the need to use Israeli's iterative procedure (Ref. 28) for determining surface vorticity such that the tangential velocity is zero. Second, the surface vorticity also dictates the determination of the stream function in the interior, as observed from the right-hand side of Eq. (39), just as one would expect from the application of Biot-Savart law. When second-order finite-difference schemes are used normal to no-slip boundary, we do not have these advantages. However, the error introduced by the lack of these advantages is not serious as long as it is of the same order of magnitude as the truncation error of discretization procedure.

The surface vorticity is calculated from Eq. (15) in which $\partial^2\Psi/\partial\rho^2$ is evaluated subject to zero tangential velocity. Following the derivation of Woods (Ref. 29), the finite-difference expression of Eq. (15) with a truncation error of $O(\Delta\rho^2)$ is

$$\omega^n_{i,JL} = -\left[\frac{6}{\Delta\rho^2}\left(\frac{d\rho}{dr}\right)^2_{JL}\Psi^n_{i,JL-1} + r^2_{JL-1}H^2_{i,JL-1}\omega^n_{i,JL-1}\right]H^{-2}_{i,JL}\left\{2 + 3\Delta\rho\left[\frac{dr}{d\rho} + \frac{d^2\rho}{dr^2}\left(\frac{dr}{d\rho}\right)^2\right]_{JL}\right\}^{-1} \qquad (42)$$

Wu (Ref. 13) has shown with the Rayleigh problem for an infinite flat plate how a second-order formula may violate the principle of total vorticity conservation by introducing a grid point outside the fluid domain. This introduction of a grid point with "midpoint" vorticity values, that is a second mesh system for ω, is not recommended (Ref. 30). Further, Fromm has also considered the above Rayleigh problem and obviously stated that there should "not be loss of vorticity as a consequence of transport or diffusion at the wall" (Ref. 31). He has shown a way of achieving this while introducing a point outside the fluid domain. It appears that Wu has used a second-order formula which one would not use. Consequently, his conclusions that second-order formulae "are usually ad-hoc" and "there are serious uncertainties regarding the range of usefulness of each second-order formula" are misleading.

The tangential velocity at the outer boundary is advanced by solving Eq. (18) with $O(\Delta\theta^4)$ accuracy:

$$\begin{aligned}&\left(T_1 rH - \frac{6\Delta t}{\Delta\theta} u_2^{n-1}\right)_{i-1,1} (u_2{}^n)_{i-1,1} + (4T_1 rHu^n)_{i,1} + \left(T_1 rH + \frac{6\Delta t}{\Delta\theta} u_2^{n-1}\right)_{i+1,1} (u_2{}^n)_{i+1,1} \\ &= (rHR^*)_{i-1,1} + 4(rHR^*)_{i,1} + (rHR^*)_{i+1,1} - \frac{6\Delta t}{\Delta\theta}\left[\left(u_1^{n-1} u_1{}^n\right)_{i+1,1} - \left(u_1^{n-1} u_1{}^n\right)_{i-1,1}\right] \\ &+ 2\Delta t\left\{\left[-rH\left(\omega^{n-1} u_1{}^n + u_1^{n-1}\omega^n\right)\right]_{i+1,1} - \left[4rH\left(\omega^{n-1} u_1{}^n + u_1^{n-1}\omega^n\right)\right]_{i,1} - \left[rH\left(\omega^{n-1} u_1{}^n\right.\right.\right. \\ &\left.\left.\left. + u_1^{n-1}\omega^n\right)_{i-1,1}\right]\right\} \qquad (43)\end{aligned}$$

where

$$R^* = -\left(T_2 u_2^{n-1} + T_3 u_2^{n-2}\right) + \frac{\Delta t}{rH}\frac{\partial(u_1{}^2 + u_2{}^2)^{n-1}}{\partial\theta} + 2\Delta t\left\{\omega^{n-1} u_1^{n-1} + \frac{1}{2H}\left[-\frac{d\Omega}{dt}^n \frac{\partial(x^2 + y^2)}{\partial r} + \frac{(\Omega^n)^2}{r}\frac{\partial}{\partial\theta}(x^2 + y^2)\right]\right\} \qquad (44)$$

The above equation has been derived using the "delta" formulation of Warming and Beam (Ref. 32).

The computational sequence is as follows: solve Eqs. (33) and (34) simultaneously; determine $\omega_I{}^n$ from Eq. (36); obtain $\partial\psi/\partial\rho$ with the help of Eq. (43) or from Eq. (22); solve Eqs. (39) and (40) to determine ψ; and then calculate surface vorticity from Eq. (42). This sequence is repeated until the surface vorticity changes less than some prescribed value. In order to speed up the convergence of this process, the surface vorticity is changed using the formula

$$\omega_{i,JL}^{n,s} = \omega_{i,JL}^{n,s-1} + \beta\left(\omega_{i,JL}^{n} - \omega_{i,JL}^{n,s-1}\right) \qquad (45)$$

where $\omega_{i,JL}^n$ is determined from Eq. (42) and s is the iteration counter. The variation of β with θ is given as

$$\begin{aligned}\beta &= \beta_1 , & i &= 2, 4 \\ \beta &= \frac{\beta_1}{4} i , & i &= 5, 34 \\ \beta &= \frac{\beta_1}{4}\beta_2(i - 1) , & i &= 35, 63 \\ \beta &= \beta_1\beta_2 , & i &= 64, 66\end{aligned} \qquad (46)$$

where $\beta_1 < 1$ and $1 \le \beta_2 \le 2$. The same sequence is used along the upper surface. The basic reasoning behind this sequence is that the flow around the airfoil is much better behaved away from the leading and trailing edge; and the vorticity near the trailing edge is the most sensitive quantity in an iterative procedure.

The arrangement of the block periodic tridiagonal system, Eqs. (33) and (34) and $\tilde{k}^2$ in Eq. (39), is changed at each iteration so that the round-off error does not predominantly accumulate in any one location for each value of j. This is done so that the increasing value of i changes θ as follows: at sth iteration, θ increases from 0 to $2\pi - \Delta\theta$; at $s + 1$ iteration, it decreases from 2π to $\Delta\theta$; at $s + 2$ iteration, it increases from π to $3\pi - \Delta\theta$; and at $s + 3$ iteration, it decreases from π to $-\pi + \Delta\theta$.

Oscillations in the vorticity field above some Reynolds number (depending on the physical problem, numerical scheme, and grid resolution), in an incompressible external flow computation are troublesome just as the oscillations in dependent variables are, near shocks with shock-capturing numerical schemes (Refs. 33 and 34). In latter computations some numerical dissipation is added or schemes with inherent dissipations are used to somewhat smear out the sharp gradients across shocks. For incompressible computations, addition of dissipative terms has not been tried so far to control the vorticity oscillations. On the other hand, the equivalent of shock-fitting technique is not available for vorticity sheet-fitting.

The preliminary results with a second-order numerical scheme described in the next section for $R = 10{,}000$ developed oscillations at $\alpha \sim 16°$ on the upstroke of the airfoil. See the equivorticity loops below the trailing edge of the airfoil in Fig. 4. On these loops the value of vorticity is of $O(1)$, which is much less than vorticity in the immediate neighborhood of the airfoil, particularly around the leading edge. The erroneous vorticity in these loops, therefore, does not appreciably effect the overall flow pattern. Unless these oscillations are controlled they tend to grow and make the solution meaningless as explained in Section 1. Similar oscillations were observed for $R = 5{,}000$, during the downstroke of the airfoil, around the leading edge. These oscillations in vorticity primarily appear in θ direction.

Orszag and Jayne (Ref. 35) have reported for a linear hyperbolic equation that the higher order methods give better accuracy and smaller amplitude oscillations than the lower order methods. Because of the vorticity oscillations in the preliminary results with a second-order scheme, the fourth-order scheme discussed above was developed. However, for the present nonlinear problem with these fourth-order scheme oscillations appeared in front of the leading edge of a stationary airfoil started impulsively at zero incidence with $R = 10{,}000$. Eventually, it was impossible to determine the steady-state solution. In nonlinear problems, it appears that higher order numerical methods require more smoothness in the dependent variables than the lower order methods. Obviously, the former give more accurate solution than the latter when the dependent variables are smooth.

The computations presented in Section 5 are determined with a sixth-order dissipative term added to both the vorticity Eq. (26) and the tangential momentum Eq. (43), see also Section 2. To the right-hand side of Eq. (35) and Eq. (44), respectively,

$$\frac{T_2 \Delta t \beta_3 \Delta\theta^6}{64 T_1 L} \frac{\partial^6}{\partial\theta^6} \left(\left| \frac{d\rho}{dr} \frac{1}{H} \frac{\partial\Psi^{n-1}}{\partial\rho} \right| \omega_I^{n-1} \right) \tag{47}$$

and

$$\frac{T_2 \Delta t \beta_3 \Delta\theta^6}{64 T_1 L} \frac{\partial^6}{\partial\theta^6} \left(\left| u_2^{n-1} \right| u_2^{n-1} \right) \tag{48}$$

is added. The variable β_3 is a constant. Central finite differences are used to discretize these terms.

Computations of pressure coefficients on the surface and loads are conducted as in Ref. 8.

4. PRELIMINARY REMARKS AND RESULTS

The computations were conducted for $R = 5{,}000$ and $R = 10{,}000$ respectively with $k_1 = k_2 = 2.0$, and $k_1 = 2.25$, and $k_2 = 2.0$ in transformation (8). The grid distribution is determined from $IL = 130$, $JL = 84$, and $r_o = 0.04$. The shape of the airfoil is defined by $\xi = -0.0647384$, $\eta = 0$, and $\delta = 0.04$ in Eq. (2). The above value of r_o corresponds to a distance of about 6.4 chord lengths from the trailing edge of the airfoil, where the downstream boundary is placed. In the vicinity of the airfoil, the grid distribution for $R = 10{,}000$ computations is shown in Fig. 5. The above constants defining the shape of the airfoil give a modified NACA 0012 airfoil. It has a 12.0011% thick symmetric profile with maximum thickness at 30.71% chord length and with the leading-edge radius of curvature of 1.4178% chord. These statistics are valid for $IL = 130$. The differences around the leading and trailing edge between the modified and unmodified NACA 0012 airfoil (Fig. 6) give primarily different inviscid pressure coefficients near the trailing edge (Fig. 7).

After a fully developed flow is determined at zero incidence, the airfoil is oscillated in pitch (Fig. 1) through an angle-of-attack range from 0° to 20° given by $\alpha = 10° (1 - \cos ft)$. The computations are done for two cases: (1) $R = 5{,}000$ and $k = 0.5$, and (2) $R = 10{,}000$ and $k = 0.25$, where the reduced frequency of oscillation is based on half chord, $k = f\ell/2U$. The pitch axis is located at the quarter-chord point with $\sigma = -0.917095$ and $\alpha = 0$ in Eq. (1).

Some of the computed results are presented in the form of instantaneous streamlines both in inertial and rotating frame of reference. These are compared with flow visualization pictures obtained by Werlé (Ref. 36) with a NACA 0012 airfoil under identical conditions. The experiments were carried out with air bubbles in the water tunnel of Châtillon as described in Ref. 37. Photographs showing air bubble trajectories with black airfoils for $R = 5{,}000$ and $k = 0.5$, other photographs with air bubbles (from Ref. 36) and the dye pictures were respectively taken at an exposure time of 1/10, 1/28 and 1/1000 sec (Ref. 38). Therefore, in unsteady flow the air bubble trajectories near the surface of the airfoil represent neither streamlines (Ref. 38) nor streaklines (Ref. 39) as the pictures are of many paths over the exposure time. In addition, these pictures are taken in the inertial frame of reference. These points should be kept in mind while comparing the computed streamline patterns with the experimental air bubble trajectories.

As in Ref. 8, the unsteady instantaneous separation point, in the rotating coordinate system, is the point at which the surface (or zero) streamline bifurcates. This is the point at which instantaneously both vorticity and velocity, defined in the rotating coordinate system, are zero. This latter definition allows for bifurcation of a streamline in the flow field. Sears and Telionis (Ref. 40) have proposed a definition of separation point as a point at which the Goldstein (Ref. 41) singularity appears. This singularity is a pecularity of the boundary-layer equation and not of the Navier-Stokes equation. In this study, the reattachment point is the unification point of the two branches of streamlines formed at the separation point. A bubble is a region enclosed by zero streamline in the rotating coordinate system. Likewise, a vortex is defined locally by closed equivorticity lines with a relative extremum of vorticity in the center. The shape of the vortex or bubble need not be circular. Bubbles and vortices are separate entities that may have some regions in common.

It is generally believed that once laminar separation takes place on the upper surface of the airfoil, the flow cannot reattach without going through transition and becoming turbulent. This belief is primarily based on the work of Crabtree (Ref. 42) on leading edge laminar separation bubbles. In explaining the above flow reattachment process Crabtree states: "If the bubble reattaches, however, there must be a considerable widening ofthe streamlines over the rear end. This cannot be imagined as a laminar process at the Reynolds number we are concerned with, but is more akin to turbulent mixing as it occurs in, say, a pipe with a sudden enlargement of cross section. We are, therefore, led to assume that there is transition to a turbulent state . . . ." The phrase, which has been overlooked, in this quote is "at the Reynolds numbers we are concerned with." There is a Reynolds number below which, for a given airfoil shape and angle of incidence, the laminar reattachment on the surface of the airfoil is feasible (see Refs. 8, 14, and 15). In this study, bubbles with laminar separation and reattachment are called laminar bubbles and the so-called laminar separation bubbles are called transition bubbles.

The preliminary results presented in this section for the oscillating airfoil were obtained using second-order finite differencing procedures both in ρ and θ direction. The vorticity Eq. (9) was solved with the procedure given by Eqs. (29) and (30). The nonlinear terms were represented using Arakawa's formulation (Ref. 43) as it was done in Ref. 8. (This procedure was abandoned in the numerical procedure that is developed in the previous section for the sake of accuracy and efficiency, Ref. 25.) The disturbance stream function Eq. (10) was solved using the odd-even cyclic reduction procedure (Ref. 44). For $R = 5{,}000$, Eq. (18) was used at all points along the outer boundary. However, for $R = 10{,}000$, the following equation was used.

$$\frac{\partial u_{2I}}{\partial t} = -\left[\frac{1}{2rH}\frac{\partial(u_1^{\,2} + u_2^{\,2})_I}{\partial\theta} + (u_1\omega)_I\right] \tag{49}$$

The preliminary results determined using the above numerical procedures are shown in Fig. 8 for $R = 10{,}000$ and $k = 0.25$. First the instantaneous streamlines in rotating coordinates, which give the airfoil chord aligned with the x axis are plotted, and then the airfoil is rotated to give the angle of incidence corresponding to that in the inertial frame of reference. Qualitatively, these computed streamlines are in excellent agreement near the trailing edge of the airfoil and in the near wake region with the trajectories of air bubbles observed in experiments. When $R = 5{,}000$ and $k = 0.5$, the streamline pattern shown in Fig. 9 compare remarkably well except near the trailing edge, with air bubble paths shown in Fig. 10d. One of the reasons for the difference is that in the experiment, downstream of the trailing edge the air bubbles are disorganized or the trajectories of the bubbles intersect locally. Further discussion of the above results is given in the next section.

The equivorticity lines in Fig. 4 and Fig. 9 and elsewhere in this paper are plotted in the inertial frame of reference. As discussed in the previous section, the fourth-order scheme with a sixth-order numerical dissipation in θ direction was developed in order to improve the resolution of the vorticity field and alleviate the problem of oscillations in vorticity field (Figs. 4 and 9). In addition, the total number of points in θ directions were increased from 82 in Ref. 8 to 130. This two-sided attack on the problem of resolution is better for the moderate Reynolds number computations than what has been generally done in high Reynolds number computations of flow fields around airfoils (Refs. 11, 12, 45, and 46).

The computed answers are obviously not the exact solutions of the Navier-Stokes equation and the continuity equation. There are engineering judgments and computational and physical insight involved in deciding whether to accept the data generated by a computer. Just as wind tunnel data is subject to certain errors, the computed numbers are subject to errors. However, a careful attempt should be made to minimize errors from different sources. Such an attempt is made in the present study (see, for example, Section 3). Further, a good computation practice is to study the effect of grid size on the solution. In the present study, the total number of grid points, 130×84, are so chosen that both small and large core memory of CDC 7600 are completely used with most of the auxiliary variables required during computation stored along with the primary variables, stream function and vorticity. We do not consider (130×84)/2 grid points sufficient for the present problem and computations with 2(130×84) points are time consuming, at present, as they require a disk pack in addition to the large core memory. Therefore, the results presented in the next section are at least qualitatively accurate. Quantitative validation must await quantitative experimental data, other numerical studies solving the same problem or grid refinement studies.

5. ANATOMY OF THE FLOW FIELD AROUND AN OSCILLATING AIRFOIL

The numerical method described in Section 3 is used to obtain fully developed flow past the modified 0012 airfoil. The pressure distribution for this flow are shown in Fig. 7. These pressure coefficients are lower than those for the inviscid flow near the trailig edge because the Reynolds number is not high enough and the boundary layer displacement effect is appreciable. When $R = 5{,}000$, the pressure coefficients upstream of the trailing edge are slightly lower than for $R = 10{,}000$ as it should be. The differences in suction peak correspond to the differences in the front stagnation-point pressure coefficients which are 1.028 and 1.015, respectively, for $R = 5{,}000$ and $R = 10{,}000$. Again, these values are greater than unity, because the Reynolds number is not large enough. In both cases, flow separates near the trailing edge: at 98.4% chord length for $R = 5{,}000$ and at 86.11% chord for $R = 10{,}000$.

During the computations of oscillating airfoil results, time increment was varied such that the changes in the solution were not significant over a time step. The time increment ranged from 0.02 to 0.08 for $R = 5{,}000$ and from 0.016 to 0.064 for $R = 10{,}000$. These values may be converted to the distance travelled by the airfoil by division with $L = 3.61906$, the nondimensional chord length. The constant β_3 in Eqs. (47) and (48) is generally taken to be $4L$. In the relaxation procedure for determining the surface vorticity, $\beta_2 = 1.1$ and 1.5 are, respectively, used for $R = 5{,}000$ and $R = 10{,}000$ with $\beta_1 = 0.02$ for both cases. The relaxation procedure is generally terminated when the absolute maximum residue or change in the evaluation of surface vorticity between iterations is less than 10^{-4}. At times, this criteria was not maintained, if the rate of convergence was too slow and consequently the number of iterations became excessive, and if the solution was considered to be valid. Table 1 lists the total number of time steps, the average number of iterations, the average error in the surface vorticity, average CDC 7600 computation

Table 1. Some Statistics of Computed Results.

No.	R	k	Oscillation cycle	Time steps	Average iterations	Average residue in ω_{JL}	Average CPU time per time step, min	Error in C_p, %
1	5,000	0.5	1 and 2	778	54.5	0.005	0.712	1.12
2	10,000	0.25	1	855	48.5	0.003	1.086	0.578
3	10,000	0.25	2 (Incomplete)	638	54.2	0.086	0.828	2.20

time per time step (FTN 4.4 compiler with OPT = 2 and R = 3) and the percentage error in evaluation of the surface pressure coefficient using two different paths of integration (Ref. 8). This percentage is based on the difference in the maximum and minimum pressure coefficient.

Except for the preliminary results presented in the previous section, the values assigned to the plotted stream function, vorticity and velocity vectors are as follows: The numerical values of the stream function for the plotted streamlines vary from -0.42 to 0.42 with an increment of 0.06. In Figs. 10-13, streamlines are plotted both in the rotating and inertial (or fixed) coordinate system with the former on top. Both vorticity and velocity vectors are plotted in the inertial coordinate system. The vorticity values for the plotted equivorticity lines vary from -14.0 to 16.0 with an increment of 3.0. The magnitude of the velocity vectors is one-fourth the actual value. These vectors are plotted near the airfoil at every fourth value of i (except near the leading and trailing edge of the airfoil) and at every other value of j. The three lines upstream of the airfoil in the velocity vector plots indicate the minimum, instantaneous, and maximum incidence of the airfoil during oscillation.

Interpretations for plotted results are given below for both cases, R = 5,000 and k = 0.5, and R = 10,000 and k = 0.25, together. Similarities and differences between these cases are discussed. The computed results are compared with the water tunnel experiments of Werlé (Ref. 36). Comparison is also made with the preliminary results presented, with a second-order numerical scheme, in the previous section.

Symmetric, steady-state flow with a small separation bubble is observed in Fig. 10a at $\alpha = 0$. The equivorticity lines are not symmetric because the values of vorticity chosen above for plotting are not symmetric about zero. As the airfoil incidence increases from zero, the separation point (defined in the rotating coordinate system) on the upper surface moves upstream (Figs. 10b and 12a) and the separation bubble on the lower surface is shed downstream. In the fixed coordinate system, the airfoil surface is not a streamline and hence there is no bifurcation or unification of streamlines on the surface of airfoil. Figure 10b shows streamlines penetrating the upper surface and streamlines emerging from the lower surface. This pattern is also indicated by the air bubbles in the experiment. Further, there is strictly no front stagnation point in the experiment as well as in the streamline plots. There is, however, an apparent stagnation point.

While the separation point is moving up the airfoil the suction peak builds up as more net positive vorticity is shed in the wake, leaving behind more clockwise circulation. Figure 10b does not show a bump in the pressure distribution, which is observed across a transition bubble. The characteristics of this bump, namely, a plateau and a rapid recovery of pressure, are observed in Fig. 10c. This is coupled with the formation of a neck along the upper surface in both equivorticity lines and streamlines just downstream of the axis of oscillation (Figs. 10c and 12c). As the incidence of the airfoil is increased, both the flow velocity around the leading edge and the angle of separation streamline (with respect to x-axis) increase. This tends to take separated flow further away from the airfoil surface; and yet, the flow downstream remains next to the airfoil surface. Continuity of flow, therefore, suggests that the separated flow needs to come back towards the surface producing the neck in the streamline pattern. This neck in streamline or equivorticity line structure gets narrower as the incidence is increased and eventually the flow reattaches on the surface Figs. 10d and 12d. The pressure coefficient rises where this neck is developing (Fig. 12c). In addition, a suction peak develops on the surface below the center of the vortex or the center of closed streamlines in the bubble. This is consistent with large reverse flow velocities in the separation bubble. The difference between the two cases is that for R = 10,000 and k = 0.25, the reattachment of the separated flow takes place at smaller incidence than for R = 5,000 and k = 0.5. This difference is primarily a Reynolds number effect.

The reattachment of the separated flow from the leading edge region, just downstream of the pitch axis, breaks up the original long bubble into two as shown in Fig. 12d. The bubble along the second half of the airfoil has two centers and another bubble in between these centers, as also seen in the experiment. The structure of the leading-edge bubble is complex. There is an adverse pressure gradient for the flow moving upstream in the bubble between the two suction peaks. This develops the inner bubble in Figs. 10d and 12d. This double bubble structure is clearly confirmed by the air bubble trajectories in Fig. 10d. (The experimental picture in Fig. 12d is not clear enough to see this double bubble structure.) In addition, the dye visualization in Fig. 14a compares extremely well with the structure of the vortex as observed from the equivorticity lines in Figs. 10d and 11c. Superposition of streamlines and air bubble trajectories in Fig. 15a indicate that the double bubble structure in experiment is bigger than in computation; however, qualitatively the flow field is the same. Free streams in Figs. 15a and 15b suggest different exposure times.

The diffused dye pattern in Fig. 14b suggests that the separated flow may be turbulent. This conclusion is based on the assumption the boundary layers on the four walls of the water tunnel do not contaminate the main features of the flow around the oscillating airfoil. The level of turbulent intensity is probably quite low at the Reynolds numbers considered here. In addition, if the disorganization of air bubbles or intersection of their trajectories (Figs. 10g, 12e-12g, etc.) imply three-dimensional flow structure and hence turbulence, then the present laminar calculations are strictly meaningful only for the upstroke of the airfoil just short of the maximum incidence, α_{max}.

Some preliminary results with a second-order scheme were presented in the previous section. These are compared with the present results. In Figs. 8 and 9 the numerical values of the stream function for the plotted streamlines vary with an increment of 0.04 instead of 0.06 for the present results. In Figs. 4 and 9 the vorticity values for the plotted equivorticity lines vary with an increment of 2.0 instead of 3.0. The patterns of streamlines for R = 5,000 and k = 0.5 in Fig. 9 are essentially the same as in Fig. 10d, the main difference being just downstream of the trailing edge. The equivorticity lines have the same patterns except again just downstream of the trailing edge. The use of a fourth-order finite-differencing with a sixth-order dissipative term in θ direction for the present results do not give oscillations downstream of the trailing edge of the airfoil Fig. 10d as those observed with the second-order scheme in Fig. 9. This is further confirmed by the comparison between Figs. 4 and 12d for R = 10,000 and k = 0.25. The computed streamlines compare somewhat better downstream of the trailing edge with the air bubble trajectories in the water tunnel (Fig. 8) than those shown in Figs. 12b-12d. However, Fig. 12d shows a small bubble between the two centers of the large bubble both in computation and experiment, but the second-order scheme does not give this small bubble.

As stated in the previous section, the preliminary and present results for $R = 5,000$ were obtained with the same outer boundary condition, at least along the downstream half of the boundary. However, for $R = 10,000$, Eq. (49) was used instead of Eq. (18). If, after rewriting Eq. (49) in the convective form, the convective velocity in Eq. (49) were of the rotating coordinate system instead of in the fixed coordinate, then the resulting equation would be constraining the flow at the outer boundary the same as Eq. (18). Equation (49) was used to somehow take into account the interaction of top and bottom walls of the water tunnel (Ref. 38) with the unsteady flow field due to the oscillating airfoil. (The physical distance between these walls is unavailable.) The differences in the wake of the airfoil between the streamlines of the preliminary and present results ($R = 10,000$) are not due to the differences between Eqs. (18) and (49). Recall the boundary conditions are applied at about 6.4 chord lengths from the trailing edge of the airfoil along almost a circular boundary. In addition, for $R = 5,000$ computations, Eq. (18) was applied for both the preliminary and present results which have differences in the near wake of the airfoil. As indicated above, these differences are due to the oscillations in vorticity values in this region with the second-order scheme. The above discussion was motivated because if the experimental results are to be reproduced, the boundary conditions in computation need to be appropriate.

Coming back to the discussion of only the present results, a third suction peak is seen developing at the trailing edge of the airfoil in Figs. 12d and 12e. This indicates the flow along the lower surface of the airfoil turns around the trailing edge at large velocities but less than the free-stream velocity. While the leading edge suction peak was developing, the velocities around the leading edge were larger than the free-stream velocity.

The changes in the flow field at $R = 10,000$ and $k = 0.25$ (Figs. 12f-12i) are much more rapid around α_{max} than for $R = 5,000$ and $k = 0.5$ (Figs. 10c-10e). This appears to be a Reynolds number effect and not a reduced frequency effect.

The vorticity next to the downstream half of the upper surface of the airfoil is predominantly positive and away it is negative (Fig. 10d and 12e). The positive vorticity is created by the flow moving upstream and the negative vorticity is convected from the leading edge region. The open separation bubble (Ref. 8) located here has both positive and negative vorticity. These different kinds of vorticity form eventually two vortices as the separation bubble is swept off the airfoil surface (Figs. 10f and 12f). This shedding of pair of vortices takes place just after α_{max} is passed for $R = 5,000$ and $k = 0.5$; whereas, it takes place just before α_{max} is reached for $R = 10,000$ and $k = 0.25$. The centers of these vortices rotate clockwise as they move downstream. The strength of the vortex with negative vorticity is more than that with positive vorticity. Thus, the first identifiable vortex pair is shed from the second half of the upper surface and not from the leading edge. While this pair is being shed, the leading edge vortex extends further downstream (Figs. 10e and f and Figs. 12f and g). As this vortex passes over the upper surface of the airfoil, the suction peak associated with it also travels downstream. In addition, the separation bubble associated with this vortex obviously moves downstream. The magnitude of reverse flow velocity is frequently comparable to that of free-stream velocity (Figs. 10e, 10f, 12g, and 12h).

There is one major difference in the flow patterns computed for the two reduced frequencies. The number of leading edge vortices or separation bubbles that pass over the airfoil and are shed (along with vortices with positive vorticity) during the downstroke of the airfoil depends upon the reduced frequency. A strong and a weak vortex are shed for $k = 0.5$; whereas, two strong and two weak vortices are shed for $k = 0.25$. The strong vortices can easily be identified in Werlé's movie (Ref. 36). The number of vortices observed in the movie appears to be the same as those predicted in the present computed results. These vortices are identified and discussed below.

Figures 10f-10i show the downstream motion of the leading edge vortex. The sequence starts with the inner separation bubble of the double bubble structure opening up to the outer flow in Fig. 10g. The outer bubble is broken into two with the downstream half moving in downstream direction. A vortex is correspondingly shed from the leading region. Whatever negative vorticity is left behind forms a vorticity tongue from the leading edge or locally, just downstream of the axis of oscillation, a vortex consisting of closed equivorticity lines. Between this small vortex and the above large one, there is predominantly positive vorticity which was created by the downstream travelling bubble. As the incidence is decreased, the whole flow pattern on the upper surface qualitatively moves downstream. In Fig. 10i, we see a pair of positive and negative vortices being shed. Again, the vortex with negative vorticity is stronger than the other. The shedding of this vortex pair is observed in Werlé's movie (Ref. 36). Next, the weak vortex or bubble seen at about three-fourths of chord length in Fig. 10i is shed before the incidence of the airfoil is zero. This weak vortex pair can be identified in Ref. 36. As bubbles are swept off the upper surface of the airfoil, the flow reattachment proceeds from the leading edge towards the trailing edge. The flow is not symmetric at $\alpha = 0°$.

Two strong vortices are shed followed by two weak ones for $k = 0.25$ (Figs. 12g-12p). In Fig. 12h, the two suction peaks, away from the leading edge, correspond to the leading edge vortex and the vortex shed from the leading edge region. Between these two, there is positive vorticity. A pair of vortices with opposite vorticity is distinctly seen in Fig. 12i. Note the boundary of the vortex with negative value is not the same as the large bubble. After the above pair passes into the wake another vortex is shed from the leading edge (Fig. 12k). Again we see a pair of vortices in Fig. 12m moving downstream. Both the above pairs can be observed in Ref. 36. Next two small vortices are shed (Fig. 12n-12p). As in $k = 0.5$ case, the flow reattaches from the leading edge to the trailing edge with some residual asymmetry at $\alpha = 0°$.

Above, the evolution of flow field during the first cycle of oscillation was described. During the second cycle of oscillation the flow field is qualitatively the same as during the first cycle for $R = 5,000$ and $k = 0.5$. The computations were carried out only up to $\alpha = 12°\downarrow$ for $R = 10,000$ and $k = 0.25$. In this case also, the flow patterns during the upstroke are qualitatively the same as those observed above. Figures 11 and 13 show the flow development as follows: development of a neck in streamlines and equivorticity lines (Figs. 11b and 13a), reattachment of the separated flow from the leading edge region forming the leading edge vortex and giving rise to a double bubble structure (Figs. 11c and 13b), shedding of a vortex pair from the trailing edge region (Fig. 11d), shedding of leading edge vortex (Figs. 11e and f), the reattachment of the flow from front to rear accompanied with a shedding of a small bubble and finally, asymmetric flow at zero incidence with a bubble near the trailing edge (Fig. 11g). Superposition of streamlines and air bubble trajectories in Fig. 15b is excellent.

The computed patterns of streamlines and air bubble trajectories do not appear to correspond as well during the downstroke of the airfoil as they do during the upstroke. This is primarily because the air bubbles are disorganized or their trajectories intersect during the downstroke of the airfoil. However, the overall flow patterns are similar to those observed in the experiment as described above.

The computations for $R = 10{,}000$ did develop some oscillations in vorticity during the pitch down motion of the airfoil. A series of black dots upstream of the leading edge of the airfoil in θ direction, in Fig. 12h, represent these oscillations. The dissipation term added in the vorticity equation did control these oscillations in the sense that they appear and disappear; compare Figs. 12h and 12i. Similar series of black dots or small equivorticity loops roughly of the size of local grid spacing in physical plane are seen near the trailing edge region in Fig. 12m. In this region these oscillations are also controlled by the dissipation term (Figs. 12m and 12n). As long as these oscillations remain controlled and the vorticity in the above loops is of $O(1)$, these oscillations do not qualitatively affect the overall flow patterns. It is possible to completely eliminate these oscillations simply by using a larger value of β_3 in Eq. (47) than $4L$ that was generally used in the present study. However, both inherent and intentionally added dissipation in a numerical scheme may alter the effective viscosity of the flow. Care needs to be exercised in choosing a numerical scheme and in adding a dissipative term for a given physical problem. As the overall flow patterns for $R = 10{,}000$ were physically meaningful, no attempt was made to completely eliminate these oscillations for presentation at this symposium. However, the solutions for the downstroke during the second cycle were questionable or hard to interpret and hence the computations were stopped at about $\alpha = 12^\circ\downarrow$ as indicated above.

Figures 16 and 17 show the location of front stagnation point, respectively, for $R = 5{,}000$ and $k = 0.5$ and $R = 10{,}000$ and $k = 0.25$. The ordinate in these figures gives the normalized distance measured from the leading edge along the chord of the airfoil. The stagnation point is defined in the rotating coordinate system. It is always located along the lower surface of the airfoil for $\alpha > 0^\circ$. These figures indicate that even the stagnation region experiences hysteresis.

It was concluded in Ref. 8 for a stationary stalled airfoil that an increase in the strength of a clockwise (or a counterclockwise) bubble accompanies lower (or higher) pressures along the airfoil surface in contact with it. Further, the lift increases when attached clockwise bubbles grow and when counterclockwise bubbles are swept away from the surface of the airfoil. It diminishes when counterclockwise bubbles grow and clockwise bubbles are shed. These conclusions are valid in the present oscillating airfoil study in the rotating coordinate system. Recall, a bubble has closed streamlines with the surface of the airfoil forming part of the bubble boundary. A pattern of closed streamlines whose boundary is not the airfoil surface is defined as free bubble, in the present viscous calculations. This definition is required because the forces acting on the oscillating airfoil are defined in the inertial frame of reference. Then the lift coefficient increases when clockwise free bubbles in contact with the upper surface of the airfoil grow and counterclockwise free bubbles are swept away from the surface. It diminishes when counterclockwise free bubbles grow and clockwise free bubbles are shed. As soon as a clockwise free bubble picks up a streamline from below the lower surface of the airfoil, it is in a process of being shed. These conclusions are based on Figs. 10-13 and Figs. 18 and 19.

The lift coefficient increases as the incidence is increased. It decreases with decreasing incidence. Figures 18 and 19 show hysteresis loops. Maximum lift is achieved around α_{max}. No sudden increase in lift coefficient is observed for $R = 5{,}000$ and $k = 0.5$. But we do observe such increase for $R = 10{,}000$ and $k = 0.25$. In this latter case, the airfoil experiences a moment stall but not in the former case (Figs. 20 and 21).

The variations of the lift coefficient (Figures 18 and 19) and the moment coefficient (Figures 20 and 21) with incidence suggest that generally when lift coefficient increases, the moment coefficient decreases. Therefore, those free bubbles in the inertial frame of reference that increase lift also decrease moment. Both the lift and drag coefficients increase or decrease simultaneously (Figs. 18, 19, 22, and 23). But the rate of change may be different. The primary contribution to the lift and moment coefficients is due to pressure and not due to skin friction. This is valid also for the drag coefficient except at small incidences when the friction drag is greater than or comparable to pressure drag.

As mentioned above, solutions for the downstroke of the airfoil during the second cycle of oscillation, when $R = 10{,}000$ and $k = 0.25$, are questionable (Figs. 17, 19, 21 and 23). The most probable cause for this is explained as follows: The iteration procedure, discussed in Section 3, was actually executed such that there was an inner and a complete iteration loop. The former covered the flow region next to the surface and the latter covered the complete computational region. The outer boundary conditions for the inner iteration loop was determined during the complete iteration loop. At nth time step, the first three iterations were the complete iterations. Then four inner iterations were executed followed by one complete iteration. This sequence of five iterations was repeated until convergence criteria or acceptable solution was achieved (Section 5). The check for convergence was done at the end of the complete iteration loop. Typically, the inner iteration region extended from $J = 42$ to 84, for $R = 10{,}000$ and $k = 0.25$. This procedure helped in reducing the computational time (Table 1). However, under certain flow conditions it may force the solution to deviate from that obtained from only the complete iteration loop, if the outer edge of the inner iteration loop is not chosen properly. This is particularly true during the downstroke of the airfoil. Lack of time has prevented a satisfactory solution of this problem.

The classification of dynamic stall as stated in Section 1 has been deduced from experiments at high Reynolds numbers with airfoils differing in leading-edge geometry (Refs. 4 and 47). This classification was primarily based on the time history of location of the separation point during the upstroke of the airfoil (Fig. 15 of Ref. 4). In the present study, the gradual progression of flow separation from trailing edge towards the leading edge suggests that there would be the trailing-edge stall. However, at high Reynolds number the present modified NACA 0012 airfoil would be expected to exhibit leading-edge stall caused by an abrupt breakdown of the turbulent flow on the forward portion of the airfoil, just as does the basic NACA 0012 airfoil since the difference in the leading-edge geometry between these two airfoils is probably negligible (Fig. 6).

In this section, a description of the anatomy of the flow field past an oscillating airfoil is given. In addition, the general features of this flow are verified by the water tunnel experiments of Werlé (Ref. 36) even though during the downstroke of the airfoil the separated flow is turbulent in the experiment. (Obviously, there is a need for quantitative experimental data for validating this type of Navier-Stokes results.)

6. CONCLUDING REMARKS

The principal features of dynamic stall of an oscillating airfoil are flow separation, formation of vortices and passage of these vortices over the airfoil surface. The secondary features, such as strength, location, instant of formation and the number of vortices depend upon the airfoil geometry, frequency of oscillation, amplitude of oscillation and Reynolds number. These principal and secondary features together determine the aerodynamic characteristics of the oscillating airfoil.

The formation of the leading-edge vortex, having concentric equivorticity lines, starts with convection of vorticity from the leading-edge region, giving rise to equivorticity lines that turn around towards the leading edge forming a vorticity tongue (Figs. 10a, 10b, and 11a). As the incidence of the airfoil is increased, the flow going around the leading edge remains attached to the surface until the flow separation from trailing edge reaches the leading-edge region. Further increase in incidence moves the flow above the separated region near the leading edge away from the surface as it whips around the leading edge. Continuity of the flow requires the separated flow to come closer to the surface in order to resume the approximate direction of the surface, developing a neck in streamlines and equivorticity lines (Figs. 10c, 11b, 12c, and 13a). Next, the upstream flow near the surface separates, upstream of this neck in the streamlines, forming a small bubble (Fig. 12c). As the incidence is further increased, the separated streamline moves further outward, and the above neck narrows. Eventually the separated flow reattaches, forming a bubble which encloses the above bubble. Comparison of the experimental "vortex" as seen in Figs. 11c and 14a with the leading-edge vortex formed of concentric equivorticity lines speaks for itself. This description of the formation of the leading-edge vortex essentially holds for the trailing-edge stall and the stall due to the abrupt turbulent boundary layer separation in the forward portion of the airfoil. In the transition bubble bursting type of stall, laminar separated flow cannot maintain its course moving away from the airfoil and hence reattaches as turbulent flow forming, thereby the leading-edge vortex. The above discussion suggests that the essential ingredients are flow separation and a constriction in streamline pattern with possible flow reattachment for the formation of the leading-edge vortex observed in experiments during the dynamic stall of oscillating airfoils.

The actual formation of the leading-edge vortex does not cause moment or lift stall, and consequently, it does not initiate dynamic stall. In fact, during the formation of this vortex, lift continues to increase along the inviscid trend. The growth and initial downstream travel of this vortex initiate the moment stall, followed by lift stall. Another characteristic of this vortex is that generally when it increases lift, the pitching moment around the quarter chord location decreases. The key to preventing dynamic stall seems either to control the position and strength of this vortex, or not let it be formed at all, during the entire cycle of oscillation.

There are simplified, theoretical methods to determine dynamic stall and aerodynamic characteristics of oscillating airfoils. These methods are the discrete potential vortex approach, the thin boundary-layer approach and the strong interaction approach (Ref. 1). At present, these approaches do not give satisfactory results (Ref. 1). Apart from that, the thin boundary-layer approach cannot solve the above problem. (See also Ref. 1, page 23, and Ref. 47, page 26.) Further, we believe that strong interaction approach would be complex to implement and would be as time-consuming (computationally) as solutions of the Navier-Stokes equation. This approach would solve the potential flow region, the boundary-layer region and the separated region, respectively, with potential flow methods, the unsteady boundary-layer equation and the Navier-Stokes equation. One has to iterate between these three regions that would have to be continuously matched. These iteration and matching procedures make this approach considerably more difficult to solve the above problem. Alternatively, it is possible to use discrete vortices to represent the separated region and solve this region along with the potential flow region, and then couple this solution with that for the boundary-layer equation. But this would suffer generally from the same limitations as the discrete potential vortex approach. In short, a lot of work needs to be done in perfecting the simplified methods; and the Navier-Stokes solutions presented in this paper would provide some insight for doing just that.

Laminar studies of flow field around bluff and slender bodies at $R > 100$, using the Navier-Stokes and continuity equation in terms of stream function and vorticity must include plots of equivorticity lines because vorticity is a good indicator of the quality of solutions. Studies without this information suffer seriously. In the present study, the results for $R = 10,000$ are not completely satisfactory as stated in Section 5. However, the qualitative flow behavior is correct.

In summary, there are three important contributions of this paper: (1) the solutions of the Navier-Stokes and continuity equation around an oscillating airfoil, (2) the explanation as to how the leading-edge vortex is formed, and (3) a higher order numerical method to solve the stream function and vorticity equation.

ACKNOWLEDGMENT

Dr. W. J. McCroskey has monitored this work. His interest in the physics of oscillating airfoils has been a valuable source of encouragement to the author. During the final stages of this work, his comments and suggestions have helped in improving the contents of this paper. At his request, Monsieur Werlé

(ONERA) conducted water tunnel experiments and kindly provided flow visualization pictures under France - U.S. Army Memorandum of Understanding. Discussions with Mr. R. MacCormack led to the form of dissipation term used in the vorticity equation.

This research was supported by USAARMDL and NASA Ames Research Center. The work was done under NASA grants NCA 2 OR745-602 and NAG 2255.

REFERENCES

1. McCroskey, W. J., "Some Current Research in Unsteady Fluid Dynamics — The 1976 Freeman Scholar Lecture," *ASME Journal of Fluids Eng.*, Vol. 1, 1977, pp. 8-39.
2. McCroskey, W. J. and Fisher, R. K., Jr., "Detailed Aerodynamic Measurements on a Model Rotor in the Blade Stall Regime," *Journal American Helicopter Society*, Vol. 17, No. 1, 1972, pp. 20-30.
3. Dadone, L. U. and Fukushima, T., "Investigation of Rotor Blade Element Airloads for a Teetering Rotor in the Blade Stall Regime," NASA CR-137,534, 1975.
4. McCroskey, W. J., Carr, L. W., and McAlister, K. W., "Dynamic Experiments on Oscillating Airfoils," *AIAA Journal*, Vol. 14, No. 1, 1976, pp. 57-63.
5. Ham, N. D., "Aerodynamic Loading on a Two-Dimensional Airfoil During Dynamic Stall," *AIAA Journal*, Vol. 6, No. 10, 1968, pp. 1927-1934.
6. Ham, N. D. and Garelick, M. S., "Dynamic Stall Considerations in Helicopter Rotors," *Journal American Helicopter Society*, Vol. 13, 1968, pp. 49-55.
7. McCroskey, W. J., "Recent Developments in Dynamic Stall," *Proceedings of the University of Arizona/ USAF OSR Symposium on Unsteady Aerodynamics*, Vol. 1, Kinney, R. B., ed., 1975, pp. 1-33.
8. Mehta, U. B. and Lavan, Z., "Starting Vortex, Separation Bubbles, and Stall — a Numerical Study of Laminar Unsteady Flow Around an Airfoil," *Journal Fluid Mechanics*, Vol. 67, 1975, pp. 227-256.
9. Theodorsen, T. and Garrick, I. E., "General Potential Theory of Arbitrary Wing Sections," NACA TR-452, 1933.
10. Ives, D. C., "A Modern Look at Conformal Mapping Including Multiply Connected Regions," *AIAA Journal*, Vol. 14, No. 8, 1976, pp. 1006-1011.
11. Thompson, J. F., Thames, F. C., and Mastin, C. W., "Boundary-Fitted Curvilinear Coordinate Systems for Solution of Partial Differential Equations on Field Containing any Number of Arbitrary Two-Dimensional Bodies," NACA CR-2729, 1977.
12. Steger, J. L., "Implicit Finite Difference Simulations of Flow About Arbitrary Geometries with Application to Airfoils," AIAA Paper 77-665, June 1977.
13. Wu, J. C., "Numerical Boundary Conditions for Viscous Flow Problems," *AIAA Journal*, Vol. 14, No. 8, 1976, pp. 1042-1049.
14. Lugt, H. J. and Haussling, H. J., "Laminar Flow Past an Abruptly Accelerated Elliptic Cylinder at 45° Incidence," *Journal Fluid Mechanics*, Vol. 65, 1974, pp. 711-734.
15. Lugt, H. J. and Ohring, S., "Rotating Elliptic Cylinders in a Viscous Fluid at Rest or in a Parallel Stream," *J. Fluid Mechanics*, Vol. 73, 1977, pp. 127-156.
16. Wu, J. C. and Thompson, J. R., "Numerical Solutions of Time-Dependent Incompressible Navier-Stokes Equations Using an Integro-Differential Formulation," *Computers and Fluids*, Vol. 1, 1973, pp. 197-215.
17. Stone, H. L., "Iterative Solution of Implicit Approximations of Multidimensional Partial Equations," *SIAM, J. Num. Anal.*, Vol. 5, No. 3, 1968, pp. 530-558.
18. Yanenko, N. N., *The Method of Fractional Steps*, Springer-Verlag, 1971.
19. Douglas, J., Jr. and Gunn, J. E., "A General Formulation of Alternating Direction Methods, Part I, Parabolic and Hyperbolic Problems," *Num. Math.*, Vol. 6, 1964, pp. 428-453.
20. Lin, C. L., Pepper, D. W., and Lee, S. C., "Numerical Methods for Separated Flow Solutions Around a Circular Cylinder," *AIAA Journal*, Vol. 14, No. 7, July 1976, pp. 900-907.
21. Wu, J. C. and Sampath, S., "A Numerical Study of Viscous Flow Around an Airfoil," AIAA Paper 76-337, AIAA 9th Fluid and Plasma Dynamics Conference, July 1976.
22. Briley, W. R., "A Numerical Study of Laminar Separation Bubbles Using the Navier-Stokes Equations," *Journal Fluid Mechanics*, Vol. 47, 1971, pp. 713-736.
23. Briley, W. R. and McDonald, H., "Numerical Prediction of Incompressible Separation Bubbles," *Journal Fluid Mechanics*, Vol. 69, 1975, pp. 631-656.
24. Kopal, Z., *Numerical Analysis*, 2nd ed., John Wiley & Sons, 1961.

25. Orszag, S. A. and Israeli, M., "Numerical Simulation of Viscous Incompressible Flows," *Annual Review of Fluid Mechanics*, Vol. 6, van Dyke, M., *et al.*, eds., Annual Reviews, Inc., Palo Alto, Calif., 1974, pp. 281-318.

26. Kreiss, H. and Oliger, J., "Methods for the Approximate Solution of Time Dependent Problems," GARP Publications Series, No. 10, 1973.

27. Bramble, J. H. and Hubbard, B. E., "On the Formulation of Finite Difference Analogues of the Dirichlet Problem for Poisson's Equation," *Numerische Mathematik*, Vol. 4, 1962, pp. 313-327.

28. Israeli, M., "A Fast Implicit Numerical Method for Time Dependent Viscous Flows," *Studies in Applied Math.*, Vol. 39, No. 4, 1970, pp. 327-349.

29. Woods, L. C., "A Note on the Numerical Solution of Fourth-Order Differential Equations," *Aero. Quart.*, Vol. 5, 1954, p. 176.

30. Roache, P. J., *Computational Fluid Dynamics*, Hermosa Publishers, 1972, pp. 146-148.

31. Fromm, J. E., "A Method for Computing Nonsteady, Incompressible, Viscous Fluid Flows," Los Alamos Scientific Laboratory Report LA-2910, 1963.

32. Warming, R. F. and Beam, R. M., "On the Construction and Application of Implicit Factored Schemes for Conservation Laws," *SIAM-AMS Proceedings of the Symposium on Computational Fluid Dynamics*, New York, 1977.

33. MacCormack, R. W., "An Efficient Numerical Method for Solving the Time-Dependent Compressible Navier-Stokes Equations at High Reynolds Number," *Computing in Applied Mechanics*, AMD Vol. 18, Dec. 1976, pp. 49-64.

34. Beam, R. M. and Warming, R. F., "An Implicit Finite-Difference Algorithm for Hyperbolic System in Conservative-Law Form," *J. Comput. Phys.*, Vol. 22, 1976, pp. 87-110.

35. Orszag, S. A. and Jayne, L. W., "Local Errors of Difference Approximations to Hyperbolic Equations," *J. of Comp. Phys.*, Vol. 14, 1974, pp. 93-103.

36. ONERA Film OAh No. 2506, Jan. 1976.

37. Werlé, H., "Hydrodynamic Flow Visualization," *Annual Review of Fluid Mechanics*, Vol. 5, van Dyke, M., *et al.*, eds., Annual Reviews, Inc., Palo Alto, Calif., 1973, pp. 361-382.

38. Werlé, H., "Visualisation Hydrodynamique de L'écoulement Autour d'une Pale Oscillante," ONERA Rapport Technique No. 56/1369 AN, Jan. 1976.

39. Morkovin, M. V., private communication.

40. Sears, W. R. and Telionis, D. P., "Unsteady Boundary-Layer Separation," in Recent Research of Unsteady Boundary Layers, *Proceeding International Union of Theoretical and Applied Mechanics*, Quebec, Vol. 1, E. A. Eichelbrenner, ed., 1971, pp. 404-447.

41. Goldstein, S., "On Laminar Boundary-Layer Over a Position of Separation," *Quart J. Mech. Appl. Math.*, Vol. 1, 1948, p. 43.

42. Crabtree, L. V., "Effects of Leading-Edge Separation on Thin Wings in Two-Dimensional Incompressible Flow," *J. of the Aero. Sci.*, Vol. 24, No. 8, 1957, pp. 597-604.

43. Arakawa, A., "A Computational Design for the Long Term Integration of the Equations of Atmospheric Motion," *J. Comp. Phys.*, Vol. 1, 1966, p. 119.

44. Buzbee, B. L., Golub, G. H., and Nielson, C. W., "On Direct Methods for Solving Poisson's Equation," *SIAM J. Num. Anal.*, Vol. 7, 1970, pp. 627-656.

45. Deiwert, G. S., "Computation of Separated Transonic Turbulent Flows," *AIAA Journal*, Vol. 14, No. 6, June 1976, pp. 735-740.

46. Levy, L. L., Jr., "An Experimental and Computational Investigation of Steady and Unsteady Transonic Flow Field About an Airfoil and a Solid Wall Test Channel," AIAA Paper 77-678, June 1977.

47. Carr, L. W., McAlister, K. W., and McCroskey, W. J., "Analysis of the Development of Dynamic Stall Based on Oscillating Airfoil Experiments," NASA TN D-8382, Jan. 1977.

48. Sampath, S., "A Numerical Study of Incompressible Viscous Flow Around Airfoils," Ph.D. Thesis, Georgia Institute of Technology, Sept. 1977.

49. Kwak, D., Reynolds, W. C., Ferziger, J. H., "Three-Dimensional Time-Dependent Computation of Turbulent Flow," Report No. TF-5, Dept. of Mech. Engrg., Stanford University, May 1975.

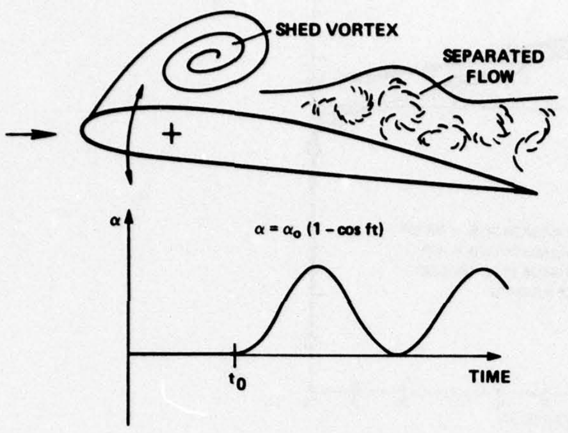

Fig. 1 Problem definition.

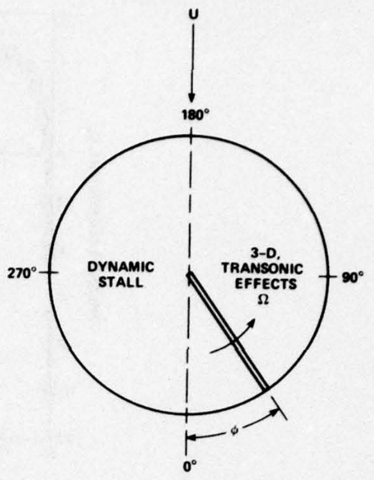

Fig. 2 A rotating helicopter blade in uniform flow.

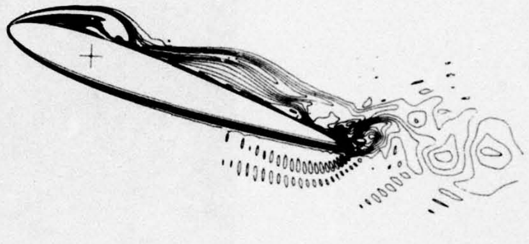

Fig. 4 Equivorticity lines, second-order scheme, first cycle; $R = 10{,}000$, $k = 0.25$, $\alpha = 16.52°$ ↑.

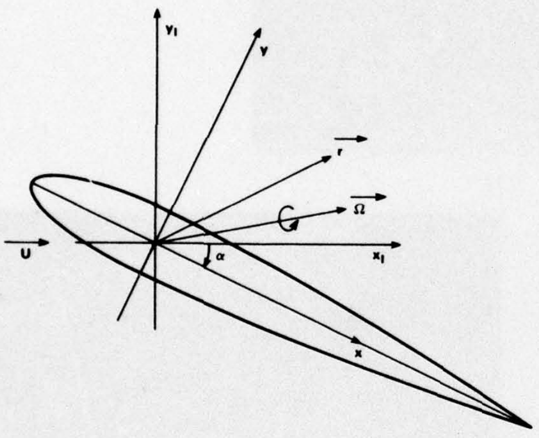

Fig. 3 Fixed and rotating coordinate systems.

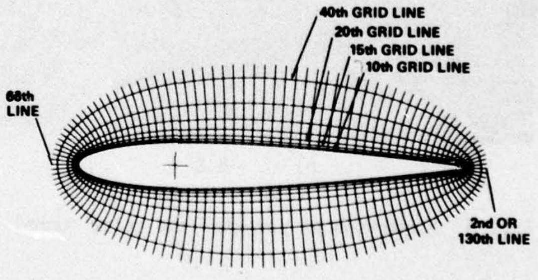

Fig. 5 Grid distribution around 12% airfoil for $R = 10^4$.

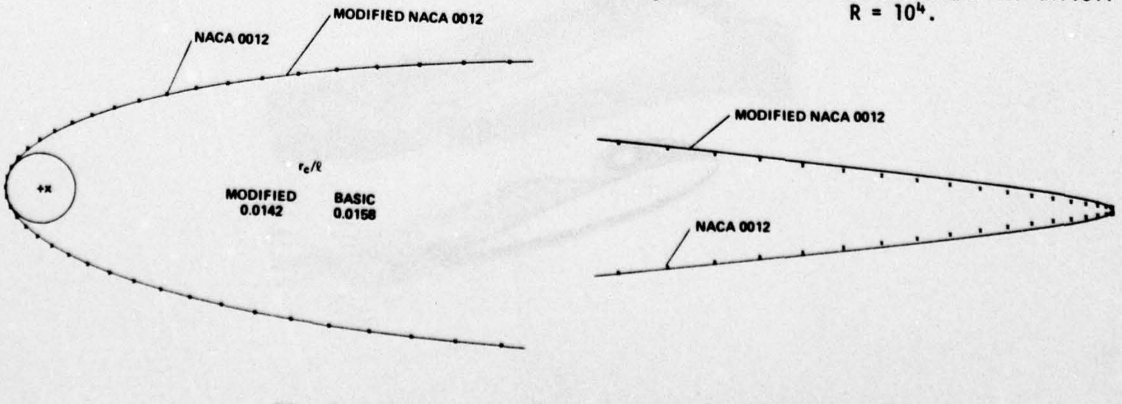

Fig. 6 Leading and trailing edge geometry of 0012 airfoil.

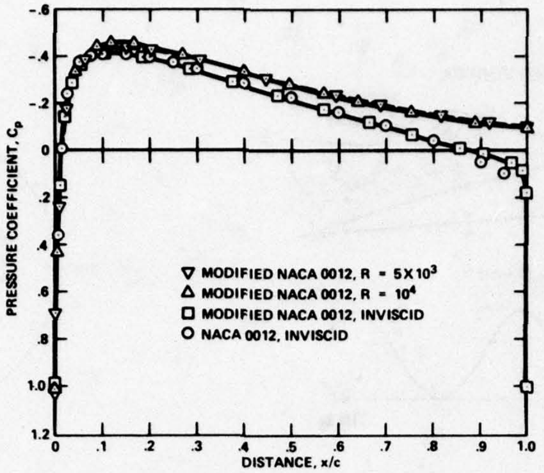

Fig. 7 Pressure distribution on 0012 airfoil at α = 0°.

a) α ~ 14°

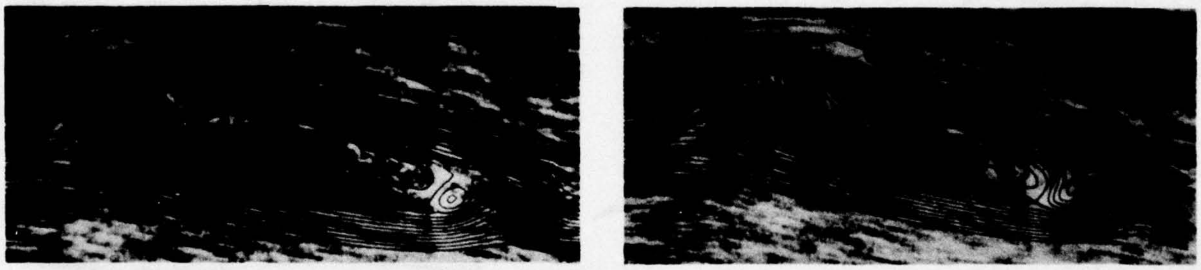

b) α ~ 15.8°

c) α ~ 16.56°

Fig. 8 Comparison of computer and water tunnel flow simulations, Re = 10^4, k = 0.25, second-order scheme.

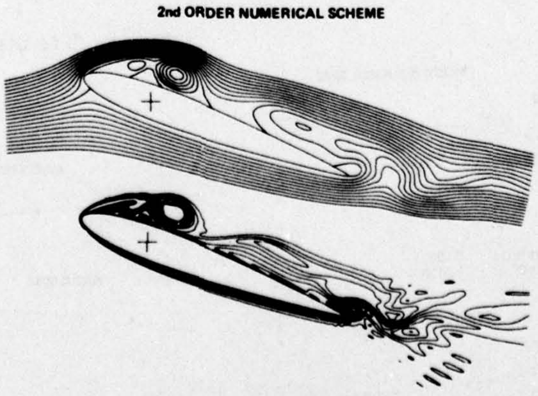

Fig. 9 Streamlines and equivorticity lines, R = 5000, k = 0.5, α = 20°.

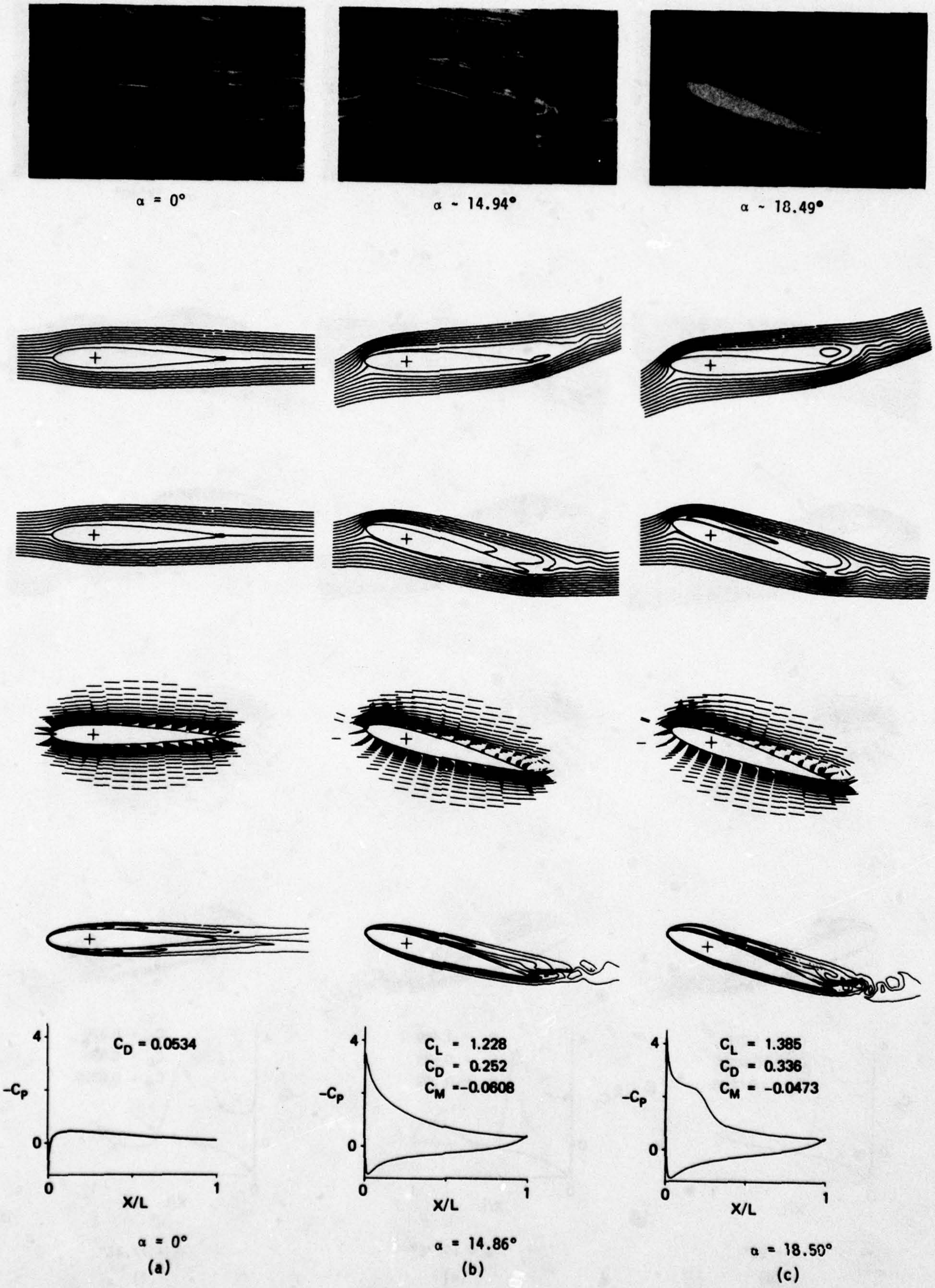

Fig. 10 Flow characteristics, first cycle; R = 5000, k = 0.5.

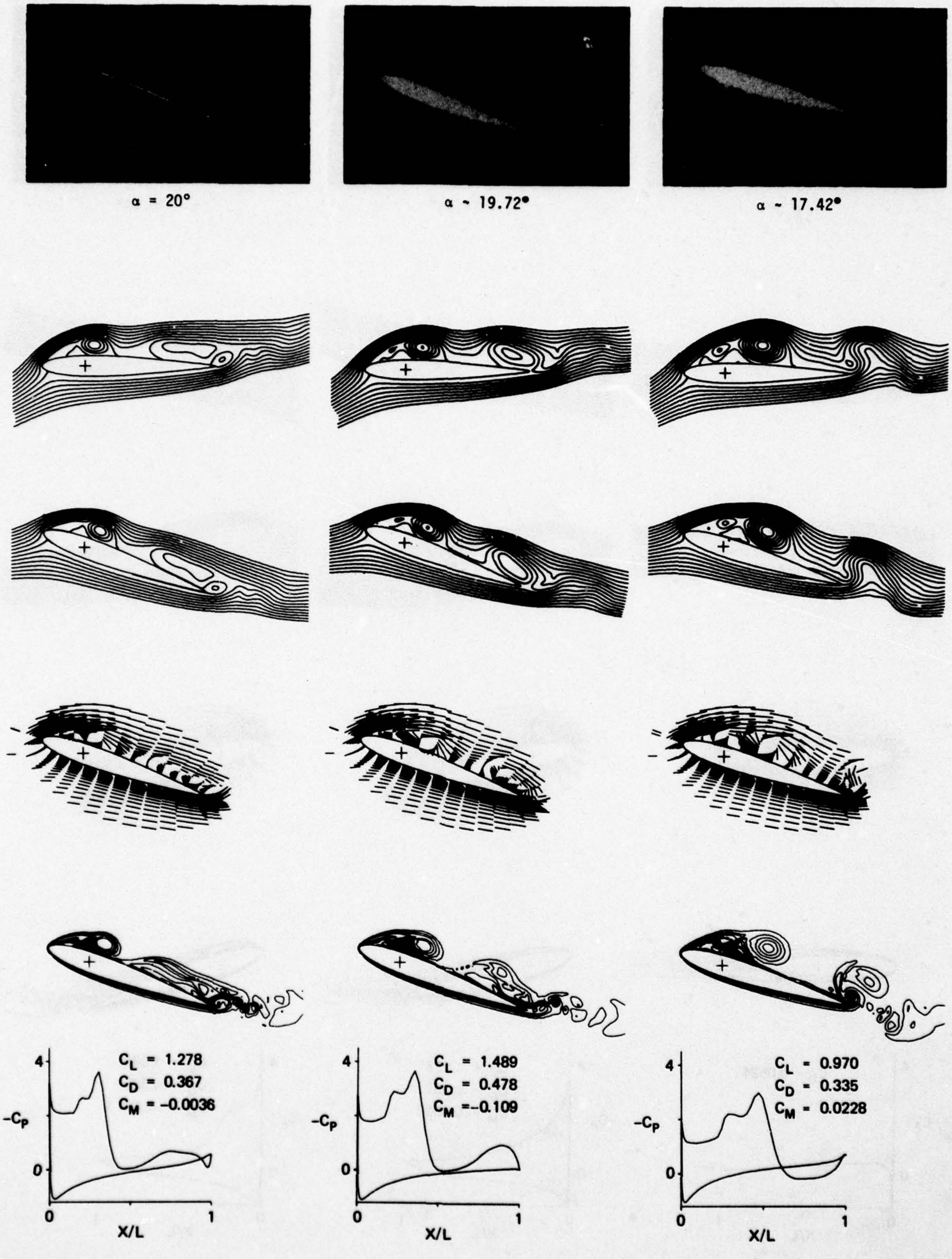
α = 20°

α ~ 19.72°

α ~ 17.42°

α = 20°
(d)

α = 19.76°
(e)

α = 17.47°
(f)

Fig. 10 (Continued).

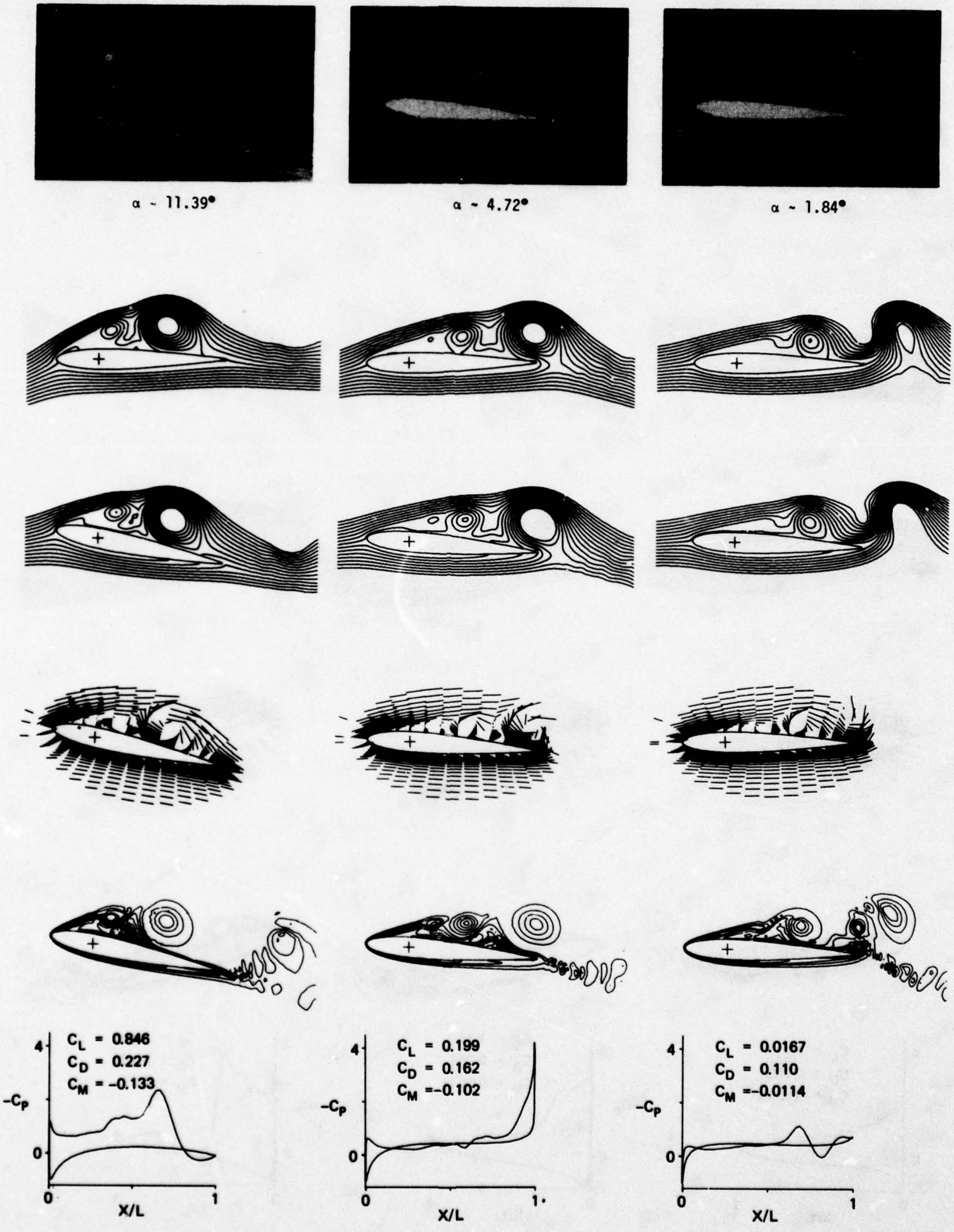

α = 11.36°
(g)

α = 4.78°
(h)

α = 1.82°
(i)

Fig. 10 (Concluded).

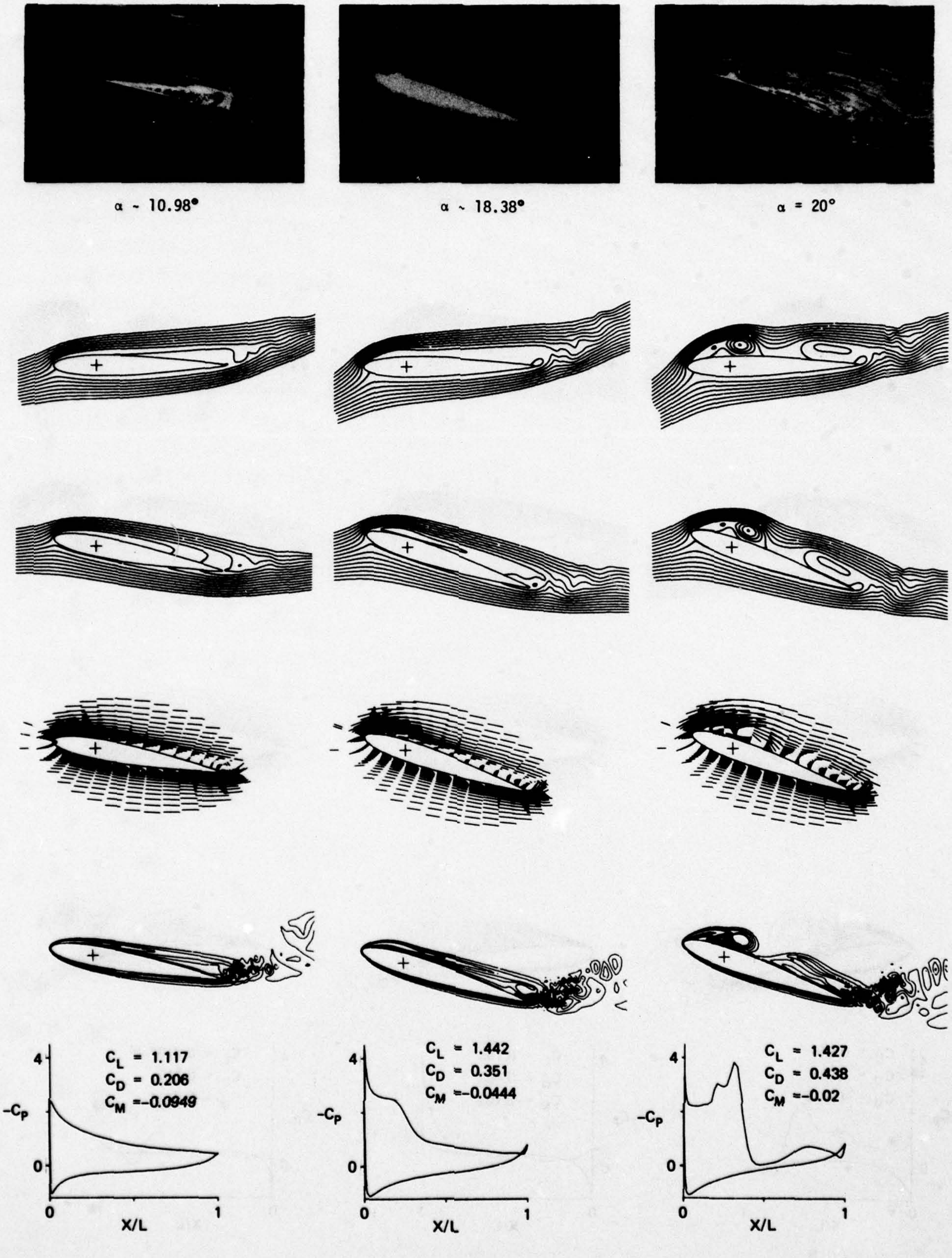

α = 11.04°
(a)

α = 18.35°
(b)

α = 20°
(c)

Fig. 11 Flow characteristics, second cycle; R = 5000, k = 0.5.

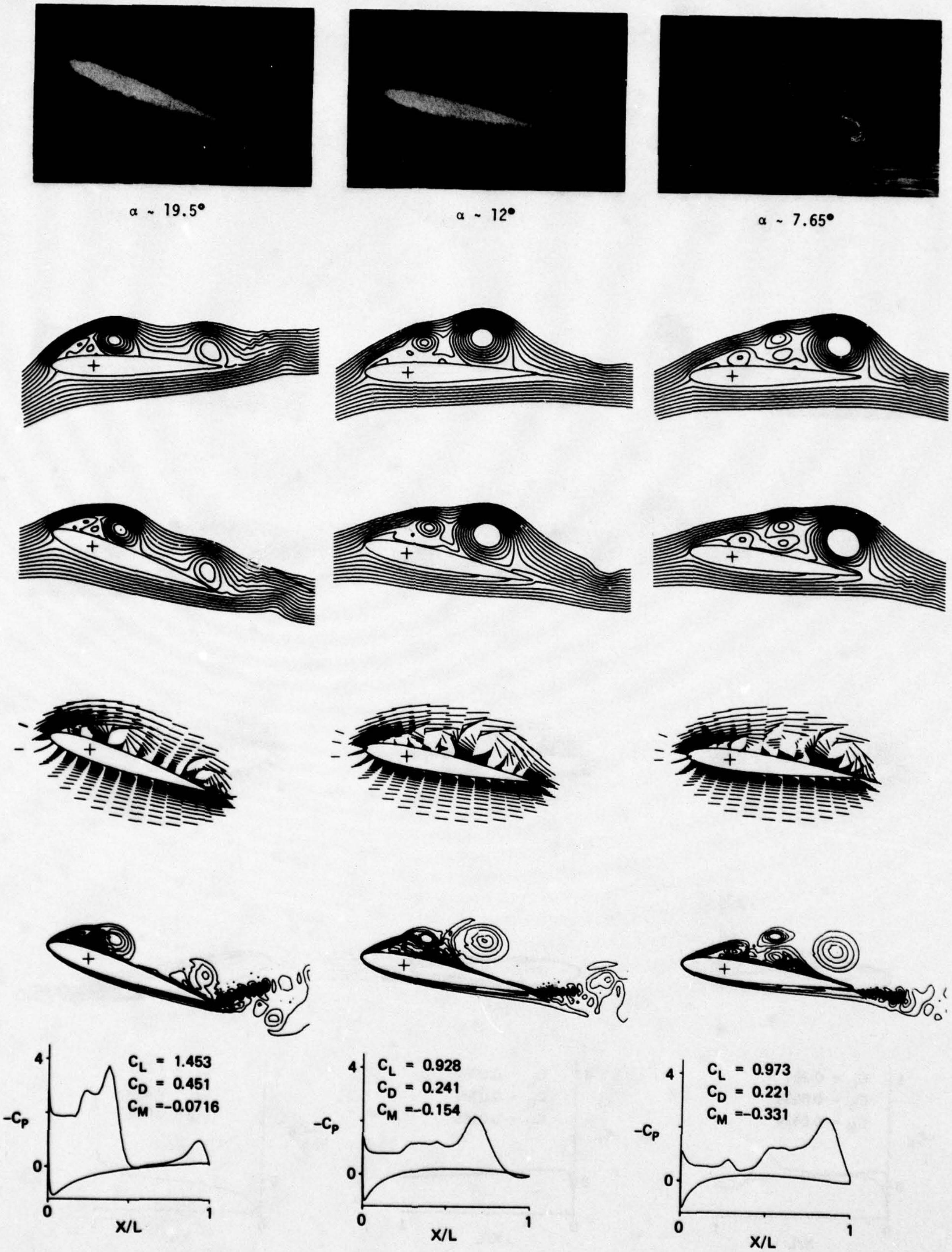

α = 19.48°
(d)

α = 11.63°
(e)

α = 7.68°
(f)

Fig. 11 (Continued).

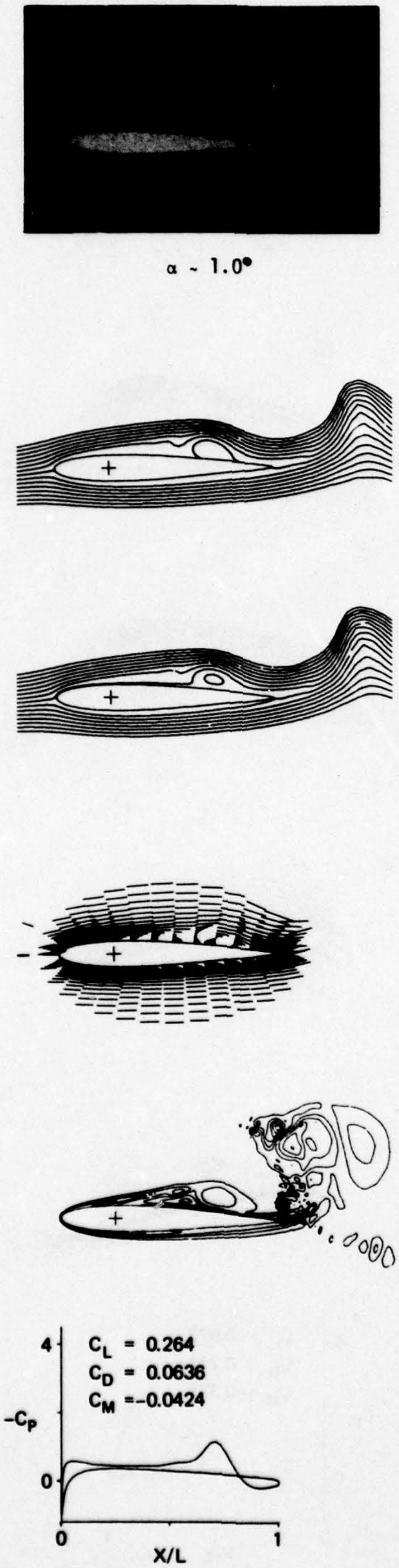

α = 0.58°

(g)

Fig. 11 (Concluded).

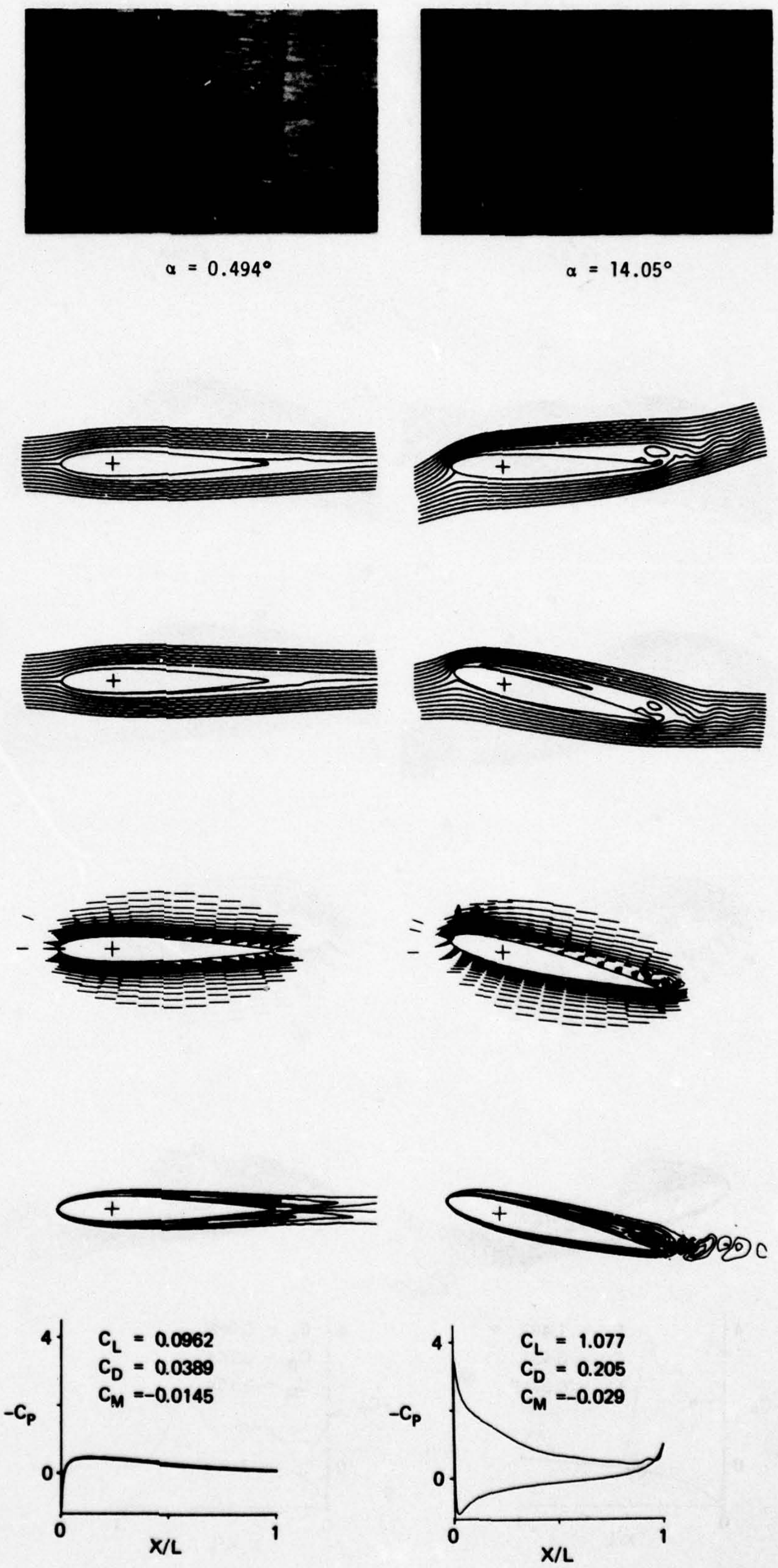

α = 0.475° (a)

α = 14.06° (b)

Fig. 12 Flow characteristics, first cycle; R = 10,000, k = 0.25.

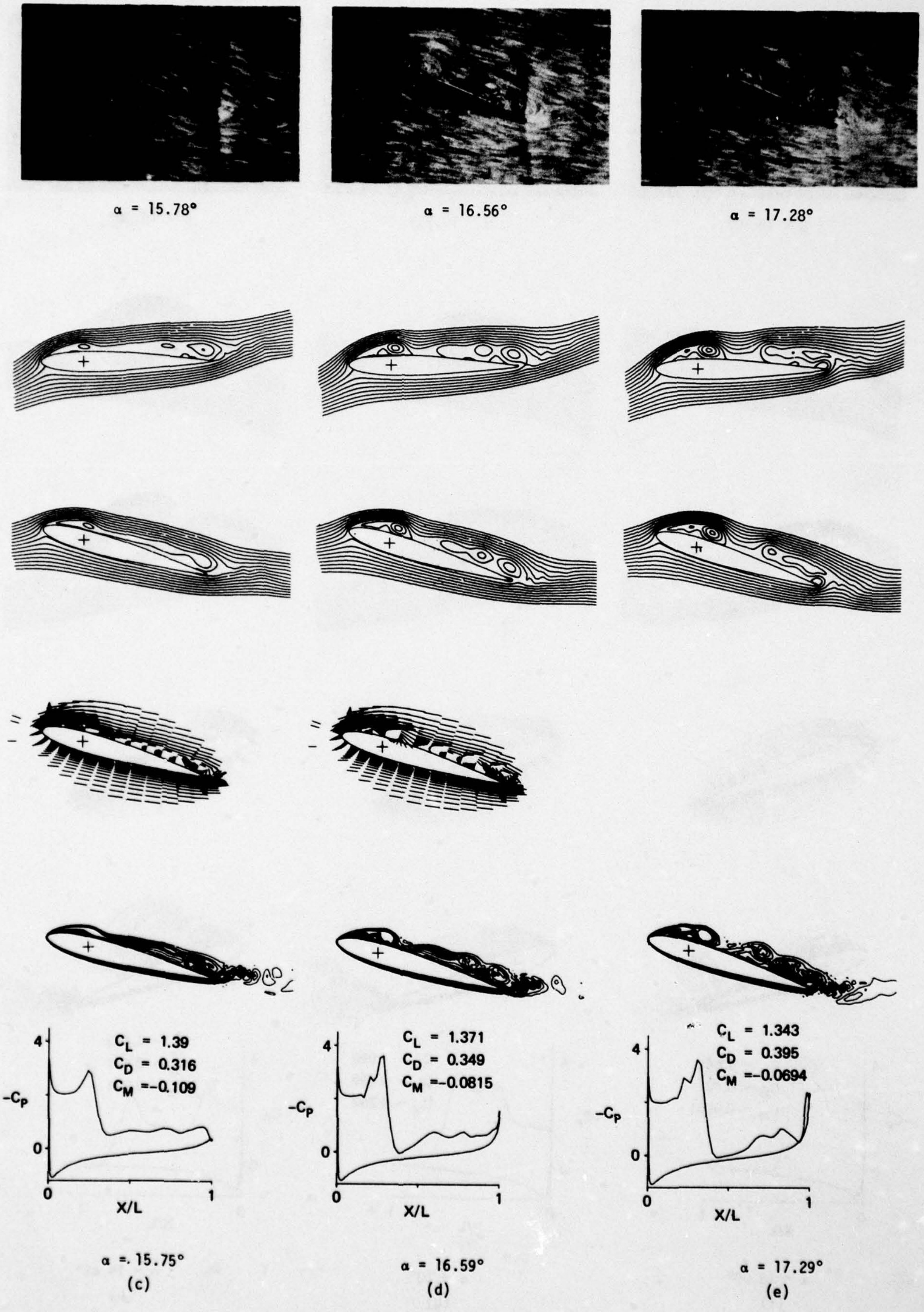

α =. 15.75°
(c)

α = 16.59°
(d)

α = 17.29°
(e)

Fig. 12 (Continued).

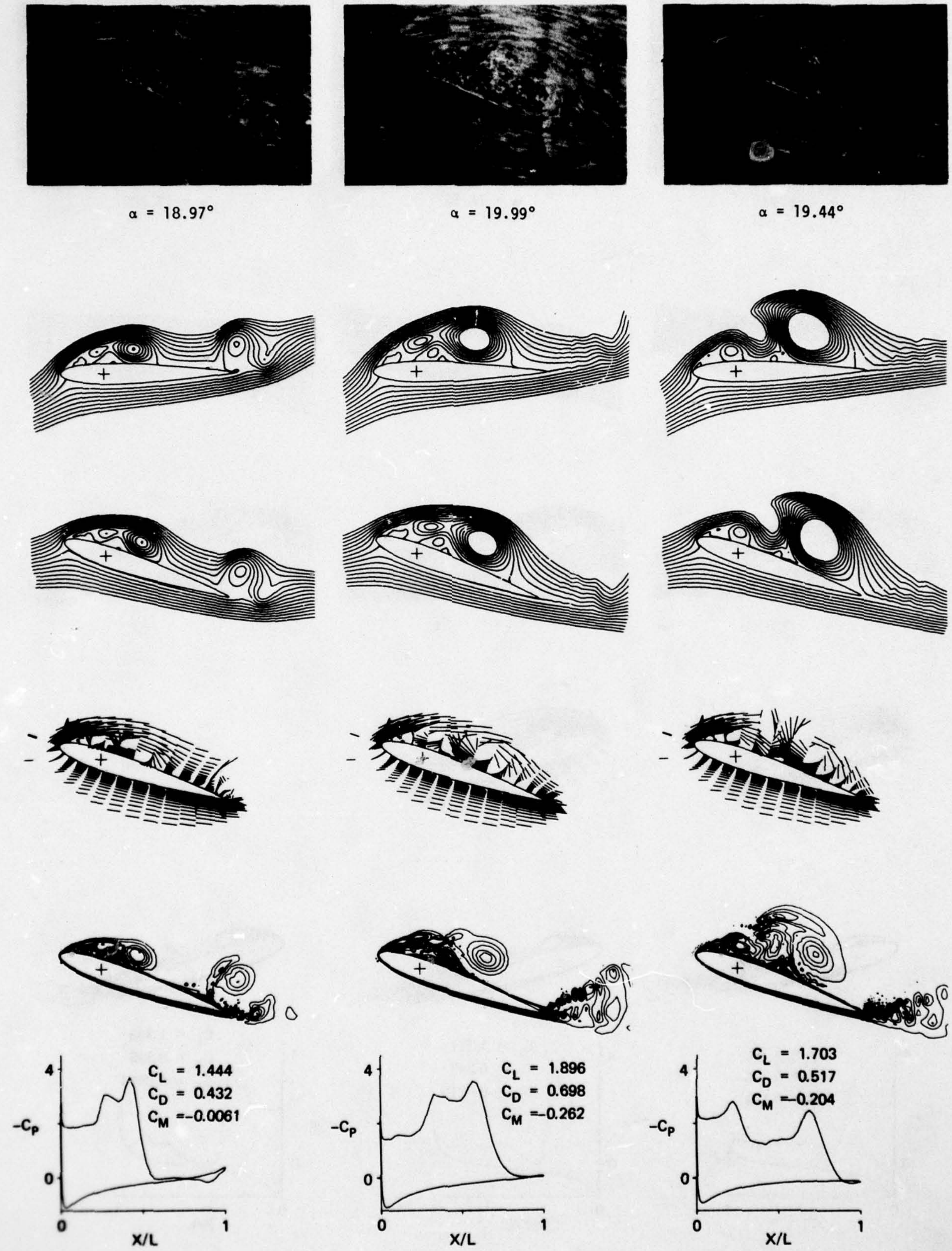

α = 18.99°
(f)

α = 20°
(g)

α = 19.45°
(h)

Fig. 12 (Continued).

α = 19.06°　　α = 15.95°　　α = 14.24°

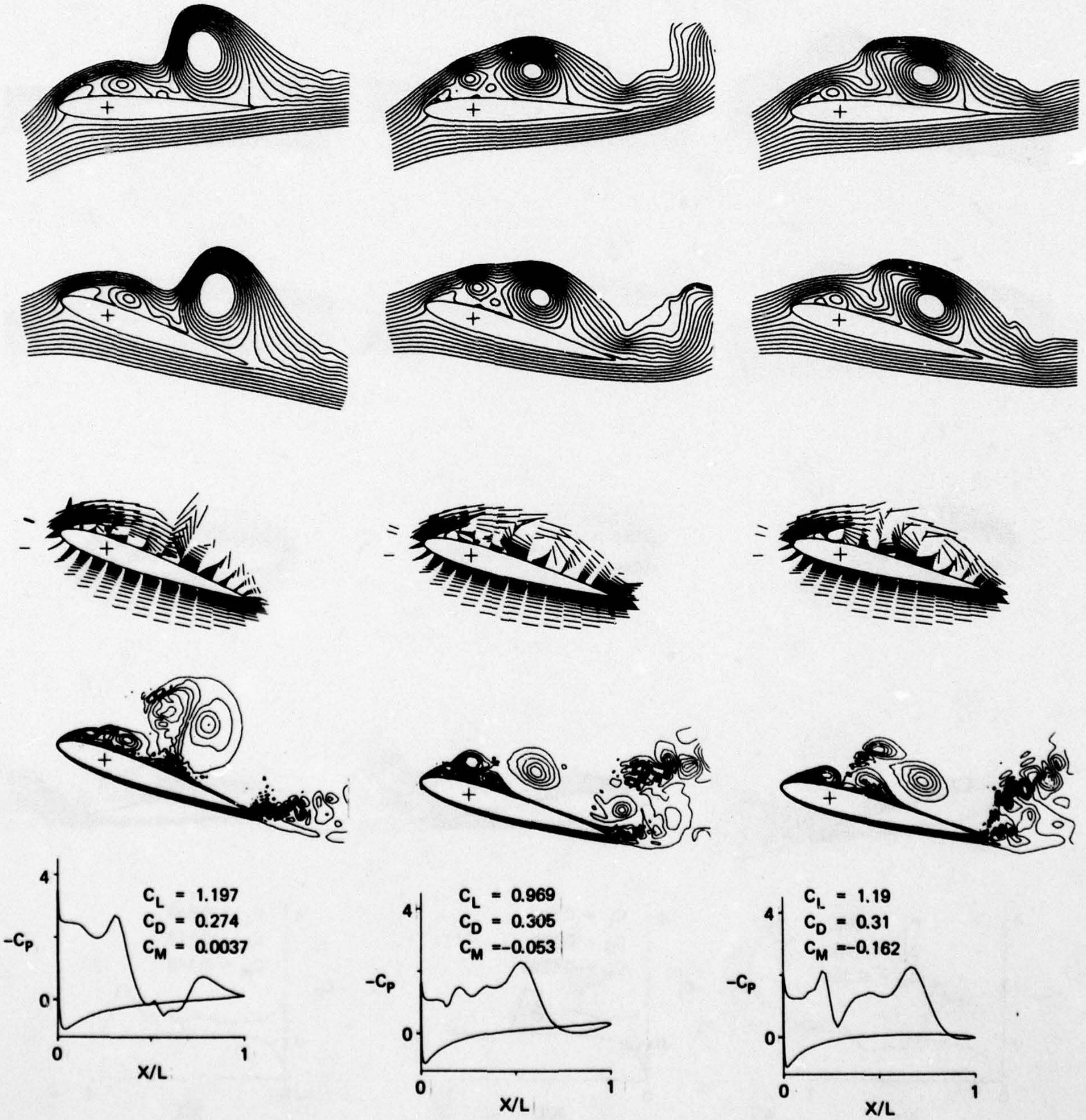

α = 19.07°
(j)

α = 15.94°
(k)

α = 14.27°
(l)

Fig. 12 (Continued).

α = 12.37°

α = 7.45°

α = 5.59°

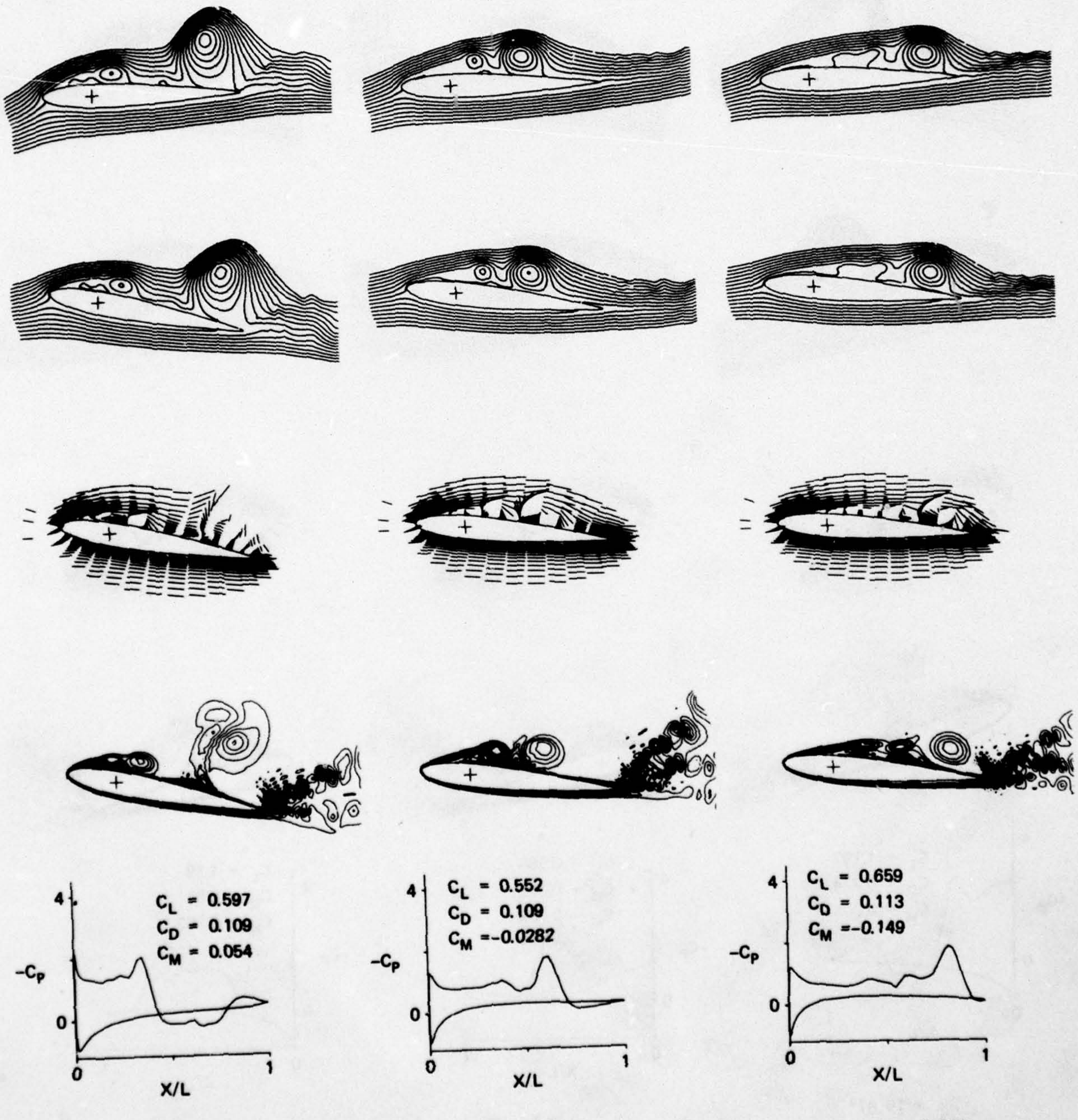

α = 12.36°
(m)

α = 7.46°
(n)

α = 5.56°
(o)

Fig. 12 (Continued).

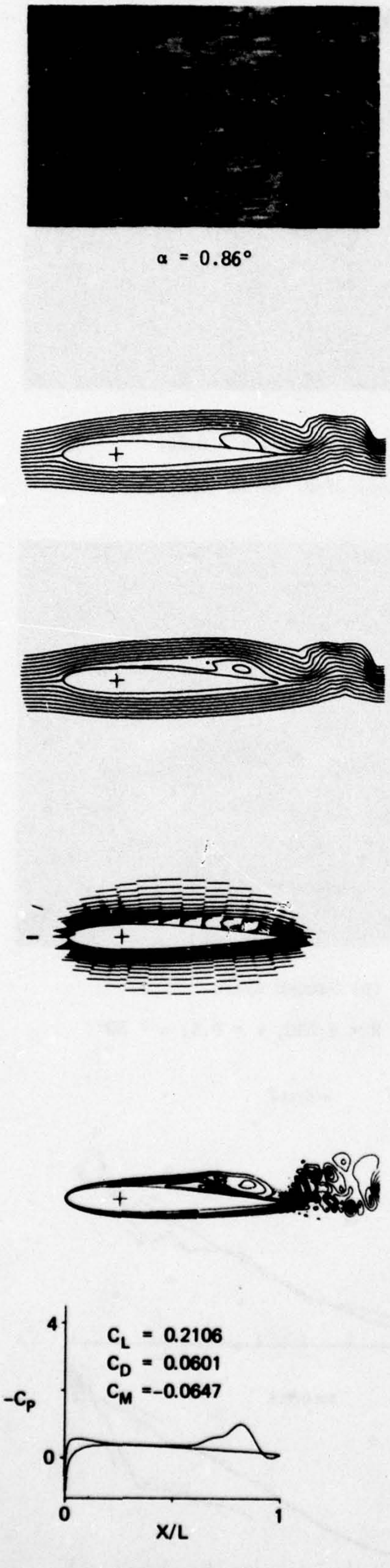

α = 0.89°
(p)

Fig. 12 (Concluded).

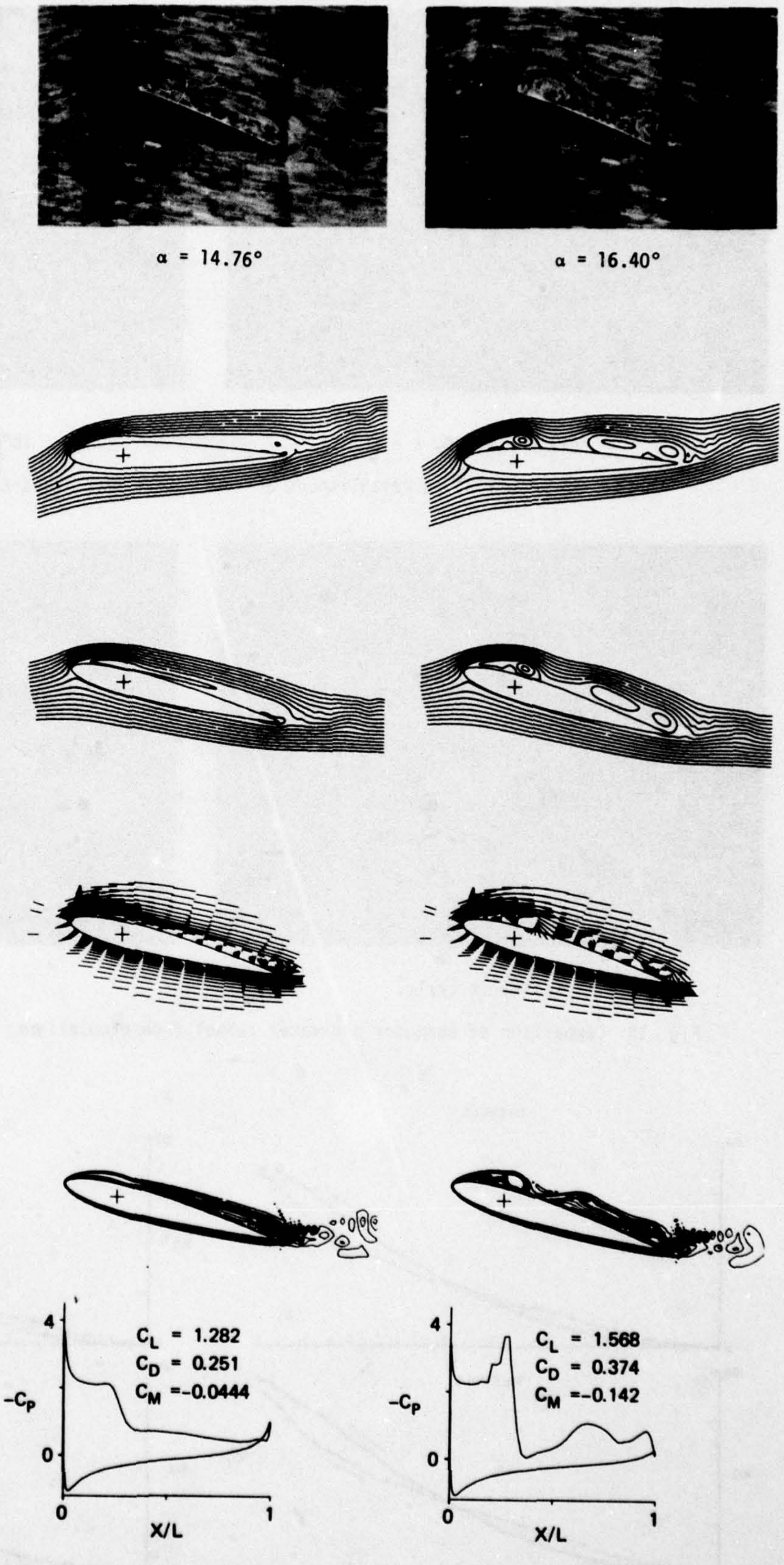

α = 14.73°
(a)

α = 16.41°
(b)

Fig. 13 Flow characteristics, second cycle; R = 10,000, k = 0.25.

(a) R = 5,000, k = 0.5.

(b) R = 10,000, k = 0.25.

Fig. 14 Oscillation established, α = 20°, NACA 0012 (courtesy of H. Werlé (ONERA).

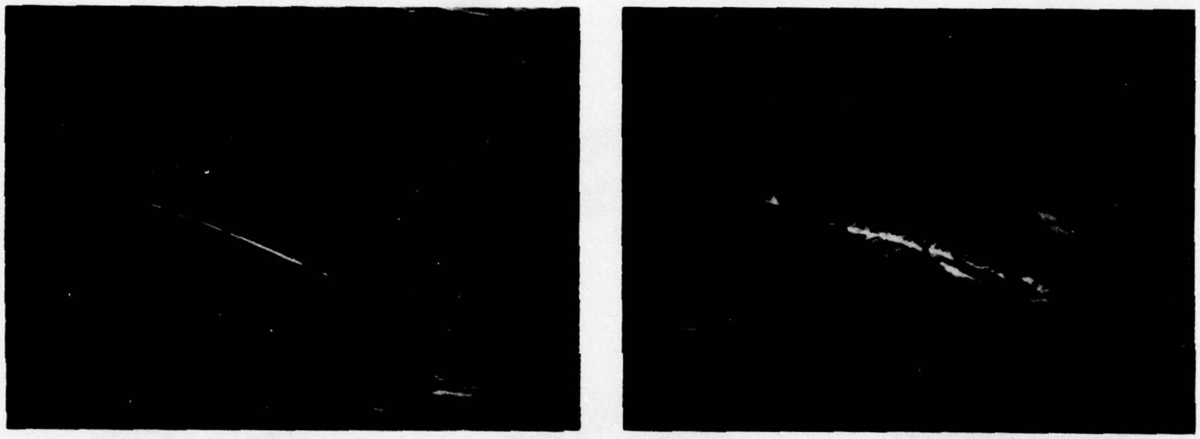

(a) First cycle.

(b) Second cycle.

Fig. 15 Comparison of computer and water tunnel flow simulations; R = 5,000, k = 0.5, α = 20°.

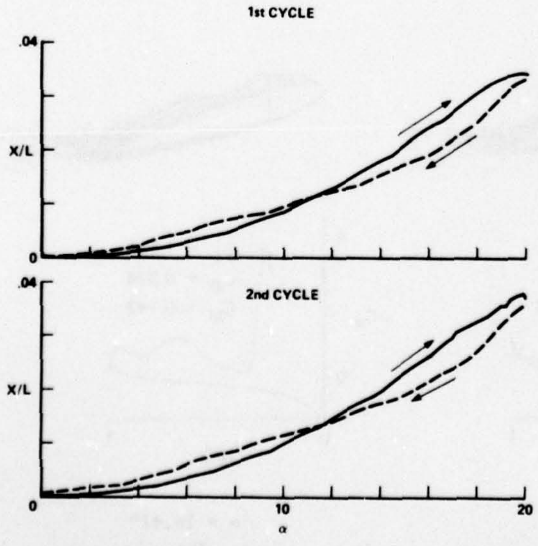

Fig. 16 Location of front stagnation point; $R = 5\times10^3$, k = 0.5.

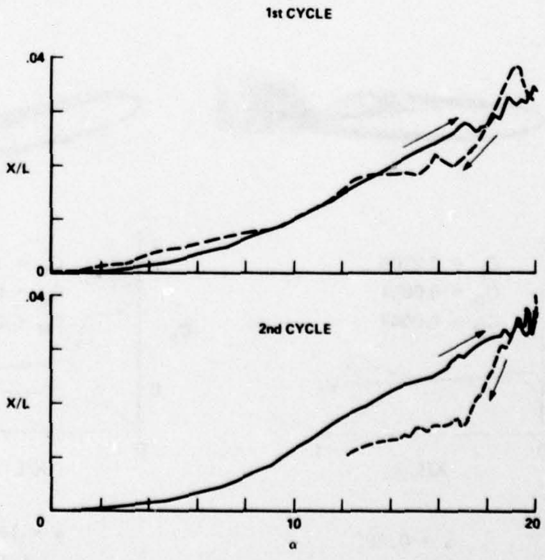

Fig. 17 Location of front stagnation point; $R = 10^4$, k = 0.25.

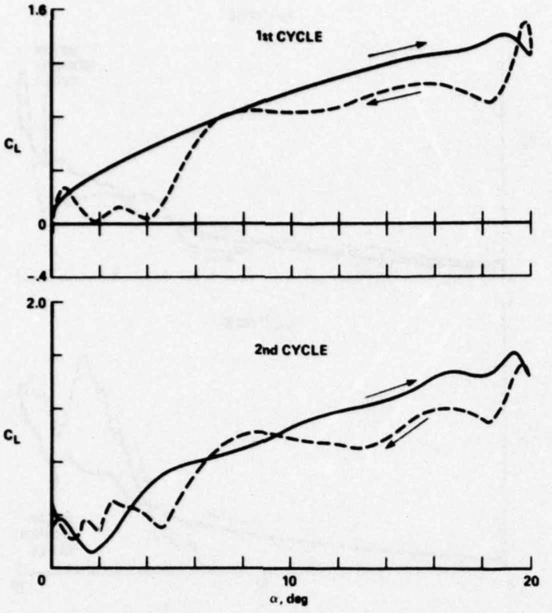

Fig. 18 Lift coefficient, R = 5×10^3, k = 0.5.

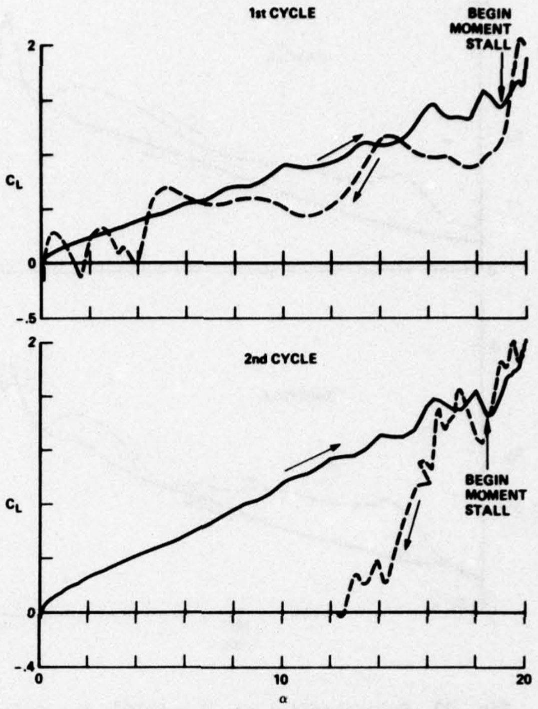

Fig. 19 Lift coefficient, R = 10^4, k = 0.25.

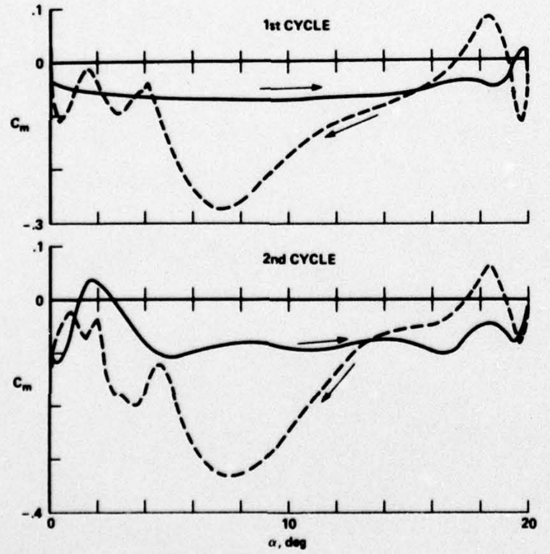

Fig. 20 Moment coefficient, R = 5×10^3, k = 0.5.

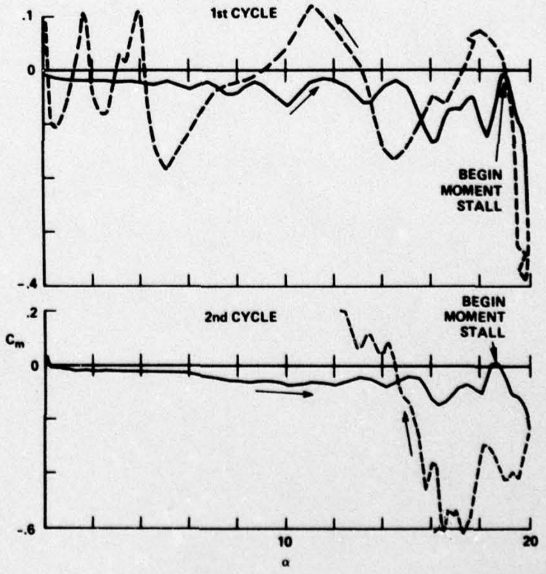

Fig. 21 Moment coefficient, R = 10^4, k = 0.25.

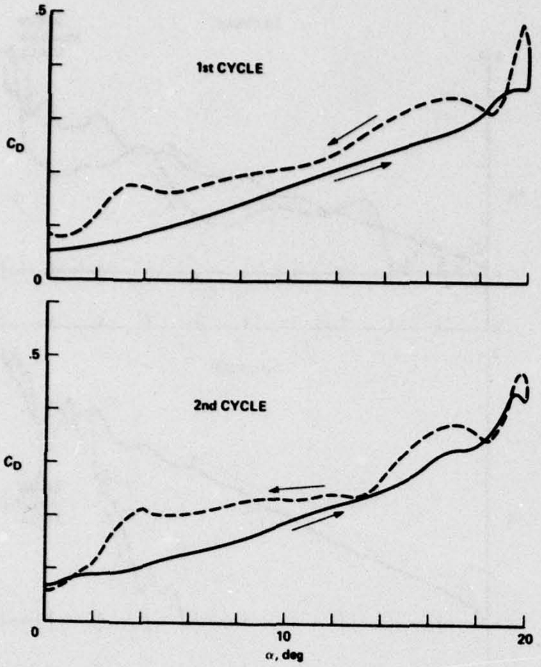

Fig. 22 Drag coefficient, R = 5×10^3, k = 0.5.

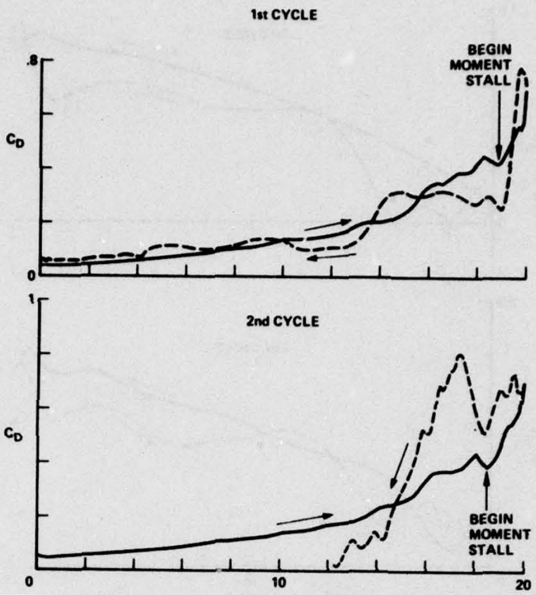

Fig. 23 Drag coefficient, R = 10^4, k = 0.25.

A NUMERICAL STUDY OF UNSTEADY VISCOUS FLOWS AROUND AIRFOILS

J. C. Wu, Professor
S. Sampath, Research Assistant
and N. L. Sankar, Research Assistant
School of Aerospace Engineering
Georgia Institute of Technology
Atlanta, Georgia 30332
U.S.A.

SUMMARY

The application of an integro-differential approach in the numerical study of unsteady viscous flows about airfoils is described. Two different procedures are presented. A procedure based on a stream function-vorticity formulation and on a transformation technique is used in a study of a flow about an impulsively started 9% thick Joukowski airfoil at an angle of attack of 15° and a Reynolds number of 1000. Numerical results are presented and compared with available finite-difference results. A second procedure based on a velocity-vorticity formulation and on a hybrid finite difference-finite element technique is used in a study of a flow about an oscillating 12% thick Joukowski airfoil at a Reynolds number of 1000. With either procedure, the unique ability of the integro-differential approach to confine the solution field to the vortical region of the flow is utilized. It is shown that this ability offers great computational advantages.

1. INTRODUCTION

During the past two decades, there has been a gradual but persistent increase in the willingness of aerodynamicists to accept the computer as a valuable, perhaps indispensable, tool in the prediction of fluid flows. This willingness is a consequence of the impressive progress made in recent years in the routine numerical solutions of differential equations describing many types of potential and boundary layer flows. For general viscous flows, i.e., flows past finite solid bodies and involving appreciable regions of separation, a capability for the routine computation of the flows has yet to be established, and the willingness to accept computer solutions has spurred extensive research efforts in this regard.

Because of its fundamental nature and practical importance, the general viscous flow problem has been a focal point of fluid dynamic research for more than a century. The mathematical difficulties attendant to the analytical solution of the equations describing the general viscous flow are known to be formidable. Numerical methods offer at the present the only prospect of accurate quantitative solutions under reasonably general circumstances.

Until relatively recently, computational aerodynamicists have emphasized the application of the finite-difference approach to the general viscous flow problem. This emphasis is an outgrowth of the success enjoyed by the finite-difference methods in the solution of various boundary layer problems. Although the boundary layer equations are simpler than the Navier-Stokes equations describing the general viscous flow, the two types of equations are both non-linear partial difference equations. Furthermore, the momentum equation for the time-dependent general viscous flow is parabolic, as is the boundary layer momentum equation. It had been hoped, therefore, that the finite-difference approach would lead to a routine computational capability for the time-dependent general viscous flow, with steady flow solutions, when they exist, considered as asymptotic limiting solutions at large time levels. In reality, however, the application of the finite-difference approach to the general viscous flow problem has fallen far short of earlier expectations. Most of the general viscous flows of practical importance in aerodynamics today remain beyond the scope of the finite-difference approach.

Several years ago, the first author of this article identified several major obstacles that caused the disparity of successes of the finite-difference approach as applied to the boundary layer and to the general incompressible viscous flows. Subsequently, a program of research was initiated with the goal of developing new approaches transcending the limitations of the finite-difference approach. This research program has now reached a reasonable stage of completeness. Progress made to date in applying a new approach to the study of unsteady incompressible laminar flows is summarized in this paper. Selected numerical results are presented for flows past airfoils to illustrate the application of this new approach. Additional numerical results as well as detailed descriptions of the specific numerical procedures are presented in doctoral dissertations of the second author (Ref. 1) and of the third author, the latter still being prepared. A major emphasis of the present article is to bring into focus the authors' understanding, acquired during the past few years of research, of the interplay between the numerical and physical aspects of the general viscous flow problem.

The distinguishing feature of the present approach is the formulation of the general viscous flow problem as a set of integro-differential equations. This feature represents a major departure from finite-difference methods based on the formulation of the problem as differential equations. Various attributes of the integro-differential approach have been studied and described in earlier articles (Refs. 1 to 11). In particular, it has been conclusively demonstrated by analyses and numerical illustrations that the approach possesses a unique ability to confine the solution field to the vortical region of the flow. For most problems of practical interest, the flow Reynolds number is high and the vortical region represents only a small fraction of the total flowfield. The ability to confine the solution field to the vortical region therefore offers the possibility of a drastically improved computational efficiency.

Although the present paper is concerned only with unsteady incompressible laminar flows, the utility of the integro-differential approach is not restricted to such flows. In a recent article (Ref. 3), the use of the integro-differential approach in conjunction with a two-equation turbulence model was demonstrated. Turbulent flow results obtained were found to agree well with experimental data. An integro-differential formulation was presented for compressible flows three years ago (Ref. 4). Because of the limited resources available, however, efforts of the present authors in implementing the integro-differential approach have been limited to incompressible flow problems. It has also been found that the general viscous flow problem may be formulated as a set of integral representations (Ref. 5) of field variables. The solution procedures developed for the integro-differential approach are directly applicable to methods based on the integral-representation approach. In particular, for steady flows, a method based on the integral representation approach has been established (Ref. 6) and a general computer code for internal flow problems is being prepared.

Recent literature contains several articles by other researchers describing results obtained using the integro-differential approach (Refs. 12 to 15). The relatively large amounts of computing needs associated with these efforts as well as with our earlier work (Ref. 7) led to the opinion that, even though the integro-differential approach permits the solution field to be confined to the vortical region of the flow, the approach is computationally inefficient (Ref. 16). This impression is misleading. The present authors have, in the past few years, progressed through several stages of development of the integro-differential approach; each stage has led to a substantial reduction in computing need. The present computing need is about 1/20 of that reported in Ref. 7 and for two-dimensional problems is about 1/5 of that required by the more efficient finite-difference methods available today. The reduction in needed computer time is expected to be much greater for three-dimensional problems.

Two different numerical procedures are outlined in this paper. A procedure utilizing a transformation technique is used in a study of a flow about an impulsively started 9% thick airfoil. A second procedure utilizing a hybrid finite difference-finite element technique is used in a study of flows about an oscillating 12% thick airfoil.

2. KINETICS AND KINEMATICS OF THE FLOW

The time-dependent Navier-Stokes and continuity equations for a fluid with constant density ρ, constant kinematic viscosity ν, and subject to negligible body forces are well-known and are expressible in terms of the velocity $\vec{v}$ and pressure p as:

$$\frac{\partial \vec{v}}{\partial t} + (\vec{v}\cdot\nabla)\,\vec{v} = -\frac{1}{\rho}\vec{\nabla}p + \nu\nabla^2\vec{v} \tag{1}$$

and

$$\vec{\nabla}\cdot\vec{v} = 0 \tag{2}$$

where t is the time.

Equations (1) and (2) are in principle sufficient for the determination of $\vec{v}$ and p, provided that adequate initial and boundary conditions are known. The boundary conditions occuring most frequently are the "no-slip" condition at the surface of solid bodies over which the fluid passes. For problems involving an infinite fluid domain, $\vec{v}$ and p at infinity must also be specified.

It is convenient to introduce the vorticity vector $\vec{\omega}$ defined by

$$\vec{\nabla}\times\vec{v} = \vec{\omega} \tag{3}$$

and to consider the "vorticity transport" equation

$$\frac{\partial\vec{\omega}}{\partial t} = \vec{\nabla}\times(\vec{v}\times\vec{\omega}) + \nu\nabla^2\vec{\omega} \tag{4}$$

obtained by taking the curl of both sides of Eq. (1) and using Eqs. (2) and (3).

The set of equations (2) to (4), with $\vec{v}$ and $\vec{\omega}$ as dependent variables, replaces the set of equations (1) and (2) in which $\vec{v}$ and p are dependent variables. There are several reasons for using $\vec{\omega}$ in the formulation of the problem. A principal reason is that the formulation in terms of $\vec{\omega}$ allows clear and separate delineation of the kinetic and kinematic aspects of the problem. As a consequence of this clear delineation several important characteristics of the general viscous flow problem, not obvious in the p and $\vec{v}$ formulation, become manifest. Major obstacles to the finite-difference solution of the general viscous flow problem are then traceable to physical processes involved in the development of the flow patterns. The identification of the physical origin of these obstacles is of course a prerequisite for the establishment of solution methods that overcome these obstacles.

The kinetic aspect of the problem deals with the change of the vorticity field $\vec{\omega}$ with time. This aspect is described by Eq. (4). For an inviscid fluid, the last term in Eq. (4) vanishes and the vorticity is convected with the fluid in the sense that the vorticity flux $\vec{\omega}.\vec{n}ds$, where $\vec{n}$ is a unit normal vector of the surface element ds, associated with each material element ds moving with the fluid remains a constant for all times. This well-known theorem of Helmholtz is modified in the case of a real fluid by the process of vorticity diffusion. According to Eq. (4), changes in the flux of vorticity across a surface element that is moving with the fluid and is in the interior of the fluid domain takes place only by diffusion. Vorticity flux cannot be created in the interior of a fluid.

If the fluid is in contact with solid bodies in motion, the no-slip condition provides a mechanism for the generation of vorticity at the solid surfaces. In the case where the fluid is initially at rest and occupies an infinite domain bounded internally by surfaces of solid bodies also initially at rest, the vorticity is obviously zero everywhere initially. Subsequent motion of the solid bodies sets up corresponding motion of the fluid. Immediately after the onset of the motion, since the vorticity flux in the interior of the fluid domain can change only as a consequence of diffusion, the vorticity is everywhere zero except at the solid surfaces. That is, the flow immediately after the onset of the motion has a non-zero tangential velocity relative to the solid bodies at the solid boundaries. The discontinuity in tangential velocity represents a sheet of concentrated vorticity at the solid boundaries. At subsequent time levels, this concentrated vorticity at the solid boundaries spreads into the interior of the fluid domain by diffusion and, once there, is transported away from the boundaries by both convection and diffusion. At the same time, vorticity is continually generated on the solid boundaries. The general flow pattern therefore includes vortical regions surrounding the solid bodies and vortical wake regions trailing the solid bodies. Outside of these vortical regions, the flow is essentially free of vorticity and is therefore potential. If the Reynolds number of the flow is not small, then the vorticity spreads by diffusion only a short distance from the solid surface before being carried away with the fluid. Thus there exists a large region of the fluid, ahead and to the side of the solid bodies, which is free of vorticity. In fact, at any finite time level after the onset of the motion, the vortical regions are finite in extent while the potential flow region is infinite in extent.

The kinematic aspect of the problem relates the velocity field at any given instant of time to the vorticity field at that instant. This aspect is described by Eqs. (2) and (3) together with appropriate velocity boundary conditions on the solid surfaces and at infinity. If the velocity field is known at any given instant of time, the corresponding vorticity field is immediately obtainable by differention, using Eq. (3). If the vorticity field is known, the velocity field is obtainable by integrating Eq. (3), subject to the solenoidal condition, Eq. (2). One method of evaluating $\vec{v}$ is to take the curl of Eq. (3) and, by using Eq. (2), obtain a vector Poisson's equation for $\vec{v}$ in the form

$$\nabla^2\vec{v} = -\vec{\nabla} \times \vec{\omega} \tag{5}$$

Alternatively, Eq. (2) implies the existence of a vector potential $\vec{\Psi}$ which is related to $\vec{v}$ by

$$\vec{v} = \vec{\nabla} \times \vec{\Psi} \tag{6}$$

Equation (3) and (6) gives a vector Poisson's equation:

$$\nabla \times \nabla \times \vec{\Psi} = \vec{\omega} \tag{7}$$

A general solution procedure based on the kinetic-kinematic formulation which enables the pattern of flow development to be followed computationally is as follows. With known spatial distributions of $\vec{v}$ and $\vec{\omega}$ at a given time level, the kinetic aspect, i.e., Eq. (4) together with appropriate boundary conditions on $\vec{\omega}$, is treated numerically and a new distribution of vorticity at a subsequent time level is established. The kinematic aspect, i.e., Eqs. (2) and (3), or Eq. (7), together with appropriate boundary conditions for $\vec{v}$, or $\vec{\Psi}$, is then treated and a new velocity distribution corresponding to the new vorticity distribution at the new time level is obtained. This completes a computational loop to advance the solution from an old time level to a new one. Repeated applications of this computational loop yields a transient solution. In the limit of large time, if the velocity boundary conditions are independent of time, then either a steady state solution or a periodic vortex shedding solution is obtainable.

The implementation of the above outlined solution procedure consists of a number of component problems as shown in Figure 1. The literature contains a variety of numerical methods that differ from one another in the specific techniques for treating the component problems. The general framework for these numerical methods, however, are identical. If the "primitive" variable p is used in place of the "derived" variable $\vec{\omega}$, or if $\vec{\Psi}$ is used in place of $\vec{v}$, the component problems are then concerned with the computation of these different variables. The spirit of the general solution-procedure framework, however, remains the same. The major difficulties encountered by researchers can be conveniently reviewed by a critical examination of the component problems.

3. MAJOR OBSTACLES AND ALTERNATIVES

In this section, several major obstacles experienced in previous finite-difference solutions of the general viscous flow problem are reviewed. As stated earlier, the finite-difference approach enjoys remarkable success in the prediction of boundary layer flows. The present obstacles are traceable to the important differences between the boundary layer flow and the general viscous flow in flow patterns and in the physical processes of flow development. It is worthy of note that except the establishment of the initial solution, each of the component problems for the general viscous flow, as shown in Fig. 1, present difficulties that are absent in the boundary layer flow. These difficulties dictate the development of innovative approaches for the general viscous flow problem. Several such approaches are described here.

3.1. Grid System--Coordinate-Transformation and Finite-Element Methods

As discussed earlier, the flowfield in general consists of vortical regions surrounded by a potential flow region. For high Reynolds number flows, if no appreciable flow reversal occurs near the solid bodies, the vorticity spreads to the sides of the solid bodies mainly by diffusion. Since the diffusive process is relatively slow at high Reynolds numbers, the vortical regions near the solid bodies are thin and the boundary layer simplifications are justifiable there. The vortical wakes derive their vorticity from the thin boundary layers and are therefore also thin. The success of the boundary layer theory is attributable to the fact that the effects of these vortical layers on the potential flow may be treated as a relatively small perturbation to the potential flow past the solid bodies in the absence of the vortical layers. This fact permits the potential region to be studied separately from the vortical regions. In particular, it becomes possible to establish the flow velocity immediately adjacent to the boundary layer through potential flow analyses, employing iterative or matching procedures if needed to properly account for the effects of the vortical layers. Consequently, it is possible to confine the solution field of the boundary layer equation to the thin vortical layers near the solid bodies.

In general viscous flows, appreciable regions of flow reversal occur near the solid bodies. The vorticity now spreads to the sides of the solid bodies by both diffusion and convection. The vortical regions are not thin and their presence "strongly" influences the potential flow. With the finite-difference approach, the solution field must include the potential region as well as the vortical regions. Matching procedures are not easily applicable.

For attached boundary layers, it is permissible to employ an orthogonal coordinate system with one of the coordinate axes coinciding with the solid surface. Such a coordinate system is curvilinear. However, since the solution field is restricted to the thin region of the boundary layer, the scale factor of the curvilinear system changes negligibly across the solution field. The differential equations describing the flow, when expressed in terms of the curvilinear coordinates, are formally identical with the equations expressed in the Cartesian coordinates, the curvature terms being negligibly small within the context of boundary-layer approximations. As a consequence, it is straightforward to use a finite-difference grid system with the airfoil surface represented by a grid line. Such a grid system is "boundary-fitted" in the sense that data points on the solid boundaries are permitted to coincide with grid points.

For the general viscous flow problem, the solution field is not thin and the scale factor in a curvilinear coordinate system fitted to the solid boundaries can change substantially across the solution field. The differential equations describing the flow, when expressed in the curvilinear coordinates, contain curvature terms that are not negligible. The use of a boundary-fitted finite-difference grid is considerably more complex than it is in the case of an attached flow.

Much of the earlier works using the finite-difference approach to treat the general viscous flow problem attempted to avoid the complexity introduced by the use of curvilinear coordinate system. In these works, the differential equations are expressed in Cartesian Coordinates and a rectangular grid system in the physical plane is used. Such a system is not boundary-fitted. That is, grid points representing the boundary in general do not coincide with the solid boundaries, and interpolation procedures are needed to accommodate the boundary geometry.

Various authors treating different types of flow problems (Refs. 17 to 21) are in agreement that the proper handling of the boundary conditions are of dominant importance in the numerical solution of flow problems. Existing evidence points to the use of grid systems that are not body-fitted as one of the culprits for the very limited capability of earlier methods in treating the general viscous flow problem. As is well-known, the Navier-Stokes equations describing the general viscous flow are common to an astonishingly rich variety of flow phenomena drastically differing from one another not only quantitatively but also in character. The drastic differences are results of differences in the geometries and the imposed conditions at the flow boundaries. Clearly, accurate representation of the flow boundaries and of the boundary conditions are of paramount importance in the prediction of general viscous flows.

Boundary-fitted grid systems are obtainable by the use of coordinate transformation methods. Alternatively, the finite-element methods (Ref. 18) accomplish the same purpose. With either approach, the relative simplicity of the Cartesian finite-difference representation are bartered for a better numerical representation of the boundary geometry.

Until recently, successful numerical solutions of the general viscous flow problem have been obtained only for those boundary geometries for which convenient analytical transformation formulas are available. In particular, conformal transformations which permit straight forward calculation of the scale factor for the curvilinear coordinate system and of the curvature terms in the differential equations have been utilized by several researchers. In recent years, numerical methods for the establishment of boundary-fitted coordinate systems have been developed (Ref. 17). The numerical transformations need not be conformal and is not restrictive regarding the boundary geometry.

The basic finite-element methods involves the following components: (a) the reformulation of the differential equations as integral relations, (b) the division of the solution field, i.e., the region of integration, into small subregions, called elements, of arbitrary sizes and shapes, (c) the use of interpolation functions, usually polynomials, to express the dependent variables in each element in terms of their values at selected data points, called nodes, associated with the element, and (d) the evaluation of the integrals over each element, yielding a set of algebraic equations containing the nodal values of the dependent variables as unknowns. Since the elements are of arbitrary sizes and shapes, it is straightforward to devise a boundary-fitted system of elements. The resulting set of algebraic equations, however, possesses coefficient matrices more complex than those of finite-difference equations.

In the present work, both the transformation method and the finite-element method are utilized in conjunction with the integro-differential approach in studies of viscous flows about airfoils. The studies demonstrated that both methods are effective in removing the difficulty of accurate numerical representation of the solid boundaries. The added algebraic complexity of either method is not excessive for two-dimensional flows. There exist, however, several other difficulties that are not removed by either method. These difficulties are described below.

3.2. Vorticity Solution - Kinetics

A major source of difficulty in the kinetic part of general viscous flow computation is the simultaneous occurrence of the diffusive and convective processes in the flow. These two processes proceed at drastically different rates at high Reynolds numbers. The length and time scales of these processes are vastly different. This fact leads to vastly different, often overly stringent, requirements on the time interval and grid spacing because of accuracy and stability considerations. In comparison to problems in which either the diffusive process or the convective process is alone important, the kinetic aspect of the general viscous flow is immensely more complex. For boundary layer flows in two-dimensions, the diffusive process is of negligible importance in comparison to the convective process along the direction parallel to the body surface. In the direction perpendicular to the body surface, the convective and diffusive processes are of comparable importance and the length scales of the two processes are not vastly different. Consequently, the boundary layer momentum equations do not contain the above described difficulty associated with the general viscous flow.

In Ref. 5, an integral representation for the vorticity vector is presented. This integral representation is completely equivalent to the differential vorticity transport equation (4). A solution procedure based on this representation is suggested in Ref. 5. This procedure has been calibrated recently using simple problems with known analytical solutions. A noteworthy feature of this procedure is that the kinetic processes of diffusion and convection are represented by separate integrals and the contributions of these two processes to the time variation of vorticity can be evaluated separately in a convenient manner. This new procedure is being developed for complex time-dependent problems. The work reported in the present paper, however, are based on extensions of existing finite-difference and finite-element methods. For the impulsively started airfoil, a method of flowfield segmentation is developed and used in conjunction with a modified strongly implicit procedure. For the oscillating airfoil, a hybrid finite difference-finite element method is established. These methods will be outlined in later sections of this paper.

3.3. Kinematics - Integral Representation and Flowfield Segmentation

It is well known that the computer time requirement for the finite-difference solution of a general viscous flow problem in general increases rapidly with the flow Reynolds number. The basic cause of this difficulty is that the kinematic aspect of the general viscous flow problem is described by elliptic differential equations, e.g. Eq. (5) or Eq. (7). The finite-difference solution of $\vec{v}$ at any given point in the flowfield depends on the value of $\vec{v}$ at the neighboring points. It is therefore not possible to evaluate the value of $\vec{v}$ explicitly, point by point, using a finite-difference method. The solution field, in fact, should be infinite so as to satisfy the freestream condition at infinity. For numerical solution, the infinite solution field needs to be represented by a finite number of grid points. Substantial inaccuracy can result if one truncates the solution field and specifies freestream velocity condition, or some other condition, on some outer boundaries at finite distances from the solid boundary (Reference 8). In many previous works, this outer boundary is placed at a distance of ten chord lengths or more from the solid boundary in hope that the inaccuracy resulting from the replacement of an infinite region by a finite one is then unimportant. Such practices may lead to fundamental difficulties and must be handled with great caution. For example, it can be shown that if the steady state equations are to be treated and the freestream velocity boundary condition is applied at a closed outer boundary at finite distances from the airfoil, then no solution for an airfoil with non-zero lift force is possible.

As discussed earlier, for high Reynolds number flows, the vortical regions surrounding and trailing the solids are relatively small. The effects of viscosity are important only in this region. The gradients of field variables are large and the corresponding length scale for this region is small, particularly in the boundary layer. Consequently, in order to have sufficient solution resolution in this region, the grid lines must be very finely spaced. If this fine spacing is continued into the potential region of the flow, which has been made finite but is still large, a gigantic number of grid points invariably enter the computation procedure. This implies that an excessive amount of computer time is needed to solve the equations. With increasing Reynolds number, the length scale in the vortical region decreases. The number of grid points, and hence also the needed computer time, therefore increases with increasing Reynolds number.

The coordinate transformation and finite-element methods provide a degree of relief from the excessive computing needs at high Reynolds numbers. For example, Ref. 17 describes a method which maps the fluid region into the interior of a rectangle. A uniformly spaced grid system is used in the transformed plane to numerically solve the transformed differential equations. In the physical plane, the corresponding spacing between grid lines increases as the distance from the solid boundaries increases. With the "expanding" grid system in the physical plane, it is possible to substantially reduce the number of grid points entering the solution procedure and to make this number less sensitive to the Reynolds number.

With a finite-element method, since the elements can be of arbitrary sizes and shapes, an expanding grid system is not difficult to devise. To researchers accustomed to the finite-difference approach, the finite-element procedure for setting up a set of algebraic equations may appear to be circuitous. It should be noted, however, that the coordinate transfomration approach, usually considered an improved finite-difference procedure, also would appear to be circuitous to those accustomed to the use of uniformly spaced finite-difference grid in the physical plane. The added complications of coordinate transformation, or of the finite-element approach, however, are amply justified by their ability to accurately represent the boundary geometry, as discussed in Section 3.1. The ability to have an expanding grid system is an additional important property of these approaches. However, these approaches by themselves do not permit an explicit, point by point, evaluation of the velocity values, and therefore the solution field needs to include the potential region as well as the vortical regions of the flow.

As discussed in Section 3.1, in treating the attached flow problem, the solution field for the boundary layer equations can be confined to the thin vortical layers near the solid bodies. There is no need to concurrently solve the potential and the vortical flow problems. Rather, the two problems are solved individually and matched. With attached flows, therefore, the difficulty of simultaneously accommodating the potential and vortical regions is absent. This fact is a major reason contributing to the success of the finite-difference approach in solving boundary layer problems.

For the general viscous flow problem, the kinetic aspect of the computation can be confined to the vortical regions of the flow. From Eq. (4), it is obvious that if the vorticity and velocity fields in the vortical regions are known at any given time level, then the time rate of change of vorticity at that time level is determinate. There is no need to go beyond the vortical regions and their immediate neighborhood to establish a new vorticity distribution at the subsequent time level. Consequently, if the kinematic aspect of the computation can also be confined to the vortical region, then the solution field need not extend into the potential flow region and the difficulty of simultaneously accommodating the potential and the vortical regions is removed. In Ref. 2, it is shown that the confinement of the kinematic aspect of the computation to the vortical region is possible if the differential equations describing the kinematics of the general viscous flow problem is recast into an integral representation of the velocity vector (or of the vector potential). In this research, the integral representation for the kinematics of the problem is used together with the differential vorticity transport equation (4). The formulation of the overall problem is named the integro-differential formulation.

In Ref. 2, it is shown that Eqs. (2) and (3), together with velocity boundary conditions, can be recast into the following integral representation for the velocity vector:

$$\vec{v}(\vec{r}, t) = -\frac{1}{A}\left[\int_R \frac{\vec{\omega}_o \times (\vec{r}_o - \vec{r})}{|\vec{r}_o - \vec{r}|^d}\, dR_o - \oint_B \frac{(\vec{v}_o \cdot \vec{n}_o)(\vec{r}_o - \vec{r}) - (\vec{v}_o \times \vec{n}_o) \times (\vec{r}_o - \vec{r})}{|\vec{r}_o - \vec{r}|^d}\, dB_o\right] \tag{8}$$

where $\vec{r}$ is the position vector, $\vec{\omega}$ is the vorticity vector, R is any region occupied by the fluid or the solid, B is the boundary of R, and $\vec{n}$ is the unit normal vector directed outward from R, $A = 4\pi$ and $d = 3$ in three-dimensional problems and $A = 2\pi$ and $d = 2$ in two-dimensional problems. The subscripts "o" in dR_o and dB_o indicate that the integrations are in the $\vec{r}_o$ space.

Equation (8) is valid for all position vectors in R and on B and is completely equivalent to Eqs. (2) and (3) together with the velocity condition on the boundary B. The use of Eq. (8), in place of Eqs. (2) and (3), permits the explicit, point by point, computation of the velocity distribution in R, provided that the vorticity distribution in R and the velocity condition on B are known.

The second integral in Eq. (8) represents the contribution of the velocity boundary condition to the velocity field within the boundary. For the problem of an external flow past a solid body undergoing translation and rotation, it has been shown (Ref. 8) that this contribution can be expressed in terms of the instantaneous rectilinear and angular velocities, $-\vec{v}_\infty$ and $\vec{\Omega}$, of the solid. Equation (8) then reduces to

$$\vec{v}(\vec{r}, t) = -\frac{1}{A}\left[\int_{R_f} \frac{\vec{\omega}(\vec{r}_o, t) \times (\vec{r}_o - \vec{r})}{|\vec{r}_o - \vec{r}|^d} dR_o + 2\int_{R} \frac{\vec{\Omega}(\vec{r}_o, t) \times (\vec{r}_o - \vec{r})}{|\vec{r}_o - \vec{r}|^d} dR_o\right] + \vec{v}_\infty(t) \tag{9}$$

where R_f and R_s are respectively the regions occupied by the fluid and the solid body. The coordinate system translates with the solid but does not rotate with it.

The vortical regions at any finite time level after the onset of the motion are of finite extent and are within finite distances from the solid boundaries. The region of integration is therefore finite. Furthermore, as $\vec{r}$ goes to infinity, the integrands in Eq. (9) vanish. The freestream boundary condition is therefore satisfied at infinity.

Equation (7), together with appropriate boundary conditions, can be recast into an integral representation for the vector potential $\vec{\Psi}$. For two-dimensional flows, $\vec{\Psi}$ has only one non-vanishing component in the direction perpendicular to the plane of the flow. This component is familiarly interpreted as the stream function Ψ. An integral representation for Ψ is (Ref. 10):

$$\Psi(\vec{r}, t) = \frac{1}{2}\int_{R} \omega(\vec{r}_o, t) \ln \frac{|\vec{r}|}{|\vec{r}_o - \vec{r}|} dR_o + \frac{1}{2\pi}\int_{B} \{(\vec{\nabla}_o \Psi(\vec{r}_o, t))\cdot\vec{n}_o - (\Psi(\vec{r}_o, t)\vec{n}_o\cdot\vec{\nabla}_o)\} \ln \frac{|\vec{r}|}{|\vec{r}_o - \vec{r}|} dB_o \tag{10}$$

The second integral in Eq. (10) again represents the contribution of the boundary condition. For a solid body translating in an infinite fluid, this contribution is simply $(\vec{v}_\infty \times \vec{r}).\vec{k}$, where $\vec{k}$ is the unit vector in the direction perpendicular to the flow. Equation (10) becomes for this case

$$\Psi(\vec{r}, t) = \frac{1}{2\pi}\int_{R_f} \omega(\vec{r}_o, t) \ln \frac{|\vec{r}|}{|\vec{r}_o - \vec{r}|} dR_o + (\vec{v}_\infty \times \vec{r})\cdot\vec{k} \tag{11}$$

Equations (10) and (11) are valid in the physical plane (x, y) and in any plane, say (ξ, η), related to the physical plane by a conformal transformation, with the stream function Ψ an invariant under the transformation. The vorticity in the (x,y) plane is related to that in the (ξ, η) plane by the following formula

$$\omega(\xi, \eta, t) = H^2\omega(x, y, t) \tag{12}$$

where H is the scale factor for the transformation and is defined by

$$H^2 = \left(\frac{\partial x}{\partial \xi}\right)^2 + \left(\frac{\partial x}{\partial \eta}\right)^2 = \left(\frac{\partial y}{\partial \xi}\right)^2 + \left(\frac{\partial y}{\partial \eta}\right)^2 \tag{13}$$

The position vector in the (x,y) plane is given by $\vec{r} = x\vec{i} + y\vec{j}$ and that in the (ξ, η) plane is given by $\vec{r} = \xi\vec{i} + \eta\vec{j}$.

Equation (11) or, equivalently, Eq. (9) forms the basis of earlier studies of the integro-differential approach by the present authors and by others. It has been pointed out (Ref. 8) that the operation count of numerical procedures based on these equations can be high. For example, suppose the vortical region of the flow contains N grid points. Equation (11) is represented by the algebraic equations

$$\Psi_i(t) = \sum_{j=1}^{N} \omega_j(t)F_{ji} + G_i, \quad i = 1, 2, \ldots, N \tag{14}$$

where i refers to a grid point at which the value of Ψ is to be computed, j refers to a boundary point or a vortical point, F_{ji} are geometric coefficients whose values depend on the relative position of the points i and j, and G_i are constant values corresponding to the last term of Eq. (11). The computation of each stream function value using Eq. (14) requires about 2N algebraic operations (N multiplicatons and N additions), provided that the geometric coefficients F_{ji} are known and need not be computed. The use of Eq. (14) to evaluate stream function values at all the N grid points requires a total of $2N^2$ algebraic operations. It is well known that an efficient finite-difference or finite-element solution of the two-dimensional form of Eq. (7) for a field containing N grid points requires a much smaller number of operations than $2N^2$. The use of the integral representation in the form of Eq. (11), or, equivalently, Eq. (9), is therefore computationally efficient only if the confinement of the solution field to the vortical regions results in a substantial reduction in the number of grid points required.

For many high Reynolds number flows, the vortical region constitutes only a small portion of the entire flowfield so that a substantial reduction in the needed number of grid points is indeed accomplished by the use of Eq. (11). It should be emphasized, however, that even if the reduction in the number of grid points is not substantial, the integro-differential approach still offers highly efficient numerical procedures.

One method of accomplishing superior computational efficiency is to use Eq. (11) only in the computation of stream function (or velocity) values at grid points surrounding the vortical regions. Once this is completed, the computation of stream function values at grid points in the vortical regions can be carried out using a finite-difference or a finite-element method. In this manner, the superiority of the integro-differential approach is assured since an optimum method, including a method that may appear in the future, can be incorporated into the numerical procedure and the solution field can be confined to the vortical regions.

Another method of improving the computational efficiency is to utilize a flowfield segmentation technique (Ref. 11). This technique has been suggested in conjunction with the velocity integrals, Eqs. (8), and (9) and tested on the problem of a flow past a finite flat plate. The application of this technique in conjunction with the stream function formulation is outlined here.

The flowfield is segmented into compartments each containing a suitable number of grid points. With known vorticity values at all grid points at a new time level, new stream function values at grid points located on the boundary of the compartments are computed from Eq. (14). Values of the normal gradient of the stream function at the compartment boundary are computed from an equation similar to Eq. (14) derived by differentiating Eq. (11) and representing the result by algebraic equations.

Stream function values at grid points located interior of the compartments are now computed using Eq. (10). Suppose the vortical region is segmented into several compartments each containing P number of grid points, with Q number of grid points located on the compartment boundary. Equation (10) is now represented for each compartment by the algebraic equations:

$$\Psi_i(t) = \sum_{j=1}^{P} \omega_j(t)F_{ji} + \sum_{j=1}^{Q} \left(\Psi_j M_{ji} + \frac{\partial\Psi}{\partial n}_j N_{ji}\right), \qquad i = 1, 2, \dots P \tag{15}$$

where the first summation is over all grid points of the compartment and the second summation is over all grid points on the compartment boundary. The use of Eq. (15) to compute each stream function value requires 2(P+2Q) algebraic operations. This operation count is clearly substantially smaller than 2N if N is large. If the solution field is segmented into a larger number of compartments, then the operation count 2(P+2Q) decreases. On the other hand, with an increasing number of compartments, the total number of grid points located interior of all the compartments decreases. As a result, there are fewer grid points in the solution field for which the segmentation technique offers a computational advantage. At the same time, the number of grid points located on compartment boundaries increases with the number of compartments; and on these grid points not only the stream function value but also its normal gradient must be computed. There exists, therefore, an optimum number of compartments for each problem considered. This optimum number depends on the total number of grid points in the vortical region and the geometric distribution of these grid points. It is not difficult to show, however, that the optimum number of compartments in general increases with the total number of grid points. Consequently, the factor of reduction in the operation count also increases with the total number of grid points. For example, with 1089 grid points arranged in a 33 x 33 array, the operation count can be reduced by a factor of about 2.5 with the segmentation technique. With 4225 grid points arranged in a 65 x 65 array, the operation count can be reduced by a factor of about 4.6.

Substantial reductions in the total operation count for problems requiring a large number of grid points is a highly significant feature of the flowfield segmentation technique since it is precisely for these problems that excessive computer time presents a serious obstacle. An additional highly significant feature of this technique is the inherent flexibility it offers. The compartments utilized in the solution procedure can be of any arbitrary size or shape. Once the stream function (or velocity) values are established on the boundary of a compartment, the computation within that compartment can be performed independently of that in other compartments. Consequently, the flowfield segmentation technique is well suited for parallel programming.

Since the compartments can be chosen to be of standard simple shapes, such as rectangles, except near solid boundaries of irregular shape, various efficient methods can be adopted for the interior point computation. That is, one does not always need to use Eq. (15) for the interior point computation. Rather, highly efficient methods such as the fast Fourier transform method that are particularly well suited for simple boundary geometries can be utilized. If Eq. (15) is used, then the number of geometric coefficients that enters the computation procedure is drastically reduced by the use of compartments of standard shapes. Note that with Eq. (14), the number of geometric coefficients entering the computation is N^2. These geometric coefficients are independent of time. However, if N is very large, then the storage of the N^2 coefficients may present a problem, and the coefficients may need to be computed repeatedly for different time levels. With Eq. (15) and standard shape for compartments, the number of geometric coefficients is

AD-A054 028   ADVISORY GROUP FOR AEROSPACE RESEARCH AND DEVELOPMENT--ETC   F/G 20/4
UNSTEADY AERODYNAMICS.(U)
FEB 78

UNCLASSIFIED   AGARD-CP-227   NL

5 OF 7
ADA
054028

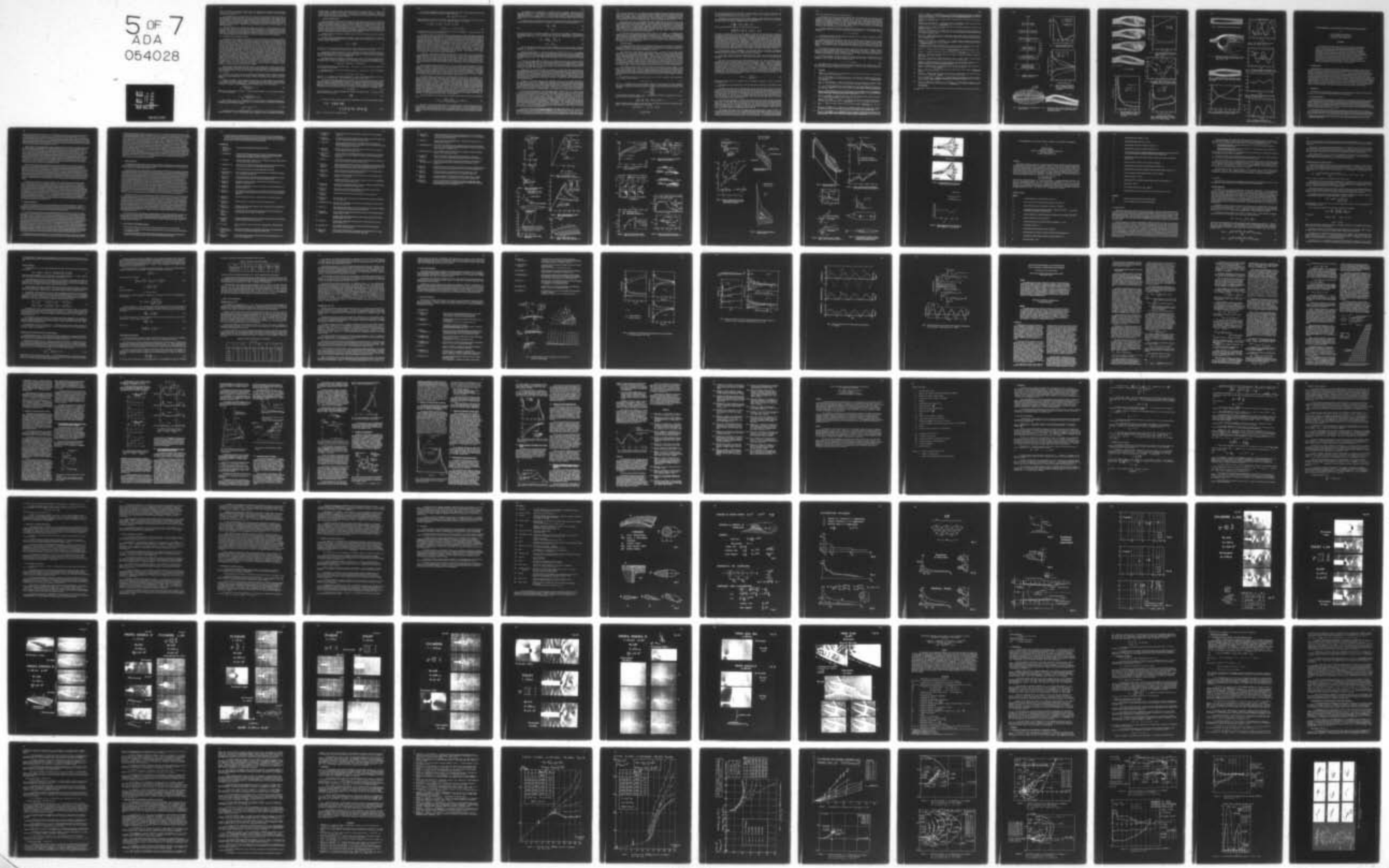

P(P+2Q). This number can be further reduced to P+2Q if the compartments are rectangles and uniformly spaced grid is used in each compartment. These numbers are generally small enough so that all geometric coefficients can be stored.

As discussed earlier, the length scales for the potential and vortical regions of the flow are generally vastly different in magnitude. The use of the integral representation for the kinematic aspect of the problem makes it possible to confine the solid field to the vortical regions only. However, in the general viscous flow, the length scale within the vortical regions varies greatly. In the boundary-layers, the length scale is represented by the boundary layer thickness in the direction perpendicular to the solid surface. In the wake and recirculating regions, the length scale is represented by the body dimensions. The segmentation technique offers a convenient means of separating these parts of vortical regions in the solution procedure.

The above features of the segmentation technique are expected to be highly important for three-dimensional flows requiring the use of very large number of grid points. For the present studies of two-dimensional flows, only a few of these features of flowfield segmentation are incorporated into the solution procedure. It is noteworthy that the segmentation technique is useful also in the solution of the kinetic aspect of the problem. In the present study of the impulsively started airfoil problem, the solution field is divided into compartments in the kinetic part as well as the kinematic part of the computation.

3.4. Extraneous Vorticity Boundary Condition

The solution of Eq. (4) requires a knowledge of the vorticity values on the boundaries of the fluid as a function of time. The establishment of new vorticity values on solid boundaries is a necessary part of the overall solution procedure. In most of the previous investigations, one-sided difference formulas have been used to estimate the vorticity values on solid boundaries from the no-slip condition and the computed stream function (or velocity) values at grid points near the boundary. The computer time required for such calculations is very small compared to that required for the calculation of field values of vorticity. It has been found, however, that one-sided difference formulas of first-order accuracy tend to yield stable solutions, while second-order accurate formulas tend to give unstable results at high Reynolds numbers. In fact, for some problems, second-order formulas, even when stable, gave less accurate solutions than did the first-order formulas (Reference 19). The use of first-order formulas, however, restricts the overall accuracy of the solution. In particular, it has been shown (Reference 8) that first-order formulas do not permit the effect of tangential pressure gradient on the local boundary vorticity generation to be accounted for. There existed, therefore, considerable uncertainties regarding the correct one-sided formula to use, and regarding the limitations of each formula. These difficulties are independent of the computer time needed for the component problem under consideration, and are discussed more fully in Reference 8. They are referred to as the extraneous boundary-condition problem since the proper boundary condition for the physical problem is that for the velocity (or the stream function). The specification of the vorticity on the boundary of the fluid domain overspecifies the problem. These difficulties of extraneous boundary conditions, however, are not peculiar to the formulation of the problem using the vorticity as a field variable. If Eq. (1) is to be solved numerically instead of Eq. (4), then it is necessary to know the pressure on the solid boundaries in addition to the velocity.

The extraneous boundary-condition problem is absent in the boundary layer problem since the pressure in a direction normal to the boundary (vortical) layer is practically constant. Thus the pressure on the solid boundaries is equal to that at the outer edge of the boundary layer where it is determined by the outer flow. For the general viscous flow, the vortical region is not necessarily thin and the above simplification may not be valid.

In Ref. 8, it is shown that the prescribed velocity boundary condition imposes a kinematic restriction on the boundary vorticity values. The integral representation for the velocity vector then permits an accurate determination of the boundary vorticity value through the solution of an integral equation.

Consider, for example, a solid undergoing translation only. The second integral in Eq. (9) vanishes. If the vorticity distribution is known interior of the fluid domain R_f', then the first integral in Eq. (9) can be written as a sum of an integral over R_f' and an integral over the solid boundary B_s on which a layer of vorticity ζ exists. For two-dimensional flow, one then has, since $\vec{v} = 0$ in the solid,

$$\int_{B_s} \frac{\zeta_o(\vec{r}_o - \vec{r}_o^{\,-})_n}{|\vec{r}_o - \vec{r}_o^{\,-}|^2}\, dB_o = F_b \tag{16}$$

where r_o^- is a point interior of the solid, n indicates a normal component, F_b is the tangential component of $\vec{F}$, which is defined by

$$\vec{F} = \int_{R_f'} \frac{\omega_o \times (\vec{r}_o - \vec{r}_o^{\,-})}{|\vec{r}_o - \vec{r}_o^{\,-}|^2}\, dR_o - 2\pi\, \vec{v}_\infty \tag{17}$$

With $\vec{\omega}$ known in R_f'., $\vec{F}$ is determinate. Equation (16) therefore is a Fredholm integral equation containing ζ as the unknown function. This function ζ is rendered unique by the principle of conservation of total vorticity (Ref. 8) which requires

$$\int_{B_s} \zeta dB + \int_{R_f'} \omega\, dR = 0 \tag{18}$$

In previous studies, the integral equation (17) is approximated by a set of simultaneous algebraic equations containing ζ values at boundary grid points as unknown. The set of equations is solved using iterative methods. In the present study, closed form solutions of the integral equation (17), subject to the restriction (18), are obtained. These closed form solutions make it possible to evaluate values on the solid boundaries explicitly, point by point. It is found that these explicit calculations yield highly accurate values of vorticity on solid boundaries. The derivations of the closed form solutions are presented in Ref. 1 and will also appear in future articles.

4. IMPULSIVELY STARTED AIRFOIL

The integro-differential formulation in terms of the stream function and vorticity is particularized, transformed, and applied to the study of the time-dependent incompressible viscous flow past an impulsively started 9% thick symmetric Joukowski airfoil at an angle of attack of 15° and a Reynolds number of 1000. This problem has been studied previously by Mehta (Ref. 22) who mapped the fluid domain into the interior of a unit circle and used a finite-difference method to solve the transformed vorticity transport and Poisson's equations. In the present study, the geometry of the airfoil is identical to the one studied by Mehta. The vorticity transport equation and the integral representation are re-expressed in Mehta's transformed plane and Mehta's grid spacings are adopted in order to facilitate a comparison between the integro-differential results of the present study and the finite-difference results of Mehta.

The major features of the numerical procedures used in this study is described below for the component problems shown in Fig. 1.

The grid system is obtained through a transformation. This system is boundary-fitted and expanding. The shape of the 9% symmetric Joukowski airfoil is given in Figure 2 in the complex plane $z = x + iy$. By using the conformal transformation

$$z = \frac{1}{\kappa} + \gamma + \frac{\kappa C^2}{1 + \kappa} \tag{19}$$

where $\kappa = re^{i\theta}$, C and γ are real constants, the airfoil surface transforms into a circle and the exterior of the airfoil, i.e., the fluid domain, is mapped in the κ plane as the interior of the circle.

For the present problem, the values of C and γ are taken to be 0.9241635 and -0.05214 respectively. The coordinates and the flow variables are to be non-dimensionalized with respect to the radius of the circle and the freestream velocity. The non-dimensional chord length, L, of the airfoil is, according to equation (19), 3.71281277. The airfoil is 8.9998% thick.

The kinematic part of the computation is performed in the κ plane. A non-conformal transformation is utilized to obtain an efficient distribution of grid points for the kinetic part of the computation. The coordinate in the κ plane is not modified. The r coordinate is "stretched" by the relation (Ref. 22)

$$\rho = \frac{1}{4.8} \tanh^{-1}(1.996590918r - 1.032563339) + 2.8 \tag{20}$$

This transformation maps the annular region between $r = 0.02$ and $r = 1$ in the κ-plane into the interior of a unit circle in the ρ-θ plane.

The grid system in the $\rho - \theta$ plane is formed by using $\Delta\rho = 1/47$ and $\Delta\theta = \pi/40$. The coordinates of the grid point i,j are

$$\rho = 1.0 - (j - 1)\Delta\rho \quad \text{and} \quad \theta = (i - 1)\Delta\theta$$

Note that $j = 1$ corresponds to the airfoil surface and $j = 48$ ($\rho = 0$) corresponds roughly to a circle of radius 13 L in the physical plane. The corresponding grid system is shown in Fig. 2.

The vorticity distribution immediately after the start of the airfoil motion consists only of a vortex sheet on the airfoil. The determination of the initial vorticity distribution does not require a special procedure. Rather, the procedure outlined in Section 3.4. is applicable. With the vorticity everywhere zero in R_f', the vector $\vec{F}$, defined by Eq. (17), is simply $-2\pi\vec{v}_\infty$. With this value of $\vec{F}$, Eq. (16) can be solved numerically to give the initial distribution of vorticity (vortex strength) on the airfoil surface. Alternatively, the closed form solution of Eq. (16), subject to the condition (18), is recognized to be

$$\zeta = 2v_\infty \mathrm{Sin}(\theta+\alpha) \tag{21}$$

in the transformed plane . The corresponding vortex strength in the physical plane z is equal to ζ/H, H being the scale factor defined by

$$H = \left|\frac{dz}{d\kappa}\right| \tag{22}$$

The vorticity transport equation expressed in the working plane in terms of non-dimensional variables is

$$r^2H^2 \frac{\partial\omega}{\partial t} = r\frac{d\rho}{dr}\left(\frac{\partial\Psi}{\partial\rho}\frac{\partial\omega}{\partial\theta} - \frac{\partial\Psi}{\partial\theta}\frac{\partial\omega}{\partial\rho}\right) + \frac{L}{Re}\left[\left(r\frac{d\rho}{dr}\right)^2\frac{\partial^2\omega}{\partial\rho^2} + r\left(\frac{d\rho}{dr} + r\frac{d^2\rho}{dr^2}\right)\frac{\partial\omega}{\partial\rho} + \frac{\partial^2\omega}{\partial\theta^2}\right] \tag{23}$$

where ω is the vorticity in the physical plane.

The vorticity transport equation (23) is approximated by an implicit finite-difference equation using a 3-point backward differencing to represent the time derivative:

$$\frac{\partial \omega}{\partial t} = \frac{1}{2\Delta t}\left(3\omega^{n+1} - 4\omega^{n} + \omega^{n-1}\right)$$

where the superscript refers to the time level. Space derivatives of vorticity are represented by central differencing at the time level n+1. The finite difference equation is of the form

$$B_{i,j}\,\omega^{n+1}_{i,j-1} + D_{i,j}\,\omega^{n+1}_{i-1,j} + E_{i,j}\,\omega^{n+1}_{i,j} + F_{i,j}\,\omega^{n+1}_{i+1,j}$$

$$+ H_{i,j}\,\omega^{n+1}_{i,j+1} = J_{i,j}\left(-2\omega^{n}_{i,j} + \frac{1}{2}\,\omega^{n-1}_{i,j}\right) \qquad (24)$$

The coefficients B, D, F and H contain derivatives of Ψ and are time-dependent. In the present work, the coefficients are evaluated at the time level n.

The selection of central differencing for the space derivatives of vorticity was made after comparing computed results for the first few time steps using central differencing with those using upwind differencing and using Arakawa differencing (Ref. 23). No significant deviations between the numerical values of vorticity was revealed. Mehta (Ref. 22) used Arakawa differencing, which requires more arithmetical operations than central differencing, to ensure total vorticity conservation. Since the present method of determining surface vorticity distribution conserves the total vorticity, the use of central differencing requiring fewer arithmetic operations is appropriate. Small amounts of spurious values of vorticity was found to occur in portions of the outer field where the vorticity values are expected to be negligible. Such occurences are perhaps attributable (Ref. 24, 25) to the large grid spacing, and hence cell Reynolds numbers, used in the present study in regions of the flow far from the airfoil surface. The use of upwind differencing in place of central differencing removes this anomalous solution behavior. Arakawa differencing was not found to be effective in removing this spurious vorticity. Since spurious vorticity values are very small and since they do not seriously affect the solution, it was decided to use central differencing which is higher ordered than upwind differencing.

A modified strongly implicit procedure (SIP) (Ref. 26) was used to solve the set of simultaneous algebraic equations (24) for vorticity values at the time level n+1. This method is selected amongst several competing methods on the basis of its solution efficiency and accuracy. The relative requirements of computer time using the various methods were, for the first few time steps, (a) Modified SIP - 100%, (b) SIP - 220%, (c) Alternating Direction Implicit (ADI) method - 154%, (d) Successive Line Relaxation - 254%, and (e) Successive Point Relaxation Method (used in Reference 22) - 365%. The ADI method is faster than the SIP method; but did not yield acceptable solution using the same time step sizes employed by the SIP method.

The SIP method was proposed by Stone (Ref. 26). Lin et al. employed the method successfully to obtain solutions for viscous flows past a cylinder. The basic concepts of this method as applied to the present problem is as follows. The coefficient matrix for Eq. (24) is sparse and contain only five non-zero diagonals. With a direct elimination procedure, one would factorize the coefficient matrix into the product of a lower and an upper triangular matrix, or use a procedure that is essentially equivalent. In such cases the triangular matrices generated are not in general sparse. With the SIP, the coefficient matrix is altered in such a manner that the altered matrix is easily factored into a product of a lower and an upper triangular matrix and that the matrices each have only three non-zero elements in each row.

With the SIP method, the solution field is bounded by the solid surface ($\rho = 1$) and a constant ρ line, say $\rho = \rho_1$ which is sufficiently removed from the non-negligible vorticity region. The value of ρ_1 is generally determined by the extent of the wake region. At large time levels, the wake extends far behind the airfoil while the vortical regions to the sides and ahead of the airfoil extend only a relatively short distance from the airfoil. As a result, a large number of data points where vorticity values are negligible enter into the solution procedure. The modification of the SIP method introduced in the present study consists of a division of the solution field into several compartments along constant θ lines, the individual application of SIP method in each compartment, and the use of successive line relaxation method for obtaining vorticity values along the dividing constant θ lines. With the solution field divided in this manner, each solution block is bounded by two constant θ lines, a part of the $\rho = 1$ line, and $\rho = \rho_i$ lines. ρ_i can be different for different blocks. Therefore much fewer data points at which vorticity values are negligible enter into the computation. In the present study, the solution field is divided into four compartments. The location of the constant θ dividing lines and ρ_i values are kept flexible and are changed in accordance with the shape of the non-negligible vorticity region as time progresses.

The vortex strengths on the airfoil surface are computed using an explicit formula in the transformed plane:

$$\zeta = \frac{1}{2\pi}\int_{R_f'} \frac{\omega_o\left(r_o^2 - 1\right)\,{}_o dR_o}{1 + r_o^2 - 2r_o \operatorname{Cos}\left(\theta_o - \theta\right)} + 2V_\infty \operatorname{Sin}(\alpha + \theta) \qquad (25)$$

The value of the airfoil-boundary vorticity in the physical plane at a grid point located on the airfoil boundary is then obtained by dividing ζ by the scale factor H and by the physical distance corresponding to $\frac{1}{2}\Delta\rho$ nearest the airfoil surface. The surface vorticity values are re-calculated for each iteration. New boundary vorticity values for the subsequent iteration are obtained using a relaxation procedure and used in the SIP procedure for the calculation of vorticity values at grid points away from the boundary.

The computation of the stream function is accomplished using the flowfield segmentation technique described in Section 3.3. The flowfield is divided into several compartments. The boundary of the compartments are the $\theta = 0$ line and two ρ = constant lines. Stream function values on constant ρ compartment boundaries are computed using Eq. (14) in the transformed plane. Stream function values at the interior points of each compartment are then calculated using the strongly implicit method described earlier.

Instantaneous pressure distributions and shear stress on the airfoil surface are determined from the computed vorticity values and gradients on the surface in accordance with the following equations

$$\frac{\partial p}{\partial s} = \rho \nu \frac{\partial \omega}{\partial n} \tag{26}$$

and

$$\tau = \rho \nu \omega \tag{27}$$

Note that the direction of the normal coordinate is away from the fluid domain. Equation (26) is a specialization of Eq. (1) to the solid boundary S where the "no-slip" condition applies. The pressure and skin friction coefficients C_p and C_f are, from Eqs. (36) and (37), expressible as a function of θ as follows:

$$C_p(\theta) = \frac{2L}{Re} \frac{d\rho}{dr}\bigg|_{\rho=1} \int_0^{\theta} \frac{\partial \omega}{\partial \rho}\bigg|_{\rho=1} d\theta \tag{28}$$

and

$$C_f(\theta) = \frac{2}{Re} \omega\bigg|_{\rho=1} \tag{29}$$

The force and moment are readily obtained from the computed values of $C_p(\theta)$ and $C_f(\theta)$, by numerical quadrature. In the present work, the values of $\partial\omega / \partial\rho$ are obtained by numerical differentiation using the values of $\omega_{i,1}$ and $\omega_{i,2}$.

Numerical results obtained for the airfoil problem are presented in Figs. 4 to 9. The chordwise distances from the leading edge, x_c and the load coefficients C_L, C_D, and C_M shown in the figures are normalized with respect to the chord length. The Reynolds number of 1000 is based on the chord length and the freestream velocity. All other quantities shown were normalized with respect to the freestream velocity and the radius of the unit circle. The reference time is the radius of the circle divided by the freestream velocity.

A check on the program coding was carried out by obtaining the solution for a flow past a circular cylinder at a Reynolds number of 40. The solutions were carried out up to a dimensionless time level of t = 9.5, the reference time being the cylinder radius divided by the freestream velocity. The drag coefficient at this time level is found to be 1.67 which is in reasonable agreement with an experimental value of 1.5 for steady state flow. The computed pressure distribution on the cylinder is compared with the experimental values (Ref. 28) in Figure 3.

Additionally, for the airfoil problem, the acceptibility of block subdivision was checked out by comparing the numerical results for a few first time steps of the following cases: (1) Successive Point and Line Relaxation Procedures without block subdivisions (2) Strongly Implicit Procedure (SIP) with no flow field subdivision (3) SIP method with four block subdivisions and for three different locations of block boundaries for the block enclosing the trailing edge. The excellent agreement of computed vorticity values for all these cases indicated the acceptability of block subdivision technique. The major aspects of the flow phenomena past the impulsively started airfoil at an angle of attack of 15° and at a Reynolds number of 1000 are described below.

At time t = 0, the flow around the airfoil corresponds to that of a non-circulatory potential flow. After the impulsive start the rear stagnation point (RSP) moves very rapidly to the trailing edge (TE) from its potential flow location of $X_C = 0.9808$. This rapid movement of the rear stagnation point is accompanied by a small separation bubble located between RSP and TE at time levels 0.003 and 0.004. After the RSP has reached the TE, plots of equi-vorticity contours show "curling up" of vorticity field near trailing edge with positive vorticity values in the curled up regions. The curling up of vorticity field is indicative of vortex roll-up and the formation of starting vortex. The vorticity in this starting vortex diffuses rapidly.

An adverse pressure gradient on the upper surface becomes noticeable at time t = 0.068. At time t = 0.404 this adverse pressure gradient is more pronounced (Fig. 4) and this leads to the birth and growth of the first separation bubble with clockwise flow. This bubble eventually extends over almost the entire upper surface of the airfoil, at time t = 6.228 (Fig. 5a). At the very next time level, t = 6.74, its reattachment point separates from the airfoil. In Figure 5, streamlines are shown around the airfoil for several time levels. The values of the stream function are in the range -0.48 to 0.48 in steps of 0.04. As the bubble size increases the pressure gradient on the upper surface decreases as seen from Fig. 4. The lift coefficient which has been rapidly decreasing after the impulsive start (Fig. 6), begins to increase with the growth of the clockwise bubble A, as seen from Fig. 7. This increase in lift is associated with the fact that the attached bubble effectively increases the camber of the airfoil. After the bursting of the bubble at time t = 6.74, the lift coefficient increases at much slower rate and it starts falling off at time t = 9.0 (Fig. 8). The bursting of the bubble causes the drag coefficient to increase (Fig. 8), since the wake width is increased for the separated flow.

An adverse pressure gradient for the reversed flow on the upper surface from X_c 0.82 to X_c 0.6 is noticeable in Fig.9.A counterclockwise bubble, B, appears in this region and grows with time. The growth of this counterclockwise bubble causes the lift coefficient to fall off rapidly (Fig. 8). From time t = 6.74 to t = 17.62 there is no rear stagnation streamline and the rear stagnation point becomes the separation point of a counterclockwise bubble, C (Fig. 56). The growth cf bubble B partitions the recirculating region

A into regions A' and D (Fig. 5b). Also bubbles B and C merge together and then lift off from the surface at time $t = 17.748$ (Fig. 5c). At this time level region D becomes an attached clockwise bubble, and subsequently at time $t = 18.26$ a counterclockwise bubble, E, appears within the attached bubble D. Growth of this counterclockwise bubble E divides bubble D into two parts (Fig. 5d). As time progresses, bubble D' of Fig. 5d moves towards the trailing edge and bursts. After the bursting of D', the bubble D grows rapidly in size and at time $t = 25.428$ it extends over almost the entire upper surface of the airfoil.

The present results are in good agreement with those of Mehta (Ref. 22) until the bursting of the first separation bubble. After this the sequence of occurence of bubbles and their bursting or lift off from surface are different between these two studies. The key differences are the following: (1) In the present study, whenever there is no rear stagnation streamline, a small counterclockwise trailing edge bubble is always present and the rear stagnation point becomes the separation point of this bubble. This is not found true in Mehta's study. (2) After bubbles B and C merge they stay merged and lift off from the surface together. In Mehta's study they separate again and only bubble C lifts off to surface. Bubble B stays on the surface to play the roll of bubble E of the present case.

The following general conclusions are similar between the two studies. (1) Immediately after impulsive start the rear stagnation point moves very rapidly to the trailing edge. (2) Subsequently a "starting vortex" is visualized through concentric equivorticity lines. (3) The formation of a separation bubble is preceded by an adverse pressure gradient (4) Clockwise bubbles extend or move towards trailing edge and burst (5) Anticlockwise bubbles either lift off the surface or open up to streamlines from above the surface (6) The lift increases with increase in the size of attached clockwise bubbles and decreases when attached anticlockwise bubbles grow.

5. OSCILLATING AIRFOIL

The integro-differential formulation in terms of the velocity vector and the vorticity is utilized in the study of incompressible flows past a 12% thick symmetric Joukowski airfoil oscillating in pitch about a pitching axis located 1/4 chord from the leading edge. The major features of the numerical procedures are described below in terms of the component problems shown in Fig. 1.

The solution field, already confined to the vortical region, is divided into an inner region and an outer region. In the inner region, the grid system consists of grid points, or nodes, that are not uniformly spaced. The nodes represent vortices of triangular elements. In Fig. 10 is shown the specific grid system for the inner region used with the 12% thick airfoil. This system has 232 nodes, including 48 nodes on the airfoil surface and 62 nodes on the outer boundary of the inner region. This system gives 354 triangular elements. The grid system for the outer region consists of uniformly spaced grid points forming a rectangular array. The outer region overlaps the inner region by one layer of elements. That is, in the outermost layer of triangular elements, each pair of elements form a rectangle whose boundaries coincide with the rectangular grid lines of the outer region. The grid spacings used for the airfoil are $\Delta x = 0.05$ and $\Delta y = 0.025$. This grid system for the outer region is not shown in Fig. 10. The number of grid points in the outer region is large. In the oscillating airfoil case, more than 3500 points are used in the outer region.

A finite-element method is used to treat the kinetics of the problem in the inner region. In the outer region, finite-difference methods are used. This hybrid finite element-finite difference method permits the grid system to "fit" the airfoil boundary geometry and to have relatively closely spaced grid points near the airfoil boundary. By using a relatively small number of nodes in the inner region, the size of the relatively complex coefficient matrices involved in the finite-element method is kept small. Most of the solution field is covered by the finite-difference grid which leads to relatively simple coefficient matrices.

Associated with each node "i" in the inner region at (x ,y), there is a composite linear interpolation function $N_i(x\,,y\,)$ with the property

$$N_i(x_j,\ y_j) = \zeta_{ij} \tag{30}$$

where ζ_{ij} is the Kronecker delta. The interpolation function is continuous across the element boundaries (It is zero in elements not containing the node i) though its first derivatives are not necessarily continuous. The velocity and the vorticity fields are assumed to vary linearly within each element. Thus one writes

$$\omega = \left(N_i,\ N_j,\ N_k\right)\begin{Bmatrix}\omega_i\\ \omega_j\\ \omega_k\end{Bmatrix} \tag{31}$$

for the triangular element with nodes i, j and k. Using Galerkin's procedure, an approximation to the two-dimensional vorticity transport equation is

$$\int_R \left(\frac{\partial\omega}{\partial t} + u\,\frac{\partial\omega}{\partial x} + v\,\frac{\partial\omega}{\partial y} - \nu\nabla^2\omega\right) N_i(x,\ y)\,dxdy = 0 \tag{32}$$

The above weighting process is applied at all nodes in the inner region except those on the boundary of that region. By the use of the divergence theorem, one obtains

$$\nu\int_R (\nabla^2\omega)N_i\,dx\,dy = -\,\nu\int_R \vec{\nabla}N_i \cdot \vec{\nabla}\omega\,dxdy$$

$$+\ \nu\int_B N_i(\vec{\nabla}\omega\,)\cdot\vec{n}\,dB \tag{33}$$

The line integral is performed over the boundary of the inner region. Since i is not a boundary node, this line integral vanishes by virtue of Eq. (30). By the use of Eq. (33), the integrand in Eq. (32) is re-expressed as one containing only first derivatives of ω.

Equation (32) can be written as the sum of component integrals over all elements in the inner region. Upon introducing Eq. (31) into the integrals, each of the component integrals in the sum can be integrated, yielding a system of simultaneous differential equations of the form

$$[H]\left\{\frac{d\omega}{dt}\right\} + [C]\{\omega\} + [D]\{\omega\} = \{E\} \tag{34}$$

Using a backward difference scheme for the time derivative, one obtains

$$[H]\left\{\frac{\omega^{n+1}-\omega^{n}}{\Delta t}\right\} + [C^{n}]\left\{\omega^{n+1}\right\} + [D]\left\{\omega^{n+1}\right\} = \left\{E^{n+1}\right\} \tag{35}$$

The terms on the left hand side of Eq. (32) represent respectively the local time rate of change of vorticity, the convection of vorticity, and the diffusion of vorticity. The coefficient matrices $[H]$ and $[D]$ are depdendent only on the node coordinates and are independent of time, they do not need to be evaluated repeatedly for different time levels. The matrix $[C]$ represents convective processes and is dependent on time through the time-varying velocity distribution. To avoid iterative computation of the velocity values for each time step, the velocity field is computed only for the old time step "n". The column matrix $\{E\}$ on the right hand side of Eq. (35) is also time dependent. It represents the contributions of the boundary nodes of the inner region. With known vorticity values on the boundary nodes, $\{E\}$ can be explicitly computed. In the present work, the boundary of the inner region consists of the solid surface and the boundary located within the outer region. (Recall that the two regions overlap). Vorticity values at boundary nodes that are located inside the outer region are computed as a part of the finite-difference procedure. Vorticity values at the solid surface are determined as a part of the kinematic computation as described in Section 3.4.

Since the matrix $[C]$ is time-dependent, the coefficient matrix of the system of simultaneous algebraic equations for the unknown ω^{n+1} must be inverted at each time step. It should be noted, however, that fairly large time intervals can be used in the solution procedure.

In the outer region, the vorticity transport equation is treated using a two-point backward time differencing scheme, with successive point overrelaxation method used to solve the resulting algebraic equations.

The velocity values are computed by a numerical quadrature of Eq. (9). The first integral in Eq. (9) is expressed as a sum of component integrals over individual elements. (For this purpose, each rectangle bounded by grid lines in the outer region is treated as a rectangular element). The use of interpolation functions then leads to exact analytical expressions for the component integrals. These exact expressions have been derived for interpolation functions of all degrees. In the present work, linear interpolation functions are used for the triangular elements of the inner region of the grid system. The vorticity in the rectangular elements of the outer region, however, are represented by a concentrated vortex filament placed at the centroid of the element and its contribution to the velocity field is computed in accordance with the Biot-Savart law. The evaluation of the second integral in Eq. (9) is simplified by considering the rotating coordinate system and the nonrotating coordinate system to coincide with one another at the time t. The second integral can then by re-expressed as

$$2\,\vec{\Omega}(t) \times \int_{R_s} \frac{\vec{r}_o - \vec{r}}{|\vec{r}_o - \vec{r}|^d}\, dR \tag{36}$$

The integral therefore needs to be evaluated only for unit angular velocity $\Omega = 1$ since it is directly proportional to Ω.

The computation of the pressure and skin friction coefficients are carried out in the manner described in Section (4).

The numerical procedures used in this study were calibrated by treating the problem of a flow past an impulsively started finite flat plate at a Reynolds number of 1000 and at zero angle of attack. The results obtained are in excellent agreement with earlier results (Ref. 8) obtained using finite-difference methods instead of the present hybrid method in treating the vorticity transport equation. The solution was carried to a dimensionless time level of 2.4, the reference time level being the plate length divided by the freestream velocity. At this time level, the solution varies very slowly with time in the vicinity of the plate. The velocity and vorticity profiles at midplate obtained for this large time level are, as expected, in excellent agreement with the Blasius profile.

As an additional calibration, the flow past an impulsively started circular cylinder at a Reynolds number based on the cylinder diameter of 40 was treated. The solution was carried to a dimensionless time level of 20.4. At this time level, the computed drag coefficient varies only in the fourth significant digit between successive time levels, the time step being 0.125. The computed streamline and constant vorticity contours are shown in Fig. 11, in the upper and lower halves of the figure respectively, for this large time level. The computed pressure distribution around the cylinder is shown in Figure 3, compared with the results described in Section 4 and experimental results (Ref. 28).

The case where the airfoil is set into translational motion impulsively at an angle of attack of 3° and a Reynolds number of 1000 was studied. The transient solution after the onset of the motion is carried to a dimensionless time level of 2.07, the reference time being the chord length divided by the freestream velocity. The streamline pattern at a time level of 0.87 is shown in Fig. 12. The adverse pressure gradient on the upper surface was not sufficiently strong to cause flow separation. The streamline pattern, however, shows a thick boundary layer region on the upper surface.

The loads on the airfoil are very high immediately after the impulsive start. They decrease rapidly at small time levels, up to a dimensionless time level of 0.35. Prior to this time level, the loads are due primarily to the impulsive start effects. Subsequent to this time level, viscous effects, particularly the thickening of the boundary layer, results in further changes of the loads. The surface pressure decreases relative to the trailing edge pressure. The upper surface pressure, however, decreases at a more rapid rate so that the lift coefficient increases with time. Figure 13 shows the variation of the lift coefficient C_L and of the drag coefficient C_D over the time interval form 0.3 to 2.07. Both the lift and the drag coefficients vary relatively slowly at the time level 2.07.

A flow past the airfoil oscillating at a moderate reduced frequency of 0.3 and a Reynolds number of 1000 was treated. The airfoil is set into translational motion impulsively at $t = 0$. The angle of attack α is given by

$$\alpha = 3^{\circ} + 1^{\circ} \operatorname{Sin}(0.6t) \tag{37}$$

The solution was carried to a non-dimensional time level of 10.4. The airfoil undergoes a complete cycle of oscillation during this period.

The main feature of the load history is that the lift and moment agree qualitatively with the time-dependent linearized potential flow solution. The calculated lift variation is in phase with the potential flow result. The magnitude of the lift coefficient is lower than the lift predicted by the potential flow analysis. This is expected since at the moderate Reynolds number of 1000, the boundary layer on the upper surface is thick and its displacement thickness results in a significant change in the effective shape of the airfoil.

The viscous drag is much larger than the pressure drag for the present case of low angle of attack. This viscous drag is relatively insensitive to the pitching motion of the airfoil. Numerical results indicate a very small separation bubble appearing near the trailing edge on the upper surface during the down stroke (not at maximum angle of attack). However, the size of this bubble is very small and the presence of the bubble does not affect the integrated load significantly.

The solution obtained at the end of the moderate-frequency oscillation cycle was used as the initial solution for a high frequency oscillation computation. The flow Reynolds number is 1000 and the reduced frequency is 3 for this case. The angle of attack is given by

$$\alpha = 3^{\circ} + 1^{\circ} \operatorname{Sin}(6t) \tag{38}$$

The computation was performed for more than two cycles of oscillation. The transient effect, due to the initial condition used, is present during the first cycle but became very small during the second cycle. The load history is presented in Figures 14, 15, 16 and 17.

6. REFERENCES

1. Sampath, S., "A Numerical Study of Incompressible Viscous Flow Around Airfoils, " Ph.D. Thesis, Georgia Institute of Technology, 1977.

2. Wu, J. C. and Thompson, J. F., "Numerical Solutions of Time-Dependent Incompressible Navier-Stokes Equations Using an Integro-Differential Formulation," Vol. 1, No. 2, pp. 197-215, Journal of Computers and Fluids, 1973.

3. Wu, J. C., and Sugavanam, A., "A Method for the Numerical Solution of Turbulent Flow Problems," AIAA Paper No. 77-649, Proceedings of AIAA 3rd Computational Fluid Dynamics Conference, 1977.

4. Wu, J. C., "Integral Representations of Field Variables for the Finite Element Solution of Viscous Flow Problems," Proceedings of the 1974 Conference on Finite Element Methods in Engineering, Clarendon Press, 1974.

5. Wu, J. C., "Finite Element Solution of Flow Problems Using Integral Representation," Proceedings of Second International Symposium on Finite Element Methods in Flow Problems, International Centre for Computer Aided Design, Conference Series No. 2/76, June, 1976.

6. Wu, J. C., and Wahbah, M., "Numerical Solution of Viscous Flow Equations Using Integral Representations," Lecture Series in Physics, Springer-Verlag, Vol. 59, 1976.

7. Thompson, J. F., Shanks, S. P., and Wu, J. C., "Numerical Solution of Three-Dimensional Navier-Stokes Equations Showing Trailing Tip Vortices," AIAA Journal, Vol. 12, No. 6, pp. 787-794, June 1974.

8. Wu, J. C., "Numerical Boundary Conditions for Viscous Flow Problems," AIAA Journal, Vol. 14, No. 8, 1976.

9. Wu, J. C., and Sankar, N. L., "Explicit Finite Element Solution of the Viscous Flow Problem," Proceedings of the 1976 International Conference on Finite Element Methods in Engineering, 1976.

10. Wu, J. C., and Thompson, J. F., "Numerical Solution of Unsteady, Three-Dimensional Navier-Stokes Equations," Proceedings Project SQUID Workshop on Fluid Dynamics of Unsteady, Three-Dimensional, and Separated Flows, October, Purdue University, Lafayette, Indiana, October, 1971.

11. Wu, J. C., Spring, A. H. and Sankar, N. L., "A Flowfield Segmentation Method for the Numerical Solution of Viscous Flow Problems," Proceedings of the Fourth International Conference on Numerical Methods in Fluid Dynamics, Lecture Notes in Physics, Vol. 35, Springer-Verlag, 1975.

12. Schmall, R. A., and Kinney, R. B., "Numerical Study of Unsteady Viscous Flow Past a Lifting Plate," AIAA J., Vol. 12, No. 11, 1974.

13. Kinney, R. B., and Paolino, M. A., "Flow Transient Near the Leading Edge of a Semi-Infinite Flat Plate Moving Through a Viscous Fluid, J. Applied Mech., Vol. 41, No. 4, 1974.

14. Panniker, P. K. G. and Lavan, Z., "Flow Past Impulsively Started Bodies Using Green's Functions," J. Computational Phys., Vol. 18, No. 1, 1975.

15. Reddy, R. N., and Thompson, J. F., "Numerical Solution of Incompressible Navier-Stokes Equations in the Integro-Differential Formulation," AIAA Paper No. 77-650, Proceedings of AIAA 3rd Computational Fluid Dynamics Conference, 1977.

16. Davis, R. T., "Numerical Solution of the Incompressible Navier-Stokes Equations for Two Dimensional Flows at High Reynolds Number," Rept. No. AFL 76-8-22, Department of Aerospace Engineering, University of Cincinnati, 1976.

17. Thompson, J. F., Thames, F. C., and Mastin, C. W., "Automatic Numerical Generation of Body-Fitted Curvilinear Coordinate System for Field Containing Any Number of Arbitrary Two-Dimensional Bodies," J. Computational Phys., Vol. 15, No. 3, 1974.

18. "Proceedings of the Second International Symposium on Finite Element Methods in Flow Problems," International Centre for Computer Aided Design, Conference Series No. 2/76, 1976.

19. Roache, P. J., "Computational Fluid Dynamics," Hermosa Publishers, Albuquerque, New Mexico, 1972.

20. Cheng, S. I., "Numerical Integration of Navier-Stokes Equations," AIAA Journal, Vol. 8, No. 12, 1970.

21. Moretti, G., "Importance of Boundary Conditions in the Numerical Treatment of Hyperbolic Equations," Phys. Fluids, Vol. 12, No. 12, 1969.

22. Mehta, U. B., "Starting Vortex, Separation Bubbles and Stall -A Numerical Study of Laminar Unsteady Flow Around an Airfoil," Ph.D. Thesis, Illinois Inst. of Tech., Chicago, 1972.

23. Arakawa, A., "Numerical Solution of Large Scale Atmospheric Motions," SIAM-AMS Proceedings, Vol. 2, Numerical Solution of Field Problems in Continuum Physics, American Math. Soc., 1970.

24. Lugt, H. J., and Hausling, H. J., "Laminar Flow Past an Abruptly Accelerated Elliptic Cylinder at 45 degree Inclination," J. Fluid Mechanics, Vol. 65, Oct. 2, 1974, pp. 711-734.

25. Lin, C. L. and Lee, S. C., "Transient State Analysis of Separated Flow Around a Sphere," Computers and Fluids, Vol. 1, pp. 235-250, 1973.

26. Stone, H. L., "Iterative Solution of Implicit Approximations of Multi-dimensional Partial Differential Equations," SIAM J. Num. Analysis, Vol. 5, No. 3, pp. 530-558, 1969.

27. Lin, C. L., Pepper, D. W., and Lee, S. C., "Numerical Methods for Separated Flow Solution Around a Circular Cylinder," Proc. of AIAA 2nd Computational Fluid Dynamics Conference, Hartford, Connecticut, June 19-20, 1975, pp. 91-100.

28. Grove, A. S., Shair, F. H., Petersen, E. E., and Acrivos, A., "An Experimental Investigation of the Steady Separated Flow Past a Circular Cylinder," J. Fluid Mech., Vol. 33, Part 1, 1964, pp. 60 80.

7. ACKNOWLEDGEMENT

This paper is based on research supported by the Office of Naval Research under Contract No. N00014-75-C-0249.

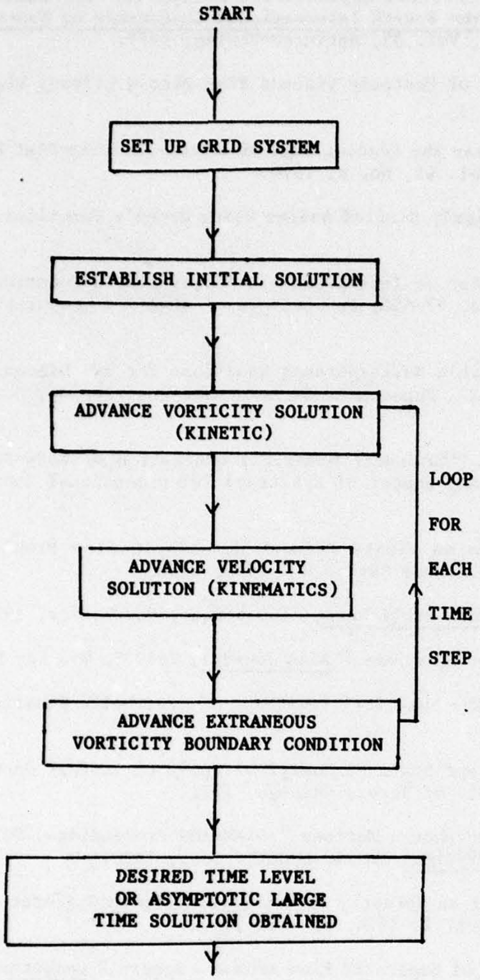

Fig. 1. COMPONENT PROBLEMS FOR THE GENERAL VISCOUS FLOW

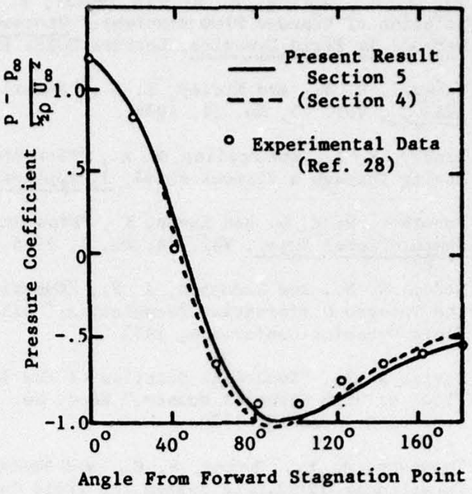

Fig. 3. PRESSURE DISTRIBUTION OVER A CIRCULAR CYLINDER ($U_\infty D/\nu = 40$)

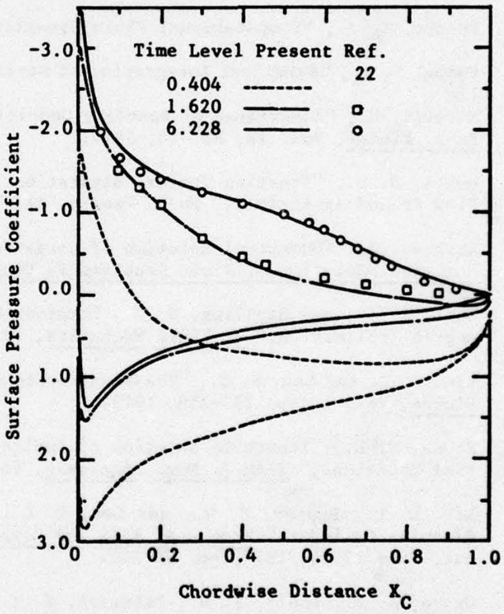

Fig. 4. SURFACE PRESSURE DISTRIBUTION OVER A 9% JOUKOWSKI AIRFOIL AT 15° ANGLE OF ATTACK FOR EARLY TIME LEVELS

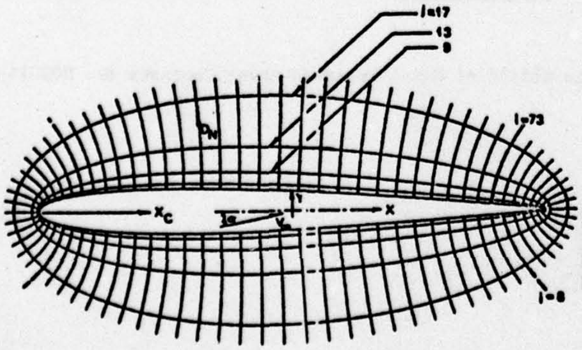

Fig. 2 GRID DISTRIBUTION AND NOTATIONS IN PHYSICAL PLANE

(a) T = 6.228

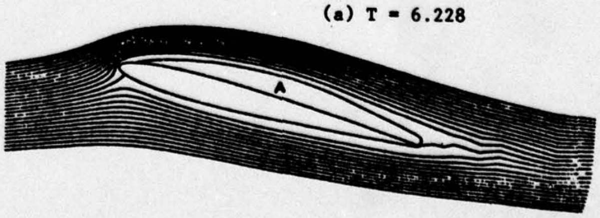

Fig. 5. STREAMLINE PATTERN AROUND AN IMPULSIVELY STARTED 9% JOUKOWSKI AIRFOIL AT 15° ANGLE OF ATTACK AT SELECTED TIME LEVELS

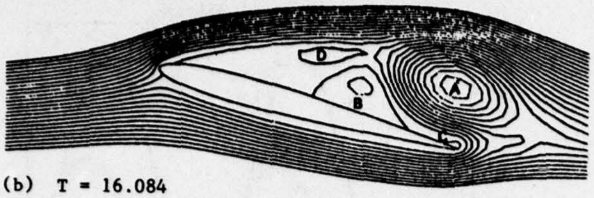

(b) T = 16.084

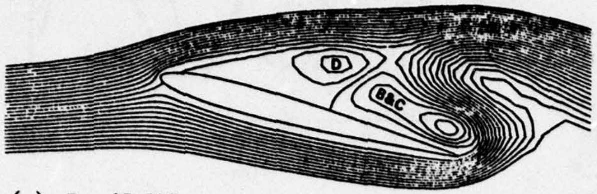

(c) T = 17.748

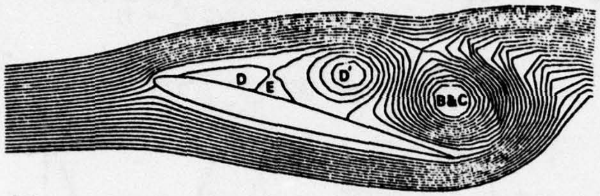

(d) T = 19.284

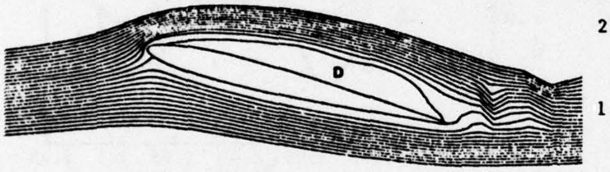

(e) T = 25.428

Fig. 5 Continued

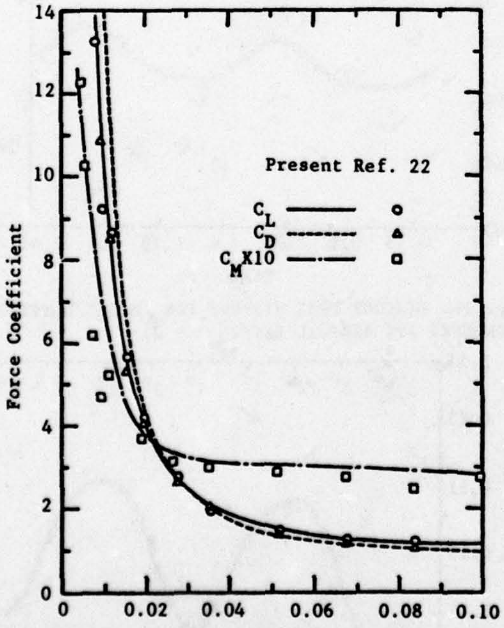

Fig. 6. LOAD HISTORIES FOR AN IMPULSIVELY STARTED JOUKOWSKI 9% AIRFOIL AT 15° ANGLE OF ATTACK AT EARLY TIME LEVELS

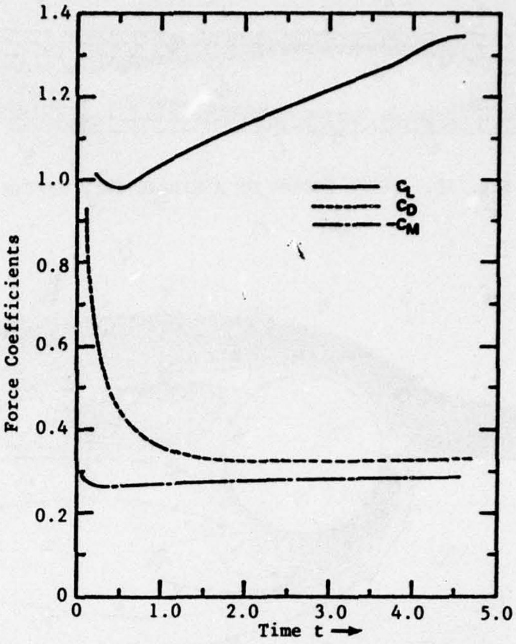

Fig. 7. LOAD HISTORIES FOR AN IMPULSIVELY STARTED 9% JOUKOWSKI AIRFOIL AT 15° ANGLE OF ATTACK

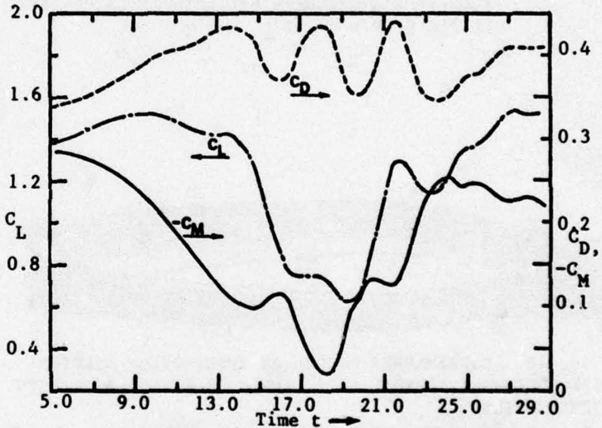

Fig. 8. LOAD HISTORIES FOR AN IMPULSIVELY STARTED 9% JOUKOWSKI AIRFOIL AT 15° ANGLE OF ATTACK

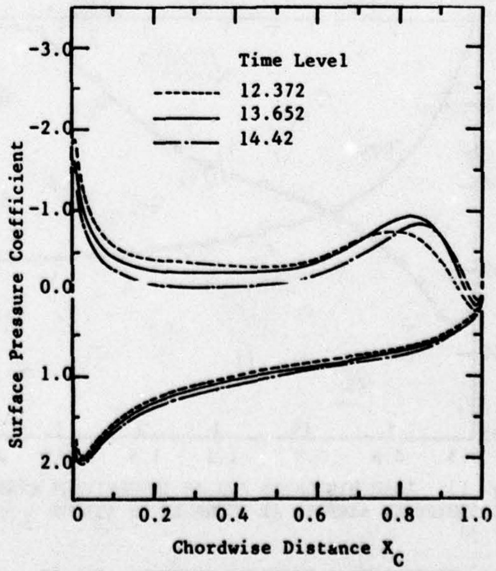

Fig. 9. SURFACE PRESSURE DISTRIBUTION OVER AN IMPULSIVELY STARTED 9% JOUKOWSKI AIRFOIL AT 15° ANGLE OF ATTACK

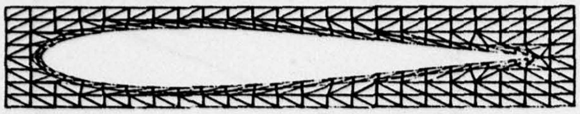

Fig. 10. INNER REGION OF A HYBRID GRID SYSTEM

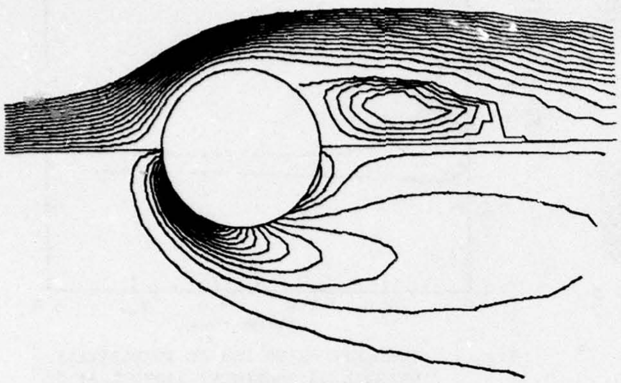

Fig. 11. STREAMLINES AND VORTICITY CONTOURS FOR VISCOUS FLOW OVER A CIRCULAR CYLINDER AT LATER TIME LEVELS ($U_\infty D/\nu = 40$)

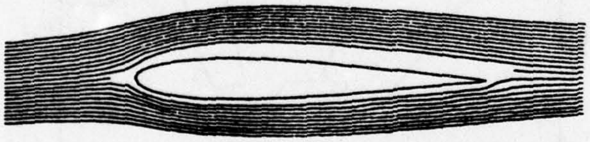

Fig. 12. STREAMLINES AROUND AN IMPULSIVELY STARTED 12% JOUKOWSKI AIRFOIL AT 3° ANGLE OF ATTACK AT EARLY TIME LEVELS

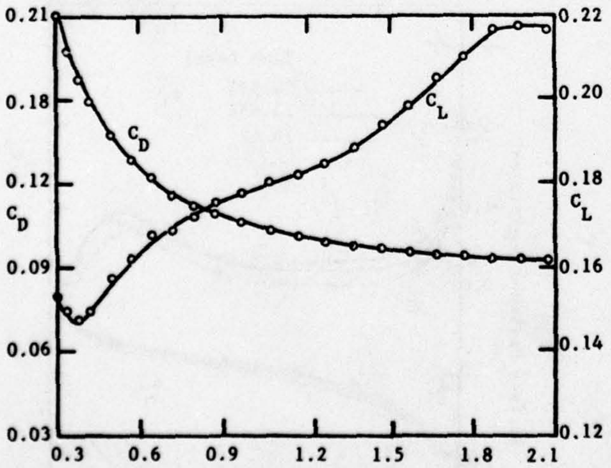

Fig. 13. LOAD HISTORIES FOR AN IMPULSIVELY STARTED 12% JOUKOWSKI AIRFOIL AT 3° ANGLE OF ATTACK

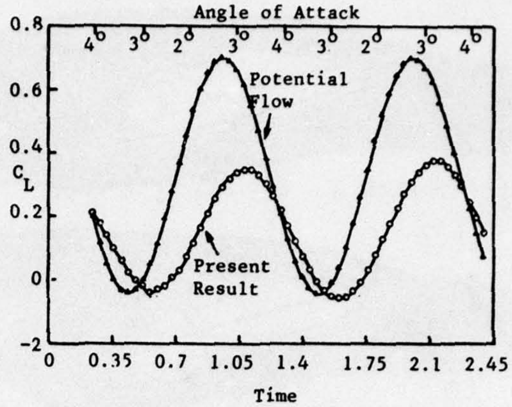

Fig. 14. LIFT HISTORY FOR AN OSCILLATING JOUKOWSKI 12% AIRFOIL ($\omega C/2 U_\infty = 3$)

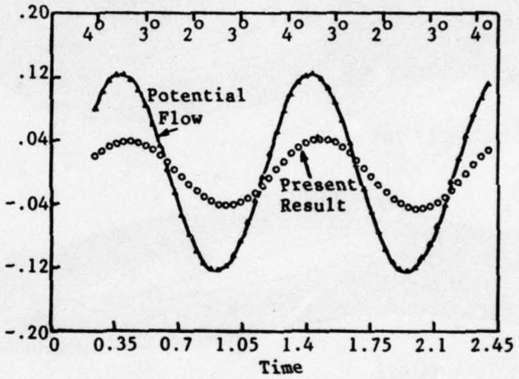

Fig. 15. MOMENT COEFFICIENT ABOUT QUARTER CHORD FOR AN OSCILLATING JOUKOWSKI 12% AIRFOIL ($\omega C/2U_\infty = 3$)

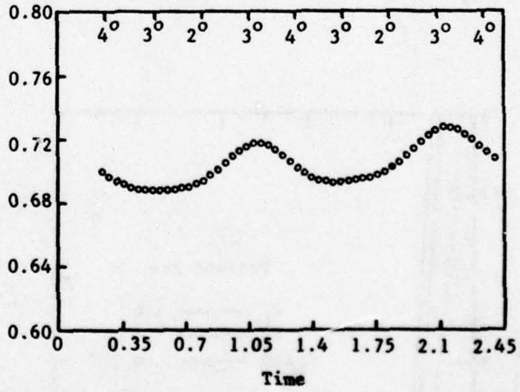

Fig. 16. VISCOUS DRAG HISTORY FOR AN OSCILLATING JOUKOWSKI 12% AIRFOIL ($\omega C/2U_\infty = 3$)

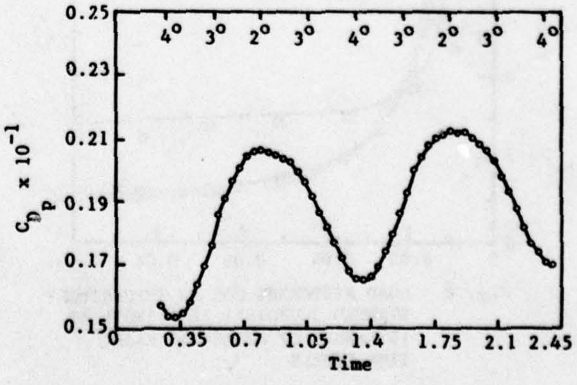

Fig. 17. PRESSURE DRAG HISTORY FOR AN OSCILLATING JOUKOWSKI 12% AIRFOIL ($\omega C/2U_\infty = 3$)

SCALING PROBLEMS IN DYNAMIC TESTS OF AIRCRAFT-LIKE CONFIGURATIONS*

by

Lars E.Ericsson and J. Peter Reding
Lockheed Missiles & Space Company, Inc.
Sunnyvale, California, 94088, USA

SUMMARY

To extrapolate from subscale wind tunnel tests to full scale flight is a well-recognised problem. It is especially critical for present day high performance aircraft and the space shuttle orbiter which operate under flight conditions where separated flow effects often dominate the vehicle aerodynamics. In the case of dynamic tests it may not be possible to simulate flight conditions at subscale Reynolds number. This is illustrated by example from two-dimensional dynamic stall tests at low speeds and dynamic tests of fully three-dimensional configurations at transonic speeds, such as the space shuttle orbiter. It is shown how analytical means can be developed establishing theoretical relationships between dynamic and static aerodynamic characteristics and how such means make it possible to extrapolate analytically from subscale tests to full scale flight. The role of future high Reynolds number facilities in establishing such "analytic extrapolation" tools is discussed.

1. INTRODUCTION

The extrapolation from subscale wind tunnel data to full scale flight is a well-recognized problem. It becomes especially serious at subsonic speeds when stall is involved and at high subsonic and transonic speeds where shock-boundary layer interaction can dominate the aerodynamics (Refs. 1–3). In the case of dynamic testing, valid subscale simulation is often impossible. For example, whereas the static shock-boundary layer interaction on an airfoil can in some cases be simulated at subscale Reynolds numbers by a strategic application of surface roughness (Ref.4), the unsteady aerodynamic characteristics cannot be simulated in this manner. The reason for this is that the coupling existing in full scale flight between the location of the free (unfixed) boundary layer transition and the airfoil motion has been changed drastically, if not eliminated completely. Thus, even in a simple two-dimensional flow case, dynamic simulation of shock-boundary layer interaction at subscale Reynolds numbers is all but impossible. When considering the complex three-dimensional flow existing on high performance aircraft or the space shuttle orbiter, the problem becomes more difficult, and full scale Reynolds number simulation is often necessary for both dynamic and static testing.

2. DISCUSSION

The scaling problem will be illustrated by examples from two-dimensional dynamic stall tests at subsonic speeds and dynamic tests of fully three-dimensional configurations at transonic speeds.

2.1 Two-Dimensional Flow

Dynamic stall is a phenomenon that still is not well understood. As a consequence, heavy reliance has to be placed on experimental data which as a rule are obtained in dynamic tests where the full scale Reynolds number cannot be simulated. Philippe has presented results (Ref.5) that demonstrate how such lack of Re-simulation can distort the dynamic results (Fig.1). The leading edge modification to the NACA-0012 airfoil is of the type investigated by Poisson-Quinton and deSievers (Ref.6), which reduces the adversity of the pressure gradient near the leading edge thereby causing a delay of stall with resultant increase of $C_{l_{MAX}}$ (Fig.2).

It has been shown (Ref.7) how the dynamic stall characteristics can be related directly to the static stall characteristics, provided that the frequency is not large enough to introduce significant transient effects of the "spilled" leading edge vortex (Ref.8). The effect of the leading edge modification in Figure 1 is to elevate the static stall and deep-stall

---

* The paper is in large part based upon results obtained in work sponsored by NASA, Marshall Space Flight Center, under Contracts NAS 8-28130 and NAS 8-30652.

levels from which the dynamic perturbation occurs, thus raising the whole $C_l(\alpha)$-loop. In the present case (Fig.3), the "infinite Reynolds number limit" for dynamic $C_{l_{MAX}}$ is reached already for the unmodified airfoil. Thus, only the lower loop boundary is elevated, resulting in the observed decrease of the $C_l(\alpha)$-loop (Ref.7). How to construct the complet $C_l(\alpha)$-loop is discussed in Reference 7. The point to be illustrated here is that even larger differences in static characteristics are caused by improper Reynolds number simulation (Ref.9) than those discussed here (compare Figures 2 and 4). Attempts to simulate dynamic section characteristics in two-dimensional subscale tests are impeded further by severe side-plate or side-wall interference effects (References 8, 10 and 11).

Figure 1 illustrates the scaling difficulties existing in incompressible flow. The problem is complicated greatly when considering the effects of compressibility which are always significant at stall. Even if the free stream Mach number is $M_\infty = 0.1$, the maximum Mach number on the stalling airfoil can easily exceed the "incompressible limit" $M_\infty = 0.4$ (Ref.12). This is true even for the NACA-0012 airfoil with its relatively large nose radius of 1.58% (Fig.5). Thus, there does not exist any incompressible stall data (dynamic or static). As most low speed wind tunnels cannot change the Reynolds number significantly without simultaneously changing the free stream Mach number, stall experiments (dynamic and static) normally show Reynolds number effects that are distorted by compressibility effects. The results in Figure 6 for the dynamic overshoot of static lift maximum in airplane pull-up maneuvers (Ref.13) illustrate this. It can be shown (Ref.12) that the compressibility effect actually dominates over the Reynolds number effect in the data shown in Figure 6. Figure 7 illustrates how such compressibility effects can influence greatly the size of the negative damping loop measured in dynamic stall tests (References 8 and 14).

When the subsonic Mach number exceeds $M_\infty \approx 0.5$, the stall type changes from the shock-augmented leading edge stall to shock-augmented trailing edge stall. The shock-induced boundary layer separation is very sensitive to Reynolds number (see Reference 15 and Figure 8). The difficulty in trying to simulate full scale Reynolds number by tripping the boundary layer is well known (Reference 16 and Figure 9). The trip causes the boundary layer to be thicker than in the case of free transition, thereby causing earlier shock-induced separation with associated large effects on the aerodynamic characteristics. Blackwell (Ref.4) has shown that the correct shock position can be obtained in the subscale wind tunnel test if the boundary layer characteristics at the trailing edge are simulated rather than the transition location. That is, the transition is allowed to occur downstream of the full scale location. One problem with this method is that it is limited to profile shapes that do not get the transition in the wind tunnel upstream of this desired, tripped transition location.

A severe problem in dynamic tests is the lack of simulation of the strong coupling existing between the airfoil motion and the transition location, as is illustrated in Figure 10 by the experimental results for a 7.3% thick airfoil (Ref.17). Using a trip wire, the measured amplitude and phase characteristics as a function of reduced frequency ($\bar{\omega}$) were in reasonable agreement with theoretical predictions. However, when the transition was free, large anomalous deviation from the expected characteristics were observed. With the oscillation center at 22.7% chord, the attached flow lift, centered at 25% chord, has little effect on the pitching moment. This is the reason for the large effects observed for free transition even in the absence of shock-boundary layer interactions. The reduced frequency was varied by changing the tunnel velocity, keeping the oscillation frequency constant. Thus, the velocity, and hence the Reynolds number, increases with decreasing reduced frequency ($\bar{\omega}$). As a consequence, transition moves foward from the trailing edge towards the leading edge with decreasing $\bar{\omega}$. The results in Figure 10 were used in Reference 18 to illustrate the dynamic phase characteristics of trailing edge separation, showing that the phase angle and amplitude perturbations could be predicted by the analytic method of Reference 19.

2.2 Three-Dimensional Flow

Figures 8, 9 and 10 demonstrate that it is practically impossible to simulate shock-boundary layer interaction in a dynamic test at subscale Reynolds number even for the relatively simple case of two-dimensional flow. The three-dimensional flow effects that occur on high performance aircraft (Ref.20) and the space shuttle orbiter (Ref.21) involve multiple shocks that severely complicate the shock-boundary layer interaction (Fig.11).

For a swept wing the spanwise flow generated by leading edge sweep produces another mechanism for boundary-layer transition, which further complicates the problems of Re-simulation (Ref.22). At transonic speeds, the wing flow pattern shown in Figure 12 results (Ref.23). On the inboard wing, transition is dominated by the chordwise flow and occurs well aft of the leading edge (in unseparated flow) and the flow separation is of the regular two-dimensional stall type. However, outboard towards the wing tip the transition is dominated by the spanwise flow component causing it to occur near the leading edge, thereby eliminating leading edge stall and causing separation to occur well downstream of the leading edge due to shock-boundary layer interaction. This mixed-separated flow pattern cannot presently be simulated at subscale Reynolds numbers even in a static test. In a dynamic test with rigid or elastic wings, the streamwise location of the change in stall pattern will be sensitive to the wing motion. Dynamic tests at subscale Reynolds number will have different spanwise separation patterns that alter the motion dependence of the aerodynamic loads, thereby invalidating the simulation. Especially critical is the inability of the subscale test to simulate the angle of attack at which the retarded, shock-induced, separation on the outboard wing jumps to the leading edge causing a discontinuous change of the outboard wing loading with associated large effects on wing bending and rolling moments (Refs. 24–27).

The large discontinuous load change observed on a slab wing (Ref.28) shown in Figure 13 is the result of separation suddenly jumping to the leading edge. The rigid body dynamic data in Figure 14 for the space shuttle orbiter (Ref.29) reveal that a similar dramatic change in flow pattern occurs at $\alpha \approx 8°$. The measured large increase of dynamic stability and corresponding moderate decrease of static stability are typical for the nonlinear, possibly discontinuous, aerodynamic characteristics associated with a sudden increase in the extent of flow separation. It is shown in References 26, 27, 30–32 how the dynamic characteristics of the space shuttle orbiter can be predicted using static experimental data in a quasi-steady analysis that accounts for the separated flow time lag effects. Figure 15 illustrates how the discontinuous net negative force produces a statically destabilizing and hence damping effect on the rigid body orbiter, oscillating in pitch, all in agreement with the results shown in Figure 14. The effect for the elastic mode sketched in Figure 15 will be the opposite, with the force couple providing a statically restoring and hence undamping moment. The flow visualization pictures in Figure 16 show that the first torsional mode of the orbiter wing will feel the full dynamically destabilizing effect of the separation-induced force couple. The sudden separation-change will, of course, also affect the wing bending and rigid body rolling moments. Recent experimental results for the coupling between lateral and longitudinal degrees of freedom (Ref.33) show a sharp peak at $\alpha = 17°$, $\beta = \pm 5°$, $M_\infty = 0.7$ of the roll-due-to-pitch-rate cross-coupling derivative (Fig.17). This angle of attack agrees well with that at which one would expect the sudden separation change to take place for the wing with its 40°–5° swept upwind leading edge. For the TACT-F111 aircraft, the sudden flow change was observed for $\alpha = 12°$, $\beta = 0$, $M_\infty = 0.9$, $\Lambda = 35°$ (References 24 and 25). One would expect the critical angle of attack to increase with decreasing subsonic Mach number.

3. GROUND TESTING

The foregoing illustrates that sudden stall is a flow phenomena shared by high performance aircraft and the shuttle orbiter. Furthermore, it will affect both the rigid body dynamics and the aeroelastic stability. Thus, valid prediction of the sudden stall effects for full scale flight simulation is vital.

The obvious solution to these scaling problems is to supply ground testing facilities with the capability of simulating full scale Reynolds number. One existing tunnel with some such capability is the two-dimensional NAE high speed wind tunnel (Ref.34). A tunnel with more complete simulation capability will be the N(ational) T(ransonic) F(acility) planned to become operational in the early eighties (Ref.35). And others will undoubtedly become available later on. However, they will all be in too much demand to be able to accommodate all the development testing. The facilities will have to be used in a more sophisticated manner. They can be used most effectively by developing a basic understanding of the effects of Reynolds number, especially in regard to flow separation with its dramatic effects on vehicle dynamics and aeroelastic stability. The goal should be to provide the vehicle designer with the information needed to determine when theory and/or tests at subscale Reynolds numbers will suffice and when he needs the full scale Reynolds number simulation that very few facilities will be able to furnish, and in many cases probably only in regard to static aerodynamics. With the present state-of-the-art, it does not appear that dynamic simulation at full scale Reynolds number will always be possible, especially in the case of the fully elastic vehicle (Ref.36). What is needed, then, is means by which the unsteady aerodynamics can be determined using static experimental data. Examples of such analytic means have already been given (Refs.7, 8, 11, 12, 18, 19, 26, 27, 30–32). In addition, it is shown in Reference 37 how Lambourne's experimental results for unsteady shock-boundary layer interactions (Ref.38) can be predicted using static experimental data.

"Analytic extrapolation tools" are not only needed to account for Reynolds number effects, but they will also allow the vehicle designer to account for effects of post test design changes on rigid and elastic vehicle dynamics. For example, the analytic method developed in Reference 39 made it possible to account for the changes in vehicle trajectory and in configurational and structural design that had been made after the completion of the dynamic tests of the elastic Apollo-Saturn vehicle (Ref.40). As the analytic method could predict the dynamic test results for the "obsolete" configuration, it could be used with confidence to "extrapolate analytically" and predict the elastic vehicle dynamics for the current flight vehicle design (References 39 and 41). It is shown in Reference 27 that rigid body dynamic experimental data can be used to check important aspects of the "analytic extrapolation tool" before it is applied to an elastic vehicle. As it appears that dynamic tests of rigid bodies will be possible in NTF and similar facilities (References 3 and 42), the effect of Reynolds number could be included in the "analytic extrapolation" of elastic vehicle dynamics by methods similar to those discussed in Reference 27.

An area of present concern is the pitch-yaw-roll coupling existing for modern military aircraft and the space shuttle. There is a need for both subscale dynamic testing capability (Ref.43) and "analytic extrapolation tools" (Ref.44). Whereas progress is being made in regard to multi-degree-of-freedom dynamic testing (Refs. 33, 45–48), the development of analytic means of extrapolation to full scale from data obtained at subscale Reynolds numbers largely remains to be accomplished (References 44 and 49).

4. CONCLUSIONS AND RECOMMENDATIONS

A review of scaling problems in dynamic tests of aircraft-like configurations has revealed the following:

- It is impossible to simulate full scale unsteady aerodynamics in dynamic tests at subscale Reynolds numbers when flow separation is involved.
- It may often not be possible to simulate full scale elastic vehicle dynamics in dynamic tests on subscale models performed at full scale Reynolds numbers due to model loads and instrumentation problems.

- **It is recommended that the large Reynolds number facilities be used to improve our basic understanding of Reynolds number scaling of static aerodynamics and aid in the development of analytic means for prediction of full scale unsteady aerodynamic characteristics using subscale static experimental data, together with selective rigid body dynamic data for full scale Reynolds numbers whenever possible.**

REFERENCES

1. Zonars, D., Lowndes, H.B., Kolb, A.W. — *Ground Testing*, AIAA Paper No.68-1084, October 1968.

2. Various authors — *Facilities and Techniques for Aerodynamic Testing at Transonic Speeds, and High Reynolds Numbers*, AGARD CP-83, Papers presented at the Fluid Dynamics Panel Specialists' Meeting, Göttingen, Germany, 26–28 April, 1971.

3. Anonomous — *National Transonic Facility*. Report of the 1974 National Aeronautical Facility Sub-panel to the Aeronautics Panel, AACB. May 1975.

4. Blackwell, J.A., Jr — *Preliminary Study of Effects of Reynolds Number and Boundary Layer Transition Location on Shock-Induced Separation*, NASA TND-5003, January 1969.

5. Philippe, J.J. — *Le Decrochage Instationnaire d'un Profil*, ONERA TP No.936, 1968.

6. Poisson-Quinton, P., deSievers, A. — *Etude Aerodynamique d'un Element de Pale d'Helicoptere*, AGARD-CP-22, Supplement, pp.4-1 through 4-35, September 1967.

7. Ericsson, L.E., Reding, J.P. — *Dynamic Stall Analysis in Light of Recent Numerical and Experimental Results*, Journal of Aircraft, Vol.13 No.4, April 1976. See also AIAA Paper No.75-76.

8. Ericsson, L.E., Reding, J.P. — *Quasi-Steady and Transient Dynamic Stall Characteristics*, AGARD-CP-204, pp.25-1 through 25-12, September 1976.

9. Jacobs, E.N., Sherman, A. — *Airfoil Section Characteristics as Affected by Variations in the Reynolds Number*, Tech. Report 586, NACA, 1937.

10. Moss, G.F., Murdin, P.M. — *Two-Dimensional Low-Speed Tunnel Tests on the NACA 0012 Section Including Measurements Made During Pitch Oscillations at the Stall*, CP No.1145, Aer. Res. Council, Great Britain, 1971.

11. Ericsson, L.E., Reding, J.P. — *Dynamic Stall Simulation Problems*, J. Aircraft, Vol.8, No.7, pp.579-583, July 1971.

12. Ericsson, L.E., Reding, J.P. — *Stall Flutter Analysis*, J. Aircraft, Vol.10, No.1, pp.5-13, January 1973.

13. Harper, P.W., Flanagan, R.E. — *The Effect of Rate of Change of Angle of Attack on the Maximum Lift of a Small Model*, NACA, TN 2061, 1949.

14. Liiva, J., Davenport, F.J., Gray, L., Walton, I.C. — *Two-Dimensional Tests of Airfoils Oscillating Near Stall*, TR 68-13A and B, US Army Aviation Material Labs., Port Eustis, Va., April 1968.

15. Vaucheret, X., Bazin, M., Armand, C. — *Comparaison d'Essais Transsoniques Bi- et Tridimensionels Effectués dans diverses Grandes Souffleries*, ONERA TP No.1975-61, June 1975.

16. Loving, D.L. — *Wind-Tunnel-Flight Correlation of Shock-Induced Separation Flow*, NASA TN D-3580, 1966.

17. Greidanus, J.H., Van de Vooren, A.I., Bergh, H. — *Experimental Determination of the Aerodynamic Characteristics of an Oscillating Wing with Fixed Axis of Rotation*, NLL Report F101, January 1952.

18. Ericsson, L.E., Reding, J.P. — *Dynamic Stall of Helicopter Blades*, Journal of the American Helicopter Society, Vol.17, No.1, pp.10-19, January 1972.

19. Ericsson, L.E.; Reding, J.P. — *Unsteady Airfoil Stall. Review and Extension*, J. Aircraft, Vol.8, No.8, pp.609-616, August 1971.

20. Lock, R.C.; Rogers, E.W.E. — *Aerodynamic Design of Swept Wings and Bodies for Transonic Speeds*, Proceedings of the 2nd International Congress of Aeronautical Sciences, 1960.

21. Nichols, M.E. — *Results of Investigations on the 0.004 – Scale Model 74-0 of the Configuration 4 (Modified) Space Shuttle Orbiter in the NASA/MSFC 14-by-14 Inch Trisonic Wind Tunnel (OA131)*, NASA-CR-141, 521, March 1975.

22. Owen, P.R.; Randall, P.G. — *Boundary Layer Transition on a Sweptback Wing*, Tech. Memo No. Aero 277, Royal Aircraft Establishment, Great Britain, 1952.

23. Rogers, E.W.E.; Berry, C.J.; Townsend, J.E.C. — *A Study of the Effect of Leading Edge Modifications on the Flow Over a 50 Deg. Sweptback Wing at Transonic Speeds*, R&M No.3270, Royal Aircraft Establishment, Great Britain, 1962.

24. Riddle, D. — *TACT Unsteady Aerodynamics*, Transonic Aircraft Technology Briefing to Industry and Government, Santa Monica, California, November 10, 1975.

25. Coe, C.F.; Riddle, D.W.; Hwang, C. — *Separated Flow Unsteady Pressures and Forces on Elastically responding Structures*, 44th Meeting of AGARD Structures and Materials Panel, Specialists' Meeting on Unsteady Airloads in Separated and Transonic Flow, Lisbon, Portugal, April 12–22, 1977.

26. Ericsson, L.E.; Reding, J.P. — *Unsteady Aerodynamic Flow Field Analysis of the Space Shuttle Configuration. Part I: Orbiter Aerodynamics*, NASA CR 144332, April 1976.

27. Reding, J.P.; Ericsson, L.E. — *The Effects of Flow Separation on Shuttle Dynamics and Aeroelastic Stability*, AIAA Paper No.77-116, January 1977.

28. – — *Compilation of Information on the Transonic Attachment of Flows at the Leading Edges of Airfoils*, NACA TN 4204, February 1958.

29. Boyden, R.P.; Freeman, D.C. — *Subsonic and Transonic Dynamic Stability Derivatives of a Modified 089B Shuttle Orbiter*, NASA TMX-72631, DMS-DR-2107, December 1974.

30. Ericsson, L.E.; Reding J.P. — *Unsteady Aerodynamics of Slender Delta Wings at Large Angles of Attack*, Journal Aircraft, Vol.12, No.9, pp.721-729, September 1975.

31. Ericsson, L.E.; Reding, J.P. — *Nonlinear Slender Wing Aerodynamics*, AIAA Paper No.76-19, January 1976.

32. Ericsson, L.E.; Reding, J.P. — *Effect of Angle of Attack and Mach Number on Slender Wing Aerodynamics*, AIAA Paper No.77-667, June 1977.

33. Orlik-Rückemann, K.J. — *On Aerodynamic Coupling Between Lateral and Longitudinal Degrees of Freedom*, AIAA Paper No.77-4. January 1977.

34. Ohman, L.H. — *The NAE High Reynolds Number 15 in x 60 in. Two-Dimensional Test Facility*, LTR-HA-4, NAE, National Research Council, Ottawa, Canada, April 1970.

35. Howell, R.R.; McKinney, L.W. — *The US 2.5 Meter Cryogenic High Reynolds Number Tunnel*, 10th ICAS Congress, Ottawa Canada, October 3–9, 1976.

36. – — Workshop on High Reynolds Number Research, NASA Langley Research Center, NASA SP-2009, October 27–28, 1976.

37. Ericsson, L.E. — *Dynamic Effects of Shock-Induced Flow Separation*, Journal of Aircraft, Vol.12, No.2, pp.86-92, February 1975.

38. Lambourne, N.C. — *Some Instabilities Arising from the Interaction Between Shock Waves and Boundary Layers*, C.P. No. 473, February 1958.

39. Ericsson, L.E.; Reding, J.P. — *Analysis of Flow Separation Effects on the Dynamics of a Large Space Booster*, J. Spacecraft and Rockets, Vol.2, No.4, pp.481-490, July–August 1965.

40. Hanson, P.W.
Dogget, R.V., Jr
Wind Tunnel Measurements of Aerodynamic Damping Derivatives of a Launch Vehicle Vibrating in Free-Free Bending Modes at Mach Numbers from 0.7 to 2.87 and Comparison with Theory, NASA TN D-1391, 1962.

41. Rainey, A.G.
Progress of Launch Vehicle Buffeting Problem, J. Spacecraft and Rockets, Vol.2, No.3, pp.289-299, May–June 1965.

42. Orlik-Rückemann, K.J.
Demonstration of a Hydraulic Forced Oscillation Rig Capable of Handling Aerodynamic Loads of up to 3000 lbs. Field trip at the AGARD Conference on Unsteady Aerodynamics, Ottawa, Canada, 26–28 September 1977.

43. Orlik-Rückemann, K.J.
Dynamic Stability Testing of Aircraft-Needs Versus Capabilities, Progress of Aerospace Sciences, Vol.16, No.4, pp.431-447, 1975.

44. Ericsson, L.E.
Reding, J.P.
Unsteady Aerodynamic Analysis of Space Shuttle Vehicles, Part II: Steady and Unsteady Aerodynamics of Sharp-Edged Delta Wings, NASA CR-120123, August 1973.

45. Hanff, E.S.
Orlik-Rückemann, K.J.
A Wind Tunnel Test and Calibration Technique for the Measurement of Damping and Dynamic Cross Derivatives due to Pitching and Yawing, AIAA Paper No.77-80, January 1977.

46. Schiff, L.B.
Tobak, M.
Results from a New Wind-Tunnel Apparatus for Studying the Coning and Spinning Motions of Bodies of Revolution, AIAA Journal, Vol.8, No.11, pp.1953-1957, November 1970.

47. Tobak, M.
Schiff, L.B.
Generalized Formulation of Nonlinear Pitch-Yaw-Roll Coupling: Part I – Non-Axisymmetric Bodies, AIAA Journal, Vol.13, No.3, pp.323-326, March 1975.

48. Tobak, M.
Schiff, L.B.
Generalized Formulation of Nonlinear Pitch-Yaw-Roll Coupling: Part II – Nonlinear Coning-Rate Dependence, AIAA Journal, Vol.13, No.3, pp.327-332, March 1975.

49. Reding, J.P.
Ericsson, L.E.
Review of Delta Wing Shuttle Vehicle Dynamics, Vol.III, Proceedings Space Shuttle Aerothermodynamics Conference NASA/Ames Research Lab., Moffett Field, California, (NASA TMX-2508), pp.861-931, December 15–17.

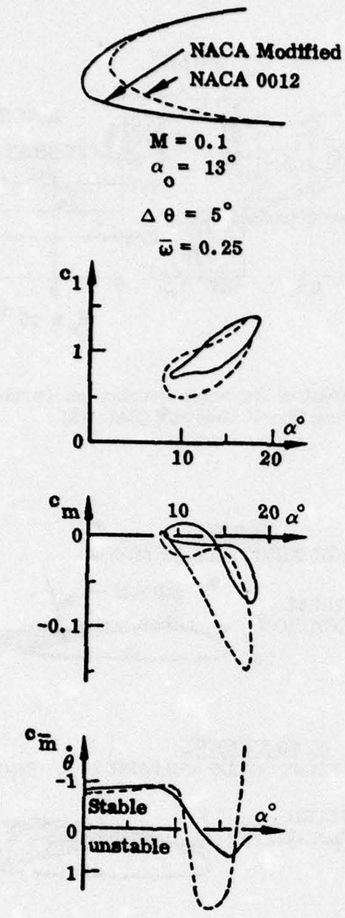

Figure 1. Effect of Leading Edge Droop on Dynamic Stall (Ref. 5)

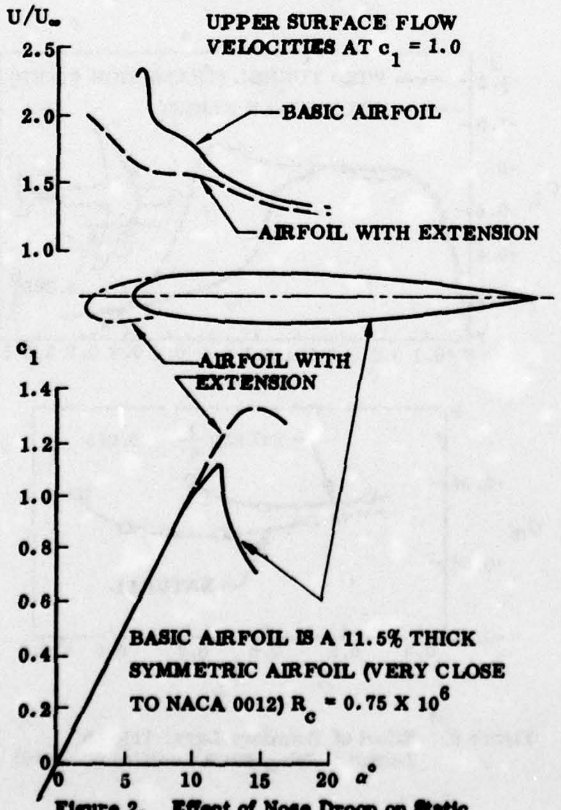

Figure 2. Effect of Nose Droop on Static Stall (Ref. 6)

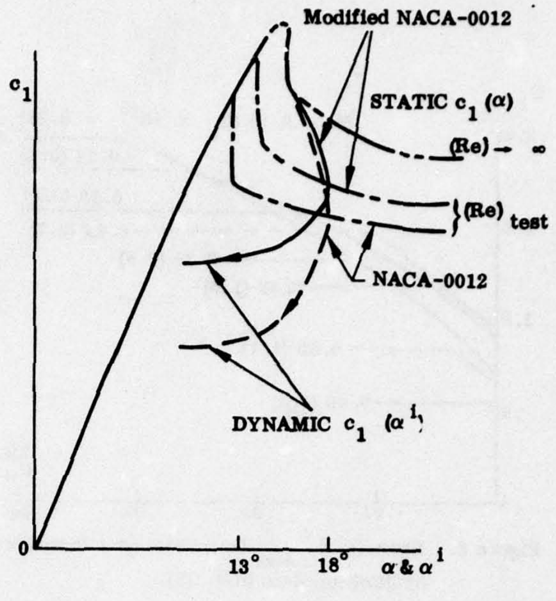

$$\alpha(t) = \alpha_o + \Delta\theta \sin\omega t$$

$$\alpha_o = 13^\circ;\ \Delta\theta = 5^\circ;\ \bar{\omega} = 0.25$$

Figure 3. Effect of Leading Edge Droop on Static and Dynamic Lift Curves (Ref. 7)

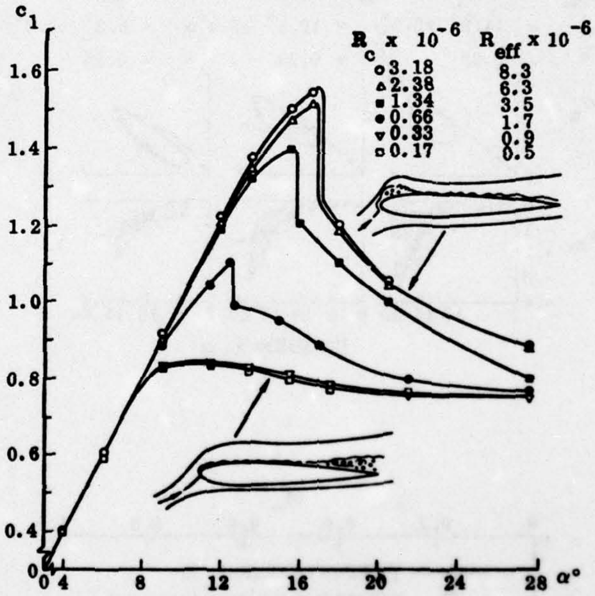

Figure 4. Effect of Reynolds Number on Static Stall of NACA-0012 (Ref. 9)

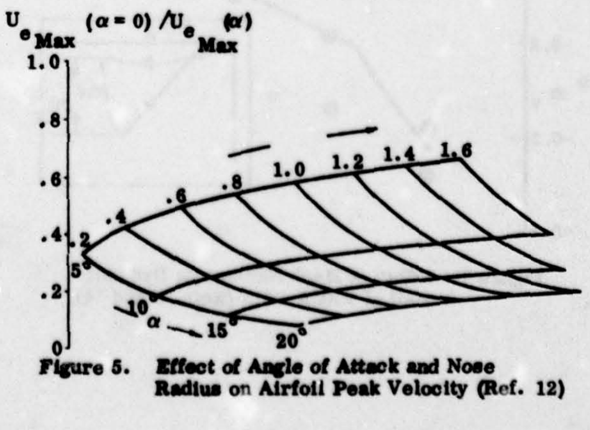

Figure 5. Effect of Angle of Attack and Nose Radius on Airfoil Peak Velocity (Ref. 12)

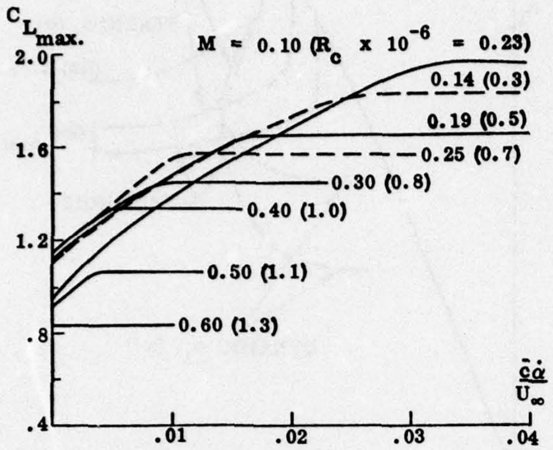

Figure 6. Dynamic $C_{\ell\ Max}$ Overshoot as a Function of Pitch-up Rate (Ref. 13).

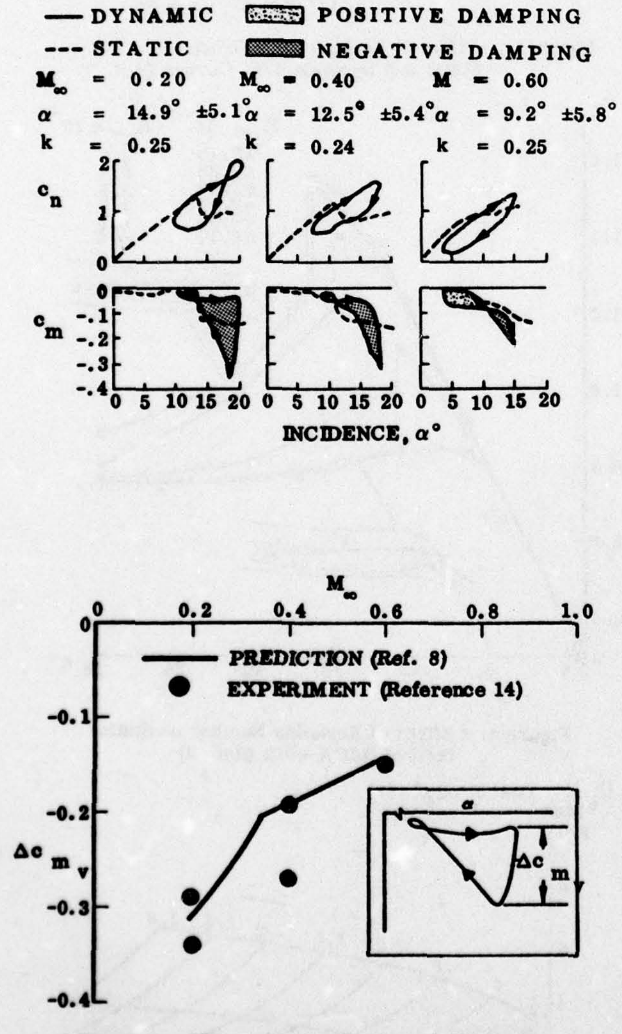

Figure 7. Effect of Mach Number on Dynamic Stall of NACA-0012 (Refs. 8 and 14)

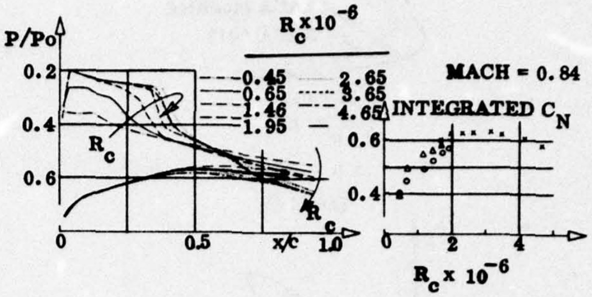

Figure 8. Effect of Reynolds Number on Terminal Wing Shock Location (Ref. 15)

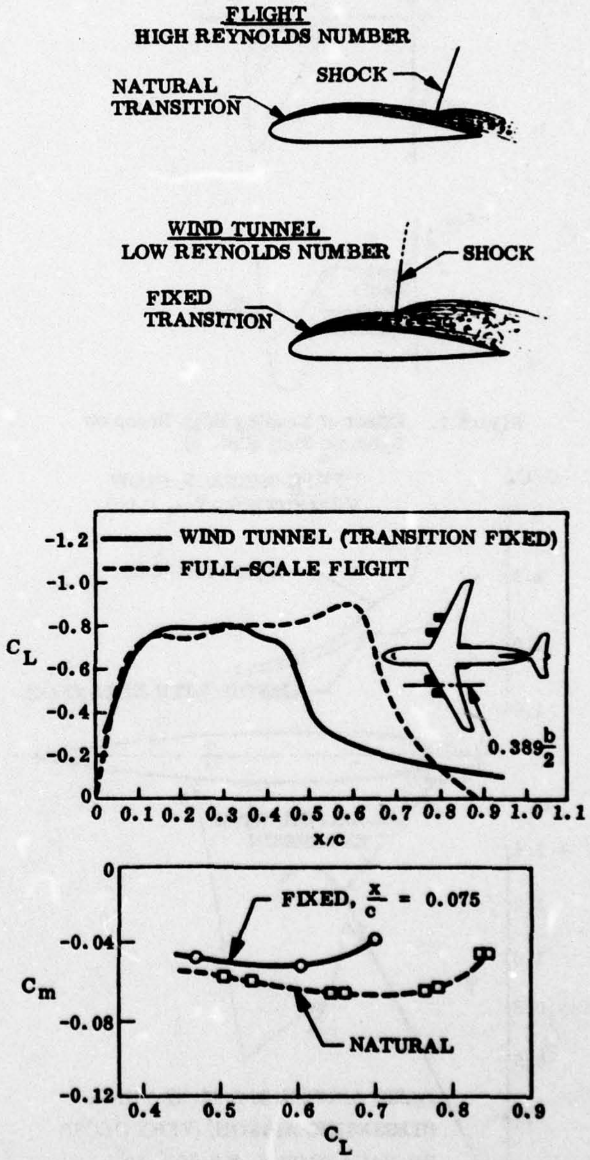

Figure 9. Effect of Boundary Layer Trip on Terminal Wing Shock Location (Ref. 16)

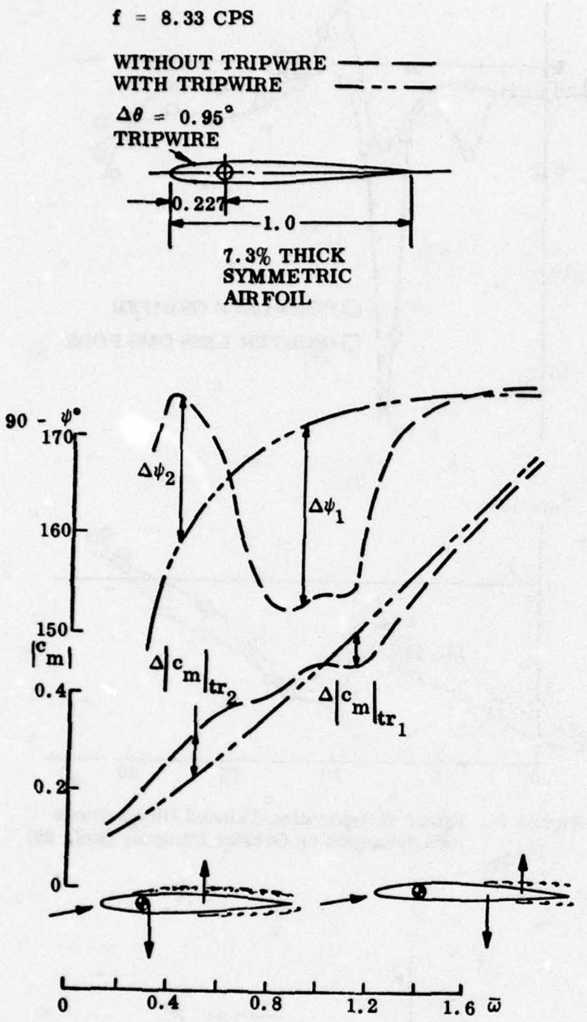

Figure 10. Effect of Boundary Layer Transition Movement on Unsteady Airfoil Aerodynamics (Refs. 17 and 18)

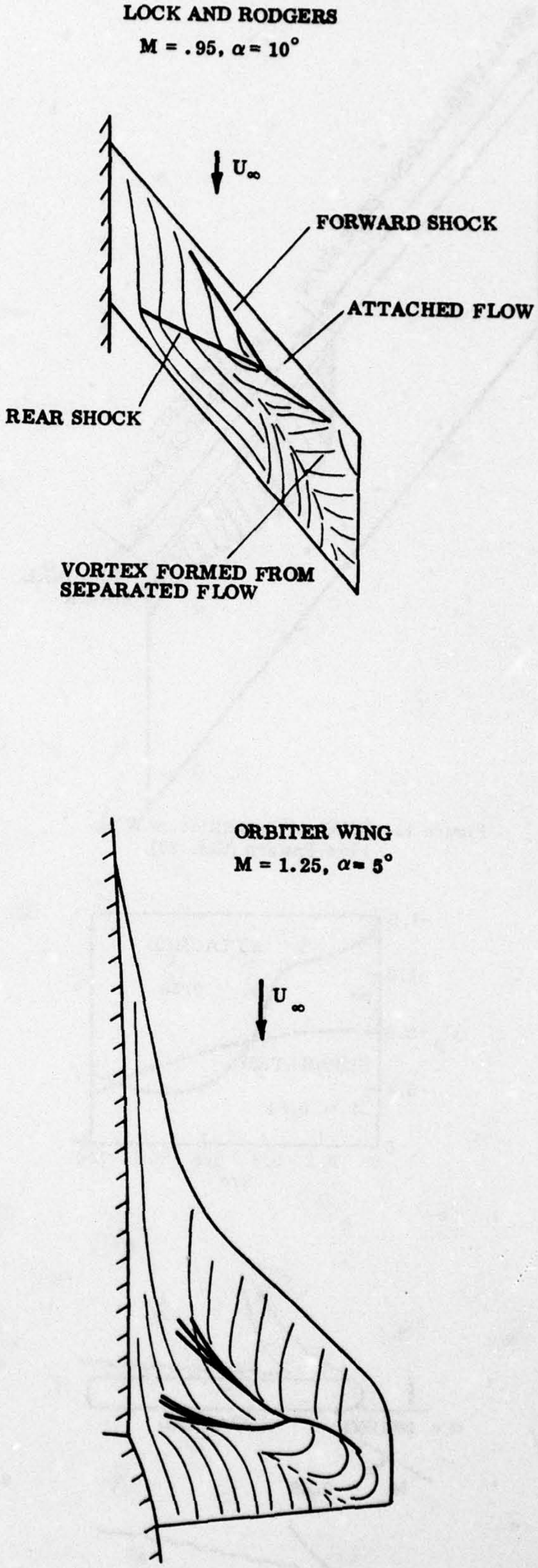

Figure 11. Transonic Wing Shock Patterns (Refs. 20 and 21)

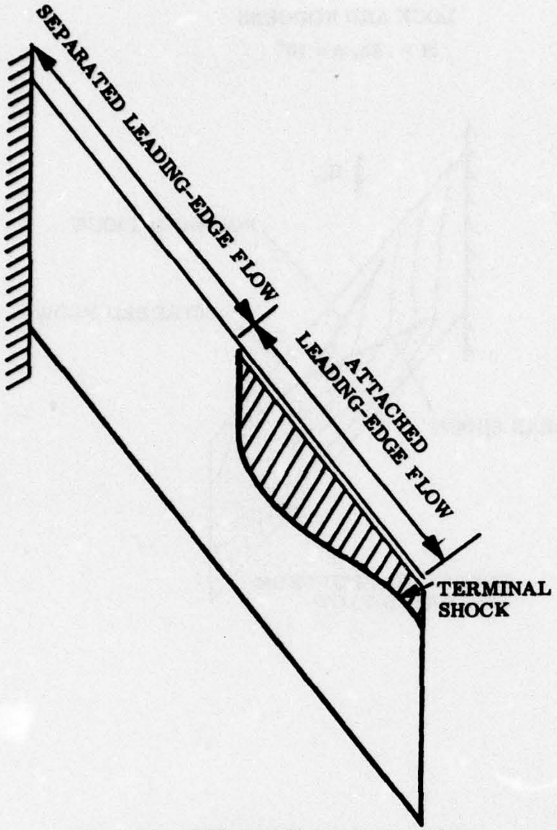

Figure 12. Effect of Transition on Wing Flow Pattern (Ref. 23).

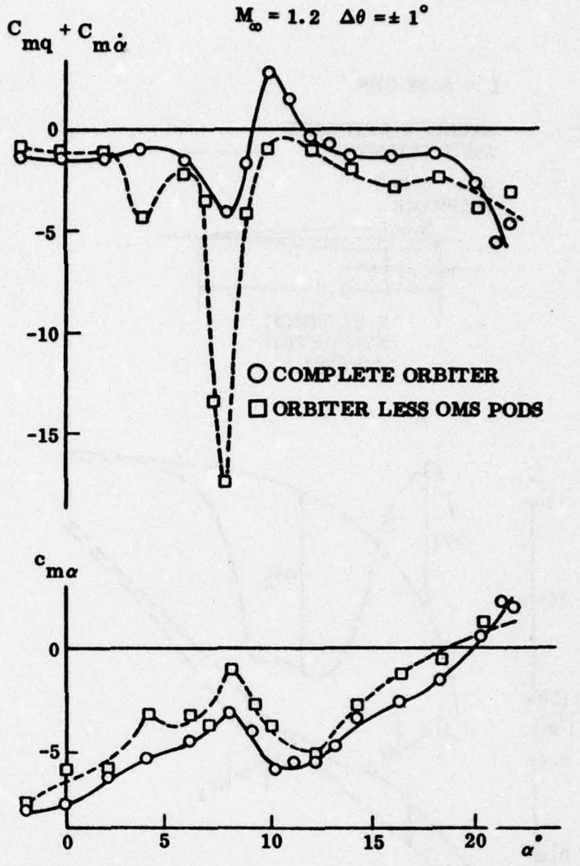

Figure 14. Effect of Separation-Induced Discontinous Aerodynamics on Orbiter Damping (Ref. 29)

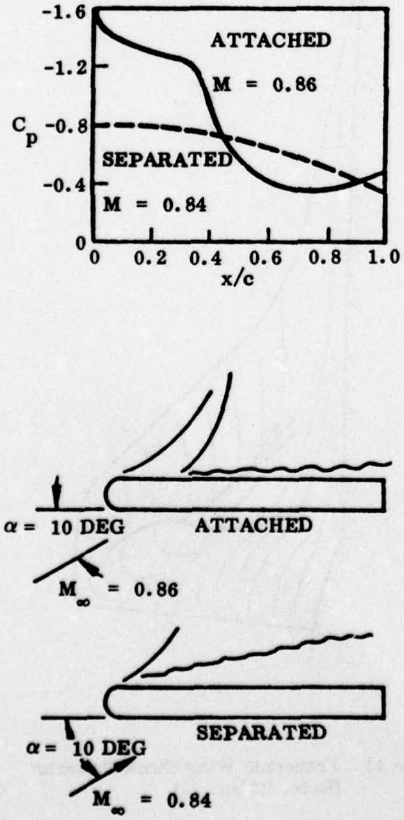

Figure 13. Effect of Separation Jump to Leading (Edge on Airfoil Aerodynamics (Ref. 28).

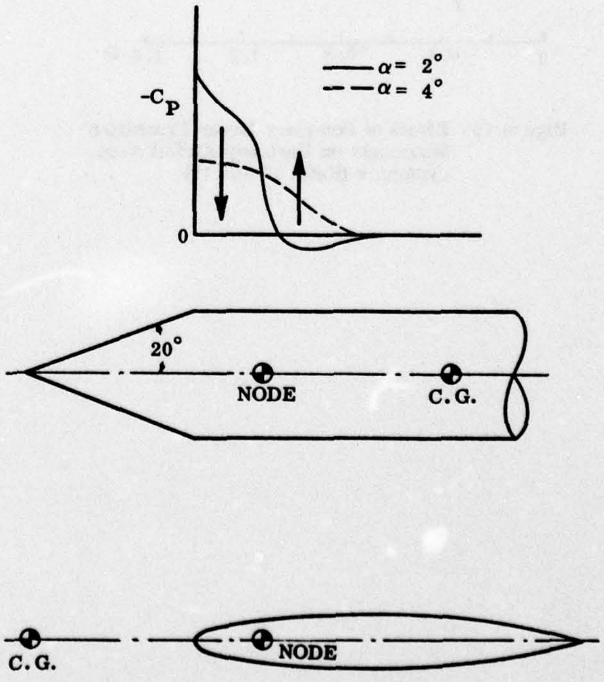

Figure 15. Conceptual Effect of Separation-Induced Discontinuous Aerodynamics on Vehicle Damping and Aeroelastic Stability.

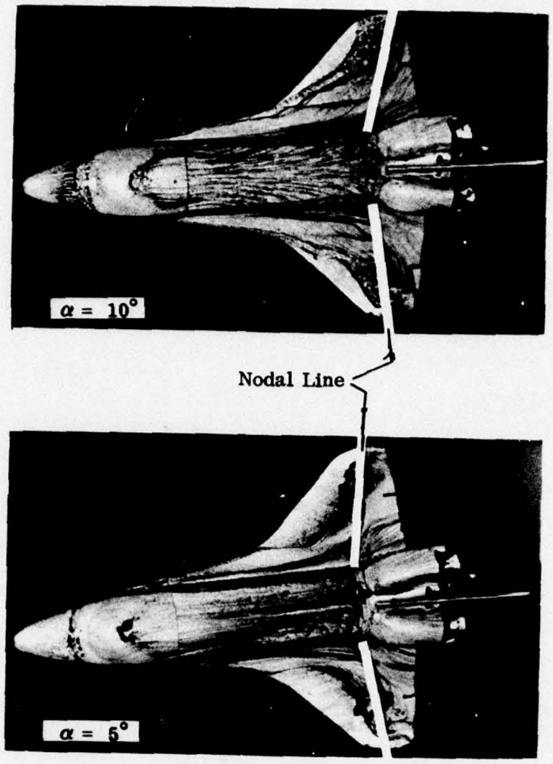

Figure 16. Sudden Separation Jump Occurring on the Space Shuttle Orbiter (Ref. 21)

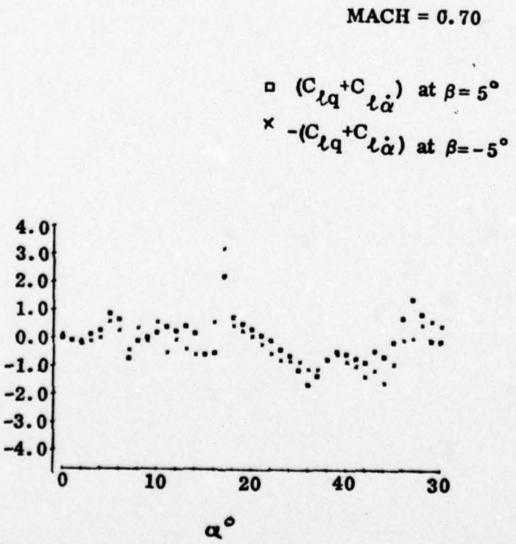

Figure 17. Effect of Separation-Induced Discontinuous Aerodynamics on $(C_{l_q} + C_{l_{\dot{\alpha}}})$ (Ref. 33).

TWO-DIMENSIONAL VISCOUS-FLOW PAST AN AIRFOIL IN AN UNSTEADY AIRSTREAM

by

Robert B. Kinney
Associate Professor
Aerospace and Mechanical Engineering Department
University of Arizona
Tucson, Arizona 85721, USA

SUMMARY

Numerical predictions are made for the viscous flow-field near an airfoil in an unsteady airstream of infinite extent. Using an extension of techniques familiar to ideal-fluid aerodynamic analyses, the body is represented by bound-vortex singularities. These coexist with the free vorticity, which forms the boundary layer and wake. Application of the no-slip condition at the airfoil surface plus the law of conservation of total vorticity, allows the production of free vorticity at the airfoil surface to be modeled. The velocity field is calculated using the law of induced velocities. Results are presented for a symmetrical Joukowski airfoil of 9% thickness. The airfoil is held fixed, and initially the fluid is at rest. At some instant, the fluid is set into motion. Two cases are treated:

(A) the impulsive gust, and
(B) the periodic gust.

In the former, the onset flow angle, α, is fixed. In the latter, α changes periodically with time. For Case (A), the Reynolds number is 10^3, and calculations are performed for $\alpha = 5^\circ, 10^\circ, 15^\circ$. For Case (B), the Reynolds number is 10^4, and α varies periodically between 0° and 5°, with a reduced frequency of 2. In addition to results which illustrate the flow behavior, curves showing the variation of the force coefficients with time are presented. Comparisons are also made with existing Navier-Stokes solutions for Case (A), with $\alpha = 15^\circ$ and $Re = 10^3$. The agreement is excellent.

NOMENCLATURE

Symbols

$\hat{A}$	constant appearing in complimentary solution for γ
A	area of non-zero free vorticity in boundary layer and wake, m^2
C_D	drag coefficient in onset flow direction, Drag Force $\Big/ \frac{1}{2}\rho U^2 L$
C_L	lift coefficient normal to onset flow direction, Lift Force $\Big/ \frac{1}{2}\rho U^2 L$. C_{LP} is lift coefficient from pressure distribution only
C_M	moment coefficient in clockwise direction about the midchord, Moment $\Big/ \frac{1}{2}\rho U^2 L^2$
C_P	pressure coefficient, $(P - P_{TE}) \Big/ \frac{1}{2}\rho U^2$
h	dimensionless scale factor in body-oriented coordinates, $1 + \eta/R$
L	chord length of airfoil, m
$\hat{P}$	dimensionless static pressure (relative to $\frac{1}{2}\rho U^2$)
R	dimensionless local radius of curvature of airfoil surface (relative to L)
r	dimensionless linear distance between two points (relative to L)
Re	Reynolds number, UL/ν

t	dimensionless time (relative to L/U)
U	speed of undisturbed onset flow, m/sec
u	dimensionless velocity in ξ-direction (relative to U)
v	dimensionless velocity in η-direction (relative to U)
x	dimensionless cartesian coordinate measured along chord from the midpoint (relative to L). x_C is fraction of the chord measured from the leading edge
y	dimensionless cartesian coordinate measured normal to chord from the midpoint (relative to L)
α	angle of onset flow relative to chord, degrees or radians
γ	dimensionless bound vorticity on airfoil surface (relative to U)
η	dimensionless body-oriented coordinate normal to airfoil surface (relative to L)
θ	local slope angle of airfoil surface relative to chord, radians
ν	kinematic viscosity, m^2/sec
ξ	dimensionless body-oriented coordinate along airfoil contour (relative to L)
ρ	fluid density, kg/m^3
ϕ	polar angle measured from x-axis, radians
ω	dimensionless free vorticity in boundary layer and wake (relative to U/L)

Subscript

CL	value along centerline downstream of trailing edge
TE	value at trailing edge or in its immediate vicinity

1. INTRODUCTION

Modern high-speed digital computers have made it possible to study many complicated aerodynamic flows which are not readily amenable to experimental investigation. Indeed, numerical solutions to the unsteady two-dimensional Navier-Stokes equations are now being performed almost routinely for realistic aerodynamic shapes. Although presently restricted to low to moderate Reynolds numbers ($\sim 10^3$), the computed results have nevertheless revealed important physical aspects of the flow development. The work of MEHTA and LAVAN [1] and LUGT and OHRING [2] are excellent examples of what has been achieved to date.

With few exceptions, the popular two-dimensional prediction methods are based on the vorticity-stream function formulation. However, other promising techniques have recently been developed which are well suited to aerodynamic analyses. These are of a broad class which also treat the vorticity as the fundamental transport variable of the flow, but the stream function is eliminated in favor of a direct integral determination of the velocity field. LIGHTHILL [3] apparently first discussed the foundations for this approach nearly 15 years ago. Nevertheless, it has only been in the last several years that numerical formulations have been developed and put to practice. Specific details can be found in the works of WU and THOMPSON [4], KINNEY and PAOLINO [5], SCHMALL and KINNEY [6], and WU [7]. Recent applications to two-dimensional unsteady flows past airfoils have been made by KINNEY and CIELAK [8], CIELAK [9], and WU and SAMPATH [10]. Three-dimensional flows have also been treated by BRATANOW and ECER [11].

In the present paper, the method of [8,9] is used to predict the unsteady viscous flow past an airfoil. The airfoil is assumed to be held fixed, and initially, the surrounding fluid is at rest. At some instant in time, the fluid is abruptly set into motion. Two cases are considered as follows:

- The Impulsive Wind Gust. The speed of the onset flow U and the flow direction relative to the airfoil chord are constant.
- The Periodic Wind Gust. The speed of the onset flow U is held constant, but the onset flow direction is a periodic function of time.

In both cases, the fluid is taken to be incompressible and the development of the unsteady flow field and the resulting forces on the airfoil are predicted.

The first case is the one most frequently treated in the literature [1,8,9,10]. The second case is novel, and no prior studies using airfoil geometries have yet been reported.

The airfoil is taken to be a 9% thick symmetrical Joukowski profile. This is a profile shape which has been used in previous numerical investigations [1,10]. For the impulsive gust, a Reynolds number of 10^3 (based on the chord length) is specified, and results are presented for the flow angle α equal to 5°, 10°, and 15°. This case for $Re = 10^3$ and $\alpha = 15^\circ$ was also studied in [1,10], thus allowing a direct comparison of the present and earlier results to be made.

For the periodic wind gust, a Reynolds number of 10^4 is chosen. The flow angle varies periodically between 0° and 5°, with a reduced frequency of 2. This is so defined that α goes through two complete cycles during the time a fluid particle with constant speed U moves one chord-length.

2. ANALYSIS

The details of the theoretical and computational approach have already been given in [8,9]. Only the fundamental ideas and important governing equations will be summarized here.

Vorticity Kinematics

The outline of the body shape is represented by bound-vortex singularities. For the symmetrical profile, a total of 80 vortex singularities are used, 40 each being on the upper and lower surfaces of the airfoil. In addition, the external flow field near the body is covered by a system of fluid cells, with node points positioned approximately at the center of each. A scale drawing showing the distribution of fluid cells and vortex singularities (surface-points) in the region near the leading and trailing edges is shown in the right-hand portion of Fig. 1. To be noted is the close spacing of the bound-vortex points near the leading and trailing edges. However, the spacing need not be so close over the entire airfoil. Over the central portion, vortex points on the surface are arranged directly below the node points corresponding to the fluid cells in contact with the airfoil. A total of 40 fluid cells are in contact with the airfoil surface.

An expression for the velocity at any point P in the fluid may now be written down directly using the Biot-Savart law of induced velocity. Let d^2u_ω and du_γ denote the perturbation velocity components due to the free and bound vorticities, ω and γ, respectively. These are shown in the upper left-hand portion of Fig. 1, for ω and γ with counter-clockwise sense of rotation (considered positive).

A body fitted coordinate system (ξ, η) is used, as shown in Fig. 1. Using kinematic principles only, the velocity at P in the positive ξ-direction can be written as follows:

$$u(P) = \cos(\alpha - \theta_P) + \int_A d^2u_\omega + \oint_C du_\gamma \quad , \tag{1}$$

where all velocity components are non-dimensionalized using the speed of the onset flow U. Thus the term $\cos(\alpha - \theta_P)$ represents the velocity contribution due to the undisturbed onset flow, which approaches the airfoil with the angle α, as measured from the chord. As illustrated in Fig. 1, the second and third terms of (1) contribute a negative perturbation to the actual velocity, u(P). For our convention, we have

$$d^2u_\omega(P) = -\frac{1}{2\pi}\left[\frac{(y_P - y_Q)\cos\theta_P - (x_P - x_Q)\sin\theta_P}{r_{PQ}^2}\right](\omega h\, d\xi\, d\eta)_Q \quad , \tag{2}$$

$$du_\gamma(P) = -\frac{1}{2\pi}\left[\frac{(y_P - y_S)\cos\theta_P - (x_P - x_S)\sin\theta_P}{r_{PS}^2}\right](\gamma\, d\xi)_S \quad . \tag{3}$$

where all length, velocity, and vorticity quantities are non-dimensionalized using U and L. To be noted is the fact the integration of (2) and (3) need be carried out only over the airfoil surface and the region of non-zero ω.

The point P can be any point in the fluid. However, it is convenient to let P be at the center of the control faces (of each fluid cell) which lie along a line of ξ = constant. In this manner, the velocity u(P) can be computed at the precise point at which it is needed in the numerical solution of the vorticity transport equation. This point will be recalled in the section dealing with the vorticity dynamics.

The vorticity fields, γ and ω, have yet to be determined. They must, of couse, satisfy constraining equations. The determination of ω is discussed in a later section. The determination of γ can be made using techniques common to ideal-fluid aerodynamic analyses.

Integral Equation for the Bound Vorticity

Following the classical approach, (1) is now written for any point P just interior to the airfoil surface. Since (1) represents the velocity relative to the stationary airfoil, the velocity at this interior point must be zero. Taking into account the discontinuity in the tangential velocity component (i.e. in the ξ-direction) across the airfoil surface, this being equal to $-\gamma$, one obtains the following integral equation for γ

$$\gamma(P) - \frac{1}{\pi} \oint \left[\frac{(y_P - y_S) \cos\theta_P - (x_P - x_Q) \sin\theta_P}{r_{PQ}^2} \right] (\gamma \, d\xi)_S = -2 \left[\cos(\alpha - \theta_P) + u_\omega(P) \right] \quad , \tag{4}$$

where P must be considered to be constrained to the airfoil surface.

The derivation of (4) was first made for potential flows by PRAGER [12]. Except for nomenclature, his result differs from (4) only in the absence of the induced contribution of the viscous layer (i.e. due to ω) to the tangential velocity at the airfoil surface. This is given by $u_\omega(P)$ and appears only as a contribution to the non-homogeneous term on the right-hand side.

The solution properties of (4) are well known. They have been studied by MARTENSEN [13] and exploited in numerous studies of potential flows past airfoils (see for example [14]). The presence in this analysis of $u_\omega(P)$ in (4) does not alter any of the solution properties previously documented.

It is known that the solution to (4) is composed of a particular solution to the complete equation and a complimentary solution to the homogeneous equation. Thus one can write

$$\gamma(\phi) = \gamma_{part}(\phi) + \frac{\hat{A}}{\sqrt{\dot{x}_S(\phi)^2 + \dot{y}_S(\phi)^2}} \quad . \tag{5}$$

In the foregoing, $\hat{A}$ is a constant, and ϕ is the polar angle shown in Fig. 1. The term containing $\hat{A}$ is the complimentary solution.

In (5), $y_S(x_S)$ is the equation for the outline of the airfoil. By definition

$$\dot{y}_S(\phi) \equiv \frac{dy_S}{d\phi} = \frac{dy_S}{dx_S} \left(\frac{dx_S}{d\phi} \right) = \frac{dy_S}{dx_S} \dot{x}_S(\phi) \quad . \tag{6}$$

We also have

$$dy_S/dx_S = \tan\theta \quad , \qquad x_S(\phi) = .5 \cos\theta \quad ,$$

and

$$\dot{x}_S(\phi) = -.5 \sin\phi \quad .$$

Thus the complimentary solution can be written $2\hat{A} / [\sin\phi (1 + \tan^2\theta)^{1/2}]$. The algebraic sign is immaterial, since $\hat{A}$ has yet to be determined.

The particular solution of (4) can be obtained using standard numerical techniques. This is usually necessary, since $u_\omega(P)$ is known only at discrete points. Details can be found in [9].

Note that since the complimentary solution contains the term $(\sin\phi)^{-1}$, the complete solution can become singular at $\phi = 0$ and $\phi = \pi$. This singular behavior is no surprise, since it also arises in the classical aerodynamic theories. It is well known that the solution for γ is integrable over the entire profile. Thus the singularity offers no particular difficulties.

The solution for γ is, in principle, known from (5). It remains only to evaluate $\hat{A}$. In the classical theories, this is done by invoking some dynamical principle, such as the Kutta-Joukowski condition, or its generalization for unsteady flows (see SEARS [15]). Since this involves the dynamics of the viscous boundary layer and wake, further discussion of this point is delayed until the end of the next section.

Vorticity Dynamics

The distribution of ω in the viscous boundary layer and wake is governed by the following transport equation

$$\frac{\partial\omega}{\partial t} + \frac{1}{h}\left[\frac{\partial}{\partial\xi}(u\omega) + \frac{\partial}{\partial\eta}(hv\omega)\right] = \frac{1}{h\mathrm{Re}}\left[\frac{\partial}{\partial\xi}\left(\frac{1}{h}\frac{\partial\omega}{\partial\xi}\right) + \frac{\partial}{\partial\eta}\left(h\frac{\partial\omega}{\partial\eta}\right)\right] \quad . \tag{6}$$

In the body-fitted coordinates (ξ, η), the quantity h is a scale factor given by $h = 1 + \eta/R$, where R is the local radius of curvature of the surface. On the airfoil surface, $h = 1$.

Eq. (6) expresses the conservation of vorticity at a point in the fluid. In the actual calculations, (6) is rewritten in finite-difference form. This is achieved by performing a vorticity balance on each individual fluid cell. A typical cell is shown in the right-hand portion of Fig. 1, where the arrows depict the fluxes of vorticity (by diffusion and convection) across the control faces.

As noted earlier, the velocity components in the ξ-direction are evaluated at each face of the control volumes, using a direct application of (1). The velocity components in the η-direction are obtained from the continuity equation. This procedure ensures that the mass is conserved at each fluid cell.

In evaluating (1), the expressions in (2) and (3) must be integrated numerically. The free vorticity ω is assumed to be constant over a given fluid cell, and the integration of (2) is carried out analytically for each of N fluid cells. Likewise, γ is held constant over a surface-segment, and (3) is integrated analytically for each of P surface-segments. After the results are summed and the velocity components at each of M points are computed, the results can be summarized as follows:

$$\begin{bmatrix} u_1 \\ \vdots \\ u_M \end{bmatrix} = \begin{bmatrix} a_{11} & \cdots & a_{1N} \\ \vdots & & \vdots \\ a_{M1} & \cdots & a_{MN} \end{bmatrix} \begin{bmatrix} \omega_1 \\ \vdots \\ \omega_N \end{bmatrix} + \begin{bmatrix} b_{11} & \cdots & b_{1P} \\ \vdots & & \vdots \\ b_{M1} & \cdots & b_{MP} \end{bmatrix} \begin{bmatrix} \gamma_1 \\ \vdots \\ \gamma_P \end{bmatrix} \quad . \tag{7}$$

The matrices [a] and [b] contain only geometrical influence coefficients, which do not change during the calculation cycle. These coefficients were computed once for a given Reynolds number and grid arrangement (see later section), and then stored on magnetic tape. They were then read into the computer whenever necessary. This is very efficient and led to fast execution times. A similar procedure was used in [10].

In modeling the convective transport of free vorticity, the velocity components were assumed to carry the vorticity corresponding to the node point of the upwind cell. The diffusion of vorticity between cells was calculated using a linear relationship involving the vorticity difference between node points. This is according to standard practice.

The advancement in time of the solution for ω was obtained using the explicit method. That is, the transport terms were all evaluated at time level t, and the time derivative in (6) was approximated by $[\omega(t + \Delta t) - \omega(t)]/\Delta t$ at each fluid cell.

Modeling of the Vorticity Production at the Airfoil Surface

In solving (6) numerically, it is important that the surface conditions for the vorticity be carefully prescribed at the airfoil. In this work, the process of vorticity production was modeled using the concept originally given by LIGHTHILL [3]. Additional discussion is given in [8].

Suppose that the distribution for γ is known from (4) at some time-level t, taking account of the free vorticity that is already in the fluid. This bound vorticity γ is in the form of a sheet of infinitesimal thickness, and it represents locally the amount of free vorticity which must enter the fluid by diffusion in the subsequent time-interval Δt. Thus the bound vorticity at time t must show up as free vorticity at time $t + \Delta t$. This idea is expressed by the following boundary condition:

$$-\frac{1}{\mathrm{Re}}\int_{t}^{t+\Delta t}\left(\frac{\partial}{\partial\eta}\,\omega\right)_s dt' = \gamma(t) \quad , \tag{8}$$

which is also valid at the initial instant of time $t = 0^+$. The incremental amount of free vorticity which enters a finite-volume fluid cell in contact with the airfoil is obtained from (8) by integrating the distribution for γ over the incremental surface element of the cell.

Although not explicitly mentioned by LIGHTHILL [3], the vorticity production must be determined in such a way that the total vorticity is conserved. For streaming flow past the airfoil (i.e. without rotation), the total free vorticity entering the fluid in a time interval Δt must be zero. That is, the integral of (8) around the airfoil surface must be zero. As shown below, this is the essential condition which must be used in order to make the solution for γ unique. It is the counterpart of the Kutta-Joukowski condition used in the classical theories.

Recall from (5) that $\hat{A}$ is a constant which was left unspecified. It can now be evaluated using the principle of conservation of total vorticity. As previously mentioned, one must have

$$\oint_C \gamma \, d\xi = 0 \quad . \tag{9}$$

From this plus (5), one obtains

$$\oint_C \left(\gamma_{\mathrm{part}} + \frac{\hat{A}}{\dot{S}}\right) d\xi = \oint_C \gamma_{\mathrm{part}} \, d\xi + \hat{A} \oint_C \frac{d\xi}{\dot{S}} = 0 \quad , \tag{10}$$

where

$$\dot{S} = \sqrt{\dot{x}_S(\phi)^2 + \dot{y}_S(\phi)^2} \quad .$$

On the airfoil surface,

$$\dot{S} \equiv dS/d\phi \equiv d\xi/d\phi \quad .$$

Thus the term in (10) which multiplies $\hat{A}$ is simply 2π. Solving for $\hat{A}$ from (10) and substituting into (4), one obtains

$$\gamma(\phi) = \gamma_{\mathrm{part}}(\phi) - \frac{\frac{1}{2\pi} \oint_C \gamma_{\mathrm{part}} \, d\xi}{\sqrt{\dot{x}_S(\phi)^2 + \dot{y}_S(\phi)^2}} \quad . \tag{11}$$

The above solution for γ, when used with the boundary condition (8), ensures that the production of free vorticity is modeled correctly. As a consequence, the single-valuedness of the pressure field is guarenteed. This follows from the dynamical equations of motion, which when written for the airfoil surface, reduce to

$$\left(\frac{\partial \hat{P}}{\partial \xi}\right)_S = -\frac{2}{Re}\left(\frac{\partial \omega}{\partial \eta}\right)_S \tag{12}$$

If it is assumed that the rate of vorticity production is uniform over the time interval Δt, then one obtains from (8) $-(1/Re)(\partial\omega/\partial\eta)_S = \gamma/\Delta t$. Thus

$$\left(\frac{\partial \hat{P}}{\partial \xi}\right)_S = 2\,\frac{\gamma}{\Delta t} \tag{13}$$

and from (9),

$$\oint_C \left(\frac{\partial \hat{P}}{\partial \xi}\right)_S d\xi = \frac{2}{\Delta t} \oint_C \gamma \, d\xi = 0 \quad . \tag{14}$$

Finite-Difference Parameters

The fluid is covered by a maximum number of 2000 control volumes. These need be so arranged so as to cover only the viscous layers in the vicinity of the airfoil and extending into the wake.

The cells adjacent to the airfoil surface have the smallest lateral dimension $\Delta\eta_0$, and these expand in height away from the surface (in the η-direction) according to the ratio 1.15. The cell widths are also smallest near the leading and trailing edges (see Fig. 1), and downstream of the trailing edge these expand gradually up to a maximum dimension of .25 (fraction of a chord). They are then fixed at that value.

In order to accurately model the vorticity production at the airfoil, the finite time and distance increments must be properly scaled. According to a one-dimensional diffusion model, the diffusion distance $\Delta\eta_0$ for vorticity produced at a uniform rate over the time-interval Δt obeys the following relationship

$$\frac{\Delta\eta_0}{2}\sqrt{\frac{Re}{\Delta t}} \cong 1.5 \quad . \tag{15}$$

In this work, the time increment Δt and Reynolds number Re were specified, and $\Delta\eta_0$ was calculated from (15). A summary of the grid characteristics is given in Table 1.

Table 1: Summary of Grid Characteristics

Case	Re	Δt	$\Delta\eta_0$	$\Delta\eta_{max}$	η_{max}
Impulsive Gust	10^3	.005	.00660	.0710	.5005
Periodic Gust	10^4	.0025	.00148	.0211	.1566

In each case, the grid extended to a distance of 4.8 chord-lengths behind the trailing edge.

For the case with the larger Reynolds number, the time increment was halved. This became necessary since the initially large convective velocity around the trailing edge, in combination with the smaller cell height $\Delta\eta_0$, led to unstable solutions of (6), when the explicit method was used with $\Delta t = .005$. With the smaller time increment of $\Delta t = .0025$, the solution was always stable.

The computations were carried out in double precision (8 bytes = 64 bits) on an IBM 370-158 machine. For $Re = 10^4$, the full 2000 fluid cells were used, and the dimensions in (7) were $M = 2040$, $N = 2000$, and $P = 80$. The computation time for a complete time-cycle was 3.23 minutes. Typically, over 90% of the computation time was consumed in the velocity evaluation alone. For $Re = 10^3$, only 1800 fluid cells were used, in which case $M = 1836$, $N = 1800$, and $P = 80$ in (7). The computation time per time-cycle was 2.75 minutes. The central core memory for $Re = 10^4$ was 576 kilobytes. For $Re = 10^3$, the core memory was 512 kilobytes. All numbers are expressed in base 10.

3. RESULTS AND DISCUSSION

Impulsive Gust, $Re = 10^3$

Calculations were first performed for $\alpha = 15^\circ$. This is the case previously studied by MEHTA and LAVAN [1] and WU and SAMPATH [10]. In the latter, a comparison was made between the results obtained by the two methods. Identical airfoil geometries and grid arrangements were used, but a different vorticity-stream function formulation was adopted. The agreement was quite satisfactory.

Typical computed results for the pressure coefficient are shown in Fig. 2. To obtain C_P, the pressure gradient was first calculated at the 80 surface points using (13). Starting at the trailing edge, this was then integrated around the airfoil using the trapezoidal rule. The actual computed points are shown, and comparisons with the results of MEHTA and LAVAN [1] are made at two representative time levels. Note that the time values given in [1] must be divided by 3.713 in order to obtain those used in the present work. The agreement is judged to be entirely satisfactory. Indeed, at $t = .436$, the two distributions for the pressure coefficient on the lower surface are nearly identical. On the suction (upper) surface, there is only a slight discrepancy near the leading edge.

There is also satisfactory overall agreement between the lift, drag, and moment coefficients, the discrepancy being on the order of 10%. However, there is some question as to the proper behavior of the lift and drag coefficients for small time.

In [1], it is found that C_L and C_D are initially very high and then fall monotonically but rapidly toward plateau values. The lift coefficient reaches a minimum value of approximately 1.0 before rising slightly, as shown in Fig. 2. The results calculated in the present work have a somewhat different behavior for small time. These are summarized in Table 2. Results for two other angles of attack are also given.

Table 2: Temporal Variation of Force Coefficients

$Re = 10^3$

	$\alpha = 5^\circ$		$\alpha = 10^\circ$		$\alpha = 15^\circ$	
t	C_L	C_D	C_L	C_D	C_L	C_D
0^+	27.68	27.97	54.51	35.16	79.69	46.90
.005	-.99	.78	-1.95	.52	-2.84	.10
.010	-.14	.61	-.26	.55	-.31	.47
.015	.21	.59	.43	.62	.69	.69
.020	.30	.55	.62	.61	.99	.73
.025	.32	.52	.67	.58	1.05	.71

In all instances, the lift and drag coefficients are initially very high, but then fall immediately to low values (C_L even goes negative) and then rise to a sharp peak at $t = .025$. This behavior, although not at first expected, is in close qualitative agreement with that found experimentally by TANEDA [16] for elliptic cylinders started impulsively from rest.

The initially high peak in C_L is due to the impulsive acceleration, but this must disappear, since immediately after the impulsive start, the flow about the airfoil is nearly irrotational. The slight negative values (in comparison with the high initial value) are probably due to the finite thickness of the boundary layer and the corresponding departure of the flow from irrotationality. TANEDA's measurements also show a slightly negative lift after the initial peak. The measured lift force then increases rapidly, in accordance with the computed results of Table 2.

Curves showing the temporal variation of the lift coefficients for selectively smaller angles of attack ($\alpha = 5^o$ and 10^o) are shown in the left-hand portion of Fig. 3. The previous results are shown for comparison. The behavior of the flow downstream of the trailing edge is illustrated in the right-hand portion. The individual computed points are shown for clarity.

Immediately after the impulsive acceleration, the transverse velocity v on the centerline just downstream of the trailing edge is relatively high. As time increases, the effect of the fluid viscosity and the developing starting vortex reduces this velocity sharply. Beyond $t = .70$, the transverse velocity is nearly zero immediately behing the trailing edge, signalling the fact that the fluid is momentarily leaving smoothly from the trailing edge. Nevertheless, with increasing time, and especially at high angles of attack, the flow is expected to eventually separate from the airfoil. A region of flow reversal does indeed exist at $t = 1.0$ downstream of the point of maximum thickness, for the airfoil at $\alpha = 15^o$. This is in agreement with the results obtained in [1], although the time at which separation occurs is somewhat different. For $\alpha = 10^o$, no separation is observed up to $t = 1.0$; the calculations were not carried further. The case $\alpha = 5^o$ was calculated to $t = 5.0$, at which time the flow appeared to be at steady state. No separation occurs, and after reaching a peak value of $C_L = .385$ at $t = 1.8$, the lift coefficient drops to an asymptotic value of $C_L = .343$. The asymptotic drag and moment coefficients are $C_D = .139$ and $C_M = .073$.

Periodic Gust, Re = 10^4

Results for the periodic gust are summarized in Figs. 4 and 5. The onset flow approaches the airfoil with constant speed U and variable angle α. The latter is a periodic cosine function, which varies between 0^o and 5^o, as shown by the dashed curve in Fig. 4. The frequency of oscillation is very high, corresponding to a reduced frequency of 2 (reduced circular frequency of 4π), based on the speed U and chord L.

The gust case was chosen in order to demonstrate that unsteady flows of a rather general nature can be modeled for realistic Reynolds numbers. Other than the overall lateral schrinkage of the grid (see Table 1), accompanied by approximately a 10 % increase in the number of grid points, no changes in the numerical formulation were made.

The temporal variation of the force coefficients is depicted in Fig. 4, where the individual computed points are shown. The behavior of the lift coefficient, in particular the large negative values, was completely unexpected. The values for C_L appear to be very nearly proportional to the rate of change (i.e. slope) of α, rather than to α itself. The peak in C_L leads that in α by $\pi/2$. Although not readily discernible, each peak in the C_L-curve is slightly higher than the previous one. This is due to the fact that the effective angle of attack is 2.5^o. However this slight rise is insignificant compared to the large negative swings.

The moment coefficient (computed about the center-chord point) appears to lead the α-variation by an angle of approximately $\pi/4$. The appearance of a small negative (nose down) moment over part of the cycle is of interest from an aircraft stability point of view.

The behavior of the flow downstream of the trailing edge is illustrated in Fig. 5. Although the angle of attack never goes negative, there is nevertheless backflow around the trailing edge from top to bottom. This can be seen from the instantaneous velocity profiles shown in the main portion of the figure. Additional profiles are shown for the times when α is at its maximum and minimum values.

The periodic behavior of the transverse velocity component immediately downstream of the trailing edge, v_{TE}, is shown in the lower portion of Fig. 5. Clearly this is nearly in phase with the α-variation, and the negative undershoot is regular. The interrelationship between the velocity variations and those of the force coefficients is obviously quite complicated. This is to be expected, since the full non-linear effects of the body thickness plus boundary layer and wake development come into play.

Before concluding this section, some remarks are in order concerning the nature of the periodic gust used in this investigation. It was assumed that the entire fluid domain approaches the airfoil as an ensemble with instantaneous flow angle α. The instantaneous dimensionless x- and y-velocity components are thus cos α and sin α, respectively. The onset flow has no rotation. Such a time-varying outer flow may not actually be found in aerodynamic applications. Nevertheless, this gust case is believed to approximate what occurs in a field of clear-air or wake-generated turbulence, whose length scale is very much greater than the chord of the airfoil.

4. CONCLUDING REMARKS

The present results clearly demonstrate that unsteady aerodynamic analyses, based on solutions to the two-dimensional Navier-Stokes equations, are entirely feasible. The effects of airfoil thickness, wake development, flow separation, and outer-flow unsteadiness can all be accounted for. Realistic Reynolds numbers of the order 10^4 can also be treated.

Unfortunately, such numerical calculations are not at a stage where they are presently suitable for design studies. Rather, they are but another research tool with which fundamental information about complicated flows can be obtained.

Nevertheless, the time is near when the accuracy and reliability of such flow predictions can be established through actual comparisons with experimental measurements. To date, it has only been possible to compare the results of one numerical analysis with those of another. However, once the numerical approaches are validated, they may then play an important role in validating the more practical, but also more approximate, first order theories used in design calculations. Thus fully numerical approaches, of the type described in the present paper, should continue to be developed and improved.

5. ACKNOWLEDGEMENTS

This work was completed while the author was on leave from the University of Arizona to the Institute für Aeroelastik, DFVLR-AVA Göttingen. The helpful cooperation of Prof. Dr. H. FÖRSCHING is gratefully acknowledged. Financial support was provided by the Alexander von Humboldt Foundation, Bad Godesberg, Germany.

6. REFERENCES

[1] MEHTA, U.B.
LAVAN, Z.
Starting Vortex, Separation Bubbles and Stall: A Numerical Study of Laminar Unsteady Flow around an Airfoil.
J. Fluid Mech., Vol. 67, Part 2 (1975) pp. 227-256.

[2] LUGT, H.J.
OHRING, S.
Rotating Elliptic Cylinders in a Viscous Fluid at Rest or in a Parallel Stream.
J. Fluid Mech., Vol. 79, Part 1 (1977) pp. 127-156.

[3] LIGHTHILL, M.J.
Introduction. Boundary Layer Theory.
Laminar Boundary Layers, J. Rosenhead, editor, Oxford University Press, Oxford (1963) pp. 54-61.

[4] WU, J.C.
THOMPSON, J.F.
Numerical Solution of Time-Dependent Incompressible Navier-Stokes Equation Using an Integro-Differential Formulation.
Computers and Fluids, Vol. 1, No. 2 (1973) pp. 197-215.

[5] KINNEY, R.B.
PAOLINO, M.J.
Flow Transient Near the Leading Edge of a Flat Plate Moving through a Viscous Fluid.
J. Appl. Mech., Vol. 41, No. 4 (1974) pp. 919-924.

[6] SCHMALL, R.A.
KINNEY, R.B.
Numerical Study of Unsteady Viscous Flow past a Lifting Plate.
AIAA J., Vol. 12, No. 11 (1974) pp. 1566-1573.

[7] WU, J.C.
Numerical Boundary Conditions for Viscous Flow Problems.
AIAA J., Vol. 14, No. 8 (1976) pp. 1042-1049.

[8] KINNEY, R.B.
CIELAK, Z.M.
Impulsive Motion of an Airfoil in a Viscous Fluid.
Proc. Symposium on Unsteady Aerodynamics, edited by R.B. Kinney, University of Arizona, Tucson (1975) pp. 487-512.

[9] CIELAK, Z.M.
Vorticity-Oriented Analysis of Viscous Flow over a Two-Dimensional Airfoil.
Ph.D. Dissertation, University of Arizona, Tucson (1976).

[10] WU, J.C.
SAMPATH, S.
A Numerical Study of Viscous Flow around an Airfoil.
AIAA Paper No. 76-337, presented at AIAA 9th Fluid and Plasma Dynamics Conference, San Diego, July 1976.

[11] BRATANOW, T.
ECER, A.
Analysis of Three-Dimensional Unsteady Viscous Flow around Oscillating Wings.
AIAA J., Vol. 12, No. 11 (1974) pp. 1577-1584.

[12] PRAGER, W.
Die Druckverteilung an Körpern in ebener Potentialströmung.
Physik. Zeitschr., Band XXIX (1928) pp. 865-869.

[13] MARTESEN, E.
Berechnung der Druckverteilung an Gitterprofilen in ebener Potentialströmung mit einer Fredholmschen Integralgleichung.
Arch. Rat. Mech. and Analysis, Vol. 3 (1959) pp. 235-270.

[14] JACOB, K.
Berechnung der inkompressiblen Strömung um dicke Tragflügel- und Gitterprofile mit eckiger Hinterkante.
Z. f. Flugwiss., Vol. 15 (1967) pp. 341-346.

[15] SEARS, W.R.
Unsteady Motion of Airfoils with Boundary Layer Separation.
AIAA J., Vol. 14, No. 2 (1976) pp. 216-220.

[16] TANEDA, S.
The Development of the Lift of an Impulsively Started Elliptic Cylinder at Incidence.
J. Phys. Soc. Japan, Vol. 33, No. 6 (1972) pp. 1706-1711.

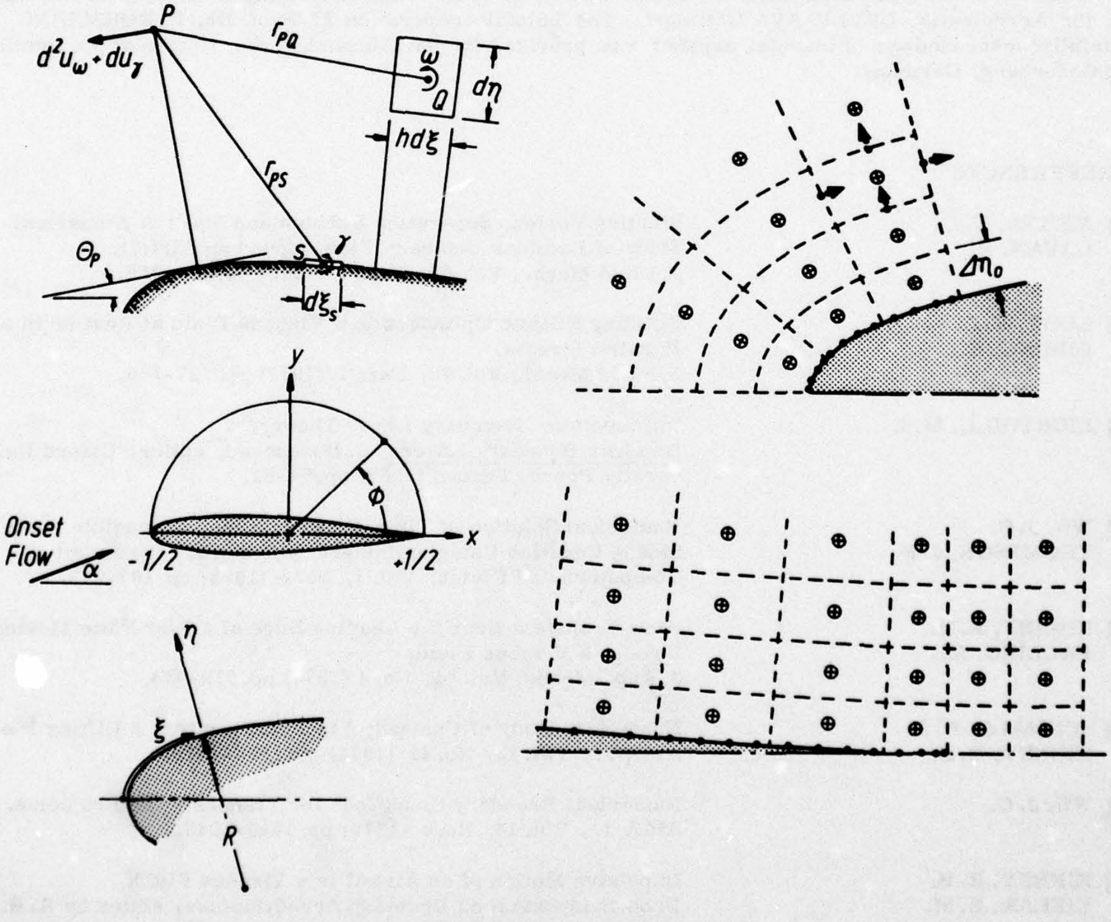

Fig. 1 Coordinate system and node arrangement in the fluid near the leading and trailing edges

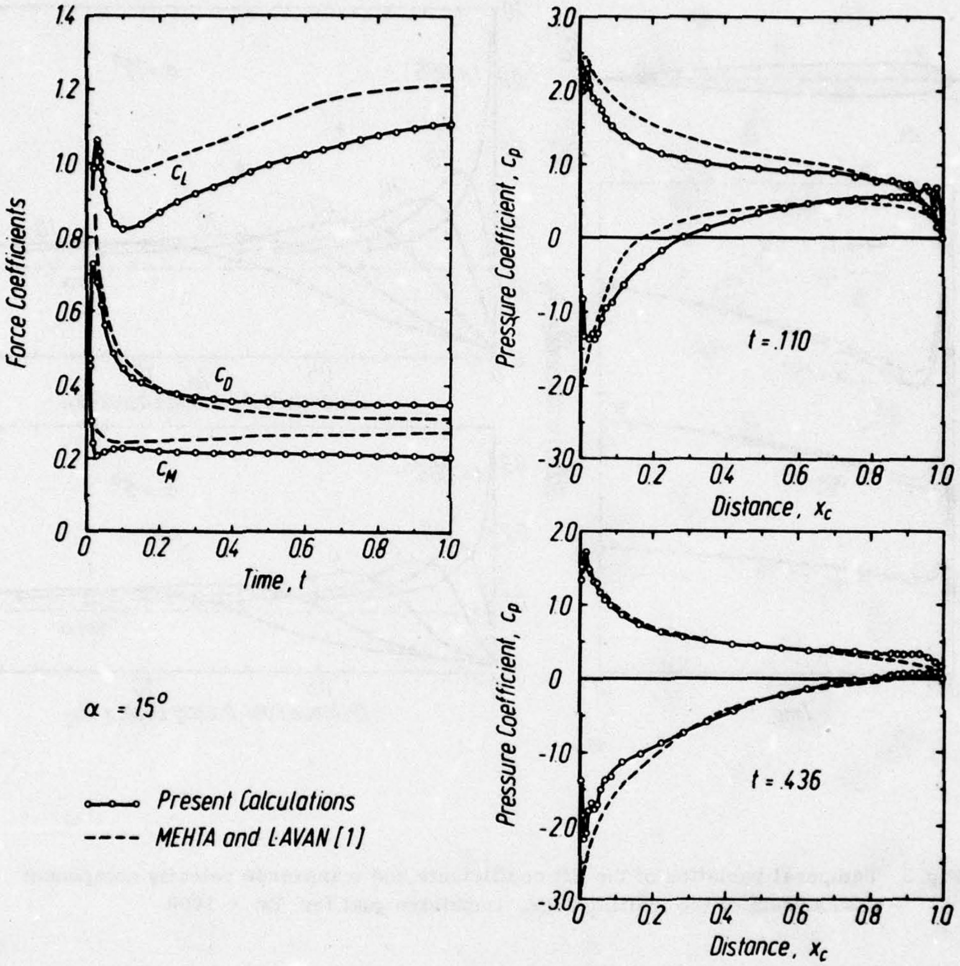

Fig. 2 Comparison of computed pressure distributions and force coefficients for the impulsive gust, Re = 1000

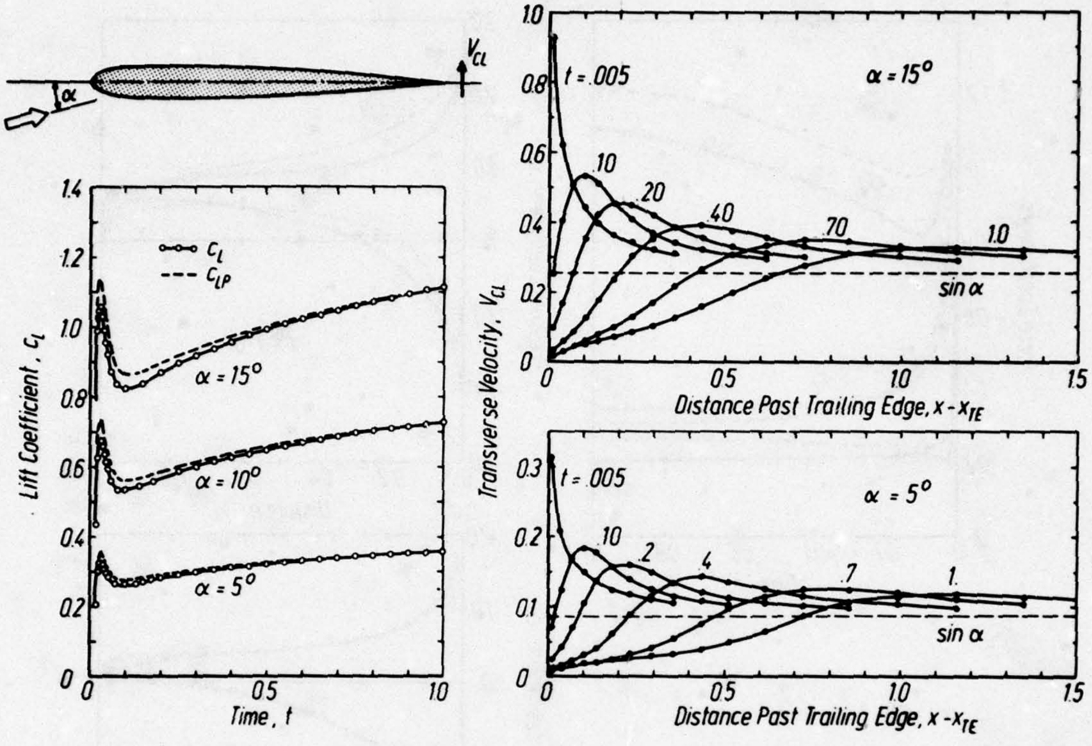

Fig. 3 Temporal variation of the lift coefficients and transverse velocity component downstream of the trailing edge. Impulsive gust for Re = 1000

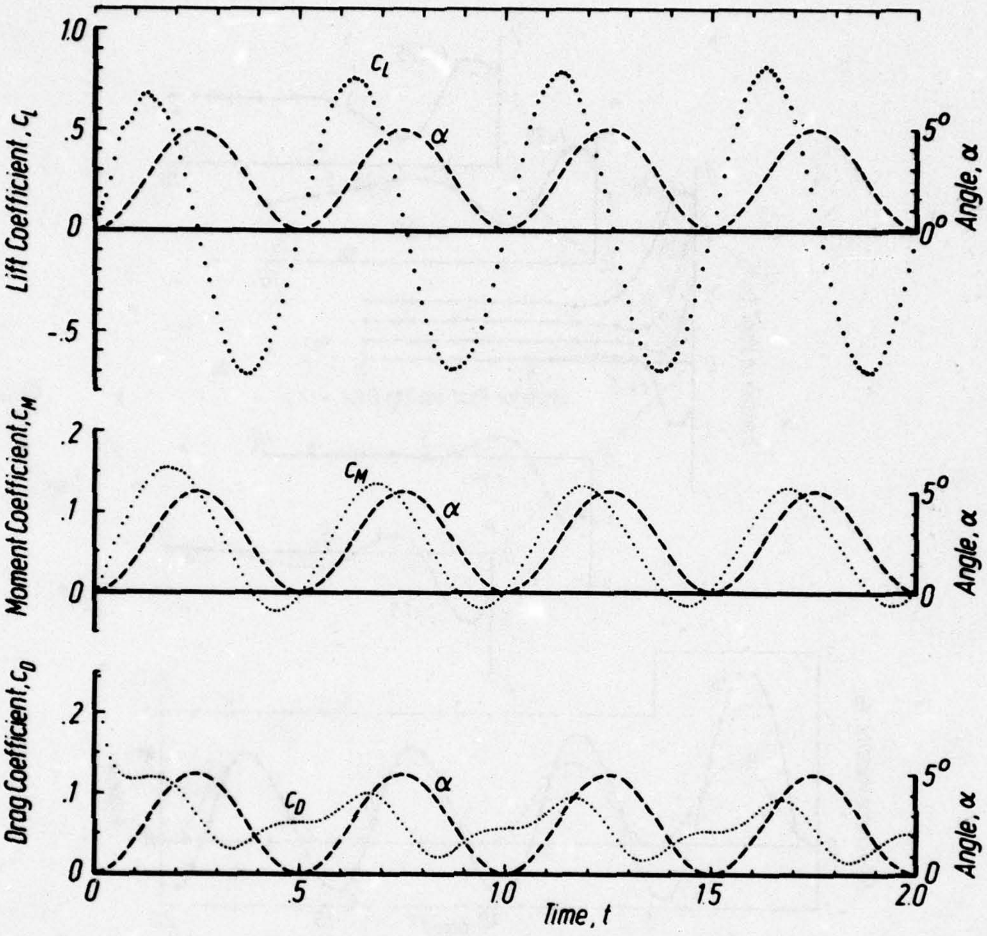

Fig. 4 Temporal variation of force coefficients for periodic gust, Re = 10000

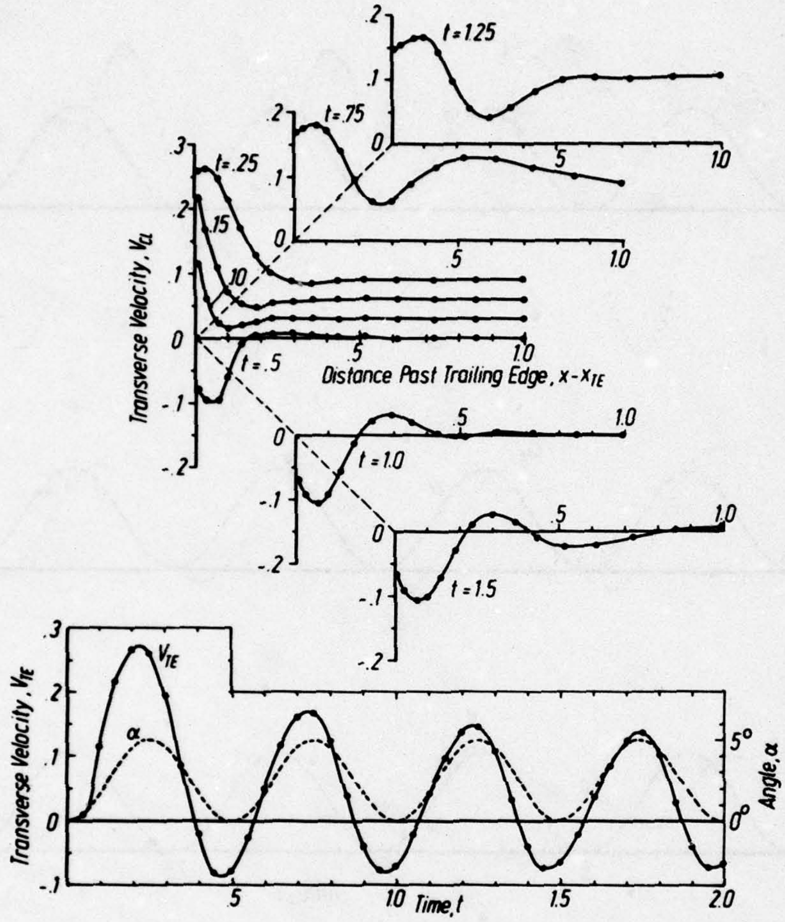

Fig. 5 Temporal variation of transverse velocity component downstream of the trailing edge. Periodic gust for Re = 10000

LES DIFFICULTÉS RENCONTRÉES PAR LES AÉROÉLASTICIENS DANS LE DOMAINE DE L'AÉRODYNAMIQUE INSTATIONNAIRE

par Rolland DAT et Jean-Jacques ANGÉLINI

Office National d'Etudes et de Recherches Aérospatiales (ONERA)
92320 Châtillon (France)

Résumé

Les aéroélasticiens ont besoin de méthodes de calcul de forces aérodynamiques instationnaires souples et rapides. La formulation classique, à partir de la théorie linéaire de la surface portante est présentée comme exemple de méthode satisfaisante par sa souplesse. Sa précision est illustrée par quelques applications qui ne s'écartent pas trop de son domaine de validité. Les problèmes d'écoulement supercritique ou de décollements, qui sortent de ce domaine de validité, sont malheureusement les plus importants du point de vue du flottement. Des résultats expérimentaux sont présentés pour illustrer les phénomènes propres à ces écoulements. Les approches adoptées pour développer de nouvelles méthodes sont indiquées à la fin. Elles vont des méthodes rigoureuses de résolution des équations d'Euler jusqu'à l'élaboration de corrections ou de modèles phénomélogiques.

DIFFICULTIES ENCOUNTERED BY AEROELASTICIANS OF UNSTEADY AERODYNAMICS

Summary

The aeroelasticians have a real need of flexible and fast methods for calculating unsteady aerodynamic forces. The classical formulation based on the linear lifting surface theory is presented as an example of a method satifactory as regards its domain of validity. The problems of supercritical flow and separation, which are much outside that domain, are unfortunately the most significant as far as flutter is concerned. Several experimental results are presented to show the phenomena particular to these flows. The approaches used to develop new methods are shown at the end. They extend from strict resolutions of the Eulerian equations to the development of corrections or phenomenological models.

INTRODUCTION

L'aérodynamique instationnaire constitue un aspect fondamental de l'aéroélasticité. Pour prévoir les vibrations aéroélastiques d'une structure, en effet, il faut être en mesure de prévoir les forces aérodynamiques instationnaires engendrées par les mouvements de vibration. Il faut en outre que les méthodes de calcul utilisées soient suffisamment souples et rapides pour permettre de traiter de nombreux cas d'écoulement et des modes de vibration présentant une grande diversité de déformées et répartis dans une large bande de fréquence.

Les méthodes linéaires utilisées jusqu'à maintenant pour prévoir le flottement des avions présentent ce caractère de souplesse et leur précision est satisfaisante dans beaucoup d'applications ; cependant, étant fondées sur l'hypothèse des petites perturbations, elles cessent d'être valables dès que l'écoulement est fortement perturbé, c'est-à-dire dans de nombreux cas intéressant les aéroélasticiens. Ceux-ci, en effet, doivent souvent prévoir des vibrations provoquées ou influencées par des effets non linéaires de couche limite, de grande incidence ou de compressibilité. Les méthodes expérimentales étant, dans la plupart des cas, incapables de fournir l'ensemble des données aérodynamiques nécessaires à un calcul d'aéroélasticité, il faut donc élaborer de nouveaux outils théoriques pour pouvoir traiter ces problèmes.

Les aéroélasticiens restent très attachés aux méthodes linéaires qui, seules, peuvent avoir la souplesse requise. Les échecs des méthodes actuelles ne mettent pas toujours en cause le principe de la linéarisation mais doivent souvent être attribuées au fait que l'hypothèse des petites perturbations est appliquée à la fois au champ aérodynamique instationnaire, consécutif aux vibrations, et au champ stationnaire. Dans beaucoup de cas, cette hypothèse n'est pas valable pour le champ stationnaire qui est fortement perturbé ; par contre, on peut presque toujours admettre l'hypothèse des petits mouvements et en déduire que le champ instationnaire consécutif aux vibrations est une petite perturbation linéarisable. La formulation linéaire qui découle de cette hypothèse est valable pour l'étude des instabilités aéroélastiques dans la mesure où l'on s'intéresse à l'amortissement des vibrations de faible amplitude sans chercher à prévoir l'amplitude des cycles limites éventuels dont l'existence s'explique par le caractère non linéaire des forces aérodynamiques ou de la structure. Elle s'applique également à l'étude de la réponse à la turbulence tant que la variation d'angle d'attaque liée à la vitesse de turbulence reste faible.

Cet exposé général, destiné à montrer aux aérodynamiciens comment le problème de l'aérodynamique instationnaire se pose aux aéroélasticiens, comporte trois parties. La première partie montre de quelle façon les méthodes linéaires sont exploitées en aéroélasticité ; dans la deuxième partie on se propose d'illustrer les possibilités et les insuffisances des méthodes actuelles par quelques résultats théoriques et expérimentaux ; enfin dans la troisième partie on évoque quelques approches adoptées pour essayer de trouver de nouvelles méthodes pratiques et efficaces.

1 – COUPLAGE D'UNE STRUCTURE SOUPLE AVEC UN FLUIDE EN ECOULEMENT

On peut, en général, assimiler les vibrations aéroélastiques d'une structure à des petits mouvements qui s'effectuent autour d'une certaine configuration moyenne appelée structure de référence. Ceci est justifié soit parce que l'on s'intéresse à des vibrations forcées dont l'amplitude est effectivement faible, soit parce que l'on veut étudier les riques d'instabilité en admettant qu'une structure est instable dès que l'amortissement des vibrations, aussi petites soient-elles, devient négatif.

Considérant que ces déplacements sont des infiniment petits du premier ordre, on peut admettre que les forces internes de structure et les forces aérodynamiques comprennent une partie stationnaire, de grandeur finie, et une partie instationnaire infiniment petite du premier ordre. Ainsi, l'écoulement autour de la structure en mouvement est la superposition de l'écoulement stationnaire autour de la structure de référence et d'un écoulement instationnaire provoqué par les petits mouvements de la structure, par les fluctuations de vitesse de turbulence, et éventuellement, par des instabilités de couche limite ou d'onde de choc (buffeting). L'écoulement stationnaire autour de la structure de référence peut être étudié séparément ; par contre, l'écoulement instationnaire dépend de l'écoulement stationnaire, à moins que la perturbation apportée au fluide par la structure de référence ne soit elle-même suffisamment petite pour pouvoir être assimilée à un infiniment petit du premier ordre.

Cette hypothèse sur l'ordre de grandeur des déplacements et des forces permet de linéariser le problème du couplage fluide-structure. Il faut lui ajouter une autre approximation qui consiste à schématiser la structure continue par un système discret dont la réponse est exprimée en fonction d'un nombre fini de coordonnées généralisées qui ne dépendent que du temps.

L'application du théorème des travaux virtuels donne les équations de Lagrange qui régissent le comportement dynamique de la structure. Ce sont des équations linéaires par rapport aux coordonnées généralisées, dont la résolution ne présente pas de difficulté lorsqu'on en connaît tous les coefficients. Par contre, l'évaluation des forces aérodynamiques généralisées, qui interviennent dans ces équations, reste un problème très difficile. C'est à ce problème que nous allons nous intéresser ici.

Les petits mouvements de vibration de la structure sont définis si l'on connaît, à chaque instant, le champ de vecteur $\mathbf{r}(P,t)$ représentant la déflexion des points P, c'est-à-dire leur écart par rapport à la position qu'ils occupent dans la structure de référence. Pour se ramener à l'étude d'un système discret, il suffit de se donner un certain nombre de champs de vecteurs cinématiquement admissibles $\mathbf{r}_k(P)$ et de poser :

$$(1) \qquad \mathbf{r}(P,t) = \sum_{k=1}^{n} \mathbf{r}_k(P)\, q_k(t)$$

Les fonctions du temps ou coordonnées généralisées, $q_k(t)$, sont les inconnues du problème.

Le degré d'approximation réalisé avec la formule (1) dépend du choix des champs de vecteur $\mathbf{r}_k(P)$ et de leur nombre n. Les aéroélasticiens utilisent en général la représentation modale, c'est-à-dire qu'ils prennent comme vecteurs de base $\mathbf{r}_k(P)$ les champs de vecteurs qui définissent les déformées des modes propres de vibration de la structure supposée isolée, dans le vide. Ceci revient à considérer la structure comme un ensemble de systèmes vibrants à un degré de liberté. La grande sélectivité en fréquence de ces systèmes permet d'étudier le comportement de la structure couplée avec le fluide par bandes de fréquence, avec un nombre d'inconnues, ou de degrés de liberté, n, relativement faible. Dans l'étude du flottement d'un avion, par exemple, le nombre de degrés de liberté à introduire dans un même calcul dépasse rarement 10 à 12 ; beaucoup de flottements classiques peuvent même être prévus avec deux degrés de liberté et certaines instabilités, qui seront évoquées plus loin, obéissent à un mécanisme particulier qui ne fait intervenir, pratiquement, qu'un seul degré de liberté.

Les forces aérodynamiques généralisées sont déduites de l'expression des travaux virtuels des forces de pression. La force généralisée Q_k agissant sur la coordonnée généralisée q_k est donnée par l'intégrale de surface :

$$(2) \qquad Q_k(t) = -\rho V^2 \iint_S \bar{\mathbf{r}}_k(P)\, \mathbf{n}(P)\; C(P,t)\, dS$$

avec,

$\rho V^2 C\,(P,t)$ = pression exercée par le fluide au point P de la surface extérieure de la structure.

$\mathbf{n}(P)$ = vecteur normal extérieur unitaire au point P.

S = domaine d'intégration comprenant toute la surface extérieure soumise à la pression du fluide en mouvement.

dS = élément de surface associé au point P.

Pour simplifier la présentation, nous allons considérer les forces aérodynamiques provoquées par le mouvement de la structure (forces couplées avec la structure) et négliger les forces dues à la turbulence ou à des instabilités éventuelles de l'écoulement. Dans ce cas, le champ aérodynamique instationnaire dépend linéairement du mouvement de la structure. Les relations linéaires entre forces généralisées et coordonnées généralisées s'expriment facilement si l'on passe du domaine temporel au domaine fréquentiel en effectuant la transformée de Fourier. Les éléments de cette transformée peuvent s'obtenir en considérant des mouvements harmoniques définis par :

$$\mathbf{r}(P,t) = \sum_{\ell=1}^{n} \mathcal{R}\left(\mathbf{r}_\ell(P)\, q_\ell\, e^{i\omega t}\right)$$

où les nombres complexes q_ℓ (ou affixes) déterminent le module des fonctions harmoniques q_ℓ et leur phase par rapport à une référence de phase donnée. La notation $\mathcal{R}(\ldots)$, qui signifie partie réelle de (...), restera sous-entendue comme c'est l'usage.

Pour ce mouvement, le coefficient de pression C(P,t) prend la forme :

$$C(P,t) = C_0(P) + \sum_{\ell=1}^{n} C_\ell(P,i\omega)\, q_\ell\, e^{i\omega t}$$

où $C_0(P)$ est le coefficient de pression de l'écoulement stationnaire autour de la structure de référence.

Après substitution dans (2), il vient :

$$(3) \qquad Q_k(t) = Q_{k0} + \sum_{\ell=1}^{n} A_{k\ell}(i\omega)\, q_\ell\, e^{i\omega t}$$

avec

$$(4) \qquad A_{k\ell}(i\omega) = -\rho V^2 \iint_S \bar{\mathbf{r}}_k(P)\, \mathbf{n}(P)\, C_\ell(P,i\omega)\, dS$$

La matrice $A_{k\ell}$ est la fonction de transfert matricielle reliant les forces aérodynamiques généralisées aux coordonnées généralisées.

$C_\ell(P,i\omega)$ est l'affixe du coefficient de pression sur la structure pour une vibration harmonique de pulsation ω avec la déformée $\mathbf{r}_\ell$ (P) : l'argument de C_ℓ détermine la phase de la pression par rapport à ce mouvement.

La matrice $A_{k\ell}(i\omega)$ permet de résoudre les problèmes de stabilité aéroélastique et elle intervient dans l'étude de la réponse forcée à la turbulence.

Mais la formule (4) doit être complétée lorsqu'il y a une onde choc dont la position est affectée par les petits mouvements de la structure. L'onde de choc forme alors une frontière mobile entre deux domaines où la pression est différente. On tiendra compte de ce mouvement en décomposant le domaine d'intégration de l'intégrale (4).

Soit par exemple une aile d'avion en écoulement stationnaire supercritique, avec une onde de choc sur l'extrados. L'intégration en corde de l'intégrale (4) sur l'extrados, s'écrit :

$$-\rho V^2 \left[\int_{x_A}^{\xi} \bar{\mathbf{r}}_k \mathbf{n}\, C\, dx + \int_{\xi}^{x_F} \bar{\mathbf{r}}_k \mathbf{n}\, C\, dx\right]$$

où x_A, x_F et ξ sont les abscisses, respectivement, du bord d'attaque, du bord de fuite et du pied de l'onde de choc.

Comme précédemment, considérons un mouvement harmonique défini par $\mathbf{r}(P,t) = \sum_\ell \mathbf{r}_\ell(P)\, q_\ell\, e^{i\omega t}$ et admettons toujours que le coefficient de pression et le déplacement du choc dépendent linéairement des petits mouvements de la structure (nous verrons que cette hypothèse n'est pas toujours valable en ce qui concerne le déplacement du choc). On a :

$$C(x,t) = C_0(x) + \sum_{\ell=1}^{n} C_\ell(i\omega)\, q_\ell\, e^{i\omega t}$$

et l'abscisse de l'onde de choc se met sous une forme analogue :

$$\xi(t) = \xi_0 + \sum_{\ell=1}^{n} \xi_\ell(i\omega)\, q_\ell\, e^{i\omega t}$$

Ces deux expressions doivent être substituées dans l'intégrale en corde qui est ensuite développée jusqu'au premier ordre en considérant que les q_ℓ sont des infiniments petits du 1er ordre. On évalue également l'intégrale en corde nu sur l'intrados, puis on procède à l'intégration en envergure et l'on retrouve la forme linéaire (3) avec $A_{k\ell}(i\omega)$ donné par :

$$(5) \quad A_{k\ell}(i\omega) = \iint_S \bar{\mathbf{r}}_k(P)\,\mathbf{n}(P)\,C_\ell(P)\,dS + \cdots$$
$$\cdots + \int_{-L}^{L} \bar{\mathbf{r}}_k(P)\,\mathbf{n}(P)\,\xi_\ell(y)\,\Delta C_0(y)\,dy$$

où

$C_\ell(P,i\omega)$ est l'affixe du coefficient de pression induit par le mouvement harmonique $\mathbf{r}(P,t) = \mathbf{r}_\ell(P)e^{i\omega t}$

$\xi_\ell(y,i\omega)$ est l'affixe du déplacement du choc pour le même mouvement ;

$\Delta C_0(y)$ est le saut de pression stationnaire à travers le choc ;

y est la coordonnée en envergure et $[-L, L]$ le domaine d'intégration en envergure.

Le saut de pression ΔC_0 est considéré comme une grandeur finie ; c'est une caractéristique importante de l'écoulement stationnaire ; ξ_ℓ dépend à la fois de l'écoulement stationnaire et de la déformée de vibration $\mathbf{r}_\ell$ (P).

Enfin l'affixe de la pression instationnaire, $C_\ell(P,i\omega)$ dépend de l'écoulement stationnaire. Celui-ci agit notamment en modifiant la propagation des ondes acoustiques émises par la structure en vibration. Cet effet peut être important, même en l'absence d'onde de choc, mais il se manifeste surtout en écoulement supercritique lorsque les perturbations qui se propagent d'aval en amont doivent contourner la zone supersonique.

Dans les calculs d'aéroélasticité, la matrice $A_{k\ell}(i\omega)$ vient s'ajouter à l'impédance matricielle de la structure et détermine l'évolution des modes propres de la structure couplée avec l'écoulement, c'est-à-dire, en particulier, l'évolution de ses fréquences propres et de ses amortissements. La difficulté principale réside dans la détermination de cette matrice. La linéarisation des relations entre forces généralisées et coordonnées généralisées, qui a permis de l'introduire, est une approximation justifiée par l'hypothèse des petit mouvements. Mais celle-ci ne suffit pas toujours à justifier la linéarisation des équations du fluide en écoulement : la linéarité peut être mise en défaut localement, par exemple au voisinage d'une onde de choc en mouvement. Dans ce cas, il faut résoudre les équations non linéaires de l'écoulement sans chercher à tirer parti de l'hypothèse des petits mouvements. Cela n'empêche évidemment pas de calculer la matrice si elle a un sens, c'est-à-dire si l'hypothèse de linéarité est une approximation acceptable pour les forces généralisées.

L'expérience en soufflerie montre qu'elle l'est dans la majorité des cas, même en présence de décollements, pour les amplitudes de vibration considérées en aéroélasticité. Nous verrons cependant qu'il existe des exceptions, notamment lorsqu'il y a une onde de choc dont la position est très sensible au champ de vitesse. Dans ce cas, les petits mouvements de la structure peuvent provoquer un déplacement fini du choc, voire même le repousser en dehors du profil.

Mais à l'inverse de ces cas fondamentalement non linéaires, où un petit mouvement peut provoquer une variation finie de l'écoulement, il existe de nombreuses configurations d'avions et de vol avec aile mince, lisse, à faible incidence, en dehors du domaine transonique, dans lesquelles l'écoulement stationnaire lui-même peut être considéré comme une perturbation infiniment petite justiciable des méthodes linéaires. Les problèmes stationnaire et instationnaire deviennent alors complètement indépendants et peuvent être traités séparément. Le fluide étant supposé parfait, on définit un potentiel de vitesse qui est régi par l'équation des ondes acoustiques. L'aile est assimilée à une plaque plane sans épaisseur effectuant de petits mouvements de vibration de part et d'autre de son plan moyen. Puisque l'écoulement stationnaire n'intervient pas dans le calcul instationnaire, on peut supposer que la position moyenne est le plan $x\,o\,y$ qui contient la vitesse V.

Le mouvement de vibration est défini par une fonction $h(x,y,t)$ qui représente la déflexion normale à la surface portante, suivant l'axe Oz.

On pose :

$$h(x,y,t) = \sum_{k=1}^{n} h_k(x,y)\, q_k(t)$$

Les fonctions $h_k(x,y)$ s'identifient aux composantes normales des déformées de base, $\mathbf{r}_k(P)$ définies dans le cas général.

La formule (4) qui donne les coefficients $A_{k\ell}$ s'écrit dans ce cas :

$$A_{k\ell} = -\rho V^2 \iint_{S_0} h_k(x,y)\, \Delta C_\ell(x,y,i\omega)\, dx\, dy$$

où (S_0) est la forme en plan de l'aile et ΔC_ℓ l'affixe du saut de pression instationnaire à travers la surface portante, c'est-à-dire $C_\ell(x,y,0^+) - C_\ell(x,y,0^-)$ pour un mouvement harmonique défini par :

$$h(x,y,t) = h_\ell(x,y)\, e^{i\omega t}$$

Ce mouvement impose au fluide une vitesse normale

$$w_\ell(x,y) = V\frac{\partial h_\ell}{\partial x} + i\omega h_\ell$$

Le problème aux limites, dont la solution donne ΔC_ℓ lorsqu'on connaît w_ℓ est suffisamment connu pour n'avoir pas à être explicité ici (voir ref. [1] à [9]). Il existe plusieurs méthodes de résolution dont l'une, qui est la plus fréquemment utilisée par les aéroélasticiens, passe par l'équation intégrale singulière exprimant la vitesse normale $w(x,y)$ en fonction du saut de pression $\Delta C(x,y)$:

$$w(x,y) = \iint_S K(x-\xi, y-\eta, i\omega)\,\Delta C(\xi,\eta)\,d\xi\,d\eta$$

où K est un noyau singulier.

A partir de cette équation on peut calculer une matrice de coefficients d'influence aérodynamiques reliant les valeurs de ΔC sur un ensemble de N points de pression, aux valeurs de W sur un ensemble de N points de vitesse normale :

$$(6) \qquad \Delta C(P_u) = \sum_{v=1}^{N} S_{uv}(i\omega)\, w(P'_v)$$

Les points de pression $P_u (u=1,\dots N)$ et les points de vitesse normale $P'_v (v=1,\dots N)$ sont répartis en corde et en envergure suivant des règles de répartition optimale, et forment deux ensembles distincts.

Le calcul de la matrice S_{uv} à partir de l'équation (5) est devenu classique pour les aéroélasticiens ; les méthodes utilisées diffèrent par la façon d'effectuer la discrétisation.

Dans la méthode de collocation, la répartition de pression est représentée par une superposition de fonctions de base auxquelles on donne un comportement approprié en les faisant tendre vers l'infini sur le bord d'attaque et vers zéro sur les bords latéraux et sur le bord de fuite. Après substitution dans l'équation (5) on obtient un système d'équations algébriques exprimant les vitesses normales aux points de vitesse (qui deviennent des points de collocation) en fonction des coefficients de superposition qui déterminent la fonction inconnue

Dans la méthode des doublets [3], l'aile est décomposée en mailles trapézoïdales comportant un segment portant (ou ligne de doublets), situé au 1/4 avant de la maille, et un point de vitesse normale situé au 1/4 arrière. L'équation (5) permet alors de calculer le coefficient d'influence entre un segment portant et un point de vitesse appartenant à la même maille ou à deux mailles distinctes.

Dans la méthode de collocation l'optimisation des points de vitesse normale, des fonctions de pression et des points de pression, permet de limiter le nombre d'inconnues introduites dans la discretisation et la difficulté principale réside dans le calcul des intégrales singulières.

La méthode des doublets au contraire part d'une représentation discontinue et grossière de la surface portante et elle exige, de ce fait, un grand nombre de mailles. Par contre, le calcul des vitesses induites par les segments portants est facile et répétitif. La difficulté principale réside alors dans l'inversion de matrice, puisque le nombre de mailles est élevé.

Le nombre d'inconnues qu'il faut prendre dans l'une ou l'autre méthode pour obtenir des résultats satisfaisants dépend de la complexité des déformées $h_k(x,y)$ qui sont introduites dans les calculs d'aéroélasticité. La participation de modes de vibration de rang élevé, dont la déformée comporte beaucoup de lignes de noeuds, oblige à prendre un nombre de points de collocation assez grand ou à faire un maillage fin. L'expérience montre que pour traiter les problèmes du flottement d'un avion, il faut de l'ordre de 25 points de collocation par demi aile avec la première méthode et au moins une centaine de mailles avec la seconde.

Les matrices de coefficients d'influence d'un avion peuvent être calculées pour différentes valeurs du Mach et de la fréquence dès que la forme en plan des surfaces portantes est définie. Elles sont alors mises en mémoire et peuvent être utilisées à n'importe quel moment. Cette organisation convient tout particulièrement aux aéroélasticiens qui peuvent ainsi effectuer des calculs de stabilité ou de réponse forcée dans de nombreuses configurations et reprendre ces calculs chaque fois qu'une modification est apportée à la structure. Le calcul des forces aérodynamiques généralisées, qui doit être répété souvent, est simple et rapide, et les seules difficultés résident dans le calcul des coefficients d'influence S_{uv} qui n'est effectué qu'une fois pour un même avion. Ce dernier calcul peut devenir assez coûteux lorsqu'il faut étudier des configurations de structure complexes : c'est le cas, par exemple, lorsque les couplages entre aile-empennage et dérive doivent être pris en considération et qu'il faut traiter les trois surfaces portantes simultanément.

Il convient de remarquer que les méthodes linéaires ne s'appliquent pas seulement aux surfaces portantes mais permettent également de prévoir les forces aérodynamiques instationnaires sur des nacelles de réacteur ou des corps fuselés tels que fuselage, réservoir extérieur ou charges militaires, à condition que l'écoulement stationnaire autour de ces éléments puisse être assimilé à une petite perturbation, fig. (1). Beaucoup d'organismes ont développé

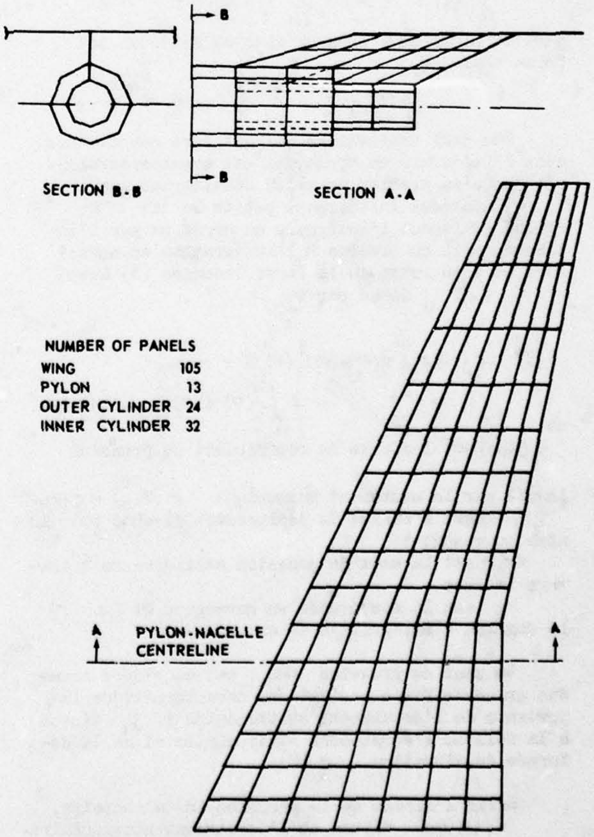

Fig. 1 – Maillage utilisé pour le calcul, par la méthode des doublets, d'une configuration aile-pylône-nacelle (extrait de la réf. [7]).

des programmes de calcul qui donnent des matrices de coefficients d'influence pour des configurations d'avion comportant plusieurs surfaces portantes et plusieurs corps fuselés en tenant compte des interactions entre ces différents éléments. Certains de ces programmes sont comparables, par leur importance et par l'étendue de leurs possibilités à des programmes d'éléments finis de structure (voir par ex. ref[7]).

Remarquons enfin que la notion de matrice de coefficients d'influence aérodynamiques s'applique également dans le cas où l'écoulement instationnaire est affecté par l'écoulement stationnaire. La matrice S_{uv} dépend alors du champ stationnaire autour de la structure de référence, mais elle conserve l'avantage, par rapport à la matrice A_{kl}, de pas dépendre des déformées $f_k(P)$ introduites dans les calculs d'aéroélasticité et peut être évaluée dès que l'on connaît les configurations de vol stationnaire de l'avion, sans attendre de connaître ses caractéristiques vibratoires.

2 - PRESENTATION DE QUELQUES RESULTATS TYPIQUES

L'hypothèse des petits mouvements et la linéarisation qui en découle permettent de distinguer deux types de forces aérodynamiques instationnaires : les forces couplées, qui sont déterminées par le mouvement de la structure et les forces imposées qui n'en dépendent pas (cas des forces dues à la turbulence). Bien que cette distinction ne soit en général pas valable lorsqu'interviennent des phénomènes non linéaires, nous admettrons qu'elle peut être faite dans la plupart des cas étudiés par les aéroélasticiens et nous continuerons à nous intéresser essentiellement aux forces couplées qui sont à l'origine des instabilités.

La prévision d'une instabilité de flottement nécessite une connaissance plus ou moins précise et plus ou moins complète des forces aérodynamiques instationnaires selon la nature de cette instabilité.

Le flottement classique fait intervenir plusieurs degrés de liberté de la structure, et c'est le déphasage entre ces degrés de liberté qui favorise le transfert d'énergie du fluide à la structure. Ce sont les forces aérodynamiques qui couplent des degrés de liberté de nature différente tels que flexion et torsion ou flexion et braquage de gouverne, qui sont à l'origine de l'instabilité. Dans beaucoup de cas, il suffit de connaître les coefficients qui déterminent ces couplages et les coefficients de "raideur" aérodynamique, qui agissent sur l'évolution des fréquences, pour prévoir la vitesse critique de flottement. Mais ceci n'est pas toujours vrai en pratique et, de toute façon, la prévision des amortissements avant le flottement nécessite une connaissance au moins approchée des autres coefficients aérodynamiques.

Mais il existe aussi des flottements "à un degré de liberté" (ainsi nommés parce qu'ils peuvent se produire avec un seul mode propre de vibration de la structure) qui s'expliquent par le déphasage entre la *force généralisée* et le mouvement, l'instabilité se produisant lorsque la force admet une composante en phase avec la vitesse d'oscillation. Le déphasage peut provenir soit du changement de signe d'une dérivée aérodynamique de portance ou de moment, à grande incidence, soit du fait que l'écoulement ne répond qu'avec un certain retard aux petits mouvements de la structure. Le flottement à un degré se manifeste plus fréquemment lorsque l'écoulement comporte un décollement ou une onde de choc. L'effet défavorable du décollement provient souvent du temps de réponse relativement élevé qui intervient lorsque le mouvement de la structure le fait évoluer ; de même, l'effet défavorable de l'écoulement supercritique s'explique par l'augmentation des délais de propagation des ondes acoustiques de retour, qui doivent contourner la zone supersonique, et par les temps de réponse qui interviennent dans le déplacement de l'onde de choc sous l'action du mouvement de la structure.

Le nombre de coefficients ou de dérivés aérodynamiques intervenant dans ces instabilités est suffisamment faible pour que l'on puisse parfois utiliser l'expérience en soufflerie pour les évaluer. Dans ce cas, il est intéressant de remarquer, pour les simplifications que cela peut apporter aux essais, que la *composante de force généralisée* en phase avec le mouvement a un effet en général négligeable et qu'il suffit de connaître la composante en phase avec la vitesse de vibration.

Mais quel que soit le type de flottement étudié, les grandeurs intervenant dans les calculs sont les coefficients des matrices A_{kl}, c'est-à-dire les intégrales (4) ou (5). Or, l'intégration a tendance à rendre négligeable l'effet de certains accidents locaux de la répartition de pression. Cette remarque justifie l'emploi de méthodes de calcul présentant des désaccords locaux avec l'expérience mais capables de restituer correctement l'évolution générale de la pression ; elle s'applique en particulier à la théorie linéaire de la surface portante et explique pourquoi celle-ci donne des résultats satisfaisants dans un large domaine d'application.

2.1 - Résultats obtenus dans le domaine d'application de la théorie de la surface portante.

Les résultats donnés par la théorie linéaire de la surface portante sont en accord avec l'expérience dans tous les cas où l'on ne s'écarte pas trop des hypothèses de calcul. Pour cela, l'aile doit être mince, vibrer autour d'une incidence moyenne nulle ou faible, être lisse, c'est-à-dire dépourvue de charges militaires ou de réservoirs extérieurs. Il faut également que le nombre de Mach soit hors du domaine transsonique pour que la linéarisation de l'équation du potentiel soit justifiée.

La figure (2) montre les valeurs théoriques et expérimentales du coefficient de pression sur une maquette trapézoïdale oscillant en roulis, à Mach 0,8. On voit que la comparaison est extrêmement satisfaisante.

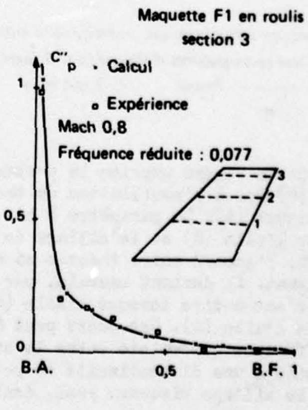

Fig. 2 – Exemple de confrontation théorie-expérience sur aile lisse (sans charge).
Répartition en corde de la pression instationnaire sur une demi-aile à la paroi oscillant en roulis. Composante en phase avec la vitesse d'oscillation.

La même méthode de calcul s'applique aussi à un ensemble de surfaces portantes telles que l'aile et l'empennage ou l'empennage et la dérive.

Des résultats numériques obtenus sur un ensemble de deux maquettes rectangulaires situées dans des plans parallèles sont comparés aux résultats expérimentaux dans la figure (3). Le coefficient représenté sur la figure exprime la portance de l'aile aval (B) due à l'oscillation de tangage de la maquette amont (A). Le paramètre H est la distance réduite entre l'aile (B) et le sillage de l'aile (A). Pour H = 0,25, l'accord entre théorie et expérience est satisfaisant. Il devient mauvais, par contre, pour H = 0, c'est-à-dire lorsque l'aile (B) est dans le sillage de l'aile (A). Cet écart peut être attribué à la différence qui existe entre le sillage théorique, assimilé à une discontinuité de potentiel de vitesse, et le sillage visqueux réel, dont l'épaisseur est finie.

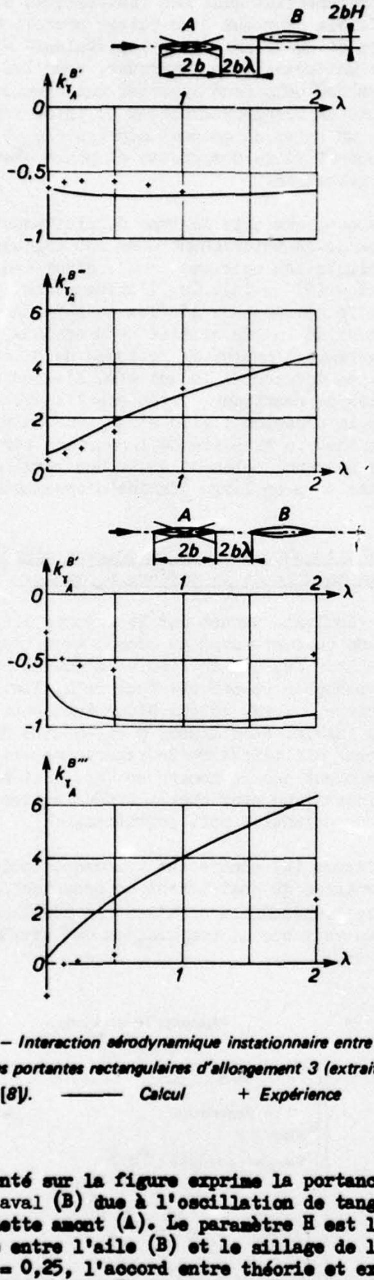

Fig. 3 – Interaction aérodynamique instationnaire entre deux surfaces portantes rectangulaires d'allongement 3 (extrait de la réf. [8]). ——— *Calcul* + *Expérience*

On constate également que les écarts entre pressions aérodynamiques théoriques et expérimentales sont plus importantes lorsque la pression instationnaire est engendrée par l'oscillation d'une gouverne que lorsqu'elle est produite par une oscillation de l'aile (figure 4). L'origine de cette aggravation est généralement attribuée aux variations d'épaisseur de couche limite qui accompagnent l'oscillation de la gouverne. Ces déformatiosn affectent le mouvement de la frontière du fluide parfait, sur laquelle la condition de glissement devrait, en principe, être appliquée, et elles peuvent compromettre la validité de la condition de bord de fuite, telle qu'elle est appliquée en instationnaire.

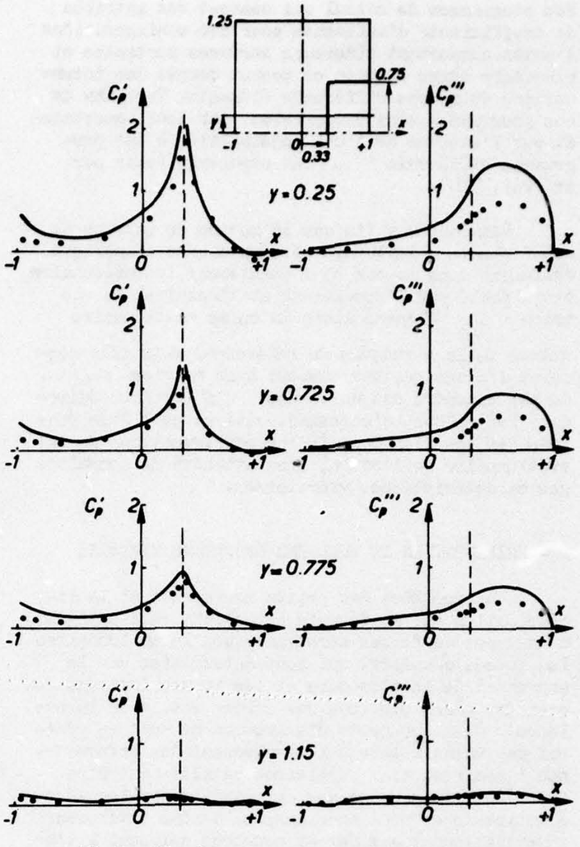

Fig. 4 – Répartition de pression instationnaire induite par l'oscillation d'une gouverne, à faible vitesse. (extrait de la réf. [9]). ——— *Calcul* • *Expérience*

2.2 - Forces aérodynamiques instationnaires sur une aile en écoulement supercritique.

Les exemples qui viennent d'être présentés ne s'écartent pas trop du domaine de validité de la théorie linéaire. Mais ce domaine ne couvre malheureusement qu'une partie des besoins des aéroélasticiens.

Les difficultés de prévision des forces aérodynamiques instationnaires apparaissent, même à incidence faible ou modérée, dès que la non uniformité de l'écoulement stationnaire au voisinage de l'aile devient importante et affecte les conditions locales et la propagation des ondes acoustiques. Lorsque l'écoulement est supercritique ces effets modifient profondément les couplages qui sont à l'origine du flottement classique et peuvent même créer des instabilités particulières à un degré de liberté dont la plus connue est le "buzz" des gouvernes [10], [11] et [12]. Dans les références [14] et [15], H. Tijdeman interprète des résultats de mesures effectuées sur un profil en présence d'une onde de choc, pour une oscillation de gouverne. Par une représentation graphique de la propagation des ondes acoustiques provenant d'une source pulsante située près du bord de fuite, dans le champ stationnaire du profil, il montre l'importance des retards consécutifs au contournement de la zone supersonique par les ondes de retour se propageant de la gouverne vers le bord d'attaque. Ces retards et le mouvement du choc expliquent parfaitement les tendances observées, à savoir :

- le déplacement de l'onde de choc qui accompagne l'oscillation de gouverne avec un certain déphasage provoque une forte bosse dans la répartition de pression instationnaire au voisinage du pied du choc.
- le contournement de la zone supersonique par les ondes acoustiques qui se propagent vers l'amont provoque une atténuation et un déphasage de la pression instationnaire en amont du choc.

Ces tendances se retrouvent également dans des mesures de pression effectuées à l'ONERA sur un profil d'aile épais muni d'une gouverne oscillante, figure (5).

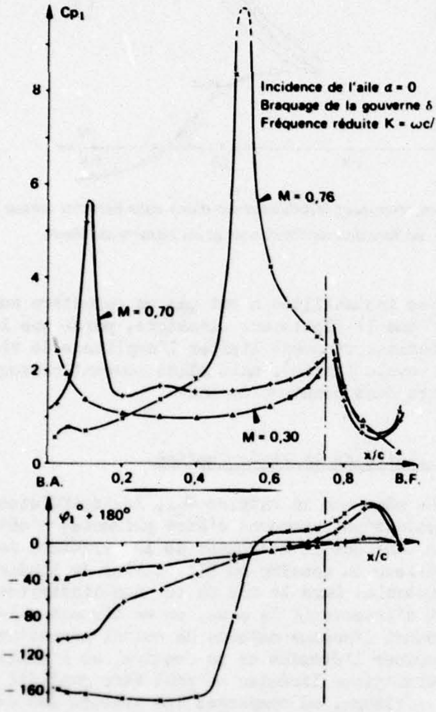

Fig. 5 – Pression instationnaire induite par l'oscillation d'une gouverne sur un profil supercritique (module et phase du coefficient de pression).

L'amplitude du mouvement du choc a tendance à diminuer avec la fréquence et elle dépend beaucoup des conditions d'écoulement stationnaire. Dans le cas des basses fréquences, H. Tijdeman distingue trois cas [15] :

- le cas (a) où l'onde de choc effectue un mouvement presque sinusoïdal en restant sur l'aile,
- le cas (b) où l'onde de choc ne quitte pas le profil mais s'évanouit pendant une partie du cycle,
- le cas (c) où, à chaque cycle, le choc se forme sur le profil puis se propage vers l'amont et sort du profil au bord d'attaque.

En admettant que l'amplitude de vibration de la gouverne reste faible, les cas (b) et (c) ne peuvent se produire que si l'écoulement est faiblement supercritique.

La linéarisation est bien justifiée dans le cas (a). Par contre, le cas (c) présente un caractère non-linéaire très prononcé puisque le choc se déplace d'une distance finie, même pour de petites oscillations de gouverne. La gravité de cette non-linéarité est toutefois limitée, du fait qu'elle ne peut se produire qu'en écoulement faiblement supercritique c'est-à-dire dans une gamme de Mach étroite et avec un choc de faible intensité.

Les tendances observées avec une gouverne oscillante se retrouvent, mais avec moins de netteté, en ce qui concerne l'atténuation et le déphasage de la pression en amont du choc, lorsque c'est l'ensemble de l'aile qui est en vibration. La figure (6) montre comment la zone supersonique due à la présence d'un engin modifie la pression induite par l'oscillation de tangage de l'aile.

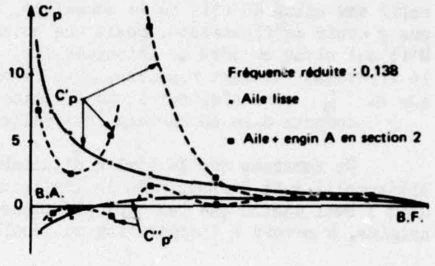

Engin A sous l'aile - Répartition de pression instationnaire mesurée dans la section 2.

Composante en phase avec l'oscillation (C'_p) et composante en quadrature (C''_p), pour une oscillation de tangage.

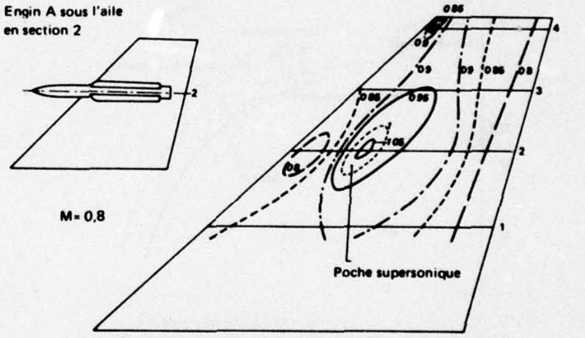

Engin A sous l'aile - Répartition du Mach stationnaire local sur l'intrados de l'aile.

Fig. 6 – Influence de la zone supersonique due à la présence d'un engin.

2.3 - Instabilités liées à l'incidence.

La présence de décollements est à l'origine de phénomènes parfois assimilables à des instabilités propres à l'écoulement et d'une complexité telle qu'il est souvent difficile de faire la distinction entre forces couplées et forces imposées. L'apparition d'une zone de décollement sur une aile s'accompagne d'une vibration de tremblement ou "buffeting". Sur une aile suffisamment rigide pour que sa réponse n'affecte pas l'écoulement, le tremblement prend l'apparence d'une excitation aléatoire à spectre continu.

Mais la présence d'un décollement a aussi pour effet de modifier de façon profonde le mécanisme du couplage entre l'écoulement et la structure : c'est l'évolution du décollement avec ce mouvement qui constitue la source principale du couplage. Comme on l'a déjà remarqué, le temps de réponse relativement important qui intervient dans ce mécanisme a tendance à provoquer des flottements à un degré de liberté.

Aucune méthode de calcul ne permet de prévoir ces instabilités. Par contre, l'expérience en soufflerie permet de faire l'étude paramètrique complète des conditions d'instabilité sur un profil indéformable.

La figure (7) montre l'effet de l'incidence moyenne sur la stabilité d'un profil monté avec un seul degré de liberté. La configuration mécanique du profil est définie par la position de l'axe d'oscillation, x_o , et par la fréquence propre f_o . La figure définit un domaine d'instabilité conditionnelle dans le plan Mach-incidence. Si le point figuratif est situé du côté de la stabilité, il ne peut pas y avoir de flottement, quels que soient x_o et f_o . S'il est situé du côté de l'instabilité, au contraire, le flottement devient possible, mais il ne se produit que si f_o est inférieur à une certaine valeur et x_o compris dans un certain intervalle.

On remarque que la limite d'instabilité conditionnelle suit d'assez près la limite de tremblement ; ceci montre que les deux phénomènes ont la origine, à savoir : l'apparition du décollement.

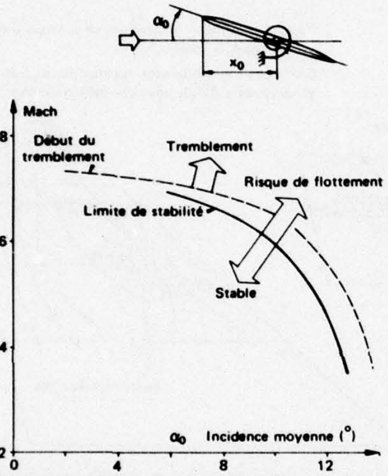

Fig. 7 – Limites de stabilité et de tremblement observées sur un profil en écoulement plan (réf. [16]). Le domaine d'instabilité délimité sur cette figure définit une condition nécessaire mais non suffisante de flottement.

Les instabilités de cette nature peuvent affecter la pale reculante des hélicoptères et les aubes de compresseur. Dans le cas des pales d'hélicoptère le phénomène est compliqué par la vitesse d'avancement et les variations périodiques du champ de vitesse qui en résultent.

L'étude en soufflerie de ces instabilités reste difficile, bien que le nombre de paramètres intervenant, pour un profil donné, soit relativement faible. La principale difficulté réside dans le fait que les forces aérodynamiques couplées doivent être extraites d'un bruit de fond important provenant du bruit et de la turbulence du vent et des fluctuations propres à l'écoulement autour du profil à grande incidence.

Les méthodes d'analyse harmonique des signaux permettent de séparer la composante de pression ou de force aérodynamique corrélée avec le mouvement du profil ; mais, du fait des non-linéarités, cette composante peut, elle-même, dépendre de la turbulence du vent et ne pas caractériser uniquement le couplage entre écoulement et mouvement de la structure. D'ailleurs, la séparation entre forces couplées et forces non couplées n'est valable que dans la mesure où toutes les perturbations instationnaires, y compris la turbulence, restent petites.

La figure (8) montre des résultats obtenus sur un profil d'aube monté dans une soufflerie de grille droite. On remarque une zone d'amortissement négatif (c'est-à-dire d'instabilité) au delà de Mach 0,7, pour une incidence de 9° [19] .

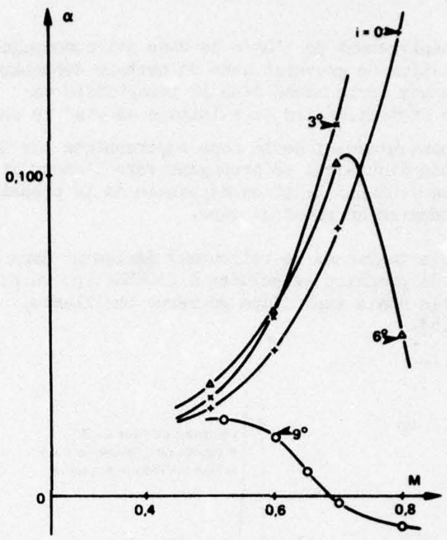

Fig. 8 – Amortissement aérodynamique d'une aube oscillant autour de la mi-corde, en fonction de l'incidence et du nombre de Mach.

Ces instabilités n'ont pas un caractère aussi explosif que le flottement classique, parce que les non-linéarités viennent limiter l'amplitude de vibration (cycle limite), mais elles peuvent provoquer la rupture dans beaucoup de cas.

2.4 – Validité de la linéarisation.

De même que la matrice $A_{k\ell}$, les coefficients expérimentaux qui viennent d'être présentés n'ont de sens que tant que le mouvement de la structure reste à l'intérieur du domaine où l'hypothèse de linéarité est acceptable. Dans le cas où les non-linéarités risquent d'intervenir le plus, on ne dispose malheureusement d'aucune méthode de calcul permettant de déterminer l'étendue de ce domaine, et l'emploi d'une formulation linéaire ne peut être justifié que par l'expérience, en comparant les valeurs des dérivés aérodynamiques mesurées avec des amplitudes de vibration différentes. La figure (9) montre les

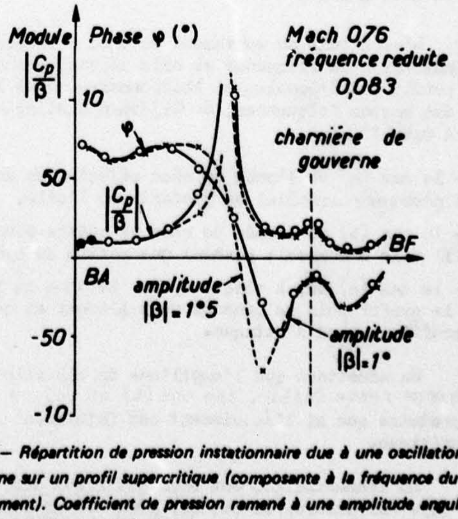

Fig. 9 – Répartition de pression instationnaire due à une oscillation de gouverne sur un profil supercritique (composante à la fréquence du mouvement). Coefficient de pression ramené à une amplitude angulaire unitaire, vérification de la linéarité.

○ *Amplitude* $|\beta| = 1°$ × *Amplitude* $|\beta| = 1,5°$

résultats d'un contrôle de linéarité dans un cas particulièrement difficile, puisqu'il s'agit d'un profil en écoulement supercritique avec oscillation de gouverne. La variation de C_{φ}/β lorsque l'amplitude de l'oscillation passe de 1° à 15° montre qu'à 1°5 on est déjà sorti du domaine où la linéarisation est acceptable pour la pression. Bien que les écarts importants ne se trouvent qu'au voisinage du choc et que l'intégration ait tendance à atténuer l'effet des écarts locaux, on doit considérer que l'amplitude de 1°5 est déjà en dehors du domaine où la linéarité est admissible pour les forces généralisées. Mais cet exemple est un des plus sévères; dans la plupart des cas la linéarité peut être admise sans réserve pour des amplitudes de l'ordre du degré.

3 - RECHERCHE DE NOUVELLES METHODES DE PREVISION

La création de nouvelles méthodes de prévision des forces aérodynamiques instationnaires répondant aux besoins des aéroélasticiens nécessite un effort important de recherche et de développement.

Pour que ces méthodes ne soient pas trop lourdes à exploiter, elles doivent être développées à partir de modèles aussi simples que possible. Dans le cas où c'est un décollement qui joue le rôle essentiel, on peut s'orienter vers la recherche d'un modèle phénoménologique ou d'un modèle théorique dans laquelle le point de décollement est imposé. Dans le cas où il n'y a pas de décollement, on peut développer des méthodes théoriques plus ou moins complexes selon qu'elles tiennent compte ou non de la couche limite. Les résultats de la figure (4) montrent qu'il faut en tenir compte pour prévoir le champ de pression induit par les vibrations de gouverne. Dans les autres cas, par contre on peut se demander s'il ne suffit pas de recherche les solutions des équations d'Euler non linéarisées. La réponse à cette question serait malheureusement négative si l'on en juge par les résultats présentés par H. Tijdeman dans la référence [15] . L'auteur compare la répartition de pression expérimentale sur un profil, en stationnaire et en quasi-stationnaire, aux valeurs théoriques obtenues dans les conditions suivantes :

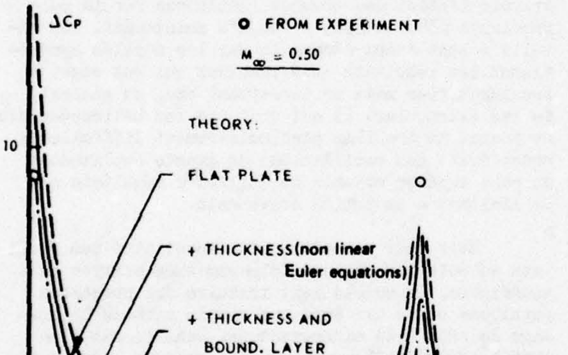

Fig. 10 – Influence de l'épaisseur et de la couche limite sur la répartition de pression, pour une oscillation de gouverne en quasi-stationnaire (résultat extrait de la réf. [15]).

- avec la théorie linéaire,
- avec effets non linéaires en fluide parfait (équations d'Euler non linéarisées),
- avec effets non linéaires et couplage couche limite-fluide parfait.

Le meilleur résultat est donné par le troisième calcul, comme on pouvait s'y attendre, mais on constate que la solution non linéaire en fluide parfait est moins bonne que la solution linéaire, figure (10).

D'après ces résultats, il serait donc illusoire de tenir compte des effets non linéaires de fluide parfait sans tenir compte en même temps du couplage du fluide parfait avec la couche limite.

3.1 - Résolution des équations du fluide parfait.

Nous n'insisterons pas sur les méthodes de résolution des équations d'Euler non linéaires en écoulement plan, par éléments finis, différences finies ou volume fini (référence [20] à [25]). Ces méthodes fonctionnent déjà : elles ne répondent pas encore aux besoins des aéroélasticiens, parce qu'elles exigent des temps de calcul prohibitifs, mais elles peuvent déjà être utilisées pour contrôler des méthodes moins rigoureuses et plus rapides. La rapidité du calcul est une des préoccupations essentielles de ceux qui les étudient. Sur ce plan, W.F. Ballhaus et P.M. Goorjian montrent que l'on peut obtenir une amélioration décisive en utilisant un algorithme de différences finies implicite [23] . Il est vrai que ces auteurs ne résolvent pas les équations d'Euler exactes mais l'équation du potentiel en quasi stationnaire, avec un terme non linéaire en $\Phi_x \Phi_{xx}$, qui en constitue la forme approchée généralement admise pour traiter les problèmes de perturbation en transsonique. Les résultats présentés recoupent bien les résultats de Magnus - Yoshihara [21] , qui partent des équations d'Euler exactes et utilisent un algorithme explicite, mais les temps nécessaires pour calculer un même cycle d'oscillation sur CDC 7600 sont respectivement de 8 sec et de 1500 sec.

On peut également rechercher la simplification du calcul en linéarisant les équations autour de la solution stationnaire exacte, comme le fait M. Fenain [26] à l'ONERA. Cette méthode est intéressante tant que l'écoulement est subcritique mais elle s'applique mal en écoulement supercritique.

3.2 - Méthode linéaire avec correction de Mach

La nécessité de répéter un grand nombre de fois les calculs de forces aérodynamiques en tenant compte des effets tridimensionnels oblige encore les aéroélasticiens à utiliser la méthode de calcul fondée sur la linéarisation autour de l'écoulement uniforme, en essayant de rattraper les insuffisances de cette méthode par des corrections.

Dans la référence [13] , Tijdeman et Zwaan ont proposé une méthode qui restitue assez bien les effets non linéaires de fluide parfait en écoulement subcritique ou faiblement supercritique. Les auteurs remarquent que chacun des coefficients d'influence aérodynamiques S_{uv} dépend beaucoup plus de la répartition du Mach entre les points P_u et P'_v que du Mach infini. Ils proposent alors de prendre pour valeur du coefficient S_{uv} la valeur correspondant à une valeur moyenne du Mach entre ces deux points. Ce Mach moyen peut être évalué en se raccordant aux valeurs quasi stationnaires données par la résolution des équations d'Euler. A cette correction vient s'ajouter une correction sur la vitesse normale qui est évaluée aussi en considérant le Mach local, comme l'avait déjà fait Rowe [27] .

Des résultats numériques sont présentés par Roos [7] . La comparaison avec les résultats du calcul exact est assez satisfaisante, figure (11), mais la comparaison avec l'expérience n'est pas améliorée tant que l'on ne tient pas compte de la couche limite.

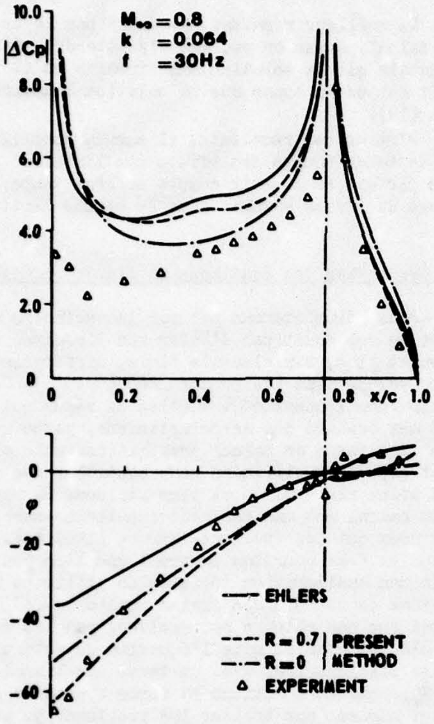

Fig. 11 — Résultat donné par la correction de Mach local sur un profil avec gouverne oscillante en subsonique. R = 0 est le cas sans correction. (extrait de la réf. [7]).

3.3 - Méthode simplifiée d'introduction de la couche limite.

L'influence de la couche limite peut être déterminée par une méthode de couplage couche limite-fluide parfait. Il s'agit d'une méthode itérative dans laquelle chaque pas d'itération comporte un calcul de couche limite et un calcul de fluide parfait. Le couplage est défini si l'on admet que la condition de glissement doit être appliquée à la frontière des deux domaines.

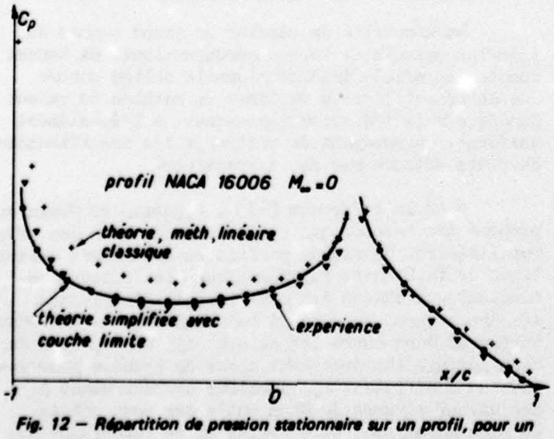

Fig. 12 — Répartition de pression stationnaire sur un profil, pour un braquage de gouverne ; linéarisation autour du profil de couche limite.

Dans un travail qui n'a pas encore été publié, J.J. Angélini décrit une méthode plus simple, qui s'adapte particulièrement bien aux techniques de calcul utilisées par les aéroélasticiens. Comme l'avait fait C.S. Ventres [28] avant lui, l'auteur linéarise les équations du fluide parfait autour d'un profil de vitesse dans la couche limite supposée connue et il détermine une équation intégrale analogue à [5] , mais avec un noyau plus complexe. La méthode n'a pas encore été mise en oeuvre en instationnaire, mais l'application au stationnaire se révèle prometteuse malgré une schématisation très rudimentaire de la couche limite (figure 12).

3.4 - Recherche de modèles phénoménologiques.

L'interaction entre onde de choc et couche limite, qui est souvent à l'origine des instabilités de gouverne et du tremblement des ailes, est un phénomène trop complexe pour pouvoir être traité de façon complète sur le plan théorique. Dans la référence [29] , L. Trilling en présente une théorie simplifiée qui en explique bien le mécanisme et les tendances et qui pourrait être à l'origine de calculs utiles pour les aéroélasticiens. Toutefois, ceux-ci sont encore obligés d'avoir recours surtout à l'expérience.

Dans le cas d'un profil indéformable, dont la position et les mouvements d'ensemble peuvent être définis avec un nombre de paramètres relativement faible, la recherche d'un modèle phénoméologique peut palier les insuffisances des méthodes théoriques en écoulement supercritique ou en présence de décollements. La mise au point d'un modèle et son identification nécessitent un grand nombre d'essais en soufflerie sur profil oscillant en courant plan.

Ce sont surtout les spécialistes des hélicoptères qui s'attachent à élaborer des modèles, pour prévoir l'effet des grandes incidences sur la pale reculante [30] et [31] . Jusqu'à maintenant, les résultats sont assez décevants car les modèles synthétisent les résultats expérimentaux qui ont servi à les identifier mais ne permettent pas, en général, de les extrapoler. Il est vrai que les hélicoptèristes se posent un problème particulièrement difficile en considérant des oscillations de grande amplitude ; on peut espérer obtenir de meilleurs résultats en se limitant à de petits mouvements.

Mais pour permettre l'extrapolation des résultats au delà des valeurs de paramètres balayés en soufflerie, le modèle doit traduire des processus physiques et ne pas être une simple méthode de lissage de résultats expérimentaux. Dans le cas d'un profil avec décollement, ou avec onde de choc, par exemple, il est important de représenter les effets de retard qui sont à l'origine de la plupart des instabilités à un degré de liberté.

3.5 - Couplage d'une méthode bidimensionnelle non-linéaire avec la théorie linéaire tridimensionnelle.

Dans beaucoup de problèmes d'aéroélasticité, les effets non-linéaires et les effets tridimensionnels sont également importants. Or, en dehors de certaines méthodes de correction, comme celle du paragraphe 3.2, les méthodes théoriques ou même expérimentales utilisées pour caractériser des écoulements non linéaires ne s'appliquent encore qu'en écoulement plan, de sorte que les aéroélasticiens disposent de modèles bidimensionnels non-linéaires et d'une théorie tridimensionnelle linéaire.

Pour obtenir des résultats tenant compte à la fois des effets tridimensionnels et des effets non linéaires, il faut utiliser ces deux outils en les couplant de façon rationnelle. Ce couplage devient possible en faisant les hypothèses suivantes :

a - les sections d'aile peuvent être assimilées à des profils en écoulement plan se déplaçant dans un fluide perturbé par les interactions tridimensionnelles.

b - à une distance suffisamment grande, un élément d'aile induit la même vitesse qu'un élément de surface portante sans épaisseur de même portance, et ceci même si l'écoulement est fortement perturbé au voisinage de l'aile.

L'hypothèse (a) justifie l'emploi de modèles bidimensionnels pour exprimer la relation locale entre portance et incidence, et l'hypothèse (b) justifie l'emploi de la théorie linéaire pour évaluer la vitesse induite par les interactions tridimensionnelles. On en déduit une méthode de calcul itérative.

Cette approche a été utilisée par J.J. Costes [32] pour calculer les forces aérodynamiques sur les pales d'hélicoptère. La formulation utilisée dans le calcul linéaire est une généralisation de l'équation intégrale (5) à des mouvements plus complexes que ceux de l'aile [33] et le modèle bidimensionnel est emprunté à Gros et Harris [30]. La méthode est également décrite dans la référence [35]. Les résultats présentés dans la figure (13) montrent que l'effet du modèle bidimensionnel est surtout ressenti sur la pale reculante, pour un azimut de 270°.

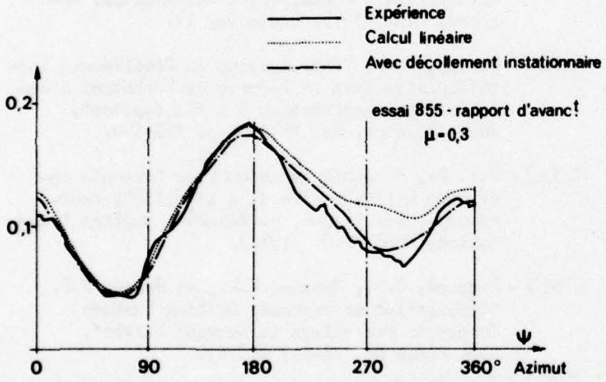

Fig. 13 – Calcul de la portance sur les pales d'un rotor expérimental section de coordonnée radiale r/R = 0,855. (extrait de la réf. [34]).

CONCLUSION

La théorie linéaire de la surface portante est un outil de prévision des forces aérodynamiques d'une remarquable souplesse, mais son domaine de validité ne couvre qu'une partie des problèmes pratiques posés aux aéroélasticiens, et ceux-ci se trouvent désarmés dans un grand nombre de cas. L'absence de moyens de prévision des écoulements avec onde de choc et/ou décollements est particulièrement regrettable parce que ces écoulements sont critiques du point de vue du flottement.

La situation évolue pourtant favorablement.

Les méthodes de résolution des équations du fluide parfait et la méthode du couplage couche limite-fluide parfait ne permettent pas encore une exploitation systématique en raison notamment du temps de calcul prohibitifs et de la difficulté de représentation réaliste du comportement instationnaire de la couche limite, mais elles commencent à donner des résultats fort utiles pour le contrôle de méthodes moins rigoureuses mais plus rapides.

D'autre part, les effets de l'écoulement supercritique ou des décollements sont mieux compris, même si l'on n'est pas encore capable d'en faire une prévision quantitative ; or une bonne interprétation qualitative n'est pas négligeable car elle peut aider à orienter les recherches expérimentales et faciliter la modèlisation.

On remarque enfin l'apparition d'une certaine rationalisation dans les méthodes de correction, telles que l'introduction du Mach local, qui se fondent maintenant sur des hypothèses précises alors qu'il y a quelques années encore les seules corrections qui étaient pratiquées consistaient à multiplier les coefficients d'influence aérodynamiques par un coefficient multiplicateur qui les rapprochait des valeurs expérimentales disponibles.

REFERENCES

[1] - Jones, W.P., ed., AGARD Manual on Aeroelasticity, Part II, Aerodynamic Aspects, (1961).

[2] - Landahl, M.T., and Stark, V.J.E., "Numerical Lifting-Surface Theory - Problems and Progress", AIAA Journal, Vol. 6, No. 11, Nov. 1968, p. 2049-2060.

[3] - Albano, E., and Rodden, W.P., "A doublet-Lattice Mehtod for Calculating Lift Distributions on Oscillating Surfaces in Subsonic Flows", AIAA Journal, Vol. 7, No 2, Feb. 1969, p. 279-285 ; errata Vol. 7 No 11, Nov. 1969, p. 2192.

[4] - Roos, R., Bennekers, B., and Zwaan, R.J., "A Calculation Mehtod for Unsteady Subsonie Flow about Harmonically Oscillating Wing-Body Combinations", AIAA Paper 75-864, June 1975.

[5] - Laschka, B., "Unsteady Aerodynamic Prediction Methods Applied in Aeroelasticity, " Unsteady Aerodynamics, AGARD Report No. 645, (1976) dans No. 1.

[6] - Rodden, W.P., "State-of-the-Art in Unsteady Aerodynamics", AGARD Report No. 650, (1976).

[7] - Roos, R., Application of panel Methods for Unsteady Subsonic Flow, NLR MP 76010 U, (1976).

[8] - Akamatsu, Y., et Dat, R., "Calcul par la Méthode du potentiel des forces instationnaires agissant sur un ensemble de surfaces portantes". Rech. Aérosp., No. 1971-5, p. 283-295.

[9] - Darras, B., et Dat, R., "Application de la théorie de la surface portante à des ailes munies de gouvernes", dans "Symposium on Unsteady Aerodynamics-Aéroelastic Analysis of interfering Surfaces", AGARD CP 80, Part II (1971), No. 13.

[10] - Lambourne, N.C., Control Surface Buzz. R and M No. 3364, (1962).

[11] - Coupry, G., et Piazolli, G., Etude du Flottement en Régime Transonique, Rech. Aérosp., No.63, (mars-avril 1958), p. 19-28.

[12] - Eckhaus, W., Two-dimensional transonic unsteady flow with shock waves, OSR TR 59-491, (1959).

[13] - Tijdeman, H., and Zwaan, R.J., On the prediction of aerodynamic loads on oscillating wings in transonic flow, AGARD Report No. 612 (1974) also : NLR MP 7 3026 U (1973).

[14] - Tijdeman, H., On the motion of shock waves on an airfoil with oscillating flap in two-dimensional transonic flow, NLR Report TR 75038 U, (1975).

[15] - Tijdeman, H., High subsonic and transonic effects in unsteady aerodynamics, AGARD Report No. 636 (1976), also : NLR TR 75079 U (1975).

[16] - Szechenyi, E., Experimental studies of dynamic forces on fixed and vibrating two-dimensional airfoils, Third European Rotorcraft and Powered Lift Aircraft Forum, Aix en Provence, 7-9 septembre (1977).

[17] - McCroskey, W.J., "Recent Developments in Dynamic Stall", Symposium on Unsteady Aerodynamics, Kinney, R.B., ed., Univ. Arizona, Tucson, (1975), p. 1-33.

[18] - McCroskey, W.J., and Philippe, J.J., "Unsteady Viscous Flow on Oscillating Airfoils", AIAA Journal, Vol. 13, No. 1, Jan. 1975, p. 71-79.

[19] - Loiseau, H., Lepoint, G., and Maquennehan, B., "Exploratory Research on the Aeroelasticity of Turbine and Grid Blades", dans Unsteady Phenomena in Turbomachinery, AGARD CP 177 (1975), Mémoir No. 8.

[20] - Ehlers, F.E., "A Fine Difference Method for the Solution of the Transonic Flow around Harmonically Oscillating Wings", AIAA Paper 74-543, June 1974 ; also NASA CR-2257, July 1974.

[21] - Magnus, R.J., and Yoshihara, H., "Calculations of Transonic Flow over an Oscillating Airfoil", AIAA Paper 75-98 (1975).

[22] - Ballhaus, W.F., and Goorjian, P.M., "Implicit Finite Difference Computations of Unsteady Transonic Flows about Airfoils, Including the Treatment of Irregular Shock Wave Motions", AIAA Paper 77-205 (1977).

[23] - Ballhaus, W.F., Goorjian, P.M., "Efficient Solution of Unsteady Transonic Flows about Airfoils", AGARD/SMP Lisbonne, 17-22 avril 1977.

[24] - Lerat, A., et Sidès, J., Calcul numérique d'écoulements transsoniques instationnaires, AGARD/SMP, Lisbonne 17-22 avril 1977, TP ONERA No. 1977-19 F (1977-19 E for English version).

[25] - Couston, M., Time Marching Finite Area Method, Lecture Series 84, Transonic Flows in Axial Turbomachinery, VKI, Feb. 2-6 (1976).

[26] - Fenain, M., Méthodes de relaxation pour la résolution d'équations elliptiques dans des domaines de frontières quelconques. Applications au calcul d'écoulements subcritiques. Journal de Mécanique Appliquée, Vol. 1, No. 1, (1977), p. 27-67.

[27] - Rowe, W.S., Sebastian, J.D., and Redman, M.C., "Some Recent Developments in Predicting Unsteady Loadings Caused by Control Surface Motions", Journal of Aircraft, Vol. 13, No. 12, (1976), p. 955-961.

[28] - Ventres, C.S., "Shear Flow Aerodynamics : Lifting Surface Theory", AIAA Journal, Vol. 12, No. 9 (1975), p. 1183-1189.

[29] - Trilling, L., "Oscillating Shock Boundary-layer Interaction", Jour. of Aero. Sc., Vol. 25, No. 5, (May 1958), p. 301-304.

[30] - Gross, D.W., Harris, F.D., "Prediction of In-flight stall Airloads from Oscillating Airfoil Data", 25th Annual National Forum of the American Helicopter Society, Washington, (May 1969).

[31] - Beddoes, T.S., "A Synthesis of Unsteady Aerodynamic Effects, Including Stall Hysteresis", Proc. First European Rotorcraft and Powered Lift Aircraft Forum, Univ. Southampton, England, Sept. 1975, Paper No. 17.

[32] - Costes, J.J., "Introduction du Décollement Instationnaire dans la Théorie du Potentiel d'Accélération, Application à l'Hélicoptère", Rech. Aérosp., No. 1975-3, p. 175-188.

[33] - Dat, R., "Théorie de la Surface Portante Appliquée à l'Aile Fixe et à l'Hélice", Rech. Aérosp., No. 1973-4, p. 245-254, English translation, ESRO TT-90 (1974).

[34] - Hammond, C.E., Runyan, H.L., et Mason, J.P., "Application of Unsteady Lifting Surface Theory to Propellers in Forward Flight", AIAA Paper No. 74-419 (1974).

[35] - Dat, R., "Aérodynamique Instationnaire des Pales d'Hélicoptère", dans "Unsteady Aerodynamics", AGARD Report No. 645 (1976), No. 3, English Translation ESA TT 327 (1977).

ETUDE D'ECOULEMENTS TURBULENTS SUBSONIQUES ET SUPERCRITIQUES PAR VISUALISATION ULTRA-RAPIDE

par A. Dyment - Maître de Conférences
et P. Gryson - Ingénieur
Institut de Mécanique des Fluides
5, bd Paul Painlevé, 59000 - Lille (France)

SOMMAIRE.-

L'instabilité de la surface de séparation qui suit un décollement est à l'origine des structures tourbillonnaires qui apparaissent en aval d'un obstacle. Une loi générale est établie pour exprimer le nombre de Strouhal des tourbillons générés au décollement en fonction du nombre de Reynolds. Les tourbillons émis subissent des agglomérations successives dont le mécanisme est expliqué à l'aide d'une théorie simplifiée. Pour former une allée alternée dont le Strouhal est nettement inférieur à celui d'émission, les tourbillons de chaque file doivent subir une nouvelle agglomération. Le fait que l'allée alternée n'apparaît immédiatement en aval de l'obstacle qu'à Reynolds modéré s'explique en considérant un temps de relaxation nécessaire à cette agglomération.

Les visualisations ombroscopiques et strioscopiques ultra-rapides sont faites en utilisant une batterie de 24 sources éclairs. Elles apportent des informations nouvelles sur la structure du sillage proche en écoulement subsonique et supercritique. En particulier, sont mises en évidence certaines propriétés concernant la propagation des tourbillons émis aux décollements, la formation des allées alternées, le couplage entre l'allée alternée et le décollement. En écoulement supercritique on obtient une description de l'interaction entre tourbillons et ondes de choc : la propagation des ondes acoustiques créées par cette interaction révèle que la poche supersonique n'est pas à l'abri des perturbations en provenance de l'aval.

SUMMARY.-

The instability of the free boundary which follows separation is at the origin of large eddies existing downstream of a body in a flow. A general law is given which expresses the Strouhal number of eddies generated at a separation point as a function of the Reynolds number. The emitted eddies undergo successive coalescences whose process is explained by a simplified theory. To form a vortex street whose Strouhal number is much lower than the emission one, the eddies of both sides have to coalesce once again. The fact that the vortex street does appear immediatly behind the body only at moderate Reynolds numbers can be explained in considering a relaxation time necessary for coalescing.

Ultra-short duration shadowgraph and Schlieren visualisations are done with twenty four spark light sources. They give new informations on the structure of the wake near the body in subsonic and supercritical flows. Are emphasized some properties regarding the spreading of eddies emitted at separation points, the formation of vortex streets, the coupling between the vortex street and the separation. In supercritical flow one obtains a description of the interaction between eddies and shock waves : the propagation of acoustic waves created by this interaction shows that the supersonic pocket can be influenced by disturbances coming from downstream.

NOTATIONS PRINCIPALES.-

c	corde d'un profil d'aile
L	dimensions de l'obstacle (obstruction géométrique en général)
ℓ	dimensions du domaine de Navier Stokes
M	nombre de Mach au loin en amont de l'obstacle
N	fréquence
q	exposant défini dans l'équation (1)
R	nombre de Reynolds $\frac{UL}{\nu}$
r	rayon d'une structure tourbillonnaire
S	nombre de Strouhal $\frac{NL}{U}$
t	temps
U	vitesse au loin en amont de l'obstacle
u	vitesse dans le domaine de Navier Stokes
V	vitesse de propagation des tourbillons d'une file
W	vitesse de propagation des structures tourbillonnaires de l'allée alternée
x	abscisse
x_n	abscisse à laquelle commence la n^e agglomération

α	incidence d'un profil d'aile
Γ	circulation de la vitesse
Δt	intervalle de temps entre deux éclairs successifs
λ_n	longueur nécessaire à la n^e agglomération
ν	viscosité cinématique
τ	durée d'un éclair

Indices :	e	relatif à l'émission des tourbillons
	a	relatif à l'allée alternée
	o	relatif à l'extrémité des domaines de recirculation

1 - *INTRODUCTION.-*

Les moyens de calcul offerts actuellement par les ordinateurs ont permis un important développement de l'étude des phénomènes turbulents. Il s'agit essentiellement de turbulence développée que l'on aborde à l'aide de modèles mathématiques plus ou moins élaborés. Le but de cette modélisation est d'éviter le recours direct aux équations de Navier Stokes qui nécessite des calculs numériques prohibitifs. Ainsi, à l'exception de quelques tentatives de simulation numérique directe, l'analyse de l'aspect instationnaire de la turbulence est généralement laissée de côté. Pourtant cet aspect est fondamental pour la compréhension des phénomènes, particulièrement en ce qui concerne la *naissance* de la turbulence et son *développement initial.*

Dans cette communication on étudie *la structure du sillage proche d'un obstacle en écoulement plan,* à *nombre de Reynolds grand* et tel que les *décollements* soient *laminaires.* Ces décollements apparaisent comme des *sources d'émission de tourbillons.* L'étude théorique de cette émission est faite en utilisant des propriétés locales des domaines qui englobent les points de décollement. Grâce à des hypothèses simplificatrices concernant la propagation des tourbillons émis, on montre qu'il existe un processus d'*agglomérations successives* dont on établit certaines propriétés. Les résultats obtenus permettent d'aborder sous un angle nouveau l'étude des *allées alternées.*

L'étude expérimentale des écoulements décrits ci-dessus est difficile car, le nombre de Reynolds étant grand, il s'agit de phénomènes très rapidement variables. Cette étude est faite ici à l'aide de *visualisations ultra-rapides* utilisant 24 sources éclairs.

2 - *EMISSION DES TOURBILLONS.-*

A grand Reynolds l'écoulement plan autour d'un obstacle présente nécessairement des décollements au nombre de deux au moins. Nous considérons le cas de décollements laminaires et nous nous limitons au cas d'un fluide incompressible.

Désignons par L une longueur caractéristique de l'obstacle (en général son obstruction géométrique), par U la vitesse au loin, par ν la viscosité cinématique, par R le nombre de Reynolds $\frac{UL}{\nu}$.

Autour d'un point de décollement il existe un petit domaine, sans direction privilégiée, où le mouvement obéit aux équations de Navier Stokes complètes. Ce domaine est englobé dans une couche limite du côté du courant général où on a un écoulement irrotationnel régi par les équations d'Euler, et dans une sous couche limite du côté du domaine de recirculation. Le mouvement étant permanent et les dimensions des domaines de recirculation étant d'ordre L , on sait ([1]) que dans ces domaines l'écoulement est régi par les équations d'Euler et que le rotationnel de la vitesse y est constant.

Les fig. 1 et 2 représentent l'écoulement décrit lorsque le décollement a lieu respectivement en un point de courbure finie et en un point anguleux. Sur la fig. 3 on a indiqué l'évolution des décollements sur un profil d'aile en fonction de l'incidence : à petite incidence on a deux décollements en des points de courbure finie (fig. 3a). Lorsque l'incidence augmente le décollement d'extrados remonte vers le bord d'attaque tandis que celui d'intrados progresse vers le bord de fuite (fig. 3b). Au-dessus d'une certaine incidence le décollement d'intrados reste fixé au bord de fuite (fig. 3c).

Désignons par ℓ l'ordre de grandeur des dimensions du domaine de Navier Stokes et par u l'ordre de grandeur de la vitesse dans ce domaine. Posons

$$\ell = L R^{-q} \quad , \quad u = U R^{q-1} . \tag{1}$$

De cette manière le nombre de Reynolds formé avec ℓ et u est égal à 1 conformément au fait que dans le domaine de Navier Stokes les forces d'inertie doivent être du même ordre de grandeur que les forces de viscosité.

La ligne de séparation qui suit le décollement ne peut être stable que si le nombre de Reynolds local est d'ordre 1, donc seulement sur des distances d'ordre ℓ . A des distances supérieures cette ligne se trouve dans des domaines de couche limite où le Reynolds local est grand (de l'ordre de R) et elle est donc instable. Cette *instabilité* est à l'origine de la *naissance des tourbillons* (fig. 4).

Ainsi, l'émission des tourbillons apparaît comme une propriété *locale* à l'égard des dimensions de l'obstacle, mais comme une propriété *globale* à l'égard du domaine de Navier Stokes. Par conséquent, la fréquence N_e et la circulation Γ_e des tourbillons émis ne dépendent que de ℓ et de u , en supposant que ν n'intervient pas directement.

La similitude donne $\frac{N_e \ell}{u} = C^{te}$ et $\frac{\Gamma_e}{\ell u} = C^{te}$. Désignons par $S_e = \frac{N_e L}{U}$ le nombre de Strouhal, ou fréquence réduite, d'émission. On obtient

(2) $$S_e \backsim R^{2q-1} ,$$

(3) $$\Gamma_e \backsim \nu .$$

On doit avoir $q \geqslant \frac{1}{2}$ pour que le domaine de Navier Stokes ne déborde pas des domaines de couche limite. De plus, on sait ([2]) que le Strouhal en-dessous duquel on peut négliger la viscosité est d'ordre $R^{3/4}$. De là $2q-1 < 3/4$. Il en résulte que les formules (2) et (3) sont valables pour

(4) $$\frac{1}{2} \leqslant q < \frac{7}{8} .$$

On remarque que S_e *est une fonction croissante de* R et que, quelle que soit la nature du décollement, Γ_e *a toujours le même ordre de grandeur.*

Considérons le cas le plus fréquent où le décollement se produit en un point de courbure finie. On a $q = \frac{2}{3}$ ([3]) , d'où

(5) $$S_e \backsim R^{1/3} .$$

On rencontre deux décollements de ce type sur un cylindre (fig. 1) ou sur un profil d'aile en faible incidence (fig. 3a et 3b).

Pour un décollement ayant lieu en un point anguleux, par exemple sur un culot (fig. 2), l'exposant q est égal à 3/4 si on admet que la couche limite au voisinage du point anguleux est sensiblement indépendante de la distance à ce point ([3]) . On obtient dans ce cas

(6) $$S_e \backsim R^{1/2} .$$

Il est à noter que si la courbure locale γ est telle que $\gamma \ell$ soit d'ordre 1, il faut retenir γ dans l'inventaire des grandeurs dont dépendent Ne et Γ_e . On obtient alors $S_e \backsim R^{2q-1} \; \phi\,(\gamma R L^{-q})$. On voit que les cas envisagés ci-dessus supposent $\gamma \ell \ll 1$ (courbure finie) ou $\gamma \ell \gg 1$ (point anguleux) de manière que la fonction ϕ se réduise à une constante.

3 - *AGGLOMERATION DES TOURBILLONS.-*

Les tourbillons générés à la suite d'un décollement sont entraînés vers l'aval en longeant les domaines de recirculation. Ils induisent un champ de vitesse instationnaire qui modifie légèrement l'écoulement permanent envisagé précédemment.

Schématisons et supposons que les tourbillons sont de forme circulaire et qu'ils se déplacent en ligne droite avec une vitesse constante V (fig.(5)).A mesure qu'ils progressent, les tourbillons s'étendent et leur intensité est de moins en moins concentrée : selon les propriétés de la diffusion visqueuse leur rayon r est relié au temps par $r \backsim \sqrt{\nu t}$. On peut écrire

(7) $$r = \frac{1}{b} \sqrt{\nu \frac{x}{V}}$$

où x est l'abscisse à partir du lieu d'émission et b une constante. Le rapport $\frac{r}{x}$ représente l'épaisseur de la zone de mélange : il est analogue à une épaisseur de couche limite et il doit être petit devant 1. De là $\frac{1}{b} \sqrt{\frac{\nu}{V x}} \ll 1$. Posons

(8) $$V = k\, U ;$$

la constante k est en général d'ordre 1. On obtient la condition

(9) $$b \sqrt{k R \frac{x}{L}} \gg 1 .$$

La distance qui sépare deux tourbillons successifs est V/N_e ; c'est une constante tandis que r augmente en fonction de x . Il en résulte qu'à partir d'une abscisse x_1 définie par

(10) $$\sqrt{\frac{\nu x_1}{V}} + \sqrt{\frac{\nu}{V}\left(x_1 + \frac{V}{N_e}\right)} = b\,\frac{V}{N_e}$$

les tourbillons vont *empiéter* l'un sur l'autre. La solution de cette équation est $2b\sqrt{kR\frac{x_1}{L}} = b^2k^2\frac{R}{S_e} - 1$. D'après (9) le premier terme du second membre est prépondérant ce qui est conforme à (2) et (4). On obtient donc

(11) $$\frac{x_1}{L} \simeq \frac{b^2k^3}{4}\,\frac{R}{S_e^2}$$

soit, d'après (2),

(12) $$\frac{x_1}{L} \sim R^{3-4q} .$$

On vérifie que V/N_e et $\sqrt{\nu x_1/V}$ sont du même ordre de grandeur et que V/N_e est grand à l'égard de b et petit à l'égard de x_1 .

Pour un décollement en un point de courbure finie ($q = \frac{2}{3}$) on a $x_1/L \sim R^{1/3}$, tandis qu'en un point anguleux $(q = 3/4)$ x_1/L est indépendant de R .

L'empiétement marque le début de *l'agglomération* de deux tourbillons successifs. Cette fusion donne naissance à de nouvelles structures tourbillonnaires plus étendues, mais de fréquence deux fois moindre. Il s'agit d'un phénomène qui a été observé au cours d'expériences à Reynolds modéré ([4]) et qui a été confirmé récemment au cours d'une simulation numérique ([5]) . Il reçoit ici une explication schématique simple.

Il est à noter que, contrairement à l'émission des tourbillons, l'agglomération dépend directement de ν car c'est une conséquence de la diffusion visqueuse.

Le processus d'agglomération étudié ci-dessus va recommencer avec les nouvelles structures tourbillonnaires formées. On voit qu'il y aura *une succession d'agglomérations*.

Désignons par x_n l'abscisse à laquelle commence la n^e agglomération, par λ_n la longueur nécessaire à la n^e agglomération, par N_n la fréquence à l'issue de la n^e agglomération et par $S_n = N_n L/V$ le Strouhal correspondant. Supposons que les structures tourbillonnaires obtenues à l'issue d'une agglomération ont des dimensions voisines de celles au début de l'agglomération. Pour obtenir la relation correspondant à la n^e agglomération il suffit de remplacer dans (10) x_1 par $x_n - \sum_1^{n-1}\lambda_i$ et N_e par N_{n-1} . On obtient, à la place de (11),

$$\frac{x_n - \sum_1^{n-1}\lambda_i}{L} \simeq \frac{b^2k^3R}{4S_{n-1}^2} .$$

Comme à chaque agglomération deux tourbillons sont remplacés par un seul on a $N_n = N_{n-1}/2 = N_0/2^n$. De plus, on peut négliger $\sum_1^{n-1}\lambda_i$ à l'égard de x_n , et cela d'autant plus légitimement que n est grand. On obtient donc :

(13) $$S_n = \frac{S_e}{2^n} \qquad x_n \simeq 4^{n-1}\,x_1 .$$

On constate que S_n diminue très rapidement en fonction du nombre d'agglomérations et que x_n augmente très rapidement. Autrement dit *le processus d'agglomération se ralentit* considérablement à mesure que l'on avance vers l'aval. Il en résulte, en particulier, que si on ne peut observer les tourbillons que sur un domaine peu étendu et suffisamment éloigné de l'émission, on va mesurer une fréquence à peu près constante et très petite devant N_e .

En un point défini par $x = L_0$ le nombre d'agglomérations subies par les tourbillons est égal à l'entier immédiatement inférieur à la solution de l'équation $4^{n-1} = \frac{L_0}{x_1}$. Pour $q = \frac{2}{3}$ et R grand on voit, compte tenu de (12), que n est fonction décroissante de R . Pour $q = \frac{3}{4}$ le nombre d'agglomérations est indépendant de R .

Il peut être commode de représenter les agglomérations successives par une courbe continue (fig. 7). Si on remplace R par βR il résulte de (12) et (13) que S_e et S_n sont multipliés par β^{2q-1} et x_1 et x_n par β^{3-4q} . Le Strouhal S_0 correspondant à une longueur donnée L_0 est remplacé par une valeur qui est supérieure ou inférieure à S_0 suivant que β est supérieur ou inférieur à 1 (fig. 8).

L'ensemble des résultats obtenus ci-dessus fournit un schéma de la *formation* et de l'*évolution initiale d'une zone de mélange*.

4 - FORMATION D'ALLEES ALTERNEES.-

Les deux décollements que l'on rencontre généralement sur un obstacle donnent naissance à deux files de tourbillons dont les circulations sont de signes opposés. Comme selon (3) les valeurs absolues de ces circulations sont du même ordre de grandeur, aucune des deux files ne peut prendre le dessus sur l'autre. L'ensemble de ces circonstances fait que les tourbillons des deux files peuvent *s'imbriquer* de manière à former une allée alternée qui subsiste loin dans le sillage. La raison de cette longévité peut être justifiée physiquement en faisant l'hypothèse que les cellules tourbillonnaires qui constituent l'allée alternée se propagent toutes avec la même vitesse W et en se plaçant dans le repère animé de cette vitesse : il est clair qu'à la frontière de deux cellules adjacentes du schéma de principe de la figure 9 les vitesses induites par ces cellules sont de même sens, de sorte qu'il n'y a pas tendance à la destruction.

L'étude théorique des allées alternées a été faite en fluide non visqueux en supposant que l'allée est formée de deux files parallèles de tourbillons ponctuels. Il a été montré qu'il n'existe qu'une seule disposition possible des tourbillons, mais la configuration ainsi obtenue est instable ([6]) . En fait, si on suppose que les tourbillons ne sont pas ponctuels, l'allée alternée peut être stable ([7]) . Par ailleurs, en tenant compte de la viscosité, il a été établi que l'allée alternée est constituée de files de tourbillons dont l'écartement augmente à mesure que l'on progresse vers l'aval ([8]) .

Désignons par N_a la fréquence des structures tourbillonnaires de l'allée alternée. Tous les résultats connus indiquent que le nombre de Strouhal $S_a = N_a L/U$ est d'ordre 1 et varie peu en fonction de R . Soit L_o la longueur d'un domaine de recirculation et S_o le Strouhal correspondant sur la courbe qui représente le phénomène d'agglomérations successives (fig. 8). A Reynolds élevé S_o est grand à l'égard de 1 et S_a est inférieur à S_o de sorte que pour former une allée alternée les tourbillons doivent subir une nouvelle agglomération. Celle-ci est due à l'interaction entre les tourbillons des deux files qui a pour conséquence une déformation et une fusion des tourbillons d'une même file. On assiste à un *enroulement* de ces tourbillons les uns sur les autres pour donner naissance à des structures plus étendues.

Ce phénomène qui ne fait pas intervenir la viscosité a été remarqué également au cours d'un calcul numérique ([7]) . Il faut le distinguer de l'agglomération des tourbillons d'une file isolée qui est, comme on l'a vu, le résultat de la diffusion visqueuse.

La nouvelle agglomération décrite ci-dessus nécessite *une durée de relaxation* qui est *d'autant plus longue que* S_o est éloigné de S_a , donc que *R est grand* puisque S_o est une fonction croissante de R . Ainsi, à Reynolds modéré l'allée alternée se forme immédiatement, dès l'extrémité des domaines de recirculation. Par contre, si R est très grand S_a est très petit devant S_o et l'agglomération exige une durée longue, donc un parcours important : dans ce cas l'allée alternée se forme loin de l'obstacle.

Le résultat précédent explique pourquoi en pratique on observe des allées alternées seulement pour des valeurs de R relativement modérées. En effet, à très grand Reynolds l'allée apparaît loin en aval, en général en dehors du champ d'observation ; de plus, les structures qui la composent sont de faible intensité à cause de la destruction subie depuis la rencontre des deux files.

Par ailleurs, si on essaye de déterminer la fréquence N_a à l'aide d'un appareil (par exemple un fil chaud) qui est placé trop près de l'obstacle, on commet une erreur importante car on mesure des fréquences de tourbillons dont l'agglomération n'est pas achevée et qui sont donc supérieures à N_a . C'est vraisemblablement la cause des valeurs de S_a anormalement élevées obtenues par Delany et Sorensen en ce qui concerne un cylindre en écoulement à grand Reynolds ([9]) .

Lorsqu'on considère un écoulement symétrique les valeurs de L_o relatives aux deux décollements sont égales (fig. 8). Supposons maintenant que les deux décollements sont de même nature mais que la longueur L_o correspondant à l'extrados est supérieure à celle L'_o de l'intrados (fig. 10). On a dans ce cas $S'_o > S_o$, donc l'apparition de l'allée alternée est régie par le décollement d'intrados.

Lorsque les deux décollements sont de nature différente (fig. 11) le Strouhal d'émission d'intrados S'_e est supérieur à celui d'extrados S_e à grand Reynolds car l'exposant q' qui lui correspond est supérieur à $\frac{2}{3}$. Il en résulte que l'on a encore $S'_o > S_o$. Finalement, on voit que dans tous les cas c'est le décollement d'intrados qui règle la distance à laquelle se forme l'allée alternée.

On peut retrouver les résultats précédents en introduisant un temps global de relaxation T nécessaire au passage de la fréquence d'émission N_e à la fréquence N_a . Puisqu'on a affaire à des structures tourbillonnaires de grande échelle T ne dépend pas directement de ν , mais seulement de L, U , N_e et N_a . Il est raisonnable d'admettre que T n'est pas fonction de N_e et N_a séparément, mais de leur différence puisque pour $N_e = N_a$ T serait nul.

La similitude permet d'écrire

$$\frac{UT}{L} = \Psi(S_e - S_a)$$

la fonction ψ étant croissante car physiquement il est évident que T augmente avec $N_e - N_a$.

La longueur parcourue pendant la durée T est de l'ordre de $VT = kUT$. L'allée alternée se forme immédiatement en aval des domaines de recirculation si on a $kUT \leqslant L_o$, soit

$$k\,\psi\,(S_e - S_a) \leqslant \frac{L_o}{L} \tag{15}$$

pour chacune des deux files de tourbillons.

Comme $\frac{L_o}{L}$ est sensiblement constant et comme ψ est une fonction croissante il vient $S_e - S_a \leqslant C^{te}$ ce qui se traduit d'après (2) par $R \leqslant C^{te}$. Si R est très grand cette condition n'est pas vérifiée et l'allée alternée se forme loin en aval, à une distance qui augmente avec R . On retrouve ainsi les conclusions obtenues précédemment, mais sans avoir décrit l'évolution des files de tourbillons et les mécanismes de l'agglomération.

5 - TOURBILLONS EN ECOULEMENT SUPERCRITIQUE.-

Jusqu'à présent nous avons considéré un fluide incompressible, mais la compressibilité ne peut apporter rien de fondamentalement nouveau en ce qui concerne les phénomènes étudiés ci-dessus. En effet, la compressibilité a peu d'influence sur l'émission des tourbillons qui se fait très près de la paroi, là où la vitesse est toujours petite. De même, la compressibilité ne peut pas modifier de manière sensible la progression et l'agglomération des tourbillons. Par conséquent les résultats obtenus s'étendent, au moins qualitativement, aux écoulements à grande vitesse.

Cependant, en écoulement supercritique de nouveaux phénomènes prennent naissance à cause de la présence d'ondes.

L'existence du champ de vitesse instationnaire produit par les tourbillons nous amène à introduire la notion d'écoulement *supercritique par intermittences :* il s'agit d'un écoulement au sein duquel des domaines supersoniques apparaissent seulement de manière fugitive.

Par contre, l'écoulement est *strictement supercritique* si la vitesse est supersonique à tout instant dans un domaine. Dans de tels écoulements il y a en permanence des ondes de choc et il faut s'attendre à une interaction entre ces ondes et les tourbillons créés aux décollements qui sont situés généralement en amont des ondes de choc. C'est le cas de l'interaction entre une onde de choc et une couche limite qui provoque un décollement en amont du pied du choc (fig. 12). C'est également le cas pour un obstacle épais ou pour un profil d'aile en grande incidence lorsque des poches supersoniques existent au contact des domaines de recirculation, là où le fluide subit une détente intense (fig. 13).

Dans les écoulements précédents les ondes de choc sont fortement perturbées par le passage périodique des tourbillons de sorte qu'elles vibrent autour d'une position moyenne. De plus, à la traversée d'un choc les tourbillons émettent des ondes acoustiques ([10]) qui vont nous servir à vérifier expérimentalement une théorie selon laquelle des perturbations créées en aval, dans le sillage, peuvent influencer la poche supersonique ([11]), ([12]) .

6 - VISUALISATIONS ULTRA-RAPIDES.-

L'approche expérimentale de base pour l'étude phénoménologique d'écoulements instationnaires est la visualisation.

Les visualisations faites à l'aide de produits étrangers sont difficiles à grande vitesse. Du reste, l'observation du mouvement de particules étrangères peut fournir une image déformée, et même inexacte, du phénomène étudié : en effet, à cause des effets d'inertie, ces particules ne peuvent pas toujours suivre les mouvements à grand gradient de vitesse ; cela est vrai en particulier pour l'agitation turbulente dès que les fréquences deviennent élevées.

Les méthodes de visualisation fondées sur la variation de l'indice de réfraction de l'air ne présentent pas l'inconvénient précédent. En revanche, elles ne permettent pas de suivre le mouvement des particules fluides. De plus, l'introduction de la compressibilité peut sembler apporter une complication supplémentaire : en fait, comme nous l'avons vu la compressibilité ne modifie pas l'aspect qualitatif des phénomènes, du moins tant que la vitesse sonique n'est pas atteinte.

Pour visualiser un phénomène à un instant il faut que la durée d'observation τ soit très petite à l'égard d'une durée caractéristique du phénomène. Pour les structures tourbillonnaires qui sont à l'échelle de l'obstacle il faut avoir $\tau \ll L/U$. Avec $L \sim 10^{-2}$m et $U \sim 10^{2}$m/s il vient $\tau \ll 10^{-4}$s. On peut satisfaire à cette condition en utilisant des sources lumineuses intermittentes, dites sources-éclairs, dont la durée peut être inférieure à 10^{-6}s. Il est à noter que l'ordre de grandeur de τ interdit l'utilisation de caméras ultra-rapides classiques.

Pour restituer l'évolution d'un phénomène en fonction du temps il faut disposer d'une suite d'images séparées par des intervalles de temps connus. On peut atteindre ce but en utilisant une batterie de sources-éclairs et en rendant réglable l'intervalle séparant deux éclairs successifs.

Les expériences présentées ici ont été faites dans la soufflerie transsonique de l'Institut de Mécanique des Fluides de Lille (I.M.F.L.). Il s'agit d'une soufflerie à fonctionnement continu et du type à retour. Une partie de l'air utilisé est remplacée par de l'air frais puisé dans l'atmosphère ; celui-ci traverse un dessicateur avant d'être introduit dans le circuit aérodynamique. Ce dispositif permet d'éviter la condensation et de stabiliser la température de l'air dans la soufflerie. La veine d'expériences est de section 42 x 200 mm^2 (fig. 14) ; ses parois latérales sont équipées de hublots de qualité interférométrique. Les deux autres parois sont formées de grilles inclinables à fentes longitudinales. Des contre-grilles déformables permettent de règler la perméabilité. Pour stabiliser l'écoulement un col sonique est établi à l'aide de deux volets disposés à la sortie de la veine d'expériences.

Les visualisations ont été faites essentiellement à l'aide d'un dispositif conçu par l'Institut Franco-Allemand de Recherches de Saint Louis (I.S.L.) et comportant 24 sources-éclairs et 24 objectifs photographiques ([13]) La durée de chaque éclair est d'environ 5 10^{-6}s. L'intervalle entre deux éclairs successifs est réglable de manière continue depuis une seconde jusqu'à 10^{-7}s. L'appareil peut fonctionner en ombroscopie et également en strioscopie par adjonction d'une plaque équipée de 24 couteaux strioscopiques réglables.

Un autre appareil, construit à l'I.M.F.L., comportant une source à fonctionnement continu a permis des observations complémentaires : les clichés pris avec des temps de pose de l'ordre de $\frac{1}{400}$ de seconde donnent des informations sur l'écoulement moyen.

7 - RESULTATS EXPERIMENTAUX D'ENSEMBLE.-

De nombreuses expériences ont été faites avec divers modèles : cylindres, plaques, obstacle à culot, profils d'aile à pic de vitesse, etc ... à Mach compris entre .3 et .9 et à Reynolds R formé avec l'obstruction compris entre .8 10^5 et 3.2 10^5.

Les dimensions L des obstacles sont d'ordre 10^{-2}m et la vitesse U d'ordre 10^2m/s. On sait que l'ordre de grandeur des périodes en-dessous desquelles la viscosité est à prendre en compte est $L/U \; R^{-3/4}$ ([2]) . Cette quantité est très inférieure à la durée τ des éclairs, de sorte que les visualisations faites ne permettent pas d'accéder aux échelles du mouvement turbulent où s'effectue la dissipation ; elles ne permettent de rendre compte que de l'évolution des grosses structures tourbillonnaires.

Avec les données précédentes les dimensions l des domaines de Navier Stokes sont d'ordre 10^{-5}m ce qui rend impossible l'observation du mouvement dans ces domaines. Du reste, la condition $\tau \ll l/u$ n'est pas satisfaite avec l'appareillage utilisé. Ainsi, il est impossible d'observer ni l'émission des tourbillons, ni le début de leur agglomération.

Les visualisations faites ont permis d'évaluer dans certains cas la fréquence des tourbillons qui longent les domaines de recirculation. On a trouvé que cette fréquence diminue lorsqu'on progresse vers l'aval et qu'elle est nettement supérieure à celle de l'allée alternée ce qui prouve l'existence des deux types d'agglomérations. La vitesse de propagation V est voisine de la vitesse au loin U .

Sur certains clichés de visualisation on remarque qu'à la naissance de l'allée alternée les grosses structures sont encore constituées d'agglomérats de tourbillons en train de fusionner, puis, après un certain parcours, les mêmes structures tendent à apparaître comme formées de tourbillons uniques (fig. 18, 25, 29).

La vitesse de propagation W des structures de l'allée alternée est difficile à évaluer car, à cause de l'exiguïté du champ d'observation, l'allée alternée n'est visible que sur une courte distance, juste après sa formation. La détermination de l'ordre de grandeur de W a été faite à partir des clichés strioscopiques car les noyaux tourbillonnaires y apparaissent plus nettement (fig. 18, 20, 28, 29). On constate que W augmente et se rapproche de U à mesure que l'on s'éloigne vers l'aval, c'est-à-dire à mesure que l'allée s'élargit.

Longtemps il a été admis qu'au-dessus d'une valeur de R de l'ordre de 10^2 à 10^3 l'allée alternée était remplacée par un sillage irrégulier conservant un caractère périodique, puis qu'à partir de 10^5 environ la structure ordonnée disparaissait pour faire place à un régime avec des tourbillons aléatoires. La tendance actuelle, fondée sur divers résultats expérimentaux récents est d'admettre que les écoulements turbulents ne sont pas aussi désordonnés qu'on le pensait, mais qu'ils possèdent des propriétés d'ordre et de périodicité, du moins statistiquement ([14]) , ([15]) . Nos résultats sont conformes à ce point de vue puisque nous avons observé des allées alternées jusqu'à $R \simeq 3\ 10^5$, non seulement en écoulement subsonique, mais également en écoulement supercritique.

Il peut paraître surprenant que les deux files de tourbillons aient toujours tendance à former une allée alternée car cela les oblige, comme nous l'avons vu, à une brutale adaptation des fréquences. La raison profonde est probablement que la configuration de l'allée alternée assure un minimum de dissipation d'énergie dans le sillage.

Les valeurs de S_a déduites de nos expériences sont données sur la figure 15 pour le cylindre, sur la figure 16 pour la plaque normale au vent et sur la figure 17 pour divers autres obstacles. Nos résultats sont voisins de ceux obtenus en [16] pour une plaque plane sans incidence. On note que la dépendance de S_a à l'égard de R et de M est faible surtout pour le cylindre et le culot ; elle est plus importante pour la plaque et le profil ONERA D.

Récemment diverses tentatives ont été faites pour calculer l'écoulement instationnaire autour d'un obstacle présentant des décollements en des points connus à priori ([16]), ([17]). Le calcul suppose le fluide non visqueux et il est fait en injectant des tourbillons discrets aux points de décollement. Nous avons voulu confronter ce type de calcul avec l'expérience. Le cas choisi est celui d'une plaque à l'incidence 50° ([16]). Le calcul donne $S_a = .154$ et l'analyse des visualisations .141 à .158 pour $R \simeq 10^5$ et $M \simeq .6$ ([19]). De plus, la position des structures tourbillonnaires est voisine de celle indiquée par le calcul.

Au cours des dépouillements on a constaté une certaine irrégularité dans l'émission des tourbillons. Elle est dûe au *couplage* entre le décollement et l'allée alternée. Le champ de vitesse instationnaire induit par les tourbillons provoque un battement périodique de la ligne de séparation qui suit le décollement et un déplacement périodique du décollement lorsque celui-ci se produit en un point de courbure finie. Les visualisations ultra-rapides mettent bien en évidence *l'oscillation* des domaines de recirculation. Elles permettent d'établir que la période de ces fluctuations est égale à celle de l'allée alternée et que ces fluctuations sont d'autant plus intenses que M est grand. Le phénomène est particulièrement net sur les figures 20, 23, 24, 28 et 29.

Jusqu'à présent nous avons considéré le cas le plus fréquent où l'écoulement autour d'un obstacle présente deux décollements. Mais, dans certaines circonstances, le nombre de décollements peut être plus élevé. Par exemple, sur un profil d'aile les deux décollements qui se produisent au voisinage du bord de fuite peuvent se combiner avec une bulle de décollement. Celle-ci peut se former soit parce que le profil est à pic de vitesse, soit parce qu'il est fortement cambré. On a constaté que quand il existe une troisième émission de tourbillons, l'apparition de l'allée alternée est retardée à cause de l'interaction entre les deux files de tourbillons émises du même côté de l'obstacle. Soit S' le nombre de Strouhal correspondant sur la figure 7 à la distance qui sépare les deux décollements qui se produisent du même côté. Les tourbillons émis au décollement le plus proche du bord d'attaque ont un Strouhal égal à S' lorsqu'ils arrivent au niveau du second décollement où ils rencontrent des tourbillons à Strouhal voisin de celui d'émission. Dans ces conditions il est évident que le mélange des deux files de tourbillons est chaotique : il en résulte que le sillage paraît d'abord désordonné et que l'allée alternée se forme beaucoup plus loin que dans le cas où il n'y a qu'un seul décollement de part et d'autre de l'obstacle.

Dans ce qui suit nous décrivons en détail certaines expériences. En ce qui concerne le choix des clichés de visualisation présentés nous avons été guidés par la volonté d'illustrer tous les phénomènes observés. Pour mettre en évidence les allées alternées nous avons représenté des séquences photographiques sur un intervalle de temps d'environ une période (fig. 18, 21, 30) ou une demi-période (fig. 24, 28, 29). L'oscillation latérale du sillage est illustrée par les photographies des figures 20, 23, 24, 28 et 29. La propagation des ondes instationnaires apparaît sur les figures 23, 24, 28, 29, 30, 31 et 32. Les photographies des figures 26 et 27 indiquent l'évolution des domaines de recirculation, celles de la figure 32 se rapportent à l'interaction de trois décollements et celles de la figure 33 à l'écoulement dans une prise d'air.

8 - EXPERIENCES EN ECOULEMENT SUBSONIQUE.-

Nous nous sommes efforcés d'effectuer des expériences à Mach aussi petit que possible de manière à se rapprocher de l'écoulement incompressible, mais nous avons constaté qu'en-dessous de $M \simeq .3$ la qualité des strioscopies était insuffisante.

Quelques exemples de visualisations en écoulement subsonique sont donnés sur les figures 18 à 22.

De nombreuses expériences ont été faites avec des cylindres à $M = .3$ et R de l'ordre de 10^5 ce qui correspond à des décollements laminaires. Deux cylindres ont été utilisés de diamètres L = 12,5 mm et 24 mm. La fig. 18 donne une visualisation strioscopique pour le petit cylindre.

En ce qui concerne les tourbillons qui longent les domaines de recirculation, des dépouillements ont été faits pour $M = .4$ à partir des essais avec le petit cylindre (fig. 19). On constate entre les différentes valeurs relevées une certaine dispersion qui provient de l'imprécision dans le décompte et le repérage des tourbillons et également de l'irrégularité de l'émission qui a déjà été mentionnée. On voit d'abord que la vitesse V est voisine de $\mathcal{U}$. D'autre part, le nombre de Strouhal S est notablement plus grand que S_a et il diminue lorsqu'on progresse vers l'aval. Comme les mesures sont faites loin de l'émission cette diminution est assez lente car on se trouve sur une portion aplatie de la courbe de la figure 7.

Une évaluation de la vitesse de propagation W a été faite dans l'expérience de la figure 18. On a obtenu $\frac{W}{\mathcal{U}} \simeq .5$ pour $\frac{X}{L} \simeq 2$ et $\frac{W}{\mathcal{U}} \simeq .7$ pour $\frac{X}{L} \simeq 5$.

Des expériences analogues aux précédentes ont été faites avec deux plaques de longueur $L = 12$ mm et 24 mm, normales au vent, également pour $M \simeq .3$, et avec un obstacle à culot pour $M \simeq .4$ et .6. Sur la figure 20 l'amplitude de la fluctuation des lignes de jet du culot est de l'ordre de 5° vers l'intérieur des domaines de recirculation et de 1° vers l'extérieur.

Les figures 21 et 22 concernent le profil ONERA D. La figure 21 représente l'écoulement autour d'une maquette de corde $c = 80$ mm à $M \simeq .6$ et $\alpha = 20°$. En plus des ombroscopies par train d'éclairs et d'une strioscopie de l'écoulement moyen, on a indiqué les limites approximatives des domaines de recirculation qui ont été déterminées par visualisation pariétale à l'aide d'un enduit pâteux et par exploration au fil de laine dans le plan médian de la veine. Un dépouillement fait pour les tourbillons d'extrados, au droit du bord de fuite, donne $V \simeq 150$ m/s et N entre 8.000 et 10.000 Hz, soit S entre 1.2 et 1.8. Pour les tourbillons d'intrados on obtient $N \simeq 1.800$ Hz, d'où $S \simeq .27$, à environ un quart de corde du bord de fuite.

La figure 22 illustre l'évolution du sillage du profil ONERA D en fonction de l'incidence à $M \simeq .6$. La maquette utilisée est plus petite (corde 24 mm) ce qui permet d'observer une plus grande partie du sillage (sur les clichés la maquette est cachée par le talon de fixation). Comme il s'agit d'un profil à pic de vitesse, il existe, dans un intervalle de valeurs de α , une bulle de décollement à l'extrados. A faible indicence (fig. 22a) on a une bulle courte, sans effet notable sur le sillage qui est alterné dès le voisinage du bord de fuite. A incidence plus élevée (fig. 22b) la bulle est plus étendue et les tourbillons qui s'y développent sont encore intenses en parvenant au bord de fuite : sous leur influence le sillage est agité sur une certaine longueur avant que l'allée alternée se forme. A grande incidence (fig. 22c) il n'y a plus de bulle et on retrouve une allée alternée bien organisée près de l'extrémité aval des domaines de recirculation.

9 - *EXPERIENCES EN ECOULEMENT SUPERCRITIQUE.-*

Les figures 23 et 24 représentent des écoulements supercritiques par intermittences. Sur les photographies de la figure 23 on distingue nettement le déplacement périodique du point de décollement : il se fait à la fréquence N_a et son amplitude angulaire est d'environ 15° de part et d'autre du maître couple. Une poche supersonique est créée lorsque le décollement progresse vers l'aval. On remarque que le retour du décollement vers l'amont s'accompagne de la naissance d'une petite onde. Les fluctuations précédentes provoquent évidemment un déplacement périodique du point d'arrêt. On imagine les conséquences importantes que ce phénomène peut avoir sur la loi de convection thermique d'un élément sensible chauffé (film chaud) fixé au bord d'attaque.

Pour la plaque (fig. 24) le décollement est fixe, mais la ligne de jet oscille à la fréquence N_a.

Sur les deux figures 23 et 24 on remarque les ondelettes créées par le champ de vitesse instationnaire induit par les tourbillons qui longent les domaines de recirculation. Ces ondelettes existent dans tous les cas, mais elles sont très apparentes ici car à proximité des noyaux tourbillonnaires la vitesse est voisine de la vitesse du son.

La figure 25 représente une plaque en incidence 50° où on a délimité les frontières des structures tourbillonnaires à partir d'une strioscopie ultra-rapide : la première grosse structure est encore adjacente aux domaines de recirculation tandis que celle qui la précède, dans la file du haut, appartient déjà à l'allée alternée.

Lorsqu'on passe aux écoulements strictement supercritiques on note un allongement considérable des domaines de recirculation pour la plaque (fig. 26), au contraire du cylindre et surtout du culot (fig. 27).

Des séquences de visualisation ultra-rapide d'écoulements strictement supercritiques sont données sur les figures 28 à 33. Les clichés strioscopiques à long temps de pose (400e de seconde) révèlent l'existence d'ondes de choc. Celles-ci apparaissent floues à cause de leur vibration autour d'une position moyenne. On discerne les ondes acoustiques émises par les tourbillons après leur passage à travers l'onde de choc.

L'oscillation latérale du sillage est évidente sur les figures 28 et 29. Pour le culot (fig. 29) l'amplitude de l'oscillation de la ligne de jet est environ 10° vers l'intérieur des domaines de recirculation et 4° vers l'extérieur.

Un dépouillement de l'essai à $M \simeq .85$ pour le profil ONERA D de corde 24 mm a été fait en ce qui concerne la propagation des ondes instationnaires. Sur la figure 30 on a indiqué à titre d'exemple trois positions successives d'une onde. On constate que les ondes émises par les tourbillons remontent le courant et viennent pénétrer dans la poche supersonique en contournant le choc par le sommet. Ce résultat montre que les poches supersoniques ne sont pas à l'abri de perturbations en provenance de l'aval.

Le même phénomène est visible sur la figure 31 qui représente la strioscopie d'un écoulement supercritique autour d'un profil à bec.

La figure 32 fournit un exemple d'écoulement supercritique avec trois décollements sur le profil ONERA D à l'incidence $\alpha = 4°$. L'écoulement présente une bulle d'extrados produite dans le cas $M = .7$ par le pic de vitesse et dans le cas $M = .84$ par l'onde de choc. Les tourbillons de la bulle altèrent le sillage, mais il existe une allée alternée loin en aval. Dans le cas $M = .84$ on aperçoit de grosses bouffées turbulentes entre le choc et le bord de fuite. Le dépouillement a montré que ces bouffées fugitives ont une vitesse de propagation légèrement inférieure à la vitesse locale du fluide, hors de la couche limite.

La figure 33 illustre la différence qui existe entre un écoulement subsonique et un écoulement supercritique dans une prise d'air en grande incidence ([19]). On constate que l'onde de choc provoque une rapide destruction des grosses structures tourbillonnaires de la zone de mélange issue du décollement. Sur une des photographies de la séquence d'ombroscopies présentée on remarque que l'onde de choc n'apparaît presque plus.

10 - CONCLUSION.-

Dans la première partie de cette communication nous avons proposé un schéma théorique simple de l'émission des tourbillons en un point de décollement et de leur agglomération en cours de propagation sous l'effet de la diffusion visqueuse. Ce schéma explique l'évolution initiale d'une zone de mélange.

L'application des résultats obtenus au sillage tourbillonnaire d'un obstacle permet de comprendre pourquoi les allées alternées se forment d'autant plus difficilement que le nombre de Reynolds est grand.

Les expériences qui ont consisté essentiellement en des visualisations ultra-rapides par trains d'éclairs ont permis de vérifier certaines prévisions théoriques. On a constaté que le phénomène d'agglomération des tourbillons d'une file existait. On a confirmé la présence d'allées alternées à grand Reynolds en écoulement subsonique et supercritique et on a déterminé la fréquence de ces allées pour de nombreux obstacles. On a montré que la formation d'une allée alternée nécessite une agglomération des tourbillons de chaque file. On a mis en évidence le couplage entre l'allée alternée et le décollement qui provoque une oscillation, à la fréquence de l'allée alternée, de la ligne de jet qui suit le décollement et, éventuellement, de la position du décollement. On a décrit l'interaction de plus de deux files de tourbillons.

D'une manière générale, les expériences montrent que les écoulements subsoniques ne diffèrent pas des écoulements à faible vitesse. Par contre, les écoulements supercritiques présentent des caractères spécifiques. Les visualisations ont permis de mettre en évidence l'existence, en écoulement décollé, de poches supersoniques adjacentes au sillage et de décrire l'interaction entre une onde de choc et les tourbillons qui la traversent. En particulier, il a été vérifié qu'une poche supersonique peut être influencée par des perturbations venant de l'aval.

L'ensemble des résultats obtenus souligne l'intérêt de la chronophotographie ultra-rapide pour l'étude phénoménologique d'écoulements rapidement variables qui sont généralement mal connus.

Certaines des propriétés décrites dans notre communication apparaissent plus évidentes à la projection d'un film d'animation qui a été monté à partir des clichés de visualisation. Ce film restitue l'évolution des phénomènes rapidement variables au ralenti, avec une échelle des temps de l'ordre de 10^4. Un extrait de ce film a été présenté au cours du Symposium.

BIBLIOGRAPHIE.-

[1] Batchelor
On steady laminar flow with closes steamlines at large Reynolds number
Journal of Fluid Mechanics vol. 1, 1956

[2] Landau, Lifschitz
Mécanique des Fluides, Moscou 1971

[3] François
Emploi des méthodes de perturbation pour l'étude des écoulements laminaires.
Application aux problèmes de séparation.
Publ. ONERA n° 128, 1969

[4] Winant, Browand
Vortex pairing : the mechanism of turbulent mixing layer growth at moderate Reynolds number.
Journal of Fluid Mechanics vol. 63, part 2, 1975

[5] Ashurst
Numerical Simulation of Turbulent mixing layers via Vortex dynamics
Symposium on Turbulent Shear Flows
Pennsylvania State University, April 1977

[6] Kotchin, Kibel, Roze
Theoretical Hydromechanics
Interscience 1964

[7] Christiansen, Zabusky
Instability, coalescence and fission of finite-area vortex structures
Journal of Fluid Mechanics, vol. 61, part 2, 1973

[8] Wille
Karman Vortex Streets
Advances in Applied Mechanics, vol. VI, 1960

[9] Roshko
Experiments on the flow past a circular cylinder at very high Reynolds number
Journal of Fluid Mechanics, vol. 10

[10] Fragassi, Nahas, Merle
Interaction onde de choc - tourbillon
10e Colloque d'Aérodynamique Appliquée, Lille 1973

[11] Spee
Investigations on the transonic flow around aerofoils
NLR TR 69122 *U* Amsterdam 1970

[12] Nieuwland, Spee
Transonic airfoils : recent developments in theory, experiment and design
Annual Review of Fluid Mechanics, vol. 5, 1973

[13] Merzkirch
Flow visualization
Academic Press 1974

[14] Laufer
New trends in Experimental Turbulence Research
Annual Review of Fluid Mechanics, vol. 7, 1975

[15] Brown, Roshko
The effect of density difference on the turbulent mixing layer
AGARD CP 93 Turbulent Shear Flows, 1971

[16] Heineman, Lawaczeck Bütefisch
Von Karman Vortices and their frequency determination in the wakes of profiles in sub- and transonic regimes
Symposium Transsonicum, Göttingen 1975

[17] Sarpkaya
An inviscid model of two dimensional vortex shedding for transcient and asymptotically steady separated flow over an circlined plate
Journal of Fluid Mechanics, vol. 68, part 1, 1975

[18] Clement, Maull
The representation of sheets of vorticity by discrete vortices
Progress in Aerospace Sciences, vol. 16, n° 2, 1975

[19] Dyment, Gryson
Etude d'écoulements transsoniques turbulents par chronophotographie ultra-rapide
13e Colloque d'Aérodynamique Appliquée, Lyon 1976

La partie expérimentale de la recherche faisant l'objet de la présente communication a été faite grâce à l'aide des organismes suivants : Délégation Générale à l'Aviation Civile (D.G.A.C.), Direction des Recherches et Moyens d'Essais (D.R.M.E.), Service Technique de l'Aéronautique de la Direction Technique des Constructions Aéronautiques (D.T.C.A.).

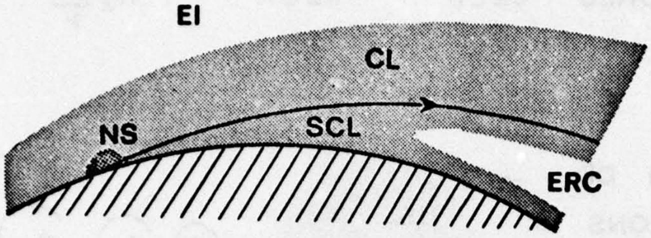

DOMAINES

EI	EULER IRROTATIONNEL
ERC	EULER A ROTATIONNEL CONSTANT
CL	COUCHE LIMITE
SCL	SOUS COUCHE LIMITE
NS	NAVIER STOKES

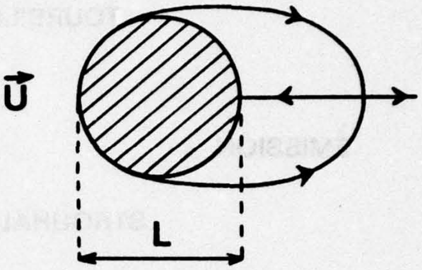

Fig: 1

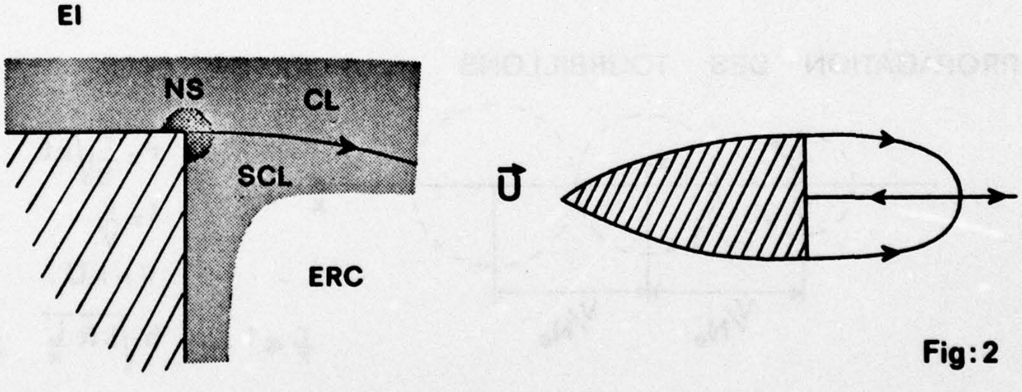

Fig: 2

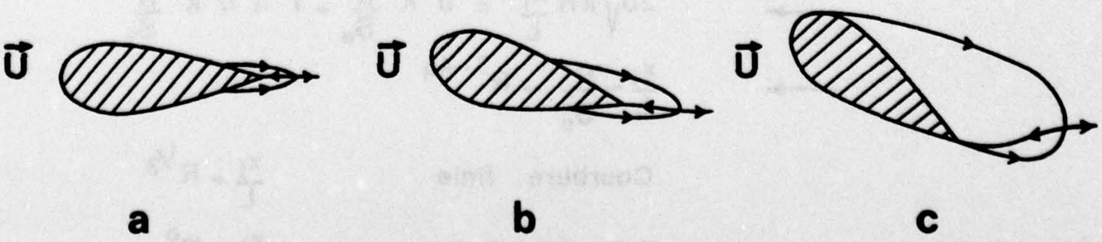

a

b

c

Fig: 3

DOMAINE DE NAVIER STOKES $\ell = L R^{-q}$ $u = U R^{q-1}$ $R = \frac{UL}{\nu}$

INSTABILITÉ → ÉMISSION DE TOURBILLONS

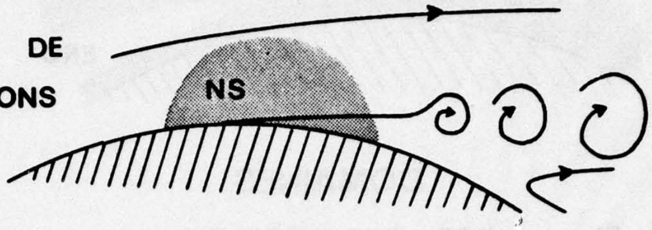

ÉMISSION :

STROUHAL $S_e = \frac{N_e L}{U} \sim R^{2q-1}$

CIRCULATION $\Gamma_e \sim \nu$

valable pour $\frac{1}{2} < q < \frac{7}{8}$

Courbure finie $q = \frac{2}{3}$ $S_e \sim R^{1/3}$

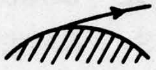

Point anguleux $q = \frac{3}{4}$ $S_e \sim R^{1/2}$

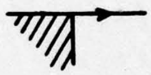

Fig:4

PROPAGATION DES TOURBILLONS

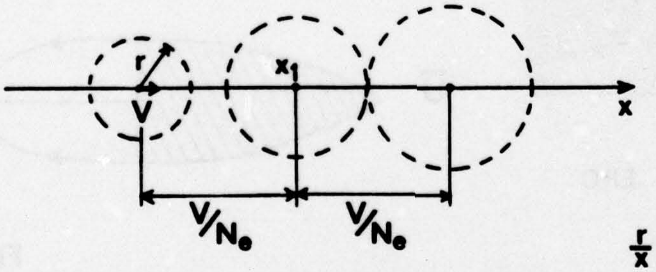

$r = \frac{1}{b}\sqrt{\nu t}$

$t = \frac{x}{V}$

$V = kU$

$\frac{r}{x} \ll 1 \longrightarrow b\sqrt{kR\frac{L}{x}} \gg 1$

EMPIÈTEMENT : DÉBUT D'AGGLOMÉRATION

$$\sqrt{\frac{\nu x_1}{V}} + \sqrt{\frac{\nu}{V}\left(x_1 + \frac{V}{N_e}\right)} = b\frac{V}{N_e}$$

$$\longrightarrow \quad 2b\sqrt{kR\frac{x_1}{L}} = b^2 k^2 \frac{R}{S_e} - 1 \simeq b^2 k^2 \frac{R}{S_e}$$

$$\longrightarrow \quad \frac{x_1}{L} \sim \frac{R}{S_e^2} \sim R^{3-4q}$$

Courbure finie $\frac{x_1}{L} \sim R^{1/3}$

Point anguleux $\frac{x_1}{L} \sim R^{0}$

Fig:5

AGGLOMÉRATIONS SUCCESSIVES

x_n	abscisse où commence la n^e^ agglomération
λ_n	longueur nécessaire à la n^e^ agglomération
S_n	Strouhal après la n^e^ agglomération

$$S_n = \frac{S_e}{2^n} \qquad x_n = 4^{n-1} x_1$$

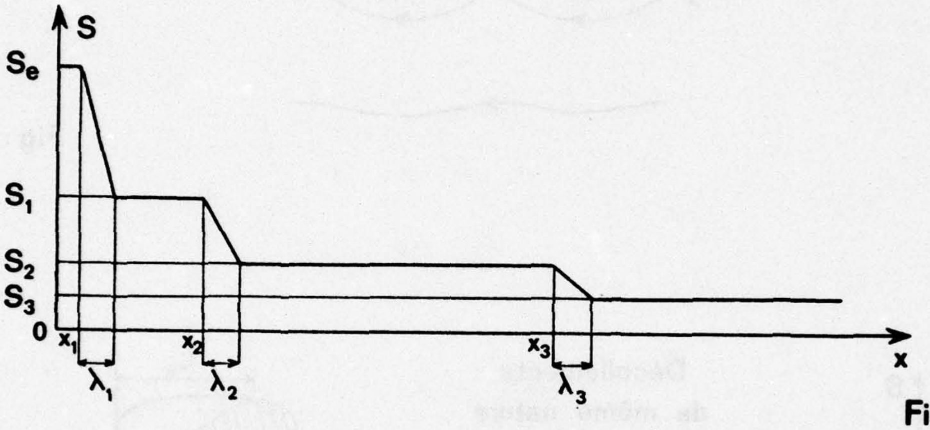

Fig : 6

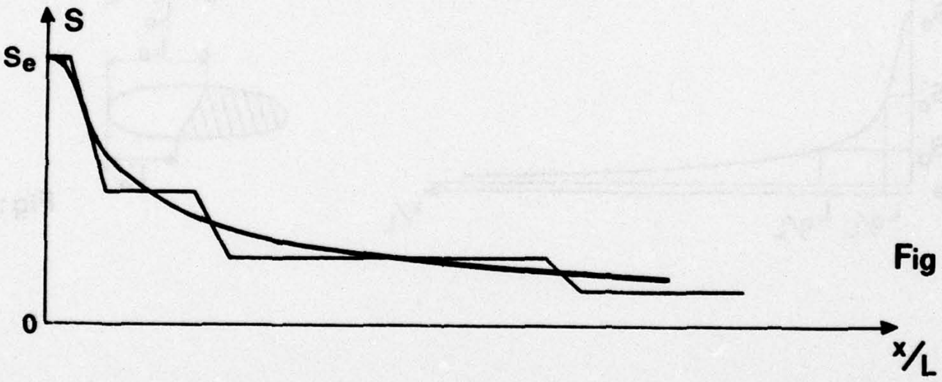

Fig : 7

$$\text{Si } R \rightarrow \beta R \left\{ \begin{array}{l} S_e \rightarrow \beta^{2q-1} S_e \\ S_n \rightarrow \beta^{2q-1} S_n \end{array} \right. \quad \begin{array}{l} x_1 \rightarrow \beta^{3-4q} x_1 \\ x_n \rightarrow \beta^{3-4q} x_n \end{array} \qquad S_o \rightarrow \gamma S_o\,,\ \gamma > 1$$
$$\beta > 1$$

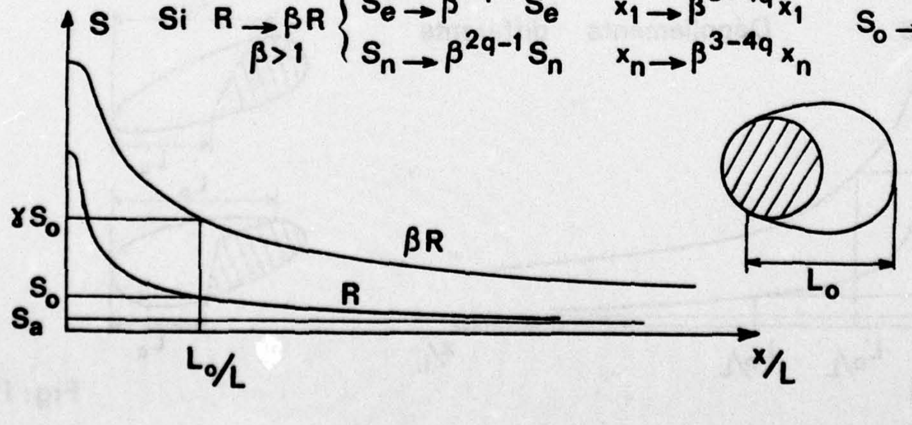

Fig : 8

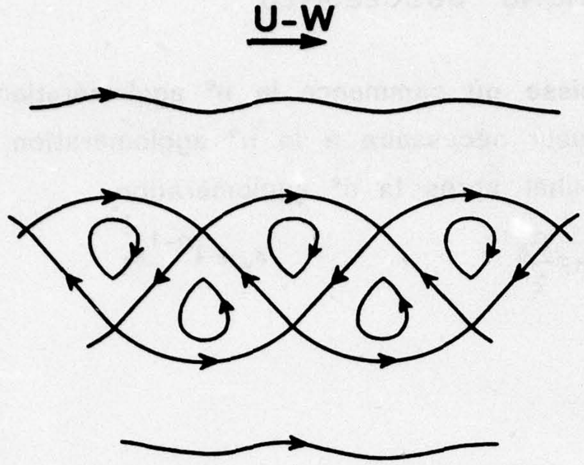

Fig : 9

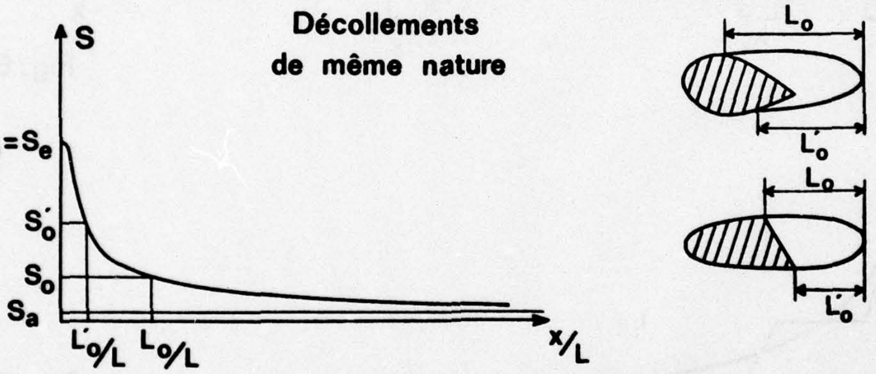

Fig : 10

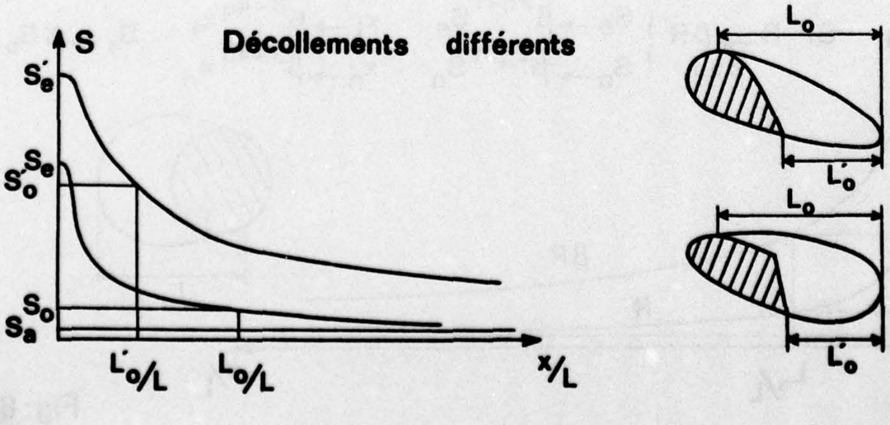

Fig : 11

Ecoulements strictement supercritiques

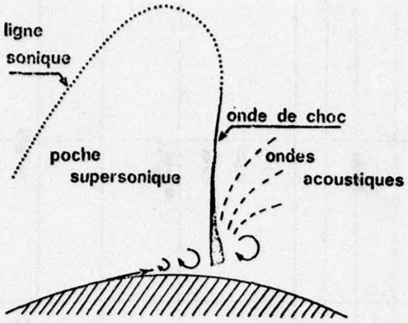

Fig: 12

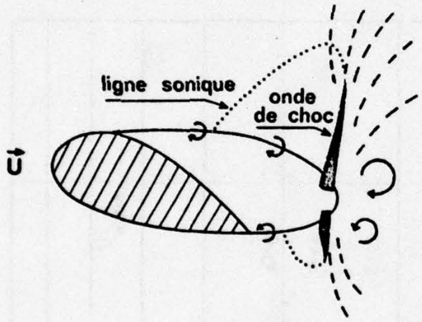

Fig: 13

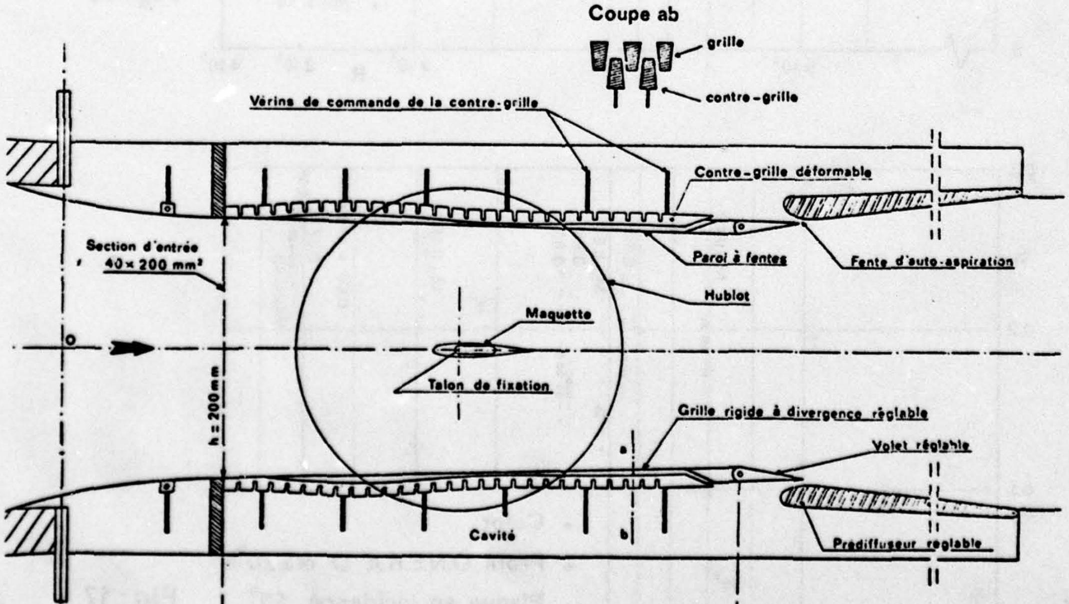

Fig: 14

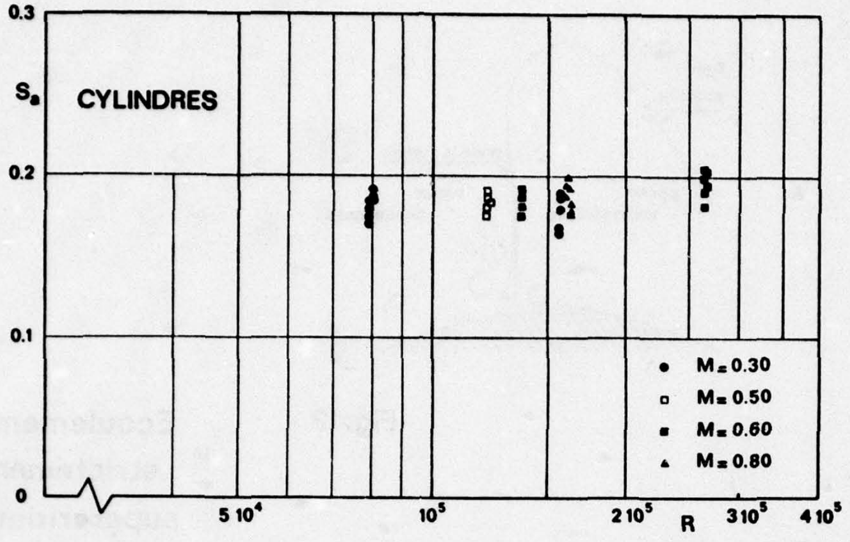

Fig : 15

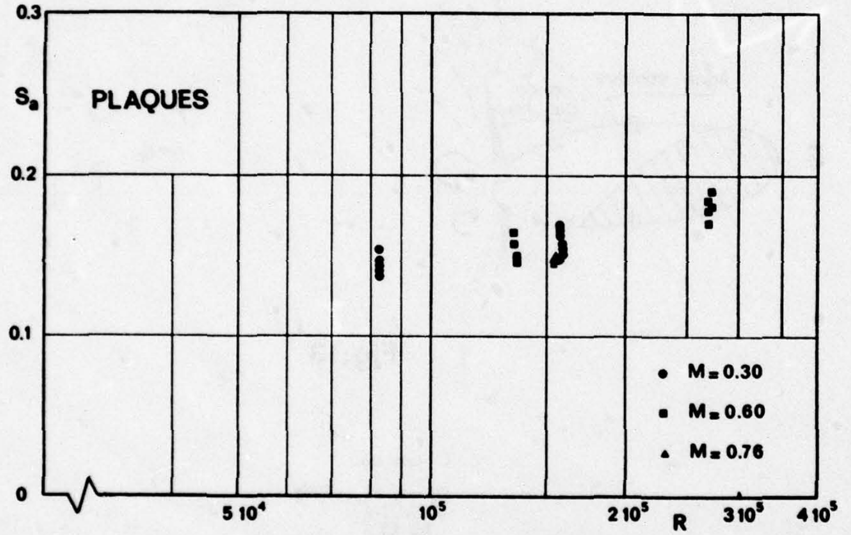

Fig : 16

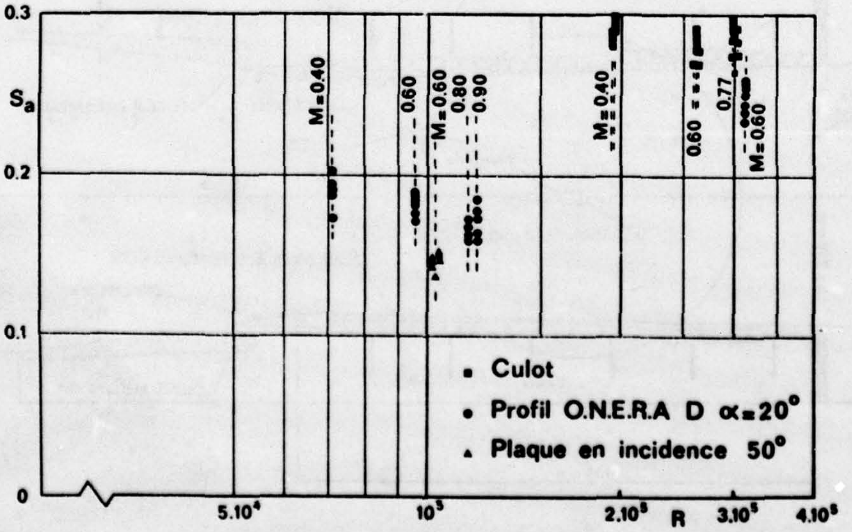

Fig : 17

Fig : 18

CYLINDRE L = 12.5

$M = 0.30$

$U = 102$ m/s

$R = 0.80\ 10^5$

Strioscopies

$\Delta t = 200\ \mu s$

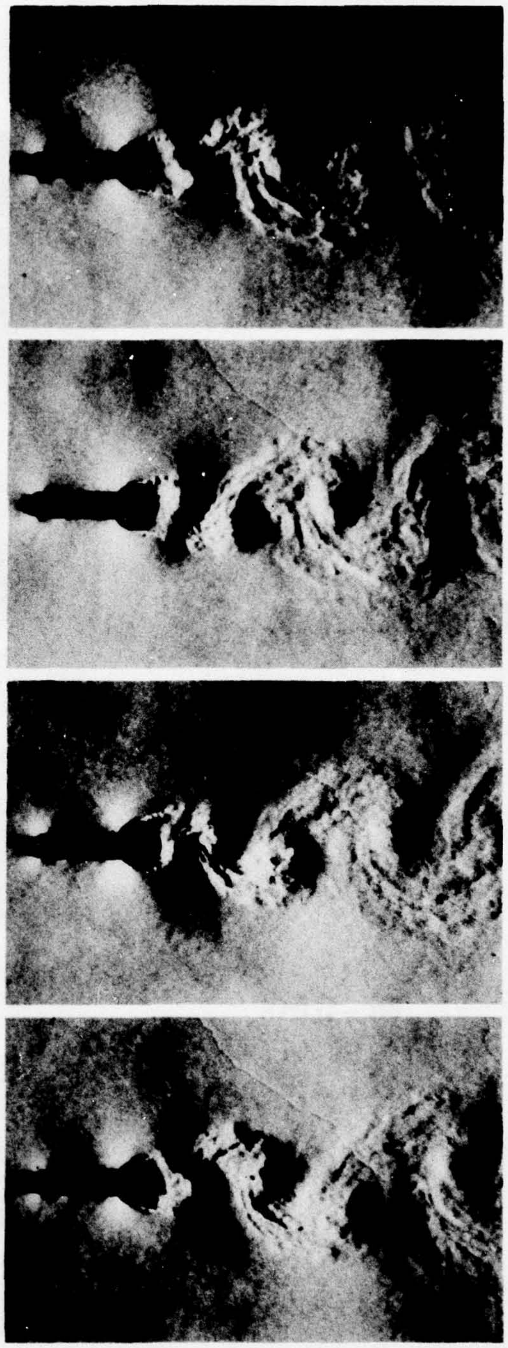

$L = 12.5$ mm
$U = 137$ m/s
$M = 0.4$
$R = 9.4\ 10^4$

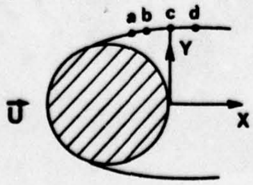

points	X/L	Y/L	S	V/U
a	-0.32	0.57	4.6 à 6.1	0.9 1.0
b	-0.20	0.60		0.9 1.1
c	0	0.64	3.7 à 4.6	1.0
d	0.20	0.63		0.9

Fig : 19

Fig : 20

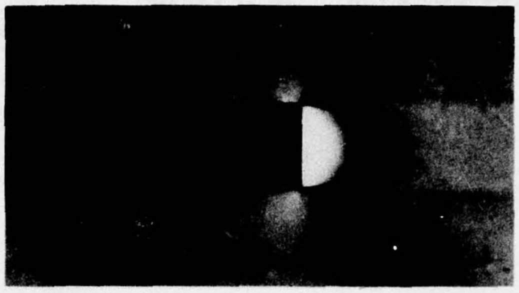

Strioscopie
1/400 s

CULOT L=24

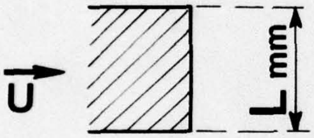

$M = 0.60$

$U = 212$ m/s

$R = 2.6\ 10^5$

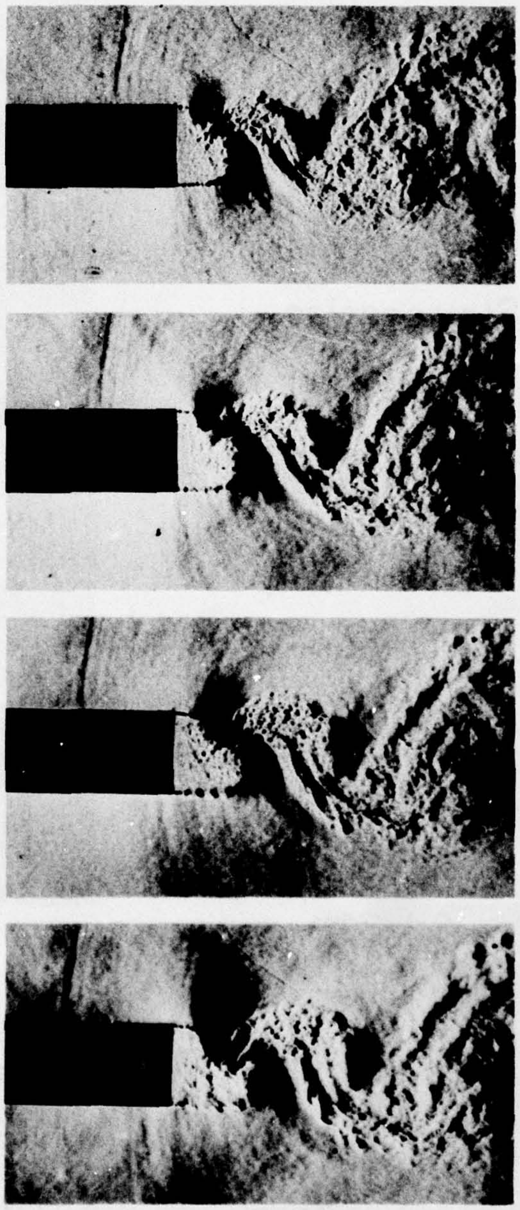

Strioscopies
$\Delta t = 40 \mu s$

Fig : 21

Strioscopie 1/400s

PROFIL O.N.E.R.A D

c = 80 mm $\alpha = 20^\circ$

$M = 0.60$

$U = 211\,\mathrm{m/s}$

$\frac{Uc}{\nu} = 8.7\ 10^5$

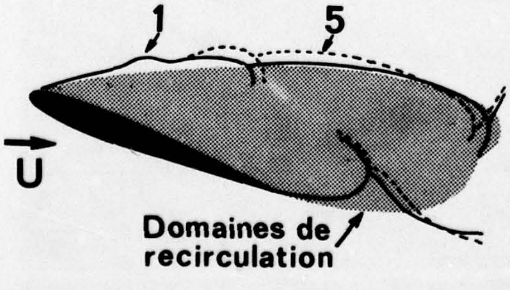

Ombroscopies

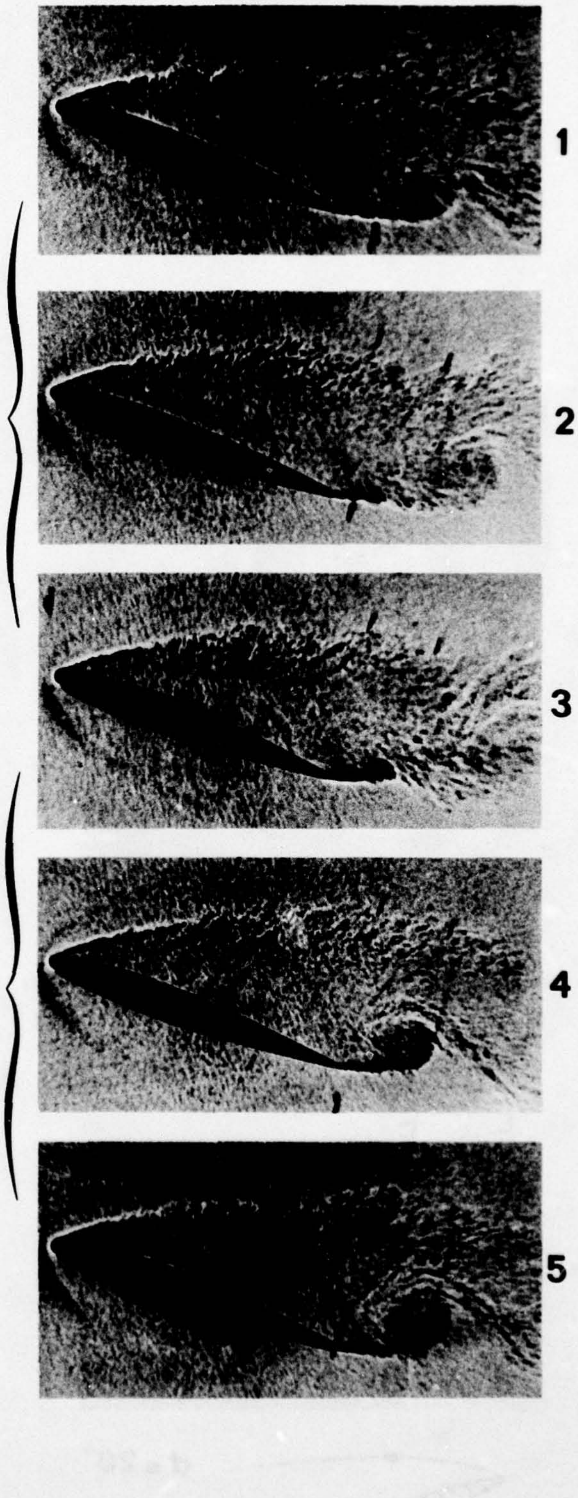

Fig: 22

PROFIL O.N.E.R.A D

c = 24 mm

M = 0.60

U = 210 m/s

$\frac{U c}{\nu} = 2.6 \; 10^5$

Strioscopies

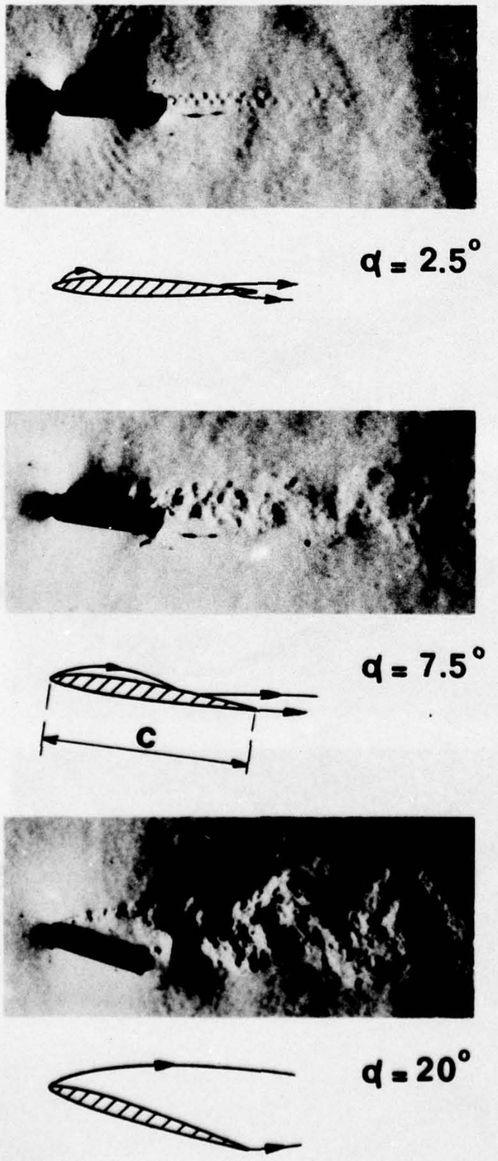

Fig: 23

CYLINDRE L = 24

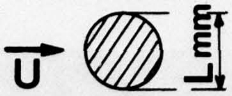

M = 0.60

U = 204 m/s

R = 2.6 10^5

Ombroscopies Δt = 50 µs

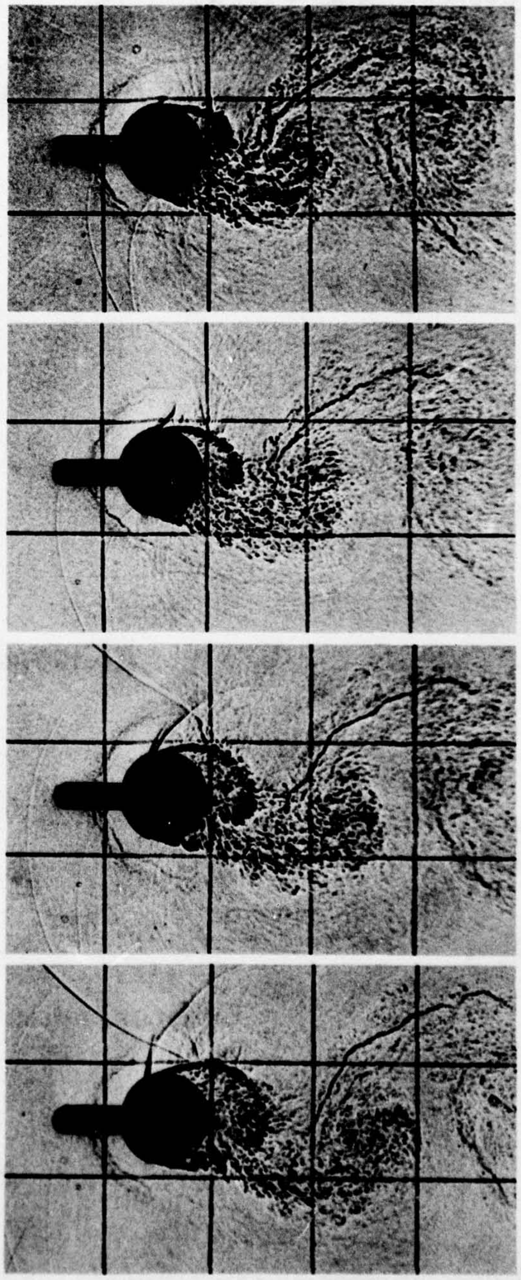

PLAQUES

L = 24 mm

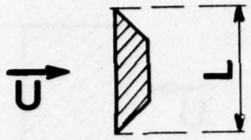

M = 0.60

U = 205 m/s

R = 2.7 10^5

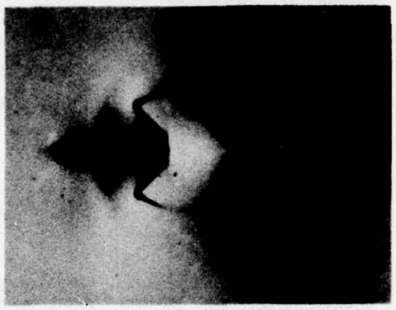

Strioscopie 1/400 s

Fig: 24

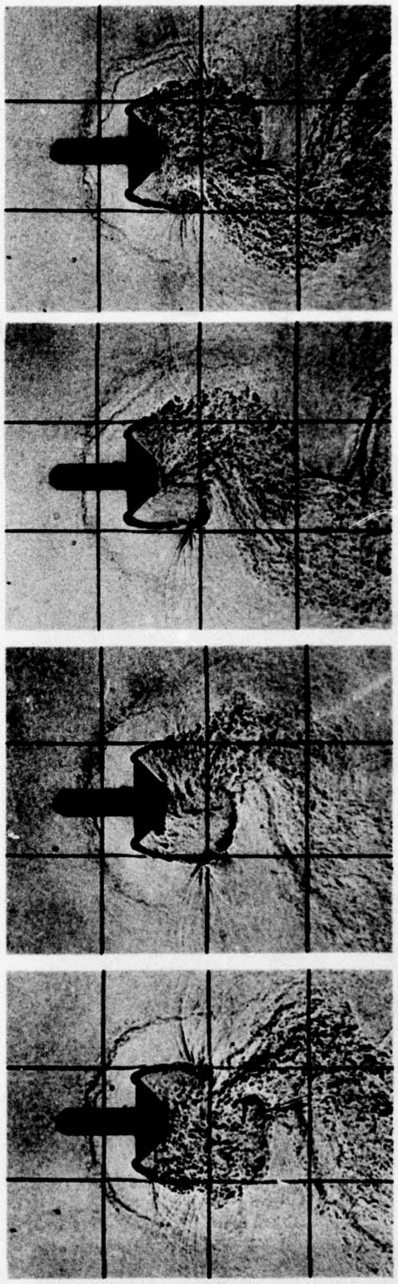

Ombroscopies

$\Delta t = 100 \mu s$

Fig: 25

Strioscopie

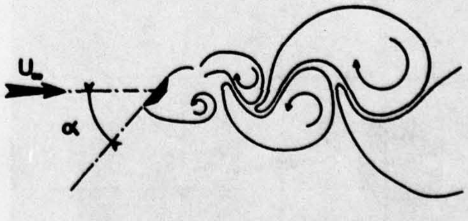

$\alpha = 50^\circ$

L = 12 mm

M = 0.60 U = 203 m/s R = 10^5

Fig:26

PLAQUE

L = 12 mm

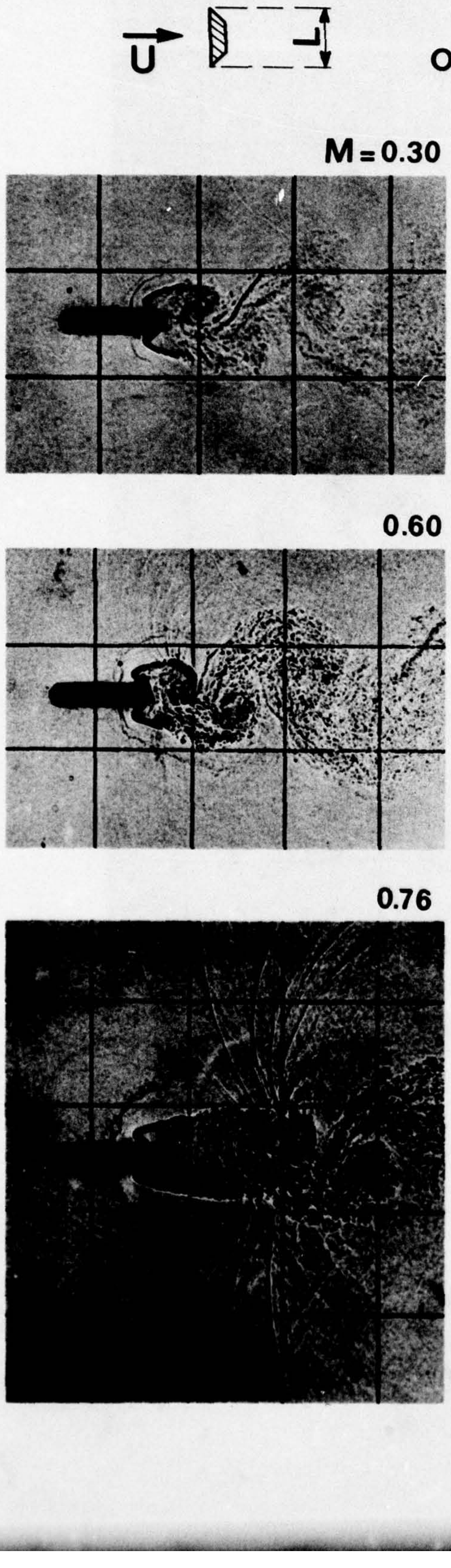

Ombroscopies

Fig: 27

CULOT

L = 24 mm

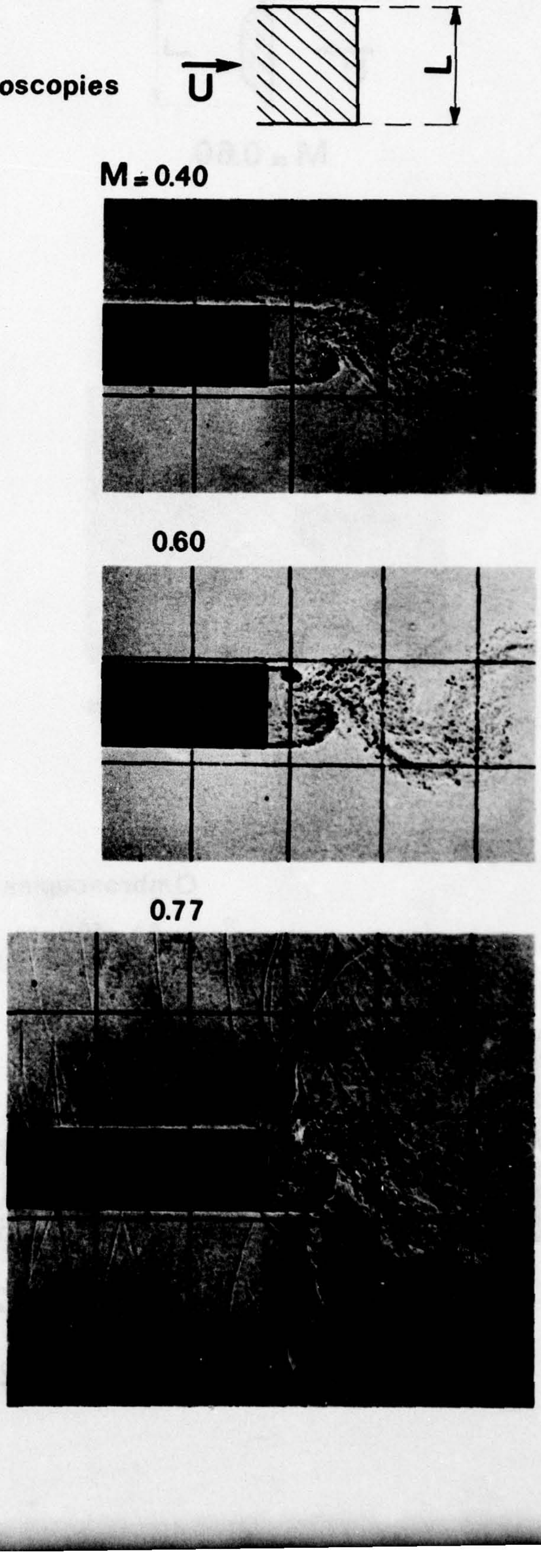

Fig: 28

CYLINDRE

L = 12.5 mm

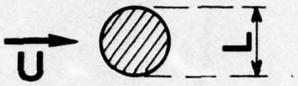

M = 0.80

U = 266 m/s

R = 1.6 10^5

Strioscopie 1/400

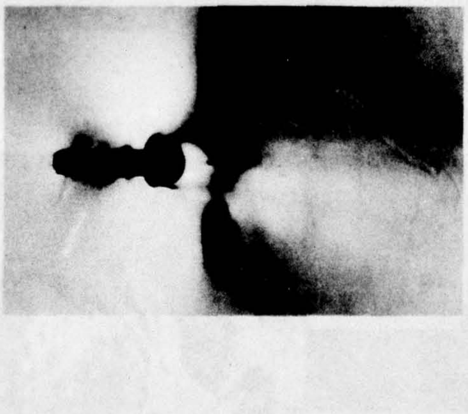

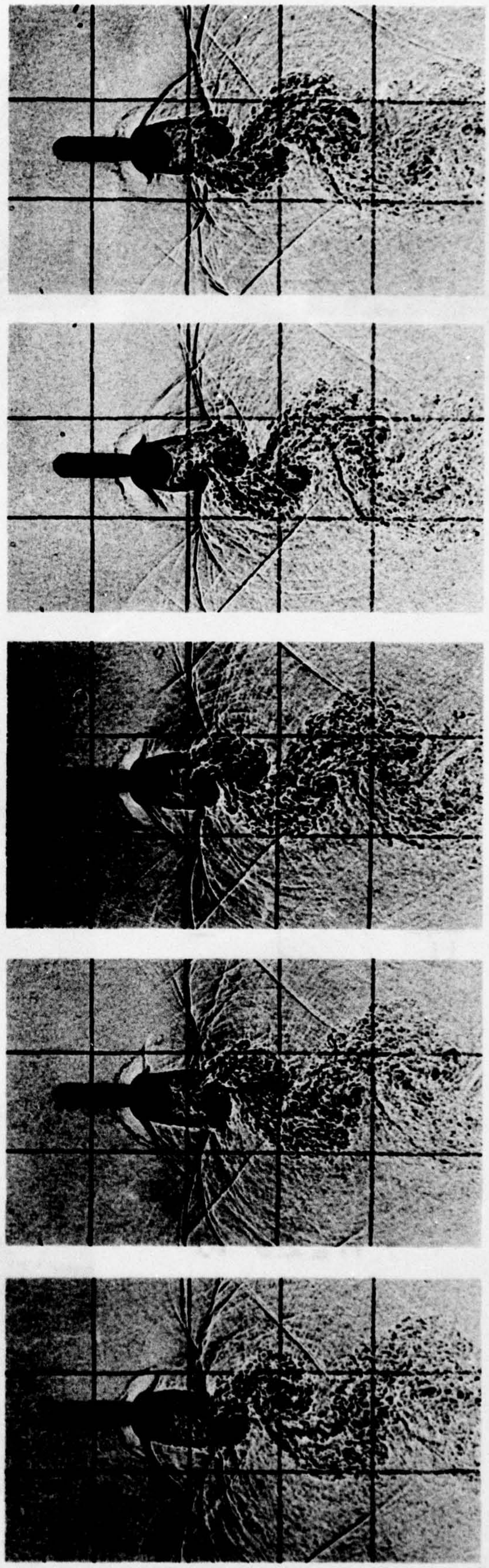

Ombroscopies

Δt = 40µs

Fig:29

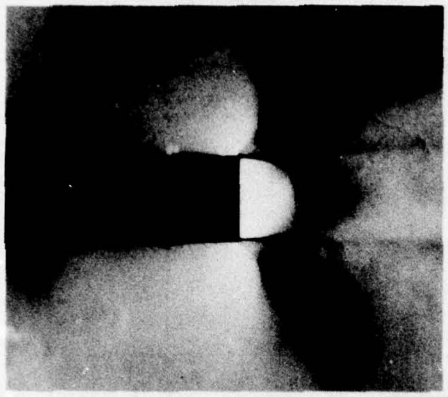

Strioscopie 1/400 s

CULOT

L = 24mm

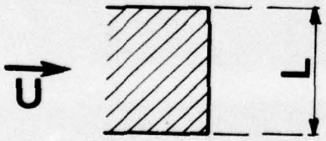

M = 0.77

U = 260 m/s

R = 2.9 10^5

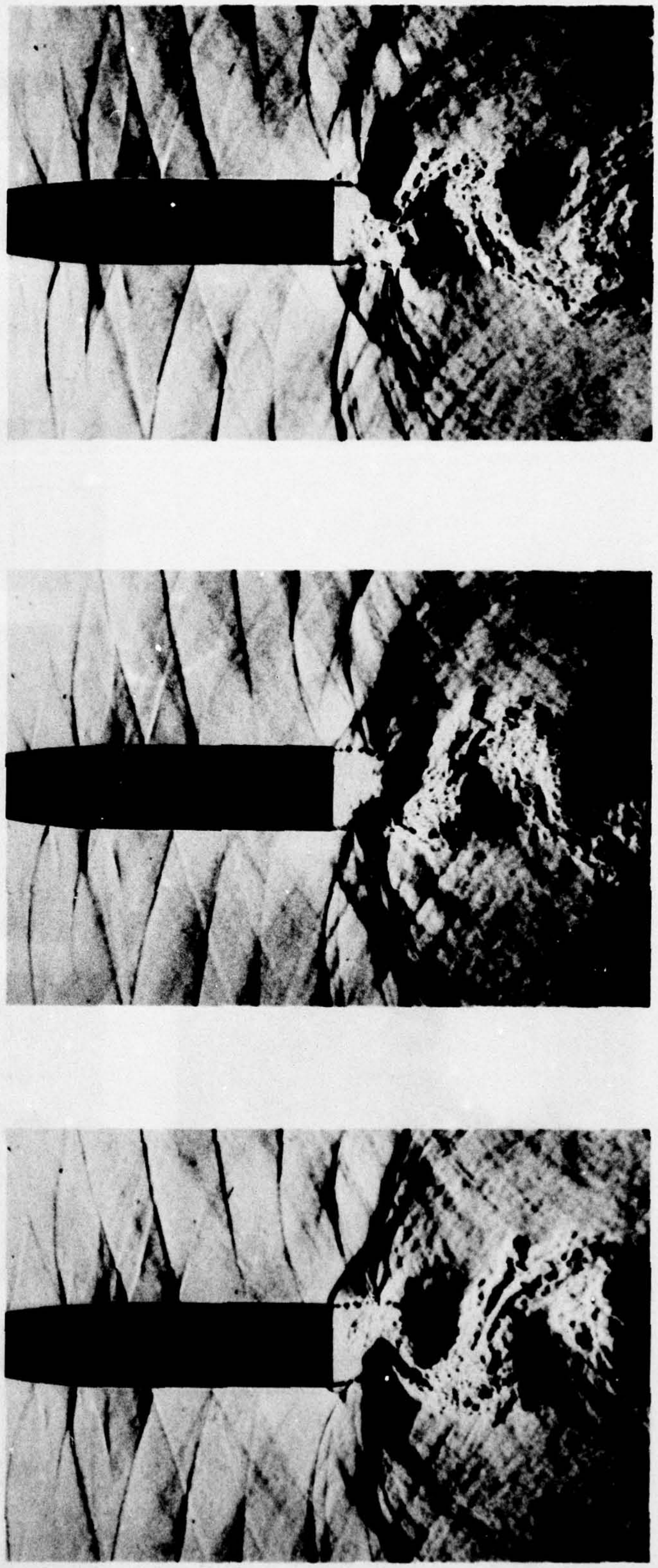

Strioscopies

Δt = 80 µs

Fig : 30

PROFIL O.N.E.R.A D

$c = 24$ mm $\alpha = 20°$

$M = 0.85$

$U = 275$ m/s

$\frac{Uc}{\nu} = 3.3\ 10^5$

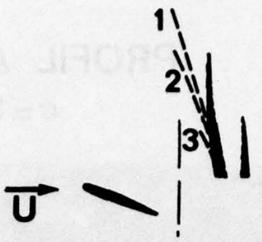

Strioscopie 1/400 s

Ombroscopies
$\Delta t = 160\ \mu s$

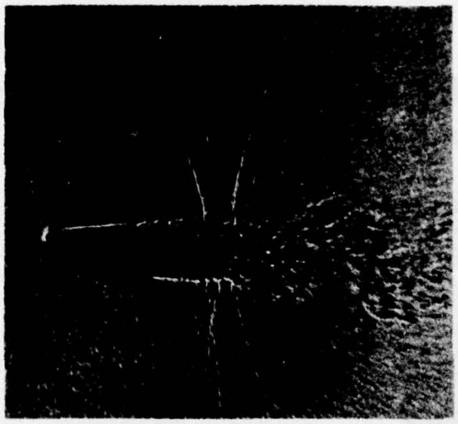
1

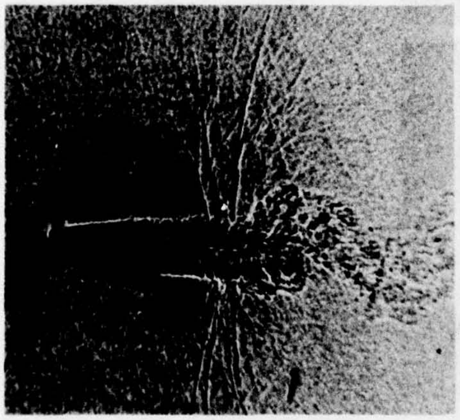
2

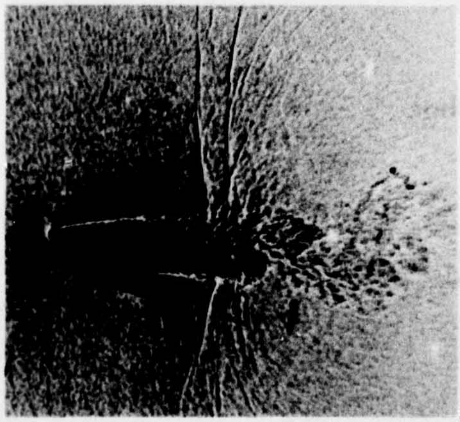
3

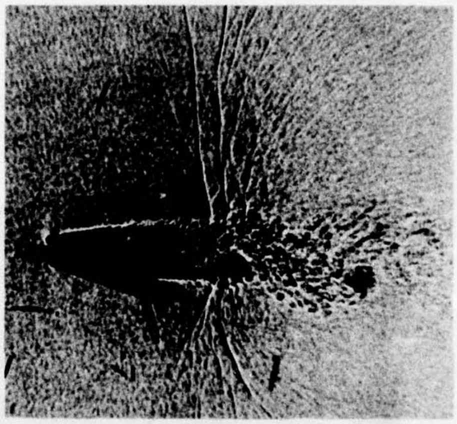
4

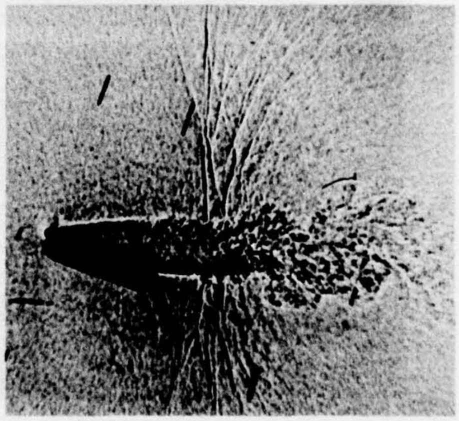
5

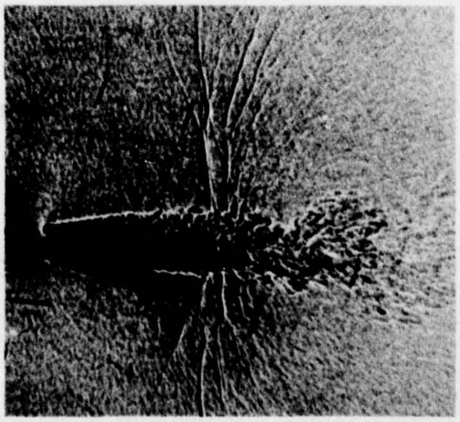
6

PROFIL AVEC BEC
c=83mm

Fig: 31

Strioscopie

M = 0.80
α = 0°

PROFIL O.N.E.R.A D
c= 80 mm

Fig: 32

Strioscopies

M = 0.70
α=4°

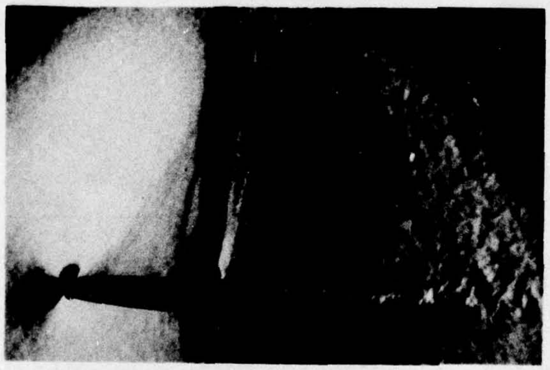

M=0.84
α=4°

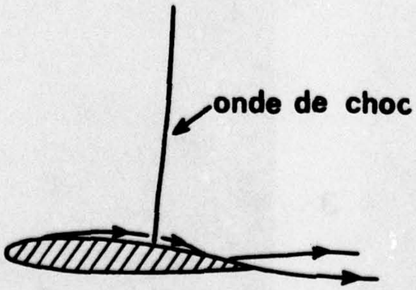

PRISE D´AIR
$\alpha = 20^\circ$

Fig:33

Strioscopies

M = 0.40 M = 0.60

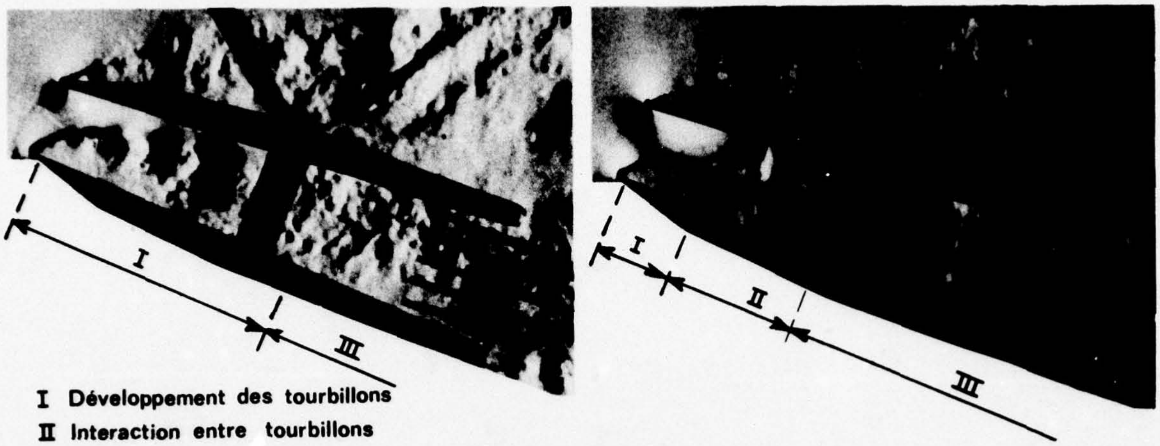

I Développement des tourbillons
II Interaction entre tourbillons et ondes
III Mélange

Ombroscopies
$\Delta t = 40\ \mu s$

M = 0.60

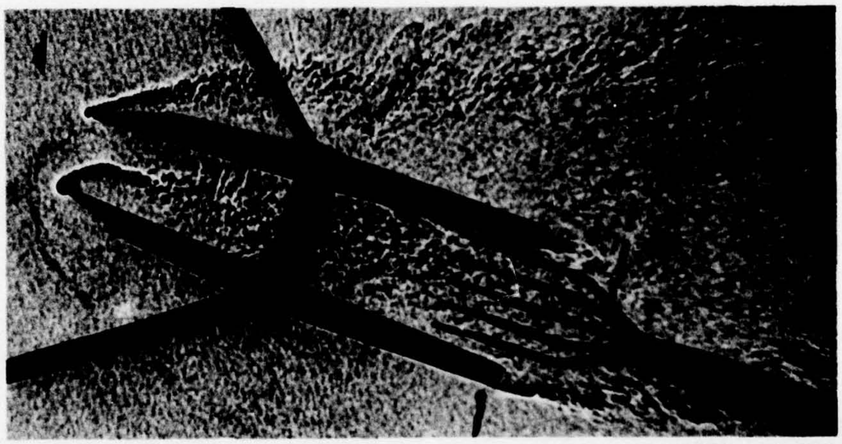
1

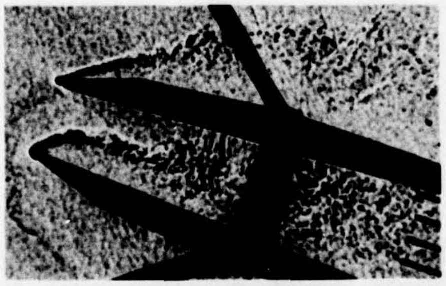
2

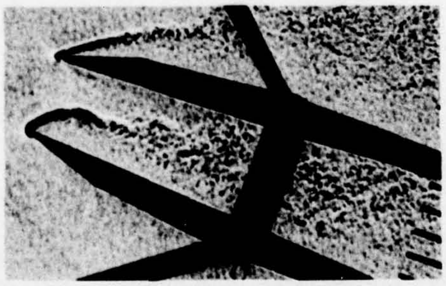
3


4


5

RECOLLEMENT DYNAMIQUE SUR UN PROFIL D'AILE EN MOUVEMENT DE TAMIS
INFLUENCE DES PARAMETRES D'OSCILLATION

J. REBONT[x], C. MARESCA[xx], D. FAVIER[xxx], J. VALENSI[xxxx]
Institut de Mécanique des Fluides de Marseille
1, rue Honnorat
13003 - Marseille - France

RESUME

Le mécanisme de recollement dynamique est étudié qualitativement et quantitativement sur un profil d'aile NACA 0012, pour lequel l'aile est placée à incidence fixe et est animée d'un mouvement d'oscillation harmonique parallèle à l'écoulement uniforme non perturbé. Le phénomène du recollement est analysé à partir de l'évolution comparée du torseur des forces aérodynamiques globales, des distributions de la pression statique et de la tension de cisaillement à la paroi du profil, ainsi que des visualisations instantanées de l'écoulement à différentes phases de la période. Les résultats obtenus mettent en évidence les effets instationnaires et notamment : l'hypersustentation moyenne de l'aile au cours d'une oscillation qui est évaluée par une formule empirique en fonction des paramètres λ, k, Rey_c, i , et la formation sur l'extrados du profil de tourbillons qui se propagent du bord d'attaque vers le bord de fuite, et qui provoquent et entretiennent des niveaux de portance bien supérieurs à ceux qui peuvent être atteints en régime stationnaire. De plus, l'analyse chronologique du phénomène instationnaire au cours d'un cycle, conduit à établir une analogie étroite entre les phénomènes observés en tamis, et ceux observés pour le décrochage dynamique dans le cas du mouvement de tangage.

NOTATIONS

A : amplitude de l'oscillation de tamis
A(i),B(i), C : fonctions définissant Co dans le cas Co = $\bar{P}/P_{stat}$
Co : premier terme de la décomposition en séries de Fourier
$C_1, C_2 \ldots C_n$: amplitudes des harmoniques de la décomposition en séries de Fourier
CYo : coefficient de portance moyen : CYo = $\bar{P}/\frac{1}{2}\rho V_\infty^2 S$
CXo : " de traînée moyen : CXo = $\bar{T}/\frac{1}{2}\rho V_\infty^2 S$
CMo : " de moment moyen : CMo = $\bar{M}/\frac{1}{2}\rho V_\infty^2 S.C$
C_p : coefficient de pression instantanée : $C_p = (p-p_\infty)/\frac{1}{2}\rho V_\infty^2$
c : corde du profil
f : fréquence du mouvement harmonique
i : incidence du profil
i_D : incidence de décrochage stationnaire
k : fréquence réduite ; $k = \frac{c\,\omega}{2\,V_\infty}$
M : moment de tangage instantané par rapport au quart avant de la corde
P : portance instantanée
P_∞ : pression statique de l'écoulement uniforme
p : pression statique instantanée
Rey_c : nombre de Reynolds rapporté à la corde et à V_∞ ; $Rey_c = \frac{V_\infty c}{\nu}$
T : traînée instantanée
t : temps
V_∞ : vitesse à l'infini amont
x : abscisse suivant la corde du profil
ω : pulsation du mouvement ; $\omega = 2\pi f$
λ : amplitude réduite ; $\lambda = \frac{A\omega}{V_\infty}$
τ : tension de cisaillement instantanée
$\phi_1, \phi_2, \ldots \phi_n$: déphasages des harmoniques de la décomposition en séries de Fourier.
Décomposition adoptée : $Co + \sum_1^n C_n \cos(n\omega t + \phi_n)$

---

[x] Ingénieur Docteur au C.N.R.S.
[xx] Maître de Recherche au C.N.R.S.
[xxx] Attaché de Recherche au C.N.R.S.
[xxxx] Professeur Honoraire de l'Université d'Aix-Marseille II

Indice supérieur :

$-$: moyenne sur une période

Indices inférieurs :

st ou stat: régime stationnaire

inst : régime instantané

I. INTRODUCTION

De nombreux travaux théoriques et expérimentaux sur le comportement aérodynamique de profils d'ailes en mouvement relatif instationnaire ont été effectués au cours de ces dernières années (voir par exemple Références 1 à 20). La plupart des études entreprises (en vue principalement de simuler en soufflerie les conditions auxquelles sont soumises les différentes sections des pales de rotors d'hélicoptères en vol de translation) concernent le cas particulier où le profil, placé dans un courant uniforme, est animé d'un mouvement propre d'oscillation en tangage autour d'une incidence voisine de l'incidence de décrochage en régime stationnaire. Ces études ont conduit à l'observation du phénomène qu'il est convenu d'appeler "décrochage dynamique".

On peut cependant envisager, pour cette simulation, d'autres modes de mouvements propres du profil ; c'est ce qui a été fait à l'I.M.F.M. en liaison avec le Service Technique de l'Aéronautique. Dans les études entreprises à l'I.M.F.M. depuis 1971, le profil placé à incidence fixe dans un courant uniforme est animé d'un mouvement d'oscillation harmonique propre, soit parallèle (tamis), soit normal (pilonnement), à l'écoulement non perturbé.

Depuis 1971, l'effort a principalement porté sur l'étude des effets instationnaires lorsque le mouvement est de tamis. Ce mémoire rend compte uniquement de cette étude qui est maintenant très complète et qui a conduit à l'observation du phénomène que nous avons appelé "recollement dynamique", par opposition à la dénomination "décrochage dynamique" dans le cas où le mouvement propre du profil est de tangage.

Un premier mémoire présenté en 1972 au Colloque A.G.A.R.D. sur l'Aérodynamique des voilures tournantes (Réf. 21) a fait état de mesures du torseur des forces aérodynamiques (P, T, M) sur le profil NACA 0012 à faible incidence et faibles amplitudes et fréquences réduites. Les effets instationnaires, dans ce cas, sont sensibles mais faibles.

Les résultats de nouvelles mesures de P, T, M sur ce même profil à $i = 16°$ ont été exposés à Tucson (Réf. 22) en 1975 ainsi que les premières mesures de frottement pariétal. Bien que l'amplitude réduite λ n'ait pas dépassé 0,26, les mesures d'efforts et de frottement ont mis en évidence le rattachement de la couche limite sur l'extrados du profil, sur la totalité de la période, rattachement qui pouvait même subsister un certain temps après que le mouvement propre du profil ait été arrêté.

Enfin en Septembre 1975 et en Septembre 1976, trois nouveaux mémoires (Réf. 23, 24, 25) ont été présentés qui rendent compte de nouvelles mesures effectuées à grande incidence et grande amplitude réduite pour λ/k constant et égal à 1,13, mesures qui mettent en évidence le recollement de la couche limite sur une partie de la période.

Depuis cette époque, des essais très complets ont été effectués ; ils comportent, toujours pour le même profil NACA 0012 les mesures instantanées d'une part et moyennes sur la période d'autre part, des grandeurs globales et locales. Ainsi les mesures d'efforts (P, T, M), de pression et de frottement pariétal en des points de la surface du profil à différents x/c (à partir du bord d'attaque jusqu'à $x/c = 0,8$), ont été réalisées pour un domaine très étendu de variation de l'incidence, de la fréquence et de l'amplitude réduites.

On a acquis ainsi, une connaissance approfondie du phénomène de recollement dynamique,ce qui a permis d'établir un parallèle entre les phénomènes observés sur la portion de la période où le recollement disparait, avec ceux observés dans le décrochage dynamique, lorsque le mouvement propre du profil est de tangage. En fait, on observe dans les deux cas, à certains instants de la période, des coefficients de portance très supérieurs au coefficient de portance maximal en régime stationnaire. Ce phénomène est dû à la propagation d'un tourbillon sur l'extrados du profil.

Il y a une analogie très frappante entre les phénomènes observés dans les deux cas de mouvement propre tamis et tangage, de sorte que le comportement instationnaire d'un profil peut être étudié valablement en mouvement de tamis, ce qui présente de grands avantages aussi bien théoriques qu'expérimentaux.

2. MONTAGES

2.1. Soufflerie, dispositif d'oscillation et conditions d'essais

Les essais ont été réalisés dans la soufflerie à refoulement de veine rectangulaire 0,5 x 1 m^2 et à faible intensité de turbulence (< 0,5 %). La vitesse de l'écoulement amont peut être réglée de 3 m/s à 20 m/s ce qui conduit à des nombres de Reynolds

Rey_c allant de 7.10^4 à 4.10^5. Le dispositif d'oscillation de la maquette déjà décrit en détail dans les références 21 et 23, permet d'obtenir des fréquences comprises entre 0,5 Hz et 5 Hz. L'amplitude du déplacement de la maquette peut varier de 0 à 17 cm. Ces conditions conduisent à faire varier λ et k dans les limites ci-dessous :

$$0 \leqslant \lambda \leqslant 1,2$$
$$0 \leqslant k \leqslant 1,2 \quad \lambda/k \text{ variable}$$
$$0 \leqslant \lambda/k \leqslant 1,13$$

La maquette est celle d'un profil symétrique NACA 0012 corde c = 30 cm, envergure : 49,5 cm.

Les dimensions de la chambre d'expérience permettent de faire varier l'incidence de la maquette de 0° à 25° et par suite d'atteindre des incidences largement supérieures à l'incidence de décrochage stationnaire qui se situe aux environs de 12°.

2.2. Equipements de mesure

2.2.1. Torseur des forces aérodynamiques (P, T, M)

Les mesures instantanées du torseur des forces aérodynamiques (P, T, M) ont été effectuées à l'aide de torsiomètres qui ont déjà fait l'objet d'une description détaillée dans les références 21 et 25.

2.2.2. Pression statique p à la paroi du profil

Les mesures de la pression statique le long de la corde du profil ont été réalisées à l'aide de capteurs différentiels semi-conducteurs du type Kulite embarqués dans la maquette (voir montage dans les références 23 et 24). Le type de capteur choisi (CQH 125) est le plus sensible de la gamme des capteurs Kulite (de l'ordre de $2.5\ 10^{-3}$ mV/Pa). Il est équipé d'un module de compensation de température. Les fréquences de 1 à 5 Hz du phénomène étudié étant faibles devant la fréquence propre des capteurs et l'insensibilité de ces capteurs aux accélérations, ont conduit à conserver l'étalonnage statique pour les mesures en régime dynamique.

2.2.3. Tension de cisaillement τ

Les jauges utilisées, dont le principe de fonctionnement est identique à celui utilisé en anémométrie à film chaud, ont été réparties aux mêmes abscisses en corde que les capteurs de pression. (Voir détail dans les références 22 et 23). Le temps de réponse, comparable à celui de jauges existant dans le commerce, est de l'ordre de quelques μ secondes. La méthode de dépouillement employée permet d'obtenir le rapport de la tension de cisaillement instationnaire τ à la valeur correspondante en régime stationnaire τ_{st} à partir des voltages recueillis aux bornes de la jauge par la relation :

$$\tau/\tau_{st} = \left[\frac{E_{inst}^2 - E_o^2}{E_{st}^2 - E_o^2}\right]^3$$ où E_o désigne la tension à vent nul, E_{st} et E_{inst} les voltages en régimes stationnaire et instationnaire.

3. METHODE DE DEPOUILLEMENT DES SIGNAUX

Les tensions électriques délivrées par les détecteurs de mesures globales ou locales décrits au §.2, sont recueillies dans un centralisateur de mesure (Intertechnique DIDAC 800).

Ces tensions numérisées puis stockées sur 800 canaux peuvent être directement soumises, de la part du centralisateur, à des opérations numériques avant de sortir sur bandes perforées exploitables par ordinateur.

Les valeurs sont ensuite décomposées en série de Fourier, et il est alors tenu compte des corrections en amplitude et en phase que nécessite l'utilisation des filtres et des capteurs dans la chaine de mesure.

Si G représente la valeur numérisée obtenue après ces corrections (effort, pression, etc...) et G_S la valeur numérisée correspondant au régime stationnaire, G/G_S est décomposée en série de Fourier suivant la forme :

$$G/G_S = Co + \sum_1^n C_n \cos (n\,\omega\, t + \phi n)$$

Le terme Co représente donc la valeur moyenne sur la période de la quantité G rapportée à sa valeur stationnaire G_S.

Le top de synchronisation initiant chaque période d'enregistrement est tel que la vitesse relative V de la maquette par rapport à la vitesse V_∞ s'écrit :

$$V/V_\infty = 1 + \lambda \cos \omega t \quad ,$$

ainsi les angles ϕn représentent les déphasages des différents harmoniques des quantités G/G_S par rapport à la vitesse relative de la maquette.

4. RESULTATS ET DISCUSSION

4.1. Influence de λ, k, i et Rey_c sur le torseur (P, T, M)

Comme il a déjà été montré dans les références 23, 25 les effets instationnaires provoquent sur l'aile placée à incidence très supérieure à l'incidence de portance maximale en régime stationnaire, un effet hypersustentateur mettant en évidence un rapport de la portance moyenne au cours d'un cycle $\overline{P_{inst}}$ à la portance stationnaire P_{stat} supérieur à 1. Ces effets sont aussi ressentis sur la traînée et le moment de tangage comme le montrent les figures 1, 2, 3. Ces résultats sont relatifs à une valeur constante du rapport $\lambda/k = 1{,}13$. Depuis, le domaine des mesures a été étendu à des valeurs de λ/k variables, et en ce qui concerne le rapport $Co = \overline{P_{inst}}/P_{stat}$ il a été possible de synthétiser les résultats obtenus àl'aide des formules empiriques suivantes :

$$Co = 1 + A(i) \left(\frac{\lambda}{k}\right)^{\alpha} . k^2 \left[1 - B(i)\, k. \left(\frac{\lambda}{k}\right)^{C(\lambda/k)}\right] \tag{1}$$

avec

Si $i \leq i_D$: $A(i) = 0{,}782(i/i_D)$; $\alpha = 4$; $B(i) = 0{,}2$; $C(\lambda/k) = 5$

et

Si $i \geq i_D$:

$$\left| \begin{array}{l} A(i) = 4 + 0{,}6\,(i/i_D) \quad ; \alpha = 1 \\ B(i) = 0{,}558 + 0{,}432\,\left|2{,}17 - (i/i_D)\right|^3 \\ C(\lambda/k) = 0{,}422 - 0{,}55\,(\lambda/k) \end{array} \right.$$

où i_D désigne l'incidence de décrochage en régime stationnaire. On constate en particulier sur ces relations que λ et k interviennent sous forme de produits des paramètres λ/k et k.

On a représenté sur la fig. 4 à titre d'exemple les résultats d'essai obtenus à i = 20° et la courbe déduite de la relation précédente concernant la variation de Co en fonction de k, pour différentes valeurs du paramètre λ/k. Il est à noter que dans la gamme des vitesses relatives à ces essais, l'influence de Rey_c peut être négligée comme le montre le regroupement des points obtenus à des mêmes k et λ/k, mais pour des Rey_c différents.

Les valeurs de P_{inst}/P_{stat} ont été décomposées en série de Fourier suivant la formule donnée au §.3 pour différentes incidences (6°, 12°, 20°) et différentes valeurs deλ/k. Les figures (5,6,7) représentent le résultat de l'analyse du premier harmonique (C_1,ϕ_1) dans le diagramme $C_1 \cos \phi_1$; $- C_1 \sin \phi_1$. Pour des incidences inférieures ou égales à i_D (6° et 12°), le déphasage ϕ_1 qui apparait pour $\lambda = 0{,}23$ est fonction croissante de λ, fonction lentement décroissante de λ/k et atteint environ 40° pour $\lambda = 1{,}16$ et $\lambda/k = 1{,}13$ (fig. 5 et 6). Par contre, on observe des fortes variations du déphasage ϕ_1 (i = 20°, fig. 7) qui peut atteindre 80° à $\lambda = 1$ et $\lambda/k = 1{,}13$. Il est à noter dans ce cas que l'amplitude C_1 passe par un maximum d'autant plus grand que λ/k est grand. La phase de ce maximum décroît avec λ/k.

Les variations de l'harmonique 2 (C_2,ϕ_2) de P_{inst}/P_{stat} dans le diagramme $C_2 \cos \phi_2$; $- C_2 \sin \phi_2$ sont représentées sur la figure 8 pour i = 20°. L'amplitude C_2 demeure dans tous les cas inférieure à 0,7 et donc toujours inférieure à C_1. Contrairement à ϕ_1, la variation de la phase ϕ_2 est très importante puisqu'elle peut atteindre 360°. Ce maximum de phase peut être atteint pour des λ d'autant plus faibles que λ/k est faible.

De plus, il est à remarquer que l'influence de Rey_c peut être également négligée sur les harmoniques 1 et 2, comme le montre le regroupement des points relatifs à des mêmes λ et λ/k mais obtenus à des nombres de Reynolds différents (figures 7 et 8).

Une analyse analogue à celle effectuée sur la portance et concernant le premier harmonique (C_1,ϕ_1) de T_{inst}/T_{stat} et M_{inst}/M_{stat} pour i = 6°, 12°, 16°, 18°, 20° et λ/k = cte = 1,13 est représentée sur les figures 9 et 10.

Les résultats relatifs à la trainée (fig. 9) font apparaître une analogie d'allure avec les variations (C_1, ϕ_1) de la portance, montrant toutefois une amplitude C_1 inférieure à celle de la portance (voir figures 7 et 9).

L'évolution de C1 et ϕ_1 dans le cas de M_{inst}/M_{stat} (fig. 10) met en évidence des fortes variations de phase et d'amplitude ($0 \leq \phi_1 \leq 360°$ et $0 \leq C_1 \leq 7$).

Il ressort des figures 5 à 7 pour P_{inst}/P_{stat} et 9 pour T_{inst}/T_{stat} que lorsque l'incidence est inférieure ou égale à i_D, la phase ϕ_1 demeure pratiquement constante et faible dans les domaines de λ et λ/k considérés. Par contre pour ces mêmes incidences et en ce qui concerne le moment, la figure 10 fait apparaître des variations de ϕ_1 importantes. Lorsque l'incidence est supérieure à i_D la phase ϕ_1 de P_{inst}/P_{stat}, T_{inst}/T_{stat} et M_{inst}/M_{stat} varie fortement avec λ. (Fig. 7, 9, 10)

A partir des résultats précédents, l'influence des paramètres λ, k, i et Rey_c a également pu être analysée directement en fonction du temps. Il a été ainsi possible d'effectuer une comparaison entre les valeurs instantanées des rapports P_{inst}/P_{stat}, T_{inst}/T_{stat} et M_{inst}/M_{stat} et les valeurs quasi-stationnaires de ces mêmes rapports aux mêmes incidences. Ces valeurs quasi-stationnaires sont identiques pour ces trois rapports et égales en fait à $(1 + \lambda \cos \omega t)^2$. Une discussion plus approfondie de l'évolution du torseur aérodynamique en fonction du temps est effectuée au § 4.2 dans le cas particulier de $i = 20°$, $\lambda = 0{,}74$, $\lambda/k = 1{,}13$, $Rey_c = 0{,}714.10^5$.

Néanmoins, on constate d'une façon générale que les courbes des valeurs instantanées sont pratiquement confondues avec la courbe $y = (1 + \lambda \cos \omega t)^2$, aussitôt que λ et k atteignent des niveaux suffisamment faibles (λ inférieur à 0,26 et k inférieur à 0,23).

Autrement dit, les valeurs instantanées de P, T et M sont pratiquement égales aux valeurs quasi-stationnaires de ces mêmes grandeurs dès que λ est inférieur à 0,26 et k inférieur à 0,23 ; les effets instationnaires sont donc à peine visibles dans ces conditions.

Par contre, pour λ et k supérieurs respectivement à 0,26 et 0,23, les effets instationnaires sont très marqués ; en particulier, pour des incidences supérieures à l'incidence de décrochage stationnaire, les oscillations de tamis provoquent un effet favorable hypersustentateur de l'aile (réf. 23, 25). Cet effet hypersustentateur moyen est d'ailleurs bien confirmé par les enregistrements de la pression statique sur le profil. A titre d'exemple, la figure 11 obtenue pour $i = 20°$, $\lambda = 0{,}74$ et $\lambda/k = 1{,}13$, compare la répartition du C_p moyen en régime instationnaire avec celle obtenue en régime stationnaire et met en évidence le gain moyen de portance (de l'ordre de 2,1). La figure 12 obtenue dans les mêmes conditions de λ et k à 6° fait apparaître au contraire un faible gain de portance (1,15) attestant les faibles effets instationnaires à faible incidence.

L'effet hypersustentateur observé à forte incidence s'accompagne d'un fort moment piqueur, et d'un accroissement marqué de la traînée moyenne comme on a déjà pu le remarquer sur les fig. 2 et 3. Une conséquence de ces effets instationnaires marqués sur le torseur aérodynamique (P, T, M) se retrouve également sur la fig. 13, qui représente la distribution locale du rapport de la tension de cisaillement moyenne ($\bar{\tau}$) à sa valeur locale stationnaire (τ_{stat}), le long de la corde du profil. On constate sur cette figure une augmentation du rapport $\bar{\tau}/\tau_{stat}$, d'autant plus forte que l'incidence est forte, alors que sur l'intrados, pour $i = 6°$ comme pour $i = 20°$, aucun accroissement notable du frottement n'est visible, exception faite de 6° à $x/c = 0{,}6$, abscisse à partir de laquelle doit se produire la transition de la couche limite.

Afin d'analyser plus finement les phénomènes observés, il a été procédé à des visualisations qui ont été confrontées aux mesures locales instantanées de pression statique et de frottement pariétal le long de la corde du profil ainsi qu'aux valeurs globales instantanées du torseur des forces aérodynamiques.

4.2. Visualisations et interprétation du phénomène dynamique

Les photographies instantanées de l'écoulement au-dessus de l'extrados du profil prises au 1/1000 de seconde, à différentes phases de la période, par application de la méthode des fumées, révèlent d'une façon satisfaisante à grande incidence (planche 14) la nature de l'écoulement dans la couche limite et la formation des tourbillons.

La comparaison de la photo (ST.), en bas à droite qui représente la configuration de l'écoulement en régime stationnaire à $i = 20°$, $Re_c = 0{,}714.10^5$ avec les instantanés réalisés à différentes phases de la période pour $\lambda = 0{,}74$ et $\lambda/k = 1{,}13$, montre que la couche limite se rattache sur l'extrados du profil, puis décolle fortement par un mécanisme d'éclatement de la bulle de bord d'attaque accompagnée d'un détachement de tourbillons. Le diagramme situé à gauche de la planche 14 permet de suivre l'évolution de la maquette, sa vitesse, et son accélération au cours d'un cycle.

De façon à établir chronologiquement les correspondances qui existent entre l'évolution de la configuration de l'écoulement sur l'extrados du profil au cours de la période et l'évolution du torseur instantané (P, T, M), des distributions de pression statique C_p, et de frottement pariétal τ/τ_{stat} instantanées, il a été sélectionné cinq instants particuliers de la période ($3\pi/2$; $1{,}76\pi$; $1{,}9\pi$; $0{,}2\pi$; $0{,}74\pi$) qui font l'objet des planches (15, 16, 17, 18, 19).

a) $\omega t = 3\pi/2$ (planche 15)

La visualisation de la planche 15, montre que la couche limite commence à se rattacher sur l'extrados du profil à cet instant, tandis que le profil va amorcer sa marche à contre courant. La vitesse relative est celle de l'écoulement amont et son accélération maximale est égale à $A\omega^2$. Le rattachement de la couche limite se produit jusqu'à $x/c = 0,5$, il y a au-delà écoulement de retour et séparation de la couche limite.

La portance prend alors une valeur très voisine de celle qui correspondrait à un régime quasi-stationnaire, elle est donc très voisine de celle qui correspond au régime stationnaire. Il en est de même pour la traînée et pour le moment de tangage.

La valeur du gradient de pression instationnaire (Réf. 25) obtenue à $x/c=0,1$ par un calcul tenant compte de l'effet de la traînée tourbillonnaire montre qu'à cet instant $(dp/dx)/(dp/dx)_{qs}$ est inférieur à 1 et que par conséquent le gradient de pression instationnaire est favorable à un recollement de la couche limite.

La distribution des pressions statiques confrontée à la distribution stationnaire montre qu'à cet instant une dépression marquée est rétablie sur l'extrados indiquant un début de recollement de la couche limite.

En ce qui concerne la distribution de τ/τ_{stat}, on constate un accroissement global de ce rapport sur tout l'extrados montrant qu'en aucun point du profil le frottement stationnaire n'est atteint, ce qui peut être attribué à un début de recollement de la couche limite.

b) $\underline{3\pi/2 < \omega t < 1,9\pi}$ (planche 16)

Pour cette fraction de la période, le profil poursuit sa marche en avant avec une vitesse accrue ($0,8\ A\omega$ pour $\omega t = 1,83\pi$), la couche limite devient attachée sur toute l'étendue de l'extrados du profil.

La portance devient supérieure à la courbe quasi-stationnaire. La traînée croît en demeurant inférieure à la valeur quasi-stationnaire qu'elle n'atteindra que vers $\omega t = 0,1\pi$. Le moment de tangage devient positif, c'est-à-dire qu'il est cabreur lorsque l'écoulement sur l'extrados est rattaché.

Le gradient de pression théorique dans cette fraction de la période est toujours favorable au recollement, et la dépression présente sur l'extrados est devenue plus importante qu'à $\omega t = 3\pi/2$ indiquant ainsi un recollement plus complet de la couche limite sur l'extrados.

L'accroissement de τ/τ_{st} est également plus important qu'à $\omega t = 3\pi/2$.

c) $\underline{1,9\pi < \omega t < 0,3\pi}$ (planches 17, 18)

La photographie de la planche 17 ($\omega t = 1,9\pi$) montre qu'à cette phase un écoulement de retour s'amorce dans la couche limite jusqu'à $x/c = 0,5$ et que se forme sur la partie avant du profil précisément jusqu'à la même abscisse une bulle de décollement laminaire. On notera d'ailleurs que l'écoulement de retour dans la couche limite à l'arrière du profil, ne s'accompagne pas de la séparation de la couche limite, caractère qui différencie le décollement en régime dynamique du décollement en régime stationnaire. L'accélération est alors égale à $0,3\ A\omega^2$ environ, tandis que la vitesse du profil est très voisine de son maximum.

La courbe de portance commence à se détacher du régime quasi-stationnaire, la traînée comme le moment de tangage croissent fortement dans cette zone vers leur maximum.

Le gradient de pression théorique est toujours favorable. La dépression sur l'extrados est maintenue à un niveau élevé comme le montre la distribution des C_p.

Sur la planche 18, ($\omega t = 0,2\pi$), la photographie montre un éclatement de la bulle de décollement de bord d'attaque et la formation d'un tourbillon qui se propage sur l'extrados du bord d'attaque vers le bord de fuite.

Pour $0,2\pi < \omega t < 0,3\pi$, la portance et la traînée passent par un maximum nettement accusé pour $\omega t = 0,25\pi$, et le moment atteint un premier maximum vers $\omega t = 0,3\pi$.

Le gradient de pression théorique commence à devenir défavorable, et la dépression sur l'extrados commence à décroître sensiblement.

La distribution du rapport τ/τ_{stat} fait apparaître deux pics marqués à $x/c = 0,2$ et $x/c = 0,6$ qui peuvent être attribués à l'éclatement de la bulle et à la formation de tourbillons.

d) $\underline{0,3\pi < \omega t < 3\pi/2}$ (planche 19)

Lorsque ωt varie entre $0,3\pi$ et $3\pi/2$, portance et traînée décroissent en fluctuant et en se rapprochant de leur valeur en régime stationnaire, qu'elles atteignent, ainsi qu'il a été dit plus haut, pour $\omega t \approx 3\pi/2$. Mais, ωt augmentant à partir de $0,3\pi$, le tourbillon qui résulte de l'éclatement de la bulle de bord d'attaque, atteint le bord de fuite et le dépasse. L'écoulement sur l'extrados devient complètement séparé, et un deuxième tourbillon se forme au milieu de la corde, qui se propage vers le bord de fuite. La propagation de ce deuxième tourbillon explique les fluctuations de la portance et de la traînée entre $\omega t = 0,74\pi$ et $\omega t = 1,2\pi$ environ.

En ce qui concerne le moment, on remarque qu'il n'est positif, c'est-à-dire cabreur, que pour ωt compris entre $1,66\pi$ et $1,9\pi$, lorsque l'écoulement sur l'extrados est rattaché. Lorsque ωt est extérieur à cet intervalle, le moment est fortement piqueur et l'on observe sur la courbe deux maximums (en valeur absolue) l'un pour $\omega t = 0,3\pi$, l'autre pour $\omega t = \pi$. Le premier se produit lorsque le premier tourbillon atteint le bord de fuite du profil ; le deuxième doit se produire lorsque le deuxième tourbillon atteint le bord de fuite.

Le gradient de pression théorique redevient fortement défavorable, et la distribution de la pression de paroi présente un plateau sur l'extrados du profil ; la dépression, à cet instant de la période, est au minimum de sa valeur.

Le rapport τ/τ_{stat} met en évidence un pic très marqué à $x/c = 0,6$ et un pic plus atténué à $x/c = 0,2$ dûs à la présence de tourbillons sur l'extrados.

La propagation de ces tourbillons sur l'extrados de l'aile a pu être mise en évidence sur la figure 20 qui représente les enregistrements simultanés sur tous les capteurs de la variation de pression sur l'extrados et au cours de deux périodes. La vitesse de progression du tourbillon, d'après ces enregistrements est égale à 43 % de la vitesse relative obtenue à $\omega t = 2\pi$.

Sur la figure 21, qui représente l'enregistrement du frottement simultanément sur tous les capteurs, la perturbation qui apparait à $x/c = 0,12$ à la phase $\omega t = 300°$ (en accord avec l'apparition à la même abscisse de la perturbation en pression fig. 20), se propage vers le bord de fuite à une vitesse sensiblement identique à celle précédemment déterminée. On notera toutefois l'atténuation de la perturbation à $x/c=0,4$.

Les résultats obtenus dans les mêmes conditions sur l'intrados sont représentés en ce qui concerne τ/τ_{st} sur la figure 22 qui montre que la couche limite reste laminaire sur tout l'intrados et qu'aucune perturbation du type de celle observée sur l'extrados n'est visible. Les variations du frottement au déphasage près que fait ressortir les théories de couches limites laminaires (Réf. 2, 20), suivent l'évolution de la vitesse et oscillent autour de la valeur stationnaire comme on a déjà pu l'observer sur la figure 13.

5. ANALOGIE ENTRE LES MOUVEMENTS DE TAMIS ET DE TANGAGE

La comparaison des phénomènes observés précédemment, avec ceux observés dans le cas du profil NACA 0012 en mouvement de tangage (Réf. 16), met en évidence, ainsi qu'on va le voir, leur très étroite et frappante analogie. La seule différence réside dans le mécanisme de la séparation dynamique de l'écoulement sur l'extrados : dans le cas des essais effectués à l'I.M.F.M., lorsque l'oscillation propre est de tamis, la séparation dynamique est due à la formation et à l'éclatement d'une bulle de séparation au bord d'attaque, tandis que dans les essais effectués aux Etats-Unis, le mécanisme de séparation en oscillation de tangage est celui de séparation turbulente au bord d'attaque.

La planche (23) tirée de la réf. 16 représente la configuration correspondante des écoulements dans le cas du mouvement de tangage ($i = 15° + 10° \sin \omega t$) ; sont représentés également sur cette planche les variations du coefficient de force normale et du coefficient de moment en fonction de l'incidence. On remarque que lorsque l'incidence dépasse en croissant 23°, le coefficient de portance (ou plus exactement de la composante normale de la résultante aérodynamique), commence à croître plus vite que ne le prévoit la théorie en régime non décroché. Ce coefficient est maximal lorsque l'incidence en croissant, atteint 24°. Le décrochage de la portance se produit donc avant que l'incidence n'atteigne 25° ; le C_N passe ensuite par un premier minimum lorsqu'en décroissant l'incidence franchit 23°.

L'accroissement de la portance se produit en même temps que se propage le tourbillon formé au bord d'attaque, du bord d'attaque au bord de fuite. Le tourbillon a atteint le milieu de la corde lorsque le coefficient de force normale est maximal.

Par conséquent, en ce qui concerne cet aspect des phénomènes, il y a là analogie avec les phénomènes observés sur l'aile en mouvement de tamis, l'oscillation en incidence étant remplacée par l'oscillation en tamis.

En ce qui concerne le moment, celui-ci passe par un minimum négatif après l'époque du maximum de la portance (comme dans le mouvement de tamis) le tourbillon d'extrados a alors atteint le bord de fuite. Toutefois, l'on n'observe pas de nouveau minimum du coefficient de moment lorsque l'incidence passe par 15° (incidence moyenne) par valeurs décroissantes.

Le moment est cabreur aussitôt que l'incidence a dépassé 5° en croissant, tout comme dans le mouvement de tamis le moment devient cabreur, lorsque l'aile reprend son mouvement en avant après avoir atteint la position arrière extrême.

Dans les deux cas,de mouvement propre, la configuration de l'écoulement sur l'extrados est identique, recollement de la couche limite progressant du milieu de la corde vers le bord de fuite. Il faut toutefois insister sur ce recollement de la couche limite qui, dans le cas du mouvement de tangage, existe déjà en écoulement stationnaire pourvu que l'incidence soit suffisamment faible, alors que dans le cas du tamis le recollement que l'on observe à très forte incidence ne peut absolument pas se produire en écoulement stationnaire et doit être attribué à un effet purement instationnaire.

Il a aussi semblé intéressant de tenter d'établir un parallèle entre les répartitions de pression statique. Comme il a été vu dans le paragraphe précédent et dans les figures 11 à 19, la distribution de la pression sur l'extrados ne comporte en général pas de pic négatif au voisinage du bord d'attaque, sauf peut-être, à la phase 1,76π, lorsque la couche limite est rattachée. La distribution de la pression au voisinage du bord d'attaque est particulièrement plate dans l'intervalle de la période au cours duquel se propagent les tourbillons d'extrados.

Par contre, un pic négatif très prononcé est observé au voisinage immédiat du bord d'attaque, lorsque le mouvement propre est de tangage et l'incidence croissante, tant que l'écoulement de retour dans la couche limite sur l'extrados n'a pas atteint le bord d'attaque.

Le pic disparait aussitôt que se forme et se propage le tourbillon de bord d'attaque, tandis qu'incidence et portance vont en croissant. Le moment piqueur croît en valeur absolue et atteint une valeur maximale lorsque le tourbillon de bord d'attaque atteint le bord de fuite du profil ; le déplacement de ce tourbillon se traduit par la propagation d'un renflement dans la courbe de distribution de la pression, du bord d'attaque au bord de fuite.

La discussion effectuée précédemment montre qu'il peut être indiqué, dans le cas du mouvement de tamis, de représenter la portance et le moment par exemple, non plus en fonction de la phase mais plutôt en fonction du déplacement du profil en x/c.

C'est ce qui a été fait dans la figure 24 et la figure 25, respectivement pour la portance et le moment. Dans cette dernière, le moment, sous sa forme réduite a été porté vers le bas lorsqu'il est piqueur et vers le haut lorsqu'il est cabreur.

En ce qui concerne la courbe de portance, on observe une certaine parenté de forme avec la courbe de portance en tangage (pl. 23). On note en particulier la large boucle d'hysteresis apparent. Cependant, l'accroissement de la portance entre la phase 1,9π et 0,25π dans le mouvement de tamis, est beaucoup moins rapide que lorsque l'angle d'incidence, dans le mouvement de tangage, croît de 23° à 24°.

Il serait intéressant de faire des essais en tamis à $i = 25°$ de façon à se rapprocher des conditions correspondant à la planche 23 pour lesquelles la variation d'incidence s'écrit : $i = 15° + 10° \sin \omega t$.

On peut noter d'ailleurs que la comparaison avec le cas où l'incidence varie selon la loi : $i = 15° + 6° \sin \omega t$ n'est pas concluante. En effet, si l'on se rapporte à la figure 39 de la référence 16, le tourbillon d'extrados, dans ce cas, prend naissance seulement pour $i = 21°$, alors que l'incidence de l'aile commence à décroître. Il y a d'abord augmentation de portance, puis décrochage de sorte que l'on observe une boucle dans la courbe de portance.

Dans les essais en tamis, le tourbillon prend naissance avant que l'aile n'ait atteint sa position la plus avancée, de même que dans les essais en tangage à $i = 15° + 10° \sin \omega t$, où le tourbillon prend naissance avant que l'incidence n'ait atteint 25°.

En ce qui concerne la courbe des moments en tamis, l'allure est assez différente de celle observée lorsque le profil est en mouvement propre de tangage, le décrochage du moment dans le cas du tamis étant beaucoup moins brutal.

Il a été tenté en rapportant la composante normale de la force aérodynamique à sa valeur maximale au cours de la période et le moment à sa plus forte valeur maximale au cours de la période, de trouver une courbe unique à l'incidence 20°, représentative des trois valeurs différentes de λ, (0,74 ; 0,52 ; 0,37) (fig. 26).

On note que la courbe $\lambda = 0{,}37$ se différencie nettement des courbes $\lambda = 0{,}74$ et $\lambda = 0{,}52$, le moment ne devenant jamais cabreur lorsque $\lambda = 0{,}37$ autrement dit : pour $\lambda = 0{,}37$, il y a décrochage du moment sur toute l'étendue de la période. L'analyse effectuée à des incidences de 16°, 18° et 20° a montré qu'il existe une bonne ressemblance entre les courbes $(FN/FN_{max}, M/(M)_{max})$, pour $\lambda = 0{,}74$ et 0,52.

On a noté en particulier que les courbes $i = 20°$ et $i = 18°$, $\lambda = 0{,}74$ et 0,52, sont très sensiblement superposables, principalement autour des phases correspondant pour chacune d'elles, aux valeurs positives du moment (moment cabreur).

De sorte que l'on peut considérer que l'une de ces courbes, par exemple $i = 20°$, $\lambda = 0{,}74$ et 0,52 (fig. 26) est bien représentative du phénomène de recollement dynamique pour le profil NACA 0012.

Une telle représentation fait d'ailleurs ressortir un certain nombre de caractères particuliers.

Par exemple on voit que lorsque l'on fait décroître le maximum de la force normale, c'est-à-dire, par conséquent, le détachement du premier tourbillon d'extrados, se produit pour une position du profil de plus en plus proche de sa position moyenne.

D'autre part, si pour $\lambda = 0{,}74$, le plus grand maximum (en valeur absolue), du moment, se produit toujours lorsque dans son mouvement rétrograde le profil passe par sa position moyenne, par contre lorsque λ est inférieur à 0,74, le deuxième maximum est, pour certaines incidences, inférieur au premier. C'est le cas pour les trois incidences considérées pour $\lambda = 0{,}37$. La grandeur,(en valeur absolue) du maximum est liée à l'intensité du tourbillon, qui en est la cause. C'est dire, par exemple, que pour $i = 20°$ et $\lambda = 0{,}74$, le deuxième tourbillon est plus intense que le premier.

6. CONCLUSION

Les caractères principaux du phénomène de recollement dynamique sur le profil NACA 0012, en mouvement propre de tamis à grande incidence, dans un écoulement uniforme, ont bien été étudiés qualitativement et quantitativement, grâce aux mesures effectuées, du torseur des forces aérodynamiques globales (P, T, M) des distributions de la pression et de la tension de cisaillement et grâce aux visualisations de l'écoulement sur l'extrados du profil aux différents instants de la période.

Les résultats obtenus sur l'effet hypersustentateur ont conduit à représenter le gain de portance moyen $Co = \overline{P_{inst}}/P_{stat}$ par une formule empirique faisant intervenir les paramètres λ, k et i, l'effet du nombre de Reynolds pouvant être négligé dans la gamme de vitesse envisagée ici. Les effets instationnaires ont également pu être évalués sur les rapports T_{inst}/T_{stat} et M_{inst}/M_{stat} en fonction de ces mêmes paramètres.

Par ailleurs, l'analyse des mesures et des visualisations fait apparaître une similitude entre les phénomènes observés, et ceux observés dans le décrochage dynamique, lorsque le mouvement propre du profil est de tangage. En particulier, l'accroissement remarquable de la portance, au-delà des valeurs qui peuvent être atteintes en régime stationnaire, est dû à la propagation sur l'extrados du profil d'un tourbillon, du bord d'attaque au bord de fuite.

Dans le cas du mouvement de tamis, ce tourbillon se forme et se propage, tandis que le profil achève son mouvement à contre courant,avec une vitesse tendant vers zéro. Dans le cas du mouvement de tangage, le tourbillon se forme et se propage tandis que l'incidence croissante se rapproche de son maximum avec une vitesse tendant vers zéro.

Dans les deux cas, le décrochage du moment se produit chronologiquement avant le décrochage de la portance. Dans les deux cas, on observe la propagation de deux tourbillons sur l'extrados, le premier, ainsi qu'il a été dit plus haut, prenant naissance au bord d'attaque, tandis que le second prend naissance en plein régime de décrochage (mouvement rétrograde du profil ou incidence décroissante), à l'abscisse 0,5c.

Une différence importante doit être notée cependant ; elle concerne la nature de l'écoulement durant le recollement de la couche limite. En effet dans le cas du mouvement en tangage, la maquette passe par des incidences suffisamment faibles pour atteindre un recollement que l'on pourrait observer également en régime stationnaire. Alors que dans le mouvement de tamis, la maquette oscillant a une incidence fixe et très supérieure à l'incidence de décrochage, le recollement dynamique conduit à une couche limite purement instationnaire.

REFERENCES

1. THEODORSEN, T. "General Theory of Aerodynamic Instability and the Mechanism of Flutter" NACA Report 496, 1935.
2. LIGHTHILL, M.J. "The Response of Laminar Skin Friction and Heat Transfer to Fluctuations in the Stream Velocity" Proc. Royal Society. Series A, Vol.224, pp.1-23, June 1954.
3. McCROSKEY, W.J. "Inviscid Flow Field of an Oscillating Airfoil" J. AIAA, Vol. 11, N° 8, pp.1130-1137, Aug. 1973.
4. HAM, N.D. and GARELICK, M.S. "Dynamic Stall Considerations in Helicopter Rotors" J. Am. Helicopter Soc., Vol. 13, N° 2, pp.49-55, April 1968.
5. CRIMI, P. and REEVES, B.L. "A Method for Analyzing Dynamic Stall" NASA CR-2009, May 1972 ; also AIAA Paper 72-37.
6. PATEL, V.C. and NASH, J.F. "Unsteady Turbulent Boundary Layers with Flow Reversal, Unsteady Aerodynamics" Vol. 1, Univ. of Arizona (R.B. Kinney, ed.), 1975.
7. NASH, J.F., CARR, L.W. and SINGLETON, R.E. "Unsteady Turbulent Boundary Layers in Two-Dimensional Incompressible Flow" J. AIAA, Vol.13, N° 2, Feb. 1975, pp.167-173.
8. DWYER, H.A. "Calculation of Unsteady and Three-Dimensional Boundary Layer Flows" J. AIAA, Vol.11, N°6, pp.773-774, June 1973 ; also AIAA Paper 72-109.
9. McCROSKEY, W.J. "Recent Developments in Rotor Blade Stall" AGARD Conference Proceedings N° 111 on Aerodynamics of Rotary Wings, Paper N° 15, Sept. 1972.

10. PHILIPPE, J.J. and SAGNER, M. "Calcul et mesure des forces aérodynamiques sur un profil oscillant, avec et sans décrochage", AGARD Conference Proceedings N° 111 on Aerodynamics of Rotary Wings, Paper N° 11, Sept. 1972.
11. MARTIN, J.M., EMPEY, R.W., McCROSKEY, W.J. and CARADONNA, F.X. "An Experimental Analysis of Dynamic Stall on an Oscillating Airfoil" J. am. Helicopter Soc. Vol.19, N°1, Jan. 1974.
12. KARLSSON, S.K.F. "An Unsteady Turbulent Boundary Layer", J. Fluid Mechanics, Vol.5, pp. 622-636, 1959.
13. McCROSKEY, W.J. and DURBIN, E.J. "Flow Angle and Shear Stress Measurements Using Heated Films and Wires" ASME J. Basic Engr. Vol. 94, N° 1, pp.46-52, March 1972.
14. PARKER, A.G. "Force and Pressure Measurements on an Airfoil Oscillating through Stall" J. Aircraft, Vol.13, n° 10, October 1976, pp.823-827.
15. ZOLAN, J.J. "Dynamic Stall on Airfoils in Oscillating Flow" Master of Sciences in Mechanical Engineering. Illinois Institute of Technology, May 1976.
16. CARR, L.W., McALISTER, K.W. and McCROSKEY, W .J. "Analysis of the Development of Dynamic Stall Based on Oscillating Airfoil Experiments" NASA TN D 8382, January 1977.
17. SEARS, W.R. and TELIONIS, D.P. "Unsteady Boundary Layer Separation" IUTAM Symposium on Unsteady Boundary Layers, Quebec 1971.
18. WILLIAMS III, J.C., JOHNSON, J.D. "Semi-Similar Solutions to Unsteady Boundary Layer Flows Including Separation" J. AIAA, N°12, 1974, pp.1427-1429.
19. TELIONIS, D.P. "Calculations of Time-Dependent Boundary Layers" Proc. Univ. Ariz./ USAF - Symposium on Unsteady Aerodynamics, Kinney R.B. Editor, Tucson, 1975.
20. McCROSKEY, W.J. and PHILIPPE, J.J. "Unsteady Viscous Flow on Oscillating Airfoils", AIAA Paper N° 74-182, February 1974.
21. VALENSI, J. et REBONT J. "Efforts aérodynamiques sur un profil d'aile animé d'un mouvement harmonique parallèle à l'écoulement - Mouvement de tamis" Congrès AGARD 13/15 Septembre 1972, Marseille.
AGARD Conference Proceedings N° 111 - Aerodynamics of Rotary Wings.
22. MARESCA, C., REBONT, J. et VALENSI, J."Separation and Reattachment of the Boundary Layer on a Symmetrical Aerofoil" Proc. Univ. Ariz./USAF - Symposium on Unsteady Aerodynamics Kinney R.B. Editor, Tucson, 1975.
23. REBONT. J., MARESCA, C., GUILLERMINET, A. et FAVIER,D. "Etude expérimentale relative à l'aérodynamique d'un rotor d'hélicoptère en vol de translation : simulation en écoulement plan des effets dûs aux variations cycliques du vecteur vitesse", 12ème Colloque d'Aérodynamique Appliquée ENSMA-CEAT, Poitiers, Septembre 1975.
24. MARESCA, C., REBONT, J., GUILLERMINET, A. et FAVIER, D."Mesures instationnaires sur un profil d'aile animé d'un mouvement harmonique parallèle à l'écoulement non perturbé" 2ème Congrès Français de Mécanique, Toulouse, Septembre 1975.
25. MARESCA, C., REBONT, J. et VALENSI, J., "Caractéristiques d'un profil d'aile en mouvements instationnaires" 14th International Congress of Theoretical and Applied Mechanics,Delft, September 1976.

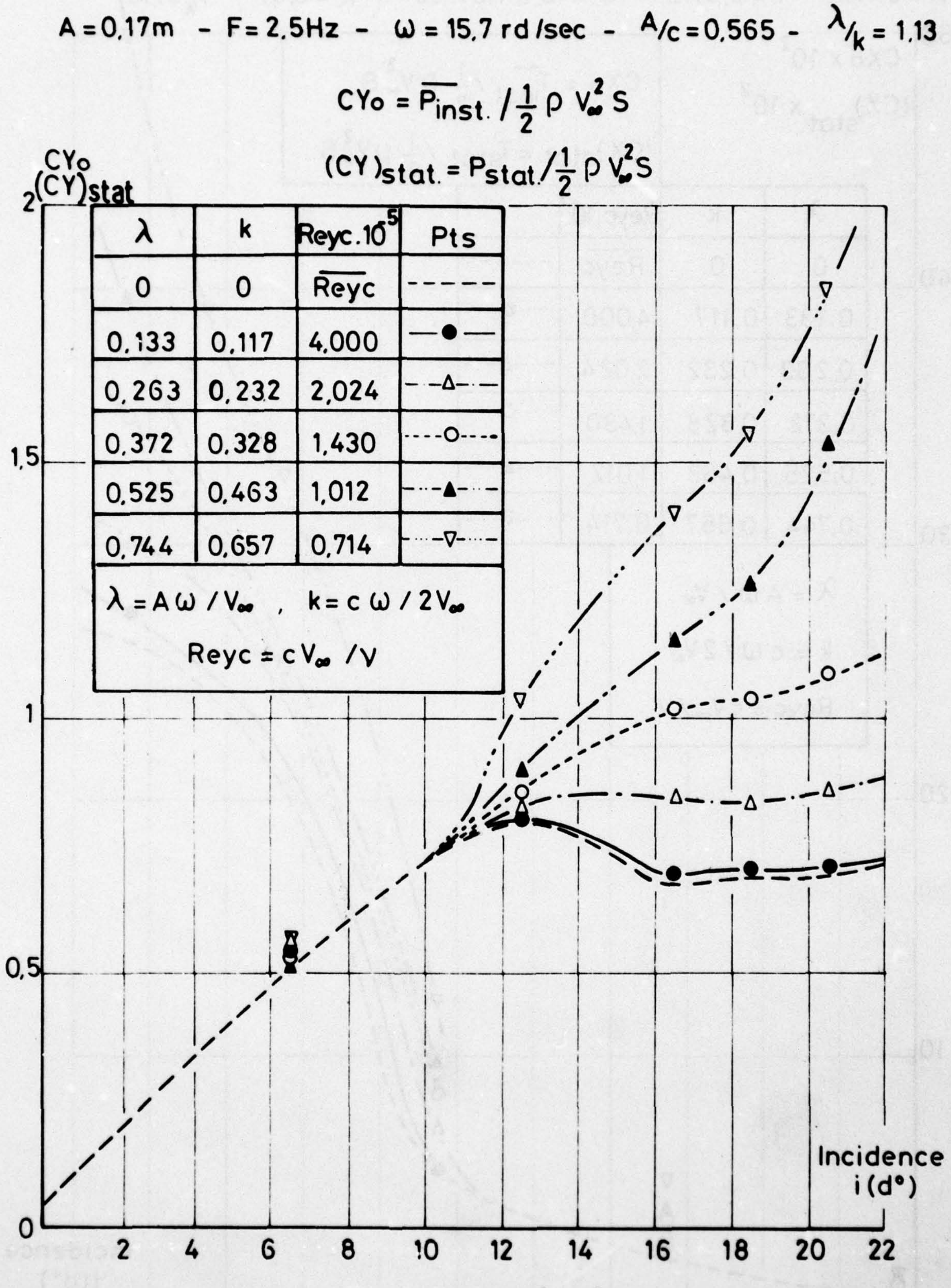

Figure 1 : Variation de $CY_o = \overline{Pinst}/\frac{1}{2}\ \rho\ V_\infty^2\ S$ avec l'incidence i et à λ/k = 1.13.

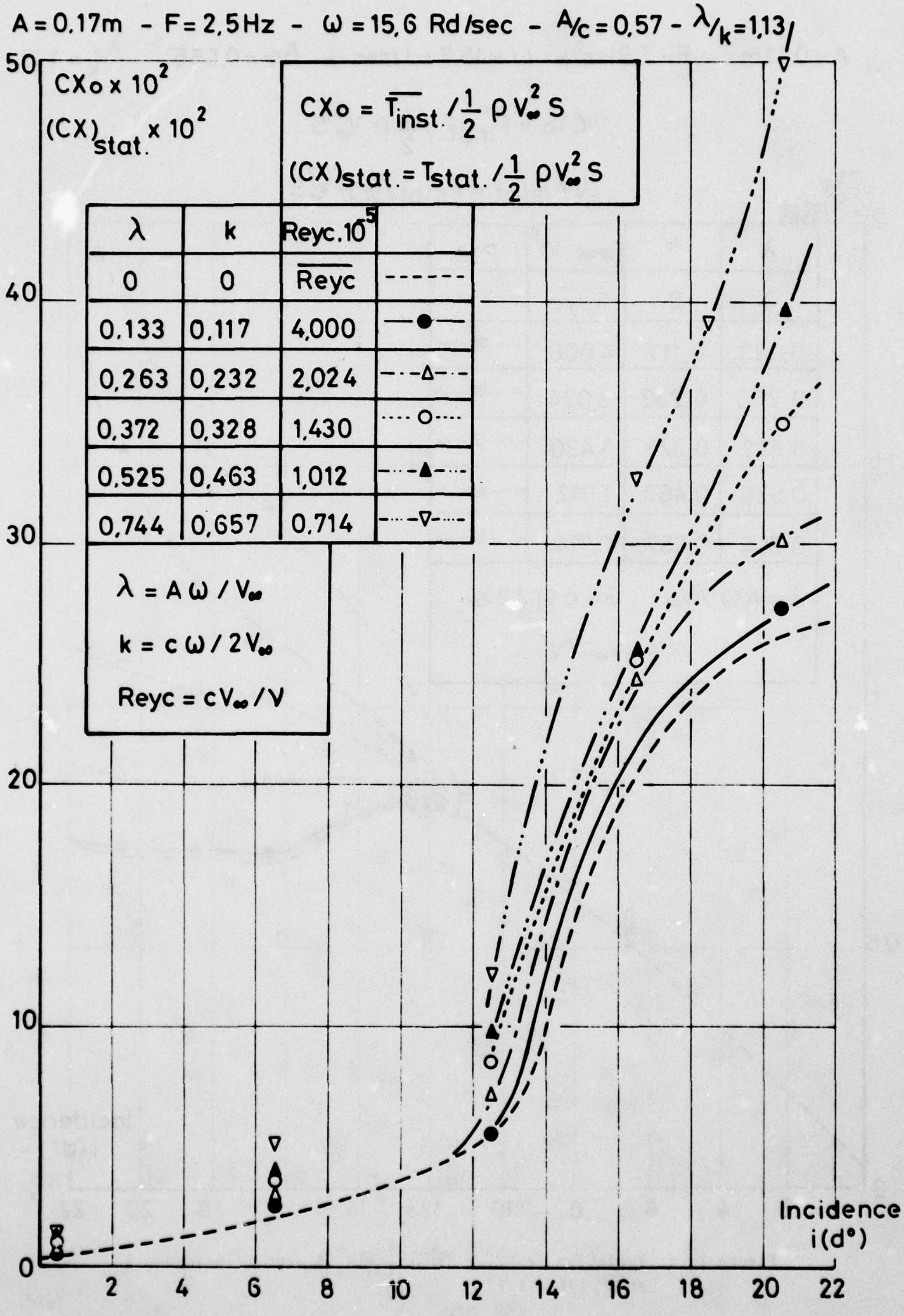

Figure 2 : Variation de $CX_0 = \overline{Tinst}/\frac{1}{2}\,\rho\,V_\infty^2\,S$ avec l'incidence i et à $\lambda/k = 1.13$.

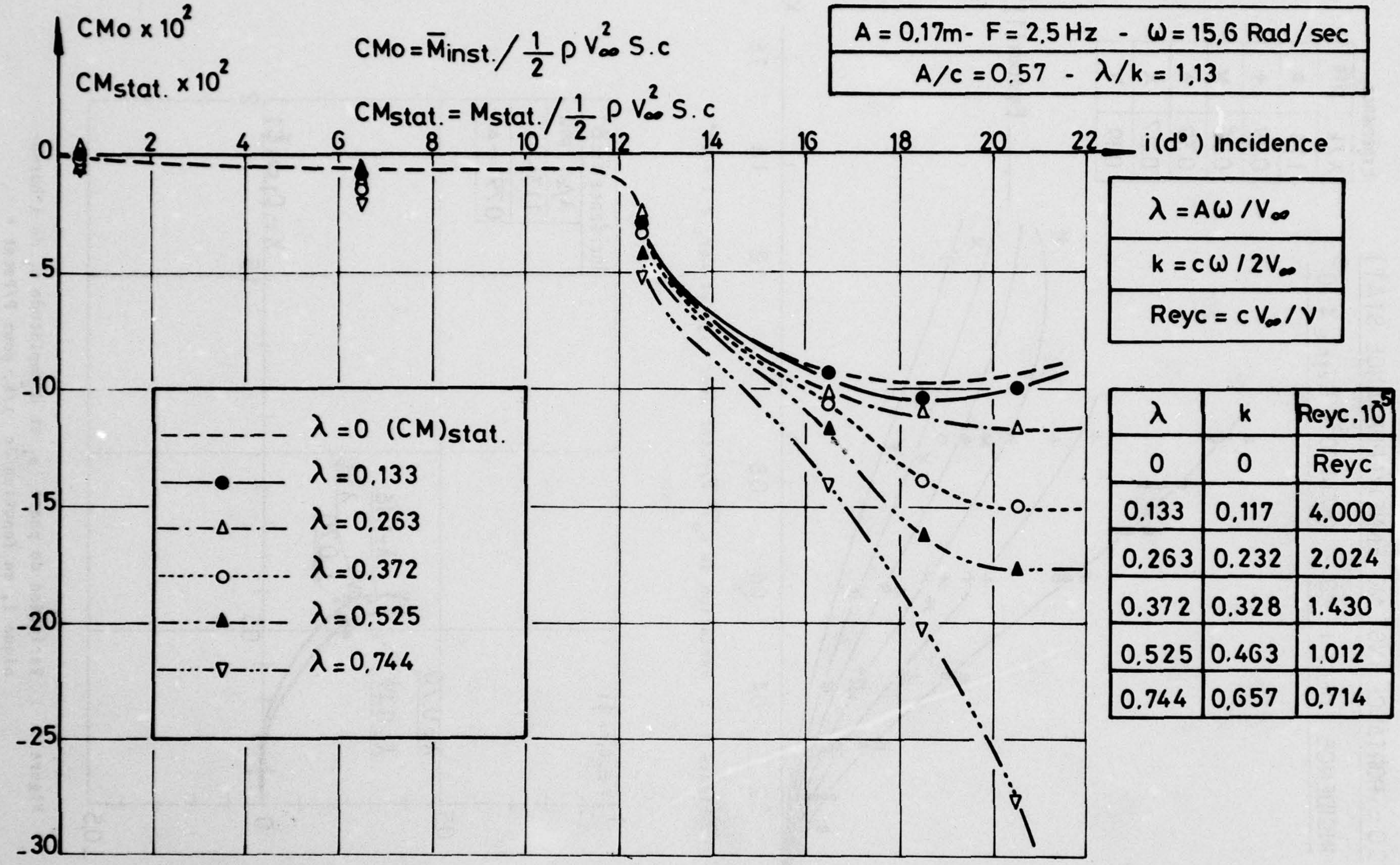

$CMo = \overline{M}inst. / \frac{1}{2} \rho V_\infty^2 S.c$

$CMstat. = Mstat. / \frac{1}{2} \rho V_\infty^2 S.c$

A = 0,17m - F = 2,5 Hz - ω = 15,6 Rad/sec

A/c = 0.57 - λ/k = 1,13

$\lambda = A\omega / V_\infty$

$k = c\omega / 2V_\infty$

$Reyc = c V_\infty / \nu$

λ	k	Reyc.10^5
0	0	$\overline{Reyc}$
0,133	0,117	4,000
0,263	0.232	2,024
0,372	0,328	1.430
0,525	0.463	1,012
0,744	0,657	0,714

Figure 3 : Variation de $CM_o = \overline{Minst}/\frac{1}{2} \rho V_\infty^2 S$ avec l'incidence i et à λ/k = 1.13.

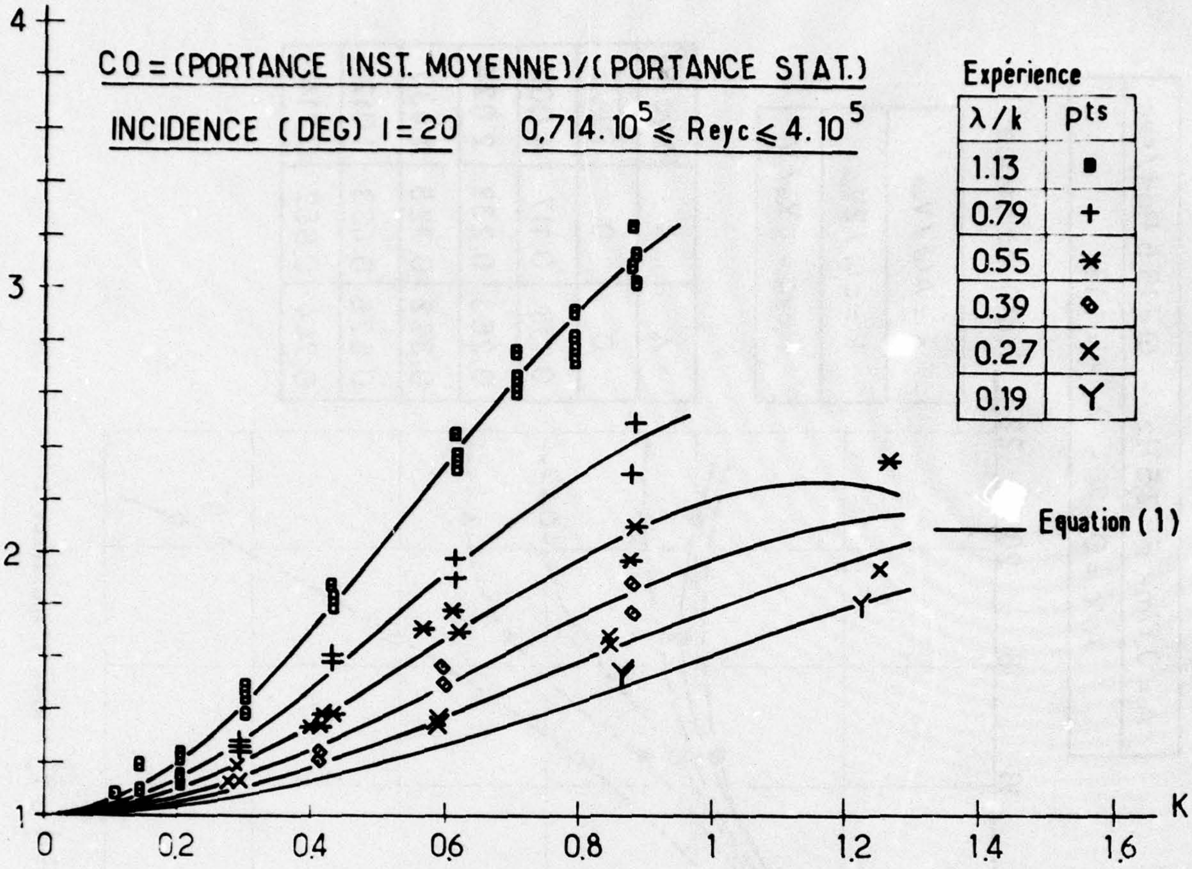

Figure 4 : Variation de $C_o = \overline{P}/Pstat$ avec λ,k et Rey_c à i = 20°

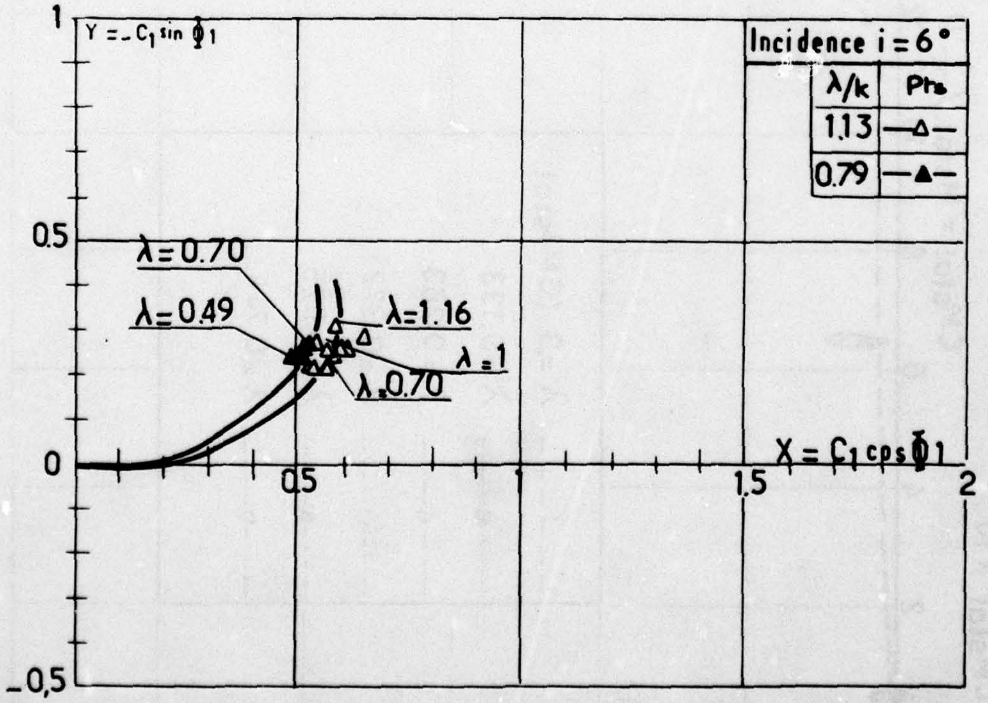

Figure 5 : Variation de phase ϕ_1 et d'amplitude C_1 de l'harmonique 1, en fonction de λ/k, pour $P/Pstat = C_o + C_1 \cos(\omega t + \phi_1) + \ldots$ à i = 6°.

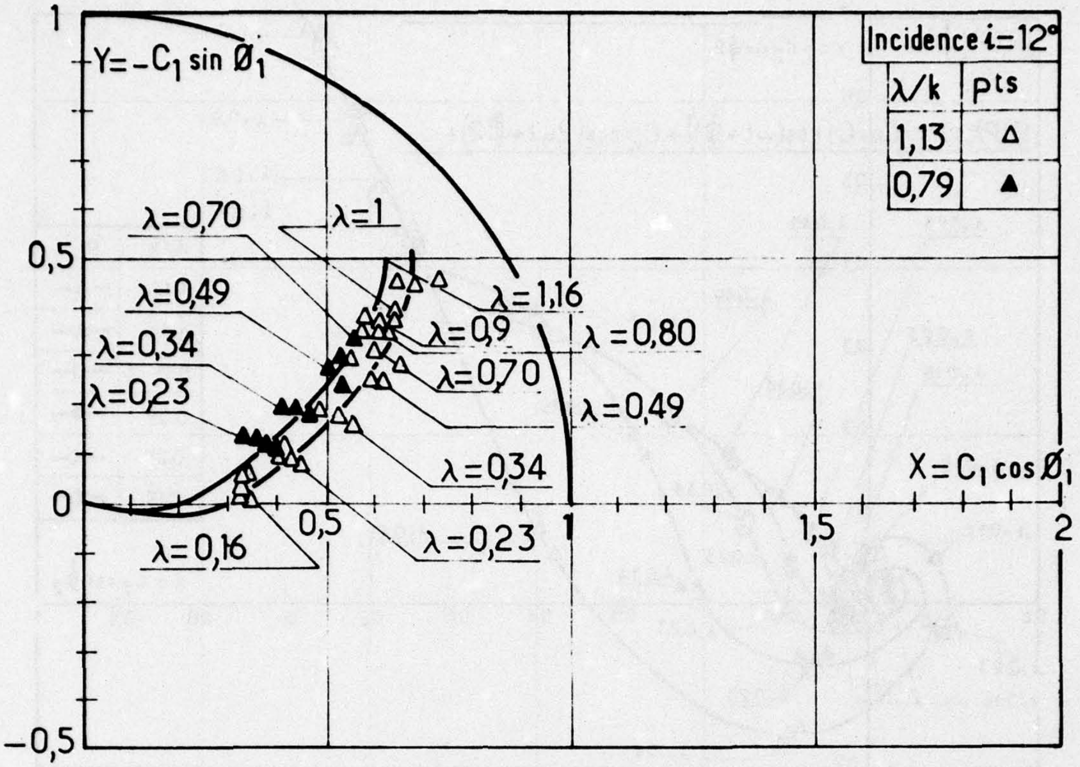

Figure 6 : Variation de phase ϕ_1 et d'amplitude C_1 de l'harmonique 1, en fonction de λ/k, pour P/Pstat = $C_o + C_1 \cos(\omega t + \phi_1) + \ldots$ à i = 12°.

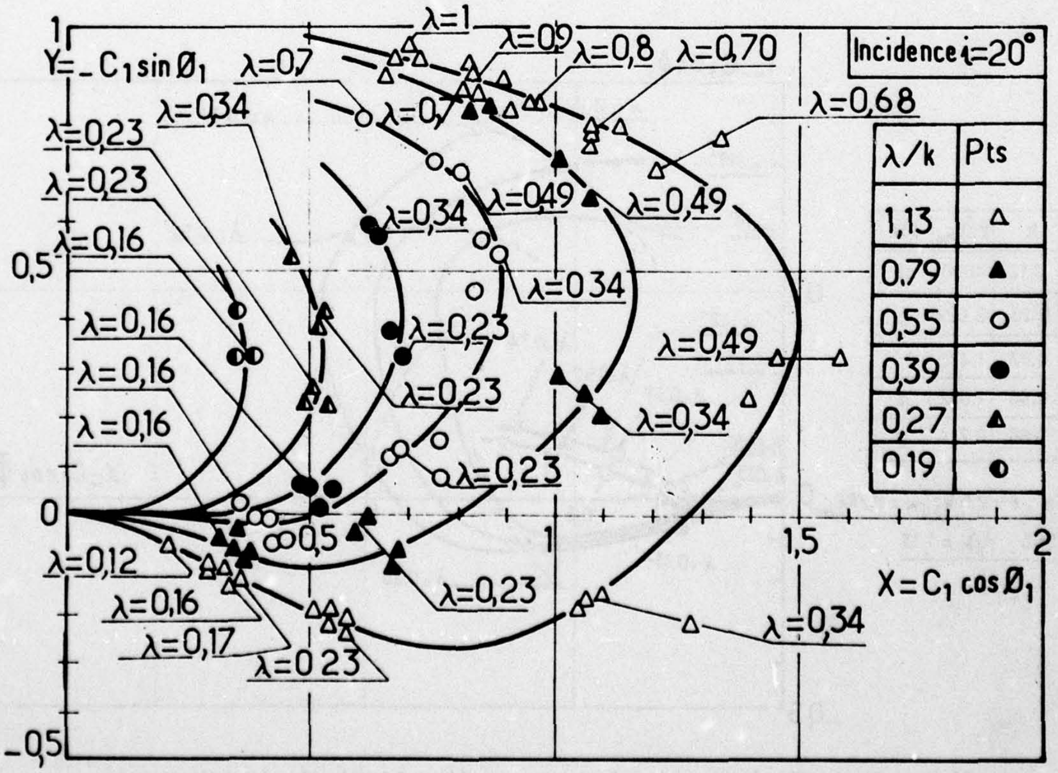

Figure 7 : Variation de phase ϕ_1 et d'amplitude C_1 de l'harmonique 1, en fonction de λ/k, pour P/Pstat = $C_o + C_1 \cos(\omega t + \phi_1) + \ldots$ à i = 20°.

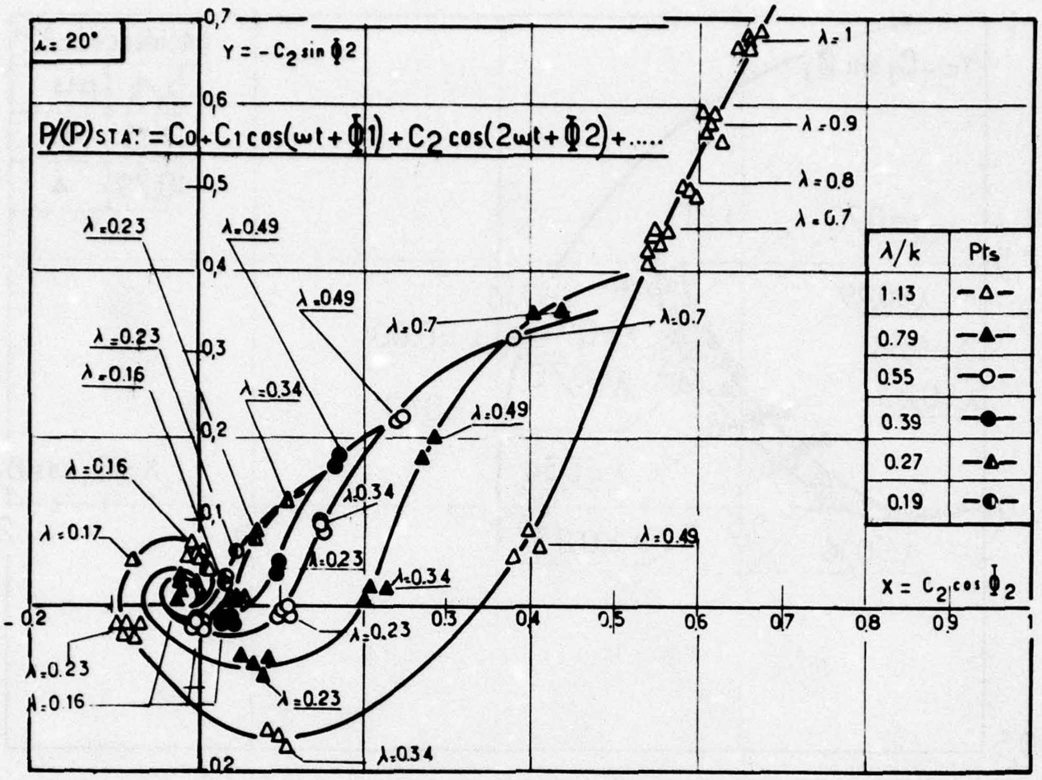

Figure 8 : Variation de phase ϕ_2 et d'amplitude C_2 de l'harmonique 2, en fonction de λ/k, pour P/Pstat = $C_o + C_1 \cos(\omega t + \phi_1) + C_2 \cos(2\omega t + \phi_2) + ...$ à i = 20°.

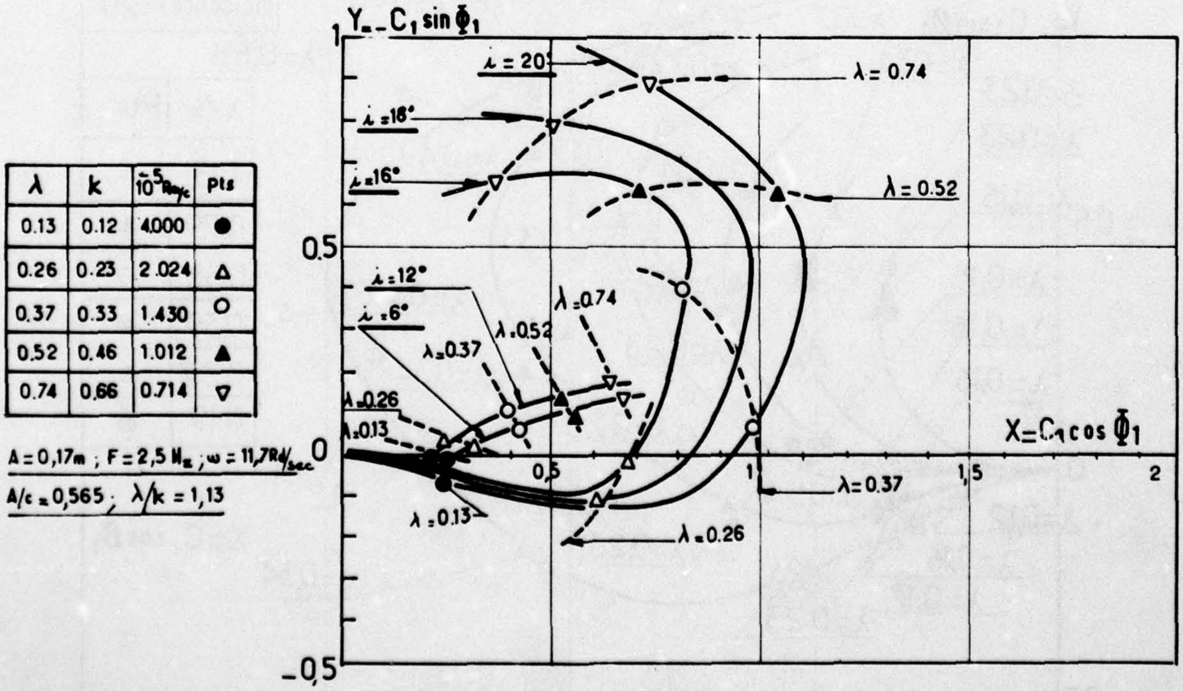

λ	k	10^{-5} Re	Pts
0.13	0.12	4.000	●
0.26	0.23	2.024	△
0.37	0.33	1.430	○
0.52	0.46	1.012	▲
0.74	0.66	0.714	▽

Figure 9 : Variation de phase ϕ_1 et d'amplitude C_1 de l'harmonique 1, en fonction de i, pour T/Tstat = $C_o + C_1 \cos(\omega t + \phi_1) + ...$ à λ/k = 1.13.

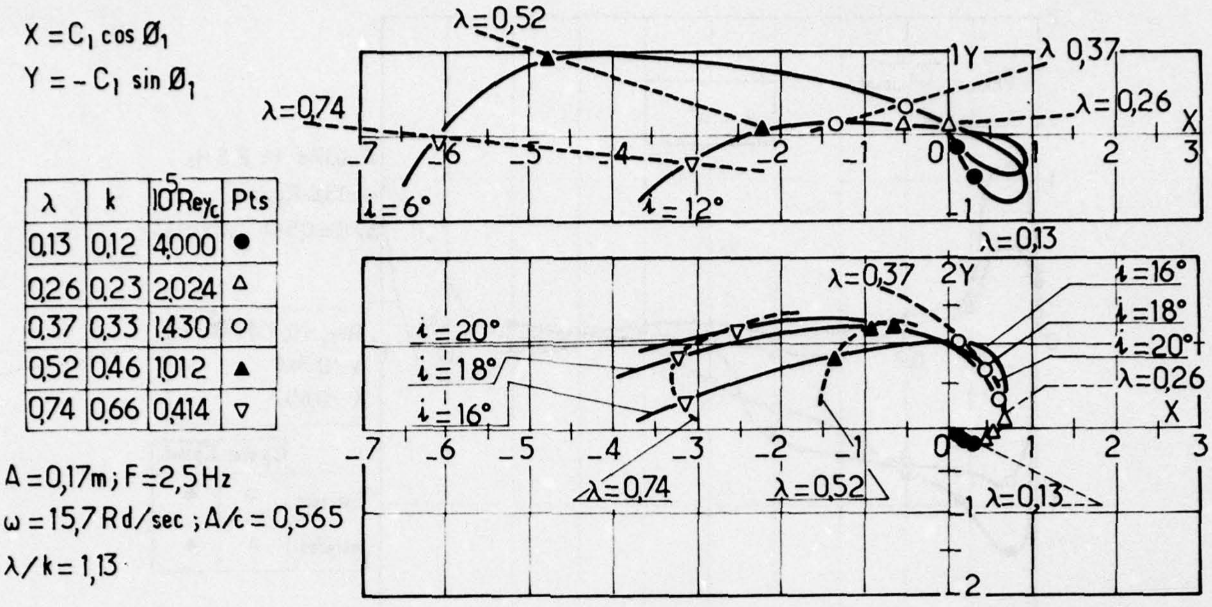

λ	k	10^5 Rey/c	Pts
0,13	0,12	4,000	●
0,26	0,23	2,024	△
0,37	0,33	1,430	○
0,52	0,46	1,012	▲
0,74	0,66	0,414	▽

A = 0,17m ; F = 2,5 Hz
ω = 15,7 Rd/sec ; A/c = 0,565
λ/k = 1,13

Figure 10 : Variation de phase ϕ_1 et d'amplitude C_1 de l'harmonique 1, en fonction de i, pour M/Mstat = $C_o + C_1 \cos (\omega t\ \phi_1) + \ldots$ à λ/k = 1.13.

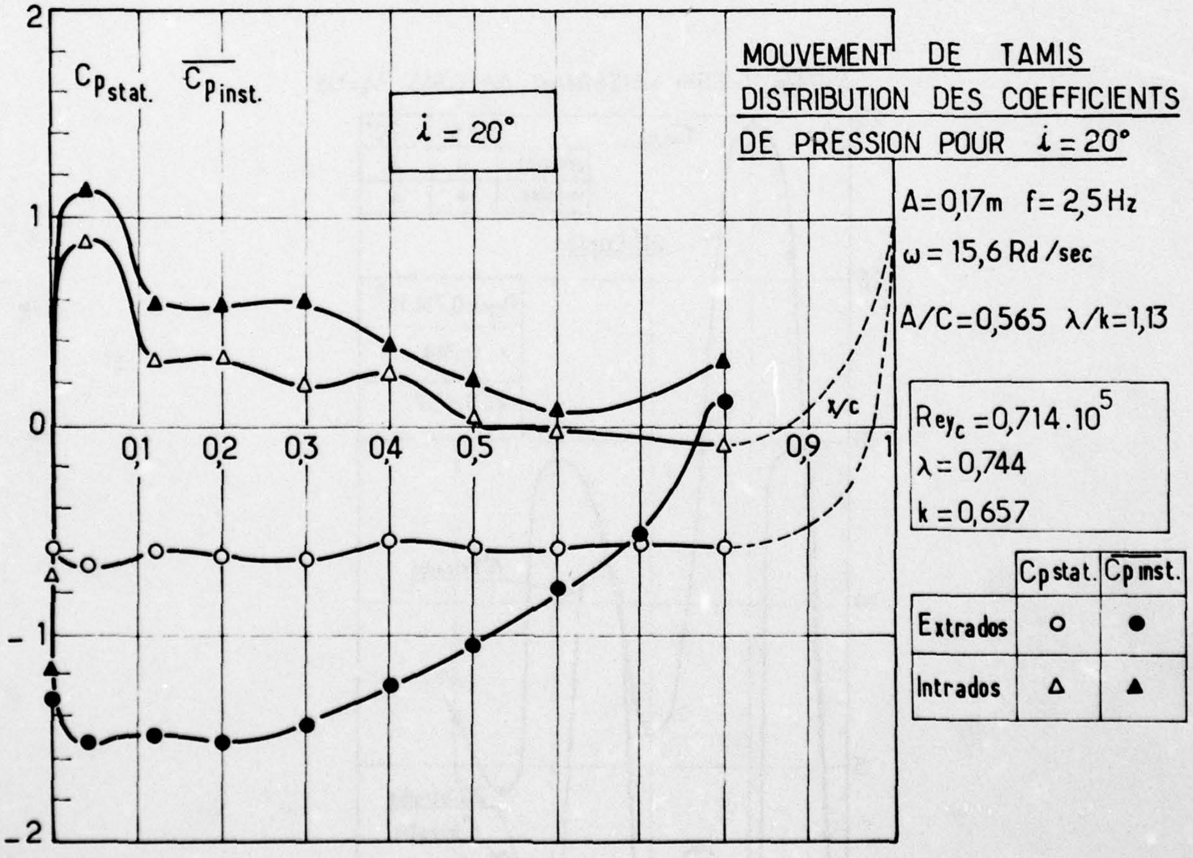

	Cp stat.	$\overline{\text{Cp inst.}}$
Extrados	○	●
Intrados	△	▲

Figure 11 : Distribution des coefficients de pression, $\overline{\text{Cpinst}}$ et Cpstat, pour i = 20°.

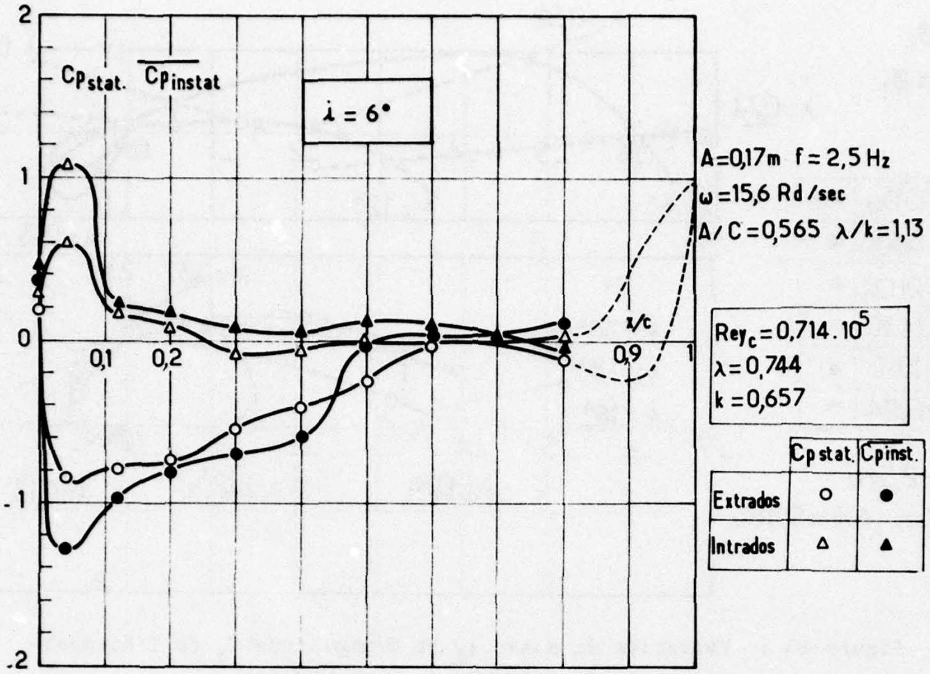

Figure 12 : Distribution des coefficients de pression, $\overline{Cpinst}$ et Cpstat, pour i = 6°.

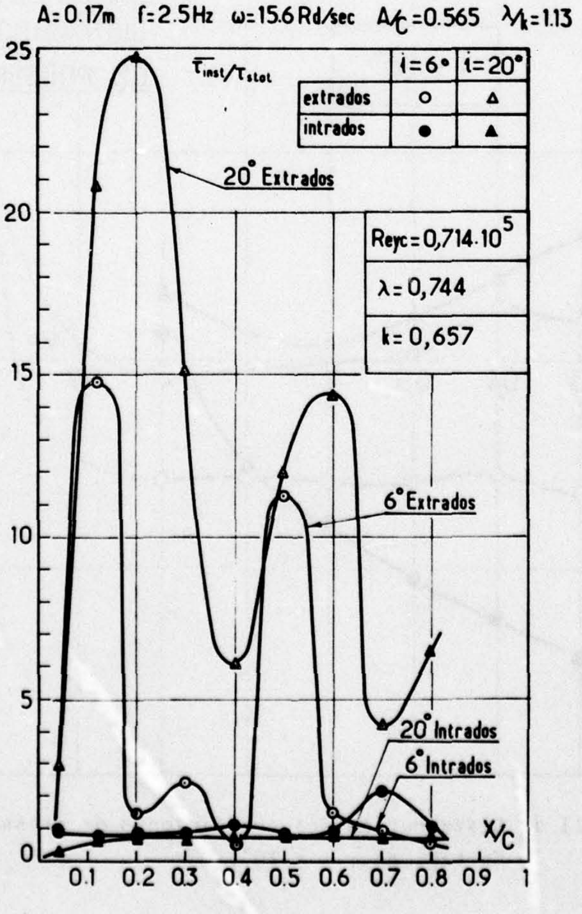

Figure 13 : Distribution de $\overline{\tau inst}/\tau stat$, pour i = 6° et i = 20°.

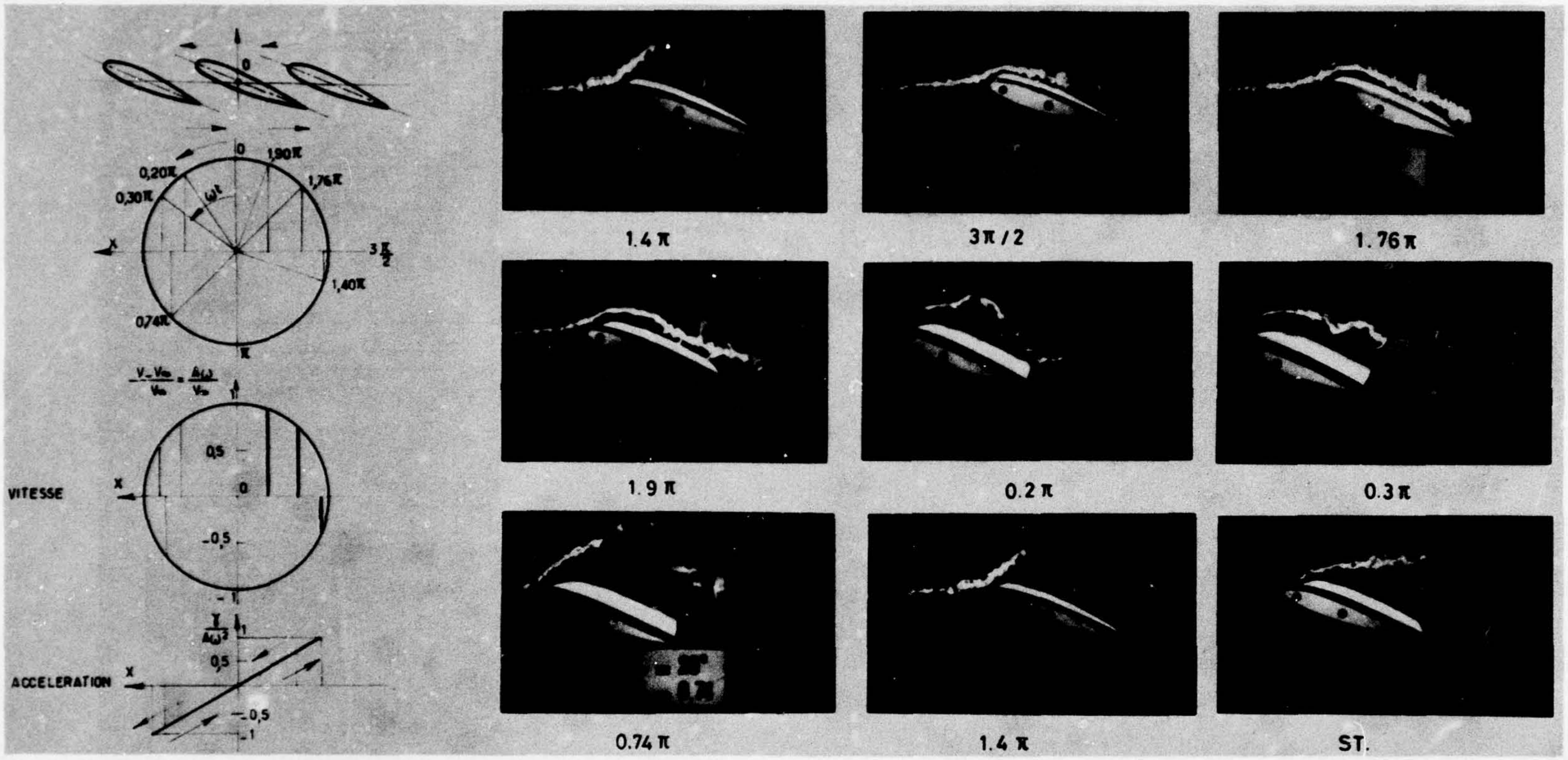

Figure 14 : Visualisations de l'écoulement à différentes phases de la période.

AD-A054 028 ADVISORY GROUP FOR AEROSPACE RESEARCH AND DEVELOPMENT--ETC F/G 20/4
UNSTEADY AERODYNAMICS.(U)
FEB 78

UNCLASSIFIED AGARD-CP-227 NL

6 OF 7
ADA
054028

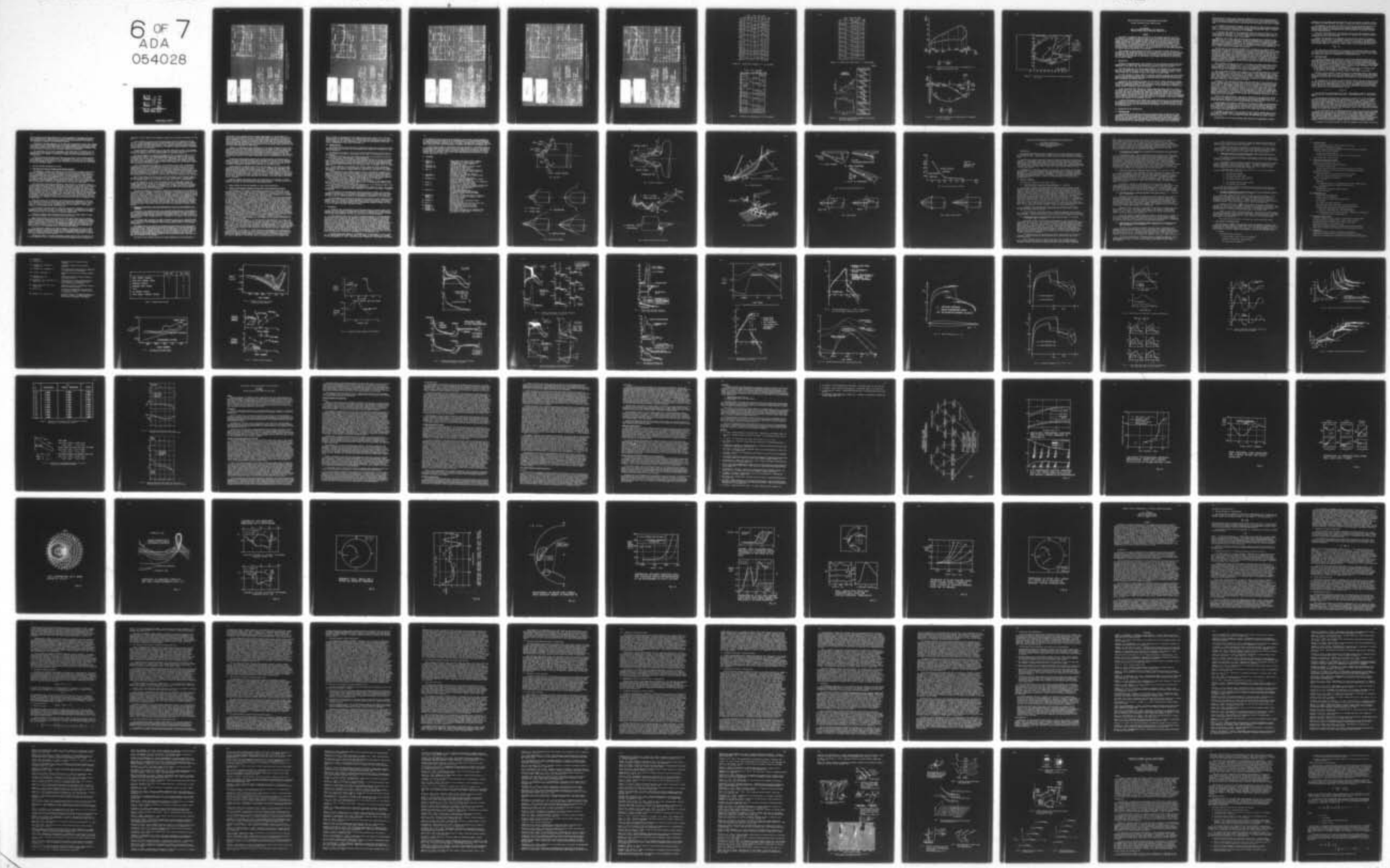

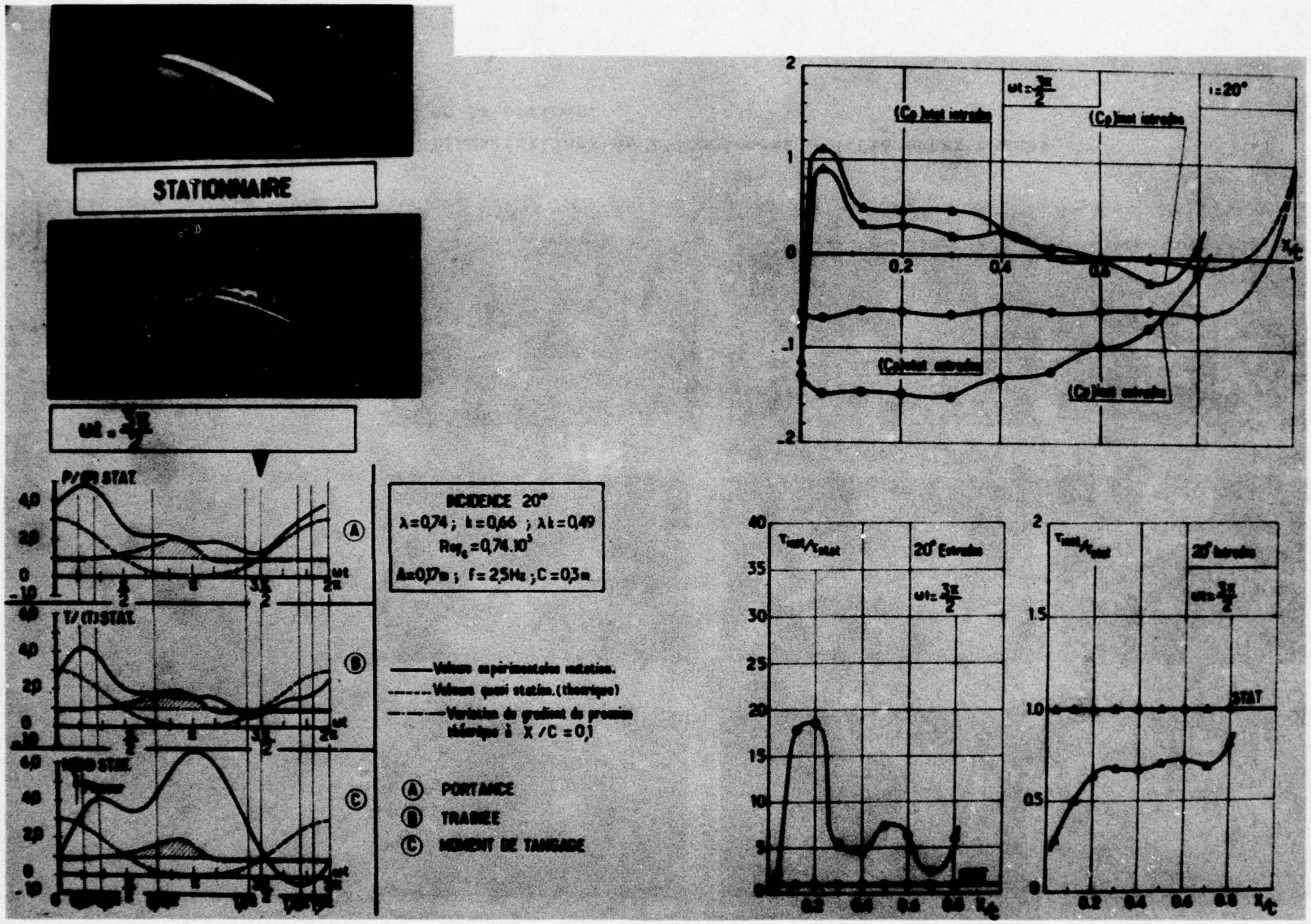

Figure 15 : Visualisation, torseur aérodynamique, coefficient de pression et frottement à ωt = 3 π/2.

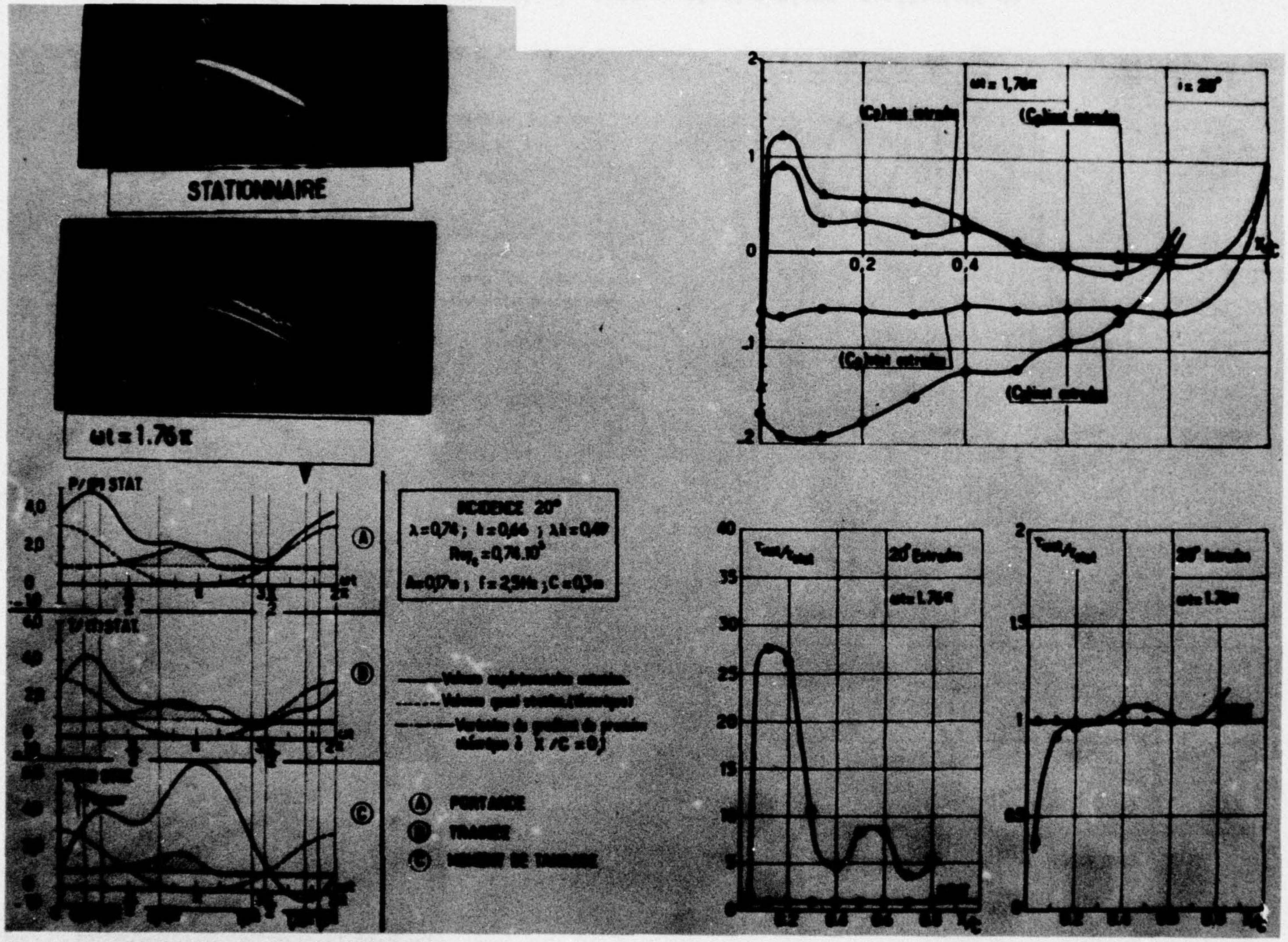

Figure 16 : Visualisation, torseur aérodynamique, coefficient de pression et frottement à ωt = 1.76 π.

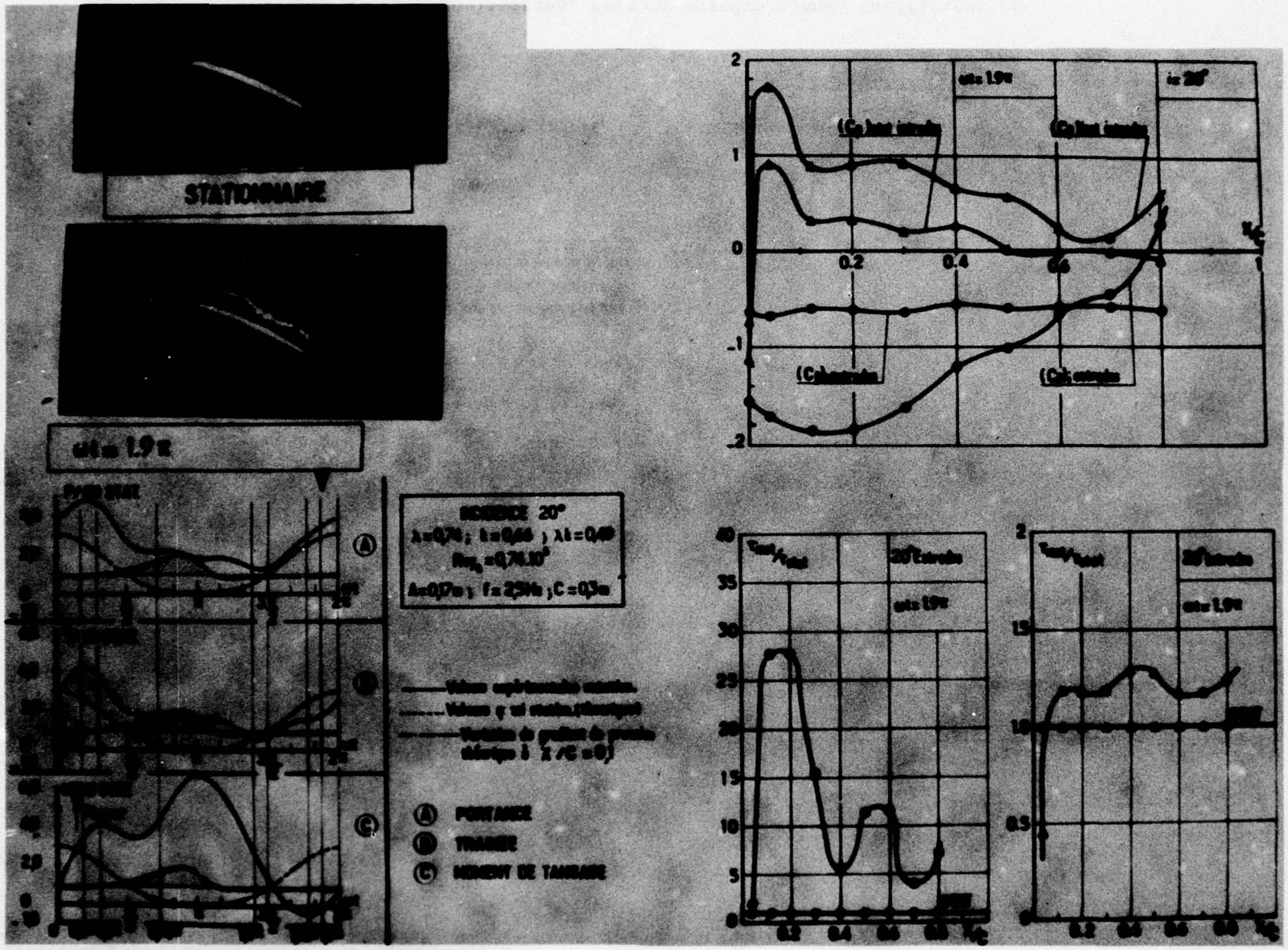

Figure 17 : Visualisation, torseur aérodynamique, coefficient de pression et frottement à $\omega t = 1.9\,\pi$.

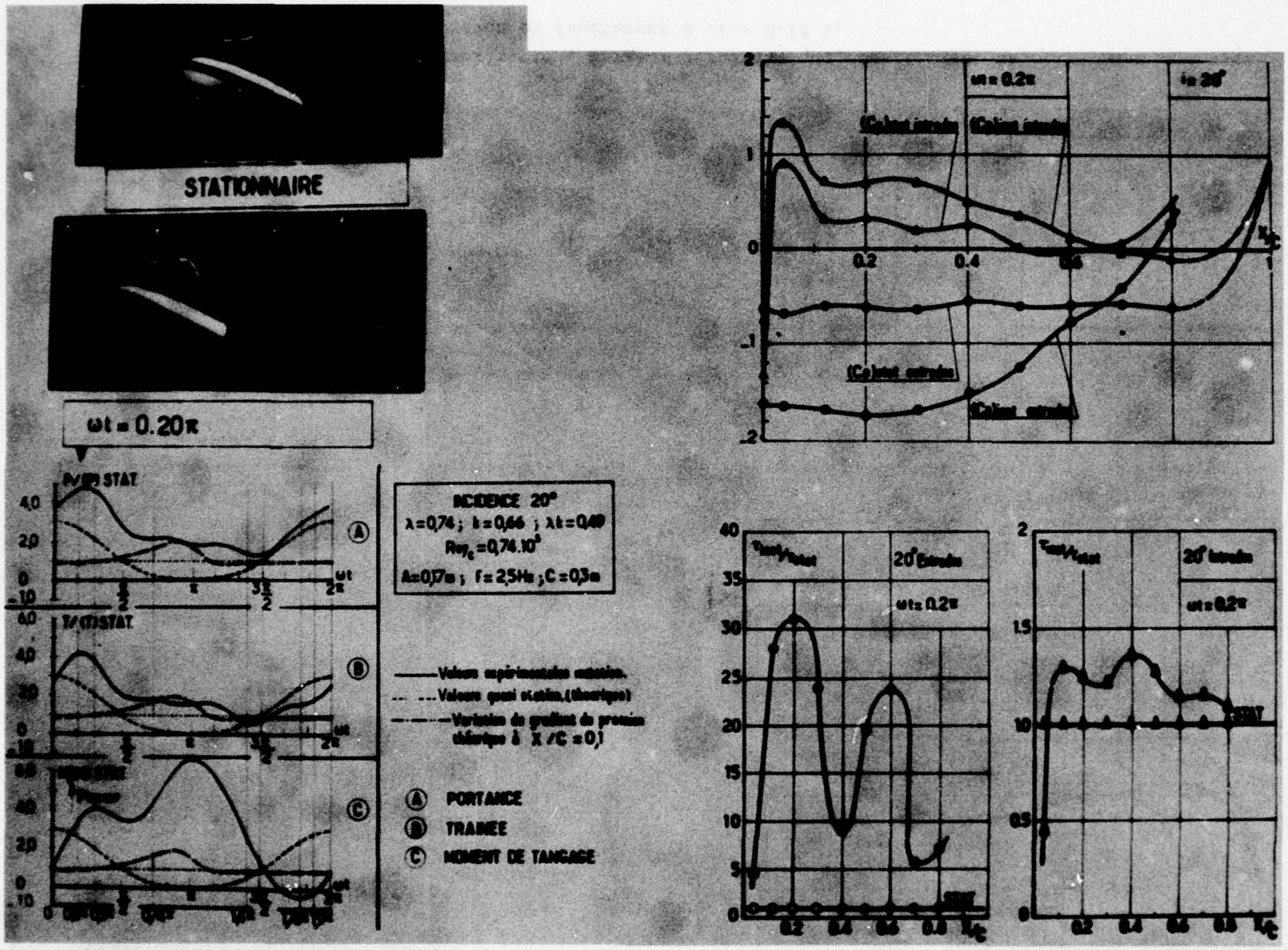

Figure 18 : Visualisation, torseur aérodynamique, coefficient de pression et frottement à ωt = 0.2 π.

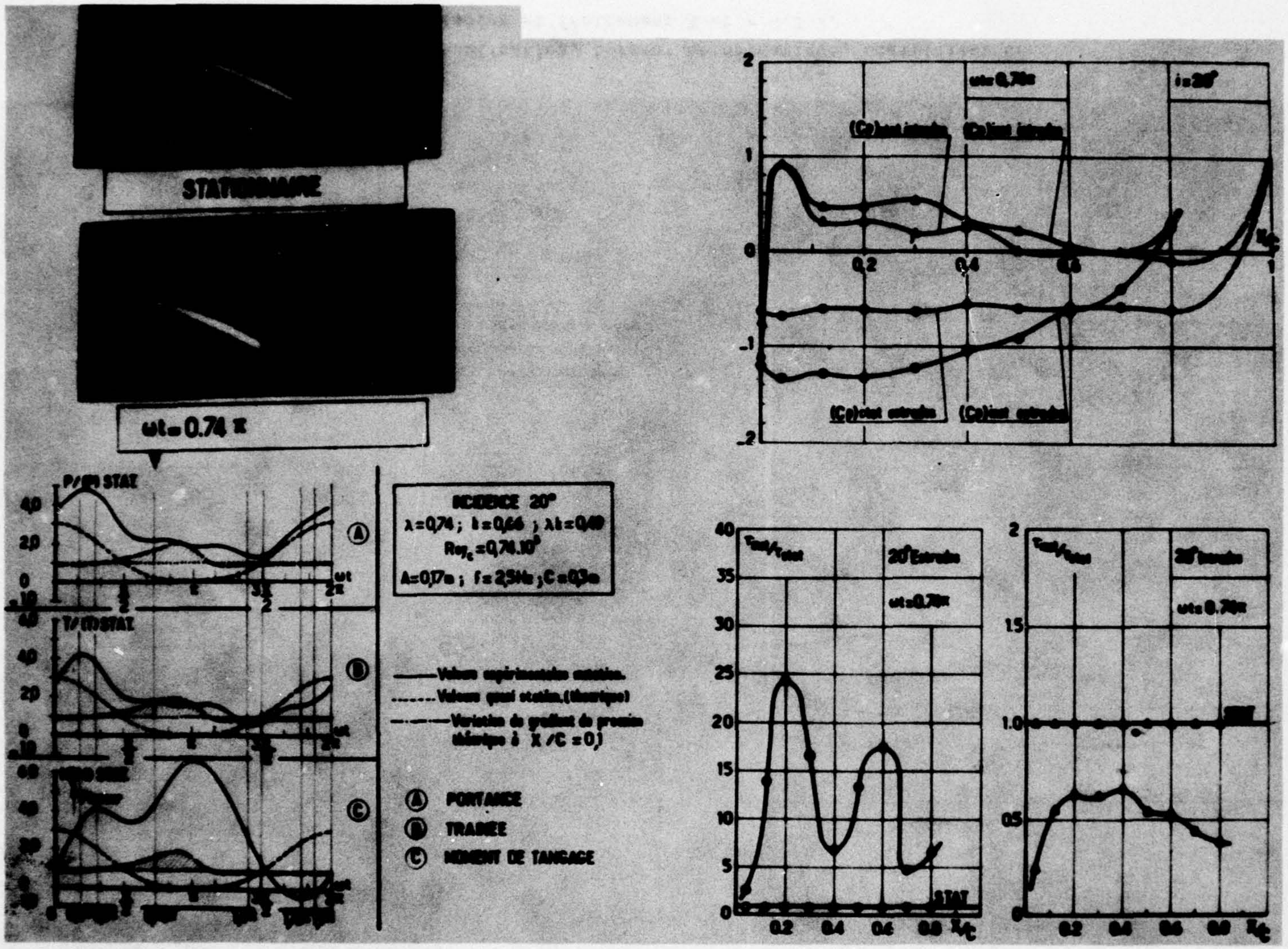

Figure 19 : Visualisation, torseur aérodynamique, coefficient de pression et frottement à ωt = 0.74 π.

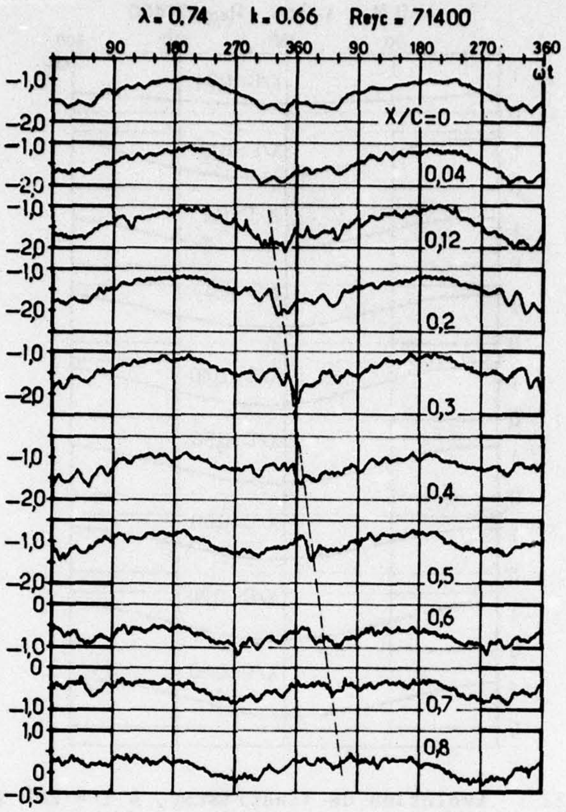

Figure 20 : Evolution de (Cp)inst, à i = 20° extrados.

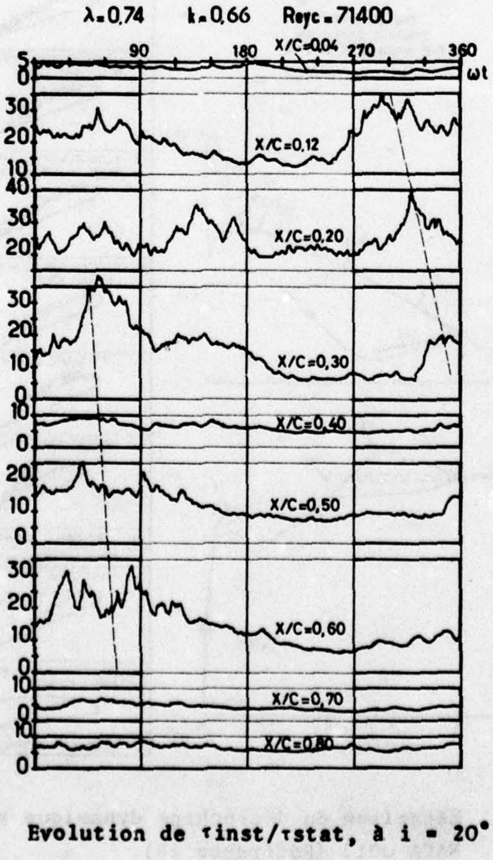

Figure 21 : Evolution de τinst/τstat, à i = 20° extrados.

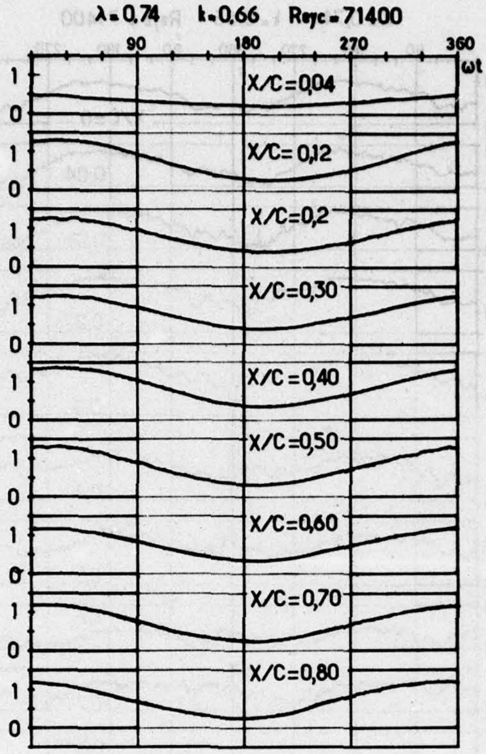

Figure 22 : Evolution de $\tau inst/\tau stat$, à i = 20° intrados.

PL.23

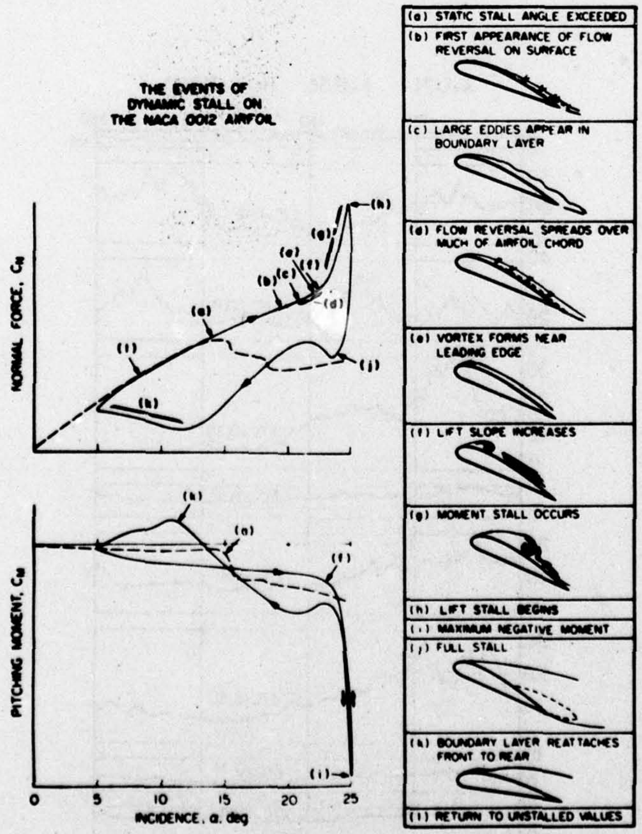

Figure 23 : Mécanisme du décrochage dynamique sur le profil NACA 0012 (Référence 16).

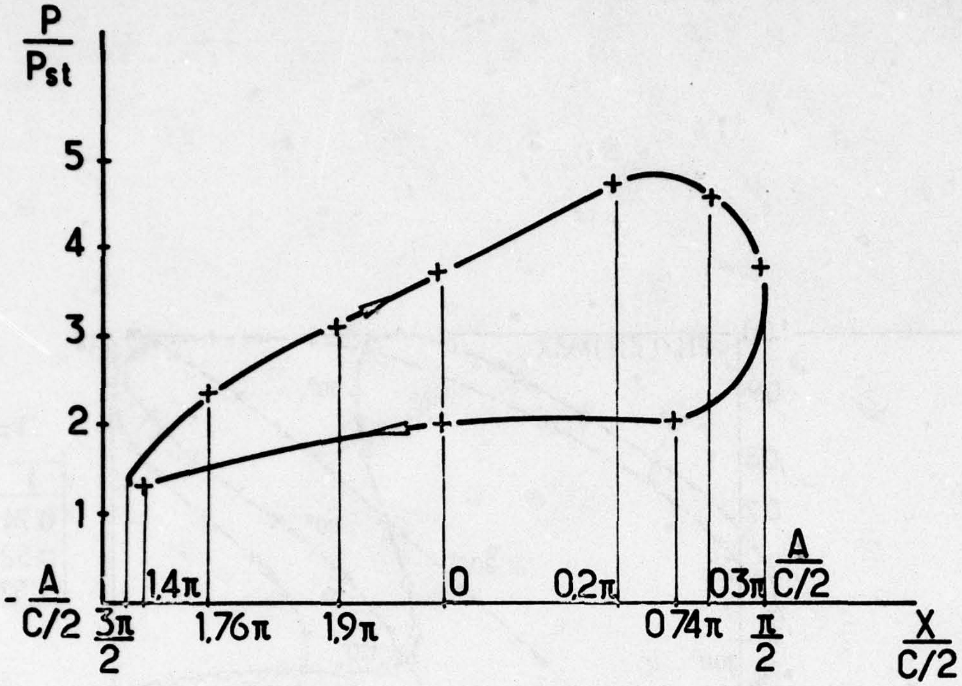

$$\frac{P}{P_{st}} = f\left(\frac{X}{C/2}\right)$$

Figure 24 : Variation de la portance avec le déplacement de la maquette au cours d'un cycle.

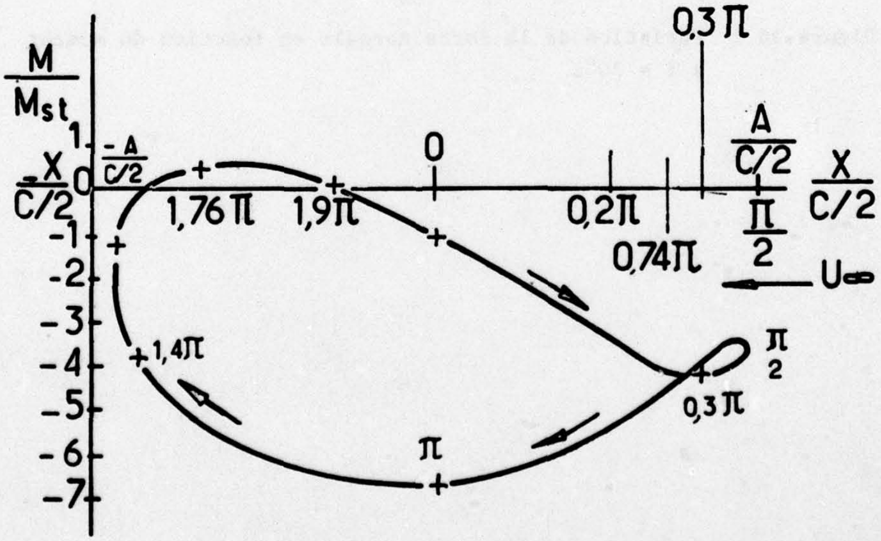

$$\frac{M}{M_{st}} = f\left(\frac{X}{\frac{C}{2}}\right)$$

Figure 25 : Variation du moment avec le déplacement de la maquette au cours d'un cycle.

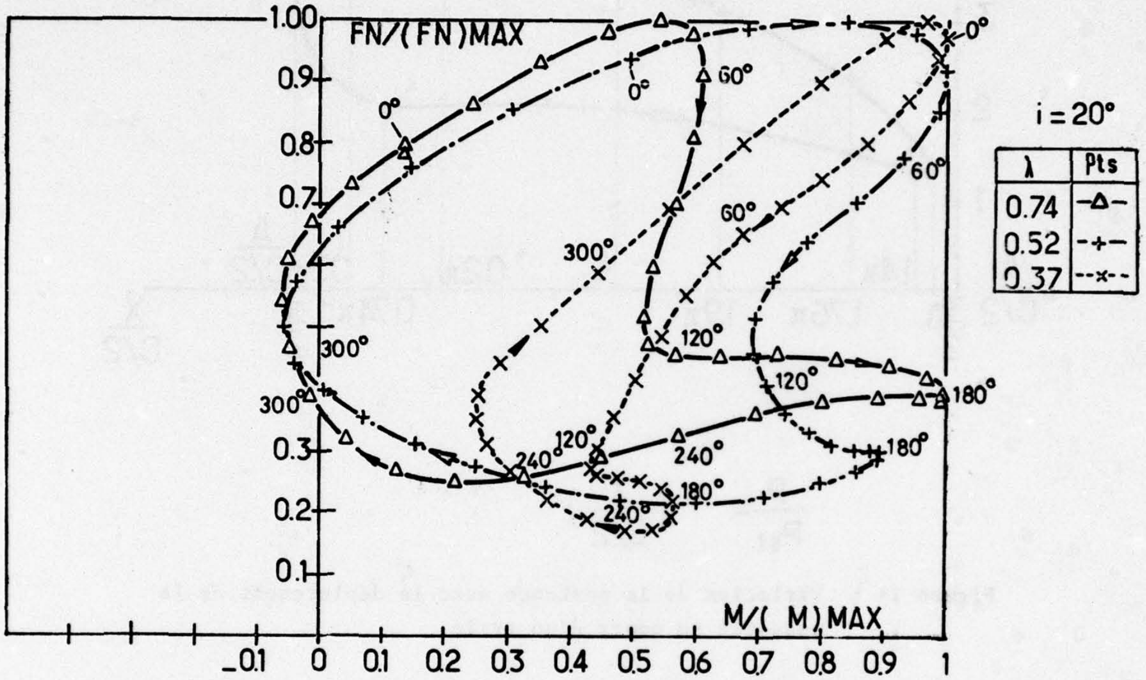

Figure 26 : Variation de la force normale en fonction du moment à i = 20°.

DESIGN CRITERIA FOR THE NON-OCCURRENCE OF HIGH SPEED UNSTEADY SEPARATION ABOUT CONCAVE BODIES

by

A.G. Panaras
Head of Aerodynamics Section, HAF Technology
Research Center, Paleon Phaleron, Athens,Greece

SUMMARY

Two modes of instability have been observed in the unsteady separated flow about some families of axisymmetric concave bodies. In the "pulsation" mode the conical separation bubble periodically inflates and expands radially. In the "oscillation" mode the conical foreshock and the accompanying shear layer oscillate laterally and their shape changes periodically from concave to convex. By means of theoretical arguments and an interpretation of the experimental data we have shown that the pulsation mode is caused by the formation of an annular supersonic jet at the intersection point of two shock envelopes evident during a brief part of the cycle. Additionally, we have found that the oscillation mode is most probably due to the non-satisfaction of the reattachment mechanism in a manner securing equilibrium of the pressure.

The knowledge of the mechanisms which induce the instabilities makes possible the derivation of some designing criteria for their non-occurence. As far as the pulsation mode is concerned, the criteria are centered on the avoidance of the intersection of the shock envelopes above the blunt part of the bodies or on the non-production of the supersonic jet. For the oscillation mode the criteria are quite simple; the shoulder of the body has to be properly rounded.

1. INTRODUCTION

Purpose of the present paper is the examination of the high-speed separated flow about concave bodies of shape as the one shown in fig. 1. By proper variation of the geometric parameters of this model body, many interesting families of bodies are derived.

The spiked body, that is a blunt axially symmetric body equipped with a spike protruding from its stagnation point, is the simplest and yet more extensively studied concave body. The interest in the study is due to the possibility of designing a missile of controlled drag, just by equipping its nose with a spike of variable length.

As other families of concave bodies of practical interest we mention the tension shells tested by Jones, Bushnell and Hunt (Ref.1) as possible Martian spacecrafts and the configurations achieved by ablation nose-caps of missiles during re-entry, which have been studied by Kenworthy and Richards (Ref.2).

According to the experimental evidence the flow about a concave body may be attached or separated. The shape of the compression arc (bc), fig.1, of the body is most probably the critical geometric parameter for the occurence or not of separation. If separation occurs, the established flow is not always steady but it may be periodically unsteady. Two distinct modes of instability have been observed.

In the "pulsation" mode (fig.2a) the conical separation bubble, which is formed on the concave part of the body, periodically inflates and expands radially. In the "oscillation" mode the conical foreshock, which envelops the separation bubble, and the accompanying shear layer oscillate laterally and their shape changes periodically from concave to convex (fig.2b). The pulsation mode was first observed by Mair (Ref.3) while the oscillation mode by Bogdonoff and Vas (Ref.4). The terminology is due to Kabelitz (Ref.8). The frequency of both modes of instability is rather high. The order of magnitude of the reduced frequency based on the diameter of the afterbody, is 0.20.

A physical explanation of the instabilities, whose main points will be presented here, was recently given by the author in Ref.5. The existence of this explanation makes feasible the evaluation of the effect which the geometric parameters of a concave body have on the development of the flow, and the derivation of some design criteria for the non-occurrence of the instabilities.

2. EXPLANATION OF THE INSTABILITIES

2.1 Pulsation Mode

The mechanism of the pulsation mode has been detected after an examination of the development of the flow field, about a geometry similar to that in fig.1, as it might seem if the flow starts impulsively at a supersonic Mach number. The impulsive start of the flow has been selected not only because it simulates the starting of the operation of the high speed tunnels. It has also been selected because a study of the experimental data reveals that at the starting phase of each cycle of pulsation the flow conditions

prevailing about a concave body, resemble an impulsive flow in which the shock envelope retains a position corresponding to an inviscid flow field. By using experimental data we have shown that the impulsive nature of the flow field is due to the violent radial expansion of the separation bubble, which occurs during the final phase of each cycle of pulsation.

An assumption concerning the geometry of the model body is that the mean inclination angle δ_t of the afterbody must be greater than the conical detachment angle corresponding to M_∞. This condition, according to the experimental evidence (Wood, Ref.6), is necessary for the flow about a concave body to be unsteady.

At the early development of the impulsively started flow about the model body, the flow is inviscid. Thus, with the first flow pulse, the weak foreshock SA (fig.1) and the strong aftershock AB appear. If the flow is quasi-steady a shock discontinuity point, A, a weak shock, Ar, and a shear layer Af must appear.

Meanwhile, the boundary layer develops along the forebody and it separates at the compression arc (bc). The existence of the shock discontinuity point in the field has a remarkable effect in the flow development during the inflation of the separation bubble. That is, the free-stream air contained in the streamtube F (fig.3) passes through the foreshock and is channeled between it and the inflating surface DA of the separation bubble. This channeled supersonic air is directed, in the vicinity of the shock discontinuity point, towards the body and impinges on its surface.

The direction of the channeled supersonic air is defined by the pressure forces prevailing in the adjacent low speed regions. As we have already mentioned, a third oblique shock Ar has to appear for the equilibrium of the flow around the shock discontinuity point. This shock, in the case of a non-separated flow extends to the surface of the body and prevents the high pressure air, existing behind the strong shock AB, from flowing into the low pressure region behind the oblique foreshock SA. But in the case examined here the growing separation bubble causes the continuous shortening of the length of the weak shock Ar and its consequent detachment from the surface of the body. In this way, the annular supersonic stream which impinges on the surface of the body is bounded between the low pressure region of the separation bubble and the high pressure field which exists behind the strong shock AB (fig.3).

This difference in pressure will act to turn inwards the annular supersonic stream, in the direction of the compression arc (bc) of the body. Thus, a certain fraction of the air contained in the streamtube (F) is fed into the separation bubble. This air is characterized by a high pressure, which is due to the appearance of a strong detached shock at the region of impingement of the annular supersonic stream.

But as the volume available for the expansion of the separation bubble which is filled with high pressure air is limited, the foreshock itself will be pushed radially outwards and will eventually cover the afterbody. If the pressure in the separation region is much higher than the pressure of the surrounding free stream, a radial pressure imbalance exists and a radial expansion will occur. On the contrary, if the radial pressure imbalance is small, no reason for a radial expansion exists and the excess air in the separation region may expand downstream at the shoulders of the body.

According to the experimental evidence, when the conditions for the occurence of the radial expansion exist, the foreshock inflates abruptly and takes a hemispherical shape. However, as this hemispherical strong shock is due to the expansion of the high pressure air contained in the separation bubble and not to the existence of a proper blunt body in the flow, it cannot stand there attached to the tip of the forebody, but it has to approach the surface of the afterbody. Obviously, as the strong shock moves towards the afterbody, the forebody is exposed to the free stream and as a result the foreshock must reappear. We note that at this phase of the flow development no separation bubble exists; hence, simultaneously with the appearance of the conical foreshock, the growth of the boundary layer along the surface of the forebody and its subsequent separation at the compression arc (bc) will start.

Obviously the reestablishment of the initial conditions of the impulsively started flow leads to the repetition of the appearance at the shock discontinuity point of the annular supersonic stream, the filling of the separation bubble with high pressure air, etc. We may say that the pulsation mode of instability has been established.

The dependence of the explosive inflation of the separation bubble on the appearance of an annular supersonic stream, at the vicinity of the shock discontinuity point, is a basic requirement of the above analysis. This supersonic stream acts as a supersonic jet at the region of its impingement and the flow at the vicinity of the shock discontinuity point may be viewed as the unsteady counterpart of the steady type IV shock formation (fig.4) observed by Edney (Ref.7).

A fundamental difference is that the Edney IV shock formation appears only when the flow behind the embedded shock Ar is supersonic and this condition is not present if M_∞ is low (Ref.5). However, in the unsteady flow case, the supersonic jet seems to appear even for low M_∞.

The main points of the present analysis were verified by an experimental program, conducted in the Von Karman Institute hypersonic ($M=6$) H-3 tunnel. The models studied were spiked flat-ended cylinders with sharp or rounded shoulders and concave conic bodies.

The hypothesis of the impulsive character of the flow at the starting phase of the pulsation mode was verified with a series of schlieren photographs of the flow field about a spiked cylinder of relatively large diameter (d=46 mm). These photographs also revealed the formation of the supersonic jet at the intersection of the weak foreshock and the strong aftershock.

After the optical detection of the supersonic jet, we performed sublimation tests. At the region of the surface where the supersonic jet impinges, the sublimation material disappeared and a dark ring was formed.

Finally, the existence of the supersonic jet was detected indirectly by pressure measurements. The amplitude of the pressure fluctuation at the face of the afterbody at $r/R=0.25$ was measured with a flush mounted Kistler 601A piezo-electric transducer. This amplitude was found to be independent of spike length. If we normalize the measured value of the pressure amplitude (ΔP) by the pressure p_3 behind the strong shock AB we find :

$$\frac{\Delta P}{p_3} = 2.0$$

This shows that the fluctuation of the pressure in the separation region is greater than the pressure behind the strong shock and consequently the air which fills the dead-air region cannot have come from the adjacent subsonic region, but actually comes through the conical shock wave and is compressed at the impingement region.

2.2 Oscillation Mode

The rapid addition of high pressure air in the growing separation bubble and its consequent radial expansion are the peculiar characteristics of the pulsation mode. However, the geometry of the body may be such that during the hypothetical impulsive start of the flow the inflating separation bubble may cover the afterbody before a considerable amount of high pressure air is trapped within the bubble. If this happens the flow develops as steady separated or as an unsteady one of the oscillation mode. According to the experimental evidence, the oscillation mode appears when :

a. The mean inclination angle of the afterbody is greater than the detachment angle.
b. The length of the forebody is smaller than a critical value.
c. The shoulder of the afterbody is sharp (small or zero radius of curvature).

The above special geometric characteristics have a significant effect on the development of the separated flow; if the flow were steady, both the separation and reattachment points would be fixed. The shear layer would begin at the tip of the forebody and it would reattach on the sharp edge of the afterbody (tip separation and shoulder reattachment, fig.5).

The determination of the dead-air region pressure solely by the free-stream conditions and the inclination of the conical surface (F in fig.5) which envelops the concave part of the body, is one significant result of the combined tip separation and shoulder reattachment. Neither the free-interaction equation nor the reattachment relation of Chapman (Ref.9) participate in the determination of the flow conditions in the separation region. This is obvious from the following relations (fig.5) :

$$\sigma = \sigma' + \sigma_0 \qquad \sigma' = \frac{\rho}{(OS)} \cos\delta$$

We note that for a sharp shoulder ($\rho \ll (OS)$) the separation angle σ' , which determines the dead-air pressure becomes insensitive to small variations of the reattachment angle δ .

The forementioned relations may be interpreted in another way. If the reattachment point moves slightly downstream of the equilibrium position (i.e. values of δ smaller than the one required for equilibrium) and the shoulder is sharp, air from the dead-air region will escape downstream. On the contrary, if it moves slightly upstream of the equilibrium point (i.e. values of δ greater than the required for equilibrium) air from the external part of the shear layer will turn inwards at the reattachment region. Furthermore we observe that if the velocity gradient of the outer part of the shear layer is large, then the pressure gradient at the reattachment region is also large and the inwards turning of the shear layer is more easy.

In the case examined here the separation starts at the tip of the body and the length of the shear layer is not free to be determined by the coupled separation and reattachment mechanisms but is physically restricted because of the limited length of the forebody. Thus the velocity gradient of the outer part of the shear layer is the largest possible. This conclusion comes from an examination of the tip separation analysis of Chapman (Ref.9,10). According to his analysis a shorter shear layer has a larger velocity gradient ($\partial u/\partial y$) because the thickness of the shear layer grows parabolically with increasing length, while its velocity profile remains similar at different streamwise stations.

A conclusion of the above analysis is that the sharpness of the shoulder of the afterbody in conjuction with high values of the velocity gradient of the shear layer seem to be the reasons for the observed addition of air coming from the reattachment region to the separation bubble, during the initial phase of an oscillation mode of instability. This hypothesis is supported by experimental evidence.

According to the above analysis, if the radius of the shoulder is large, small changes in the position of the reattachment point do not induce unstable conditions and an equilibrium may be reached. Indeed testing spiked flat-ended cylinders and conic concave bodies with rounded shoulder we have found that a flow which should otherwise be unsteady of the oscillation mode is stabilized by a very small rounding of the shoulder.

The significance of the velocity gradient of the shear layer is concluded from the observation that the oscillation is established when the length of the shear layer (or equivalently of the forebody) is small and it ceases when the length increases above a critical value.

Though the shock discontinuity point does not participate in the forcing mechanism of the oscillation, still the position of the foreshock is critical for the definition of the amplitude of the instability. In our experiments we observed that if the foreshock envelops the afterbody the amplitude of the oscillation is small and the flow stabilizes for a shorter forebody length.

3. FACTORS AFFECTING THE BEHAVIOUR OF FLOW

3.1 The Quantity of the Air Trapped in the Separation Bubble

The fundamental element of our analysis is the influence of the shock discontinuity point on the behaviour of the flow. The existence of such a point initially, that is before the appearance of the separation bubble, above the afterbody is the necessary but not the sufficient condition for the occurrence of unsteady separation. Basic for the development of the flow is the appearance or not of the supersonic jet. If it appears the flow does not "feel" the geometry of the shoulder and so even if the shoulder can accomodate a steady reattachment (large radius of curvature), the flow will pulsate. On the contrary, if the supersonic jet does not appear, the flow feels the shoulder geometry and if the shoulder is sufficiently rounded the flow develops as a steady one.

The force which induces the unsteadiness is mass addition in the conical cavity of limited volume behind the foreshock. The effect of the size of this volume in the behaviour of the flow may be understood if we examine the mass-addition phase of the cycle of the pulsation mode. As we have mentioned in section 2.1, during this phase the foreshock itself is pushed radially outwards and eventually covers the afterbody. This can be clearly seen in schlieren pictures of the flow field. In order for the radial expansion of the separation bubble to occur, an expansion that is an essential element for the establishment of the pulsation mode, the air trapped in the bubble must have a pressure much higher than the pressure of the surrounding free stream. It is obvious that the greater the conical volume behind the foreshock, available for the growth of the separation bubble, the lower the pressure of the trapped air and the lower the possibilities for the occurrence of the pulsation mode.

Thus, if the mass of the added air can be controlled the unsteadiness of the flow may be avoided. The control of the added air may be performed by application of suction (i.e. perforation of the surface and communication with a low pressure region), by provision of a large cavity for the conveyance of the initially added air, or by proper design for the downstream escape of the added air.

For the case of the large cavity we mention a special test performed by Loll (Ref.11). Varying the dead-air region volume of a spiked flat cylinder, by connecting it through a concentric hole with the inner part of the (hollow) cylinder, Loll found that for sufficient cylinder volume the flow instead of pulsating became steady.

The way the design of non-axisymmetric devices affects the establishment of large-scale unsteady separated flows, is illustrated in fig.6 and 7a.

Fig.6 shows a sketch of the interaction flow field past a blunt fin on a surface, according to Kaufman, Korkegi and Morton (Ref.12). The fin bow shock causes the boundary layer to separate from the surface ahead of the fin, resulting in a separated flow region composed of horse-shoe vortices near the surface and a lambda type shock pattern in the plane of symmetry ahead of the fin. The experiments revealed that the flow was very unsteady, with the separation point moving upstream and downstream. The unsteadiness has been attributed to the scavenging action of the horse-shoe vortices.

It is clear that because of the small thickness of the fin, the air which is added at the reattachment to the separation region, instead of increasing the volume of the separated region and inducing the movement of the reattachment point towards the end of the fin, it escapes downstream and there appears the apparently strange case of a shear-layer face reattachment on a 90° surface.

Although the action of the shock intersection points (one for the tip shock and one for the separation shock) is intense (peak pressures and heating rates at the shock impingement) it has no effect on the separation region, as the points lie outwards, far from it.

On the contrary, in fig.7a we see the model-space shuttle of Goldman and Obremski (Ref.13), in zero incidence and with the flap extended more than required for the generation of a strong aftershock. Although the width of the flap is limited, not all the air, which is added at the reattachment because of the pressure imbalance, escapes downstream from the sides of the flap, and consequently the separation region extends to the maximum possible and the flow oscillates.

On non-axisymmetric configurations, as the above space-shuttle flap, or on axisymmetric concave bodies in sufficient incidence angle, the pulsation mode of instability will certainly not appear at all, as the high pressure air can escape sidewards.

One typical example of pulsating two-dimensional flow is included in Ref.3. In his pioneer work Mair has not only studied axisymmetric spiked cylinders but also similar two-dimensional devices, i.e. double forward steps having small ratio of the horizontal protruding plate to the height of the step (l/h). The plates were extended laterally from wall to wall, preventing the air to escape sidewards. For small values of the parameter l/h the flow presented the typical inflation and expansion of the separation bubble which characterize the pulsation mode.

In the proposed physical explanation of the pulsation mode a point of fundamental importance is the extent of the separation bubble. As it has been shown in Ref.5, if a steady separated flow is established about the model body, then the separation region covers all the concave part of the body; the shear layer reattaches on the shoulder of the body and never on the conical part of the afterbody. Thus, as the bubble grows, during the early development of the impulsive flow, the embedded shock Ar (fig.3) intersects the shear layer which bounds the separation bubble. This intersection causes the flowing of the high pressure air (supersonic jet) into the bubble and its subsequent radial expansion.

But in other families of bodies there exists the possibility for the shear layer to reattach on the main part of the body and not on its shoulder: hence it may be possible for the impinging shock Ar not to intersect the shear layer before its reattachment.

As an illustration in fig.7c the flow pattern about the model-space shuttle of Goldman and Obrenski is shown, with the flap down but also in incidence. Goldman and Obrenski observed that, as far as the impinging shock Ar meets the surface at the region of reattachment of the shear layer or upstream of it, the shear layer and the impinging shock exhibit periodic excursions about a mean position, while the flow stabilizes for *intersection downstream of the reattachment*.

The material presented in this section indicate the significance of the existence of an intersection point between a weak and a strong shock in a separated flow, as far as the condition (steady - unsteady) of the flow is concerned. If the pulsation mode occurs the whole flow field is disturbed by the periodic explosive expansion of the separation bubble, and the life expectancy of the vehicle may be seriously affected by the interaction of the flow with the structure. If the conditions are not proper for the establishment of the pulsation mode, the amplitude of the established instability is smaller and the aeroelasticity problems may be less critical. However in this case the shock discontinuity point may be constantly visible (oscillation mode excluded). Then the supersonic jet impinges continuously on a certain part of the structure. Thus, the well known problem of the destructive heating of the surface (Ref.12), which was first investigated by Edney (Ref.7), appears.

3.2 Effect of the Position of the Shock-Discontinuity Point and of the Geometry of the Afterbody

The effect of the initial position of the shock discontinuity point on the behaviour of the flow may be concluded from the already mentioned observation that the foreshock itself is pushed radially outwards, during the mass-addition phase of the pulsation mode. This pushing out happens because a fraction of the quantity of the air which is fed in the separation bubble, from the supersonic jet, is diffused in the region of the shock discontinuity point.

It is evident that the nearer the shock discontinuity point lies to the surface and to the shoulder of the afterbody, the faster it will be pushed radially outwards; and the smaller the quantity of the trapped air will be (fewer possibilities for the occurrence of pulsation).

The significance of the distance of the shock discontinuity point from the surface of the afterbody, or equivalently of the stand off distance of the strong aftershock, is illustrated in fig.8. From existing data we show for Mach number 6 and 1.96 the position of the initial shock intersection point for the non-occurrence of the pulsation mode of instability. For $M_\infty=6$, though the point is far from the shoulder of the body ($r/R=0.72$) the instability has changed from the pulsation into the oscillation mode, while for $M_\infty=1.96$ the pulsation mode persists though the shock discontinuity point lies above the edge of the shoulder of the cylinder.

The effect of the initial position of the shock discontinuity point relatively to the shoulder of the afterbody has been studied experimentally at the VKI Mach 6 H-3 tunnel. For spiked cylinders and for a constant Mach number, the initial position of the shock discontinuity point is affected by the spike length, the shape of the spike tip and the diameter of the spike. If the spike length is increased the shock discontinuity point moves outwards towards the shoulder of the cylinder. Thus by increasing the spike length one may study the effect of the initial position of the shock point. Actually, for each Mach number and Reynolds number there exists a critical spike length beyond which the flow turns from pulsating into oscillating.

However by increasing the spike length not only the shock discontinuity point moves outwards but also the volume behind the foreshock is increased. In order to isolate the effect of the position of the shock discontinuity point we have tested flat-ended cylinders equipped with spikes of constant diameter and of conical tips of variable angle. Testing step by step we measured the spike length for which the pulsation turns into oscillation. The results are plotted in fig.9 and confirm our hypothesis of the importance of the initial position of the shock discontinuity point in determining the type of the flow.

Furthermore testing spiked cylinders with rounded shoulders we discovered that as long as the initial shock discontinuity point lies above the flat part of the forebody the flow pulsates, while when it approaches the shoulder of the body the flow oscillates or becomes steady. As we have mentioned in section 2.2 the radius of curvature of the shoulder is the geometric parameter that stabilizes the oscillation mode.

Another geometric parameter which affects the development of the flow is the mean inclination angle of the forebody (angle δ_t in fig.1). Surveying the experimental data (Ref.2,5,14) we discovered that there is a limit of δ_t for which the occurrence of the pulsation mode of instability for any forebody length is not possible. This limit was found to lie between δ_t=80° to 70°. For 80° the pulsation appears regularly while for 70° the flow oscillates.The data cover a range of M_∞=6 to 18. Most probably this limit exists because for a constant Mach number the stand off distance of the aftershock is decreased and the shock discontinuity point approaches the surface, if the cone angle of the afterbody is decreased.

Finally, tripping the boundary layer, by covering the tip of the spike of spiked cylinders with sand or metallic particles proved very effective in reducing the critical length of the spike for the elimination of the pulsation mode.

4. DESIGN CRITERIA FOR THE NON-OCCURRENCE OF LARGE SCALE INSTABILITIES

4.1 Effect of the Geometric Parameters of the Body on the Behaviour of the Flow

The knowledge of the effect of each geometric parameter of a concave body on the behaviour of the flow is necessary, if an optimization of the body is desired, for the non-occurrence of a large scale unsteady flow (pulsation - oscillation). In this section a classification of the subject will be done. The main geometric parameters of a concave body are shown in fig.1. They affect the flow field as follows :

a. The forebody angle, σ_t , its length l and the shape of the tip of the body determine the initial position of the foreshock and approximately of the shock discontinuity point. By the term "initial" we mean the position the corresponding to an inviscid flow field. We remind that according to the experimental evidence due to the explosive character of the radial expansion of the separation bubble, the flow field at the starting phase of the pulsation mode is almost identical with the initial one of an impulsively started flow.

b. The length of the forebody, l, affects significantly the behaviour of the flow. If the flow is unsteady there exists a critical value of this parameter beyond which a steady separation is established. In case of bodies with a slender forebody and a sharp shoulder an approximate estimation of this critical value may be performed by using the free-interaction analysis of Chapman et al. (Ref.9). The calculation consists of the estimation of the length of the forebody required for the establishment of a tip separation, assuming a shoulder reattachment (fixed reattachment point). If the actual forebody length is greater than this critical length then the separation is steady independently of the values of the other geometric parameters. The calculation procedure is included in Ref.5.

c. The form of the compression arc (bc) determines whether the flow separates or remains attached. In the present analysis we have assumed that the geometry of the body is such that separation occurs.

d. The mean inclination angle, δ_t , of the surface of the afterbody is a critical parameter. If the shock discontinuity point initially lies above the curve (bcd) and δ_t is greater than a critical value, whose theoretical calculation is not possible at the present time, the flow will most probably be unsteady of the pulsation mode. If δ_t is smaller than the critical value but greater than the conical detachment semiangle, the flow may be steady or unsteady of the oscillation mode, depending on the existence or not of rounded shoulder (de). An empirical value for the critical δ_t is 70°, which is valid for a Mach number greater than 6.

e. The radius of curvature, ρ , of the shoulder is the parameter that stabilizes the oscillation mode. In our tests the radius $\rho/d = 1/10$ proved effective in stabilizing the laminar flow (Reynolds number based on the diameter of the body equal to $R_{ed} = 5 \times 10^5$) which should otherwise be oscillating, while the radius $\rho/d = 1/15$ proved ineffective. The order of magnitude of the critical radius of curvature may also be concluded from

Ref.2. A radius of the shoulder of the concave biconic model, equal to $\rho/d = 1/8$, was sufficient for the stabilization of the separated flow at $M = 15$, and $R_{ed} = 2.5 \times 10^6$ while a radius of $\rho/d = 1/22$ was not so. If the radius of curvature is greater than the critical value and the shock discontinuity point lies above the shoulder, the flow is steady, independently of the value of the angle δ_t.

4.2 Design Criteria

The design criteria which follow have a qualitative rather than a quantitative value. They may be used as a guideline for the experimental optimization of the shape of a specific configuration.

The pulsation mode may not occur if the shock discontinuity point at its initial position lies above or outwards of the shoulder of the body, or if the supersonic jet is not produced.

1. The initial position of the shock discontinuity point is approximately controlled by the position of the foreshock and it may be affected by :

a. Proper design of the forebody. A spiked cylinder is shown in fig. 10, as an example. If the spike is thick and flat ended, the foreshock envelops the cylinder for smaller spike lengths, than when it is thin and cone-tipped. For $M_\infty = 6$, we found experimentally that for a spike/afterbody diameter ratio equal to 1/10 the flow becomes steady for flat ended spikes at length $l/d = 1.5$ while for cone capped spikes of semiangle $\sigma_t = 7.5°$ at length $l/d = 2.0$.

If the speeds are low supersonic this critical length may become considerably small. However, the effect of the optimization of the shape of the forebody will become very small at high hypersonic speeds, where the foreshock lies very near to the surface of the forebody.

b. Air injection into the dead-air region. If air is continuously injected at the base of the forebody, a nearly conical region is formed at the area of injection and the foreshock, feeling this region as a solid body, may be displaced outwards. Wood (Ref.6) observed at $M_\infty = 10$ that on a spiked flat cylinder a mass injection coefficient $(m/\rho_\infty u_\infty S)$ of only 0.08 was sufficient to change the spike length on the unsteady boundary from 2.3 1.2 body diameters. The symbol S denotes the cross-section of the cylinder.

2. The non-production of the supersonic jet is affected by :

a. The value of the mean inclination angle of the afterbody. If this angle is lower than a critical value the pulsation mode does not occur. The experimental evidence indicate that for $M \geq 6$ this value is about 70°.

b. The quantity of the air added by the supersonic jet in the separation bubble. This quantity may be controlled as it is cited in section 3.1.

c. The condition of the shear layer which envelops the separation bubble. The tripping of this shear layer, by means of surface roughness, is effective to an extent to suppress unsteadiness.

The occurrence of the oscillation mode can be avoided quite simply, just by proper rounding of the shoulder of the afterbody. The minimum radius of curvature for the stabilization of the flow cannot be predicted theoretically by this analysis. The value $\rho/d = 1/10$ may be used as a starting value for an experimental optimization of the flow field.

On non-axisymmetric configurations the pulsation mode does not occur because the high pressure air, which induces the radial expansion of the separation bubble, can escape sidewards. Thus, it is enough to optimize the shoulder shape. As an application in fig.7b the flow field about the model-space shuttle of Goldman and Obrenski is shown, as it has to be if the edge of the flap is properly rounded.

5. CONCLUSIONS

1. "Pulsation" and "oscillation" are the terms describing two distinct modes of the unsteady flow which exists in the high speed flow about a concave body for some specific combinations of the geometric parameters of the body. The experimental evidence indicates that the governing mechanisms of those two instabilities are quite different.

2. In the pulsation mode the flow field is strongly disturbed by the high-frequency periodic explosive expansion of the separation bubble which appears at the concave part of the body. We have shown that the pulsation is caused by the formation of an annular supersonic jet at the intersection point of two shock envelopes evident during a brief part of the cycle. Thus the significance of the existence of a shock intersection point between a strong and a weak shock is apparent once more. In this case a shock intersection point between a strong and a weak shock does not only induce local high heating of the structure of a configuration, in case the flow is steady or unsteady of small amplitude; it may equally well induce a large scale instability. The knowledge of the mechanism of the pulsation makes possible the determination of the effect of each geometric parameter of a concave body and the derivation of some rather qualitative design criteria for the non-occurrence of the instabilities (avoidance of the intersection of the shock envelopes above the blunt part of the body or non-production of the supersonic jet).

3. The oscillation mode appears if the generation of the supersonic jet is not possible, for reasons explained in the text, and if the length of the forebody is not enough for the establishment of a free - interaction type of separation. Additionally the shoulder

of the afterbody, where the shear layer reattaches, must be sharp. Forcing mechanism of the oscillation has been shown to be the non-satisfaction of the reattachment mechanism in a manner securing the equilibrium of the pressure. This hypothesis is strongly supported by the experimental observation that a very small rounding of the shoulder of the body, which reduces the local pressure gradients, stabilizes the otherwise oscillating flow.

4. Some critical points of the analysis, such as the effect of the maximum volume of the conically shaped separation bubble and of the mean inclination angle of the afterbody on the behaviour of the flow, need to be further investigated. We hope that the material of this paper will stimulate further systematic testing, so that some details of the mechanisms will be clarified, in the task of developing mathematical models for the quantitative description of the flow.

6. REFERENCES

1. Jones, R., Bushnell, D., Hunt, J. - Experimental flow field and heat transfer investigation of several tension shell configurations at a Mach number 8. NASA TN D-3800, 1964.
2. Kenworthy, M., Richards, B.E. - A study of the unsteady flow over concave conic models at Mach 15 and 20. AFML TR 75-137, Sept. 1975.
3. Mair, W. - Experiments on separated boundary layers on probes in front of blunt nosed bodies in a supersonic air stream. Phil.Mag. Vol.43, 1952, pp. 695-716.
4. Bogdonoff, S., Vas, I.E. - Preliminary investigations of spiked bodies at hypersonic speed. J.A.S., Vol. 26, 1959, pp. 65-74.
5. Panaras, A.G. - High speed unsteady separation about concave bodies. A physical explanation. Von Karman Institute, Tech. Note, to be published.
6. Wood, C. - Hypersonic flow over spiked cones J.F.M., Vol. 12, 1962, pp. 614-624.
7. Edney, B. - Anomalous heat transfer and pressure distributions on blunt bodies at hypersonic speeds in the presence of an impinging shock. FFA Rep. 115, 1968.
8. Kabelitz, H. - Zur Stabilität geschlossener Grenzschichtablösegebiete an Konischen Drenkörpern bei Hyperschallansströmnug. DLR FB 71-77, 1971.
9. Chapman, D., Kuehn, D., Larson, H. - Investigation of separated flows in supersonic and subsonic streams with emphasis on the effect on transition. NACA TN 3869, 1957.
10. Chapman, D. - Laminar mixing of a compressible fluid. NACA Rep.958, 1950.
11. Loll, V. - Unsteady supersonic flow around a spiked body. Von Karman Institute PR 74-4, 1974.
12. Kaufman, L., Korkegi, R., Morton, L. - Shock impingement caused by boundary layer separation ahead of blunt fins. ARL 72-0118, 1972.
13. Goldman, R.L., Obremski, H.J. - Experimental investigation of hypersonic buzz on a high cross range shuttle configuration. AIAA paper N° 73-157, 1973.

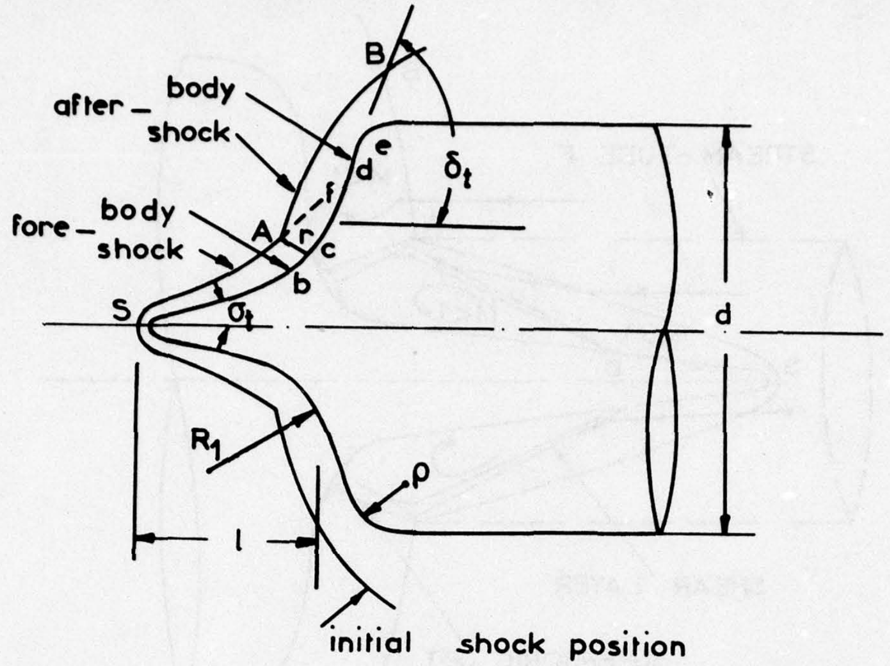

Fig.1 Model body

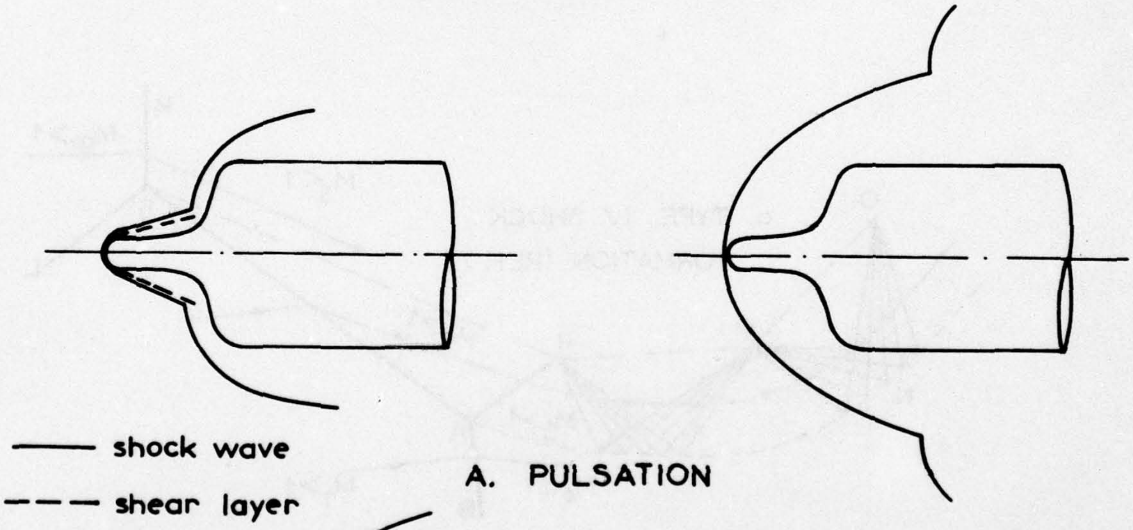

A. PULSATION

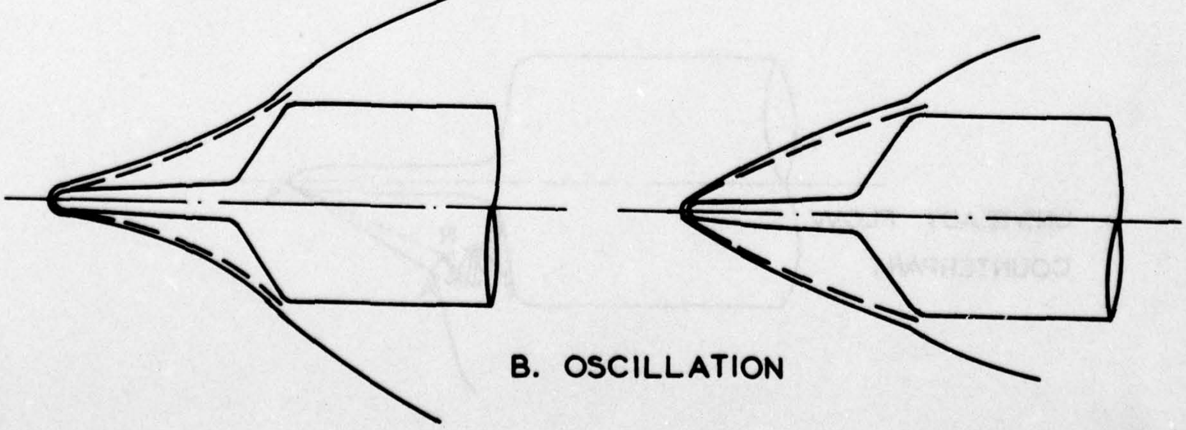

B. OSCILLATION

Fig.2 Classification of instabilities

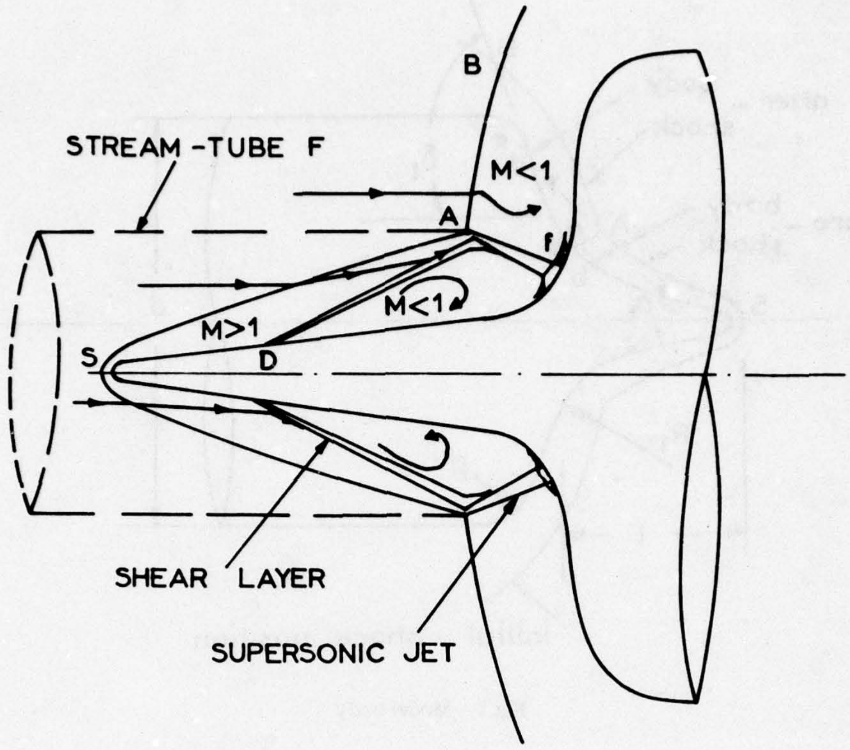

Fig.3 Generation of supersonic jet

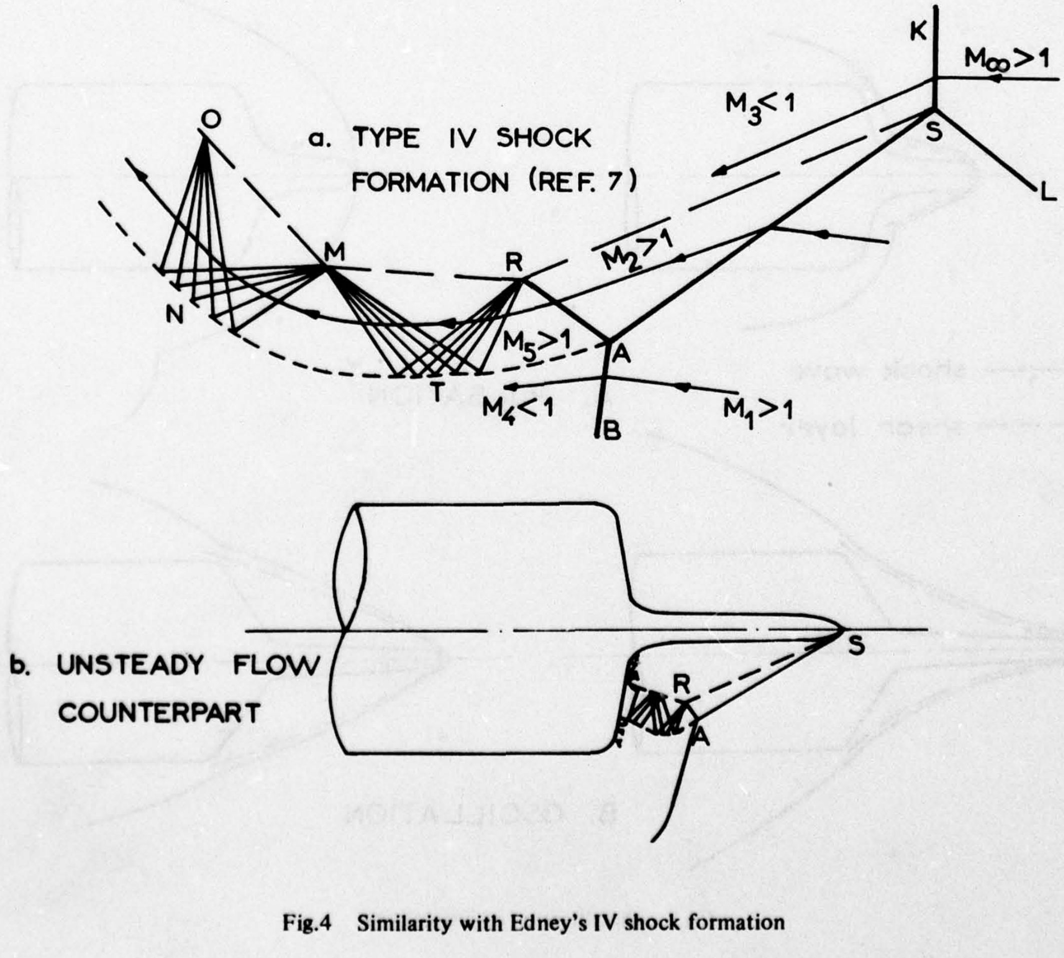

Fig.4 Similarity with Edney's IV shock formation

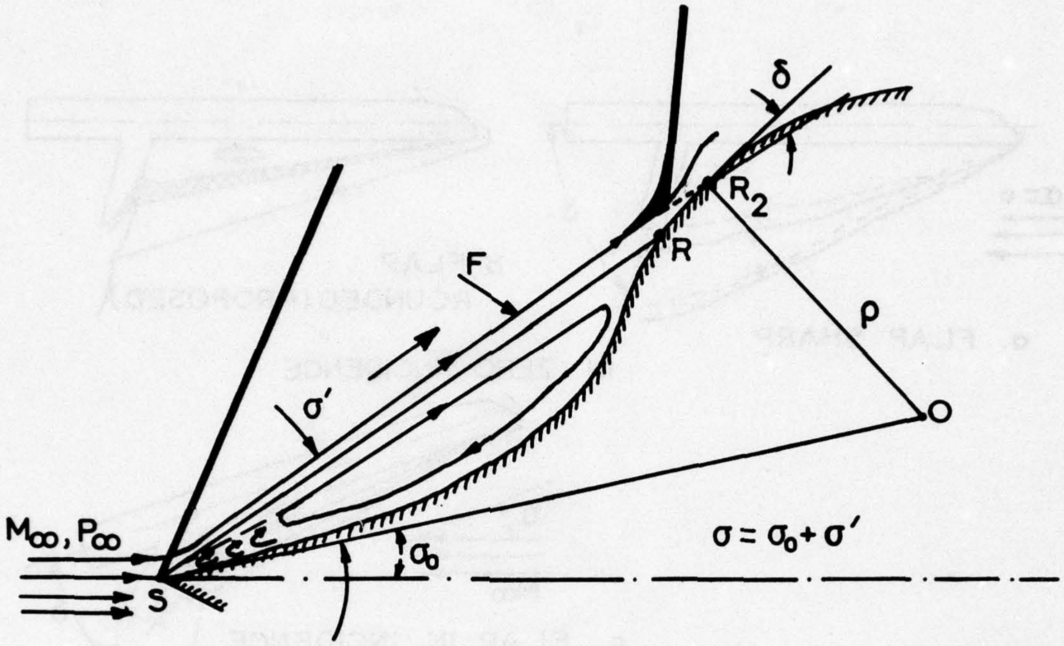

Fig.5 Leading-edge separation

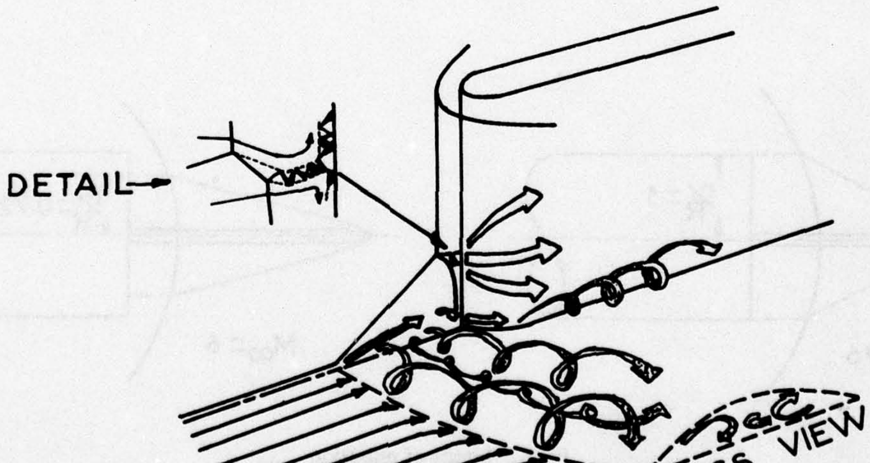

Fig.6 A blunt fin on a surface (Ref.12)

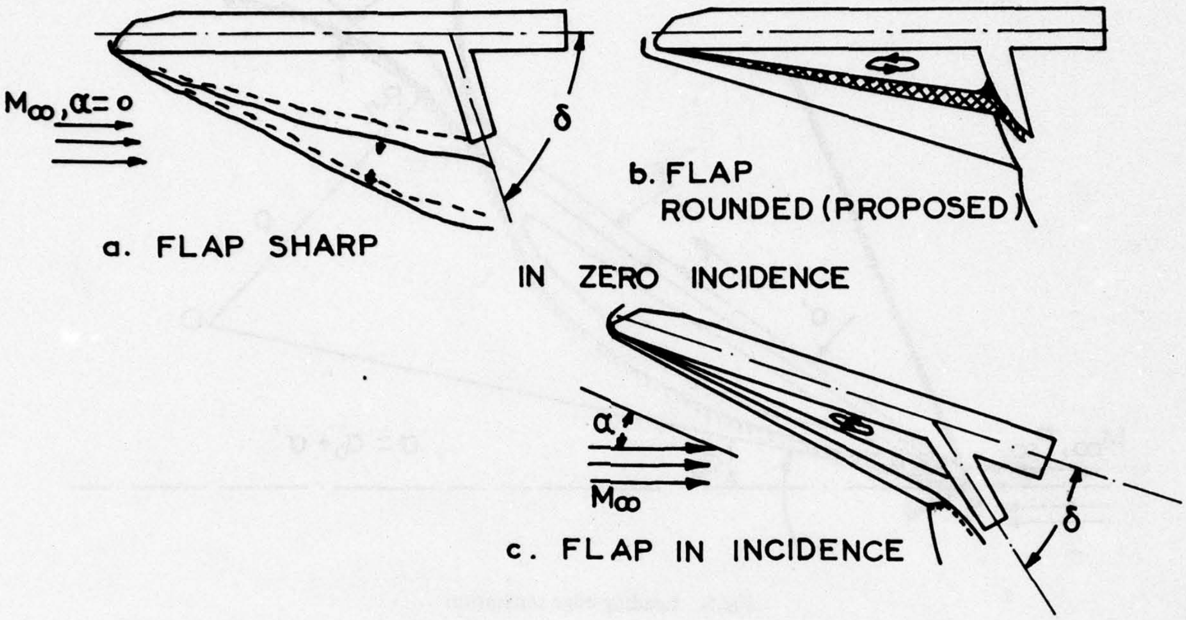

Fig.7 Space shuttle of Goldman-Obremski (Ref.13)

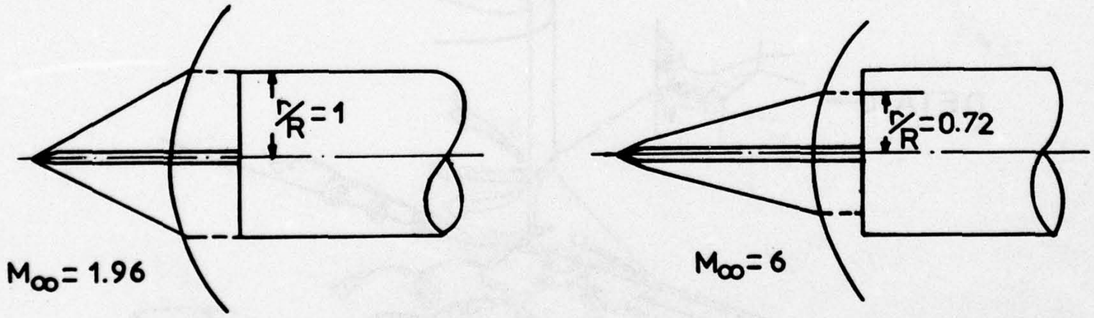

Fig.8 Limits of pulsation

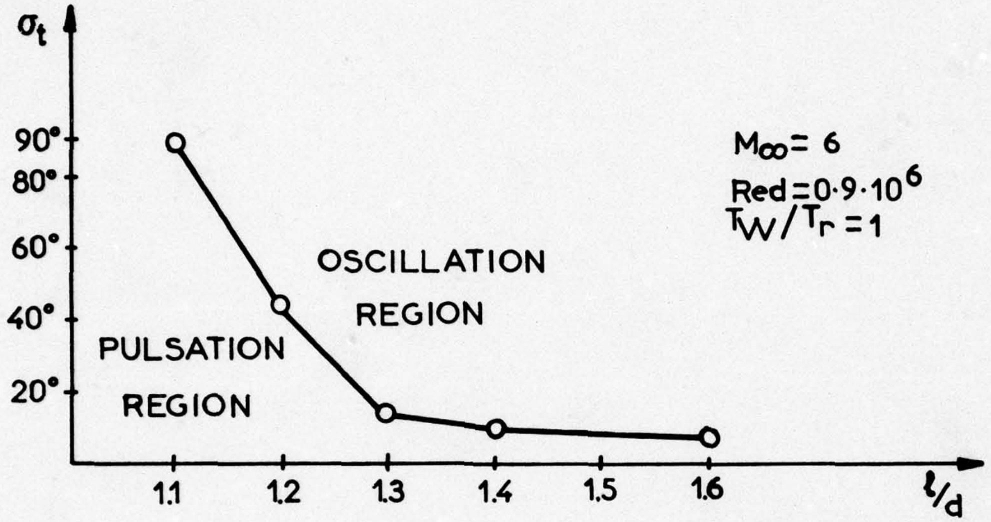

Fig.9 Transition from pulsation to oscillation

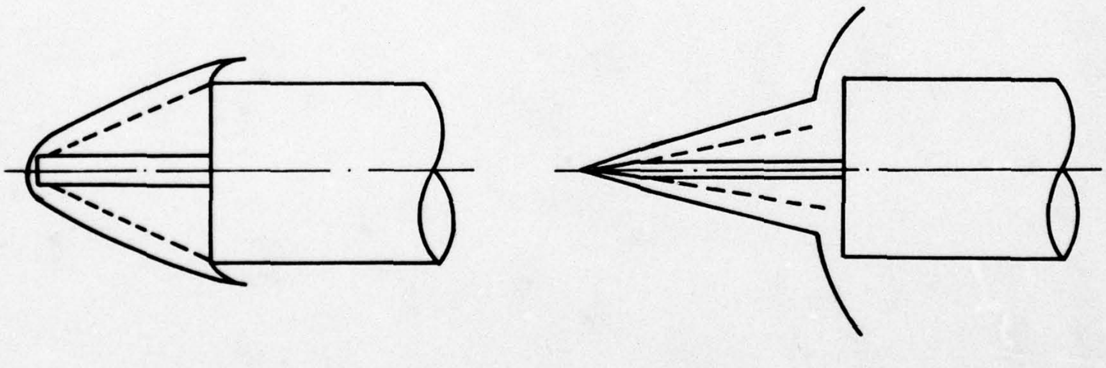

Fig.10 Influence of spike geometry

A RESUME OF AGARD SMP MEETING ON TRANSONIC UNSTEADY AERODYNAMICS

Mr W.J.Mykytow and Dr J.J.Olsen
The United States Air Force Flight Dynamics Laboratory
Wright-Patterson Air Force Base, Ohio
USA 45433

1. INTRODUCTION

The Structures and Materials Panel of AGARD held two one-day specialists' meetings on "Unsteady Airloads in Separated and Transonic Flow" in Lisbon, Portugal during the week of 18 April 1977. The first day's papers concerned "Airframe Response to Separated Flow."

The second day's papers concerned "Transonic Unsteady Aerodynamics for Aeroelastic Phenomena." The purpose of this second session was to report the rapid progress being made in transonic unsteady aerodynamics, to discuss the state of the art and future requirements, and to acquaint aeroelasticians with recent advances. Another purpose was to re-emphasize the long and urgent need to estimate reliable transonic unsteady airloads required for load, deflection, stress, stability, flutter and gust analyses in this critical speed region.

A condensation of the papers presented, an evaluation and a summary of conclusions and recommendations of the second session has been prepared and is contained in AGARD SMP Report , "Evaluation Report, the AGARD SMP Specialists' Meeting on Transonic Unsteady Aerodynamics for Aeroelastic Phenomena." This paper is a further condensation and summary to coordinate mutual interests between the Fluid Dynamics Panel and Structures and Materials Panel, as well as to highlight needs of aeroelasticians to aerodynamicists.

2. TECHNICAL SUMMARIES

Brief techiical summaries of each paper follow.

2.1 "Brief Overview of Transonic Flutter Problems," W. J. Mykytow

Previous to 1952, most flutter problems concerned control surfaces or tabs, and remedies were relatively straightforward. Higher speed flight and more flexible aircraft in the brief period 1952-1956 resulted in wing-external store, transonic control surface, T-tail, all movable surface, and fixed surface bending-torsion flutter (Table I). Reliable methods for estimating transonic unsteady airloads are lacking, so main reliance for research and aircraft development information is still the transonic flutter model. Figure 1 gives flutter model data for a straight wing and shows that the critical region extends to Mach 1.2 for lower aspect ratio wings. (A flutter condition exists when an applicable constant altitude line intersects or is tangent to the flutter stability curve. The flutter region is above the curve. b is the reference semi-chord; ω_α the torsional frequency; and μ the wing-air mass ratio.) Figure 2 shows that a large detrimental wing-air mass ratio effect exists for this swept wing model near M = 1.05. More dramatic and sudden drops in flutter speeds have been observed for T-tail and supercritical airfoil models. Causes are largely unexplained.

Transonic flight damping data (Figures 3 and 4) furnished by the British Aircraft Corporation show the continued care needed today to avoid control surface, all movable surface and store flutter.

Thus, methods for predicting transonic unsteady airloads have been required for twenty years. Without such capability, early design optimization cannot be achieved with confidence. Reliable methods would reduce risks and costs of model and flight tests.

2.2 "Unsteady Airloads on An Oscillating Supercritical Airfoil," H. Tijdeman, P. Schippers and A. J. Persoon

The authors present rare and needed information on an oscillating 16.5% thick supercritical airfoil. Thin airfoil theory predicts subsonic pressures reasonably (Figure 5). The strong shock case (Figure 6) shows the large shock motions with static angular changes. A sharp pressure peak occurs in quasi-steady and unsteady pressures which linear theory does not predict. This peak decreases with frequency and its phase angle shifts to 90° due to shock wave motion lag. The "shock free" data (Figure 7) show the bulge in quasi-steady and unsteady pressures produced by the supersonic flow. Again, thin airfoil theory is completely inadequate. The bulge region decreases with frequency, and a small and sharper peak near 65% chord occurs as a weak shock wave strength increases with frequency.

The authors discuss the decreased amplitude of shock motion with increasing frequency. Shock lag increases linearly because of the constant time lag of the Kutta wave travel.

They illustrate the large effects of boundary layer on steady flow and quasi-steady pressures (Figure 8). When boundary layer and thickness effects are included. The more forward pressure peak on the upper surface is better predicted.

Quasi-steady integrated coefficients show large increases in normal force coefficients (50%) produced by including thickness and incidence, but boundary layer effects decrease the change (-35%). For the shock free case (Figure 9), the quasi-steady theoretical design pressures for the upper surface show a bulgy pressure distribution over the supersonic region which agrees reasonably well with experimental design condition data. The lower surface data also show an improvement compared to thin airfoil theory. Several important conclusions and recommendations made by the authors have been assembled together with others at the end of this report.

2.3 "The Transonic Oscillating Flap; A Comparison of Calculations with Experiments," H. Yoshihara and R. Magnus

A displacement ramp is used to approximate viscous effects in two dimensional, finite difference calculations based on the exact inviscid Euler equations. Comparisons are made with the oscillating flap experiments reported by Tijdeman and Schippers. They show (Figure 10) a more aft mean position and less shock motions than measured. A mis-match of calculated and measured pre-shock pressure data is observed (Figure 11) and agreement is significantly improved when calculations at M = 0.854 are compared with M = 0.875 experimental data (Figure 12). The authors question the tunnel flow simulation. Shock positions and motions computed for M = 0.85 are in much better agreement with experimental data at M = 0.875.(Figure 13). While the mis-match in pre-shock pressures had an important effect on shock history, the authors state the effect would be far less on unsteady lifts and moments used in flutter analyses.

2.4 "Numerical Calculation of Unsteady Transonic Flows," A. Lerat and J. Sides

The full hyperbolic Euler equations are solved, satisfying the tangency conditions at the exact instantaneous surface positions, the Kutta conditions at the trailing edge, and allowing nonisentropic flow. The exact space domain is mapped by a product of two transformations where the first specifies the airfoil rigid body motion and the second maps the exterior part of the flow onto a rectangle. Equations, cast into conservation form, are solved by variants of MacCormack's scheme. The time step is restricted by stability conditions. Artificial viscosity and mesh refinements improve capture of the shock.

The method is applied to a NACA 0012 airfoil pitching about 25% chord, reduced frequency of 10 based on chord, and Mach = 0.8. Results are compared with those of Garabedian and Korn in Figure 14, and these results show that the shock jump satisfied the Rankine-Hugoniot conditions with good accuracy. Unsteady periodic results for 0, 90, 180 and 270° of the cycle are shown in Figure 15. They were obtained after two cycles of motion. There is very little shock motion at this high reduced frequency.

2.5 "Efficient Solution of Unsteady Transonic Flows About Airfoils," W. F. Ballhaus and P. M. Goorjian

The authors use efficient, conservative form, alternating direction, implicit finite difference procedures where the time step is based on accuracy rather than stability considerations. They apply the method to the low frequency, transonic small disturbance approximation of Euler's equations. Good agreement is obtained for the upstream blown shock wave motion, the part-time disappearing shock wave motion, and the oscillating shock wave motion reported by Tijdeman and Schippers for an oscillating flap at successively higher subsonic Mach numbers. Good agreement with the much longer calculations of Magnus and Yoshihara is also obtained.

Numerical results in Figure 16 show that the shock wave is stronger for solid, free air and free jet wall conditions, respectively. They suggest a shock weakening wall effect in NLR tests, since experimental phenomena are reported at higher Mach numbers. Figure 17 shows an oscillating shock for free air and an interrupted shock (picture B) for the free jet wall condition.

Use of the indicial response method and Duhamel's integral shows, in Figure 18, that the linear perturbation assumption produces valid lift and moment data compared to the time integration method for the NLR oscillating flap case of upstream propagating shock waves (Condition C) and interrupted shock wave motions (Condition B). Differences are noted for the stronger continuously oscillating shock Condition A.

2.6 "Application of a Finite Difference Method to the Analysis of Transonic Flow Over Oscillating Airfoils and Wings," W. H. Weatherill, J. D. Sebastian, and F. E. Ehlers

The authors use relaxation techniques to solve the small disturbance, high frequency transonic velocity potential which is separated into a steady term and an unsteady term linearized about the non-linear steady solution. Tangency conditions are satisfied on the line y = 0. Substantial numerical stability problems were encountered with purely subsonic as well as mixed subsonic-supersonic flows. The instability depended on mesh dimensions and increased with frequency and as Mach number approached 1.0.

The authors examine finite difference solutions of Hemholtz' equation, various outgoing waves, and wall conditions. No combination of boundary conditions gave a converged solution above a certain reduced frequency which depends on Mach number and mesh geometry.

Direct solutions of the large matrix equations markedly improved numerical stability, but accuracy was poor above the frequency at which relaxation techniques became unstable, possibly due to the crude mesh.

Unsteady pressures are calculated for a pitching wing at M = 0.875 and a reduced frequency of 0.06 (based on semi chord) using Ballhaus' and Bailey's steady state results. These are shown in Figures 19 and 20. They question their results at the 57% station, which seemingly had a stronger shock than the root station.

2.7 "Numerical Solution of the Unsteady Transonic Small Disturbance Equations," M. M. Hafez, M. H. Rizk, and E. M. Murman

The numerical instability problems of relaxation solutions are examined and consistent shock jump conditions which allow shock movement in the first order unsteady solutions are developed.

They propose a positive-definite system matrix obtained by premultiplying the original system matrix by its conjugate transpose. Relaxation procedures will then usually converge, even though they converge slowly. The authors demonstrate their method by application to a one dimensional problem. Results are shown in Table 2 and are compared with those of direct matrix solutions.

In developing consistent shock jump conditions for first order treatment of unsteady flows, the authors considered:

a. The potential expansion.
b. The consistent shock motion.
c. The steady potential jump condition.
d. The mean or average value of $K - \phi_{o_x}$
e. The unsteady potential jump condition.
f. The unsteady shock movement.

They gave simplified forms for a normal shock, developed a shock-fitting procedure for the unsteady potential problem, and discussed an alternate approach by Nixon using strained coordinates.

2.8 "A Practical Framework for the Evaluation of Oscillatory Aerodynamic Loading on Wings in Supercritical Flow," H. C. Garner

Non-linear steady pressures, taken from small perturbation theory or static measurements, and theoretical linear oscillatory loadings are used to produce an economic and approximate method applicable below 0.9. Numerical results are in fair agreement with measurements (Figure 21). Greater lags due to delays in upstream propagation are noticed. These need to be better simulated since they occur in regions of higher loadings. Higher lead angles on the aft chord are evident also.

Spanwise loadings for a wing oscillating about a swept axis at mid-chord are shown in Figure 22. Transonic small perturbation (TSP) methods give higher in-phase loadings than linear theory, the method using measured steady data and experiment. The measured quadrature loading in phase with velocity is more negative than the three predicted values. This is due to larger phase lags at the forward chord.

Figure 23 shows center of pressure locations. TSP theory, thin airfoil theory, the method using measured static data and experimental values are more aft, respectively. Aft aerodynamic centers frequently raise flutter speeds. Predictions based on inviscid supercritical flow could be overoptimistic, but those based on low Reynolds number tests might be too conservative.

More applications are needed to evaluate the subject approximate method.

3. CONCLUSIONS AND RECOMMENDATIONS

The following is a summary of the conclusions and recommendations reached by the authors who presented papers at the AGARD SMP specialists' meeting on transonic unsteady aerodynamics in Lisbon, Portugal in April 1977. Also included are thoughts of the present authors during their review and evaluation. The Structures and Materials Panel would appreciate receipt of comments and suggestions from the Fluid Dynamics Panel.

3.1 General

Aeroelastic Design and Analysis

Transonic Range - Most critical and dangerous

Unsteady load prediction methods lacking

Thin plate theory inadequate

3.2 Basic Principles

Unsteady Phenomena closely linked to steady flow field

Large changes in magnitudes and phases

Thickness, camber, incidence, amplitudes and shock motions are important

Viscous and wall effects important

- Porous wall research required
- viscous effects noticeable and opposite to thickness effects

Quasi-steady data provide insight

3.3 Aerodynamic Computational Methods

Methods must be extended to M = 1.2+

Large disturbance explicit methods expensive
  - Difficult to extend to 3D
  - Viscous ramp for 2D promising, but requires further exploration
  - Boundary conditions may be satisfied at instantaneous conditions

Relaxation Techniques
  - Numerical Stability problems not efficiently resolved
  - Shock jump conditions can and should be included

Implicit time-integration techniques
  - More efficient
  - Promising
  - Time integrated analysis of aerodynamic-elastic-mass system possible
    - Substantial change to frequency domain analysis

Engineering Methods
  - Intermediate and temporary methods emerging
  - Require evaluations

3.4 Experimental Data

- High priority and urgent need
- General lack of information
- Viscous effects and high Reynolds number data
- Wall effects
- U.S. lags in the state of the art
- Two dimensional flutter model tests for basic research?
- Correlate good flutter model data with emerging theories
- Limited flight measurements of unsteady pressures
  - Effects of wind tunnel walls and Reynolds numbers
- Cost information trade-off studies for multi pickups and configurations
  - In-situ versus tube type measurements

3.5 Aeroelastic Applications

Transonic aeroelastic design, analysis, optimizations cannot be made

3D methods lacking; incorporation of viscous effects difficult

Unsteady applications lagging steady transonic code usage

Approximate methods will find interim use

AGARD should encourage exchange of information and special meetings

Wind tunnel or theory could conceivably yield unconservative results

3.6 Cooperation

Standard Configurations should be defined and coordinated

Coordinations between steady and unsteady aerodynamicists increase

Transition of information to and applications by aeroelasticians required

4. REFERENCES

[1] Mykytow, W.J. "Brief Overview of Transonic Flutter Problems"

[2] Tijdeman, H.; Schippers, P.; Persoon, A.J. "Unsteady Airloads on an Oscillating Airfoil"

[3] Yoshihara, H. and Magnus, R. "The Transonic Oscillating Flap; A Comparison of Calculations with Experiments"

[4] Lerat, A. and Sides, J. "Numerical Calculation of Unsteady Transonic Flows"

[5] Ballhaus, W.F. and Goorjian, P.M. "Efficient Solution of Unsteady Transonic Flows About Airfoils"

[6] Weatherill, W.J.; Sebastion, J.D.; and Ehlers, F.E. "Application of A Finite Difference Method to the Analysis of Transonic Flow Over Oscillating Airfoils and Wings"

[7] Hafez, M.N.; Rizk, M.H.; and Murman, E.M. "Numerical Solution of the Unsteady Transonic Small-Disturbance Equations"

[8] Garner, H.C. "A Practical Framework for the Evaluation of Oscillatory Aerodynamic Loading on Wings in Supercritical Flow"

[9] Mykytow, W.J. and Olsen, J.J. "Evaluation Report: The AGARD SMP Specialists' Meeting on Transonic Unsteady Aerodynamics for Aeroelastic Phenomena" SMP Report

	1947 - 1951	1952 - 1956
TABS; CONTROL SURFACES	11	8
WING WITH EXTERNAL STORES	1	6
AUTOPILOT COUPLING	1	
TRANSONIC BUZZ RELATED		21
T-TAIL		1
ALL MOVABLE SURFACE		4
FIXED SURFACE - BENDING - TORSION		1

Table 1. Some Past Flutter Incidents

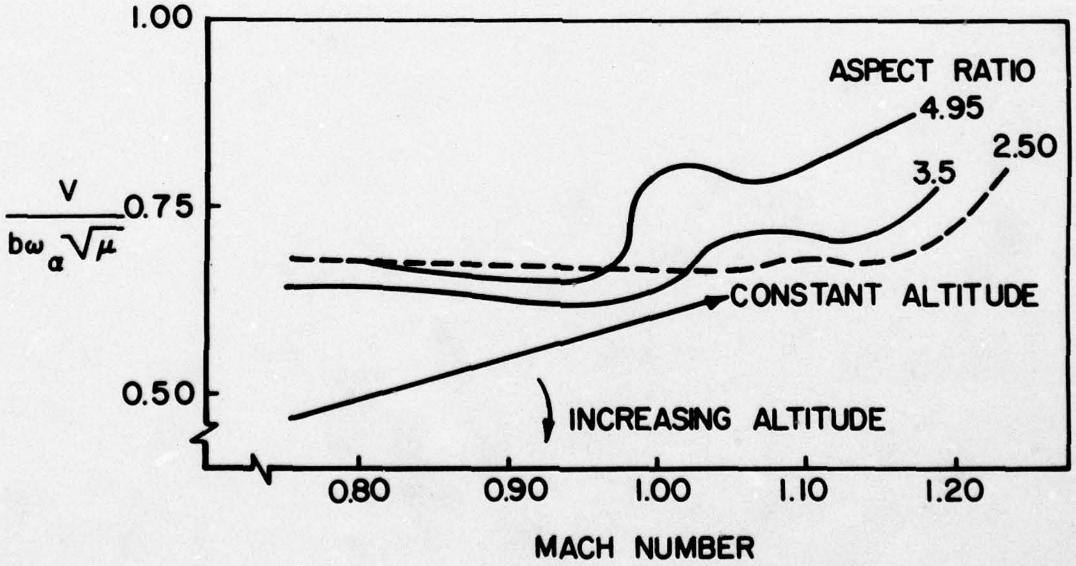

Fig. 1. Transonic Flutter Model Tests for Unswept Cantilever Wings.

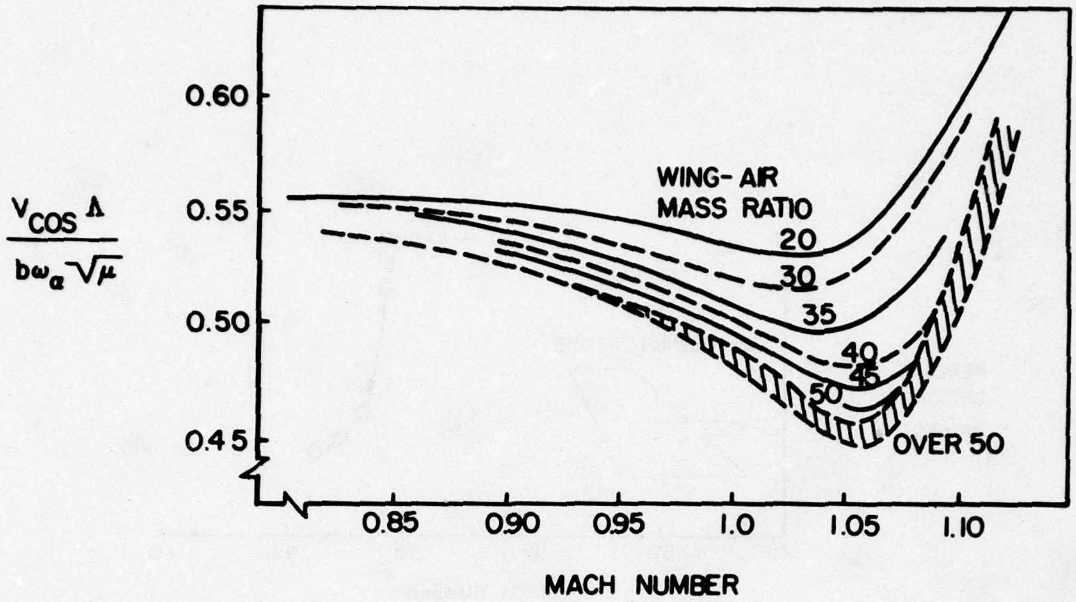

Fig. 2. Transonic Flutter Model Tests on Swept Cantilever Wings

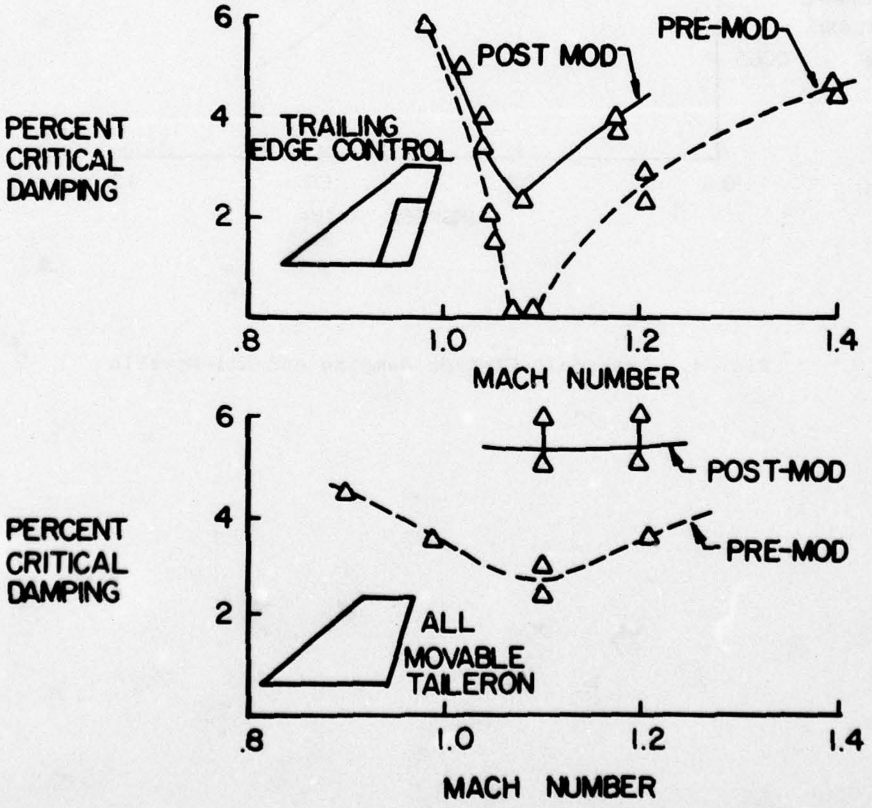

Fig. 3. Transonic Flutter Damping.

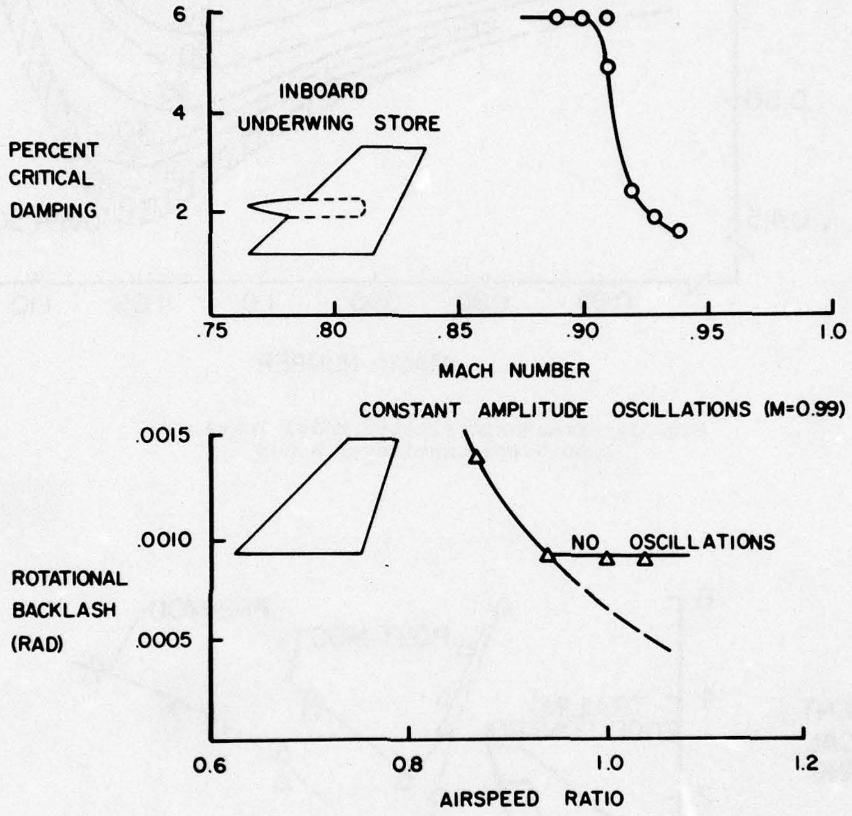

Fig. 4. Transonic Flutter Damping and All-Movable

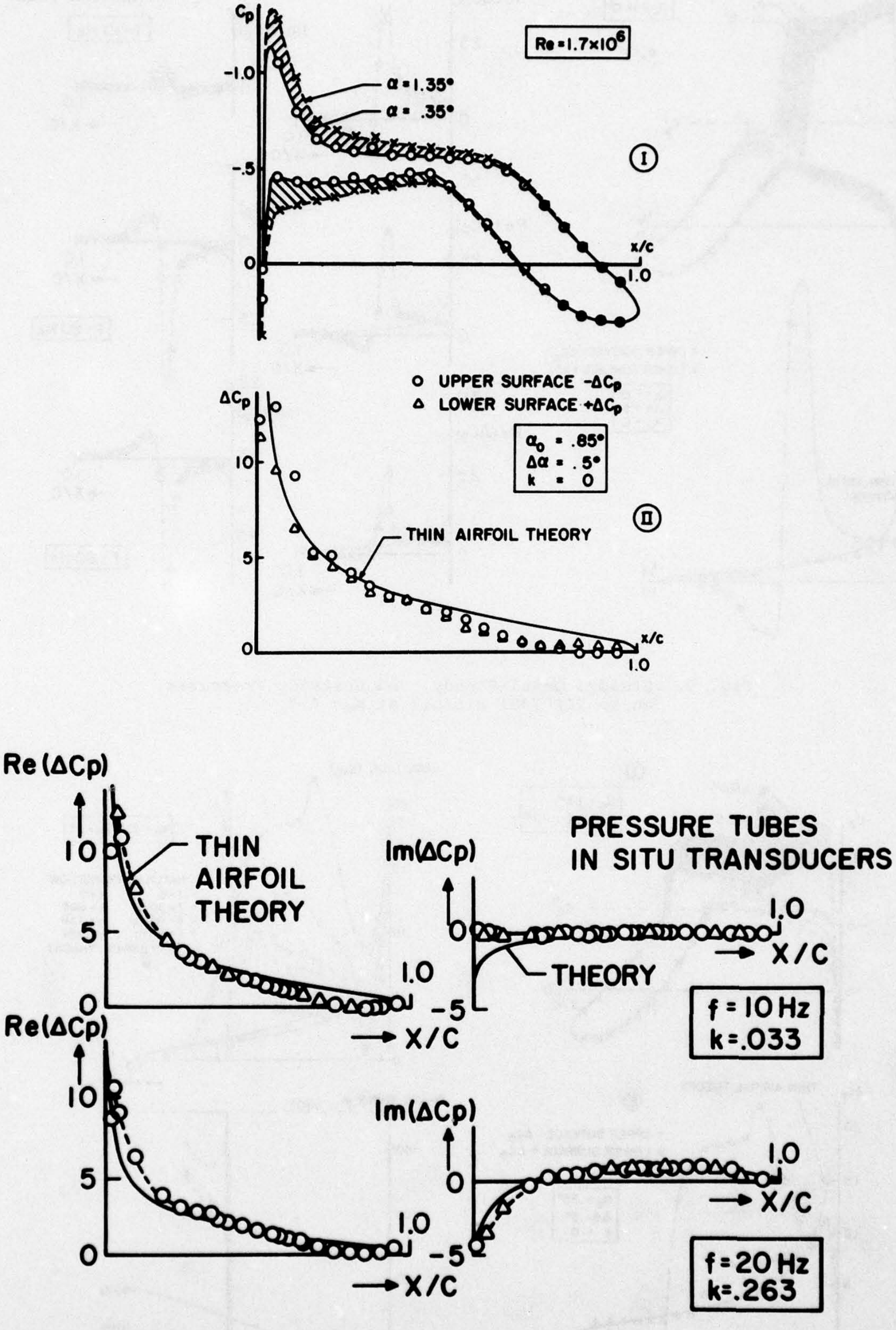

Fig. 5. Steady, Quasi-Steady, and Unsteady Pressures on an NLR 7301 Airfoil at M_∞=0.5.

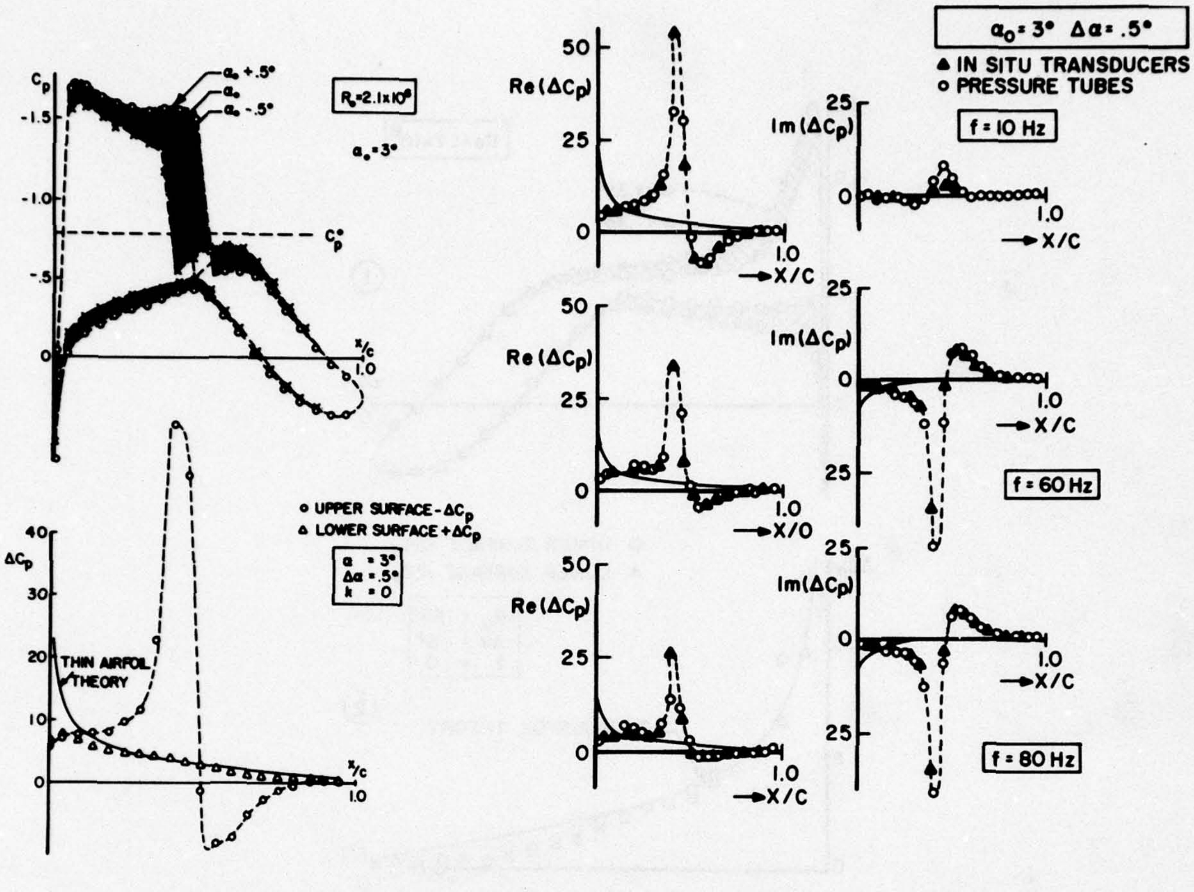

Fig. 6. Steady, Quasi-Steady, and Unsteady Pressures on an NLR 7301 Airfoil at M_∞= 0.7.

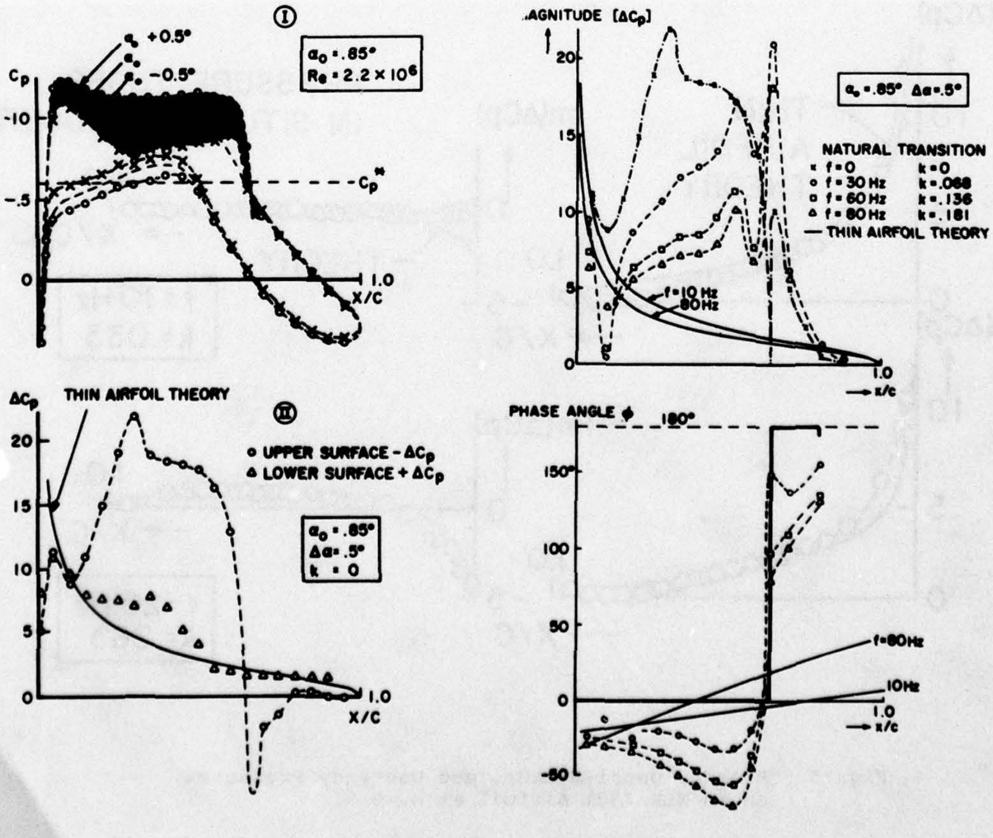

Fig. 7. Steady, Quasi-Steady, and Unsteady Pressures on an NLR 7301 Airfoil at M_∞ = 0.745.

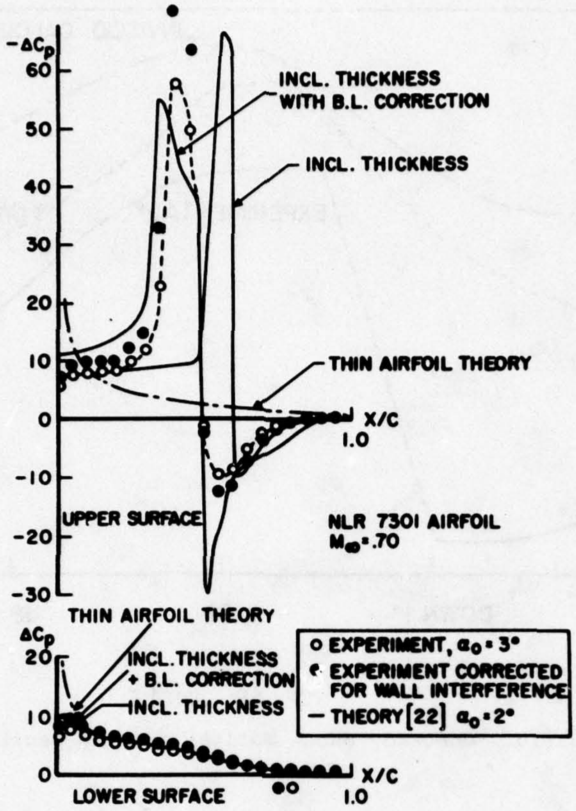

Fig. 8. Viscous and Thickness Effects on Quasi-Steady Transonic Pressures

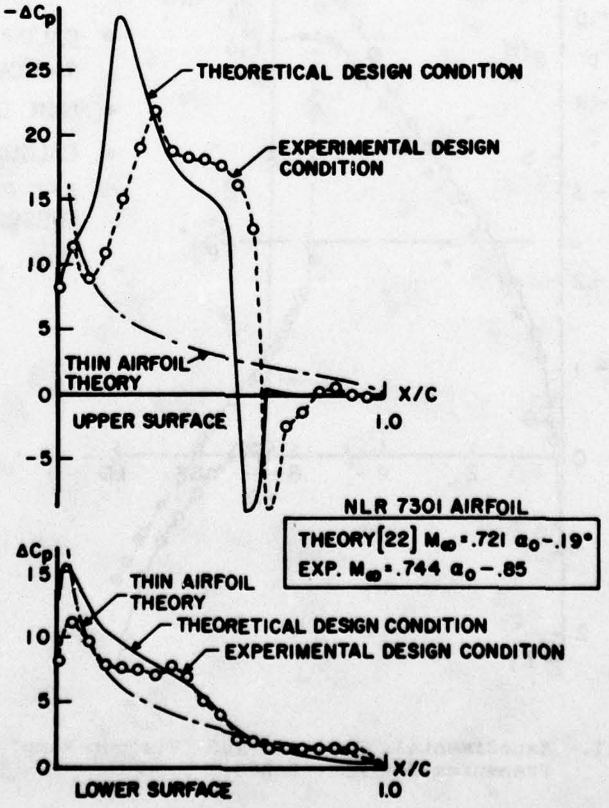

Fig. 9. Quasi-Steady Pressures for the "Shock-Free" Condition.

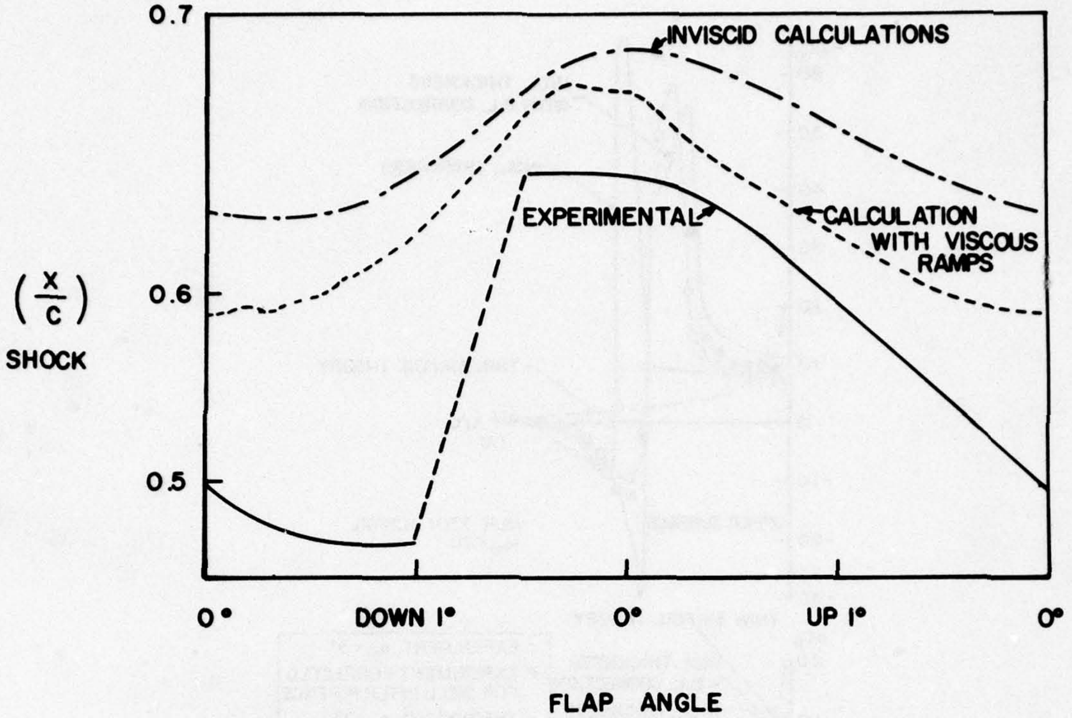

Fig. 10. Unsteady Shock Motions for the Oscillating Flap.

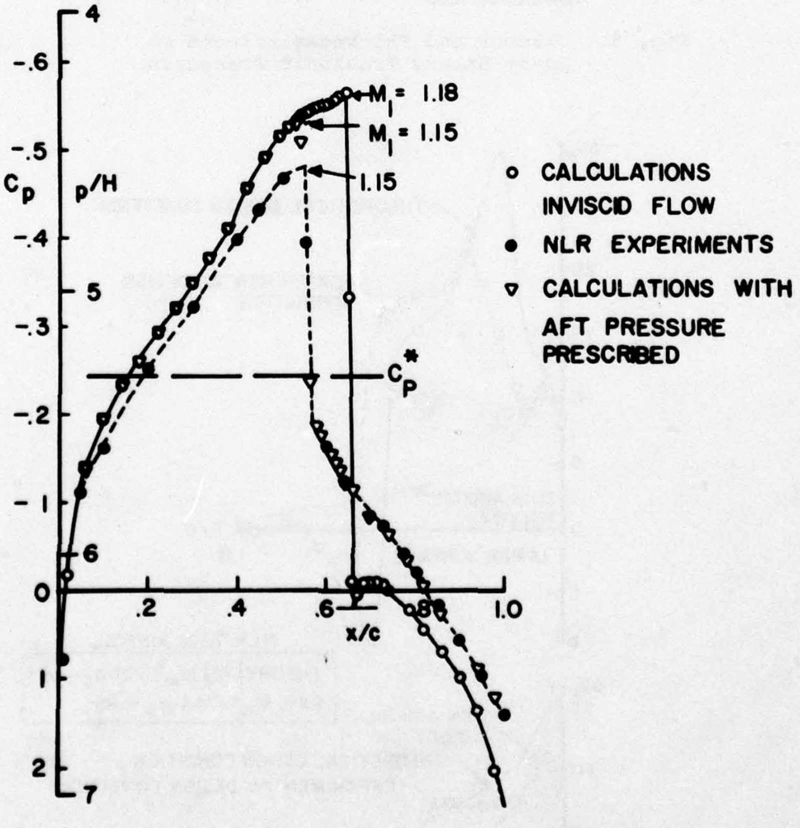

Fig. 11. Experimental, Inviscid and "Viscous-Ramp" Pressures for $M_\infty = 0.875$.

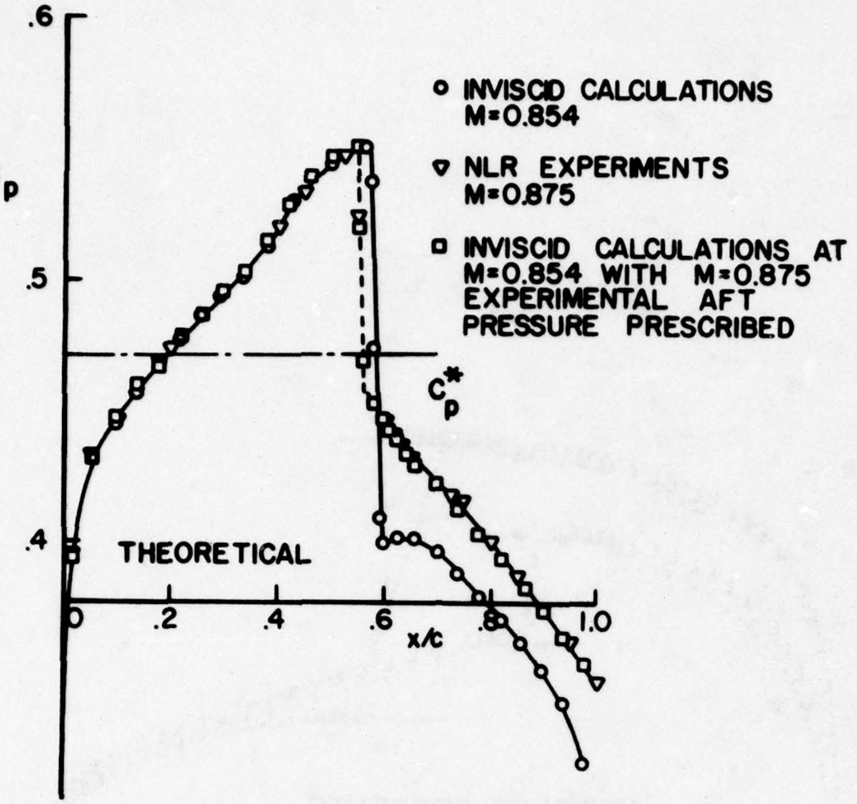

Fig. 12. Inviscid Pressures at M_∞ = 0.854 vs. Experimental and "Viscous-Ramp" Pressures at M_∞ = 0.875.

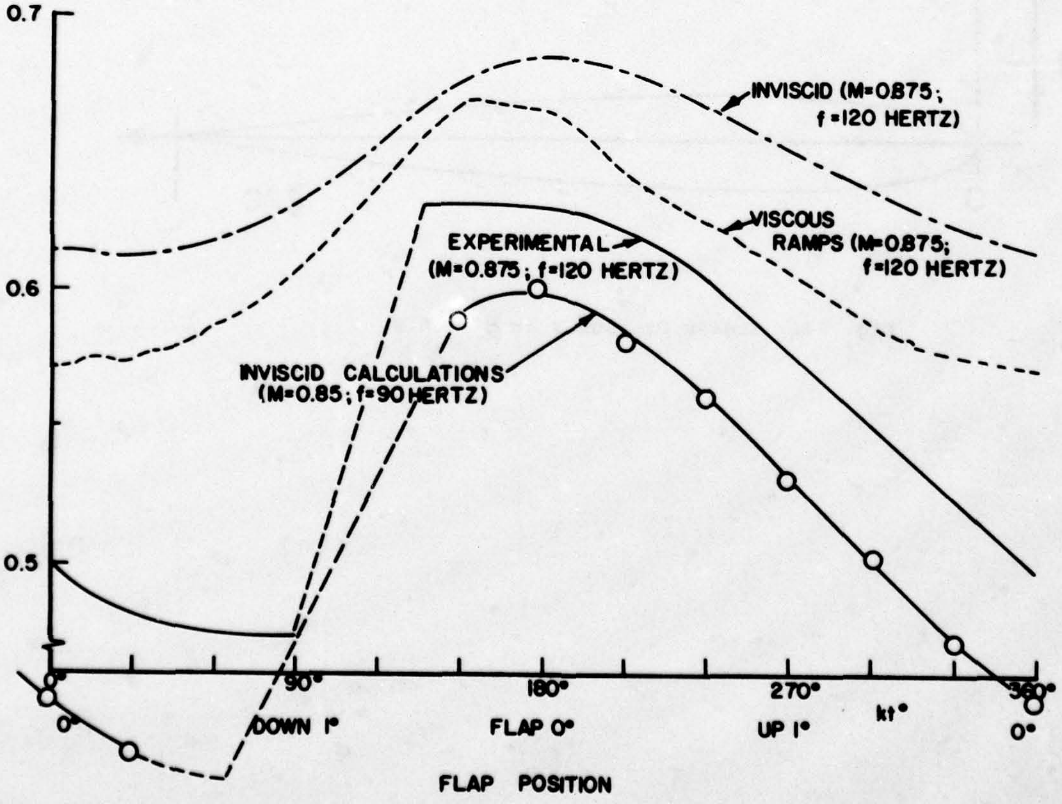

Fig. 13. Unsteady Shock Motions for the Oscillating Flap.

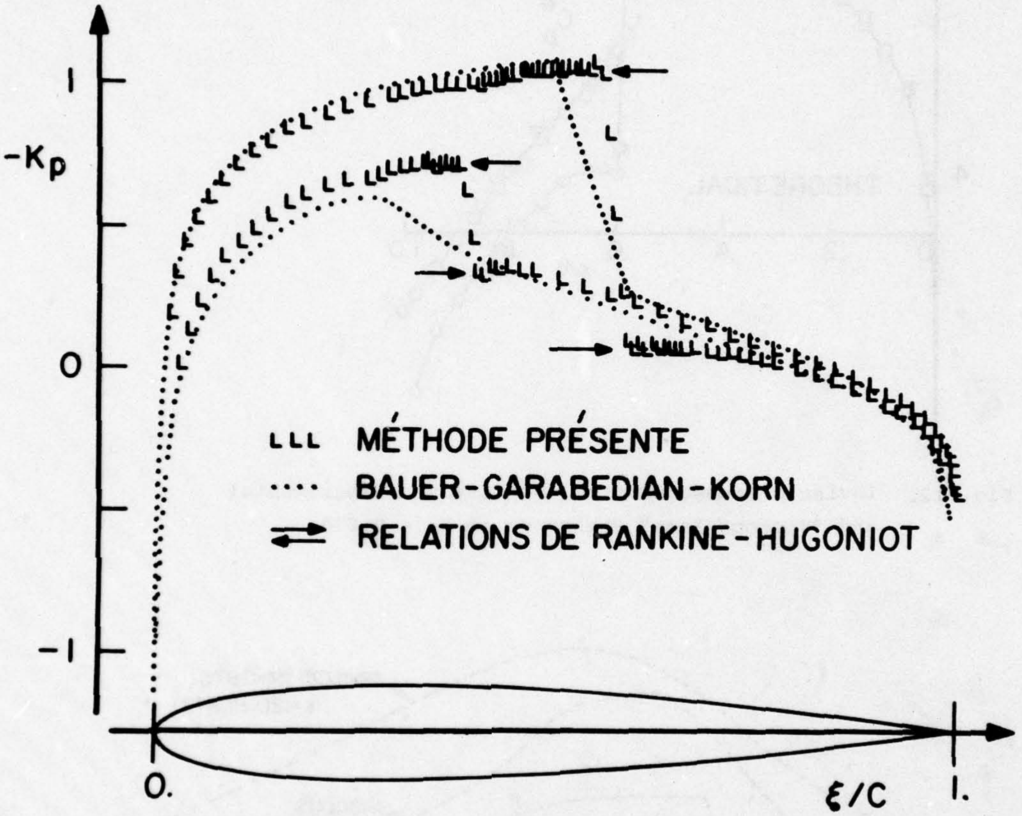

Fig. 14. Steady Pressures at $M_\infty = 0.8$.

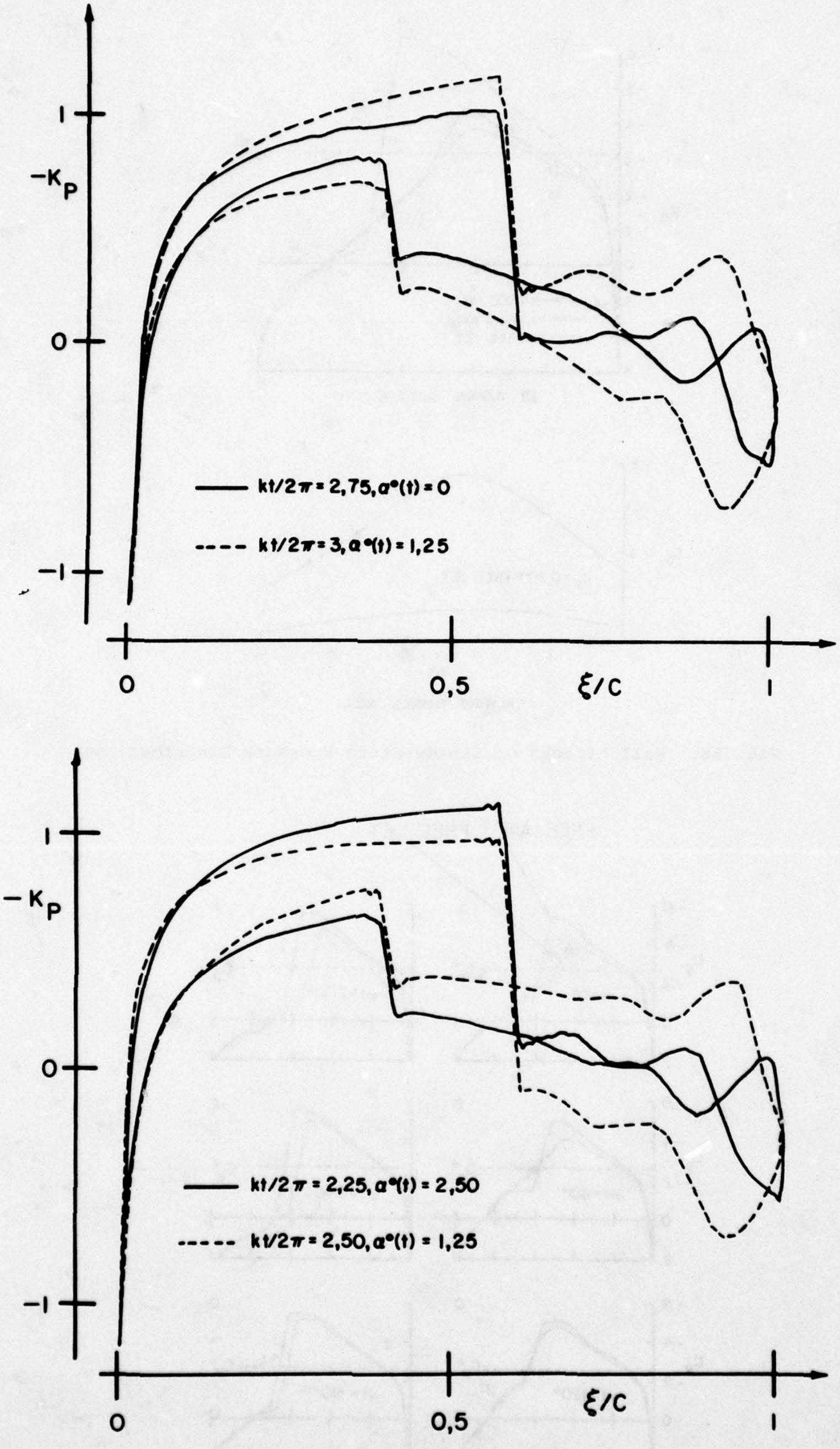

Fig. 15. Unsteady Pressures at $M_\infty = 0.8$, $k = 10.0$

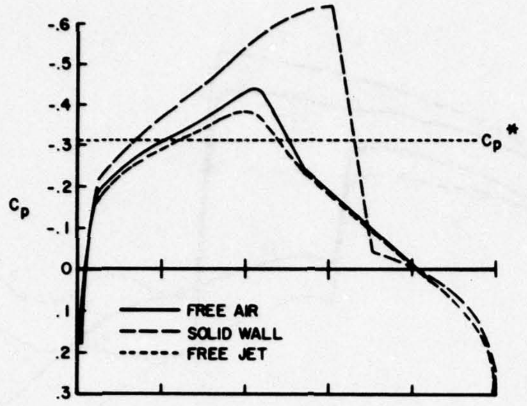

(a) AIRFOIL SURFACE

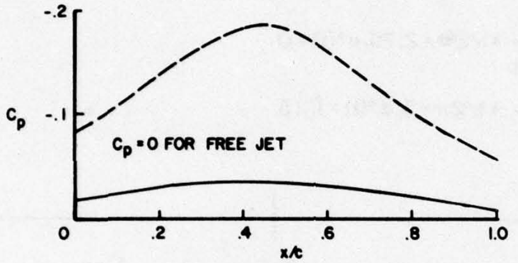

(b) WIND TUNNEL WALL

Fig. 16. Wall Effects on Steady-State Pressure Distributions.

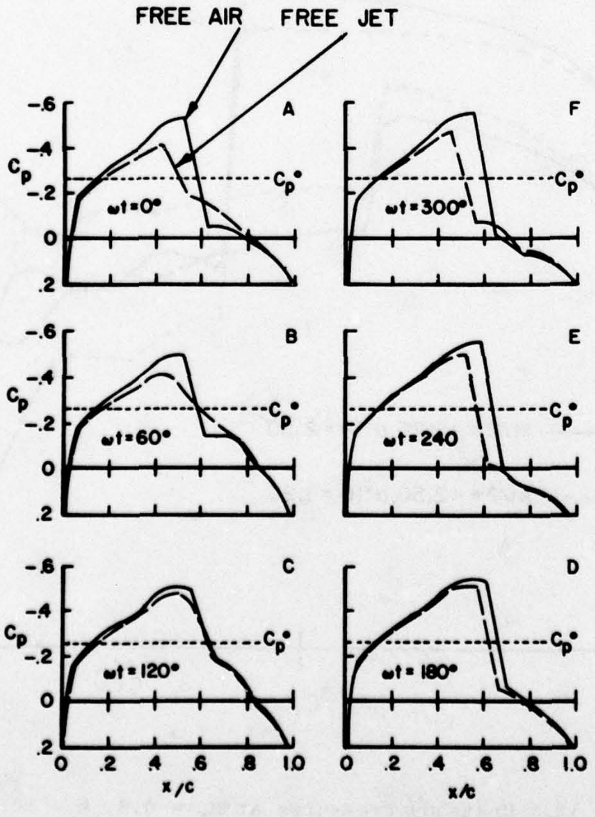

Fig. 17. Wind Tunnel Wall Effects on Unsteady Pressures, Oscillating Flap, M_∞ = 0.865, k = 0.468.

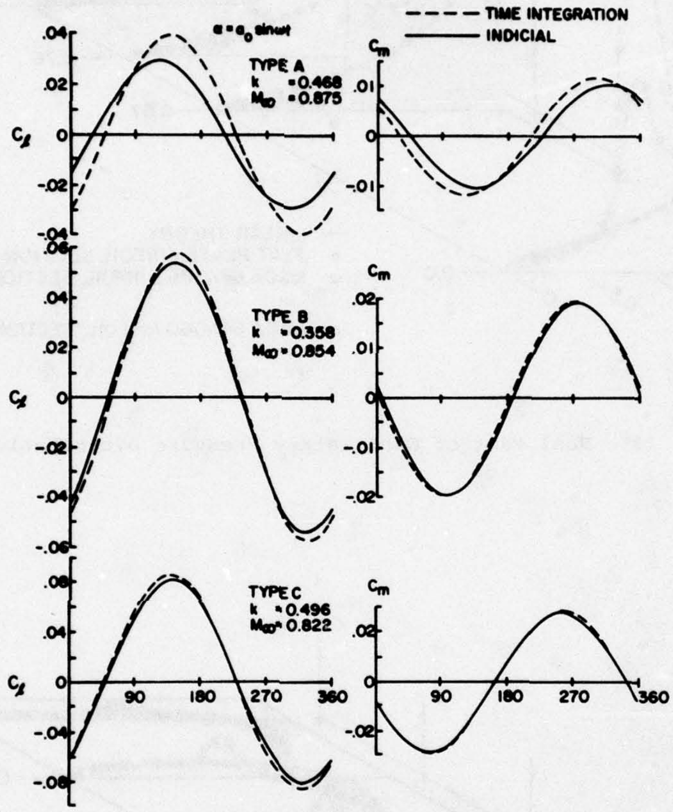

Fig. 18. Direct Integration and Indicial Calculation and Transient Lift and Moment.

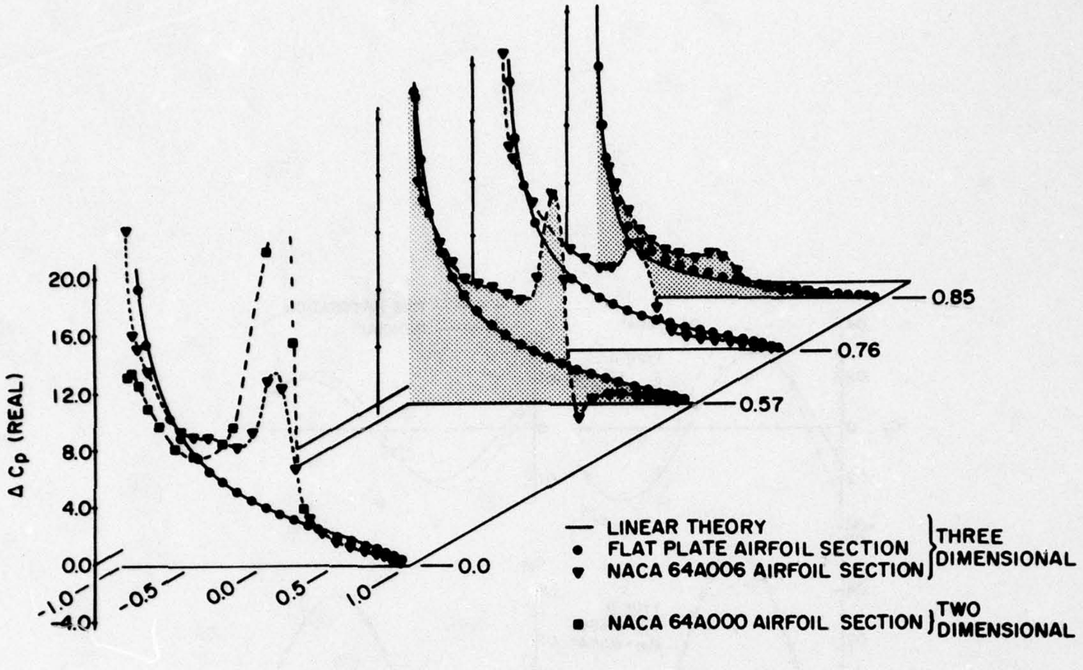

Fig. 19. Real Part of Oscillatory Pressure Distribution.

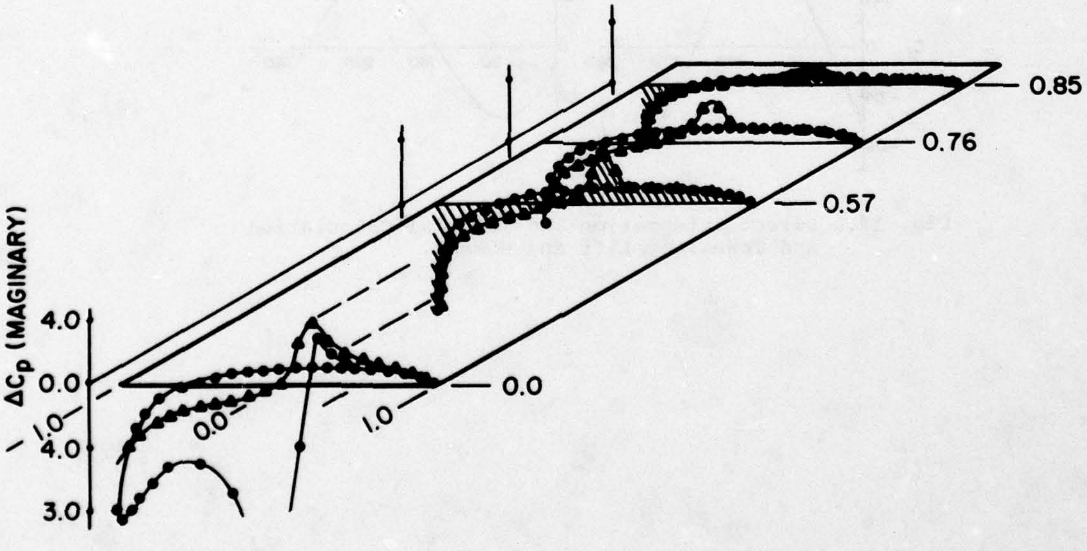

Fig. 20. Imaginary Part of Oscillatory Pressure Distribution.

x_j	ϕ_j RELAXATION	 DIRECT INVERSION	 EXACT
0.0	0.5000	0.5000	0.5000
0.1	-0.0025	-0.0036	-0.0084
0.2	-0.5195	-0.5065	-0.5151
0.3	-0.9428	-0.8969	-0.9094
0.4	-1.1776	-1.0881	-1.1055
0.5	-1.1667	-1.0377	-1.0606
0.6	-0.9067	-0.7568	-0.7845
0.7	-0.4518	-0.3078	-0.3374
0.8	0.0980	0.2094	0.1823
0.9	0.6204	0.6802	0.6640
1.0	1.0000	1.0000	1.0000

Table 2. Comparison of Relaxation, Direct Inversion, and Exact Solutions of a One-Dimensional Problem.

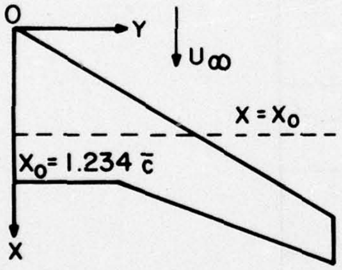

$M_\infty = 0.84, \bar{\nu} = 0.393$

MODE 1 $z_1 = \bar{c}$

MODE 2 $z_2 = x_0 - x$

LINEAR THEORY

$$(Q_{ij}) = \begin{pmatrix} -0.210 & 2.480 \\ -0.049 & -0.041 \end{pmatrix} + i \begin{pmatrix} -0.896 & -0.141 \\ 0.021 & -0.417 \end{pmatrix}$$

PRESENT METHOD WITH STATIC DATA FROM TSP THEORY

$$(Q_{ij}) = \begin{pmatrix} -0.338 & 3.526 \\ -0.043 & -0.327 \end{pmatrix} + i \begin{pmatrix} -1.276 & -0.087 \\ 0.137 & -0.455 \end{pmatrix}$$

SEMI-EMPIRICAL METHOD WITH MEASURED STATIC DATA

$$(Q_{ij}) = \begin{pmatrix} -0.133 & 1.895 \\ -0.077 & -0.006 \end{pmatrix} + i \begin{pmatrix} -0.689 & -0.169 \\ 0.015 & -0.310 \end{pmatrix}$$

Fig. 21. Theoretical and Experimental Effects of Initial Incidence on Oscillatory Pressures.

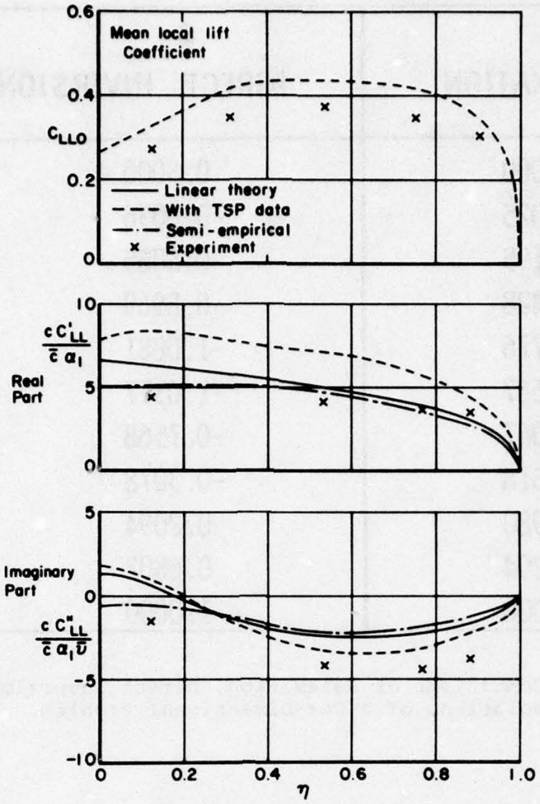

Fig. 22. Spanwise Distributions of Mean and Oscillatory Lift Section Lift Coefficients.

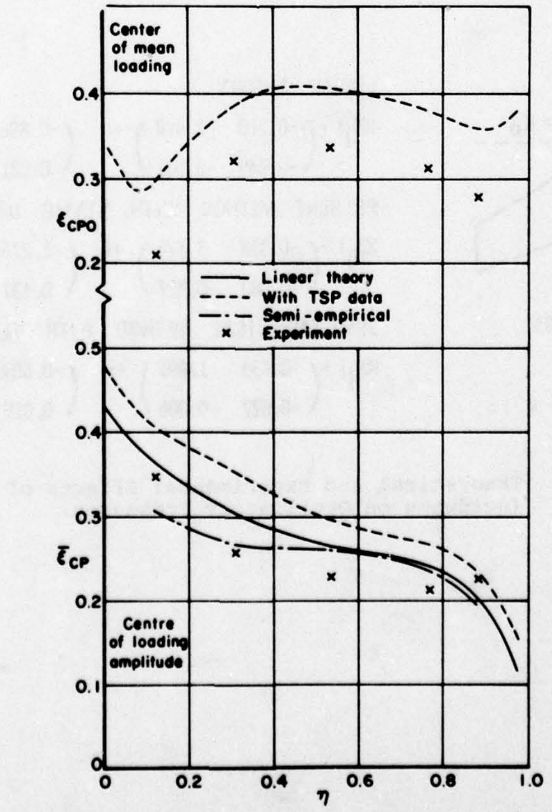

Fig. 23. Spanwise Distributions of Mean and Oscillatory Chordwise Centres of Pressure (M_∞ = 0.84, ν = 0.393)

The Importance of Unsteady Aerodynamics in Rotor Calculations

G.M. Byham
T.S. Beddoes
Westland Helicopters Ltd., Yeovil BA20 2YB, England

Summary

Unsteady aerodynamics is an important feature of detailed helicopter rotor loads calculation, and has special significance at the extremities of the flight envelope. This paper reviews briefly the background which has allowed considerable simplification of the aerodynamic model required for rotor calculation methods. The impact of compressibility and dynamic stall on the limiting behaviour of the rotor is also discussed, and it is shown, particularly for the condition of stall flutter, that the interaction of blades with discrete tip vortices is a major factor in controlling the blade torsional motion. As a result of these observations it appears likely that wake distortion, particularly in the vertical plane, will be necessary for detailed calculation of stall flutter.

Introduction

Since W.P. Jones reviewed helicopter rotor unsteady aerodynamics in 1972 (Reference 1), a growth has taken place in our knowledge of how to determine and quantify the aerodynamic limitations of the rotor in forward flight.

Work on the dynamic stall of aerofoils has continued and its coupling to a rotor calculation has allowed the prediction of helicopter "stall-flutter" with consequent growth in root torsional loads. With experience of calculating rotor stall flutter conditions a better understanding has been developed of how the phenomenon may possibly be controlled, and what extensions to the theoretical model may be needed to improve detailed evaluation.

Developments have also taken place in the calculation of rotor blade flows at high Mach numbers. Test/theory comparisons now lead us towards refinements of the theory which will allow study of suitable tip planforms for the advancing blade, and possibly a more precise definition of the advancing blade limitations experienced by the rotor.

In the field of hover wake flutter, high Mach number flutter and vibratory load prediction the discussion in W.P. Jones' paper stands and a reiteration in this discussion appears unprofitable. It is therefore my intention to concentrate more on the part that unsteady aerodynamics plays in determining the limiting conditions on the rotor in forward flight. To accomplish this it is necessary to start by reviewing how the unsteady behaviour of the rotor in linear aerodynamic conditions must be modelled, as a basis for the more empirical non linear aerodynamic phenomena.

Elements of Unsteady Aerodynamics on Rotor Blades

The strong time dependent nature of the rotor environment originates from a number of basic elements of the flow field. For instance local angle of attack is forced to vary through the application of once per rev pitch variations (to produce the required rotor attitude) combined with inflow variations brought about by the passage through a time varying downwash field and blade flapping response. More complicated quasi-incidence effects are produced by the passage of a blade close to discrete vortex trailed from previous blades. Variations in the velocity of a blade element give rise to large dynamic head changes, varying Mach number and Reynolds number; furthermore the variations in vector addition of the velocity components yield timewise variations in local sweep on the rotor blade. Flow fields from external sources such as the helicopter fuselage, give rise to significant high frequency or impulsive inputs to the inflow variation, in areas where the produce of C_L and dynamic head are large. Flow field interactions from one rotor on another in many cases compound features already mentioned but can in addition give rise to strong time varying characteristics that have a large impact on noise and vibration. Beyond the fundamentals of unsteady aerodynamics already covered there follows the more complicated hierarchy which originates in the response of the blade. At high Mach numbers the possibility of blade flutter is present with consequent vibration issues and non repeatable flapping. At high incidences penetration of stall can give rise to negative damping and a consequent non-linear torsional degree of freedom flutter which may damage the control circuit, generate vibration and produce handling issues.

Figure 1 is a schematic degeneration of the elements of unsteady aerodynamic effects outlined above and is set out mainly to give some perspective to the variety of sources that are present on a helicopter rotor and the way in which they couple. Blade control inputs and the first order flexural response they induce generate a low frequency, high amplitude variation in angle of attack around the rotor in forward flight. Higher frequency flexural response tends to contribute little to the aerodynamic conditions of the blade since incidence perturbations are small compared with the first order impacts. Blade torsional response is an important factor and features in two significant ways. High frequency, high amplitude response is a major part of stall flutter and is properly modelled by considering the full non-linear unsteady characteristics of the motion and aerodynamic time history. Low frequency high amplitude response can be brought about by the action of basic aerodynamic torsional loads (C_{MO}, lift offsets, etc.) in combination with an appropriate torsional stiffness and may have performance or handling impacts.

From the flow field the periodic events are largely self explanatory. The inflow characteristics give rise to low frequency quasi heave perturbations which must be properly accounted for in the linear unsteady representation. In addition the variation of inflow, combined with fuselage flow effects distort the wake geometry and tend to accentuate the presence of wake singularities which are brought closer to the blades. As with the high frequency torsional response this has a significant impact on the onset of non-linear unsteady effects and is a prime feature for the detailed quantitative prediction of the flight envelope.

The extent to which a fully developed representation of each unsteady element is required depends very largely on identifying what aspects of the helicopter it influences. For instance the most basic rotor calculations of blade fundamental deflections and rotor power at flight conditions well inside the aerodynamic envelope can be adequately made using a linear quasi-static approach. At the other extreme analysis of the flight boundary of the rotor requires a proper model of the non-linear unsteady aerodynamics of a blade section through to separated flow whether at high or low Mach number, and in addition a proper understanding of the structure, position and influence of the discrete vortices in the rotor wake.

The following sections of this paper are set out to identify those elements of unsteady aerodynamics which group together to form particular problem areas, and where possible to illustrate how their components are at present being analysed and with what success.

Unsteady Aerodynamics in Attached Flow

The Wake

Modelling of the rotor wake has been considerably influenced by the development of computing capacity. In the mid sixties effort was directed at producing vortex models of the wake structure with the inclusion of both trailing and shed vorticity. Vortex elements were aligned along the geometric trajectories of the blade elements in space as the rotor translated in forward flight. Downwash effects at a blade from the overall wake were computed and a closed solution was sought where blade element loading time histories, produced by the computed variations, were compatible with the wake strength distribution.

The complexity and computing effort required to model a rotor with fully representative wake makes the calculation unwieldy for design uses, and as a result more recent approaches have used a simplified wake representation, based largely on the form of the fundings of those workers who first tackled the problem. For instance, Miller, References 2 and 3, developed a full wake model including shed and trailed elements of vorticity. He shows in Reference 2 how removal of wake elements in turn affected the lift deficiency and phase of the loads produced at a particular blade station for a rotor in forward flight. Figure 2a, taken from Reference 2, illustrates Miller's findings. Here equivalent Theodorsen functions are plotted for the 80% span station of a three bladed rotor, in response to the 3 cycles/revolution downwash variation. At low advance ratio removal of the trailing wake has only a small effect on the response and phase of lift, while further removal of the far shed wake, (wakes left by all other blades than the subject) is significant. As advance ratio increases, the relevance of the far shed wake diminishes until the unsteady behaviour of the blade section is well approximated by considering only the influences of its own shed wake on itself. Figure 2b, also taken from Reference 2, broadens this point by comparing the classical 2-dimensional unsteady behaviour of a section to that computed using the full rotor wake model, at a range of downwash harmonics. The histograms at each frequency represent changes in advance ratio, and it can be seen that for of 0.3, which is typical of helicopter cruise conditions, the classical 2-D model for the section behaviour compares well for a wide range of frequencies. The dependence on is explained to a first order by considering the wake geometry. As speed increases blades encounter previous shed wakes for progressively smaller portions of the azimuth, and thus experience a progressively decreasing influence.

The implications of this work have found their way into a number of the calculation procedures at present used for rotor aerodynamic prediction. Vertol, as described by Tarzanin, References 4 and 5, use a Theodorsen function to represent the rotor blade shed wake and model only the trailing wake structure explicitly. Similarly Westland Helicopters, as described by Beddoes Reference 6, represent the unsteady aerodynamic terms through the successive application of a Wagner function at each azimuthal step, again with an explicit trailing wake.

Within Reference 6 it is shown that the Wagner model, applied in this fashion, compares well with measurements for harmonic motion in both phase and amplitude of lift, - this is shown in Figure 5. The application of the Wagner model falls radily into line with the structure of rotor calculations which tend to be based on calculation procedures which step round the disk in small increments of azimuth. In addition it eases some of the problems of distinguishing between pitching and heaving motion (periodic and non-periodic) in a flow field where time variations are produced by combinations of downwash, blade motion and in-plane velocity. Furthermore such an approach links readily into a time delay representation of dynamic stall.

Tarzanin, in Reference 4, shows that in fact the unsteady terms do not play a large part in defining for instance control loads (and hence section pitching moments) in sub stall flight conditions. Figure 3, taken from Reference 4, indicates the behaviour of the control loads (sub-stall) with and without the unsteady terms. Figure 4 helps to show why this conclusion may be formed. Here control load time histories around the azimuth are shown and it can be seen that the peak-peak loads are derived from what is basically a once-per-revolution oscillation with some small higher frequency contamination. In this condition therefore little significant high frequency forcing is being generated by the blade, reduced frequency is low and the use of a quasi-static theory should be a good approximation.

It is noticeable in Figure 3 however that at the onset of some blade stall phenomena the proper calculation of blade loads depends on the presence of a linear flow unsteady airloads representation.

So far the discussion has assumed that current practice in rotor modelling makes use of blade element techniques to piece together the problem. Other approaches are in use which treat the rotor as a closed problem, solving the airloads and blade response characteristics as a combined system. Costes, Reference 7, has developed such a model where the lifting surface of the blade and its wake are treated together with the motions which define the aerodynamic boundary conditions. Implicit in this approach is the assumption of a prescribed wake geometry and calculation from first principles of the lift/incidence relationships for the blade. Extension of the model to account for stall has been included, breaking into the closed nature of the problem to make the appropriate non linear representations of the blade aerodynamics.

Unconventional Rotors

The developments in rotor unsteady modelling and the approximations which may be used in producing useful results sub-stall are based on the assumption that the rotor system is conventional and operating at conventional advance ratios. A similar justification does not at present exist for say a co-axial rotor operating at high where the wake of an upper disk naturally passes close to blades of the lower rotor. Here very strong interactions of blades with both shed and trailing wake are commonplace, and could lead readily to unsteady air loads of significant proportions.

Casting the net further, rotor-borne aircraft are now being considered which operate at very high advance ratios (greater than unity) and maintain trim by use of blade blowing. Williams, References 8 and 9, indicates the form of loading that may be encountered around the rotor in high speed forward flight where a high level of loading is extracted from the reversed flow region of the disk, Figure 6. Taking this radial and azimuthal distribution Jupe at WHL has constructed the vorticity vector distributions around the disk and plotted its location as it is left in space by the passage of the blades. Some interesting features can be noted from this result as seen on Figure 7. Of major importance is the fact that the vorticity is highly concentrated near the edge of the reversed flow region. This is largely a result of the blowing reversal in the reversed flow region to maintain positive thrust. As the edge of the reversed flow region is traversed the bound circulation on the blade changes sign and the vortex wake, especially the trailed component, is reinforced. Because of the low relative velocity in this region the wake vorticity becomes concentrated geometrically and the distribution of Figure 7 is generated. Figure 7 clearly shows that the blade lies essentially parallel to the vortex filaments, in a region where the wake vorticity can be as much as twice that on the blade and of opposite sign to the blade vorticity. It is questionable whether a rotor which does not extract thrust from the reversed flow region would suffer the same occurrence since in this case the sign of circulation does not change and thus reinforcement of the strength of the trailing wake would not take place in the same way.

Wake modelling is a current concern in analysis of concepts such as the X wing, and in view of the vorticity distribution produced in Figure 7, it is clear that influences through the wake will be large. It seems therefore that the approximations for the modelling of unsteady characteristics as used for conventional, low rotors, would not carry through and an attack from first principles would be necessary. In addition wake distortion can clearly be an important feature, as well as the need for a careful approach to the forces and moments produced on a blade when passing obliquely through an almost discrete vortex.

Unsteady Compressibility Effects

The basic once per revolution variation in local velocity seen by the rotor blade clearly excites unsteady phenomena at a range of Mach numbers. On the advancing blade where the local Mach number is highest the presence of shock waves on the aerofoil must be expected, and measurements on models and in flight (References 10 and 11) have demonstrated supercritical flows. Thus one of the unsteady characteristics associated with the helicopter rotor stems from the variation of incidence and stream velocity on a blade section which is experiencing a mixed flow. One aspect of this type of unsteady aerodynamics can be the generation of rotor noise by the propagation of strong fluctuating pressure levels on the advancing blade. Tijdeman (Reference 12) has shown on a model wing with time-varying flap deflections that at appropriate combinations of stream Mach number and lift coefficient it is even possible for free shock waves to be projected into the upstream flow, leaving the aerofoil as a discrete front.

In view of the likelihood of such characteristics on the rotor, and the strong limitations that can be experienced from conditions at the advancing blade effort has been directed over the past three years to extend the existing rotor TSP calculations to include a time dependence. Caradonna and Philippe (Reference 11) have made a direct comparison between model tests and a 2-D theory to identify some of the likely characteristics that might be encountered on a rotor with strong supercritical unsteadiness. Figure 8, taken from Ref. 11 shows some of the comparisons between experiment and theory that were obtained from the test programme. It is particularly interesting to note the distinct phase shift around the azimuth defining the movement of the shock wave across the 30% chordwise station. Correlation with the theoretical model is clearly very good at this radial station (approximately 10% in from the tip). At a station closer to the tip (0.946 radius) correlation with the azimuthal phasing of the shock wave remains good, although some differences appear in the variation of supercritical pressures ahead of the shock. A likely explanation for this is found in the development of a strong 3-dimensional character to the flow. Inboard from the tip the variations in sweep around the rotor can be largely accounted for by using only the component of flow normal to the leading edge. On an infinite wing the differences produced by sweep forward or sweep back on the pressure distribution over the front of the chord are small and such a model is representative. At the tip of the rotor, (the .946 radius station in this case), strong end effects are present. At azimuths before zero sweep (= 70°) a swept back condition will exist and isobars would concentrate towards the leading edge at the tip, whilst beyond = 90° sweep forward would be produced and therefore the leading edge would see a relief in pressure gradients. This is clearly the trend of characteristics shown in Figure 8 where at the later azimuth station the strength of the shock wave has clearly been reduced, compared with the Caradonna theory which is based on a 2-D representation. It seems therefore that a combination of the time dependent characteristics with a 3-D model should reproduce more successfully the measured characteristics at the extreme tip of the rotor.

Clearly a proper understanding of the structure of supercritical flows on the blade tip is important in order that planform modifications can be made which alleviate compressibility effects and benefit the aims towards reducing noise. Philippe's experiments have indicated that time dependent terms must be considered for a properly balanced design.

Non-Linear Unsteady Effects

One of the major limitations experienced on the helicopter rotor is the generation of large torsional loads associated with the penetration of stall on the blade. The mechanism for this phenomena is rooted in the behaviour of aerofoils experiencing time varying excursions into and out of stall. I don't propose to develop the aerofoil mechanism discussion any further than necessary in view of the time already devoted to the subject in this symposium, but where necessary it may be appropriate in this section to intrude a little.

A number of workers in the helicopter field have set about the task of introducing dynamic stall effects into a rotor calculation. As instances Tarzanin, Reference 4 and Carter Reference 13 have produced rotor calculations which allow dynamic amplification of both lift and moment, through the use of measured aerofoil unsteady data. Beddoes, Reference 6, has developed a time-delay model which generalises the behaviour of the section and synthesises the resultant lift and moments.

Proper calculation of a rotor blade behaviour under the influence of dynamic stall requires the presence of a torsional degree of freedom to the blade motion in order that the pitch response of the blade may influence the loads. The need for higher order flapwise bending deflections has not to date been demonstrated, although it is feasible that in particular cases some representation may be necessary. For instance, the similarity of the advancing blade airload distribution to the second flapping mode shape could well produce in a resonance condition second mode deflections which are significant in generating local angle of attack. The estimation of vibratory load levels generated by dynamic stall would introduce the need for all natural frequencies of the blade, but it is unlikely that the higher flatwise modes would produce significant changes to the incidence history seen by the aerofoil. On the basis of these rationalisations the calculation of stall flutter at Westland Helicopters is based on one flapping mode shape and frequency and one torsional mode and frequency.

Tarzanin, References 4 and 5, successfully reproduced torsional waveforms for a rotor undergoing stall flutter, and from analysis of the flight test results instanced a number of areas in the rotor where strong stall characteristics can prevail, Figure 9. Similar calculations carried out at Westland Helicopters on experimental results obtained from Wessex (S58) and Lynx have shown the same characteristic response of the blade at the torsional natural frequency with the consequent growth in root control loads, Figure 10. Further analysis of the results to examine the areas on the disk where strong torsional forcing exists lead to a representation from theory of local stall patches. Figure 11 indicates the stall areas for the S58 rotor as weight is increased near the flight envelope. The calculation was based on a rigid trailing vortex wake with shed effects represented by an indicial term in the rotor loads, as described earlier. The most significant feature of Figure 11 is the strong alignment of the stall areas with the intersection locus of the blade and tip vortex from the previous blade. Clearly the strong incidence grading and elevation of local angle of attack produced by the vortex is a major initiator of the dynamic stall mechanism, with the subsequent blade response producing the amplification of the loads. Without a vortex wake model the initiation of dynamic stall depends upon a far higher level of mean incidence being produced before torsional motion is excited, and as a result the prediction in the break of control loads with speed or weight is significantly delayed. To illustrate this point Figure 12 shows a comparison of control load growth with weight for an S58 for a vortex calculation and a trapezoidal (Glauert) smoothed downwash model. The two models differ by approximately 10% in weight at which control load growth is obvious. At the breaks however control loads appear to rise at similar rates, and it was noted that torsional motion developed in a similar manner beyond the break for each wake model. In both of these cases torsional motion was initiated near the 270° azimuth position and therefore the discrepancies are limited to the increment in and its derivatives associated with the vortex.

The presence of discrete vortices on dynamic stall development can have other impacts on the calculation of rotor behaviour. Depending on the number of blades of the rotor, the advance ratio and the upwash field at the front of the disc, strong blade vortex interactions can be produced inboard near the 180° azimuth. This characteristic has been noted by Riley, Reference 14, where tests on systematically roughened blades on a Wessex showed the development of high control loads at the front of the disk. The behaviour was accentuated in shallow dives where the disk attitude was reduced relative to the free stream. In addition the level of control loads associated with the event at the front of the disk did not increase with speed, but remained nominally constant until the more usual retreating blade stall flutter became prominent. Similar characteristics have been identified and modelled on the Lynx. Figure 13 shows the growth with speed of the Lynx control load, having isolated the event at the front of the disk. Lower on Figure 13 the full Lynx waveform is shown and the presence of the event between 170° and 230° is clearly indicated. The rotor calculation was modified to accentuate the presence of the vortex crossing at $= 180^\circ$ in order that vertical distortion could be represented. As a result the control load behaviour was reproduced.

Having identified the presence of strong wake effects at the front of the rotor it is clear that increasing speed will lead to inboard movements of the vortex crossing with a resultant conflicting mechanism. The forcing will move to areas of lower dynamic head, while the incidence perturbations will be accentuated. As a result the variation of control load is not seen to change rapidly with speed. However gross changes to the aircraft geometry can have large effects. Local is dependent on fuselage upwash field and blade twist, and the combination of small rotor/fuselage separation and high twist can clearly be damaging. Vibration levels generated at the front of the disk have been quoted as the reason for increasing the mast height on the UTTAS aircraft, References 16 and 17, both of which had high overall twist and small rotor/fuselage separations. It is worth noting that the CH53 has a small fuselage/rotor clearance, combined with low overall twist and does not appear to suffer similar vibration or inboard blade stall problems.

Rotor Design Freedoms to Alleviate Stall Flutter

Sections

With the arrival of a fundamental predictive capability for the behaviour of rotor blades encountering dynamic stall it is clearly necessary to investigate how rotor designs should be directed to alleviate stall-flutter as a problem. In the first case the search for an aerofoil type which eases the problem through the development of unsteady loads is a prime target. It is clearly necessary to continue research in the development of separation on the section in order that ultimately aerofoils can be designed on primarily unsteady requirements. McCroskey, Reference 19 has studied the behaviour of the boundary layer on aerofoils in unsteady conditions. He has concluded as a result of this work that the use of a time delay based on static stall data to represent dynamic stall development is not totally satisfactory. Further work in this field is clearly necessary to allow a move away from aerofoil design based primarily on static characteristics which require subsequent studies aimed at confirming benefits in the unsteady environment.

Blade Dynamics

In addition to the basic section characteristics there exists the possibility of selecting rotor structural and geometric parameters to ease the stall flutter behaviour of the rotor. Tarzanin has studied the implications of changing torsional frequency of the rotor blade and concludes on the basis of both experimental and theoretical work that development of control loads is significantly affected. It is suggested by Tarzanin that a suitable trend would be towards low torsional frequencies of the order of 4 cycles/revolution, in which condition control loads are kept small while residual torsional motion is still acceptable. There are however a number of arguments which support an alternative high frequency solution. A similar parametric study has been carried out by Beddoes, Reference 15 and an inspection of the stalled areas of the disk has led to a number of valuable points. Figure 14 indicates the stall patches in the fourth quadrant of the disk and shows that after stall flutter initiation at $= 270^{\circ}$ the phasing of blade motion and the subsequent vortex intersection is important. At frequencies of 6 and 8 cycles per revolution the blade meets the vortex intersection at a critical point in its torsional motion with the result that torsional amplitude is sustained or even grows. At extreme frequencies the motion is so phased as to benefit from the vortex intersection and shows therefore a decrease in amplitude.

Tarzanin points out that choice of frequency depends on the advance ratio under consideration, and this is reinforced by the vortex interaction arguments discussed above. At higher advance ratios the vortex intersection moves aft and lower frequency torsional motions may well suffer adversely, while high torsional frequency would have more cycles of motion in which to decay before subsequent impacts.

The low frequency solution to torsional tuning can give rise to a persistent torsional motion of significant magnitude as seen in Figure 14. This in itself can give rise to handling issues. Furthermore if low torsional frequency is produced by a low stiffness design (as opposed to high inertia) response of the blade in torsion to low frequency inputs, say once per revolution can become significant. Thus problems associated with parasitic pitch are introduced, and the subsequent handling issues can well be severe, even in the unstalled region of the flight envelope.

Tarzanin also suggests that high frequency solutions for blade torsion have a beneficial influence on the advancing blade compressibility flutter, and this furthers the argument that the high frequency solution seems at present the most profitable approach.

Spanwise Lift Characteristics

Flight tests carried out by Riley, Reference 14, showed that degrading C_{lMAX} near the tip of the rotor blade had a dramatic effect on the onset of stall flutter. The likely benefits to the behaviour of the rotor from improvements to the blade tip therefore appear to be worth analysis. A brief theoretical study has been carried out at Westlands in which the dynamic stall characteristics of the blade sections were progressively removed from the tip inboard. Figure 15 shows the growth in control loads for several spanwise extents of dynamic stall suppression. The most interesting feature is the fact that control load break and thus the onset of stall flutter changes little, although the subsequent growth of loads and motion is significantly affected. The possible explanation for this can be arrived at by combining the findings of Riley's experiments with the theoretical study.

A rotor using constant section blades, such as NACA 0012 stalls out to some 90-92% radius on the retreating blade; stations outboard of this are in a region of decreasing loading and are thus not critical. However degrading C_{lMAX} of tip sections leads to condition where tip loadings are critical and an impact is made on the development of stall flutter. Improvement in local stall behaviour will not be felt by the rotor until sufficient spanwise extent of the tip has been influenced to encroach on an originally stalled section. Here an increment in torsional forcing is removed and a valuable increment in positive damping is introduced, in a region of high dynamic head. Thus control loads and torsional motions grow more slowly. Other mechanisms which can contribute to the pitch damping at the extreme tip would also appear to be of value in controlling stall flutter. Sikorsky, Reference 18, make use of a swept extreme tip on the basis that it suppresses torsional loads at stall, and this appears to align with the view that torsional damping has been added in the tip region.

Features Affecting the Satisfactory Prediction of Rotor Blade Stall

In the previous discussion of rotor non-linear unsteady aerodynamics one significant mechanism appears to dominate the problem, namely the interaction of the blade lifting surface with a discrete vortex. The three dominant locations for this occurrence, namely the front of the disk, the retreating side (= 270) and the rear quadrant align closely with the positions Tarzanin identified experimentally for stall, shown in Figure 16. This is clearly an area where effort must be concentrated both through modelling of the rotor aerodynamic structure as well as through proper synthesis of the local aerofoil characteristics.

For the aerofoil dynamic stall characteristics the large body of available information is based on harmonic motion of the section into and out of stalled conditions. The essentially non harmonic nature of passage near a vortex requires more detailed appraisal and its approximation by a harmonic representation requires validation. In the U.K. the unsteady aerofoil facility at ARA, Bedford is being exercised both in harmonic and non-harmonic (ramps, steps, etc.) tests. The aim is to produce a theoretical model for lift and moment histories which can cope with a range of motions.

In modelling the rotor environment some of the deficiencies produced by the use of a rigid wake structure have already been encountered, namely modelling loading peaks at the front of the disk. It is not yet resolved how far wake distortion must be accounted for in rotor calculations. Certainly the trajectories (especially the vertical location) of the wake from the preceding pair of blades should be properly represented, although wake location may not be so important for older segments which do not interact directly with later blades.

Conclusions

In reviewing helicopter unsteady aerodynamics, an attempt has been made to highlight a limited number of the problem areas which present themselves in the development of prediction tools for rotors. It is noted that W.P. Jones has reviewed the activity covering helicopter rotor unsteady aerodynamics and has examined the problems of flutter, both at high Mach numbers and associated with wake interactions at low speeds. Without wishing to repeat Jones' paper the scope of the discussion presented here is aimed largely at developments which aid our prediction of the flight envelope in cruise flight. Thus in broad terms the problems addressed are:

1. Adequate/necessary wake modelling
2. Advancing blade supercritical characteristics
3. Stall flutter

Modelling the effects of the wake away from discrete vortices and separation has been guided by early work on full wake models, particularly that of Miller. Current practice in structuring only the trailing wake, while treating the shed wake through the application of Theodorsen or Wagner models has its justification in findings such as those of Miller.

The prediction of rotor blade stall flutter is based on the aerodynamic model of the rotor as described above. It is noticeable that in many cases where stall flutter is promoted a parameter in the mechanism is found to be the passage of the blade over a discrete trailing vortex. The essentially non-harmonic nature of the vortex intersection must be properly dealt with in the aerofoil dynamic stall model. Work is still required to ensure that developments in dynamic stall representations can account for events which approximate to discontinuous changes in incidence through stall.

A further implication of the important part that discrete vortices play in the development of stall flutter is that the location of the vortex in space must be given more attention. The need to allow the early vortex trajectory to be determined by such inputs as local induced velocity field and fuselage fl[illegible] field can be important, especially at the front of the rotor.

The control of supercritical flows on the advancing blade of the rotor has been receiving attention for some time. The development and apparent hysterisis in the supercritical patch has an important effect on the choice of planform. Furthermore the possible relief to be gained by the three-dimensional effects at the rotor tip must be accounted for, as noted by Philippe and Caradonna.

References

1. W.P. Jones. Unsteady Aerodynamics of Helicopter Rotors. AGARD Structures and Materials Panel, 1972.
2. R.H. Miller. Unsteady Air Loads on Helicopter Rotor Blades. 4th Cierva Memorial Lecture, R.Ae.S., 1964.
3. R.H. Miller. Rotor Blade Harmonic Air Loading. AIAA Journal, Vol. 2, No. 7, 1962.
4. F.J. Tarzanin, Jr. Prediction of Control Loads due to Blade Stall. 27th Annual National Forum of AHS, 1971.
5. R. Gabel and F.J. Tarzanin, Jr. Blade Torsional Tuning to Manage Large Amplitude Control Loads. AIAA 2nd Atmospheric Flight Mechanics Conference, 1972.
6. T.S. Beddoes. A Synthesis of Unsteady Aerodynamic Effects Including Stall Hysterisis. Vertica, 1976, Vol. 1, pp 113-123, Pergamon Press.
7. J.J. Costes. Calcul des forces aerodynamiques instationnaires sur les pales d'un rotor d'helicoptere. AGARD Report No. 595.
8. R.M. Williams. Application of Circulation Control Rotor Technology to a Stepped Rotor Aircraft Design. 1st European Rotorcraft and Powered Lift Aircraft Forum, Southampton, England, September 1975.
9. R.M. Williams, R.T. Leitner, E.O. Rogers and D.W. Taylor. X-Wing; a New Concept in Rotary Wing VTOL. AHS Symposium on Rotor Technology, August 1976.
10. P. Brotherhood. Flight Measurements of Helicopter Rotor Aerofoil Characteristics and some Comparisons with Two-Dimensional Wind Tunnel Results. AGARD Symposium on Flight/Ground Testing Facilities Correlations, Modane 1975.
11. F.X. Caradonna, J.J. Philippe. The Flow over a Helicopter Blade Tip in the Transonic Regime. 2nd European Rotorcraft and Powered Lift Aircraft Forum, Buckeburg, Germany, September 1976.
12. H. Tijdeman. On the Motion of Shock Waves on an Airfoil with Oscillating Flap. IUTAM Symposium Transsonicum II, Gottingen, September 1975.
13. F.O. Carta, et al. Analytical Study of Helicopter Rotor Stall Flutter. 26th Annual National Forum of the AHS, June 1970.
14. M.J. Riley. A Flight Investigation of the Spanwise Lift Requirements of a Helicopter Rotor Blade by Measurement of the Control Loads Arising from Locally Applied Roughness. Royal Aircraft Establishment, Technical Report 76117, September 1976.
15. T.S. Beddoes. Retreating Blade Stall Flutter. ARC 36966, Aerodynamics, AC2112, November 1976.

16. W.C. Wetmore. Reliability Emphasized in UH-60 Design. Aviation Week, April 11th 1977, page 44-47.

17. W.C. Wetmore. Vertol Assured Full Lamps Evaluation. Aviation Week, August 1st 1977, page 47-54.

18. P. Arcidincano and R. Zincone. Titanium UTTAS Main Rotor Blade. 31st Annual National Forum of AHS, May 1975.

19. W.J. McCroskey. Recent Developments in Dynamic Stall. Presented at the Symposium on Unsteady Aerodynamics, Tucson, March 1975.

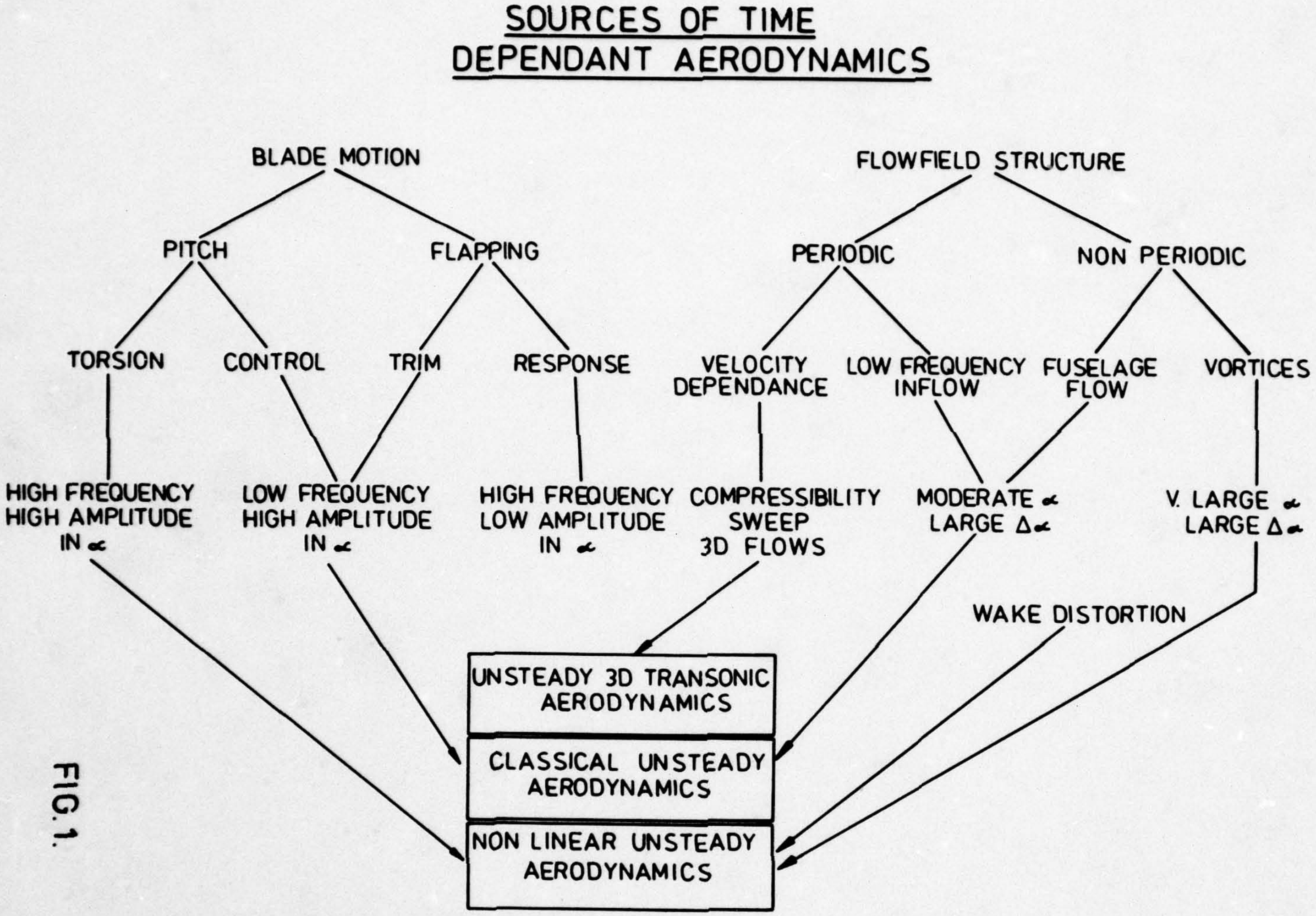
SOURCES OF TIME
DEPENDANT AERODYNAMICS
BLADE MOTION
FLOWFIELD STRUCTURE
PITCH
FLAPPING
PERIODIC
NON PERIODIC
TORSION
CONTROL
TRIM
RESPONSE
VELOCITY DEPENDANCE
LOW FREQUENCY INFLOW
FUSELAGE FLOW
VORTICES
HIGH FREQUENCY HIGH AMPLITUDE IN α
LOW FREQUENCY HIGH AMPLITUDE IN α
HIGH FREQUENCY LOW AMPLITUDE IN α
COMPRESSIBILITY SWEEP 3D FLOWS
MODERATE α LARGE Δα
V. LARGE α LARGE Δα
WAKE DISTORTION
UNSTEADY 3D TRANSONIC AERODYNAMICS
CLASSICAL UNSTEADY AERODYNAMICS
NON LINEAR UNSTEADY AERODYNAMICS

FIG. 1.

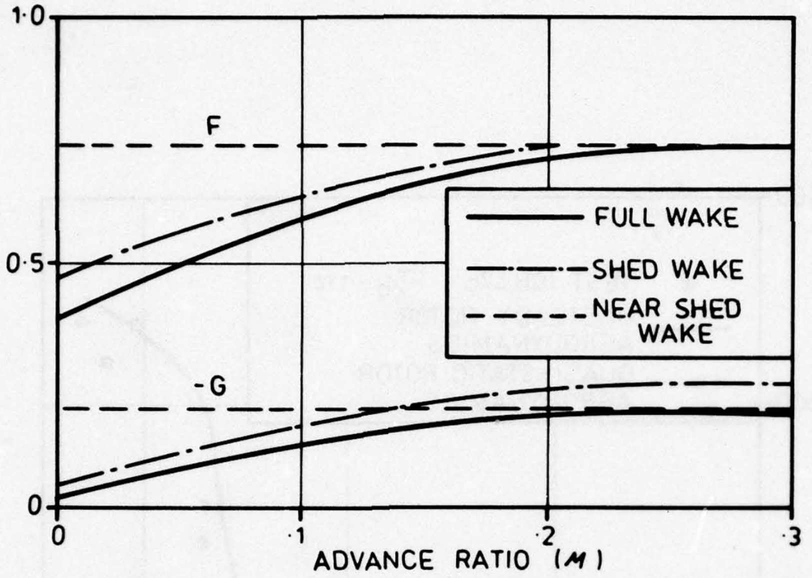

a. EQUIVALENT THEODORSEN FUNCTIONS FOR A ROTOR (THRD. HARMONIC OF DOWNWASH).

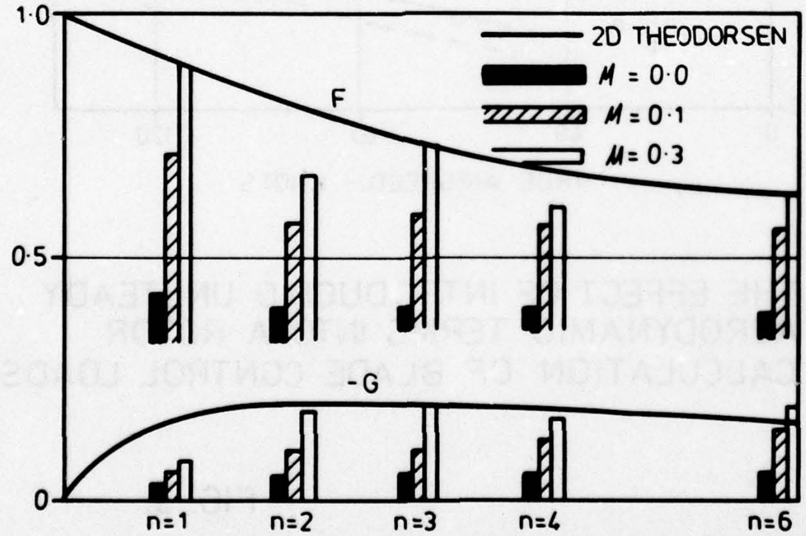

b. 2 D THEODORSEN FUNCTION COMPARED WITH FULL ROTOR WAKE CALCULATION FOR VARIOUS HARMONICS OF DOWNWASH (n).

FIG. 2.

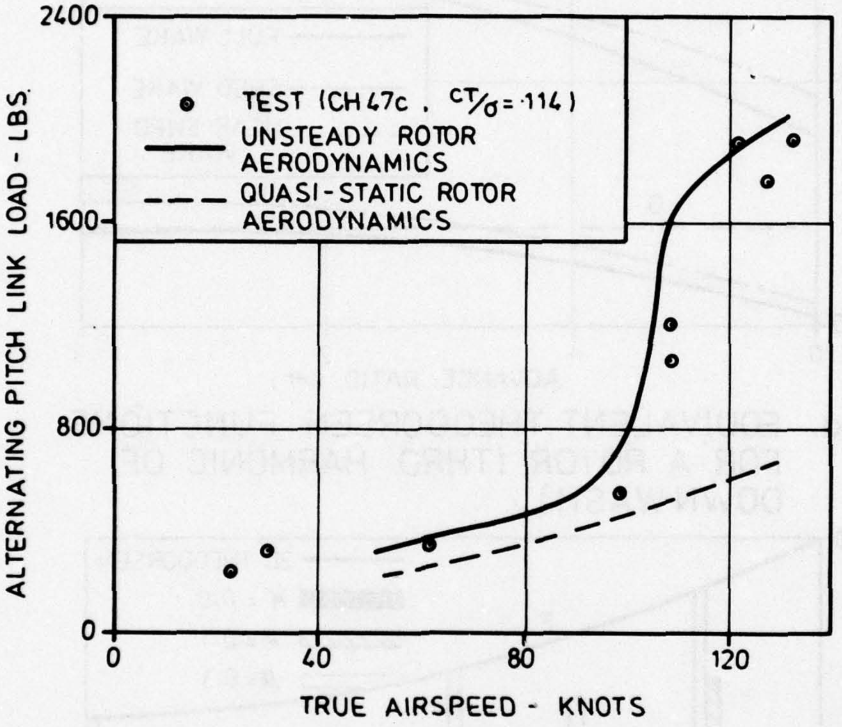

THE EFFECT OF INTRODUCING UNSTEADY AERODYNAMIC TERMS INTO A ROTOR CALCULATION OF BLADE CONTROL LOADS.

FIG. 3.

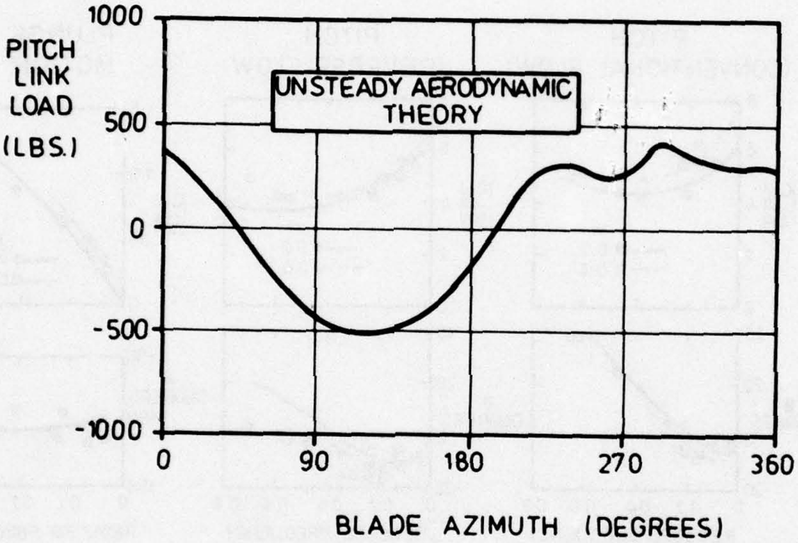

ROOT TORSIONAL LOAD WAVEFORM FOR A ROTOR WITHIN THE FLIGHT ENVELOPE

FIG. 4.

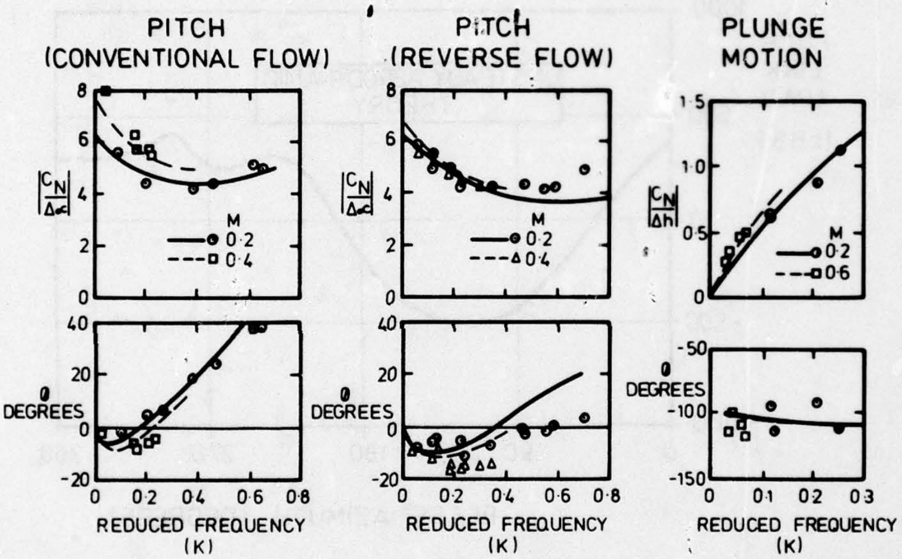

COMPARISON OF HARMONIC OSCILLATION TEST DATA WITH THEORY.

FIG. 5.

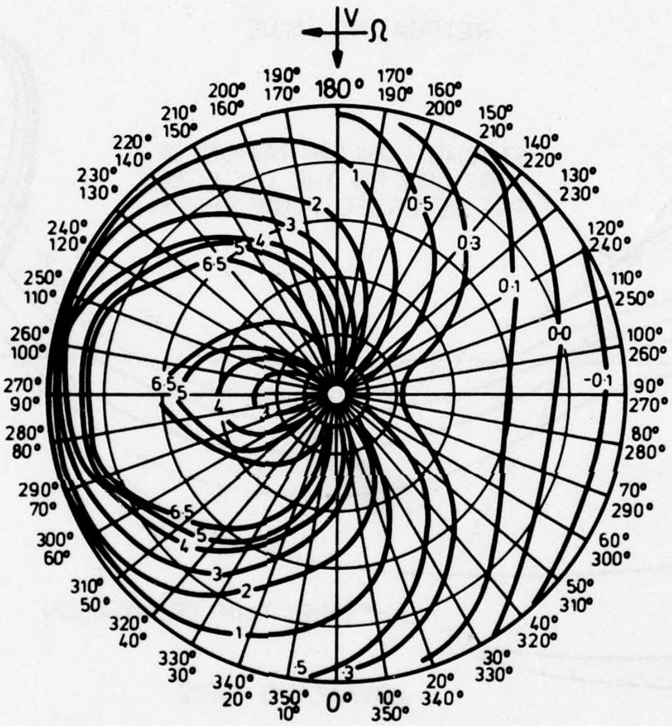

LIFT DISTRIBUTION OF "X WING" ROTOR AT $M = 0{\cdot}7$

FIG. 6.

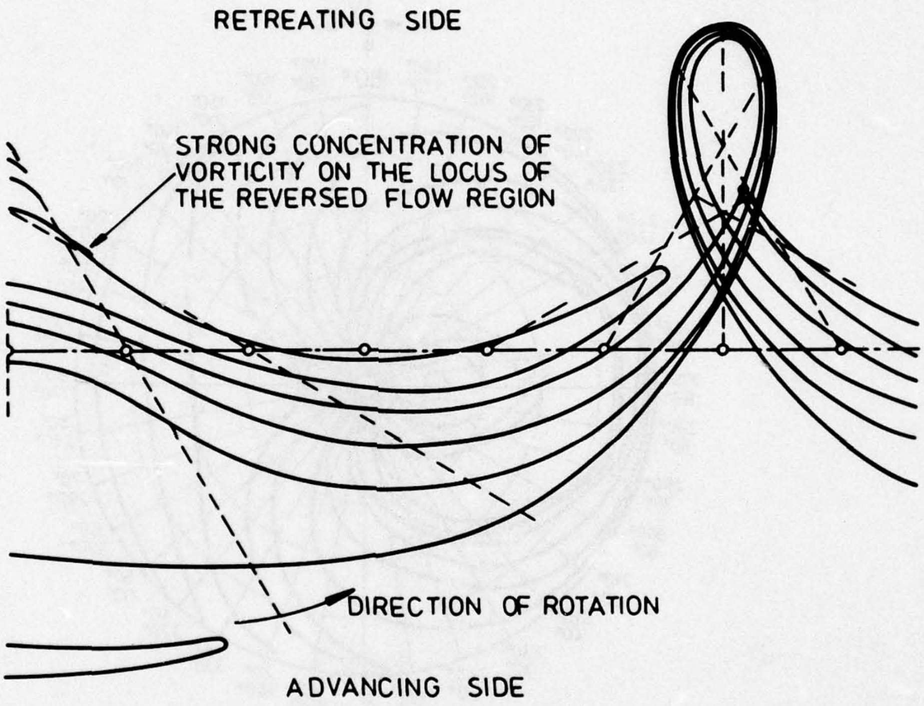

CONTOURS OF CONSTANT VORTICITY
FOR THE "X WING" AIRCRAFT AT $M = 0{\cdot}7$

FIG. 7.

THEORETICAL AND MEASURED PRESSURES ON A ROTOR BLADE.

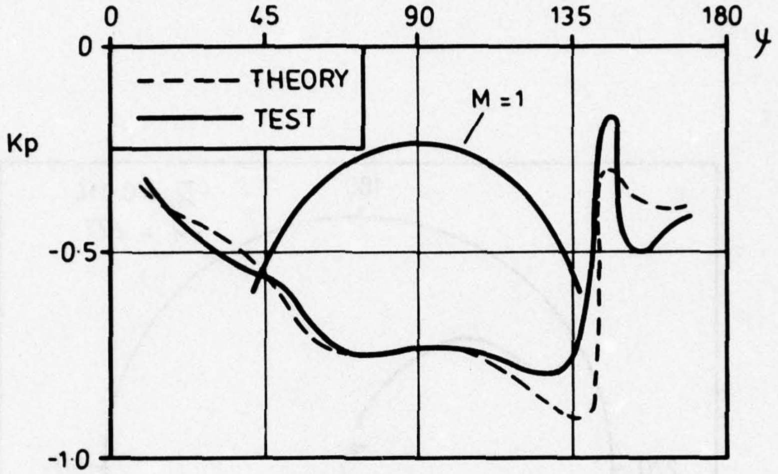

NACA 0012, r/R = 0·892, Vo = 110 M/SEC., WR = 200 M/SEC.
CHORDWISE STATION = 0·3C.

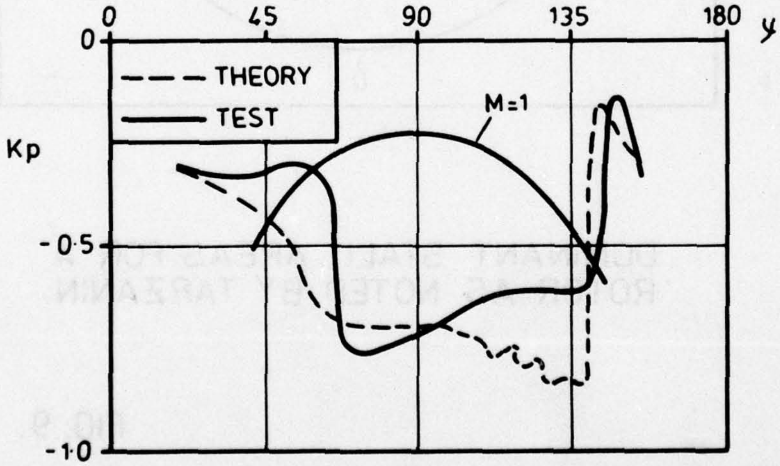

NACA 0010·5, r/R = 0·946, Vo = 110 M SEC., WR = 200 M/SEC.
CHORDWISE STATION = 0·4C

FIG. 8.

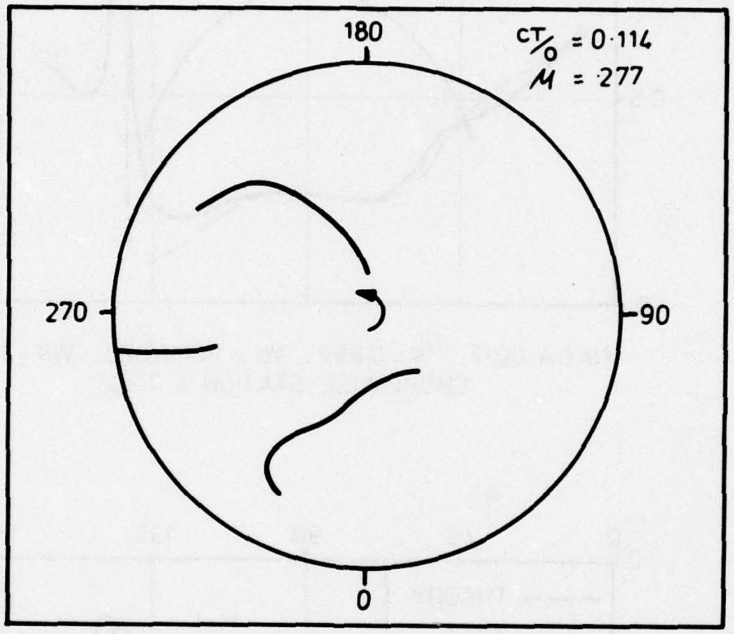

DOMINANT STALL AREAS FOR A ROTOR AS NOTED BY TARZANIN.

FIG. 9.

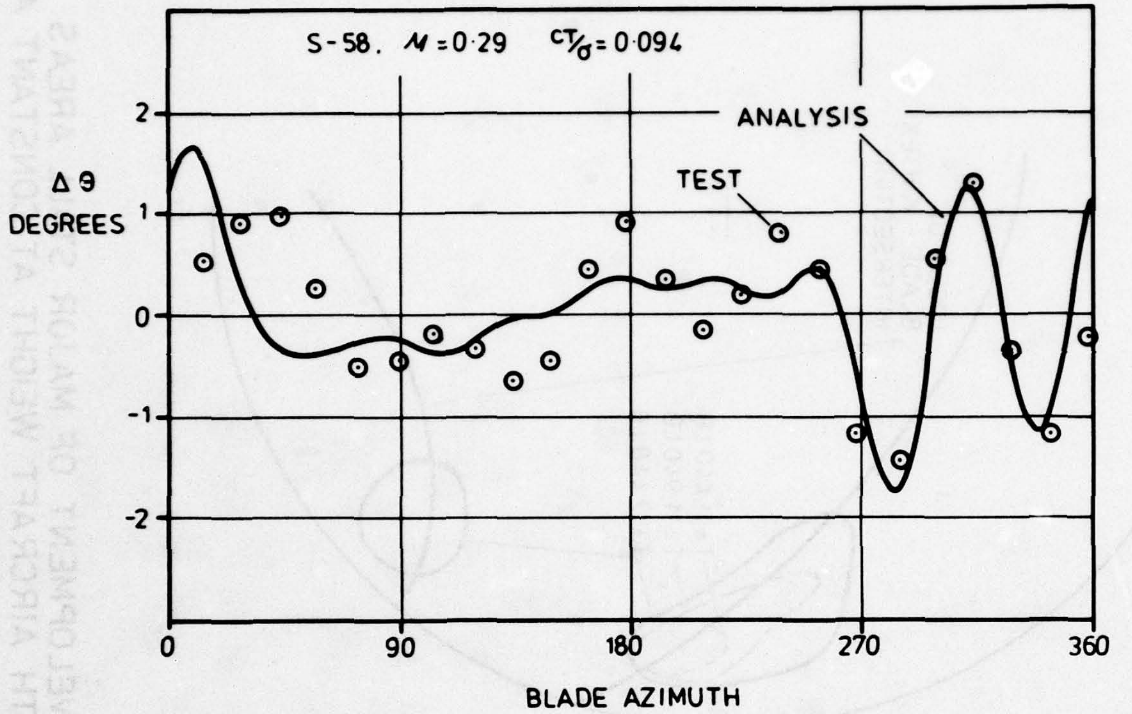

COMPARISON BETWEEN FLIGHT TEST AND THEORY FOR BLADE TORSIONAL MOTION IN STALL FLUTTER.

FIG. 10.

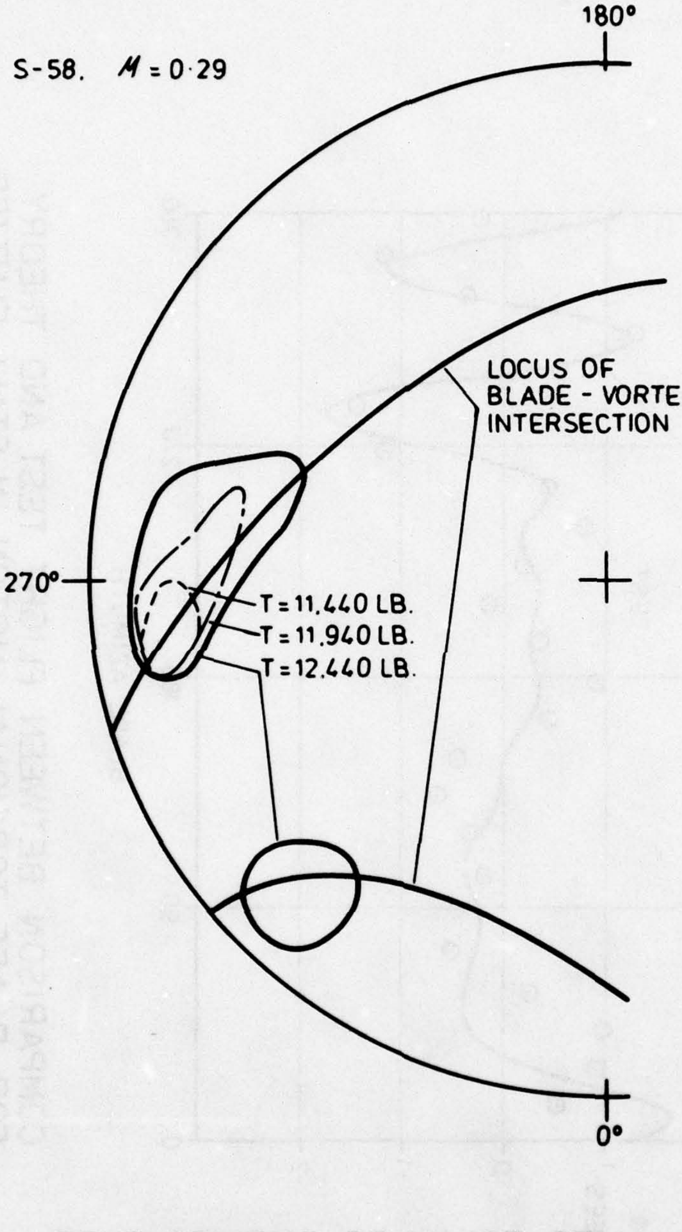

DEVELOPMENT OF MAJOR STALL AREAS WITH AIRCRAFT WEIGHT AT CONSTANT $\mathcal{M}$.

FIG. 11.

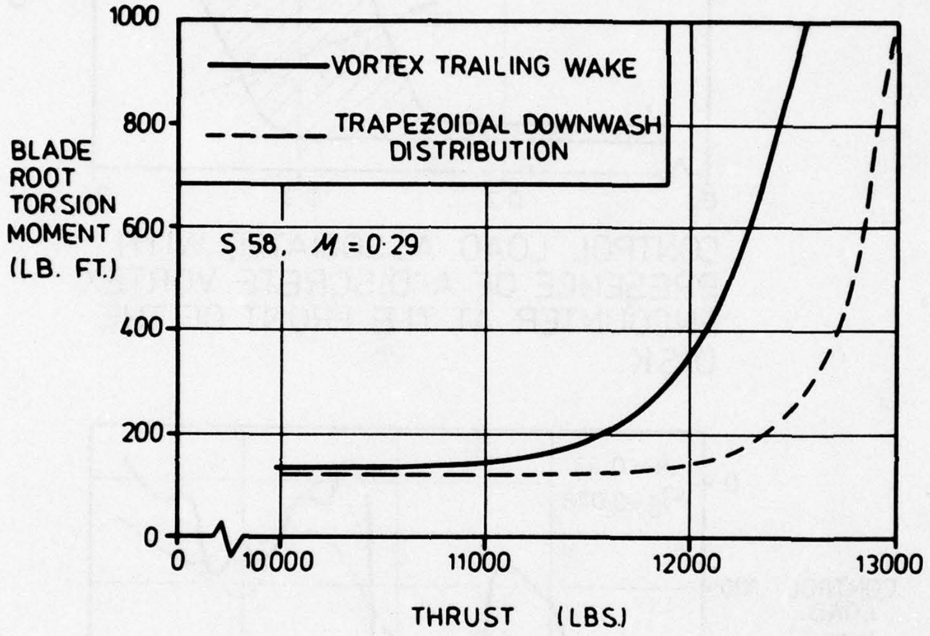

COMPARISON BETWEEN SMOOTHED WAKE AND DISCRETE VORTEX REPRESENTATION IN THE DEVELOPMENT OF STALL FLUTTER.

FIG. 12.

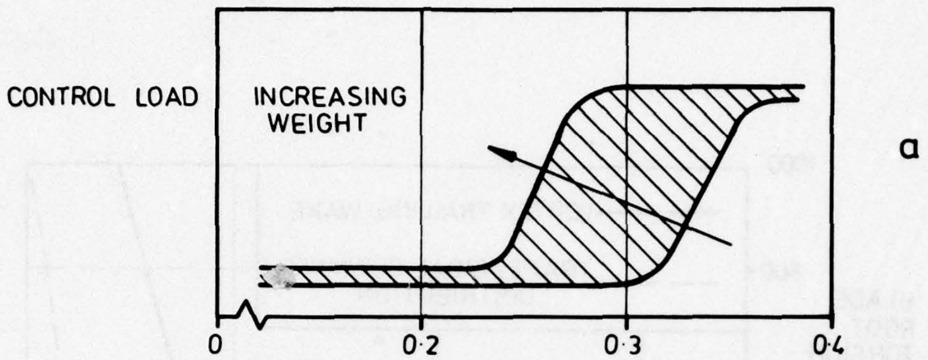

CONTROL LOAD ASSOCIATED WITH PRESENCE OF A DISCRETE VORTEX ENCOUNTER AT THE FRONT OF THE DISK.

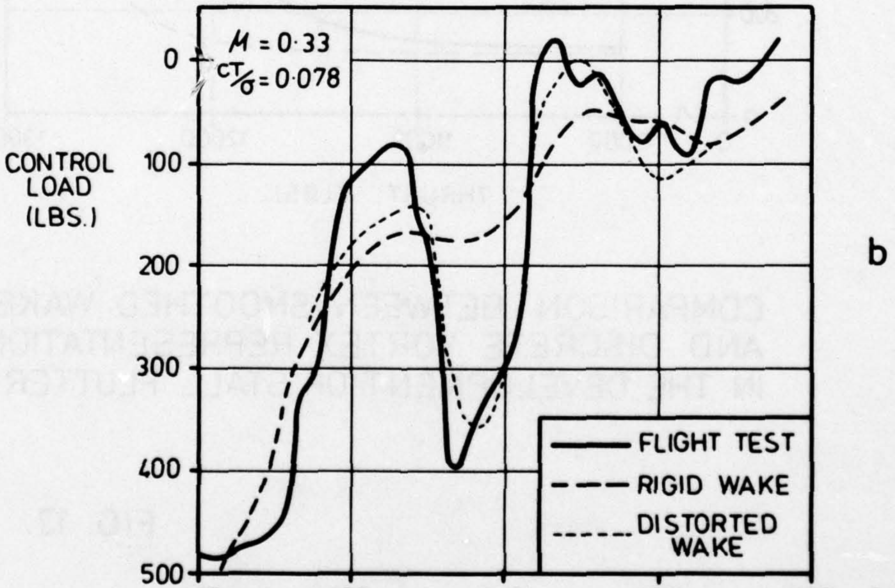

COMPARISON OF FLIGHT TEST CONTROL LOADS WITH RIGID WAKE THEORY AND THE EFFECTS OF WAKE DISTORTION.

FIG. 13.

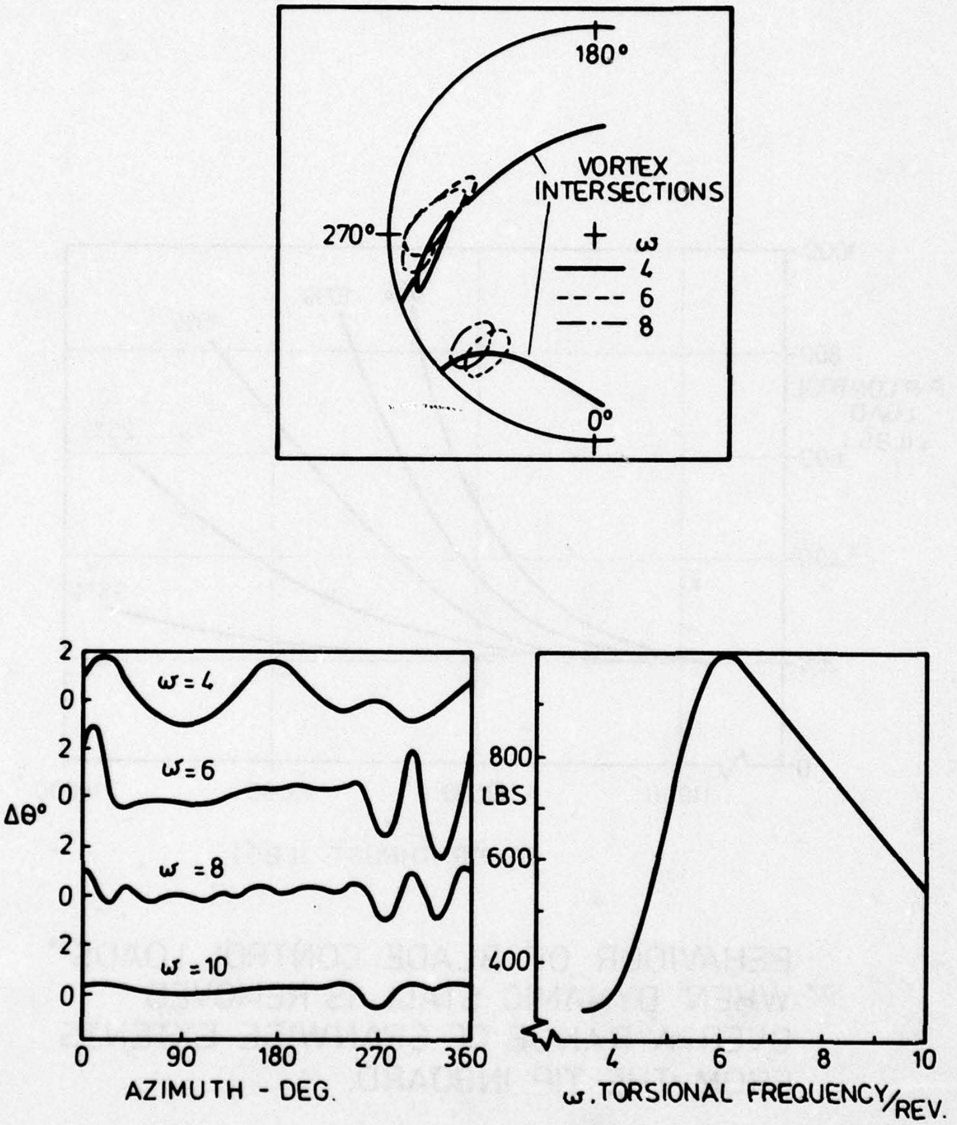

STALL AREAS WITH RESULTANT
WAVEFORM AND LOADS FOR
VARIOUS TORSIONAL FREQUENCIES

FIG. 14.

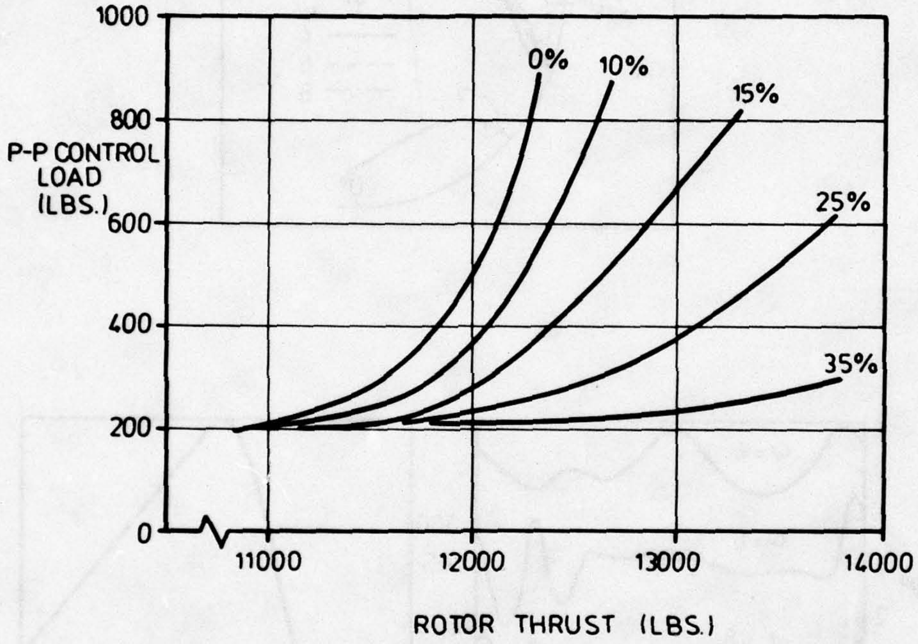

BEHAVIOUR OF BLADE CONTROL LOADS WHEN DYNAMIC STALL IS REMOVED OVER A RANGE OF SPANWISE EXTENTS FROM THE TIP INBOARD.

FIG. 15.

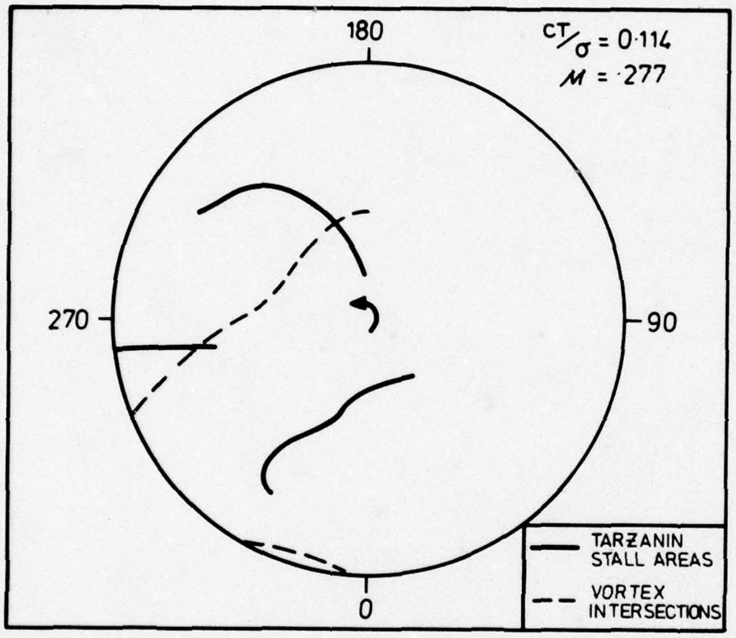

COMPARISON OF NOTED STALL AREAS ON A ROTOR WITH LOCATION OF DOMINANT VORTEX INTERSECTIONS.

FIG. 16.

UNSTEADY FLOWS IN TURBOMACHINES - A REVIEW OF CURRENT DEVELOPMENTS

by
M. F. Platzer
Professor of Aeronautics
Naval Postgraduate School
Monterey, California 93940
USA

SUMMARY

Recently, the study of unsteady flows in turbomachines has received increased attention due to the growing realization of the impact of unsteady flow effects on engine performance and stability in distorted inlet flow, engine efficiency, aeroelastic stability and noise generation. For this reason, a number of symposia have been held during the past few years on various aspects of the unsteady flow phenomena in turbomachines, e.g., the Project SQUID meetings on Aeroelasticity in Turbomachines 1972, Unsteady Flow in Jet Engines 1974, the AGARD 46th Propulsion and Energetics Panel Meeting on Unsteady Phenomena in Turbomachinery 1975 and the IUTAM Symposium on Aeroelasticity in Turbomachines 1976. It is the objective of this paper to review the past developments and the current status of turbomachinery unsteady aerodynamics as reflected in these symposia as well as in other related meetings and papers. One of the major recommendations of the AGARD PEP meeting was the need for a review and assessment of the current state-of-the-art of theoretical unsteady turbomachinery aerodynamics. Therefore, an attempt is made to highlight the theoretical treatment of the various unsteady flow phenomena in turbomachines and to indicate the relationship of these phenomena and methods with those encountered in external unsteady aerodynamics. Also, recommendations for future directions and work are given.

1. Introduction

Recently, the study of unsteady flows in turbomachines has received increased attention due to the growing realization of the impact of unsteady flow effects on engine performance, efficiency, stability and noise generation. The latter three problems have acquired new and obvious importance in the last few years because of the worsening energy situation, the occurrence of new flutter problems in high-speed fans and compressors, and the increasingly strict noise regulations.

As has been known for some years, it is the very fact of fluctuating flow in turbomachines which allows work to be done on the fluid by pressure forces and therefore provides the basic mechanism for energy transfer. Yet, in the past, unsteady flow calculations have been avoided by considering only the time averaged equations or by assuming the flow to be steady in rotor fixed coordinates. The latter assumption is valid only for single rotating blade rows operating in uniform inlet flow but fails to describe the complex interactive flows in a multi-stage machine. Here, even with uniform inlet flow there occur strong unsteady potential and viscous flow interactions between stationary and rotating blade rows which are further complicated by wake cuttings, viscous vortices shed from blade tips and cross flows at the end walls. In supersonic flow, additional shock cuttings and reflections take place as evidenced by recent flow visualization studies using laser holography. Flow separation caused by blade operation at large incidence angles can lead to various flow instabilities (rotating stall, surge) which may impose large vibratory or transient blade stresses. All these phenomena are further complicated by operation with inlet distortions or disturbances created further downstream (such as afterburner light in a turbofan engine), by aero-structural interactions (flutter) and by noise generation phenomena.

Various aspects of these unsteady flow phenomena occurring in modern turbomachines have been the subject of recent symposia, such as the Project SQUID meetings on Aeroelasticity in Turbomachines (Fleeter 1972), Unsteady Flow in Jet Engines (Carta 1974), AGARD 46th Propulsion and Energetics Panel Meeting on Unsteady Phenomena in Turbomachinery (AGARD 1975), and the IUTAM Symposium on Aeroelasticity in Turbomachines (IUTAM 1976). Also, it should be noted that this subject receives considerable attention in the USSR as indicated by various conference proceedings, e.g. the papers presented at the Fourth Conference on Problems of Aeroelasticity of Turbomachines (Pisarenko and Ol'shtein 1974), the Fifth Congress on Problems of Aeroelasticity of Turbomachines held in Riga (Ol'shtein 1976) and books by G. S. Samoylovich (1969, 1975) and Gorelov and collaborators (1971, 1974). Further recent surveys are those of Fabri (1971), Platzer (1975), Fleeter (1977) and Sisto (1977).

It is the objective of this paper to review the past developments and the current status of turbomachinery unsteady aerodynamics as reflected in the above references and other related meetings and papers. In view of the great amount of available material a certain selectivity is unavoidable. Therefore, an attempt is made to highlight the theoretical treatment of the various unsteady flow phenomena since one of the major recommendations of the AGARD-PEP-Meeting concerned the need for such a review. Experimental studies will be discussed primarily from the point of view of providing insight into the basic phenomena and of furnishing comparisons with the theoretical predictions. Unsteady phenomena in hydraulic turbomachines due to cavitation, for example, are excluded from this discussion.

2. Unsteady Phenomena in Turbomachinery

It is well worth to remember that the flow in turbomachines must, of necessity, be unsteady if work is to be done on or by the fluid. This important fact follows from the relation between the stagnation enthalpy h, the density ρ and the pressure p

$$\frac{Dh}{Dt} = \frac{1}{\rho}\frac{\partial p}{\partial t}$$

which shows that the static pressure must fluctuate locally if work is to be done on the fluid by pressure forces. Although pointed out by B. Eck (1957) and R. C. Dean (1959) this fact is not always sufficiently appreciated in the turbomachinery community because current design procedures are based on time-averaged analyses.

To quantify the amount of flow unsteadiness it is convenient to introduce a reduced frequency parameter

$$k = \frac{\omega b}{V}$$

where V is the fluid velocity, b a length scale such as blade chord or engine length and ω the frequency of oscillation. This parameter shows that many phenomena such as flutter, resonance, surge and rotating stall are basically unsteady phenomena which require unsteady rather than quasi-steady analyses. Engine acceleration or deceleration effects, on the other hand, are quasi-steady phenomena because the time of an acceleration or deceleration is typically from 1 to 10 seconds whereas the transport particle time through the engine is a few milliseconds.

Before discussing the currently available prediction methods for unsteady turbomachinery flows an overview of the most important phenomena and problems is first given in this section.

2.1 Unsteady Flow Effects in Turbomachines Exposed to Uniform Inlet Flow

As already pointed out, the flow through a turbomachine is a fluctuating one even though the inlet flow may be uniform and steady. This fact can be appreciated from Fig. 1 which shows the primary sources of flow fluctuations generated in multi-stage axial turbomachines, i.e., potential flow interactions between stator and rotor blade rows, vortex shedding from blade tips, wake formations and cuttings, cross-flow developments at the end walls, and, in supersonic flow, intricate shock formations, reflections and shock boundary layer interactions.

A simplified picture of the rotor-stator interaction process is shown in Fig. 2 which is obtained by unwrapping a stage annulus of differential radial height into a rectilinear two-dimensional cascade. The vortex wakes shed from the rotor blades are intersected by the stator blades and, as can be seen from the velocity triangles, acquire a slip velocity which transports them towards the pressure side of the stator passage. Thus, the rotor wake fluid tends to be collected on the pressure side of the stator blades and, ultimately, merges into the stator wakes. Because of the higher stagnation temperature of the rotor wakes compared to the inviscid flow stagnation temperature, the temperature profile at the stator exit tends to be that shown in Fig. 3. These intra-stator transport processes of rotor wakes therefore cause a substantial redistribution of stagnation enthalpy and have an important effect on compressor performance (Kerrebrock and Mikolajczak 1970).

Even without blade interaction, the wakes shed off a single stage can generate significant flow non-uniformity and unsteadiness. Thompkins and Kerrebrock (1975) measured the exit flow field of a single transonic rotor and found large radial velocity components and large static pressure fluctuations near the blade wakes. A typical measurement is shown in Fig. 4. In addition, they observed an interesting transition of the flow field from a 23-lobe pattern (the number of blades) to a 16-lobe pattern further downstream which suggests the existence of remarkable wake instabilities under certain circumstances. Some evidence supporting this observation has been supplied by Kerrebrock (1974) who identified two classes of wake shear disturbances, one of which is unstable, thus promoting rapid initial wake decay whereas the other is oscillatory and therefore may persist much longer. Also, as shown by Lakshminarayana (1975), important differences exist in the wake spreading and decay behavior of rotor wakes compared to airfoil or cascade wakes. Rotor wakes decay much faster close to the trailing edge but change to a much slower decay further downstream. Again, the underlying physical mechanism is not fully understood.

Additional complexities arise from compressibility effects. Fig. 5 shows a schematic of the rarefaction and shock wave pattern generated by a cascade with supersonic exit flow. The interaction with the neighbouring rotor blade row is seen to produce complicated shock cuttings and thus additional important flow non-uniformity and unsteadiness. These interaction effects have recently been studied in some detail by Arnoldi (1974), Gallus (1975), Weyer (1974) using rotating test rigs and two examples taken from Arnoldi (1974) and Gallus (1975) are shown in Figs. 6 and 7.

It is important to remember, however, that viscous wake and shock interactions are not the only mechanisms generating pressure fluctuations. Even purely potential flow interactions may cause significant fluctuations and stresses as exemplified in Fig. 8. Here, a thick strut located in a cascade of airfoils one chord downstream of a rotor is seen to induce a strong disturbance. Furthermore, small changes in strut geometry and angle of attack are apt to produce significant changes. A similar effect can be exerted by probes located downstream of a rotor. More generally, the potential flow interactions due to closely spaced blade rows - in addition to the effects of unsteady wake transport and wake mixing - can have an important impact on turbomachinery performance and vibratory stress levels. This can be understood by visualizing the blades as emitters of acoustic waves which propagate in all directions and which are reflected from neighbouring blades and solid boundaries. Under certain conditions standing wave patterns are possible such as the case of regular wave reflection shown in Fig. 9. The impact of these wave interaction phenomena on vibratory stress and noise levels requires a detailed analysis. The current status of these techniques is discussed in Section 3.

2.2 Response to Distorted Inlet Flow

Inlet flow distortions are commonly encountered in many situations, e.g., during aircraft operations in cross winds or on military aircraft subjected to steam ingestion during carrier launches or to exhaust gas ingestion from forward firing weapons. These and similar conditions cause pressure, temperature, or foreign gas type of distortions which can severely affect engine operations.

The resulting flow problem can be visualized by considering a rotor blade moving through a distorted flow which is stationary in the stator frame of reference. The blade experiences velocity and angle of attack fluctuations at a rate given by the non-dimensional frequency

$$k = \frac{b}{r} \cdot \frac{360}{\Theta} \cdot \frac{U}{C}$$

where b is the axial projection of rotor chord, r is the compressor radius at the blade section, Θ is the distortion extent in degrees, U is the tangential blade speed and C is the axial air velocity. This parameter compares the time spent by a fluid particle in a rotor passage to the time spent by the rotor in the distorted segment. Typical values of k vary from nearly zero for short chord compressors subjected to large distortions to well over unity for long chord compressors subjected to distortion of small extent. As a result, the aerodynamic lift response of the blade may vary from quasi-steady for low frequency values to a highly oscillatory response for large frequencies. A number of prediction methods have been worked out using various concepts and assumptions, e.g., the parallel compressor model, the two-dimensional linear body force model, the two- and three-dimensional linear actuator disc models, nonlinear actuator disc models and lumped volume models. A comprehensive review of these approaches has recently been given by Mokelke (1974).

Large inflow distortions are also observed in partial admission turbines. The importance of the resulting unsteady flow effects on turbine performance was pointed out by H. Kraft (1957, 1968) who also described interferometric flow visualization studies in radial in-flow turbines with partial admission. These investigations proved the existence of large pressure pulsations and of highly three-dimensional flow effects thereby demonstrating the inadequacy of loss estimate based on two-dimensional steady flow assumptions. Examples of additional unsteady flow studies in partial admission turbines are those of Woods et al. (1968) and Chu (1965).

2.3 Surge and Rotating Stall

Throttling of the flow through a compressor from its deisgn flow condition towards the stall limit eventually causes a flow instability which may take the form of surge or of rotating stall (Fig. 10). During surge the average annulus flow through the compressor exhibits large amplitude oscillations. Rotating stall, on the other hand, is a flow phenomenon where stall cells rotate around the circumference but where the average annulus flow remains virtually constant. Both phenomena produce large vibratory blade stresses making it necessary to avoid engine operations in either surge or rotating stall for any substantial length of time. Recently, progress has been made in the prediction of compression system instability (Greitzer 1976).

2.4 Turbomachinery Flutter

The self-excited oscillation (flutter) of an aerodynamically lifting surface has been of concern to aeronautical engineers since its first occurrence on a Handley Page bomber in WWI. Two different types of flutter can be distinguished at the outset, i.e., attached flow and separated flow (stall) flutter. Both types of flutter also occur in turbomachines. However, there are important differences between aircraft and turbomachinery flutter.

Wing bending oscillations in an attached incompressible flow are found to be always damped and wing flutter is excited only by the coupling of two or more degrees of freedom (bending/torsion etc.). In a turbomachinery cascade the situation is more complex because the neighbouring blades interact with the reference blade. Nevertheless, their effect usually is a damping one. Indeed, the greatest aerodynamic damping results when the blades oscillate in counterphase because in this case the normal velocities induced by neighbouring profiles are directed against the motion of the reference blade. However, if the cascade is oscillating in a non-uniform flow (corresponding to a highly loaded cascade which produces large flow turning) an unsteady force component may originate which can extract energy from the main flow and thus reinforce the oscillation. In contrast to the highly dangerous coupled wing flutter cases encountered in attached low speed flow the mass/inertia ratios and center of gravity positions of typical turbomachinery blades are usually such that they preclude blade flutter in this flow situation.

Compressibility effects, on the other hand, can drastically alter this conclusion. Here, single degree of freedom flutter is a definite possibility and it is now well recognized that mixed subsonic/supersonic or purely supersonic flow may easily induce negative aerodynamic pitch damping. Indeed, many transonic and supersonic airplanes have experienced single degree of freedom control surface flutter. Recent studies have shown that the interaction between neighbouring blades in a transonic or supersonic cascade are highly destabilizing for certain parameter combinations. This fact together with the current design trends to operate modern turbomachines at transonic/supersonic tip speeds in order to achieve higher pressure ratios per compressor stage and higher work extraction ratios per turbine stage places increased emphasis on the study of high-speed turbomachinery flutter phenomena.

Fig. 11 shows the commonly encountered compressor flutter boundaries. The supersonic unstalled flutter boundary is seen to cross the operating line and thus imposes a definite design constraint. Also shown is the choke flutter boundary which may be encountered when the blade is operating at near-choke conditions and the flow is transonic over most of the blade chord. The other two flutter boundaries are stall flutter boundaries. The subsonic boundary may occur in a high-speed fan operating at part-speed or in a low- or high-pressure compressor operating at or near design speed. This type of stall flutter has been a recurring problem in turbomachinery design for many years. The supersonic stall flutter boundary is of more recent origin and is encountered during supersonic operation near the surge line. Additional flutter problems have been found in the last stages of steam and gas turbines which are described in some detail by Pigott and Abel (1974) and Samoylovich (1969).

3. Aerodynamic Prediction Methods

The analyst of unsteady flow effects in turbomachines is confronted with the problem of determining the unsteady three-dimensional viscous flow through geometric configurations of enormous complexity. This task clearly requires the introduction of considerable simplifying assumptions in order to make the problem mathematically tractable. Therefore, the effects of viscosity are usually neglected at the outset and the occurring disturbances are usually assumed to be sufficiently weak as to permit a potential flow analysis. This makes it possible to use the wave equation for moving media discussed by Garrick (1957) as the basic governing equation

$$\frac{1}{a^2}\left(\frac{\partial}{\partial t} + \vec{V}\cdot\nabla\right)^2\varphi = \nabla^2\varphi \qquad (1)$$

$\vec{V}$ is the local flow velocity, a the local velocity of sound and φ the velocity potential. For low speed flows the incompressibility assumption can readily be made which, of course, reduces Eq. (1) to the Laplace equation

$$\nabla^2\varphi = 0 \qquad (2)$$

For compressible flows, solution of the Euler equations or of Eq. (1) for unsteady internal flow problems has been attempted only in a few cases. Rather, in analogy to the well proven methods of unsteady external aerodynamics discussed in several texts, e.g., Bisplinghoff et al. (1955) and Jones (1962), the further assumption of linearized perturbations superimposed upon a uniform flow is generally made leading to the well known linearized unsteady potential equation

U = free-stream speed
c = velocity of sound

$$\frac{1}{c^2}\left(\frac{\partial}{\partial t} + U\frac{\partial}{\partial x}\right)^2\varphi = \nabla^2\varphi \qquad (3)$$

This equation has been the subject of detailed investigations since aircraft speeds approached the speed of sound in WWII. A comprehensive exposition of the various solution methods and results for external unsteady aerodynamics can be found in the above mentioned texts. No similar treatment of unsteady internal aerodynamics is available in the English literature but two Russian textbooks (Samoylovich 1969, Gorelov et al. 1971) have recently been published.

As first shown by Lin, Reissner and Tsien (1948) for mean flow velocities close to the speed of sound Eq. (3) is valid only if the flow is sufficiently unsteady. For flows with small unsteadiness (low frequencies) the proper small perturbation approximation of Eq. (1) is given by

$$\left[1 - M^2 - (\gamma + 1)\frac{M^2}{U}\varphi_x\right]\varphi_{xx} + \varphi_{yy} + \varphi_{zz} - \frac{1}{c^2}\varphi_{tt} - \frac{2M}{c}\varphi_{xt} = 0 \qquad (4)$$

where M is the free-stream Mach number. Its solution still presents formidable difficulties. For a recent discussion of transonic flow problems in turbomachinery compare Adamson and Platzer (1977).

Over the last quarter century a number of solutions of increasing complexity have been developed for unsteady turbomachinery flows whose review will be attempted in the following sections. Still today, most analyses are based on the two-dimensional flow approximation of the actual flow which is obtained by unwrapping an annulus of differential radial height from the flow passage of an axial flow turbomachine. This produces the cascade flow model of staggered blade rows embedded in a main flow. Further limiting the analysis to the study of a single blade row finally leads to a well defined and rather widely investigated class of problems.

3.1 The Lightly Loaded Cascade in Unsteady Incompressible Flow

Work on incompressible unsteady cascade aerodynamics started in the early fifties with the investigations of Billington (1949), Lilley (1952), Sohngen (1953), Kemp and Sears (1955), Legendre (1954), Mendelson and Carrol (1954) Sisto (1952, 1955), Woods (1955), Chang and Chu (1955) and Nickel (1955). The related problem of wind tunnel interference was studied by W. P. Jones (1950) and Timman (1951). Here, an airfoil situated between two wind tunnel walls is equivalent to an unstaggered cascade whose blades are oscillating in counterphase. These approaches were mostly based on the modelling of the blades by vortex distributions which lead to integral equations for the unknown vortex strength although other methods were also pursued, e.g. the conformal mapping techniques of Legendre (1954), Chang and Chu (1955) and Woods (1955). Sisto (1955) produced the first detailed results for the case of unstaggered cascades.

Further studies of oscillating cascades in the following years are those of Isay (1958), Khaskind (1958), Popescu (1957, 1958), Sohngen and Meister (1958), Meister (1960), Samoylovich (1961a, b), Belotserkovskiy et al (1961), Musatov (1963), Kurzin (1964), Gorelov and Dominas (1965), Vakhomchik (1965a, b) and Lefcort (1965).

The vortex modelling approach was further exploited by Whitehead (1960) who published extensive tables of force and moment coefficients for vibrating airfoils in cascade and later (Whitehead 1962) extended it to finite mean incidences while the Northern Research and Engineering Company (1964) accounted for both finite mean incidence and camber. Musatov's (1963) work is an extension of Sisto's solution to the case of finite angle of attack. Belotserkovskiy et al (1961) used discrete vortices rather than continuous vortex distributions for the blade modelling. The theory of analytic functions was the basis for the work by Popescu (1957), Vakhomchik (1965), Samoylovich (1961), Meister (1960) and Sonngen and Meister (1958). Khaskind's oscillating airfoil solution was extended by the same author (1958) to the oscillating cascade and exploited more extensively in the work of Gorelov and Dominas (1965).

The gust response of cascades in incompressible flow was considered by Samoylovich (1962), Onashi (1968), Lotz and Raabe (1968), Henderson and Daneshyar (1970), Schorr and Reddy (1971), Hawthorne (1973) and Naumann and Yeh (1973).

Gorelov (1969) also published a paper showing the possibility of parametric resonance whose existence was first suspected by Sabatiuk and Sisto (1956).

Very recently, a conceptually quite simple solution method for flat plate cascade in oscillatory incompressible flow has been developed by Rao and Jones (1974) and shown to be in good agreement with the results of Schorr and Reddy (1971). Also, Kemp and Ohashi (1975) gave an exact analytical solution for incompressible flow through an unstaggered flat-plate cascade executing harmonic in-phase oscillations or being exposed to generalized gusts. Whitehead's (1960) numerical results were found to be in excellent agreement with this exact solution. The most recent study of this subject appears to be that of Horlock, Greitzer and Henderson (1977) which resolves a previously noted discrepancy for low frequency gusts.

The above analyses are all based on small perturbation theory, i.e., the blades are assumed to be flat plates or slightly cambered blades set at zero or small incidence and the unsteady disturbances are assumed to be small. Hence, the vortices shed from the blades are assumed to follow straight lines at the free-stream speed or to follow curved lines according to the steady flow solution for the given cambered cascade. Hence, there is either zero coupling or weak coupling between the unsteady and the steady flow problems which greatly facilitates the solution process. A rather thorough exposition of the underlying theory and the main solution methods, especially those developed by Russian investigators, is contained in the texts by Samoylovich (1969) and Gorelov et al. (1971). These references and a recently published atlas on unsteady cascade aerodynamics (Gorelov et al. 1974) also provide extensive numerical results.

3.2 The Highly Loaded Cascade in Unsteady Incompressible Flow

The previously noted effect of steady blade loading on the unsteady aerodynamic cascade characteristics motivated several investigators during the past decade to develop solutions for highly loaded cascades having highly cambered finite thickness blades and thus causing a strong coupling between the steady and the unsteady flow.

The problem of a cascade with arbitrary blade profiles executing small harmonic oscillations at an arbitrary interblade phase angle appears to have been first considered by Samoylovich (1962). Further studies of this problem are those of Kazimirski, Nitusov and Samoylovich (1968), Saren (1968), Kurzin (1967), Kapelovich and Samoylovich (1967) and Nitusov and Samoylovich (1970). An exposition of the basic theory is also given in the textbooks by Samoylovich (1969) and Gorelov et al. (1971). The most recent work appears to be that of Ryabchenko and Saren (1972) and Ryabchenko (1973, 1974, 1976) and of Adamczyk (1975), Atassi and Goldstein (1976) and Atassi (1978) in the United States.

The first approach to this problem was based on quasi-steady concepts which neglected the influence of the vortex wakes. This method appears to have been first outlined by Stepanov (1962) using conformal mapping of a given cascade into a circle and was further developed by Samoylovich (1962) and Kapelovich and Samoylovich (1967). The quasi-steady approach was also used by Saren (1968) who formulated an integral equation approach and presented numerical results for cascades with symmetric profiles. A formulation which accounts for the wake influence was given by Kurzin (1967) and Kazimirski, Nitusov and Samoylovich (1968) using analytic continuation principles or a Fredholm integral equation formulation, respectively. (See also the detailed description of these methods in the textbooks by Samoylovich 1969 and Gorelov et al. 1971.) The latter paper also contains several numerical examples. In an extension of this method Nitusov and Samoylovich (1970) also investigated the influence of cascade non-uniformity (blade offset) on the unsteady aerodynamic forces and determined regions of negative aerodynamic damping. Ryabchenko (1973, 1974, 1976), in a series of papers, succeeded to drop the assumption of small amplitude vibrations and to numerically solve the problem in a general nonlinear formulation which accounts for nonlinear vortex wake motions. Comparisons with the linear solutions showed the influence of finite amplitude of vibration and complex shape of the vortex wakes on the unsteady forces to be small for amplitudes less than 10% of cascade spacing and reduced frequencies less than 10.

The first American study of highly loaded cascades appears to be due to Nemesh (1970). Later, Adamczyk (1975) considered the passage of a timewise periodic total pressure distortion through a highly loaded cascade and found a substantial influence of blade loading on the unsteady forces. This approach was based on a combined analytical/numerical solution of the Laplace and vorticity transport equations. The most recent results for small amplitude vibrations of highly loaded cascades with arbitrary thickness and camber distributions have been obtained by Atassi and Goldstein (1976) and Atassi (1978) who split the problem into quasi-steady and wake-induced components and numerically solved the resulting integral equations. Current work by Atassi (1977) also includes the interaction of three-dimensional gusts with highly loaded cascades.

3.3 The Flat Plate Cascade in Unsteady Subsonic Flow

In compressible flow through oscillating cascades the phenomenon of acoustic resonance arises which can have a substantial effect on the aerodynamic damping characteristics of the blades. This phenomenon was first investigated by Runyan and Watkins (1951), W. P. Jones (1953) and Woolston and Runyan (1955) in relation to wind tunnel interference effects. Its significance in axial turbomachines appears to have been first explored by Sohngen and Quick (1960) and Lane and Friedman (1958) and work on subsonic flow solutions for oscillating cascades was started by Hamamoto (1957), Lane and Friedman (1958) and Meister (1962). In the early sixties studies of this problem were also begun in the USSR by Kurzin (1962, 1964, 1966) and by Gorelov and Dominas (1966). The latter papers also contain numerical results. A thorough exposition of the solution methods used by these authors, (i.e., integral equation and Mathieu function approaches) as well as detailed tables and graphs of aerodynamic coefficients can be found in the texts by Gorelov et al. (1971, 1974). The resonance phenomena occurring both in subsonic and supersonic cascade flows are discussed by Samoylovich (1967, 1969) and further papers devoted to this effect are those of Kurzin (1969, 1970, 1974) and Parker (1966, 1967).

The first American study of this problem was performed by Lane and Friedman (1958) who developed a solution for cascades with arbitrary stagger and interblade phase angles using Fourier transform techniques. The lifting pressure distributions were expressed as a Bessel function series which required a rather tedious computational procedure. More recently, this problem was considered again by Mani (1970), Fleeter (1973) and Rao and Jones (1975). Fleeter's work is related to Lane and Friedman's original approach, whereas Rao and Jones' method is an extension of Jones' and Moore's (1972) incompressible flow solution to subsonic compressible flow. At about the same time interest in this problem also arose in Japan (Kaji and Okazaki 1970), England (Smith 1971), and France (Leclerc (1971), Salaun (1973)). An additional very recent contribution is that of Carstens (1976) in Germany.

3.4 The Unsteady Subsonic Cascade with Finite Blade Loading

The inclusion of finite blade loading effects on the subsonic unsteady aerodynamic cascade characteristics was attempted only in the last few years by Nishiyama and Kobayashi (1973), Namba (1975) and Verdon et al. (1975). The Japanese studies are still based upon linearized thin airfoil theory and thus neglect all the nonlinear terms and cross products in Eq. (1) but account for the effect of relative displacement of the blades with finite mean blade circulation. Namba improved upon Nishiyama and Kobayashi's solution by taking into account the finite velocity of sound in dealing with the effect of the relative movement. Verdon et al. assumed small amplitude vibrations of the blades which allowed them to transform Eq. (1) into a linear equation with variable coefficients and thus to account for the interaction with the steady flow field. The paper describes a numerical near-field solution which is matched with analytical far-field solutions.

A company-proprietary computer code has been written but the results have not yet been published. Another method potentially applicable to this problem is the time-marching solution developed by Ni and Sisto (1976). However, so far results have been reported only for flat plate cascades. A further problem formulation has recently been given by Legendre (1976).

3.5 Unsteady Transonic Cascade Aerodynamics

The treatment of transonic cascades is hampered by the well known difficulties of computing mixed subsonic/supersonic flows. Therefore, only a few highly simplified solutions have so far been published although several recently developed methods are potentially quite capable to provide much better approximations to the real flow. Hamamoto (1960) gave a solution for sonic flow past unstaggered oscillating flat plate cascades by applying Fourier transform techniques to the linearized transonic small disturbance equation. An extension of this analysis to cascades with finite blade thickness using Oswatitsch's (1955) parabolic linearization technique as well as an investigation of other solution techniques, such as Laplace transform and collocation methods, was recently given by Schlein (1975). This study revealed that cascading usually is strongly destabilizing. The related problem of sonic wind tunnel interference was recently also studied by Savkar (1975) on the basis of linearized theory. Two very recent studies by Ginzburg et al. (1976) and Goldstein et al. (1977) also attempted to include the presence of normal shocks and to assess their effect on the unsteady aerodynamic characteristics. Further considerations about the inclusion of shocks have also been published by Legendre (1977). The validity of the above approaches can be assessed only by comparison with more accurate procedures. Magnus and Yoshihara's (1975) computation of transonic flow past a single oscillating airfoil using the time marching technique is the first "exact" solution of this problem. As already mentioned, this technique has been applied by Ni and Sisto (1976) to oscillating flat plate cascades and further studies are those of Ni (1974) and Pigott (1975). Efforts are presently underway to apply it to oscillating cascades with arbitrary blade shapes and thus to provide a valuable standard for the evaluation of more approximate but faster procedures. Another class of solutions which provides valuable insight into the effect of unsteady disturbances on transonic channel flows are being developed by Adamson and collaborators, e.g. Richey and Adamson (1976), Messiter and Adamson (1976) and Adamson and Liou (1977), using asymptotic expansion methods. Their analysis shows that small pressure changes downstream of a shock wave can cause large variations in the position of the shock wave and thus large variations in the aerodynamic loading of the blades. Also, their approach permits a detailed analysis of the shock boundary layer interactions. So far, only the steady interactions have been studied, but a preliminary analysis by Adamson and Liou (1977) indicates that unsteady effects are not important. Finally, a viscous transonic cascade solution using a highly efficient time-dependent implicit Navier-Stokes computer code developed by Briley and McDonald (1973) is presently being developed (Eisemann 1976).

3.6 The Flat Plate Cascade in Unsteady Supersonic Flow

The case of supersonic cascade flow requires differentiation depending on the axial through-flow Mach number as follows:

(1) For subsonic axial flow the flow disturbance can propagate upstream of the blade leading edges. Hence, each blade in the cascade is influenced by every blade below it and by the single adjacent blade above it (Fig. 12). This case therefore is often referred to as a cascade with subsonic leading edge locus, which is of great current interest because many fans and compressors have blades fully or partly exposed to locally supersonic flow.

(2) For moderately supersonic axial flow each blade is influenced only by its adjacent blades (Fig. 13). Cascades with supersonic leading edge locus therefore are much simpler to analyze.

(3) For high supersonic axial flow the disturbance created by each blade will entirely miss the adjacent blades. In this case, no blade interference takes place and the well-known problem of supersonic flow past a single airfoil is recovered.

Interest in the analysis of unsteady supersonic cascade flow first arose because of the need to understand supersonic wind tunnel interference effects. As previously mentioned an oscillating airfoil situated between two solid wind tunnel walls is equivalent to an unstaggered cascade whose blades are oscillating in counterphase. Using the linearized Eq. (3), Miles (1956) first obtained a complete solution using Laplace transform techniques. Lane (1957) generalized this solution to staggered cascades with an arbitrary interblade phase angle but provided no numerical results. Using quite different techniques, Hamamoto (1957) and Gorelov (1966) obtained the first numerical results. More recently, Platzer and Chalkley (1972) applied the method of characteristics to this case and presented torsional flutter boundaries. Cascade interference effects were found to be strongly destabilizing. They also showed that a quite elementary solution can be found for cascades oscillating at low reduced frequency. Gorelov et al. (1971) first attempted a solution for cascades with subsonic leading edge locus using collocation techniques. In this country, work on this problem started only a few years ago. Considering a semi-infinite cascade with subsonic leading edge locus, Verdon (1973) and Brix and Platzer (1974) obtained numerical results using finite difference and method of characteristics techniques, respectively. Also, Nagashima and Whitehead (1974) gave a third approach using dipole distributions and Yates (1975) developed another linearized characteristics approach. These solutions are in good agreement with each other.

Computing the flow past a sufficient number of blades until an asymptotic behavior for the aerodynamic forces and moments can be recognized, the authors made the assumption that these asymptotic values are representative of the infinite cascade. Due to the generally slow convergence (usually, the flow past 20 or 30 blades needs to be computed), a considerable computing effort is needed. This is aggravated by the fact that any subsequent flutter analysis requires the recomputation of this flow field for many combinations of parameters. Moreover, questions were raised about the equivalence between finite and infinite cascade analyses. Using Laplace transform techniques Kurosaka (1974) succeeded to obtain a solution for infinite cascades valid for low frequency blade motion and, more recently, to extend this solution to higher frequencies (Kurosaka 1977). Also, in the same year an alternate analysis of the infinite cascade was completed by Ni and Sisto (1976) using the previously mentioned time marching technique. Another approach to satisfy the flow periodicity condition explicitly was given by Verdon and McCune (1975) which was further developed by Verdon (1977). Comments on this approach and on the existence of resonance in supersonic flow were made by Kurosaka (1975). The question of the difference between finite and infinite cascades was studied by Chadwick (1975) and Platzer et al. (1976) who developed explicit analytical expressions for both cases using a quite elementary approach valid for small frequencies which was first suggested by Sauer (1950) for the single oscillating airfoil. Still other solutions for the oscillating flat plate cascade were obtained by Goldstein (1975), Adamczyk and Goldstein (1977) using the Wiener-Hopf technique, and Caruthers (1976). The only exposition of unsteady transonic and supersonic cascade theory available at this time has been given by Gorelov et al. (1971) which, of course, does not contain the more recent work described above.

3.7 The Unsteady Supersonic Cascade with Finite Blade Loading

While analyses by Carrier (1949), van Dyke (1953) and Teipel (1965) have established a significant effect of airfoil thickness on the aerodynamic forces and moments experienced by a single airfoil oscillating in unbounded supersonic flow, similar analyses of thickness and camber effects on the unsteady aerodynamic characteristics of supersonic cascades are only now being started. Gorelov and Meshman (1973) appear to have been the first ones to consider the influence of weak shocks. Chadwick (1975) and Platzer et al. (1976) also accounted for the presence of weak shocks and for the coupling between steady and oscillatory flow by solving the transonic small disturbance equation with a characteristics method and computed the inflow into a cascade with subsonic leading edge locus. Blade thickness was found to have a substantial effect in the lower frequency range. Recently, Strada (1977) extended this approach to the blade passage and confirmed the blade thickness effect in this frequency range. A quite different approach is presently being pursued by Kurosaka and Edelfelt (1976) who use the strained coordinate technique of Lighthill, Whitham and Lin. Again, preliminary results indicate a significant thickness influence.

3.8 Blade Row Interactions

The interaction between moving blade rows and the wake characteristics due to unsteady incompressible cascade flow were first investigated by Kemp and Sears (1953), (1955) and Meyer (1958) using small disturbance concepts i.e., restricting the analysis to lightly loaded thin blades. Further analyses using such concepts were later given by Lotz (1966) who studied the excitation of blade oscillations by adjacent blade cascades and by Jones and Moore (1972) who obtained a simplified solution for the flow in the wake of an oscillating cascade. Lefcort (1965) built on Meyer's (1958) work by considering wakes of finite thickness.

The interaction of highly loaded cascades in incompressible flow has been considered in a quasi-steady formulation by several authors using either conformal mapping, singularity or successive approximation methods (Isay 1957, Feindt 1961, 1962, a, b, Oellers 1962, Kazimierski 1966). Parker (1967) used the finite difference method to compute the quasi-steady potential flow through cascades in relative motion and Ispas (1974) further exploited this method in a series of calculations. This quasi-steady approximation which disregards the wake influence is also discussed in some detail by Samoylovich (1969). More recently, Saren (1971) developed another quasi-steady solution by expansion in powers of the cascade spacing and Kulyaev (1976) and Gorelov et al. (1976) attempted to account for the wake influence by direct computation of the wake development or by introducing the limiting case of infinitely large reduced frequency (Gorelov 1974). Comparisons of these latter solutions with the quasi-steady results show significant differences. Another solution accounting for the wake influence was developed by Lienhart (1973) using vortex representations of the blade surfaces.

Other interactions occur due to the presence of structural struts, stiffeners, and the like, which may cause blade excitations. A simplified method of estimating the excitation of such forced vibrations was recently proposed by Samoylovich et al. (1974) who also conducted experiments on the excitation of turbine blades. In the United States, Barber and Weingold (1977) used the Douglas-Neumann technique (Smith and Pierce 1958) to analyze the interaction of a stator cascade with a finite thickness strut cascade behind it or within it and predicted the magnitude and location of the non-uniform pressure distortion caused by it.

A similar interaction problem is caused by cascade non-uniformities such as blade displacements within a blade row. This problem was studied by Musatov (1963), Saren (1966) and Nitusov and Samoylovich (1970). Other blade row interaction studies are those of Adachi et al. (1974), Rao and Rieger (1975) and Sauer (1973).

The extension of the Kemp-Sears (1953, 1955) blade row interaction study to subsonic compressible flow was accomplished by Mani (1970) who gave a detailed account of the possible resonance effects. A similar study for supersonic flat plate blade row interactions - again using linearized theory - was begun by Ryhming (1957). However, this problem is so complex that no complete solutions could be obtained. Most recently, Favrat and Suter (1977) have tried to incorporate the shock wave diffractions and reflections which occur due to the interaction of the rotor blades with upstream stator vanes.

3.9 Unsteady Three-Dimensional Flows in Turbomachines

The above described two-dimensional cascade model (strip theory) remains, of course, a tool of questionable utility in the absence of a three-dimensional theory which allows to assess its range of validity. To shed some light on this question Gorelov (1963), Gorelov and Dominas (1967) and Gorelov et al. (1971) considered a three-dimensional cascade model which consists of an infinite blade row of finite blade height situated between end plates. Adopting again the small disturbance concept they were able to develop a solution for subsonic flow past a flat-plate cascade which executes small amplitude harmonic vibrations. In this way they were able to study the influence of the wave reflections from the end plates and thus to assess the effect of blade height.

More recently, both Salaun (1974, 1976) and Namba (1976) have succeeded to formulate solutions for compressible flow through a single annular blade row with a finite number of vibrating blades which are rotating at a constant angular velocity in an infinitely long cylindrical duct. Both authors used small disturbance theory thus excluding the effects of blade loading and by means of doublet representations for the oscillating blades they were able to obtain numerical solutions for subsonic flow. In addition, Namba (1976) also succeeded to study the response of this rotating annular cascade to inlet distortions. The results show that three-dimensional effects are small for the cases studied if the vibration frequency is well above the resonance frequency but large deviations from strip theory occur in the subresonant regime. Both authors also show the possibility of torsional flutter in subsonic flow. Furthermore, Salaun (1976) succeeded to extend his solution to the case of supersonic relative flow with subsonic axial velocity.

3.10 Response to Inlet Distortion

In view of the availability of the AGARD lecture series on inlet distortion problems and of Mokelke's (1974) review of the currently available prediction methods contained therein only a few remarks concerning the latest developments will be made here. Most of the unsteady cascade theories discussed in the previous sections are, of course, either directly applicable to inlet distortion calculations or after proper modification of the boundary conditions. The two most significant recent developments appear to be the inclusion of three-dimensional effects using small disturbance theory as demonstrated by Namba (1976) and the incorporation of viscous loss hysteresis and exit pressure non-uniformity effects into a multi-segment parallel compressor model as demonstrated by Mazzawy (1975). Both approaches are likely to contribute toward a better understanding of the major physical effects which are presently lumped together in the empirically derived distortion indices used in current design practice.

3.11 Stall Flutter Analysis

Stall flutter is a phenomenon which has plagued compressor development efforts for many years. At first, it was thought that it occurred only in the first bending mode but Shannon (1945) also identified the possibility of torsional stall flutter. Comprehensive reviews and bibliographies of stall flutter problems have been given by Schnittger and Sisto (1966) and Carta (1970). Unfortunately, the dynamic stall processes that occur in turbomachines are extremely complicated and thus confront the analyst with an exceptionally difficult problem. However, recent dynamic stall investigations on single airfoils have yielded many new insights into the basic flow phenomena and a conceptual description of the dynamic stall process has been given by Ham (1968). Semi-empirical models were developed by Ericsson and Reding (1976) and Beddoes (1975) which appear to be quite successful in certain cases and work is proceeding to analyze dynamic airfoil stall on the basis of unsteady boundary layer and Navier Stokes computations. The present state of the art of dynamic stall analysis has recently been reviewed rather comprehensively by McCroskey (1975, 1977) where further information can be found. It is generally agreed that the dynamic stall phenomena occuring in rotating turbomachinery blade rows are quite different from those encountered on a single airfoil embedded in an unbounded uniform flow. At this time, the only stall flow models available (Tanida and Okazaki 1963, Sisto 1967, Perumal 1976, Yashima and Tanaka 1977) are based on two-dimensional cascade flow assumption with a prescribed flow separation point. Yashima and Tanaka (1977) assumed leading-edge separation and achieved fairly good agreement with an experiment which was designed to reproduce this type of flutter. An experimental program is presently being conducted by Carta (1977) on highly loaded cascades oscillating near stall which should provide more definitive information and guidance for the development of more sophisticated models. For additional comments on this problem also compare Sisto (1977).

3.12 Compression Stability Analyses

The analyses of the previous sections always considered either a single blade row or the interactions of several blade rows. It is well known that the compressor does not merely respond to an externally imposed disturbance flow field but actively interacts with that flow field. Thus, study of a blade row or of a complete compressor as an isolated component of the total flow system can be grossly misleading. In a very recent paper Greitzer et al. (1977) have shown that the interactions between an axial compressor and the downstream compression system components strongly affect the operation in an inlet distortion. Their analysis is based on a nonlinear multi-segment parallel compressor model coupled to a quasi-two-dimensional flow analysis of the downstream diffuser or nozzle. Exit diffusers were found to increase the velocity distortion seen by the compressor thus causing increased blade loading whereas exit nozzles decreased the distortions and thus improved the compression stability. These predictions were confirmed by an experimental test program.

The concept of total system dynamics was also incorporated by Greitzer (1976) for the prediction of rotating stall or surge. In this model the compressor and its ducting are replaced by an actuator disk to account for the pressure rise and by a constant area pipe to account for the dynamics of the fluid in the compressor duct. Similarly, the throttle is replaced by another actuator disk and a constant area duct. The stability analysis of the resulting nonlinear model leads to the definition of a non-dimensional parameter B and to the prediction of surge for operation at values greater than B and of rotating stall for values below B. While previous linearized analyses were aimed at the prediction of the instability onset this new analysis makes it possible to study the nonlinear behavior of a compression system during the large amplitude transients that occur after the initial linear instability. The usefulness of one-dimensional flow concepts together with measured steady-state stage characteristics for the prediction of surge was recently also demonstrated in a theoretical study by Corbett and Elder (1975).

The question of the prediction of compressor performance in rotating stall was addressed by Day et al. (1977) who showed that the stall cell blockage is an important parameter which permits the prediction of full-span or part-span stall on the basis of a heuristic stall model. The problem of rotating stall prediction was recently also taken up by Orner et al. (1975) who presented preliminary results of a stability analysis based on a quasi-three-dimensional flow model.

4. **Experimental** Studies of Unsteady Flows in Turbomachines

The two major tools for the experimental investigation of the unsteady flow phenomena in turbomachines are the cascade tunnel and the single rotor test rig. Although both facilities entail inherent limitations it is generally agreed that the advantage of simplicity and lower cost outweigh these limitations and that cascades and isolated rotors are tools which, when applied correctly, are quite useful in identifying the major unsteady flow effects. In addition, unsteady flow measurements in multi-stage machines are also being carried out.

4.1 Unsteady Flow Studies in Linear Cascades

During the last few years a number of cascade tunnels have been built or adapted for use in unsteady turbomachinery flow studies. A linear oscillating cascade wind tunnel is available at the United Technologies Research Center. The 10 x 25 in test section can accommodate 11 shaft-mounted blades which can be oscillated in a frequency range between 3 to 150 cps. Further information has recently been given by Carta and St. Hilaire (1976) In this report the authors also describe a test program to measure the aerodynamic response of a cascade oscillating near stall at wind speeds up to 200 ft/sec. The most recent test results are summarized by Carta and St. Hilaire (1977). The United Technologies Research Center also operates a supersonic linear cascade wind tunnel over a Mach number range from 1.3 to 2.0. The 4 x 8 in. test section accommodates five blades plus upper and lower boundary layer scoops. In recent years, this tunnel was used to establish the torsional and bending flutter characteristics of typical supersonic compressor blades. These studies are documented in the reports by Snyder (1973), Arnoldi et al. (1975) and in the papers by Snyder and Commerford (1974) and Mikolajczak et al. (1975). Another supersonic cascade wind tunnel is in operation at the Detroit Diesel Allison Division of the General Motors Corporation which permits cascade testing over a wide range of Mach numbers, incidence angles and pressure ratios. Over the past few years, this facility has provided both flutter and oscillatory pressure information on five-bladed supersonic cascades which is reported by Fleeter et al. (1975 a,b) Novick et al. (1975), Fleeter et al. (1976) and Fleeter and Riffel (1976). Another cascade tunnel has recently been completed in the United States by Ostdiek (1975) who used an oscillating inlet to generate a nearly sinusoidal variation in the flow direction of a low-speed flow and completed a first series of oscillatory pressure measurements on a five-bladed cascade.

Unsteady cascade testing is also being carried out in Europe and Japan. A linear cascade tunnel has been built at the DFVLR-Goettingen in Germany (Lawaczek 1970) which has been used over the last several years to measure the pressure distributions on an oscillating seven-bladed cascade up to Mach numbers of 0.6 as reported by Triebstein et al. (1975) and Triebstein (1976). This same tunnel was also used by Lawaczek and Heinemann (1975) to investigate the Karman vortex street shed from a ten-bladed turbine cascade in subsonic, transonic and supersonic flow. Tests were also performed in the intermittent high-speed wind tunnel of the DFVLR-AVA Goettingen to investigate the aeroelastic characteristics of a nine-bladed highly cambered turbine cascade in the Mach number range 0.4 to 1.0. According to Bublitz (1976) large pressure fluctuations and dynamic stresses were recorded during transonic operation. Another subsonic cascade tunnel at ONERA with a test section of 0.6 x 0.12 meters covering a Mach number range from 0.3 to 0.8 was used by Loiseau and Nicolas (1976) to measure the pressure distributions of an oscillating cascade with NACA 65A006 blade profiles. Also, Loiseau and Maquennehan (1976) indicated the completion of another cascade tunnel which permits the testing of seven to eleven-bladed cascades at subsonic, transonic and supersonic Mach numbers. Subsonic and supersonic cascade flutter tests and aerodynamic damping measurements in linear cascade tunnels have also been conducted in the USSR by Korostelev (1974), Tikhonov (1974), Pisarenko et al. (1976) and Kaminer and Balalaev (1976). In England, the new gust tunnel of the University of Cambridge which has oscillating flexible walls to generate controlled sinusoidal gusts was used by Satyanarayana (1975) to make rather detailed transitional boundary layer measurements on single airfoils and cascades in low speed flow. Finally, in Japan Hanamura (1971, 1973) studied incompressible attached flow flutter of a blade row whereas Yashima and Tanaka (1977) completed a stall flutter test of a linear cascade.

4.2 Unsteady Flow Studies in Annular Cascades

Linear cascades suffer from uncertainties caused by the "finiteness" of the cascade due to wall interference effects. Annular cascades offer the advantage of eliminating such end effects. At present, only two annular cascades seem to be in operation. Whitehead et al. (1976) developed an annular cascade of 16 blades which permits testing at subsonic and supersonic Mach numbers up to $M = 1.4$. Using electromagnetic excitation of the blades they measured the aerodynamic moments due to torsional oscillations over a Mach number range from 0.6 to 1.2. Both a fixed and a rotating supersonic annular cascade are available at ONERA which were used by Fabri and Paulon (1975) and Paulon (1976) to study unsteady flow phenomena and shock motions caused by overspeed operation of a transonic compressor.

4.3 Unsteady Flow Studies in Rotating Rigs

Several extensive measuring programs have been or are being conducted on a number of single rotors or on multi-stage machines in order to explore the major unsteady aerodynamic flow effects which occur in turbomachines. The problem of wake production, transport and interaction has received considerable attention over the years with major contributions by Meyer (1958), Tyler and Sofrin (1962), Smith (1966), Kerrebrock and Mikolajczak (1970), Parker and Watson (1972), Walker and Oliver (1972), Whitfield et al. (1972), Kiock (1973), Lockhart and Walker (1974), Evans (1972, 1973, 1975, 1976, 1977), Hirsch and Kool (1976), Lakshminarayana (1975), Gallus et al. (1976), Thompkins and Kerrebrock (1975), Kerrebrock (1976) and Schmidt and Okiishi (1976), 1977). These investigations were carried out in both single rotors (Kerrebrock, Lakshminarayana), single-stage compressors (Walker, Evans, Gallus) as well as three-stage compressors (Okiishi) using various measuring techniques, such as hot-wire anemometry, pressure transducers and Schlieren stroboscopy. These studies show a significant difference between the rotor wake characteristics and wakes of linear cascades or isolated airfoils as well as the possibility of certain wake instabilities (Kerrebrock 1974) which hamper the theoretical modelling of rotor wakes. Also, over the last few years detailed measuring programs of the steady and unsteady flow and pressure characteristics of transonic turbomachines have been initiated. These activities have recently been reviewed in considerable detail by McNally (1976) where a listing of the current test programs using modern instrumentation (high-response transducers, hot wire probes, hot film gages, laser velocimetry, laser fluorescence, laser holography) can be found. Many of these tests are only internally documented but a few studies, notably the measurements in the MIT blowdown compressor facility (a transonic rotor which is operated in a pulsed mode with a test time of about 30 milliseconds) reported by Thompkins and Kerrebrock (1975) and Kerrebrock (1976), the measurements in the DFVLR single-stage transonic compressor reported by Weyer and Hungenberg (1975) and by Lecht and Weyer (1976), the transducer and schlieren-optical investigations of two types of supersonic compressor stages with tandem cascades as stator as reported by Gallus (1975), Gallus et al. (1976), Gallus et al. (1977) are available in the open literature. Further noteworthy measurements are those of Einsfield (1970) and Fasso and Larguier (1970). Also, the feasibility of subscale flutter testing has recently been explored by Jay (1975) who tested an 8 inch model rotor of an advanced design fan which experienced both subsonic stall and supersonic flutter. Good correlation between model and full scale rig results was noted for the subsonic flutter boundary but little correlation could be achieved for supersonic flutter. Nevertheless, this low cost method of flutter testing appears to have good potential for further development. Supersonic unstalled flutter of two 1800 ft/sec tip-speed NASA fan rotors was also investigated by Snyder and Commerford (1974).

Detailed measurements of the unsteady blade response characteristics due to inlet distortion have recently been initiated by Bruce and Henderson (1975) who measured the blade response on a single-stage low-speed axial flow fan with strain gauges and pressure transducers and by Peacock and Overli (1975) who determined the dynamic stall characteristics of a lightly-loaded single-stage low speed axial flow compressor due to various inlet distortions. In the latter study normal force hysteresis loops were measured which exhibit certain similarities with the single airfoil dynamic stall phenomena which were reviewed by McCroskey (1977). The complicated character of these loops and the accompanying wave propagation and vortex shedding processes vividly illustrate the enormous obstacles toward the analytical modelling of dynamic stall.

Recent advances in measuring techniques have also stimulated detailed compressor stall investigations. Sexton et al. (1975) investigated rotating stall of a low-speed single-stage axial-flow fan using blade mounted transducers in connection with a multichannel telemetry system. Another rotating stall investigation of a low speed compressor stage has been completed by Ludwig et al. (1973) who also tested a rotating stall control system and developed a small disturbance theory for the onset of stall. (Nenni and Ludwig 1974). Further rotating stall information was obtained by Nagano (1974) in a five-stage transonic compressor. The deep-stall characteristics of a low-speed three-stage compressor were determined by Day (1975) who used a conditional sampling technique for hot wire and pressure transducer measurements. Contrary to earlier models postulating wake-type stall cells Day's results indicate that the rotating stall cell has a size and speed of rotation which forces unstalled flow to enter from the side and to be transported across the cell.

Also, it should be noted that a substantial amount of experimental information on unsteady phenomena in turbomachines has been gathered in the USSR. The individual papers are too numerous to be cited here. However, readers interested in specific references can probably orient themselves rather quickly by studying the introductory overview articles of Pisarenko and Ol'shtein (1974) and Ol'shtein (1976) which summarize the papers presented at the conferences on aeroelasticity in turbomachines held in Kanev (1973) and Riga (1975). Further references as well as a detailed exposition on "Excitation of the Fluctuations of the Blades of Turbomachines" can be found in Samoylovich's latest book (1975) on this topic. It is a 285-page book whose major chapters are: heterogeneity of flow - measurement of pulsating fluxes - unsteady aerodynamic phenomena in stages - damping of the oscillations of blades - unsteady aerodynamic forces which excite blade oscillations - effect of design peculiarities on exciting forces - blade flutter - excitation of acoustic waves by cascades, their reflection and passage through cascades. His reference list mentions 151 Russian papers out of a total of 225.

Finally, attention is drawn to two more topics, i.e., unsteady flows in centrifugal compressors and unsteady boundary layer measurements. While both problems have as yet attracted much less attention and work than the above described topics it should be noted that a two-component LDV is being used by Runstadler and Dolan (1976) and Kulite pressure transducers and hot wire probes by the Northern Research and Engineering Company to investigate the flow in a centrifugal compressor and that detailed unsteady flow measurements in centrifugal compressors have been reported from Germany by Bammert (1972), Eckardt (1975, 1976) and Gallus (1975). Direct measurements of the unsteady boundary layer development on an axial-flow compressor stator blade have recently been reported by Evans (1973, 1977) who found that great caution should be used in attempting to predict boundary-layer development from cascade test results or steady calculation procedures.

5. Discussion

In the preceding Sections 3 and 4 an attempt was made to summarize the major theoretical and experimental approaches to the study of the unsteady aerodynamic and aeroelastic phenomena in turbomachines which are currently being pursued. Several observations are offered here to characterize the current status of these developments.

The theoretical treatment of unsteady incompressible flow past lightly loaded single cascades has attracted considerable attention over the past quarter century. As a result, a number of computational procedures have been evolved and catalogues of tables and graphs have been produced (notably Whitehead 1960, Samoylovich 1969, Gorelov 1971, 1974) which provide rather detailed information on the unsteady aerodynamic characteristics of such cascades. Several of these procedures have been checked against each other, e.g. Whitehead's, Sisto's, Belotserkovskiy's and Gorelov's results as shown in Samoylovich (1969) or Rao and Jones' and Schorr and Reddy's results as shown in Carta (1974). Also, both cascade (Triebstein 1976, Loiseau and Nicolas 1976) as well as fan tests (Bruce and Henderson 1975) have recently become available which provide generally encouraging experimental verification. In contrast, the computation of highly loaded unsteady incompressible cascades has only recently been studied more extensively by Ryabchenko, Gorelov, Samoylovich and Atassi but little comparative theoretical or experimental verification appears to be available at this time.

Also, in recent years, a number of solutions for unsteady subsonic flat-plate cascades have become available and detailed tabulations have been provided by Gorelov et al. (1971, 1974). Few comparative evaluations of the methods developed in various AGARD countries seem to have been conducted and, in fact, contradictory statements can be found. As an example, Whithead et al. (1976) state that Smith's theory (1972) predicts torsional flutter whereas Carstens (1976) flatly excludes such a possibility in the absence of steady blade loading. Also, the question of resonance effects on the aerodynamic damping appears to require further study. Fortunately, several cascade and rotating rig test programs (Triebstein 1976, Loiseau 1976, Gallus 1976) are presently underway which have already yielded valuable experimental information. The problem of unsteady subsonic flow past highly loaded cascades, on the other hand, is still unresolved although at least one theoretical solution (Verdon et al. 1975) is close to completion.

Work on the unsteady transonic cascade flow problem has also increased over the last few years and several linearized solutions have been obtained. Furthermore, numerical solution of the nonlinear equations as well as asymptotic matching techniques (Adamson et al.) are being applied to this problem and the latter technique has already provided valuable new insight about the possible shock motions in response to downstream disturbances. The question of unsteady viscous effects, shock boundary layer interactions and, most importantly, of three-dimensional flow effects is still unanswered although several approaches could be applied to this problem. The possible significance of three-dimensional flow effects was first studied by McCune (1958) and the new approaches by Namba (1976), Salaun (1976) could be extended to provide new insight. The detailed measurements in the DFVLR single-stage compressor by Weyer et al. also provide helpful guidance for the formulation of theoretical flow models.

The unsteady supersonic flat-plate cascade problem has been considered quite extensively over the past few years and several solution methods have been developed. Comparative evaluations of the numerical results show substantial agreement although certain questions about the equivalence of finite and infinite cascades and about the significance of resonance effects are not yet completely resolved. Work on blade-thickness and three-dimensional effects has been initiated only recently (Platzer et. al., Kurosaka, Salaun) but some preliminary results have already become available. Cascade and rotating rig testing is underway (Fleeter, Gallus, Loiseau) which is providing detailed flow and pressure information. In addition, cascade and fan flutter tests (Snyder, Jay, Loiseau) have provided information on the supersonic blade flutter boundaries. The agreement with the theoretically predicted boundaries is generally encouraging but much more theoretical and experimental work is required to establish confidence in these prediction techniques and to understand their range of validity.

The theoretical analysis of blade row interaction effects has benefitted from the recent advances in numerical fluid mechanics which permit a detailed computation of the potential flow interactions (e.g. Barber and Weingold 1977) and of the vortex wake development (Ryabchenko) in a two-dimensional approximation. However, the available experimental evidence (in particular, the recent measurements of Lakshminarayana and Kerrebrock) indicates large differences between rotor wakes and cascade wakes and the presence of strong three-dimensional effects. Further advances in modeling the viscous wake effects therefore will have to depend on additional detailed measuring programs (e.g., Schmidt and Okiishi) coupled with new approaches such as those proposed by Kerrebrock 1974, 1976 and McCune 1976.

It is evident from the preceding survey that the theoretical modeling of unsteady flow effects in turbomachines is largely limited to the analysis of lightly loaded cascades (i.e., to two-dimensional flow assumptions). The methods used involve direct extensions of the well known external flow solutions for oscillating airfoils in unbounded flow to the more difficult boundary value problem of unsteady flow past airfoil arrays. Thus, there is a direct relationship with the current status of unsteady external aerodynamics and the methods used in this field (airfoil modeling by vortex distributions, conformal mapping, transform techniques, characteristics and other numerical methods etc.) are directly applicable to turbomachinery unsteady aerodynamics and, indeed, pace its rate of progress. This is most obvious in the analysis of unsteady transonic effects. The development of more efficient solution methods for unsteady transonic airfoils, as reviewed e.g. by Spreiter and Stahara (1976) and by McCroskey (1977) or as proposed at this meeting for example by Liu and Winther (1977)is of direct benefit in internal flow studies. Furthermore, it should also be noted that the methods developed for the flutter and forced vibration analysis of turbomachinery blading are, of course, equally applicable to turbomachinery noise studies and, indeed, Namba's (1976) new three-dimensional rotating cascade solution includes results for the sound power output. However, a detailed discussion of specific turbomachinery noise problems and of the current analyses methods is outside the scope of this paper and the reader is referred to Cumpsty's (1977) review.

McCroskey (1977), in his review of unsteady external aerodynamics, concluded that numerical analyses have generally outpaced detailed experiments in problems that are mostly inviscid, whether in the regime of flutter and unsteady airloads predictions, or in the field of transonic aerodynamics. It should be obvious from the preceding pages that a similar statement can be made for the field of unsteady turbomachinery aerodynamics - with two important qualifications. First, the current methods are mostly restricted to two-dimensional analyses of lightly loaded cascades thus severely limiting the range of applicability and usefulness of such methods. Second, their practical utility is still further hampered by the inaccessibility of the currently available results. In contrast to the systematic documentation of unsteady turbomachinery aerodynamics (theory and experiment) in the USSR (Samoylovich 1969, 1975, Gorelov et al. 1971, 1974) no such documentation exists in the AGARD countries. As a result, the appreciation for the unsteady aerodynamic effects in turbomachines and the access to the available results is limited to a small number of specialists.

The work on viscous unsteady flow effects in turbomachines, on the other hand, is still largely limited to experiments (e.g., the wake measurements) and, even there, the detailed measurements of the unsteady blade boundary layer characteristics (Evans) or of the dynamic stall characteristics (Carta, Peacock) is of only very recent origin. The theoretical analysis of unsteady boundary layer effects and the development of reliable estimates of unsteady flow losses and of unsteady loads due to viscous or separated flow phenomena (in particular, rotating stall, surge, stall flutter) are problems requiring much further work. Additional remarks can be found in the panel discussions and summaries given at the Project SQUID Workshop (Carter 1974) and the AGARD-Meeting (Platzer 1975).

6. Conclusions and Recommendation

Only a few years ago Kraft (1968) and Legendre (Fleeter 1972 p. 114) deplored the low level of activity in turbomachinery research due to the preoccupation of the scientific/engineering community with space exploration and emphasized the need for a better understanding of the unsteady flow phenomena that occur in turbomachines. The above review of past and current efforts in unsteady turbomachinery aerodynamics shows that a significant change in attitude and increase in research effort has taken place in the seventies. It also shows, incidentally, that a similar hiatus did not occur in the USSR where the literature reveals a steady and systematic buildup of research activities in this field since the late fifties.

The following major developments and results can be distinguished:

a) Incompressible, subsonic and supersonic unsteady flow past lightly loaded single cascades has been studied in considerable detail, but relatively little comparative evaluation and documentation of the various solutions is available in the AGARD countries. However, rather comprehensive texts on this subject have been published in the USSR.

b) Recently, solutions for incompressible unsteady flow past highly loaded cascades have also been published, but little information is still available for subsonic and supersonic cascades with finite blade thickness and loading.

c) The unsteady transonic cascade problem is still unsolved, but some new approaches are presently in progress which are likely to provide new insight.

d) Work on the analysis of three-dimensional unsteady flow effects is in progress and some valuable new results for lightly loaded rotors have already been published.

e) New measuring techniques coupled with modern data acquisition systems are being applied to the investigation of unsteady cascade and rotor flows throughout the whole speed regime. A number of papers have recently been published which provide detailed unsteady flow and pressure information for comparison with the available theoretical models.

f) Progress has also been made towards the prediction of compression system instabilities (rotating stall, surge) using nonlinear unsteady analyses, but much more experimental and theoretical work is required to understand and describe highly viscous and separated unsteady flow phenomena (wake formations and interactions, stall flutter etc.).

In 1974 Horlock (Carta, 1974 p. 502) advocated the development of an "unsteady flow tool kit" which should be available to the turbomachinery designer of the 1980's as a supplement to the steady flow tools (three-dimensional meridional flow programs, steady flow cascade data, two-dimensional blade-to-blade programs etc.) which are presently in use. The validity and importance of Horlock's recommendation was further endorsed by the participants of the AGARD Conference on Unsteady Phenomena in Turbomachinery, AGARD 1975. In view of the relatively rapid advances in the field of unsteady turbomachinery aerodynamics it appears that the following recommendations are warranted:

- To promote acceptance and use of unsteady flow information in turbomachinery design and engineering increasing emphasis will have to be placed on the problem of data access, evaluation and documentation. Therefore, systematic comparisons and evaluations of various theoretical methods and experimental results should be conducted for well defined and mutually agreed-upon test configurations. Such a plan of action was also suggested at the IUTAM 1976-Meeting by Prof. Stepanov, USSR, as the topic for another IUTAM meeting on unsteady turbomachinery aerodynamics.
- Further engine performance improvements and the avoidance of expensive engine modifications due to aerodynamic/aeroelastic stability problems will not only depend on the continued systematic research in unsteady turbomachinery aerodynamics. Rather, the transfer of highly specialized unsteady aerodynamic and aeroelastic information to the design community and the introduction of young engineers to this problem suggest an equally important need for a "Manual on Aeroelasticity in Turbomachines" similar to the well known "AGARD Manual on Aeroelasticty" for the design of flight vehicles.

Acknowledgments

Preparation of this review was supported under a partial task of Naval Air Systems Command Project No. WR024-03-001 with Dr. Herbert J. Mueller, Code AIR-310, as program manager. The assistance of Mr. Gregory L. Shaffer, AFSC-FTD, WPAFB, in providing many foreign references is gratefully acknowledged. Also, the author is grateful to Prof. Atassi, University of Notre Dame, and Prof. Gallus, Technical University of Aachen, for valuable suggestions.

References

Adachi, T., Fukusada, K., Takahashi, N. and Nakamoto, Y. (1974), "Study on the Interference between Moving and Stationary Blade Rows in Axial-Flow Blower", Bulletin of the JSME, Vol. 17, No. 109, July 1974

Adamczyk, J.J. (1975), "The Passage of a Distorted Velocity Field through Cascade of Airfoils", AGARD-CP -177

Adamczyk, J.J. and Goldstein, M.E. (1977), "Unsteady Flow in a Supersonic Cascade with Subsonic Leading-Edge Locus", to be published

Adamson, T.C. and Liou, M.S. (1977), "Unsteady Motion of Shock Waves in Two-Dimensional Transonic Channel Flows", University of Michigan Technical Report UM014534-F, June 1977

Adamson, T.C. and Platzer, M.F. (Editors)(1977), "Transonic Flow Problems in Turbomachinery", Hemisphere Publishing Corporation, Washington, DC, 1977

AGARD Conference Proceedings No. 177 on "Unsteady Phenomena in Turbomachinery", 1975

Arnoldi, R.A. (1974), "Holographic Visualization of Compressor Blade Wake Interaction", Pratt & Whitney Aircraft Report No. PWA-TM-4925, March 1974

Arnoldi, R.A. et al. (1975), "Supersonic Chordwise Bending Flutter in Cascades", Pratt & Whitney Aircraft Report No PWA-5271, May 1975

Atassi, H. (1977), Private Communication

Atassi, H. (1978), "Effect of Blade Loading and Thickness on the Aerodynamics of Oscillating Cascades", AIAA-paper No. 78-227, January 1978

Atassi, H. (1978), "Aerodynamic Force and Moment on Oscillating Airfoils in Cascade", ASME-paper to be presented at 23rd Annual International Gas Turbine Conference, London, April 1978

Attassi, H. and Goldstein, M.E. (1976), "Unsteady Aerodynamic Forces Acting on Loaded Two-Dimensional Blades in Nonuniform Incompressible Flows", Revue Francaise de Mecanique, Numero Special, pp. 47-56, 1976

Bammert, K. (1972), "Nonsteady Flow Measurements of a Centrifugal Compressor", paper presented at the JSME Symposium, Tokyo, 5 September 1972

Barber, T.J. and Weingold, H.D. (1977), "Vibratory Forcing Functions Produced by Nonuniform Cascades", ASME paper No. 77-GT-57

Beddoes, T.S. (1975), "A Synthesis of Unsteady Aerodynamic Effects, Including Stall Hysteresis", Proc. First European Rotorcraft and Powered Lift Aircraft Forum, University of Southhampton, Paper No. 17

Belotserkovskiy, S.M., Ginevsky, A.S. and Polonsky Ya.Ye. (1961), "Aerodynamic Forces Acting Upon a Cascade of Profiles in the Case of Unsteady Streamline Flow. In: Promyshlennaya Aerodinamika (Industrial Aerodynamics), Oborongiz, 1961

Billington, A.E. (1949), "Aerodynamic Lift and Moment for Oscillating Airfoils in Cascade", Rep. E.63, Aeronautical Council of Scientific & Industrial Research, Australia

Bisplinghoff, R.L., Ashley, H., Halfman, R.L. (1955), "Aeroelasticity", Addison-Wesley Publishing Company

Briley, W.R. and McDonald, J. (1973), "An Implicit Numerical Method for the Multi-Dimensional Compressible Navier-Stokes Equations", United Aircraft Research Laboratories Report M911363-6, November 1973

Brix, C.W.,Jr. and Platzer, M.F. (1974), "Theoretical Investigation of Supersonic Flow Past Oscillating Cascades with Subsonic Leading Edge Locus", AIAA 12th Aerospace Science Meeting, Washington, DC, AIAA Paper No. 74-14 (January 30- February 1, 1974)

Bruce, E.P. and Henderson, R.E. (1975), "Axial Flow Rotor Unsteady Response to Circumferential Inflow Distortions", AGARD-CP -177, paper No. 18

Bublitz, P. (1976), "Experimental Aeroelastic Investigation on a Cascade in Compressible Flow", Revue Francaise de Mecanique-Numero Special, pp. 143-150, 1976

Carrier, G.F. (1949), "The Oscillating Wedge in a Supersonic Stream", JAS 16, 150-152

Carstens, V. (1976), "Unsteady Pressure Distributions on an Oscillating Cascade in Subsonic Flow", Revue Francaise de Mecanique-Numero Special, pp. 25-33, 1976

Carta, F. (1970), "Turbomachinery Flutter", United Aircraft Research Laboratories Report No. UAR-J242, October 1970

Carta, F. (Editor)(1974), "Unsteady Flows in Jet Engines", United Aircraft Research Laboratories Report No. UARL-3-PU, November 1974

Carta, F.O. and St. Hilaire, A.O. (1976), "An Experimental Study on the Aerodynamic Response of a Subsonic Cascade Oscillating Near Stall", Project SQUID Technical Report UTRC-2-PU, July 1976

Carta, F.O. and St. Hilaire, A.O. (1977), "Experimentally Determined Stability Parameters of a Subsonic Cascade Oscillating Near Stall", ASME-paper No. 77-GT-47

Caruthers, J.E. (1976), "Theoretical Analysis of Unsteady Supersonic Flow Around Harmonically Oscillating Turbofan Cascades", Ph.D. Thesis, Georgia Tech. September 1976

Chadwick, W.R. (1975), "Unsteady Supersonic Cascade Theory Including Nonlinear Thickness Effects", Ph.D. Thesis, Naval Postgraduate School, June 1975

Chang, C.C. and Chu, W.H. (1955), "Aerodynamic Interference of Cascade Blades in Synchronized Oscillation". J. of Appl. Mech., No. 4, 1955

Chu, F.K.H. (1965), "A Theoretical and Experimental Investigation of Two-Dimensional Effects on Unsteady Flow in a Partial Admission Turbine", ScD Thesis, MIT, September 1965

Corbett, A.G. and Elder, R.L. (1975), "Mathematical Modelling of Compressor Stability in Steady and Unsteady Flow Conditions", AGARD-CP -177, paper No. 12

Cumpsty, N.A. (1977), "A Critical Review of Turbomachinery Noise", ASME Journal of Fluids Engineering, pp. 278-293, June 1977

Day, I.J. (1975), "Detailed Flow Measurements During Deep Stall in Axial Flow Compressors", AGARD-CP -177, paper No. 34

Day, I.J. et al. (1977), "Prediction of Compressor Performance in Rotating Stall", ASME paper No. 77-GT-10

Dean, R.C. (1959), "On the Necessity of Unsteady Flow in Fluid Machines", ASME Journal of Basic Engineering pp. 24-28, March 1959

Eck, B. (1957), "Technische Stroemungslehre", Springer Co. p. 50, 1957

Eckardt, D. (1975), "Instantaneous Measurements in the Jet-Wake Discharge Flow of a Centrifugal Compressor Impeller", Journal of Engineering for Power, Trans. of ASME 97.3, July

Eckardt, D. (1976), "Detailed Flow Investigations within a High-Speed Centrifugal Compressor Impeller", ASME 76-FE-13, ASME International Gas Turbine Conference, New Orleans

Einsfeld, K. (1970), "Comparative Electromechanical and High-Frequency Interferometric Measurement of Unsteady Blade Forces on a Turbine Cascade", Thesis, Technical University Stuttgart, Germany, 1970

Eiseman, P.R. (1976), "A Coordinate System for a Viscous Transonic Cascade Analysis", United Technologies Research Center Technical Report R76-Q12149-5, May 1976

Ericsson, L.E. and Reding, J.P. (1976), "Spilled Leading Edge Vortex Effects on Dynamic Stall Characteristics", Journal of Aircraft, Vol. 13, No. 4, pp. 313-315, April 1976

Evans, R.L. (1972), "Stream Turbulence Effects on the Turbulent Boundary Layer in a Compressor Cascade", ARC Report 34 587, U.K.

Evans, R.L. (1973), "Turbulent Boundary Layers on Axial-Flow Compressor Blades", Ph.D. dissertation, Cambridge University

Evans, R.L., (1975), "Turbulence and Unsteadiness Measurements Downstream of a Moving Blade Row", Trans. ASME, Journal of Engineering for Power, 97, pp. 131-139

Evans, R.L. (1976), "Some Turbulence and Unsteadiness Effects in Turbomachinery", Project SQUID-Report PU-R1-77, June 14-15, 1976

Evans, R.L. (1977), "Boundary Layer Development on an Axial Flow Compressor Stator Blade", ASME-paper No. 77-GT-11

Fabri, J. (1971), "Review of Recent French Research on Unsteady Aerodynamics of Axial Flow Compressors and Turbines", Project SQUID Workshop on Fluid Dynamics of Unsteady, Three-Dimensional and Separated Flows, Atlanta, June 1971

Fabri, J. and Paulon, J. (1975), "Unsteady Phenomena in Turbomachines, as Revealed by Visualizations and Measurements", AGARD-CP -177

Fasso, G. and Larguier, R. (1970), "Experimental Determination of Pressure Fluctuations on Stationary Blades of a High Power Axial Compressor", Recherche Aerospatiale No. 5, pp. 272-273, Sept-Oct 1970

Favrat, D. and Suter, P. (1977), "Interaction of the Rotor Blade Shock Waves in Supersonic Compressors with Upstream Stator Vanes", ASME-paper No. 77-GT-93

Feindt, E.G. (1961), "Flow Calculation of a Tandem Cascade with a Second Moving Blade Row", Ing. Archiv., Vol. 30, No. 2, 1961

Feindt, E.G. (1962a), Flow Calculation for a Nonstationary Multistage Plate Cascade", Ing. Archiv., Vol. 30, No. 5, 1961

Feindt, E.G. (1962b), "Flow Calculation of a Nonstationary, Multistage, Staggered Plate Cascade", Ing. Archiv., Vol. 31, No. 5, 1962

Fleeter, S. (1972) (Editor), "Aeroelasticity in Turbomachines", Proceedings of a Project SQUID Workshop held at Detroit Diesel Allison, June 1-2, 1972

Fleeter, S. (1977), "Aeroelasticity Research for Turbomachine Applications", AIAA-paper No. 77-437

Fleeter, S. (1973), " The Fluctuating Lift and Moment Coefficients for Cascaded Airfoils in a Nonuniform Compressible Flow", Journal of Aircraft, March 1973

Fleeter, S., Holtman, R.L., McClure, R.B. and Sinnet, G.T. (1975), "Supersonic Inlet Torsional Cascade Flutter", AIAA Journal of Aircraft, 12:9, August

Fleeter, S., Novick, A.S. and Riffel, R.E. (1975), " The Unsteady Aerodynamic Response of an Airfoil Cascade to a Time Varying Supersonic Inlet Flow Field", Proceedings of AGARD Conference on Unsteady Phenomena in Turbomachinery, AGARD-CP -177, September

Fleeter, S., Novick, A.S. and Riffel, R.E. (1976), "Experimental Determination of the Unsteady Aerodynamics in a Controlled Oscillating Cascade", ASME 76-GT-17, ASME International Gas Turbine Conference, New Orleans

Fleeter, S., and Riffel, R.E. (1976), "An Experimental Investigation of the Unsteady Aerodynamics in an Oscillating MCA Airfoil Cascade Including Loading Effects", Office of Naval Research Technical Report, Detroit Diesel Allison EDR 9028, December 1976

Gallus, H.E. (1975), "Results of Measurements of the Unsteady Flow in Axial Subsonic and Supersonic Compressor Stages", AGARD-CP -177, paper No. 10 (see also the remark about radial-flow compressors)

Gallus, H.E., et al. (1976), "Measurement of the Rotor-Stator-Interaction in a Subsonic Axial-Flow Compressor Stage", Revue Francaise de Mecanique, Numero Special, pp. 169-176, 1976

Gallus, H.E., et al. (1977), "Measurements of Quasi-Steady and Unsteady Flow Effects in in a Supersonic Compressor Stage", ASME- paper Mo. 77-GT-13

Garrick, I.E. (1957), "Nonsteady Wing Characteristics", High Speed Aerodynamics and Jet Propulsion, Vol. VII, pp. 658-792, Princeton Univ. Press, Princeton, NJ, 1957

Ginzburg, S.I., et al. (1976), "A Supersonic Flutter Excitation Mechanism for Compressor Blades", Problemy Prochnosti No. 3, pp. 62-65, March 1976

Goldstein, M.E. (1975), "Cascade with Subsonic Leading Edge Locus", AIAA Journal, Vol. 13, No. 8, pp. 1117-1119, August 1975

Goldstein, M.E., Braun, W., Adamczyk, J.J. (1977), "Unsteady Flow in a Supersonic Cascade with Strong In-Passage Shocks", accepted for publication in Journal of Fluid Mechanics

Gorelov, D.N. (1963), "Three-Dimensional Flow About a Blade Circle of an Axial Turbomachine in a Subsonic Unsteady Gas Stream", Izvestiya Akademii Nauk, SSSR, Otdeleniye Tekhnicheskikh Nauk, Mekhanika i Mashinostroyeniye, No. 6, 1963

Gorelov, D.N.,(1966), "Oscillations of a Plate Cascade in a Transonic Gas Flow", Mekhanika Zhidkosti i Gaza 1(1), 69-74, 1966

Gorelov, D.N. (1966), "Lattice of Plates in an Unsteady Supersonic Flow", Mekhanika Zhidkosti i Gaza 1(4), 50-58, 1966

Gorelov, D.N. (1969), "Oscillations of Cascade Profiles in Nonuniform Incompressible Flow", Mekhanika Zhidkosti i Gaza, Vol. 4, No. 4, pp. 31-40, 1969

Gorelov, D.N. (1974), "On Hydrodynamic Interaction between Flat Plate Cascades during their Relative Motion", Prikladnaya Mekhanika i Tekhnicheskaya Fizika, No. 1, 1974

Gorelov, D.N., Kurzin, V.B., Saren, V.E., (1971), "Aerodynamics of Lattices in an Unsteady Flow", Izd-vo "Nauka", Novosibirsk 1971

Gorelov, D.N., Kurzin, V.B., Saren, V.E. (1974), "Atlas of Non-Steady Aerodynamic Characteristics of Profile Cascades", Nauka Publishers, Norosibirsk 1974

Gorelov, D.N., Kulyaev, V.E., Saren, V.E. (1976), "Theoretical Investigation of Hydrodynamic Interaction between Profile Cascades", Revue Francaise de Mecanique, Numero Special, pp. 19-23, 1976

Gorelov, D.N. and Dominas, L.V. (1965), "Calculation of the Aerodynamic Forces and Moments Acting Upon a Cascade of Plates that Oscillate in a Two-Dimensional Flow of Incompressible Fluid", Izvestiya Akademii Nauk SSR, Mekhanika, No. 3, 1965

Gorelov, D.N. and Dominas, L.V. (1966), "A Cascade of Plates in a Subsonic Unsteady Gas Stream", Mekhanika Zhidkosti i Gaza, No. 6, 1966

Gorelov, D.N. and Dominas, L.V. (1967), "Determination of Unsteady Aerodynamic Forces for a Three-Dimensional Cascade of Plates in a Two-Dimensional Gas Stream", Mekhanika Zhidkosti i Gaza, No. 6, 1967

Gorelov, D.N. and Meshman, V.A. (1973), "On Unsteady Flow with Shocks in Supersonic Compressor Cascades", P,M.T.F. (Russian Journal for Applied Mechanics and Technical Physics) No. 5, p. 41, 1973

Greitzer, E.M. (1976), "Surge and Rotating Stall in Axial Flow Compressors", ASME Journal of Engineering for Power, Vol. 98, No. 2, pp. 190-217, April 1976

Greitzer, E.M., Mazzawy, R.S., Fulkerson, D.A. (1977), "Flow Field Coupling between Compression System Components in Asymmetric Flow", ASME-paper No. 77-GT-17

Ham, N.D. (1968), "Aerodynamic Loading on a Two-Dimensional Airfoil during Dynamic Stall", AIAA Journal, Vol. 6, No. 10, pp. 1927-1939, October 1968

Hamamoto, I. (1957), "Minute Harmonic Oscillation of Flat Plate Cascade in Subsonic Flow", Proc. 7th Japanese National Congress for Applied Mechanics, pp. 273-276, 1957

Hamamoto, I. (1957), "Minute Harmonic Oscillation of Flat Plate Cascade in Supersonic Flow", Second Japanese Natl. Congress for Appl. Math. and Mech. (May 1957)

Hamamoto, I. (1960), "Minute Harmonic Oscillations of a Flat Plate Cascade in Transonic Flow", Proc. 10th Japanese Natl. Congr. for Appl. Mech., pp. 227-231, 1960

Hanamura, Y. (1971, 1973), "Flutter of Cascading Blade Row", Report No. 459 and 503, Institute of Space and Aeronautical Science, University of Tokyo, February 1971 and December 1973

Hawthorne, W.R. (1973), "Flow through Moving Cascades of Lifting Lines with Fluctuating Lift", Journal of Mechanical Engineering Science, Vol. 15, No. 1, pp. 1-10, 1973

Henderson, R.E. and Daneshyar, H. (1970), "Theoretical Analysis of Fluctuating Lift on the Rotor of an Axial Turbomachine", Aeronautical Research Council R & M 3684, September 1970

Hirsch, C. and Kool, P. (1976), "Measurement of the Three-Dimensional Flow Field behind an Axial Compressor Stage", ASME-paper No. 76-GT-18, 1976

Horlock, J.H. (1968), "Fluctuating Lift Forces on Aerofoils Moving Through Transverse and Chordwise Gusts", Journal of Basic Engineering Vol. 90, No. 4, 1968, pp. 494-500

Horlock, J.H., Greitzer, E.M., Henderson, R.E. (1977), "The Response of Turbomachine Blades to Low Frequency Inlet Distortions", Journal of Engineering for Power, Vol. 99, No. 2, pp. 195-203, April 1977

Isay, W.H. (1957), "Zur Berechnung der Stroemung durch axiale Schaufelgitter", Z. angew. Math. Mech. 37, p. 321, 1957

Isay, W.H. (1958), "Flow Through an Oscillating and Rotating Radial Blade Cascade", Z. Flugwiss, No. 11, 1958

Ispas, I. (1974), "Contribution to the Calculation of Inviscid Subsonic Flow through Cascades and Stages of Axial Turbomachines by Means of Finite Difference Procedures", Ph.D. Thesis, Technical University of Aachen, Germany, 1974

IUTAM (1974), "Symposium on Aeroelasticity in Turbomachines", sponsored by the International Union for Theoretical and Applied Mechanics, Paris, France, October 18-23, 1976

Jay, R.L. (1975), "Subscale Flutter Testing of TF-41-A-100 LP1 Blades", AFAPL-TR-75-82, December 1975

Jones, W.P. (1950), "Wind Tunnel Interference Effects on Measurements of Aerodynamic Coefficients for Oscillating Aerofoils", Aeronautical Research Council R & M 2786, September 1950

Jones, W.P. (1953), "Wind Tunnel Wall Interference Effects on Oscillating Aerofoil in Subsonic Flow", Aeronautical Research Council R & M 2943, December 1953

Jones, W.P. (Editor)(1962), "Manual on Aeroelasticity", AGARD 1962

Jones, W.P. and Moore, J.A. (1972), "Flow in the Wake of a Cascade of Oscillating Aerofoils", AIAA Journal, Vol. 10, No. 12, pp. 1600-1605, December 1972

Kaji, S. and Okazaki. T. (1970), "Propagation of Sound Waves through a Blade Row", Journal of Sound and Vibration, Vol. II, No. 3, pp. 355-375, 1970

Kaminer, A.A. and Balalaev, V.A. (1976), "Determination of the Aerodynamic Damping in Flexural-Torsional Vibrations of Turbomachine Blades", Problemy Prochnosti No. 3, 1976

Kapelovich, B.E. and Samoylovich, G.S. (1967), "Integral Characteristics of Quasi-Steady Flow Past a Cascade of Arbitrary Profiles Oscillating with Arbitrary Phase Shift", Mekhanika Zhidkosti i Gaza, Vol. 2, No. 1, pp. 154-157, 1967

Kazimierski, Z. (1966), "Plane Flow through an Axial Stage of Flow Machines having Arbitrary Geometry", Archiwun budowy maszyn, No. 2, 1966

Kazimierski, Z.B., Nitusov, V.V., Samoylovich, G.S. (1968), "Plane Incompressible Fluid Flow Past an Array of Arbitrary Profiles Vibrating with Arbitrary Phase Shift", Mekhanika Zhidkosti i Gaza, Vol. 3, No. 5, pp. 47-53, 1968

Kemp, N.H. and Ohashi, H. (1975), "Forces on Unstaggered Airfoil Cascades in Unsteady In-Phase Motion with Applications to Harmonic Oscillation", Proc. Symp. Unsteady Aerodynamics, University of Arizona, March 18-20, 1975

Kemp, N.H. and Sears, W.R. (1953), "Aerodynamic Interference between Moving Blade Rows", J. Aeron. Sci. Vol. 20, pp.585-597, 1953

Kemp, N.H. and Sears, W.R. (1955), "The Unsteady Forces due to Viscous Wakes in Turbomachines", JAS, No. 7, 1955

Kerrebrock, J.L. (1974), "Waves and Wakes in Turbomachines Annuli with Swirl", AIAA-paper No. 74-87, 1974

Kerrebrock, J.L. (1976), "Flow in a Transonic Compressor Rotor", Proc. Workshop on Transonic Flow Problems in Turbomachinery, February 11-12, 1976, Hemisphere Publishers, Washington, DC

Kerrebrock, J.L. and Mikolajczak, A.A. (1970), "Intra-Stator Transport of Rotor Wakes and Its Effect on Compressor Performance", Journal of Engineering for Power, p. 359, October 1970

Khaskind, M.D. (1958), "The Oscillation of a Cascade of Thin Profiles in an Incompressible Stream", Prikladnaya Matematika i Mekhanika, No. 2, 1958

Kiock, R. (1973), "Turbulence Downstream of Stationary and Rotating Cascades", ASME-paper No. 73-GT-80, 1973

Korostelev, A.E. (1974), "Experimental Study of the Aerodynamic Interaction in a Cascade of Vibrating Blades", Problemy Prochnosti No. 8, pp. 34-40, August 1974

Kraft, H. (1957), "Nonsteady Flow through a Turbine", ASME Nonsteady Flow Symposium, December 5-6, 1957

Kraft, H. (1968), "Nonsteady Flow in the Turbine, Recent Work and Thinking", ASME Symposium on Unsteady Flow, May 6-8, 1968

Kulyaev, R.L. (1976), " Calculation of Hydrodynamic Interaction between Cascades of Thin Profiles Taking Account of Evolution of Vortex Wakes", Prikladnaya Mekhanika i Tekhnicheskaya Fizika, No. 4, 1976

Kurosaka, M. (1974), "On the Unsteady Supersonic Cascade with a Subsonic Leading Edge--An Exact First Order Theory", ASME J. Engr. for Power, pp. 13-31, January 1974

Kurosaka, M. (1975), "On the Issue of Resonance in an Unsteady Supersonic Cascade", AIAA Journal, Vol. II, pp. 1514-1516, November 1975

Kurosaka, M. (1977), "Supersonic Cascade Study", work currently performed for the Air Force Office of Sci. Res.

Kurosaka, M. and Edelfelt, I.H. (1976), "Some Recent Developments in Unsteady Aerodynamics of a Supersonic Cascade", Revue Francaise de Mecanique, Numero Special, pp. 57-64, 1976

Kurzin, V.B. (1962), "The Oscillation of a Cascade of Thin Profiles in a Compressible Subsonic Stream", Prikladnaya Mekhanika i Teknicheskaya Fizika, No. 1, 1962

Kurzin, V.B. (1964), "Concerning the Calculation of Forces in the Case of Arbitrary Small Oscillations of Profiles in a Cascade", Izvestiya Akademii Nauk SSSR, Ser. Mekh. Mas., No. 2, 1964

Kurzin, V.B. (1966), "Concerning the Aerodynamic Interference of Profiles in a Subsonic Unsteady Stream", Mekhanika Zhidkosti i Gaza, No. 1, 1966

Kurzin, V.B. (1967), "Solution of the Problem of Flow past a Thick Blade Cascade by the Splicing Method", Mekhanika Zhidkosti i Gaza, Vol. 2, No. 3, pp. 145-150, 1967

Kurzin, V.B. (1969), "Natural Oscillations of Gas Flowing past a Lattice of Flat Plates", Zhurnal Prikladnoi Mekhaniki i Tekhnicheskoi Fiziki, Vol. 10, No. 5, pp.-68-75, September 1969

Kurzin, V.B. (1970), "The Damped Natural Oscillations of a Gas Flowing past a Cascade of Flat Plates", Mekhanika Zhidkosti i Gaza, No. 5, pp. 84-88, September 1970

Kurzin, V.B. (1974), "Acoustic Resonance in Turbomachines", Problemy Prochnosti, No. 8, pp. 94-98, August 1974

Lakshminarayana, B. (1975), "The Nature of Flow Distortions caused by Rotor Blade Wakes", AGARD-CP -177

Lane, F. (1957), "Supersonic Flow Past an Oscillating Cascade with Supersonic Leading Edge Locus", J. Aeronaut. Sci. 24(1), pp. 65-66, 1957

Lane, F. and Friedman, M. (1958), "Theoretical Investigation of Subsonic Oscillatory Blade-Row Aerodynamics", NACA TN 4136, 1958

Lawaczek, O. (1970), "Cascade Tunnel of the AVA Goettingen", AVA-Report 70A46, 1970

Lecht, M. and Weyer, H.B. (1976), "Unsteady Aerodynamic Rotor Blade Loading in a Transonic Axial Flow Compressor with Steady-State Inlet Distortion", Revue Francaise de Mecanique, Numero Special-Complement, 1976

Leclerc, J. (1971), "Linearized Theory of Unsteady Subsonic Flow in a Linear Two-Dimensional Subsonic Flow in a Linear Two-Dimensional Cascade", La Recherche Aerospatiale No. 1971.3

Lefcort, M.D. (1965), "An Investigation Into Unsteady Blade Forces in Turbomachinery", J. of Engng. for Power, No. 4, pp. 345-354, 1965

Legendre, R. (1954), "First Calculations of the Aerodynamic Damping of Compressor Blade Oscillations", La rech. aeronaut., No. 37, 1954

Legendre, R. (1976), "Highly Cambered Blades in Cascades, Oscillating in a Compressible Gas", La Recherche Aerospatiale No. 6, pp. 301-305, November-December 1976

Legendre, R. (1977), "Highly Cambered Blades, Mounted in Cascades and Oscillating in a Fluid in Transonic Flow", La Recherche Aerospatiale No. 2, pp. 129-130, March-April 1977

Lienhart, W. (1973), "Computation of the Unsteady Flow and the Blade Forces on Blade Rows in Relative Motion to Each Other", VDI-Berichte No. 193 and VDI Forschungsheft No. 562 1973

Lilley, G.M. (1952), "An Investigation of the Flexure - Torsion Flutter Characteristics of Aerofoils in Cascades", College of Aeron., Cranfield - Rep.n° 60, 1952

Lin, C.C., Reissner, E. and Tsien, H. (1948), "On Two-Dimensional Nonsteady Motion of a Slender Body in a Compressible Fluid", J. Math. and Phys., 27(3), pp. 220-231, 1948

Liu, D.D. and Winther, B.A. (1977), "Unsteady Transonic Flow Analysis by a Mixed Kernel Function Method", AGARD-Symposium on Unsteady Aerodynamics, Ottawa, September 26-28, 1977

Lockhart, R.C. and Walker, G.J. (1974), "The Influence of Viscous Interactions on the Influence of Viscous Interactions on the Flow Downstream of an Axial Compressor Stage", Proc. 2nd Int. Symp. Air Breathing Engines, Univ. of Sheffield, London, 1974

Loiseau, H. and Nicolas, J. (1976), "Unsteady Aerodynamic Forces and a Rectilinear Cascade of Subsonic Blades", Revue Francaise de Mecanique, Numero Special, pp. 105-114, 1976

Loiseau, H. and Maguennehan, B. (1976), "Aeroelastic Instabilities in Compressors and Wind Tunnel Tests of Straight Cascades, Revue Francaise de Mecanique, Numero Special, pp. 157-168, 1976

Lotz, M. (1966), "Excitation of Blade Oscillations in Axial Turbomachines by Adjacent Blade Cascades", Warme, No. 2, 1966

Lotz, M. and Raabe, J. (1968), "Blade Oscillations in One-Stage Axial Turbomachinery", Journal of Basic Engineering, Vol. 90, No. 4, pp. 485-493, December 1968

Ludwig, G.R., et al. (1973), "Investigation of Rotating Stall in Axial Flow Compressors and the Development of a Prototype Rotating Stall Control System", AFAPL-TR-73-45, May 1973

Magnus, J. and Yoshihara, H. (1975), "Calculations of Transonic Flow over an Oscillating Airfoil", AIAA Journal 13, 1622-1628, December 1975

Mani, R. (1970), "Compressibility Effects in the Kemp-Sears Problem", NASA-SP-304, pp. 513-533, 1970

Mazzawy, R.S. (1975), "Multiple Segment Parallel Compressor Model for Circumferential Flow Distortion", AGARD-CP -177

McCroskey, W.J. (1975), "Recent Developments in Dynamic Stall", Symp. Unsteady Aerodynamics, Univ. of Arizona, March 18-20, 1975, pp. 1-34

McCroskey, W.J. (1977), "Some Current Research in Unsteady Fluid Dynamics", ASME Journal of Fluids Engineering, Vol. 99, pp. 8-38, March 1977

McCune, J.E., (1958), "A Three-Dimensional Theory of Axial Compressor Blade Rows - Application in Subsonic and Supersonic Flows", J. Aerosp. Sci., pp. 544-560, September 1958

McCune, J.E. (1976), "Three-Dimensional Inviscid Flow through a Highly Loaded Transonic Compressor Rotor", Proc. Project SQUID Workshop on Transonic Flow Problems in Turbomachinery, pp. 20-59, Hemisphere Publishers, February 11-12, 1976

McNally, W.D. (1976), "Review of Experimental Work on Transonic Flow in Turbomachinery", Proc. Project SQUID Workshop on Transonic Flow Problems in Turbomachinery, pp. 457-484, Hemisphere Publishers, February 11-12, 1976

Meister, E. (1960), "Flow of an Incompressible Fluid through an Oscillating Staggered Cascade", Arch. for rat. Mech. and Anal., No. 3, 1960

Meister, E. (1962), "Contribution to the Aerodynamics of an Oscillating Cascade in Subsonic Flow", ZAMM, No. 1/2, 1962 and ZAMM No. 6, 1962

Mendelson, A. and Carroll, R.W. (1956), "Lift and Moment Equations for Oscillating Airfoils in an Infinite Unstaggered Cascade", NACA-TN n° 3263, October 1954

Messiter, A.F. and Adamson, T.C. (1976), "Asymptotic Solutions for Nonsteady Transonic Channel Flows", Symposium Transsonicum II, pp. 41-48, Springer Verlag, 1976

Meyer, R.X. (1958), "The Effect of Wake on the Transient Pressure and Velocity Distributions in Turbomachinery", Trans. ASME, No. 7, 1958

Mikolajczak, A.A., et al. (1975), "Advances in Fan and Compressor Blade Flutter Analysis and Predictions", J. Aircraft, Vol. 12, No. 4, pp. 325-332, April 1975

Miles, J.W. (1956), "The Compressible Flow Past an Oscillating Airfoil in a Wind Tunnel", J. Aeronaut. Sci. 23(7), pp. 671-678, 1956

Mokelke, H. (1974), "Prediction Techniques", AGARD-LS-No. 72 on Distortion Induced Engine Instability

Musatov, V.V. (1963), "Concerning the Calculation of Unsteady Flow About a Cascade of Profiles in an Incompressible Fluid", Izvestiya Akademii Nauk, SSSR. Ser. Mekh. Mash., No. 3, 1963

Nagano, S. (1974), "Rotating Stall in a 5-Stage Transonic Compressor", Proc. Project SQUID Workshop on Unsteady Flows in Jet Engines. UARL-3-PU, pp. 465-468, 11-12 July 1974

Nagashima, T. and Whitehead, D.S. (1974), "Aerodynamic Forces and Moments for Vibrating Supersonic Cascade Blades", CUED/A-Turbo/TR59, 1974

Namba, M. (1975), "Subsonic Cascade Flutter with Finite Mean Lift", AIAA Journal Vol. 13, No. 5, pp. 586-593, May 1975

Namba, M. (1976), "Lifting Surface Theory for Unsteady Flows in a Rotating Annular Cascade", Revue Francaise de Mecanique, Numero Special, pp. 39-46, 1976

Naumann, H. and Yeh, H. (1973), "Lift and Pressure Fluctuations of a Cambered Airfoil under Periodic Gusts and Applications in Turbomachinery", ASME Journal of Engineering for Power, Vol. 95, No. 1, pp. 1-10, January 1973

Nemesh, J. (1970), "Thickness Effects in Nonstationary Cascade Flow", Ph.D. Thesis, Stevens Institute of Technology, 1970

Nenni, J.D. and Ludwig, G.R. (1974), "A Theory to Predict the Inception of Rotating Stall in Axial Flow Compressors", AIAA-paper No. 74-528

Ni, R.H. (1974), "Nonstationary Aerodynamics of Arbitrary Cascades in Compressible Flow", Ph.D. Thesis, Stevens Institute of Technology , 1974

Ni, R.H. and Sisto, F. (1976), "Numerical Computation of Nonstationary Aerodynamics of Flat Plate Cascades in Compressible Flow:, ASME Journal of Engineering for Power, Vol. 98, No. 2, pp. 165-170, April 1976

Nickel, K. (1955), "Lifting Wing Systems in Plane Flow for Arbitrary Unsteady Flow", Ing. Archiv., Vol. 24, No. 3, 1955

Nishiyama, T. and Kobayashi, H. (1973), "Theoretical Analysis for Unsteady Characteristics of Oscillating Cascade Airfoils in Subsonic Flows", Technology Reports, Tohoku Univ., Vol. 38, No. 1, pp. 287-314, 1973

Nitusov, V.V. and Samoylovich, G.S. (1970), "Calculation of Flow past Cascade of Arbitrary Profiles Vibrating with Arbitrary Phase Shift and with Account for Profile Displacement", Mekhanika Zhidkosti i Gaza, Vol. 5, No. 3, pp. 170-173, 1970

Northern Research and Engineering Co. (1966), "Unsteady Force Coefficients in Axial Turbomachinery Blades", Report No. 1094-3, 1966

Novick, A.S., et al. (1975), "An Experimental Investigation of Unsteady Airfoil Motion in a Supersonic Stream", Proc. Symposium on Unsteady Aerodynamics, Univ. of Arizona, pp. 609-630, March 18-20, 1975

Oellers, H.J. (1962), "Incompressible Potential Flow in a Plane Cascade Stage", Sonderdruck aus dem Jahrbuch der WGLR, 1962

Ohashi, H. (1968), "Analytical and Experimental Study of Dynamic Characteristics of Turbopumps", NASA TND-4298, April 1968

Ol'shtein, L.E. (1976), "New Aspects of the Aeroelasticity of Turbomachines", Problemy Prochnosti, pp. 3-6, March 1976

Orner, N., et al. (1975), "The Prediction of the Behavior of Axial Compressors near Surge", AGARD-CP-177, paper No. 36

Ostdiek, F.R. (1975), "A Cascade in Unsteady Flow", AGARD-CP-177, paper No. 26

Oswatitsch, K. and Keune, F. (1955), "The Flow Around Bodies of Revolution at Mach Number One", Proc. Conf. High Speed Aeronaut. Polytech, Inst. Brooklyn, New York, NY, January 1955

Parker, R. (1966, 1967), "Resonance Effects in Wake Shedding from Parallel Plates", J. Sound & Vibration Vol. 4, No. 1, (1966) and Vol. 5, No. 2 (1967)

Parker, R. (1967), "Calculation of Flow through Cascades of Blades having Relative Motion and the Generation of Alternating Pressures and Forces due to Interaction Effects", Proc. Instn. Mech. Engrs., 182 (Ptl), pp. 229, 1967-68

Parker, R. and Watson, J.F. (1972), "Interaction Effects between Blade Rows in Turbomachines", Heat and Fluid Flow, Vol. 2, No. 1, pp. 33-42, 1972

Paulon, J. (1976), "Flow Instabilities in Supersonic Compressors at Low Compression Regime", Revue Francaise de Mecanique, Numero Special, pp. 177-186, 1976

Peacock, R.E. and Overli, J. (1975), "Dynamic Internal Flows in Compressors with Pressure Maldistributed Inlet Conditions", AGARD-CP-177, paper No. 17

Perumal, P.V.K. (1976), "Thin Airfoil in Eddy Array and Part-Stalled Oscillating Cascade", Ph.D. Thesis, Stevens Institute of Technology, June 1976

Pigott, R. (1975), "Forced and Self-Excited Vibration of Transonic Turbine Cascades", Ph.D. Thesis, Univ. of Pennsylvania, Philadephia, 1975

Pigott, R. and Abel, J.M. (1974), "Vibrations and Stability of Turbine Blades at Stall", ASME Journal of Engineering for Power, July 1974

Pisarenko, G.S. and Ol'shtein, L.E. (1974), "Problems of Aeroelasticity of Blades of Turbomachines", Problemy Prochnosti, pp. 3-8, August 1974

Pisarenko, G.S., et al. (1976), "Experimental and Theoretical Investigations of the Aerodynamic Damping of Turbojet Rotor Blade Vibrations", Revue Francaise de Mecanique, Numero Special, pp. 89-06, 1976

Platzer, M.F. (1975), "Transonic Blade Flutter--A Survey", Shock and Vibration Digest, Vol. 7, No. 7, pp. 97-106, July 1975

Platzer, M.F. (1975), "Technical Evaluation Report on Unsteady Phenomena in Turbomachinery", AGARD CP-177

Platzer, M.F. and Chalkley, H.G. (1972), "Theoretical Investigation of Supersonic Cascade Flutter and Related Interference Problems", AIAA/ASME/SAE 13th Struc., Struc. Dynam. and Matl. Conf., San Antonio, TX, AIAA Paper No. 72-377, April 10-12, 1972

Platzer, M.F., Chadwick, W.R., Schlein, P.B. (1976), "On the Analysis of the Aerodynamic and Flutter Characteristics of Transonic Compressor Blades", Revue Francaise de Mecanique, Numero Special, pp. 65-74, 1976

Popescu, I.L. (1957), "Nonsteady Fluid Flow Through a Profile Network", Nota I, Acad. RPR, sec. mat. fiz. No. 1., 1957

Popescu, I.L. (1958), "Nonsteady Fluid Flow Through a Profile Network", Nota II, Communic. Acad. RPR, No. 10, 1958

Raj, R. and Lakshminarayana, B. (1976), "Three-Dimensional Characteristics of Turbulent Wakes behind Rotors of Axial Flow Turbomachinery", ASME Journal of Engineering for Power, pp. 218-228, 1976

Rao, B.M. and Jones, W.D. (1974), "Unsteady Airloads on a Cascade of Staggered Blades in Incompressible Flow", Proc. Project SQUID Workshop on Unsteady Flow in Jet Engines, UARL-3-PU, 11-12 July 1974

Rao, B.M. and Jones, W.D. (1975), "Unsteady Airloads on a Cascade of Staggered Blades in Subsonic Flow", AGARD-CP-177, paper No. 32

Rao, J.S. and Rieger, N.F. (1975), "Computer Program for Aerodynamic Interference between Moving Blade Rows", Technical Memo 75 WRL MIO, Rochester Institute of Technology, July 1975

Richey, G.K. and Adamson, T.C. (1976), "Analysis of Unsteady Transonic Channel Flow with Shock Waves", AIAA Journal Vol. 14, pp. 1054-1061, 1976

Runstadler, P.W. and Dolan, F.X..(1976), "A Laser Velocimeter System for Small Radial Turbomachinery", Proc. Project SQUID Workshop on Transonic Flow Problems in Turbomachinery, pp. 546-565, MICH-16-PU, 11-12 February 1976

Runyan, H. L. and Watkins, C. E., "Considerations of the Effect of Wind Tunnel Walls on Oscillating Air Forces for Two-Dimensional Subsonic Compressible Flow", NACA TN 2552, September 1951

Ryabchenko, V. D. (1973), "Nonlinear Problem about the Nonstationary Flow around a Cascade of Profiles", TSAGI (Central Aeromechanics Institute Vol. 4, No. 6, (1973)

Ryabchenko, V.D. (1974), "Nonstationary Aerodynamic Characteristics of Cascades of Arbitrary Profiles Vibrating in a Potential Stream of Incompressible Fluid", Izv. Akad. Nauk SSR, Mekhan. Zhidki i Gaza, No. 1, 1974

Ryabchenko, V.D. (1976), "Analysis of the Nonstationary Aerodynamic Characteristics of Cascades of Arbitrary Shaped Profiles", Problemy Prochnosti, No. 3, pp. 29-32, March 1976

Ryabchenko, V.D. and Saren, V.E. (1972), "On the Analysis of Aerodynamic Characteristics of Profiles of Arbitrary Shape", Izv. Akad. Nauk SSR, Mekhan. Zhidl. i Gaza, No. 2, 1972

Ryhming, I. (1957), "Uber die instationare Uberschallstromung durch Schaufelgitter mit Ruckwirkung", Z. Angew. Math. Mech. 37(11/12), 416-431, December 1957

Sabatiuk, A. and Sisto, F. (1956), "A Survey of Aerodynamic Excitation Problems in Turbomachines", Trans. ASME, Vol. 78, No. 3, April 1956

Salaun, R. (1973), "Calculation of the Subsonic Unsteady Aerodynamic Pressures on Compressor Blades", La Recherche Aerospatiale, No. 1, 1973

Salaun, R. (1974), "Unsteady Aerodynamic Pressures in an Annular Cascade in Subsonic Flow", Ph.D. Thesis, University of Paris, May 1974

Salaun, R. (1976), "Flutter Instability in an Annular Cascade", Revue Francaise de Mecanique, Numero Special, pp. 35-38, 1976

Salaun, R. (1976), Private Communication

Samoylovich, G.S. (1961a), "A Nonstationary Vortex Stream About a Cascade of Thin Vibrating Profiles", Prikladnaya Matematika i Mekhanika, No. 5, 1961

Samoylovich, G.S. (1961b), "Flow About an Aerodynamic Cascade of Thin Vibrating Profiles", Prikladnaya Matematika i Mekhanika, No. 4, 1961

Samoylovich, G.S. (1962), "On the Calculation of the Unsteady Flow around an Array of Arbitrary Profiles Vibrating with Arbitrary Phase Shift", PMM, Vol. 25, No. 1, 1962

Samoylovich, G.S. (1967), "Resonance Phenomena in Sub-and Supersonic Flow through an Aerodynamic Cascade", Mekhanika Zhidkosti i Gaza, Vol. 2, No. 3, pp. 143-144, 1967

Samoylovich, G.S. (1969), "Unsteady Flow Around and Aeroelastic Vibration in Turbomachine Cascades", Izd-vo Nauka, Moscow, 1969 (Translated as WPAFB-FTD-HC-23-242-70, February 1971)

Samoylovich, G.S. (1975), "Excitation of the Fluctuations of the Blades of Turbomachines", "Mashinostroyeniye", Moscow 1975

Samoylovich, G.S. (1976), "Theoretical and Experimental Investigation of Aeroelastic Effects in Turbomachines", Revue Francaise de Mecanique, Numero Special, pp. 75-80, 1976

Samoylovich, F.S., Nitusov, V.V., Yurkov, E.V. (1974), "Excitation of Forced Vibrations in Turbomachine Blades in a Peripherally Uneven Flow", Problemy Prochnosti, No. 8, pp. 106-109, August 1974

Saren, V.E. (1966), "Unsteady Incompressible Fluid Flow past a Cascade of Thin Curved Plates", Mekhanika Zhidkosti i Gaza, Vol. 1, No. 1, pp 75-84-1976

Saren, V.E. (1968), "Cascade of Arbitary Vibrating Profiles in Incompressible Fluid Flow", Mekhanika Zhidkosti i Gaza, Vol. 3, No. 3, pp. 81-87, 1968

Saren, V.E. (1971), "On Hydrodynamic Interaction between Profile Cascades in a Potential Flow", Mekhanika Zhidkosti i Gaza, No. 4, 1971

Satyanarayan, B. (1975), "Some Aspects of Unsteady Flow past Airfoils and Cascades", AGARD-CP -177, paper No. 25

Sauer, H. (1973), "Aerodynamic Excitation in Turbomachines as a Result of Blade Rows with Differing Blade Numbers", Maschinenbautechnik 22, No. 10, pp. 469-472, 1973

Sauer, R. (1950), "Elementary Theory of the Slowly Oscillating Supersonic Airfoil", ZAMP pp. 248-253, 1950

Savkar, S.D. (1976), "A Note on Transonic Flow past a Thin Airfoil Oscillating in a Wind Tunnel", J. Sound & Vibration 46 (2), pp. 195-207, 1976

Schlein, P.B. (1975), "A Study of Unsteady Transonic Interference Effects", Ph.D. Thesis, Naval Postgraduate School, Monterey, CA, March 1975

Schmidt, D.P. and Okiishi, T.H. (1976), "Multistage Axial-Flow Turbomachine Wake Production, Transport and Interaction", Iowa State University Report ISU-ERI-AMES-77130, November 1976

Schmidt, D.P. and Okiishi, T.H. (1977), "Detailed Measurements of the Periodically Unsteady Flow Produced by Rotor and Stator Wake Interaction in a Multi-Stage Turbomachine", AIAA-paper No. 77-202

Schnittger, J.R. and Sisto, F. (1966), "Blade Flutter in Axial Turbomachines", Applied Mechanics Surveys, Spartan Books, Washington, DC, 1966

Schorr, B. and Reddy, K.C. (1971), "Inviscid Flow through Cascades in Oscillatory and Distorted Flow", AIAA- Journal, Vol. 9, No. 11, pp.2043-2050, October 1971

Sexton, M.R., O'Brien, W.F.O., Moses, H.L. (1975), "An On-Rotor Investigation of Rotating Stall in an Axial-Flow Compressor", AGARD-CP -177, paper No. 33

Shannon, J.F. (1945), "Vibration Problems in Gas Turbines, Centrifugal and Axial-Flow Compressors", ARC-R&M No. 2226, 1945

Sisto, F. (1952), "Flutter of Aerofoils in Cascade", So.D. Thesis - MIT, September 1952

Sisto, F. (1955), "Unsteady Aerodynamic Reactions of Airfoils in Cascade", Journal of Aeron. Sci., Vol. 22, No. 5, May 1955

Sisto, F. (1967), "Linearized Theory of Nonstationary Cascades at Fully Stalled or Supercavitated Conditions", ZAMM, pp. 531-542, 1967

Sisto, F. (1977), "A Review of the Fluid Mechanics of Aeroelasticity in Turbomachines", ASME Journal of Fluids Engineering, pp. 40-44, March 1977

Smith, A.M.O. and Pierce, J. (1958), "Exact Solution of the Neumann Problem", Douglas Aircraft Report No. ES26988, 1958

Smith, S.N. (1971), "Discrete Frequency Sound Generation in Axial Flow Turbomachines", Cambridge University Report CUED/A-Turbo/TR29, 1971 or ARC R&M 3709

Snyder, L.E. (1973), "Supersonic Torsional Flutter in Cascades", Pratt & Whitney TR-PWA-TM-4701, April 1973

Snyder, L.E. and Commerford, G.L. (1974), "Supersonic Unstalled Flutter in Fan Rotors; Analytical and Experimental Results", ASME Journal of Engineering for Power, pp. 379-386, October 1974

Sohngen, H. (1953), "Air Forces Acting on an Oscillating Blade Ring With a Small Division", ZAMP, No. 4, 1953

Sohngen, H. and Meister, E. (1958), "Contribution to Aerodynamics of an Oscillating Cascade", ZAMM, No. 11/12, 1958

Sohngen, H. and Quick, A.W. (1960), "Oscillations in Axial Compressors", Deutsche Versuchsanstalt fur Luftfahrt, No. 105, 1960

Spreiter, J.R. and Stahara, S.S. (1975), "Unsteady Transonic Aerodynamics - An Aeronautics Challenge", Symp. on Unsteady Aerodynamics, University of Arizona, pp. 553-581, March 18-20, 1975

Stepanov, G.Yu. (1962), "The Hydrodynamics of Turbomachine Cascade", Fizmatgiz, 1962

Strada, J.A. (1977), Thesis, Naval Postgraduate School, Monterey, CA, USA, September 1977

Tanida, Y. and Okazaki, T. (1963), "Stall Flutter in Cascade", Bulletin of the JSME, Vol. 6, No. 24, p. 644, 1963

Teipel, I. (1965), "Calculation of Unsteady Aerodynamic Forces in Transonic Flow", Journal de Mecanique, Vol. 4, No. 3, pp. 335-360, September 1965

Thompkins, W.T. and Kerrebrock, J.L. (1975), "Exit Flow from a Transonic Compressor Rotor", AGARD-CP -177, paper No. 6

Tikhonov, N.D. (1974), "Influence of the Geometrical Parameters of the Profile and Cascade on the Critical Flutter Velocity of a Pack of Compressor Blades", Problemy Prochnosti, No. 8, pp. 57-62, August 1974

Timman, R. (1951), "The Aerodynamics of an Oscillating Airfoil between Two Parallel Walls", Appl. Sci. Res., No. 31, 1951

Triebstein, H. (1976), "Unsteady Pressures on a Harmonically Oscillating Staggered Cascade in Incompressible and Compressible Flow", Revue Francaise de Mecanique, Numero Special, pp. 115-122, 1976

Triebstein, H., et al. (1975), "Unsteady Pressures on a Harmonically Oscillating Staggered Cascade", Report DLR-FB75-57, DLR-FB-75-58

Tyler, J.M. and Sofrin, T.G. (1962), "Axial Compressor Noise Studies", Trans. SAE, Vol. 70, pp. 309-332, 1962

Vakhomchik, V.P. (1965a), "Determination of Unsteady Forces in a Cascade of Profiles", Inzhenernyy Zhurnal, No. 1, 1965

Vakhomchik, V.P. (1965a), "Analytic Solution of the Oscillation of Thin Profiles in a Cascade", Inzhenernyy Zhurnal, No. 2, 1965

vanDyke, M.D. (1953), "Supersonic Flow past Oscillating Aerofoils Including Nonlinear Thickness Effects", NACATN 2982, 1953

Verdon, J.M. (1973), "The Unsteady Aerodynamics of a Finite Supersonic Cascade with Subsonic Axial Flow", J. Appl. Mech., pp. 667-671, September 1973

Verdon, J.M. (1977), "Further Developments in the Aerodynamic Analysis of Unsteady Supersonic Cascades", ASME-paper No. 77-GT-44 and 45

Verdon, J.M., Adamczyk, J.J., Caspar, J.R. (1975), "Subsonic Flow past an Oscillating Cascade with Steady Blade Loading-Basic Formulation", Proc. Symp. Unsteady Aerodynamics, University of Arizona, pp. 827-851, March 18-20, 1975

Verdon, J.M. and McCune, J.E. (1975), "Unsteady Supersonic Cascade in Subsonic Axial Flow", AIAA Journal, Vol. 13, No. 2, pp. 193-201, February 1975

Walker, G.J. and Oliver, A.R. (1972), "The Effect of Interaction between Wakes from Blade Rows in an Axial Flow Compressor on the Noise Generated by Blade Interaction", ASME Journal of Engineering for Power, pp. 241-248, 1972

Weyer, H.B. (1974), "Techniques for the Experimental Study of Unsteady Flow Effects in Turbomachines", Proc. Project SQUID Workshop on Unsteady Flows in Jet Engines, UARL-3-PU, 11-12 July 1974

Weyer, H.B. and Hungenberg, H.G. (1975), "Analysis of Unsteady Flow in a Transonic Compressor by Means of High-Response Pressure Measuring Techniques", AGARD-CP-177, paper No. 11

Whitehead, D.S. (1960), "Force and Moment Coefficients for Vibrating Airfoils in Cascade", A.R.C. R. & M. No. 3254, February 1960

Whitehead, D.S. (1962),"Bending Flutter of Unstalled Cascade Blades at Finite Deflection", ARC R. a. M., No. 3386, 1962

Whitehead, D.S. et al. (1976), "An Experiment to Measure Moment Coefficients for Aerofoils Oscillating in Cascade", Revue Francaise de Mechanique, Numero Special, pp. 123-139, 1976

Whitfield, C.E., et al. (1972), "A Three-Dimensional Analysis of Rotor Wakes", The Aeronautical Quarterly Vol. 23, pp. 285-300, 1972

Woods, L.C. (1955), "On Unsteady Flow Through a Cascade of Airfoils", Proc. Roy. Soc., ser. A, No. 1172, 1955

Woods, W.A., et al. (1968), "The Formation of a Shock Wave in the Blade Passage of a Partial Admission Turbine", ASME-paper No. 68-FE-25, ASME Symposium on Unsteady Flow, May 6-8, 1968

Woolston, D.S. and Runyan, H.L. (1955), "Some Considerations on the Air Forces on a Wing Oscillating Between Two Walls for Subsonic Compressible Flow", JAS, No. 1, 1955

Yashima, S. and Tanaka, H. (1977), "Torsional Flutter in Stalled Cascade", ASME-paper No. 77-GT-72

Yates, J.E. (1975), "Analysis of Supersonic Unsteady Cascades with the Method of Characteristics", AFFDL-TR-75-159, December 1975

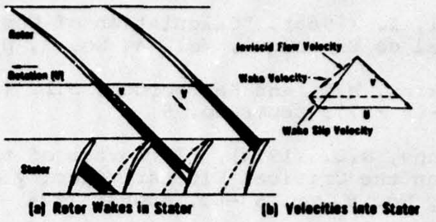

(a) Rotor Wakes in Stator (b) Velocities into Stator

Fig. 2. Schematic of a stage showing rotor wakes passing through stators; wakes have transport velocity towards the stator pressure surface. (from Mikolajczak AGARD CP 177)

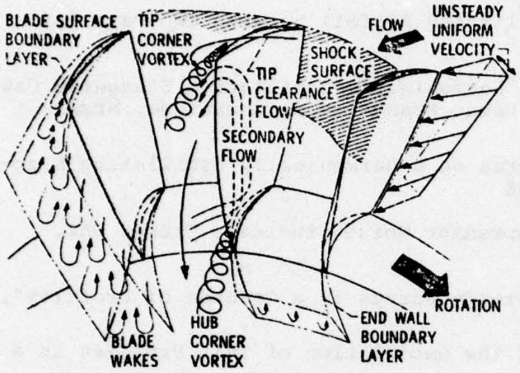

Fig. 1. Rotor Blade Row Flow Phenomena (from McNally 1976)

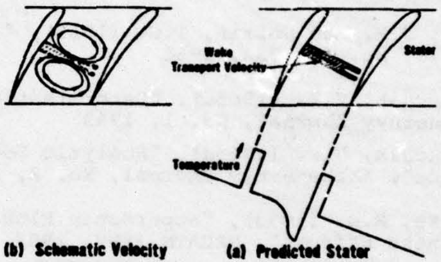

(b) Schematic Velocity Distribution Near Wake (a) Predicted Stator Temperature Wake

Fig. 3. Wake transport leads to a time averaged stagnation temperature profile at stator exit, and a flow circulation inside stator passages. (from Mikolajczak AGARD CP 177)

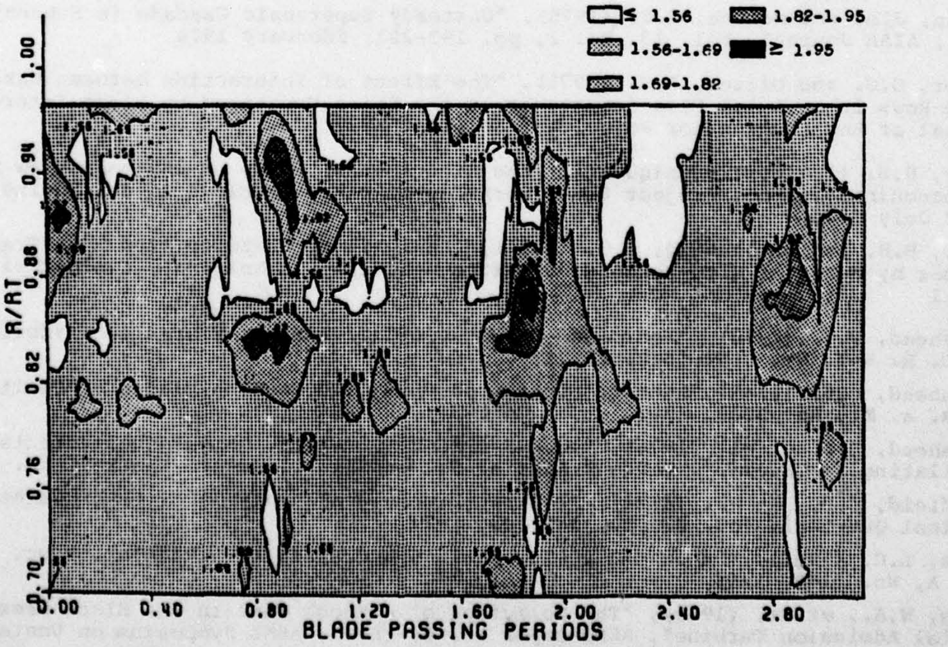

Fig. 4. Contour Plot of Total Pressure 0.1 Chords Aft of Rotor (from Thompkins & Kerrebrock AGARD CP 177)

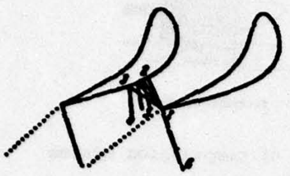

Fig.5 Rarefaction (1-2-3-4) and Shock Wave Formation (1-6) at the Outlet from a Cascade with Convergent Channels (from Samoylovich 1969)

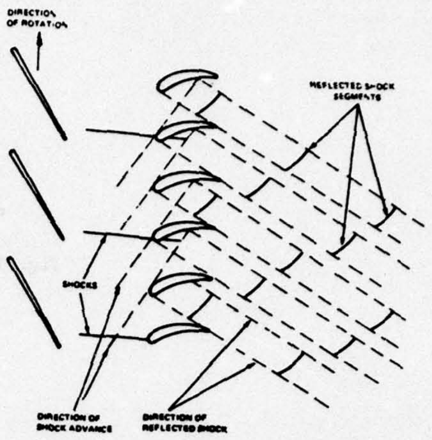

Figure 6 Ordered Array of Reflected Shock Segments
(from Arnoldi 1974)

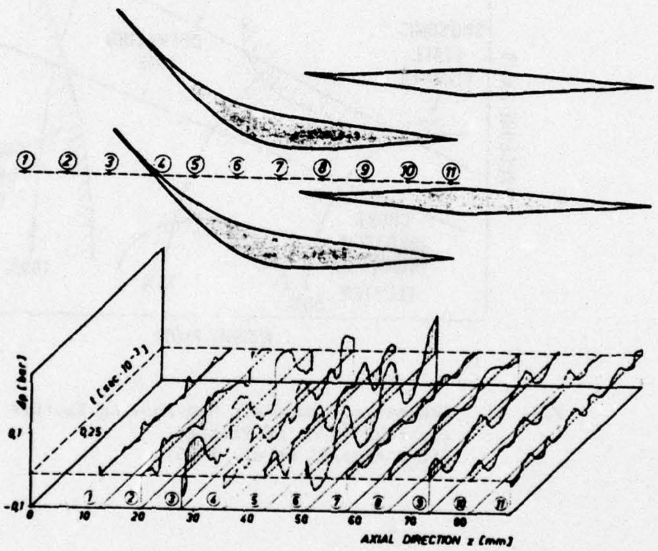

Fig. 7. Pressure Oscillations at Various Stator Stations (from Gallus AGARD CP 177)

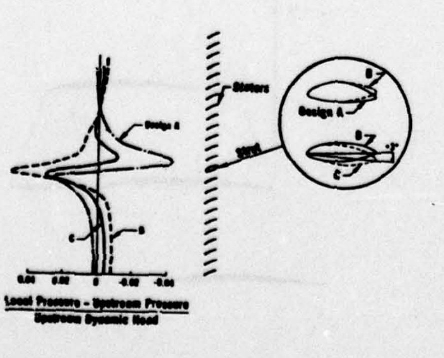

Fig. 8. Effect of strut geometry and angle of attack on static pressure distribution one stator chord upstream of stator cascade. (from Mikolajczak AGARD CP 177)

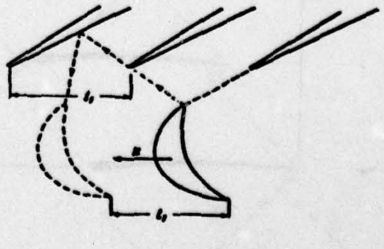

Fig. 9. Regular reflection of acoustic waves in a turbine stage. (from Samoylovich 1969)

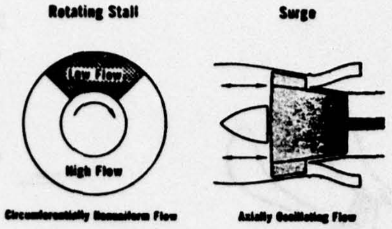

Fig. 10. Possible modes of compression system instability.
(from Mikolajczak AGARD CP 177)

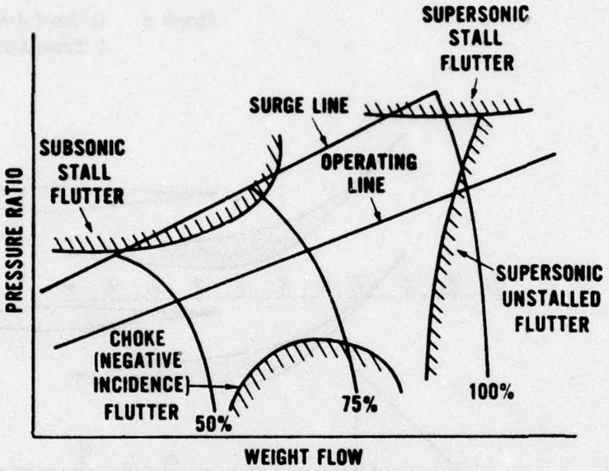

Fig. 11. Schematic Compressor Map Showing Flutter Boundaries for Four Types of Flutter.
(from Arnoldi et al. 1975)

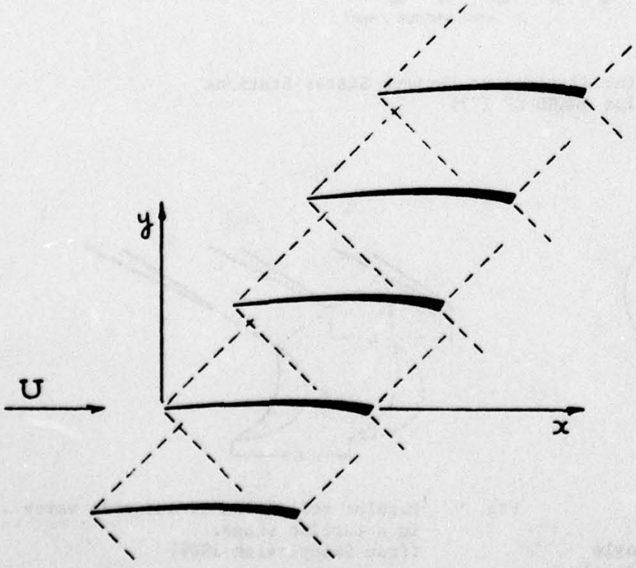

Fig. 13. Supersonic Cascade with Supersonic Leading Edge Locus

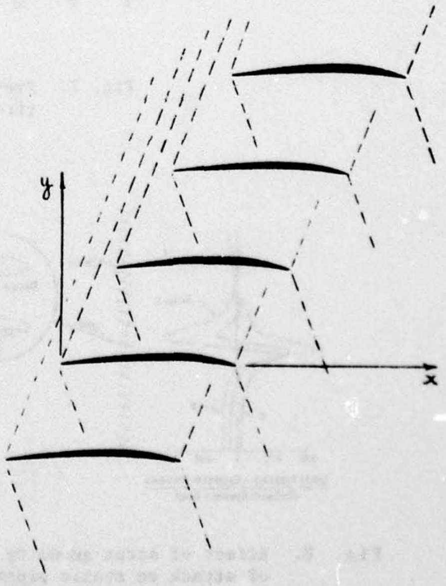

Fig. 12. Supersonic Cascade with Subsonic Leading Edge Locus

AERODYNAMIC PHENOMENA IN AN OSCILLATING TRANSONIC MCA AIRFOIL CASCADE INCLUDING LOADING EFFECTS

by

Sanford Fleeter
Ronald E. Riffel
Cascade and Flow Systems Research
Detroit Diesel Allison Division
GENERAL MOTORS CORPORATION
Indianapolis, Indiana 46206

SUMMARY

A unique unsteady cascade experiment directed at providing fundamental aerodynamic data needed to verify or direct refinements to the basic model of unstalled supersonic torsional flutter in turbomachines is presented. In particular, the steady, quasi-static, and unsteady aerodynamics were determined for a multiple circular arc (MCA) airfoil cascade which modeled the tip section of an advanced design fan blade. The steady airfoil surface aerodynamic performance of the cascade was measured at two levels of aerodynamic loading and correlated with the predictions from a time-marching, steady, transonic flow analysis. The chordwise distribution of the quasi-static unsteady pressure coefficient for a 0° interblade phase angle was then determined and correlated with two appropriate predictions: one based on the steady transonic analysis and the other on steady inviscid supersonic flat plate theory. Finally, the MCA cascade was harmonically oscillated in the torsional mode at a reduced frequency value of 0.14. The fundamental unsteady aerodynamic data was then obtained at a Mach number equal to 1.55 over a range of interblade phase angles for two values of the cascade static pressure ratio. These unsteady results were then correlated with the predictions from state-of-the-art unsteady flat plate cascade analyses.

INTRODUCTION

The demand for increased engine performance, while maintaining a minimum weight, has taken the compressor designer into flow regimes wherein he has no apriori experience. These advanced design fans and compressors have encountered unstalled supersonic flutter at the design operating condition, demonstrating that current flutter prediction systems, based on empirical correlations of prior engine aerodynamic flutter data, are inadequate for the task of extrapolating these past experiences, to the new high speed designs. Thus, the need for a phenomenological modeling approach to the development of a well-founded flutter design system, substantiated by key critical experiments which model the fundamental unsteady aerodynamic phenomena, is clearly evident.

The generally used flow model for unstalled supersonic flutter is that of inviscid flow through a compressor stage of differential radial height, which is developed into a two-dimensional rectilinear cascade. The airfoils are assumed to be zero thickness flat plates which are harmonically oscillating in the torsional mode. Even with this simplified model, the problem is still very complex, particularly as the flow involves a subsonic axial velocity component.

Recently, a number of solutions to this basic model involving various mathematical techniques have been developed, as noted and discussed in Reference 1. For the designer to make use of these solutions in a quantitative predictive design system, it is necessary to determine the validity of the mathematical assumptions and to extend the model to more realistic airfoil configurations. To accomplish this, however, fundamental experimental aerodynamic data is needed to verify the model and to further the understanding of the basic unsteady flow physics.

The results of an experimental investigation of the fundamental unsteady aerodynamics associated with an harmonically oscillating airfoil cascade which closely simulates that of the analytical model are presented in Reference 2. The correlation of the experimental data with an appropriate theory is excellent, thereby indicating the validity of the experimental techniques, and the data acquisition and analysis procedures.

The present work is directed at the experimental investigation of an aerodynamic configuration which more closely resembles the physical and aerodynamic conditions of an advanced design rotor blade, including the aerodynamic loading. In particular, the steady, quasi-static, and unsteady aerodynamics are determined for a multiple circular arc (MCA) airfoil cascade which models the tip section of an advanced design fan blade at two levels of aerodynamic loading. All of the experimental results are correlated with appropriate predictions obtained from state-of-the-art analyses.

AIRFOIL CASCADE AND INSTRUMENTATION

The two-dimensional cascade utilized in this investigation is comprised of five double-trunnioned steel airfoils modeled from the tip section of an advanced design fan blade. These airfoils are characterized by a 3.00 inch (7.62 cm) span, 2.50 inch (6.35 cm) chord and a 0.075 inch (0.19 cm) maximum thickness at the 50% chord location. The cascade physical parameters are noted in Table I. The airfoil profile is of multiple circular arc (MCA) design with the airfoil coordinates presented in Table II.

The airfoil mounting arrangement in the cascade is shown schematically in Figure 1. An array of torsional frequencies are provided by attaching various thickness spring bars to the trunnions. The double-trunnion airfoils and spring bar assemblies are mounted in plexiglas wind tunnel test section walls, thereby permitting schlieren flow visualization. Driving arms are attached to the airfoil trunnions which are in turn driven by electromagnets controlled by an on-line computer system, as described in References 2 and 3. In this manner, the torsional frequency of the airfoils and the interblade phase angle are precisely controlled. Strain gages mounted on the spring bars exhibit excellent sensitivity to the torsional movement of the airfoil, and allow measured strain gage signals to be converted to rotational amplitudes.

The choice of proper steady-state aerodynamic instrumentation is important to quantitatively determine the details of the cascade steady flow field. Sidewall static pressure taps were used to establish the cascade inlet and exit pressure distributions. This information combined with schlieren flow visualization was used to establish the steady-state periodicity. In addition, the static pressure distributions on the suction and pressure surfaces of the second and fourth airfoils of the cascade respectively, were measured at the chordwise locations specified in Table II.

The center airfoil (third) of the cascade was machined to permit the chordwise embedding of twelve miniature Kulite LQ series dynamic pressure transducers such that the airfoil contours were preserved. This was accomplished by placing a thin pliable coating over the transducer diaphragms which resulted in no depreciation in sensitivity. The chordwise transducer locations, presented in Table IV, are schematically indicated in Figure 2. These flush mounted transducers were staggered across the span of each surface, as indicated in Figure 3 which shows a view of the pressure surface.

EXPERIMENTAL FACILITY

The Detroit Diesel Allison (DDA) rectilinear cascade facility, shown in Figure 4, was conceived and built as a research tool to evaluate the aerodynamic characteristics of compressor and turbine blade sections. The facility is a continuous flow, non-return, pressure-vacuum type wind tunnel with the test section evacuated by means of two primary steam ejectors. Up to 10 lbm/sec of filtered, dried, and temperature-controlled air may be used.

The major features of the facility include the following.

- Continuous operation for extended time periods
- A mechanized test section which permits a cascade of airfoils to be rotated with the tunnel in operation
- A schlieren optical system for visual observation and photography of the test section while the facility is in operation
- A sophisticated instrumentation system centered on a laboratory-size digital computer. The computer provides on-line control of data acquisition, data reduction, and calculates performance parameters while the test is in progress for both steady-state and dynamic testing of airfoil cascades.

In this cascade facility, the entrance flow to the test section is generated by fixed nozzle blocks yielding a Mach number of 1.50. The orientation of a wedge with respect to this nozzle exit flow specifies the test section Mach number, i.e., the shock or expansion wave generated by the wedge determines the cascade inlet conditions.

The wind tunnel facility is completely automated using a dedicated digital computer. For steady-state and/or dynamic investigations, the computer is used for control of instrumentation, data acquisition, and data reduction. The computer and associated peripheral equipment were used in this investigation to:

- Determine the steady-state flow parameters including the inlet Mach number, inlet air density, and instrumented airfoil surface static pressure parameters
- Control cascade excitation such that a torsional mode is imparted to the airfoils at a prescribed frequency and interblade phase angle
- Digitize the time-dependent strain gage and miniaturized high response pressure transducer signals at rates to 100,000 points per second
- Store permanently the cascade steady-state parameters and dynamic data on removable magnetic disks

- Control a dual channel storage oscilloscope to provide an analog record of the time-variant pressure transducer signals
- Control a high speed motion picture camera for schlieren movies of the unsteady phenomena.

DYNAMIC DATA ACQUISITION AND ANALYSIS

With the tunnel in operation and the airfoil cascade harmonically oscillating at the prescribed frequency and interblade phase angle, the time-variant strain gage and pressure transducer signals were digitized at rates to 100,000 points per second by a 16-channel analog-digital converter and multiplexer system, and stored on a magnetic disk. These digitized data were analyzed on-line to determine the fundamental aerodynamic characteristics of the unsteady phenomena. The parameters of interest are the amplitude of the airfoil motion and the pressure disturbance, the frequency, the interblade phase angle, and the phase difference between the unsteady pressures and the airfoil motion as characterized by the strain gage signal on the dynamically instrumented airfoil, i.e., the pressure phase shift data is referenced to the motion of the dynamically instrumented center airfoil in the cascade.

The amplitude of the airfoil motion and the pressure disturbance is determined by fitting a second order least square function to the data, differentiating it, and evaluating the maximum. The pressure disturbance amplitude is then non-dimensionalized into an unsteady pressure coefficient, C_p, as defined in Equation 1.

$$C_p = \frac{p}{\frac{1}{2}\rho U^2 \alpha} = \frac{p}{\frac{1}{2}\gamma M^2 p_s \alpha} \tag{1}$$

where p is the measured unsteady pressure amplitude, ρ is the fluid density, U is the inlet velocity, α is the torsional amplitude of oscillation (in radians), γ is the ratio of specific heats, and p_s is the inlet static pressure.

The frequency of the time-dependent data is determined through the autocorrelation function. This function describes the dependence on the values of the data at one time, X_i, on the values at another time, X_{i+r}. The normalized autocorrelation function, R_{xr}, is defined in series form as

$$R_{Xr} = \frac{1}{N-r}\sum_{i=1}^{N-r} X_i X_{i+r} \Big/ \frac{1}{N}\sum_{i=1}^{N} X_i X_i \quad r = 0,1,2\ .\ .\ .\ m \tag{2}$$

where:

X_i = $X(i\Delta t)$

r = lag number

N = total number of dynamic data points

m = number of lags.

A lag time, Δt, is inversely proportional to the rate at which the data is digitized. A typical autocorrelogram of the digitized data exhibits the features of a sine wave plus random noise. A second order least square function is fit to the data in the second positive peak of the autocorrelogram. The inverse of the time at which this least square function is a maximum is equal to the frequency, f, of the time-dependent data.

The phase difference of the pressure disturbance along the airfoil chord in relation to the airfoil motion is calculated through the cross-correlation function. This function, for two sets of data, X_i, Y_i, describes the dependence of the values of one set of data on the other. The normalized cross-correlation function, R_{xyr}, is defined as:

$$R_{xyr} = \frac{1}{N-r}\sum_{i=1}^{N-r} X_i Y_{i+r} \Big/ \frac{1}{N}\sum_{i=1}^{N} X_i Y_i \quad r = -m,\ \ldots -1,0,1,\ \ldots \tag{3}$$

where the variables are defined analogous to those in Equation (2).

AD-A054 028 ADVISORY GROUP FOR AEROSPACE RESEARCH AND DEVELOPMENT--ETC F/G 20/4
UNSTEADY AERODYNAMICS.(U)
FEB 78

UNCLASSIFIED AGARD-CP-227 NL

7 OF 7
ADA
054028

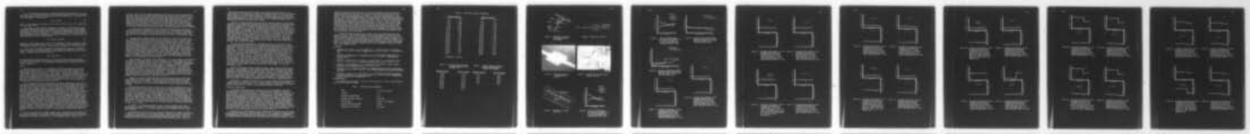

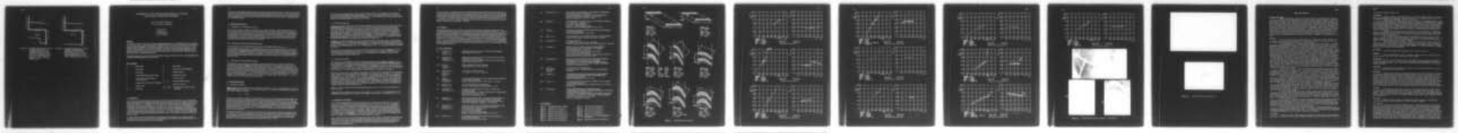

END
DATE
FILMED
6 78
DDC

As in the frequency calculation, a second order least square function is fit to the data in the first positive peak of the cross-correlogram. The time, t_p, at which this least square function is a maximum is analytically determined. The phase difference, in degrees, is calculated as

$$\theta_p = t_p f\, 360 \tag{4}$$

where f is the frequency calculated for the airfoil motion from the strain gage data, utilizing Equation (2).

Two sources of phase relation discrepancy are inherent in the electronic data acquisition system and correlation computation. The analog-digital (A/D) converter-multiplexer unit does not permit data to be digitized simultaneously on all channels. Consequently, an inherent phase shift is introduced into the physical data when the cross-correlation function operates on the raw digitized data. This phase shift, for the sinusoidal data in this experiment, is directly proportional to the "cut rate" of the multiplexer, as shown in Equation (5):

$$\theta_s = f_x(K_y - K_x)\, 350/R_a \tag{5}$$

where θ_s is the AD phase shift inherent in the computation between channels K_y and K_x, representing the respective data, Y_i and X_i. The frequency, f_x, corresponds to the disturbance in channel K_x, and R_a is the rate at which the data is being digitized.

Prior to acquiring data the electronic data acquisition system is calibrated for phase shift, θ_a, using the A/D converter and the computation described in the foregoing. Therefore, the phase difference of the pressure disturbance along the airfoil surface in relation to the airfoil motion is

$$\theta_{xy} = \theta_p - \theta_s - \theta_a \,. \tag{6}$$

This computational procedure results in a valid on-line data analysis system and provides the experimentalist with meaningful information with which to make judicious decisions during the test. All analyzed results are stored on a magnetic disk for further examination.

RESULTS

The procedure followed in this experiment included first obtaining a periodic steady-state cascade flow field. This periodicity was determined by means of the schlieren flow visualization and the sidewall static pressure taps located at the leading edge of each of the airfoils in the cascade. The resulting steady-state leading edge static pressure variation of the airfoil cascade was less than ± 2 percent. Figure 5 is a schematic of the steady-state cascade flow field, determined from the static pressure measurements and the schlieren flow visualization. As indicated, the bow shock intersects the suction surface of the adjacent airfoil near the trailing edge with the shock reflection as well as the adjacent airfoils trailing edge shock intersecting the pressure surface near mid-chord.

With the cascade periodicity established, the steady cascade airfoil surface performance was determined for the aerodynamic conditions of the unsteady experiments. These conditions are characterized by a 1.55 cascade inlet Mach number value and 1.05:1 and 1.30:1 static pressure ratios. The airfoil surface performance data for these conditions are presented in Figures 6 and 7, respectively. Also presented are the predictions of the steady-state cascade aerodynamic performance obtained from the transonic, time-marching, steady flow analysis of Reference 3. This analysis considers the time-dependent Navier-Stokes equations in conservation-law form which allows for viscous shock wave formation. As can be seen from these figures, the steady aerodynamic loading of the cascade is taken up by the trailing edge shock system, as characterized by the absence of any effects due to the increased loading indicated over: (1) the leading 42% of the pressure surface; (2) the entire suction surface. Overall the airfoil steady surface pressure distribution data correlates very well with the predictions from the transonic flow analysis. The correlation is not as good near to the leading and trailing edges, regions where the analysis does not accurately model the profile of the airfoil. Also, it should be noted that the current state-of-the-art inviscid unsteady flutter aerodynamic model assumes a uniform steady flow field with small perturbations generated by the harmonic oscillations of zero thickness flat plate cascaded airfoils, as previously discussed. Figures 6 and 7 demonstrate clearly the differences between this uniform steady flow of the model and the actual steady flow field.

Prior to oscillating the cascade, a quasi-static experiment was undertaken to obtain the zero frequency limit of the unsteady pressure coefficient for an interblade phase angle value equal to zero degrees. This was accomplished by measuring the airfoil surface static pressure distributions with the cascaded airfoils in their nominal position. The airfoils were then rotated and locked into a position corresponding to that 180° later in the 0° interblade phase angle oscillation, and the resulting static pressure distributions measured. This permitted the chordwise distribution of the quasi-static unsteady pressure coefficient to be determined for each airfoil surface. These results were then correlated with a quasi-static prediction based on inviscid supersonic flat plate theory as well as with one obtained from the time-marching steady transonic flow analysis of Reference 3. These quasi-static predictions were accomplished by maintaining the inlet flow vector and rotating the airfoil cascade. It should be noted that this quasi-static flat plate prediction is the zero frequency limit of the current state-of-the-art supersonic unstalled aerodynamic flutter analyses.

The quasi-static unsteady pressure coefficient data-prediction correlations on the suction surface are excellent, as seen in Figure 8. The discrepancies between the two predictions in the vicinity of the leading and trailing edges is attributed to the fact that the time-marching transonic analysis recognizes, to some extent, that the airfoils have a profile in these regions, whereas inviscid flat plate theory does not.

The quasi-static unsteady pressure coefficient data on the airfoil pressure surface correlates with the two predictions, as indicated in Figure 9. However, these correlations are not as good as those previously presented for the suction surface. The 50.64 percent chord data point is under the direct influence of the previously noted shocks which impinge on the airfoil pressure surface near mid-chord. Also, this pressure surface data is offset in level as compared to the quasi-static inviscid flat plate cascade prediction. However, the prediction overall trends as well as the magnitude of the increase in the value of the unsteady pressure coefficient across the mid-chord position shocks agree well with the quasi-static data. The time-marching steady flow analysis predicts a continuous, relatively smooth, static pressure distribution on the pressure surface at this level of loading, Figure 6. This results in the continuous, smooth, quasi-static unsteady pressure coefficient prediction on the airfoil pressure surface seen in Figure 9. Hence, the quasi-static prediction based on the transonic analysis does not correlate as well with the data as the one based on inviscid supersonic flat plate theory.

Upon completion of the quasi-static experiment, the airfoil cascade was harmonically oscillated in a torsional mode at a reduced frequency ($k = \omega b/U_\infty$) equal to 0.14 for specified interblade phase angle values. At selected points the cascade static pressure ratio was increased from the nominal 1.05:1 to 1.30:1. Fundamental time-dependent aerodynamic data were then obtained, analyzed, and correlated with the predictions from the current state-of-the-art cascade analysis of Reference 4. This analysis assumes small perturbations which are generated by oscillating zero thickness flat plate cascaded airfoils in a uniform inviscid steady flow field. Predictions were obtained for a variable blade-to-blade amplitude of oscillation, accomplished through input of the measured amplitudes into the analysis. The chordwise distribution of the complex data and the corresponding prediction is presented in the form of an aerodynamic phase lag as referenced to the motion of the instrumented airfoil, and the unsteady pressure coefficient, C_p, defined in Equation 1.

Figures 10 through 21 present the time-variant chordwise suction surface data and correlation with the variable amplitude flat plate cascade prediction for interblade phase angle values between - 32.3° and 193.8° and for two values of cascade static pressure ratio. It should be noted that the front portion of the suction surface is relatively flat, with a small precompression region located near the leading edge.

The aerodynamic phase lag data is seen to be in excellent agreement with the flat plate cascade prediction over the flat front portion of this suction surface. Over the rear half of this surface where the surface camber becomes significant, the data is seen to deviate from the flat plate prediction. For interblade phase angles near 45°, Figures 12 through 15, it is seen that the suction surface camber results in a decrease in the aerodynamic phase lag as compared to the flat plate prediction. For the other interblade phase angles investigated, the effect of the surface camber is to increase the phase lag as compared to the flat plate prediction. The absolute magnitude of the camber effect on the aerodynamic phase lag data is seen to be approximately equal for all of the cases. It is interesting to note that in this experiment, the cases for interblade phase angles near 45° were much more difficult to physically set up, i.e., it was much more difficult to achieve a constant interblade phase angle in the vicinity of 45°.

The effect of increased aerodynamic loading on the aerodynamic phase lag is demonstrated in Figures 14, 18, and 20. As seen, increased cascade static pressure ratio generally results in an increased phase lag over the cambered portion of the suction surface.

The chordwise trend of the suction surface unsteady pressure coefficient data is to decrease in the direction of the trailing edge. The data is increased significantly in value over the prediction for the front of the surface, decreasing in value and generally approaching the flat plate prediction near the trailing edge. This is an interesting contrast to the previously discussed phase lag data on this surface, in that the phase lag data correlated well with the flat plate prediction over the front portion of this surface. A similar trend has been previously noted in an experimental study of this instrumented blade as an isolated airfoil. It was speculated therein that this overall trend was caused by the leading edge region including the small precompression zone. Also, Figures 14, 18 and 20 demonstrate that an increased cascade static pressure ratio generally results in an increased unsteady pressure coefficient value over the rear of this surface.

Figures 22 through 33 present the time-variant chordwise pressure surface data together with the predictions obtained from the variable amplitude flat plate cascade prediction. The time-variant phenomena occurring on this surface are extremely complex as a cambered airfoil surface with two impinging shock waves are involved, depicted schematically in Figure 5. Generally the aerodynamic phase lag data exhibits some correlation with the flat plate cascade prediction over the front portion of the pressure surface. The exception to this is the phase lag data for the cases with an interblade phase angle near 45°, Figures 24 through 27. For these cases, the leading edge phase lag data point, 14 percent chord, is noticably decreased in value as compared to the second chordwise data point, 34.5 percent chord, as well as the flat plate prediction. On the suction surface, a discrepancy was noted in the trend of the phase lag data over the cambered back portion of this surface for these same interblade phase angle cases. The pressure surface phase lag trend discrepancy is observed over the cambered front portion of this surface. Thus, this effect may be related to the influence of camber.

For the case of approximately 0° interblade phase angle, Figure 23, the aerodynamic phase lag data at the rearward chordwise data points downstream of the two shock wave impingement locations, are in relatively good agreement with the flat plate prediction. For all of the other interblade phase angle cases, Figures 22 and 28 through 33, the value of the aerodynamic phase lag approaches 360° in this trailing edge region. This may be attributable to the physical phenomena not modeled in the state-of-the-art flat plate cascade analysis. For example, the analysis does not predict the pressure surface impingement of the shock wave originating at the trailing edge of the adjacent airfoil. Also, the steady flow field is modeled as a uniform flow with small unsteady perturbations superimposed. The nonlinearities of the flow field including airfoil camber, shock waves, their reflections and motion, are not modeled. That this may be significant is reflected in the fact that the 0° interblade phase angle case correlates well with the prediction over the back portion of the pressure surface whereas the other interblade phase cases do not. This 0° interblade phase angle case is special in that the shock systems do not interact with one another. For the other interblade phase angles investigated, this was not generally the case.

Overall, the unsteady pressure coefficient data on the pressure surface shows a relatively large decrease in value between the leading edge and the second chordwise data points, 14.0 percent and 34.5 percent chord, with this second data point demonstrating reasonable agreement with the flat plate prediction. The 65 percent chord data point is located in the immediate vicinity of the impinging trailing edge shock wave, hence the scatter exhibited by the data at this chordwise location between the various interblade phase angle cases. Over the approximate aft 40 percent of the pressure surface, behind the trailing edge shock intersection, the unsteady pressure coefficient data is in reasonable agreement with the flat plate cascade prediction.

The effect of increased aerodynamic loading on the pressure surface unsteady data is demonstrated in Figures 26, 30, and 32. As indicated, increased cascade static pressure ratio generally results in an increased aerodynamic phase lag on the pressure surface, analogous to the suction surface results previously discussed.

SUMMARY AND CONCLUSIONS

The unsteady cascade experiment directed at providing fundamental aerodynamic data necessary for the verification or the direction of refinements in the basic analytical model of unstalled supersonic torsional flutter in fans and compressors has been presented. This was accomplished by investigating an instrumented MCA airfoil cascade which modeled the tip section of an advanced design rotor blade. The steady airfoil surface aerodynamic performance was measured at two levels of aerodynamic loading and demonstrated very good correlation with the corresponding predictions obtained from a time-marching, steady, transonic flow analysis. A quasi-static experiment was then conducted at a 0° interblade phase angle value. The resulting quasi-static unsteady pressure coefficient data was correlated with appropriate predictions from inviscid supersonic flat plate cascade theory as well as one obtained from the time-marching transonic analysis. The quasi-static unsteady pressure coefficient data exhibited excellent correlation with both predictions in the suction surface. On the pressure surface, however, the correlation was not as good, with somewhat better correlation of the data obtained with the flat plate prediction.

The dynamically instrumented MCA airfoil cascade was then harmonically oscillated in the torsional mode at an inlet Mach number of 1.55 over a range of interblade phase angle values for two cascade static pressure ratios. The fundamental unsteady MCA cascade aerodynamic obtained were then correlated with predictions from a state-of-the-art unsteady cascade variable blade-to-blade amplitude of oscillation analysis. The chordwise aerodynamic phase lag data is in excellent agreement with the flat plate cascade prediction over the flat front portion of the suction surface whereas the unsteady pressure coefficient data is increased in value over the prediction in this region. Over the rear cambered portion of this surface the phase lag data deviates from the flat plate prediction whereas the unsteady pressure coefficient data approaches the prediction. The correlation of the flat plate prediction with the unsteady data on the cambered pressure surface is extremely complex. This is a result of the surface camber and the impingement of two shock waves on this surface. Generally, the phase lag data exhibits some correlation with the prediction over the front portion of the pressure surface. The unsteady pressure coefficient data exhibits a large decrease in the leading edge region of this surface, approaching the predicted value. Over the aft portion of this surface where the impinging shock waves are significant, the phase lag data correlates with the prediction for the case where the two shock systems do not intereact. When these two systems do interact, the flat plate prediction and the phase lag data do not correlate.

It should be noted that many of the trends of this MCA unsteady data have been previously noted. The increased values of the unsteady pressure coefficient in the leading regions were found in an isolated airfoil investigation using this same airfoil. Also, Reference 6 presents the results of an unsteady cascade experiment wherein the airfoils were fixed but the upstream wedge was oscillated to generate an unsteady inlet flow field. The same MCA profile blading was used, although not the same instrumented airfoil. Therein are presented aerodynamic phase lag and unsteady pressure magnitude data in the pressure and suction surfaces which show a remarkable similarity in trend to the data presented herein.

REFERENCES

1. Chadwick, W. R., Bell, J. K., and Platzer, M. F., "On the Analysis of Supersonic Flow Past Oscillating Cascades", AGARD-CP-177, Unsteady Phenomena in Turbomachinery, 1975.

2. Fleeter, S., Novick, A. S., and Riffel, R. E., "An Experimental Determination of the Unsteady Aerodynamics in a Controlled Oscillating Cascade", ASME Paper No. 76-GT-47, 1976.

3. Fleeter, S., McClure, R. B., Sinnet, G. T. and Holtman, R. L., "Supersonic Inlet Torsional Cascade Flutter", Journal of Aircraft, Vol. 12, No. 8, August, 1975.

4. Kurzrock, J. W. and Novick, A. S., "Transonic Flow Around Rotor Blade Elements", Journal of Fluids Engineering, Vol. 97, December 1975.

5. Caruthers, J. E., "Theoretical Analysis of Unsteady Supersonic Flow Around Harmonically Oscillating Turbofan Cascades", Ph.D. Thesis, Georgia Institute of Technology, June 1976.

6. Fleeter, S., Novick, A. S., and Riffel, R. E., "The Unsteady Aerodynamic Response of an Airfoil Cascade to a Time-Variant Supersonic Inlet Flow Field", AGARD-CP-177, Unsteady Phenomena in Turbomachinery, 1975.

ACKNOWLEDGEMENTS

This research was supported, in part, by the Power Branch, Office of Naval Research, under Contract N00014-72-C-0351.

TABLE I. CASCADE PHYSICAL PARAMETERS

CHORD	2.50 INCH (6.35 CM)
SOLIDITY	1.21
MAXIMUM THICKNESS/CHORD	0.03
MAXIMUM THICKNESS LOCATION	50% CHORD
SETTING ANGLE	66.09° (1.15 RADIANS)
LEADING EDGE RADIUS/CHORD	0.0015
TORSIONAL AXIS LOCATION	50% CHORD

TABLE II. MCA AIRFOIL PROFILE COORDINATES

SUCTION SURFACE		PRESSURE SURFACE	
X/C*	Y/C*	X/C*	Y/C*
0.00	0.86	0.00	0.71
5.21	0.98	6.29	0.04
11.53	0.96	12.59	- 0.53
17.84	0.96	18.90	- 1.00
24.14	0.97	25.21	- 1.37
30.45	0.99	31.53	- 1.64
36.75	1.02	37.85	- 1.81
43.05	1.08	44.18	- 1.88
49.35	1.12	50.51	- 1.85
55.65	1.22	56.83	- 1.72
61.95	1.31	63.15	- 1.48
68.25	1.41	69.47	- 1.15
74.55	1.53	75.78	- 0.71
80.88	1.62	82.06	- 0.25
87.21	1.58	88.36	0.16
93.53	1.38	94.66	0.50
99.85	1.02	99.86	0.88

*Expressed in percent.

TABLE III. PERCENT CHORD LOCATIONS OF AIRFOIL SURFACE STATIC PRESSURE TAPS

PRESSURE SURFACE	SUCTION SURFACE
13.99	14.05
24.08	24.14
32.93	32.97
41.79	41.79
50.64	50.61
67.08	66.99
75.92	75.81
84.72	84.67

TABLE IV. PERCENT CHORD LOCATIONS OF AIRFOIL SURFACE DYNAMIC PRESSURE TRANSDUCERS

PRESSURE SURFACE	SUCTION SURFACE
14.0	36.0
34.5	55.0
65.0	65.0
75.5	74.5
87.0	85.0

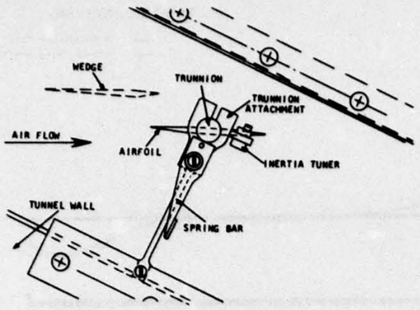

Figure 1. Schematic of Airfoil-Spring Bar Mounting Arrangement

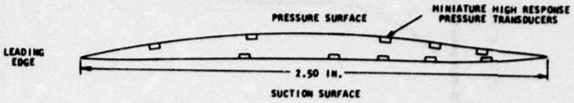

Figure 2. MCA Airfoil Profile

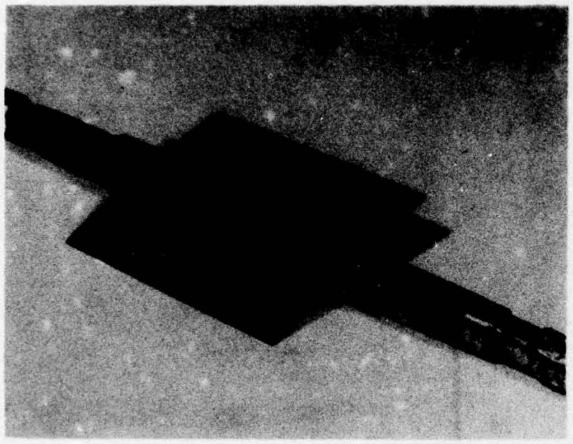

Figure 3. Pressure Surface of Instrumented MCA Airfoil

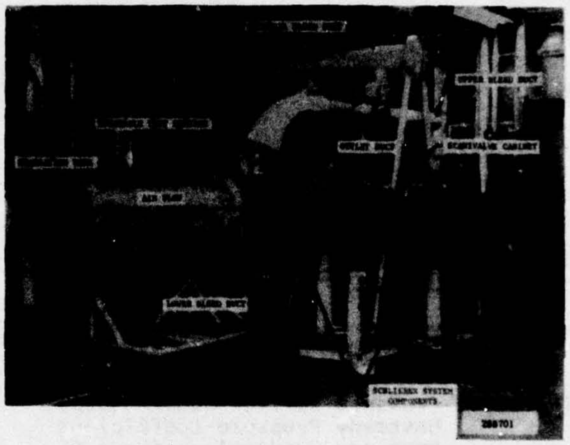

Figure 4. Overall View of Rectilinear Cascade Facility

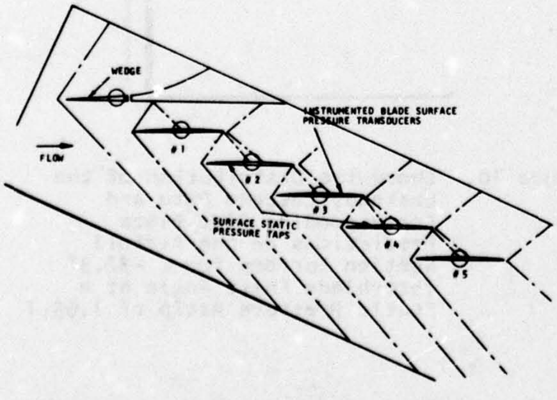

Figure 5. Schematic of Cascade Flow Field

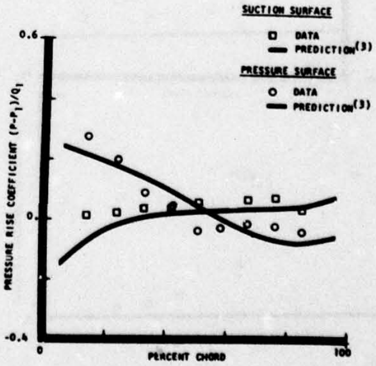

Figure 6. Airfoil Surface Steady Aerodynamic Performance for an Inlet Mach Number of 1.55 and a Cascade Static Pressure Ratio of 1.05:1

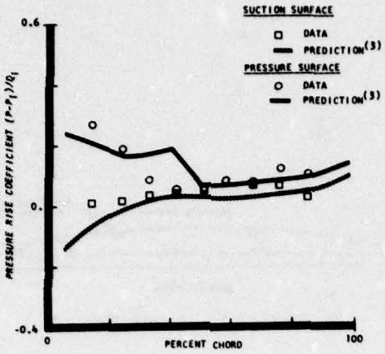

Figure 7. Airfoil Surface Steady Aerodynamic Performance for an Inlet Mach Number of 1.55 and a Cascade Static Pressure Ratio of 1.30:1

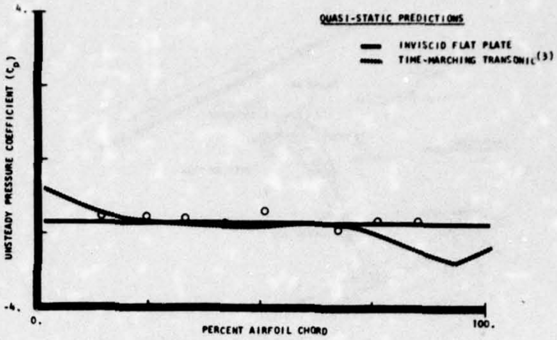

Figure 8. Suction Surface Quasi-Static Unsteady Pressure Coefficient Data and Predictions for a 0° Interblade Phase Angle

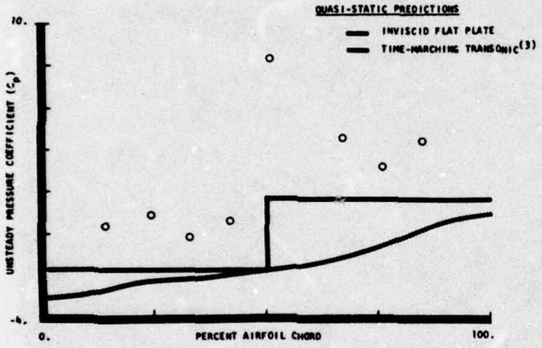

Figure 9. Pressure Surface Quasi-Static Unsteady Pressure Coefficient Data and Predictions for a 0° Interblade Phase Angle

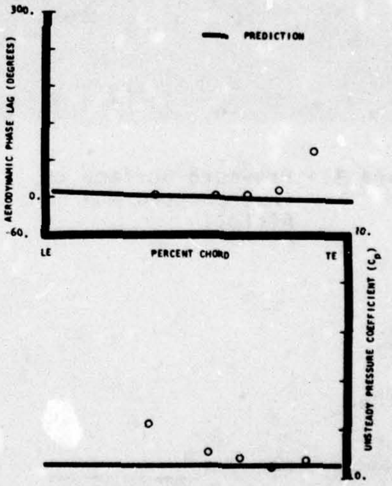

Figure 10. Chordwise Distribution of the Unsteady Cascade Data and Corresponding Flat Plate Predictions on the Airfoil Suction Surface for a -32.3° Interblade Phase Angle at a Static Pressure Ratio of 1.05:1

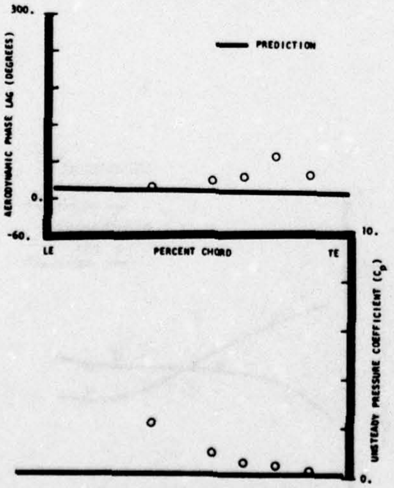

Figure 11. Chordwise Distribution of the Unsteady Cascade Data and Corresponding Flat Plate Predictions on the Airfoil Suction Surface for a -4.4° Interblade Phase Angle at a Static Pressure Ratio of 1.05:1

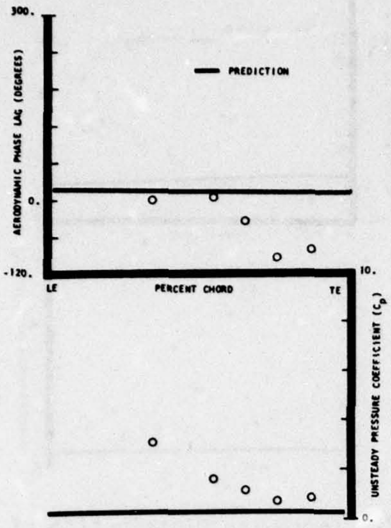

Figure 12. Chordwise Distribution of the Unsteady Cascade Data and Corresponding Flat Plate Predictions on the Airfoil Suction Surface for a 46.6° Interblade Phase Angle at a Static Pressure Ratio of 1.05:1

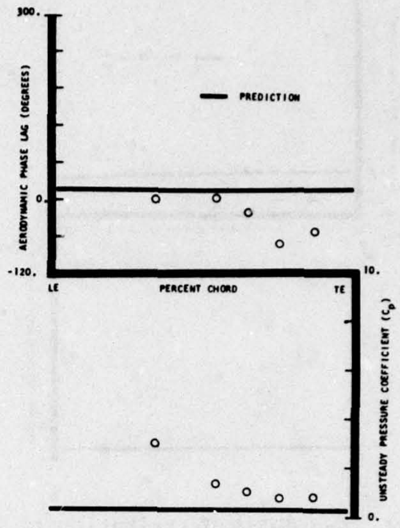

Figure 13. Chordwise Distribution of the Unsteady Cascade Data and Corresponding Flat Plate Predictions on the Airfoil Suction Surface for a 58.2° Interblade Phase Angle at a Static Pressure Ratio of 1.05:1

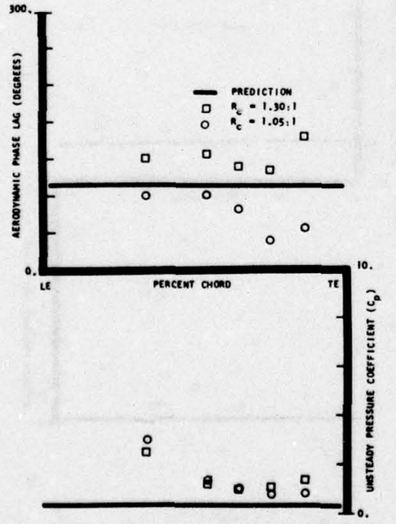

Figure 14. Chordwise Distribution of the Unsteady Cascade Data and Corresponding Flat Plate Predictions on the Airfoil Suction Surface for 56.7° and 58.2° Interblade Phase Angles at the Static Pressure Ratios of 1.30:1 and 1.05:1, Respectively

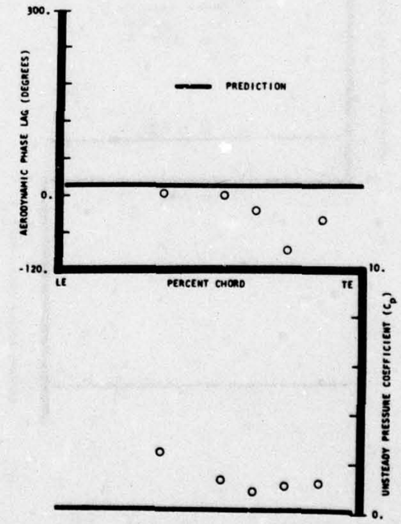

Figure 15. Chordwise Distribution of the Unsteady Cascade Data and Corresponding Flat Plate Predictions on the Airfoil Suction Surface for a 70.2° Interblade Phase Angle at a Static Pressure Ratio of 1.05:1

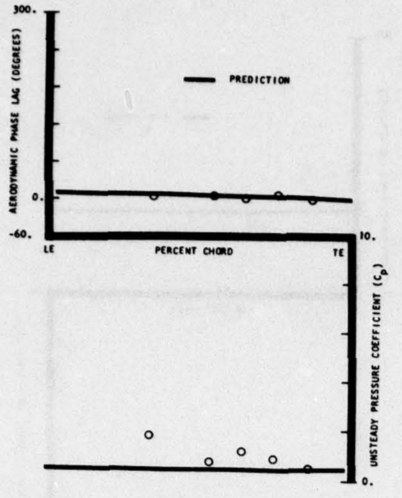

Figure 16. Chordwise Distribution of the Unsteady Cascade Data and Corresponding Flat Plate Predictions on the Airfoil Suction Surface for a 130.6° Interblade Phase Angle at a Static Pressure Ratio of 1.05:1

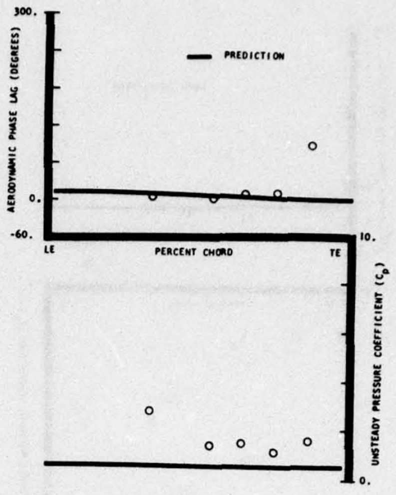

Figure 17. Chordwise Distribution of the Unsteady Cascade Data and Corresponding Flat Plate Predictions on the Airfoil Suction Surface for a 162.1° Interblade Phase Angle at a Static Pressure Ratio of 1.05:1

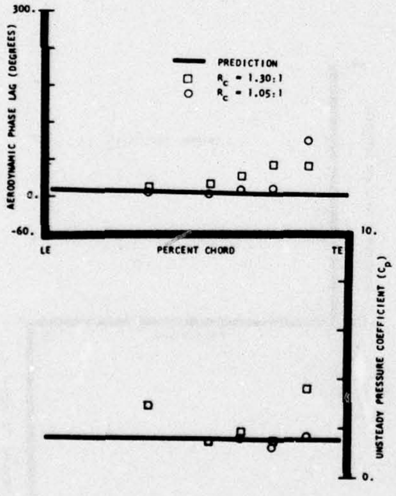

Figure 18. Chordwise Distribution of the Unsteady Cascade Data and Corresponding Flat Plate Predictions on the Airfoil Suction Surface for 163.1° and 162.1° Interblade Phase Angles at Static Pressure Ratios of 1.30:1 and 1.05:1, Respectively

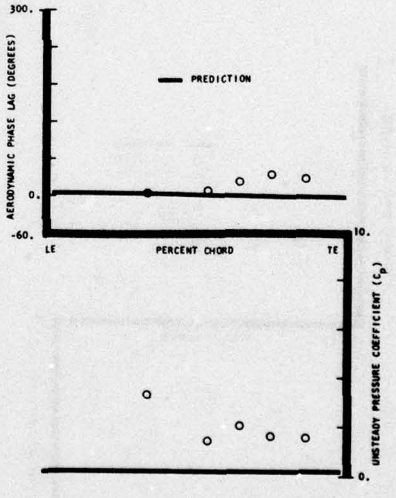

Figure 19. Chordwise Distribution of the Unsteady Cascade Data and Corresponding Flat Plate Predictions on the Airfoil Suction Surface for a 170.2° Interblade Phase Angle at a Static Pressure Ratio of 1.05:1

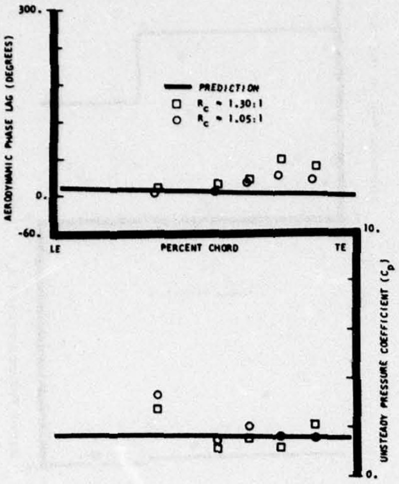

Figure 20. Chordwise Distribution of the Unsteady Cascade Data and Corresponding Flat Plate Predictions on the Airfoil Suction Surface for 173.4° and 170.2° Interblade Phase Angles at Static Pressure Ratios of 1.30:1 and 1.05:1, Respectively

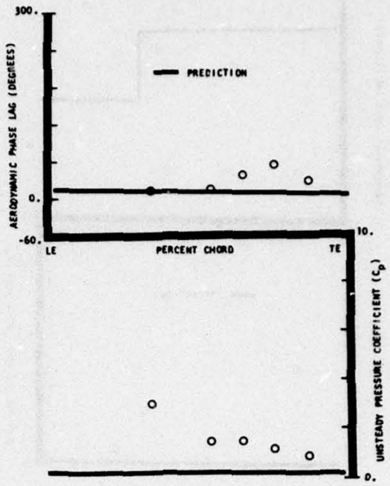

Figure 21. Chordwise Distribution of the Unsteady Cascade Data and Corresponding Flat Plate Predictions on the Airfoil Suction Surface for a 193.8° Interblade Phase Angle at a Static Pressure Ratio of 1.05:1

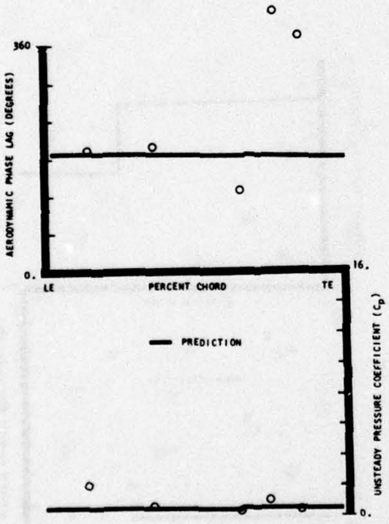

Figure 22. Chordwise Distribution of the Unsteady Cascade Data and Corresponding Flat Plate Predictions on the Airfoil Pressure Surface for a -32.3° Interblade Phase Angle at a Static Pressure Ratio of 1.05:1

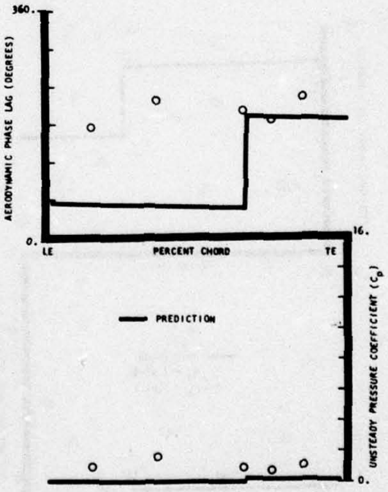

Figure 23. Chordwise Distribution of the Unsteady Cascade Data and Corresponding Flat Plate Predictions on the Airfoil Pressure Surface for a -4.4° Interblade Phase Angle at a Static Pressure Ratio of 1.05:1

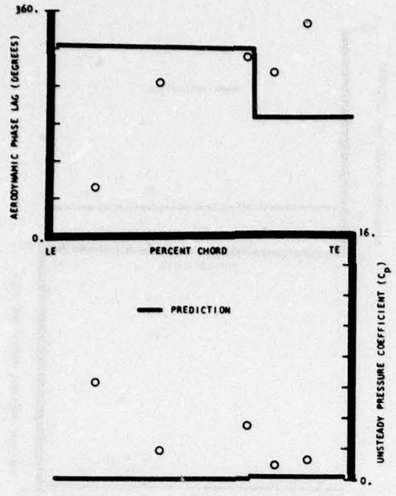

Figure 24. Chordwise Distribution of the Unsteady Cascade Data and Corresponding Flat Plate Predictions on the Airfoil Pressure Surface for a 46.6° Interblade Phase Angle at a Static Pressure Ratio of 1.05:1

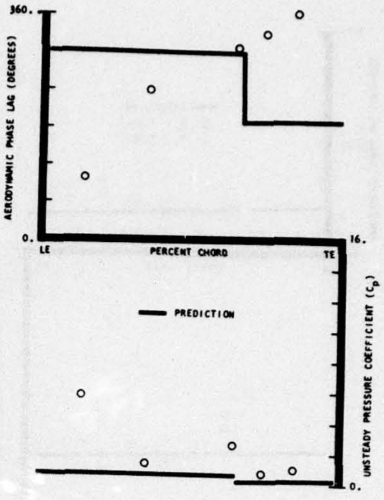

Figure 25. Chordwise Distribution of the Unsteady Cascade Data and Corresponding Flat Plate Predictions on the Airfoil Pressure Surface for a 58.2° Interblade Phase Angle at a Static Pressure Ratio of 1.05:1

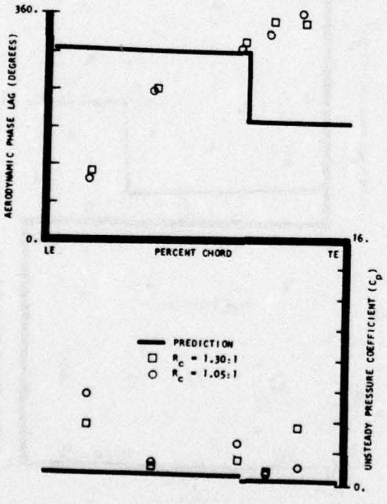

Figure 26. Chordwise Distribution of the Unsteady Cascade Data and Corresponding Flat Plate Predictions on the Airfoil Pressure Surface for 56.7° and 58.2° Interblade Phase Angles at Static Pressure Ratios of 1.30:1 and 1.05:1, Respectively

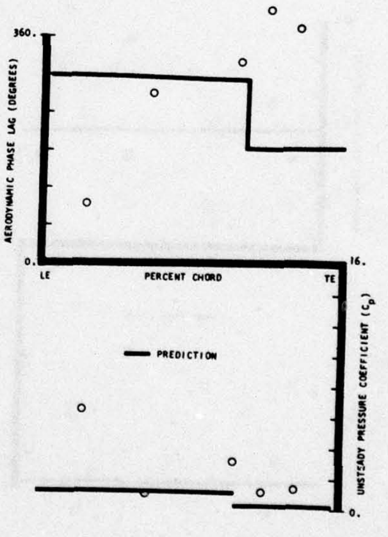

Figure 27. Chordwise Distribution of the Unsteady Cascade Data and Corresponding Flat Plate Predictions on the Airfoil Pressure Surface for a 70.2° Interblade Phase Angle at a Static Pressure Ratio of 1.05:1

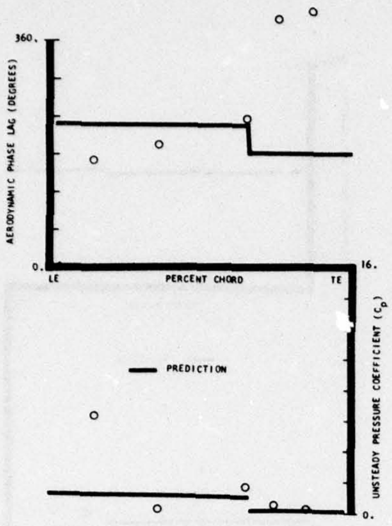

Figure 28. Chordwise Distribution of the Unsteady Cascade Data and Corresponding Flat Plate Predictions on the Airfoil Pressure Surface for a 130.6° Interblade Phase Angle at a Static Pressure Ratio of 1.05:1

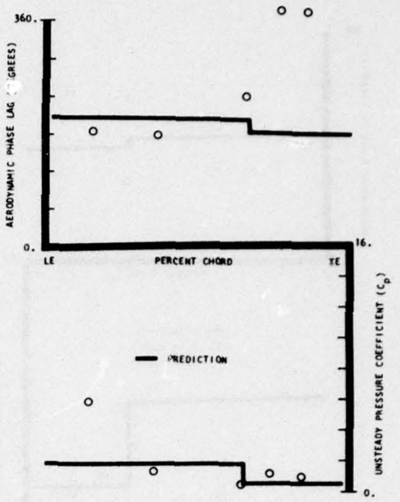

Figure 29. Chordwise Distribution of the Unsteady Cascade Data and Corresponding Flat Plate Predictions on the Airfoil Pressure Surface for a 162.1° Interblade Phase Angle at a Static Pressure Ratio of 1.05:1

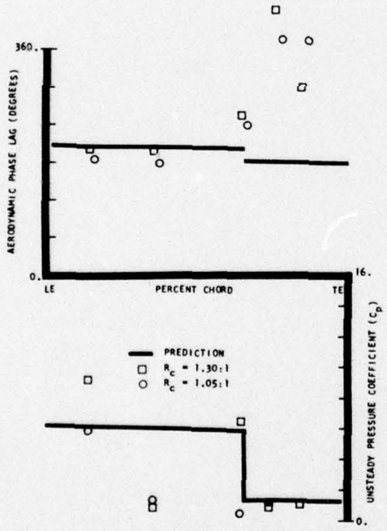

Figure 30. Chordwise Distribution of the Unsteady Cascade Data and Corresponding Flat Plate Predictions on the Airfoil Pressure Surface for 163.1° and 162.1° Interblade Phase Angles at Static Pressure Ratios of 1.30:1 and 1.05:1, Respectively

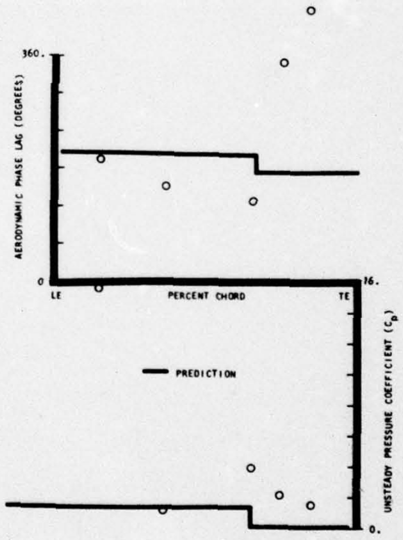

Figure 31. Chordwise Distribution of the Unsteady Cascade Data and Corresponding Flat Plate Predictions on the Airfoil Pressure Surface for a 170.2° Interblade Phase Angle at a Static Pressure Ratio of 1.05:1

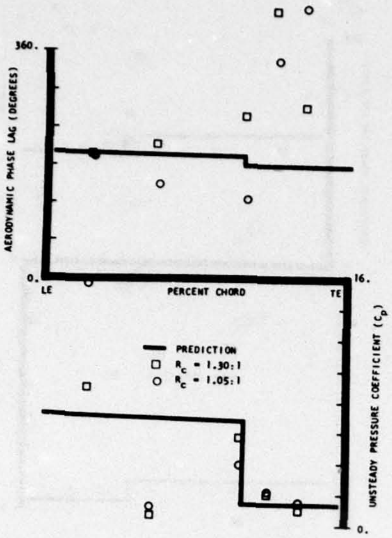

Figure 32. Chordwise Distribution of the Unsteady Cascade Data and Corresponding Flat Plate Predictions on the Airfoil Pressure Surface for 173.4° and 170.2° Interblade Phase Angles at Static Pressure Ratios of 1.30:1 and 1.05:1, Respectively

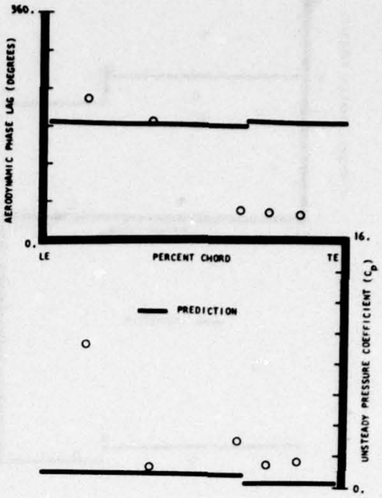

Figure 33. Chordwise Distribution of the Unsteady Cascade Data and Corresponding Flat Plate Predictions on the Airfoil Pressure Surface for a 193.8° Interblade Phase Angle at a Static Pressure Ratio of 1.05:1

DETERMINATION OF THE VORTEX SHEDDING FREQUENCY OF CASCADES WITH DIFFERENT TRAILING EDGE THICKNESSES

Dipl.-Ing. Hans-J. Heinemann
Dr. rer. nat. Karl A. Bütefisch

DFVLR-AVA
Bunsenstraße 10
D - 3400 Göttingen

Summary

The wake flow of isolated airfoils and turbine cascade blades appears to consist generally of vortex streets. Vortex streets appear in incompressible and compressible flow. Recently in the DFVLR-AVA an electronic-optical method was developed to determine the shedding frequency of the vortices in the wake flow. This method is used in testing the flow through various hub-, mid- and tip-section turbine cascades for various downstream Mach numbers in the sub- and transonic flow regimes. The trailing edge thicknesses of the blades vary from 0.8 to 5 percent of the blade chord length. Thin trailing edges lead to higher frequencies than thicker ones at constant Mach numbers.

The experiments give a survey of the region of possible shedding frequencies and the corresponding Strouhal numbers of turbine cascades which in use today.

List of Symbols

b	blade height	β_2	outlet angle
c	blade chord	f	frequency of vortex shedding
g	pitch length	St	Strouhal number
d	trailing edge thickness of the blade	u	downstream velocity
d'	reduced trailing edge thickness (see figure 13)	a	velocity of sound
		$M = \frac{u}{a}$	downstream Mach number
δ	boundary layer displacement thickness	ν	kinematic viscosity
γ	stagger angle	$Re_d = \frac{u \cdot d}{\nu}$	Reynolds number, based on blade thickness
β_1	inlet angle		

1. Introduction

It is well known that the agreement of theoretical flow calculations, which are based e.g. on Martensen's method, and experimental investigations strongly depend on assuptions of the flow conditions at the trailing edge of the profiles [1, 2]. Changing the position of the last calculation points at the suction-side and at the pressure-side of the trailing edge, in a region less than one percent of the chord length of the blade, the pressure distributions may be affected considerably [2]. Therefore it appears to be necessary to investigate the wake flow at the trailing edge in order to get a better understanding of the flow field. This is especially of importance for gas turbines, the blades of which have a comparatively thick trailing edge. The trailing edges of gas turbine blades are rather large - up to 5 % thick based on the chord length of the blade. In cases of such large trailing edge thicknesses the wake flow consists of vortex streets with very distinct vortices.

For single airfoils the vortex shedding at the trailing edge was investigated for two reasons: firstly, it was assumed that flutter could be caused by vortex shedding [3] and secondly, some publications [4, 5, 6] indicate that noise is generated due to vortex shedding.

At DFVLR-AVA Göttingen schlieren pictures of the flow through different cascades and of the flow past isolated airfoils were taken, which showed vortex streets in the wakes of the profiles [7, 8] . An electronic-optical method was developed in order to determine the shedding frequency of the vortices [9] . The method is used for the investigation of various turbine cascades to get a survey of the region of possible shedding frequencies of turbine cascades.

2. Experimental Facilities

2.1 Windtunnel for 2-Dimensional Cascades

The cascade-windtunnel of the DFVLR-AVA is a suction type windtunnel. A detailed description of the facility is given in [10] . There is a rectangular nozzle upstream of the cascade and either a free jet or in some cases a tail-board downstream. The test section can accomodate up to about 16 blades depending on the geometry of the cascade and on the inlet angle β_1. In general, the blade chord, c, is 60 mm and the blade height, b, 125 mm. Thus the height/chord ratio, b/c, is 2.08. For taking schlieren pictures or frequency measurements the blades are fixed within the glass-wall with the aid of two pins at each side of the blade. The pins do not protrude into the flow.

2.2 Arrangement for the Frequency Measurements

The electronic-optical frequency measurement method is described in detail in [2, 9, 11] .

The determination of the frequency is independent on the test location within the vortex row. In the case of a flat plate the shedding frequency can be determined even one chord length downstream [11] . In [2] it is shown that for constant flow conditions one gets the same results for the frequency when the measurements are taken behind different blades of the cascade. To get best results for the experiments described in the following the test position within the wake varies, because the outlet angle β_2 changes with Machnumbers M [12] .

2.3 Description of the Investigated Cascades

Ten different turbine cascades are investigated: 2 tip-section cascades, 5 mid-section cascades and 3 hub-section cascades. In figure 1 the profiles and the geometries of the cascades are shown. The two tip-section cascades consist of flat plates with different geometries, chord lengths and thicknesses. The first mid-section cascade, the profile of which is called M 1, is investigated in the original version (M 1A) and in addition with two different trailing edge thicknesses (M 1B and M 1C). In all three versions the blade contour is equal except for the fact that the profiles are shortened at the trailing edges. The profile M 1B has a trailing edge thickness, d, of 1.25 mm and the profile M 1C a trailing edge thickness, d, of 1.82 mm. Because of the shortening of the profiles M 1B and M 1C the stagger angle, γ, and the chord , c, of the cascades vary a little. The values are given in figure 1.

3. Experimental Results

3.1 Tip-Section Cascades

Figure 2 and 3 show the results for the two tip-section cascades, T 1 and T 2. The frequency, f, is plotted versus the downstream velocity, u, and the Strouhal number, St, versus the downstream Mach number, M. The Strouhal number is defined as

$$St = \frac{f \cdot d}{u} \qquad (1)$$

There are two different downstream test Mach numbers. The first one is the isentropic Mach number. The isentropic Mach number is used because wake flow measurements are not available for all flow conditions for which the vortex shedding is determined. The losses of the cascades are not included. The results are shown in the diagrams by + symbols. The second Mach number is based on the homogeneous flow conditions far downstream of the cascade. The evaluation of the homogeneous downstream flow is described in [13] . The results are given by o symbols. For the trailing edge thickness, d, a value twice the trailing edge radius is taken. This is a geometric value, not including the boundary layer displacement thickness, δ , as done for example in [14] .

The results for the profile T 1 show that the frequency, f, increases linearly with the downstream velocity, u, over the entire velocity range (figure 2a). It is remarkable that also for transonic and supersonic velocities vortices occur and the range of Strouhal number, St, is nearly the same as for a circular cylinder in incompressible flow (see [15] , figure 2. 9). The Reynolds number range based on the trailing edge thickness, d, for the measurements shown here is $0.3 \cdot 10^4 < Re_d < 1.6 \cdot 10^5$.

The results of the second flat plate cascade T 2 are shown in figure 3. The thickness of these blades is only one half of the thickness of the cascade blades T 1 Up to $u \sim 250$ m/s the frequency, f, increases again almost linearly (figure 3a), and the Strouhal number, St, is 0.2 (figure 3b). For higher Mach numbers the value of the Strouhal number is larger ($0.2 < St < 0.3$).

3.2 Mid-Section Cascades

In figure 4, 5 and 6 the results for the mid-section cascades M 1A, M 1B and M 1C are given. The trailing edge thickness of the blades of M 1A is $d = 0.45$ mm. This is the thinnest trailing edge investigated. Figure 4a shows that the frequency increases up to 160 kHz. The Strouhal number obtained for cascade M 1A (inlet angle $\beta_1 = 110^{\circ}$) is about 0.24 (figure 4b). In the case of M 1B two different inlet angles are investigated $\beta_1 = 90^{\circ}$ and 120°. It can be seen, that there is no significant influence of the different inlet angles on the results (figure 5). The diagram of the frequency, f, versus the velocity, u, shows again a linear dependence. The Strouhal number is about 0.35 (figure 5b). The results for the cascade M 1C with the thickest trailing edge ($d = 1.82$ mm) show lower shedding frequencies (figure 6a) but nearly the same Strouhal number (figure 6b) as obtained for the cascade M 1B (figure 5b).

In figure 7 the results for another mid-section cascade with a similar turning are given. The thickness of the trailing edge, $d = 0.75$ mm is again rather small. The maximum measured shedding frequency is about 100 kHz. The frequency shows again a linear dependence on u (figure 7a). The value of the Strouhal number increases up to the Mach number $M = 0.4$. For Mach numbers $M > 0.4$ the Strouhal number is constant ($St \sim 0.28$).

The results of the measurements for the third mid-section cascade M 3 are shown in figure 8. M 3 is the cascade with the smallest pitch/chord ratio, g/c. The turning is small, compared with the other mid-section cascades. The trailing edge is thicker ($d = 2.15$ mm) than for the cascades M 1 and M 2. The value of the Strouhal number is about 0.25 .

3.3 Hub-Section Cascades

The results of the three different hub-section turbine cascades are given in figures 9, 10 and 11. In the past, investigations of unsteady flow effects [16] and secondary flow effects [17] were already performed for the profile H 1. The results of the shedding frequency measurements are shown in figure 9. There is a sudden increase of the frequency, f, at $u \sim 300$ m/s, corresponding to an increase of the Strouhal number, St, at $M \sim 0.9$. In the case of lower velocities the Strouhal number is constant, $St \sim 0.23$. The trailing edge thickness of $d = 0.85$ mm is the smallest one investigated for the hub-section cascades.

In the case of the profile H 2 two different inlet angles $\beta_1 = 120^{\circ}$ and 140° are investigated. The frequencies shown in figure 10 are not influenced by the inlet angles. The increase of the frequency, f, with the downstream velocity, u, is linear again up to $u \sim 300$ m/s. The Strouhal number, St, decreases moderately with higher velocities (figure 10b) up to $M \sim 0.9$ and increases for Mach number $M > 0.9$. The value of the Strouhal number is $0.3 < St < 0.4$. The trailing edge thickness of $d = 3.1$ mm is comparatively large. Profiles of this type are used to eject coolant air from the trailing edges of the blades. The cascade H 2 is designed by the v.Karman Institut (VKI), Belgium [18]. It was proposed by the VKI to investigate this cascade in different cascade windtunnels for purpose of comparison. All the theoretical and experimental results of the DFVLR-AVA are given in [19].

Figure 11 shows the results of the third hub-section cascade (H 3). The value of the Strouhal number is about $St \sim 0.28$.

In figure 12 schlieren pictures are shown for the cascades T 1, M 3 and H 3. Photographs taken from all other cascades investigated here, which show the vortices in the wake flow, are published in [2, 7, 9].

4. Discussion of the Results

It was already mentioned that the Strouhal number in the case of the flat plate cascade T 1 is $St = 0.2$. This value is also obtained for a single flat plate with $d/c = 0.03$ and $d/c = 0.05$ [9]. The shedding frequency for the isolated flat plates was investigated for Mach numbers $M < 0.9$. Up to this Mach number range there is no difference in the Strouhal number between flat plate cascades and the isolated flat plate. The reason for this is, that a flat plate cascade of comparatively large pitch/chord ratio , g/c, behaves like a single flat plate. Proceeding to higher velocities a shock system appears behind the trailing edge as shown in figure 13 for cascade T 2. In this case it is useful to base the Strouhal number not on the geometric blade thickness, d, but on the wake height (d') at the position of the confluence (see figure 13). Using d' the Strouhal number for the cascade T 2 is reduced.

In [7] a schlieren picture of the same cascade and a similar flow condition is published. In the photograph the vortices are not visible. Nevertheless the vortex street exists as one can recognize on figure 13. Whether the vortex street is visualized depends on the position of the knife edge of the schlieren optical system and an extremely sensitive adjustment. Obviously the adjustment was not sufficient for the schlieren picture published in [7].

In [2] the question is considered on which velocity the Strouhal number should be based. In the case of cylinders [6, 20] and single airfoils [5, 9] the free stream velocity is used. In [2, 21] the trailing edge velocity obtained by surface pressure measurements is used for the computation of the Strouhal number. This velocity is interpreted as the mean value of the suction and pressure side velocity. Using this value it was expected to get equal Strouhal numbers for different cascades. Thus, Strouhal numbers are computed in this way for the ten cascades investigated here. However, equal Strouhal numbers could not be achieved. The results are, therefore, not shown.

5. Conclusion

The shedding frequency of the vortices of a v. Karman vortex street is determined with the aid of an electronic-optical method developed in the DFVLR-AVA. Ten turbine cascades of tip-section, mid-section and hub-section are investigated. The trailing edge thicknesses of the cascade blades vary between 0.8 and 5 % of the blades chord length. The downstream Mach number used for the computation of the Strouhal number is mainly in the range of $0.2 < M < 0.9$, but in the case of the two tip-section cascades also supersonic flow conditions were examined. The Strouhal numbers for all ten cascades lie within a range of $0.2 < St < 0.4$. The Reynolds number range is $0.3 \cdot 10^4 < Re_d < 1.6 \cdot 10^5$. The highest shedding frequency, which is obtained in the case of the thinnest trailing edge, is about 160 kHz. It is not possible to achieve constant Strouhal numbers for different cascades by using the velocity at the trailing edge instead of the downstream velocity.

6. List of References

[1] Langston, L. S.; Nice, M. L.; Hooper, R. M.
Three-Dimensional Flow within a Turbine Cascade Passage
ASME Paper No. 76-GT-50

[2] Lawaczeck, O.; Bütefisch, K. A.; Heinemann, H.-J.
Sillages Tourbillonnaires dans les Grilles d'Aubes de Turbines Subsoniques et Transsoniques
IUTAM Symposium sur l'Aéroélasticité dans les Turbomachines
Paris, 18.-23. Octobre 1976

[3] Blenk, H.; Fuchs, D.; Liebers, F.
Über Messungen von Wirbelfrequenzen
Luftfahrtforschung 12 (1935), p. 38-41

[4] Paterson, R. W.; Vogt, P. G.; Fink, M. R.; Munch, C.
Vortex Noise of Isolated Airfoils
J. Aircraft, Vol. 10, No. 5, May 1973

[5] Fathy, A.; Rashed, M. I.; Lumsdaine, E.
A Theoretical Investigation of Laminar Wakes behind Airfoils and the Resulting Noise Pattern
Journal of Sound and Vibration (1977), 50(1), p. 133-144

[6] Blevins, R. D.; Burton, T. E.
Fluid Forces Induced by Vortex Shedding
Journal of Fluids Engineering, March 1976, p. 19-24

[7] Lawaczeck, O.; Heinemann, H.-J.
Von Karman Vortex Streets in the Wakes of Subsonic and Transonic Cascades
AGARD-PEP-Meeting on Unsteady Phenomena in Turbomachinery
Sept. 1975 Monterey/Cal. / USA
AGARD-Conf. Proceedings, No. 177

[8] Lawaczeck, O.; Bütefisch, K. A.
Geplante Untersuchungen über v. Karmansche Wirbelstraßen als eine mögliche Ursache für das Entstehen des Buffet-Onset
DFVLR-Arbeitssitzung 'Probleme der experimentellen transsonischen Aerodynamik', Göttingen, 2.-3. Juni 1976

[9] Heinemann, H.-J.; Lawaczek, O.; Bütefisch, K. A.
Von Karman Vortices and their Frequency Determination in the Wakes of Profiles in the Sub- and Transonic Regimes
IUTAM Symposium Transsonicum II
8.-13. Sept. 1975, Göttingen
Editors: K. Oswatitsch and D. Rues,
Springer Verlag, Berlin/Heidelberg/New York (1976)

[10] Lawaczeck, O.
Der Prüfstand für ebene Schaufelgitter der Aerodynamischen Versuchsanstalt Göttingen
DFVLR-AVA-Bericht 70 A 46 (1970)

[11] Heinemann, H.-J.
Zum Stand der Untersuchungen an v. Karmanschen Wirbelstraßen in sub- und transsonischer Strömung
DFVLR-Arbeitssitzung 'Probleme der experimentellen transsonischen Aerodynamik', Göttingen, 2.-3. Juni 1976
DFVLR-AVA-Bericht 251 76 A 18 (1976)

[12] Lehthaus, F.
Flow Phenomena of Transonic Flow in Two-Dimensional Cascades
IUTAM Symposium Transsonicum II
8.-13. Sept. 1975, Göttingen
Editiors: K. Oswatitsch and D. Rues
Springer Verlag, Berlin/Heidelberg/New York (1976)

[13] Amecke, J.
Anwendung der transsonischen Ähnlichkeitsregel auf die Strömung durch ebene Schaufelgitter
VDI-Forschungsheft 540, S. 16-28 (1970)

[14] Bauer, A. B.
Vortex Shedding from Thin Flat Plates Parallel to the Free Stream
Journal of the Aerospace Sciences, April 1961, p. 340-341

[15] Schlichting, H.
Grenzschicht-Theorie
5. Auflage, 1965, Verlag G. Braun, Karlsruhe
see also: Boundary Layer Theory, 6ed. 1968, McGraw Hill, New York

[16] Lehthaus, F.
Transonic Flow in a Turbine Cascade with high Deflection (Colour-schlieren-film with high-speed-film passages)
DFVLR-AVA-Bericht 251 74 A 24
IIIrd Conference on Steam Turbines of Great Output, 24.-27. Sept. 1974, Gdansk/Poland,
Polska Akademia Nauk, Transactions of the Institute of Fluid-Flow Machinery, 70-72, Warszawa-Poznan (1976)

[17] Heinemann, H.-J.
Influence of Secondary Flow Effects on Blade Surface Pressure Measurements in 2-D Transonic Turbine Cascades
49th AGARD-PEP Specialists' Meeting on Secondary Flows in Turbomachines, 28.-30. March 1977, The Hague, Netherlands
AGARD-Conf. Preprints No. 214

[18] Chauvin, J.
Sieverding, C.
(Editors)
Transonic Flows in Turbomachinery
Lecture Series 59, Von Karman Institute, Brussels, Belgium, May 1972

[19] Lehthaus, F.
Anwendung eines Zeit-Schritt-Verfahrens zur Berechnung der transsonischen Durchströmung ebener Turbinengitter und experimentelle Überprüfung
DFVLR-AVA-Bericht 251 77 A 01 (1977)

[20] Fung, Y. C.
Fluctuating Lift and Drag Acting on a Cylinder in a Flow at Supercritical Reynolds Numbers
Journal of the Aerospace Science, November 1960, Vol. 27, No. 11, page 801-814

[21] Sieverding, C.
Unstead Flow Measurements in Straight Cascades
Communication de l'Institute de Thermique Appliquée de l'école polytechnique fédérale de Lausanne, No. 5
Proceedings of the Symposium 'Measuring Techniques in Transonic and Supersonic Cascades and Turbomachines', held in Lausanne, Switzerland, on November 18.-19., 1976
Editors: A. Bölcs and T. Fransson

List of Figures

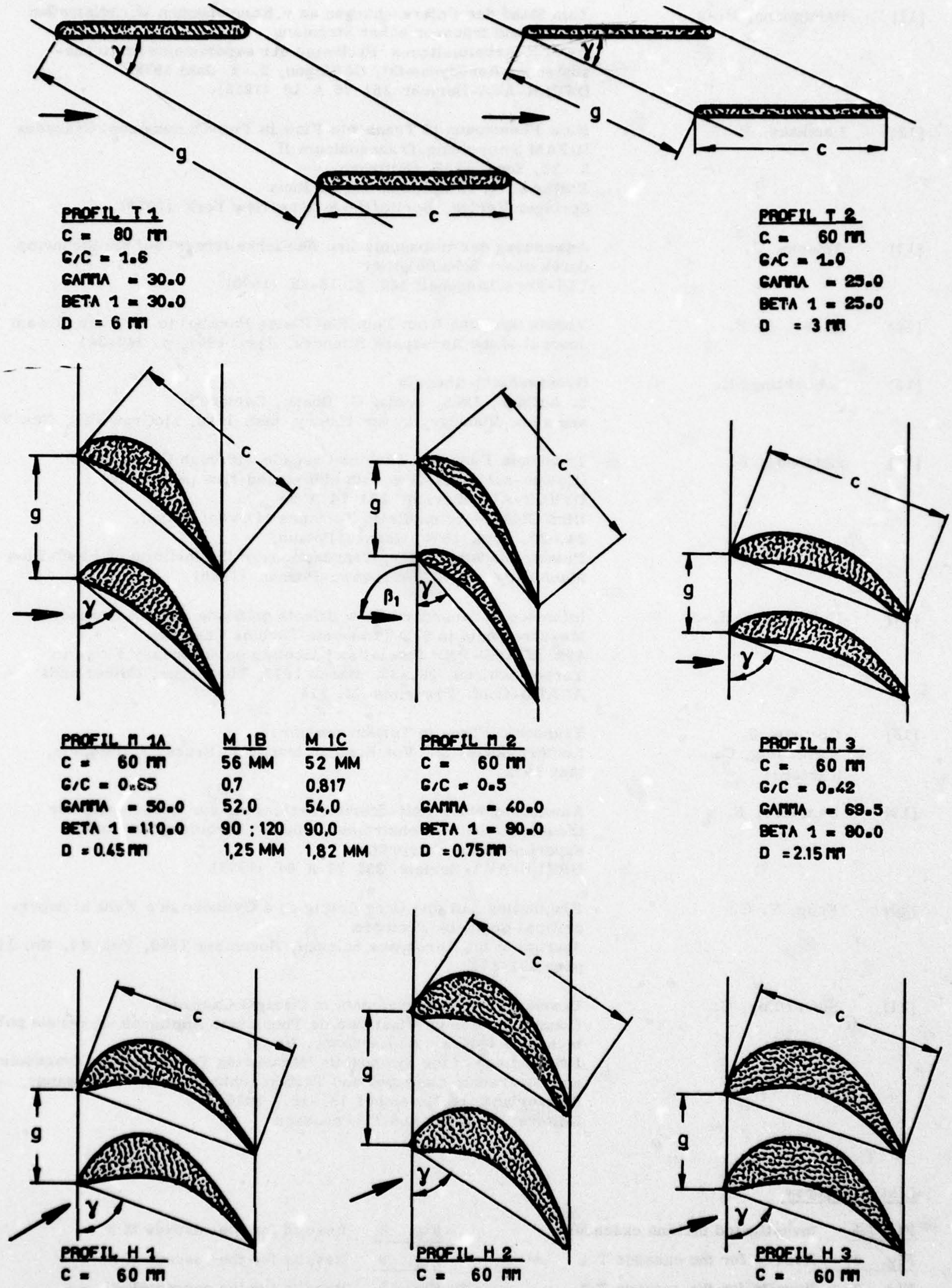

Figure 1: Investigated turbine cascades

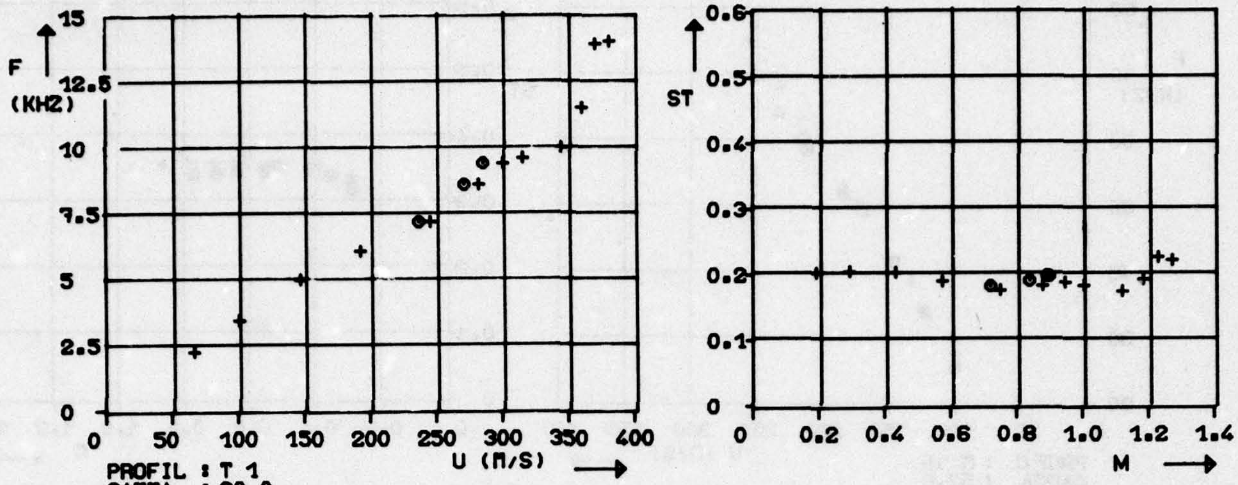

PROFIL : T 1
GAMMA : 30.0
G/C : 1.600
BETA 1 : 30.0
D : 6.10 MM

Figure 2a: Figure 2b:

Results for the cascade T 1

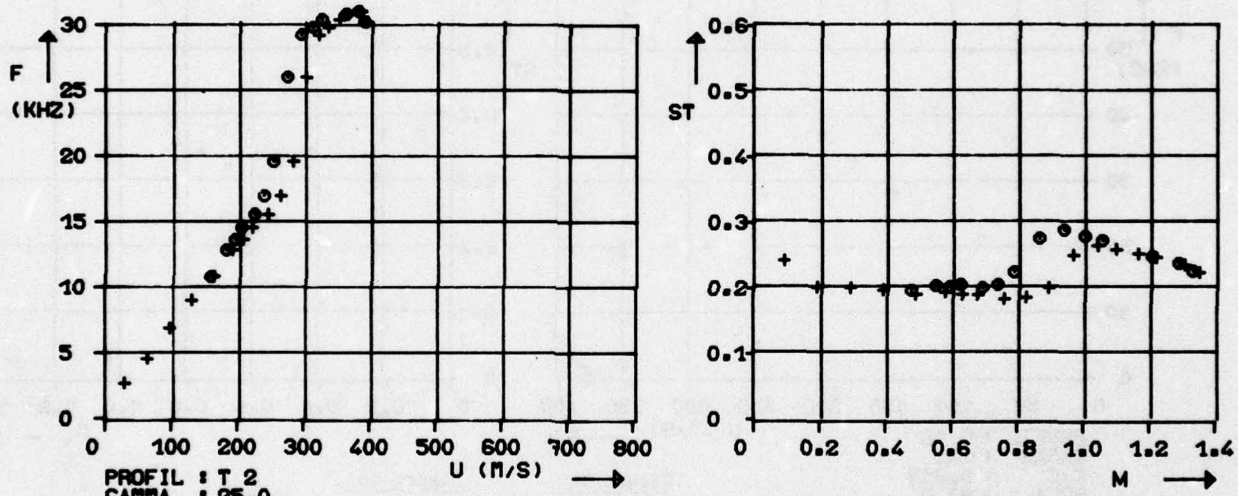

PROFIL : T 2
GAMMA : 25.0
G/C : 1.000
BETA 1 : 25.0
D : 3.00 MM

Figure 3a: Figure 3b:

Results for the cascade T 2

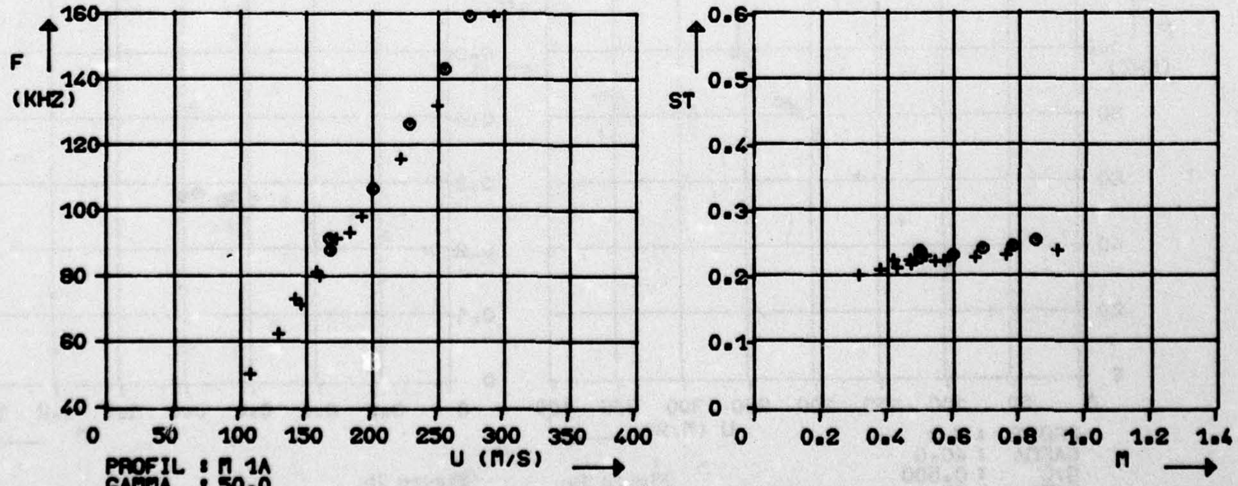

PROFIL : M 1A
GAMMA : 50.0
G/C : 0.650
BETA 1 : 110.0
D : 0.45 MM

Figure 4a: Figure 4b:

Results for the cascade M 1A

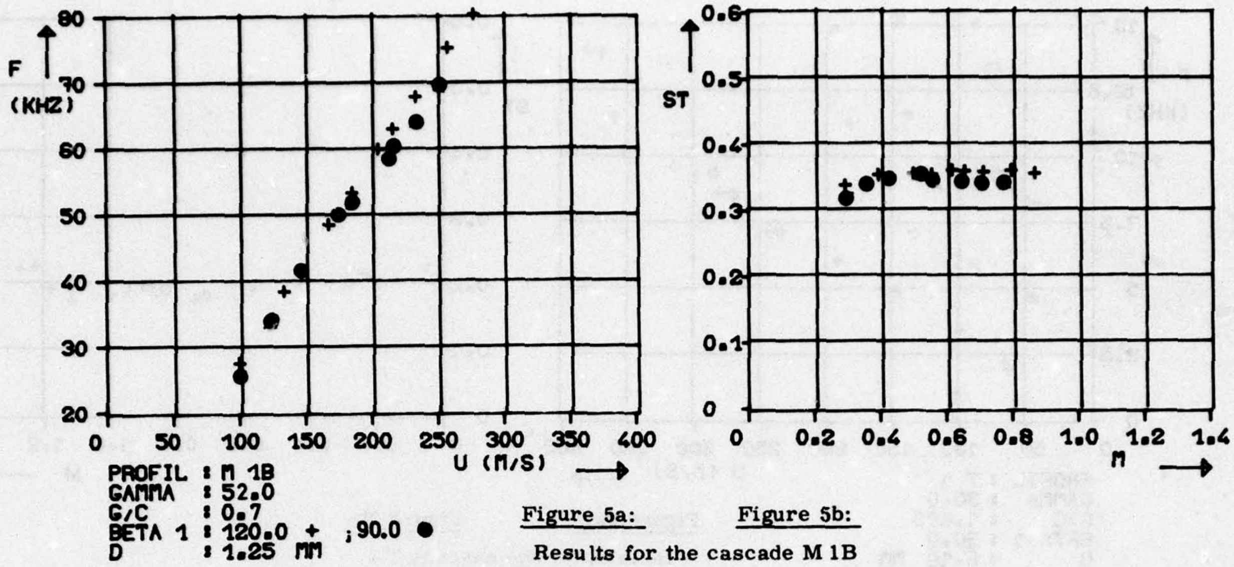

Figure 5a: **Figure 5b:**

Results for the cascade M 1B

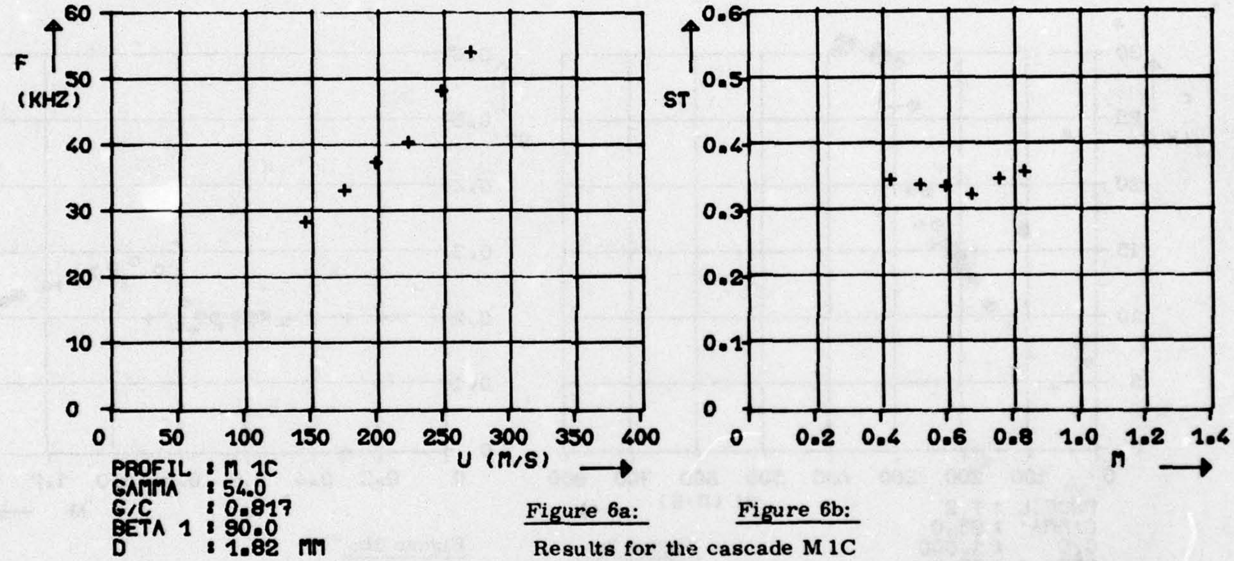

Figure 6a: **Figure 6b:**

Results for the cascade M 1C

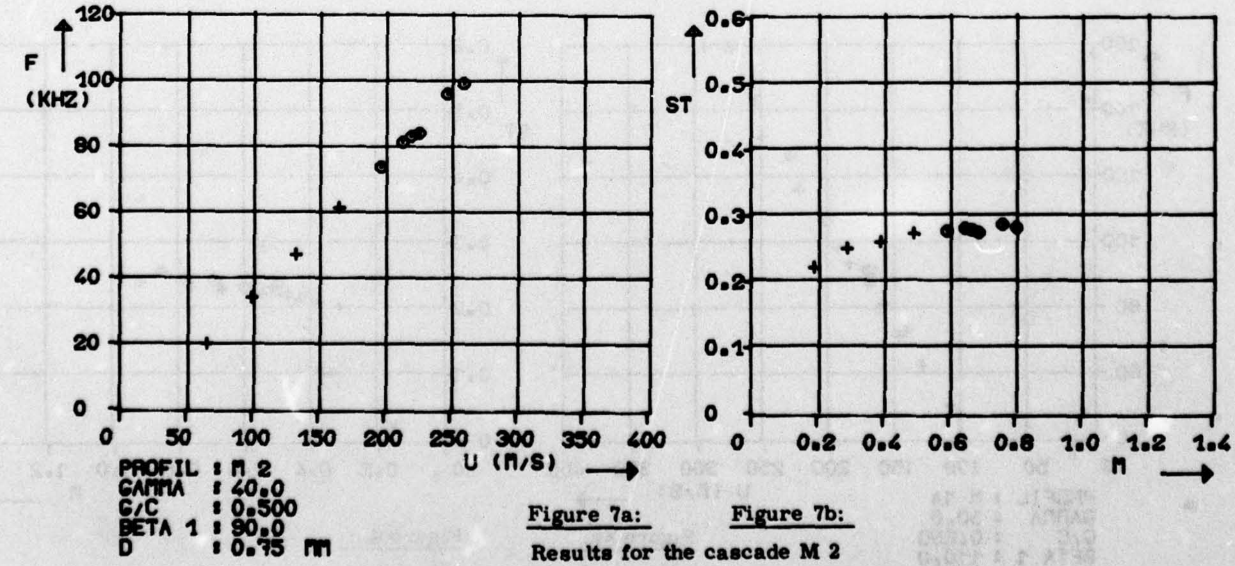

Figure 7a: **Figure 7b:**

Results for the cascade M 2

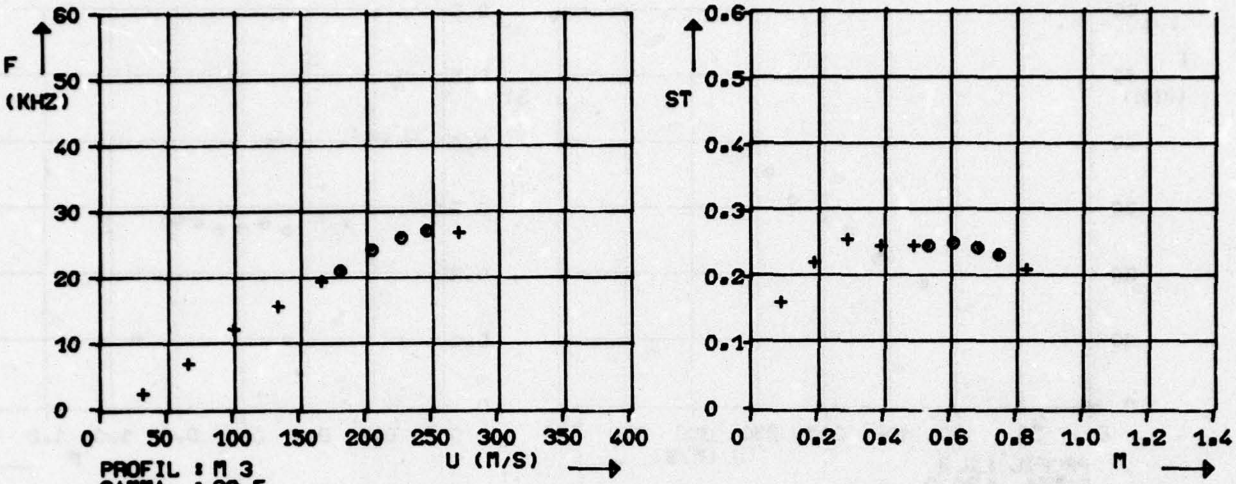

Figure 8a: Figure 8b:

Results for the cascade M 3

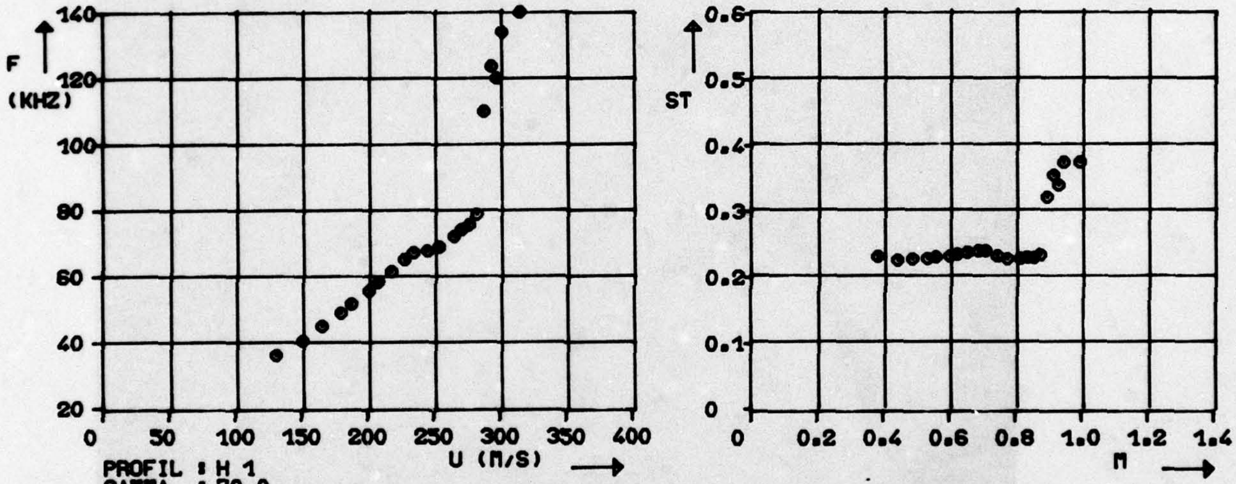

Figure 9a: Figure 9b:

Results for the cascade H 1

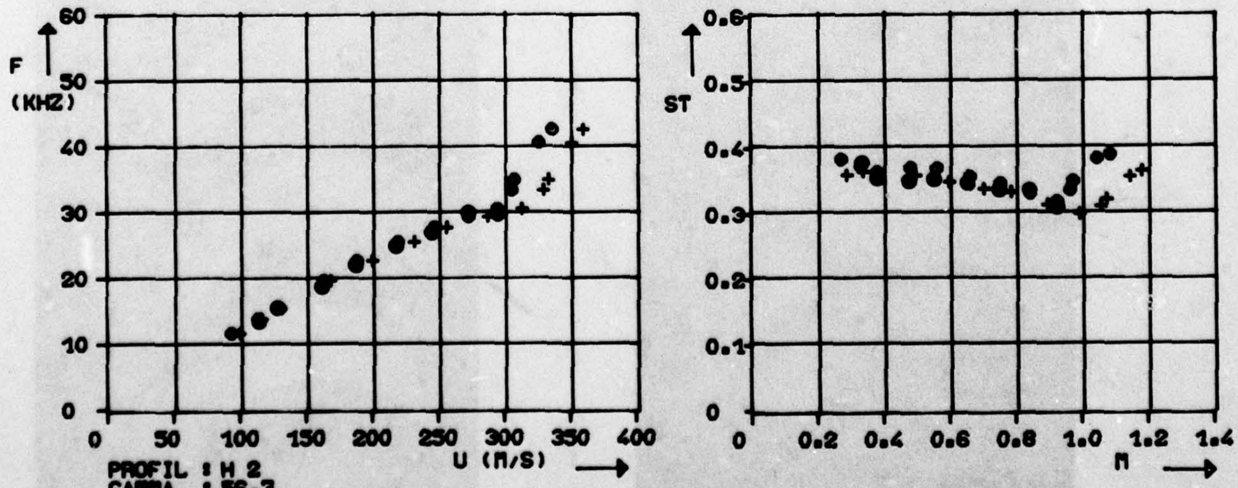

Figure 10a: Figure 10b:

Results for the cascade H 2

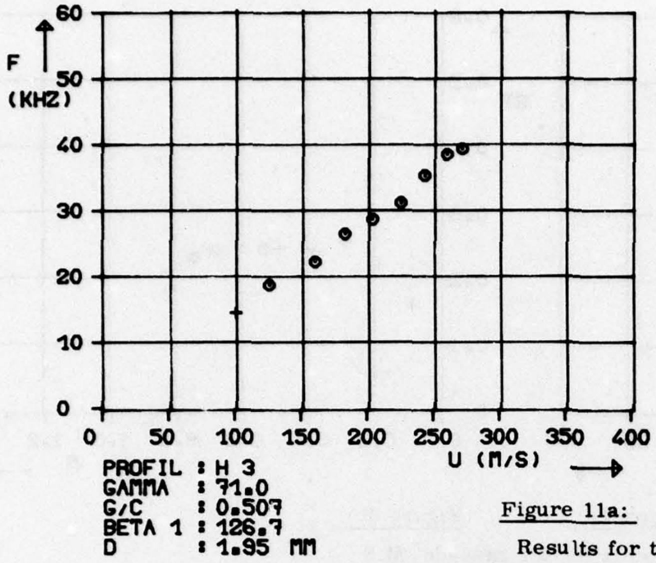

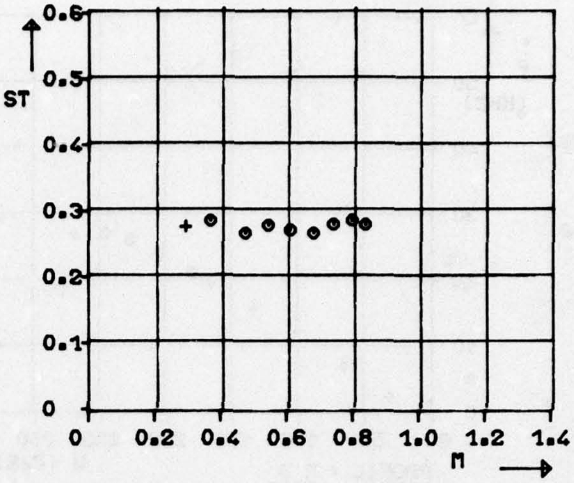

Figure 11a: Figure 11b:

Results for the cascade H 3

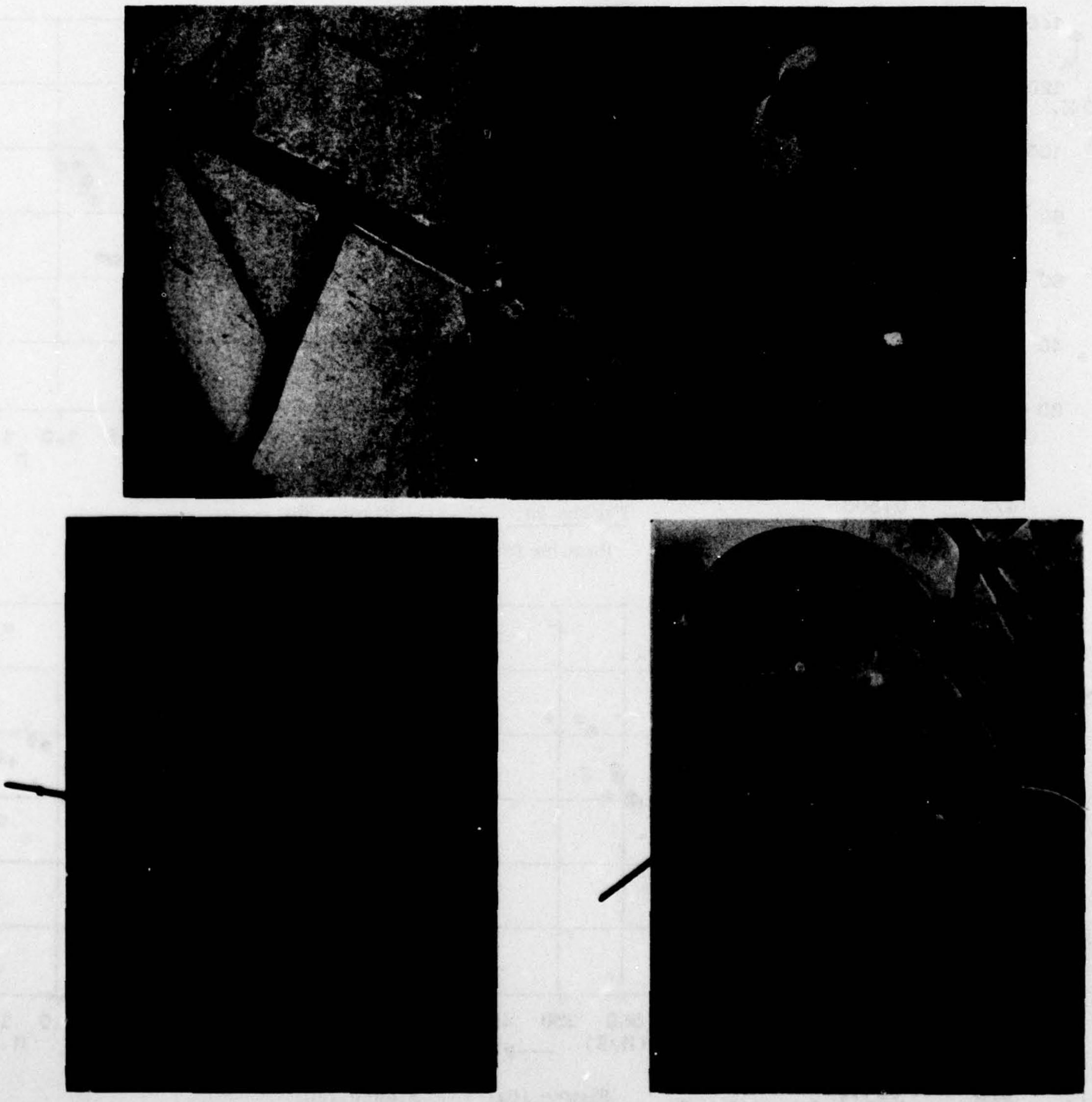

Figure 12: Schlieren pictures of the cascades T 1 , M 3 and H 3

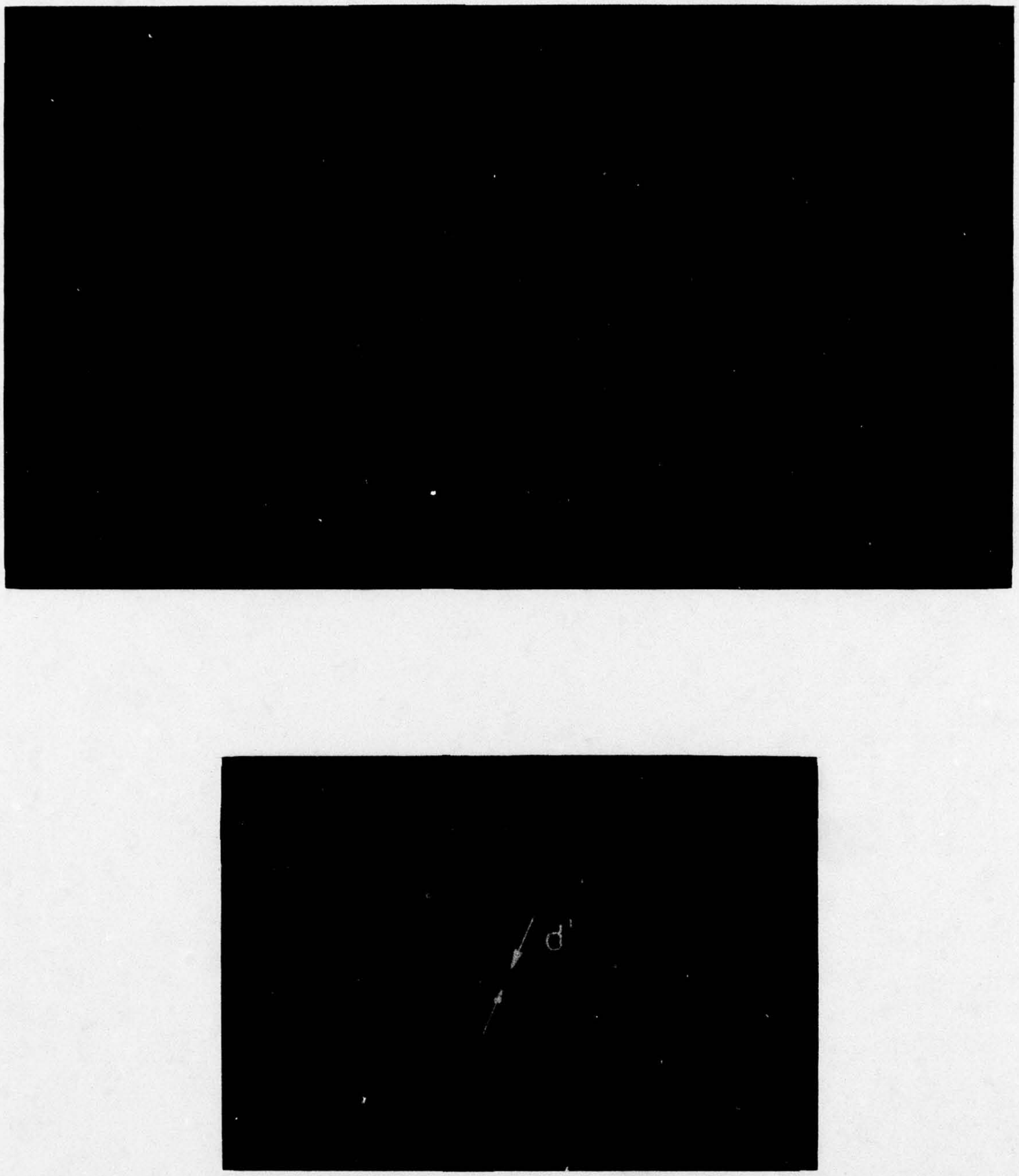

Figure 13: Schlieren picture of the cascades T 2

ROUND TABLE DISCUSSION

Chairman, Prof. Young

Ladies and Gentlemen, we have come to the final stage of this meeting, and I think that most people are feeling rather overwhelmed with all they have heard. Perhaps we should try to make this session short and bright. I have asked up here with me the people who can offer informed comments on the various sections of the meeting. On my left is Prof. Telionis. On my immediate right is Dr. McCroskey. On his right is Mr. Garner, and on his right Dr. Tijdeman. What I would like to do is to ask each of them in turn to talk about the area with which they are most concerned, and to discuss very briefly what they think are the main points that they feel have arisen from the appropriate session or sessions and where they think future research activities should be directed. At each stage I shall be glad to have you get up and offer your comments on the points that are made. I should tell you that this particular session is being recorded, so if you get up and say anything, would you please give your name and affiliation, so that you can be suitably credited with your remarks when the final recorded version comes to be printed. I will start off by inviting Mr. Garner to say a few words about his impressions on the subject of Session 1, which was unsteady subsonic and supersonic flow, where the emphasis was on inviscid flow solutions.

Mr. Garner

I am very conscious that I am deputizing for Prof. Ashley and not fully qualified to do so. However, I will go through the eight papers in that session, trying to be as provocative as I can. Provocative means calling forth, and I hope to call forth discussion.

In the opening paper the field was admirably reviewed by Prof. Holt Ashley. In conclusion he reiterated that linearized theory was in danger of over-refinement and voiced his dream of a unified methodology of computational fluid dynamics. I would also call attention to the appeal in his written paper for careful measurements of pressures and other field variables in unsteady flows. The theoretician must check all aspects of his solutions. Dr. Tijdeman has rightly emphasized that linearization in unsteady perturbations may often suffice for the overall quantities needed in practical application. Nevertheless, while theories are still being developed, the details of solutions must receive thorough appraisal. Now I come to Prof. Kandil's paper in which he describes a new treatment of delta wings in steady and unsteady asymmetric flows with leading-edge separations. In such flows the leading-edge vortices are the dominant feature and a rather special one. It is important, therefore, that the treatment is applicable to general planform. Nevertheless, I wonder whether further investigation is needed to deal with swept wings having attached flow over the inner portion of the span and part-span vortices over the outer portion, also with flows where the separation is intermittent, and with swept wings having non-zero tip chord and edge forces that influence the yawing moment. Prof. Morino's SOUSSA lends a touch of reality to Prof. Ashley's dream. The version of SOUSSA after February 1978 will be eagerly awaited, with its facilities for a complex aircraft configuration with rolled-up vortex wake, with shock-free mixed flow and 85 % time reduction on the current version. If all this is achieved, the name will need to be expanded! I would suggest, however, that there is scope for replacing uniformly loaded planar panels by ones with continuity in loading and curvature at their edges.

In Dr. Patel's paper the 'old hat' aerodynamics of linearized theory gets a considerable lift from experimental results in a gust tunnel. The theoretical man conveniently builds his gust from the figment of an elementary sinusoidal gust. Dr. Patel has turned figment into reality, and by combining sinusoidal gusts of different wavelength in a low-speed wind tunnel he has vindicated the principle of superposition upon which the theoretical treatment relies. In this respect, full reassurance would demand a reduction of the wavelength in the experiments by an order of magnitude to, say, one chord length.

In the written paper by Dr. Geissler, his subsonic panel method has been applied and compared with experiment for a thin swept wing with oscillating flaps, for a pitching body of revolution and for an oscillating thick rectangular wing with zero and non-zero mean lift. I hope that the final version will include the improved calculations in this last case when the boundary layer is taken into account. Thus encouraged, is Dr. Geissler now able to turn his attention to the wing-body combination?

Perhaps the generality of Prof. Das' treatment of the disturbances propagated from moving sources, dipoles and quadrupoles will encourage the realization of Prof. Ashley's dream! Some basic distinctions have been made between subsonic and supersonic streams and between the characteristics of near-field and far-field disturbance potentials. A topic for discussion would be how to turn this academic 'tour de force' to practical use. I wonder if Prof. Morino would be able to say whether any features of Prof. Das' analysis would enhance SOUSSA.

I come now to Mr. Bosch's paper which provides an interesting analytical demonstration of the substantial equal and opposite streamwise forces on interacting aerofoils in potential flow. In unsteady flow it is reassuring to find that a stationary trailing plate calms the energy losses in the wake of an oscillating aerofoil. One can envisage the efficiency of transporting felled timber on the Ottawa River. An intriguing application of the study, we are told, is to traffic in muddy canals, but surely this is of no interest in Ottawa itself!

In his paper, Dr. Roos has explained how combined theoretical and experimental studies have tamed the problem of wing-store interference. Should the theoretical prediction be doubted, there are confirmatory pressure measurements in the wind tunnel. Should there be lingering doubts about pressure measurements by the scanning-valve technique, one can turn to the validation of the theory against model flutter tests with and without stores. Should wall interference be a source of worry, then there is encouraging confirmation of the flutter predictions from free flight.

In conclusion I return to Prof. Ashley's paper and his remark that AGARD Report 643 on interfering surfaces is already becoming out of date. In the light of an accumulation of fresh theoretical evidence and Mr. Angelini's illustration (Paper 27, Fig. 3) of discrepancies between theory and experiment for coplanar tandem surfaces, we can surely see scope for some reappraisal.

Prof. Young

Thank you very much. Perhaps some of you would like to reply or add to these comments of Mr. Garner. No, in that case I will ask Dr. Tijdeman to comment on the particular area which I know he is concerned with, unsteady transonic flow.

Dr. Tijdeman

In fact, the session on unsteady transonic flow covered a number of subjects. Four papers dealt with oscillating airfoils and wings. Further there was an ad hoc investigation on the flow in a two-dimensional diffuser, and a paper about the influence of noise.

Talking about oscillating airfoils, it can be concluded that considerable progress is made in two-dimensional flow computation. This was demonstrated for instance, by Dr. Yoshihara and his associates, who easily generated various types of unsteady pressure distributions on an airfoil with both leading and trailing edge flap. While watching their film, I got the impression that it was nice entertainment, but that in the examples shown, no real problems were solved. I would like to ask the authors to focus their attention to the questions that the aeroelastic specialists are struggling with, namely, the generation of unsteady transonic aerodynamic loads in a form which is suitable for practical application in aeroelastic calculations.

The paper of Prof. Seebass et al. on a technique to include shock waves in unsteady aerodynamic calculations was very interesting. The extension of the idea of "shock matching" to three-dimensional finite-difference methods for transonic flow do require an enormous amount of computer time and therefore are still far from practical.

The experimental investigations performed by ONERA (Grenon and Thers) are very useful. A variety of different flow conditions has been studied. I would like to ask the authors whether it is possible to release the contour data of the airfoil investigated, since it certainly will be an attractive example for the theoreticians to verify calculation methods.

The remaining papers in the session on unsteady transonic flow are somewhat difficult to judge for me, since I do not know much about flows in diffusers or noise problems. I got the impression that Dr. Sajben et al. did a good job to improve the understanding of the physical phenomena in transonic diffuser flow and that the extensive investigation of Mr. Vaucheret is a valuable contribution in judging the effect of noise in wind tunnel experiments.

Prof. Young

Are there any comments that anybody would like to make on this area?

M. Grenon

Pour les coordonnées de ce profil, il faudrait prendre contact avec l'Aerospatiale qui a dessiné ce profil. C'est tout ce que je peux vous dire pour le moment.

Dr. McCroskey

In fact, it would be useful to have the coordinates and also the numerical tabulations of these data because as you say, it is an area for which the theoreticians, particularly the numerical analysts, are crying for data. This is a set which I presume was done carefully enough to be considered worthy in this way.

Prof. Young

Would anyone like to comment on the problem of what was called the transonic dip, particularly in connection with supercritical wings?

Prof. Bergh

Concerning the influence of supercritical properties on the flutter behavior, I think many aeroelasticians put the question too academic by comparing flutter speeds of two identical wings, only different in aerodynamic possibilities, the one being conventional, the other supercritical. Of course, then you have an indication of the difference in flutter behavior of these two types of airfoils, but in practice, the situation is different. If you will develop an airplane with a supercritical wing, the question is how do you take advantage of the typical supercritical properties? For instance, if you keep the Mach number identical, but you use less sweep or a thicker wing having higher torsion rigidity, then the answer may be that the supercritical wing is less critical for flutter than the conventional one. Another possibility is that you make use of the supercritical properties by taking a higher aspect ratio. Then you are extending the beam in such a way that it may become critical again from a flutter standpoint.

Mr. Garner

On the question of the effect on flutter as you enter the supercritical regime, there is the consideration that your aerodynamic center moves aft for a considerable range of incidence once the supercritical flow is established. At least, that is what one calculates, and I think sometimes what one measures. If that is so, the tendency is beneficial towards flutter. However, I have expressed a warning that one should be careful not to rely on the increased flutter speeds that one might calculate using inviscid flow theory.

Prof. Young

Shall we now pass on then to the third section, namely, unsteady, non-separated and separated boundary layers. Here I would like to ask Prof. Telionis to comment.

Prof. Telionis

I would like to refrain from taking one by one the papers presented here and commenting upon them; instead, I would rather offer some general comments. I will start first with unsteady separation, which is my dear topic. I will try to be as honest and down to earth as possible. The reason I start with this is because I then intend to pass the ball to someone else in this room, when we come to unsteady turbulent boundary layers. For a long time, so I was told, before I started getting involved in this research 10 years ago, unsteady separation was a big and important problem. I now observe, that some investigators have ceased to be interested in this area. After all, the people who work with the full Navier-Stokes equations simply say, "who cares? my streamlines and my vorticity lines give me all I need to know, I do not even need to define unsteady separation". This is a good point. Next, we would like to see this group extend their theories to larger Reynold's numbers, and maybe we will not need to know anything more. The fact remains, that in a realistic fluid flow, we are going to have turbulence in thin boundary layers that cover our aerodynamic surfaces, we are going to have attached and free shear layers and the phenomenon whereby the fluid ceases to follow the contour of the body and turns sharply, I do not know how sharply, into the flow. I think that this phenomenon will still be called separation and what follows downstream of it, wake. However, I also feel that these past few years, important evidence became available, that makes us readjust our understanding of what is a wake. I always liked to believe that the point of separation marks the initiation of the wake. This is where the wake begins. Separation and wake are therefore intimately linked. I felt that there was no doubt that a wake ought to be a region of the flow where the velocities are very, very small. It used to be called dead air or dead water. It is definitely erratic in its motion and contains large scale turbulence. I believe that we may have to reconsider our understanding, because, at least in unsteady aerodynamics, we have seen in many pictures of large-Reynolds-number flow visualizations, a very well organized vortical motion which is definitely unsteady. This is nothing, for example, but the vortex generated at the leading edge which you have seen in Dr. Metha's and Dr. Wu's beautiful results. It is also there, in the flow visualizations of stalling airfoils of Dr. Carr, McCroskey and their associates. I may add that we have seen in our experiment a classical slow-moving turbulent wake suddenly being "energized", getting a lot of energy from somewhere, somehow, and suddenly taking the entity of a vortex. The problem is whether, even in this case, separation could be the magical point where somehow the energy from the free flow is channeled, through viscosity, into this vortical motion, which is moving and changing its size and shape and breaking down to other vortices. This much I would have to say about separation.

Now I will go on to unsteady laminar and mostly turbulent boundary layers. I would like to tell you that yesterday was an excruciating day for most of the people who have been related to this problem, because we had a very, very long but fruitful session from 7 until 11:30 in the evening. During this session we talked about the experimental needs and the way the theoreticians should follow. We have heard many opinions with regard to the experimental data. The opinion was expressed that we probably have enough information already to start improving theoretical models, that would at least provide us with engineering estimates. However, some people suggested that it is necessary, if we really want to understand the mechanism and the real physics of the phenomenon, to collect even more data and especially with regard to the statistics of an unsteady turbulent boundary layer. In fact, all the experimentalists were urged to try to get more accurate data. Specifically, it was suggested that the experimentalist should keep in mind that the theoretician who attempts to calculate the same flow field, will also need very accurate initial and boundary data. Of course, we would need to have data for turbulent boundary layers over a flat plate, with adverse or favorable pressure gradients and turbulent boundary layers that separate. With regard to the attempts of improving the theoretical models, again different opinions were suggested. One group felt that as far as the engineering applications of the immediate future are concerned, it would be perhaps quite satisfactory to go ahead with approximate empirical models (after all, they are all empirical). It would be quite satisfactory to come up with an integral method, for example, that would really give us some quick answers. The opposite opinion was also expressed. Most of all, it was agreed that the efforts internationally, or at least in the western world, ought to be somehow organized and, at least, the minimum we could do would be to try to collect in a unified way all the existing experimental data and try to standardize it. The place was decided to be Ames, California. Now I will pass the ball to Dr. Carr, who organized yesterday's meeting, led the discussion and volunteered to run a "data bank".

Dr. Carr

Prof. Telionis has covered quite well what went on in our two-hour session last night. The essence of our conclusions is that we have done much in terms of theoretical prediction, without having much experimental data to back this up or test the theories. At this point, we are hoping that experimental work will be done accurately and with the specific intent of identifying the minimum set of information that could test the theories. For example, measurements of velocity profiles should be made before separation, where we can make measurements accurately and know that they can be satisfactorily documented. These profiles can then be given to the theoreticians as test cases.

Prof. Young

Would anyone else who was present at the gathering last night like to comment on the discussion?

Dr. Patel

We have heard some excellent contributions to the science of separated flows. Going off on a slightly different tack, however, in progressing towards the refinement of theoretical models for tackling the unsteady separation problem, would it not be advisable to concentrate first on obtaining "reasonable" agreement between these models and experiment for attached unsteady turbulent boundary layers over a variety of flow conditions? More experimental data are obviously necessary for this to be possible and the work of Cousteix and his co-workers is a step in the right direction. I feel that there is some way to go before theoretical models can adequately predict the attached unsteady turbulent boundary layer. Once this is done, however, the separation problem in unsteady flow can be considered with a more complete understanding of the flow field preceding it.

Prof. Young

I wonder if there is any intention when calling on people to provide data to issue some written guidance as to the sort of data that you think would be most helpful.

Dr. Patel

We discussed it adequately last night, and perhaps Prof. Telionis or Dr. Carr would like to continue that.

Dr. Carr

We are not yet in a position to say what the "complete" set of data would be like. However, reviewing what we discussed last night, the point that Dr. Patel has made was excellent. We should look at the flow ahead of the separating region. For example, we should fully document the flow field for an attached unsteady boundary layer with a strong pressure gradient so that there is a very clear indication that you are imposing unsteady flow conditions on an attached boundary layer, rather than in the region of flow reversal. The minimum level of documentation would be velocity profiles, the next level of detail may be measurement of turbulent spectra. For a long time the question of measuring turbulent spectra was thought of as almost passé. I think that at this point it might be a subject to be reconsidered. We do not have a written set of guidelines at this time, but we hope to be able to give such guidance in the future.

Prof. Young

Prof. Bogdonoff, I was waiting for your comments.

Prof. Bogdonoff

I come to this meeting from quite a different background, so my comments have a certain perspective, but also reflect some ignorance about the detailed problems. Let me discuss the questions of boundary layers, which I know a little bit about. There are currently many people who are working on turbulent boundary layers, and turbulent boundary layer separation in high speed flows. Many of the comments which came up in this meeting are similar to comments that have been made in other fields.

There are a couple of general views that I would like to express: First; I was glad to hear that the group last night decided that you need more experiments. I was overwhelmed, and very much impressed, by what this group was able to do with computational techniques. I would like to express a great deal of skepticism with regard to whether there is any connection whatsoever between what many people are calculating and the real world. There is, as has been pointed out by Mr. Carr, a lack of experimental results to show that the computations match real flows. Your field, as with other fields, is going to have to determine some guidelines or guideposts, i.e., some critical well-defined, experiments which tell you whether any of the computational methods are correct. The check of one computational method against another, at least to me, lends no validity to the truth of the final result. Second: A very personal observation which has something to do with the fact that, for the last couple of years my own group has been involved in three-dimensional flows, after some 30 years of work on two-dimensional flows. I say, with a great deal of feeling at this point, that I am not sure that much of the work which I did over the past 30 years makes a lot of sense in real applications. The work is being used as a base to check computational programs. It has been used in many applications, but our work over the last 3 or 4 years in the three-dimensional flows has opened up completely new fields. My background in two-dimensional flows has been a hindrance, not a help. At least, in many of the things that we have looked at recently, starting with a well understood two-dimensional flow, does not prepare you for many aspects of three-dimensional flows.

I would like to suggest that there is perhaps a philosophical question that ought to be considered. Many people have done two-dimensional work and are going to do it better and better and better. I hear that all we need is a turbulence model. I doubt whether anything unique is going to happen in turbulence modelling in the next several years. Many computational people seem to feel that you simply do it better and better, with a finer grid, and a bigger computer, and more memory, and faster. Then we will add a turbulence model. I would suggest that perhaps a more productive view might be not to get into finer detail for two-dimensions, but very crudely try to do three-dimensions. If there is any parallel at all between your boundary layers and my boundary layers, and I think that they come from the same place, I believe you will find all sorts of new things - not new in that they have been there all the time, we just have not really looked at them - in three-dimensions. I really hope that some of you will consider this.

In our own field, we have found three-dimensional shock wave boundary layer interactions which are completely different than anything that we thought about before we started making these experiments. I hear you talking about two-dimensional vortices, but you know that there is no such "animal". Vortices are going to drive you mad!! They are not two-dimensional, and you will not find out about what they do to you until you look in three-dimensions. I hope that you will not wait until you get the two-dimensional problems completely solved, but will start now to look at three dimensions. I think the real problems are there, and it is clearly the real world.

Prof. Young

Thank you very much. Those were very stimulating remarks which I am sure we will all think about.

Dr. Tijdeman

Watching the session of unsteady boundary layers, I got a little bit confused about the way the methods have to be used in applications to oscillating airfoils. In my review on unsteady transonic flows, I mentioned the important effect of the boundary layer on the airloads of oscillating airfoils and stressed the need for some knowledge to increase the accuracy of the theoretical predictions by implementation of unsteady boundary layers. As far as I know the only approach that works at this moment is the so-called "viscous-ramp" method presented by Dr. Yoshihara. I would like to ask him what he needs for that type of calculation and whether he has got some new ideas about the way in which the effect of the boundary layer can be introduced after the sessions on unsteady boundary layers presented during this meeting.

Dr. Yoshihara

The viscous ramp concept was conceived to bypass the need of detailed boundary layer measurements. It requires only measurements of surface pressure distributions, but such measurements must be free of wind tunnel wall interference. The viscous displacement modeling is then accomplished by a numerical computation by using the above measured pressure distributions. On a longer time scale, the experimentalist could be very helpful by developing information to evolve even the crudest of turbulent transport models applicable for shock-induced separations.

Prof. Young

We should now pass on to the next session, which is a major one of viscous inviscid interactions and includes the dynamic stall. Here I would like to ask Dr. McCroskey to offer his comments. He is one of our best experts on this area.

Dr. McCroskey

I will make a few brief comments on this session, and if I have time and can think of the right words before the end, I will see if I can refute my former Professor about the two-dimensional assumptions. You will recall that the last paper in our regular session was by Mr. Panaras of Greece, with a spike in front of the body. I cannot comment a great deal on the ultimate utility and significance of that paper, but it struck me as a most interesting investigation that will find a useful place in some parts of the engineering community.

The paper by Mr. Dyment included both the high speed flow visualization and some discrete vortex modelling of blunt bodies. The latter is an area which has been worked on for a long time and is far from totally resolved. It seems to me that in this subject of what you might call vortex shedding from bluff bodies, that the real crux of whether or not a method is going to ultimately be correct and useful to engineers, is whether it can correctly predict the side forces, the unsteady lift. Unfortunately, that aspect is seldom examined when an analysis is first published, and such was the case here.

M. Angelini touched on one aspect of the problem of aeroelasticity, the retreating blade stall problem on helicopter blades, and that leads me into the discussion of the remaining papers. You recall M. Philippe's excellent review that gave you a good impression of the dynamic two-dimensional approximation to the aerodynamic loads on a helicopter blade. In the real world there are certainly three-dimensional effects which are sometimes important and sometimes appear to be not so important. We think we have identified this vortex shedding phenomenon as being responsible for the large change in the unsteady pitching moment, which translates into vibrations in the control system of the rotor. This can be explained pretty well with the two-dimensional model. However, in the actual rotor application, there is a portion of the rotor disc, after the flow is fully separated, in which the three-dimensional effects are, in fact, quite important. In this case the (nominally) two-dimensional tests do not seem to give the right aerodynamic forces.

I would like to return now to the papers which discuss various aspects of separation on oscillating airfoils. Dr. Ericsson spoke about, among other things, Reynolds number effects in these kinds of unsteady situations. He addressed what I would call the high end of the Reynolds number spectrum, from about one million on up, corresponding to many of the practical applications. We find in the papers here, that with all these other unsteady parameters we have to contend with, Reynolds number may be rather important. New results were shown for relatively low Reynolds numbers from the point of view of applications, but for rather high Reynolds numbers from the point of view of the computational community. There were three papers on laminar Navier-Stokes calculations, with Re of order 10^3 to 10^4. The two experimental papers were for Reynolds numbers of the order of 10^5 or so. In his review, M. Philippe showed that the general qualitative features of the vortex shedding look very similar at Re = 5000 and at 1.5 million. But when you look at the hysteresis loops of the aerodynamic forces and moments as a function of the incidence, they are much more different than I had hoped, when I first encouraged these laminar Navier-Stokes calculations.

Regardless of their practical utility for high Reynolds numbers, we are still left with the question of how to validate these Navier-Stokes codes. Dr. Mehta mentioned the possible contamination of the low-Reynolds number experiment by turbulence. We were fortunate to have three authors calculate the same problem, the impulsively-started airfoil at a Reynolds number of 1000, calculated by three different codes. The agreement was stated to be satisfactory. However, Mehta's and Wu's calculations appear to be diverging at large times. Mehta's and Kinney's calculations differed by about 10 % in lift coefficient and by about the same numerical value in pitching moment, but the percentage discrepancy in C_M was quite a bit more. After going through this, I feel that the codes are probably basically correct, but they are really not fully validated. The question is where to go next and how much emphasis to put on continuing these kinds of calculations. I really do not know what recommendation to make at this point.

There are three-dimensional effects, and other things that were not mentioned in this session, such as the difference between pitching and plunging motion. I mentioned briefly, in connection with the paper by Rebont and Maresca this morning, the importance to the engineer of the unsteady drag.

In terms of trying to get practical information out of all of these basic studies of dynamic stall, as well as the unsteady boundary layer work, someone needs to determine how the boundary-layer vorticity, i.e., the surface-generated vorticity, feeds this vortex shedding phenomenon that seems to be responsible for the unusual aerodynamic forces. From a fundamental point of view, that is a very important question, but it is also crucial to the development of good engineering analyses. There is a great need for further empirical correlations, but that approach will always be marginal until we have a better theoretical understanding of this general flow problem.

Prof. Young

Does anyone want to comment or add to these last remarks?

Dr. Peake

This is not directly relevant to your remarks, but perhaps I could address a question to Prof. Telionis. Would he expect that his unsteady flow separation model would have any relevance in three dimensions?

Prof. Telionis

Yes.

Dr. Peake

Why and how?

Prof. Telionis

I would rather avoid answering your question directly, because I am not sure what I want to put forward just now. I ended my discussion on this topic, by saying that we may need to find a way in which energy is transferred into a clearcut unsteady vortex. I say clearcut, because wakes are usually made up of a large number of vortices whose size and strength are random quantities. To tell you the truth, I am amazed with the fact that those nice recirculating flows can exist in flows with very large Reynolds numbers. I feel that maybe there is still a lot of information contained in the boundary layer that could tell us something about the mechanism of this phenomenon. We should be able to find out, what portion of the free flow which is coming on, is going to be entrapped in the growing vortex and become wake. I think this happens through the boundary layer. There is no doubt that it is due to the presence of the skin. This is not an inviscid flow phenomenon. You asked me about our model. There has never been any particular model proposed by our group. The only thing that we tried to put forward was that first of all, zero-skin friction has nothing to do with separation in general. Experimental justification followed our numerical analysis. Then our main argument was that the first-order unsteady boundary layer contains the information that something peculiar is happening as separation is approached. As such, we have interpreted the fact that the boundary layer is thickening, some properties grow suddenly very large; perhaps in an orderly way, like with the inverse square root of the distance from separation. I do not want to say that it is exactly the Goldstein singularity. All I am saying is that the boundary layer equation, the unsteady or steady, if correctly integrated, could probably tell us that something is going to happen, and that the outer flow will finally be forced to cease following the contour of the body. Does this answer your question?

Dr. Peake

Not really. I am going to throw it over to Jim McCroskey. Perhaps I could ask him very briefly how much of the rotor, for example, on the typical helicopter, would he feel he could allow his two-dimensional representation of the flow field to be a reasonable model. Then could he say what changes to the models that we really have been seeing all through this meeting, would he expect to happen as he went out towards the tip? What does the spanwise bleeding effect in the viscous flow do to the situation?

Dr. McCroskey

It is difficult to address in a few words the helicopter rotor, but there are large segments of the rotor blade which are neither transonic nor separated, on which fluctuating aerodynamic forces act. Apart from some uncertainty about the trailing vorticity and the wake problem, the airloads in these segments can be predicted rather well. However, severe problems occur in those narrow zones that are transonic or that have separation. As I was saying a moment ago, the early stages of the onset of stall on rotor blades appear to be roughly analogous to this nominally two-dimensional oscillating airfoil business that we have been doing. But after the primary vortex passes off the trailing edge, there is strong evidence that the three-dimensional aspect of the flow becomes very important, and that the aerodynamic loads are no longer the same as the two-dimensional results.

I have been talking in rather large-scale, gross engineering terms. What I had hoped to address to your initial question was something a bit different, as follows: One of the characteristic features that we observe in the analyses, in the computational experiments, and in a few experiments with limited separated regions, is a basic difference between steady and unsteady two-dimensional boundary layers. This difference is the appearance of the thin layer of reversed flow near the surface before any catastrophic breakdown of the main flow field. With the exception of leading edge laminar bubbles, there are not many examples of such behavior in two-dimensional steady flows. But it is a characteristic feature that often precedes large-scale turbulent separation in real flows and it is distinctly different in the unsteady and the steady case. We have identified this phenomenon within the framework of two-dimensional ideas. I feel that something analogous will be carrying over into three dimensions, but we do not know very much about that problem at all. Just as three-dimensional steady separation is quite different in practice from two-dimensional, I suspect that three-dimensional unsteady separation will have some more hidden features that we have not looked at. Nevertheless, the utility of what has been done so far is to tell you in your three-dimensional problems to look for this thin layer of reversed flow beneath a well-organized outer boundary layer flow, something that is not found in a steady boundary layer.

Dr. Ericsson

I would like to emphasize Prof. Bogdonoff's point. There is no such thing as two-dimensional or axisymmetric separated flow. One finds, for example, that there is a spanwise (or axial) flow component in the wake of a (two-dimensional) cylinder, and that this is necessary for unsteady Karman type vortex shedding to exist. Restricting this spanwise (or axial) flow exchange by the use of side plates stops the Karman vortex shedding, as was shown mathematically and experimentally by Theisen in the Fifth AIAA Aerospace Sciences Meeting, Jan. 1967 (AIAA Paper No. 67-34). Moss and Murdin (ARC CP No. 1145,1971) and Gregory, et al. (ARC CP No. 1146,1971) found similar large spanwise flow effects on the dynamic stall of a NACA-0012 airfoil. McCroskey, et al. found in their oscillatory dynamic stall test that this spanwise flow influence was present unless they increased the frequency above k = 0.2, when it effectively was filtered out (AIAA Paper No. 75-125). Furthermore, to emphasize Peake's comment, I believe strongly that there is a spanwise flow influence. I thought I saw data presented yesterday showing that even a moderate sweep, like 35° or 25°, gave widely different dynamic stall loops than those measured at zero sweep. Finally, if you consider a highly swept wing, such as the delta wing, you find that the effect of leading edge roundness on the unsteady aerodynamic characteristics is largely accounted for if one considers the effect of roundness to delay the static stall if the crossflow plane normal to the leading edge (AIAA Paper No. 76-19). This is in sharp contrast to the two-dimensional case, where leading edge roundness can provide as much as 100 % "extra" dynamic overshoot of static $c_{\ell MAX}$. For the delta wing it appears that a strong three-dimensional organization of the flow dominates over these two-dimensional dynamic effects in the crossflow plane. I think that the comments made earlier by Prof. Bogdonoff and Dr. Peake are very, very pertinent. We need to look further into these three-dimensional flow complications. There is no such thing as two-dimensional separated flow.

Prof. Young

There is time for another comment, but I do not want to get into another discussion going to half past eleven tonight, because I do not think many of you will survive it.

Mr. Dixon

We are also studying the leading edge vortex flow with a viscous model, a Navier-Stokes model, a hybrid model which includes potential flow for boundary conditions and a boundary layer for leading edge vorticity and direction to feed into the Navier-Stokes model. We have found that the position and strength of the leading edge vortex, is highly a function of the strength of the leading edge vorticity and its direction as it comes off the leading edge. Of course, this depends on the shape of the leading edge. I would also like to make another comment about two papers today concerning the oscillating airfoil in the horizontal plane; one in which the wind tunnel flow was oscillating, and one in which the model was oscillating. The one where the wind tunnel was oscillating, the pressure was also oscillating. I have a question. Is that really a good simulation of free-stream conditions?

Prof. Young

I think perhaps I might comment on that particular point. Clearly, the situation when you have the model oscillating is different in a number of respects from that where you have the flow oscillating. But when you come to an actual aircraft, you might have both types of motion involved or either, so we really want to know something about what happens in both cases. When an aircraft is flying in gusts, of course, it is the airflow that is moving, so to speak, whereas for flutter problems, you are more particularly concerned with the aeroelastic effects and therefore with the motion of the aircraft. I do not think that one can say that one is correct and the other is incorrect. They are both inputs toward the general problem.

Mr. Dixon

What I was referring to was the oscillating pressure. You do not have oscillating pressure in flight conditions. In a tunnel where you are oscillating the wind tunnel velocity you do have oscillating static pressure. I wonder what effect that has.

Prof. Young

Oscillating static pressure, by this do you mean the main stream pressure? I do not know that the situation there is really any different from flying into a gust, is it?

Dr. Patel

If I may just make a comment on that; during work related to paper No. 4 on the gust tunnel studies of forces on a rectangular and swept wing, I looked at this question of the static pressure varying. The static pressure would, in fact, vary for any test section which has an oscillating device that restricts the flow in order to alter the wind velocity periodically. In these cases, there is nothing that can be done to alleviate the effects of the oscillating static pressure. For the gust tunnel work described in paper No. 4, the static pressure in the flow remains constant. The vertical velocity gust oscillations are induced by the tunnel flow streamlines which are altered in shape as they are approaching the models.

Prof. Young

I think perhaps that the time has come to wind up these proceedings. If I may be allowed one comment on this question that Dave Peake raised which threatened to start off a completely new session, it seems to me that it is a very difficult problem to define in a precise way what we mean by separation in general. Insofar as it involves the diffusion of vorticity into the mainstream flow at a certain stage, whether in two dimensions or three, it also implies a very radical change in the flow pattern and a change in the energy of the flow. The separated flow has a good deal of inertia, and if you start trying to move it around by oscillating the body or by oscillating the stream, you must expect that its response is going to be less marked and more sluggish, because of its inertia, than the flow in the attached boundary layer. To this extent it seems to me, that the kind of picture that Prof. Telionis has put forward, and which we have seen demonstrated in many experiments in two-dimensions is valid in general. (I will put the two-dimensions in inverted commas if you like.)

Dr. Peake

I think I would agree with that, but I understood Prof. Telionis to say that one of the characteristic distinctive features of the flow fields that he has seen, has been this reversal of the layer very close to the wall prior to or perhaps as providing the signal that "things are really happening in an unsteady two-dimensional separation fashion". What my query would be is, would the spanwise effect of flow in the third dimension just remove this particular reverse flow or would it not?

Prof. Young

I would expect it to have much the same effect whether it is in two dimensions or three. However, I think perhaps we ought to close these proceedings, and it is my pleasant task at this late hour to thank all of my colleagues on the program committee for their help in organizing this meeting, and to thank all the lecturers who gave us their presentations through these three rather full days. In particular, I would like to thank my fellow colleagues of this Round Table Discussion for their final inputs into the meeting. Again, thank you all for coming.

Mr. Hartzuiker

From the movement in the room and the noise, I am quite sure you are eager to go out, but I can not let you go yet. I think, from my own experience, it is well known that a tremendous amount of preparation goes into a symposium like this. It is a lot of time and effort and from that point of view I think we should thank Prof. Young for what he has done as Chairman of the Program Committee for this symposium. Furthermore, I would like to thank the local coordinator for this meeting, Mr. Markham and his "assistant" Dr. Orlik-Rückemann, for what they have done locally. I am quite sure that without their efforts this meeting would not have been possible. I would like to thank the interpreters. I am quite sure that without their excellent contributions we would not have had the success we have had. Thank you very much. After also thanking the technicians who recorded the final Round Table Discussion, I think I can close off this meeting. I hope it has been inspiring to you. If there is any possibility that the Fluid Dynamics Panel could help you in the future or if you have suggestions, please contact us. Thank you very much.

REPORT DOCUMENTATION PAGE

1. Recipient's Reference	**2. Originator's Reference** AGARD-CP-227	**3. Further Reference** ISBN 92-835-0212-4	**4. Security Classification of Document** UNCLASSIFIED

5. Originator
Advisory Group for Aerospace Research and Development
North Atlantic Treaty Organization
7 rue Ancelle, 92200 Neuilly sur Seine, France

6. Title
UNSTEADY AERODYNAMICS

7. Presented at
the Fluid Dynamics Panel Symposium held at the Government Conference Centre, Ottawa, Canada, 26–28 September, 1977.

8. Author(s) Various	**9. Date** February 1978
10. Author's Address Various	**11. Pages** 624

12. Distribution Statement
This document is distributed in accordance with AGARD policies and regulations, which are outlined on the Outside Back Covers of all AGARD publications.

13. Keywords/Descriptors

Unsteady flow
Turbulent boundary layer
Critical flow
Numerical analysis
Aeroelasticity
Stalling
Transonic flow
Supersonic flow

14. Abstract

The Symposium identified the need for carefully conceived experimental unsteady flow data, particularly for both unseparated and separated two- and three-dimensional turbulent boundary layers. Detailed, accurate measurements of critical flow parameters was encouraged. It was agreed that linearized theories of unsteady inviscid flows provided a useful basis for many engineering applications, particularly in the early design stages of aircraft, but for more reliable calculations in the transonic and supersonic regimes the emphasis should be on development of non-linear numerical methods. Transonic numerical codes are increasingly efficient but their validity and accuracy needs assessment. Future calculations should include boundary layer effects even if no shock-wave interaction is included. The importance of Reynolds number on the dynamic stall was indicated. It was advised that serious consideration should be given to the development of a manual aeroelasticity for turbo-machines. An important factor in determining the characteristics of a rotor blade is the interaction of the blade with vortices shed by other blades. Research is required on the nature of this interaction and its effect on the dynamic stall of the blade.

AGARD Conference Proceedings No.227
Advisory Group for Aerospace Research and Development, NATO
UNSTEADY AERODYNAMICS
Published February 1978
624 pages

The Symposium identified the need for carefully conceived experimental unsteady flow data, particularly for both unseparated and separated two- and three-dimensional turbulent boundary layers. Detailed, accurate measurements of critical flow parameters was encouraged. It was agreed that linearized theories of unsteady inviscid flows provided a useful basis for many engineering applications, particularly in the early design stages of aircraft, but for more reliable calculations in

P.T.O.

AGARD-CP-227

Unsteady flow
Turbulent boundary layer
Critical flow
Numerical analysis
Aeroelasticity
Stalling
Transonic flow
Supersonic flow

AGARD Conference Proceedings No.227
Advisory Group for Aerospace Research and Development, NATO
UNSTEADY AERODYNAMICS
Published February 1978
624 pages

The Symposium identified the need for carefully conceived experimental unsteady flow data, particularly for both unseparated and separated two- and three-dimensional turbulent boundary layers. Detailed, accurate measurements of critical flow parameters was encouraged. It was agreed that linearized theories of unsteady inviscid flows provided a useful basis for many engineering applications, particularly in the early design stages of aircraft, but for more reliable calculations in

P.T.O.

AGARD-CP-227

Unsteady flow
Turbulent boundary layer
Critical flow
Numerical analysis
Aeroelasticity
Stalling
Transonic flow
Supersonic flow

AGARD Conference Proceedings No.227
Advisory Group for Aerospace Research and Development, NATO
UNSTEADY AERODYNAMICS
Published February 1978
624 pages

The Symposium identified the need for carefully conceived experimental unsteady flow data, particularly for both unseparated and separated two- and three-dimensional turbulent boundary layers. Detailed, accurate measurements of critical flow parameters was encouraged. It was agreed that linearized theories of unsteady inviscid flows provided a useful basis for many engineering applications, particularly in the early design stages of aircraft, but for more reliable calculations in

P.T.O.

AGARD-CP-227

Unsteady flow
Turbulent boundary layer
Critical flow
Numerical analysis
Aeroelasticity
Stalling
Transonic flow
Supersonic flow

AGARD Conference Proceedings No.227
Advisory Group for Aerospace Research and Development, NATO
UNSTEADY AERODYNAMICS
Published February 1978
624 pages

The Symposium identified the need for carefully conceived experimental unsteady flow data, particularly for both unseparated and separated two- and three-dimensional turbulent boundary layers. Detailed, accurate measurements of critical flow parameters was encouraged. It was agreed that linearized theories of unsteady inviscid flows provided a useful basis for many engineering applications, particularly in the early design stages of aircraft, but for more reliable calculations in

P.T.O.

AGARD-CP-227

Unsteady flow
Turbulent boundary layer
Critical flow
Numerical analysis
Aeroelasticity
Stalling
Transonic flow
Supersonic flow

the transonic and supersonic regimes the emphasis should be on development of non-linear numerical methods. Transonic numerical codes are increasingly efficient but their validity and accuracy needs assessment. Future calculations should include boundary layer effects even if no shock-wave interaction is included. The importance of Reynolds number on the dynamic stall was indicated. It was advised that serious consideration should be given to the development of a manual of aeroelasticity for turbo-machines. An important factor in determining the characteristics of a rotor blade is the interaction of the blade with vortices shed by other blades. Research is required on the nature of this interaction and its effect on the dynamic stall of the blade.

Papers presented at the Fluid Dynamics Panel Symposium held at the Government Conference Centre, Ottawa, Canada, 26–28 September, 1977.

ISBN 92-835-0212-4

the transonic and supersonic regimes the emphasis should be on development of non-linear numerical methods. Transonic numerical codes are increasingly efficient but their validity and accuracy needs assessment. Future calculations should include boundary layer effects even if no shock-wave interaction is included. The importance of Reynolds number on the dynamic stall was indicated. It was advised that serious consideration should be given to the development of a manual of aeroelasticity for turbo-machines. An important factor in determining the characteristics of a rotor blade is the interaction of the blade with vortices shed by other blades. Research is required on the nature of this interaction and its effect on the dynamic stall of the blade.

Papers presented at the Fluid Dynamics Panel Symposium held at the Government Conference Centre, Ottawa, Canada, 26–28 September, 1977.

ISBN 92-835-0212-4

the transonic and supersonic regimes the emphasis should be on development of non-linear numerical methods. Transonic numerical codes are increasingly efficient but their validity and accuracy needs assessment. Future calculations should include boundary layer effects even if no shock-wave interaction is included. The importance of Reynolds number on the dynamic stall was indicated. It was advised that serious consideration should be given to the development of a manual of aeroelasticity for turbo-machines. An important factor in determining the characteristics of a rotor blade is the interaction of the blade with vortices shed by other blades. Research is required on the nature of this interaction and its effect on the dynamic stall of the blade.

Papers presented at the Fluid Dynamics Panel Symposium held at the Government Conference Centre, Ottawa, Canada, 26–28 September, 1977.

ISBN 92-835-0212-4

the transonic and supersonic regimes the emphasis should be on development of non-linear numerical methods. Transonic numerical codes are increasingly efficient but their validity and accuracy needs assessment. Future calculations should include boundary layer effects even if no shock-wave interaction is included. The importance of Reynolds number on the dynamic stall was indicated. It was advised that serious consideration should be given to the development of a manual of aeroelasticity for turbo-machines. An important factor in determining the characteristics of a rotor blade is the interaction of the blade with vortices shed by other blades. Research is required on the nature of this interaction and its effect on the dynamic stall of the blade.

Papers presented at the Fluid Dynamics Panel Symposium held at the Government Conference Centre, Ottawa, Canada, 26–28 September, 1977.

ISBN 92-835-0212-4